Springer Series in Optical Sciences 209

Michael Bukshtab

Photometry, Radiometry, and Measurements of Optical Losses

Second Edition

Springer

Springer Series in Optical Sciences

Volume 209

Springer Series in Optical Sciences is led by Editor-in-Chief William T. Rhodes, Georgia Institute of Technology, USA, and provides an expanding selection of research monographs in all major areas of optics:

- lasers and quantum optics
- ultrafast phenomena
- optical spectroscopy techniques
- optoelectronics
- information optics
- applied laser technology
- industrial applications and
- other topics of contemporary interest.

With this broad coverage of topics the series is useful to research scientists and engineers who need up-to-date reference books.

More information about this series at http://www.springer.com/series/624

Michael Bukshtab

Photometry, Radiometry, and Measurements of Optical Losses

Second Edition

Springer

Michael Bukshtab
Optoelectronics Research Centre
University of Southampton
Southampton
UK

ISSN 0342-4111 ISSN 1556-1534 (electronic)
Springer Series in Optical Sciences
ISBN 978-981-10-7744-9 ISBN 978-981-10-7745-6 (eBook)
https://doi.org/10.1007/978-981-10-7745-6

Library of Congress Control Number: 2017962029

This Springer imprint is published by the registered company Springer Nature Singapore Pte Ltd.
The registered company address is: 152 Beach Road, #21-01/04 Gateway East, Singapore 189721, Singapore

Preface to the Second Edition

The second edition of the book "Applied Photometry, Radiometry, and Measurements of Optical Losses" includes a vast majority of material published in its first edition in 2012, while also expanding and extending some of its sections. Due to continuous enhancement of measurement techniques and methodologies, this edition adds Chap. 12 on the Spectroscopic Interferometry, including FTIR, Brillouin Scattering, Frequency Comb, Terahertz Spectroscopies, plus upgrades paragraph 6.4 with techniques for Enhancement of Sensitivity and Mitigation of Fluorescence in Raman Scattering. These additions could be seen as broadening the scope of the book somewhat beyond commonly assigned subject areas of photometric and radiometric studies and expanding measurement techniques into far-infrared and even terahertz spectral regions, overlapping with spectral interferometry, biomedical and biotech sensing, and more; although such developments, while enhancing techniques and methods of laser spectroscopy, exemplify essential broadening of spectroradiometric methodologies via lasers or newer sources or detectors of optical radiation.

I wish to express my sincere appreciation to all readers of the first edition of this book, and, especially, to Jonathan Barletta for pointing out to an erroneous typo in Eqs. (2.1)–(2.3). I sincerely appreciate the curtesy of David Wright for thoroughly reviewing sections of the newly written Chap. 12 of the 2nd edition and am grateful to Mikhail Smirnov for helpful suggestions.

This edition is dedicated to my dearest and ever caring mother, to my dear brother and to Alla and Roberta, to my lovely daughter and to Pierre, and to my two loveliest granddaughters Anastasia and Laetitia, and also to the memory of Avrush Shwartsman.

Cranbury, CT, USA and Southampton, England — Michael Bukshtab

Preface to the First Edition

The broad variety of technical challenges has attracted the lasting attention of optical scientists and engineers to develop sensitive and accurate optical measurements – such as creating pure colors and making efficient laser systems or sensors. This interest resulted in the appearance of diverse measurement methods and technologies, often claiming unprecedented and even contradicting results, with the individual attention focused on achieving either high specular reflectance, direct transmittance, low absorptance, scattering, birefringence, or phase dispersion. Increased usage of lasers and pulse-modulated light sources intensified the interest – as a result, an orientation dilemma exists. Publications on the subject (see [0.1–0.47]) describe contrasting methods of measurements or implementations, and the methods can often appear to be different in terms of physical principles and realization conditions, but, at first sight, may remain almost indistinguishable from the standpoint of the accuracy and sensitivity achieved.

In this book, the analysis of measurement methods and techniques is given not only by the totality of light sources, detectors, and recording systems, but rather by detailed classification of the measurements performed and by the optimized conditions for the recognition of the optical property examined, by the objects and the aims of the study, by the boundaries of applicability, by advantages and shortcomings, and by the measurement methods, appropriate devices, and the examination systems themselves. The main considerations are given to measurements of the optical properties of highly reflecting mirrors for laser resonators and high-resolution interferometers, transparent optical crystals, glasses, and fibers, and the materials for their fabrication. Substantial features for studying weakly absorbing liquids and gases, including air pollutions, are examined as well. In spite of the existence of a fairly ample literature on radiometry and light measurements, even the conventional material is revisited from the point of executing the methods of photometric and radiometric measurements. Analyzed techniques are separated by determination of the parameters and extents of radiation and the optical properties of bodies and substances in that radiation. Special attention is given to approaches involving laser radiation. The high spectral density of laser light and the broad dynamics of modern photodetectors permit one to perform experiments

which are incompatible with routine radiometric and photometric methodologies, reaching sensitivity or accuracy unattainable with conventional approaches. At the same time, high spatial and temporal coherence, and sometimes unavoidable instabilities of laser radiation, complicate the measurement processes. This book provides an analysis of and solutions to the various measurement situations and describes ways to design some nontrivial equipment.

The sequence adopted for the analysis in the second part of the book reflects development processes for the advanced low optical loss measurement technologies – from the conventional spectrophotometric methods, reaching up to 10^{-3}–10^{-5} cm^{-1} sensitivity, to modern techniques, sensing losses down to 10^{-6} cm^{-1} and lower. Certain advanced methods may not necessarily lead to increasing sensitivity for a given study of optical loss and the accuracy of detection, while the increased diversity of optical-examination techniques being developed could be caused by the difficulties in detecting changes of optical characteristics at levels of thousandths and millionths of the measured extents. The challenges are enhanced by dependencies of measured optical losses not only on the properties of analyzed objects, but also on specific measurement conditions, such as light wavelength, its angle of incidence and state of polarization, viewing and irradiation conditions, etc. At high exposure to laser light, the expected outcome can be influenced by the power extents of an incident beam of such laser radiation. The results of measurements may also be dependent on the spatial configuration used to study sample surfaces and localization of the light beam itself. Any desirable increase of measurement accuracy, achieved by some decrease of locality, could make informativity higher only by way of not resolving thus concealed nonuniformity of the object being studied.

Traditional photometric methods do not possess extremely high sensitivity without special measures being taken, but they allow one to obtain information about the characteristics of an object under study as a whole by a direct measurement. Application of laser light with low divergence and high power density enables spatial and spectral selectivity of conventional measurements, thus expanding the prospects of low-loss detection. Exceptionally, high sensitivity to the bulk or surface absorption may be realized by focusing a laser beam into the object being studied, while registering changes of the object's temperature, its index of refraction, or noticing laser-induced birefringence. Under certain conditions, the process of stimulated emission of light is characterized by high sensitivity to selective optical losses introduced into a laser resonator, but it could be obstructed even by low-reflecting surfaces of the object being studied. Furthermore, the tasks of identifying absolute optical losses remain challenging and may require added comparisons with known standards.

Consequently, this book starts by deriving the main radiometric and photometric laws, definitions, and assumptions, and analyzing apparently simple methodologies, followed by more complex and sensitive optical techniques, while highlighting, within the bounds of every method, the exact features of each measurement procedure. The methods for low-loss detection – from interferometric, calorimetric, resonator, polarization, phase-shift and ring-down decay, wavelength- and frequency-modulation to pulse-separation, resonant, multipass, emissive, and

colorimetric ones – are analyzed and compared for the applicability of studying free-space and polarization optics, fibers, and waveguides. Ultimately, the content returns to the direct laser and spectroradiometric methods, but executed with the knowledge sequentially accumulated by experience of precision optical measurements. Every section of the book is completed with a description of the major results obtained by the most characteristic experiments.

Acknowledgements from the First Edition

I express my sincere gratitude and appreciation to all the people who helped in this vast book journey: my family and my lovely daughter, every teacher, friend, and colleague – overseas and in the USA – whose support and encouragement made the quarter-century-long project possible. Let me also thank those who, one way or another, opposed that effort – without certain resistance, my commitment could have lacked some willpower to overcome challenges along the way. Special thanks to my distinguished colleagues Prof. Leonid Glebov of CREOL and Dr. Kent Rochford of NIST Boulder Laboratories for supporting the proposal for this book with Springer, to Prof. H. Weber of Berlin Technical University for helpful suggestions and remarks, to Robert Nicolet and Kevin Viteri, to the language editor of the book manuscript and to members of editorial staff of Springer Science. Let me also extend my appreciation to libraries and librarians – The Library of the Russian Academy of Sciences (BAN), the libraries of Case Western Reserve University and Massachusetts Institute of Technology, and Westport Public Library, as well as to The Optical Society for its Optics InfoBase as my main reference source.

I dedicate this work to the memory of my teacher and doctorate adviser Andrei A. Wolkenstein.

Cranbury Village, Connecticut Michael Bukshtab

Abstract

This book provides an expansion into the radiometric and photometric approach to physical optics for measuring the energy and power extents of optical radiation, while exploring diverse, but not necessarily photometric, measurement techniques for examining the optical properties of the mediums, bodies, and substances using light. The major objective of that effort is to review all the accumulated knowledge and the essence of optical methods and techniques expanded within photometry and radiometry of quasi-monochromatic continuous, pulsed, spontaneous, coherent, and laser radiation, as well as of polychromatic light by analyzing up-to-date methodologies and metrology for the detection of ultra-low optical losses in various objects, materials, and elements, and comparing the majority of relevant measurement equipment. Conceptually, the initial thoughts of the analysis emphasized here were developed for two previous books: Measurements of Low Optical Losses, published by Energoatomizdat in Leningrad (now St. Petersburg) in 1988, and Photometry and Radiometry for Engineers, written in close cooperation with A. A. Wolkenstein and A. S. Doynikov, the publication of which was announced by Polytechnika (Mashinostroenie), St. Petersburg, in 1991, but only proofs of the manuscript were printed, and the book was left unpublished.

This book consists of two interconnected parts. In the first part, fundamental photometric and radiometric principles, designations, methods, and devices are discussed via fundamental laws and methods developed within the concepts of physical optics applicable to photometric and radiometric systems. Attention is given to specifics of optical measurements, partially with coherent and pulsed radiation, corrections for diffraction, verification of authenticity for analyzing methods, and confirmation of photometric accuracy for photometers and radiometers. The second part of the book focuses on methods and systems, designed for evaluation of low optical losses in radiation interacting with transparent crystals and glasses, highly reflecting mirrors, thin-film coatings, weakly absorbing solids, liquids or gases, optical fibers, or any other objects. Optical losses may occur anywhere when reflection, scattering, or absorption of radiation causes a noticeable reduction of efficiency for the radiant energy transfer. Multitudes of pulsed, resonator, calorimetric, interferometric, polarization, acousto-optic, active

or passive, and other methods are analyzed side by side and in comparison with the conventional spectrophotometric and radiometric techniques for accurate optical measurements. Finally, advancements in direct methods of precision measurements attributing to the newest developments of highly stabilized laser light sources, balanced detectors, and computerized registration systems are described with insights into certain novel applications.

The book is intended for practicing scientists and engineers of need to apply measurement methods and procedures for optical analysis and practical evaluation of transparent, reflecting, scattering, absorbing, and aggregated objects, as well as for determination of power and energy parameters, and the extents of radiation and color properties of light. It is also hoped that this book will serve as an accommodating resource of optical measurement ideas for students of optics.

Contents

Part I
Applied Photometry and Radiometry

I.1. Background

As the term photometry is the derivative of words "*light*" and "*metrein*", radiometry may be defined as a measurement science, studying the parameters and characteristics of radiative energy transfer. Photometry deals with photometric and radiometry deals with radiometric quantities, determining the temporal, spatial, and spectral distributions of radiation and optical properties of the substances, mediums, and bodies as intermediates or detectors of such a transformation. Radiometry, in which photometry could be seen as the discipline for visible light, studies the properties of optical radiation by ignoring the finiteness of space, time continuity, and related phenomena. It deals with the observable space- and time-averaged parameters of radiation emitted by sources, propagating in mediums, and interacting with substances and material bodies in ultraviolet, visible, and infrared wavelength regions.

The radiant intensity, as a main parameter of energy transport of light, may be defined as a surface integral over the product of radiation Poynting vector by an outer normal to an enclosing surface at a given instance of time. Therefore, the radiometric interpretation of optical radiation power and energy, as its time derivative, is by definition provided via introduction of the finite time and space intervals. The dimensions of the finite intervals must, respectively, exceed the oscillation times or the wavelengths of optical radiation. The finiteness causing additivity of photometric and radiometric quantities or the independence of individual light components, combined or summed, arises not from imperfection or incomprehension of radiometric theory but from imposed limits of observation for the phenomena considered. Under such limitations, the finiteness of light wavelengths can be disregarded by setting them as tending to zero. Thus, mutual independence of amplitude and phase fluctuations remains valid for any radiometric or photometric superposition of radiation.

The concept of photometric and radiometric quantities distinguishes the power and energy extents of light and their derivatives using various systems of measurement, such as the radiant, photon, luminous, or otherwise reduced system. Such a distinction is only terminological and concerns units of measurements without regard to fundamentals of science, methods of study, or temporal, spatial, and spectral distributions of light. Diverse radiometric quantities are always derivatives with respect to a small, but finite interval of length, area, bulk, frequency, or time, and may also be represented as integrals of basic radiant or luminous parameters. The variety of names does not alter the nature of the phenomenological understanding of every phenomenon.

Chapter 1
Radiometric and Photometric Quantities and Notions

1.1 Physical Sense of Radiometric Conception

1.1.1 Statistical Field of Optical Radiation

The energy conservation law for any electromagnetic field implies, that the time derivative $\partial Q/\partial t$ of the field energy for optical radiation, which ranges from a wavelength as short as 1 nm to one as long as 1 mm, when propagating in a homogeneous, isotropic, and low-absorbing medium whose properties satisfy the material equations $\mathbf{D} = \varepsilon\mathbf{E}, \mathbf{B} = \mu\mathbf{H}, \mathbf{J} = \sigma\mathbf{E}$ and whose elements are in a steady position or in slow motion, is [1.1]:

$$\frac{dQ}{dt} = -\frac{d\Pi}{dt} - \Lambda - \int_{\mathbf{A}} \mathbf{S} \bullet \mathbf{r}\, dA, \tag{1.1}$$

where Π is the work done for the travel time t; Λ is the total loss, caused by resistive dissipation of energy Q, if the medium is a conductor; $\mathbf{S}$ is the Poynting vector; $\mathbf{r}$ is the outward normal unit vector to any arbitrary boundary surface A situated far away from a source of the field; $\mathbf{E}$ and $\mathbf{H}$ are the electric and the magnetic vectors; $\mathbf{D}$ is the vector of electric displacement, $\mathbf{B}$ is the vector of magnetic induction; ε is the dielectric constant (permittivity), μ is the magnetic permeability, and σ is the specific conductivity of the medium. The integral in Eq. (1.1) identifies the flow of energy crossing the boundary surface A reached by the optical wave. Thus, when dealing with a transfer of energy of optical radiation in the absence of moving elements or conductors, the space-time derivative in Eq. (1.1) represents the flow of optical energy crossing such a boundary surface A per unit of time. By definition, the *radiant flux*, or the *flux* of optical radiation or *flux*, is:

$$\Phi \equiv \frac{dQ}{dt} = -\int_{A} \mathbf{S} \bullet \mathbf{r}\, dA. \tag{1.2}$$

M. Bukshtab, *Photometry, Radiometry, and Measurements of Optical Losses*, Springer Series in Optical Sciences 209,
https://doi.org/10.1007/978-981-10-7745-6_1

As follows from Eq. (1.2), the integral of a scalar product of vectors **S** and **r** has the physical meaning of the average power of a beam of radiation. On the basis of such a definition, it is impossible to resolve the detailed distribution of vector **S**, which defines the density of the energy flow of radiation. Radiometrically speaking, for a steady flow of optical energy emitted from any given point of space within an enclosing surface A, it is only possible to speak about the mean radiant flux Φ and the mean Poynting vector **S** of radiation for small but finite space and time intervals.

Consequently, the radiometrically observable energy action of optical radiation is identified not by the instantaneous electromagnetic field, but by parameters of the averaged statistical field of that radiation. The statistically averaged domain may be defined as the *field of optical radiation* or the *field of optical vector*. *The optical vector* can be identified by the following statistical equation:

$$D_l = \langle \mathbf{S} \rangle = \frac{1}{t} \int \bar{\mathbf{S}} dt. \tag{1.3}$$

Here angular brackets identify time averaging and t is the mean time interval, much larger than the fundamental period of oscillation for the wave component at wavelength λ: $t \gg 2\pi/\omega = 1/\nu = \lambda/c$.

The defined concept of statistical field and statistically averaged vector of optical radiation is very closely allied with the character of observation of light waves in the optical domain and originates from the impossibility to construct the instant power density operator of the photon flux at any single point [1.2]. Thus, the statistical parameters of optical radiation may be observed or measured only in some space and time domains, or in some enclosed vicinity of frequency or k-space. The nature of that notion is stipulated by extraordinary high frequencies of electromagnetic oscillations for the optical domain allowing one not to consider, at least within the photometric and radiometric averaging concept, principal correlations between oscillations for optical radiation.

1.1.2 Propagation of Light Waves

The electromagnetic field, denoting optical radiation, consists of waves having wavelengths approximately from 1 nm to 1 mm and frequencies from $3 \cdot 10^{17}$ to $3 \cdot 10^{11}$ Hz. For lots of processes of emission of optical radiation or its interactions with substances, bodies, and mediums the high oscillation frequencies of light can be considered as tending to infinity without violating the integrity of the analysis. Hence, the physical phenomena particularly studied by radiometry and photometry are concerned with any propagation of optical radiation in isotropic dielectric substances and observed at distances much longer than the wavelength or a set of wavelengths of radiation. The radiometric concept of optical-radiation transfer considers frequencies of radiation oscillations to be infinitely high and ignores the finiteness of radiation wavelengths, which subsequently interact with all real

apertures of optical systems by way of propagation. The smallness of radiation wavelengths in comparison with material apertures and propagation distances identifies the specifics of observation for optical radiation.

Applying the concept of geometrical optics [0.1–0.50, 1.1–1.3] for the notion of photometry and radiometry, one may represent the light wave having a tending-to-zero solitary wavelength $\lambda \to 0$, propagating in a substance with refractive index $n = \sqrt{\varepsilon\mu}$, in the direction of a unit vector **s** and in the far field from its source at the position of a unit vector **r**, as a plane homogeneous electromagnetic wave of number k_0 and of electric **E** and magnetic **H** vectors:

$$\mathbf{E}_0 = \mathbf{e}\exp[ik_0 n(\mathbf{s}\cdot\mathbf{r})] = \mathbf{e}(\mathbf{r})\exp[ik_0 L(\mathbf{r})]; \quad \mathbf{H}_0 = \mathbf{h}\exp[ik_0 n(\mathbf{s}\cdot\mathbf{r})] = \mathbf{h}(\mathbf{r})\exp[ik_0 L(\mathbf{r})]. \tag{1.4}$$

Here **e** and **h** are the constant vector amplitudes; λ_0 is the wavelength in vacuum; $k_0 = \omega_0/c = 2\pi/\lambda_0$; and **r** is the distance to a light source and is much larger than the wavelength: $\mathbf{r} \gg \lambda_0$. In contrast to the generally complex vector functions **e**(**r**) and **h**(**r**), the function L(**r**) is the scalar function of a position and a direction along a way from the source to the point of the radiation field at distance **r** and identifies the optical path for the propagation of the plane light wave.

Since the subjects of radiometric studies are monochromatic waves with big k_0 values in homogeneous and low scattering mediums, restricting radiometric observations to limits of not large changes for **grad** L, ε, μ and in the absence of electric currents or charges, one can rewrite Maxwell's equations in simplified forms [1.1]:

$$\mathbf{grad}\,\mathbf{L} \times \mathbf{h} + \varepsilon\mathbf{e} = 0\,; \tag{1.5a}$$

$$\mathbf{grad}\,\mathbf{L} \times \mathbf{e} - \mu\,\mathbf{h} = 0\,; \tag{1.5b}$$

$$\mathbf{e} \bullet \mathbf{grad}\,\mathbf{L} = 0\,; \tag{1.5c}$$

$$\mathbf{h} \bullet \mathbf{grad}\,\mathbf{L} = 0\,. \tag{1.5d}$$

For **grad** L, **ε**, **μ** values on the order of 1.0, the radiometric restriction is justified if changes of **e** and **h** at distances compatible with the radiation wavelength are small in comparison with the individual values of **e** and **h**. That condition is violated at sharp changes of radiation intensity, for example, around light or shade boundaries, in nonisotropic and highly scattering mediums, near an optical focus, and in the presence of a sizeable medium conductivity or polarization. A nontrivial (other than zero) solution for the system of Maxwell's equations (1.5) is obtained via substitution for **h** from (1.5b) into (1.5a) [1.1]:

$$(1/\mu)\left[(\mathbf{e} \bullet \mathbf{grad}\,\mathrm{L})\,\mathbf{grad}\,\mathrm{L} - \mathbf{e}(\mathbf{grad}\,\mathrm{L})^2\right] + \varepsilon\mathbf{e} = 0. \tag{1.6}$$

According to the third equation in (1.5): $\mathbf{e} \bullet \mathbf{grad}\,\mathrm{L} = 0$, expression (1.6) transforms at $\mathbf{e} \neq 0$ and $\sqrt{\varepsilon\mu} = n$ into the eikonal equation – the fundamental law of geometrical optics and radiometry:

$$(\mathbf{grad}\,\mathrm{L})^2 = \mathrm{n}^2. \tag{1.7}$$

The explicit form of Eq. (1.7) in the Cartesian system is given by the eikonal equation as:

$$(\mathrm{dL}/\mathrm{dx})^2 + (\mathrm{dL}/\mathrm{dy})^2 + (\mathrm{dL}/\mathrm{dz})^2 = \mathrm{n}^2(\mathrm{x}, \mathrm{y}, \mathrm{z}). \tag{1.8}$$

In consequence with the eikonal equation, any monochromatic beam of light, which acts or is viewed at distances of many wavelengths from a source, can be treated as a plane homogeneous wave in every homogeneous and isotropic substance. Therefore, for monochromatic light the surface:

$$\mathrm{L}(\mathbf{r}) = \mathrm{const}, \tag{1.9}$$

is the equal-phase geometrical wave surface determining a singular position of the geometrical wave front of radiation. Since the field of a plane wave is characterized by equality to zero of the scalar products $\mathbf{E} \bullet \mathbf{s}$ and $\mathbf{H} \bullet \mathbf{s}$, in such a specific case, the electric and magnetic vectors of the optical radiation lie in the planes perpendicular to the direction of light propagation, and since these two vectors form the right-handed orthogonal coordinate system, the Poynting vector is:

$$\mathbf{S} = (\mathrm{c}/4\pi)|\mathbf{E} \times \mathbf{H}| = (\mathrm{c}/4\pi)\left(\sqrt{\varepsilon/\mu}\right)|\mathbf{E}|^2\mathbf{s} = (\mathrm{c}/4\pi)\left(\sqrt{\mu/\varepsilon}\right)|\mathbf{H}|^2\mathbf{s}, \tag{1.10}$$

and represents the spatial density of electric or magnetic energy in the direction of propagation.

1.1.3 Intensity of Radiation and Light Rays

For identified statistically observable radiation, it is impossible to instantly measure the **E** and **H** or **S** magnitude of a single-wave oscillation. Thus, radiometry and photometry deal with both space or time averages in the stationary and ergodic field of optical radiation.[1] Radiometry observes an electric or a magnetic energy density of light at a time interval longer than the principal period of oscillation at a mean frequency of radiation $\bar{\omega} : T = 2\pi/\bar{\omega}$. The equations for these averaged electric and magnetic energies respectively are:

$$<\mathrm{Q_e}> = (\varepsilon/16\pi) \cdot \mathbf{e} \bullet \mathbf{e}^*; \quad <\mathrm{Q_m}> = (\mu/16\pi) \cdot \mathbf{h} \bullet \mathbf{h}^*, \tag{1.11}$$

where the complex conjugate magnitudes are marked with an asterisk. Considering a light beam with a tending-to-infinity wavelength, it may be shown [1.1, 1.3] that

[1]It is more correct to speak about the averaging with respect to some appropriate ensemble of values, which characterizes statistical properties of the electromagnetic field of radiation, but as long as the optical radiation fields are, by vast majority, ergodic and statistically homogeneous, their space and time averages coincide with the average by the ensemble.

the time-averaged electric and magnetic energy densities with accuracy $\lambda \to 0$ are $<Q_e> = <Q_m> = <Q>/2$ and the Poynting vector is:

$$<\mathbf{S}> = (c/n) \cdot (<Q_e> + <Q_m>) \cdot \mathbf{grad}\, L/n = v <Q> \mathbf{s}. \tag{1.12}$$

According to the eikonal equation (1.7), beam unit vector **s** lies in the direction of the average Poynting vector $<\mathbf{S}>$ and is collinear with vectors $\mathbf{grad}\, L/n$ and $\mathbf{grad}\, L/|\mathbf{grad}\, L|$ pointing in the same direction, where $v = c/n$ is the light velocity. Equation (1.12) confirms that statistical vector $<\mathbf{S}>$ lies in the direction of the outer normal to a geometrical wave front of light and, within apparent accuracy of the conventional approximation $\lambda \to 0$, the time-averaged energy density $<Q>$ of the light field propagates with the light velocity $v = c/n$.

From Eq. (1.12) it also follows that in any homogeneous medium the wave normal to the geometrical wave front of the beam of quasi-monochromatic radiation coincides with its optical vector (see Eq. (1.3)) and, consequently, with the direction of the energy transfer. Therefore, if the wavelength of that light can be considered as notably small in comparison with obstacles it interacts with, such as various substances, instrument apertures, and radiation receivers, the time-averaged density of that radiation energy $<Q>$ propagates with the velocity of light v_i, being defined by every specific medium index of refraction: $v_i = c/n_i$. Therefore, the direction of energy transfer coincides with the outer normal to the wave front of radiation, which is characterized, in turn, by constancy of the eikonal. When such conditions are observed, light is transmitted according to the laws of geometrical optics and the correlation of energy and power parameters of specific fluxes of radiation obeys linear and additive interactions. Studies of that radiation and of the radiation's interactions with material objects are the subject of *photometry and radiometry*.

Following Eq. (1.12), the absolute value of the Poynting vector equals the product of the average energy density of a given wave group of radiation and the velocity of its propagation:

$$|<\mathbf{S}>| = v <Q> \equiv I, \tag{1.13}$$

where the sign $\equiv$ indicates the introduction of a new designation. Expression (1.13) characterizes the average angular power density at a point of the electromagnetic field or the energy of radiation per unit of time, in the selected direction per unit of solid angle, which falls, propagates, or is irradiated from one imaginary platform perpendicular to that direction. Since such a product defines the angular power density of the electromagnetic field at a given time or the power action of radiation per unit of solid angle, it designates the *angular intensity* or the *intensity I* of the optical field at any given point of space per unit of time. Intensity *I* is an inclusive power extent of optical radiation, which is not affiliated with any specific process of emission of radiation by the sources, its propagation through material objects, or its actions on such radiation receivers.

According to Eqs. (1.12) and (1.13), the outer normal to a wave front of the radiation flow may serve as an approximation of that radiation beam indicating the straightforward propagation of electromagnetic energy. Therefore, light propagation in a homogeneous and isotropic medium occurs in a straight line. Since every light beam whose symmetry axis coincides with its wave normal carries energy other than zero, a real beam of optical radiation would be considered as a certain material line. For example, it could be radiated from a source through a small aperture of any opaque baffle, whose dimensions in comparison with actual distances permit one to consider that aperture as the material point. Moreover, in consequence of the diffraction phenomenon, the bounds of a light beam with the surroundings are not sharp and the intensities of the shade regions are not reduced to zero in comparison with the highest intensity of radiation in the irradiated zone. However, the dimensions of the respective inhomogeneous transition regions are approximately equal to a set of wavelengths for the propagating light beam. That is why the tending-to-zero wavelength requirement $\lambda \to 0$ also allows one to ignore phenomena which overstep the limits of geometrical optics. As a result, while realizing photometric and radiometric analysis and specific experiments with objects or apertures at considerably large dimensions, compared with light wavelengths, one can consider the flow of quasi-monochromatic optical radiation as a *beam of rays* or as a *light tube*.

Up to now monochromatic radiation has been considered under the assumption of a single received or emitted wave. A monochromatic wave could be seen as a single Fourier component of a multiwave optical field. From that angle, the intensity I of a physical light beam is given by the entirety of single-component intensities, formed by compound elementary radiating harmonic oscillators:

$$\mathrm{I} = |\langle \mathrm{S} \rangle| = \frac{\mathrm{c}}{4\pi} \sum_{\mathrm{n,m}} |\langle \mathbf{E_n} \times \mathbf{H_m} \rangle| = \frac{\mathrm{c}}{4\pi} \sum_{\mathrm{n}} |\langle \mathbf{E_n} \times \mathbf{H_n} \rangle| + \frac{\mathrm{c}}{4\pi} \sum_{\mathrm{n} \neq \mathrm{m}} |\langle \mathbf{E_m} \times \mathbf{H_m} \rangle|, \tag{1.14}$$

The second sum in Eq. (1.14) characterizes the correlations among fluctuations of different light components. In every case, when correlations are absent, or more accurately, if they can be disregarded while presuming these different components of radiation to be incoherent, the total field is given by the additive sum of individual fields of each single oscillator:

$$I = \sum_{n} |\langle \mathbf{S_n} \rangle|, \tag{1.15}$$

making the light beam a stochastic mixture of incoherent, monochromatic, infinitely long waves.

On the basis of Eqs. (1.9)–(1.15), one could define radiometry and photometry as the science of analysis and measurement of the parameters and characteristics of radiant and luminous energy transfers operating with observable optical radiation of uncorrelated waves, i.e., with the electromagnetic field of time- and space-averaged Poynting vectors. According to that concept [1.1–1.8], light in radiometry and

photometry propagates in the isotropic medium and meets particles having dimensions considerably larger than light wavelengths. The validity of the radiometric and photometric laws of light propagation obtained according to the $\lambda \to 0$ assumption can be violated in anisotropic, highly scattering, and absorbing substances,[2] when radiation is passing small, compared with the light wavelength, particles, at shade boundaries, or in regions of sharp intensity changes, as well as when there is considerable correlation among fluctuations of individual radiation components, i.e., when light beams are coherent. This does not necessarily mean that particular radiometers or photometers are not capable of measuring exact intensity distributions of optical radiation in any diffraction and interference patterns or for any specific power level of laser radiation with any plausible coherence length, or in other situations. These conditions only restrict the application of radiometric and photometric laws to particular phenomena of light propagation and bounds of radiometric correlations between parameters of light beams related to some potentially strong interactions and to the existence of particles having dimensions comparable to or smaller than light wavelength.[3]

1.2 Parameters of Optical Radiation

1.2.1 Radiometric Quantities and Units

By definition, radiometry and photometry operate with space- and time-averaged Poynting vectors. As a result, radiometric and photometric quantities are the ones that identify temporal, spatial, and spectral distributions of optical radiation, and properties of substances, mediums, and bodies as intermediaries of emission, transformation, and reception of radiation energy. The additivity principle, emphasized by that identification, fundamentally regulates radiometric and photometric considerations. The additivity principle substantiates the presumption of statistically averaged physical processes of emission, reception, and interaction of light with the substances in which propagation occurs. For each such process it is possible to disregard, on one hand, the finiteness of the light wavelength and relevant diffraction phenomena and, on the other hand, interdependence of individual intensity fluctuations in diverse light beams comprising the total optical field, additively averaging the results of interference for radiometrically added beams.[4]

---

[2]In optical glasses any practical anisotropy of scattering molecules is averaged by their great quantity even for a volume on an order of λ^3.

[3]Correlation between fluctuations of Fourier components of optical radiation, and criteria of practical exposures of coherence and diffraction effects in radiometry will be analyzed in Chap. 3.

[4]The term "no interference" means no interference effect may affect the radiometric concept, which from the standpoint of the law of conservation of energy means that all effects of any actual interference pattern, which may occur while adding coherent light beams, are to be averaged over the space or time of the specific radiometric or photometric observation.

Concepts of radiometric and photometric quantities unite the means of expressing energy and power extents of optical radiation and its time and space derivatives. These quantities may differ by a system of units, compliant or reduced to a given law of energy or power conversion: radiant, photon, luminous, or otherwise. The radiant quantities X_e are derived to be compliant with the universal physical energy and power units: joule and watt. The photon units X_p are not dimensional and correspond to the number of photons in a given light beam. The optical science which expresses all physical parameters and characteristics of optical radiation as the radiant power or energy quantities is called *radiometry of optical radiation*, or *radiometry*.

A system of reduced photometric quantities X_r may be formed using a mathematical model of any linear spectrally additive receiver executing a physical process. Such a process transforms the units of a given radiant spectral quantity to units of the reduced quantity. The conversion law is:

$$X_r = K \int_0 X_{e,\lambda} S'(\lambda) d(\lambda), \tag{1.16}$$

where K is the conversion factor from a specific radiant quantity to the unit based on any given reduced system; $X_{e,\lambda}$ is the spectral density of the radiant photometric quantity, with respect to which a specific reduction is realized; and $S'(\lambda)$ is the relative spectral response of a receiver making the transformation. The *reduced photometric quantity* is called the *luminous* quantity, if the values of $S'(\lambda)$ are defined by the relative spectral efficiency function $V(\lambda)$ of the monochromatic radiation for photopic vision with the coefficient $K_{max} = 683\ \mathrm{lm} \cdot \mathrm{W}^{-1}$ [1.5]. This magnitude corresponds to the maximum luminous spectral effectiveness, which coincides with a wavelength of approximately 555 nm for the photopic vision. A receiver for the transformation is not a perfect eye of a concrete person, but the model reflecting the average responsiveness of human vision and representing the standard colorimetric observer of the *International Commission on Illumination* (CIE) for the visual field of 2°. The optical science that concerns visible radiation and considers the parameters and characteristics of such radiation to be expressed by means of the luminous quantities is called the *photometry* or *light measurements*.

To describe a spectral, spatial, and temporal distribution of the energy of radiation recognizing a distinct system of units, the physical parameters of radiation are named to specifically characterize spectral densities and spectral distributions of radiometric and photometric quantities. These quantities specify the *spatial, angular,* and/or *spectral density* of a light beam at a given region of space, the *distribution* of the light beam surface density over its cross section, and the *dependency* of a given quantity on time. From the standpoint of time-dependent quantities, two types of light envelopes are distinguished: the *continuous radiation*, existing at any instant of the observation time *t*, and the *pulsed radiation*, existing during a time interval τ smaller than the observation time. The time interval τ_p, at which the values of a photometric or

radiometric quantity of a light pulse exceed a given relative level, typically 0.5 of its maximum, is called the *duration of the light pulse*.

The *spectral density* X_λ of a given radiometric or photometric quantity is recognized as the physical quantity identified by the ratio of any considered quantity dX within a small spectral interval containing a mean light wavelength λ to width $d\lambda$ of that spectral interval: $X_\lambda = dX/d\lambda$. Analogously, the spectral density can be formed on various scales: X_f by a frequency f, X_ν by a wave number ν, or by their logarithms, etc. The *spectral distribution* of a photometric or radiometric quantity is the dependence of its spectral density versus wavelength, frequency, wave number, etc. Respectively, the section of radiometry in which the parameters of optical radiation are expressed through the spectral densities of radiometric quantities is called *spectroradiometry*. One specific section, in which the properties of materials, bodies, or substances are identified via relations between spectral densities and the radiometric quantities to be analyzed, is called *spectrophotometry*.

The study of parameters and characteristics of emission, transfer, and reception of optical radiation is provided by *photometers and radiometers*. Two basic types of photometers and radiometers are distinguished. A radiometer utilizes some physical receiver of radiation as the primary optical transformer, directly converting the energy or power of a light beam into a signal to be registered. For a *visual photometer*, the receiver is the human eye, establishing photometric equilibrium between analyzing and comparing light waves due to equality of surface-angular densities of the viewed luminous fluxes as the equality of luminance values of the visible spots.

The availability of such a natural photometric observer as the human eye enabled the establishment of the luminous units of measurements in photometry historically independent of the system of radiant units. It was natural in the early years of photometry to use a standard candle, emitting a given luminous flux into the space region limited by a unit solid angle of one steradian. The luminous intensity of such a standard source was initially designated as the *candle* (cd). Later, the unit of luminous measurements was reproduced via the spectral emittance of the blackbody radiator under a specific fixed temperature. As a result, the following definition was introduced: the *candela* equals the luminous intensity irradiated in the perpendicular direction from $1/600,000$ of a square meter of a blackbody with its surface at the temperature of platinum solidification at a pressure equal to $101,325\,\mathrm{N/m^2}$.

The existence of various units of measurement for energy or power extents of radiation defines varieties for quantitative estimations of radiant or luminous actions. Nevertheless, reproduction of the dimension of any unit of measurement can be realized on the basis of one unified systematic approach. For that purpose the relative spectral luminous efficiency of monochromatic radiation for photopic vision can be normalized within one system. That is based on the correlation between radiant flux expressed in radiant units and luminous flux of radiation in the maximum of the responsiveness for a standard CIE photometric observer, which represents one statistically averaged eye. In October 1979 the 16th General Conference on Weights and Measures ultimately adopted a new conclusive definition for the candela within the radiometric-term system: “The *candela* is the

luminous intensity, in a given direction, of a source that emits monochromatic radiation of frequency $540 \cdot 10^{12}$ Hz and that has a radiant intensity in that direction of $1/683\,\mathrm{W} \cdot \mathrm{sr}^{-1}$."

The adopted radiometric definition for the candela allows one to practically reproduce the actual dimensions of radiant, photon, luminous, and, by analogy, any arbitrary reduced unit of measurement by the sources of optical radiation of a consecutive spectrum: from continuous to pulsed sources in any state of coherence at a fixed or changeable wavelength. The reduced units can be, in turn, determined by measuring the radiant or luminous fluxes, or any other spatial, spectral, or temporal extents of radiation by a given radiometer or photometer with either unselective, preferential, or accordingly corrected optical characteristics of its radiometric or photometric response.

1.2.2 Parameters of Optical Radiation

The normal radiometric viewpoint on any radiant transfer presumes that an electromagnetic field, localized in finite spatial and temporal regions, is being averaged in these regions near every given point of observation. Thus, if there is a superposition of different beams of radiation with equal spectral and temporal distributions, providing the phase statuses of radiation components are independent of each other, then the radiometric effect at a chosen point is identified by the combined intensity of those radiation components. The combined intensity is set in a unit area, a unit volume, within a unit solid angle, or in a unit temporal or spectral interval. The spatial or temporal distributions of radiation in space and time may be characterized by the respective radiometric quantities, which represent the spatial or the temporal integral or derivative of the flux or energy of optical radiation over any enumerated coordinate.

The primary radiometric and photometric quantity is, respectively, the radiant or luminous *flux of radiation* Φ, which is equal to the power P of radiation as the ratio of the energy Q transferred by radiation to the time t of the transfer that greatly exceeds the period of electromagnetic oscillation of radiation: $\Phi = P = dQ/dt$. The radiant flux is measured in the radiant unit *watt* (W), and is designated by radiant index e: $\Phi_e = dQ_e/dt$. The luminous flux is measured in the luminous unit *lumen* (lm), identified by the luminous energy Q_v per unit of time t. The luminous flux is designated by the visual index v: $\Phi_v = \mathrm{dQ}_v/\mathrm{dt}$. The mean or average power of radiation $\bar{\Phi}$ or $\bar{\Phi}_e$ (observation of luminous quantities practically always implies averaging) represents the radiant flux, defined as the radiant energy transferred by continuous or by pulsed radiation during the time of such a transformation. In the pulsed mode, the maximum power $\Phi_{\max}$ of a beam of optical radiation is determined as the greatest magnitude of the radiation power during the time of its observation.

The utmost spatially localized power parameter of the statistically averaged field of optical radiation is the *radiance* $\mathrm{L_e}$, measured in radiant units, or the *luminance* L_v, measured in luminous units. Radiance or luminance denotes a surface-angular density of light. It is given by a radiant flux $\mathrm{d}^2\Phi_\mathrm{e}$ or a luminous flux $\mathrm{d}^2\Phi_v$ related to

a geometric extent d^2G of a light beam irradiated from a small platform dA containing a specified point of observation into a small solid angle $d\Omega$ of a direction ℓ forming an angle Θ with the normal to the platform dA of the light beam formed:

$$L = \frac{d^2\Phi}{d^2G} = \frac{d^2\Phi}{dA\ \cos\Theta d\,\Omega} = \frac{d^2\Phi}{dA_n d\,\Omega}. \tag{1.17}$$

The radiance and luminance have the physical meaning of flux of optical radiation propagating in a given solid angle into a chosen direction from a normally situated (dA_n) platform of a unit area. The measurement units are watts per steradian per square meter for radiance $[W/(sr \cdot m^2)]$, and lumens per steradian per square meter $[lm/(sr \cdot m^2)]$ or candela per square meter for luminance $[cd/m^2]$.

The angular density of radiation is characterized by the *radiant intensity* I_e for radiant units, and by the *luminous intensity* I_v for luminous units. The angular density or the *intensity* of light is defined by ratio of flux $d\Phi$, propagating from a given source of radiation in a small solid angle of observation $d\Omega$ containing an analyzing direction ℓ, into solid angle $d\Omega$ of light propagation:

$$I = \frac{d\Phi}{d\Omega} = \int_A L\ \cos\Theta dA. \tag{1.18}$$

The units of measurement are watts per steradian for radiant intensity $[W/sr]$, and candela, which is equivalent to lumens per steradian $[lm/sr]$, for luminous intensity.

The designations of photometric quantities characterizing the spatial density of light depend on the localities. The *radiant emittance* M_e and the *luminous emittance* M_v designate the surface density of the emitted flux. Each is defined by the ratio of radiant or luminous flux $d^2\Phi$ flowing out from a small part of an emitting surface, containing any observation point, to an area dA of that part:

$$M = \frac{d^2\Phi}{dA} = \int_\Omega L\ \cos\Theta d\Omega. \tag{1.19}$$

The units of measurement are watts per square meter $[W/m^2]$ and lumens per square meter $[lm/m^2]$. Two supplementary quantities, the *irradiance* Ξ_e and the *illuminance* Ξ_v, characterize the surface density of radiating flux falling on an object under study and irradiating or illuminating that object. These quantities are defined by the ratio of the radiant or luminous flux $d^2\Phi$ falling on a small surface containing a given point to an area dA of the surface:

$$\Xi = \frac{d^2\Phi}{dA}. \tag{1.20}$$

The units of measurement are watts per square meter $[W/m^2]$ and lux (lx). The *surface density* of radiant flux $d\Phi_e/dA$ or radiant energy dQ_e/dA characterizes the

surface density of either continuous or pulsed radiation. The flux density is defined by the ratio of radiant flux transferred by a small section of a physical beam, retaining a point being studied, to an area of that section and is measured in watts per square meter $[W/m^2]$. The radiant flux surface density integrated over time characterizes the radiant energy density or *fluence*, which defines the surface energy density and the strength of radiation field, and is measured in joules per square meter $[J/m^2]$.

The three-dimensional spatial density of optical radiation is characterized by the *spherical irradiance* $\Xi_{0,e}$ and by the *spherical illuminance* $\Xi_{0,v}$, identifying the entirety of normal irradiance or illuminance values $d\Xi_n$ originating from the totality of the beams contained in small solid angles of all directions ℓ_i, in the space with a vertex at an observation point P, which fall on the small platforms dA_i perpendicular to each named direction ℓ_i, which contain the observation point P:

$$\Xi_O = \int d\Xi_n = \int_{4\pi} L d\Omega. \tag{1.21}$$

The units of measurement for the spherical irradiance and spherical illuminance are as for irradiance and illuminance.

The three-dimensional angular intensity of light is defined by the *spherical density of radiant intensity* $I_{0,e}$ and the *spherical density of luminous intensity* $I_{0,v}$, respectively identified by the ratio of the radiant intensity $dI_e(\varphi, \theta)$ or the luminous intensity $dI_v(\varphi, \theta)$ of a small volume V of an emitting, scattering, or fluorescent medium, containing an observation point, in a direction formed by angles φ and Θ to that volume dV. The spherical densities are measured in watts per steradian per cubic meter $[W/(sr \cdot m^3)]$ and in candelas per cubic meter $[cd/m^3]$, respectively.

Alternatively to instantaneous observation, pulse radiometry and photometry study time-sensitive events. For pulsed radiation, when a temporal action is observed, the energy extent of light may be identified by an integral of a respective photometric or radiometric quantity over the observation time. Depending on the units of the study, the following quantities may be used: the *integral radiant intensity* θ_e and the *integral luminous* intensity θ_v, identified by integrals of radiant and luminous intensities over time and measured in joules per steradian [J/sr] and candela seconds [cd · s]; the *radiant exposure* H_e and the *light exposure* H_v, identified by integrals of the irradiance and the illuminance over time and measured in joules per square meter and lux seconds $[J/m^2]$ [lx · s]; the *integral radiance* Λ_e and the *integral luminance* Λ_v, defined by the integrals of the radiance and the luminance over time and measured in joules per steradian per square meter $[j/sr \cdot m^2]$ and in candela seconds per square meter $[cd \cdot s/m^2]$; as well as the *spatial radiant exposure* $H_{0,v}$ and the *spatial light exposure* $H_{0,v}$, identified by integrals of the spatial irradiance and the spatial illuminance over time and measured in joules per square meter $[J/m^2]$ and in lux seconds [1x · s].

1.2.3 Invariable Parameters of a Light Tube

Consider a beam of optical radiation at wavelength λ propagating in free space with the wave front of the beam defined by the eikonal equation (1.7). In that optical beam an arbitrary element of volume dV at a point P could radiate or be irradiated, and by the Huygens principle the element can be viewed as a source of secondary waves. Equation (1.2) defines the flux dΦ of radiation inside volume dV. To provide for radiometric observation, the volume's dV dimensions should be notably larger than wavelength λ. The smallest element of volume dV for the integration in (1.2), while radiometrically observing optical radiation in any ultraviolet–visible–near infrared spectral domain, can be considerably smaller than common apertures of optical systems and the distances between their elements. Therefore, such a volume dV may be considered as one material point, from which radiation beams or rays are irradiated forming the *light tube*.

To determine the distribution of radiant or luminous intensity in a light tube, let us take a look (see Fig. 1.1) at a beam of light propagating from an element dA_1 of a given wave front $L_1(\mathbf{r}) = \text{const}$, at a distance ℓ_1 from a designated point P, to an element dA_2 at a distance ℓ_2 forming a wave front $L_2(\mathbf{r})$. If the volume dV enclosed by the tube and elements dA_1 and dA_2 contains no internal light sources and no energy absorbers, the law of conservation of energy Eq. (1.2) of the time- and space-averaged optical field inside the light tube can be expressed using a curve integral over volume dV as [0.5]:

$$\oint_{dV} \langle \mathbf{S} \rangle \bullet \mathbf{r}\, dA = 0. \tag{1.22}$$

Taking into account relations (1.12, 1.13) for the radiant intensity I, Eq. (1.22) transforms into:

$$\oint \mathrm{I}\, \mathbf{s} \bullet \mathbf{r}\, dA = 0. \tag{1.23}$$

Here **s** is the unit vector of a wave normal and **r** is the unit vector of an outer normal to the element.

Since the scalar product $\mathbf{s} \bullet \mathbf{r}$ of vectors **s** and **r** is $+1$ on irradiated surface dA_2 and -1 on radiating surface dA_1, as well as zero on the lateral tube surface, Eq. (1.23) converts to:

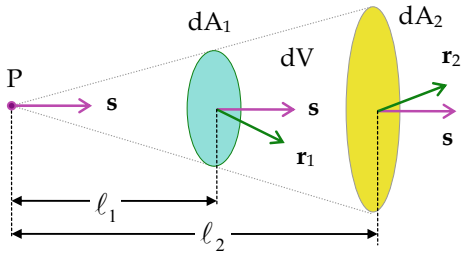

Fig. 1.1 A physical beam forming a light tube

$$I_2 dA_2 - I_1 dA_1 = 0 \quad \text{or} \quad I_1 dA_1 = I_2 dA_2. \tag{1.24}$$

Hence, the flux $d\Phi$ of radiation inside the light tube is invariable along direction of its propagation, and the normal cross section of the tube serves as a measure of the surface density of radiation flux.

The processes of emission and reception of optical radiation by arbitrary surfaces inside the light tube can be analyzed via individual material points, interconnected by inscribed light beams (Fig. 1.2). Elements dA_1 of emitting surface A_1 are connected with elements dA_2 of irradiated surface A_2, and vice versa. Every light beam that irradiates surface A_2 from each arbitrary element dA_1 is inscribed in the solid angle $\Omega_1 = A_2 \cos\Theta_2 / {r_1}^2$. Every beam irradiating each arbitrary element dA_2 from the surface A_1 is inscribed in solid angle $\Omega_2 = A_1 \cos\Theta_1 / {r_2}^2$. Angles Ω_1 and Ω_2 define how surfaces A_1 and A_2 are observed from elements dA_2 and dA_1. The full entirety of all the beams that have reached surface A_2 from elements dA_1 represents one material beam of optical radiation emitted from surface A_1 and irradiating surface A_2. Since $r_1 = r_2 = r$, that beam has a physical constant:

$$\Omega_1 A_1 \cos\Theta_1 = \Omega_2 A_2 \cos\Theta_2 = \text{const} \equiv G. \tag{1.25}$$

Such a physical constant G serves as the measure of the angular-surface density of optical radiation carried by a light beam or by the light tube [0.5, 1.4]. G is called the *geometric extent* of a light beam, which may be directly approximated by the light tube. Equation (1.25) defines that the intensity of an optical beam forming the light tube remains constant independent of the position of an inner point for which the intensity is analyzed: emitting, irradiated, or situated in between.

If a light beam propagates through substances with unequal refractive indices, the invariance of the geometric extent is more general. In the case of incidence of a beam of light falling within solid angle $d\Omega = \sin\varphi \cdot d\varphi \cdot d\alpha$ onto a border of two dielectric substances, having refractive indices n_1 and n_2 (Fig. 1.3), the beam's angle φ_2 of refraction should satisfy Snell's law:

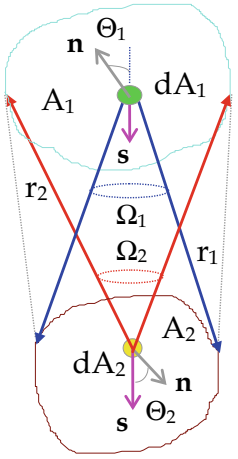

Fig. 1.2 Geometry of a beam of radiation

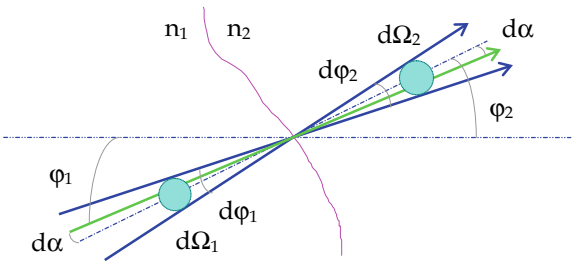

Fig. 1.3 Refraction of a light beam on a boarder of two mediums

$$n_1 \sin\varphi_1 = n_2 \sin\varphi_2. \tag{1.26}$$

The azimuth angle α in the plane perpendicular to the plane of incidence does not change, and after raising the left and right sides of Eq. (1.26) to the second power and differentiating, one can obtain:

$$n_1^2 \sin\varphi_1 \cos\varphi_1 d\varphi_1 = n_2^2 \sin\varphi_2 \cos\varphi_2 d\varphi_2. \tag{1.27}$$

Further multiplying both sides by dA·dα gives:

$$n_1^2 (dA \cos\varphi_1) \sin\varphi_1 d\varphi_1 d\alpha = n_2^2 (dA \cos\varphi_2) \sin\varphi_2 d\varphi_2 d\alpha, \tag{1.28}$$

and re-writing the equation in the form separating the geometric extent for the element 1 and 2:

$$n_1^2 d\Omega_1 dA \cos\varphi_1 = n_2^2 d\Omega_2 dA \cos\varphi_2, \tag{1.29}$$

one may obtain Gershun's invariant [0.5]. The invariant may also be re-written in the form:

$$n_1^2 d^2 G_1 = n_2^2 d^2 G_2 = \text{const}. \tag{1.30}$$

Gershun's invariant states that in a light tube the product of the square of the optical refractive index and the tube's geometric extent is a constant of the tube's material beam propagating in substances with unequal refractive indices. By analogy, the geometric extent is sometimes called the optical extent (*étendue*) of a light beam (see, for example, (1.25)), since it specifies the medium properties for a geometric extent [1.4, 1.5]. The term d^2G in (1.30) indicates that the geometric extent is a function of two variables: dA and dΩ.

1.2.4 Flux and Radiance of Optical Radiation

Let a surface dA represent any single element of an emitting or irradiated surface in a light tube. In the tube a material beam at an arbitrary point *P* in a direction ℓ

makes an angle φ with the inner or outer normal **n** to the surface (see Fig. 1.2). The radiant flux $d^2\Phi$ propagating in a small solid angle dΩ in a direction **s** via element *dA* and carrying a portion of energy in a small but finite time interval longer than the period of electromagnetic oscillation is:

$$d^2\Phi = L\cos(\mathbf{s}^{\wedge}\mathbf{n})dA\,d\Omega. \tag{1.31}$$

Here L is the proportionality factor – a function of two spatial variables: point *P* and direction **s**. Taking into consideration Eq. (1.25), relation (1.31) can be re-written in a one-factor form:

$$d^2\Phi = L \cdot d^2G. \tag{1.32}$$

Equation (1.32) defines that the flux carried by a light beam, is related in radiant units to its geometric extent, which identifies the beam geometry, by only one variable—called the *radiance*. The radiance has the physical meaning of the radiant flux passing a unit surface by a surface normal in the unit solid angle. The *luminance* determines the luminous flux carried by a beam of light in proportion to the geometric extent. The two factors define *the surface-angular density* of radiation.

Equation (1.32) identifies the radiance and luminance, as well as the geometric extent, being invariant parameters of a light beam. According to Eq. (1.25), the radiance, the luminance, and the geometric extent of a given beam remain unchanged, $L = \text{const}_1, d^2G = \text{const}_2$, for any propagation of radiation in nonabsorbing or nonscattering mediums if the flux $d^2\Phi$ remains constant. In the first-known work devoted to photometry [0.1] this statement was misformulated as equality of the luminance of an object and of its image, formed by optically perfect lenses or mirrors, but the statement only applies to the no-loss approximation of image formation and radiation transfer [1.4].

If a beam passes a border of two substances with a relative refractive index $n = n_2/n_1$, the flux $d^2\Phi$ carried by the light beam is altered, even if the border absorption and scattering losses are negligible:

$$d^2\Phi_2 = d^2\Phi_1(1 - \rho). \tag{1.33}$$

Here ρ is the *specular reflectance* of the border of two substances, given by the Fresnel formulae [0.3, 1.1]:

$$\rho_{||} = \left|\frac{n\cos\varphi_1 - \cos\varphi_2}{n\cos\varphi_1 + \cos\varphi_2}\right|^2 = \frac{\tan^2(\varphi_1 - \varphi_2)}{\tan^2(\varphi_1 + \varphi_2)}, \tag{1.34}$$

for a light wave polarized in the plane of incidence. For the wave polarized perpendicularly to the plane of incidence:

$$\rho_{\perp} = \left|\frac{\cos\varphi_1 - n\,\cos\varphi_2}{\cos\varphi_1 + n\,\cos\varphi_2}\right|^2 = \frac{\sin^2(\varphi_1 - \varphi_2)}{\sin^2(\varphi_1 + \varphi_2)}. \tag{1.35}$$

When light is incident on the border normally, the differences vanish: $\rho_{||} = \rho_{\perp} = \rho_0$, and the specular reflectance is:

$$\rho_n \equiv \rho_0 = \left(\frac{\mathrm{n} - 1}{\mathrm{n} + 1}\right)^2, \tag{1.36}$$

At normal incidence the border reflectance is independent of the state of light polarization. The designated angles $\Theta_1(\varphi_1)$ and $\Theta_2(\varphi_2)$ are, respectively, the *angle of incidence* and the *angle of refraction* defined by Snell's law (relation (1.26)); n is the *relative refractive index* of the boundary of two substances: $n = n_2/n_1$.

Combining Eqs. (1.30), (1.32), and (1.33), one can obtain the following relationship:

$$\mathrm{L}_2 = (1 - \rho)\,(\mathrm{n}_2/\mathrm{n}_1)^2\mathrm{L}_1. \tag{1.37}$$

It implies that any given radiance or luminance of a light beam, transferred from the less dense to the denser medium, increases in proportion to the square power of mediums' relative refractive index, owing to a decrease of the solid angle filled by the beam after refraction on the mediums' border. If either the medium or the border absorbs and scatters radiation, by the law of conservation of energy:

$$\mathrm{d}^2\Phi_1 = (1 - \rho - \alpha - \sigma)\mathrm{d}^2\Phi_2, \tag{1.38}$$

where α and σ are the *absorptance* and the *scattering factor* of the border. If necessary, the factual absorptance and scattering factor of a given border can be taken into account in Eq. (1.37):

$$\mathrm{L}_2 = (1 - \rho - \alpha - \sigma)\,(\mathrm{n}_2/\mathrm{n}_1)^2\mathrm{L}_1. \tag{1.39}$$

1.2.5 Intensity and Emittance of a Light Beam

Let us rewrite Eqs. (1.31) and (1.32) for the flux $\mathrm{d}^2\Phi$ of a beam via its dependence on the solid angle $\mathrm{d}\Omega$ and the area dA of a light-emitting element (Fig. 1.2):

$$\mathrm{d}^2\Phi = \mathrm{L} \cdot \cos(\mathbf{s}\,\hat{}\,\mathbf{n})\mathrm{dA}\,\mathrm{d}\Omega = \mathrm{dI} \cdot \mathrm{d}\Omega, \tag{1.40}$$

$$\mathrm{d}^2\Phi = \mathrm{L} \cdot \cos\Theta\ \mathrm{dA}\ \mathrm{d}\Omega = \mathrm{dM} \cdot \mathrm{dA}. \tag{1.41}$$

Designated by Eqs. (1.40) and (1.41), the proportionality factors dI and dM are:

$$\mathrm{dI} = \mathrm{d}^2\Phi/\mathrm{d}\Omega = \mathrm{L}\ \cos\Theta \mathrm{dA}, \tag{1.42}$$

$$\mathrm{dM} = \mathrm{d}^2\Phi/\mathrm{dA}\ = \mathrm{L}\ \cos\Theta \mathrm{d}\Omega. \tag{1.43}$$

Here Θ is the planar angle between the beam's direction **s** and the normal **n** to dA. The angular extent:

$$I(\Theta) = \int_A L\ \cos\Theta dA \underset{L=const;\,\theta=0}{=} LA, \tag{1.44}$$

is the *intensity of optical radiation* in direction **s** (relation (1.18)). It converges to the *radiant intensity* or the *luminous intensity* for radiant or luminous units. The intensity is the measure of the flux of radiation propagating from a point in a unit solid angle in a given direction. The surface extent:

$$M(\mathrm{P}) = \int_\Omega L\ \cos\Theta d\Omega, \tag{1.45}$$

is the *emittance of optical radiation* at point *P* (relation (1.19)): the *radiant emittance* and the *luminous emittance* for radiant and luminous units. The emittance describes the functionality of a source emitting a beam of radiation or the spatial density of a light beam irradiating or illuminating a surface. The emittance is a measure of the flux of radiation propagating from or onto a unit platform containing a point of observation.

The magnitude L of radiance or luminance in the integral in relations (1.44) and (1.45) is dependent on the direction of observation and on the coordinate of a given point of a wave front at which the integration is realized. In many cases, the angular-surface density of a light beam emitted by a primary or a secondary source of light is a constant of the source or changes according to a particular law. For example, under thermodynamic equilibrium, a blackbody at a steady-state temperature totally absorbs, i.e., with absorptance $\alpha = 1.0$ and reflectance $\Sigma\rho = 0$, all incident radiation independently of its spectral composition, direction, or state of polarization. Only under such specified conditions do diverse parts of a blackbody exchange equal portions of energy. Since the radiance and luminance of each point of the blackbody represent equivalent fluxes, radiated by the unit platform into the unit solid angle, the surface-angular density of the radiation energy within the blackbody remains unchanged for any point in any direction. It only changes as a function of the blackbody temperature and thus is called *blackbody* (or *black-cavity*) *radiation.*

The angular intensity $\mathrm{I}(\Theta)$ of radiation for a uniformly emitting source whose radiance and luminance does not depend on the direction of observation: $\mathrm{L}(\Theta) = \mathrm{const} \equiv \mathrm{L}_0$, is defined by Lambert's law [0.2]:

$$I(\Theta) = \cos\Theta \int L(\ell)dA = \cos\Theta \int L_0 dA = I_0 \cos\Theta. \tag{1.46}$$

Here $I_0(\Theta)$ is the radiant or luminous intensity of the uniform source with any constant radiance or luminance L_0. From (1.43) the radiant emittance and radiance of the uniformly emitting source or the luminous emittance and luminance are interrelated to each other by the equation:

$$M(P) = L_0 \int_{\pi} \cos\Theta d\Omega = L_0 \int \cos\Theta \, 2\pi \sin\Theta d\Theta = \pi L_0. \tag{1.47}$$

Here $d\Omega = 2\pi \sin\Theta d\Theta$ is the elementary solid angle into an angle of observation $d\Theta$ at a point P, which defines the elementary emittance dM(P). Factoring of L_0 outside the integrals in Eqs. (1.46) and (1.47) is enabled by the constancy of radiance (luminance). If Lambert's law is not satisfied, relations (1.46) and (1.47) become incorrect, and intensity and radiance are governed by relations (1.44) and (1.45).

The spatial distributions of radiance or luminance and of radiant or luminous intensity for real light sources mostly do not satisfy Lambert's law. A distinction as a function of observation direction can be defined via the *indicatrix* of a relative distribution of the radiance or luminance:

$$\gamma(\Theta) = \mathrm{L}(\Theta)/\mathrm{L}(0), \tag{1.48}$$

or via the indicatrix of relative distribution of radiation intensity:

$$\mathrm{f}(\Theta) = \mathrm{I}(\Theta)/\mathrm{I}(0), \tag{1.49}$$

where $\mathrm{L}(\Theta)$ and $\mathrm{I}(\Theta)$ are the radiance and radiant intensity in the direction of angle Θ to the outer normal to a given surface, and L(0) and I(0) are the values in the normal direction of the beam for $\Theta = 0$.

The indicatrix of either radiance (luminance) or intensity can be expressed via L_0 and I_0 magnitudes for the *isotropic diffuser*, which by analogy to the uniform source would reflect or emit optical radiation according to Lambert's law (see Eq. (1.46)), making a *Lambertian reflector or emitter*:

$$\gamma_0 = \mathrm{L}(\Theta)/\mathrm{L}_0, \tag{1.50}$$

$$\mathrm{f}_0 = \mathrm{I}(\Theta)/\mathrm{I}_0. \tag{1.51}$$

The isotropic or uniform diffuser emits the *uniformly diffused radiation*. Owing to the equivalence:

$$\mathrm{dI}(\Theta) = \mathrm{L}(\Theta)\mathrm{dA}\cos\Theta = \gamma(\Theta)\ \mathrm{L}(0)\mathrm{dA}\cos\Theta = \gamma(\Theta)\mathrm{dI}(0)\cos\Theta, \tag{1.52}$$

indicatrixes of radiance (luminance) and radiant (luminous) intensity are related by the following equations:

$$\mathrm{f}(\Theta) = \gamma(\Theta)\cos\Theta, \quad \mathrm{f}_0 = \gamma_0\cos\Theta. \tag{1.53}$$

By comparing them with the isotropic diffuser, Eqs. (1.47), (1.48) may be analogously written as:

$$I(\ell) = I(\Theta) = \int\limits_A \gamma(\Theta)L(\Theta)\cos\Theta d\Omega = \int\limits_A \gamma(\Theta)L_0\cos\Theta dA = I_0 f(\Theta), \tag{1.54}$$

$$M(P) = \int\limits_\pi \gamma(\Theta)L(\Theta)\cos\Theta d\Omega = L_0\int f(\Theta)d\Omega = L_0\Omega_e. \tag{1.55}$$

Here the integral of intensity indicatrix Ω_e is the *equivalent solid angle* containing the uniformly distributed flux of optical radiation and having a total emittance matching that of the actual source:

$$\Omega_e = \int\limits_\pi f(\Theta)d\Omega. \tag{1.56}$$

Besides a blackbody at thermodynamic equilibrium, some secondary light sources may be considered as nearly uniform emitters or diffusers, such as coatings based on barium sulfate or magnesium oxide or their compositions, and highly reflective or translucent opal glasses or polymers in reflected or in transmitted light. Some sources have almost uniform distribution not of radiance or luminance, but of radiant or luminous intensity. The spatial distribution of radiation emitted by such sources corresponds not to Lambert's law, but to Euler's law. One example of a uniform-intensity source is a mirror sphere viewed in reflected light if it is irradiated by a parallel light beam [0.1, 1.4].

Analogously to the absolutely perfect emittance of such an ideally isotropic, effective, uniform primary source of radiation as a blackbody of emissivity $\varepsilon = \alpha = 1$, the *perfect diffuser* is a model for a perfectly isotropic and effective secondary source of light of unity reflectance and uniform radiance or luminance. The perfect diffuser reflects radiation with complete reflectance $\rho = 1.0$ and at a constant radiance or luminance such that the radiant or luminous intensity in any direction Θ is $\mathrm{I}(\Theta) = \mathrm{I}_0\cos\Theta$, where the intensity I_0 in the normal direction is defined by that constant radiance L_0 over its surface A: $I_0 = \int L_0 dA$. Despite the fact that the actual light distribution and reflectance indicatrix of all known white objects deviate from the ideal model for the secondary light source providing ideal transformation factors, evaluation of discrepancies between optical properties of

existing and perfect diffusers can reasonably simplify computations of parameters of radiation reflected by such actually imperfect, but realizable objects. Therefore, in theory, the "perfect diffuser" provides support in verifying correlations among different objects themselves.

Conformity of a particular radiance or luminance profile of any actual diffuser in reference to the perfect diffuser can be identified versus either the *radiance factor* or the *luminance factor*:

$$\beta = L(\ell)/L_P(\ell). \tag{1.57}$$

The factor defines the ratio L/L_p of the radiance or luminance L of the object being studied and of the perfect diffuser L_p for equivalent irradiation or illumination settings. According to Eqs. (1.50)–(1.53), the radiance (luminance) factor relates to the indicatrix of radiance (luminance) or intensity as:

$$\beta(\Theta) = \beta(0)\gamma(\Theta) = \beta(0)\, f(\Theta)/\cos\Theta. \tag{1.58}$$

If an actual diffuser reflects or transmits optical radiation while maintaining its radiance and luminance unchanged in every direction of the hemisphere to which such radiation is being reflected and transmitted, respectively, such a diffuser is called an *isotropic diffuser* [1.5].

1.2.6 Irradiance and the Inverse-Square and Cosine Law

Let us consider a narrow beam of light emitted from element dA into solid angle $d\Omega$, crossed by two arbitrary planes A_1 and A_2, making angles Θ_1 and Θ_2 with the outer normal to the beam wave front at points P_1 and P_2 (Fig. 1.4). If we presume the beam exists in a transparent – nonabsorbing as well as nonscattering – medium, the flux $d^2\Phi$ carried by the beam over planes A_1 and A_2 is the constant of the beam, and is identified by the beam radiance L and by its geometric extent d^2G:

$$d^2\Phi = L \cdot d^2G = LdA\,\cos\Theta d\Omega = Id\Omega. \tag{1.59}$$

The solid angle $d\Omega$ filled by the beam defines the beam intensity I and is identified by the ratios:

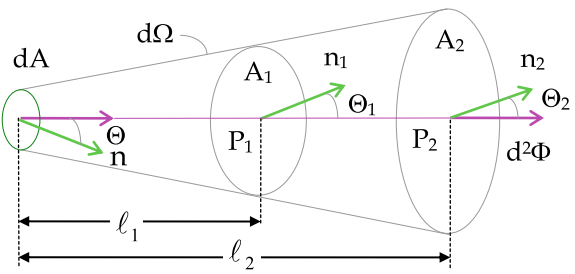

Fig. 1.4 Surface-density concept for a beam of radiation

$$d\Omega = \frac{dA_1 \cos\Theta_1}{\ell_1^2} = \frac{dA_2 \cos\Theta_2}{\ell_2^2}. \tag{1.60}$$

Since by definition (Eq. (1.20)) irradiance dΞ of a surface reached by the wave front at a point P is the ratio of the radiant (luminous) flux $d^2\Phi$ falling on that element to the element area dA, the surface irradiance (illuminance) from point P_1 to point P_2 changes according to the distance ℓ_i and the angle Θ_i:

$$\Xi(P_1) = \frac{d^2\Phi}{dA_1} = \frac{Id\Omega}{dA_1} = \frac{IdA_1 \cos\Theta_1}{dA_1\ell_1^2} = \frac{I \cos\Theta_1}{\ell_1^2}. \tag{1.61}$$

$$\Xi(P_2) = \frac{d^2\Phi}{dA_2} = \frac{Id\Omega}{dA_2} = \frac{IdA_2 \cos\Theta_2}{dA_2\ell_2^2} = \frac{I \cos\Theta_2}{\ell_2^2}. \tag{1.62}$$

Equations (1.61) and (1.62) define the main relationship in photometry and radiometry: the *inverse-square and cosine law*. Alterations of the area of an emitting or irradiated surface, created by changes in the inclination of falling rays or in the distance to the light source, cause corresponding changes of the surface density of the flux of radiation and of the irradiance or illuminance made by such a constant flux. At a constant intensity across any irradiated surface, the optical flux itself may be identified by a product of that intensity and the solid angle under which the surface is irradiated.

If a light beam is transformed by lenses or mirrors, making an intermediate image of a source of radiation, expressions (1.61) and (1.62) change. Evidently, the intensity of radiation transmitted by a lens objective I_τ or reflected by a mirror objective I_ρ is lower than the intensity of an incident beam in proportion to the transmission or reflection factor of an objective. Assuming absence of aberrations or diffraction, the radiant or luminous intensity I' of an image O' of a given point source O (Fig. 1.5) becomes:

$$I'_\tau = \tau I_\tau d\Omega_1/d\Omega_2 = \tau I_\tau(\ell_2/\ell_1)^2; \quad I'_\rho = \rho I_\rho(\ell_2/\ell_1)^2, \tag{1.63}$$

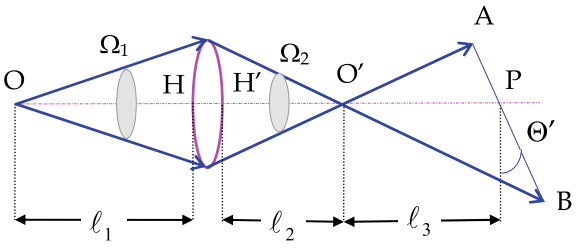

Fig. 1.5 Modification of irradiance or illuminance by a lens

where τ and ρ are the transmittance and the reflectance of each objective, respectively. The ratio of transmitted flux or the ratio of reflected flux or any extent of angular (surface) density of radiation to the incident extent give the transmission or the reflection factor. Angles Ω_1 and Ω_2 are small solid angles, under which the clear aperture of the objective is seen from the given point source O and from its image, respectively; ℓ_1 and ℓ_2 are the distances from the source O and the image O′ to principal planes H and H′ of each lens system.

The irradiance created by the secondary source O' at a point P of an imaging plane AB that makes an angle $\Theta' \neq 90°$ with the optical system axis becomes (see Eqs. (1.62), (1.63)):

$$\Xi' = \frac{I' \cos\Theta'}{\ell_3^2} = \tau I \cos\Theta' \left[\frac{\ell_2}{\ell_1 \ell_3}\right]^2 = \left[\tau \frac{\ell_2}{\ell_1}\right]^2 \frac{I \cos\Theta'}{\ell_3^2}, \tag{1.64}$$

where the multiplier in square brackets is the factor for transformation of the intensity of the source to the intensity of the image. Thus, transformation of a radiant flux by any optical system converts the inverse-square and cosine law from the space of objects to the space of images. That holds true for transformation of irradiance or illuminance by any image of any light source [0.1, 1.4].

Realization of the inverse-square and cosine law in actual photometric and radiometric experiments may be applied to confirm either calibration or evaluation of photometric accuracy of radiometers and photometers. Verifications can be made by measuring conversions of power and energy extents of radiation to corresponding responses, as functions of distances from light sources to images, or as functions of inclinations of the planes of observations. Deviations from the values predicted by law conversions identify the limits of the radiometric and photometric description, in terms of geometric optics, at which light sources can be seen as point sources at given distances.

Deviations of the inverse-square and cosine law can appear not only owing to the finiteness of the dimensions of the light sources and their images at insufficiently large distances, but also in astigmatic beams of light, for which a beam emerges as not being emitted from a single material point. For example, a homocentric physical beam of light transmitted by a border of mediums of unequal bulk indices of refraction at an angle deviating from the normal to the border becomes astigmatic (Fig. 1.6a) since the refraction of the beam takes place only in the plane containing the wave normal to the border and the incident beam. For the process of refraction for meridional beams OA and OB reaching two observation points A and B, the beams look as if they have been emitted from meridional image O'_m of light source O. Sagittal beams OA and OC appear to have been emitted from sagittal image O'_s, situated on the outer normal to adjacent border substances. Wide-beam reflection from a spherical mirror leads to similar astigmatism via two images O′ and O″ (Fig. 1.6b).

In consequence of the fact that solid angle Ω_{ast} filled by an astigmatic beam is defined by the product of the respective distances to meridional r_m and sagittal r_s images of its vertex O as:

$$d\Omega_{ast} = dA\cos\Theta/(r_m r_s), \tag{1.65}$$

the irradiance or illuminance created by such an astigmatic light beam is [0.1, 1.4]:

$$dE_{ast} = dI'\cos\Theta'/(\ell_m \ell_s). \tag{1.66}$$

Here dI' is the radiant or luminous intensity of the image, and ℓ_m and ℓ_s are the distances from the transmission or reflection image, respectively, of the source to the point of image observation.

If a light beam interacts with a border of two mediums, the law of conservation of energy:

$$M = \tau\Xi = (1 - \rho - \alpha - \sigma)\Xi, \tag{1.67}$$

$$M = \rho\Xi = (1 - \tau - \alpha - \sigma)\Xi, \tag{1.68}$$

defines losses of light intensity on the border. Here M and Ξ are the radiant or luminous emittance and the irradiance or illuminance of the border; τ and ρ are the factors of the energy transformation process of radiation at such a border, which is either transmittance or reflectance, respectively; and α and σ are the absorptance and the scattering factor of the border, considered as losses. Therefore, in expression (1.66), the radiant intensity of the image has to be considered as given by $I' = \tau I$.

In reflected light, owing to equivalence of the angles of incidence and of reflection (Fig. 1.6b):

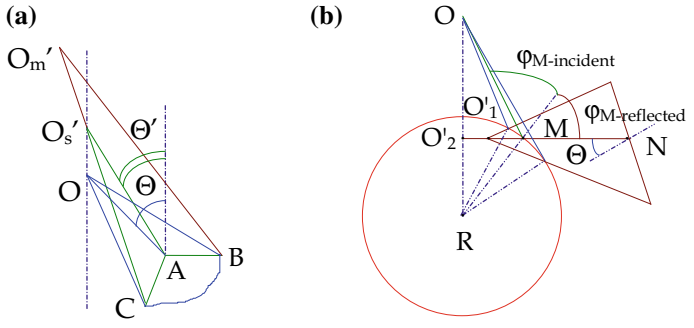

Fig. 1.6 Transformation of a homocentric beam into an astigmatic one: in transmitted (**a**) and in reflected (**b**) radiation

$$\frac{I}{OM^2} = \frac{I'}{O'_1M \cdot O'_2M}, \tag{1.69}$$

where $I' = \rho I$. According to Eq. (1.69), irradiance or illuminance E_N at arbitrary point N due to mirror astigmatism is defined by the inverse-square law, transformed via the meridional and the sagittal prolongation of the astigmatic image, formed in reflection from the spherical mirror:

$$E_N = \rho \frac{I}{OM^2} \frac{O'_1M \cdot O'_2M}{O'_1N \cdot O'_2N} \cos\Theta = \rho \frac{I}{\ell^2} \frac{r_m}{\ell_m} \frac{r_s}{\ell_s} \cos\Theta. \tag{1.70}$$

1.3 Interactions of Radiation with Material Objects

1.3.1 Factors and Coefficients of Attenuation

During propagation of radiation, any changes of its intensity, such as angular and surface density, like irradiance, illuminance, radiance, and luminance, may be caused by changes in the parameters of light beams due to refractive index transformations at medium borders. Concurrently, interactions of light with bodies, substances, or propagation mediums, in the absence of added sources of energy, inevitably cause attenuation of light intensity. Only under specially taken measures may the magnitude of attenuation be negligible.

Three fundamental mechanisms of attenuation of radiation are to be considered: reflection on borders of substances with unequal indices of refraction, absorption causing transformation of electromagnetic energy to thermal, chemical, or any other form of energy, and scattering, or diffraction, of light by the composition, inhomogeneities, and/or density fluctuations of elements of light propagation. The transmission action of a given cross section ΔX of any attenuating, but homogeneous, substance under study that interacts with optical radiation can be written as:

$$Q - Q_0 = \Delta Q = -Q\,\mu\,\Delta X, \tag{1.71}$$

where Q_0 and Q are the input and output energy for the given layer with thickness ΔX and μ is the attenuation factor dependent on the attenuation properties of the substance being studied. The negative sign indicates the decrease of energy in the interaction (the only exception is the inverted active medium, having a negative absorption coefficient due to supply of energy from external sources).

If the optical properties of irradiating substance are independent of coordinate X along length ℓ of propagation with a constant attenuation coefficient μ_ℓ, integration of Eq. (1.71) gives:

$$\int_{Q_0}^{Q} \frac{dQ}{Q} = -\int_{0}^{\ell} \mu \, dX. \tag{1.72}$$

The solution for input and output energies of radiation gives the Bouguer–Beer–Lambert law:

$$\mathrm{Q} = \mathrm{Q}_0 \exp(-\mu_\ell \, \ell). \tag{1.73}$$

If the attenuation is not a function of time, a similar dependence holds true for the power of radiation $\Phi = dW/dt$ at an arbitrary instant of time t or for a mean power over period $\Delta \mathrm{t} = \mathrm{t} - \mathrm{t}_0$:

$$\overline{\Phi}\big|_{\Delta t} = \overline{\Phi}_0\big|_{\Delta t} \exp(-\mu_\ell \ell). \tag{1.74}$$

If the attenuation factor μ varies over thickness ℓ for $\mu_\ell \neq$ const, the extinction process can be integrated:

$$Q_\ell(\lambda) = Q_0(\lambda) \exp\left[-\int_{0}^{\ell} \mu_\ell(\ell) d\ell\right]. \tag{1.75}$$

Equations (1.72)–(1.75) provide the physical sense for function μ_ℓ as the *linear attenuation coefficient* defining the energy or power loss, caused by the object being studied at a unit distance. That function determines the specific internal reduction of power or energy of radiation transmitted by a medium and the rate of its exponential decay. The units of the measurements are per meter, per centimeter, per millimeter [m^{-1}, cm^{-1}, mm^{-1}], etc.

Natural attenuation by length ℓ of an object is defined by the *Napierian optical density*:

$$\mathrm{D_N} = \mu\ell = \ln \mathrm{Q}_0 - \ln \mathrm{Q}. \tag{1.76}$$

The decimal logarithm of the ratio of two radiant fluxes or energies that are, respectively, incident upon and emerging from the object or substance defines the *optical density* of the object:

$$\mathrm{D} = \mu_d \ell = \lg(\mathrm{Q}_0/\mathrm{Q}). \tag{1.77}$$

Accordingly, μ_d is the *decimal coefficient of attenuation*. From expressions (1.74)–(1.77), it follows that:

$$\mu_d = 0.434\mu; \quad D_N = 2.303D. \tag{1.78}$$

The total loss in a beam of radiation propagating via any homogeneous object or substance that does not contain specifically reflective inclusions is due to absorption and scattering losses:

$$Q = Q_0 \exp\left[-(\alpha + \sigma)\,\ell\right]. \tag{1.79}$$

Here α is the *linear absorption coefficient* and σ is the *linear scattering coefficient*. These coefficients are defined by analogy with the linear attenuation coefficient. The scattering phenomenon is seen here as any deflection of radiation propagation from directions defined by Snell's law (Eq. 1.26) from the lines of a compass set by specular reflection at the angles opposite to the angles of light incidence: $\varphi_{ref} = -\varphi_{inc}$. Therefore, the coefficient σ characterizes the actions of inhomogeneities and fluctuations of the density of the medium or the composition of the irradiated or illuminated substance.

From the radiometric standpoint, i.e., from the point of energy transfer, which is integrated over dimensions larger than the light wavelength, the task of defining the radiation intensity totally or partially scattered into the entire reflection and transmission 4π space can be characterized by one integral scattering coefficient or factor. Such a factor at any given wavelength λ can be independent of a specific interaction phenomenon, such as a coherent light interaction without phase changes conserving the propagation direction, an incoherent interaction distributed in 4π space, or even any combination of both. In every case, only a specific localization of the scattering phenomenon is required to define the intensity commensurate with the given scattering mechanism.

If radiation is incident upon a boundary of two mediums with distinctively different indices of refraction, the change of radiation velocity can be very sharp. Alteration of the optical properties of contacting mediums is often distributed over such a small distance that the border's action may be considered to be described by a step function. Consequently, each interaction of radiation with such a border – transmission, reflection, scattering, or absorption – can be expressed by a single dimensionless factor equal to the ratio of the power, or energy, or other radiation extent (see Sect. 1.2) directly transmitted Q_τ, specularly reflected Q_ρ, absorbed Q_α, or scattered Q_σ into spherical solid angle 4π to a respective extent: flux Φ_0, energy Q_0, or other radiation extent of light incident on the border:

$$\tau_r = \frac{Q_\tau}{Q_0} = \frac{\Phi_\tau}{\Phi_0}; \quad \rho_r = \frac{Q_\rho}{Q_0} = \frac{\Phi_\rho}{\Phi_0}; \quad \alpha = \frac{Q_\alpha}{Q_0} = \frac{\Phi_\alpha}{\Phi_0}; \quad \sigma = \frac{Q_\sigma}{Q_0} = \frac{\Phi_\sigma}{\Phi_0}. \tag{1.80}$$

The factors are respectively called *the direct (regular) transmittance* (τ_r), *the direct reflectance or specular reflectance* (ρ_r), *the absorptance* (α), and *the scattering factor or total scattering factor* (σ).

The specular reflectance of a perfect, i.e. nonabsorbing and nonscattering, border of uniform and homogeneous dielectrics, is identified by the Fresnel formulae: (1.34)–(1.36). The magnitude of that reflectance depends on the relative refractive index n of two bordering dielectrics, the state of radiation polarization, and the angle of incidence of a given light beam. The relative refractive index n is a function of wavelength λ, as the respective indices of bordering dielectrics are: $n(\lambda) = n_2(\lambda)/n_1(\lambda)$. Accordingly, a beam transmitted by such an idealized border is not attenuated by nonexisting border absorption and does not contain scattered components; thus, a border transmission factor *or the transmittance* τ is equal to *the direct transmittance* τ_d defined by the ratio of the energy or power of total radiation transmitted through the border to the energy or power of the incident beam of light. According to the law of conservation of energy, in the absence of scattering and absorption on the border, that border direct transmittance $\tau_{d,ideal}$ complements its specular reflectance $\rho_{s,ideal}$ and thus $\tau_{d,ideal} = 1 - \rho_{s,ideal}$:

$$\tau_{d,ideal} + \rho_{s,ideal} = \left(Q_\tau + Q_\rho\right)/Q_\Sigma = \left(\Phi_\tau + \Phi_\rho\right)/\Phi_\Sigma \underset{\substack{\alpha \to 0 \\ \sigma \to 0}}{\equiv} 1.0. \tag{1.81}$$

The Fresnel formulae [0.3] for transmission (see Eqs. (1.34)–(1.36) for reflection) of light polarized orthogonally to the plane of incidence $\tau_\perp$, $\rho_\perp$, in the plane of incidence $\tau_\parallel$, $\rho_\parallel$, and at normal incidence of light τ_n, ρ_n (Fig. 1.7) are:

$$\tau_\perp = \frac{\sin 2\varphi_1 \sin 2\varphi_2}{\sin^2(\varphi_1 + \varphi_2)}; \tag{1.82}$$

$$\tau_\parallel = \frac{\sin 2\varphi_1 \sin 2\varphi_2}{\sin^2(\varphi_1 + \varphi_2)\cos^2(\varphi_1 - \varphi_2)}; \tag{1.83}$$

$$\tau_n \equiv \tau_0 = 4n/(n+1)^2. \tag{1.84}$$

In the absence of scattering or absorption: $\tau + \rho = 1$, the border's reflection factor is specular *reflectance* ρ_r, being the power or energy of reflected light related to the power or energy of the incident light. If radiation polarized in the plane of incidence

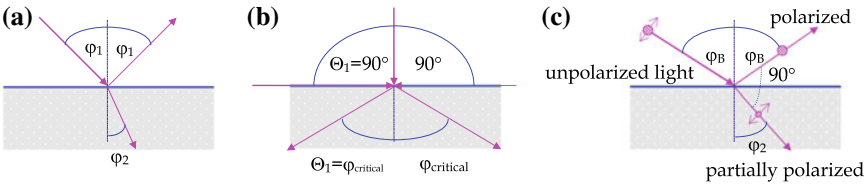

Fig. 1.7 Incidence of direct (**a**) and diffused (**b**) light on the infinite border of two dielectrics, and polarization in reflection at the Brewster angle (**c**)

is incident at the Brewster angle φ_B on the border of two dialectics with relative refractive index n, the border reflectance $\rho_{\parallel} = 0$ at:

$$\tan\varphi_B = n, \tag{1.85}$$

since at this angle (Fig. 1.7c), the reflected and the transmitted light rays are orthogonal to each other: $\sin\varphi_2 = \sin(90^\circ - \varphi_1) = \cos\varphi_1$, thus the reflected light beam has no component in the plane of incidence.

The scattering factor σ defines the ratio of the flux or energy of light scattered into spherical angle 4π related to the flux or energy of incident light. The relative intensity of light scattered by a material object backward into solid angle 2π defines the *diffuse reflectance* ρ_d. Similarly, the relative intensity of light, scattered forward into solid angle 2π, defines the *diffuse transmittance* τ_d. For the case of a mixed reflectance and transmittance, when every beam contains direct and diffuse light components, the total reflectance equals to the sum of direct and diffuse components: $\rho = \rho_r + \rho_d$, and the total transmittance is the sum of direct and diffuse factors: $\tau = \tau_r + \tau_d$, with scattering factor: $\sigma = \rho_d + \tau_d$.

When a substance exhibits some permittivity, which most optical materials do, its dielectric constant $\hat{\varepsilon}$ is a complex function of the complex phase velocity $\hat{v}$ and dielectric permeability $\hat{e}$:

$$\hat{n} = c/\hat{v} = \sqrt{\mu\hat{\varepsilon}} = n(1 + i\chi) = n - i\kappa. \tag{1.86a}$$

Here χ and κ are the attenuation or absorption index and the extinction coefficient, respectively:

$$n^2(1 - \chi^2) = \mu \cdot \varepsilon; \quad \hat{\varepsilon} = (n - i\kappa)^2. \tag{1.86b}$$

The Bouguer-Beer-Lambert law Eq. (1.73) defines the relationship between the extinction κ and absorption α coefficients of a conducting medium for angular frequency ω of incident light (see also Sect. 12.4 for details):

$$\frac{I}{I_0} = e^{-\mu\cdot\ell} = e^{-(\alpha+\sigma)\ell}; \text{ at scattering coefficient } \sigma \to 0; \alpha = \frac{2\omega}{c}n\kappa = \frac{4\pi}{\lambda_0}n\kappa = \frac{4\pi}{\lambda}\kappa, \tag{1.87}$$

where λ_0 is the wavelength of light in a vacuum; the other designations are as in Eq. (1.1). Following from Bouguer's law (Eqs. (1.73) and (1.87)), the physical quantity reciprocal to the absorption coefficient is the distance d, at which the density of the radiation energy decreases over e times:

$$d = \frac{1}{\alpha} = \frac{\lambda_0}{4n\kappa} = \frac{\lambda}{4\kappa}. \tag{1.88}$$

Therefore, at high levels of conductivity, the exponential distance $d = \alpha^{-1}$ could be much smaller than the radiation wavelength λ in the UV (ultraviolet), VIS (visible), or IR (infrared) optical domains.

When radiation is incident on a border dividing a dielectric and a conductor, the refraction law and the reflectance amplitude R versus the incident amplitude A and the state of polarization become:

$$\sin\varphi_1 = \hat{n}\sin\varphi_2; \tag{1.89}$$

$$R_{\parallel} = \frac{\tan(\varphi_1 - \hat{\varphi}_2)}{\tan(\varphi_1 + \hat{\varphi}_2)} A_{\parallel}; \quad R_{\perp} = -\frac{\sin(\varphi_1 - \hat{\varphi}_2)}{\sin(\varphi_1 - \hat{\varphi}_2)} A_{\perp}. \tag{1.90}$$

In that case, the equivalent angle of refraction $\widehat{\varphi}_2$, and, respectively, both ratios $R_{\parallel}/A_{\parallel}$ and $R_{\perp}/A_{\perp}$ are complex. The presence of absorption by a substance that interacts with light makes surfaces of constant amplitude and phase be detached from each other and refracted beams become heterogeneous; thus linearly polarized light reflected by a conductor is elliptically polarized [1.1, 1.6–1.8]. At normal incidence $R_{\parallel} = R_{\perp}$ and, similarly to (1.36), the reflectance becomes:

$$\rho_0 = \left|\frac{\hat{n} - 1}{\hat{n} + 1}\right|^2 = \frac{n^2(1 + \kappa^2) + 1 - 2n}{n^2(1 + \kappa^2) + 1 + 2n}. \tag{1.91}$$

Here n and κ are the refractive index and the extinction coefficient for wavelength λ, respectively.

1.3.2 Localized Optical Properties

Considering interactions of optical radiation with a material object, which is likely more dense than its surroundings, let us review the local properties of the object, separating surface and bulk actions. In view of various types of optical losses, the law of conservation of energy for any border of two adjacent substances (see Eq. (1.80)) becomes:

$$\rho_r + \rho_d + a + \tau_r + \tau_d \underset{\rho_d + \tau_d \equiv \sigma}{=} \rho_r + a + \sigma + \tau_r \equiv 1.0. \tag{1.92}$$

Here σ is the total scattering factor of the border given by the sum of its diffuse reflectance ρ_d and its diffuse transmittance τ_d. The total scattering factor defines the ratio of the energy or power extent of the radiation scattered at the border into 4π spherical space to the incident energy, except in the directions of direct transmission and specular reflection. Subsequently, any act of interaction of radiation with a material object under study can be characterized by a total attenuation factor γ. By that definition, the transformation factor K of the light's interaction with the border is $K = 1 - \gamma$.

The action of all local and bulk factors and coefficients for the direct propagation of a beam of radiation by a contingent totality of several homogeneous plain elements may be given as a sum:

$$\begin{aligned} \mathrm{Q}_{\tau,m} &= Q_0 \prod_{i=1;j=1}^{m+1} \tau_{i,j} \exp[\sum_{i=1}^{m} (-\mu_i \ell_i)] \\ &= Q_0 \prod_{i=1;j=1}^{m+1} [1 - (\rho_r)_{i,j} - (\rho_d)_{i,j} - a_{i,j} - (\tau_d)_{i,j}] \exp(-\sum_{i=1}^{m} \mu_i \ell_i), \end{aligned} \tag{1.93}$$

where index i refers to the uniform and homogeneous i^{th} layer of any given substance or element, indices i and j correspond to a border of i^{th} and j^{th} elements, and m is the number of elements. Identifying the total factors and the average bulk attenuation coefficient $\bar{\mu}$, (1.93) transforms to:

$$Q_{\tau,m} = Q_0 \tau_\Sigma \exp(-\Sigma \mu_i \ell_i) = Q_0 (1 - \rho_{r\Sigma} - \alpha_\Sigma - \sigma_\Sigma) \exp(-\bar{\mu} \ell_\Sigma). \tag{1.94}$$

Let us separate every action and consider transmission of light via a relatively thin sample of a transparent dielectric in any dielectric homogeneous surrounding medium. The accepted designation of the "transparent" sample presumes its scattering and absorption losses are low in comparison with the regular reflectance for each flat homogeneous sample surface: front and back, with the direct transmittance through the entire sample. Let us characterize three possible configurations of the front and of the back surface for that sample (Fig. 1.8a–c): (a) – infinitely large, in comparison with the beam dimensions, but not parallel to each other; (b) – parallel to each other, but not perpendicular to the optical axis of the beam; and (c) – parallel to each other and perpendicular to the optical axis of the light beam incident on that sample.

For a small angle of incidence, in each configuration of a dimensionally unrestricted plate, either the transmitted or the reflected beam contains an infinite sequence of individual components of retroreflected light with amplitudes dependent on the reflectance ρ of the sample surfaces, the linear attenuation coefficient μ of the sample bulk and its length ℓ_i, and a number of notable reflections, defined by the sensitivity of the relative intensity measurements. The first component in the transmission semispace represents the light beam transmitted directly:

$$\mathrm{Q}_{\tau 1} = \mathrm{Q}_0 (1 - \rho) \exp(-\mu \ell_1)(1 - \rho) \equiv \mathrm{Q}_0 (1 - \rho)^2 \tau_1. \tag{1.95}$$

The first component in the reflection semispace is due to specular reflection on the front surface:

$$\mathrm{Q}\rho_1 = \mathrm{Q}_0 \rho. \tag{1.96}$$

In Eq. (1.95) τ_1 is the internal transmittance of the sample bulk for thickness ℓ_1. The second pair of components is defined by light retroreflected twice within the sample's bulk and transmitted through the sample:

$$Q_{\tau 2} = Q_0(1-\rho)^2\tau_1\tau_2\tau_3\rho^2, \tag{1.97}$$

and by light transmitted twice via the first surface after being reflected from the second surface:

$$Q_{\rho 2} = Q_0(1-\rho)^2\tau_1\tau_2\rho. \tag{1.98}$$

The m^{th} components of the sample as a plate with flat front and back surfaces are:

$$Q_{\tau m} = Q_0(1-\rho)^2\rho^{2m}\exp[-(2m+1)\mu\ell_{2m+1}]; \tag{1.99a}$$

$$Q_{\rho m} = Q_0(1-\rho)^2\rho^{2m+1}\exp[-2(m+1)\mu\ell_{2(m+1)}]. \tag{1.99b}$$

In Fig. 1.8a, the first transmitted beam is incident normally on the first surface of the plate, having relative refractive index n, and reaches the second surface at angle Θ', passing through at angle: $\varphi_1 = \arcsin(n \cdot \sin\Theta) - \Theta$. The second component, which goes via two reflections, is deflected at angle $\varphi_2 = \arcsin(3n \cdot \sin\Theta) - \Theta$, the third component is deflected at angle $\varphi_3 = \arcsin(5n \cdot \sin\Theta) - \Theta$, etc., until total internal reflection occurs. Analogously, in reflection the beams diverge at incidence on the wedge-shaped plate at expanding angles $\varphi_1, \varphi_2, \ldots$. In the case of oblique incidence onto the plane-parallel plate depicted in Fig. 1.8b, the direction of the transmitted beam having 2 m refractions remains unchanged with respect to direction of the incident beam. After the first displacement during beam propagation, the beam is displaced at every cycle of two retroreflections by the double distance d:

$$d = 2\ell tg\varphi' \cos\varphi = 2\ell \sin\varphi\left(1 - \frac{n\cos\varphi}{n'\cos\varphi'}\right) \underset{\varphi\to 0}{\cong} 2\ell\sin\varphi. \tag{1.100}$$

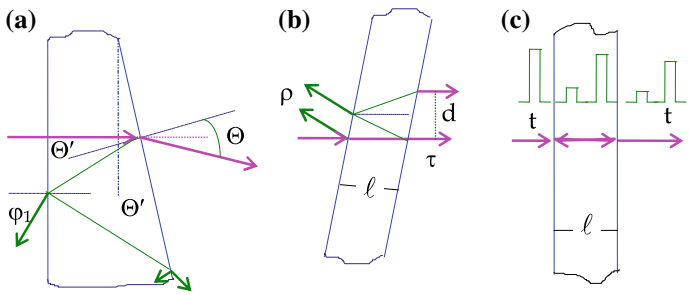

Fig. 1.8 Propagation of a light beam via a single, variously-shaped sample **a** wedged; **b** and **c** plane-parallel tilted and perpendicular to the beam axis

In every configuration it is possible to separate each spatially distributed component, or at least some of them, by using apertures and detectors. The intensity I_ρ of the beam reflected at angle φ by the first surface with reflectance ρ_φ is $I_\rho = I_0\rho_\varphi$, where l_0 is the intensity of the incident radiation. The single-pass transmittance of a plate of length ℓ and internal bulk loss μ irradiated at angle φ is:

$$\tau_{\mathrm{pl-par,single}} = \frac{I_{\tau,\mathrm{single}}}{I_0} = (1-\rho_\varphi)\,\exp(-\mu\ell)(1-\rho_\varphi) \underset{\mu\to 0,\ell\to 0}{=} (1-\rho)^2. \quad (1.101)$$

Imagining a semi-space wide detector, which collects all retro-reflected components at infinite number of inner-sample reflections $m \to \infty$, the total reflectance and total transmittance respectively are:

$$\tau_\Sigma = \frac{(1-\bar{\rho})^2\exp(-\bar{\mu}\ell_\tau)}{1-\bar{\rho}^2\exp(-2\bar{\mu}\bar{\ell})}, \quad (1.102)$$

$$\rho_\Sigma = \rho\left\{1+\frac{(1-\bar{\rho})^2\,\exp[-\bar{\mu}(\ell_\tau+\ell_r)]}{1-\bar{\rho}^2\,\exp(-2\bar{\mu}\bar{\ell})}\right\}, \quad (1.103)$$

where the additive summation law applies and $\bar{\rho}$ is the mean reflectance averaged from the angle of incidence Θ to the angle of total internal reflection $\Theta' = \arcsin(1/n)$; ℓ_τ and ℓ_ρ are, respectively, the length of the first radiation pass in transmission and the length in reflection from the second to the first sample surface, $\bar{\ell}$ is the average length of the internal pass via the sample bulk, and $\bar{\mu}$ is the average linear bulk attenuation coefficient for the sample material.

In Fig. 1.8c, a quasi-parallel beam of light is incident on the plane-parallel plate as its wave normal; thus, multiple reflected light components propagate via the normal-to-plate direction. Both transmittance and reflectance of the dielectric plate are sums of retroreflected light components:

$$\tau_{\Sigma,n} = \frac{(1-\rho_0)^2\,\exp(-\mu\ell_0)}{1-\rho_0^2\,\exp(-2\mu\ell_0)}, \quad (1.104)$$

$$\rho_{\Sigma,n} = \rho\left[1+\frac{(1-\rho)^2\,\exp(-2\mu\ell_0)}{1-\rho_0^2\,\exp(-2\mu\ell_0)}\right], \quad (1.105)$$

where ℓ_0 and ρ_0 are the plate thickness and its surface reflectance at normal incidence. If $\mu\ell_\Sigma \ll \rho_0$, making the internal loss inside the sample negligibly low in comparison with the surface reflectance, the low-bulk-loss equations for the total transmittance and total reflectance of the plate are:

$$\tau_n = \frac{(1-\rho_0)^2}{1-\rho_0^2} = \frac{1-\rho_0}{1+\rho_0}, \tag{1.106}$$

$$\rho_n = \frac{2\rho_0}{1+\rho_0}. \tag{1.107}$$

Either single-pass transmittance or single reflectance of any plane-parallel plate at normal incidence may only be distinguished in space if the multiple reflection factor $\rho_0^2 \exp(-2\mu\ell)$ is negligibly low. If internal multiple reflections do contribute to the entire-plate reflectance, each retroreflected component may be separated in time (see Fig. 1.8c). If the duration t_p of a light pulse is shorter than the time interval needed for the pulse to pass the plate twice: $t_p < 2n\ell_0/c$, every beam reflected by either the front or the back surface can be separated with sufficient time resolution.

1.3.3 Multiple Optical Elements

Let us consider interactions of a beam of light of low divergence with a set of parallel optical elements, such as plane-parallel plates of an identical material, having refractive index $n \geq 1$ and identical thickness ℓ (Fig. 1.9). Equations (1.71)–(1.79) and (1.94)–(1.99) can be rewritten for the incident beam intensity I_0 by assigning a single transmission factor $\tau_{int,\varphi}$ describing attenuation via one internal pass of each single plate at any defined angle of light incidence φ, as well as individual reflection and transmission factors ρ_φ and τ_φ defining a plate surface interaction with light at the angle φ. Considering one pile of consecutive parallel plates, unchanged in relation to the positions of transmitted and reflected beams, the equations are:

$$\begin{aligned}
I_{\tau,1} &= I_0\tau_\varphi\tau_{int,\varphi}\tau_\varphi = I_0(1-\rho_\varphi)^2\tau_{int,\varphi}; \quad I_{\tau,2} = I_0(1-\rho_\varphi)^2\tau_{int,\varphi}\times\rho_\varphi^2\tau_{int,\varphi}^2;\\
I_{\tau,n} &= I_0(1-\rho_\varphi)^2\left(\rho_\varphi^2\tau_{int,\varphi}^2\right)^{n-1};\\
I_{\rho,1} &= I_0\rho_\varphi; \quad I_{\rho,2} = I_0(1-\rho_\varphi)^2\tau_{int,\varphi}^2\rho_\varphi; \quad I_{\rho,3} = I_0(1-\rho_\varphi)^2\tau_{int,\varphi}^2(\tau_{int,\varphi}\rho_\varphi)^2\rho_\varphi;\\
I_{\rho,n} &= I_0(1-\rho_\varphi)^2\left(\rho_\varphi^2\tau_{int,\varphi}^2\right)^{n-1}\rho_\varphi.
\end{aligned} \tag{1.108}$$

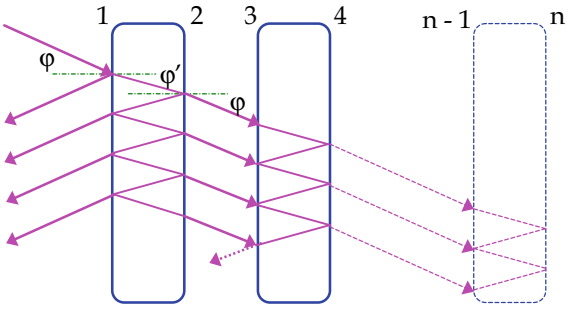

Fig. 1.9 Transmission and reflection beams via a pile of plates

Assuming all plates to be infinitely large at $\tau_\varphi < 1$, $\rho_\varphi < 1$, the intensity of the beam eventually decays to $I = 0$, and presuming the law of additive summation to be valid (see Chap. 3 for interference-bound computations and effects), the total transmitted and reflected intensities for the plate are:

$$\begin{aligned} I_{\tau,1-2,ad} &= I_0\tau_{1-2,\varphi} = I_0(1-\rho_\varphi)^2\left[\tau_{\text{int},\varphi}\left(1+\rho_\varphi^2\tau_{\text{int},\varphi}^2+\cdots+\rho_\varphi^{2(n-1)}\tau_{\text{int},\varphi}^{2(n-1)}\right)\right] \\ &= I_0(1-\rho_\varphi)^2\frac{\tau_{\text{int},\varphi}}{1-\rho_\varphi^2\tau_{\text{int},\varphi}^2}; \end{aligned}$$

$$\begin{aligned} I_{\rho,1-2,ad} &= I_0\rho_{1-2,\varphi} = I_0\left[\rho_\varphi+(1-\rho_\varphi)^2\tau_{\text{int},\varphi}^2\rho_\varphi+(1-\rho_\varphi)^2\tau_{\text{int},\varphi}^2\rho_\varphi^2\tau_{\text{int},\varphi}^2\rho_\varphi+\cdots\right] \\ &= I_0\rho_\varphi\left[1+(1-\rho_\varphi)^2\frac{\tau_{\text{int},\varphi}^2}{1-\rho_\varphi^2\tau_{\text{int},\varphi}^2}\right] = I_0\rho_\varphi\frac{1+(1-2\rho_\varphi)\tau_{\text{int},\varphi}^2}{1-\rho_\varphi^2\tau_{\text{int},\varphi}^2}. \end{aligned} \tag{1.109}$$

Note that at $\tau_{\text{int},\varphi} \to 1$, Eqs. (1.109) for the beams transmitted and reflected by each plate at angle φ converge to (1.106) and (1.107) for the total transmittance and reflectance of the plate at normal incidence:

$$\begin{aligned} I_{\tau,plate,ad} &\underset{\tau_{\text{int}}\to 1}{=} I_0\frac{(1-\rho_\varphi)^2}{1-\rho_\varphi^2} = I_0\frac{1-\rho_\varphi}{1+\rho_\varphi}; \\ I_{\rho,plate,ad} &\underset{\tau_{\text{int}}\to 1}{=} I_0\rho_\varphi\frac{1+(1-2\rho_\varphi)}{1-\rho_\varphi^2} = I_0\frac{2\rho_\varphi}{1+\rho_\varphi}. \end{aligned} \tag{1.110}$$

When light exits the first plate and is reflected from and transmitted by the first surface of the second plate (plane 3, Fig. 1.9), light transformation can be viewed as the combined action of surfaces 1 and 2 with known factors $\tau_{1-2,\varphi}$ and $\rho_{1-2,\varphi}$ and of surface 3 for reflected and transmitted intensities:

$$\begin{aligned} I_{\tau,1-2-3,ad} &= I_0\tau_{1-2-3,\varphi} = I_0\tau_{1-2,\varphi}\left(\tau_{3,\varphi}+\tau_{3,\varphi}\rho_{1-2,\varphi}\rho_{3,\varphi}+\cdots\right) \\ &= I_0\frac{\tau_{1-2,\varphi}\tau_{3,\varphi}}{1-\rho_{1-2,\varphi}\rho_{3,\varphi}} \underset{\tau_{\text{int}}\to 1}{=} I_0\left(\frac{1-\rho_\varphi}{1+\rho_\varphi}\right)\frac{1-\rho_\varphi}{1-2\rho_\varphi^2/(1+\rho_\varphi)}; \\ I_{\rho,1-2-3,ad} &= I_0\rho_{1-2-3,\varphi} = I_0\left(\rho_{1-2,\varphi}+\frac{\tau_{1-2,\varphi}^2\rho_{3,\varphi}}{1-\rho_{1-2,\varphi}\rho_{3,\varphi}}\right) \\ &\underset{\tau_{\text{int}}\to 1}{=} I_0\left(\frac{2\rho_\varphi}{1+\rho_\varphi}+\frac{\left[(1-\rho_\varphi)/(1+\rho_\varphi)\right]^2\rho_\varphi}{1-2\rho_\varphi^2/(1+\rho_\varphi)}\right). \end{aligned} \tag{1.111}$$

Presuming the additive summation of retroreflected components, the intensities in transmission and reflection for the first two infinite plates are:

$$
\begin{aligned}
I_{\tau,1-4,ad} &= I_0\tau_{1-4,\varphi} = I_0\tau_{1-2-3,\varphi}\left(\tau_{\mathrm{int},\varphi}\tau_{4,\varphi} + \rho_{4,\varphi}\tau^2_{\mathrm{int},\varphi}\rho_{1-2-3,\varphi}\tau_{\mathrm{int},\varphi}\tau_{4,\varphi} + \cdots\right)\\
&= I_0\frac{\tau_{1-2-3,\varphi}\tau_{\mathrm{int},\varphi}\tau_{4,\varphi}}{1-\rho_{1-2-3,\varphi}\tau^2_{\mathrm{int},\varphi}\rho_{4,\varphi}};\\
I_{\rho,1-4,ad} &= I_0\rho_{1-4,\varphi} = I_0\left(\rho_{1-2-3,\varphi} + \left(1-\rho_{1-2-3,\varphi}\right)^2\tau^2_{\mathrm{int},\varphi}\rho_{4,\varphi} + \cdots\right)\\
&= I_0\left(\rho_{1-2-3,\varphi} + \frac{\tau^2_{1-2-3,\varphi}\tau^2_{\mathrm{int},\varphi}\rho_{4,\varphi}}{1-\rho_{1-2-3,\varphi}\tau^2_{\mathrm{int},\varphi}\rho_{4,\varphi}}\right).
\end{aligned}
\tag{1.112}
$$

Another way of seeing the action of four surfaces is by considering them as two plates at $\tau_{\mathrm{int},\,\varphi} \equiv 0$:

$$
\begin{aligned}
I_{\tau,1-4,ad} &\underset{\tau_{\mathrm{int}}\to 1}{=} I_0\frac{\tau_{1-2,\varphi}\tau_{1-2,\varphi}}{1-\rho_{1-2,\varphi}\rho_{1-2,\varphi}} = I_0\left(\frac{1-\rho_\varphi}{1+\rho_\varphi}\right)^2\frac{1}{1-\left(2\rho_\varphi/\left(1+\rho_\varphi\right)\right)^2}\\
&= I_0\frac{\left(1-\rho_\varphi\right)^2}{\left(1-\rho_\varphi\right)^2-4\rho_\varphi^2} = I_0\frac{1-\rho_\varphi}{1+3\rho_\varphi};\\
I_{\rho,1-4,ad} &\underset{\tau_{\mathrm{int}}\to 1}{=} I_0\left(1-I_{\tau,1-4,ad}\right) = I_0\left(1-\frac{1-\rho_\varphi}{1+3\rho_\varphi}\right) = I_0\frac{4\rho_\varphi}{1+3\rho_\varphi}.
\end{aligned}
\tag{1.113}
$$

Let us now rewrite Eq. (1.111) for three identical reflective surfaces with the same reflectance ρ_φ:

$$
\begin{aligned}
I_{\tau,1-2-3,ad} &\underset{\tau_{\mathrm{int}}\to 1}{=} I_0\left(\frac{1-\rho_\varphi}{1+\rho_\varphi}\right)\frac{1-\rho_\varphi}{1-2\rho_\varphi^2/\left(1+\rho_\varphi\right)} = I_0\frac{1-\rho_\varphi}{1+\rho_\varphi}\frac{\left(1-\rho_\varphi\right)\left(1+\rho_\varphi\right)}{1+\rho_\varphi-2\rho_\varphi^2}\\
&= I_0\frac{\left(1-\rho_\varphi\right)^2}{1-\rho_\varphi^2+\rho_\varphi-\rho_\varphi^2} = I_0\frac{1-\rho_\varphi}{1+2\rho_\varphi};\\
I_{\rho,1-2-3,ad} &\underset{\tau_{\mathrm{int}}\to 1}{=} I_0\left(1-\frac{1-\rho_\varphi}{1+2\rho_\varphi}\right) = I_0\frac{3\rho_\varphi}{1+2\rho_\varphi}.
\end{aligned}
\tag{1.114}
$$

One can see the particular tendency from Eq. (1.110) to (1.114) and in (1.113) at $m \to \infty$, $\tau_{\mathrm{int}} \to 1$, whereas the straightforward solutions [1.9–1.21] can be derived by considering either interactions of dual sets of surfaces M =1, 2, … for the respective plate sets N =1, 2, … [1.9, 1.14] or by resolving the determinant for the sequence of 2 m single parallel surfaces [1.11, 1.18]:

$$
I_{\tau,\varphi,n} \underset{\tau_{\mathrm{int}}\to 1}{=} I_0\frac{1-\rho_\varphi}{1+(m-1)\rho_\varphi};\quad I_{\rho,\varphi,n} \underset{\tau_{\mathrm{int}}\to 1}{=} I_0\frac{m\rho_\varphi}{1+(m-1)\rho_\varphi},
\tag{1.115}
$$

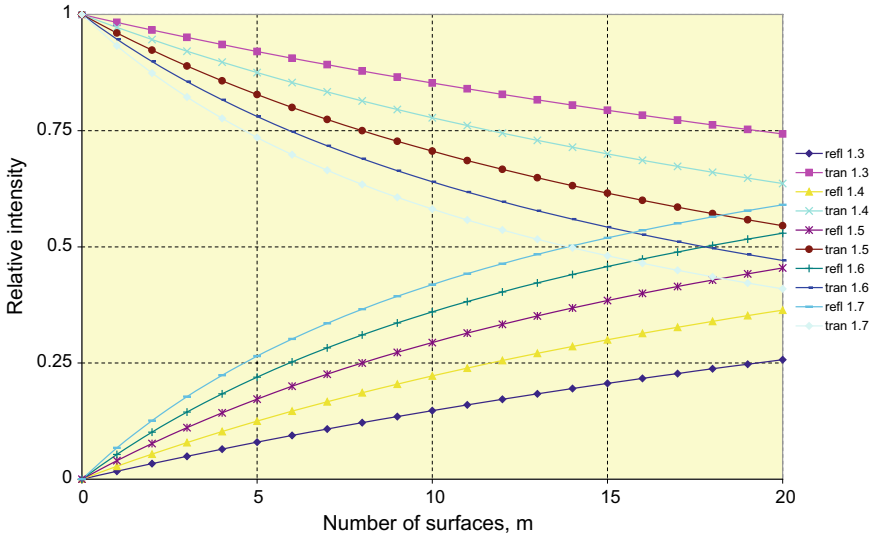

Fig. 1.10 Transmittance-reflectance of a pile of parallel-plate plates for refractive index from 1.3 to 1.7 n steps of 0.1

where m is the number of infinitely wide nonabsorbing and nonscattering surfaces divided by the transparent plate's bulk or by the plate's separation distance in the nonattenuating air. Figure 1.10 shows the transmittance and reflectance of a pile of plane-parallel plates versus the number of surfaces in the pile and versus the change of the refractive index of the plate's internal bulk.

1.3.4 Diffuse Irradiation

Previously, optical radiation interacting with any material object was viewed as quasi-parallel physical beams of light of low divergence. Uniformly diffused radiation of intensity I given by Eq. (1.46) defines spatially symmetric propagation opposite to the light-ray concept. Owing to defined spatial symmetry, the parameters of uniformly diffused beams of radiation and the optical characteristics of material objects – transmittance, reflectance, scattering factor – can be determined by spatial integration of light beams in all possible directions for 2π or 4π space.

Consider a point source of uniformly diffused radiation (see Fig. 1.7b) emitting at constant radiance or luminance L in any arbitrary direction and to which an infinite plane in the far field is exposed. Let us presume that the intensity distribution of radiation conforms to Lambert's law (relations (1.46), (1.47)). If such an isotropic source irradiates an infinite border of two homogeneous dielectrics, either the modification factor of the border or its optical response does not depend on the coordinates of the irradiated points. Thus, it is sufficient to determine the surface transmittance

and reflectance for the single and arbitrary radiating elementary flux $d\Phi$. Using the conversion of solid angle $d\Omega$ in Eq. (1.47) as a function of the vertex angle Θ of a light cone (cone of radiation): $d\Omega = 2\pi \sin\Theta d\Theta$, and integrating all radiation components emitted from a platform dA within the limits: $0 \leq \Theta \leq \pi/2$, the entire radiant or luminous flux irradiated by every elementary source of the platform dA is:

$$d\Phi = \int_{\Omega} d^2\Phi = 2\pi LdA \int_0^{\pi/2} \cos\Theta \sin\Theta d\Theta = \pi LdA. \tag{1.116}$$

The total elementary flux reflected by that infinite border with specular reflectance $\rho = \rho(\Theta, n)$ is:

$$d\Phi_{\rho}^{d} = 2\pi LdA \int_0^{\pi/2} \rho(\Theta, n) \cos\Theta \sin\Theta d\Theta, \tag{1.117}$$

where n is the relative index of refraction for a chosen monochromatic component of radiation.

Consequently, the *diffuse reflectance* of an object can be defined as the reflectance on either irradiation or observation within 2π-angle of the irradiation or observation semispace, which is:

$$\rho^d = d\Phi_{\rho}^{d}/d\Phi = 2 \int_0^{\pi/2} \rho(\Theta, n) \cos\Theta \sin\Theta d\Theta. \tag{1.118}$$

The components of the diffuse reflectance for S and P polarization, namely S and P *diffuse reflectance*, for light polarized either in the parallel or in the perpendicular plane to the plane of incidence are [1.4]:

$$\begin{aligned} \rho_S^d = \rho_{\parallel}^d &= 2 \int_0^{\pi/2} \frac{tg^2(\Theta_1 - \Theta_2)}{tg^2(\Theta_1 + \Theta_2)} \cos\Theta_1 \sin\Theta_1 d\Theta \\ &= \frac{n^7(n-4) - 8n^5(n-1) + 2n^3(3n-2) + 1}{(n^4-1)^2} \\ &\quad + \frac{16n^4(n^4+1)}{(n^4-1)^2(n^2+1)} \ln n - \frac{2n^2(n^2-1)^2}{(n^2+1)^3} \ln\left(\frac{n+1}{n-1}\right), \end{aligned} \tag{1.119}$$

$$\rho_P^d = \rho_{\perp}^d = 2 \int_0^{\pi/2} \frac{\sin^2(\Theta_1 - \Theta_2)}{\sin^2(\Theta_1 + \Theta_2)} \cos\Theta_1 \sin\Theta_1 d\Theta = \frac{(n-1)(3n+1)}{3(n+1)^2}. \tag{1.120}$$

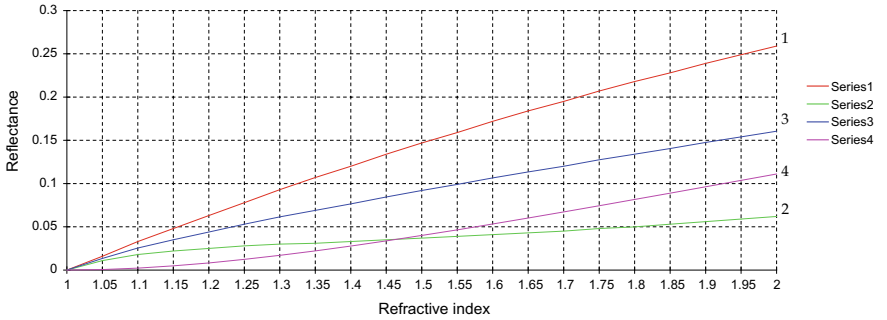

Fig. 1.11 surface reflectance of a glass plate at diffused irradiation 1-s polarization, 2-p polarization, 3-unpolaried light, 4-direct irradiation

The reflectance of an infinitely-wide plane surface: $\rho_U^d = (\rho_S^d + \rho_P^d)/2$, for unpolarized diffuse irradiation follows its specular reflectance for direct irradiation as a function of the refractive index n (Fig. 1.11).

In the $1.4 < n < 1.8$ range, the diffuse and specular reflectance are different by a nearly constant term:

$$\rho_U^d \cong \rho_r^{dir.} + 0.05. \tag{1.121}$$

The transmittance of an infinite plane-parallel plate for uniformly diffused irradiation is affected by internal multiple reflections. Assuming ideal transparency of the plate's bulk for diffuse irradiation by flux $d\Phi = \pi L dA$, hemispherical integration similarly identifies the total diffuse transmittance of the plate:

$$\tau_{pl.}^d = 2\int_0^{\pi/2} \frac{[1-\rho(\Theta,n)]^2}{1-\rho^2(\Theta,n)} \cos\Theta \, \sin\Theta \, \mathrm{d}\Theta = 2\int_0^{\pi/2} \frac{1-\rho(\Theta,n)}{1+\rho(\Theta,n)} \cos\Theta \, \sin\Theta \mathrm{d}\Theta. \tag{1.122}$$

The plate diffuse-transmittance components for S and P polarization respectively become [1.4]:

$$\tau_{pl.P}^d = \tau_\perp^d = 2\int_0^{\pi/2} \frac{\sin^2(\Theta_1+\Theta_2) - \sin^2(\Theta_1-\Theta_2)}{\sin^2(\Theta_1+\Theta_2) + \sin^2(\Theta_1-\Theta_2)} \cos\Theta_1 \, \sin\Theta_1 d\Theta \tag{1.123}$$
$$= n - (n^2-1)\arctan(1/n),$$

$$\tau_{pl.S}^d = \tau_{||}^d = 2\int_0^{\pi/2} \frac{\tan^2(\Theta_1+\Theta_2) - \tan^2(\Theta_1-\Theta_2)}{\tan^2(\Theta_1+\Theta_2) + \tan^2(\Theta_1-\Theta_2)} \cos\Theta_1 \, \sin\Theta_1 d\Theta$$
$$= \frac{2n^3}{n^4+1} - \frac{4n^4(n^2-1)}{(n^4+1)^2}\arctan n + \frac{n^2(n^2-1)(n^4-1)}{(n^4+1)^2}\ln\frac{n+1}{n-1}. \tag{1.124}$$

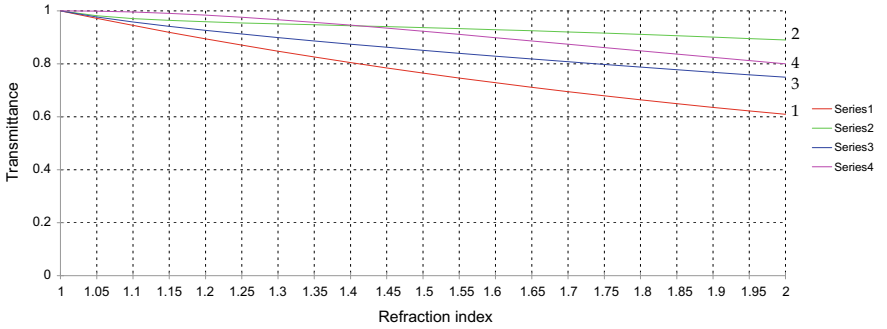

Fig. 1.12 Transmittance of a plane-parallel plate at uniformly diffused irradiation 1-s polarization, 2-p ppolarization, 3-unpolarized light, 4-direct transmittance of the plate

The diffuse transmittance functions of a plane-parallel plate versus the plate's refractive index are seen in Fig. 1.12. The graphs also show the plate's average transmittance (line 3): $\bar{\tau}^{d}_{pl.} = (\tau^{d}_{pl.S.} + \tau^{d}_{pl.P})/2$, and the direct (not diffuse) transmittance $\tau^{dir.}_{pl.}$ of such a plate (line 4) for comparison.

The internal attenuation coefficient μ of any homogeneous infinite layer of an absorbing or a scattering substance which is irradiated by the uniformly diffused light can be identified as:

$$\tau^{d}_{\text{int.}} = 2\int_{0}^{\pi/2} \exp(-\mu\ell/\cos\Theta)\cos\Theta\,\sin\Theta d\Theta$$
$$= (1-\mu\ell)\,\exp(-\mu\ell) + \mu^2\ell^2\int_{\mu l}^{\infty}\frac{\exp(-t)dt}{t}. \qquad (1.125)$$

Solutions for Eq. (1.125) can be found by numerical integration of the exponential function for variable $t = \mu\ell/\cos\Theta$. If the optical density $\mu\ell$ of the internal layer is small, an approximate solution is:

$$\tau^{d}_{\text{int.}transp.} \cong (1-\mu\ell)\exp(-\mu\ell) \cong (1-\mu\ell)^2 \cong 1 - 2\mu\ell. \qquad (1.126)$$

Consequently [1.4], the total internal attenuation factor for the uniformly diffused radiation in a transparent, i.e., nonabsorbing and nonscattering substance, is only about 2 times higher than the total internal attenuation factor for direct radiation having the same spectral composition.

If integral properties of one diffusely irradiated plate are known, behavior of a pile of plates are defined by Eqs. (1.108)–(1.115). For i + 1 infinitely wide plates at i^{th} diffuse transmittance $\tau_{i,d}$ and reflectance $\rho_{i,d}$, single-surface factors $\tau_s = 1 - \rho_s$, bulk

thicknesses ℓ and linear attenuation coefficient μ being under the uniform diffuse irradiation, transmittance and reflectance become:

$$\begin{aligned}\tau_{i+1,d} &= \frac{\tau_{i,d}\tau_{\text{int},d}(1-\rho_s)^2}{1-\rho_{i,d}\tau_{\text{int},d}^2\rho_s} = \frac{\tau_{i,d}\tau_d}{1-\rho_{i,d}\rho_d};\\ \rho_{i+1,d} &= \rho_{i,d} + \frac{\tau_{i,d}^2\tau_{\text{int},d}^2\rho_s}{1-\rho_{i,d}\tau_{\text{int},d}^2\rho_s} = \rho_{i,d} + \frac{\tau_{i,d}^2\rho_d}{1-\rho_{i,d}\rho_d}.\end{aligned} \tag{1.127}$$

The equations for the diffuse transmittance and reflectance of a pile of plates are quite elaborate [1.12–1.18]. Nevertheless, on the basis of the observation that for tending-to-infinity number i of plates the pile reflectance reaches its maximum: $\rho_{\max,i+1} \underset{i\to\infty}{\to} \rho_{\max,i}$, Eq. (1.127) for the diffuse reflectance of the pile can be rewritten by swapping the $(i+1)^{\text{th}}$ pile and the $(1+i)^{\text{th}}$ one, and thus [1.13]:

$$\begin{aligned}\rho_{pile,i+1,d} &= \rho_d + \frac{\tau_d^2\rho_{i,d}}{1-\rho_d\rho_{i,d}} \underset{i\to\infty}{\equiv} \rho_{i,d};\\ \rho_{pile\,\max,d} &= \frac{\left(1-\tau_d^2+\rho_d^2\right) - \sqrt{\left(1-\tau_d^2+\rho_d^2\right)^2 - 4\rho_d^2}}{2\rho_d}.\end{aligned} \tag{1.128}$$

Besides extreme cases of direct and diffuse irradiation or reception, in many instances other mixed conditions may be realized. Figure 1.13 illustrates intermediate settings of the incident (view *a*) and reflected (view *b*) geometry of light irradiation and observation, being not strictly direct or uniformly diffused (similar conditions occur in transmitted radiation). Respective modification factors for the intensity of radiation in these settings can be derived from known ones, not necessarily remaining constant under various irradiation and reception conditions.

The model-based reflectance of the perfect diffuser does not depend on the irradiation settings, such that the amount of light reflected by the perfect diffuser and dispersed into any solid angle $\Omega \leq 2\pi$ depends only on the magnitude of the angle. Conversely, for diffuse irradiation of a regular object, not only reflectance and transmittance, but also the geometry of the irradiation and of the observation define this object transformation factor. Consider element dA of an opaque surface

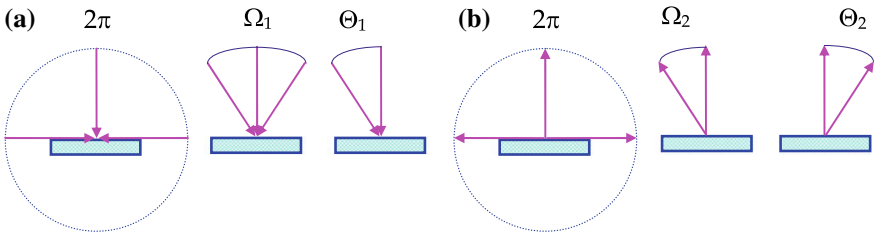

Fig. 1.13 Diffused irradiation (**a**) and reception (**b**)

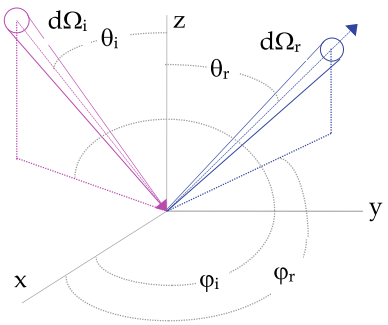

Fig. 1.14 Bidirectional reflectance settings

irradiated by a light beam at constant radiance L_i within solid angle Ω_i in the direction specified by elevation Θ_i and azimuth φ_i angles (Fig. 1.14). The radiant flux $d\Phi_i$ incident on the surface element dA is: $d\Phi_i = L_i \cos\Theta_i \cdot dA d\Omega_i = L_i \cdot dA d\Omega_i'$, where $d\Omega_i'$ can be viewed as the projected solid angle [0.1, 0.12]. The radiation flux $d\Phi_r$ reflected to elementary solid angle $d\Omega_r$ in direction Θ_r, φ_r respectively is: $d\Omega_r = L_r dA d\Omega_r'$, where L_r is the reflected elementary radiance of irradiated surface in a given direction. By definition, the reflectance ρ_r of element dA directed into elementary solid angle $d\Omega_r$ is:

$$\rho_r = d\Phi_r/d\Phi_i = L_r d\Omega_i'/L_i d\Omega_i' = \left(L_r/L_i d\Omega_i'\right) d\Omega_i' \equiv \rho_b(\Theta_i, \varphi_i, \Theta_r, \varphi_r) d\Omega_i', \tag{1.129}$$

and describes the properties of the surface element and the geometry of irradiation and observation.

Here the sign $\equiv$ introduces the bidirectional reflectance ρ_b, defining such a reflectance of an opaque surface per unit solid angle in observation space. That function of irradiation and reception geometry is identified as the *bidirectional reflectance distribution function* (BRDF) [1.22]. The analogous bidirectional transmission function can be introduced for translucent objects. By definition, the bidirectional reflectance distribution function defines the radiance to irradiance ratio of any irradiated surface: $\rho_b = dL_r/dL_i d\Omega_i' = dL_r/dE_i$. For the perfect diffuser, the bidirectional reflectance ρ_b is constant in every direction and its total diffuse reflectance is simply $\rho\Sigma_b = \rho_b = {}_{\pi}\int d\Omega' = \pi\rho_b$. According to Helmholtz's reciprocity theorem [1.1], the bidirectional reflectance distribution function is a symmetrical function of coordinates $\rho_b(\Theta_1, \varphi_1, \Theta_2, \varphi_2) = \rho_b(\Theta_1, \varphi_1, \Theta_2, \varphi_2)$. Consequently, full integration of either the bidirectional-reflection function or the bidirectional-transmission function yields the total radiation conversion.

Clearly, only two ideal optical transformers, such as the *perfect diffuser* and the *ideal mirror*, can be considered as geometrically transforming substances. Their optical properties are predetermined and the intensities of light transformed by them are only functions of the irradiation and observation geometries. For either the perfect diffuser or the ideal mirror, the entire reflectance is 1. The ideal mirror

Table 1.1 Interdependence of irradiation and observation geometries

No	Type of reflectance (irradiation/observation)	Transformation factors	
		Ideal mirror	Perfect diffuser
1	$\rho(2\pi/2\pi)$	1	1
2	$\rho(2\pi/\Omega_2)$	$(1/\pi)\int_{\Omega_2}\cos\Theta_2 \mathrm{d}\,\Omega$	$(1/\pi)\int_{\Omega_2}\cos\Theta_2 \mathrm{d}\,\Omega$
3	$\rho(2\pi/\Theta_2)$	$(1/\pi)\cos\Theta_2 \mathrm{d}\,\Omega$	$(1/\pi)\cos\Theta_2 \mathrm{d}\,\Omega$
4	$\rho(\Omega_1/2\pi)$	1	1
5	$\rho(\Omega_1/2\pi)$	$\int_{\Omega_2}\cos\Theta_2 \mathrm{d}\Omega / \int_{\Omega_1}\cos\Theta_1 \mathrm{d}\Omega$	$(1/\pi)\int_{\Omega_2}\cos\Theta_2 \mathrm{d}\,\Omega$
6	$\rho(\Omega_1/\Theta_2)$	$\cos\Theta_2 \mathrm{d}\Omega / \int_{\Omega_1}\cos\Theta_1 \mathrm{d}\Omega$	$(1/\pi)\cos\Theta_2 \mathrm{d}\,\Omega$
7	$\rho(\Theta_1/2\pi)$	1	1
8	$\rho(\Theta_1/\Omega_2)$	1 or 0	$(1/\pi)\int_{\Omega_2}\cos\Theta_2 \mathrm{d}\,\Omega$
9	$\rho(\Theta_1/\Theta_2)$	1 or 0	$(1/\pi)\cos\Theta_2 \mathrm{d}\,\Omega$

reflects light by Snell's law and the perfect diffuser reflects light by Lambert's law. The intensity of any beam reflected by an ideal mirror of $\rho_0 = 1$ remains unchanged. The perfect diffuser redistributes all incident light spatially. Hence, its radiance (luminance), emittance, and irradiance (illuminance) are given via a straightforward relation: $L = M/\pi = E/\pi$ (Eq. 1.47). Only for these two opposite cases of ideal objects is the radiation-transformation factor defined by the spatial geometry of emission and reception [1.23, 1.24]. Common spatial conversion factors of optical radiation reflected by an ideal mirror and a perfect diffuser are given in Table 1.1.

In particular, the incident flux $\mathrm{d}\Phi_{in}$ irradiating an object may be viewed as the product of the object's radiant emittance M and the incident beam cross section d*A* (Eq. 1.46): $\mathrm{d}\Phi_{in} = M \cdot \mathrm{d}A$. The total flux Φ_{refl} reflected in solid angle $\Omega_{refl} = \Omega_2$ by the perfect diffuser for radiance L and irradiance E is:

$$\Phi_{refl} = LA \int_{\Omega_{refl.}} \cos\Theta_{refl} d\Omega = \frac{EA}{\pi} \int_{\Omega_2} \cos\Theta_2 d\Omega. \tag{1.130}$$

Here $\Theta_{refl} = \Theta_2$ is the reflection observation angle. The total reflectance ρ_P of the perfect diffuser is:

$$\rho_P = \left(\frac{1}{\pi}\right) \int_{\Omega_2} \cos\Theta_2 d\Omega. \tag{1.131}$$

Owing to the fact that the ideal mirror converts the semispace of incident light into the specularly reflected semispace, it acts as an ideal directional converter and its light conversion factors are defined only by the geometry of incidence and

observation. Therefore, loss factors of actual objects due to reflection, absorption, and scattering can be defined via the performance of the ideal mirror.

The characteristics of real diffusers with respect to perfect diffuser can be given by the radiance factor β (see Eqs. (1.57), (1.58) and Table 1.1). For example, for any reflective object and arbitrary irradiation and observation geometry Ω_1/Ω_2, the relative intensity $dI_{1,2}$ of its surface is a function of an unknown for now radiance $L_{1,2}$: $dI_{1,2} = L_{1,2}d\Omega_2$. The total radiant flux Φ_{sc}, scattered by the object into solid angle Ω_2, can be determined via integration over Ω_2:

$$\Phi_{sc} = A \int_{\Omega_2} L_{1,2} \cos\Theta_2 d\Omega, \tag{1.132}$$

where A is the irradiated area of the object and Θ_2 is the angle of observation. Since for the perfect diffuser $\Phi_P = \pi L_P A$, the reflectance of the object is given by the ratio $\rho = \Phi/\Phi_P$; thus:

$$\rho = \left(\frac{1}{\pi}\right) \int_{\Omega_2} \beta_{1,2} \cos\Theta_2 d\Omega, \tag{1.133}$$

where $\beta_{1,2} = L_{1,2}/L_P$ is the radiance factor of the object at the irradiation and observation geometry given by solid angles Ω_1 and Ω_2 in directions of irradiation Θ_1 and observation Θ_2 (see Fig. 1.14). That derived dependence can be obtained from the fifth row in Table 1.1 by substitution of the radiance factor into the expression specifying the actual geometry of $\rho_{1,2}$ reflectance for the perfect diffuser.

Table 1.1 also allows one to distinguish the optical properties of any actual diffuser for inverted irradiation and observation directions. Under limited irradiation within a given solid angle Ω_1 and for observation over the entire 2π semispace (see Eq. (1.131)), the reflectance is:

$$\rho_{\Omega_1,2\pi} = \left(\frac{1}{\pi}\right) \int_{2\pi} \beta_{1,2} \cos\Theta_2 d\Omega. \tag{1.134}$$

According to the second row in Table 1.1:

$$\rho^p_{2\pi,\Omega_2} = \left(\frac{1}{\pi}\right) \int_{\Omega_2} \cos\Theta_2 d\Omega. \tag{1.135}$$

Consequently, for the actual diffuser one obtains:

$$\rho_{2\pi,\Omega_2} = \left(\frac{1}{\pi}\right) \int_{\Omega_2} \beta_{2\pi,\Omega_2} \cos\beta_2 d\Omega. \tag{1.136}$$

The reflectance of an actual diffuser can also be seen as its radiance factor under the equivalent irradiation to observation geometry, providing the geometric extent of the beam remains constant: $d^2G = \text{const}$; thus, the ratio of radiances is equal to the ratio of fluxes (Eq. 1.32). Under inverse geometry: $\Omega_1 = -\Omega_2$, and because of Snell's law, the inverted radiance factors are equal: $\beta_{\Omega_1,2\pi} = \beta_{2\pi,\Omega_2}$. Accordingly, the reflectance of the diffuser at the inverse geometry is:

$$\rho_{\Omega,2\pi} = \beta_{2\pi,\Omega}. \tag{1.137}$$

As a result, the magnitude of the diffuse reflectance of a practical diffuser irradiated within the solid angle Ω, restricted to be smaller than 2π, can be represented by the radiance factor of that diffuser, irradiated by radiation of uniformly diffused radiance of the perfect diffuser within the 2π semispace, for the respective observation of reflected light at the defined limited solid angle Ω.

Chapter 2
Methods of Photometric and Radiometric Measurements

2.1 Evaluation of Power and Energy Extents of Optical Radiation

The ability of any flow of optical radiation to make energy actions is identified by the statistical average of the Poynting vector designated as the optical vector satisfying (Eq. 1.3). The spatial, temporal, and spectral densities of the space- or time-averaged flow of radiation in the UV, visible, and IR optical-frequency domains identify the radiometric and photometric extents of radiation. Luminous actions of optical radiation are given by the vector, which forms luminous power and energy extents with the relative spectral luminous efficiency of radiation for the photopic vision of the human eye. In every case, a particular extent or parameter of radiation transfer, as intensity, radiant intensity, radiance or luminance, and radiant or luminous flux, can be identified via the spatial, surface, angular, or temporal density of radiation. The specifics of any measurement of a power or energy derivative for the radiation flow define the choice of the density of either radiant or luminous flux or the energy density of a beam at a given localized space and time region.

2.1.1 Methods of Optical Flux and Energy Measurements

Two balancing main approaches are viable for the measurement of the power or energy extent of a light beam. For the first one, the power or energy extent of radiation is obtained directly by an objective physical detector, which is already calibrated in power or energy units (watts or joules). For the second measurement approach, the power or energy extent of the radiation is obtained in comparison with the same extent of calibrating light, presumably with spectral intensity distribution equivalent to that of the radiation being studied.

M. Bukshtab, *Photometry, Radiometry, and Measurements of Optical Losses*, Springer Series in Optical Sciences 209,
https://doi.org/10.1007/978-981-10-7745-6_2

Until recently, the latter approach was used for the photometric system of luminous-power quantities comparing luminous actions of light beams by a subjective receiver, such as a human eye. The candela, conventionally determined by a model candle emitting within a fixed solid angle under unaltered conditions, was chosen as the basic unit for luminous intensity. A model source reproduced the unit of luminous intensity given by the flux to angle ratio by expression (1.18). Luminous parameters of secondary sources were determined in comparison with the luminous intensity of the primary source. Since the joule and the watt are units of any kind of power and energy, the approach based on a coequal system of radiant units was recently established in radiometry and photometry. Comparison of statistically averaged power actions of a calibrating electrical current of known magnitude and of a light beam under test provides a conversion for such a radiant unit transfer. Knowledge of the specific time term is required for conversion to the measure of the radiant energy.

For direct measurement of the power or energy of a beam of radiation, the entire beam must be completely transferred into heat by a physical detector with absorptance $\alpha \equiv 1.0$, and the heat needs to be measured or substituted by an electrical current, carrying an equivalent amount of thermal power (energy). The measurement results for energy Q and power Φ transformations become:

$$\mathrm{Q}\alpha = J^2 R t = \frac{\partial}{\partial T}(\mathrm{CV}\Delta\mathrm{T}), \tag{2.1}$$

$$\Phi\alpha = \mathrm{J}^2\mathrm{R} = \mathrm{qA}_\Sigma\Delta\mathrm{T}. \tag{2.2}$$

Here α is the absorptance for the radiation being measured, J and t are the magnitude and the duration of the heat-substituting current, respectively, R is the resistance of the heat-generating resistor, C and V are the heat capacity and the volume of the heat detector used, ΔT is the stable rise of the detector's temperature, q is the convective heat transfer in the detector in the state of thermal equilibrium, and A_Σ is the total area of the detector's surface [2.1, 2.2]. An identical method of measurement can be applied for the reverse power or energy conversion for measuring the transformation factor of other forms of energy: electric, thermal, or chemical, into optical radiation by equations:

$$\mathrm{Q} = \varepsilon \mathrm{J}^2 \mathrm{Rt}; \quad \Phi = \varepsilon \mathrm{J}^2 \mathrm{R}, \tag{2.3}$$

where $\varepsilon = \mathrm{Q_r}/\mathrm{Q_o} = \Phi_\mathrm{r}/\Phi_\mathrm{o}$ is the *emission factor*, or the *emissivity*, of the light source being studied, Q_0 and Φ_0 are the optical energy and power which are emitted by the light source, and $\mathrm{Q_r}$ and Φ_r are the electrical energy and power supplied to the light source to initiate the emission, and t is the time interval of that action.

Consequently, an identical method of measurement for the power or energy of radiation can be used for either electrical or thermal calibration of a source or a detector and for determination of the emission and absorption factors. Without attention to the specifics of the calibration in one or another unit of measurement (see Chap. 4 for details), let us note some assumptions in relations (2.1)–(2.3). For

either emittance or absorptance measurement in any given spectral interval, the same section of the object being examined must be used. Otherwise, possible nonuniformity of the radiating or absorbing properties of the object must be known. Under radiation or irradiation Q_i and calibration Q_c conditions, a strict linearity of each energy-transformation step needs to be maintained, such as:

$$(Q_i)_a/(Q_i)_b = (Q_c)_a/(Q_c)_b. \tag{2.4}$$

Here subscripts a and b characterize arbitrary points within the full dynamic range of measurement and calibration. The entire process must be performed in the steady-state mode while random changes of object's absorptance and emissivity and any unknown functions of temperature fluctuations not to exceed the margins of measurement errors. Systematic errors, as nonlinearity, nonuniformity, and unsteady conditions, need to be known and taken into account, introducing correction factors. Extremely sensitive but relative measurements may be made via displacement sensing by light-weight oscillator in a calibrated interferometer [2.96].

An example of the goniophotometric method for measuring the flux or energy of a beam emitted into 2π or 4π space, for which the notes above are applicable, is seen in Fig. 2.1. The total flux Φ emitted by source S is determined as: $\Phi_\Sigma = \sum_{i=0}^{\pi} \Phi_i(\Theta)\Delta\Theta_i + \sum_{j=0}^{\pi} \Phi_j(\psi)\Delta\psi_j$, and detector D integrates elementary fluxes Φ_i within $\Delta\Theta_i$ and $\Delta\psi_j$ for $0 \le \Theta_i, \psi_j \le \pi$. The comparison of radiant or luminous fluxes for various light sources is presumed to be performed under identical conditions. If the spatial distributions of radiation emitted by sources to be compared differ, the diffusing integrating sphere can integrate and balance out any nonequivalence [2.3, 2.4]. For source S in the integrating sphere, having diffuse wall reflectance ρ_0, flux Φ_S emitted by source S and retroreflected by sphere walls makes the sphere irradiance Ξ:

$$\begin{aligned}\Xi &= \Xi_0 + \Xi_1 \cdots + \Xi_\infty \\ &= \Phi_S/A_0 + \rho_0\Phi_S/A_0 + \cdots \underset{\rho \le 1}{=} \Phi_S\left(1-\rho_0^m\right)/[A_0(1-\rho_0)] \underset{m\to\infty}{=} \Phi_S/[A_0(1-\rho_0)],\end{aligned} \tag{2.5}$$

where A_0 is the entire internal area of the sphere. Equation (2.5) denotes Kirchhoff's law for the sphere, since at thermal equilibrium the flux introduced into

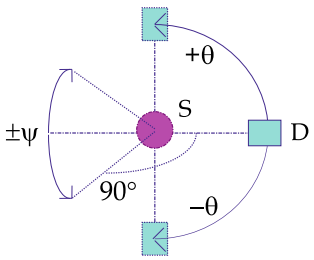

Fig. 2.1 Goniometric measurement of the angular distribution of a source flux

the sphere and that absorbed with factor α by its surface, exposed to sphere irradiance Ξ, are complementary functions [0.12, 1.12]:

$$\Phi = \Xi A_0 \alpha = \Xi A_0 (1 - \rho_0) \rightarrow \alpha = 1 - \rho_0. \tag{2.6}$$

If the sphere of surface A_0 has a small output aperture of area A, screened by a not large opaque baffle of area A_B, any external detector D, protected by the baffle from source S (Fig. 2.2), measures signal J_S, defined by sphere irradiance Ξ, due to flux Φ_S, and area A: $J_S = A \cdot \Phi_S/[A_0(1 - \rho_0)]$. Referencing for comparison the detector signal J_S to another signal J_C of the calibrating light source emitting its known total flux Φ_C, the source flux Φ_S can be obtained via the ratio of two consecutive readings of external detector D: $\Phi_S = \Phi_C \cdot J_S/J_C$.

From the standpoint of the detailed distribution of the sphere's irradiance or illuminance by a light source, the direct-irradiation component of sphere wall irradiance Ξ_0 at a point-size source inside and with no baffles and openings – $\Xi_0 = \Phi\rho_0/A_0$; $\Xi_1 = \Phi\rho_1/A_0$; … $\Xi_m = \Phi\rho_m/A_0$ – can be distinguished from irradiance of the sphere for the baffled source: $\Xi a_0 = k_0 E_0$; $\Xi a_1 = k_1 E_1$; $\Xi a_m = k_m \Xi_m$. Here ρ_0, $\rho_1 = \rho_0^2$, …, $\rho_m = \rho_0^{m+1}$ are the total reflectance of the sphere wall for the first, second, and m^{th} reflection cycles, respectively, and k_0, k_1, and k_m are the correction factors for the respective irradiance component Ξa for the ideal sphere versus the baffled one. Comparing multiple-reflection totals, one obtains [2.5]:

$$k_m(\rho) = \Xi a_m/\Xi_m = (k_0 + \rho k_1 + \cdots + \rho^{(m-1)} k_m)(1 - \rho_0), \tag{2.7}$$

providing in the integrating sphere of uniformly diffuse reflectance at point-size inclusions all successive reflectances are constant $\rho_{0,1} = \rho_{0,2} = \rho_{0,m}$ (see Sect. 2.4, Eqs. (2.102), (2.103)).

At $m \rightarrow \infty$, correction factor $k_m = k_\infty$ for irradiance of a one-baffle sphere versus an ideal unbaffled sphere is:

$$k_\infty \underset{m \rightarrow \infty}{=} A_0/(A_0 + 2S), \tag{2.8}$$

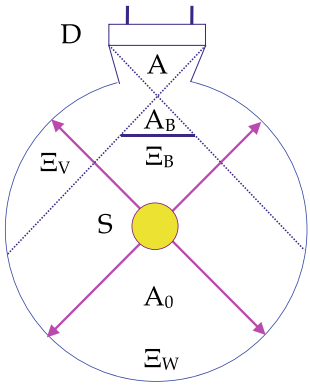

Fig. 2.2 Comparison of source emissions via an integrating sphere

where since the baffle is irradiated from two opposite directions inside the sphere, its surface S is counted twice. Factor k_{∞} may also be seen as the ratio of irradiances of ideal and baffled spheres irradiated by any given flux Φ. Three major zones can be considered in the integrating sphere for flux measurement (see Fig. 2.2): (1) the baffle zone for which flux Φ_S creates irradiance Ξ_B; (2) the wall zone, not seen from the center of port A, on which flux Φ_S creates irradiance Ξ_W; and (3) the viewing zone, opened to a detector D and for which irradiance Ξ_V is seen on the first reflection m = 1, whereas irradiances Ξ_B and Ξ_W are both seen only on the second reflection m = 2. The irradiance of each zone can be determined via the portion of the source flux Φ_S received by the zone [2.5].

$$\Xi_V = \Phi_V \rho^m/(A_0 + 2S); \quad \Xi_W = \Phi_W \rho^m/(A_0 + 2S); \quad \Xi_B = \Phi_B \rho^m/(A_0 + 2S). \tag{2.9}$$

Owing to the definition above, $\Phi_V = \Phi_S - \Phi_B - \Phi_W$, where Φ_B, Φ_W, and Φ_V are the flux components for irradiances Ξ_B, Ξ_W, and Ξ_V. From Eqs. (2.5) and (2.7), the respective relations follow:

$$\Xi_V = \frac{\Phi_V}{(A_0 + 2S)} \frac{\rho}{1-\rho}; \quad \Xi_W = \frac{\Phi_W \rho}{(A_0 + 2S)} \frac{\rho}{1-\rho}; \quad \Xi_B = \frac{\Phi_B \rho}{(A_0 + 2S)} \frac{\rho}{1-\rho}. \tag{2.10}$$

The combined irradiance (illuminance) Ξ_Σ of the integrating sphere surface at the center of port A is:

$$\begin{aligned} \Xi_\Sigma &= \Xi_V + \Xi_W + \Xi_B = \frac{\Phi_V + \Phi_W \rho + \Phi_B \rho}{(A_0 + 2S)} \frac{\rho}{1-\rho} \\ &= \frac{\Phi_S - (\Phi_W + \Phi_B)(1-\rho)}{(A_0 + 2S)} \frac{\rho}{1-\rho} = \frac{\Phi_S - \alpha(\Phi_W + \Phi_B)}{(A_0 + 2S)} \frac{\rho}{1-\rho}, \end{aligned} \tag{2.11}$$

where the total source flux is $\Phi_S = \Phi_V + \Phi_W + \Phi_B$ and the absorption factor of the entire sphere is $\alpha = 1 - \rho$ (see Eqs. (2.5) and (2.6)). Relations (2.11) confirm that the accuracy of any flux measurement using a real-dimension auxiliary integrating sphere versus the ideal sphere of negligibly small apertures and openings is limited by the discrepancy of the reflectance values from 1.0 for the wall and the baffle of the auxiliary sphere. Instead of baffling a port, two spheres can be used sequentially: one collecting the flux and one uniformly irradiating the detector [2.97].

2.1.2 Measurement of Surface Density of Light

By definition, irradiance (illuminance) represents the surface density created by the radiant (luminous) flux: $\Xi = d\Phi/dA$. To determine the surface density, the mean or averaged power of a given beam of radiation of any known area $A_{c.s}$ of the beam

cross section can be measured. Within the first-order approximation neglecting higher-order diffraction effects, the beam may be formed by an aperture with the flux being a product.

$$\Phi = \Xi \cdot A_{c.s.} \tag{2.12}$$

To determine the irradiance or illuminance by measurement of a radiant or luminous flux, one should notice that Eq. (1.20) defines irradiance as a function of a point and a direction.

$$d\Xi = \frac{d^2\Phi \cos\Theta}{dA} = d\Xi_n \cos\Theta = d^2\Phi / dA_n. \tag{2.13}$$

The result of such a measurement is identified not only by area A_n of an irradiated aperture, which should be practically defined by the beam's cross section $A_{c.s}$, but also by the angle of observation Θ_i, being the slope angle between the axis of the incident beam and the wave normal to the aperture. In (2.13), Ξ_n is the normal irradiance for irradiation by a wave normal to the direction of observation and A_n is the area of the aperture, viewed by the normal, defining cross section $A_{c.s}$ of the beam making the irradiance on the surface element of area A. The reduction of surface density due to the inclination (slope) angle is given by optical vignetting (see Fig. 2.3).

Equations (2.12) and (2.13) also allow one to determine the average surface density created by any arbitrarily distributed radiant or luminous flux existing in the entire semispace above the test surface and falling onto a region limited by the defining aperture of area A_n. A radiometric detector, by virtue of limitations to its transverse dimensions and time constants, will react only to time and space averages of the square amplitudes of all contributing electromagnetic oscillations, therefore summing the entire actions of the total number of light fluxes passing through the aperture within semispace solid angle 2π. Even if the emitted light beams are partially coherent and make a randomly localized but steady-state interference pattern, the result can be averaged over the measured interference pattern across the observation area. Consequently, the irradiance and illuminance may remain additive radiometric and photometric parameters, each representing the arithmetic totality of

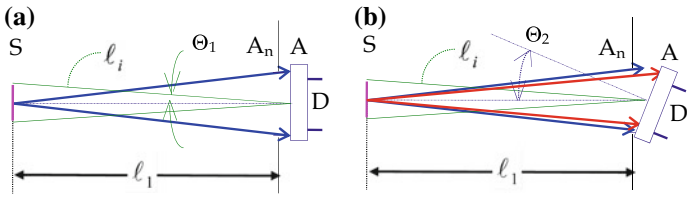

Fig. 2.3 Irradiance or illuminance as a function of angle of incidence

either the local irradiance or the local illuminance transmitted by the aperture. If the distance to the light source is notably larger than the linear dimensions of the source, the irradiance or illuminance created by the source is given by Eq. (2.13) and defined by the inverse-square and cosine law (see Chap. 1). The criterion in the point-source approach is also based on potential observability of fluxes radiated from unequally spaced emitting elements. Hence, in every practical situation the source of radiation must be the *point source*. Only for the point source can the distance ℓ_i to each diverse i^{th} element of the source (see Fig. 2.3) be considered unchanged when crossing from the center of the source to its edges. Any practical margins of that approximation are always defined by the required accuracy of the observation.

2.1.3 Absolute Flux Measurement Via an Integrating Sphere

Applying the inverse-square distance law (Eqs. (1.61), (1.62)) for an integrating sphere, one may accomplish measurements of the absolute flux for radiation emitted by a given source into the entire 4π space [2.6, 2.7]. A known flux Φ_{SS} of radiation (Fig. 2.4) from a standard source SS enters the sphere via the opening A_S and creates irradiance E_{ss}. A measuring flux Φ_S from source S in the sphere center irradiates the sphere walls, but baffles B_1 and B_2 protect it from being directly viewed by internal sphere detector D. According to Eqs. (1.61) and (2.13), the normal irradiance Ξ_n of standard SS at the plane of aperture A_{ss} is $\Xi_n = I_{SS}/\ell^2$, where I_{SS} is the standard's radiant (luminous) intensity. Equation (2.5) for the measured source irradiance Ξ_S on sphere detector D seeing only radiation retro-reflected by sphere walls becomes:

$$\Xi_S = \Phi_S \rho / \left(4\pi R^2 (1-\rho)\right), \tag{2.14}$$

where R is the sphere radius. At the same time, the detector D is exposed to the first reflection of flux emitted by the standard: $\Phi_{SS} = \Xi_n A_{SS}$, thus reacting to

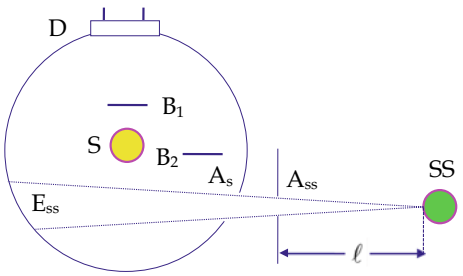

Fig. 2.4 Absolute flux measurement via an integrating sphere

first-reflection-added sphere irradiance: $\Xi_{SS} = \Phi_{SS}\rho/(4\pi R^2(1-\rho))$. The ratio of the sphere's irradiances Ξ_s/Ξ_{ss} for baffled detector D gives the flux Φ_S:

$$\Xi_S/\Xi_{SS} = \Phi_S/\Phi_{SS} = J_S/J_{SS}; \quad \Phi_S = \left(I_{SS}A_{SS}/\ell^2\right)(J_S/J_{SS}). \tag{2.15}$$

Here J_S and J_{SS} are the readings of detector D measuring the light flux from the source and standard.

2.1.4 Spherical Density of Radiation

The irradiance or illuminance in a point of space created by a sum of any arbitrary light sources averaged within the limits of a solid angle Ω can be defined as:

$$\Xi_\Omega = \int_\Omega \Xi d\Omega/\Omega. \tag{2.16}$$

Similarly, the mean or averaged spherical irradiance due to any radiation existing in 4π space is:

$$\Xi_{4\pi} = \frac{1}{4\pi}\int_{4\pi} \Xi d\Omega. \tag{2.17}$$

The mean spherical irradiance at a given point can be identified and measured via the irradiance of the outer surface of a sphere of negligibly small diameter with its center at the given point. The elementary flux $d\Phi_s$ falling on element $dA = R^2 d\Omega$ of that spherical surface becomes:

$$d\Phi_s = \Xi \cdot dA = R^2 \Xi d\Omega, \tag{2.18}$$

where dΩ is the elementary solid angle at which dA is seen from the center of the small sphere of radius R. The radiant or luminous flux Φ_s irradiating the entire surface of the sphere is given by:

$$\Phi_0 = R^2 \int_{4\pi} \Xi d\Omega = 4\pi R^2 \Xi_{4\pi}. \tag{2.19}$$

According to Eq. (2.19), one way to measure the mean spherical illuminance or irradiance becomes straightforward – by making the sensitive area of the light detector as a solitary spherical receiver or making such a receiver from a number of negligibly small flat detectors [1.4].

Another possibility for spherical irradiance measurement at a given point is associated with implementing a sphere formed from a translucent material, which transmits radiation diffusely and which center coincides with that point [2.8]. The main feature of the translucent sphere is due to effects of multiple reflections and transmission via low-absorbing walls. If that sphere transmits a given spectrum of radiation diffusely for diffuse transmittance $\tau_d \equiv 1 - \rho_d$, owing to its wall absorptance α being lower than the error of the radiance measurement to be made, then the initial flux Φ_0 of direct or diffuse irradiation will be uniformly distributed inside the sphere, resulting in multiple reflections for internal sphere flux Φ_{sph}:

$$\Phi_{sph} = \Phi_{int,\Sigma} = \Phi_0\tau + \Phi_0\tau\rho + \cdots + \Phi_0\tau\rho^n \underset{\substack{n\to\infty,\\ \rho\le 1.0}}{=} \Phi_0 \frac{\tau}{1-\rho} \underset{\substack{\tau=1-\rho,\\ \alpha\to 0}}{=} \Phi_0. \tag{2.20}$$

The error of the assumption for the derivation is $\Delta\Phi/\Phi = \Delta\tau = \alpha$. For most opal glasses and translucent synthetic materials the values of the linear absorption coefficient α are not higher than $0.001-0.0001\ \mathrm{cm}^{-1}$. Hence, actual errors attributed to using equation (2.20) at the translucent sphere wall thickness under 1 cm should not exceed ones of accurate spectrophotometric measurements.

The fact that such a translucent sphere of diffuse nonabsorbing material reflects or transmits incident light with no attenuation seems unusual and is only true in the absence of absorption, $\alpha \le \Delta\Phi/\Phi$, diffusing incident power Φ_0 into total external flux $\Phi_{ext.\Sigma}$:

$$\begin{aligned}\Phi_{ext,\Sigma} &= \Phi_0\rho + \Phi_0\tau^2 + \Phi_0\tau^2\rho + \cdots + \Phi_0\tau^2\rho^n \\ &\underset{n\to\infty}{=} \Phi_0\rho + \Phi_0\frac{\tau^2}{1-\rho} \underset{1-\rho=\tau}{=} \Phi_0(\rho+\tau) \underset{\alpha\to 0}{=} \Phi_0.\end{aligned} \tag{2.21}$$

The explanation for this straightforward, but a bit deceptive phenomenon [2.8] described by Eqs. (2.20) and (2.21) relates to the spatial separation of incoming and outgoing fluxes uniformly distributed in 4π space owing to the properties of a diffusely reflecting sphere (see Sect. 2.4). For no wall absorption, a sphere formed by the uniformly diffuse reflecting and transmitting material balances the incident radiation into the surroundings, not adding or diminishing anything and flux Φ_0 is contained within every imaginary sphere coincident with the integrating one (Fig. 2.5).

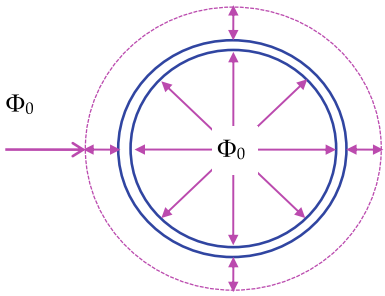

Fig. 2.5 Translucent sphere irradiation and observation

If a small detector makes up a spherical segment of area A_d on surface A_s of the translucent sphere, the A_d/A_s ratio defines the detector's signal. If the irradiance of the internal surface of the sphere is:

$$\Xi_s = \frac{\Phi_s}{A_s} = \frac{\Phi_0}{4\pi R^2}. \tag{2.22}$$

then, the radiant flux Φ_d measured by the detector is equal to:

$$\Phi_d = \Xi_s A_d \cong \frac{\pi r^2}{4\pi R^2}\Phi_s = \Phi_0 r^2/4R^2, \tag{2.23}$$

where r and R are the radii of the segment and of the sphere. Using Eq. (2.19) relation (2.23) becomes:

$$\Phi_d = \Xi_s A_d \cong \pi r^2 \Xi_{4\pi}. \tag{2.24}$$

The total flux received by the sphere from the surroundings may be seen as the sum of normal irradiations by flux components. Since the area of sphere projection on any plane is πR^2, and the elementary flux $d\Phi$ is $d\Phi = \pi R^2 d\Xi_n$, the total flux inside the sphere can be written as:

$$\Phi_s = \pi R^2 \int_{4\pi} d\Xi_n. \tag{2.25}$$

Since the mean spherical and normal irradiances are $\Xi_{4\pi} = \Phi_s/4\pi R^2$ and $\Xi_n = L\cos 0^\circ\, d\Omega$, one obtains:

$$\Xi_{4\pi} = \frac{1}{4}\int_{4\pi} d\Xi_n = \frac{1}{4}\int_{4\pi} L d\Omega. \tag{2.26}$$

Finally, the spherical and mean spherical irradiances (see Sect. 1.2 and Eq. (2.17)) are:

$$\Xi_0 \equiv 4\Xi_{4\pi} = \int_{4\pi} L d\Omega \cong 4\Phi_d/\pi r^2. \tag{2.27}$$

Spherical irradiance Ξ_0 characterizes, up to the inverse of the velocity of light *1/c* [1.4], the spherical density of radiant energy in adjoining space: $Q_0 = (1/c)\Xi_0$. Assumptions of low absorption and smallness of a spherical segment removed by a detector of actual area $A_D = \pi r^2/4\pi R^2$ define actual systematic errors of spherical irradiance measurements using a low-absorbing translucent sphere.

2.1.5 Measurement of Angular Density of Radiation

One method for measurement of radiation intensity comes directly from its definition. Expressions (1.61) and (1.62) defining the cosine and inverse-square law give essential conditions for the realization of such a measurement. The ratio of normal irradiances $\Xi_{n,i}$ created by the light source under study at respective distances ℓ_1 and ℓ_2 is inversely proportional to the one for distances, since the light intensity I remains constant:

$$\Xi_{n,1}\ell_1^2 = \Xi_{n,2}\ell_2^2 \equiv I; \quad \Xi_{n,1}/\Xi_{n,2} = \ell_2^2/\ell_1^2. \tag{2.28}$$

The accuracy of the respective substitution of irradiances measured via the distances to the point source determines the accuracy of measurements and the minimum allowed distance ℓ_1 for the source to remain a point source. For the minimum distance identified, the first magnitude of the irradiance or illuminance can be measured. The second magnitude can be measured at the distance $\ell_2 = \ell_1 + \Delta\ell$, at which the second magnitude can be positively distinguished from the first one over the error of the measurement. As a result, two equations to be studied are $E = \Xi_1\ell_1^2$ and $E = \Xi_2(\ell_1 + \Delta\ell)^2$. After removing the parentheses and using $\ell_1 = \sqrt{I/\Xi_1}$, the irradiance E is [0.6].

$$E = \Xi_1\Delta\ell^2\left[\left(\Xi_2 + \sqrt{\Xi_1\Xi_2}\right)/(\Xi_1 - \Xi_2)\right]^2. \tag{2.29}$$

The first distance ℓ_1 does not need to be measured. Its magnitude only establishes the validity of the square-power character for a changing irradiance or illuminance given by the source studied.

Another procedure, called the *telecentric method*, does not require measurements to be made at several observation points and can be accomplished via an optical system of an aplanatic lens and an aperture stop imitating a test source as placed at infinity (Fig. 2.6). The aperture stop A_f is installed in the focal plane of lens *L* to select from all beams radiated by the source only the cones of a small solid angle Ω. Aperture A_f is seen from the lens plane under angle Ω to the optical axis of the system independently of the traverse distance from a point P of the source or the lens. Since the lens is aplanatic, the system's sine term: $h/\sin\Theta = f$, remains constant independently of distance *h* from the object's or lens's point P to the optical axis of the system. If the lens maintains a constant transmittance τ_h for traverse points, the radiant (luminous) flux Φ through aperture A_f is:

$$\Phi = \tau_h\left(A_f/f^2\right)I. \tag{2.30}$$

Here *I* is the emission intensity of the source of radiation, *f* is the focal length of the lens being used, and $A_f/f^2 = \Omega$ is the solid angle, which defines the fixed solid angle Ω of radiation emission for all points of the source, viewed via aperture stop

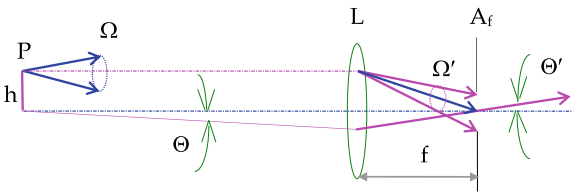

Fig. 2.6 Telecentric method for beam-intensity measurement

A_f [2.9]. Within the limits of the unchanging transmittance τ for different zones of the system's lens, the telecentric method allows one to realize every measurement of the radiant or luminous intensity independently of a distance between the system's lens and the source. Likely restrictions of the method are bound by vignetting of the beam by the lens mounting if the following condition is not satisfied:

$$(h_{\max} + \ell_{\max} tg\Theta) \leq D_{\det}/2. \tag{2.31}$$

Here h_{max} is the maximum source height across the optical axis, ℓ_{max} is the maximum distance from the source to the detector of diameter D_{det}, and 2Θ is the plane vertex angle for solid angle Ω.

2.1.6 Radiance and Luminance Measurements

The spatial-angular density of radiation making a beam of known spatial geometry defines the beam radiance (luminance) and can be measured via radiant (luminous) intensity or irradiance (illuminance) for a beam of known cross section. The measurement layout follows from Fig. 1.2, where indices 1 and 2 refer to the source and detector for appropriate beam wavelengths. When the radiant or luminous intensity of the source is measured via the area of the emitting surface, the radiant or luminous flux identified by these parameters is:

$$d^2\Phi = dI_1 d\Omega_1 = L_1 dA_1 d\Omega_1. \tag{2.32}$$

Likewise, the radiance or luminance of the source at a defined emitting area A_{em} is given by the ratio:

$$L = I/A_{em}, \tag{2.33}$$

where A_{em} is the area of the source emitting surface. By analogy, irradiance Ξ_e or illuminance Ξ_v measured within a solid angle dΩ, at which the entire source is seen from the detector's center:

$$d^2\Phi = d\Xi_n dA_2 = L_1 dA_1 d\Omega_1, \tag{2.34}$$

determines the radiance or luminance via the irradiance or illuminance by the normal or at angle Θ:

$$L = \Xi_n/\Omega_0 = \Xi/\Omega_0 \cos\Theta. \tag{2.35}$$

Here Ω_0 is the solid angle of observation and Θ is the inclination angle of the detector plane to the beam's axis.

If the area of the emitting section of the source is unknown, there are difficulties in determining it, and if the radiance distribution over the source does not remain constant, it is possible to designate only some limited solid angle defining a beam coming from the restricted part of the source (Fig. 2.7). Since the geometric extent is a constant of a physical beam of light (see Eq. (1.25)) and does not depend on the selection of the cross section of that beam, an aperture stop of area A_f placed at a distance ℓ_f from detector D limits the solid angle Ω_2 viewed from the test source S. The aperture stop explicitly defines a specific physical beam of light that is emitted from the restricted area A_s of the source at any mutually parallel position of the source and of the detector surfaces: $A_1\Omega_1 = A_2\Omega_2$.

Thus, knowing area A_f of the aperture and distance ℓ_f defined by the detector's pupil (see Fig. 2.7a), one can identify the radiance or luminance of the zone restricted this way by a specific measurement of irradiance or illuminance in the structured beam. In such a case, owing to Eq. (2.35), the angle is $\Omega_0 = \Omega_2 = A_f'/\ell_f$, where A_f' is the area of the spherical segment cut out by the aperture A_f from an imaginary sphere with radius ℓ_f. By cross-scanning the source or detector across the optical axis of the system, one will register any radiance changes as a function of coordinate for the zone pointed out by the detector. The dimensions of that zone are limited by the aperture size, the tube length, and sensitivity of the detector to the radiation spectrum.

Similar measurements can be realized by a lens of known integral transmittance τ_{ob} (see Fig. 2.7b). With the lens, the lateral dimensions of the measured beam are set by diameter D_{cl} of the lens's clear aperture and by distance ℓ_1 from its principal plane to the source. Since no vignetting of the detector is allowed, the total flux Φ transmitted by the lens objective to the detector is: $\Phi = \tau_{ob} \cdot L \cdot A_s \cdot \Omega$, where L is the test source radiance or luminance. For paraxial beams when the measurements are made at large distances in comparison with sizes of the apertures to comply with: $\ell_1 \gg D_{cl}$, the radiance is:

$$L = 4\Phi\ell_1^2/\pi D_{cl}^2 A_s. \tag{2.36}$$

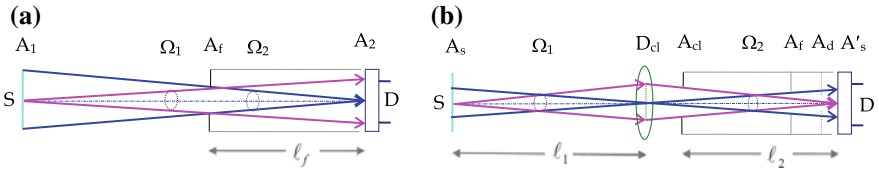

Fig. 2.7 Measurement of radiance (luminance) via irradiance (illuminance) using an aperture (**a**) and an objective plus an aperture (**b**)

If image area A'_s is known, the measurement with the lens permits determination of the average radiance or luminance of a source by setting up a limit on the solid angle Ω_2 of detection. This can be done by implementing an aperture stop of area A_f (Fig. 2.7b). Such a stop can only restrict the amount Φ' of flux received from the source, but cannot change image area A'_s. Hence, the radiance is:

$$L = \Phi' \tau_{ob} / A' \Omega_2. \tag{2.37}$$

Further installation of an auxiliary aperture with a much smaller area, $A_d \ll A'_s$, over the detector's sensitive surface allows one to create a receiving geometry similar to that for the procedure with no lens objective. Consequently, the source radiance L in this case is straightforwardly identified by the transmittance of the lens objective and the ratio of the measured irradiance Ξ to the solid angle Ω_2:

$$L = \tau_{ob} \Xi / \Omega_2. \tag{2.37'}$$

2.2 Analysis of Attenuation Factors

A straightforward method for measurement of attenuation, such as of the attenuation factor of a given object, is based on two consecutive measurements of either the power or the energy extent of some stable beam of defined radiation measured before and after its interaction with the object. Virtually any energy or power parameter of radiation can be used for measurements: flux, intensity, radiance, luminance, illuminance, etc. The main feature of attenuation measurements distinguishing them from methods of power or energy determination is affiliated with no need to measure the chosen power or energy extent by way of absolute units, since only the ratio of two values of one extent is used for obtaining the result of measurements. The primary task of attenuation measurement is in ensuring sufficient stability of emission of the source of radiation and sensitivity of the detector during the measurement cycle, reproducing initial and intermediate states of measurement and maintaining linearity in the full system. Mutual orientation of light sources, detectors, projection optics, dynamic and spectral ranges of their performance, etc. cumulatively determine, in every specific case, the most suitable method for the measurement of the optical characteristic being studied.

2.2.1 Measurements in Transmitted Light

As follows from Eqs. (1.101)–(1.107), attenuation of a light beam transmitted by an object made from a test substance with a refractive index distinct from the refractive index of its surrounding is determined by the entire loss inside that substance and at its front and back surfaces. Therefore, a comparison of the incident and of the

transmitted energy or power of the beam of light makes it possible to identify only the total transmittance τ_Σ of that object:

$$\tau_\Sigma = \tau_{1s}\tau_{int}\tau_{2s}K, \tag{2.38}$$

where τ_{1s} and τ_{2s} are the transmittances of the first and of the second surfaces of the object under study, τ_{int} is the object's internal transmittance defined as: $\tau_{int} = \exp(-\mu\ell_0)$ (see Chap. 1), where ℓ_0 and μ are the thickness and the linear attenuation coefficient of the substance, and K is the factor of multiple reflections. Equation (2.38), owing to too many undetermined variables (see, e.g., expressions (1.93)–(1.99)), does not allow one to distinguish a particular coefficient or factor for the test substance or either surface. Nevertheless, for a variety of practical tasks and under specially taken measures, potential discrepancies between the ideal surface, not having any absorbing or scattering layers, and the high-quality polished optical surface may be disregarded. As a result, if multiple reflections are absent or are presumed to be negligible, the measurement formula becomes:

$$\tau_\Sigma(\lambda) = \tau_s^2(\lambda)\tau_{int}(\lambda) = [1 - \rho_s(\lambda)]^2\tau_{int}(\lambda). \tag{2.39}$$

Two possibilities for exclusion of the effect of internal multiple reflections on the measurement result are shown in Fig. 2.8. Either the object to be studied is made as a wedge or the object having plane-parallel faces is tilted by such an angle φ that, after a double reflection cycle inside, the retroreflected beam does not overlap with the incident beam in the forward direction transmitted directly. To determine the internal attenuation of that object in transmitted light, its front and back surface reflectance values need to be measured at the spectral distribution of light as for attenuation studies to compute surface losses via Fresnel formulae (relations (1.34)–(1.36)). At the normal or 90°-slide incidence, differences between reflectances $\rho_\parallel$ and $\rho_\perp$ vanish and the transmittance of each surface is independent of the state of radiation polarization. In other cases, the angles of incidence φ_1 and of refraction $\varphi_2(\lambda)$ or the index of refraction $n(\lambda)$ for any given wavelength and states of polarization must be known. For the measurement in statistically averaged unpolarized light, the mean surface reflectance ρ_{unp} is:

$$\rho_{unp} = \frac{1}{2}\left[\frac{\sin^2(\varphi_1 - \varphi_2)}{\sin^2(\varphi_1 + \varphi_2)} + \frac{\tan^2(\varphi_1 - \varphi_2)}{\tan^2(\varphi_1 + \varphi_2)}\right]. \tag{2.40}$$

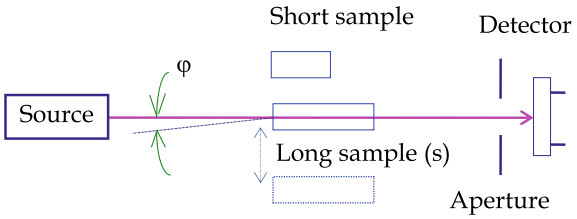

Fig. 2.8 Attenuation coefficient measurements in transmitted light

Only when studying a thin slab of a transparent substance, where its internal transmittance $\exp(-\mu\ell_0)$ may not be distinguished from 1.0 with guided-away internal multiple reflections, can the total transmittance of the slab, viewed not at normal incidence but with sliding irradiation via its surfaces of one equivalent reflectance ρ_0 (see Eq. (1.101)), be determined as $\tau_{sgl} = (1 - \rho_0)^2$. If all multiple reflections are included in the directly transmitted beam, the transmittance is (formula (1.106)): $\tau_{mul} = (1 - \rho_0)/(1 + \rho_0)$. When refractive index $n = 1.5$ and thus $\rho_0 = 0.04$, the relative difference $\delta\tau$ between single τ_{sgl} and multiple τ_{mul} factors becomes $\delta\tau = (\tau_{mul} - \tau_{sgl})/\tau_{sgl}$, corresponding to 0.0016. For some applications such a distinction can be considered as negligible, whereas for others it may be significant. The validity of all supposed assumptions: $\exp(-\mu\ell) = 1.0; \rho = \rho_0 \neq \rho(\varphi)$, has to be verified, for example, by sufficient-to-sense inclinations of a sample from normal incidence.

A more sensitive and reliable method of internal loss measurements is associated with irradiation of several identical, or as similar as possible, samples of a test substance. Then, the determination of internal attenuation is realized by comparing changes of the energy or power of a light beam transmitted by a long sample with changes of the energy or power of a light beam propagating not in a surrounding medium, but in a shorter sample of the test substance, at all four equivalent surfaces. The relative transmittance τ_{rl} at reflectances $\rho_{1,lg}$, $\rho_{2,lg}$, $\rho_{1,sh}$, $\rho_{2,sh}$ is:

$$\tau_{rl} = \frac{\tau_{lg}}{\tau_{sh}}_{\rho_i \neq \rho_j} = \frac{(1 - \rho_{1,lg})(1 - \rho_{2,lg})}{(1 - \rho_{1,sh})(1 - \rho_{2,sh})} \exp[-\mu(\ell_{lg} - \ell_{sh})] \frac{1 - \rho_{1,sh}\rho_{2,sh}\exp(-\mu\ell_{sh})}{1 - \rho_{1,lg}\rho_{2,lg}\exp(-\mu\ell_{lg})}, \tag{2.41}$$

where indices *lg* and *sh* refer to the long and the short samples and the indices *1* and *2* mark the first surface and the second surface of each sample. Equation (2.41) shows that for such a technique of attenuation measurements, the surface reflectance ratio and the multiple reflection factor both become the order of a magnitude lower variables in comparison with the transmittance of every sample (see also Chaps. 4 and 5).

Comprehending the evident practical limitation for realizing high accuracy of the transmission measurement method just described, consider the results obtained via interdependence of the variables involved in the measurement process. Possible alterations of the transmittance and reflectance: $\tau = 1 - \rho$, of any perfectly polished optical surface via negligibly low absorptance and low scattering surface factors are defined only by the changes of its specular reflectance:

$$\frac{\Delta\tau}{\tau} = \frac{\Delta\rho}{1 - \rho} = \frac{\Delta\rho}{\tau}. \tag{2.42}$$

Here $\Delta\tau$ and $\Delta\rho$ are the changes of transmittance and reflectance. An accidental change of specular reflectance ρ can be expressed via conceivable variations Δn of the surface refraction index n:

$$\Delta\rho = \frac{4(n-1)}{(n+1)^3}\Delta n. \tag{2.43}$$

Considering normal incidence of light onto a surface to be measured and the following equality:

$$\tau = 1 - [(n-1)/(n+1)]^2 = 4n/(n+1)^2, \tag{2.44}$$

the relative alteration of such a single-surface transmittance becomes:

$$\delta\tau \equiv \Delta\tau/\tau = \Delta\rho/\tau = (\Delta n/n)\cdot(n-1)/(n+1). \tag{2.45}$$

Allowing for variations of optical properties of four surfaces of two compared samples, the relative magnitude of uncontrollable changes of the measured relative internal transmittance is:

$$\frac{\Delta\tau_{rl}}{\tau_{rl}} = \Delta\tau_{int} = 4\frac{\Delta n}{n}\cdot\frac{n-1}{n+1}. \tag{2.46}$$

Depending on the accuracy requirements of the measurement provided, one or another difference or variation of a surface refraction may be allowed. Thus, within the scope of random error caused by the allowance, sensitivity to the studies of the internal loss may be considered from the following equations:

$$\tau_{int} = \exp[-\mu(\ell_{lg} - \ell_{sh})], \quad \delta\tau_{int} = \Delta\tau_{int}/\tau_{int} \underset{\mu=const}{=} -\mu\Delta\ell. \tag{2.47}$$

For the capability of sensing $\pm 0.01\%$ transmission changes at $\mu = 0.1\ \mathrm{cm}^{-1}$, $\Delta\ell$ must be constant to at least $\pm 10\ \mu\mathrm{m}$.

To conclude, let us consider one main aspect of any transmittance measurement: conversion of the optical path length of the beam of radiation having two comparative transmissions: first, via the surroundings, which are usually air, and, second, via a test sample. Depending on the angle φ of incidence on the sample surface and on the divergence of the beam during normal irradiation, the changes of the beam diameter D_0 on passage via the sample bulk of thickness ℓ and on passage in air are:

$$\begin{aligned} D_{air} &= D_0 + 2\ell\ \tan\varphi, \\ D_{smp} &= D_0 + 2n\ell\ \tan[\arcsin(\sin\varphi/n)]. \end{aligned} \tag{2.48}$$

Consequently, the larger the magnitudes of ℓ, n, and φ, the stronger should be the requirements for uniformity of sensitive area of the detector and the

measurement system itself. The system can also be arranged with some compensation of an extended optical path length of light propagation via a long test sample by diminishing spot-size variations of the beam which irradiates the detector.

2.2.2 *Measurements of Reflectance*

The principal measurement concept for specular reflectance is the same as for direct transmittance: the change of intensity of the incident beam before and after its interaction with an object is to be resolved and measured. One insignificant, as may seem, aspect of reflectance studies, i.e., opposite directions of light incidence and reflection, notably complicates the process, especially if high accuracy is required. Figure 2.9 reveals a few approaches for a direct measurement of specular reflectance. Four conceivable source-detector combinations are seen. After the measurement by the first detector of the intensity of the beam incident directly from light source S, the reflective object under study can be positioned in the incident beam at any desired angle φ with the detector accordingly relocated to new position D′ matching dual angle 2φ for the incidence and reflection. An identical measurement can be made via the source moved into new position S′ for the object rotated 180°. Two other combinations are realized by having the second detector identical to the first one set at position D′ or the second source, as the first one, set at position S′. The requirement for the first two measurements is to reproduce the initial position of the incident beam on the detector to be moved. For the second measurement pair, the emittance of sources S and S′ or the sensitivity of detectors D and D′ must be identical. In every specific case, the choice among the four procedures considered above, or even more complicated ones (see later), is defined by the required accuracy, the spectral and dynamic ranges of measurements, sensitivity to determining specular reflectance under study, accessibility of the components, overall setup dimensions, etc.

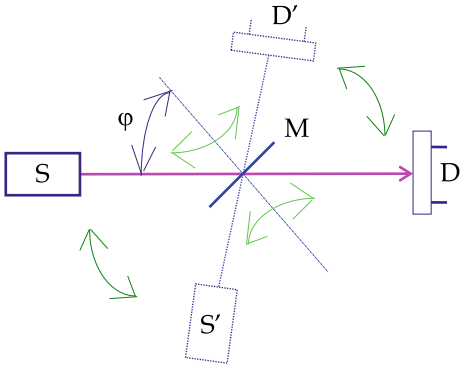

Fig. 2.9 Measurement arrangements for specular reflectance: S—source, D—detector, M—mirror under study

Compared with transmission measurements, measurements in reflected light have a definite advantage – high sensitivity to the state of the reflective surface. At normal incidence (relation (1.36)), reflectance-based sensitivity to refractive index change Δn for a single surface irradiated by a wave normal is (see Eq. (2.43)):

$$\delta\rho \equiv \frac{\Delta\rho}{\rho} = \frac{\Delta n}{n} \cdot \frac{4n}{n^2 - 1}. \tag{2.49}$$

For light reflected by a glass-air border and glass relative index of refraction n = 1.5, the changes of glass-surface specular reflectance are nearly 5 times greater than respective variations of the refractive index. Compared with transmittance measurements for a single glass surface (see Eq. (2.45)):

$$\frac{\delta\rho}{\delta\tau} = \frac{\tau}{\rho} = \frac{4n}{(n-1)^2}, \tag{2.50}$$

reflection-based sensitivity is much higher. For glass with n = 1.5, ratio (2.50) becomes Δ(ρ/τ) = 24.

The high sensitivity to changes of reflectance versus transmittance may be useful for achieving higher accuracy of surface studies in reflected light. However, if relatively low magnitudes of reflectance are to be measured, a higher dynamic range and a higher sensitivity of the detector may be required. For glass with n = 1.5 and ρ = 0.04, the intensity of light reflected from its single surface is 25 times lower than the intensity of the incident light. Thus, it becomes necessary to have not only much higher spectral responsivity of the detector, but also a higher dynamic range to achieve the same accuracy of measurements for reflected light – compare the ratios of the incident $\delta\Phi_0 = \Delta\Phi_0/\Phi_0$ versus reflected $\delta\Phi_\rho = \Delta\Phi_\rho/\Phi_\rho$ fluxes of radiation for the single surface analyzed. For that reason, the specular reflectance measurement is often provided via the so-called standard sample. Reflectance ρ_s of the standard is measured by means of more precise equipment, taking care of the requirements mentioned above. Therefore, the reflectance ρ_i of a test surface is measured via the reflectance ρ_s of the standard, having similar characteristics:

$$\rho_i = \rho_s \Phi_i / \Phi_s, \tag{2.51}$$

thus, only high detector sensitivity is required. The accuracy of that measurement is defined by error $\Delta\rho_s$ of determining the standard's reflectance ρ_s and by error $2\Delta(\Phi_i/\Phi_s)$ of two flux measurements.

One concept for direct absolute measurement of specular reflectance following from Fig. 2.9 is seen in Fig. 2.10. Utilization of two mirrors in sequence – one as a standard and the other as one to be measured – instead of a single mirror addresses the dynamic-range concern. First, intensity I_1, not of a source light, but of radiation reflected from a mirror standard is measured (Fig. 2.10a), giving $I_1 = \text{const} \cdot \rho_{stand}$. Then (Fig. 2.10b), rearranging the entire system, one places the standard and the sample in the light path at an unchanged angle of incidence Θ_1 for the standard and

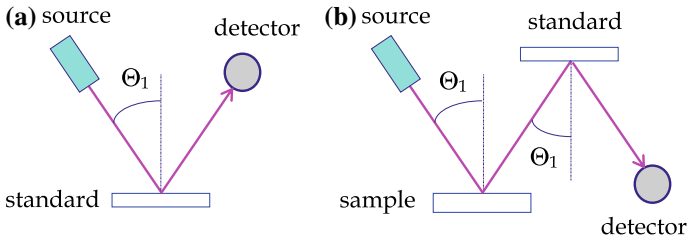

Fig. 2.10 Absolute measurements of reflectance

the same angle of incidence $\Theta_2 = \Theta_1$ for the sample, and makes another intensity measurement, $I_2 = \text{const} \cdot \rho_x \cdot \rho_{stand}$, where ρ_x is the reflectance of the sample. Accordingly $\rho_x = I_2/I_1$.

For the absolute measurement of specular reflectance performed by altering the positions of the sample mirror and of the standard, the reflection-symmetry approach can be used [0.6] (Fig. 2.11). The flux Φ_{std} of radiation reflected once by the standard in position 1 is measured first (view *a*). Second, the standard is rotated 180° around the system's symmetry axis into position 2 (view *b*), and the total flux Φ_Σ reflected by the standard once and twice by the wide sample in its axis plane is measured. The standard's reflectance may be unknown, but must remain stable during the measurement cycle. The ratio of two measured intensities provides the twofold specular reflectance $\bar{\rho}_S^2$ of the sample averaged over surface spots M and N: $\bar{\rho}_s^2 = \Phi_\Sigma/\Phi_{std}$.

Figure 2.12 illustrates the approach for absolute measurements of specular reflectance and direct transmittance at oblique incidence of radiation onto a plane opaque or transparent sample S [2.10]. For symmetrically aligned mirror pairs M_2, M_4 and M_3, M_5, presumed to have equal reflectance, detector D measures the ratio of the light fluxes incident on and reflected by the sample. When sample S is transparent, the ratio of detector readings with and without the sample gives the difference and the sum of attenuation for transmittance τ and reflectance ρ: $(1 - \tau - \rho)/$

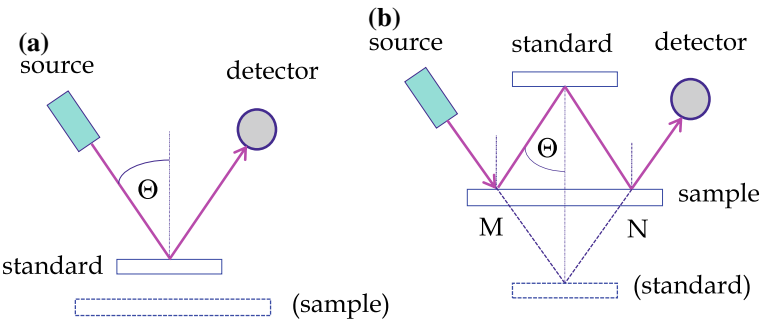

Fig. 2.11 Relative (**a**) and absolute (**b**) measurements of reflectance

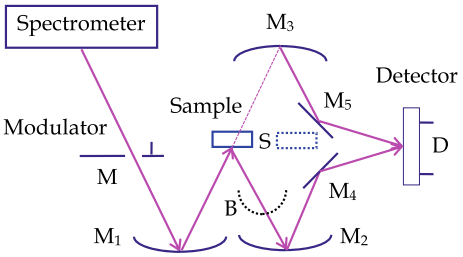

Fig. 2.12 Spectral evaluation of absolute reflectance

$(1+\tau+\rho)$, measuring the total absorption and scattering loss: $(\sigma + \alpha)/(2-\sigma-\alpha)$. Chopping the incident beam by modulator M for two separate time instances in detection of the reflected and transmitted beams permits one to measure the τ/ρ ratio. Rotating transparent sample S in and out of the beam at low modulation frequencies allows one to detect the difference-to-sum ratios: $(1-\rho)/(1+\rho)$ or $(1-\tau)/(1+\tau)$ (see Chap. 10), when either reflectance or transmittance is measured. In the latter case, the reflected beam is blocked by black light trap B and only the transmitted beam reaches detector D with and without sample S in its rotating holder (Fig. 2.12).

When measuring optical properties of objects in reflected light, special measures need to be taken for studies at normal light incidence. Since reflectance at normal incidence is not sensitive to random polarization changes of incident radiation, measurements at normal incidence appeal to a variety of applications. One way to capture normally reflected light from specularly reflective objects is to use a semitransparent beam splitter [2.11]. Figure 2.13 illustrates such a method of relative measurement of specular reflectance at normal incidence. A quasi-parallel beam of light is incident on beam splitter 1 from a light source or a spectral selector, such as a monochromator. Test sample 2 and reference standard 3, installed on one sliding carrier providing parallel displacement, are inserted sequentially into the beam's path. Light reflected and transmitted back via beam splitter 1 is received by detector 4, which may be used with an objective. Dark-glass reflector 5 and absorber 6 help reduce multiple reflections of incident light and can be replaced by a telescope to align the measurement system.

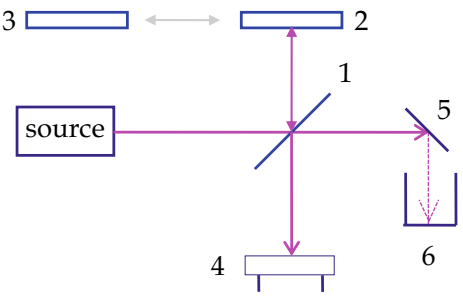

Fig. 2.13 Reflectance study at normal incidence

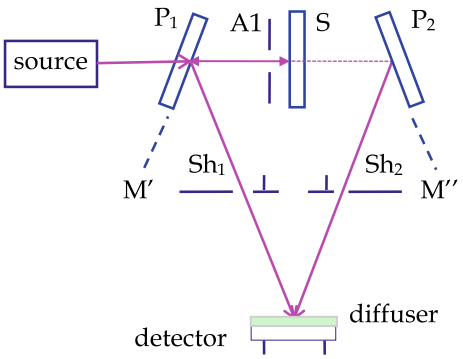

Fig. 2.14 Reflectometer for normal incidence

Another concept for measurement at normal incidence via two equivalent transparent plates aligned to redirect light to same spot on a single detector [2.12, 2.13] is seen in Fig. 2.14. A light beam from a source or a monochromator propagates via inclined plate P_1 and is reflected from test sample S and from plate P_1 to the detector. Without sample S incident light is reflected from equalizing plate P_2 to same detector spot. Added aperture A1 selects images only from the first, but not the second, surfaces of plates P_1 and P_2. When sample S is transparent, shutters Sh_1 and Sh_2 sequentially allow either the transmitted or the reflected beam to pass [2.13]. An earlier version of that design intended for normal or variable incidence of light [2.12] had single mirror M placed at positions M′ and M″ instead of the plates, allowing one to measure the intensity of incident light and the intensity of light reflected by crystal sample S by varying the angle of incidence.

A system for absolute reflectance measurement at normal incidence of light via a 45° rotating beam splitter is seen in Fig. 2.15. Semitransparent beam splitter B having a 50% reflecting and 50% transmitting coating on its first surface, and an antireflection coating on another surface, is set to be rotatable into two orthogonal but fixed positions *a* and *b*. In position *a*, the respective signal N_a of detector D is created by radiation directly incident from a source S and reflected by splitter B:

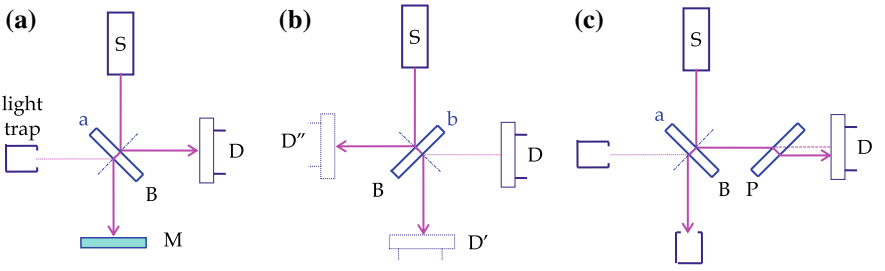

Fig. 2.15 Absolute measurement of specular reflectance at normal incidence of radiation: S—source; B—beam splitter; M—reflective sample; D, D′, D″—detector in altered positions

$$N_a = k\Phi_0\rho_B. \tag{2.52}$$

The detector's signal N_b in splitter position b, while sample M remains as shown in view a, is defined by the properties of two elements – the sample and the splitter – as splitter B transmits light and both the sample and the splitter reflect light to detector D:

$$N_b = k\Phi_0\tau_B\rho\rho_B. \tag{2.53}$$

Here Φ_0 is the flux emitted by source S, ρ is the reflectance under study, k is the sensitivity factor of steady measurements defined by the detector's sensitivity and the system's spectral transmittance, and τ_B and ρ_B are the transmittance and reflectance of beam splitter B. From Eqs. (2.52) and (2.53), we obtain:

$$\rho\tau_B = N_b/N_a. \tag{2.54}$$

The two measurements described above determine only the product of the sample reflectance and the splitter transmittance. The splitter transmittance τ_B is to be measured in the exactly same position as in Fig. 2.15b. This can be accomplished, for example, by replacing sample M by detector D at position D′. Fundamentally, the concept of measurement via rotating beam splitter B needs to be supported by at least $(\tau_B\rho_B)^{-1}$ times higher sensitivity than for the direct transmittance measurement. Thus, a semitransparent beam splitter with $\tau_B = \rho_B = 0.5$ provides the highest intensity of the conversion: $C = \tau_B\rho_B = 0.25$, being the most efficient. Another disadvantage is due to displacement of the beam passing the splitter. This could result in errors caused by likely nonuniformity of detector D. To prevent such errors, a balancing plate P (see Fig. 2.15c) with the same transmittance: $\tau_P = \tau_B$, and same thickness as beam splitter B can be inserted into the sample's light path. Another way is to set splitter B in one permanent position (Fig. 2.15b), adding two detectors D′ and D″, or moving detector D to position D″ and making the third reading of splitter transmittance τ_B at position D′.

In that case, the semitransparent beam splitter enables absolute measurement of mirror reflectance not only at normal incidence as in Figs. 2.14 and 2.15, but at any confined angle Θ desired (Fig. 2.16). Since a nonscattering beam splitter BS yields no light in the direction of incidence, added standard mirror M serves here to confine the back reflection. Light from source S is normally incident on mirror M. Beam splitter BS splits light reflected by the mirror into detector D. When any mirror sample is implemented at a desired angle Θ, mirror M is rotated around the sample into its new position determined by the dual angle 2Θ maintaining normal incidence of light. The ratio of these measurements gives the twofold reflectance of the sample at the desired incidence angle Θ for the section of its surface selected by the beam.

One distinctive way for the absolute measurement of reflectivity [2.14] deploys the absolute blackbody emitter, as depicted in Fig. 2.17. First, the blackbody emissivity is measured via small aperture A, selecting only radiation retroreflected by walls of the emitter to detector 1. Then, the detector or blackbody itself is rotated

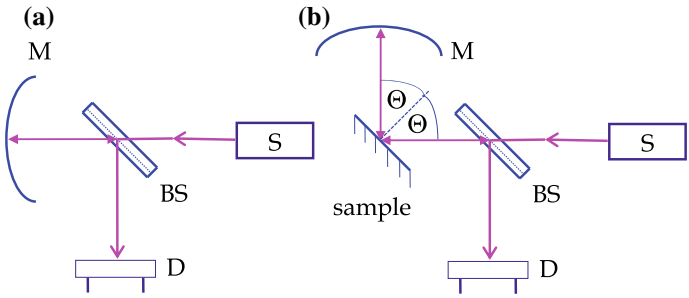

Fig. 2.16 Absolute reflectance measurement at confined incidence of light

Fig. 2.17 Emissivity-based reflectance study

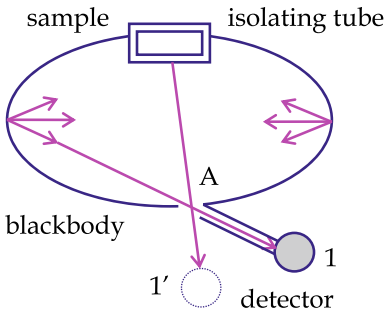

such a way that light reflected by an isolated sample inside the blackbody cavity is seen by the detector in position 1′ and measured. The ratio of signals gives absolute sample reflectance $\rho_s^{\,d}$ for hemispherical irradiation. For the sample, which does not violate the blackbody equilibrium and has graybody emissivity $\varepsilon_s = 1 - \rho_s^{\,d}$ at wavelength λ (see Sect. 9.3 for detail), the measured diffuse reflectance of sample S becomes:

$$\rho_s^d = \frac{M_{\lambda,2}}{M_{\lambda,1}} = \frac{M_{\lambda,c}\rho_s^d + \varepsilon_s M_{\lambda,s} - M_0}{M_{\lambda,c} - M_0} \underset{\varepsilon_s = 1-\rho_s^d}{=} \frac{\rho_s^d\left(M_{\lambda,c} - M_{\lambda,s}\right) + \left(M_{\lambda,s} - M_0\right)}{M_{\lambda,c} - M_0}, \tag{2.55}$$

where ρ_s^d is the diffuse reflectance of the sample at the thermal equilibrium and $M_{\lambda,c}$, $M_{\lambda,s}$, and M_0 are the emissivity of the emitter, sample, and surroundings, all at a blackbody temperature.

2.2.3 Directional Scattering Measurements

As long as scattered light can be diffused into 4π or 2π space surrounding an object under study, the spatial distribution of the object's scattering factor with arbitrary irradiation and observation geometry Ω_1/Ω_2 can be determined by a goniometer [0.4, 0.5]. The goniometric technique essentially allows determination of the object's scattering indicatrix at any conceivable geometry of irradiation and observation with regard to the object positioned in the center of the goniometer's rotation. The measurement formula for direct irradiation does not differ from that for transmittance or reflectance: $\sigma_{\Omega_1/\Omega_2} = \Phi_\sigma/\Phi_0$, where $\Phi_\sigma(\Omega_2)$ and $\Phi_0(\Omega_1)$ are, respectively, the flux of radiation scattered into solid angle Ω_2 of reception and the flux incident within solid angle Ω_1 of irradiation. Relations for the scattering factor for diffuse irradiation with uniform irradiance follow from Table 1.1. If either irradiation or illumination is not uniform and the object's radiance or luminance is therefore dependent on the point and the direction of observation, the magnitudes for the radiance or luminance indicatrix can be defined according to expressions (1.55)–(1.57). Likewise, the object's scattering indicatrix expresses the distribution of scattered light.

The total radiant or luminous flux Φ_σ scattered into the hemisphere of solid angle 2π is:

$$\Phi_\sigma = \int_0^{2\pi} d\psi \int_0^{\pi/2} I(\Theta, \psi) \sin\Theta d\Theta, \tag{2.56}$$

where $I(\Theta,\psi)$ is the radiant or luminous intensity of the secondary light source formed by the scattering object, and Θ and ψ are the radial and the azimuth angles which the light makes with the normal to the sample. The radiant or the luminous intensity I_P of radiation scattered by a perfect diffuser under identical conditions of irradiation and observation as for the sample (see Eqs. (1.57), (1.58)) is:

$$I(\Theta, \psi) = \beta(\Theta, \psi) I_p \cos\Theta. \tag{2.57}$$

Thus, the equivalent radiant or luminous flux scattered by a perfect diffuser may be rewritten as:

$$\Phi_\sigma = I_p \int_0^{2\pi} d\psi \int_0^{\pi/2} \beta(\Theta, \psi) \cos\Theta \sin\Theta d\Theta\,. \tag{2.58}$$

Since the flux falling onto the sample may be expressed via the flux reflected by a perfect diffuser: $\Phi_0 = \pi I_P$, the sample's 2π-space scattering factor $\sigma_{2\pi,}$ or its diffuse reflectance or transmittance, becomes:

$$\sigma_{2\pi} = \frac{1}{\pi} \int_0^{2\pi} d\psi \int_0^{\pi/2} \beta(\Theta, \psi) \sin\Theta \cos\Theta d\Theta \,. \tag{2.59}$$

For any homogeneous substance of symmetrical properties in the azimuth and radial directions:

$$\sigma_{2\pi} = 2 \int_0^{\pi/2} \beta(\Theta, \psi) \sin\Theta \cos\Theta d\Theta \,. \tag{2.60}$$

That measurement method for radiance (luminance) factor $\beta(\Theta)$ and radiance (luminance) indicatrix $\gamma(\Theta)$ can be simplified in comparison with the evaluation of the angular distribution for radiation intensity. Since these factors are always ratios of space-angular densities of radiation, both can be measured as ratios of intensities of a primary light source and one formed by the test object irradiated or illuminated by that primary source [2.15]. Schematically, such a method is illustrated in Fig. 2.18. An arbitrary source S of light of a limited emitting area A_s irradiates an aperture A_1, situated at a distance ℓ_1 from S. If small area A_s of the source aperture or its long distance ℓ_2 from detector D allows that aperture to be considered as the point source, intensity I_0 on the detector is identified by the square-distance law for source S. When solid angle Ω_1 constrained by aperture A_1 is not restrained by aperture A_2, no vignetting occurs (presuming no noticeable diffraction occurs at any aperture), and signal N_1 of detector D is strictly due to solid angle Ω_1 for aperture A_1 seen from the center of source S:

$$N_1 = k \cdot I_0 \cdot \Omega_1 \cong k \cdot I_0 \cdot A_1 / \ell_1^2. \tag{2.61}$$

To determine radiant or luminous irradiance, the object is placed behind aperture A_1, confining the area of the object's irradiation (Fig. 2.18b). To measure either object's radiance or luminance factor, detector D is reinstalled in its new position corresponding to observation angle Θ, still at normal incidence. Aperture A_2 is

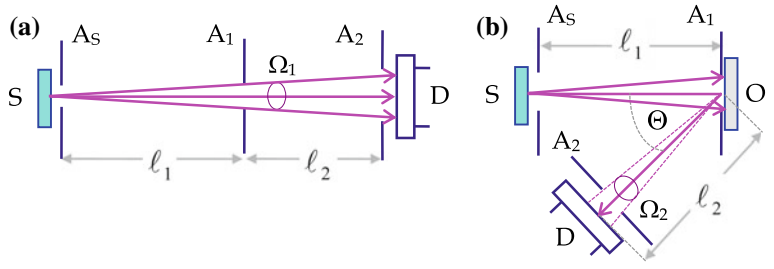

Fig. 2.18 Measuring a radiance or a luminance factor

placed in front of detector D, denoting solid angle Ω_2 at which aperture A_2 is seen from the object's center, now serving as the point source. In such an orientation:

$$N_2 = kL_{obj}(A_1 \cos\Theta)\Omega_2 \cong kL_{obj}A_{obj}A_2/\ell_2^2. \tag{2.62}$$

Here L_{obj} is the radiance or luminance of radiation scattered by the sample and $A_{obj} = A_1\cos\Theta$ is the equivalent area of the sample in the direction perpendicular to the direction identified by angle Θ. Both Eqs. (2.61) and (2.62) are obtained under the assumption that apertures A_s and A_1 are very small or are placed far away from the detector, so each can be treated as a point source (see Sect. 1.2).

Equation (2.62), rewritten via the radiance or luminance L_P of the perfect diffuser, becomes:

$$L_P = M_P/\pi = E\rho_P/\pi \underset{\rho_P=1}{=} E/\pi, \tag{2.63}$$

$$N_2 = k\beta(\Theta)\left(I/\pi\ell_1^2\right)\left(A_{obj}A_2/\ell_2^2\right) = \frac{k\sigma\gamma(\Theta)IA_2A_{obj}}{\pi(\ell_1\ell_2)^2}. \tag{2.64}$$

From Eqs. (2.61) and (2.64), the object's radiance factor β as a function of angle Θ at $A_{obj} = A_1\cos\Theta$ is:

$$\beta(\Theta) = (N_2/N_1)\left(\pi\ell_2^2A_1/A_2A_{obj}\right) = (N_2/N_1)\left(\pi\ell_2^2/A_2\cos\Theta\right). \tag{2.65}$$

Finally, at the round apertures of radii r_1 and r_2, Eq. (2.65) in reflected radiation converts to:

$$\beta(\Theta) = \rho^n{}_d \cdot \gamma(\Theta) = (N_2/N_1)(\ell_2^2/r_2^2)(1/\cos\Theta), \tag{2.66}$$

where ρ_d^n is the diffuse reflectance of the test object viewed in the direction of the outer normal.

2.3 Measurements of Color Coordinates and Indices

The photometric additivity principle enables the existing system of colorimetry, defined by the International Commission on Illumination (CIE), based on equally weighted color excitation functions of the CIE standard reference observer [2.16–2.36]. According to the definition of relation (1.16), the system of photometric quantities X_p is formed by a mathematical model of a linear spectrally additive receiver – CIE-standardized reference human eye executing a color-sensitive process of visualizing optical radiation within spectral domain $\lambda_p \in 360$–830 nm (for all practical purposes $\lambda_p \cong 380$–780 nm), with the luminance-to-radiance conversion factor $K_p = 683\ \text{lm} \cdot \text{W}^{-1}$ [1.3]. K_p provides the maximum luminous spectral

efficiency at wavelength $\lambda_{max} \cong 555$ nm for photopic vision. The conversion factors and λ_{max} are different for scotopic vision and other reduced quantities.

The sensation of color is associated with all the sensations arising from the activity of the retina of a human eye and its attached nervous mechanisms produced by visible radiation [2.18]. The system of colorimetry is based on three standardized and equally weighted spectral distributions for the equienergy *reference stimuli* [X], [Y], [Z] of the CIE standard reference observer. Any color stimulus C is, respectively, defined as a space vector $C = X[X] + Y[Y] + Z[Z]$, where X, Y, and Z are the *tristimulus values* of vector C; [X], [Y], and [Z] are unit vectors of CIE-defined reference stimuli for the reference colorimetric observer [2.22]. Other colors are located inside Maxwell's triangle (Fig. 2.21) drawn as a two-dimensional X–Y projection for space vector C [2.16]. For a set of reference stimuli [X], [Y], [Z], the *normalized tristimulus values* $\bar{x}(\lambda), \bar{y}(\lambda), \bar{z}(\lambda)$ for monochromatic radiations λ_i are derived as the equal sums over all wavelengths λ_i of the equienergy spectrum having $\bar{y}(\lambda)_{max} = 1$:

$$\sum_i \bar{x}(\lambda_i) = \sum_i \bar{y}(\lambda_i) = \sum_i \bar{z}(\lambda_i). \tag{2.67}$$

By that definition $\bar{y}(\lambda)$ is the spectral luminous efficiency function $V(\lambda)$ for the photopic vision specified by the CIE for the reference observer. Normalized tristimulus values $\bar{x}(\lambda), \bar{y}(\lambda), \bar{z}(\lambda)$ are the color-matching functions $\bar{x}(\lambda_i), \bar{y}(\lambda_i), \bar{z}(\lambda_i)$ for determining tristimulus values X, Y, Z of a color stimulus standardized by CIE as x-, y-, and z-bars for reference colorimetric observers (Figs. 2.19 and 2.20).

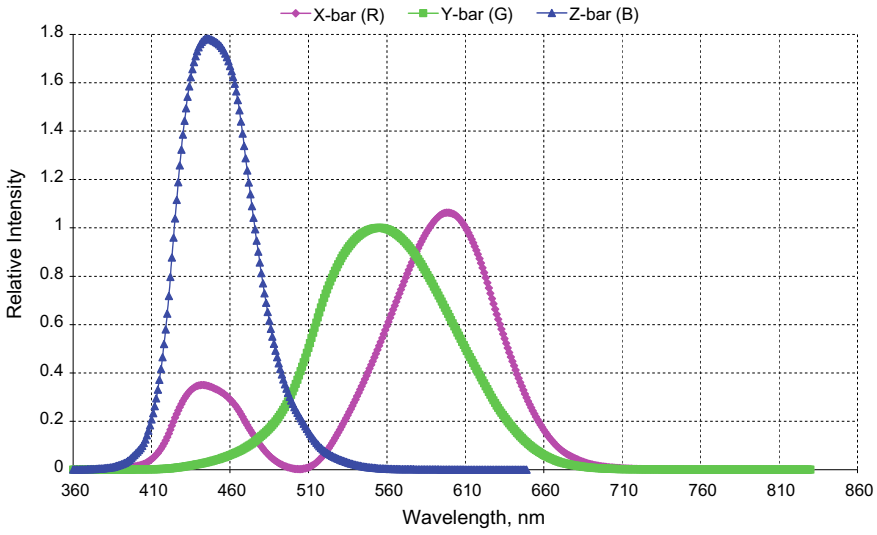

Fig. 2.19 CIE 2° color matching functions: 360–830 nm for x-bar, y-bar; 360–649 nm for z-bar

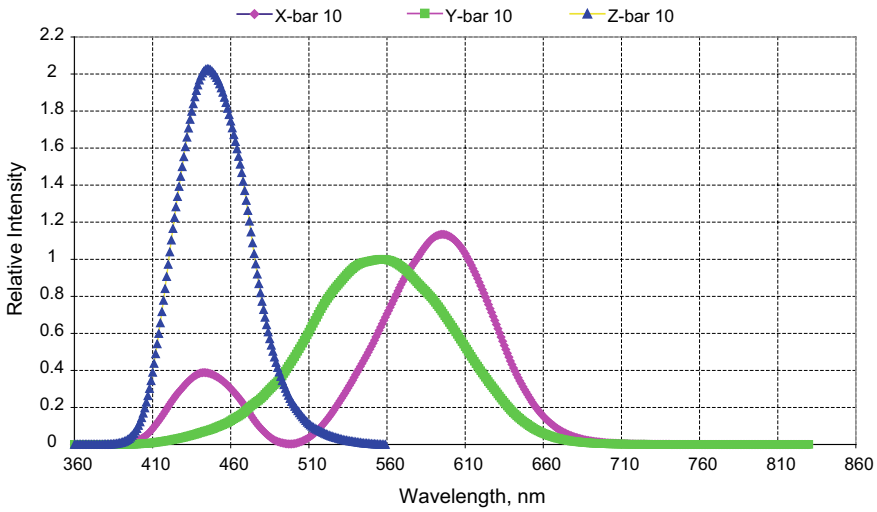

Fig. 2.20 CIE 10° color matching functions: 360–830 nm x-bar10, y-bar10; 360–559 nm z-bar10

The chromaticity, or color, coordinates x, y, z are derived from tristimulus values X, Y, Z as:

$$x(\lambda) = \frac{X}{X+Y+Z}; \quad y(\lambda) = \frac{Y}{X+Y+Z}; \quad z(\lambda) = \frac{Z}{X+Y+Z}. \tag{2.68}$$

By definition, $x + y + z \equiv 1$. The color coordinates for the normalized tristimulus values are similarly:

$$\begin{aligned} x(\lambda) &= \frac{\bar{x}(\lambda)}{\bar{x}(\lambda)+\bar{y}(\lambda)+\bar{z}(\lambda)}; \quad y(\lambda) = \frac{\bar{y}(\lambda)}{\bar{x}(\lambda)+\bar{y}(\lambda)+\bar{z}(\lambda)}; \\ z(\lambda) &= \frac{\bar{z}(\lambda)}{\bar{x}(\lambda)+\bar{y}(\lambda)+\bar{z}(\lambda)}. \end{aligned} \tag{2.69}$$

The chromaticity coordinates x_E, y_E, z_E for the equienergy spectrum are derived as equal sums:

$$\begin{aligned} x_E &= \sum_i \bar{x}(\lambda_i) = 0.333334; \quad y_E = \sum_i \bar{y}(\lambda_i) = 0.333331; \\ z_E &= \sum_i \bar{z}(\lambda_i) = 0.333335. \end{aligned} \tag{2.70}$$

If there is a color stimulus described by a spectral function $\varphi_\lambda(\lambda)$, then the tristimulus values of a color stimulus $\varphi_\lambda(\lambda)$ are defined as sums carried out at 1 nm intervals $\Delta\lambda = 1$ nm over the entire visible spectrum from 360 to 830 nm for the CIE matching functions $\bar{x}(\lambda), \bar{y}(\lambda), \bar{z}(\lambda)$:

$$X = k\sum_{\lambda} \varphi_{\lambda}(\lambda)\bar{x}(\lambda)\Delta\lambda; Y = k\sum_{\lambda} \varphi_{\lambda}(\lambda)\bar{y}(\lambda)\Delta\lambda; Z = k\sum_{\lambda} \varphi_{\lambda}(\lambda)\bar{z}(\lambda)\Delta\lambda. \tag{2.71}$$

Here k is the normalizing constant, the value of which is set to maximum spectral luminous efficiency $k_m = 683$ lm/W for illuminants or self-luminous objects, being set to give $Y = 100$ for objects with reflectance $\rho(\lambda)$ or transmittance $\tau(\lambda)$ equal to unity at all wavelengths: $\rho(\lambda_i) = 1$; $\tau(\lambda) = 1$, thus:

$$k = k_{\rho,\tau} = 100/\sum_{\lambda} S(\lambda)\bar{y}(\lambda)\Delta\lambda, \tag{2.72}$$

where $S(\lambda)$ is the relative spectral distribution function of the object's illuminant, such as any of the CIE standard illuminants applied to illuminate the reflective or transmissive object being studied.

Similarly, the measures for objects to be colorless are defined conversely for transparent and for reflective observation. For transparent objects, any coloration, such as yellowness, may be identified by the definition of Eq. (2.67): $\Delta_c = [(X - Z)/Y] \neq 0$. Depending on specific illumination and observation conditions, the yellowness index YI is defined by ASTM [4.68] for CIE sources and observers as:

$$YI = 100 \cdot (C_x X - C_z Z)/Y. \tag{2.73}$$

The equation constants for CIE illuminant D65 and 2° reference observer are $C_x = 1.2985$ and $C_z = 1.1335$. For reflective objects two characteristics – whiteness index and tint index – are defined by the CIE [2.33]:

$$WI = Y + 800(x_n - x) + 1700(y_n - y); \tag{2.74}$$

$$TI = 1000(x_n - x) - 650(y_n - y), \tag{2.75}$$

where $x_n = 0.333334$ and $y_n = 0.333331$ are the color coordinates of the perfect diffuser (see Chap. 1, Eq. (1.52)) and Y is the object's reflectivity – equal to 100 for the perfect (*perfectly white*) diffuser.

Since visual perception of color depends on the geometry of illumination and observation, the CIE defines two fields of view: 2° and 10°. All viewing angles between 1° and 4° are considered as 2° and angles above 4° are considered as 10°. If marked by no specific indices, as all definitions above, 2° or 1–4° is the angle for CIE color matching functions, also called $\bar{x}$, $\bar{y}$, and z-bars, or the spectral coordinates for 2° reference observer, or 2° reference stimuli, or primary colors red (R), green (G), and blue (B) (Fig. 2.19).

For 10°-visual field as for 2°-visual field specified by Eqs. (2.67)–(2.72), the normalized tristimulus values $\bar{x}_{10}(\lambda), \bar{y}_{10}(\lambda), \bar{z}_{10}(\lambda)$ of the monochromatic radiations for the reference stimuli $[X_{10}]$, $[Y_{10}]$, $[Z_{10}]$ match wavelength λ_i of the equienergy spectrum: $\sum_i \bar{x}(\lambda_i) = \sum_i \bar{y}(\lambda_i) = \sum_i \bar{z}(\lambda_i)$, with the maximum

$\bar{y}_{10}(\lambda)_{\max} = 1$. The chromaticity coordinates x_{10}, y_{10}, z_{10} of tristimulus values X_{10}, Y_{10}, Z_{10} are:

$$x_{10}(\lambda) = \frac{\bar{x}_{10}(\lambda)}{\bar{x}_{10}(\lambda) + \bar{y}_{10}(\lambda) + \bar{z}_{10}(\lambda)}; \quad y_{10}(\lambda) = \frac{\bar{y}_{10}(\lambda)}{\bar{x}_{10}(\lambda) + \bar{y}_{10}(\lambda) + \bar{z}_{10}(\lambda)};$$
$$z_{10}(\lambda) = \frac{\bar{z}_{10}(\lambda)}{\bar{x}_{10}(\lambda) + \bar{y}_{10}(\lambda) + \bar{z}_{10}(\lambda)}. \tag{2.76}$$

The chromaticity coordinates x_{10E}, y_{10E}, z_{10E} for the equienergy spectrum at 10° (>4°) are the sums:

$$x_{10,E} = \sum_i \bar{x}_{10}(\lambda_i) = 0.333334; \quad y_{10,E} = \sum_i \bar{y}_{10}(\lambda_i) = 0.333331;$$
$$z_{10,E} = \sum_i \bar{z}_{10}(\lambda_i) = 0.333335. \tag{2.77}$$

The CIE 10° illumination color matching functions of reference stimuli are shown in Fig. 2.20.

Figure 2.21 illustrates Maxwell's triangle, plotted for the CIE 2° reference observer. It is more precisely a semicircle construction, since its base only connects the circle, being the actual Y versus X function. The semicircle represents chromaticity coordinates for the color being perfectly neutral or white.

CIE tristimulus values X, Y, Z of a color stimulus $\varphi_\lambda(\lambda)$ are obtained via spectral coordinates of color-stimulus function $\varphi_\lambda(\lambda)$ at every wavelength by corresponding

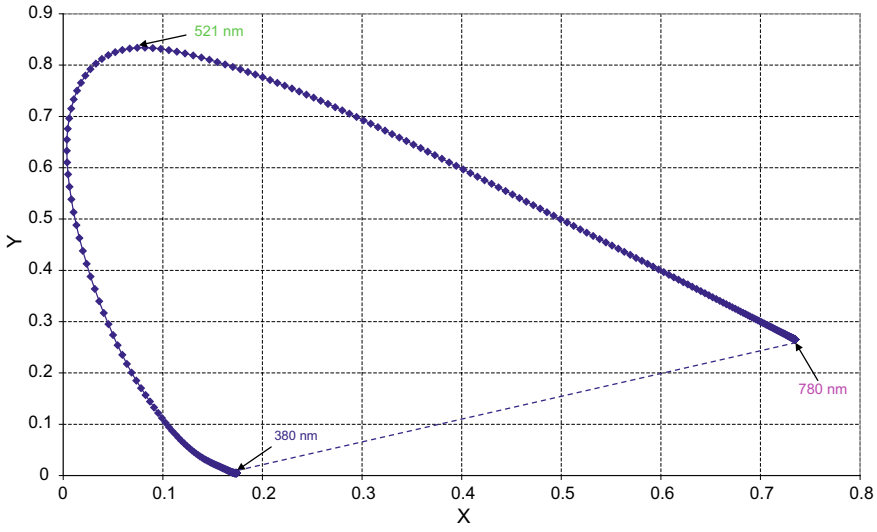

Fig. 2.21 Chromaticity plot for X-Y color coordinates of CIE 2 reference observer

to the angle-of-view CIE color-matching function integrated over the visible spectrum from 360 to 830 nm. The integration is practically carried out by numerical summation for CIE 1 nm standard tables (Eq. 2.71):

$$X = k\int_{\lambda} \varphi_{\lambda}(\lambda)\bar{x}(\lambda)d\lambda; \quad Y = k\int_{\lambda} \varphi_{\lambda}(\lambda)\bar{y}(\lambda)d\lambda \equiv V_{\lambda}; \quad Z = k\int_{\lambda} \varphi_{\lambda}(\lambda)\bar{z}(\lambda)d\lambda.$$
$$X_{10} = k_{10}\int_{\lambda} \varphi_{\lambda}(\lambda)\bar{x}_{10}(\lambda)d\lambda; Y_{10} = k_{10}\int_{\lambda} \varphi_{\lambda}(\lambda)\bar{y}_{10}(\lambda)d\lambda \equiv V_{\lambda 10}; Z_{10} = k_{10}\int_{\lambda} \varphi_{\lambda}(\lambda)\bar{z}_{10}(\lambda)d\lambda. \tag{2.78}$$

Along with defining the properties of standard observers, the CIE recommends and defines properties of standard CIE illuminants for analysis of color stimuli and for measurement of color coordinates: illuminant A and illuminant D65. Other illuminants with CIE-defined properties can also be used in specific illumination circumstances. The properties of the standard illuminants are based on a given spectral distribution of radiation emitted by the blackbody at the specified correlated color temperature $T_{D65} = 6500$ K for CIE illuminant D65 and $T_A = 2854.742$ K $\cong 2855$ K for CIE illuminant A. The spectral irradiance $L_{e,\lambda}(\lambda,T)$ of a blackbody in thermodynamic equilibrium at temperature T (K) in a medium with relative index of refraction n is defined by Plank's law:

$$L_{e,\lambda}(\lambda, T) = \frac{c_1 n^{-2}\lambda^{-5}}{\pi}\left[\exp\left(\frac{c_2}{n\lambda T}\right) - 1\right]^{-1}, \tag{2.79}$$

where $c_1 = 2\pi hc^2$ and $c_2 = hc/k$, where c is the speed of light in a vacuum, h is the Plank constant, k is the Boltzmann constant, and λ is the wavelength of radiation in a given blackbody medium. The CIE values are: $c_1 = 3741771 \times 10^{-16}\,\mathrm{W \cdot m^2}$ and $c_2 = 14388 \times 10^{-16}\,\mathrm{m \cdot K}$. From Eq. (2.79), the spectral distribution for CIE standard illuminant A in air having standardized refractive index $n = 1.00028$ becomes:

$$S_A(\lambda) = L_{e,\lambda}(\lambda, T)/L_{e,\lambda}(560\,nm, T). \tag{2.80}$$

Historically, when determining the color temperature, Plank's equation (2.79) in a vacuum and with $n = 1.0$ is used owing to wavelength dependency for the refractive index of air. The relative spectral distribution $S_A(\lambda)$ of power for CIE standard illuminant A is given by the normalized equation:

$$S_A(\lambda) = 100(560/\lambda)^5\left(\exp\left(1.435 \cdot 10^{-7}/2848 \cdot 560\right) - 1\right)/\left(\exp\left(1.435 \cdot 10^{-7}/2848 \cdot \lambda\right) - 1\right), \tag{2.81}$$

where λ is the wavelength in nanometers. The normalization in Eq. (2.81) results in $S_A(\lambda) = 100$ at $\lambda = 560$ nm. CIE standard illuminant D65 has the relative spectral distribution of a daylight phase at the nominal correlated color temperature $T \cong 6500$ K. If neither CIE illuminants A or D65 can be used, another CIE daylight

illuminant (D) is defined as having chromaticity coordinates x_D and y_D, correlated color temperature $T_{cp,D}$, and relative spectral distribution $S_D(\lambda)$ by the equations:

$$
\begin{aligned}
y_D &= -3.000x_D^2 + 2.870x_D - 0.275; \text{ for } 0.250 \le x_D \le 0.380; \\
x_D &= -4.6070 \cdot 10^9/T_{cp,D}^3 + 2.9678 \cdot 10^6/T_{cp,D}^2 \\
&\quad + 0.09911 \cdot 10^3/T_{cp,D} + 0.244063 \text{ for } 4000\,K \le T_{cp,D} \le 7000\,K; \\
x_D &= -2.0064 \cdot 10^9/T_{cp,D}^3 + 1.9018 \cdot 10^6/T_{cp,D}^2 + 0.24748 \cdot 10^3/T_{cp,D} \\
&\quad + 0.237040 \text{ for } 7000\,K < T_{cp,D} \le 25000\,K; \\
S_D(\lambda) &= S_0(\lambda) + M_1 S_1(\lambda) + M_2 S_2(\lambda), \text{ where } M_1 = \frac{-1.3515 - 1.7703x_D + 5.9114y_D}{0.0241 + 0.2562x_D - 0.7341y_D}, \\
M_2 &= \frac{0.0300 - 31.4424x_D + 30.0717y_D}{0.0241 + 0.2562x_D - 0.7341y_D}.
\end{aligned}
\tag{2.82}
$$

Spectral distributions of the relative intensity for CIE illuminants A and D65, and for color-temperature dependent CIE daytime illuminant D via functions $S_0(\lambda)$, $S_1(\lambda)$, and $S_2(\lambda)$ are shown in Figs. 2.22 and 2.23.

Other color systems can be derived by linear transformation of the specified functions. For example [2.20], an infinite number of excitation curves: χ, γ, ξ, may be found for $\bar{x}(\lambda_i), \bar{y}(\lambda_i), \bar{z}(\lambda_i)$:

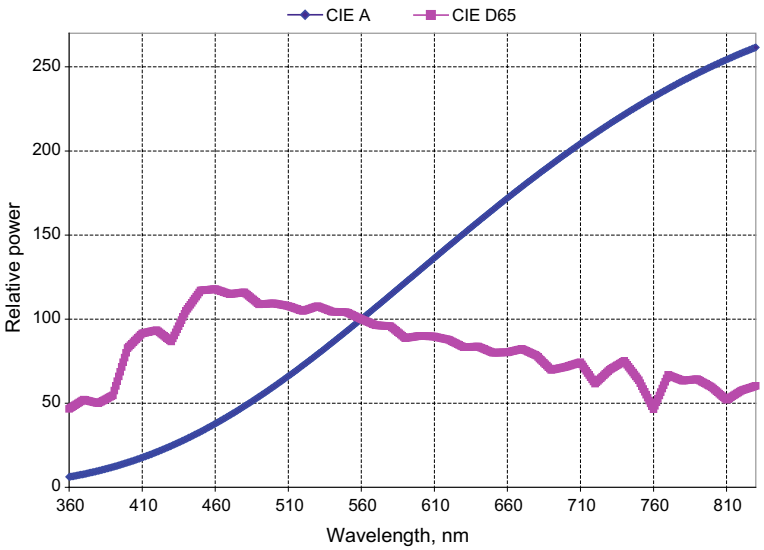

Fig. 2.22 Relative spectral power distributions of CIE standard illuminants A and D65

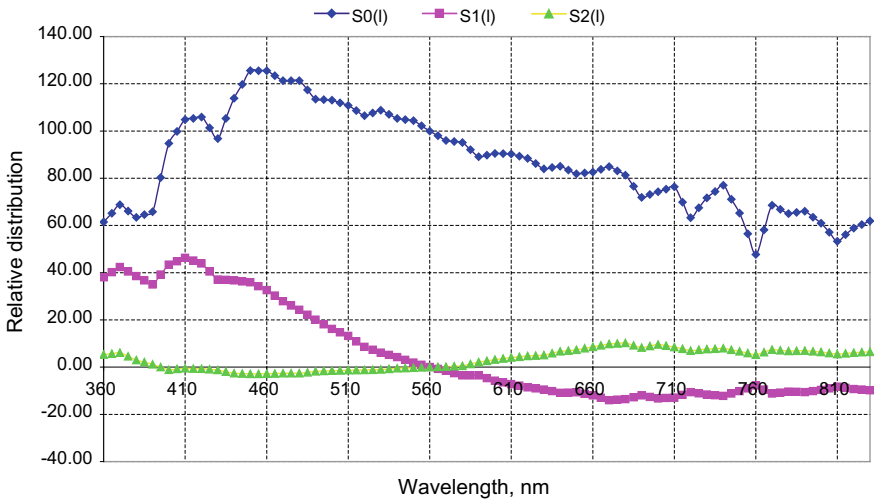

Fig. 2.23 Relative spectral power distributions of CIE functions for the daytime illuminants D

$$\begin{aligned} \chi &= K_1 x + K_2 y + K_3 z; \\ \gamma &= K_4 x + K_5 y + K_6 z; \\ \xi &= K_7 x + K_8 y + K_9 z. \end{aligned} \tag{2.83}$$

where K_1–K_9 are arbitrary constants, forming the determinant which is distinguished from zero:

$$\begin{vmatrix} K_1 & K_2 & K_3 \\ K_4 & K_5 & K_6 \\ K_7 & K_8 & K_9 \end{vmatrix} \neq 0. \tag{2.84}$$

$$X_\chi = \frac{\chi}{\chi+\gamma+\xi}; \quad Y_\gamma = \frac{\gamma}{\chi+\gamma+\xi}; \quad Z_\xi = \frac{\xi}{\chi+\gamma+\xi}. \tag{2.85}$$

$$x = \frac{\bar{\chi}(\lambda)}{\bar{\chi}(\lambda)+\bar{\gamma}(\lambda)+\bar{\xi}(\lambda)}; \quad y = \frac{\bar{\gamma}(\lambda)}{\bar{\chi}(\lambda)+\bar{\gamma}(\lambda)+\bar{\xi}(\lambda)};$$

$$z = \frac{\bar{\xi}(\lambda)}{\bar{\chi}(\lambda)+\bar{\gamma}(\lambda)+\bar{\xi}(\lambda)}. \tag{2.86}$$

In the case of a visual mixture of two color stimuli, $\bar{\chi}_1(\lambda), \bar{\gamma}_1(\lambda), \bar{\xi}_1(\lambda)$, $\bar{\chi}_2(\lambda), \bar{\gamma}_2(\lambda), \bar{\xi}_2(\lambda)$, the mixture's stimulus is identified as the combination $\bar{\chi}_m = \bar{\chi}_1(\lambda) + \bar{\chi}_2(\lambda), \bar{\gamma}_m = \bar{\gamma}_1(\lambda) + \bar{\gamma}_2(\lambda), \bar{\xi}_m = \bar{\xi}_1(\lambda) + \bar{\xi}_2(\lambda)$. The tristimulus coordinates of the visual color mixture as the linear combination of the two are:

$$x(\lambda) = \frac{\bar{\chi}_1 + \bar{\chi}_2}{\bar{\chi}_1 + \bar{\chi}_2 + \bar{\gamma}_1 + \bar{\gamma}_2 + \bar{\xi}_1 + \bar{\xi}_2}; \quad y(\lambda) = \frac{\bar{\gamma}_1 + \bar{\gamma}_2}{\bar{\chi}_1 + \bar{\chi}_2 + \bar{\gamma}_1 + \bar{\gamma}_2 + \bar{\xi}_1 + \bar{\xi}};$$
$$z(\lambda) = \frac{\bar{\xi}_1 + \bar{\xi}_2}{\bar{\chi}_1 + \bar{\chi}_2 + \bar{\gamma}_1 + \bar{\gamma}_2 + \bar{\xi}_1 + \bar{\xi}}. \tag{2.87}$$

From the additivity principle of the CIE color system, the color coordinates of any composite summation object Σ are:

$$x_\Sigma = \frac{x_1 + x_2}{2}; \quad y_\Sigma = \frac{y_1 + y_2}{2}; \quad x_\Sigma + y_\Sigma = \frac{x_1 + x_2}{2} + \frac{y_1 + y_2}{2} = \frac{x_1 + y_1}{2} + \frac{x_2 + y_2}{2}. \tag{2.88}$$

Since correlations among color stimuli may be represented in vector forms considering each color as one vector in X, Y, Z space with respective unit vectors $\vec{x}, \vec{y}, \vec{z}$ for three color coordinates:

$$\vec{C} \equiv X\vec{x} + Y\vec{y} + Z\vec{z}, \tag{2.89}$$

color difference ΔC between two stimuli can be seen as the difference of two vector modules:

$$\Delta C_{i,j} = \vec{C}_i - \vec{C}_j = \sqrt{(X_i - X_j)^2 + (Y_i - Y_j)^2 + (Z_i - Z_j)^2}. \tag{2.90}$$

Color coordinates for the CIE 2° reference observer given by Eqs. (2.67)–(2.72) (Figs. 2.19 and 2.20) lead to a nonuniform x–y color space and unequal transformation factors among diverse colors. The CIE 1976 uniform chromaticity scale is reset by transforming the projected x–y diagram into:

$$Abscissa: u' = 4X/(X + 15Y + 3Z); \quad Ordinate: v' = 9Y/(X + 15Y + 3Z), \tag{2.91}$$

at tristimulus values X, Y, Z, with w′ being the third uniform chromaticity coordinate $w' = 1 - u' - v'$.

The three-dimensional CIE 1976 uniform color space is formed by establishing a white color object stimulus, such as that of the perfect diffuser (see Chap. 1), plotted in rectangular coordinates:

$$L* = 116 \cdot f(Y/Y_n) - 16; \quad a* = 500[f(X/X_n) - f(Y/Y_n)];$$
$$b* = 200[f(Y/Y_n) - f(Z/Z_n)], \tag{2.92}$$

where X, Y, Z and X_n, Y_n, Z_n are the tristimulus values of the test color object and the white color object. For a perfectly white object, X_n, Y_n, Z_n are the tristimulus values of a CIE standard light source applied for illumination of the test object, and

$Y_n = 100$ is the normalizing constant in Eq. (2.72). The values of the functions in Eq. (2.92) depend on the ratios of the tristimulus values for two objects:

$$f(X/X_n) = (Y/Y_n)^{1/3} \quad \text{if} \quad f(X/X_n) > (24/116)^{1/3}; \tag{2.93}$$

$$f(X/X_n) = (841/108)(Y/Y_n) + 16/116 \quad \text{if} \quad f(X/X_n) \le (24/116)^{1/3}. \tag{2.94}$$

Identical correlations exist for $f(Y/Y_n)$ and $f(Z/Z_n)$ as in Eqs. (2.93) and (2.94) [2.33]. The CIE 1976 color difference between color stimuli 1 and 2 can be calculated as the Euclidian distance between space points 1 and 2 representing the two color stimuli in three-dimensional uniform space:

$$\Delta E^*_{a,b} = \sqrt{(\Delta L^*)^2 + (\Delta a^*)^2 + (\Delta b^*)^2}, \tag{2.95}$$

where the above-mentioned differences for points 1 and 2 are $\Delta L^* = L^*_2 - L^*_1$, $\Delta a^* = a^*_2 - a^*_1$, and $\Delta b^* = b^*_2 - b^*_1$.

When the CIE standard reference observer views optical radiation with an equienergy spectral distribution function, making the tristimulus values X, Y, Z equal, the resultant observer response represents an unaltered white color. If the radiation viewed consists of the three primary colors red, green, and blue with uneven spectral distribution, having respective spectral radiances $L_R(\lambda)$, $L_G(\lambda)$, and $L_B(\lambda)$ (see Fig. 2.19), the resultant tristimulus values converted to luminance units, seen by the observer, are as shown for the red color component:

$$\begin{aligned}
X_R &= 683 \int_\lambda L_{\lambda,R} y\bar{x}\,(\lambda)d\lambda = 683R \int_\lambda L_{\lambda,R,\max}\bar{x}\,(\lambda)d\lambda \equiv RX_{R,\max};\\
Y_R &= 683 \int_\lambda L_{\lambda,R}\bar{y}\,(\lambda)d\lambda = 683R \int_\lambda L_{\lambda,R,\max}\bar{y}\,(\lambda)d\lambda \equiv RY_{R,\max};\\
Z_R &= 683 \int_\lambda L_{\lambda,R}\bar{z}\,(\lambda)d\lambda = 683R \int_\lambda L_{\lambda,R,\max}\bar{z}\,(\lambda)d\lambda \equiv RZ_{R,\max},
\end{aligned} \tag{2.96}$$

where the primary color luminances are $L_{\lambda,R} = R \cdot L_{\lambda,R,\max}$, $L_{\lambda,G} = G \cdot L_{\lambda,G,\max}$, and $L_{\lambda,R} = B \cdot L_{\lambda,B,\max}$. The linear superposition of red, green, and blue color components is observed with the tristimulus values:

$$
\begin{aligned}
X &= 683 \int_{360nm}^{830nm} \left(L_{\lambda,R} + L_{\lambda,G} + L_{\lambda,B}\right)\bar{x}_\lambda d\lambda = RX_{R,\max} + GX_{G,\max} + BX_{B,\max};\\
Y &= 683 \int_{360nm}^{830nm} \left(L_{\lambda,R} + L_{\lambda,G} + L_{\lambda,B}\right)\bar{y}_\lambda d\lambda = RY_{R,\max} + GY_{G,\max} + BY_{B,\max};\\
Z &= 683 \int_{360nm}^{830nm} \left(L_{\lambda,R} + L_{\lambda,G} + L_{\lambda,B}\right)\bar{z}_\lambda d\lambda = RZ_{R,\max} + GZ_{G,\max} + BZ_{B,\max}.
\end{aligned}
\tag{2.97}
$$

The system of linear Eqs. (2.97) can be solved in matrix notations for the matrix inverse as:

$$
\begin{aligned}
\begin{bmatrix} X \\ Y \\ Z \end{bmatrix} &= \begin{bmatrix} X_{R,\max} & X_{G,\max} & X_{B,\max} \\ Y_{R,\max} & Y_{G,\max} & Y_{B,\max} \\ Z_{R,\max} & Z_{G,\max} & Z_{B,\max} \end{bmatrix} \begin{bmatrix} R \\ G \\ B \end{bmatrix};\\
\begin{bmatrix} R \\ G \\ B \end{bmatrix} &= \begin{bmatrix} X_{R,\max} & X_{G,\max} & X_{B,\max} \\ Y_{R,\max} & Y_{G,\max} & Y_{B,\max} \\ Z_{R,\max} & Z_{G,\max} & Z_{B,\max} \end{bmatrix}^{-1} \begin{bmatrix} X \\ Y \\ Z \end{bmatrix}.
\end{aligned}
\tag{2.98}
$$

The founding principle of tristimulus colorimetry is the assumption which states that if for any pair of two light stimuli there is a precise match of each tristimulus value, the CIE standard observer experiences a color match for the pair. That assumption is based on two fundamentals: (1) cone photoreceptors of the CIE standard reference observer generate an invariant response to the same stimuli and (2) the photoreceptors of the standard reference observer individually carry no information about any spectral distribution of light absorbed by them. Therefore, only by comparing signals for the defined three classes of eye photoreceptors for the standard reference observer can one extract the information needed for perception of each individual color [2.29–2.31]. Another factor is that the CIE color matching functions are based on relative spectral radiometric measurements but their connections to the absolute luminance scale are provided by mathematical transformation of the measured data while normalizing one color matching function $\bar{y}(\lambda) \equiv V(\lambda)$. Future photometric and color systems could be based on measuring actual spectral sensitivities of three color classes of the eye cones, while not necessarily relying on linear assumptions [2.29] and addressing likely UV corrections for photopic luminous efficiency function $V(\lambda)$ [2.31–2.32].

A color stimulus associated with an object may be identified by measuring the transmission, reflection, or scattering spectrum of that object in the visible domain. The associated tristimulus coordinates for such an object can be determined by converting the spectrum measured as the mathematical model for the product of the spectrum of the object itself, the emission spectrum of a standardized source of observation, illuminating the object, and the normalized tristimulus values

$\bar{x}(\lambda), \bar{y}(\lambda), \bar{z}(\lambda)$ of the CIE reference observer. Measurements of the object's spectral transmission, reflection, or scattering must be provided by means of absolute spectral measurements, such as made by an absolute spectrophotometer, matching spectral and illumination characteristics of a specified standard source and spectral and observation characteristics of the CIE standard reference observer. Any standardized color index of interest, such as the yellowness or the whiteness index, may be acquired from the measured tristimulus spectral color coordinates of the object.

The perception of color in the CIE-standardized scale for an object being studied can be obtained directly by illuminating that object by a source spectrally matching the standard source and by observing the reaction of the object to that radiation using a receiver matching the spectral sensitivity of one of the standardized observers. That straightforward principle was the foundation for using spectrophotometers for detecting spectral functions of color objects [2.23]. Nevertheless, specific applications and developments of tristimulus colorimeters led to measuring color coordinates by trying to physically emulate CIE-standardized sources and reference observers, and building them into the spectrophotometer's hardware. Such an approach made systems inflexible while imbedding emulation errors into measured color coordinates, since the properties of standard CIE sources and observers or specific geometries were not matched for one or another reason in devices as intended [2.37–2.40]. Similar matching errors affect color measurements modeled by color measurement and analysis software tools [2.41] when the standard emulation approach is applied for determining the test object's color coordinates and indices. Special calibration measures utilized to correct colorimeter measurements could reduce but not eliminate errors [2.42–2.44].

To enable true and absolute color measurements, the measurements of spectral distribution functions $\varphi_\lambda(\lambda)$ for color stimuli must establish a direct correlation to standardized CIE spectrums, for example, by deploying actual data for standard sources and reference observers. A common approach for measurements of tristimulus values X, Y, Z consists in irradiating a color object by a quasi-standard source $S'(\lambda)$ with spectral mismatch error $A(\lambda)$ and obtaining a quasi geometry-matching spectrum $T'(\lambda)$ of the reflection, transmission, or scattering of the object for mismatch error $O(\lambda)$ by a quasi-standard observer with color coordinates x',y',z' at respective mismatch spectral errors $R(\lambda)$, $G(\lambda)$, and $B(\lambda)$, and finally determining the tristimulus values $\tilde{X}, \tilde{Y}, \tilde{Z}$ by approximations:

$$\begin{aligned}
\tilde{X} &= k \int_{\lambda} S'(\lambda) \cdot T'(\lambda) \cdot x'(\lambda) d\lambda; \\
\tilde{Y} &= k \int_{\lambda} S'(\lambda) \cdot T'(\lambda) \cdot y'(\lambda) d\lambda; \\
\tilde{Z} &= k \int_{\lambda} S'(\lambda) \cdot T'(\lambda) \cdot z'(\lambda) d\lambda;
\end{aligned} \tag{2.99}$$

$$\begin{aligned}\tilde{X} &= k\int_{\lambda}[A(\lambda)S(\lambda)]\cdot[T(\lambda)O(\lambda)]\cdot[R(\lambda)x(\lambda)]d\lambda;\\ \tilde{Y} &= k\int_{\lambda}[A(\lambda)S(\lambda)]\cdot[T(\lambda)O(\lambda)]\cdot[G(\lambda)y(\lambda)]d\lambda;\\ \tilde{Z} &= k\int_{\lambda}[A(\lambda)S(\lambda)]\cdot[T(\lambda)O(\lambda)]\cdot[B(\lambda)z(\lambda)]d\lambda.\end{aligned} \tag{2.100}$$

Here T(λ) is the true transmittance, reflectance, scattering or another color transformation factor of the object being studied, S(λ) is the relative spectral power of a CIE standard illuminant applied for the object's illumination, x(λ), y(λ), and z(λ) are the color matching functions of a standard reference observer, such as any CIE-defined reference observer used, and k = 683 lm/W. Owing to absolute source–observer mismatches, $A(\lambda)\cdot R(\lambda)$, $A(\lambda)\cdot G(\lambda)$, $A(\lambda)\cdot B(\lambda)$, the $\tilde{X},\tilde{Y},\tilde{Z}$ values measured by applying imperfect sources and observers deviate from tristimulus X, Y, Z values by substantial margins. Various calibration methods may correct some mismatches, but leave inevitable residual errors.

A true color stimulus function of any object can be determined by applying a substitution method of absolute measurements in such a way that all color measurements are to be made via utilizing exact CIE color functions [2.45]. First, the color stimulus function $\varphi_\lambda(\lambda)$ of a test object is identified by measuring its absolute transmission, reflection, or scattering functionality within an applicable standardized spectral region of visible radiation defined by the CIE. Second, absolute data of the object's measured color stimulus $\varphi_\lambda(\lambda)$ are fitted into a mathematical model combining the emission spectrum of a CIE standard source matching an illumination condition and tristimulus values: the color matching functions $\bar{x}(\lambda),\bar{y}(\lambda),\bar{z}(\lambda)$ of the CIE reference observer for an observation condition. The object's actual transmission, reflection, or scattering spectrum must be provided by means of the absolute spectral measurement, such as performed by any absolute spectrophotometer, satisfying the conditions of illumination and observation defined by the CIE and reproducing precise wavelengths, but not necessarily intensities of illumination and observation spectrums for the CIE standard source and the reference observer used. The limits for the sensitivity for such measurements are only restricted by the principal discrimination confinements to measure color differences, as determined by a vector difference of two color stimuli—true and measured – which must be discriminable, as long as the discrimination defining spectrum $\varphi_\lambda(\lambda)$ is detectable.

The defined absolute color evaluation concept implies that each measurement provides the object's absolute transformation spectrum at the specified optical-geometry condition of the illumination and observation. That absolute

transformation spectrum in reflection, transmission, or scattering can be further embedded into any CIE-standardized color-coordinate determination technique, such as that defined by Eqs. (2.67)–(2.75), to determine the object's tristimulus values X, Y, Z. If absolute measurement processes for obtaining the object's characteristics are realized under specified irradiation and observation conditions, the properties measured may be further used to identify the object's color coordinates for either CIE-standardized sources or reference observes, specifically under the irradiation and observation condition of the measurement provided.

The absolute measurement method described can use actual standard CIE functions for optical radiation sources and for CIE matching functions X, Y, Z. The concept is illustrated in Figs. 2.24 and 2.25. The principal functional arrangement for the absolute color measurement method is shown in Fig. 2.24. A CIE standard source, a color test object, and a CIE reference observer are all deployed at CIE-standardized geometry for the object's illumination and observation. CIE standard illuminant A, D65, or D (Figs. 2.22 and 2.23) can be deployed as a source for that system.

The CIE standard illumination geometry for illumination by the normal and normal observation at identical right-circular conic geometry for a light beam, having up to 5° half-angle divergence in transmission, may be applied. The CIE standard observer is provided by a daytime CIE X, Y, Z reference observer with CIE 2° color matching functions $\bar{x}, \bar{y}, \bar{z}$ [2.45] (see Sects. 4.1, 4.2) that defines $\bar{x}, \bar{y}, \bar{z}$ values for every 1 nm from 360 to 830 nm (Fig. 2.19). Figure 2.25a shows a physically separable measurement insert, which contains three of the five elements in Fig. 2.24: the illumination geometry, the color object, and the observation geometry, leaving out the source and the observer. The remaining two system

Fig. 2.24 Absolute color measurement methodology

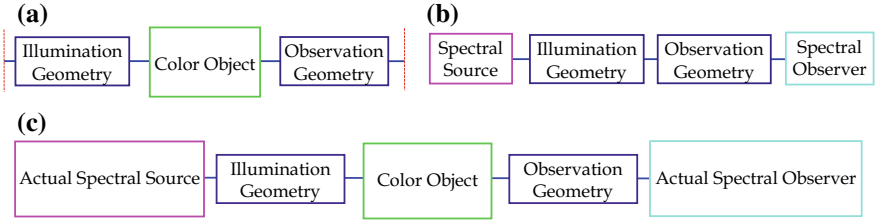

Fig. 2.25 **a** Concept of absolute color measurement insert. **b** Absolute spectral color measurement calibration. **c** Absolute spectral measurement for a color object

elements – the CIE standard source and the CIE standard reference observer are to be recombined with the first three elements of the measurement insert depicted when the results of the absolute color measurements are obtained, as shown below.

Figure 2.25b depicts the calibration step for the absolute color spectrophotometer enclosure per CIE-defined spectral and spatial conditions. Figure 2.25c depicts the color measurement step. When the spectrophotometer completes any absolute spectral measurement for the color object, and while the absolute spectrum measured only contains information about the object itself, the actual functions of the spectral source and of the spectral observer of that spectrophotometer for a specific spectral region measured are replaced by the model mathematical functions of the CIE standard source and the CIE reference observer matching the spectral region of the source and the observer of the spectrophotometer (see Fig. 2.26). The color characteristics of the color object, as its color coordinates and tristimulus values, are determined via its absolute spectrum T(λ):

$$\begin{aligned}\widetilde{X} &= k\int_{\lambda} S(\lambda)\cdot T(\lambda)\cdot \bar{x}(\lambda)d\lambda;\\ \widetilde{Y} &= k\int_{\lambda} S(\lambda)\cdot T(\lambda)\cdot \bar{y}(\lambda)d\lambda;\\ \widetilde{Z} &= k\int_{\lambda} S(\lambda)\cdot T(\lambda)\cdot \bar{z}(\lambda)d\lambda.\end{aligned} \tag{2.101}$$

Since the absolute measured spectrum T(λ) of the object and the spectrums of the standardized source S(λ) and the reference observer x (λ), y (λ), z (λ) are all used for such absolute determination of the object's tristimulus values $\tilde{X}, \tilde{Y}, \tilde{Z}$, mismatch errors ΔT_λ of measurements can only be caused by measurement errors of the object's absolute spectrum T(λ) versus the true one T_λ: $\Delta T(\lambda) = |T_\lambda - T(\lambda)|/T_\lambda$. Spectral values of the error function ΔT(λ) will be much smaller than those for common color measurements, since typical absolute spectrophotometric measurement errors amount to tens or even hundreds of parts of 1% (0.01−0.1%), while errors of color measurements are orders of magnitudes higher and even in standardizing institutions can be several percentage points. Another advantage of that absolute method is for any future corrections in standard source or reference observer data to be directly included in the color coordinate measurement results, if

Fig. 2.26 Absolute spectral color measurement model

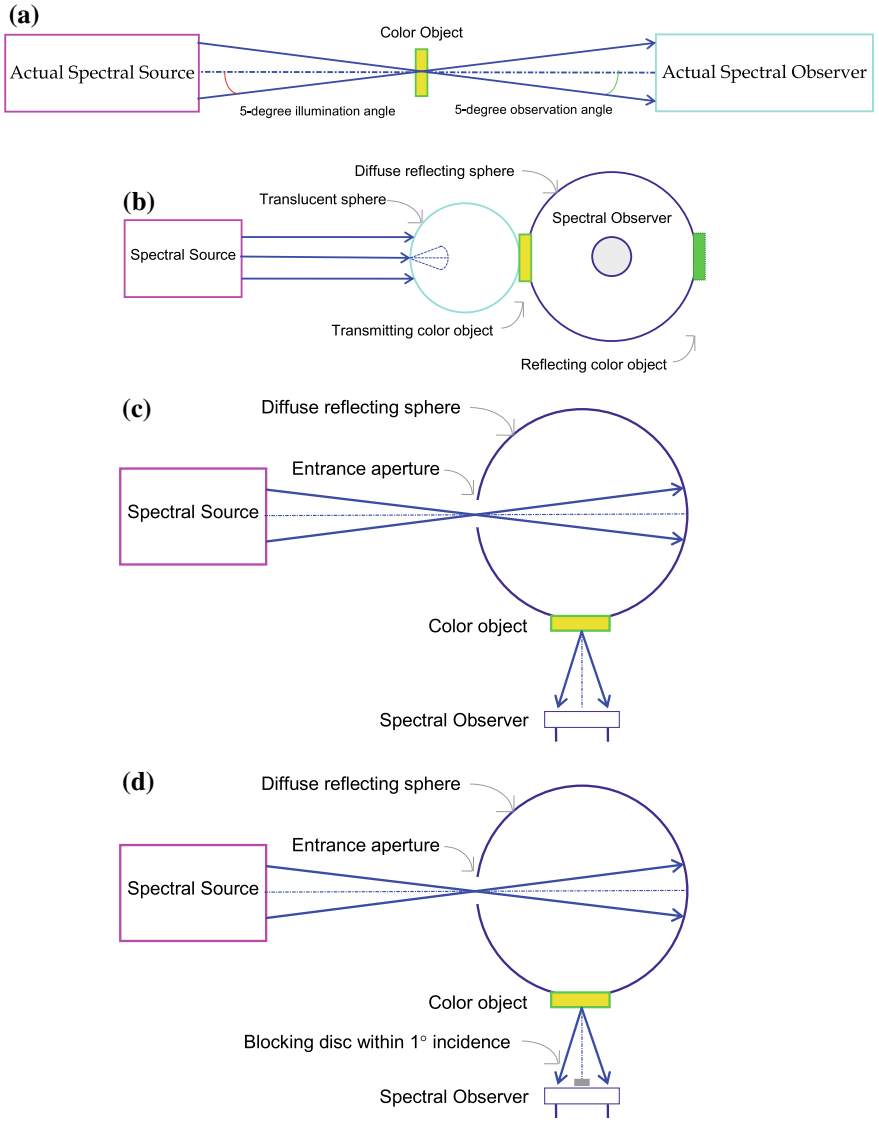

Fig. 2.27 **a** Absolute spectral measurement in transmission for normal illumination/observation geometry. **b** Absolute color measurement in transmission or reflection for diffuse illumination/observation geometry. **c** Absolute color measurement in transmission or reflection for diffuse illumination/observation geometry: the direct component of the object's transmission is included. **d** Absolute color measurement in transmission or reflection for diffuse illumination/observation geometry: the direct component of the object's transmission within 1° angle of incidence is excluded

the CIE, for example, would adopt the short-wavelength correction for the luminous efficiency function $\bar{y}_\lambda(\lambda)$ relying on flicker photometry of matching radiances for alternating colors [2.31].

Several specific examples of illumination and observation geometries for the absolute color measurements are illustrated in Fig. 2.27: normal illumination and observation in transmission (Fig. 2.27a); diffuse-diffuse illumination–observation in either transmission or reflection (Fig. 2.27b); and diffuse illumination and normal observation with (Fig. 2.27c) and without (Fig. 2.27d) a direct component in transmission.

The example in Fig. 2.27b involves application of a translucent sphere (see Sects. 2.2 and 2.4) for uniform diffuse illumination of the object in transmitted and in reflected radiation incident on an object from a source. Other illumination-observation geometries specified by the CIE can be used [2.45].

2.4 Photometry of Integrating Spheres

2.4.1 Uniformly Scattering Spheres

It may not be obvious for the integrating sphere with a highly diffuse-reflecting isotropic coating on its internal surface to be the device to collect light scattered by a test object into a 2π hemisphere or a 4π sphere if the object's hemispherical or spherical scattering factor is measured. One could instead suggest utilizing a specularly reflecting wall for a mirror-bound integrating sphere. Let us consider irradiation of the internal surface of a partially reflective and transmissive integrating sphere of radius R via a small opening by a direct light beam with radiant flux Φ_0 and having cross section A_0. If the entire internal sphere wall reflects light as a solitary mirror having specular reflectance ρ_r, then the sequence of multiple reflections inside the sphere should create either uniform or close-to-uniform irradiance E only when an infinitely high number of reflections inside is approached. That condition is satisfied if the wall's reflectance ρ_r tends to unity: $\rho_r \to 1.0$. Presuming that ρ_r weakly depends on the angle of incidence, the total irradiance $E_{r,\Sigma}$ of a specular sphere wall dispersed over the sphere surface A_{sph}, is:

$$E_{r,\Sigma} = \frac{1}{4\pi R^2}\left(\Phi_0 + \Phi_0\rho_r + \cdots + \Phi_0\rho_r^n\right) = \frac{\Phi_0}{4\pi R^2}\frac{1-\rho_r^n}{1-\rho_r} \underset{n\to\infty}{\overset{\rho_r\to 1}{=}} \frac{\Phi_0}{A_{sph}}\frac{1}{1-\rho_r}. \tag{2.102}$$

The distinction of wall specular reflectance from 1.0 defines the closeness of consecutive irradiances E_i and E_j and distinction of the total irradiance E_Σ from the irradiance created by the directly irradiating beam: $E_0 = \Phi_0/A_0$. Therefore, irradiance inside a mirror sphere is affected by unequal irradiance terms of multiple reflections arbitrary distributed over the sphere surface. Consequently, only if $\rho_r \to$

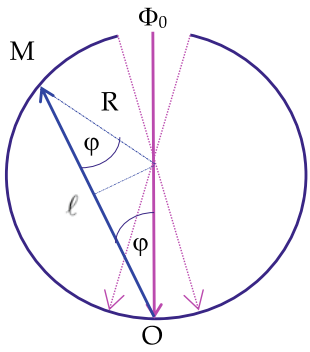

Fig. 2.28 Irradiation of sphere wall

1.0 can a specularly reflecting sphere become uniformly irradiated by its own internal reflections.

In contrast, any isotropic diffuser converting light with uniform radiance or luminance creates perfectly uniform irradiation of an ideally spherical surface even for diffuse reflectance not equal to 1.0 [2.3, 1.4, 0.4]. Arbitrary point O of the sphere (Fig. 2.28) under the condition of uniform diffuse reflectance ρ_d is the isotropic second source of radiant intensity: $I = I(0)\cos\varphi$. Light reflected in direction φ to point M creates irradiance E_M for the surface tilted to an inner normal by a given angle φ such that:

$$E_M = \frac{I\cos\varphi}{\ell^2} = \frac{I(0)\cos^2\varphi}{(2R\cos\varphi)^2} = \frac{I(0)}{4R^2}. \tag{2.103}$$

Here I(0) is the intensity of radiation reflected by the normal to irradiated point O. Thus, irradiance inside the diffusely reflecting sphere does not depend on the coordinates of observation point M.

Each subsequent sphere reflection contributes to supplemental but constant irradiance or illuminance. The only difference between the first reflection and further reflections from a sphere wall made of an isotropic diffuser consists in receding magnitudes of the reflection terms. The first beam irradiating the wall is reflected at the direct-diffuse factor of the irradiation–observation geometry. Table 1.1 defines this is as (0/d) geometry. Further reflections from the wall have diffuse-diffuse or other (d/d) geometry. The effective sphere reflectance changes from the first to the second reflection and then to other reflections since it is impossible to launch a material beam of light into a sphere and lead it out if the sphere's inner surface is covered by any opaque reflecting material with no apertures. Depending on the number of apertures, their entire area, and their ability to reflect light back to the sphere, the *effective* hemispherical reflectance ρ_0' of the total surface of the sphere for uniform diffused irradiation is:

$$\rho_0{}'(d/d) = \rho_0(d/d)\left\{1 - \frac{\sum\limits_{i=1}[1 - \rho_i(d/d)/\rho_0(d/d)]A_i}{A_{sph}}\right\}. \tag{2.104}$$

Here $\rho_0(d/d)$ is the reflectance of the sphere's aperture-free zone for uniform diffuse irradiation, A_i and $\rho_i(d/d)$ are the area and reflectance of the i^{th} aperture, and $A_{sph} = 4\pi R^2$ is the sphere's area for no apertures. If distinctions of sphere-diffuser properties for direct and diffused irradiation may be disregarded, the sphere's reflectance is $\rho_0(0/d) = \rho_0(d/d) \equiv \rho_0$. If $\rho_{\Sigma,i} = 0$, the effective reflectance becomes:

$$\rho_0{}' = \rho_0(1 - A_{\Sigma,i}/A_{sph}). \tag{2.105}$$

When summing the actions of all multiple reflections inside the diffusely reflecting sphere, the equation for internal irradiance E of an integrating sphere beyond any zone of its first irradiation is:

$$E_{sph} = \frac{\Phi_0}{4\pi R^2}[\rho_0(0/d) + \rho_0(0/d)\rho_0{}'(d/d) + \cdots] = \frac{\Phi_0}{4\pi R^2}\frac{\rho_0(0/d)}{1 - \rho_0{}'(d/d)}, \tag{2.106}$$

where $\rho_0{}'$ designates the effective reflectance. In the simplified form expression Eq. (2.106) becomes:

$$E_s = \frac{\Phi_0}{4\pi R^2}\frac{\rho_0}{1 - \rho_0{}'}. \tag{2.107}$$

One may conclude that irradiance or illuminance of an integrating sphere is inversely proportional to the square of the sphere's radius and is directly proportional to the diffuse reflectance of the directly irradiated wall, and to the effective reflectance of its entire internal surface for diffuse irradiation. The internal sphere irradiance differs in the area A_0 directly irradiated by the incident beam. Within that area, the sphere irradiance increases by the term Φ_0/A_0. If instead of a direct first irradiation the entire sphere is irradiated diffusely by flux $\Phi_0(d)$, Eq. (2.106) becomes:

$$E_{sph}(d) \underset{A_0 = A_{sph}}{=} \frac{\Phi_0(d)}{4\pi R^2}\left[1 + \rho_0'(d/d) + \cdots\right] = \frac{\Phi_0(d)}{4\pi R^2}\frac{1}{1 - \rho_0'(d/d)}. \tag{2.108}$$

If the first irradiation is uniformly diffused over a 4π angle, Eq. (2.108) is even correct for the mirror sphere, inverting the distribution according to Snell's law after each reflection (Table 1.1).

Inclusion of entrance or exit ports, baffles, detectors, and samples into an integrating sphere will change the sphere irradiance created by the beam reflected from or transmitted by a sample. Owing to these necessary inclusions, the sphere's effective reflectance $\rho_0{}'$ changes via any irradiated area of each successive

reflection, but the internal sphere irradiance E_d created by a beam reflected from the uniform diffuser of diffuse reflectance ρ_d follows from Eq. (2.106).

$$E_d = \frac{\Phi_0 \rho_d}{4\pi R^2} \frac{1}{1 - \rho_0'(d/d)}. \tag{2.109}$$

For a specularly reflecting sample having specular reflectance ρ_r, when the directly reflected sample beam irradiates an unbound spot of the sphere wall but not the detector, the equation for the irradiance becomes:

$$E_r = \frac{\Phi_0 \rho_r}{4\pi R^2} \frac{\rho_0(0/d)}{1 - \rho_0'(d/d)}. \tag{2.110}$$

If the sample is a nonuniform diffuser of any arbitrary scattering indicatrix $f(\Theta)$ characterized by equivalent solid angle Ω_e (Eq. 1.55) and if the detector is baffled against direct irradiation by light reflected or transmitted by that sample, the resulting irradiance E_x for the baffled detector is:

$$E_x = \frac{\Phi_0 \rho_x}{4\pi R^2} \frac{\rho_0'(\Omega_e/d)}{1 - \rho_0'(d/d)}. \tag{2.111}$$

2.4.2 Relative Measurements

Relative, i.e., in reference to any standard, measurements of diffuse reflectance or transmittance of an object may be obtained by having the integrating sphere as an integrator of radiation diffused by that object into a 2π or 4π solid angle. An object and a standard may substitute one another at a sphere spot for comparison. The effective sphere reflectance ρ_0' may be unknown if that reflectance remains unchanged during one measurement cycle of irradiating the object and the standard. If the sphere reflectance ρ_0' changes, the measurement equation becomes:

$$\rho_{ob} = \rho_{st} \frac{N_{st}}{N_{ob}} D, \tag{2.112}$$

where D is the correction factor accommodating the effective sphere reflectance variation $\rho_{0,ob}' \neq \rho_{0,st}'$ from the object to the standard of equivalent solid angle Ω_{ob} or Ω_{st}, respectively (Eq. 1.56).

There are two general methods for making relative measurements. The first method involves direct irradiation by incident flux Φ_0 of the standard and object installed consecutively behind one sample port of an integrating sphere. Another method consists in irradiation in turn of the standard and of the test object (samples) while both are placed simultaneously into one sphere behind equivalent ports. The first measurement procedure, the *substitution method*, uses a pair of small ports –

one, for the entrance of light into the sphere and another, for the installation of each sample. The second technique, the *comparison method*, requires either an extra pair of ports or one larger entrance opening and two sample ports to concurrently set the sample and the standard in the sphere, having the advantage of the effectiveness of multiple reflections in the comparison integrating sphere, identified by Eq. (2.103), remaining unchanged. To identify the effectiveness of the two methods, under the assumption of perfect diffuse reflectance of the sphere's surface, several intuitive [2.3–2.5] and exact [2.46–2.59] approaches were used, and obtaining the exact solution requires solving the integral or matrix equations for the irradiated internal surface of a sphere with actual samples, sample ports and entrance openings, and other inclusions with finite-difference equation [2.50] or matrix [2.54] methods to simplify the calculations. Let us further apply the irradiance equations derived in [2.49] and slightly corrected in [2.53] for large inclusions.

Consider a small region dA' at spherical coordinates Θ', ψ' of the internal surface of an integrating sphere to be directly irradiated by a source beam (Fig. 2.29). Light diffusely reflected from that region creates irradiance $E(\Theta, \psi)$ on the entire sphere's surface. Initial irradiance $E_0(\Theta, \psi)$ for region dA' is made by direct irradiation by the input beam. The irradiance $E_0(\Theta, \psi)$ is zero everywhere in the sphere, except in irradiated region dA', situated on the sample surface or on the standard with which the sample is to be compared, both with coordinates Θ', ψ'. By that designation, the complete irradiance for region dA' is $E_0(\Theta', \psi') + E(\Theta', \psi')$, where the first term defines the initial irradiation condition for the sphere and the second term is not known but needs to be determined. For those cases when the sample studied reflects all radiation incident on it as an isotropic diffuser with reflectance $\rho(\Theta', \psi')$ and constant radiance L', the radiant emittance M of the region dA' can be formulated as:

$$M = \pi L' = \rho(\Theta', \Psi')[E_0(\Theta', \Psi') + E(\Theta', \Psi')]. \tag{2.113}$$

Considering the relationship between the flux and the radiance in any light beam (see Eqs. (1.31, 1.47)), the flux Φ emitted by arbitrarily located platform dA' into

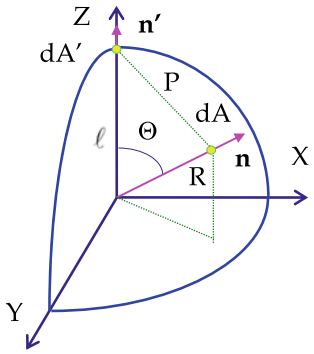

Fig. 2.29 Flat inclusions in an integrating sphere

another zone dA of the sphere with coordinates (Θ, ψ) can be identified by the following equation (see [2.49] for more details):

$$\Phi = \frac{\rho(\Theta', \psi')}{\pi}[E_0(\Theta', \psi') + E(\Theta', \psi')]dA'\left(\frac{-\mathbf{p}\cdot\mathbf{n}'}{|\mathbf{p}|}\right)dA\left(\frac{\mathbf{p}\cdot\mathbf{n}}{|\mathbf{p}|\mathbf{p}^2}\right), \tag{2.114}$$

where n' and $\mathbf{n}$ are the unit vectors of outer normal at denoted points with coordinates $\Theta', \psi'$and Θ, ψ and $\mathbf{p}$ is the vector joining small platforms dA and dA' and having a direction from dA' to dA. Finally, the irradiance of the internal sphere surface not irradiated by the direct beam is given by [2.49]:

$$\begin{aligned} E(\Theta, \psi) = &\frac{1}{\pi}\int_A E_0(\Theta', \psi')\rho(\Theta', \psi')\frac{(-\mathbf{p}\cdot\mathbf{n}')(\mathbf{p}\cdot\mathbf{n})}{\mathbf{p}^4}dA' \\ &+ \frac{1}{\pi}\int_A E(\Theta', \psi')\rho(\Theta', \psi')\frac{(-\mathbf{p}\cdot\mathbf{n}')(\mathbf{p}\cdot\mathbf{n})}{\mathbf{p}^4}dA'. \end{aligned} \tag{2.115}$$

Because irradiance $\mathrm{E}_0(\Theta', \psi')$ is known, Eq. (2.115) is a Fredholm-type integral equation for the symmetrical spherical space with only one variable of integration. Such a variable is area dA' of the elemental spherical segment irradiated by light reflected from the entire sphere's surface:

$$E(\Theta, \psi) = f(\Theta, \psi) + \lambda\int_A K(\Theta, \psi, \Theta', \psi')E(\Theta', \psi')dA'. \tag{2.116}$$

Here λ is a parameter and $\mathrm{K}(\Theta, \psi, \Theta', \psi')$ is the nucleus of that equation. The new function $\mathrm{f}(\Theta, \psi)$ represents the irradiance at a point of coordinates Θ, ψ formed by the first reflection of the direct beam carrying flux Φ from the sample occupying a particular region with spherical coordinates Θ', ψ'. Radiation reflected once again from all the internal sphere surface including the irradiated sample creates an additional irradiance $\mathrm{f}(\Theta', \psi')\mathrm{K}(\Theta, \psi, \Theta', \psi')\mathrm{dA}'$ in the sphere's Θ, ψ region, etc.

Approaching a relatively small opening port of an area $\mathrm{A}_\rho << \mathrm{A}_{sph}$ in a perfect sphere with no deviation from its geometry, Eq. (2.115), with its geometrical factor: $(-\mathbf{p}\cdot\mathbf{n}')(\mathbf{p}\cdot\mathbf{n})/\mathbf{p}^4 = 1/\left(4\mathrm{R}^2\right)$, becomes:

$$\begin{aligned} E_{perf}(\Theta, \psi) = &\frac{1}{4\pi R^2}\int_A E_0(\Theta', \psi')\rho(\Theta', \psi')\mathrm{dA}' \\ &+ \frac{1}{4\pi R^2}\int_A E(\Theta', \psi')\rho(\Theta', \psi')\mathrm{dA}'. \end{aligned} \tag{2.117}$$

For the substitution method, the irradiance ratio E_s/E_c for the spherical sample of reflectance ρ and the spherical comparison sample of reflectance ρ_c, matching the sphere curvature, is [2.49]:

$$\left(\frac{E_s}{E_c}\right)_{sub}^{sph} = \frac{\rho}{\rho_c}\left[1 - \frac{(\rho_c - \rho)A_\rho/A_{sph}}{1 - \rho_0 A_{\rho_0}/A_{sph} - \rho A_\rho/A_{sph}}\right]. \tag{2.118}$$

Here A_{ρ_0} and A_ρ are the areas of the sphere's surface with reflectance ρ_0 and of the sample studied with reflectance ρ. Equation (2.118) is obtained for an identical area A_ρ of the comparison sample having reflectance ρ_c, assuming geometrical perfection of the sphere for any one of the samples installed.

In the absence of flat inclusions, the comparison method is realized without systematic errors:

$$(E_s/E_c)_{com}^{sph} = \rho/\rho_c. \tag{2.119}$$

If both the test sample and either the comparison or the substitution sample are flat at plane areas $A_\rho = \pi(R^2 - \ell^2)$, either one or two sections of area $A'_\rho = 2\pi R^2(1 - \ell/R)$ of the active sphere surface are substituted by flat sample inclusions at distance ℓ from the center of the sphere (see Fig. 2.29). For small samples, the geometry may be approximated as:

$$\frac{(-\mathbf{p}\cdot\mathbf{n}')(\mathbf{p}\cdot\mathbf{n})}{\mathbf{p^4}} \cong \frac{(R - \ell\cos\Theta)(\ell - R\cos\Theta)}{(R^2 + \ell^2 - 2R\ell\cos\Theta)^2}. \tag{2.120}$$

For the assumption of small diffuse-reflecting samples inside a relatively large – in comparison with the dimensions of the samples – integrating sphere, the substitution method with two flat samples gives [2.49]:

$$\left(\frac{E_s}{E_c}\right)_{sub}^{flt} = \frac{\rho}{\rho_c}\left[1 - \frac{(\rho_c - \rho)(A'_\rho/A_{sph})(\rho_0 A_{\rho_0}/A_{sph})}{1 - (\rho_0 A_{\rho_0}/A_{sph})(1 + \rho A'_\rho/A_{sph})}\right]. \tag{2.121}$$

For the comparison method, flat samples also bring imperfections to the sphere. By contrast to the substitution method, in the latter case the diffuse reflectance ρ being measured is diminished when it is smaller than the reflectance ρ_c of the comparison sample. The correction factor for the flat samples, using the comparison method, is still considerably lower than that for the substitution method:

$$\left(\frac{E_s}{E_c}\right)_{com}^{flt} = \frac{\rho}{\rho_c}\left[1 + \frac{(\rho_c - \rho)A'_\rho/A_{sph}}{1 + \rho A'_\rho/A_{sph}}\right]. \tag{2.122}$$

Sufficient experimental studies [2.51, 2.60–2.62, 4.49] verified that Eqs. (2.118)–(2.122), derived in [2.49] for relatively small samples are true for most practical applications. Studies also confirmed the absolute accuracy of 0.1% or less reached at high and low levels of reflectance measured [2.55]. For relatively large dimensions of sphere inclusions, a second-order correction for the equations can be used [2.53]. Since the only approximation made was for integration of area A_s over a presumed negligibly small sample, and thus not resolved coordinates Θ', ψ' (see Fig. 2.29), at the polar angle $\Theta_s = \arcsin\left(\sqrt{R^2 - \ell^2}/R\right)$ of the sample, Eq. (2.120) transforms to:

$$\frac{(-\mathbf{p}\cdot\mathbf{n}')(\mathbf{p}\cdot\mathbf{n})}{p^4} = \frac{(\cos\Theta_s - \cos\Theta)\{1 - \cos\Theta_s[\cos\Theta + \sin\Theta\,\tan\Theta'\cos(\psi' - \psi)]\}}{\{1 - 2\cos\Theta_s[\cos\Theta + \sin\Theta\,\tan\Theta'\cos(\psi' - \psi)] + \cos^2\Theta_s\sec^2\Theta'\}^2}, \tag{2.123}$$

where $\cos\Theta_s = \ell/R$. Owing to such a detailed integration factor for the geometry of the sphere, Eq. (2.121) for two flat samples is converted to [2.53]:

$$\left(\frac{E_s}{E_c}\right)_{sub}^{Flt.Lrg} = \frac{\rho_s}{\rho_c}\left\{1 - \frac{(\rho_c - \rho)(\rho_0 A_{\rho_0}/A_{sph})\left(A'_\rho/A\rho\right)\left(A'_\rho/A_{sph}\right)}{1 - (\rho_0 A_{\rho_0}/A_{sph})\left[1 + \rho\left(A'_\rho/A\rho\right)\left(A'_\rho/A_{sph}\right)\right]}\right\}. \tag{2.124}$$

For the comparison method with a flat sample versus a spherical standard of area A'_ρ:

$$\left(\frac{E_s}{E_c}\right)_{com}^{Flt.Lrg} = \frac{\rho}{\rho_c}\frac{A'_\rho/A_\rho}{1 + \rho\left(A'_\rho/A_\rho\right)\left(A'_\rho/A_{sph}\right)}. \tag{2.125}$$

2.4.3 Samples Performing as Nonuniform Diffusers

Equations (2.118)–(2.125) were derived for the integrating sphere of an isotropic diffuser, where every component of the internal sphere irradiance except the component of irradiance created by an entrance beam does not depend on its coordinate. In that case, there is no certainty only about the irradiance distribution due to light reflected or transmitted by a sample, since that distribution may not remain constant over all points and directions, while each reflectance from the sphere wall itself creates the uniformly distributed irradiance. Thus, it is sufficient to install an isotropically reflecting baffle protecting a sphere detector from directly viewing the sample and from being affected by nonuniformly diffused light. When the protective baffle has same properties as the sphere wall, the irradiance or illuminance starting from the second reflection from the sphere wall also does not

depend on the coordinate. As a result, all derived equations for the determination of diffuse reflectance remain unchanged. Irradiation of the specularly reflecting sample in any integrating sphere is accompanied by a similar effect as having the baffle for the nonuniformly reflecting diffuser. The beam specularly reflected from the sample can be directed to the sphere wall, making the following reflection from the sphere uniformly diffused when viewed by a detector. The substitution or comparison measurement for objects of mixed, i.e., specular or direct plus diffuse, reflectance and transmittance in the integrating sphere at the isotropically reflecting baffle between the object and sphere detector is not linked to additional systematic errors, except the ones accounted for in Eqs. (2.118)–(2.125).

2.4.4 Absolute Measurements in an Integrating Sphere

The prospects of obtaining absolute reflectance measurements in the integrating sphere of either the comparison or the substitution method follow from Eqs. (2.106)–(2.111). Here the term *absolute measurement* implies that a given method does not require any extra calibration of the absolute magnitude of either reflectance or transmittance, measured by inherently relating to an internal comparison object, such as the integrating sphere wall itself. The irradiance or illuminance for a geometrically symmetrical integrating sphere at its section protected against direct irradiation from the sample by an isotropically reflecting baffle is:

$$E_{smp}^{sph}(0/d) = \frac{\Phi_0 \rho_d(0/d)}{4\pi R^2} \frac{\rho_0{}'(d/d)}{1 - \rho_0{}'(d/d)}, \tag{2.126}$$

where $\rho_d(0/d)$ is the diffuse sample reflectance for direct irradiation. Comparing irradiance $E_{smp}^{sph}(0/d)$ with irradiance E_0^{sph} (Eq. 2.106) for direct irradiation of the wall with reflectance ρ_0(0/d) without inclusions, any internal sphere detector exposed to wall reflectance directly has:

$$\frac{E_{smp}^{sph}}{E_0^{sph}} = \rho_d(0/d) \frac{\rho_0'(d/d)}{\rho_0(0/d)}. \tag{2.127}$$

Only under uniform diffuse irradiation of the internal sphere surface, creating constant radiance L_0 irradiating directly the detector and the sphere's surface, do any measurements of diffuse reflectance and transmittance have no systematic error, since in Eq. (2.127): $\rho_0(0/d) \rightarrow \rho_0'(d/d)$, and:

$$E_{smp}^{sph}/E_{L=const}^{sph} = \rho_d(0/d)\left[\rho_0'(d/d)/\rho_0'(d/d)\right] \equiv \rho_d(0/d). \tag{2.128}$$

Accordingly, for the absolute measurement in the integrating sphere to be realized without systematic error, the internal sphere detector must be irradiated by

the radiation either reflected from or transmitted through the sample studied not directly, but via the sphere wall, causing the isotropic diffuse reflection to be sustained further. An ideal comparison measurement would be obtained by comparing detector readings for the direct irradiation of the baffled sample and the unbaffled internal sphere surface, while maintaining its irradiation geometry as of light diffused by the sample. Studies of specularly reflecting and directly transmitting samples do not require diffuse irradiation of the sphere since from Eqs. (2.106) and (2.110) the specular reflectance is:

$$\rho_r = E_{smp}^{sph}(r/d)/E_0^{sph}(0/d). \tag{2.129}$$

For specularly reflecting and directly transmitting samples, it is only necessary to preserve the equivalence of optical properties for sections of the sphere wall irradiated directly by an incident beam and specularly reflected/directly transmitted by the sample. Equations (2.127)–(2.129) are true while multiple reflection factor $1/[1 - \rho_0'(d/d)]$ remains constant, i.e., a spherical sample having the same radius of curvature as the integrating sphere is measured by the comparison method.

2.4.5 *Baffling Method*

Let us note certain impediments to performing sequential irradiation of a test sample by a parallel beam of light having constant irradiance and of the internal sphere surface by a power- or energy-equivalent beam with a spherical wavefront normally and uniformly irradiating the entire sphere, conditionally converting Eq. (2.127)–(2.128) in a straightforward manner. The major reason for such a conversion is that the actual properties of many white diffusers can be approximated as those of near-perfect isotropic diffusers, deviating at angles of observation only near 90°. Presuming equalities $\rho_0(0/d) \cong \rho_0(d/d)$ and $\rho_0(d/d) \cong \rho_0'(d/d)$ by supposing that the area of all apertures and material inclusions inside the absolute sphere is much smaller than the area of the entire internal surface, $\sum A_i \ll 4\pi R^2$, we can convert measurement Eq. (2.127) for either a diffusely reflecting or a diffusely transmitting sample into the form:

$$\rho_d(0/d) \cong E_{smp}^{sph}(0/d)/E_0^{sph}(0/d). \tag{2.130}$$

The concept of simplified absolute measurement of diffuse reflectance and transmittance by Eq. (2.130) defines the generalized Taylor method [2.46] (Fig. 2.30). Figure 2.30 illustrates one realization of the method and can be modified depending on applications. To obtain the irradiance $E_{smp}^{sph}(0/d)$ created by a test sample, a beam of incident light from source 1 is directed by mirror 2 at near

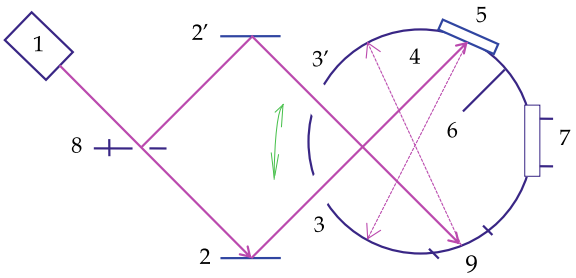

Fig. 2.30 Absolute reflectance measurements in the integrating sphere

normal incidence though aperture 3 onto the sample under test 5, placed behind a poling aperture of the integrating sphere 4. The specular component of light reflected by the sample is directed onto the sphere's wall (dotted line). An opaque baffle 6 fabricated from the sphere material protects internal sphere detector 7 from being directly irradiated by the diffused component of light reflected by the sample. To obtain the second irradiance $E_0^{sph}(0/d)$, mirror modulator 8 is placed into the beam and mirror 2 is rotated into position 2′ (dashed lines); thus, the redirected beam irradiates wall spot 9. Possible specular reflection from spot 9 is directed to the wall, but its diffuse component irradiates detector 7. The method may also be realized in the unchanged direction of propagation by alternating the positions of sample 5 and of removable sphere cap 9 as the absolute comparison sample. The entire sphere may be rotated around its center, shifting the positions of the entrance openings (dual arrow in Fig. 2.30).

2.4.6 *Efficiency Approach*

Another option for absolute measurements in an integrating sphere can be accommodated by consecutive alterations of the effective sphere reflectance (Eqs. (2.104) and (2.105)). The measurement process is multistaged [2.47]. First, with no test sample, two sphere-wall caps are located at positions 5 and 9, with second-beam port 3′ closed (Fig. 2.30). The cap replacing a sample is irradiated, and the first sphere irradiance is measured. For the second measurement, the second cap is removed, decreasing the sphere's effective reflectance. For equal areas A_{sph} of sphere caps and of the input port at a small area of the sphere detector the measurement ratio is:

$$\frac{N_1}{N_2} = \frac{1 - \rho_0(d/d)(1 - 2A/A_{sph})}{1 - \rho_0(d/d)(1 - A/A_{sph})}. \tag{2.131}$$

Relation (2.131) defines the sphere cap's reflectance ρ_0(d/d). For unknown reflectance ρ_x(d/d), a third identical measurement is needed with the sample installed, but not in the incident beam:

$$\frac{N_1}{N_3} = \frac{1 - \rho_0\{1 - A/A_{sph} - [1 - \rho_x(d/d)/\rho_0(d/d)]A/A_{sph}\}}{1 - \rho_0(d/d)(1 - A/A_{sph})}. \tag{2.132}$$

By contrast to the method using Eq. (2.130), efficiency measurements are made with uniform diffuse irradiation, altering the reflectance of the integrating sphere, but at least three measurements are necessary. At the same time, the latter measurements are practically free of systematic errors and require only maintaining a relatively small area of the sphere detector, considered to be negligibly small by expressions (2.131) and (2.132). However, a more substantial requirement of the efficiency method is that, besides somewhat higher total measurement error due to one extra measurement being required, it is necessary to distinguish a difference in the effective reflectance $\rho_0'(d/d)$ by means of the sample under study in the presence and the absence of the sphere cap inside the integrating sphere. To provide for such a difference significant enough to be registered by the sphere's detector, the most efficient way consists in making the magnitude of $[1 - \rho_0'(d/d)]^{-1}$ as high as possible. Another but not so effective way consists in increasing the relative area of the samples and caps compared with that of the sphere itself. Such an approach decreases the effectiveness of the sphere's surface and, therefore, increases systematic errors due to the imperfect sphere's surface during any study of flat samples.

2.4.7 *Viewing Method*

Internal sphere measurements of reflectance under diffused irradiation can be realized via the reciprocity concept (see Chap. 1) for the irradiation and the observation directions (Fig. 2.31). If the internal sphere wall emittance due to multiple reflections is observed via various openings in the inner sphere surface and also via direct irradiation of the sphere wall by the source beam, the ratio of irradiance magnitudes depends not only on the reflectance values of specific wall sections being irradiated, but on the effective number of internal sphere reflections as well [2.15, 2.48, 2.56]. Consider Sections 1 and 2 being irradiated as simply distinct zones of the integrating sphere wall having unaltered wall reflectance ρ_0, but let the first zone be directly irradiated by light reflected from the sphere wall and the

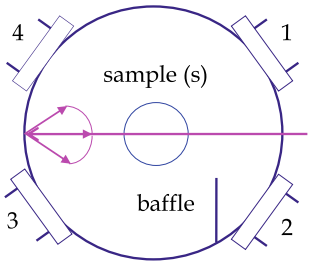

Fig. 2.31 Viewing-method technique

second zone be protected from the direct irradiation via an opaque baffle. If the detector is consequently placed into these zones, it readings become:

$$M_1 = \frac{\Phi_0}{4\pi R^2}\left[\rho_0 + \rho_0\rho_0' + \cdots\right] = \frac{\Phi_0}{4\pi R^2}\frac{\rho_0}{1-\rho_0{}'}, \tag{2.133}$$

$$M_2 = \frac{\Phi_0}{4\pi R^2}\left[\rho_0\rho_0' + \rho_0\rho_0'\rho_0' + \cdots\right] = \frac{\Phi_0}{4\pi R^2}\frac{\rho_0\rho_0'}{1-\rho_0'}. \tag{2.134}$$

$$M_2/M_1 = \rho_0'(d/d). \tag{2.135}$$

For equally irradiated zones 3 and 4 having sphere effective reflectance ρ'_{0x} and ρ'_0 as with a sample and sphere cap installed in position 5 in sequence, the ratio of detector irradiances 3 and 4 by analogy is:

$$M_3/M_4 = \left(\rho_{0x}'/\rho_0'\right)\left((1-\rho_0')/(1-\rho_{0x}')\right). \tag{2.136}$$

Under the assumption of relatively small ports of known area A_p compared with the sphere of internal spherical surface $A_0 = A_{sph} = 4\pi R^2$, $A_p \ll A_0$:

$$\frac{M_3 \cdot M_2}{M_4 \cdot M_1} = \rho_{0x}'(d/d)\frac{(1-\rho_0'(d/d))}{(1-\rho_{0x}'(d/d))} \underset{A_p \ll A_0}{=} \rho_{0x}'(d/d). \tag{2.137}$$

Measurements of diffuse wall plus sample reflectance $\rho'_{0x}(d/d)$ by the *Sharp–Little* method just described are like the *Taylor* method under a similar approximation of effective sphere reflectance $\rho'_0 \approx \rho'_{0x}$, giving:

$$\rho_{0x}(d/d) \cong (M_2 \cdot M_3)/(M_1 \cdot M_4). \tag{2.138}$$

The anomaly of *viewing* versus *efficiency* study is the necessity to measure ρ'_0 before determining ρ_x.

2.4.8 Reduction of Systematic Errors of Absolute Measurements

Let us rewrite Eq. (2.106) for irradiance of the internal sphere surface when the sphere cap is directly irradiated by light entering the sphere with flux Φ_0. Since the sphere irradiance created by reflection from the isotropic diffuser covering the sphere's surface does not depend on the directions of irradiation or observation, the sphere irradiance can always be considered as the sum of the first reflection and all other reflections:

$$E_0(0/d) = \frac{\Phi_0 \rho_0(0/d)}{4\pi R^2}\left[1 + \frac{\rho_0'(d/d)}{1 - \rho_0'(d/d)}\right]. \tag{2.139}$$

The consequent irradiation by input flux Φ_0 of a sample having an arbitrary scattering indicatrix f(Θ), equivalent solid angle of scattering $\Omega_e \leq \pi$, and reflectance ρ(0/d) leads to the next sphere irradiance, which can also be represented in the form of only two additive components [2.58]:

$$E_{sph}(0/d) = \frac{\Phi_0 \rho_0(0/d)}{4\pi R^2}\left\{\frac{\pi f(\Theta)}{\Omega_e \cos\Theta} + \left[1 - \frac{\sum_{i=1}^{m} f(\Theta)(1 - \rho_i/\rho_0)A_i}{4R^2 \Omega_e \cos\Theta}\right]\frac{\rho_0(\Omega_e/d)}{1 - \rho_0'(d/d)}\right\}. \tag{2.140}$$

Here ratios f(Θ)/cosΘ and Ω_e/π characterize the alterations from the cosine law and inequalities of scattering characteristics of the sample and of the sphere cap from the ones of the isotropic diffuser.

Baffling radiation due to the first reflection from the sample and the sphere wall, and assuming $f(\Theta) = \cos\Theta$, which is true for the majority of known samples at small angles of observation, Eqs. (2.139) and (2.140) lead to Eqs. (2.118) and (2.119) or (2.121) and (2.122) for absolute measurements of diffuse reflectance. The supposition of flat-to-spherical irradiation equivalence for the sphere's wall reflectance, which closely resembles a perfect diffuser: $\rho_0(0/d) \cong \rho_0(d/d)$, confirms the validity of Taylor's ratio:

$$\frac{E_{sph}}{E_o} = \rho\frac{\rho_0'}{\rho_0} \cong \rho\left[1 - \frac{\sum_{i=1}(1 - \rho_i/\rho_0)A_i}{A_{sph}}\right] \equiv \rho'. \tag{2.141}$$

As a result, the absolute Taylor method measures not the actual but the effective sample reflectance.

The inherent systematic error due to preset parity: $\rho_0(0/d) \cong \rho_0(d/d)$, by Eq. (2.130) may be avoided if direct irradiation of the sample under study leads to internal sphere irradiance:

$$E_{sph} = \frac{\Phi_0 \rho}{4\pi R^2}\frac{\rho_0(0/d)}{1 - \rho_0'(d/d)}. \tag{2.142}$$

To comply with Eq. (2.142), the sphere baffle could be made having radiation reflected from the sample to irradiate an internal sphere detector via baffle transmittance τ satisfying the anticipation [2.60]:

$$E = \frac{\Phi_0 \rho}{4\pi R^2} \left\{ \tau + \left[1 - \frac{\sum_{i=1} (1 - \rho_i/\rho_0) A_i}{A_{sph}} \right] \frac{\rho_0}{1 - \rho_0'} \right\} \equiv \frac{\Phi_0 \rho}{4\pi R^2} \frac{\rho_0}{1 - \rho_0'}. \quad (2.143)$$

To convert equation (2.143) to (2.142), the baffle diffuse transmittance τ should satisfy the following equation:

$$\tau = (\rho_0 - \rho_0')/(1 - \rho_0'). \quad (2.144)$$

According to equations (2.127)–(2.129), the presence of the specular component in the sample reflection irradiating the inner sphere wall but not passing out via sphere openings does not change relation (2.144). A certain paradox of using a partially transparent baffle is defined only by the loss of diffused radiation reflected from the sample into sphere openings proportionally compensating for the loss of light effectively reflected by the integrating sphere itself. Any material may be used for such a baffle: from a transparent material, when the sample's reflectance is practically isotropic, to a translucent material, when discrepancies from quasi-isotropic reflection can occur.

For a centered layout (Fig. 2.32) of an integrating sphere [2.57], a similar error-correction method can be applied [2.60]. Illustrated by Fig. 2.32, design allows a measurement when no protecting baffle is required at all, since the sample under study is situated near the center of the sphere, and the bottom hemisphere is totally in shade. When detector 2 is placed in the shade of the sample's irradiation, the top hemisphere serves as a retroreflecting section for the first reflection from sample 1. When sample 1 is turned out of the entrance beam into new position 1′, detector 2 is irradiated as in all previous absolute methods by the direct reflection from the sphere wall. In this case, the relative loss of the first component of light reflected by sample 1 into the entrance aperture is 4 times higher, owing to the 2 times smaller distance to the entrance aperture and the reduced area of the effective retroreflecting surface of the sphere, compared with when the same sample is placed onto the sphere wall. For compensation of that error, the detector can be moved into new position 2′ in the top hemisphere. The location of the detector is identified by angle Θ_i versus the direction of the incident beam. In that case, the irradiance E_i of the detector's sensitive surface is:

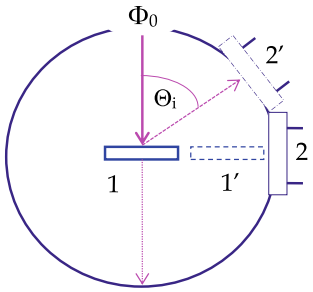

Fig. 2.32 Absolute sphere for the internal placement of a test sample

$$E_i = \frac{\Phi_0 \rho}{4\pi R^2} \left\{ 4\cos\Theta_i + \left[1 - \frac{4\sum_{i=1} (1 - \rho_i/\rho_0) A_i}{A_{sph}} \right] \frac{\rho_0}{1 - \rho_0{}'} \right\}. \tag{2.145}$$

If angle Θ is selected to convert the right side of Eq. (2.145) to that in (2.144), this leads to:

$$\cos\Theta = (\rho_0 - \rho_0{}')/(1 - \rho_0{}'). \tag{2.146}$$

Accordingly, the sphere surface irradiance directed by angle Θ corresponds to that predicted by relation (2.142). To irradiate the detector by diffuse reflectance of wall cap 3, the sample is moved out of the beam into position $1'$ to make its irradiance determined by Eq. (2.139) as in Taylor's design. If a shading effect of a sample holder in transmitted light is absent, the totality of the sample diffuse reflectance and its diffuse transmittance $\rho + \tau$ can also be measured as:

$$\begin{aligned} E_\Sigma &= \frac{\Phi_0 \rho}{4\pi R^2} \left\{ \rho \frac{4(\rho_0 - \rho_0{}')}{1 - \rho_0{}'} + \rho \left[1 - \frac{4\sum_{i=1} (1 - \rho_i/\rho_0) A_i}{A_{sph}} \right] \frac{\rho_0}{1 - \rho_0{}'} + \tau \frac{\rho_0}{1 - \rho_0{}'} \right\} \\ &= \frac{\Phi_0}{4\pi R^2} \frac{\rho_0}{1 - \rho_0{}'} (\rho + \tau). \end{aligned} \tag{2.147}$$

Similar techniques may be applied to compensate for systematic errors for all of the methods of absolute measurements mentioned and all types of integrating spheres. The alteration procedure is based on the creation of a supplemental sphere irradiance equivalent to that which is actually reflected from the sample under study, but that is lost in sphere apertures. The opposite way to perform the correction is to subtract the irradiance lost on irradiation of the sample from the irradiance falling on the sphere during measurements of irradiance E_0 (Eq. 2.139). The correction may be made by the sphere cap with a remedial aperture of relative proportions, reducing the sphere cap's reflectance or the wall's reflectance from ρ_0 to $\rho_0{}'$. The corrective effect of such an error reduction is independent of whether the corrective sphere cap is acting under direct or under diffuse irradiation for the absolute method.

Let us consider an error-correcting opening of reflectance ρ_c and area A_c in a sphere cap of an internal sphere surface with reflectance ρ_0 and area A_0. That opening, when it is covered, for example, by a certain protective glass, can have higher than zero reflectance. The properties of a sphere cap with the correcting opening should be such that the subsequent equality is satisfied:

$$1 - (1 - \rho_c/\rho_0) A_c/A_0 = 1 - \sum_{i=1}^{m} [1 - \rho_i/\rho_0] A_i/A_{sph}, \tag{2.148}$$

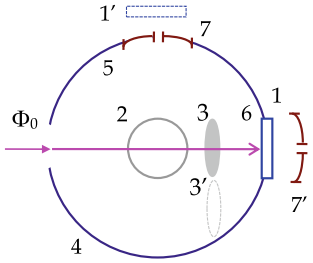

Fig. 2.33 Absolute comparison sphere settings for non spectrally-selective error compensation

where m is the number of sphere openings, each with a reflectance ρ_i. As a result, under irradiation of the correcting cap by the beam whose cross section matches cap area A_0, the cap's effective reflectance ρ_o^A is equal to reflectance ρ_0' for the sphere itself, no matter what the wavelength of incident radiation is. If the correcting sphere cap is used in the baffling method to be directly irradiated by the same beam, possible errors for $\rho_o^A \neq \rho_0'$ are defined by deviations of the sphere properties from those of the perfect diffuser. The error vanishes when either the efficiency or the viewing method is used, since both the cap and the rest of the internal sphere surface are irradiated by multiple reflections of equivalently diffused radiation.

Figure 2.33 depicts an arrangement of an integrating sphere having the correcting opening, which is designed for the absolute measurement by the comparison, the baffling, or the viewing method [2.61, 2.62]. Sample 1 and sphere cap 7, having the correcting opening, are installed in turn behind sample ports 5 and 6 and both always remained in sphere 4. A direct beam of a cross section A_0 carrying flux Φ_0 is incident on the cap or sample placed behind sample port 6. Sphere irradiance E at exit port 2 or the sphere's wall emittance M via exit port 2 is measured by a single detector, conforming to Eq. (2.130) or (2.131), respectively. If sample 1 is irradiated and irradiance E or emittance M is measured, opaque baffle 3 is placed between sample 1 and the detector in respective ports 6 and 2, or between sample 1 and the spot of the sphere wall opposite to exit port 2. Next, when cap 7 and sample 1 are swapped between ports 6 and 5, baffle 3 is moved into position 3′, and either E_0 or M_0 is measured [2.61].

2.4.9 *Spheres of Nonisotropic Diffusers*

The analyzed above absolute and relative methods of measurement using integrating spheres highlight one key drawback limiting the accuracy of each measurement – the necessity of the diffuse reflectance of the sphere wall not only to be Lambertian, but also not to change from direct to diffuse irradiation. This means the measurement must be made using a sphere of a practically perfect isotropic diffuser. Therefore, it is important to distinguish the actual difference in the properties of any actual diffuser versus the perfect diffuser, or to exclude the necessity for the diffuse sphere reflectance for direct irradiation, $\rho_0(0/d)$, to be equal to its effective

reflectance for following multiple reflections, $\rho'_0(d/d)$. The latter can be realized by irradiating an entire inner sphere surface when measuring the first sphere irradiance E_0. Let us consider the measurement of the sphere irradiance for a nonisotropic diffuser irradiated by a direct beam via its entrance aperture. Let us also extend that concept [2.8] to integrating spheres made of translucent materials directly irradiated via an input spot of the sphere wall with diffuse transmittance and reflectance $\tau_d + \rho_d = 1$.

When a collimated beam carrying flux Φ_0 is incident on an outer region of area A of a diffusely transmitting sphere wall, it in turn irradiates the rest of the internal surface of such a translucent sphere in conformity with that sphere wall's scattering indicatrix in transmission: $f(\Theta) = \gamma(\Theta)\cos\Theta = (L_\Theta/L_0)\cos\Theta$, and with the wall's diffuse transmittance τ_d (Fig. 2.34). When the beam enters via the entrance port, the reflectance indicatrix for the wall and the transmittance τ_a of the port both need to be known. Here L is the radiance of the emitting sphere wall in the observation direction, L_0 is the wall's radiance viewed from the normal, and Θ is the angle of observation. The flux $d\Phi_M{}^A$ emitted by element dA in the direction of platform dM is:

$$d\Phi_M^A = I_M^A d\Omega = I_0^A f(\Theta) d\Omega, \tag{2.149}$$

where I_M^A is the intensity of a point source equivalent to element dA viewed in the direction of platform M and $d\Omega$ is the solid angle of observation. The flux Φ^A either diffusely transmitted or reflected back into the sphere is:

$$\Phi^A = \int_\pi I_0^A f(\Theta) d\Omega = I_0^A \Omega_e, \tag{2.150}$$

where $\Omega_e = \int_\pi f(\Theta) d\Omega$ is the equivalent solid angle for such a translucent internal sphere surface, which may not remain the same in transmission and in reflection, respectively changing to $\Omega_{e,\tau}$ and to $\Omega_{e,\rho}$.

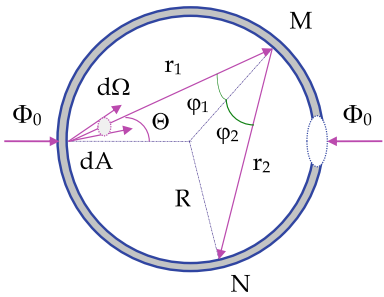

Fig. 2.34 An arbitrary scattering sphere

The irradiance E_M^A of a randomly chosen platform M due to radiation emitted by the irradiated region dA and incident at an angle φ_1 to the outer normal for the viewing platform M is:

$$E_M^A = \frac{I_M^A}{r_1^2}\cos\Phi_1 = \frac{I_0^A f(\Theta)}{4R^2\cos\Phi_1}. \tag{2.151}$$

Taking into account the relationship between indicatrixes of the radiance and irradiance: $f(\Theta) = \gamma(\Theta)\cos\Theta$ (see expressions (1.53)), and equality of the inscribed angles: $\Theta = \Phi_1$, one may obtain:

$$E_M^A = \frac{I_M^A \gamma(\Theta)\cos\Theta}{4R^2\cos\Phi_1} = \frac{I_0^A}{4R^2}\gamma(\Theta). \tag{2.152}$$

Since: $\Phi^A = \tau_d\Phi_0 = I_0^A\Omega_e$, the equation for internal irradiance of an arbitrarily nonuniform sphere, or for internal illuminance, created by light transmitted by or reflected from that sphere wall, is:

$$E_d(\Theta) = \frac{\tau_d\Phi_0}{4R^2\Omega_e}\gamma(\Theta) = \frac{\rho_d\Phi_0}{4R^2\Omega_e}\gamma(\Theta). \tag{2.153}$$

Platform M, reflecting light with a diffuse reflectance ρ_d, irradiates another arbitrary element N:

$$dE_N^M = \frac{dI_N^M}{r_2^2}\cos\varphi_2 = \frac{dI_0^M f(\Theta)}{r_2^2}\cos\varphi_2 = \frac{dI_0^M \gamma(\Phi_2)}{r_2^2}\cos\varphi_2^2. \tag{2.154}$$

Considering, for the time being, identical indicatrixes in transmitted and reflected radiation:

$$dE_N^M = \frac{L_0 dA_M f(\Theta)\cos\varphi_2}{r_2^2} = \frac{E_M^A}{\pi}\rho_d f(\Theta)\frac{dA_M\cos\varphi_2}{r_2^2} = \frac{E_M^A}{\pi}\rho_d f(\Theta)d\Omega. \tag{2.155}$$

Integration, with respect to all reflecting elements inside, provides the expression for the sphere irradiance created by the first reflection of radiation from the entire internal surface of the sphere:

$$E_{\rho_0',1} = \frac{E_d}{\pi}\rho_0'\int_\pi f(\Theta)d\Omega = E_d\rho_0'\frac{\Omega_e}{\pi}, \tag{2.156}$$

where ρ_0' is the effective diffuse reflectance of the internal sphere surface with openings:

$$\rho_0' = \int_{\pi} \rho_d(\varphi) \left\{ 1 - \sum_{i=1}^{m} [1 - \rho_i(\varphi)/\rho_d(\varphi)] A_i / A_{sph} \right\} d\varphi, \tag{2.157}$$

and $\rho_d(\varphi) = 1 - \tau_d(\varphi)$ is the reflectance of the translucent sphere wall, which may depend on the angle of incidence φ. The irradiance E_n after n reflections in the sphere, converting light at negligible losses, is:

$$E_{\rho_0',n} = E_d \left(\rho_0' \frac{\Omega_e}{\pi} \right)^n. \tag{2.158}$$

As a result, the irradiance for the translucent lossless sphere, irradiated via transmission of its wall, and the irradiance for the reflective integrating sphere, irradiated via its similarly lossless open port, are [2.8].

$$E_{\Sigma,\tau} = \frac{\Phi_0}{4\pi R^2} \frac{\gamma(\Theta)}{\Omega_e/\pi} \frac{\tau_d}{1 - \rho_d' \Omega_e/\pi}; \tag{2.159a}$$

$$E_{\Sigma,\rho} = \frac{\Phi_0}{4\pi R^2} \frac{\gamma(\Theta)}{\Omega_e/\pi} \frac{\rho_d}{1 - \rho_d' \Omega_e/\pi}. \tag{2.159b}$$

The first factor in both equations characterizes the irradiance, being created by the isotropic and nonabsorbing diffuser. The second factor identifies changes of the irradiance as a function of the nonuniformity of a scattering indicatrix for the actual diffuser. The third part finally determines the efficiency of multiple reflections, being contingent to irregularity of the indicatrix. Equation (2.159a) derived for the irradiance of a translucent lossless sphere can be further transformed by separating the transmission and reflection observations, while taking into account a potential difference of the equivalent solid angles $\Omega_{e,\tau}$ and $\Omega_{e,\rho}$ in transmitted and in reflected radiation:

$$E_{\Sigma} = \frac{\Phi_0}{4\pi R^2} \frac{\gamma(\Theta)}{\Omega_{e,\tau}/\pi} \frac{\tau_d}{1 - \rho_d' \Omega_{e,\rho}/\pi}. \tag{2.160}$$

For any translucent sphere with negligible absorption, providing its actual wall absorptance α is below the measurement sensitivity (see Sect. 2.1), the wall diffuse transmittance is $\tau_d = 1 - \rho_d$ and:

$$E_{\Sigma,\tau=1-\rho} = \frac{\Phi_0}{4\pi R^2} \frac{\gamma(\Theta)}{\Omega_{e,\tau}/\pi} \frac{1 - \rho_d}{1 - \rho_d' \Omega_{e,\rho}/\pi}: \tag{2.161}$$

If the integrating sphere reflecting light by its inner surface of high diffuse reflectance is exposed to direct radiation flux Φ_0 via its clear aperture, the factor $1 - \rho_d$ in Eq. (2.161) changes to ρ_0 and:

$$E_{\Sigma,\rho} = \frac{\Phi_0}{4\pi R^2}\frac{\gamma(\Theta)}{\Omega_{e,\rho}/\pi}\frac{\rho_0}{1-\rho_0{}'\Omega_{e,\rho}/\pi}. \tag{2.162}$$

Let us now express the nonuniformity K of the scattering indicatrix of the integrating sphere as a single factor by revealing the difference in irradiances created by an actual diffuser and the isotropic diffuser. For a translucent and lossless, i.e., weakly absorbing, sphere (Eq. 2.161):

$$K_\tau = \frac{\gamma(\Theta)}{\Omega_{e,\tau}/\pi}\frac{1-\rho_d}{1-\rho_d'\Omega_{e,\rho}/\pi}. \tag{2.163}$$

For diffuse-reflecting sphere nonuniformity K_ρ is defined by relations (2.159) and (2.162) for factor Ω_e:

$$K_\rho = \frac{\gamma(\Theta)}{\Omega_{e,\rho}/\pi}\frac{\rho_0}{1-\rho_0{}'\Omega_{e,\rho}/\pi}, \tag{2.164}$$

$$\Omega_e = \int_\pi \gamma(\Theta)\cos\Theta 2\pi\,\sin\Theta d\Theta = \pi\int_0^{\pi/2}\gamma(\Theta)\sin 2\Theta d\Theta. \tag{2.165}$$

By way of an example, let us consider the values of K for an opal glass with diffuse reflectance $\rho_d = 0.6$ and diffuse transmittance $\tau_d \cong (1-\rho_d) \cong 0.4$ and its radiance indicatrix given at fixed angles of observation as in the following table:

Θ°	0	10	20	30	40	50	60	70	80
γ(Θ)	1.00	1.00	1.00	0.99	0.98	0.96	0.92	0.83	0.64

The scattering nonuniformity for that diffuser can be approximated with error lower than 1% as:

$$\Omega_e = \pi\int_0^{60^\circ}\cos^{0.1}\Theta\,\sin 2\Theta d\Theta + \int_{60^\circ}^{70^\circ}\cos^{0.15}\Theta\,\sin 2\Theta d\Theta + \int_{70^\circ}^{90^\circ}\cos^{0.25}\Theta\,\sin 2\Theta d\Theta. \tag{2.166}$$

A trapezium calculation gives $\Omega_e = 0.925\pi$. Considering $\Omega_{e,\tau} = \Omega_{e,\rho}$, and with the detector located 45° to the emitting zone, giving $\gamma(45^\circ) = 0.97$, the K value for relative area of apertures $A/A_{sph} = 0.05$ is:

$$K = \frac{0.97\pi}{0.925\pi}\frac{0.6}{1-(1-0.6)\cdot 0.95\cdot 0.925} = 0.97.$$

If the diffuser with this table indicatrix has diffuse transmittance $\tau_d = 0.7$ and reflectance $\rho_d = 0.3$, the nonuniformity factor becomes: $K = 0.997$, making one sufficiently uniform integrating sphere at 0.3% accuracy, but at the inversed values: $\tau_d = 0.3$ and $\rho_d = 0.7$, the nonuniformity of irradiance becomes prohibitively large: $K = 0.817$. The large difference in the value of K from 1.0 is caused by the strong influence of the multiple reflection factor $(1 - \rho_0)$ at $\rho_0 \to 1.0$, enhancing the irradiance nonuniformity via highly pronounced multiple reflections in the higher reflecting sphere. That notion may explain the considerable discrepancy among published experimental data for certain absolute spectral measurements [2.56]. One cause of potential nonuniformity of sphere irradiance is due to imperfections of diffusers and nonisotropic diffuse reflectance for direct irradiation, leading to subsequent reduction of sphere efficiency as for a mirror sphere.

2.4.10 *Fully Isotropic Irradiation of Integrating Sphere*

One earlier discussed concept for absolute measurement which completely eliminates the cause of nonuniformity in the sphere's irradiance on the first direct irradiation of the sphere consists in the uniform diffused irradiation of the sphere surface by a beam of constant radiance, relating to the conversion of irradiance E_0 from Eq. (2.127) to (2.128). A combinational set of integrating spheres for absolute measurement is shown in Fig. 2.35. Translucent sphere 7 of low-absorbing opal glass or a diffuser satisfying relations (2.20) and (2.21) is placed inside primary integrating sphere 3, having typical high-diffuse reflectance. An incident flux Φ_0 from light source 1 via an entrance aperture directly irradiates any sample under study 6 protected from detector 4 by the opaque baffle 5. If the translucent sphere, having sufficiently uniform scattering indicatrix and absorptance α of its wall under the noise sensitivity limit $\Delta N/N$ of detector 4, is located at position 7 near the center of primary sphere 3, radiation that falls from source 1 is uniformly diffused in sphere 3. According to Eqs. (2.21) and (2.108), by keeping distortions of the main sphere irradiance below the detector sensitivity limit $\pm\Delta N/N$, combinational sphere irradiance E_0 at such diffuse irradiation becomes:

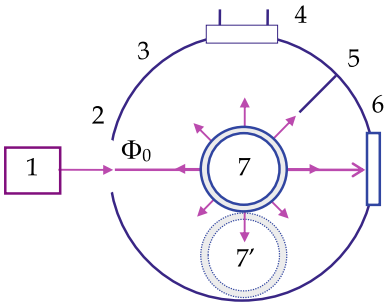

Fig. 2.35 Combination of integrating spheres

$$E_0 = \frac{\Phi_0/4\pi R^2}{1 - \rho_0'(d/d)}, \tag{2.167}$$

where $\rho_0'(d/d)$ is the effective reflectance of all internal sections of sphere 3, including translucent sphere 7. The next measurement is provided when sphere 7 is moved into position 7′ and the sample under test 6 is directly irradiated by flux Φ_0. Irradiance E of the sphere wall protected by baffle 5 is:

$$E = \frac{\Phi_0}{4\pi R^2} \frac{\rho_x(0/d)}{1 - \rho_0'(d/d)}. \tag{2.168}$$

If there are no further assumptions other than the scattering uniformity and $\alpha \leq \Delta N/N$, the sample reflectance is:

$$\rho_x(0/d) = E/E_0. \tag{2.169}$$

2.4.11 Essentials of Diffuse Transmittance Measurements

One obvious difference for any diffuse transmittance versus a reflectance study in an integrating sphere consists in the opposite directions of light scattering. Another effect makes diffuse transmittance measurements more complicated: increase of the cross section of a light beam expanded by a diffuse scattering object. That leads to the necessity of making the entrance port of the integrating sphere for diffuse transmittance studies nearly twice as big as the beam's cross section. Hence, the already considered measurement errors due to a specific method or the sample's flatness, respectively, increase, and thus error corrections require the use of precise Eqs. (2.124) and (2.125). The computations are complicated to perform, but analysis of diffuse transmittance measurement error in an integrating sphere with large input ports and flat sections can also be achieved via the more intuitive finite-difference equation method [2.50–2.52].

The derivation of the finite-difference equations is based on the reciprocity of indicatrix or the form factors K_1, K_2,…, K_n for correlation of fluxes of radiation, exchanged among emitting and irradiated surfaces A_1, $A_{2,\ldots,}$ A_n at thermal equilibrium $K_{1n}A_1 = K_{n1}A_n$. Thus [2.51], emittance M_1 of sphere section A_1 of reflectance ρ_1 which is directly irradiated by a light beam creating irradiance E_0 can be expressed via emittance values M_1,…,M_n for sequential surfaces A_1,…,A_n:

$$M_1 = \rho_1 M_1 K_{11} + \rho_1 M_2 K_{12} + \cdots + \rho_1 M_n K_{1n} + \rho_1 M_0. \tag{2.170}$$

Here K_{11} gives the fraction of radiation totally reflected from A_1 that is incident on A_1 itself. Since A_1 belongs to an *n*-surface system, the entirety of balances makes a set of linear equations [2.50] similar to ones of resistance and can be solved

as an electrical network [2.59]. Solutions due to that method are similar to relations (2.118)–(2.120), but do not necessarily predict small factors as for samples and sphere ports, correctly resolved via the integrated-equation formalism [2.49, 2.53, 2.54].

The characteristic layout of an integrating sphere for diffuse transmittance measurements is depicted in Fig. 2.36. A beam of light, carrying flux Φ, is incident at angle Θ on translucent object 1, placed in front of the entrance aperture of area A_e. The object may have the distinctive diffuse transmittance τ^{Θ} and reflectance ρ^{Θ} at angle Θ and hemispherical reflectance ρ^{π} – all different from the properties at normal incidence. The sphere has different reflectances ${\rho_0}^{\pi}$ and ${\rho_0}^{\Theta}$ for hemispherical and direct irradiation, respectively, and reflectance ${\rho_0}^{\Theta\Theta}$ in the direction of the entrance port. The port area and the absorptance for hemispherical irradiation are A_0 and ${\alpha_0}^{\pi}$. Light entering the sphere is either absorbed by its walls or by the internal detector having reflectance ${\rho_d}^{\pi}$ or lost in its apertures. The radiant flux balance in the sphere may be described similarly to Eqs. (2.5) and (2.6):

$$\begin{aligned}\Phi\tau^{\Theta} = {} & \Phi\tau^{\Theta}\rho_0^{\Theta\Theta}\left(1-\rho^{\Theta}\right)A_e/(A_0+A_e+A_s)+\Phi\tau^{\Theta}\alpha_0^{\pi} \\ & + EA_0\alpha_0^{\pi}+EA_d\left(1-\rho_d^{\pi}\right)+EA_e(1-\rho^{\pi})+EA_s.\end{aligned} \tag{2.171}$$

Here E is the irradiance of the internal sphere surface at thermal equilibrium. By re-arrangement [2.63]:

$$E=\frac{\Phi\tau^{\Theta}\left(1-\rho_0^{\Theta\Theta}\left(1-\rho^{\Theta}\right)A_e/(A_0+A_e+A_s)-\alpha_0^{\Theta}\right)}{A_0\alpha_0^{\pi}+A_d-A_d\rho_d^{\pi}+A_e-A_e\rho^{\pi}+A_s}. \tag{2.172}$$

When object 1 is moved to formerly opened port A_s at position 1′, keeping comparison settings (Fig. 2.36), the beam enters without attenuation, $\tau^{\Theta}=1$ and $\rho^{\Theta}=\rho^{\pi}=0$, causing Eq. (2.172) to converge to:

$$E_0=\frac{\Phi\left(1-\rho_0^{\Theta\Theta}A_e/(A_0+A_e+A_s)-\alpha_0^{\Theta}\right)}{A_0\alpha_0^{\pi}+A_d-A_d\rho_d^{\pi}+A_e+A_s-A_s\rho^{\pi}}. \tag{2.173}$$

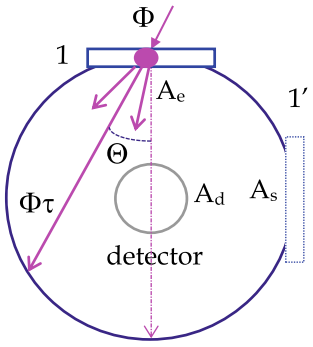

Fig. 2.36 Diffuse transmittance study

Consequently, the ratio of the two equations gives the diffuse transmittance of the sample being studied:

$$\frac{E}{E_0} = \tau^{\Theta} \frac{1 + \dfrac{\rho_0^{\Theta\Theta}\rho^{\Theta}A_e/(A_0 + A_e + A_s)}{1 - \rho_0^{\Theta\Theta}A_e/(A_0 + A_e + A_s) - \alpha_0^{\Theta}}}{1 - \dfrac{A_e\rho^{\pi} + A_s\rho^{\pi}}{A_0\alpha_0^{\pi} + A_d - A_d\rho_d^{\pi} + A_e + A_s - A_s\rho^{\pi}}}. \tag{2.174}$$

If the comparison sphere is opaque for a given wavelength and performs as a uniform diffuser:

$$\tau_{com}^{\Theta} = \frac{E}{E_0} \frac{1 - \dfrac{A_e\rho^{\pi} + A_s\rho^{\pi}}{A_0\alpha_0^{\pi} + A_d - A_d\rho_d^{\pi} + A_e + A_s - A_s\rho^{\pi}}}{1 + \dfrac{\rho^{\Theta}A_e/(A_0 + A_e + A_s)}{1 - A_e/(A_0 + A_e + A_s)}}, \tag{2.175}$$

since for a uniform diffuser $\alpha_0{}^{\Theta} = \alpha_0{}^{\pi}$, $\rho_0{}^{\Theta\Theta} = \rho_0{}^{\pi}$, and $\rho_0{}^{\pi} = 1 - \alpha_0{}^{\pi}$. For the substitution measurement with one open port, Eq. (2.175), representing the comparison method, is changed to [2.63]:

$$\tau_{sub}^{\Theta} = \frac{E}{E_0} \frac{1 - A_e\rho^{\pi}/\left(A_0\alpha_0^{\pi} + A_d - A_d\rho_d^{\pi} + A_e\right)}{1 - (1 - \rho^{\Theta})A_e/(A_0 + A_e + A_s)}. \tag{2.176}$$

It should be kept in mind that Eqs. (2.171)–(2.176) are derived assuming all integrating sphere inclusions to be spherical and to have the sphere's radius. Since flat surfaces do not result in uniform irradiance in reflected light as spherical ones, to obtain correction factors the Fredholm integral equations (2.116, 2.117) or the finite-difference (2.170) ones are to be solved.

For a small sample in a substitution sphere of a uniform diffuser, the diffuse transmittance τ becomes [2.64].

$$\tau_{sub}^{d} = \frac{E}{E_0} \frac{\Phi_{inc,0}}{\Phi_{inc}} \left[1 - \frac{\rho^{\pi}\rho_0 A_{s,pl}/A_s}{1 - \rho_0\left(1 - A_{s,pl}/A_s\right)}\right]. \tag{2.177}$$

Here ρ_0 is the reflectance of the sphere wall, presumed to be equal for direct and hemispherical irradiation, $\Phi_{inc,0}/\Phi_{inc}$ is the ratio of measured fluxes, and $A_{s,pl}/A_s$ is the ratio of the plane area of the sample port to the area of that spherical segment. Equation (2.177) is similar to (2.118) and does not account for second-order corrections as (2.121) and (2.124). A similar approach [2.64] for a comparison sphere does not distinguish correction factors of small flat samples given for reflective samples by Eqs. (2.122) and (2.125).

2.4.12 Separation of Direct and Diffuse Transmittance

Commonly, the diffuse transmittance of any translucent sample is measured as the diffuse reflectance in the integrating sphere, attached to a double-beam or single-beam spectrophotometer. The measured spectrum is then referred to the spectrum of a diffuse standard of seemingly uniform scattering indicatrix as of the perfect diffuser. Considering that correction factors for flat inclusions are accounted for by Eqs. (2.175)–(2.177), obtained under the small flat-sample assumption, one extra benefit from combination studies in transmission is to validate sphere correction factors via the specular and diffuse-scattering components measured.

The universal design of the integrating sphere for transmittance–reflectance measurement is depicted in Fig. 2.37. The sample and reference beams propagate through the sphere via ports 1 and 2, being reflected back into the sphere by a sample, a standard, or the sphere cap via ports 3 and 4. Extra port 5 lets the specular component of reflectance escape from the sphere. Round opaque baffle 6 protects sphere detector 7 from being directly irradiated by transmitted or by reflected light. When ports 3 and 4 are occupied by equal white standards, the detector readings are equalized: $N_0 = \text{const} \cdot k_{sam}\rho_1/k_{ref}\rho_2 \rightarrow 1$, where $\rho_1 \cong \rho_2 \cong \rho_{st}$ are identical reflectances of the standards and $k_{sam} \cong k_{ref} \cong k$ are the escape factors for channel losses in entrance ports. When a sample covers port 1:

$$N_s = const \cdot \left(\tau_{sp} k_{sam} \rho_{st} + (1 - D)\tau_{df} k_{sam} \rho_{st} + D\tau_{df}\right) / \left(k_{ref}\rho_{st}\right), \tag{2.178}$$

where D is the fraction of the sample diffuse transmittance, directly irradiating the sphere wall, but not the standard. Removing the standard from port 3 or replacing it by a blackbody gives:

$$N_c = const \cdot \left[(1 - D)\tau_{df} k'_{sam} \rho_{st} + D\tau_{df}\right] / \left(k'_{ref}\rho_{st}\right). \tag{2.179}$$

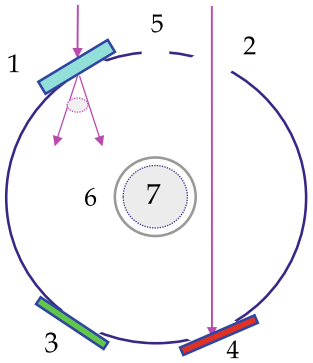

Fig. 2.37 Dual-beam sphere arrangement

Here k′ is not equal to k since one more port is opened and the effectiveness of multiple reflections is changed. If the ports are much smaller than the sphere and the escaping factors are approximately identical, the specular and diffuse transmittance can be expressed as [2.65, 2.66]:

$$\tau_{sp} = (N_s - N_c)/N_0; \tau_{df} = N_c/[N_0(1-D) + D/(k\rho_{st})]; \quad \tau_\Sigma = \tau_{sp} + \tau_{df}. \tag{2.180}$$

A single-beam integrating sphere for the measurement of specular and diffuse transmittance by the substitution method is seen in Fig. 2.38. Transmission sample 1 is either absent or installed in the sphere transmission-entrance port as for the substitution study (1′ is sphere-reflectance port). Internal detector 2 is protected by protruding baffle 3 from direct irradiation by either the sample or sphere port 1′. If the disturbance of sphere irradiance by flat inclusions is not counted, the sample's total transmittance is obtained analogously to Eqs. (2.171)–(2.180) [2.67].

$$\tau_\Sigma = \frac{1-\rho_0(1-A_{sl}/A_{sh})}{1-\left[\rho_0\left(1-A_{sl}/A_{sp}\right)+\left(A_{sl}/A_{sh}\right)\rho\right]} \times \frac{\tau_{df}+\tau_{sp}\left[\rho_0\left(1-\left(\rho_0^{sp}/\rho_0^{df}\right)\left(A_{sl}/A_{sh}\right)\right)+\left(\rho_0^{sp}/\rho_0^{df}\right)\left(A_{sl}/A_{sh}\right)\rho\right]}{\rho_0\left(1-\left(\rho_0^{sp}/\rho_0^{df}\right)\left(A_{sl}/A_{sh}\right)\right)}. \tag{2.181}$$

Here A_{sl} and A_{sh} are the areas of the sample port and the sphere, ρ and ρ_0 are reflectances of the sample and sphere wall, ρ_0^{sp} and ρ_0^{df} are the specular and diffuse components of wall reflectance ρ_0, and τ^{sp} and τ^{df} are the specular and the diffuse transmittance of a sample studied, such that $\tau_{sp} + \tau_{df} = \tau_\Sigma$. It is clear that to identify τ_Σ, the scattering indicatrixes of the sample and the wall have to be identified. When the sample scattering indicatrix is not uniform but without a

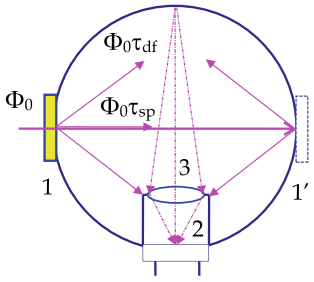

Fig. 2.38 Single-beam integrating sphere

noticeable direct transmittance, a correction factor could be introduced similarly to the diffuse reflectance (see above and [2.8]). However, if the direct transmittance is noticeable, thus leading to substantial losses to the reflectance port (marked 1′ in Fig. 2.38), a correction factor for a given geometry of the sphere and for a specific indicatrix need to be determined experimentally [2.94].

2.4.13 Coupling of Integrating Spheres

A natural step in making simultaneous measurements of diffuse reflectance and transmittance is associated with combining two integrating spheres: one in reflected and one in transmitted light [2.95, 2.98]. A joined reflection–transmission sphere is shown in Fig. 2.39. Sample 1 to be studied is fitted in between integrating spheres 2 and 3, having individual detectors 4, 5, screened from sample 1 by baffles 6, 7. A spot of sphere 2 wall is irradiated at angle of incidence φ and the sample 1 is irradiated at a design angle Θ, letting specularly reflected light be collected in sphere 2 or lost in its entrance port at normal incidence. For any translucent sample 1, light interchanges between spheres 2 and 3. To resolve additive effects of each second sphere, let us review in more detail the relations for single-sphere irradiance (2.140) and (2.162), while evaluating inputs of flat sections by Eqs. (2.121)–(2.125). All terms in the new equations will have indices rf and tr for the reflectance–transmittance spheres, indices sh, wl, en, and sl for the sphere, walls, entrance port, and the sample, and letters τ and ρ for transmittance and reflectance. The flux Φ_0 incident on each sphere wall creates single-sphere irradiance:

$$E_{wl}^{rf} = \frac{\Phi_0}{A_{sh}^{rf}} \tau_{en}^{\Theta} \rho_{0,rf}^{\Theta} \left(1 - \frac{\Delta\rho_{en}^{\pi} A_{en}^{rf}}{\rho_{0,rf}^{\pi} A_{sh}^{rf}} - \frac{\Delta\rho_{sl}^{\pi} A_{en}^{tr}}{\rho_{0,rfl}^{\pi} A_{sh}^{rf}} \right) \frac{\rho_{0,rf}^{\pi}}{1 - \rho_{0,rf}^{\pi\prime}} \equiv \frac{\Phi_0}{A_{sh}^{rf}} \tau_{en}^{\Theta} \rho_{0,rf}^{\Theta} \frac{f_{fs}^{rf} \rho_{0,rf}^{\pi}}{1 - \rho_{0,rf}^{\pi\prime}}. \tag{2.182}$$

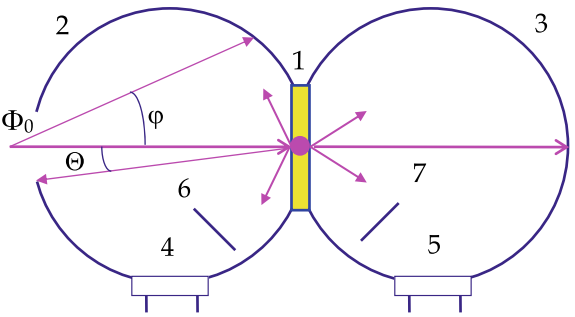

Fig. 2.39 Doubling of integrating spheres

Here ρ_0 and ρ_0' are the sphere's actual and effective reflectances (equations (2.104) and (2.105)), ρ_0^{π} and ρ_0^{Θ} are the diffuse reflectances of the wall for hemispherical irradiation and at angle Θ, A_{sl}, A_{ent}, and A_{dt} are the relative areas of the sample, entrance ports, and detectors related to area A_0 of the sphere, τ_{en}^{Θ} is the entrance port transmittance, f_{fs} is the effective factor of the sphere surface viewed from an exposed spot, $\Delta\rho_{en} = \rho_0 - \rho_{en}$, and $\Delta\rho_{sl} = \rho_0 - \rho_{sl}$. If the sample is irradiated, the first sphere irradiance is:

$$E_{sl}^{rf} = \frac{\Phi_0}{A_{sh}^{rf}} \tau_{en}^{\varphi} \left(\rho_{sl}^{sp,\varphi} \rho_{0,rf}^{\varphi} + \rho_{sl}^{df,\varphi} f_{fs}^{rf} \rho_{0,rf}^{\pi} \right) \frac{1}{1 - \rho_{0,rf}^{\pi\prime}}, \tag{2.183}$$

where ρ_{sl}^{df} and ρ_{sl}^{sp} are the specular and diffuse components of the sample reflectance at given angle φ.

The corresponding equations for transmitting sphere 3 when its wall is directly irradiated and when translucent sample 1 occupies its entrance port, being the exit port for reflecting sphere 2, are:

$$E_{wl}^{tr} = \left(\Phi_0 \tau_{en}^{\Theta} \rho_{0,rf}^{\Theta} \frac{A_{en}^{tr}}{A_{sh}^{rf}} + E_{wl}^{rf} A_{en}^{tr} \right) \tau_{sl}^{\pi} f_{wl}^{tr} \frac{\rho_{0,tr}^{\pi}}{1 - \rho_{0,tr}^{\pi\prime}}; \tag{2.184}$$

$$E_{sl}^{tr} = \left[\left(\Phi_0 \tau_{en}^{\varphi} \tau_{sl}^{df,\varphi} + E_{wl}^{rf} A_{en}^{tr} \tau_{sl}^{\pi} \right) f_{fs}^{tr} \rho_{0,tr}^{\pi} + \Phi_0 \tau_{en}^{\varphi} \tau_{sl}^{dr,\varphi} \rho_{0,tr}^{\varphi} \right] \frac{1}{1 - \rho_{0,tr}^{\pi\prime}} \frac{1}{A_{sh}^{tr}}. \tag{2.185}$$

Here A_{ent} is the relative area of the entrance port of sphere 3, related to its total surface, and $\tau_{sl}^{sp,\varphi}$, $\tau_{sl}^{df,\varphi}$, and τ_{sl}^{π} are the sample specular and diffuse transmittance at angle φ and the sample transmittance for hemispherical irradiation. Note that every specular component is incident on a sphere wall with no inclusions. For diffused light, the effective reflecting area has some inclusions identified by the specific sphere factor f_{fst}.

If both spheres perform concurrently, the four internal irradiances considered are, respectively:

$$E_{wl}^{rf+tr} = E_{wl}^{rf} + \left[E_{wl}^{rfl} \left(1 + \frac{\Delta\rho_{sl}^{\pi} A_{en}^{tr}}{\rho_{0,rf}^{\pi} A_{sh}^{rf}} \right) + \frac{\Phi_0 \tau_{en}^{\Theta}}{A_{sh}^{rf}} \rho_{0,rf}^{\Theta} \right] \frac{\left(A_{en}^{tr} \tau_{sl}^{\pi} \right)^2}{A_{sh}^{rf} A_{sh}^{tr}} \frac{f_{fs}^{tr} \rho_{0,tr}^{\pi}}{1 - \rho_{0,tr}^{\pi}}. \tag{2.186}$$

$$E_{sl}^{rf+tr} = E_{sl}^{rl} + \left\{ \left[E_{sl}^{rl} \left(1 + \frac{\Delta\rho_{sl}^{\pi} A_{en}^{tr}}{\rho_{0,rf}^{\pi} A_{sh}^{rl}} \right) \tau_{sl}^{\pi} + \frac{\Phi_0 \tau_{en}^{\varphi} \tau_{sl}^{\varphi,df}}{A_{sh}^{rf}} \right] A_{en}^{tr} \frac{f_{fs}^{tr} \rho_{0,tr}^{\pi}}{1 - \rho_{0,tr}^{\pi\prime}} + \Phi_0 \tau_{en}^{\varphi} \tau_{sl}^{\varphi,dr} \frac{\rho_{0,tr}^{\varphi}}{1 - \rho_{0,tr}^{\pi\prime}} \right\} \frac{\tau_{sl}^{\pi} A_{en}^{tr}}{A_{sh}^{rf} A_{sh}^{tr}}. \tag{2.187}$$

$$E_{wl}^{tr+rf} = E_{wl}^{tr} + \left[E_{wl}^{tr} \left(1 + \frac{\Delta\rho_{sl}^{\pi} A_{en}^{tr}}{\rho_{0,tr}^{\pi} A_{sh}^{tr}} \right) + \Phi_0 \tau_{en}^{\Theta} \rho_{0,rf}^{\Theta} \frac{A_{en}^{tr}}{A_{sh}^{rf}} \tau_{sl}^{\pi} \rho_{0,tr}^{\pi} \frac{f_{fs}^{tr}}{A_{sh}^{tr}} \right] \times \frac{\left(A_{en}^{tr} \tau_{sl}^{\pi}\right)^2}{A_{sh}^{rf} A_{sh}^{tr}} \frac{f_{fs}^{rf} \rho_{0,rf}^{\pi}}{1 - \rho_{0,rf}^{\pi\prime}}. \tag{2.188}$$

$$E_{sl}^{tr+rf} = E_{sl}^{tr} + \left[E_{sl}^{tr} \left(1 + \frac{\Delta\rho_{sl}^{\pi} A_{en}^{tr}}{\rho_{0,rf}^{\pi} A_{sh}^{rl}} \right) + \Phi_0 \tau_{en}^{\varphi} \tau_{sl}^{\varphi,df} \rho_{0,tr}^{\pi} \frac{f_{fs}^{tr}}{A_{sh}^{tr}} + \Phi_0 \tau_{en}^{\varphi} \tau_{sl}^{\varphi,dr} \frac{\rho_{0,tr}^{\varphi}}{A_{sh}^{tr}} \right] \times \frac{\left(A_{en}^{tr} \tau_{sl}^{\pi}\right)^2}{A_{sh}^{rf} A_{sh}^{tr}} \frac{f_{fs}^{rf} \rho_{0,rf}^{\pi}}{1 - \rho_{0,rf}^{\pi\prime}}. \tag{2.189}$$

In all equations, the factor $(1 + \Delta\rho A_{en}/(\rho_0 A_{sh}))$ accounts for loss of single sphere irradiance to each second sphere and the factor $(A_{en}\tau_{sl})^2/(A_{sh}A_{sh})$ stands for conversion of incident flux to irradiance in a single sphere converting back and forth via the sample aperture into another sphere irradiance.

Equations (2.186)–(2.189) for a dual sphere are based on knowledge of irradiance for each detached sphere. Expressions (2.181)–(2.185) for single reflection and transmission spheres contain two pairs of the sample's direct and diffuse reflectance and transmittance, ρ_{sl}^{df}, ρ_{sl}^{dr}, $\tau_{sl}^{df,\varphi}$, $\tau_{sl}^{dr,\varphi}$, and ones for the sphere, $\rho_{0,rf}^{\Theta(\varphi)}, \rho_{0,rf}^{\pi}, \rho_{0,tr}^{\Theta(\varphi)}, \rho_{0,tr}^{\pi}$. The equations can be resolved by performing two extra measurements of direct transmittance and specular reflectance for the sample, presuming a uniform diffuse coating for sphere surfaces: $\rho_{0,rf}^{\Theta(\varphi)} = \rho_{0,rf}^{\pi}$ and $\rho_{0,tr}^{\Theta(\varphi)} = \rho_{0,tr}^{\pi}$.

Measurements of specular reflectance and direct transmittance can be performed by adding for the joined spheres extra beam splitter 8, exit port 9 for the transmission sphere, and extra detectors 10 and 11 (Fig. 2.40). To determine the characteristics of the sample, both specular factors and two diffuse factors for the sample

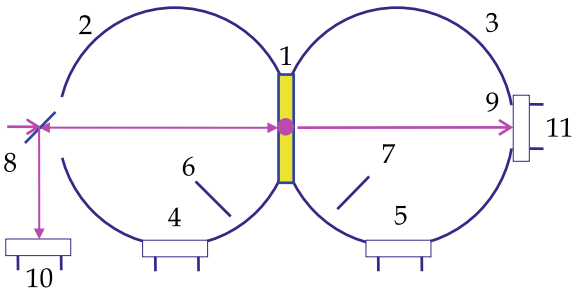

Fig. 2.40 Added specular reflectance and direct transmittance

and four factors for the spheres need to be detected in separate and connected sphere settings. In the double-sphere arrangement, each sphere irradiance must be measured separately to be resolved by Eqs. (2.182)–(2.185).

2.4.14 Integrating Spheres for Isotropic Irradiation

Ideally, the integrating sphere should produce uniform Lambertian irradiation of its inner surface – that nearly happens when sphere inclusions are infinitely small. Practical implementations can present various challenges owing to finite dimensions of the sphere entrance and exit ports, owing to dependence of wall reflectivity for practical sphere surfaces on the angle of light incidence and polarization, or owing to design errors [2.70–2.75]. Nevertheless, there are many practical ways, some of which were reviewed above, for making sphere irradiance or illuminance practically uniform for given considerations and measurements.

One straightforward way to minimize disturbance of internal sphere irradiance by a port is to cover its opening by a diffusely transmitting and reflecting material, such as an opal glass [2.76]. The sphere wall emittance at a first-order approximation of sphere irradiance (Eqs (2.5) and (2.6)) is:

$$M_0 = \frac{\Phi_0\rho_0 + \Phi_0\rho_0^2 + \cdots + \Phi_0\rho_0^n}{4\pi r_0^2} = \frac{\Phi_0}{4\pi r_0^2}\frac{\rho_0}{1-\rho_0}, \tag{2.190}$$

where ρ_0 is the effective diffuse reflectance of a perfect sphere and Φ_0 is the flux of radiation directly irradiating a wall (Eq. 2.102). For a port of diffuse reflectance ρ_p, its into-sphere emittance consists of two components: one of the sphere itself and one of input flux Φ_0 at cross section $2r_p$:

$$M_p = \frac{\Phi_0}{4\pi r^2}\frac{\rho_p}{1-\rho_0} + \frac{\Phi_0}{\pi r_p^2}. \tag{2.191}$$

Following [2.76], for total-sphere emittance to be uniform M_0 and M_p should be equal; therefore:

$$\frac{r_0}{r_p} = \sqrt{\frac{\rho_0 - \rho_p}{4\rho_p(1-\rho_0)}}. \tag{2.192}$$

Considering the measurement in a nearly ideal highly diffuse-reflecting sphere of wall reflectance $\rho_0 = 0.99$ at $\rho_p = 0.5$, the ratios of the sphere-to-port radius and of the sphere-to-port areas become $r_0/r_p = 5$ and $S_0/S_p = 100$ and make the internal sphere irradiance nearly uniform (compare Eq. (2.104)).

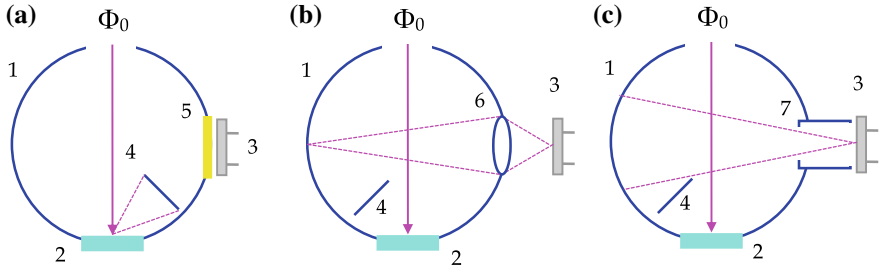

Fig. 2.41 Baffling in integrating spheres: detector (**a**), projecting area (**b**), via protrusion (**c**):1—sphere; 2—sample; 3—detector; 4—baffle; 5—translucent glass; 6—lens; 7—protruding holder

Although the first-order approximation by Eqs. (2.190)–(2.192) may not hold true for a sophisticated integrating-sphere design, the applicability of a translucent diffuser, covering detector ports, is established as the universal solution for reliable and absolute reflectance measurements using integrating spheres [2.8, 2.46, 2.49, 2.58, 2.60–2.62]. However, in certain cases, the detector cannot be directly attached to an integrating sphere especially if extensive cooling is required; therefore, a section of a sphere surface without inclusions must be projected to a remote detector (see Fig. 2.41). As an internal sphere detector (Fig. 2.41a), a remote one can be screened from direct irradiation by shielding the viewing area via a baffle (Fig. 2.41b) or by protrusion of the detector or a projecting lens (Fig. 2.41c). A common recipe for internal sphere uniformity is use of highly reflecting materials for baffles as for the primary internal sphere reflector keeping relative areas of flat samples, baffles, or protruding sections negligibly small, ultimately approaching the unbaffled sphere [2.84].

The protruding holder can also focus and collect radiation on the detector [2.77, 2.78]. The hyperbolic concentrator (see Fig. 2.42 using Fig. 2.41 designations) provides an example of supplemental light collection effort by increasing light concentration via hyperboloid mirror surface 7 [2.79]. External placement of the detector also allows adjustment of its field of view on the inner sphere surface, while portions of radiation not accepted by the concentrator are recycled back into the main sphere.

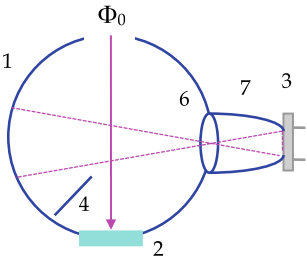

Fig. 2.42 Integrating sphere with non-imaging concentrator

Despite every design effort to create an isotropic integrating sphere, practical implementations deal with constraints and deviations from modeled design continuity and the ideal uniformity of Lambertian light scattering for actual diffusers and configurations [2.80–2.99]. Various modeling recommendations of integrating sphere reflectivity, as the linear mixture of perfectly diffuse and ideally specular scattering, predict significant measurement errors occurring for non-Lambertian sphere wall scattering. However, modeling results show the relative independence on the detector field of view, except for viewing areas irradiated by specular components, while errors are minimized [2.81] as sphere wall reflectance approaches the ideal 1.0 limit as for a mirror sphere (Eq. 2.102). Furthermore, at certain sphere arrangements, restricting areas of direct irradiation can lead to nonuniform initial irradiance, even for curved-surface interreflections [2.82]. The actual distribution functions and design models for internal sphere irradiance can serve as correction factors [2.86].

However, individual integrating sphere designs may unintentionally lead to nonuniformity of sphere irradiance at specific angles of observation, particularly owing to the restricted field of view. Figure 2.43 depicts one easier-to-model unbaffled integrating sphere, in which to avoid use of baffles and irradiation of the detector by nonuniform irradiance of a test sample, one optical fiber bundle of small dimensions and low numerical aperture is utilized [2.83]. A 10.6 cm-diameter integrating sphere with 2.54 cm circular opening has a fiber-optic cable output port positioned at 90° to the optical axis of the entrance port. The incident beam carrying flux Φ_0 is directed at zenith angles 0–80° at 10° increments and at any azimuth angle ranging from 0° to 345° with 15° increments. The fiber-optic cable has a 0.254 cm input diameter bundle of 0.28 numerical aperture [2.83]. The half-view angle is 16.32° at refractive index 1.46 and at 0.035 reflectance for normal light incidence. Via the energy-balance approach introduced in Sect. 2.1, and using input–output equilibrium of light, the ratio of the sphere's output flux Φ_r to flux Φ_0 entering the sphere is directly proportional to the loss of sphere wall reflectance due to openings (relations (2.104)–(2.110)) and to output-coupling loss at the numerical aperture to all the sphere area:

$$\frac{\Phi_r}{\Phi_0} = (1-\rho_r)\frac{A_r}{A_0}NA^2\frac{\rho_0}{(1-\rho_0(1-(A_{in}+A_r)/A_0))}. \tag{2.193}$$

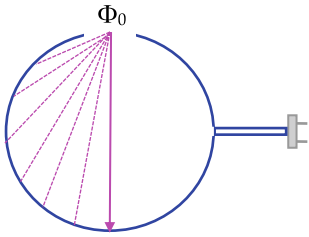

Fig. 2.43 Simple fiber-coupled and unbaffled integrating sphere

Here A_0, A_{in}, and A_r are the areas of the sphere and the input and receiving ports, ρ_0 and ρ_r are reflectances of the sphere and the bundle, and NA is the numerical aperture, where NA^2 characterizes the viewing area of the port versus the hemisphere.

Particular allocations of sphere wall reflectivity and nonuniformity can be modeled via a probability density function of the photon distribution using probabilistic techniques (see Sect. 9.4 or [0.24, 2.83, 2.86] for details). Since an integrating sphere should behave as a cosine-law collector, the intensity $I(\Theta)$ of radiation reflected at angle Θ versus input intensity I_0 is defined by Lambert's law (Eq. 1.46). By definition (see relations (1.40) and (1.47)), the total flux $\Phi(\Theta)$ reflected within solid angle Ω' subtended by the azimuth angles $\varphi' = 0 - 180°$ and zenith angles $\Theta' = 0 - \Theta°$ is:

$$\Phi(\theta) = \int_{\varphi'=0}^{2\pi} \int_{\theta'=0}^{\theta} I_0 \cos(\theta') \sin(\theta') d\Phi' d\theta' = I_0 \pi \sin^2(\theta). \tag{2.194}$$

When related to full flux Φ_0 reflected into the entire hemisphere, expression (2.194) provides the cumulative probability distribution for radiation emitted into subtended-angle range $0{-}\Theta°$ [2.83].

$$F(\Theta) = \sin^2(\Theta). \tag{2.195}$$

Despite certain nonuniformity of the specific sphere design in Fig. 2.43 for 40–50° zenith angles, revealed by Monte-Carlo simulation of the distribution function via random numbers as angles Θ per Eq. (2.195): $\Theta \sim \sin(\sqrt{F(\Theta)})$, the total flux averaged by angles within 0°–90° was found equivalent to the analytical solution via energy-balanced Eq. (2.193) at nearly 0.25% [2.83]. Similar levels of scattering uniformity, within 0–2% and 0.2–2.6%, were experimentally confirmed by in-depth radiance-gradient measurements for inclusion-free areas of integrating spheres and for the spectral regions of high diffuse reflectivity of internal-surface sphere coatings [2.85, 2.88].

Considering uniformly diffused transmission via any integrating sphere, one could think of spheres as in Figs. 2.4 and 2.5. Another transmitting integrating sphere design is shown in Fig. 2.44, which aims to use one port simultaneously for incoming and outgoing radiation [2.89]. The goal is similar to the idea of absolute

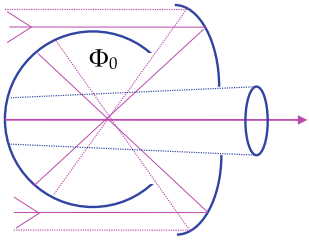

Fig. 2.44 Integrating-sphere radiator

reflectance measurements (Eqs. (2.126)–(2.128)) and that for evaluation of absolute flux (Fig. 2.4, relations (2.14) and (2.15) – to block any viewing of the first sphere reflection. Following Eqs. (2.5) and (2.6), Kirchhoff's law for the thermal equilibrium of the sphere [1.13, 2.4] states that the fraction of radiation being reflected inside the sphere must be in equilibrium with the radiation transmitted by sphere ports and absorbed by its walls. For an integrating sphere with radius r and spherical surface $A_0 = 4\pi r^2$ for diffuse reflectance ρ, except for the opening of area A with no reflectivity, its effective surface reflectance (see relation (2.104)) is $\rho' = \rho(1 - A/A_0)$. For the incoming flux Φ_0:

$$\begin{aligned}\Phi_\rho &= \Phi_0(\rho + \rho\cdot\rho' + \cdots + \rho\cdot\rho'^n) \underset{n\to\infty}{=} \frac{\Phi_0\rho}{1-\rho'} = \frac{\Phi_0\rho}{1-\rho(1-A/A_0)} \\ &= \frac{\Phi_0\rho A_0}{A_0 - \rho(A_0 - A)};\end{aligned} \tag{2.196}$$

$$\begin{aligned}\Phi_\tau &= \Phi_0\left(\rho\frac{A}{A_0} + \rho\cdot\rho'\cdot\frac{A}{A_0} + \cdots + \rho\cdot\rho'^n\cdot\frac{A}{A_0}\right) \underset{n\to\infty}{=} \frac{\Phi_0\rho}{1-\rho'}\frac{A}{A_0} \\ &= \frac{\Phi_0\rho A}{A_0 - \rho(A_0 - A)};\end{aligned} \tag{2.197}$$

$$\begin{aligned}\Phi_\alpha &= \Phi_0\left(\rho\frac{A_0 - A}{A_0} + \cdots + \rho\cdot\rho'^n\cdot\frac{A_0 - A}{A_0}\right) \underset{n\to\infty}{=} \frac{\Phi_0\rho}{1-\rho'}\frac{A_0 - A}{A_0} = \frac{\Phi_0\rho'}{1-\rho'} \\ &= \frac{\Phi_0\rho(A_0 - A)}{A_0 - \rho(A_0 - A)}.\end{aligned} \tag{2.198}$$

Here Φ_ρ, Φ_τ, and Φ_α are the reflected, transmitted, and absorbed portions of the flux Φ_0 and A/A_0 and $(A_0 - A)/A_0$ are the relative areas of the port and the sphere surface. The equilibrium is:

$$\begin{aligned}\Phi_\rho &= \frac{\Phi_0\rho}{1-\rho'} = \Phi_\tau + \Phi_\alpha = \Phi_0\frac{\rho A + \rho(A_0 - A)}{A_0 - \rho(A_0 - A)} = \frac{\Phi_0\rho A_0}{A_0 - \rho(A_0 - A)} \\ &= \frac{\Phi_0\rho}{1-\rho(1-A/A_0)}.\end{aligned} \tag{2.199}$$

One drawback of aiming to avoid not-uniform first sphere reflection by directing a viewing area outside the spot, irradiated by incident light, is in this case leading to a quite large input port. The same thermal-equilibrium set for a sphere section of reflectance ρ′ guarded from direct irradiation is:

$$\Phi_{\rho 2} = \Phi_0 \rho \rho' A_0/(A_0 - \rho(A_0 - A)) = \Phi_0 \rho^2 (A_0 - A)/(A_0 - \rho(A_0 - A));$$
$$\Phi_{\tau 2} = \Phi_0 \rho \rho' A/(A_0 - \rho(A_0 - A)) = \Phi_0 \rho^2 (A/A_0)(A_0 - A)/(A_0 - \rho(A_0 - A));$$
$$\Phi_{\alpha 2} = \Phi_0 \rho \rho' (A_0 - A)/(A_0 - \rho(A_0 - A)) = \Phi_0 \rho^2 \left((A_0 - A)^2/A_0\right)/(A_0 - \rho(A_0 - A)). \quad (2.200)$$

As discussed for measurements of reflectance, having one large opening may not benefit a sphere design, unless its practical implementation overcomes challenges and is verified experimentally. Finally, considering implementations of integrating spheres with fully or partially coherent laser radiation, one should also keep in mind that, as for any other dense diffusers, the multiple beam interference may exhibit itself via speckle effects, which may be minimized by spatial averaging and integration, though the root cause of most problems is in random phase noise conversion to intensity noise that exhibits itself via specific signal fluctuations (see Chaps. 3, 6, and 8 on the measures for reducing interference phenomena). In some cases a relatively high frequency beam modulation or agitation of the receiver, or the sphere itself, can decrease speckle effects [2.90]. Also, similarly to integrating spheres, other surface integrating elements, such as long cylinders, can be used for multiplication of reflected light as employed in solid-state laser resonators [2.91].

Since coupling of two integrating spheres provides double integration of light scattering via the spheres and likely more uniform Lambertian integration than a single sphere [4.51], coupled integrating spheres could supplement each other for auxiliary measurements of the radiant flux [2.93]. One measurement concept is based on the coupling of symmetrical integrating spheres to simultaneously detect emission of a test source in two spheres, presuming the complete equality for two sphere properties (Fig. 2.45). Concurrent use of two identical detectors in each sphere, measuring respective sphere irradiance due to a test source in a single sphere, provides for an extra sphere modification factor via the signal ratio of both detectors and could simplify absolute calibration, providing the spheres are identical. Test source S emitting flux Φ_0 is placed in the center of sphere 1 connected via a port of area A_c to sphere 2. The spheres have the same detectors of close-to-zero reflectivity observing each sphere irradiance via identical ports with spherical surface $A_d = A_c$. Matching baffles 1, 2, and 3 screen the detectors from being

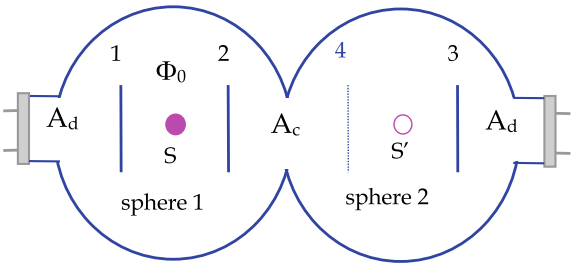

Fig. 2.45 Symmetrical coupled integrating spheres

directly irradiated by source S or by the source plus sphere 1. Irradiance E_1 of sphere 1 for its area A_0 due to source S is:

$$E_1 = \frac{\Phi_0}{A_0}\frac{\rho_0}{1-\rho_{01}'} = \frac{\Phi_0}{A_0}\frac{\rho_0 A_0}{A_0 - \rho_0(A_0 - A_c - A_d)} \equiv \frac{\Phi_0}{A_0}F_1. \tag{2.201}$$

Presuming both spheres have identical reflectivity ρ_0, irradiance E_2 of sphere 2 due to source S is:

$$E_2 = \frac{E_1 A_c}{A_0}\frac{\rho_0}{1-\rho_{02}'} = \Phi_0\frac{A_c}{A_0}F_1\frac{\rho_0 A_0}{A_0 - \rho_0(A_0 - A_c - A_d)} \equiv \Phi_0\frac{A_c}{A_0}F_1F_2. \tag{2.202}$$

To equalize the efficiencies of the spheres, identical baffle 4 and not-emitting source S′ are added to sphere 2:

$$E_2 \underset{F_1=F_2=F_0}{=} \Phi_0\frac{A_c}{A_0}F_0^2 = \Phi_0\frac{A_c}{A_0}\left(\frac{\rho_0 A_0}{A_0 - \rho_0(A_0 - A_c - A_d)}\right)^2. \tag{2.203}$$

Then, at identical efficiencies and reflectivities, efficiency $F_0 \equiv F_{1,2}$ can be measured via the ratio:

$$E_2/E_1 = A_c F_0 = A_c\rho_0/\left(1-\rho_0'\right) \underset{A_c=A_d}{=} \rho_0 A_0 A_c/(A_0 - \rho_0(A_0 - 2A_c)). \tag{2.204}$$

For certain applications while studying skin tissue or biological samples, it is advantageous to use an integrating sphere as a uniform diffuse irradiator of a sample. If light reflected by such a sample is retroreflected by the sphere wall, the probability model for sample reflection to reach the internal sphere detector or to be further absorbed by the wall can be based on Markov chains [2.87]. This way the integrating sphere system as a whole has a number n of finite states, of which m are absorbing ones, where the probability of light exiting the sphere is zero. The probability for a photon to hit a given section of the integrating sphere is determined by the spherical area of the section. For a sphere wall of uniform diffuse reflectance ρ_0 and inner-surface area A_0 having a spherical sample of reflectance ρ_s and area A_s with a fully absorbing spherical detector of area A_d, the detector signal due to the first reflectance of direct light from the sample inside the sphere is proportional to the number m of absorbing states related to the total area A_0 of the sphere surface; thus:

$$m/A_0 = A_d/1 - \rho_s A_s - A_0(1-\rho_0). \tag{2.205}$$

If the relatively small but flat sample experiences uniform diffuse irradiation via the wall of a large sphere, the large-sphere and small near-spherical sample approximation model becomes [2.87].

$$\frac{m}{A_0} = \frac{A_d\left(1-\left(1-\rho_s\right)A_s\right)}{1-A_s-A_0\left(1-\rho_0\right)\left(1-\left(1-\rho_s\right)A_s\right)}. \tag{2.206}$$

Solving Eq. (2.206) gives an estimation of the probability of sample reflectance via sphere irradiation:

$$\rho_s = \frac{\left(1-A_s\right)\left(m\left(1-A_0\left(1-\rho_0\right)\right)-A_dA_0\right)}{A_sA_0\left(A_d+m\left(1-\rho_0\right)\right)}. \tag{2.207}$$

Calibrating the detector responsivity via known reflectance references would quantify the model [2.87].

Chapter 3
Radiometry of Partially Coherent Radiation

3.1 Coherence and Radiative Transfer

3.1.1 Observability and Statistical Properties of Radiation

The origin of the photometric and radiometric concept is associated with the desire to observe and quantify radiation and to measure physical parameters of light beams via energy and power extents. Owing to the finiteness of the dimensions and time constants of visual and radiometric detectors, the observation and the measurement processes are defined not only by wave amplitudes of the electromagnetic oscillations observed, but also by the detector's response to the squared amplitude of the wave averaged by detector time and space constants. The properties of the actual detectors define the space–time averages of radiant or luminous parameters of optical radiation and cause high-frequency filtration for observable radiation, leading to an evident lack of correlation between radiometric observation and the description of wave oscillations by electric and magnetic vector amplitudes [1.2]. Only in the electromagnetic field of a plane monochromatic wave, with the phase of its oscillation being an amplitude-invariable function of time, is it possible to construct a single-valued square correlation between the field intensity and its amplitude. Light waves emitted by sources are not strictly monochromatic owing to the finiteness of source dimensions and a great number of elementary dipoles affecting one another. Each light excitation made by a physical source is always given by a sum of Fourier decompositions to infinitely long individual monochromatic groups. Therefore, the wave amplitudes and phases of light in any actual wave field undergo certain irregular fluctuations within spectral width $\Delta\nu$ of effective radiating frequency ν.

Furthermore, the amplitude of electromagnetic oscillations producing a quasi-monochromatic light wave at an average frequency $\bar{\nu}$ can be presumed to be constant only during a time interval τ considerably smaller than the wave coherence time: $\Delta\tau \cong 1/(\Delta\nu)$, and within a distance ℓ notably smaller than the spatial

M. Bukshtab, *Photometry, Radiometry, and Measurements of Optical Losses*, Springer Series in Optical Sciences 209,
https://doi.org/10.1007/978-981-10-7745-6_3

coherence length $\Delta\ell \cong c/(\Delta\nu) = (\bar{\lambda})^2/(\Delta\lambda)$ of the wave source. The constancy of the wave amplitude holds true within the coherence region at a given point of the wave field [1.1]. Such a coherence concept does not contradict traditional radiometric definitions, which presume the law of additive superposition of light beams holds true and expect the absence of observable interference phenomena. Knowledge of coherence properties of the quasi-monochromatic waves interacting by engaging in interference or diffraction and the of conditions under which these coherence properties do not manifest themselves allows one to reveal the bounds of additive radiometric concepts, the manners of diminishing interference effects, and the reasons for potential deviations from the additive laws.

Let us consider an electromagnetic field of a number of correlated wave groups interacting with each other to form the ergodic and, consequently, stationary field of radiation in statistical equilibrium. This balance means that the field averages by any ensemble of realizations have identical results as the time average [3.1]. In such a field, the second-order correlations between two arbitrarily chosen points $p_1(\mathbf{r}_1)$ and $p_2(\mathbf{r}_1)$ are characterized by the mutual coherence function:

$$\Gamma(\mathbf{r_1}, \mathbf{r_2}, \tau) = \langle U(\mathbf{r_1}, t+\tau) U^*(\mathbf{r_2}, t) \rangle, \tag{3.1}$$

where U(**r**, t) is the complex analytic representation of the wave oscillation corresponding to the amplitude of the electric component of this electromagnetic field at any established point P(**r**) of the observation defined by a radius vector **r** at an arbitrary moment of time t, and τ is the difference in propagation time of a given wave from points $P_1(\mathbf{r}_1)$ and $P_2(\mathbf{r}_2)$ to the point of superposition P(**r**). Here the angle brackets designate the statistical average either by time or by an ensemble, and the asterisk indicates the complex conjugate. The complex degree of spatial coherence is represented by the normalized correlation function of the observable field of optical radiation between spatial points designated by radius vectors $\mathbf{r}_1$ and $\mathbf{r}_2$ at instants of time separated by the delay τ [1.1]:

$$\gamma(\mathbf{r_1}, \mathbf{r}_2, \tau) = \frac{\Gamma(\mathbf{r_1}, \mathbf{r_2}, \tau)}{\sqrt{I(\mathbf{r_1}) I(\mathbf{r_2})}}. \tag{3.2}$$

The mutual coherence function $\Gamma(\mathbf{r}, \mathbf{r}, 0)$ at a field point defines the mutual radiation intensity I(**r**, 0) at $\tau = 0$:

$$I(\mathbf{r}, 0) = \langle U(\mathbf{r}, t) U^*(\mathbf{r}, t) \rangle = \Gamma(\mathbf{r}, \mathbf{r}, 0), \tag{3.3}$$

while I(**r**, t) is the average radiation intensity or the mean angular density of the field at point P(**r**) and at time instant *t*. For all possible magnitudes of the argument and by contrast to oscillations U(**r**, t) and U^*(**r**, t), the correlation function $\Gamma(r_1, r_2, t)$ and the similar, but normalized function:

$$0 \le |\gamma(\mathbf{r_1}, \mathbf{r}_2, \tau)| \le 1, \tag{3.4}$$

which is the complex degree of spatial coherence, are always observable and experimentally measurable.

The interpretation of the normalized correlation function $\gamma(r_1, r_2, \tau)$ as the degree of coherence corresponds to observation of interference of light beams emanating from points P_1 and P_2 and traveling to point P of observation. The resultant radiant intensity I(r) of two interfering light components becomes:

$$I(\mathbf{r}) = I_1(\mathbf{r}) + I_2(\mathbf{r}) + 2\sqrt{I_1(\mathbf{r})I_2(\mathbf{r})}\mathrm{Re}[\gamma(\mathbf{r_1}, \mathbf{r_2}, \tau_{1,2})], \tag{3.5}$$

where time constant τ is defined by distances PP_1 and PP_2 and the speed of light in a given medium:

$$\tau_{1,2} = (PP_1 - PP_2)/c; \tag{3.6}$$

I_1 and I_2 are the radiant intensities of beams emitted from points P_1 and P_2 as if they reached P from P_1 and P_2 with no superposition. For $P_1 = P_2$, the modulus of γ defines the fringe visibility V of the interference pattern:

$$V = \frac{I_{\max}(\mathbf{r}) - I_{\min}(\mathbf{r})}{I_{\max}(\mathbf{r}) + I_{\min}(\mathbf{r})} = \left|\gamma(\mathbf{r_1}, \mathbf{r_2}, \tau_{1,2})\right|. \tag{3.7}$$

$I_{\min}$ and $I_{\max}$ are two extreme values of the average intensity at immediate closeness to point P.

The complex degree of spatial coherence is the field-correlation criterion, defining the visibility of the interference pattern by any physical or subjective detector in either the space domain or the time domain. However, most properties of radiative energy transfer via substances, bodies, and mediums are spectrally selective. To express correlations of waves in terms of frequencies, it is natural to analyze the coherence extents of radiation in the space–frequency domain. Disregarding conceivable polarization effects, any fluctuating optical field can be represented by a complex analytical amplitude U(**r**, t), which, in that case, is the scalar function of distance and time. The resulting Fourier transform of the complex wave amplitude with respect to the time variable is [3.1, 3.2]:

$$U(\mathbf{r}, t) = \int_0^\infty U(\mathbf{r}, \nu)\, \exp(-2\pi i \nu t) d\nu. \tag{3.8}$$

The inverse Fourier transform gives:

$$U(\mathbf{r}, \nu) = \int_{-\infty}^\infty U(\mathbf{r}, t)\, \exp(2\pi i \nu t) dt. \tag{3.9}$$

The average magnitude of amplitude product $U^*(\mathbf{r}_1,\nu) \cdot U(\mathbf{r}_2,\nu')$, corresponding to correlation between points $P_1(\mathbf{r}_1)$ and $P_2(\mathbf{r}_2)$ at two different frequencies ν and ν' within the limits of all their values, is:

$$\langle U^*(\mathbf{r}_1,\nu)U(\mathbf{r}_2,\nu')\rangle = \int_{-\infty}^{\infty} \int \langle U^*(\mathbf{r}_1,t)U(\mathbf{r}_2,t+\tau)\rangle e^{2\pi i(\nu-\nu')t} e^{2\pi i\nu' t} dt d\tau, \quad (3.10)$$

where $t' = t + \tau$ and $\langle U^*(\mathbf{r}_1,t)U(\mathbf{r}_2,t+\tau)\rangle$ is the mutual coherence function $\Gamma(\mathbf{r}_1,\mathbf{r}_2,\tau)$, defined by Eq. (3.1). Since the wave amplitude in a steady-state optical field is not time-dependent, the result of direct integration over t in Eq. (3.10) is represented by Dirac's delta function δ:

$$\langle U^*(\mathbf{r}_1,\nu)U(\mathbf{r}_2,\nu')\rangle = \delta(\nu-\nu')W(\mathbf{r}_1,\mathbf{r}_2,\nu), \quad (3.11)$$

where $W(r_1,r_2,\nu)$ is the cross-spectral density function, characterizing a measure of the correlation for wave oscillations at frequency ν at points $P(\mathbf{r}_1)$ and $P(\mathbf{r}_2)$ (see, e.g., [3.3]), and is:

$$W(\mathbf{r}_1,\mathbf{r}_2,\nu) = \int_{-\infty}^{\infty} \Gamma(\mathbf{r}_1,\mathbf{r}_2,\tau)\ \exp(2\pi i\nu\tau)d\tau. \quad (3.12)$$

The inverse Fourier transform of Eq. (3.12) gives [3.1, 3.4]:

$$W(\mathbf{r}_1,\mathbf{r}_2,\tau) = \int_{0}^{\infty} \Gamma(\mathbf{r}_1,\mathbf{r}_2,\nu)\ \exp(-2\pi i\nu\tau)d\nu. \quad (3.13)$$

Expressions (3.11)–(3.13) establish that the cross-spectral density function $W(\mathbf{r}_1,\mathbf{r}_2,\nu)$ characterizes correlations between generalized Fourier components of light oscillations at given points. These Fourier components of different frequencies ν and ν' do not correlate with each other, and the correlation at frequency ν and delay τ are characterized by functions $W(\mathbf{r}_1,\mathbf{r}_2,\nu)$, $W(\mathbf{r}_1,\mathbf{r}_2,\tau)$. That assertion [3.4] presumes a continuous function of ν exists for each pair of radius vectors $\mathbf{r}_1$ and $\mathbf{r}_2$, which excludes the possibility of having rigorously monochromatic waves, which are not detected in reality.

From Eq. (3.11) it follows [3.4] that $W(\mathbf{r}_1,\mathbf{r}_2,\nu) = W(\mathbf{r}_2,\mathbf{r}_1,\nu)$, and the physical quantity:

$$\mu(\mathbf{r}_1,\mathbf{r}_2,\nu) = \frac{W(\mathbf{r}_1,\mathbf{r}_2,\nu)}{\sqrt{I(\mathbf{r}_1,\mathbf{r}_1,\nu)I(\mathbf{r}_2,\mathbf{r}_2,\nu)}}, \quad (3.14)$$

in the space–frequency domain, as the complex degree of spatial coherence $\gamma(\mathbf{r_1}, \mathbf{r}_2, \tau)$ in the space–time domain, can be normalized in such a way that for all possible magnitudes of arguments $\mathbf{r_1}, \mathbf{r}_2, \nu$:

$$0 \leq |\mu(\mathbf{r_1}, \mathbf{r}_2, \nu)| \leq 1. \tag{3.15}$$

Consequently, the function $\mu(\mathbf{r_1}, \mathbf{r_2}, \nu)$ defines the complex degree of spectral coherence and the spatial correlation factor for the random field of light of frequency ν and at points $P_1(\mathbf{r}_1)$ and $P_2(\mathbf{r}_2)$. Equation (3.14) can be rewritten similarly to (3.2) and (3.3) in terms of angular frequency $\omega = 2\pi\nu$ as:

$$\mu(\mathbf{r_1}, \mathbf{r_2}, \omega) = \frac{W(\mathbf{r_1}, \mathbf{r_2}, \omega)}{\sqrt{I(\mathbf{r}_1, \omega) I(\mathbf{r_2}, \omega)}}, \tag{3.16}$$

and the normalizing factor for the not negative continuous cross-spectral density function [3.4, 3.5]:

$$I(\mathbf{r}, \omega) = W(\mathbf{r}, \mathbf{r}, \omega), \tag{3.17}$$

represents the statistically averaged intensity I of optical radiation at each point r_1 and r_2 at frequency ω.

The theory of coherence for the statistically averaged steady-state optical field [3.1–3.10] allows one to define the law-governed nature of the spatial-angular distribution of light emitted by an isotropic planar source. The theory is also applicable to any source that can be reduced to a planar one in a far field where it can be considered as a material point. The distribution of the intensity of light emission over such a source is determined by cross-spectral density function $W^{(0)}(\mathbf{r}_1, \mathbf{r}_2, \omega)$ in that approximation plane, having the source coordinate $z = 0$. The inverse-square law for the radiant intensity $I_\omega(\mathbf{s})$ in the far field for the source, where wave number $k = \omega/c$ multiplied by distance $\mathbf{r}$ to observation point $P(\mathbf{r})$ identified by three-dimensional vector $\mathbf{s}$ tends to infinity, is given by [3.12]:

$$I_\omega(\mathbf{s})/r^2 \rightarrow const = I^{(\infty)}(r\mathbf{s}, \omega). \tag{3.18}$$

Here $I^{(\infty)}$ is the angular density of the radiation flux at infinity, which is not dependent on the modulus of $\mathbf{r}$: $|\mathbf{r}| = r$. The magnitude $I^{(\infty)}(r\mathbf{s}, \omega)$, in turn, can be determined by taking a four-dimensional Fourier transform $\tilde{W}^{(0)}(k\mathbf{s}_\perp, -k\mathbf{s}_\perp, \omega)$ of function $W^{(0)}(\mathbf{r}_1, \mathbf{r}_2, \omega)$ (see [3.11]), giving:

$$\begin{aligned} I^{(\infty)}(r\mathbf{s}, \omega) &= (2\pi k)^2 \cos^2\Theta \frac{1}{r^2} \tilde{W}^{(0)}(k\mathbf{s}_\perp, -k\mathbf{s}_\perp, \omega) \\ &= \left(\frac{k}{2\pi r^2}\right)^2 \cos^2\Theta \int_{-\infty}^{\infty} \int W^{(0)}(\mathbf{r}_1, \mathbf{r}_2, \omega) \exp[-i(k\mathbf{s}_\perp \cdot \mathbf{r_1} - k\mathbf{s}_\perp \cdot \mathbf{r_2})] d^2 r_1 d^2 r_2, \end{aligned} \tag{3.19}$$

where $\mathbf{s}_\perp = (s_x, s_y, 0)$ is the two-dimensional projection of a unit vector $\mathbf{s}$, pointing in the direction of energy flow at the angle Θ to the positive axis: $+\mathrm{z}$ (outer normal to the source). From Eqs. (3.18) and (3.19):

$$\begin{aligned} I_\omega(\mathbf{s}) &= (2\pi k)^2 \cos^2\Theta \tilde{W}^{(0)}(k\mathbf{s}_\perp, -k\mathbf{s}_\perp, \omega) \\ &= \left(\frac{k}{2\pi}\right)^2 \cos^2\Theta \int\limits_{-\infty}^{\infty} \int \mathrm{W}^{(0)}(\mathbf{r}_1, \mathbf{r}_2, \omega)\, \exp[-ik\mathbf{s}_\perp \cdot (\mathbf{r_1} - \mathbf{r_2})] d^2 r_1 d^2 r_2. \end{aligned} \tag{3.20}$$

By introducing the difference $\mathbf{r}' = \mathbf{r}_1 - \mathbf{r}_2$ and the average $\mathrm{r} = (\mathbf{r}_1 + \mathbf{r}_2)/2$ coordinates, one can express respective expressions for the radiant intensity and for the radiance, as well as for the radiant emittance of any partially coherent planar source in the following forms [3.6, 3.11]:

$$I_\omega(\mathbf{s}) = \left(\frac{k}{2\pi}\right)^2 \cos^2\Theta \int\limits_{-\infty}^{\infty} \int\limits_{-\infty}^{\infty} \mathrm{W}^{(0)}(\mathbf{r} + \mathbf{r}'/2, \mathbf{r} - \mathbf{r}'/2, \omega) \exp(-ik\mathbf{s}_\perp \cdot \mathbf{r}') d^2 r d^2 r'; \tag{3.21}$$

$$L_\omega(\mathbf{r}, \mathbf{s}) = \left(\frac{k}{2\pi}\right)^2 \cos\Theta \int\limits_{-\infty}^{\infty} \mathrm{W}^{(0)}(\mathbf{r} + \mathbf{r}'/2, \mathbf{r} - \mathbf{r}'/2, \omega)\, \exp(-ik\mathbf{s}_\perp \cdot \mathbf{r}') d^2 r'; \tag{3.22}$$

$$M_\omega(\mathbf{r}) = \left(\frac{k}{2\pi}\right)^2 \int\limits_{-\infty}^{\infty} \int\limits_{(2\pi)} \mathrm{W}^{(0)}(\mathbf{r} + \mathbf{r}'/2, \mathbf{r} - \mathbf{r}'/2, \omega) \exp(-ik\mathbf{s}_\perp \cdot \mathbf{r}') \cos^2\Theta \mathrm{d}^2 r' d\Omega. \tag{3.23}$$

Equations (3.21)–(3.23) characterize the interdependence of the angular, surface-angular, and surface densities of optical radiation on the cross-spectral density function $\mathrm{W}^{(0)}$ of the isotropic planar source for any arbitrary state of coherence. These relations make the principal consonance among observable radiometric parameters and the spatial spectrum of a random electromagnetic field. They also presume mutual correlation among radiometric parameters $\mathrm{M}_\omega(\mathbf{r})$ and $\mathrm{I}_\omega(\mathbf{s})$ and spectral radiance function $L_\omega(\mathbf{r}, \mathbf{s})$ designated by Eq. (3.22), which all are to obey radiometric relationships:

$$I_\omega(\mathbf{s}) = \cos\Theta \int\limits_A L_\omega(\mathbf{r}, \mathbf{s}) dA, \tag{3.24}$$

$$M_\omega(\mathbf{s}) = \int\limits_{(2\pi)} L_\omega(\mathbf{r}, \mathbf{s}) \cos\Theta d\Omega, \tag{3.25}$$

with such generalized radiance $L_\omega(\mathbf{r}, \mathbf{s})$ satisfying the subsequent transfer equation (see Chap. 1):

$$d[L_\omega(\mathbf{r},\mathbf{s})]/ds = 0. \tag{3.26}$$

In conjunction with the conventional concept reviewed in Chaps. 1 and 2, Eq. (3.26) confirms the generalized radiance L_ω in a material light beam remains unchanged and the energy of the optical field in free space propagates along straight lines. At the same time, the generalized spectral radiance L_ω and emittance M_ω defined by Eqs. (3.22) and (3.23) can intermittently have negative values. It also does not follow from any of the expressions above that spectral radiance L_ω given by Eq. (3.22) actually satisfies Eq. (3.26). Moreover, equivalent expressions for L_ω exist, which when substituted in Eq. (3.24) for intensity I_ω and then integrated over the equivalent plane of a given partially coherent source, give the correct formula for the angular density of its spectral flux as a function of direction. That is the consequence of the mutual Fourier conjugation for vectors **r** and **s** on which any particular radiance depends simultaneously and of the applicability of the uncertainty principle in the attempt to determine a localized property of a random wave field [3.12]. Hence, the radiance as a measurement parameter could be unobservable itself and is defined more precisely at the expense of either a spatial or an angular position [3.13]. At the same time, the angular density $\mathrm{I}_\omega(\mathbf{s})$ determined for any source with an arbitrary state of coherence by means of Eq. (3.21) is always an observable parameter of the optical field. Thus, the spectral radiant intensity $\mathrm{I}_\omega(\mathbf{s})$ of light emitted by a partially coherent source in the far-field zone from its equivalent projection plane $\mathrm{z} = 0$ can be considered as the main radiant parameter at frequency ω for any arbitrary direction **s**.

3.1.2 *Planar Sources of Incoherent and Coherent Light*

Following Eq. (3.11), the cross-spectral density function of a spatially incoherent source in the equivalent plane of emission is the product of the two-dimensional delta function and the spectral distribution $I^{(0)}$ of radiant intensity in the plane [3.4]:

$$W^{(0)}(\mathbf{r}_1,\mathbf{r}_2,\omega) = I^{(0)}(\mathbf{r},\omega)\delta(\mathbf{r}_1-\mathbf{r}_2), \tag{3.27}$$

Since the delta function is zero everywhere outside point $\mathrm{P}(\mathrm{r}_1 = \mathrm{r}_2)$, where its magnitude becomes infinite, the intensity $I^{(0)}(\mathbf{r},\omega)$ is also zero everywhere outside the plane of emission. Therefore, the substitution of expression (3.27) into Eqs. (3.21)–(3.23) gives [3.14]:

$$L_\omega(\mathbf{r},\mathbf{s}) = \left(\frac{k}{2\pi}\right)^2 \cos\Theta I^{(0)}(\mathbf{r},\omega), \tag{3.28}$$

$$M_\omega(\mathbf{r}) = \frac{k^2}{6\pi} I^{(0)}(\mathbf{r},\omega), \tag{3.29}$$

$$I_\omega(\mathbf{s}) = \left(\frac{k}{2\pi}\right)^2 \cos^2\Theta \int_A I^{(0)}(\mathbf{r},\omega)dA. \tag{3.30}$$

Equations (3.28)–(3.30) indicate that as well as conventional radiometric quantities, the radiance, radiant emittance, and radiant intensity of a spatially incoherent isotropic planar source, defined on the basis of a statistical wave approach, take positive values in semispace $z > 0$ and disappear concurrently in the emission plane with the coordinate $z = 0$, as they should in accordance with the inverse-square law at $\ell \to 0$. Nevertheless, there is a considerable distinction of the predicted spatial distribution for the source of equal-to-zero complex degree of coherence since:

$$I_\omega(\mathbf{s})|_{\mu=0} = I_{\omega,0}\ \cos^2\Theta, \tag{3.31}$$

Here $I_{\omega,0}$ is the radiant intensity along direction $\Theta = 0°$. Consequently, a source of uniform radiance and of uniform radiant intensity, distributed by the cosine law $I = I_0 \cos\Theta$, has some unequal-to-zero complex degree of coherence. Hence, oscillation fluctuations in the field of the radiation correlate inside a spatial domain approaching a length of the order of the average radiation wavelength λ.

In the limit of fully coherent light source with equal-to-unity complex degree of coherence $\mu^{(0)}$, Eq. (3.11) for the cross-spectral density function of that source can be rewritten as [3.12]:

$$W^{(0)}(\mathbf{r_1},\mathbf{r_2},\omega) = U^{(0)}(\mathbf{r}_1,\omega)U^{(0)*}(\mathbf{r_2},\omega). \tag{3.32}$$

Here $U^{(0)}(\mathbf{r}_1,\omega)$ is the scalar potential of the optical field across the plane vanishing in semispace $z > 0$ and beyond the limits of source area A. For a cophasal planar source with the Gaussian intensity distribution $I^{(0)}(\mathbf{r}_1,\omega) = I_0\exp[-r^2/(2r_0^2)]$, the field pattern in plane $z = 0$ is also a Gaussian function:

$$U^{(0)}(\mathbf{r}_1,\omega) = \sqrt{I_0}\ \exp[-r^2/(4{r_0}^2)], \tag{3.33}$$

where I_0 is the radiant intensity along the axis of the beam and r_0 is the distance at which intensity I_0 decreases $\sqrt{e}$ times. From Eqs. (3.21) and (3.22), taking into account ${\mathbf{s}_\perp}^2 = \sin^2\Theta$, one obtains:

$$\begin{aligned} L_\omega(\mathbf{r},\mathbf{s}) &= \frac{2}{\pi}(kr_0)^2 I^{(0)}(\mathbf{r},\mathbf{s})\cos\Theta\exp[-2(kr_0)^2]\sin^2\Theta \\ &= L_{w,0}(\mathbf{r})\cos\Theta\ \exp[-2(kr_0)^2]\sin^2\Theta, \end{aligned} \tag{3.34}$$

$$\begin{aligned} I_\omega(\mathbf{s}) &= (2kr_0)^2 I_0\cos^2\Theta\ \exp[-2(kr_0)^2]\sin^2\Theta \\ &= I_{w,0}(\mathbf{r})\cos^2\Theta\ \exp[-2(kr_0)^2]\sin^2\Theta. \end{aligned} \tag{3.35}$$

Figure 3.1 shows modeled angular distributions of radiant intensity (angular density) and radiance (spatial-angular density) distinguished by the cosΘ factor for

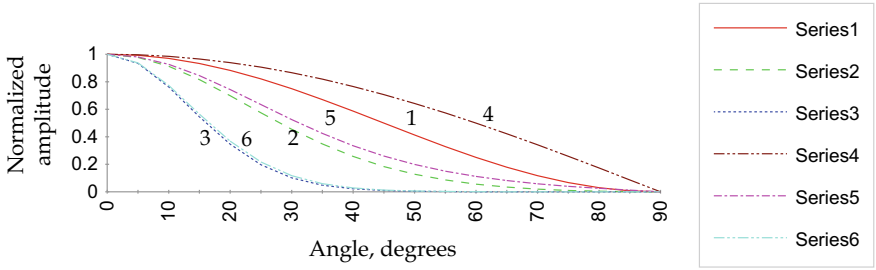

Fig. 3.1 Angular distributions of the normalized radiant intensity (1–3) and the normalized radiance (4–6) of a fully coherent laser source at kr = 0 = cosΘ(1, 4), kr = 1 (2, 5) and kr = 2 (3, 6)

fully coherent and cophasal planar sources while operating in the lowest transverse mode with the Gaussian dependence of optical intensity. Since in the optical range $kr_0 \gg 1$, such as at $\lambda = 632.8$ nm and $r_0 = 1$ nm, the product $kr_0 = 9.9 \cdot 10^4$ and the radiation intensity is reduced from that in the forward direction by the factor e^{-2} already at $\theta = 1.01 \cdot 10^{-4}$ [3.12].

3.1.3 *Quasi-Homogeneous Partially Coherent Planar Sources*

Let us presume the linear dimensions of source studied are much larger than the wavelength λ of radiation, and the spatial distribution of the radiant intensity in plane $z = 0$ is defined by the function $I^{(0)} = I^{(0)}(\mathbf{r})$ changing much more slowly than its complex degree of spectral coherence $\mu^{(0)} = \mu^{(0)}(\mathbf{r})$. Suppose μ is different from zero only in a small region $\mathbf{r}'$ in comparison with the source dimensions, then the cross-spectral density function W, according to Eq. (3.16), can be given as the radiant intensity along average coordinate $\mathbf{r} = (\mathbf{r_1} + \mathbf{r_2})/2$ multiplied by the complex degree of spectral coherence μ, which only depends on $\mathbf{r}' = (\mathbf{r_1} - \mathbf{r_2})/2$:

$$W^{(0)}(\mathbf{r_1}, \mathbf{r_2}, \omega) = I^{(0)}(\mathbf{r}, \omega)\mu^{(0)}(\mathbf{r}', \omega). \tag{3.36}$$

A corresponding substitution from Eq. (3.36) into expressions (3.21)–(3.23) leads to [3.14]:

$$I_\omega(\mathbf{s}) = k^2 \cos^2 \Theta \tilde{I}^{(0)}(0, \omega) \int_{-\infty}^{\infty} \mu^{(0)}(\mathbf{r}', \omega)\, \exp(-ik\mathbf{s}_\perp \cdot \mathbf{r}')d^2r'; \tag{3.37}$$

$$L_\omega(\mathbf{r}, \mathbf{s}) = \left(\frac{k}{2\pi}\right)^2 \cos\Theta I^{(0)}(\mathbf{r}, \omega) \int_{-\infty}^{\infty} \mu^{(0)}(\mathbf{r}', \omega)\, \exp(-ik\mathbf{s}_\perp \cdot \mathbf{r}')d^2r'; \tag{3.38}$$

$$M_\omega(\mathbf{r}) = \left(\frac{k}{2\pi}\right)^2 I^{(0)}(\mathbf{r}, \omega) \int_{-\infty}^{\infty} \int_{(2\pi)} \mu^{(0)}(\mathbf{r}', \omega) \exp(-ik\mathbf{s}_\perp \cdot \mathbf{r}') \cos^2 \Theta d^2r' d\Omega, \tag{3.39}$$

where $\tilde{I}^{(0)}(0,\omega)$ is the two-dimensional spatial Fourier spectrum of intensity $I^{(0)}(\mathbf{f},\omega)$ at $\mathbf{f}=0$:

$$\tilde{I}^{(0)}(\mathbf{f},\omega)=\frac{1}{(2\pi)^2}\int\limits_{-\infty}^{\infty} I^{(0)}(\mathbf{r},\omega)\,\exp(-i\mathbf{f}\cdot\mathbf{r})d^2r. \tag{3.40}$$

Since $\mu^{(0)}(\mathbf{r},\boldsymbol{\omega})>0$ inside region $\mathbf{r}'$, the radiance of a quasi-homogeneous partially coherent planar source, viewed from the phenomenological radiometric standpoint, remains positive over the entire semispace $z>0$. At the same time [3.12], the source radiance $L_\omega(\mathbf{r},\mathbf{s})$ expressed by Eq. (3.38) remains unchanged along any direction $\mathbf{s}$ over a distance ℓ defined by the limit:

$$\ell \ll \left(2\cos^4\Theta/\sin\Theta\right)\left(k/|\mathbf{f}|_{\max}\right)^3\lambda, \tag{3.41}$$

where Θ is the angle between the propagation direction $\mathbf{s}$ and the positive $\mathbf{z}$ axis, and $|\mathbf{f}|_{\max}$ is the maximum spatial frequency for the intensity distribution of radiation emitted by the source and identified by Eq. (3.40). By definition, changes of $I^{(0)}(\mathbf{r},\boldsymbol{\omega})$ at any distance on the order of a given light wavelength are not large and the $k/|\mathbf{f}|_{\max}$ ratio is much greater than unity. Thus, radiance constancy remains within relatively broad distances compared with wavelength λ defined for the ergodic optical field. Therefore, inequality (3.41) identifies the limits for the main Eq. (3.26) of radiant transfer and for the primary radiometric invariant derived from phenomenological considerations.

The radiant emittance of a quasi-homogeneous source due to Eq. (3.39), according to its radiometric meaning as the ratio of its flux to the source area while the source is seen as a material point, may be viewed via the distribution of the angular density multiplied by factor C_ω [3.15]:

$$M_\omega(\mathbf{r})=\Phi_\omega I^{(0)}(\mathbf{r},\omega)/\int\limits_{-\infty}^{\infty} I^{(0)}(\mathbf{r},\omega)\;d^2r=I^{(0)}(\mathbf{r},\omega)C_\omega. \tag{3.42}$$

Thus, C_ω defines the propagation efficiency of radiation emission by the source at frequency ω:

$$C_\omega=\left(\frac{k}{2\pi}\right)^2\int\limits_{-\infty}^{\infty}\int\limits_{(2\pi)}\mu^{(0)}(\mathbf{r}',\omega)\exp(-ik\mathbf{s}_\perp\cdot\mathbf{r}')\cos^2\Theta d^2r'd\Omega, \tag{3.43}$$

where Φ_ω is the total flux emitted by the source at the contributing frequency. Therefore, the radiant emittance $M_\omega(\mathbf{r})$ of any quasi-homogeneous planar source is given by the complex degree of its spectral coherence $\mu^{(0)}(\mathbf{r}',\omega)$. Owing to the restriction $0\le\left|\mu^{(0)}(\mathbf{r}',\omega)\right|\le 1$, the emittance of a quasi-homogeneous planar source can never exceed the magnitude of $I^{(0)}(\mathbf{r},\omega)$ in the source plane.

If radiation of a quasi-homogeneous source is correlated in such a way that the complex degree of its spatial coherence μ, distributed in the source plane, is a Gaussian function, represented as:

$$\mu^{(0)}(\mathbf{r}', \omega) = \exp[-\mathbf{r}'^2/(2r_\mu{}^2)], \tag{3.44}$$

major radiometric quantities can be expressed in a more traditional way. The spectral radiance of a quasi-homogeneous Gaussian planar source may be represented by the following equation [3.15]:

$$\begin{aligned} L_\omega(\mathbf{r}, \mathbf{s}) &= \left(\frac{kr_\mu}{2\pi}\right)^2 I^{(0)}(\mathbf{r}, \omega) \cos\Theta \exp\left[-\frac{(kr_\mu)^2}{2}\sin^2\Theta\right] \\ &= L_{\omega,0} \cos\Theta \exp\left[-\frac{(kr_\mu)^2}{2}\sin^2\Theta\right], \end{aligned} \tag{3.45}$$

with its radiant intensity I at frequency ω in direction **s** being consequently identified as:

$$\begin{aligned} I_\omega(\mathbf{s}) &= 2\pi(kr_\mu)^2 \tilde{I}^{(0)}(0, \omega) \cos^2\Theta \exp[-0.5(kr_\mu)^2 \sin^2\Theta] \\ &= I_{\omega,0} \cos^2\Theta \exp[-0.5(kr_\mu)^2 \sin^2\Theta]. \end{aligned} \tag{3.46}$$

Here r_μ is the effective radius of coherence. From Fig. 3.2, it is seen that the larger is the product kr_μ defining the source effective coherence area, the more directional this radiation propagation becomes. In another limiting case, $kr_\mu \to 0$, the radiance of a Gaussian-correlated quasi-homogeneous source at tending-to-zero coherence area changes as cosΘ for radiant intensity changing as $\cos^2\Theta$. Similarly, if the magnitude of $\mu^{(0)}(\mathbf{r}', \omega)$ increases, the propagation efficiency of Gaussian-correlated light emitted by such a source also increases with coherence area $kr_\mu \to \infty$ and its divergence tends to zero.

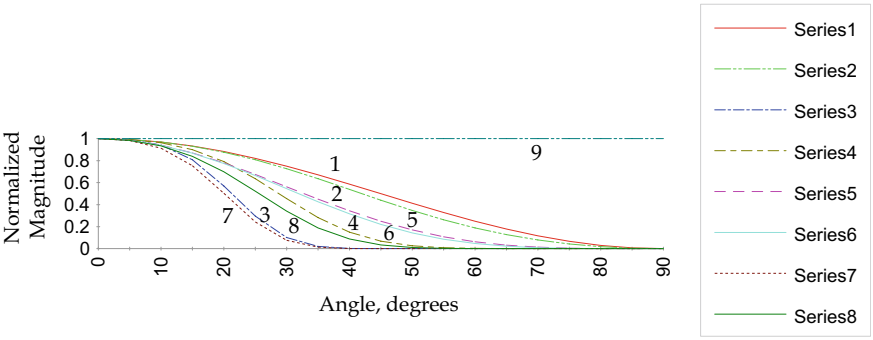

Fig. 3.2 Angular distributions of the normalized radiance (1–4) and the normalized radiant intensity (5–8) of a Gaussian correlated homogeneous source as a function of the coherence area equal to: 0 - (1, 5), 1 - (2, 6), 2 - (4, 8), 8 - (3, 7); lambertian - (9)

For a blackbody source maintained at thermal equilibrium, its radiant intensity $I_{\omega,0}$ from the effective emitting plane of coordinate z = 0 does not change when viewed via an exit aperture of negligibly small area A. The blackbody complex degree of spectral coherence becomes [3.14]:

$$\mu^{(0)}(\mathbf{r}', \omega) = \frac{\sin kr'}{kr'}, \tag{3.47}$$

where $r' = |\mathbf{r}'|$. Equations (3.37) and (3.38) make it evident that the blackbody radiance emitted by a small open aperture A, notably larger than the observed wavelengths of its radiation, remains unchanged:

$$L_\omega(\mathbf{r}, \mathbf{s}) = \frac{1}{2\pi} I_{\omega,0} = \frac{M_{\omega,0}}{\pi}. \tag{3.48}$$

Here (see Eq. (3.42)):

$$M_{\omega,0} = I_{\omega,0} C\omega = I_{\omega,0}/2, \tag{3.49}$$

is the effective radiant emittance of the blackbody source given by the product of its propagation efficiency and the angular-density distribution function across the source, defining the light intensity. The blackbody radiant intensity changes in proportion to the cosine of the observation angle:

$$I_\omega(\mathbf{s}) = \frac{A}{2\pi} I_{\omega,0} \cos\Theta = \frac{A \cdot M_{\omega,0}}{\pi} \cos\Theta. \tag{3.50}$$

Equation (3.49) indicates that the propagation efficiency of radiation in free space at thermal equilibrium is $C_\omega = 0.5$. The second equalities in Eqs. (3.48) and (3.50) coincide with fundamental radiometric dependencies derived from phenomenological considerations in Chap. 1 and confirm the imperative agreement between the phenomenological and statistical observation. This is especially significant in view of Eq. (3.47), implying that even a uniform Lambertian source of radiation is not fully spatially incoherent and the field of optical radiation correlates over a minute but finite distance compatible with the radiation wavelength [3.11].

3.1.4 *Propagation of Coherence and Observation of Polychromatic Radiation*

Further overcoming the limitations of the generalized radiance function $L_\omega(\mathbf{r}, \mathbf{s})$, introduced via Eq. (3.22), that does not necessarily follow the properties of radiometric radiance L by Eq. (1.31), the short-wavelength-limit models for generalized radiometry of light transfer define the quasi-homogeneous sources of nonstationary polychromatic optical radiation [3.16–3.25]. For any planar quasi-homogeneous secondary source of radiation, the fluctuations of which may be

represented via the statistically stationary ensemble $\{\mathrm{U}(\mathbf{r}, \nu)\exp(-2\pi i\nu t)\}$ of monochromatic oscillations, the cross-spectral density function $\mathrm{W}(\mathbf{r}_1, \mathbf{r}_2, \nu)$ at frequency ν for points p_1 and p_2 of radius vectors $\mathbf{r}_1$ and $\mathbf{r}_2$ to the center of the source, taking a finite part of the source plane $z = 0$, can be expressed in the space–frequency domain [3.13] as:

$$W(\mathbf{r}_1, \mathbf{r}_2, \nu) = \langle U^*(\mathbf{r}_1, \nu)U(\mathbf{r}_2, \nu)\rangle. \tag{3.51}$$

If each realization is expressed via the angular spectrum of plane waves, in half-space $z \geq 0$ [3.17]:

$$W(\mathbf{r}_1, \mathbf{r}_2, \nu) = \int\limits_{-\infty}^{\infty} \int \mathrm{A}(\mathbf{s}_1, \mathbf{s}_2, \nu)\exp[ik(\mathbf{s}_2 \cdot \mathbf{r}_2 - \mathbf{s}_1 \cdot \mathbf{r}_1)]d^2\mathbf{s}_{1\perp}d^2\mathbf{s}_{2\perp}, \tag{3.52}$$

where $\mathrm{A}(\mathbf{s}_{1\perp}, \mathbf{s}_{2\perp}, \nu) = \langle a^*(\mathbf{s}_1, \nu)a(\mathbf{s}_2, \nu)\rangle$ is the angular correlation function for two-dimensional projections $\mathbf{s}_{1\perp}$ and $\mathbf{s}_{2\perp}$ onto the z plane, then by designating sum and difference vectors $\mathbf{s} = (\mathbf{s}_1 + \mathbf{s}_2)/2$ and $\mathbf{s}' = (\mathbf{s}_1 - \mathbf{s}_2)$, having $\mathbf{s}_1 = \mathbf{s} - \mathbf{s}'/2$ and $s_2 = s + s'/2$, while counting contributions from homogeneous but not evanescent waves, rapidly decaying away from plane $z = 0$, Eq. (3.52) becomes [3.17]:

$$\begin{aligned} W(\mathbf{r}_1, \mathbf{r}_2, \nu) = &\int\limits_{-\infty}^{\infty} d^2s'_{\perp} \int d^2s_{\perp}\mathrm{A}(\mathbf{s}_{\perp} - \mathbf{s}'_{\perp}/2, \mathbf{s}_{\perp} + \mathbf{s}'_{\perp}/2, \nu) \\ &\times \exp\{ik[\mathbf{s} \cdot (\mathbf{r}_2 - \mathbf{r}_1) + \mathbf{s}' \cdot (\mathbf{r}_2 + \mathbf{r}_1)/2]\}. \end{aligned} \tag{3.53}$$

The omission of evanescent waves allows one to keep the integration in Eq. (3.52) within domains $\mathbf{s}_{1\perp} \leq 1.0$ and $\mathbf{s}_{2\perp} \leq 1.0$, and to introduce for this approximation a generalized radiance L_ν:

$$L_\nu(\mathbf{r}, \mathbf{s}) = s_z \int\limits_{s_\perp^2 \leq 4} \mathrm{A}(\mathbf{s}_{\perp} - \mathbf{s}'_{\perp}/2, \mathbf{s}_{\perp} + \mathbf{s}'_{\perp}/2, \nu)\ \exp(iks' \cdot \mathbf{r})d^2s'_{\perp}, \tag{3.54}$$

which for sufficiently short wavelengths, making $k = 2\pi/\lambda \to \infty$ [3.17], acquires the properties of the radiometric radiance identified by Eq. (1.31). For $z > 1.0$ the cross-spectral density is:

$$W(\mathbf{r}_1, \mathbf{r}_2, \nu) = \int\limits_{(2\pi)} B_\nu[(\mathbf{r}_1 + \mathbf{r}_2)/2, \mathbf{s}]\ \exp[ik\mathbf{s} \cdot (\mathbf{r}_2 - \mathbf{r}_1)]d\Omega, \tag{3.55}$$

where $d\Omega = ds_x ds_y/ds_z$ is the element of solid angle for unit vector $\mathbf{s}$ pointing to half space $z > 0$.

Most previous considerations of generalized radiometry were given for monochromatic and stationary optical fields. Other definitions for the generalized

radiance can be invoked for polychromatic and nonstationary fields [3.19]. In a stationary field, the correlation of amplitudes for two time–space field points are defined by the mutual coherence function $\Gamma(\mathbf{r}_1, t_1; \mathbf{r}_2, t_2)$ related to cross-spectral density function $W(\mathbf{r}_1, \mathbf{r}_2, \omega)$ at frequency ω via a temporal Fourier transform [3.18]:

$$\Gamma(\mathbf{r}_1, \mathbf{r}_1, \tau) = \int_0^{+\infty} d\omega \, \exp(-i\omega\tau) W(\mathbf{r}_1, \mathbf{r}_1, \omega), \tag{3.56}$$

where $\tau = t_1 - t_2$ is the time difference between selected field points p_1 and p_2, which in this case are not necessarily located in one plane, and for which the cross-spectral density function can be represented by a complex scalar function $U_\omega(\mathbf{r})$ of the field, while omitting evanescent waves:

$$W(\mathbf{r} - \mathbf{p}/2, \mathbf{r} + \mathbf{p}/2, \omega) = \left\langle U_\omega^*(\mathbf{r} - \mathbf{p}/2) U_\omega(\mathbf{r} + \mathbf{p}/2) \right\rangle, \tag{3.57}$$

where $\mathbf{r}$ and $\mathbf{p}$ are the mean-position and separation vectors for the given arbitrary points p_1 and p_2. For the considered approximation of a stationary and quasi-homogeneous field, the complex generalized radiance function $L_c(\mathbf{r}, \mathbf{s}, \omega)$ for the polychromatic field can be defined via the mutual coherence function $\Gamma(\mathbf{r} - \mathbf{p}/2, \mathbf{r} + \mathbf{p}/2, \tau)$ for field points $\mathbf{r} - \mathbf{p}/2$ and $\mathbf{r} + \mathbf{p}/2$ positioned symmetrically to mean point $\mathbf{r}$ as [3.20]:

$$L_c(\mathbf{r}, \mathbf{s}, \omega) = \frac{k^2}{(2\pi)^3 c} \int d^3p [-i(\mathbf{k} \cdot \mathbf{p} - \omega\tau)] \Gamma(\mathbf{r} - \mathbf{p}/2, \mathbf{r} + \mathbf{p}/2, \tau), \tag{3.58}$$

giving the Fourier-transform pair for mutual coherence $\Gamma(\mathbf{r} - \mathbf{p}/2, \mathbf{r} + \mathbf{p}/2, \tau)$ and complex generalized radiance $L_c(\mathbf{r}, \mathbf{s}, \omega)$ functions:

$$\Gamma(\mathbf{r} - \mathbf{p}/2, \mathbf{r} + \mathbf{p}/2, \tau) = c \int \frac{d^3k}{k^2} \exp[i(\mathbf{k} \cdot \mathbf{p} - \omega\tau)] L_c(\mathbf{r}, \mathbf{s}, \omega). \tag{3.59}$$

The mutual intensity function $I(\mathbf{r}, \mathbf{r}, 0)$ is obtained via mutual coherence $\Gamma(\mathbf{r} - \mathbf{p}/2, \mathbf{r} + \mathbf{p}/2, 0)$ setting $\tau = 0$; here $\mathbf{k} = k\mathbf{s}$ is the wave-number vector. The complex generalized radiance $L_c(\mathbf{r}, \mathbf{s}, \omega)$ converts to the generalized radiance function $L_\omega(\mathbf{r}, \mathbf{s})$ by Eq. (3.22) via cross-spectral density function $W^{(z)}(\mathbf{r}_{1\perp}, \mathbf{r}_{2\perp}, \omega)$:

$$L_\omega(\mathbf{r}, \mathbf{s}, \omega) = s_z \left(\frac{k}{2\pi}\right)^2 \int d^2p_\perp \, \exp(-i\mathbf{k}_\perp \cdot \mathbf{p}_\perp) W^{(z)}(\mathbf{r}_\perp - \mathbf{p}_\perp/2, \mathbf{r}_\perp + \mathbf{p}_\perp/2, \omega), \tag{3.60}$$

and defines the cross-spectral density function of a quasi-homogeneous optical field [3.20, 3.19]:

$$W(\mathbf{r} - \mathbf{p}/2, \mathbf{r} + \mathbf{p}/2, \omega) = \int d\Omega(\mathbf{s}) \, \exp(i\mathbf{k} \cdot \mathbf{p}) L_c(\mathbf{r}, \mathbf{s}, \omega), \tag{3.61}$$

where $W^{(z)}(\mathbf{r}_{1\perp}, \mathbf{r}_{2\perp}, \omega)$ is the cross-spectral density function in a given projection plane z = const, and $d\Omega(\mathbf{s})$ is the element of solid angle into the direction of unit vector **s** at the mean position **r**. The mutual coherence function of the polychromatic field within given domain $\mathbf{r} \pm \mathbf{p}/2$ is [3.20]:

$$\Gamma(\mathbf{r}-\mathbf{p}/2, \mathbf{r}+\mathbf{p}/2, \tau) = \int_0^{+\infty} d\omega \exp(-i\omega\tau) W_c(\mathbf{r}-\mathbf{p}/2, \mathbf{r}+\mathbf{p}/2, \omega), \quad (3.62)$$

where $W_c(\mathbf{r}-\mathbf{p}/2, \mathbf{r}+\mathbf{p}/2, \omega)$, is the complex version of cross-spectral density function, leading the complex generalized radiance $L_c(\mathbf{r}, \mathbf{s}, \omega)$ to be seemingly valid regardless of the state of coherence [3.19]:

$$L_c(\mathbf{r}, \mathbf{s}, \omega) = \frac{k^2}{(2\pi)^3 c} \int d^3p[(-i\mathbf{k}\cdot\mathbf{p})]\Gamma(\mathbf{r}, \mathbf{r}+\mathbf{p}). \quad (3.63)$$

The necessity to invoke the complex radiance and cross-spectral density functions evolves from inequivalence of the averaged z-component of phase vector $k_z p_z$ for points k_1 and k_2 designated by vectors **r** and **r** + **p** of the polychromatic field to the arithmetic average, which becomes [3.20]:

$$\left(\frac{k_{z,1}+k_{z,2}}{2}\right)p_z = k_z p_z + \frac{p_z}{4k_z^3}\left[k_z^2 p_\perp^2 - (\mathbf{k}_\perp \cdot \mathbf{p}_\perp)^2\right] + \text{const} \cdot \left(p_\perp^4\right). \quad (3.64)$$

3.1.5 Summary

Coherence theory provides transitions to main radiometric parameters of optical radiation via the functions of cross-spectral density and complex degree of spectral coherence of the statistically stationary and quasi-homogeneous optical field. The inverse task, which defines the coherence properties of radiation by the observable distribution of its radiant or luminous intensity, remains imperative and valuable. The primary postulate for the identification of the state of radiation coherence is formulated as the van Cittert–Zernike theorem (see [1.1, 3.6] for details) and can be summarized by the following two statements: (1) the complex degree of spectral coherence, describing the correlation among fluctuations of the light field created by any quasi-homogeneous planar source, is identical to the normalized amplitude of the diffraction pattern, commencing in the field for the aperture of the same form and dimensions as the source; (2) the pattern resulting from interference at two given points of the wave field of the planar source is equivalent to the diffraction pattern on the aperture, which is equivalent to that of a planar source of the spherical wave with the intensity distribution as that of the source [1.1]. It can be also stated [3.2, 3.15] that within the accuracy of a geometrical phase factor the complex degree of spectral coherence of a beam of optical radiation in the far-field zone of any

quasi-homogeneous planar source is equal to the normalized Fourier transform of the distribution of optical, radiant or luminous, intensity across that source. The approaches and specific methods for reduction or elimination of the coherence effects produced in respective spatial and/or temporal distributions of optical radiation intensity from those predicted by the phenomenological radiometric approach are reviewed in paragraph 3.3, while diffraction effects in photometry and radiometry and spectral or color measurements are assessed in paragraph 3.4.

3.2 Laser and Pulsed Light

3.2.1 Propagation Extents of Laser Radiation

Two major properties of optical radiation generated by lasers—high directness and narrow spectral bandwidth—noticeably distinguish laser radiation from radiation spontaneously emitted by thermal sources. Both the high directness and the high spectral density of laser light are defined by distinguishable correlations among wave oscillations in the field of laser radiation owing to the high degree of spatial and temporal coherence. The directness of laser light sets a limit on the potential applicability of all previously considered approximations of geometrical optics and on the radiometric relationships for propagation of light emitted by point sources. The ability of laser radiation to execute spatial and temporal interference of high contrast restricts the additive rule of superposition for the overlapping light beams. To consider the outcome on radiometric laws and rules of measurement due to coherence of laser radiation, let us review specific properties of laser light, such as nonisotropic angular distribution of the radiation intensity and the great ability of laser light to generate interference patterns with unequal-to-zero contrast.

Consider an ideal laser as a fully spatially coherent and cophasal planar source (see Sect. 3.1 for terminology) with a Gaussian intensity distribution profile of radiation given by equation:

$$I^{(0)}(\mathbf{r}, \omega) = \mathrm{I}_0 \exp[-\mathrm{r}^2/(\mathrm{r}_0^2)]. \tag{3.65}$$

The emittance M of such laser radiation can be obtained from Eqs. (3.23), (3.42) and (3.43) [3.8]:

$$M_\omega(\mathbf{r}) = \left[1 - \frac{F(a)}{a}\right] I^{(0)}(\mathbf{r}, \omega), \tag{3.66}$$

where $a = \sqrt{2}(kr_0)$ (see Fig. 3.1), and F(a) is the Dawson integral [3.8, 3.12, 3.26]:

$$F(a) = \exp(-a^2) \int_0^a \exp(x^2) dx. \tag{3.67}$$

Defining $\Phi_\Sigma = \int_{-\infty}^{\infty} I^{(0)}(\mathbf{r}, \omega) d^2 r$, the propagation efficiency $C_\omega = \Phi_\omega / \Phi_\Sigma$ of such coherent light is [3.8]:

$$C_\omega = 1 - \frac{F\left(\sqrt{2}(kr_0)\right)}{\sqrt{2}(kr_0)}. \tag{3.68}$$

If $kr_0 \to \infty$, efficiency $C_\omega \to 1.0$, and the wave front of radiation from this cophasal and coherent source is that of the infinite plane wave that for negligible diffraction produces one freely propagating light ray, and the efficiency diagram of such radiation is a straight line (see Fig. 3.3).

Equations (3.34), (3.35), and (3.42) define that for a cophasal and fully coherent laser of $C_\omega = 1$ with observation direction $\Theta = 0°$, the main radiometric parameters of laser light transform to:

$$I_\omega(\mathbf{s}) \to I_{\omega,0}(\mathbf{r}); \quad L_\omega(\mathbf{r}, \mathbf{s}) \to L_{\omega,0}(\mathbf{r}); \quad M_\omega(\mathbf{r}) \to I^{(0)}(\mathbf{r}, \omega). \tag{3.69}$$

In all other directions $\Theta \neq 0°$, both I_ω and L_ω, which are dependent on $\mathbf{s}$, become zero. A much less coherent laser light is emitted by a Gaussian-correlated quasi-homogeneous source with its complex degree of spatial coherence given by expression (3.44). By substitution of Eq. (3.44) into Eq. (3.43), the propagation efficiency for a Gaussian-correlated source can be expressed as [3.15]:

$$C_\omega = 1 - \frac{F\left((kr_\mu)/\sqrt{2}\right)}{kr_\mu/\sqrt{2}}. \tag{3.70}$$

Comparison of Eqs. (3.68) and (3.70) for the propagation efficiency demonstrates that at the limit $kr_0 \to \infty$, the highest degree of coherence causes the maximum propagation efficiency (Fig. 3.3).

In practical terms, in the regular optical spectral domain the product kr_μ can be large, but not extremely large; therefore, the complex degree of spatial or temporal coherence and the propagation efficiency of laser radiation defined by kr_μ all asymptotically tend to 1.0. Similarly, even the fundamental TEM_{00} mode of laser emission forms not an infinite but a limited plane wave having its divergence

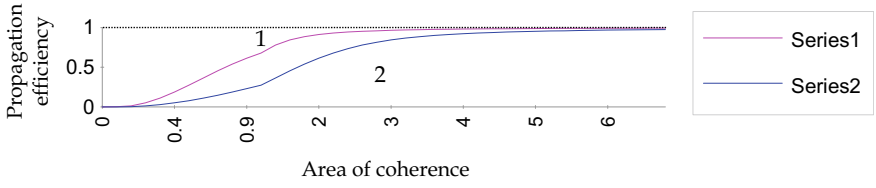

Fig. 3.3 Radiation efficiency versus effective area of coherence for quasi-homogeneous planar sources: 1 - fully coherent and cophasal laser with Gaussian intensity distribution; 2 - Gaussian correlated source

defined by diffraction on an output coupler of a respective laser resonator. In the approximation of the far-field zone, corresponding to Fraunhofer diffraction, which begins from distances on an order of magnitude larger than $\ell \cong r_0^2/2\lambda$ [3.27], the overall divergence of a laser radiation beam, defined by the half value of the radiation intensity along its optical axis, is $\Theta \cong \lambda/(2r_0)$. As a result, toward the far-field distances $\ell_F \gg \ell_0$, the cross section of a laser beam can be defined by its initial diameter $2r_0$ plus the diffraction-limited divergence:

$$D = 2r_0 + \frac{\ell_F \lambda}{2r_0}. \tag{3.71}$$

Equation (3.71) identifies conditions of the radiometric approach for representing a material beam of laser radiation. It is sufficient that at relatively long distances ℓ the first term in Eq. (3.71) can be disregarded. Then, the diameter of the beam is $D \cong (\ell_F \lambda)/2r_0$. Consequently, such a laser beam can be considered as having emerged from a single point P′ (see Fig. 3.4), and from that perspective the laser emission is to the far-field zone as of the effective point source. If at a distance ℓ_d in the far-field zone, a detector is completely irradiated by the defined laser beam, the longitudinal transformation of the detector's position will change its irradiance in square proportion to distance ℓ_d from the effective point source P′ identifying the far-field radiation. Thus, the irradiance changes at each point of this field of laser radiation, such as points 1 and 2, are given by the inverse-square law $E_2 = E_1 \ell_1^2/\ell_2^2$, as defined by radiometric and photometric phenomenological concepts for restricted conditions of these observations.

In every particular case, it is appropriate to chose a criterion to satisfy the requirement of the far-field zone: $\ell_F \gg \ell_0$. The suitable far-field conditions can be determined in each given situation, such as the particular type of laser resonator, certain projective optics, and the surrounding medium. Therefore, the applicability of the inverse-square law for laser radiation (see Chaps. 1 and 2) requires one to establish distance limits for the appropriate far-field-zone approximation.

Within the near-field region for laser radiation: $\ell_N \ll \ell_0$, which corresponds to Fresnel diffraction with an irradiance level within a laser source beam that virtually does not depend on distance, measurements of the power or energy of such a laser beam become quite straightforward. Consider a physical detector whose cross section is wider than that of the laser beam which is placed in position D_0 within its

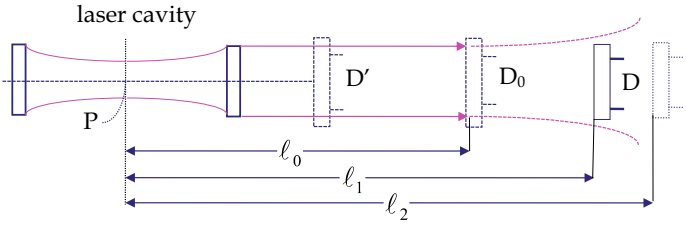

Fig. 3.4 Laser beam with Gaussian intensity distribution

near-field region defined by distance ℓ_0 in Fig. 3.4. When the detector sensitivity in absolute terms is known and is independent of beam position, the detector reading gives directly the absolute power or energy of the laser beam (see Chap. 4 for details). In particular, the lack of need to collimate laser radiation in a near-field zone considerably enhances the applicability of lasers and laser-based systems for measurements of optical properties of substances, bodies, and mediums.

3.2.2 *Applicability of Lasers for Various Optical Measurements*

The high monochromaticity and low divergence of laser radiation do not necessarily cause any unusual conditions for measurements to be made. Likely irregularities may only be caused by superposition of partially coherent laser beam components. If a free-propagation state for partially coherent laser light forming a material beam is broken by the presence of collimating optics, by bounds of separating mediums with diverse refractive indices, or by noticeable index discontinuities compared with laser light wavelengths, the interference patterns can change the rule of additive summing owing to superposition of light paths for interfering laser beam components. In every specific situation, deviations from radiometric additivity, appearing because of interference effects, are defined by the length and time of laser coherence, by particular spatial and temporal delays of interfering components, and by specific localizations of space and time regions in which the laser light observations are realized.

Since the notions of the length and time of coherence (Eqs. (3.1)–(3.17)) are set as conditioning factors over the totality of all interacting monochromatic vibrations f(ν) forming a laser beam F(t):

$$F(t) = \int_0^\infty f(\nu) \exp(-2\pi i \nu t) d\nu, \tag{3.72}$$

the larger is the number N of Fourier components passing at observation time T via a chosen spatial point, the more precisely the average intensity $\bar{I}$ of the beam is given by the additive sum [0.27, 1.1, 3.34]:

$$\bar{I} = \frac{N}{2T} \int_{-\infty}^{\infty} |f(\nu)|^2 d\nu. \tag{3.73}$$

The lower is the total number N of components, the more compressed the effective frequency domain of its Fourier spectrum $\Delta\omega \cong (2\pi)/(\Delta t)$ *or* $\Delta\nu = 1/(\Delta t)$ becomes, and the smaller is the number of randomly distributed components passing the observation point during any fixed time interval. Owing to that spectral compression, the additive rule of summing becomes less precise for this wave

group. The time and the space intervals Δt and $\Delta\ell$ of the wave group correlation, $\Delta\ell = c\Delta t$, define the time and the length of coherence and identify deviations from the additive-summation law.

At the same time, according to the law of conservation of energy, the total intensity of light components forming an interference pattern distributed in space or in time may not be different from the additive sum obtained in the absence of any interference. Therefore, an obvious way to prevent an influence of the interference on the result of the radiometric measurement is to obtain a respective space or time integral of all interfering radiation components on the sensitive surface of a physical detector. Such a notion means that when partially coherent light is measured, the additive rule of radiometric summation may be strictly observed if not enough resolution, spatial or temporal, for the measurement detector is utilized. The averaging and integrating in time and space domains considerably larger than the specific temporal and spatial dimensions of interference patterns occurring allows one to observe the averaged statistical ensemble of interfering intensities:

$$\langle E^2 \rangle = \langle E_i^2 \rangle + \left\langle E_j^2 \right\rangle. \tag{3.74}$$

Particular optical schematics for forming characteristic spatial interference patterns are well known and include plane-parallel plates as beam splitters, objectives, and interferometers (Fig. 3.5a). The origination of a temporal interference pattern distributed in time is seen in Fig. 3.5b. Laser light source 1 emits a quasi-monochromatic plane wave λ, shown as a parallel beam, in one example. Plane-parallel plate 2 of thickness ℓ with refractive index n is placed in the beam's near field in another example. Beam splitter 2 may be viewed as an effective Fizeau interferometer [1.1, 1.6] making two respective interference patterns, localized within the reflected and the transmitted beam paths. The phase shift δ_τ in the transmission pattern between two neighboring components for the infinite sequence of the light beams retroreflected within the plate becomes:

$$\delta_\tau = (4\pi/\lambda_0) n\ell \cos\varphi. \tag{3.75}$$

The consecutive phase shift δ_ρ for the respective pattern in radiation reflected from the splitter is:

$$\delta_\rho = \frac{4\pi\ell}{\lambda_0}\sqrt{1 - n^2 \sin^2\varphi} \pm \pi. \tag{3.76}$$

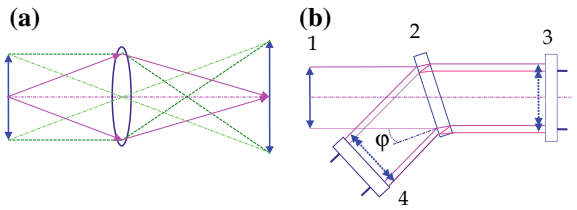

Fig. 3.5 Overlapping of light paths on superposition **a** and splitting **b** of beams

Here φ is the angle between the wave normal to splitter 2 and the optical axis of the laser beam. The interference patterns are additive to one another: the maximum in reflected light corresponds to the minimum in transmitted radiation and vice versa. The spatial patterns in the reflected and transmitted paths appear with displacement $d \cong 2\ell \sin\varphi$ (Eq. 1.100). Intensity detectors 3 and 4, set in the transmitted and reflected light paths, respectively, measure beam intensities I_τ and I_ρ transmitted by the splitter bulk and retroreflected between two splitter surfaces, then sequentially transmitted by the splitter and reflected from it. To summarize all reflected components, the effective apertures of both detectors must be larger than the cross sections of the beams. If the spatial resolution of detectors 3 and 4 does not allow one to distinguish any of these interference patterns, and if the sum of each retroreflected component intensity across every light path is registered, one will not see interference affecting the results of these measurements. Even if the source emits any number of monochromatic components in spectral interval $\Delta\lambda$, the radiometric observation may not be necessarily obscured. The spatial interference patterns become more complicated, but as long as the spatial and temporal patterns are not resolved by detectors, the sums remain unchanged.

Furthermore, the necessary steady-state condition for the measurement of spatial and temporal patterns is achieved only when the totality of all spectral components F(t) of a laser beam (Eq. 3.72) is not changed during a measurement cycle within observation time Δt. Equations (3.75) and (3.76) reveal that if a specific subset of light emitted by any given source is changed, the phases of retroreflected components compared with the phases of directly transmitted components or of other components reflected by two splitter surfaces may change. Moreover, these changes are additive in transmitted and reflected light. At diverse time instances t_i, combined spectral components λ_i in reflected and transmitted radiation have interference patterns with the supplementary to each other extrema, being functions of the $2\ell n \cos\varphi/\lambda_i$ ratio. Thus, the beam splitter conversion of spectral instabilities in laser emission into transmitted and reflected radiation enables observation of random spatial or temporal interference patterns.

A certain irregularity in the spectral composition of light emitted by every source of radiation and frequency fluctuations among its components is the fundamental characteristic of the emission process. The concept of partial coherence is defined by statistical correlations among fluctuations for the field of observable optical radiation. Particularly for any laser source, except a nonlinear regime at a high power density, the act of lasing is a Gaussian random process with an irregular structure, having the interval of correlations defined by the cavity intermode distance of the laser. The intensity distribution function $\tilde{I}(\nu)$ for any given independent single laser mode versus its averaged emission intensity $\langle \tilde{I}(\nu) \rangle$ at frequency ν can be expressed in the form [3.28, 3.29]:

$$f\left[\tilde{I}(\nu)\right] = \frac{1}{\langle \tilde{I}(\nu) \rangle} \exp\left[-\frac{\tilde{I}(\nu)}{\langle \tilde{I}(\nu) \rangle}\right], \tag{3.77}$$

and the spectrum of laser-radiation emission is defined by the statistics of its specific noise process.

When laser light interacts with an optical system, the existence of all mentioned fluctuations is manifested through various interference effects. For the plane-parallel beam splitter (Fig. 3.5b) formed as a transparent plate with surface reflectance ρ, the intensity I_τ of radiation transmitted via the plate is identified by the intensity I_0 of emission, its wavelength, and the splitter's optical thickness:

$$I_\tau = I_0 \frac{(1-\rho)^2}{(1-\rho)^2 + 4\rho \sin^2(\delta/2)}. \tag{3.78}$$

For low surface reflectance ρ of the splitter, the maximum beam intensity and the minimum beam intensity:

$$I_{\tau,\max} = I_0;\ I_{\tau,\min} = I_0 \left(\frac{1-\rho}{1+\rho}\right)^2, \tag{3.79}$$

do not significantly change from the mean intensity $\bar{I}_\tau$ of transmission in the absence of interference:

$$\bar{I}_\tau = I_0 \frac{1-\rho}{1+\rho}. \tag{3.80}$$

The opposite situation exists for the intensity of optical radiation reflected by the splitter:

$$I_\rho = I_0 \frac{4\rho \sin^2(\delta/2)}{(1-\rho)^2 + 4\rho \sin^2(\delta/2)}. \tag{3.81}$$

The maximum intensity in the multiple-beam interference pattern occurring in reflected light,

$$I_{\rho,\max} = I_0 \frac{4\rho}{(1+\rho)^2}, \tag{3.82}$$

exceeds the average intensity $\bar{I}_\rho$ of the reflected beam nearly twice (compare Eqs. (1.106), (1.107)):

$$\bar{I}_\rho = I_0[2\rho/(1+\rho)]. \tag{3.83}$$

At the same time, the intensity of the interference minimum for the reflected-light pattern becomes zero.

As a result, the relative intensity changes from the mean level to the maximum and the minimum are:

$$\delta I_\tau = \frac{\Delta I_\tau}{I_\tau} = \pm\left(1 - \frac{1-\rho}{1+\rho}\right) = \pm\frac{2\rho}{1+\rho} \underset{\rho \ll 1}{\cong} \pm 2\rho, \tag{3.84}$$

$$\delta I_\rho = \frac{\Delta I_\rho}{I_\rho} = \pm\left(\frac{2\rho}{1+\rho} - 1\right) = \pm\frac{1-\rho}{1+\rho} \underset{\rho \ll 1}{\cong} \pm(1-2\rho). \tag{3.85}$$

The practical probability of full intensity transfer of radiation from any λ_i maximum or minimum to another of λ_j, causing the opposite result of interference, is extremely small. Intensity fluctuations in actual experiments are much lower than those predicted by Eqs. (3.84) and (3.85) expecting interference extrema to be completely swapped. However, the change of the spectral distribution of light emission needed for a given extremum to be swapped is so trivial it can take place at will, especially for unstabilized laser sources. For example, for the splitter thickness $\ell = 2.5\,\text{mm}$, $n = 1.5$, $\varphi = 0^\circ$ and $\Delta\lambda = 1059 - 1061\ \text{nm}$ (Fig. 3.5b), changes of an emitting wavelength by every 0.11 nm determine the transfer from the minimum to the maximum of reflected-light interference.

Propagation of laser light can often be accompanied by multiple interactions with optical elements and mediums of propagation. This may be accompanied not only by spectral changes, but also by fluctuations of the light-propagation direction and of the divergence of the laser beams formed. Therefore, to provide accurate measurements using optical radiation emitted by lasers, one must either fully eliminate or integrate in space and time all spatial and temporal interference patterns, while achieving feasible stabilization of spectral, spatial, and temporal parameters of laser light.

3.2.3 Optical Radiation as a Pulse Train

Conventional radiometry and photometry always assume the radiant and luminous parameters of radiation can be represented and characterized as derivatives of a steady-state flux of light flowing within the entire time of observation. However, any material beam of optical radiation can almost never be actually considered as an infinitely long harmonic oscillation having a constant frequency and constant amplitude. Even the sum of two equivalent harmonic oscillations, having stable amplitudes, becomes an amplitude-modulated traveling wave:

$$E(t) = E\cos(\omega_1 t) + E\cos(\omega_2 t) = E_{\text{mod}}\cos(\bar{\omega} t), \tag{3.86}$$

where $E_{\text{mod}}(t) = 2E\cos(\omega_{\text{mod}} t)$, $\omega_{\text{mod}} = (\omega_1 - \omega_2)/2$, and $\bar{\omega} = (\omega_1 + \omega_2)/2$. Thus, when measuring a flow of quasi-continuous radiation emitted by a number of oscillators, one may consider the amplitude-modulated flux of radiation as the mean (averaged) power $\bar{\Phi}$ existing at observation time T:

$$\bar{\Phi} = \frac{1}{T}\int_0^T \Phi_i(t)dt, \tag{3.87}$$

where $\Phi_i(t)$ is the instantaneous radiant flux of quasi-continuous radiation at the i^{th} instant of time.

Let us consider a wave function Ψ(t) representing the superposition of a great number N of oscillations with equivalent amplitudes ψ(t) and initial phases $\varphi = 0$, where the oscillation frequencies ω_i are spread within frequency range $\Delta\omega = \omega_2 - \omega_1$. If single-wave oscillations are close enough to be approximated by one mean frequency $\bar{\omega} = (\omega_2 + \omega_1)/2$, the resulting oscillation represents a pulse existing only during a limited time interval: $\Delta t = 1/\Delta\omega$ [3.30]. The fact that the pulse exists clearly assumes that the pulse amplitude is not zero. The maximum potential amplitude $N \cdot \psi(t)$ of the pulse corresponds to the number N of fully synchronized oscillations in the superposition. If all oscillation phases are correlated, the time interval Δt of pulse existence is defined as $\Delta t\Delta\omega \cong 2\pi$ or $\Delta t\Delta\nu \cong 1$. The wave function Ψ(t) at interval Δt exceeds the zero level, which corresponds to isotropic distribution of independent harmonic oscillations within the 2π angular-frequency limit (see paragraph 3.1). If the phases of its components are not correlated, but just have some phase shift, the superposition, as the pulse being considered, does not reach its maximum and the time interval of the resulting pulse existence respectively increases. Consequently, in the case of a certain random harmonic phase distribution, leading to the product: $\Delta t\Delta\nu \gg 1$, the total duration of the effective pulse tends to infinity and its amplitude becomes equal to the statistical average of the component amplitudes of such a superposition. Therefore, the pulse ceases to become distinguishable, and the resulting function represents the quasi-continuous signal. Consequently, depending on the existing phase correlation among light components, the wave function of the quasi-continuous signal analyzed is equivalent to that of a certain sequence of pulses and can be represented as a set of standard pulses, the response to whose actions by a particular measurement system may already be known.

At an instance of time t, the response $\eta(t, \tau)$ of a measurement system to a unit pulse $p_i(t)$ is:

$$p_i(t) = 1[t - (i - 1/2)\Delta T] - 1[t - (i + 1/2)\Delta T], \tag{3.88}$$

being equal to 1 at $(i - 1/2)\Delta T \le t \le (i + 1/2)\Delta T$ and to zero at all other instances [3.30]. Thus, exposing the system to the pulse at time interval $\tau = (1 - 1/2)\Delta T$, the response can be expressed via operator P:

$$\eta[t, (i - 1/2)\Delta T] = P[p_i(t)]. \tag{3.89}$$

A linear system responding to input action $m[p_i(t)]$ makes a proportional reaction $mP[p_i(t)]$; thus:

$$P[p_i(t) + p_j(t)] = P[p_i(t)] + P[p_j(t)]. \tag{3.90}$$

As a result, the input action provided by any arbitrary function U(t) for a linear system can be approximated by the sequence U′(t) of N pulses expressed by means of these unit pulse impacts:

$$U'(t) = \sum_{i=-N}^{N} u(i\Delta T)\{1[t - (i - 1/2)\Delta T] - 1[t - (i + 1/2)\Delta T]\}. \tag{3.91}$$

Accordingly, the shorter time interval ΔT is, the better the function U(t) is approximated by the set of oscillations U′(t). As a result, the following response of the measurement system to the signal represented by such a sequence can be more appropriately expressed by means of reactions to unit pulses. Keeping in mind that the derivative of any step function is the Dirac delta function:

$$d1(t - \tau)/d\tau = -\delta(t - \tau), \tag{3.92}$$

at the $\Delta T \to 0$, $N \to \infty$ limit, one can replace the input action U(t) by a continuum of sequential pulses:

$$U(t) = \int_{-\infty}^{\infty} u(t)\delta(t - \tau)d\tau. \tag{3.93}$$

Thus, the system's response Y(t) to the input action can be represented by a convolution integral:

$$Y(t) = \int_{-\infty}^{\infty} u(t)h(t - \tau)d\tau. \tag{3.94}$$

Here $h(t - \tau)$ is the pulse response of the measurement system, which determines its reaction at time instant t to the delta pulse acting at moment τ. For a steady-state system, its pulse response depends only on the interval remaining after the action, and is not a function of the time instance at a start of the action. Following Eq. (3.92), pulse response h(t) represents the derivative of the transient function H(t), which itself determines the system's response to the action of a unit pulse:

$$H(t) = 1 - \exp(-t/\tau). \tag{3.95}$$

3.2.4 Measurements in Pulsed Radiation

The ability to quantitatively determine a radiometric, as well as a photometric, reaction of a specific optical system to either power or energy action of radiation arbitrary dispersed in time allows various measurements of radiation parameters and

extents to be performed. One can determine the reaction of such a radiometric system not only to an average flow of continuous radiation, but also to the energy W_Σ carried by radiation over a time interval T:

$$W_\Sigma = \int_0^T \Phi_i(t)dt, \tag{3.96}$$

or to the maximum power Φ_{max} in a single pulse, or to the power at an arbitrary instance of time t:

$$\Phi_{max} = \frac{dW}{dt}|_{d^2W/d^2t=0}. \tag{3.97}$$

The temporal response of the measurement system to a given power extent depends on relationships among the repetition time T of observing the pulse sequence, the duration τ of a single pulse, and the time constant τ_d of the system defined by the inverse magnitude of the equivalent transmission frequency band (see Fig. 3.6). At $\tau_d > \tau$, T, the entire energy of any recurrent pulse sequence is measured as that of a single long pulse. At $\tau_d < \tau$, T, the system's resolution allows one to distinguish the power parameters of a single pulse. Further possibilities for altering either power or energy extents in a sequence of light pulses are obvious and follow from Eqs. (3.96) and (3.97). At the same time, an increase of the duration of each pulse, for any specific but constant mean or average power and repetition rate, allows one to increase the energy of such a pulse; a decrease permits one to increase the maximum pulse power (see Fig. 3.6).

Typical temporal emission spectrums of prevalent light sources of pulsed radiation are not nearly such right-angled functions as in Fig. 3.6. Thus, straightforward estimations for averaged extents:

$$W = \Phi\Delta t;\ \Phi_{max} = W/(\Delta t), \tag{3.98}$$

are often used to approximate either the 0.35 or the 0.5 level of the maximum power of an actual pulse. A single pulse emitted by a pulsed lamp may be approximated by an asymmetric bell-shaped profile:

$$I(t) = I_{max}\ \exp[(t/t_{max})(1 - t/t_{max})]^b, \tag{3.99}$$

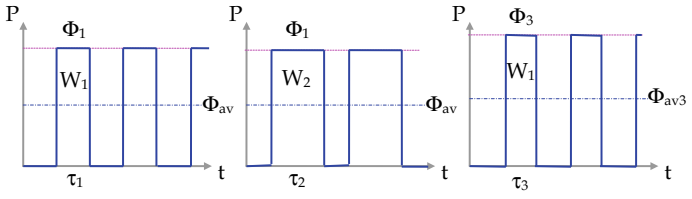

Fig. 3.6 Alteration of maximum and average power or pulse energy via parameters of the pulse

where I_{max} is the maximum pulse power, t_{max} is the time interval to reach the maximum, and b is the pulse-form approximation parameter dependent on the inductance of a discharging circuit (see Fig. 3.7a) [3.31]. Stimulated emission likely leads to creation of quasi-symmetrical pulses, but in some cases the intensity profile of the laser pulse may be similar to a symmetrical bell-shaped function [3.27]:

$$I = I_0 \exp[(\beta - \alpha)ct], \tag{3.100}$$

where α is the linear absorption coefficient in a generated spectral line and β is the linear gain factor for a small signal, which depends on a population inversion $\Delta N(t)$ changing at various stages of laser generation. A sequence of randomly distributed peaks in a laser pulse during one cycle of its stimulated emission can be examined in the following form [0.16, 3.32]:

$$I(t) = 0.5(1 - \cos\ \omega t)[1(t) - 1(t - 2\pi)]. \tag{3.101}$$

Figure 3.7b illustrates pump-light conversion to laser emission spikes and an integrated-output pulse.

Analogously to irradiance in continuous radiation, the surface energy density or fluence in pulsed light is the ratio of the energy W_τ of a pulse of duration τ falling or propagating in small-beam cross section containing a point P to area A of the section: dW_τ/dA. The angular-surface energy density of radiation in the beam of pulsed light is the radiance over the pulse duration τ:

$$\frac{d^2 W_\tau}{d^2 G} = \frac{d^2 W_\tau}{dA\ \cos\varphi d\Omega} = \frac{\tau \sum_\tau \Phi_i(t)}{dA\ \cos\varphi d\Omega}. \tag{3.102}$$

The mean surface density and mean radiance or luminance during the full pulse duration τ are:

$$\frac{d\Phi(t, A)}{dA} = \frac{1}{T} d\left[\int_0^T \Phi_i(t, A)dt\right]/dA, \tag{3.103}$$

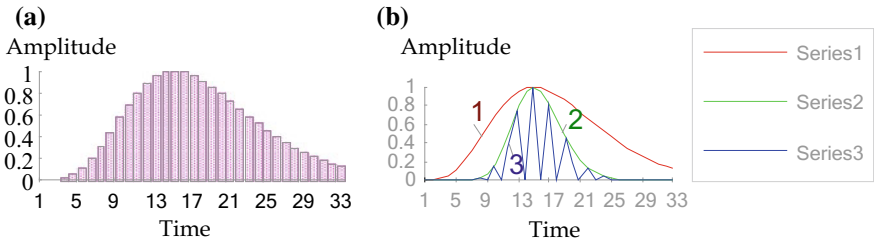

Fig. 3.7 Examples of pulse asymmetry: **a** asymmetric quisi-continuous pulse emitted by a pulsed lamp; **b** laser radiation pulses: pumping pulse (series 1), unsaturated stimulated-emission pulses (series 3), integrated output of pulsed laser-light emission (series 2)

$$\frac{d\Phi^2(t,A)}{dAd\Omega} = \frac{1}{T}d^2\left[\int_0^T \Phi_i(t,A,\Omega)dt\right]/(dAd\Omega). \tag{3.104}$$

The radiant exposure created by arbitrarily distributed in time pulsed or continuous radiation over time may be distinguished by the integral created by its irradiance over the time interval T:

$$H_e = \int_0^T E_{e,i}dt = \int_0^T [d\Phi_i(A)/dA]dt. \tag{3.105}$$

The integral radiant intensity may be similarly determined by the integral of radiation intensity:

$$\Xi_e = \int_0^T I_{e,i}dt = \int_0^A \int_0^T L_{e,i}(A,t)\cos\varphi dAdt. \tag{3.106}$$

A pulse of radiation of arbitrary shape X(t) can be defined by a generalized quantity X_{gen}:

$$X_{gen} = \frac{\int_\tau [X_r(t)]^2 dt}{\int_\tau X_r(t)dt}, \tag{3.107}$$

where $X_r(t)$ is the time distribution function of the respective rectangular pulse, the temporal action of which is equivalent to that of observing pulse X(t), for which the following relations are valid [3.33]:

$$\int_\tau X_r(t)dt = \int_\tau X(t)dt; \int_\tau [X_r(t)]^2 dt = \int_\tau [X(t)]^2 dt. \tag{3.108}$$

Comparison with that conceptually shaped pulse allows one to avoid uncertainties of referencing to a pulse of nonuniform power distribution, but requires one to concurrently measure the time dependence of the compared pulse parameters as the square power. These extra measurements necessitate using either a nonlinear optical or a nonlinear electrical element to obtain the known square-power dependence in a system.

The optical properties of mediums, substances, and bodies are inherent to the object, independently of in what kind of light—pulsed or continuous—such a property measurement is realized. However, the results of measurements in pulsed light, particularly in pulsed laser radiation, can be substantially different from those

in spontaneous continuous light owing to the considerable increase of the applied power. Depending on the portion of radiation absorbed in bulk of the object studied:

$$W_a = \int_0^T \Phi_i(t)(1-\rho)[\exp(-\alpha\ell)]dt, \tag{3.109}$$

potential extra heating, excited coloring, transparency, nonlinear frequency conversion, emission, or scattering can take place, changing the integral optical property of the object under study. In Eq. (3.109), ρ is the surface reflectance and α and ℓ are the linear absorption coefficient and thickness of the object. As a function of any conceivable surface absorptance α_s of the given object and of the surface density $d\Phi_i/dA$ of the flux Φ_i of incident radiation, even some surface evaporation for the object studied and potential destruction of its internal bulk can arise. The nonlinear effects, which are functionally associated with the increase of the radiation power above a linearity threshold, inevitably lead to a related nonlinear change of the observed power extent of radiation interacting with an object. Inconsistency of presumably linear relations:

$$(\Phi/\Phi_0)_i = (\Phi/\Phi_0)_j = k, \tag{3.110}$$

where k is the factor studied at i and j levels of the incident power, indicates the appearance of the nonlinearity, leading to a discrepancy of that pulsed measurement from one in continuous light.

Another noticeable distinction for measurements obtained in pulsed and pulse-modulated laser light is defined by likely higher intensity fluctuations than those for continuous generation of radiation, as well as for spontaneous emission of spectrally equivalent light. The smaller is the time width $\Delta\tau$ of the laser pulse, the wider is the spectrum of its effective frequency $\Delta\nu \cong 1/\Delta\tau$ and the higher is the probability of random phase fluctuations among single-pulse components, at least due to extra instability of the pulse width. The process is amplified by mode competition inside a laser resonator and by added thermal noise. Noise, i.e., an accidental disordered wave field situated in the same spectral interval as the fundamental signal, causes fluctuations of power or energy of the radiation considered in both pulsed and quasi-continuous regimes. As a result, the optical field of that laser radiation can be mostly viewed as the additive sum of two components: one being mutually uncorrelated and the other slowly changing in comparison with $\exp(i\omega t)$. The first component defines randomly distributed uncorrelated radiation components, and the second indicates cophasal light. Hence, the total mean power averaged by a statistical ensemble is [3.34]:

$$\bar{P} = U^2 + 2\sigma^2, \tag{3.111}$$

where U is the amplitude of the field of laser generation and σ^2 is the root-mean-square deviation of that amplitude. The root-mean-square deviation for the average power of laser radiation is:

$$\Delta P = \sqrt{[P(t) - \bar{P}]^2} = 2\sigma\sqrt{P + \sigma^2}, \tag{3.112}$$

where P is the radiant power measured in the absence of noise. Considering that the uncertainty of the power transferred by laser light characterizes a threshold level P_{Th}, at which fluctuations are equal to the signal itself, the magnitude P_N of laser noise can be determined from the following expression:

$$P_{Th} = P_N(1 + \sqrt{2}). \tag{3.113}$$

This added power noise in laser, and more generally, in pulsed optical radiation sets limits on the sensitivity and accuracy of measurements realized in that radiation. To diminish radiation deviations due to noise caused by peak-power or average-power fluctuations, as well as pulse-energy fluctuations, a stabilization system limiting fluctuations of the measured power or energy extent by providing an optical feedback to either the source or the detector can be used. Stabilization of both the source and the detector can also be applied simultaneously. Figure 3.8 illustrates a measurement system utilizing one stabilization and one reference channel, each completed by an optical beam splitter with transmittance τ_i and reflectance ρ_i. Every random change ΔI of emitted intensity I is manifest in each channel: the measurement, the reference, and the stabilization one. Hence, the ratios are:

$$\begin{aligned} N_1 &= \frac{k_m\tau(I + \Delta I_i)}{k_r\rho(I + \Delta I_i)} = \frac{k_m\tau(I + \Delta I_j)}{k_r\rho(I + \Delta I_j)} = \frac{k_m\tau_2}{k_r\rho_2} = const_1; \\ N_2 &= \frac{k_m\tau(I + \Delta I_i)}{k_t\rho(I + \Delta I_i)} = \frac{k_m\tau(I + \Delta I_j)}{k_t\rho(I + \Delta I_j)} = \frac{k_m\tau_3}{k_t\rho_3} = const_2. \end{aligned} \tag{3.114}$$

Keeping the two-channel ratio signal as the system's constant allows one to perform accurate measurements within such a system with no need to know the optical properties of its elements as long as the actual characteristics τ_2, ρ_2, τ_3, and ρ_3 of the channel beam splitters as well as spectral sensitivities k_m, k_r, and k_t, of all three channels involved are not altered in any way during the entire measurement cycle needed to evaluate the optical property under study. Here indices *k, r,* and *m* relate to

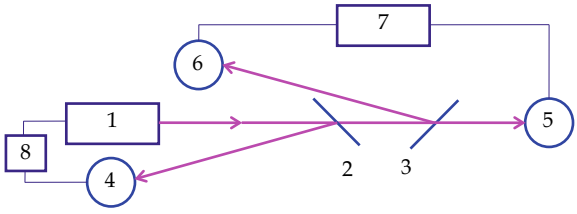

Fig. 3.8 Measurement layout for radiation-stabilization feedback and referencing: 1 - source, 2,3 - beam splitters; 3,4,5 - detectors, 7 - power or energy measuring radiometer; 8 - feedback control

the reference, the reflectance, and the transmittance channel, respectively. For related methods using the ratio-based and balanced techniques as well as other measurement-stabilization techniques, see further sections and Chap. 10 in particular.

3.3 Interference Phenomena and Optical Measurements

3.3.1 Fringe Visibility of Interference Patterns in Transmitted and Reflected Light

Every power and energy measurement of optical radiation, as well as any measurement of the optical properties of objects in such radiation, is realized using one or another optical element which transmits and reflects some portion of radiation. Consider the interaction of a light beam with a dielectric plane-parallel plate, having the transmittance of its input and output surfaces and of its internal bulk not necessarily equal to each other or to unity. That plate is an optical element, acting in transmitted and reflected light, and is widely used in power and energy measurements to create a reference channel or to seal the measurement enclosure, etc. Let it be a beam splitter having a thickness ℓ, distinct transmittances τ_1 and τ_2 and reflectances ρ_1 and ρ_2 of its two surfaces, and unequal-to-unity bulk transmittance $\tau_{\text{int}} = \exp(-\mu\ell)$, where μ is the linear attenuation coefficient of the bulk (Fig. 3.9).

The amplitude transmittance and reflectance of the splitter's surfaces at wavelength λ, viewed from a less-dense surrounding medium with refractive index n, are τ_{1a}, τ_{2a}, ρ_{1a}, ρ_{2a}, respectively. The same factors remain inside the dielectric plate of refractive index n′: τ'_{1a}, τ'_{2a}, ρ'_{1a}, ρ'_{2a}. Its internal amplitude transmittance is τ_a. In sequence of the multiple reflections for that beam splitter, made as a sufficiently

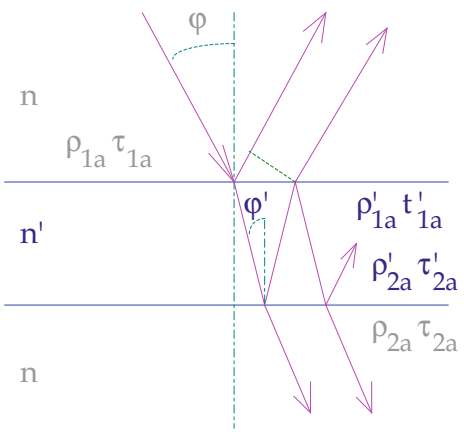

Fig. 3.9 Conversion of wave amplitudes in light transmitted by a plane-parallel dielectric plate

wide plate for all multiple reflections to decay to zero, the total light amplitude for a given quasi-monochromatic wave λ reflected from the splitter's plate is:

$$\begin{aligned} E_\rho &= E_0[\rho_{1a} + \tau_{1a}\tau_a\rho'_{2a}\tau_a\tau'_{1a}e^{i\delta} + \ldots + \tau_{1a}\tau'_{1a}\tau_a^2\rho'_{2a}(\rho'_{1a}\rho'_{2a}\tau_a^2)^{m-2}e^{i(m-1)\delta}] \\ &= E_0\left[\rho_{1a} + \tau_a^2\tau_{1a}\rho'_{2a}\tau'_{1a}e^{i\delta}\frac{1-(\rho'_{1a}\rho'_{2a}\tau_a^2)^{m-2}e^{i(m-2)\delta}}{1-\rho'_{1a}\rho'_{2a}\tau_a^2e^{i\delta}}\right], \end{aligned} \tag{3.115}$$

where E_0 is the amplitude of the radiation incident on the plate, m is the number of reflections, $\delta = 2\pi(2\ell/\lambda)n'\cos\varphi'$ is the phase difference between consecutive reflected or transmitted waves, and φ' is the angle of refraction. As the last wave term $(\rho'_{1a}\rho'_{2a}\tau_a^2)^{m-2}$ in the reflected sequence goes to zero owing to a low surface reflectance, a high internal transmittance, or a tending to infinity number of reflections, Eq. (3.115) becomes:

$$E_\rho = E_0\left[\rho_{1a} + \tau_a^2\tau_{1a}\rho'_{2a}\tau'_{1a}e^{i\delta}\frac{1}{1-\rho'_{1a}\rho'_{2a}\tau_a^2e^{i\delta}}\right]. \tag{3.116}$$

According to Snell's law, the intensity factors in reflection are: $\rho_{a,m}^2 = \rho_m$; $\tau_a^2 = \tau$; $\tau_{a,m}^2 = \tau_m$, and the sign of the amplitude reflectance at every interaction is changed to the opposite sign, $\rho_{1a} = -\rho'_{1a}$, but the transmittance is unchanged, $\tau_{1a} = \tau'_{1a}$ [1.1]. Owing to the law of conservation of energy for a plate of nonabsorbing internal medium: $\tau_{a,m}^2 + \rho_{a,m}^2 = \rho_m + \tau_m = 1$, the reflected amplitude at the unequal surface reflectances of the plate becomes:

$$\begin{aligned} E_\rho &= E_0\left[\frac{\rho_{1a} + \rho_{1a}^2\rho'_{2a}\tau_a^2e^{i\delta} + \tau_a^2\tau_{1a}\tau'_{1a}\rho'_{2a}e^{i\delta}}{1-\rho'_{1a}\rho'_{2a}\tau_a^2e^{i\delta}}\right] \\ &= E_0\frac{\rho_{1a} - \tau_a^2\rho_{2a}(\rho_{1a}^2 + \tau_{1a}^2)e^{i\delta}}{1-\tau_a^2\rho_{1a}\rho_{2a}e^{i\delta}} = E_0\frac{\sqrt{\rho_1}\left(1-\tau\sqrt{\rho_2/\rho_1}e^{i\delta}\right)}{1-\tau\sqrt{\rho_1\rho_2}e^{i\delta}}. \end{aligned} \tag{3.117}$$

For the complex conjugate:

$$E_\rho{}^* = E_0{}^*\frac{\sqrt{\rho_1}\left(1-\tau\sqrt{\rho_2/\rho_1}e^{-i\delta}\right)}{1-\tau\sqrt{\rho_1\rho_2}e^{-i\delta}}. \tag{3.118}$$

After substituting the equalities: $(1-ke^{i\delta})(1-ke^{-i\delta}) = 1+k^2-2k\cos\delta$; $\cos\delta = 1-2\sin^2(\delta/2)$, the product of Eqs. (3.117) and (3.118) gives the total intensity of fully reflected radiation [3.35]:

$$I_\rho = E_\rho E_\rho{}^* = I_0 \frac{\rho_1 + \tau^2\rho_2 - 2\tau\sqrt{\rho_1\rho_2}\cos\delta}{1 + \tau^2\rho_1\rho_2 - 2\tau\sqrt{\rho_1\rho_2}\cos\delta} = I_0 \frac{\left(\sqrt{\rho_1} - \tau\sqrt{\rho_2}\right)^2 + 4\tau\sqrt{\rho_1\rho_2}\sin^2(\delta/2)}{\left(1 - \tau\sqrt{\rho_1\rho_2}\right)^2 + 4\tau\sqrt{\rho_1\rho_2}\sin^2(\delta/2)}. \tag{3.119}$$

Accordingly, the extrema of that intensity distribution for phase difference: $\delta = 2\pi\mathrm{m}$ at $\mathrm{m} = 1, 2, \ldots$, are:

$$I_{\rho\max} = I_0\left(\frac{\sqrt{\rho_1} + \tau\sqrt{\rho_2}}{1 + \tau\sqrt{\rho_1\rho_2}}\right)^2;\ I_{\rho\min} = I_0\left(\frac{\sqrt{\rho_1} - \tau\sqrt{\rho_2}}{1 - \tau\sqrt{\rho_1\rho_2}}\right)^2. \tag{3.120}$$

Similarly, in light transmitted by the plane-parallel plate with unequal surface reflectances:

$$E_\tau = E_0\left[\tau_{1a}\tau_a\tau_{2a}\frac{1 - (\rho'_{2a}\rho'_{1a}\tau_a^2)e^{i(m-1)\delta}}{1 - \rho'_{2a}\rho'_{1a}\tau_a^2 e^{i\delta}}\right] \underset{m\to\infty}{=} E_0\frac{\tau_{1a}\tau_a\tau_{2a}}{1 - \rho'_{2a}\rho'_{1a}\tau_a^2 e^{i\delta}}; \tag{3.121}$$

$$I_\tau = E_\tau E_\tau{}^* = I_0\frac{\tau_1\tau_2\tau}{1 + \rho_1\rho_2\tau^2 - 2\tau\sqrt{\rho_1\rho_2}\cos\delta} = I_0\frac{\tau_1\tau_2\tau}{\left(1 - \tau\sqrt{\rho_1\rho_2}\right)^2 + 4\tau\sqrt{\rho_1\rho_2}\sin^2(\delta/2)}; \tag{3.122}$$

$$I_{\tau\max} = I_0\frac{\tau_1\tau_2\tau}{\left(1 - \tau\sqrt{\rho_1\rho_2}\right)^2};\ I_{\tau\min} = I_0\frac{\tau_1\tau_2\tau}{\left(1 + \tau\sqrt{\rho_1\rho_2}\right)^2}. \tag{3.123}$$

Presuming: $\rho_1 = \rho_2 = \rho; \tau_1 = \tau_1 = \tau = 1 - \rho$; at $\tau_{\mathrm{int}} = 1$, Eqs. (3.120) and (3.123) become Airy formulae:

$$I_{\rho\max} = I_0\left(4\rho\Big/(1+\rho)^2\right); \tag{3.124a}$$

$$I_{\rho\min} = 0; \tag{3.124b}$$

$$I_{\tau\max} = I_0\tau^2\Big/(1-\rho)^2 = I_0(1-\rho)^2\Big/(1-\rho)^2 \equiv I_0; \tag{3.125a}$$

$$I_{\tau\min} = I_0(1-\rho)^2\Big/(1+\rho)^2. \tag{3.125b}$$

Assuming $\rho_1 = \rho_2 = \rho$ and $\tau_{\mathrm{int}} \neq 1.0$ and designating $F \equiv 4\tau_{\mathrm{int}}\rho/(1 - \tau_{\mathrm{int}}\rho)^2$, Eqs. (3.119) and (3.122) are:

$$I_{\rho} \underset{\tau_{\text{int}}\neq 1}{=} I_0 \frac{\rho(1-\tau_{\text{int}})^2 \Big/ (1-\tau_{\text{int}}\rho)^2 + F\sin^2(\delta/2)}{1+F\sin^2(\delta/2)}, \tag{3.119c}$$

$$I_{\tau} \underset{\tau_{\text{int}}\neq 1}{=} I_0 \frac{\tau_{\text{int}}(1-\rho)^2 \Big/ (1-\tau_{\text{int}}\rho)^2}{1+F\sin^2(\delta/2)}. \tag{3.122c}$$

The maximum and minimum of interference for the plate of attenuating bulk become:

$$\begin{aligned} &I_{\rho,\max} = I_0 \frac{\rho(1+\tau_{\text{int}})^2}{(1+\tau_{\text{int}}\rho)^2}; \quad I_{\rho,\min} = I_0 \frac{\rho(1-\tau_{\text{int}})^2}{(1-\tau_{\text{int}}\rho)^2}, \\ &\frac{I_{\rho,\max}}{I_{\rho,\min}} = \frac{(1-\tau_{\text{int}}\rho)^2}{(1+\tau_{\text{int}}\rho)^2}\frac{(1+\tau_{\text{int}})^2}{(1-\tau_{\text{int}})^2}. \end{aligned} \tag{3.124c}$$

$$\begin{aligned} &I_{\tau,\max} = I_0 \frac{\tau_{\text{int}}(1-\rho)^2}{(1-\tau_{\text{int}}\rho)^2}; \quad I_{\tau,\min} = I_0 \frac{\tau_{\text{int}}(1-\rho)^2}{(1+\tau_{\text{int}}\rho)^2}; \\ &\frac{I_{\tau,\max}}{I_{\tau,\min}} = \frac{(1+\tau_{\text{int}}\rho)^2}{(1-\tau_{\text{int}}\rho)^2}; \quad \frac{I_{\rho,\max}}{I_{\rho,\min}}\frac{I_{\tau,\max}}{I_{\tau,\min}} = \frac{(1+\tau_{\text{int}})^2}{(1-\tau_{\text{int}})^2}. \end{aligned} \tag{3.125c}$$

The observability of each respective interference pattern can be described by fringe visibility V:

$$V_{\rho} = \frac{I_{\rho\max} - I_{\rho\min}}{I_{\rho\max} + I_{\rho\min}} = \frac{2\tau\sqrt{\rho_1\rho_2}(1-\rho_1)(1-\tau^2\rho_2)}{\rho_1(1-\tau^2\rho_2)^2 + \tau^2\rho_2(1-\rho_1)^2}; \tag{3.126}$$

$$V_{\tau} = \frac{I_{\tau\max} - I_{\tau\min}}{I_{\tau\max} + I_{\tau\min}} = \frac{2\tau\sqrt{\rho_1\rho_2}}{1+\tau^2\rho_1\rho_2}. \tag{3.127}$$

Since the fringe visibility gives the difference between the maxima and minima versus a twofold intensity $2I_{\Sigma} = I_{\max} + I_{\min}$, which corresponds to the case of no interference occurring, if $\tau = \tau_{\text{int}} = 1.0$ and $\rho_1 = \rho_2$, the observed visibility in reflected light is the highest: $V_{\rho} = 1$, independently of the value of $\rho_1 = \rho_2$. The same effect is produced by any absorbing plate having $\rho_1 = \tau^2\rho_2$. The only exceptions are for zero and 1.0 reflectance of each surface that removes light superposition. In transmitted light for the plate with nonabsorbing and nonscattering bulk and equal surface reflectances, the fringe visibility is a function of the surface reflectance, reaching unity at $\rho = 1$:

$$V_{\tau} \underset{\rho_1=\rho_2}{\overset{\tau_{\text{int}}=1}{=}} 2\rho/(1+\rho^2)\ . \tag{3.128}$$

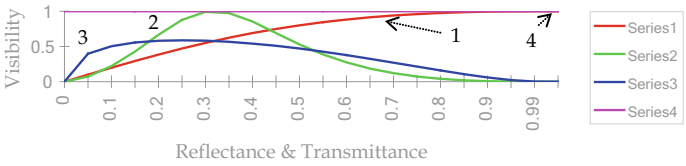

Fig. 3.10 Fringe visibility of transmitted (1, 3) or reflected (2, 4) interference pattern: 1,4 - transparent plate with equal reflectances; 2,3 - high first reflectance of transparent plate corresponds to low second reflectance and vise versa

Figure 3.10 shows how notably the effects of the interference can modify the outcome of measurements made at the presumption of the additive summation neglecting the interference.

3.3.2 Reductions of Interference Noise

As analyzed previously, the radiometric and photometric description of radiation transfer and the interaction of radiation with physical objects and mediums is valid if associated interference phenomena are either not detectable or are integrated in space and/or time. Interference infringes all photometric and radiometric laws and descriptions by breaking the additive rule of summing that forms the basis of conventional photometry and radiometry. If the surfaces of optical elements interacting with light have ideal antireflection (AR) coatings, surface-induced interference effects will be inherently absent, since no reflection, and thus no superposition, exists. One way to reduce interference effects due to surface reflections is affiliated with introducing nonparallelism among two or more reflecting surfaces, converting the multiple-beam interference among any multiple parallel surfaces to the two-beam interference among pairs of overlapping reflections. Equations (3.122)–(3.128) reveal (see Fig. 3.10) that in transmitted light such a measure only makes sense when considering highly reflecting surfaces. For reflectance ρ lower than 0.05, the multiple-reflection multiplier, $\rho_1\rho_2\tau^2$, even for internal plate transmittance $\tau = 1$, is smaller than 0.0025; thus, the influence of such reflections virtually does not manifest itself on transmitted intensity I_τ. One may keep in mind that the effectiveness of a wedge-shaped plate comes at the detriment of the radiometric or photometric goal to accomplish spatial averaging and therefore spatial integration for every interference pattern localized in both reflected and transmitted light.

Averaging effects can be seen as follows. If the phase difference δ between two interfering zones of a light beam changes by π within the cross section of the beam, the intensity of the beam averaged over that cross section should remain unchanged, as without interference at all. While applying such a concept to determine the total reflectance and the total transmittance of a plane-parallel plate of transparent bulk, one can integrate the cross-section of the incident beam at the small angle φ around the normal $\varphi \cong 0$ and obtain equations that are equivalent to (1.106) and (1.107):

$$\bar{\tau}_{pl} = \frac{1}{\pi}\int_0^{\pi} \frac{(1-\rho)(1-\rho)}{1+\rho^2-2\rho\,\cos\delta} d\delta \equiv \tau_{\Sigma,0} = \frac{1-\rho}{1+\rho}, \tag{3.129}$$

$$\bar{\rho}_{pl} = \frac{1}{\pi}\int_0^{\pi} \frac{2\rho(1-\cos\delta)}{1+\rho^2-2\rho\,\cos\delta} d\delta \equiv \rho_{\Sigma,0} = \frac{2\rho}{1+\rho}. \tag{3.130}$$

The required phase difference δ within the beam cross section, such as the beam diameter D, can be achieved by use of a small wedge-angle α between plate surfaces $\alpha \cong \mathrm{tg}\,\alpha = \Delta\ell/\mathrm{D}$. For $\delta = 4\pi\ell\mathrm{n}'\cos\varphi'/\lambda = \pi$ that angle should be equal to $\alpha = \lambda/(4Dn'\cos\varphi')$, where n′ and φ′ are the plate index and the respective angle of refraction. The Fourier transform of expression (3.129) gives [3.36]:

$$\bar{\tau}_{pl} = \tau_{\Sigma,0} + 2\tau_{\Sigma,0}\sum_{m=1}^{\infty}\rho^m\cos(m\delta), \tag{3.131}$$

and for the integrated total transmittance, averaged over the light beam diameter, it becomes:

$$\begin{aligned}\bar{\tau}_{pl} &= \tau_{\Sigma,0} + \frac{2\tau_{\Sigma,0}}{D}\int_{-D/2}^{D/2}\sum_{m=1}^{\infty}\rho^m\cos(mk_1x+k_2)dx \\ &= \tau_{\Sigma,0} + \frac{4\tau_{\Sigma,0}}{k_1D}\sum_{m=1}^{\infty}\rho^m\cos(mk_2)\sin(mk_1D/2),\end{aligned} \tag{3.132}$$

where $k_1 = 4\pi n'\alpha\cos\varphi'/\lambda$; $k_2 = 4\pi n'\ell\cos\varphi'/\lambda$. Since the right part of Eq. (3.132) is smaller than $\left(\tau_{\Sigma,0} + 4\tau_{\Sigma,0}\arcsin\rho/(k_1D)\right)$, for the purpose of determining the accuracy of averaging one may assume [3.36]:

$$\bar{\tau}_{pl} = \tau_{\Sigma,0}\left(1 + \frac{4\arcsin\rho}{k_1D}\right). \tag{3.133}$$

This way, relative averaging error $\delta_{\bar{\tau}_{pl}}$ becomes:

$$\delta\,\bar{\tau}_{pl} = \frac{\bar{\tau}_{pl} - \tau_{\Sigma,0}}{\tau_{\Sigma,0}} = \left|\frac{4\arcsin\rho}{k_1D}\right|. \tag{3.134}$$

Finally, for such a wedged plate and a parallel beam in transmission, the minimal angle is:

$$\alpha_{\tau\min} \geq \left|\frac{\lambda_{\max}\arcsin\rho}{\delta_{\bar{\tau}_{pl}}\pi n' D_{\min}\cos\delta}\right|. \tag{3.135}$$

Because:

$$\frac{\bar{\rho}_{pl} - \rho_{\Sigma,0}}{\rho_{\Sigma,0}} = \frac{1 - \bar{\tau}_{pl} - 1 + \tau_{\Sigma,0}}{\rho_{\Sigma,0}} = \frac{\tau_{\Sigma,0} - \bar{\tau}_{pl}}{\rho_{\Sigma,0}}, \tag{3.136}$$

the relative error $\delta_{\bar{\rho}_{pl}}$ of spatial beam averaging in reflection given by such a wedge plate becomes:

$$\delta_{\bar{\rho}_{pl}} = \frac{\tau_{\Sigma,0} - \bar{\tau}_{pl}}{\tau_{\Sigma,0}} \frac{\tau_{\Sigma,0}}{\rho_{\Sigma,0}} = \left|\delta_{\bar{\tau}_{pl}}\right| \frac{\tau_{\Sigma,0}}{\rho_{\Sigma,0}}. \tag{3.137}$$

As a result, to provide the spatial averaging of interference patterns for light beams reflected by the wedge-shaped plate, the required minimal wedge between the plate surfaces must be:

$$\alpha_{\rho\min} \geq \left| \frac{\tau_{\Sigma,0} \lambda_{\max} \arcsin \rho}{\rho_{\Sigma,0} \delta_{\bar{\rho}_{pl}} \pi n' D_{\min} \cos \delta} \right|. \tag{3.138}$$

Equations (3.135)–(3.138) demonstrate that the plate wedge angle for interference averaging increases with the incident beam diameter decreasing in proportion to the radiation wavelength. In reflected radiation, the requirements are nearly 1 order of magnitude higher than in transmitted light. The ratio of the plate's transmittance and reflectance determines the distinction (see Eq. (2.50)):

$$\tau_{pl} \big/ \rho_{pl} = \tau_{\Sigma,0} \big/ \rho_{\Sigma,0} = (1 - \rho)/2\rho = 4n \Big/ (n - 1)^2. \tag{3.139}$$

For example, for $n' = 1.5$, $\lambda_{\max} = 1\,\mu m$, and $D = 2.5\ mm$, to satisfy the requirement of $\delta \leq 0.1\%$, angle α_τ needs to be not less than 15′, but to achieve the same averaging in reflected light the minimal angle becomes 2°.

One reason for the mentioned wedge requirements in reflected light to be noticeably greater than those in transmitted radiation is conditioned by the considerably higher fringe visibility V_ρ in reflection versus the visibility V_τ in transmission. This is due to equality of the amplitudes of interfering waves reflected from the first and second surfaces of the thin transparent plate Eq. (3.110) being interposed within the combined cross section of both reflected beams. In transmitted radiation, incident and transmitted beams interfere only after one dual reflection within the plate. The beams' intensity ratio is $1/\rho^2$, making the interference term $\sqrt{1/\rho^2}$ lower. If the surface reflectances of a plate increase, interference effects in transmitted light become more visible than in reflected light.

The straightforward way to eliminate the effects of interference is to separate interfering beams from one another. Since for a glass plate as a beam splitter the highest visibility of interference is caused by the reflected light, the optical thickness of the splitter and its wedge may be chosen to make the reflected beams completely separated from one another (see Fig. 3.11). For a relatively thick plate, the beams reflected from the first and second surfaces are only crossed by incident

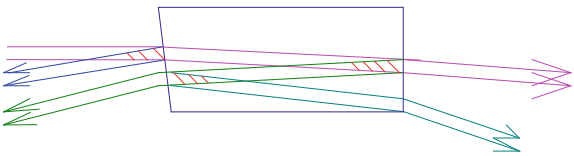

Fig. 3.11 Retroreflections in a long substrate as a wedged beam splitter

and transmitted beams once (the sections are shown patterned). In this case, any interference among the components having similar intensities is eliminated. In addition, every sequential amplitude of an intersecting beam becomes much lower owing to the very small surface reflectance ρ.

Applications of wedge-shaped optical elements, redirecting reflected beams and reducing the effects of interference, may be efficient, but are not the most advanced measure. They set limits on the choice of wavelengths, beam cross sections, and thicknesses of optical elements. Especially, when an optical system contains multiple components, any changes of a set direction of light propagation are not convenient. One more way for efficient reduction of interference follows from Eqs. (3.126) and (3.127). These equations were derived to account for the likely difference among surface reflectances of each optical element multiplied by its bulk transmittance as the square power. The fringe visibility of the interference pattern occurring in transmitted light created by a plane-parallel plate with surface reflectances ρ_1 and ρ_2 and internal transmittance τ is defined by the product $\tau\sqrt{\rho_1\rho_2}$, tending to zero as $\tau\sqrt{\rho_1\rho_2} \to 0$. Consequently, sufficient decrease of all interference phenomena in transmitted as well as in reflected light may be achieved by AR coatings applied to at least one plate surface or to both plate surfaces. Another, not so obvious, way of reducing interference may be provided by bulk absorption. It is applicable, but is not the most efficient way, since absorption can lead to overheating or even damage of the optical bulk of a transmission element when it is used in powerful laser radiation. The solutions change in reflected light. As illustrated in Fig. 3.10, equivalent reduction of both surface reflectances does not decrease the fringe visibility of interference in reflected radiation. If any internally attenuating substrate of transmittance $\tau_{\text{inner bulk}} \neq 1$ is used, the obstacle is still not fully resolved. If the properties of the surfaces and the substrate are such that $\rho_1 = \tau^2\rho_2$, the resultant fringe visibility in reflected light is unity as for a transparent plate of equal surface reflectances. Only any substantial difference of the first surface reflectance ρ_1 from the product of the bulk transmittance as the square power over the reflectance of the second surface, $\tau^2\rho_2$, significantly diminishes the fringe visibility of a beam reflected from such an attenuating optical element. Figure 3.12 illustrates contingency of V_ρ and V_τ as functions of plate properties ρ_1, τ, and ρ_2. Series 4 and 6 are not distinguished in Fig. 3.12 owing to the described transmission symmetry of the reversed positions of two plate surfaces.

Any absolute increase of the difference modulus reduces the fringe visibility of the interference in reflected light, concurrently somewhat increasing V_τ in transmitted radiation [3.35]. For some applications, a plate may be used sequentially in reflected and in transmitted light. If two fields are viewed separately, the lower is

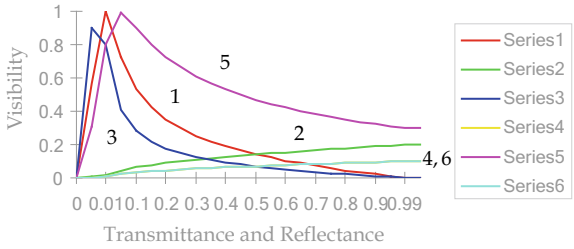

Fig. 3.12 Fringe visibility for interference patterns in reflected (1, 3, 5) and in transmitted (2, 4, 6) light versus values of surface reflectance and bulk transmittance: 1,2 - T = 1, R2 = 0.01; 3,4 - T = 0.5, R2 = 0.01; 5,6 - R1 = 0.01, T = 0.5

the visibility of every interference pattern, the better is the situation for both beams. In that case, the intersection point of the transmission and the reflection function matches the equally low visibility for both divided patterns and sets the visibility limit. Let us introduce the new function $V_{\rho,\tau}$ equal to V_ρ when $V_\rho > V_\tau$ and to V_τ when $V_\tau > V_\rho$, to be called the *function of largest fringe visibility*. Visibility $V_{\rho,\tau}$ has one minimum at $V_\rho = V_\tau$:

$$\frac{2\tau\sqrt{\rho_1\rho_2}(1-\rho_1)(1-\tau^2\rho_2)}{\rho_1(1-\tau^2\rho_2)^2+\tau^2\rho_2(1-\rho_1)^2} = \frac{2\tau\sqrt{\rho_1\rho_2}}{1+\tau^2\rho_1\rho_2}. \tag{3.140}$$

Discarding terms of second order of smallness, the reflectance leading to the intersection is:

$$\rho_1 = \frac{1-2\tau^2\rho_2}{(1-3\tau^2\rho_2)}. \tag{3.141}$$

For $\tau = 1$ and $\rho_2 = 0.1$, the magnitude $\rho_1 = 0.57$ corresponds to maintaining equal visibilities in transmitted and reflected light; for $\tau = 0.5$ and $\rho_2 = 0.01$, reflectance ρ_1 should be 0.5, but for $\tau = 0.5$ and $\rho_1 = 0.01$, no intersection point is present. Accordingly, as it is seen for curves 5 and 6 in Fig. 3.12, the optimal deployment of any absorbing beam splitter is sensitive to its orientation. In minimizing negative interference effects by a beam splitter, the specific condition which leads to the intensities of all the interfering beams being unequal rather than similar is preferable.

For any intensity-ratio measurement, such as in the two-channel system seen in Fig. 3.8, the largest fringe visibility function $V_{\rho,\tau}$ does not fully represent the outcome of the combined transmitted and reflected interference pattern when neither pattern can be disregarded. Since reflection plus transmission interference fringes are complementary, the sum of the ratios of transmitted intensity I_τ to incident intensity I_0 and reflected intensity I_ρ to incident intensity I_0 equals to unity:

$$I_\tau/I_0 + I_\rho/I_0 = 1, \tag{3.142}$$

A minimum of one pattern exactly corresponds to a maximum of another and to account for the total effect, the combined correlative interference pattern of mutual fringe visibility V_Σ needs to be analyzed. Within the temporal-spatial pattern localized not at any particular point, but in the space-time region adjoining the splitter, the single intensity magnitudes should be substituted by the ratios of matching intensities: I_τ/I_ρ or I_ρ/I_τ. Counting the fringe visibility V_Σ of the mutual pattern as:

$$\begin{aligned} V_\Sigma &= \frac{I_{\rho\max}/I_{\tau\min} - I_{\rho\min}/I_{\tau\max}}{I_{\rho\max}/I_{\tau\min} + I_{\rho\min}/I_{\tau\max}} \\ &= \frac{I_{\tau\max}/I_{\rho\min} - I_{\tau\min}/I_{\rho\max}}{I_{\tau\max}/I_{\rho\min} + I_{\tau\min}/I_{\rho\max}}, \end{aligned} \tag{3.143}$$

and bearing in mind, that $\tau_1 = 1 - \rho_1; \tau_2 = 1 - \rho_2$, from Eqs. (3.120) and (3.123), we obtain [3.37]:

$$V_\Sigma = \frac{\left(\sqrt{\rho_1} + \tau\sqrt{\rho_2}\right)^2 - \left(\sqrt{\rho_1} - \tau\sqrt{\rho_2}\right)^2}{\left(\sqrt{\rho_1} + \tau\sqrt{\rho_2}\right)^2 + \left(\sqrt{\rho_1} - \tau\sqrt{\rho_2}\right)^2} = \frac{2\tau\sqrt{\rho_1\rho_2}}{\rho_1 + \tau^2\rho_2}. \tag{3.144}$$

Mutual visibility function V_Σ, as well as visibility $V_{\rho,\tau}$ has one maximum equal to unity at: $\rho_1 = \rho_2; \tau = 1$, becomes lower at $\rho_1 \neq \rho_2$ or $\tau \neq 1$, and equals to zero along with either surface reflectance or bulk transmittance (Fig. 3.13). At $\tau \neq 1$, the *mutual fringe visibility* V_Σ, the same as $V_{\rho,\tau}$, depends on the splitter orientation to the beam propagation direction. The higher is the difference between the first surface reflectance and the product of the bulk transmittance squared and the second surface reflectance, the lower is the mutual fringe visibility of the shared pattern and the smaller are the effects of interference on the results of measurements by the two-channel optical system.

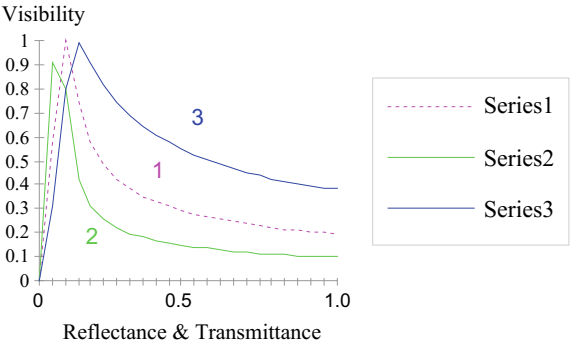

Fig. 3.13 Total fringe visibilities of mutual patterns obtained in the reflected and in the transmitted light:
1 - T = 1, R2 = 0.01;
2 - T = 0.5, R2 = 0.01;
3 - T = 0.5, R1 = 0.01

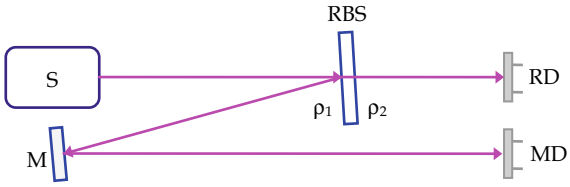

Fig. 3.14 Interference supressing dual-channel measurement system: S - light source; RBS - reflecting beam splitter; RD - reference detector; M - mirror; MD - main detector

Figure 3.13, as well as Fig. 3.12, depicts how substantially the entire influence of the interference is reduced by purely redistributing surface reflectances of the channel beam splitter. By fixing the total transmittance and total reflectance of the transparent beam splitter, but redistributing one surface reflectivity by its AR coating to $\rho_1 = 0.0025$, and increasing another surface reflectance to $\rho_2 = 0.1$, one reduces the mutual fringe visibility V_Σ for the splitter to 0.3. This is 3 times less than for the plate of the same transmittance with identical surface reflectances. A similar effect may be achieved by reducing the internal bulk transmittance of the splitter, but as a result losing the radiation throughput. To obtain visibility $V_\Sigma = 0.3$ via the bulk absorptance, the beam splitter bulk transmittance should be $\tau = 0.155$. Accordingly, the intensity of light transmitted via that absorbing splitter becomes 6.5 times lower than that transmitted by a transparent glass plate.

From Eq. 3.144 and Fig. 3.13 it also follows that among any multiple-channel optical system the highest decline of interference phenomena can be achieved if light is transformed via beam splitters and combiners of high reflectance and low transmittance. In such a system, implementation of a beam splitter with first surface reflectance $\rho_1 = 0.9$, bulk transmittance $\tau = 1$, and second surface reflectance $\rho_2 = 0.025$ provides exactly the same distribution of energy as the conventional transparent plate does. The difference is only defined by the swapped two system channels. The measurement channel receives the reflected light, but the reference channel receives radiation transmitted by the splitter (Fig. 3.14). In this case, fringe visibility $V_\Sigma \cong 0.03$ of the mutual interference pattern becomes more than 30 times lower than that for the conventional two-channel optical system, which utilizes a plane-parallel beam splitter of two similar surface reflections such as of the transparent glass plate.

3.3.3 *Interference Effects Induced by Birefringence*

Most of the optical elements considered above, for which the optical thickness is not optimized to be a multiple of the light wavelength, are arbitrarily modifying phase differences of interacting beams of light and producing certain interference noise, rather than a predictable alteration of light intensity due to a stable and observable interference pattern. Another situation occurs when radiation interacts with a linear phase retarder, which is intended to match that radiation wavelength,

such as a crystal wave plate creating a predictable phase shift, owing to the birefringence between its two orthogonal optical axes of unequal wave refraction. When one measures the phase retardance, the result of interference of light waves propagating along each optical axis of the wave plate is defined by the birefringence between the ordinary and extraordinary axes and thus can be accounted for.

As a starting point in analysis of interference effects induced by birefringent substances, let us consider a random orientation of each vibration direction P, A, singled out by a polarizer and an analyzer from radiation at a wavelength λ at normal incidence, versus the location of the ordinary N_o and extraordinary N_e axes of a birefringent plate under study, as in [1.1]. In addition, let us take into account losses induced by surface reflections of the plate. Let γ be the angle between positive directions ZP and ZA for respective transmission of radiation by the polarizer and the analyzer, and let φ be the angle between the plate's ordinary axis and direction ZP (Fig. 3.15). Let light emerging from the polarizer be incident normally onto the retarder under study. The light's amplitude E may be represented through two orthogonal projections along the ordinary and extraordinary axes of the plate: $E_O = E\cos\varphi$ and $E_e = E\sin\varphi$. The amplitudes transmitted by the wave plate are $ZO = E{\tau'_o}^2\cos\varphi$ and $ZT = E{\tau'_e}^2\sin\varphi$, where τ'_o and τ'_e are the respective amplitude transmittances of each plate surface, subsequently determined along the corresponding vibration direction N_o, N_e. The analyzer transmits only light components parallel to its vibration direction *ZA*. Thus, projections ZM and ZN of wave components ZO and ZT onto direction ZA are:

$$ZM = E\tau_O'^2\cos\varphi\cos(\varphi-\gamma); \tag{3.145}$$

$$ZN = E\tau_e'^2\sin\varphi\cos[90-(\varphi-\gamma)] = E\tau_e'^2\sin\varphi\sin(\varphi-\gamma). \tag{3.146}$$

The components of the state of polarization transmitted by the analyzer interfere as two monochromatic waves incurring a phase shift $\delta = (2\pi/\lambda)(n_e - n_o)h$ that is dependent upon the component's wavelength λ, the plate's birefringence $b = |n_e - n_o|$, and the thickness h of the plate slab. The resultant intensity becomes:

$$I = I_1 + I_2 + 2\sqrt{I_1 I_2}\cos\delta. \tag{3.147}$$

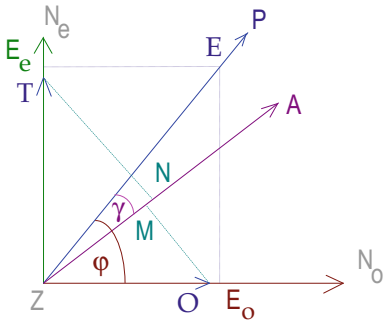

Fig. 3.15 Positions of radiation vibration components transmitted by the polarizer, retarder, and analyzer

For the waveplate with unequal transmittances: $\tau_o \neq \tau_e$, along two optical axes, we obtain:

$$\begin{aligned} I = E^2\{&[\tau_o \cos\varphi \cdot \cos(\varphi - \gamma) + \tau \sin\varphi \cdot \sin(\varphi - \gamma]^2 \\ &- (\tau_o \tau_e) \sin 2\varphi \cdot \sin 2(\varphi - \chi) \sin^2 \delta/2\}. \end{aligned} \tag{3.148}$$

Let us note that Eq. (3.148) has a solution for the phase retardance δ; therefore, if the magnitudes of φ and of γ and the measured intensities I_0 and I_τ of the incident light and the light transmitted via the system are known, the phase shift introduced by the wave plate can be resolved. It is also seen that the first term converts to $\cos^2\gamma$ only if the plate's transmittances along both optical axes are equal: ${\tau_o}^2 = {\tau_e}^2$. Another simplification comes from the arrangements of the measurement system. If the polarizer and analyzer are crossed, thus angle $\gamma = 90°$, and if the optical axis of the wave plate (usually the ordinary one) is set at $\varphi = 45°$ to directions ZP and ZA, the resultant intensity is:

$$I_\perp = (I_o/4)[(\tau_o - \tau_e)^2 + 4\tau_o\tau_e \sin^2 \delta/2]. \tag{3.149}$$

When the polarizer and analyzer axes are parallel, $\gamma = 0$, and when the wave plate remains at $\varphi = 45°$,

$$I_\parallel = (I_o/4)[(\tau_o - \tau_e)^2 - 4\tau_o\tau_e \sin^2 \delta/2]. \tag{3.150}$$

Equations (3.149) and (3.150) transform into well-known conventions [1.1] for zero reflectances ρ_o and ρ_e:

$$I_\perp = I_o \sin^2 \delta/2, \tag{3.151}$$

$$I_\parallel = I_o(1 - \sin^2 \delta/2). \tag{3.152}$$

The reduction predicted by relations (3.148)–(3.150) for the intensities of waves transmitted by the wave plate does not include all polarization components retro-reflected by plate's surfaces. To analyze the influence of reflections and changes of intensities of light beams transmitted by any measurement system, let us consider the infinite sequence of reflections as two isolated parallel wave sequences along the ordinary and extraordinary vibration directions of the retarder. Each retarder surface may have distinct reflections ρ_{o1}, ρ_{e1}, ρ_{o2}, and ρ_{e2} along each vibration direction. For convenience we will consider the wave plate to be uncoated, having two identical back and front surface reflectances: ordinary reflectance $\rho_o = [(1 - n_o)/(1 + n_o)]^2$ along the ordinary axis, and extraordinary reflectance $\rho_e = [(1 - n_e)/(1 + n_e)]^2$ along the extraordinary axis. We will also assume that every beam reflected from the first (the front) surface of the plate is not returned to the system.

After passing via the first plate surface and its crystal bulk, which we will assume to be of low scattering and low absorption, each light component for both axes splits into several beams. The first two components with intensities $I_{\tau,o}$ and $I_{\tau,e}$ along the ordinary and extraordinary directions of the plate are directly transmitted

according to Eq. (3.148). The second series are created by single reflections from each plate surface and have intensities $I_{\rho,o1}$ and $I_{\rho,e1}$. The intensities of the m^{th} components with 2^m reflections are $I_{\rho,om}$ and $I_{\rho,em}$ (Fig. 3.16). The intensity factor of each double pass is defined by ordinary or extraordinary reflectance of the first and second surfaces: $\rho_{o1}\rho_{o2}$ and $\rho_{e1}\rho_{e2}$. The phase shift does not remain constant even for the sequential components along optical axes. For every pair of coequally retroreflected light waves, the phase difference δ expands step-by-step as $\delta_m = (2m + 1)(\delta_e - \delta_o)$. Here $\delta_o = (2\pi/\lambda)(hn_o)$ and $\delta_e = (2\pi/\lambda)(hn_e)$, and $m = 1, 2, \ldots$ is the integer denoting an order of a wave term in a sequence. For $m = 0$ the phase difference is $\delta = \delta_e - \delta_o$, and between the two interfering beams, experiencing any unequal number of surface reflections $m_o \neq m_e$, the phase shift is no longer a multiple of δ.

Ordinary and extraordinary components of each optical beam transmitted by the wave plate interfere separately along every orthogonal vibration direction with each other, but not with ones of the opposite state polarization propagating via another axis. Two additional interference phenomena exist for projections of these components into the polarization direction of analyzer. Let us separate two processes for waves of equal and distinct amounts of transmission, such as the comparative and cross-reference interference events, respectively. As a result, only beams, which share each comparative interference event will have similar amplitudes. The resultant complete action for the triple-step interference event transforms Eq. (3.148) into the form:

$$\begin{aligned} I_\Sigma = {} & I_{\tau,o} + I_{\rho,o1} \ldots + I_{\rho,om} + I_{\tau,e} + I_{\rho,e1} \ldots + I_{\rho,em} \\ & + 2\sqrt{I_{\tau,o} I_{\tau,e}} \cos\delta + \ldots + 2\sqrt{I_{\rho,om} I_{\rho,em}} \cos[(2m_o + 1)\delta_o - (2m_e + 1)\delta_e] + \ldots \\ & + 2\sqrt{I_{\tau,o} I_{\rho,em}} \cos[\delta_0 - (2m+1)\delta_e] + 2\sqrt{I_{\rho,om} I_{\tau,e}} \cos[(2m+1)\delta_0 - \delta_e]. \end{aligned} \tag{3.153}$$

To categorize the infinite number of terms in Eq. (3.153), let us identify the intensities of all interfering beams to be counted. Keeping in mind that interference terms may be omitted if the intensities or amplitudes of the interfering waves, such as I_1, I_2, and I_3, are not compatible, when $I_1, I_2 \gg I_3$, we may replace the sum accounting for multiple interference: $I_1 + I_2 + I_3 + 2\sqrt{I_1 I_2}\cos\delta_{1,2} + 2\sqrt{I_1 I_3}\cos\delta_{1,3} + 2\sqrt{I_2 I_3}$

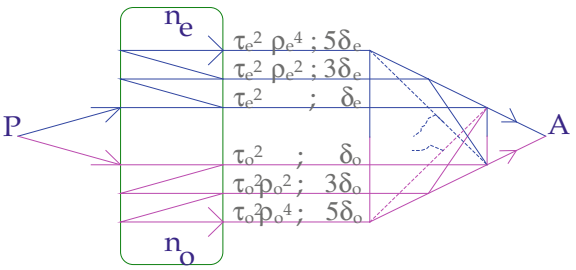

Fig. 3.16 Schematic separation of interfering waves (the dotted lines designate insignificant interactions)

$\cos\delta_{2,3}$, by $I_1 + I_2 + I_3 + 2\sqrt{I_1 I_2}\cos\delta_{1,2}$. Since the intensities of light components which participate in the cross-reference interference differ by the product of both surface reflections of the retarder, let us distinguish the most valuable retroreflected terms presuming that $(\rho_{o1}\rho_{o2})^2, (\rho_{e1}\rho_{e2})^2 \ll 1$. For identical front and back surface reflections, the presumption leads to $(\rho_o)^2 \ll 1$, $(\rho_e)^2 \ll 1$, meaning that only interference of waves separated by at least two dual-reflection cycles inside the retarder will not be counted (denoted by the wave marks in Fig. 3.16). That is the only presumption needed to obtain the following complete quantitative description of the multiple-reflection fringes with the wave plates. It also gives the succeeding order of discreteness of the interference phenomena considered in comparison with broadly identified restrictions for the wave plate refractive indices $1 < n < 2$ in early studies [3.41] and with the first-order approximation of $\rho_o \ll 1$, $\rho_e \ll 1$ in work done later [3.42]. With such a second-order approximation accounting for mutual interference interactions among all components affected by the dual transmission via the retarder (wave plate), Eq. (3.153) transforms into:

$$
\begin{aligned}
I_{\tau,\Sigma} = I_0 \Bigg[& \frac{1-\rho_o}{\sqrt{(1-\rho_o)^2 + 4\rho_o \sin^2\delta_o}} \cos\varphi\cos(\varphi-\gamma) \\
& + \frac{1-\rho_e}{\sqrt{(1-\rho_e)^2 + 4\rho_e \sin^2\delta_e}} \sin\varphi\sin(\varphi-\gamma) \Bigg]^2 \\
& - I_0\tau_o\tau_e \sum_{i=1}^{m} \left\{ \rho_o^{m-1}\rho_e^{m-1} \sin^2\left[\frac{(2m-1)\delta}{2}\right] + \rho_o^m \rho_e^{m-1} \sin^2\left(m\delta_o + \frac{\delta}{2}\right) \right. \\
& \left. + \rho_o^{m-1}\rho_e^m \sin^2\left(m\delta_e + \frac{\delta}{2}\right) \right\} \sin 2\varphi \sin[2(\varphi-\gamma)].
\end{aligned}
\tag{3.154}
$$

Equation (3.154) defines the incidence of entirely random orientation of all polarization-sensitive parts and for two most practical cases of the orthogonal and parallel orientation of the polarizer and analyzer: $\gamma = 90°$; $\varphi = 45°$ and $\gamma = 0°$; $\varphi = 45°$, respectively becomes:

$$
\begin{aligned}
I_{\perp,\Sigma} = \frac{I_0}{4} \Bigg\{ & \left(\frac{1-\rho_o}{\sqrt{(1-\rho_o)^2 + 4\rho_o \sin^2\delta_o}} - \frac{1-\rho_e}{\sqrt{(1-\rho_e)^2 + 4\rho_e \sin^2\delta_e}} \right)^2 + 4(1-\rho_o)(1-\rho_e) \\
& \times \sum_{i=1}^{m} \left[\rho_o^{m-1}\rho_e^{m-1} \sin^2\left(\frac{(2m-1)\delta}{2}\right) + \rho_o^m \rho_e^{m-1} \sin^2\left(m\delta_o + \frac{\delta}{2}\right) + \rho_o^{m-1}\rho_e^m \sin^2\left(m\delta_e + \frac{\delta}{2}\right) \right] \Bigg\},
\end{aligned}
\tag{3.155}
$$

$$I_{||,\Sigma} = \frac{I_0}{4}\left\{\left(\frac{1-\rho_o}{\sqrt{(1-\rho_o)^2+4\rho_o\sin^2\delta_o}}+\frac{1-\rho_e}{\sqrt{(1-\rho_e)^2+4\rho_e\sin^2\delta_e}}\right)^2-4(1-\rho_o)(1-\rho_e)\right.$$
$$\left.\times\sum_{i=1}^{m}\left[\rho_o^{m-1}\rho_e^{m-1}\sin^2\left(\frac{(2m-1)\delta}{2}\right)+\rho_o^m\rho_e^{m-1}\sin^2\left(m\delta_o+\frac{\delta}{2}\right)+\rho_o^{m-1}\rho_e^m\sin^2\left(m\delta_e+\frac{\delta}{2}\right)\right]\right\}. \tag{3.156}$$

The first terms in Eqs. (3.154)–(3.156) define two infinite sequences sharing multiple-beam interference along every vibration direction. The algebra applied is based on the approximation:

$$1+\rho_o\rho_e+\rho_o+\rho_e+(\rho_o\rho_e)^2+\rho_o\rho_e^2+\rho_e\rho_o^2+\rho_o^2$$
$$+\rho_e^2+\rho_o\rho_e^3+\rho_e\rho_o^3+\ldots\underset{\rho_o,\rho_e<1;m\to\infty}{\cong}[(1-\rho_o)(1-\rho_e)]^{-1}. \tag{3.157}$$

Terms under the sum signs in Eqs. (3.155) and (3.156) designate the two-beam interference of every ordinary and every extraordinary component of the first two terms further transmitted by the analyzer, and while only interference terms for wave components with vastly different amplitudes are omitted from the final results, and while each equation term counts an infinite number of reflections.

Equations (3.155) and (3.156), because of not the first but the second-order limitation used, include an unlimited number of interfering terms with distinct phases. The pattern of multiple interference of retroreflected beams overlaps the main two-beam interference with phase difference δ as a disordering factor, owing to the resolved coherence property of the particular light source with all multiple-reflection interference fringes counted. Making those fringes spatially or temporarily integrated over every distinctive optical path length, along ordinary and extraordinary directions of the retarder, or using incoherent light, one can simplify the phenomenon. We may also clarify the terms under the sum signs in Eqs. (3.154)–(3.156) by omitting the components of the higher orders of reflection. By reducing in all instances the invoked approximation to $\rho_{o1}\rho_{o2}, \rho_{e1}\rho_{e2} \ll 1$ or ${\rho_o}^2 \ll 1$, ${\rho_e}^2 \ll 1$, only the interference terms with no more than two reflections from the retarder surfaces are counted further. Consequently, the integral intensities of light sequences being spatially integrated within the double optical thickness of the wave plate, still making an angle of 45° to the vibration directions of the respectively crossed or parallel polarizers, can be rewritten as:

$$\bar{I}_{\perp,\Sigma} = \frac{I_0}{4}\left\{\left(\sqrt{\frac{1-\rho_o}{1+\rho_o}}-\sqrt{\frac{1-\rho_e}{1+\rho_e}}\right)^2+4(1-\rho_o)(1-\rho_e)\right.$$
$$\left.\times\left[\sin^2\left(\frac{\delta}{2}\right)+\rho_o\rho_e\sin^2\left(\frac{3\delta}{2}\right)+\rho_o\sin^2\left(\delta_o+\frac{\delta}{2}\right)+\rho_e\sin^2\left(\delta_e+\frac{\delta}{2}\right)\right]\right\}, \tag{3.158}$$

$$\bar{I}_{\|,\Sigma} = \frac{I_0}{4}\left\{\left(\sqrt{\frac{1-\rho_o}{1+\rho_o}}+\sqrt{\frac{1-\rho_e}{1+\rho_e}}\right)^2 - 4(1-\rho_o)(1-\rho_e)\right.$$
$$\left.\times\left[\sin^2\left(\frac{\delta}{2}\right)+\rho_o\rho_e\sin^2\left(\frac{3\delta}{2}\right)+\rho_o\sin^2\left(\delta_o+\frac{\delta}{2}\right)+\rho_e\sin^2\left(\delta_e+\frac{\delta}{2}\right)\right]\right\}. \tag{3.159}$$

The algebra used for all denominators in the first terms is based on parity:

$$1+\rho^2+\ldots+\rho^m = (1-\rho^2)^{-1}.$$

To analyze the derived equations and to verify the limits of their applicability, let us apply them to some known cases of light transmission via birefringent and isotropic substances. If any isotropic plate is located between two crossed polarizers, no light can pass through, since $\delta_{isot} = \delta_e - \delta_o = 0$. As a result, Eqs. (3.155) and (3.158) become zero and (3.156) and (3.159) convert to:

$$\bar{I}_{\tau,isot,coherent} = \frac{(1-\rho)^2}{\sqrt{(1-\rho)^2+4\rho\sin^2\delta_{thickness}}}; \bar{I}_{\tau,isot,incoherent} = \frac{1-\rho}{1+\rho}. \tag{3.160}$$

Assigning in relations (3.158) and (3.159) the average transmittance, reflectance, and phase difference between two axes of the wave plate, respectively, as $\bar{\tau} = (\tau_o + \tau_e)/2$, $\bar{\rho} = (\rho_o + \rho_e)/2$, and $\bar{\delta}_{o,e} = (\delta_o + \delta_e)/2$:

$$\bar{I}_{\perp,\Sigma,av} = I_0(1-\bar{\rho})^2\left[\sin^2\left(\frac{\delta}{2}\right)+\bar{\rho}^2\sin^2\left(\frac{3\delta}{2}\right)+2\bar{\rho}\sin^2\left(\bar{\delta}_{o,e}+\frac{\delta}{2}\right)\right], \tag{3.161}$$

$$\bar{I}_{\|,\Sigma,av} = I_0(1-\bar{\rho})^2\left[\left(1-\bar{\rho}^2\right)^{-1}-\sin^2\left(\frac{\delta}{2}\right)-\bar{\rho}^2\sin^2\left(\frac{3\delta}{2}\right)-2\bar{\rho}\sin^2\left(\bar{\delta}_{o,e}+\frac{\delta}{2}\right)\right]. \tag{3.162}$$

The first-order approximation confirms that the bulk retardance of a wave plate due to single-pass phase difference δ obtained by a transmission measurement of integral intensity $\bar{I}_\perp$ or $\bar{I}_\|$ is affected by the comparative and cross-reference interference terms within the intensity limits:

$$\begin{aligned}\bar{I}_{comp} &= \pm\bar{\rho}^2\sin^2(3\delta/2);\\ \bar{I}_{cross} &= \pm\left(\rho_o\sin^2(\delta_o+\delta/2)+\rho_e\sin^2(\delta_e+\delta/2)\right)\\ &= \pm2\bar{\rho}\sin^2\left(\bar{\delta}_{o,e}+\delta/2\right).\end{aligned} \tag{3.163}$$

The meanings of the derived mathematics may be double checked at extreme points of the wave plate's phase retardance. For a full-wave plate at $\delta = 0, 2\pi \ldots$, the intensity of radiation transmitted by the full-wave retarder deviates from zero or unity for the polarizer and analyzer if they are crossed or parallel:

$$\begin{aligned}\bar{I}_{\perp,2\pi,\Sigma} &= I_0\left[(A-B)^2\Big/4 + C\left(\rho_o \sin^2\delta_0 + \rho_e \sin^2\delta_e\right)\right];\\ \bar{I}_{||,2\pi,\Sigma} &= I_0\left[(A+B)^2\Big/4 - C\left(\rho_o \sin^2\delta_0 + \rho_e \sin^2\delta_e\right)\right],\end{aligned} \tag{3.164}$$

where $A = \sqrt{(1-\rho_o)/(1+\rho_o)}; B = \sqrt{(1-\rho_e)/(1+\rho_e)}; C = (1-\rho_o)(1-\rho_e)$. For the average terms:

$$\begin{aligned}\bar{I}_{\perp,2\pi,\Sigma,av} &= I_0(1-\bar{\rho})^2 2\bar{\rho}\sin^2\bar{\delta}_{o,e};\\ \bar{I}_{||,2\pi,\Sigma,av} &= I_0(1-\bar{\rho})/(1+\bar{\rho})\left[1 - 2\bar{\rho}(1-\bar{\rho})^2\sin^2\bar{\delta}_{o,e}\right].\end{aligned} \tag{3.165}$$

Assuming also the cross-reference interference is entirely absent, the equations convert to ones for an isotropic plate, since full-wave retardance leaves the phase status of passing light unchanged:

$$\bar{I}_{\perp,2\pi,\Sigma,av} = 0; \quad \bar{I}_{||,2\pi,\Sigma,av} = I_0(1-\bar{\rho})/(1+\bar{\rho}). \tag{3.166}$$

If the full-wave retarder is replaced by a half-wave retarder making the phase difference $\delta = \pi$, intensities $I_{\parallel}$ and $I_{\perp}$ in transmission for the crossed and parallel polarizers are interchanged. For $\delta = \pi$, relations (3.158) and (3.159) become:

$$\begin{aligned}\bar{I}_{\perp,\pi,\Sigma} &= I_0\left[(A-B)^2\Big/4 + C\left(1 + \rho_o\rho_e + \rho_o\cos^2\delta_0 + \rho_e\cos^2\delta_e\right)\right];\\ \bar{I}_{||,\pi,\Sigma} &= I_0\left[(A+B)^2\Big/4 - C\left(1 + \rho_o\rho_e + \rho_o\cos^2\delta_0 + \rho_e\cos^2\delta_e\right)\right].\end{aligned} \tag{3.167}$$

Averaging the plate's optical properties and omitting the cross-reference interference terms keeping the comparative components for any equal number of reflections to the limit $m \to \infty$, the intensity relations become the opposites of Eq. (3.166):

$$\bar{I}_{\perp,\pi,\Sigma,av} = I_0(1-\bar{\rho})/(1+\bar{\rho}); \quad \bar{I}_{||,\pi,\Sigma,av} = 0. \tag{3.168}$$

Let us note that the virtually impossible occurrence of cophasal maxima for the cross-reference interference patterns with phases δ_o and δ_e corresponds to the equivalent maxima of multiple-beam interference along each vibration direction of a wave plate (see Eqs. (3.154)–(3.156)). If such limited-probability instances occur concurrently, the intensities of light transmitted by full-wave and half-wave plates between parallel or crossed polarizers will reach respective maxima:

$$\begin{aligned}\bar{I}_{||,2\pi,\Sigma,cophasal} &= (I_0/4)[(1-\rho_o)/(1-\rho_o) + (1-\rho_e)/(1-\rho_e)]^2 = I_0;\\ \bar{I}_{\perp,\pi,\Sigma,cophasal} &= I_0(1-\bar{\rho})^2\Big/(1-\bar{\rho})^2 = I_0.\end{aligned} \tag{3.169}$$

Another specific case of the extreme influence of two-beam interference is for the quarter-wave retarder having $\delta = \pi/2, 3\pi/2, \ldots$, etc. Keeping the earlier assigned designations, we can derive:

$$\bar{I}_{\perp,\pi/2,\Sigma} = I_0\Big\{ (A-B)^2 \Big/ 4 + \mathrm{C}\Big[(1+\rho_o\rho e)/2 + \rho_o \sin^2\Big(\delta_0 + \frac{\pi}{4}\Big) + \rho_e \sin^2\Big(\delta_e + \frac{\pi}{4}\Big)\Big]\Big\},$$
$$\bar{I}_{\perp,\pi/2,\Sigma} = I_0\Big\{ (A+B)^2 \Big/ 4 - \mathrm{C}\Big[(1+\rho_o\rho e)/2 + \rho_o \sin^2\Big(\delta_0 + \frac{\pi}{4}\Big) + \rho_e \sin^2\Big(\delta_e + \frac{\pi}{4}\Big)\Big]\Big\}, \tag{3.170}$$

In terms of average transmittance and reflectance, and ignored cross-reference interference, the ratio of Eqs. (3.170) is:

$$\bar{I}_{\perp,\pi/2,\Sigma,av} = \bar{I}_{||,\pi/2,\Sigma,av} = (I_0/2)(1-\bar{\rho})/(1+\bar{\rho}). \tag{3.171}$$

For conventional assumptions of equal-to-unity transmittances along both optical axes, we obtain:

$$\bar{I}_{\perp,\pi/2,ideal} = \bar{I}_{||,\pi/2,ideal} = \mathrm{I}_0/2. \tag{3.172}$$

Figures 3.17 and 3.18 depict the actual intensities of light transmitted by two crystal quartz wave plates computed by Eqs. (3.155) and (3.156) and (3.158) and (3.159). One may clearly observe that especially for any thin (zero-order) retarder both examples of interference events are characterized by intensity noise, caused by the cross-reference interference of light components incurring different amounts of reflection (compare the 2ρ and ρ^2 factors in Eq. (3.163)). Such noise is lower if interference is not noticeable on the double pass of a plate, i.e., if the coherence length of radiation is smaller than the double thickness of the retarder. This case is depicted in Figs. 3.17b and 3.18b for two waveplates: multiple order and zero order. To verify the concept of limited coherence length, let us further reduce the approximation by disregarding the rest of the cross-reference interference terms for the wave components having different numbers of the surface reflections.

If we keep the comparative interference term for interfering beams with only two reflections, since the change of optical path lengths for these beams: $\mathrm{L}_{3\delta} = 3(\mathrm{n_e} - \mathrm{n_o})\mathrm{h}$, is much lower than the length difference for any cross-reference pair: $\mathrm{L}_{2\delta\mathrm{e}\,+\,\delta} = [2\mathrm{n_e} + (\mathrm{n_e} - \mathrm{n_o})]\mathrm{h}$ or $\mathrm{L}_{2\delta\mathrm{o}\,+\,\delta} = [2\mathrm{n_o} + (\mathrm{n_o} - \mathrm{n_e})]\mathrm{h}$, the intensities of the light beams with the limited coherence length after passing through the analyzer are:

$$\bar{I}_{\perp,\Sigma,\mathrm{lim}} = \frac{I_0}{4}\Big\{ \Big(\sqrt{(1-\rho_o)/(1+\rho_o)} - \sqrt{(1-\rho_e)/(1+\rho_e)}\Big)^2 + 4(1-\rho_o)(1-\rho_e)\big[\sin^2(\delta/2) + \rho_o\rho_e \sin^2(3\delta/2)\big]\Big\}. \tag{3.173}$$

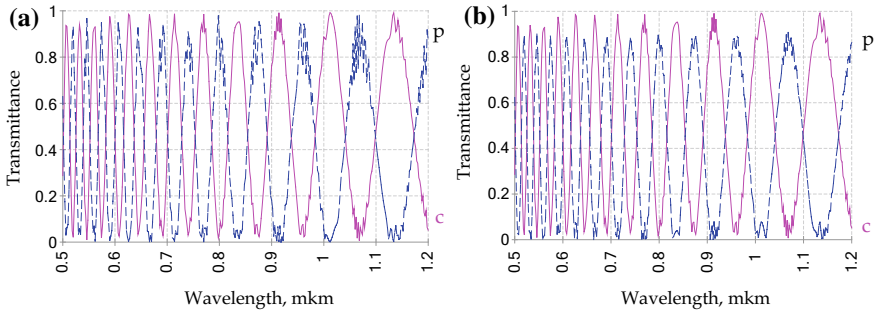

Fig. 3.17 Interference phenomena in coherent (**a**) and partially-coherent (**b**) radiation for a multiple-order retarder: the parallel and crossed axes orientations of the polarizer and the analyzer are marked as *p* and *c*, respectively

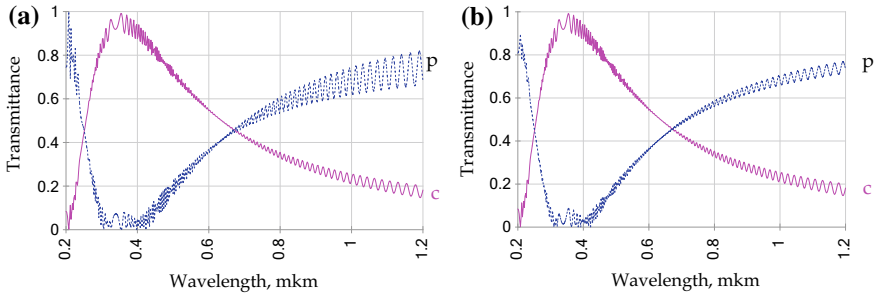

Fig. 3.18 Interference phenomena in coherent (**a**) and partially-coherent (**b**) radiation for a zero-order waveplate: the parallel and crossed axes orientations of the polarizer and the analyzer are marked as *p* and *c*, respectively

$$\bar{I}_{||,\Sigma,\mathrm{lim}} = \frac{I_0}{4}\left\{\left(\sqrt{(1-\rho_o)/(1+\rho_o)}+\sqrt{(1-\rho_e)/(1+\rho_e)}\right)^2 - 4(1-\rho_o)(1-\rho_e)\left[\sin^2(\delta/2)+\rho_o\rho_e\sin^2(3\delta/2)\right]\right\}. \tag{3.174}$$

Equations (3.173) and (3.174) opposite to Eqs. (3.158) and (3.159) have the second-order phase terms, but these terms are the derivatives of the expected retardance δ and not of cross-reference phase shifts $2\delta_o$ and $2\delta_e$ caused by the optical thickness of each extra double pass along every single vibration direction. Figure 3.19a shows the intensities resolved by Eqs. (3.173) and (3.174) (curves 3, 4) in comparison with relations (3.155) and (3.156) for fully coherent radiation (noisy curves 1, 2). The retarder, a first-order λ/8 plate for 532 nm, was notably chosen to have its phase shift δ not to be a multiple of either π/2 or π/4. The graphs clearly demonstrate that Eqs. (3.173) and (3.174) compute the space averaged intensity of radiation transmitted by the retarder, both representing integrated light whose coherence properties are not distinguished on either double cross-optical paths $3\delta_o - \delta_e$ or $3\delta_e - \delta_o$. It is also seen (curves 5, 6) that trivial expressions

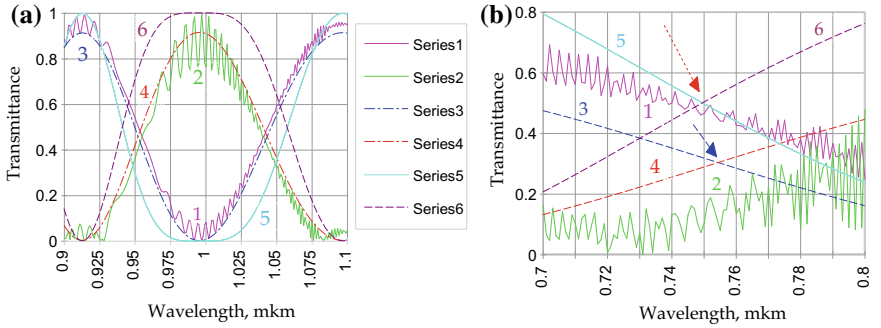

Fig. 3.19 Computed cross-reference interference effects in coherent light for a quartz (**a**) and a high-reflecting (**b**) retarder

(3.151) and (3.152) do not closely reflect the actual phase retardance caused by the wave plate even for relatively low surface reflectances. The opposite case for the surfaces of each plate having increased reflectances: $\rho_{o,\Sigma} = \rho_0 + 0.2; \rho_{e,\Sigma} = \rho_e + 0.2$, is seen in Fig. 3.19b. In this case, the spectral dependencies for a zero-order $\lambda/4$ retarder at wavelength $\lambda = 750$ nm are also computed, first, by presuming completely coherent radiation (lines 1, 2), and, second, spatially integrated, and thus not cross-interfering, light with limited coherence length (lines 3, 4). Such a plate transmittance counted as for an ultimate nonreflecting element, omitting all the reflection terms (lines 5, 6), is sufficiently different from the values obtained by Eqs. (3.173) and (3.174) (compare the indicated points of intersections). Lines 3 and 4 exhibit some consistent phase difference instead of very noisy lines 1 and 2 for coherent light. Besides, it may be demonstrated (see beginning of this paragraph), that implementation, as in Fig. 3.19b, of the auxiliary, but equal surface reflectances $\rho_{o,\Sigma}$ and $\rho_{e,\Sigma}$ becomes equivalent to materialization of unequal front plate and back plate reflectances, such as $\rho_{o,1} = \rho_o$ and $\rho_{e,1} = \rho_e$ and $\rho_{o,2} = \rho_o + 0.5$ and $\rho_{e,2} = \rho_e + 0.5$, since:

$$\left(1 - \rho_{o,\Sigma}\right)^2 = \tau_{o,\Sigma}^2 = \tau_{o,1}\tau_{o,2} = \left(1 - \rho_{o,1}\right)\left(1 - \rho_{o,1}\right);$$
$$\left(1 - \rho_{e,\Sigma}\right)^2 = \tau_{e,\Sigma}^2 = \tau_{e,1}\tau_{e,2} = \left(1 - \rho_{e,1}\right)\left(1 - \rho_{e,1}\right).$$

3.3.4 Stabilization of Radiation Emission

Owing to unavoidable correlation of light oscillations, the inevitable instabilities of emission spectrums and propagation directions are notably manifested while observing laser and pulse-modulated light. Either the spatial or the temporal interference pattern formed by optical elements interacting with unstable radiation generated by laser and pulsed sources becomes highly observable. Therefore, one way to make measurements in laser and pulsed radiation is aligned with reduction

of instabilities of intensity with concurrent decrease of fringe visibility for all likely interference events that are randomly distributed in space or time.

Let us consider a way for practical stabilization of either a spatial or a temporal distribution of partially coherent light emitted by any pulsed or continuous source, looking concurrently for an appropriate manner for minimization of observability for all coexisting interference patterns. To moderate the most notable impact of interference noise for radiation emitted by pulsed lasers and, to some extent by pulsed lamps, a two-channel measurement system is commonly realized. Any relatively large expansion, distortion, or longitudinal mode discrimination of the laser light pulses creates irregular temporal and spatial formations of pulse-to-pulse spectral patterns [3.29, 3.39]. For laser resonators a random change of localization for either an uncoated glass or a crystal surface owing to, for example, the resonator's irregular pump heating by $\lambda/2$ or the transformation of a coated surface reflectance by $\Delta\rho/\rho \cong 10^{-3}$, is sufficient for the excitation of a new longitudinal mode. Only almost complete elimination of any stray-mode discrimination providing the mode-locking state results in practically reproducible generation of laser light [3.32]. Similar effects [3.40], though to lower extents, accompany unstable settings of pulsed lamps. Accordingly, the influence of interference caused by temporal fluctuations or spatial irregularities in a spectral composition of radiation emitted by a lamp should be reduced when the lamp's disturbance factors are removed.

The two-channel measurement system using a pulsed laser or lamp source with the goal of neutralizing temporal and spatial instabilities of signal detection due to interference noise is shown in Fig. 3.20. Pulsed laser or lamp 1 irradiates two similar channels, measurement channel 5 and reference channel 8, via spectral selector or monochromator 2, spatial filter 11, and beam splitter 3. Both channels have identical detectors 6 and 7 and attenuators 4 and 5. Attenuators 4 and 5 are tunable translucent opal glass stacks or integrating spheres, if higher spatial uniformity is needed. The distances between the detectors and the attenuators may vary, but must be long enough to produce uniform irradiation of each detector. The measurement system allows one to modify channel attenuation factors, compensating for the desired dynamic range of any attenuation factors to be measured. It also maintains channel signals unchanged, concurrently integrating spatial fluctuations of the radiation intensity profile in every beam. Each channel signal is registered separately or synchronously by ratio meter 10 with a sample P_i to be tested.

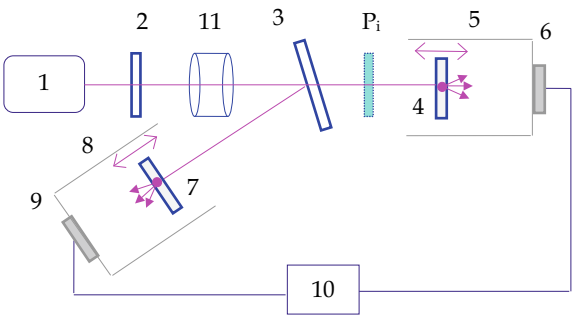

Fig. 3.20 Measurements with variable splitting and attenuation

Separate verification experiments [3.35, 3.37, 3.39] were conducted using a Nd:glass laser at $\lambda = 1.053$ μm and a flash lamp built into a pulsed spectrophotometer for the 400–750-nm spectral domain. In the laser experiment, broadband laser radiometers ΦΠМ (see Chap. 4, Fig. 4.7) were used as two combined systems of elements 4–6 and 7–9 in Fig. 3.20. A practically identical in structure dual-channel system based on a ΦМ-89 pulsed spectrophotometer (Chap. 4 and Fig. 4.15) was utilized during the lamp experiment. First, the laser measurements were made using a not optimized laser cavity consisting of a right-angled prism as its total internal reflector and a set of glass plates as the output coupler. Random error of measurements in series was evaluated by the standard deviation of the mean of up to ten ratios of signals in the measurement and reference channels. These measurements were characterized by root-mean-square deviation $2\sigma = (1.5–2)\%$. Implementation of a dense opal glass and a collimator functioning as spatial filter 11 eliminating respective spatial and polarization changes (see Fig. 3.20) due to formation of a quasi-parallel uniform beam via diffusely transmitted radiation caused 2σ reduction only by 0.3–0.5%. At the same time, when the cavity prism and glass set were replaced by a multiple-layer high-reflecting mirror and an output coupler, made using coatings on a similar wedged substrate, the initial reduction was doubled and tripled, reaching $2\sigma = (0.5–0.6)\%$. That magnitude is shown as the opening point in Fig. 3.21. These measures for redesigning the laser resonator eliminating all consecutive multireflecting surfaces led to temporal and spatial stabilization of the laser emission spectrum to a base level.

As the second step in the attempt to further reduce any potential interference effects, the notion for discrimination of laser resonator longitudinal modes was tested. These modes were created by uncoated surfaces of the active element inside the laser cavity. To suppress the effects of the surfaces, the efficiency $K = (1 - \rho_1\rho_2)^{-1}$ (see Eq. (2.5)) of total multiple reflections inside that laser resonator with a semitransparent output coupler (series 1 in Fig. 3.21) was increased from $K = 2$ to $K = 4$ by implementing the output coupler with $\rho_2 = 0.75$ (series 2). Finally, its ultimate efficiency was further increased to $K = 10$ by deploying a 90% reflecting output coupler in the system (series 3). The highest elimination of the implied interference effects during any single measurement by the dual-channel system examined was conclusively achieved by the additional AR coating of the second surface of the beam splitter, and by increasing the reflectivity of its first surface to $\rho_{sp1} = 0.2$, 0.5, and 0.8, respectively.

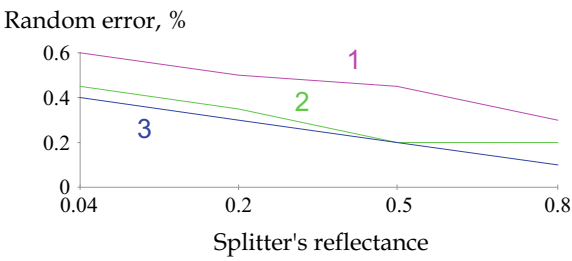

Fig. 3.21 Random error of dual-channel measurements versus splitting efficiency

Spectral measurements with pulsed lamps can be accompanied by similar effects as with lasers. Usually, a relatively slow repetition rate of lamp pulses in comparison with the pulse recovery time needed to return its heated emitting plasma to a steady-state condition is the major reason for spectral instability in the pulsed lamp's emission. As a result, the intensity of every linear spectral component of thermal emission can fluctuate with respect to a continuous portion of plasma emission as a blackbody or a graybody. Hence, the ratio of the continuous spectrum to the totality of the pulsed components emitted by a lamp does not remain constant [3.31]. The lamp interference experiments were done using a ΦM-89 pulsed spectrophotometer (see Chap. 4) with a tungsten filament flash lamp having a pulse discharge energy 90 J and time width $t = 0.9$ ms [3.39]. Initially the measurement channel (see Fig. 3.20) had a grating monochromator as a spectral selector, but the reference channel used a "white" integrated lamp spectrum. To maintain the same spectral intervals as in the measurement channel, a set of interference filters, matching the maximum wavelength λ_{max} and bandwidth $\Delta\lambda$ of the transmission spectrum, was installed in the reference channel.

The results are given in Table 3.1. A medium-density translucent opal glass was used as the spatial filter as in the laser experiment, making sure spatial fluctuations of the discharge did not affect the experimental results. Subsequently, measurements were made at short, but equal time intervals, then at medium time intervals, and, finally, at uneven time intervals between pulses, as shown in Table 3.1. To verify the effects of possible spectral distinctions between the channels, measurements were made at two levels of a spectral width in the measurement channel—unequal to and equal to $\Delta\lambda$ of the reference channel. Following that evaluation of the spectral character for the temporal fluctuations observed, the first surface of the beam splitter was high-reflection-coated to $\rho_1 = 0.2$, and the second surface was AR-coated to $\rho_2 = 0.005$. To raise the plasma temperature and increase the

Table 3.1 Root-mean-square deviation of spectral measurement with pulsed lamp

Measurement conditions	Δt (s)	Measurement channel: λ = 534 nm			
		$\Delta\lambda$ = 6 nm		$\Delta\lambda$ = 12 nm	
		Reference channel			
		λ = 534 nm $\Delta\lambda$ = 12 nm	"White light"	λ = 534 nm $\Delta\lambda$ = 12 nm	"White light"
Complement condition of the setup	10 15 10, 15, 20	1.4 0.9 1.5	1.1 0.6 1.1	1.3 0.7 1.2	1.0 0.5 1.1
Spatial filter is inserted	10	1.3	1.2	1.2	1.1
Splitter is HR & AR coated	10	0.5	0.7	0.4	0.6
Lamp is in the reflector	10 15	0.7 0.4	0.8 0.3	0.6 0.4	0.8 0.4
Pre-heated lamp in the reflector	15	0.2	0.3	0.15	0.3

effectiveness of plasma broadband emission, the lamp was placed inside a tight mirror reflector [3.39, 3.40]. The best results were obtained by a preliminary lamp heating with a pulse train of 10–15 pulses, and by providing measurements with the smallest, but sufficient time intervals for the plasma, pulsed spectrophotometer, and its registration system to fully recover (final raw).

3.3.5 *Polarization Measurements*

For the experimental verification of interference effects with the birefringent plates discussed above, likely influences of multiple reflections were measured using three equivalent quartz wave plates [3.43]. The first plate was not coated, and the other two had, respectively, a single surface and front and back surfaces coated to 10 times less residual reflectance than the plate with no coating. For a retarder with a single reflecting surface, Eqs. (3.155) and (3.156) become:

$$\bar{I}_{\perp,\Sigma,single} = I_0\left\{\left[(\sqrt{(1-\rho_o)}/2 - \sqrt{(1-\rho_e)}/2\right]^2 + \sqrt{\tau_o\tau_e}\sin^2(\delta/2)\right\}, \quad (3.175)$$

$$\bar{I}_{||,\Sigma,single} = I_0\left\{\left[(\sqrt{(1-\rho_o)}/2 + \sqrt{(1-\rho_e)}/2\right]^2 - \sqrt{\tau_o\tau_e}\sin^2(\delta/2)\right\}. \quad (3.176)$$

In terms of average ordinary–extraordinary surface transmittance $\bar{\tau}$, Eqs. (3.175) and (3.176) are:

$$\bar{I}_{\perp,\Sigma,single,av} = I_0\bar{\tau}\sin^2(\delta/2); \quad \bar{I}_{||,\Sigma,single,av} = I_0\bar{\tau}[1-\sin^2(\delta/2)]. \quad (3.177)$$

The transmission spectrums, computed via optical constants in [3.44] for the wave plates with no coatings, one face coated, and both surfaces coated leading to no face reflections (Eqs. (3.173–3.176, 3.151, and 3.152) are shown in Fig. 3.22.

The experiments were performed using a standard PerkinElmer 330 spectrophotometer in two spectral regions: 500–700 nm and 900–1100 nm. Three identical 15^{th}-order quarter-wave quartz wave plates for $\lambda = 632.8$ nm were evaluated by another method [3.45] as having identical retardance within $\lambda/500$. Broadband AR coatings had reflectances $\rho \leq (0.5–0.7)\%$ from 0.4 to 1.2 μm. Two equivalent AR-coated Glan–Thompson polarizing prisms were utilized as the polarizer and the analyzer, respectively. The alignment of the prisms and all wave plates to be tested was made via a He–Ne laser. Corrections of the 100% lines were performed for the parallel vibration directions of the polarizer and analyzer. The dark signal of the spectrophotometer at the crossed polarizer and analyzer without any wave plates did not exceed ±0.1%. The spectral resolution of all studies was set to 0.1–0.2 nm in the visible and IR regions. The measured transmission spectrums in the visible region are depicted in Fig. 3.23. Some slight differences seen among the curves in Figs. 3.22 and 3.23 were created by intensity fluctuations (the IR curves looked the same [3.43]).

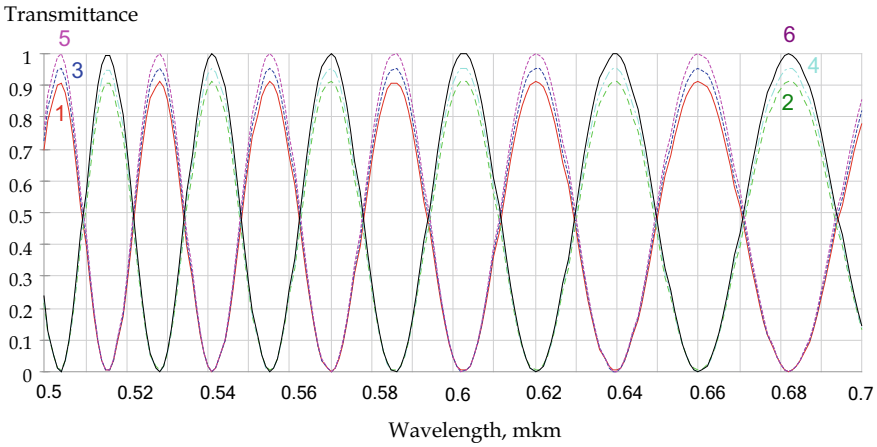

Fig. 3.22 Spectral transmittance of quartz 15th order quarter-wave retarders @ 632.8 nm between crossed (1, 3, 5) and parallel (2, 4, 6) polarizers: 1, 2 - no coatings; 3, 4 - one face AR coated; 5, 6 - no face reflections

The analysis and experiments confirm that every individual effect for retro-reflected beams participating in the comparative and cross-reference interference of ordinary and extraordinary radiation components with different and equal numbers of reflections can be quantified. The experiments demonstrated that cross-reference interference, concerning waves of the orthogonal vibration directions with an unequal number of retroreflections, is responsible for interference terms, which are manifested as errors of phase measurements. Instead, the impact of interference for

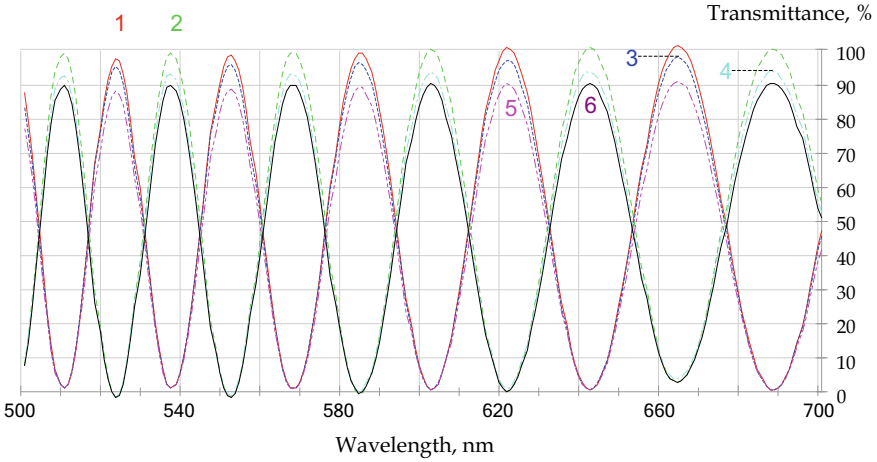

Fig. 3.23 Transmittance obtained by spectrophotometer PE 330 of 15th order quarter waveplates at 632.8 nm between crossed (1, 3, 5) and parallel (2, 4, 6) polarizers: first plate without coatings (5, 6), second and third plates with a broad band AR coating on one face (3, 4) and on both surfaces (1, 2)

light components propagating in parallel with opposite states of polarization and equivalent numbers of reflections affects the single-pass retardance in a linear and direct way. That effect is responsible for the slight shift of the total retardance in intensity measurements of any reflecting wave plate estimated as an AR-coated not reflecting retarder. The experimentally confirmed predictions of main Eqs. (3.155) and (3.156) via Eqs. (3.173) and (3.174), as well as (3.175) and (3.176), and conversions of all those equations to ones known for isotropic substances indicate that the intensity of light transmitted by a linear retarder can be correctly predicted if both bulk and surface properties are accounted for. Even when the retarder has relatively high surface reflections, its transmission intensity measurement via radiation with a limited coherence length should detect an increase of its phase retardance.

The concept of interference-effect analysis in coherent light, while omitting third-order and higher reflection terms, makes linear retardance of a deliberately reflecting wave plate virtually undistinguishable from random noise (see Fig. 3.19). Such noise is viewed as random, since it follows actual fluctuations of emission of a light source and conversions of its coherence length. The only exception corresponds to quarter-wave retardance, leading to destructive interference for retroreflected components when interference extrema are lowest (see Fig. 3.18). Depending on the applications of a retarder with reflecting surfaces, the multiple reflections in spontaneous or spatially integrated light with a restricted coherence length linearly increase or decrease the single-pass phase retardance. Other reductions of interference effects are seen at spectral points at which the intensity of light transmitted by the retarder between crossed or parallel polarizers tends to zero: the full-wave and half-wave retardance – no retroreflection effects are observed. For all other phase points, a linear retarder with reflecting surfaces, in contrast to any coated wave plate with identical internal properties, moves the expected magnitude of the transmission to a new wavelength. Thus, if a wave plate is expected to function only at spectral points of specific phase extrema, such as those leading to any multiple of the half-wave shift, that wave plate does not require any antireflection coating. That could be useful for coherence-restrained applications of uncoated wave plates.

When retardance measurements are obtained with partially coherent radiation, the resultant interference effects can make transmittance measurement results look different. As follows from Eqs. (3.154) to (3.158) in the region of a quarter-wave retardance the essential phase exchange provided by the interference terms for equivalent numbers of reflections which are participating in the comparative pattern becomes significantly diminished. This occurs since the derivative of the function $\sin^2[(2\ m - 1)\pi/2]$ tends to zero in the regions described. One can clearly observe how dramatically the oscillations in Figs. 3.17 and 3.18 drop around every quarter-wave point. The interference effect is also apparent in Fig. 3.19a, but is much less visible in Fig. 3.19b, where the cross-reference interference for the retroreflecting terms with different numbers of reflections creates intensive random noise owing to the high reflectance of the retarder surfaces. Similar effects when interference fringes are enhanced or diminished at the extrema of interference, as well as when the fringes are averaged via spatial or temporal integration of multiple optical paths of light propagation, can be observed in other experiments (see paragraphs 6.5 and 11.4 and references therein).

One notion to perceive is that multipath-interference noise occurs owing to spatial as well as temporal interpolation of multiply retroreflected light components contributing to the interference observed as a result of the interpolation. If each of these interpolating components is resolved either spatially or temporarily, no interference occurs, and multipath interference noise vanishes. Examples of measurements without interference noise when propagation of retroreflected light is guided to its own path can be seen in cavity ringdown spectroscopy applications (see paragraph 7.3) or other time-resolved and spectrally resolved multipath resonator studies [3.83–3.85]. This way, for example, the minute residual birefringence was measured in the time domain and normalized by the sum of intensities of two orthogonal components [3.84], and polarization mode-coupling in a polarization-maintaining fiber was resolved via a Fourier transform process applied to reconstruct spectral-phase changes [3.85].

3.4 Diffraction Corrections and Gratings in Radiometry and Photometry

3.4.1 Diffraction on Beam-Defining Apertures

Most radiometric and photometric methods do not intend to obstruct the radiation to be measured, thus involving apertures that do not shield beams, but rather baffle possible stray light. The only beam-defining apertures used for the measurements are detector frames typically set at immediate proximities of their sensitive elements (see Chaps. 2 and 4 for details). In circumstances for which apertures are fully or partially defining, serving as entrance pupils of optical systems, while high accuracy of photometric and radiometric measurement remains essential, diffraction phenomena at such apertures can notably destroy approximations of geometrical optics that presume infinitely small wavelengths $\lambda_i \rightarrow 0$ of the measured radiation (see Chap. 1), thus causing measurement error. Two limiting cases of aperture-defined geometry are (1) where the detector is irradiated by light from a partially viewed expanded source and (2) where the detector is overfilled by point-source light.

Figure 3.24 illustrates the geometry of either a limiting-defining or nonlimiting circular aperture between a source of light and a detector when the source or

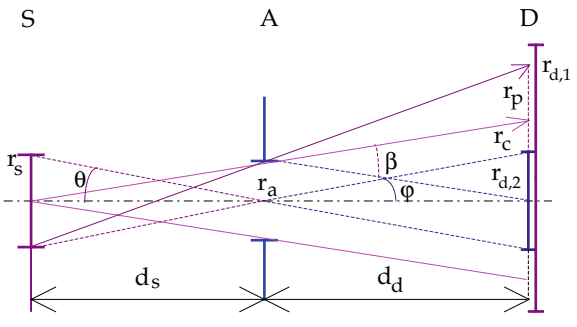

Fig. 3.24 Diffraction on limiting and nonlimiting aperture

detector or both are not necessarily point objects (see paragraphs 1.2, 2.1). From the standpoint of geometrical optics [1.1, 3.48, 3.49], for all objects with cylindrical symmetry considered, the irradiation of the detector's plane by source S of radius r_s at distance d_s to aperture A of radius r_a creates a fully irradiated circle of radius r_c:

$$\begin{aligned} r_c &= r_a + [(r_a - r_s)/d_s]d_d \\ &= r_a(1 + r_s/r_d) - r_s d_d/d_s = r_a(d_s + d_d)/d_s - r_s d_d/d_s. \end{aligned} \tag{3.178}$$

Here d_d is the distance from the detector of radius r_d to aperture A. The finite height of source S causes its geometrical projection onto the detector's plane to have a circular penumbra of radius r_p:

$$r_p = r_a + [(r_a + r_s)/d_s]d_d = r_a(d_s + d_d)/d_s + r_s d_d/d_s. \tag{3.179}$$

For radiometric observation via a defining aperture, while applying paraxial treatment enabling a small-angle approximation for viewing solid angle θ of source S from the center of aperture A: $\Omega = 4\pi\sin^2(\theta/2) \approx \pi\theta^2$, of the flux Φ_1 received by detector D for a source radiance L (see Eq. (1.31)) is:

$$\Phi_1 = \pi r_a^2 2\pi(1 - \cos\theta)L = \pi r_a^2 4\pi \sin^2(\theta/2)L \underset{\sin\theta\to\theta}{\cong} \pi^2\theta^2 r_a^2 L. \tag{3.180}$$

For the nondefining, e.g., baffling aperture, detector irradiation E_d is given by the inverse-square law (Eqs. (1.17)–(1.61)), making the flux Φ_2 received in the paraxial approximation via aperture view angles θ and φ:

$$\Phi_2 = E_d \pi r_d^2 = \pi^2 r_s^2 r_d^2 L \Big/ (d_s + d_d)^2 \underset{\tan\theta,\varphi\to\theta,\varphi}{\cong} L(\pi\theta\varphi d_s d_d/(d_s + d_d))^2. \tag{3.181}$$

Consider diffraction of source S light of wavelength λ on aperture A, first, as underfilling, and, second, as overfilling detector D. In both cases, source S makes a directly irradiated region of radius R_c and a penumbra of radius R_p. The detector irradiance in each case is formed as an image of the source S via the diffracting aperture A [1.1]. The spread function of irradiance E_d is that for Fresnel diffraction by circular aperture A given as [3.46–3.51]:

$$\begin{aligned} E_d &= \left(\pi^2 r_a^4/\lambda^2 d_s^2 d_d^2\right) \cdot \Lambda(u, v) \cdot I(u, v) \\ &= \left(\pi^2 r_a^4/\lambda^2 d_s^2 d_d^2\right) \cdot \Lambda(u, v) \cdot 4\left[U_1^2(u, v) + U_2^2(u, v)\right]/u^2, \end{aligned} \tag{3.182}$$

where β is the viewing angle of the edge of aperture A to the center of the source and detector that in the small-angle approximation is $\beta = r_a(1/d_s + 1/d_d)$, $u = (2\pi/\lambda)[(d_s + d_d)/d_s d_d]r_a^2$ and $v_{d(s)} = (2\pi/\lambda)r_a r_{d(s)}/d_{d(s)}$ are new variables, and I(u, v) is the light intensity distribution, being the spread function for Fresnel diffraction which is

defined by Lommel functions $U_1(u, v)$ and $U_1(u, v)$ [3.46]. The light intensity distribution I(u, v) in the detector's plane can be expanded into the form [3.46]:

$$I(u,v) = \frac{4}{u^2}\left[1 + V_0^2(u,v) + V_1^2(u,v) - 2V_0^2(u,v)\cos\left(\frac{u}{2} + \frac{v^2}{2u}\right) - 2V_1^2(u,v)\sin\left(\frac{u}{2} + \frac{v^2}{2u}\right)\right], \tag{3.183}$$

where n^{th} functions $V_n(u, v)$ are defined via Bessel functions of the first kind of order (n + 2s) [3.47]:

$$V_n(u,v) = \sum_{s=0}^{\infty}(-1)^s (v/u)^{n+2s} J_{n+2s}(v). \tag{3.184}$$

$\Lambda(u, v)$ in (3.182) is the autocorrelation function, that is: $\Lambda(u, v) = 0$ at $v \geq v_s + v_d$ and $\Lambda(u, v) = 1$ at $u < v_d - v_s$.

Considering the source radiance and detector sensitivity as constant, the total flux Φ integrated over the detector surface obtained via diffraction of the source radiation on aperture A is [3.51]:

$$\Phi(u, v_s, v_d) = \left(\pi^2/2\right)\theta^2 r_a^2 L \int_0^{v_s+v_d} I(u,v)\Lambda(u,v)v\,dv, \tag{3.185}$$

where $\Lambda(u, v) = 0$ for $v \geq (2\pi r_a/\lambda)(\theta + \varphi) \cong v_s + v_d$. In the first radiometric case, for detector D to view source S flux via a limiting aperture, $r_d \geq r_p$, the ratio of flux Φ due to diffraction on aperture A obtained by Eq. (3.185), to flux Φ_1 obtained by radiometric considerations by Eq. (3.180) is [3.48, 3.50]:

$$F_1(u, v_s, v_d) = \frac{1}{2}\int_0^{v_s+v_d} I(u,v)\Lambda(u,v)v\,dv \underset{v>u;\,\Lambda=1}{=} \frac{1}{2}\int_0^{v_d} I(u,v)v\,dv. \tag{3.186}$$

For a point source or a point detector, which can be treated via reciprocity: $v_s = 0$ [3.51, 3.52]:

$$F_1(u, 0, v_d) \underset{v>u}{\cong} 1 - \frac{2v_d}{\pi\left(v_d^2 - u^2\right)} + \frac{\cos^2 v_d}{\pi\left(v_d^2 - u^2\right)} + \ldots \underset{v\gg u}{\cong} 1 - \frac{2}{\pi v_d}. \tag{3.187}$$

For the radiometric case when detector D is placed within a fully illuminated region, $r_d < r_c$, thus making a factual radiance or luminance observation (see Chap. 2), and when the relation in the first case is reversed, $u > v$, the ratio of the

flux Φ obtained via diffraction on aperture A obtained by relation (3.185) to the flux Φ_2 obtained by the radiometric consideration by Eq. (3.181) is [3.51]:

$$F_2 = \left[\frac{1}{2}\left(\frac{u}{v_d}\right)^2\right] \int_0^{v_s+v_d} I(u, v_s, v_d)\Lambda(u, v)vdv \underset{u>v}{=} \frac{u^2}{2v^2}\int_0^{v_d} I(u, v)vdv. \tag{3.188}$$

Since for u $\gg$ v, successive terms multiplied by $v^2/2u$ in Eq. (3.183) decay rapidly, Eq. (3.183) can be approximated with reasonable accuracy by only the V_0 and V_1 terms [3.52]:

$$I(u, v) \underset{u\gg v}{=} \frac{4}{u^2}\left[1 + J_0^2(v) + \frac{v^2}{u^2}J_1^2(v) - 2J_0^2(v)\cos\left(\frac{u}{2} + \frac{v^2}{2u}\right) - 2\frac{v}{u}J_1(v)\sin\left(\frac{u}{2} + \frac{v^2}{2u}\right)\right]. \tag{3.189}$$

Integrating and approximating for u $\gg$ v_s, v_d in Eq. (3.185) with relation (3.189) gives [3.52]:

$$F_2(u, v) \underset{u\gg v}{\cong} 1 + J_0^2(v) + J_1^2(v) - \frac{4}{v}J_1(v)\cos\left(\frac{u}{2} + \frac{v^2}{2u}\right). \tag{3.190}$$

For v $\gg$ 1, Eq. (3.190) may be further simplified by using asymptotic forms of functions J_0 and J_1:

$$F_2(u, v_d) \underset{v_d\gg 1}{\cong} 1 + \frac{2}{\pi v_d} - \frac{4}{v_d}\sqrt{\frac{2}{\pi v_d}}\sin\left(v_d - \frac{\pi}{4}\right)\cos\left(\frac{u}{2} + \frac{v_d^2}{2u}\right). \tag{3.191}$$

On the axis of the paraxial optical system for u $\gg$ v, Eq. (3.190) and rigorous Eq. (3.183) both lead to the ratio of intensities for the diffracted and geometrically transferred light as [3.52]:

$$F_2(u, 0) \underset{u\gg v}{=} 2 - 2\cos(u/2). \tag{3.192}$$

Equation (3.192) gives the ratio of intensities for the on-axis diffraction pattern, compared to the geometrical-optics approach, and provides corrections due to diffraction effects on any baffling aperture for a radiometric measurement to be made. Figure 3.25 provides numerical values of the ratio F_2(u, 0) at λ = 500 nm, revealing dual-beam interference-like phenomena. Figure 3.26 illustrates the diffraction correction ratio F_2 obtained by Eq. (3.191) for $u/v_d = 10$ and λ 500 nm. Figure 3.27 gives diffraction ratio F_1 obtained by relation (3.186) comparing v > u and v $\gg$ u approximations. More precise, but more complicated analytical expressions for diffraction corrections can be invoked if higher accuracy is required, along with a detailed numerical evaluation [3.53–3.62].

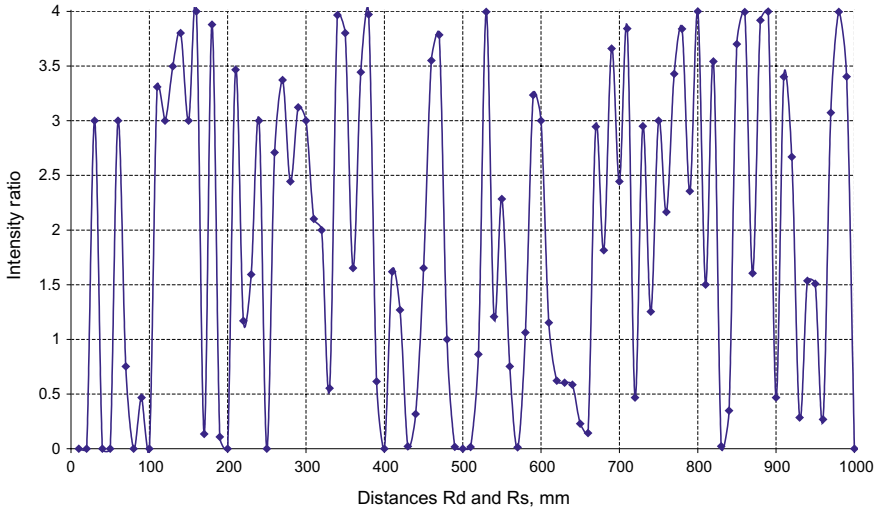

Fig. 3.25 On-axis ratio of diffracted to geometrical intensities versus distance Ds = Dd at Ra = 25 mm for 500-nm wave

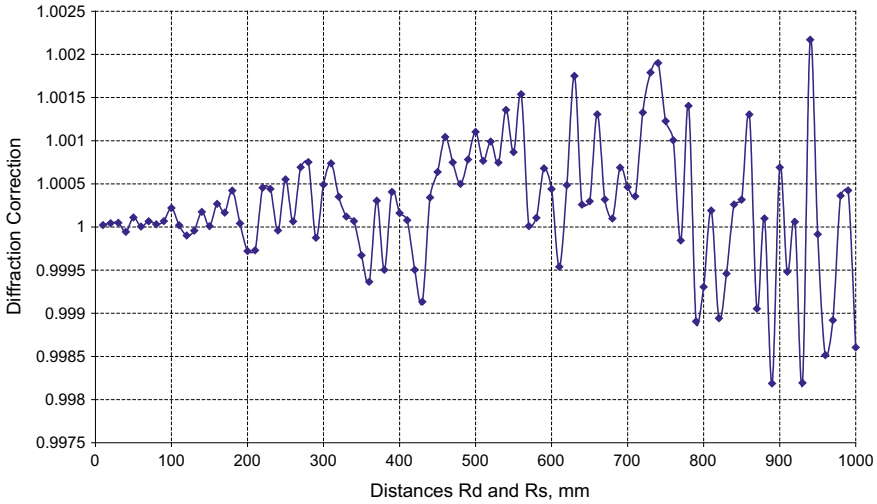

Fig. 3.26 Diffraction correction ratio F2 versus distance Ds = Dd at Ra = 25 mm, Rd = 5 mm for 500-nm wavelength

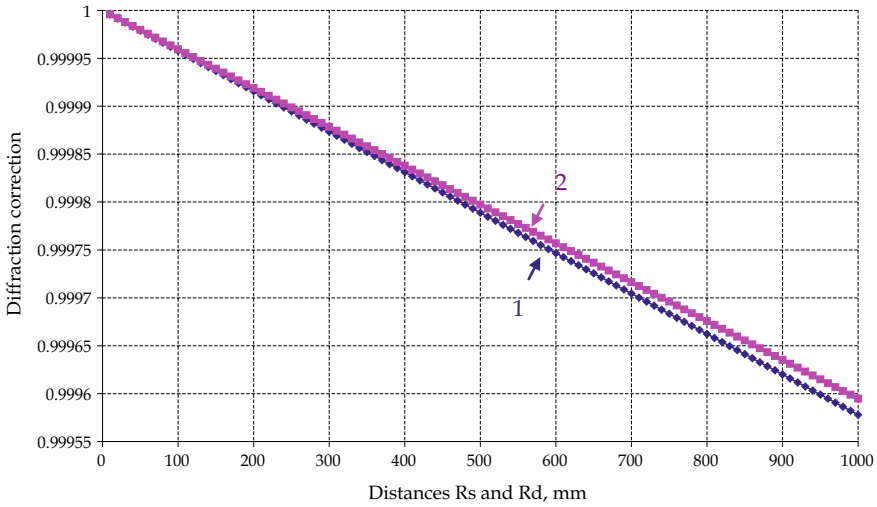

Fig. 3.27 Diffraction correction F1 versus distance Ds = Dd for Ra = 5 mm, Rd = 25 mm at approximation: (1) v > u; (2) v ≫ u

3.4.2 Maxima-Shifting Anomaly for Step-Function (Surface-Relief) Diffraction Gratings

In view of diffraction corrections in radiometry, let us examine the applicability of diffraction gratings for optical measurements. It has been known almost since introduction that diffraction gratings exhibit abrupt anomalies at critical diffraction angles or wavelengths which may occur owing to finite beam sizes for wide-angle diffraction phenomena or as deviations from the wavelength of maximum blaze efficiency for echelle gratings. Step-function (surface-relief) diffraction gratings, being susceptible to the step-shadowing effects for incident and for diffracted light, may exhibit certain angular anomalies of diffraction maxima at much smaller angles than expected in view of all other considerations. The step-function diffraction gratings often maid as the surface-relief gratings consist of recurring, mainly rectangular steps in the sub-wavelength-thick layers, could exhibit the maxima-shifting anomalies for relatively small angles of incidence or small angles of observation, when such a grating does not have the sufficiently high number of grating periods. The first-order maxima-shifting anomaly follows the phase modulation of the step around the grating normal: away from the direction of light illumination for phase thicknesses between π and π/2 or toward the illumination direction for phase thicknesses between π/2 and 0, with the tendency to be most pronounceable as the phase thickness tends to π and to zero.

Traditionally, for the diffraction grating consisting of a large number N of parallel grooves with period p, the grating equation: $\sin\Theta + \sin\Theta_0 = m\lambda/p$, that defines the positions of the maxima for the angles of diffraction Θ versus angles of incidence Θ_0 and light wavelength λ is considered fundamental and thus is not expected to change [1.1]. Nonetheless, certain grating anomalies have been

revealed and also experimentally confirmed [3.63, 3.64]. The known echelle grating anomalies reported were for wavelengths of the maximum blaze efficiency slightly different from wavelengths satisfying the wavelength equation and for the angular positions of some diffraction orders violating the grating equation. An explanation has been given [3.64] for the angular grating anomaly as the straightforward result of the finite beam size for the observed strictly wide-angle diffraction phenomena. However, for medium to small angles of incidence, the anomalies seemed vanish, with the grating equation correctly predicting the angular positions of all interference maxima. At the same time, various upcoming technologies, pushing the dimensions of the grating features into tens of nanometers, provide new ways to make diffraction gratings, such as of the step-function profile made by relieving alternating surfaces of solid-state structures and consisting of periodic rectangular steps with thicknesses being less than of the wavelength of incident light. These thin step-function gratings are often considered as making negligible shadows to affect the grating equation, especially at the angles of incidence and diffraction for which the small-angle approximation, $\cos\Theta \cong \cos\Theta' \cong 1.0$, could be used [3.65].

As detailed below, even at relatively small angles of incidence and diffraction, nearly satisfying the small-angle approximation, the step-function diffraction grating with insufficiently high numbers of grating periods N clearly exhibits certain maxima-shifting anomaly [3.75]. Such an anomaly could be identified by the step-shadowing effects due to the angles of incidence and diffraction deviating from the step-function grating normal, leading to an asymmetric step modulation of diffraction intensity and causing the positions of the centroid of at least the first-order diffraction maximum to shift about the grating normal—away from and toward the direction of incidence of radiation. The maxima-shifting anomaly is the most pronounceable, whereas the phase-modulation function of the grating step tends to its extrema at π and 0 phase values. Let us analyze the circumstances affecting the maxima-shifting anomaly and review the measures leading to improvements of the efficiency of surface-relief gratings.

In the classical case of diffraction on any periodic structure [1.1], interference defines the formation of diffraction maxima. If the diffraction grating of period p is seen in reflected light (Fig. 3.28), the optical path difference Δ for beams interfering on the grating becomes $\Delta_{ref} = AC - DB = p(\sin\beta - \sin(-\alpha))$, where α and β are the angles of incidence and diffraction, respectively. For the interference maximum to occur, the path difference must satisfy the diffraction grating equation defining the m^{th} order of diffraction with $m = 0, \pm1, \pm2,\ldots$ as:

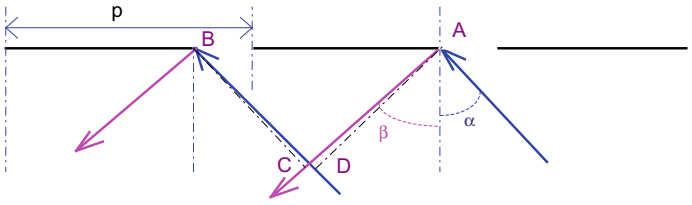

Fig. 3.28 Path difference of incident and diffracted beams for a diffraction grating in reflected light

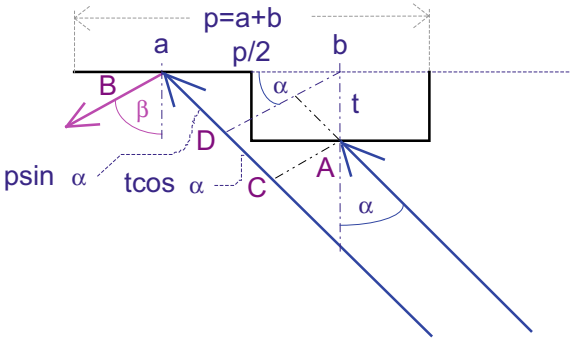

Fig. 3.29 Incident and diffracted light for one grating period

$$p(\sin\beta + \sin\alpha) \equiv m\lambda \; or \; p \equiv m\lambda/(\sin\beta + \sin\alpha). \tag{3.193}$$

The specific case of the step-function diffraction grating in reflected light is illustrated in Fig. 3.29. Let us start by following an earlier analysis [3.65] for the small-angle approximation, which omits near unity cosine terms for incidence and diffraction: $\cos(\alpha, \beta) \rightarrow 1.0$. The optical path difference Δi for all beams incident on the grating at step point A and trench point B becomes $CB = \Delta i \approx BD + DC = (p/2) \cdot \sin\alpha + t \cdot \cos\alpha \cong (p/2) \cdot \sin\alpha + t$, where the latter of the two expressions is the small-angle approximation. Continuing with the small-angle estimate, the path difference Δr in reflected light by analogy becomes $\Delta r \approx (p/2) \cdot \sin\beta + t \cdot \cos\beta \cong (p/2) \cdot \sin\beta + t$.

The resultant small-angle path difference ΔS for beams diffracted on the step-function grating is $\Delta S \cong (p/2)(\sin\alpha + \sin\beta) + 2t$ at angles of incidence and diffraction small enough for the unity approximation: $\cos\alpha \cong \cos\beta \rightarrow 1.0$. Diffracted light intensity I_S at equidistant steps and trenches $a = b = p/2$, as for a Foucault grating [3.65], is modulated by a cosine-squared function:

$$I(\alpha,\beta,p,t)_S = 4a^2 \left[\left(\frac{\sin\pi\left(\frac{\sin\alpha + \sin\beta}{\lambda}\right)a}{\pi\left(\frac{\sin\alpha + \sin\beta}{\lambda}\right)a} \right)^2 \left(\frac{\sin 2N\pi\left(\frac{\sin\alpha + \sin\beta}{\lambda}\right)a}{\sin 2\pi\left(\frac{\sin\alpha + \sin\beta}{\lambda}\right)a} \right)^2 \right] \cdot \cos^2\left(\pi\left(\frac{\sin\alpha + \sin\beta}{\lambda}\right)a + \frac{2t\pi}{\lambda} \right). \tag{3.194}$$

The first term in square brackets in Eq. (3.194) is for a Foucault grating of the equivalent period to the step grating and the second one is the modulation function of the step-function grating, vanishing for all even orders of diffraction and keeping the zero order and odd orders at $m = 0, \pm1, \pm3, \pm5, \ldots$.

Figure 3.30 illustrates the spectral distribution profile of the intensity of light modeled by Eq. (3.194) of a diffraction grating, made, for example, either lithographically or any other way, as the series of equidistant trenches in an opaque matrix. The viewing wavelength domain starting at 800 nm and ending at 900 nm

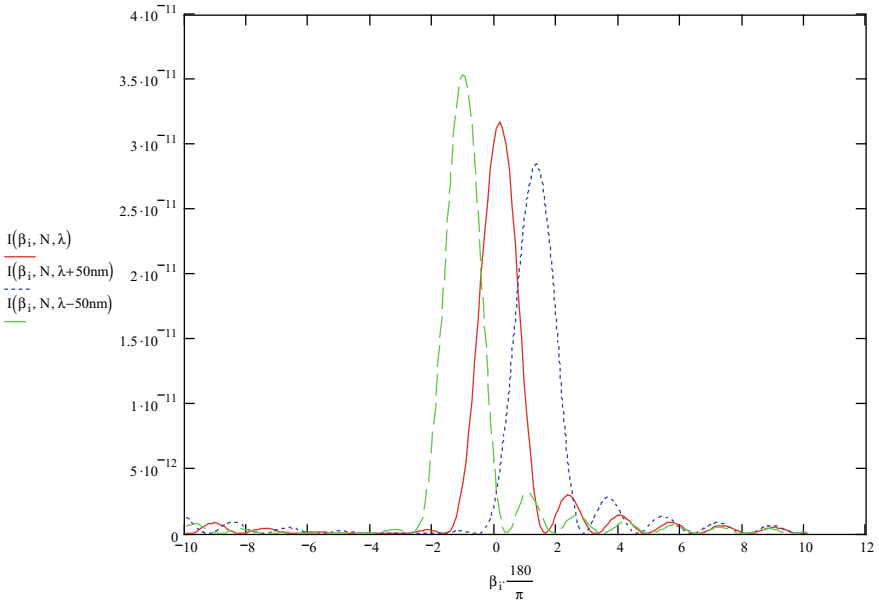

Fig. 3.30 Intensity distributions for step-grating diffraction at 20° incidence in small-angle approximation

is centered at 850 nm wavelength and is chosen to be irradiated at 20° and to be observed at the first diffraction order in the normal direction to the grating, leading to the grating period: $p = \lambda/|\sin\alpha| = 2.485$ μm. The 11-period grating comprises 12 steps, 11 trenches, all etched in a solid substrate, and is 31.065 μm wide with $a = b = 1.243$ um. Figure 3.30 shows the intensity of diffraction for a 40-nm-thick surface-relief diffraction grating.

One can clearly see the shift of the maximum intensity for the central wavelength $\lambda_0 = 850$ nm from the direction of the grating normal $\beta_0 = 0°$ to $\beta_{+,0} = 0.16°$. For the opposite incidence at −20° (see [0.50]), the shift of maximum intensity is mirrored precisely to the same extent: $\beta_{-,0} = -0.16°$.

Let us now evaluate, if the small-angle approximation is responsible for the maxima-shifting anomaly. Following the preceding steps, actual angle-path differences in reflected light (Fig. 3.29) for radiation incident onto the step-function grating Δi and for radiation diffracted by the grating Δr become: $\Delta i = (p/2) \cdot \sin\alpha + t \cdot \cos\alpha$ and $\Delta r = (p/2) \cdot \sin\beta + t \cdot \cos\beta$. The combined path difference is:

$$\Delta_A = (p/2)(\sin\alpha + \sin\beta) + t(\cos\alpha + \cos\beta). \tag{3.195}$$

Equation (3.194), with all aspects of its derivation unchanged except $\Delta S \rightarrow \Delta A$, becomes:

$$I(\alpha,\beta,N,p,t)_A = 4a^2\left[\left(\frac{\sin\pi\left(\frac{\sin\alpha+\sin\beta}{\lambda}\right)a}{\pi\left(\frac{\sin\alpha+\sin\beta}{\lambda}\right)a}\right)^2\left(\frac{\sin 2N\pi\left(\frac{\sin\alpha+\sin\beta}{\lambda}\right)a}{\sin 2\pi\left(\frac{\sin\alpha+\sin\beta}{\lambda}\right)a}\right)^2\right] \cdot \cos^2\left(\pi\left(\frac{\sin\alpha+\sin\beta}{\lambda}\right)a+\frac{t\pi}{\lambda}(\cos\alpha+\cos\beta)\right). \tag{3.196}$$

Identical to Fig. 3.30, the plot in Fig. 3.31 for 20° shows the anomaly does not vanish, but the grating's efficiency is noticeably reduced: $I_{max,1,S} = 3.17 \times 10^{-11}$ W/m^2 · rad at $\beta_{max} = 0.16°$ and $I_{max,1,A} = 2.53 \times 10^{-11}$ W/m^2 · rad at 0.20° for the small-angle approximation and the actual 20° angle; with the respective values for $\beta = 0°$, $I_{0,1,S} = 3.06 \times 10^{-11}$ W/m^2 · rad and $I_{0,1,A} = 2.42 \times 10^{-11}$ W/m^2 · rad. A lesser degree of maxima-shift occurs for a twice as thick step of the same grating modeled by Eq. (3.196) at $\beta_{max} = 0.07°$ (see Fig. 3.31b in [0.50]). Conversion of Eq. (3.194) into (3.196) and accommodating the effects of a step thickness via cosλ and cosβ does not account for the maxima-shifting anomaly seen in Figs. 3.30 and 3.31.

Figure 3.32 illustrates shadowing effects caused by the finite thickness of the grating step when deviating from the grating normal for light incidence and

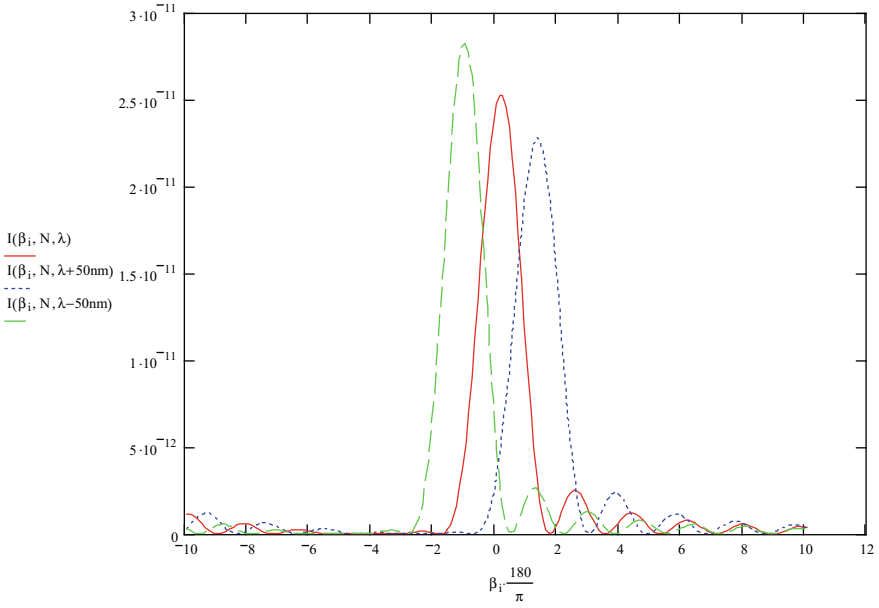

Fig. 3.31 Intensity distribution of light diffracted on a 40-nm step-grating at 20° incidence

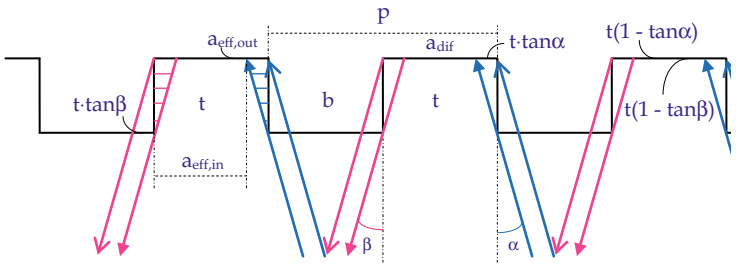

Fig. 3.32 Shadowing effects in the formation of effective grating period p for step thickness t

diffraction. Considering that the period p of the grating for step thickness t is in effect shadow-reduced by 2 t · tanα and 2 t · tanβ for both incident and diffracted light, the shadow-bound step-function grating equation could be rewritten from Eq. (3.193) by replacing grating period p by effective periods p − 2 t · tanα for irradiation and p − 2 t · tanβ for diffraction:

$$p_{eff,out}\sin\beta - p_{eff,in}\sin\alpha = (p - 2t\cdot\tan\beta)\sin\beta - (p - 2t\cdot\tan\alpha)\sin\alpha \equiv m\cdot\lambda,$$
$$p_{sh} \equiv \frac{m\cdot\lambda}{\sin\beta - \sin\alpha} + 2t\cdot\frac{\sin^2\beta/\cos\beta - \sin^2\alpha/\cos\alpha}{\sin\beta - \sin\alpha}. \tag{3.197}$$

For observation by the grating normal, β = 0, Eqs. (3.193) and (3.197), respectively become:

$$p_0 \equiv \frac{m\cdot\lambda}{|\sin\alpha|}. \tag{3.198}$$

$$p_{step,0} \equiv \frac{m\cdot\lambda}{|\sin\alpha|} + 2t\cdot\tan\alpha. \tag{3.199}$$

For the step-function grating seen in Fig. 3.31, Eq. (3.199) gives the matching period $p_{step,0}$ = 2.5144 μm and $a_{step,0}$ = $b_{step,0}$ = 1.2572 μm versus p_0 = 2.4852 μm and a_0 = b_0 = 1.2426 μm. Figure 3.33 shows the plot of Fig. 3.31 by Eq. (3.196) for a matching step grating with the shadow-bound period $p_{step,0}$ of Eq. (3.199). The maxima-shifting anomaly virtually disappears.

Let us rewrite Eqs. (3.194) and (3.196) counting the shadow-bound effects for the step grating. Keeping designations for the optical path difference as in Fig. 3.29, while

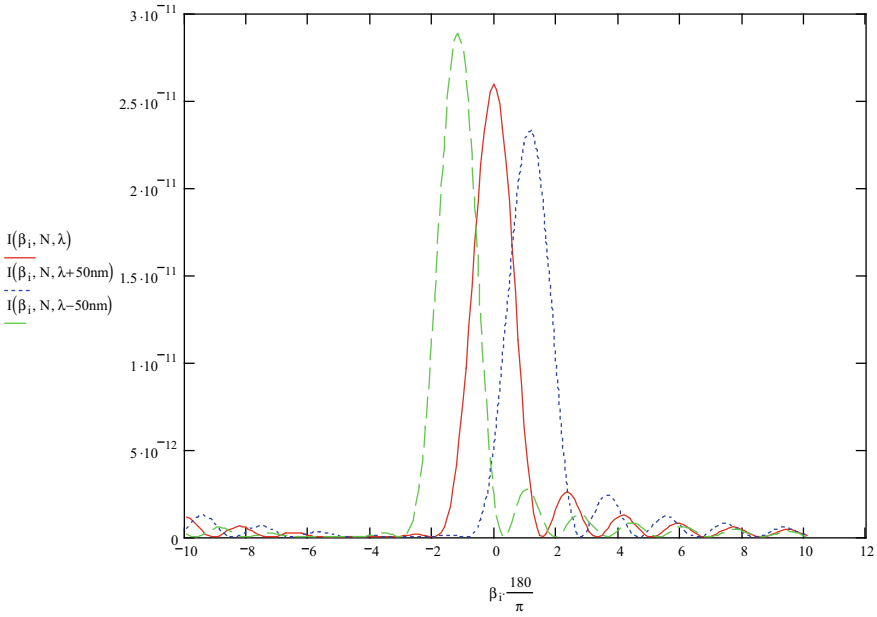

Fig. 3.33 Step-function grating diffraction intensity for the shadow-bound period at the actual angle of 20°

counting off grating shadow-bound sections in Fig. 3.32 and assigning respective effective periods $p - 2t \cdot \tan\alpha$ for illumination and $p - 2t \cdot \tan\beta$ for diffraction, the resultant path differences for $a = b = p/2$ for incident and diffracted light become: $\Delta in = ((p - 2t \cdot \tan\alpha)/2) \cdot \sin\alpha + t \cdot \cos\alpha = (a - 2t \cdot \tan\alpha/2) \cdot \sin\alpha + t \cdot \cos\alpha$, and $\Delta dif = (p/2 - 2t \cdot \tan\alpha/2) \cdot \sin\alpha + t \cdot \cos\alpha + (p/2 - 2t \cdot \tan\beta/2) \cdot \sin\beta + t \cdot \cos\beta = a \cdot (\sin\alpha + \sin\beta) + t \cdot (\cos\alpha + \cos\beta) - t \cdot (\sin 2\alpha/\cos\alpha + \sin 2\beta/\cos\beta)$. If diffracted light is viewed by the grating normal at $\beta = 0$, the later expression for the diffraction path difference becomes: $\Delta dif,\ 0 = (p/2) \cdot \sin\alpha + t \cdot (\cos\alpha + 1) - t \cdot (\sin 2\alpha/\cos\alpha)$. The resultant entire phase difference for the diffracted beam is:

$$\delta = \frac{2\pi}{\lambda}\Delta_{dif} = \pi \cdot p\frac{\sin\alpha + \sin\beta}{\lambda} + \frac{2\pi}{\lambda}t\left[(\cos\alpha + \cos\beta) - \left(\frac{\sin^2\alpha}{\cos\alpha} + \frac{\sin^2\beta}{\cos\beta}\right)\right] \equiv \pi p u + 2\pi t\varepsilon, \quad (3.200)$$

where $u = \sin\alpha + \sin\beta/\lambda$ and $\varepsilon = \left(\cos\alpha + \cos\beta - \sin^2\alpha/\cos\alpha - \sin^2\beta/\cos\beta\right)/\lambda$. For the equidistant steps, $a = b = p/2$, mainly dictated by technological reasons, the amplitude A of diffracted light becomes [3.65]:

$$A = a\frac{\sin \pi ua}{\pi ua} + b\frac{\sin \pi ub}{\pi ub} \cdot e^{i\delta} \underset{a=b}{=} a\frac{\sin \pi ua}{\pi ua}\left(1 + e^{i\delta}\right) = 2ae^{i\delta/2}\frac{\sin \pi ua}{\pi ua}\cos\frac{\delta}{2}. \tag{3.201}$$

The resultant intensity I of diffracted light for a step grating with defined designations u and ε for p = 2a is:

$$I(u,\varepsilon) = 4(p/2)^2\left(\frac{\sin \pi up/2}{\pi up/2}\right)^2 \cdot \left(\frac{\sin N2\pi up/2}{\sin 2\pi up/2}\right)^2 \cos^2[\pi up/2 + \pi\varepsilon t], \tag{3.202}$$

$$I(\alpha,\beta,N,p,t)_B = 4a^2\left[\left(\frac{\sin \pi\left(\frac{\sin\alpha + \sin\beta}{\lambda}\right)a}{\pi\left(\frac{\sin\alpha + \sin\beta}{\lambda}\right)a}\right)^2\left(\frac{\sin 2N\pi\left(\frac{\sin\alpha + \sin\beta}{\lambda}\right)a}{\sin 2\pi\left(\frac{\sin\alpha + \sin\beta}{\lambda}\right)a}\right)^2\right] \cdot \cos^2\left(\pi\left(\frac{\sin\alpha + \sin\beta}{\lambda}\right)a + \frac{t\pi}{\lambda}\left(\begin{array}{l}\cos\alpha - \dfrac{\sin^2\alpha}{\cos\alpha} + \\ \\ + \cos\beta - \dfrac{\sin^2\beta}{\cos\beta}\end{array}\right)\right). \tag{3.203}$$

Figure 3.34 depicts the intensity distribution obtained by Eq. (3.203) for the same light diffracted by the modeled 11-period, 40-nm-thick step grating with period $p_{step,0}$ defined by the shadow-bound grating Eq. (3.199) exhibiting no

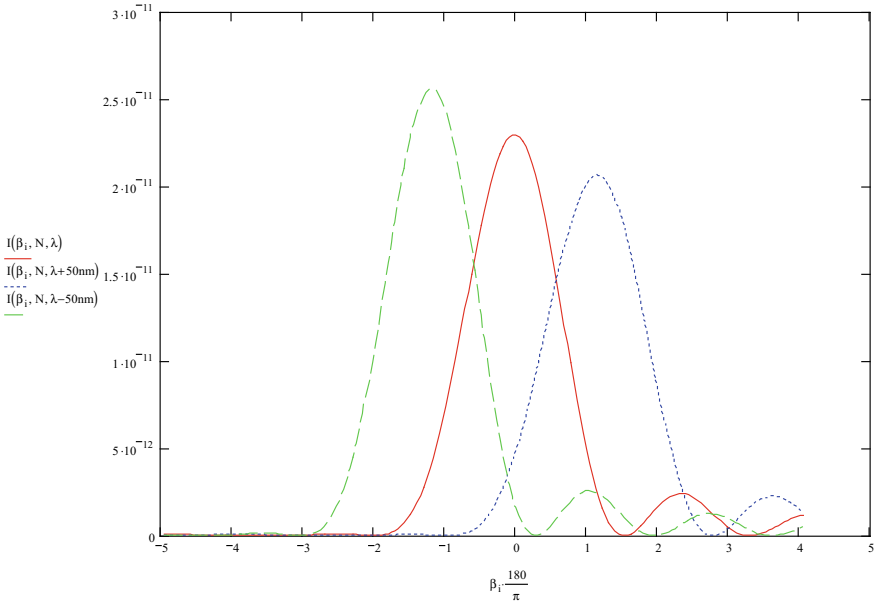

Fig. 3.34 Shadow-bound intensity distribution for a 40-nm 11-period step grating at 20°

anomaly at ±0.00° accuracy. Notice the reductions of the grating efficiency, and therefore the intensity maxima are about 10% lower than those in Fig. 3.33 and are another 10% lower than those in Fig. 3.31.

The cosine-squared function of the period, depth, and angles of incidence and diffraction in Eq. (3.203):

$$W(\alpha,\beta,p,t) = \cos^2\left(\pi\left(\frac{\sin\alpha + \sin\beta}{\lambda}\right)\frac{p}{2} + \frac{t\pi}{\lambda} \cdot \left((\cos\alpha + \cos\beta) - \left(\frac{\sin^2\alpha}{\cos\alpha} + \frac{\sin^2\beta}{\cos\beta}\right)\right)\right), \tag{3.204}$$

provides the step-thickness modulation in addition to period p and angles α and β. At $\beta = 0°$, W becomes:

$$W(\alpha,\beta=0,p,t) = \cos^2\left(\pi\frac{\sin\alpha\, p}{\lambda}\frac{}{2} + \frac{t\pi}{\lambda}\left((\cos\alpha + 1) - \frac{\sin^2\alpha}{2\cos\alpha}\right)\right). \tag{3.205}$$

Figure 3.35 gives respective profiles of function W at 20° irradiation for the nominal grating period. The obvious asymmetry in Fig. 3.35 versus the direction of the grating normal: $\beta = 0°$, contributes to the uneven modulation of diffracted light being eliminated for t = 0 nm when $p \equiv p_{sh}$ (Fig. 3.36).

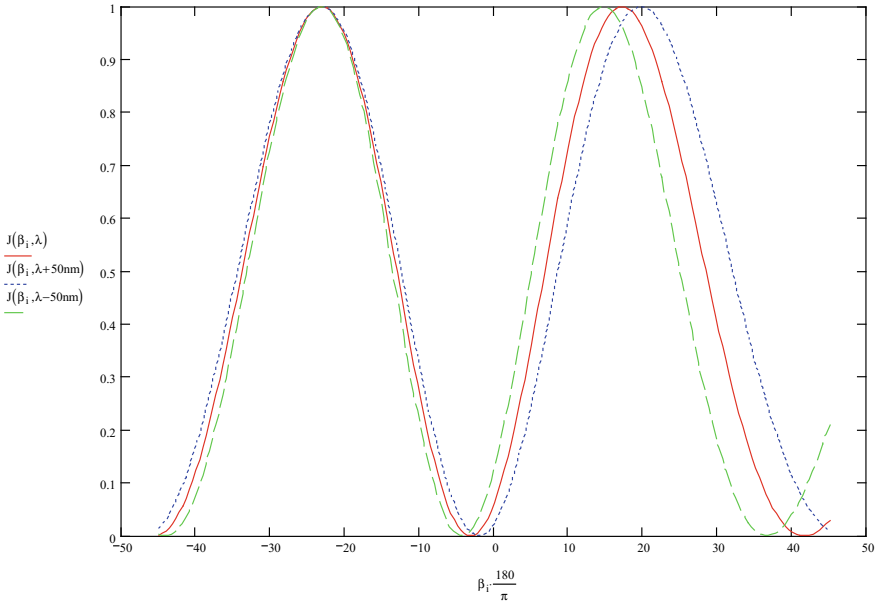

Fig. 3.35 Cosine-squared modulation function for a 40-nm thick step-function grating at 20°

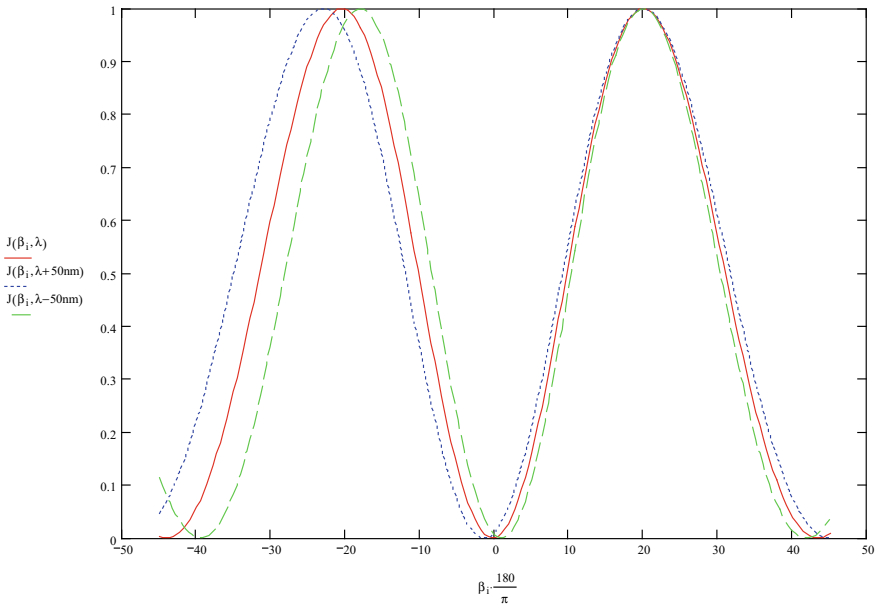

Fig. 3.36 Cosine-squared modulation function of Fig. 3.35 for $\alpha = 20°$ and $\beta = 0°$ with the eliminated step at $t = 0$

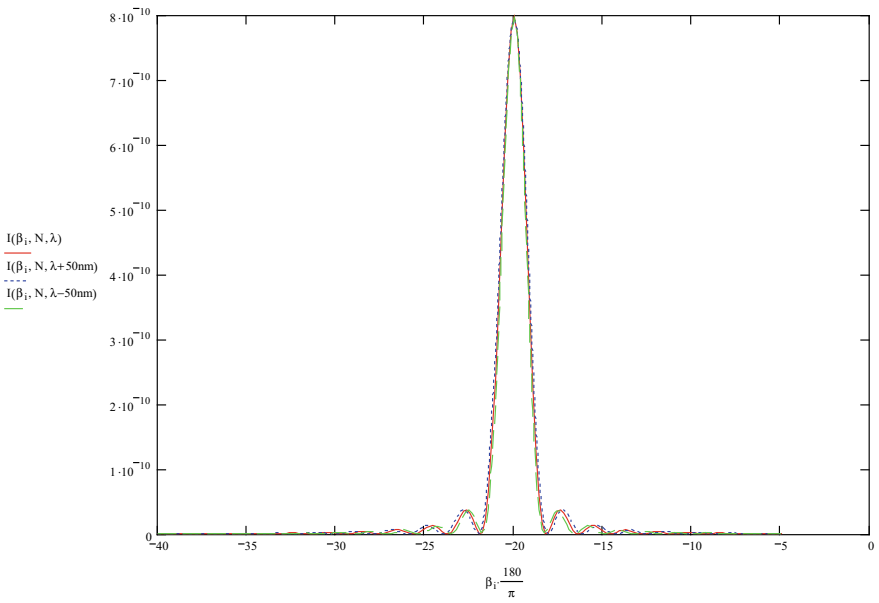

Fig. 3.37 Zero- order diffraction on the grating for zero step-thickness

If the step thickness is zero, the grating diffraction becomes that as of the mirror, and if the phase thickness is π, the first-order maximum for wavelength λ vanishes (see Fig. 3.37 and [0.50]).

If the step phase thickness is between π and π/2, function W swaps its asymmetry and the first-order maximum shifts in the opposite direction from the grating normal and from the irradiation (Fig. 3.39). The shadow-bound equation (3.203) predicts the lowest shift while relations Eqs. (3.196) and (3.194) consecutively increase the anomaly: for the 400-nm step the maxima shifts are 0.20°, 0.30°, and 0.33°, respectively. Equation (3.194) incorrectly predicts the termination of the first-order maximum for $\lambda = 800$ nm matching dual-step thickness at normal incidence owing to its small-angle approximation (see [0.50] for more detail), while relation (3.196) corrects and Eq. (3.203) normalizes the spread among modeled wavelengths.

If the value of W is optimized by the step thickness, setting $\varepsilon \cdot t = \pm 1, 2\ldots$ to give $W = \cos^2(\pi ua \pm k\pi/2)$ (Eqs. (3.203, 3.204)), the thickness modulation vanishes at $t = 234.1362$ nm, 20° incidence, and 0° observation, and hence function W becomes symmetric for central wavelength $\lambda = 850$ nm (Fig. 3.38).

For that optimized step thickness the anomaly is absent for nominal period p as seen in Fig. 3.39.

When the magnitude of W is lowered from 1.0 to $W_{0°} = \cos^2(\pi ua \pm k\pi/4) = 0.5$, the maxima-shifting anomaly in the intensity profile given by Eq. (3.203) is also absent, but the spectral profile is asymmetric (Fig. 3.40a). Conversely, the maxima-

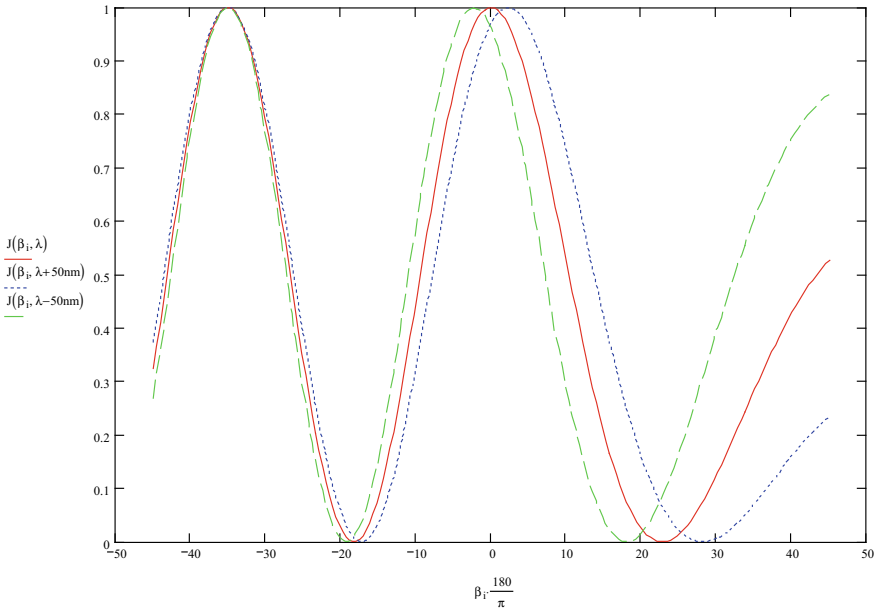

Fig. 3.38 Symmetric cosine-squared modulation function W at the optimized step for first order diffraction

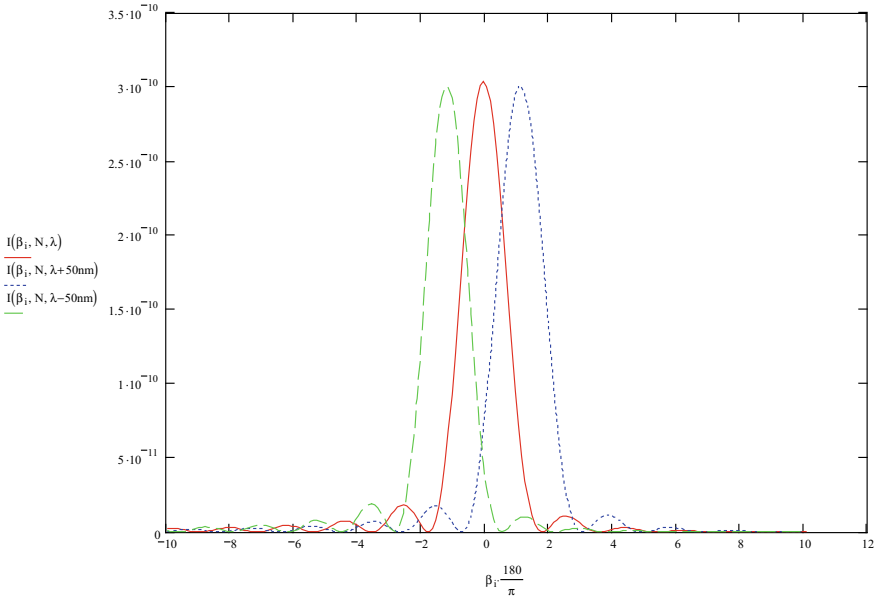

Fig. 3.39 Intensity of an optimally thick step-function grating for π/2 phase and W ≡ 1.0, thus eliminating the anomaly

shifting anomaly is manifested if Eq. (3.194) is used for the grating with $W_{0^\circ} = 0.5$, thus having λ/8 step thickness (Fig. 3.40b).

If the diffraction intensity is computed according to Eq. (3.203) for the grating of nominal period *p* satisfying grating Eq. (3.198) and when the value of W is between $\cos^2(\pi ua \pm k\pi/4)$ and $\cos^2(\pi ua \pm k\pi/8)$, the maxima-shifting anomaly is practically not noticeable. When the step thickness is lowered further from λ/16 to near λ/24, the shadow-bound grating Eq. (3.199), used alongside Eq. (3.203) for the step-matching grating period p_{step}, compensates for the maxima-shifting anomaly, as seen in Fig. 3.43 for approximately λ/21 step thickness. However, if the step thickness goes below $W = \cos^2(\pi ua \pm k\pi/12)$ levels, even Eqs. (3.203) and (3.199) together do not relieve the anomaly, giving a positive-shift maximum for $\lambda \to 0$. The negative-shift maximum is reached for thicknesses $t \to \lambda/2$ for phase thickness of the grating's step approaching π (Eqs. (3.194), (3.196), (3.203)). Since the anomaly's asymmetry is centered at step-modulation function W equal to 1.0 for step thickness $t \equiv t_c$, the compensation algorithm for grating period p_c can be written from Eqs. (3.193), (3.198), and (3.199) via the difference of the actual step thickness t from t_c:

$$p_{c,0} \equiv \frac{m \cdot \lambda}{|\sin \alpha|} + (t_c - t) \cdot \tan \alpha. \tag{3.206}$$

Figure 3.41 shows the compensation effect for 11-period, 5-nm, and 463-nm-thick step-function gratings for the intensity-spectrum obtained by

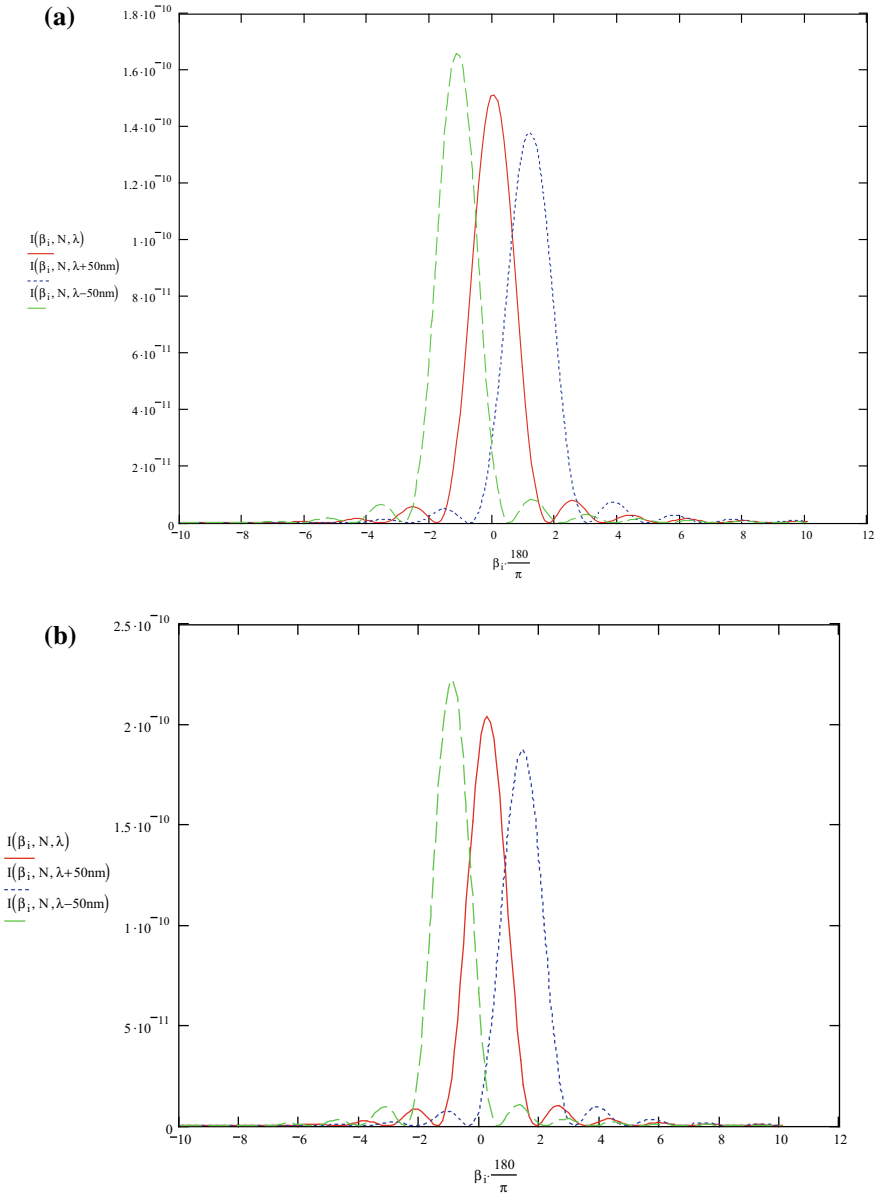

Fig. 3.40 Grating intensity for π/4 phase-thickness with no anomaly if accounted for by the shadow-bound equation (**a**), and with 0.25° maxima-shift for first-order diffraction if step-shadowing is not counted (**b**)

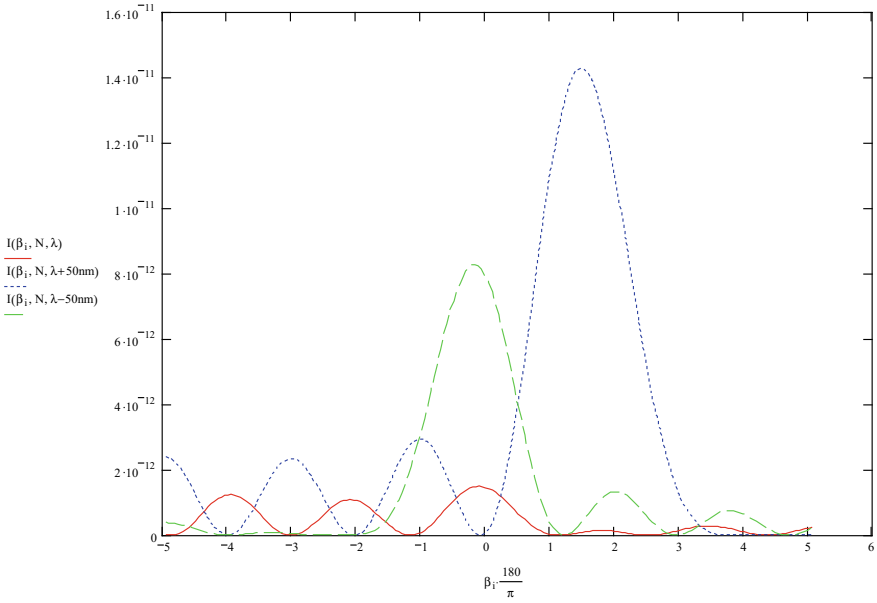

Fig. 3.41 Intensity profile for a step grating with the shift-compensation period p_c for 5-nm step

Eq. (3.203) and grating period p_c satisfying Eq. (3.206). The first-order intensity maxima for both thicknesses, being about equidistant from t = 0 and t = 468.27 nm—for the phase thickness to become π, are centered within +0.06° and −0.07° from the grating normal for otherwise +0.7°, −0.75° shifts in opposite directions from the same normal. Equations (3.203) and (3.206), providing linear compensations for the nonlinear anomaly, do not fully balance the maxima shifts for all step thicknesses, for which Eq. (3.203) provides exact matches at compensation period p_{11} fully eliminating the anomaly. For example, for 463-nm and 5-nm grating steps, the compensation periods are $p_{11\text{-}463} = 1.195$ μm versus $p_{c\text{-}463} = 1.201$ μm and $p_{11\text{-}5} = 1.2875$ μm versus $p_{c\text{-}5} = 1.284.3$ μm (see [0.50] for more detail).

For the nominal grating period, the anomaly may be substantially reduced by limiting the angle of incidence: 2° versus 20° illumination limits the anomaly from 0.7° to 4 arc minutes (Fig. 3.42).

Reduction of the angle of incidence by itself does not remove the anomaly—0.12° maxima shift at 10° incidence at 11 periods, but increasing the number of steps does—the shift is reduced to 0.03° (Fig. 3.43) which is within a calculation error for 10° incidence for the number of periods being doubled to 22. Increasing a number of periods makes the anomaly virtually disappear in otherwise largely anomalous settings –10° incidence leads to the only 0.015° shift for 44 grating periods for a 20-nm-thick step (Fig. 3.44). For a 5-nm-thick step the anomaly is equally limited to 0.015° for 88 periods [3.75].

Making the final step in modeling of the step-function grating properties for the nanoscale step thickness, let us increase the angle of incidence from 20° in our main

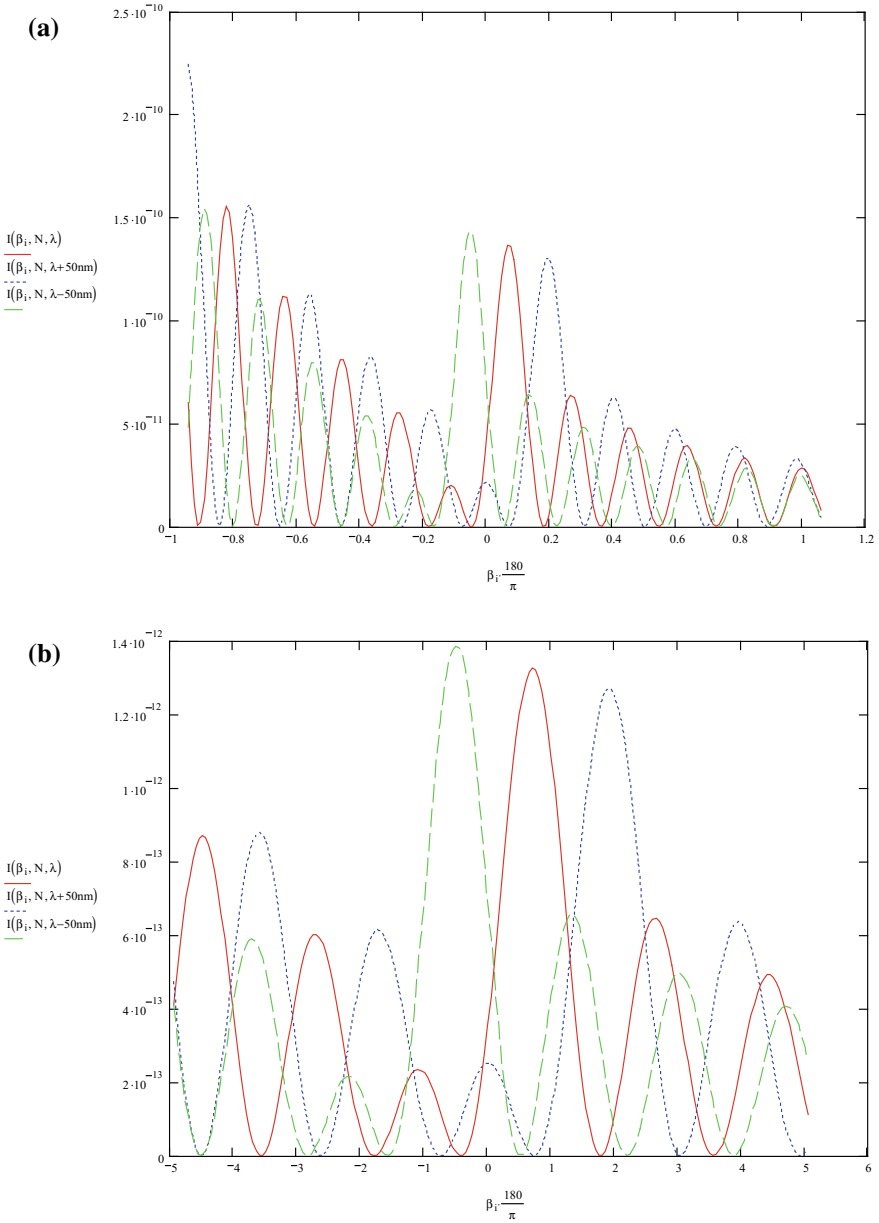

Fig. 3.42 Intensity profile of a 5-nm thick step at 2° (**a**) versus 20° (**b**) incidence for nominal grating periods

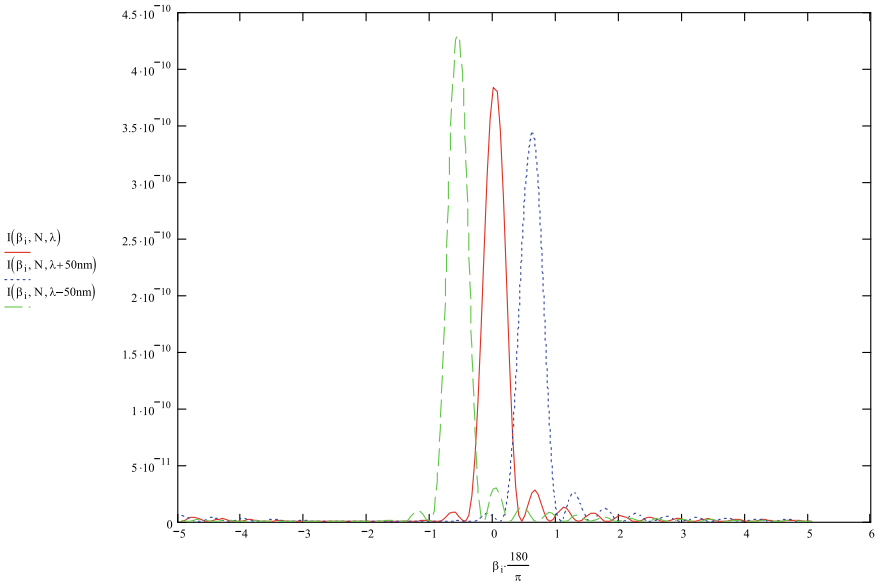

Fig. 3.43 Intensity profile of a 40-nm thick step grating for 10°-incidence at 22 grating periods

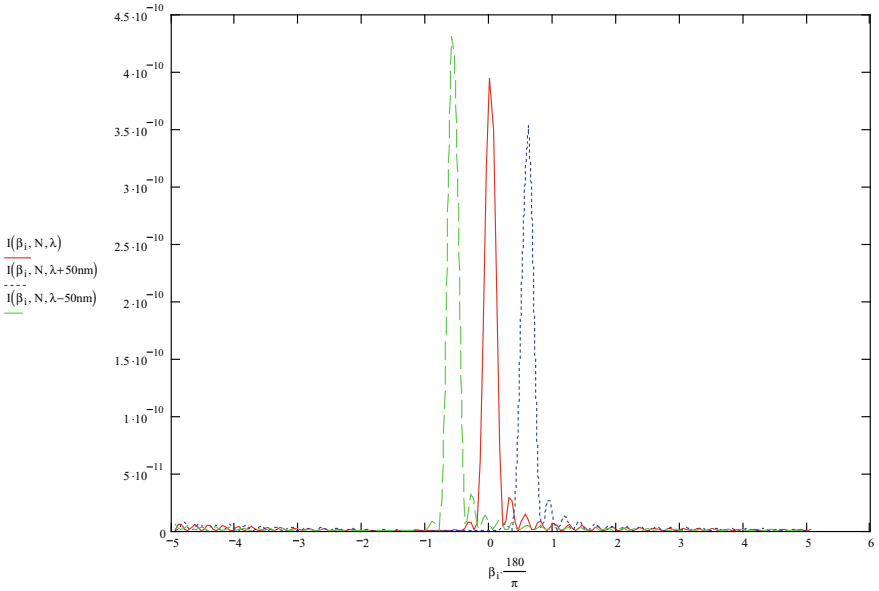

Fig. 3.44 Intensity profile of a 20-nm, 44 period step grating for 10°-incidence

example, instead of lowering it to reduce the anomaly. Such a large angle of incidence as 40° makes a 80-nm-thick step grating with period $p_{40°} = 1.3224$ um to shift its maximum to only 0.27° for 11 periods [0.50], and when the grating width is increased from 11 to 22 periods the anomaly is decreased further from 0.6° to only 0.17° for the 40-nm-thick surface-relief grating of our main example (Fig. 3.45).

The anomalies seen in Fig. 3.31 were verified by strict numerical modeling using rigorous finite-element analysis of the electromagnetic field [3.74]. The results shown in Fig. 3.46 exhibit quite evident maxima shifts for the step thicknesses of the surface-relief gratings modeled: 80 nm and 40 nm.

The irregularities in the angular positions of the diffraction maxima for thin step-function gratings can affect the performance of various devices for upcoming nanotechnologies, as well as extremely short-wave lithography applications. The magnitudes of the grating-step thickness modeled in the analysis are dictated by forthcoming applications. Already developed prototypes of absorber layers for EUV (Extreme UV) lithography are near 42–40 nm in thickness and the thickness may be lowered to 30 nm in an attempt to avoid shadowing effects due to EUV light incidence of 6° [3.67]. Shadow-bound Eq. (3.203) for the intensity of reflected light being diffracted on a surface-relief diffraction grating can be applied to mitigate the maxima-shifting anomaly increasing the otherwise lowered grating efficiency at angles of incidence or observation causing the grating step shadows. When considering the properties of the step-modulation function for a phase thicknesses between π and π/2 as mirroring those between 0 and π/2, the maxima-shifting anomaly associated with the nanoscale-level thicknesses of step-function gratings, even when approaching

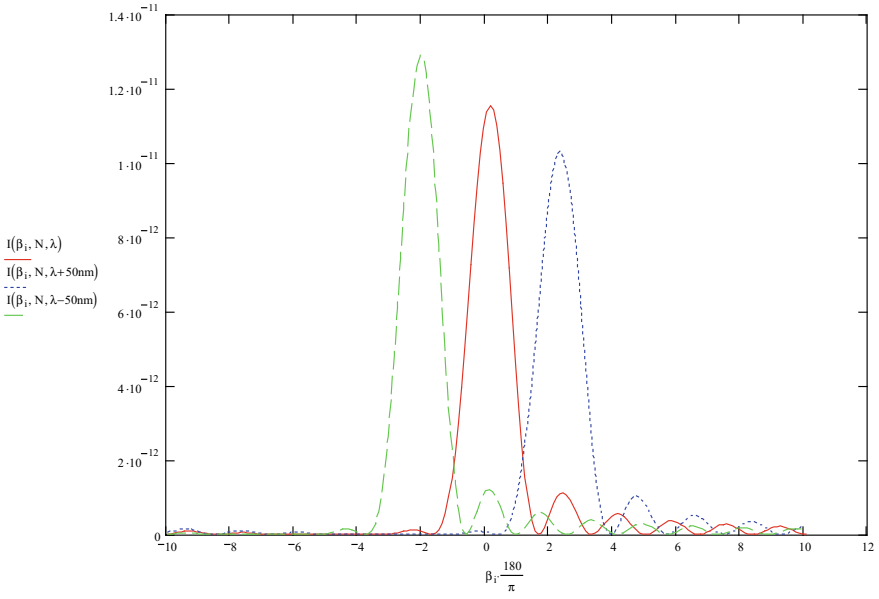

Fig. 3.45 Intensity profiles for 40° incidence at 40-nm-thick step for 22 periods

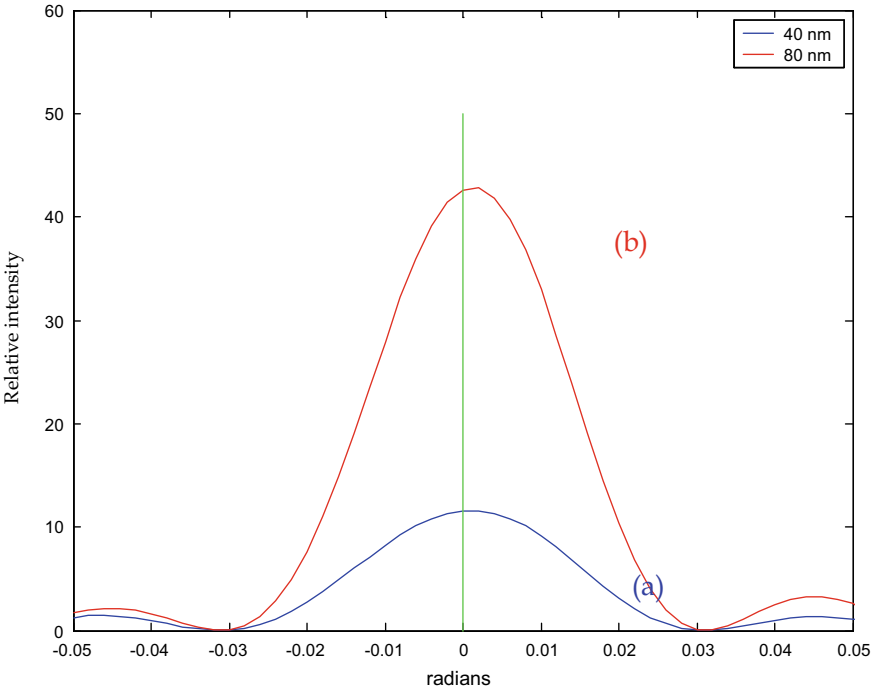

Fig. 3.46 Numerical results for 40-nm (**a**) and 80-nm (**b**) gratings: 11 periods, 20° illumination, 0° observation [3.74]

hundredths and thousandths of the illuminating wavelengths, must be affecting these novel applications. Phenomenologically, one can think of shadowing effects as shifting the effective grating toward the irradiating light, as schematically depicted in Fig. 3.47. Figure 3.47a, illustrates shadow-bound regions at incident and diffracted angles α and β; Fig. 3.47b, gives a view from the perspective of incident light schematically tilting the grating via the direction of radiation incidence. From that

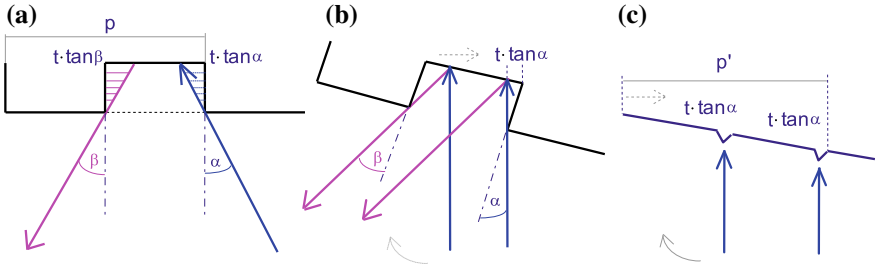

Fig. 3.47 Phenomenological illustration of the grating-step-bound maxima-shifting transformation effect

angle, the grating is seen as being shifted toward the direction of light incidence by its one shadow-bound distance: $t \cdot \tan\alpha$. When the step thickness t is reduced toward $\lambda/20$ or below, the grating profile becomes almost indistinguishable and the incident light virtually faces edge bumps of the grating structure seen from its direction to be "$(t \cdot \tan\alpha)$-shifted," as depicted in Fig. 3.47c. The $t \cdot \tan\alpha$ lateral shift is exactly half of the difference for shadow-bound period p_{step} computed by expression (3.199) versus period p given by grating Eq. (3.198). For example, for grating step thickness $t = 20$ nm, angle of incidence $\alpha = 20°$, and observation of the first diffraction order by the grating normal at $\beta = 0°$, the shift is precisely half of the period difference: $(t \cdot \tan\alpha) = (p_{step} - p)/2 = 7.2794$ nm.

Limiting the angles of incidence allows one to contain the anomaly to a minimum. For 12° versus 20° illumination for a 40-nm step, 11-period grating, the maxima shift is limited to 0.12° from 0.20° with no grating modification. Increasing the grating period from $p = 4.0883$ μm to $p_{step} = 4.1053$ μm using Eq. (3.199) brings it further down to 0.06°. Another advantage of using smaller angles of illumination, down to close to normal incidence, if the number of grating steps cannot be sufficiently high is associated with the subsequent reduction of the half-width half-maximum intensity of diffraction maxima. For 12° versus 20° illumination, the half-width half-maximum intensities of first-order maxima are reduced to 1.2° from 1.8° for an 80-nm step, to 1.1° from 1.7° for a 40-nm step, and to 1° from 1.6° for a 20-nm step—all for our main example of the step-function grating with 11 periods. The maxima widths are higher for the modeled broadband source at half-spectral width $\Delta\lambda \pm 50$ nm. Since the numerical aperture of a diffraction-observation system is always limited, the narrower is the diffraction order, the lower is the error of axial intensity registration due to a potential anomaly.

For certain applications altering the nominal grating period toward the highest efficiency of a given diffraction order by Eqs. (3.199) and (3.206) or, most straightforwardly, Eq. (3.203) versus grating Eqs. (3.193) or (3.198) provides valuable alternatives to otherwise inefficient application of that specific grating. Although such a grating modification should diminish the particular anomaly, the attempt would rather make the grating design be strictly application-specific. Limiting the angles of incidence and observation and, most importantly, increasing the number of grating periods should be the two best alternatives. At the same time, enhancements in understanding the step-function grating functionality and the performance of the grating in various applications may be accomplished by invoking a more rigorous analysis, such as a matrix-vector, finite-element, and/or weight of a ray formalism [3.68–3.73], especially for a grating-step thicknesses on the nanoscale, where phenomenological theory may not apply and errors in making uniform nanometer-thick step surface-relief gratings over all steps and trenches embody other complex challenges [3.73].

The analyzed angular-shifting anomaly of diffraction maxima for step-function gratings to satisfy the grating equation resembles the asymmetrical irradiance distribution for echelle gratings exhibiting a substantial angular shift of the centroid from the diffraction angle predicted by the grating equation for wide-angle diffraction orders [3.64, 3.75]. By analogy to phase-status formation of interference

maxima in a resonator, becoming narrower and spreading wider when the number of multiple reflections is increased (see Chap. 8, Fig. 8.35), the anomaly of small-angle approximation discussed in this section, being primarily caused by an insufficiently high number of grating periods N, resembles other incomplete multibeam interference phenomena when insufficient interactions of available interferers do not allow the diffraction pattern on the inadequately long step-function grating to become fully formed, as it happens at a tending-to-infinity number of step-function periods of the sufficiently long surface-relief grating.

3.4.3 *Diffraction Gratings as Spectral and Color Filters*

Alternatively to using diffraction gratings in reflected light at orders other than zero, avoiding overlapping by specular reflection, gratings in transmitted light allow both zero-order and higher-order applicability for spectral and color filtering [3.76–3.90]. A schematic of a surface-relief phase grating with step-function rectangular grooves made in a transparent matrix to be used in transmitted light is illustrated in Fig. 3.48. A parallel beam of light of wavelength λ is incident from source *S* on grating *G*, made of a material of refractive index *n,* by its wave normal, while the transmitted and diffracted into 0^{th} order beam is collected by lens *L* into image *Im*, whereas any i^{th} diffraction order propagating at an angle α_i is not imaged. The cross-coupled combination of two transmission gratings (compare Fig. 12.23 with reflection ones) could serve not only as a spectral filter, but as a color combiner adding red, green,

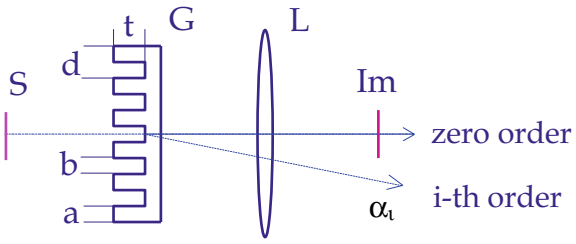

Fig. 3.48 Diffraction grating in transmitted light

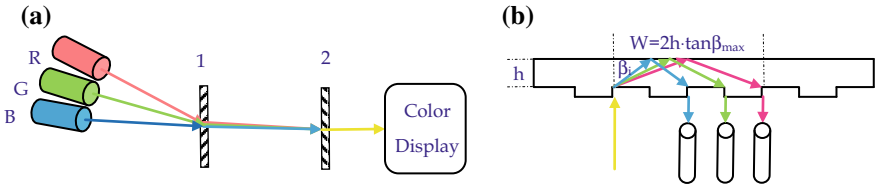

Fig. 3.49 Cross-coupled diffraction gratings as a spectral selector or a beam-shaping color combiner

and blue waves to create white light (Fig. 3.49). The cross-coupling of view (a) accommodates for physical sizes of three color sources *R*, *G*, and *B*, combining them into one white beam on a color display [3.91]. Figure 3.49b shows a substrate of thickness *h* and width *W* of a transmission grating with a mirror reflecting surface deployed for back-coupling of individual color components of a white beam separated via diffraction into fibers or waveguides [3.86–3.88].

For a transmission grating (Fig. 3.48), as only axis-centric beams are imaged, the interactions occurring within 0^{th} diffraction order are due to dual-beam interference on grating groves *b* and steps *a* via the path length $\Delta = t \cdot (n - 1)$ and phase difference $\delta = (2\pi/\lambda) \cdot \Delta = (2\pi/\lambda) \cdot t \cdot (n - 1)$. The total intensity I_Σ for dual-beam interference at the equidistant grating steps and trenches a = b is [1.1]:

$$I_\Sigma = I_1 + I_2 + 2\sqrt{I_1 I_2}\cos\delta \underset{I_1=I_2}{=} 4I_1\cos^2(\delta/2), \tag{3.207}$$

where I_1 and I_2 are the intensities of the interfering beams. Considering for a given case the one-dimensional transmission grating as depicted in Fig. 3.48 with steps and grooves of equal width, being irradiated at normal incidence by the light beam with intensity I_0, two interfering uniaxial beam components are: $I_1 = I_2 = I_0/4$, thus the transmission function $T(\lambda)$ versus wavelength λ becomes:

$$T(\lambda) = \cos^2[t \cdot \pi(n-1)/\lambda], \tag{3.208}$$

having the transmission profile changing from maxima of 1.0 to minima of zero.

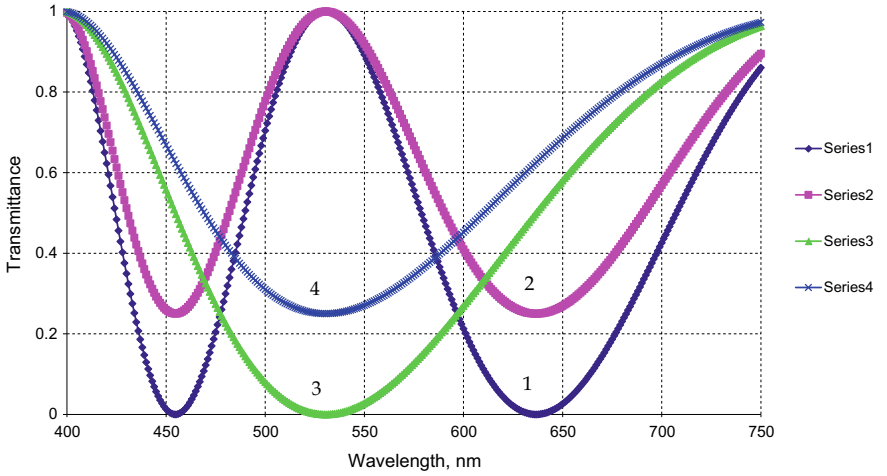

Fig. 3.50 Transmission profiles of a thick surface-relief grating at equal groove and step widths a = b (series 1, 3) and at a = 3b (series 2, 4) for the step thickness t = 10 micron (series 1, 2) and for t = 5 micron (series 3, 4) versus wavelength λ in the visible domain

When the widths of the grating steps and trenches are not equal within the period d: $a \neq b$, at $a + b = d$, the transmittance T(λ) changes to having asymmetrical maxima and minima [3.80]:

$$T(\lambda) = (1 - 2a/d)^2 + 4(a/d)(1 - a/d)\cos^2[t \cdot \pi(n-1)/\lambda], \tag{3.209}$$

with the transmission profile transitioning from unity maxima to unequal-to-zero minima [3.81], according to the aspect ratio a/d of the step versus the period of surface-relief grating, $a/d = 1 - b/d \neq 0.5$:

$$T_{\max} = 1; \quad T_{\min} = (1 - 2a/d)^2. \tag{3.210}$$

The dependence of refractive index versus wavelength λ of irradiation: (n − 1)/λ, and the aspect ratio of the grating step: $a/d = 1 - b/d$, define a color of grating conversion and its saturation depth. As seen in Fig. 3.50, either a transmission or reflection grating can serve as a broadband spectral filter or a color selector, converting radiation in a function of its step thickness and the step profile.

Chapter 4
Photometers and Radiometers

4.1 Optical Design and Absolute Calibration of Radiometers

4.1.1 Spectrally Unselective Systems

As discussed in Chap. 2, by utilizing the thermoelectric reception, having practically equal to unity absorptance over a relatively broad spectral region, one can provide direct measurements of any power or energy parameters of optical radiation "straight" with no optical component added. The linear range of measurement of a thermal detector is limited, on one hand, by low thermal noise and, on the other, by the thresholds of either nonlinearity or damage due to laser radiation. To reduce the thermal noise of the detector, hence accessing the lowest limit of power or energy to be measured, the area of its sensitive surface needs to be minimized. This measure also reduces the detector's time constant. For a direct measurement the light beam to be measured is expected to fit the detector's entrance aperture. Lenses and attenuators can be used to modify the beam's size and the detector's linear dynamic range by increasing the upper threshold at which nonlinear effects or irreversible changes of sensitivity due to thermal damage do not materialize.

Photoelectric transformation of the power or energy of light directly into an electrical signal allows one to achieve higher sensitivity for power and energy measurements, reaching photon counting levels, if needed. However, the linear limits of direct measurements are constrained to magnitudes substantially lower than the actual laser damage or nonlinear transformation threshold levels of the high power and energy to be studied. Thus, actual measurement solutions for one or another radiant and luminous power or energy extent are defined not only by all choices of detectors and registering systems, but, in many respects, also by the best design of the optical system transforming light beams in the desired manner, while having a known transformation factor, as well as by the methods used for absolute calibration of the system in the radiant or reduced units of measurements used.

M. Bukshtab, *Photometry, Radiometry, and Measurements of Optical Losses*, Springer Series in Optical Sciences 209,
https://doi.org/10.1007/978-981-10-7745-6_4

Thermocouple-based calorimetric detectors are utilized for measurement of the continuous wave (cw) or pulse-average power and single-pulse energy of laser light. Usage of surface absorbers with thermally conductive substances of broad-band absorptive coatings is typical for this kind of measurement. Since absorption in such a case occurs in a thin layer of the coating, the high peak power of a laser, especially in pulsed mode, can cause thermal damage. Volume absorbers rely on exponential attenuation in their materials, and thus can withstand a much higher maximum pulse power than surface absorbers and are more suitable for pulsed lasers. Owing to lower steady-state heat conduction, they are less sensitive and mostly have a narrower flat spectral response. A pyroelectric detector inherently reacts to a change in its temperature and is optimized to measure parameters of pulsed optical radiation or operate with continuously modulated cw light beams.

The main limitation for high-power laser pulse measurements consists in possible damage of the absorbing substance of the detector used. If intense optical radiation encounters surface absorbers, measures need to be taken to predict the actual irradiance formed by laser light, which should be below the absorber's damage threshold. When a bulk absorber, such as gas, liquid, or solid, is used, the spherical density of laser light must be limited correspondingly. Solid bulk absorbers based on neutral-density glasses are widely used since their high thermal diffusivity allows minimization of time constants for pulsed measurement of energy or power [4.1]. A laser calorimeter using two glass-plate absorbers (1 and 2) is shown in Fig. 4.1. The main fraction of the incident beam is absorbed in plate 1. Plate 2 precludes laser damage of electroformed copper-surface absorbers 4 by light reflected from the first plate. Volume absorbers are made of neutral-density glass contacting electroformed cavity via electrically calibrated heaters 3 attached to back corners. The radiation energy is measured by applying the calorimeter's electrical-calibration constant with no corrections since the entire incident energy is absorbed in the calorimeter [4.2]. By analogy, gas bulk absorbers can be used to maintain sufficient sensitivity and low damage susceptibility at high laser powers [4.3].

When a thermoelectric detector measures either radiant power or energy, the measurement transformation function is anticipated to have as close to unity total absorptance α_Σ as dictated by the task. The difference $\Delta\alpha = 1 - \alpha_\Sigma$ gives the loss of conversion of the measured energy to heat and measurement error. To minimize

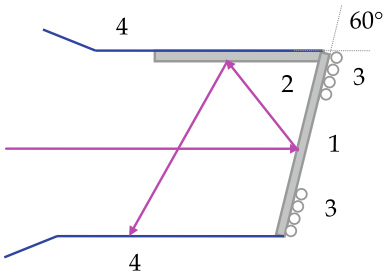

Fig. 4.1 Bulk-absorbing calorimeter

unconverted absorption, an additional multiple-reflection cavity can be formed from discrete sensitive elements. The total absorptance of the cavity becomes:

$$\alpha_\Sigma = \alpha + \rho\alpha + \ldots + \rho^m\alpha = \frac{\alpha(1-\rho^m)}{1-\rho}, \tag{4.1}$$

where ρ is the effective reflectance of the additional cavity, combining the specular and diffuse reflections of the entire cavity, and $\alpha = \alpha(\lambda)$ is the spectral absorptance of a cavity wall. The effective diffuse reflectance of the cavity depends on the entrance aperture opening: $\rho'_d = (1 - A_{\text{ap}}/A_{\text{cav}})\rho_d$. Assuming that the total loss into this aperture is not significant, thus $\rho'_{\text{d}} \cong \rho_{\text{d}}$ and $\rho = 1 - \alpha$, we have:

$$\alpha_\Sigma = 1 - \rho^m. \tag{4.2}$$

The lowest number m of required reflections, leading $\Delta\alpha_\Sigma$ to be lower than $\Delta\alpha_{\text{min}}$, can be estimated from either (4.1) or (4.2). Using the assumptions of Eq. (4.2): $A_{\text{ap}} \ll A_{\text{cav}}$, for $\alpha = 0.95$ and $\Delta\alpha_\Sigma = 0.01\%$ only four reflections are required to obtain α_Σ equal to 0.9999. Since the number of reflections may not be necessarily large, a cone-shaped sensitive cavity is frequently deployed. Such a cavity does not create any excessive increase of the detector's opening; hence, it does not increase the detector's total time constant and inclusive thermal noise of the entire measurement system.

The cone-shaped cavity allows one to utilize multiple reflections, thus increasing the absorbing power of radiation measured in proportion to the threshold-sustainable irradiance and the increased surface for the multiple reflections to be taking place. Depending on the ratio of reflectance ρ to absorptance α and the angle φ of incidence, the optimal cavity shape of angle Θ can be used. The decrease of local absorptance α_{l} may be equalized by an increase of the total energy absorbed as a result of a correspondingly increased length of multiple interactions. For the law of conservation of energy as: $\rho \cong 1 - \alpha$, Eq. (4.2) with $\rho \cong \alpha \cong 0.5$ leads to the total cavity absorption factor α_Σ reaching 0.999, while approaching only ten reflections. In the case of $\alpha = 0.1$, $\rho \cong 0.9$, that happens for 66 interactions. Several other configurations for surface-absorbing cavities may also be applied [0.12–0.20, 0.22].

Figure 4.2 shows the laser calorimeter design with a hollow glass cone and the external absorbing coating. The cone design at the optimized vertex angle 2θ

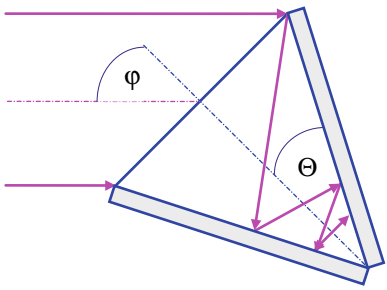

Fig. 4.2 Cone-shaped sensitive element

anticipates for its axis, approaching oblique incidence of an input light beam at angle φ, to be oriented to lead the incident beam being reflected at 90° after the m^{th} interaction. This reflected beam is returned the same way as it entered after $2m$ actions without getting to the cone vertex [4.4].

Another way of achieving nearly unselective spectral attenuation for power measurements of potent laser radiation is depicted in Fig. 4.3. The notion of that classical attenuation action is based on low dispersion of most optical glasses in the UV–VIS–near IR spectral domain. Consequently, specular reflectance of a single surface of an optical element made from that glass can be considered as a known constant. To use only the first surface reflection, the element could be made from a highly absorbing glass, totally dissipating light reflected by the second surface. To increase its damage threshold to laser radiation, the element may consist of two or more plates. The first plate could be made from any transparent and, thus, mostly radiation-resistant glass. The absorbing second plate or wedge could be optically contacted to the back surface of the first one. One pair of combined elements oriented at a desired angle of incidence φ in the two orthogonal planes (Fig. 4.3 is projected into one plane) is commonly used to compensate for polarization effects, and a 45° angle for inclination of each plate is technologically prevalent [4.5, 4.6]. Since the smaller is the angle, the lower is the constraint on adjustment and lower polarization sensitivity that can be achieved, smaller angles are advantageous.

To provide measurements with optical attenuators, a radiometer needs to have an extended linear dynamic range η covering every attenuator. Range η allows one to measure the conversion factor $k = 1/\eta$ for each given attenuator. The set of two reflective plates with reflectance ρ in Fig. 4.3 has conversion factor $k = (1/\rho)^2$, requiring the specific photometer's linear dynamic range η to be higher than at least $1/\rho^2$. To determine actual k values, at least two light power or energy measurements need to be made. First, the power or energy of light incident from source 1 is measured after it has passed each rectangular prism 3 and 5 and is then reflected with no attenuation owing to total internal reflection on the hypotenuse side of the prism. For the second intensity measurement, the prisms are removed from the light path and radiation reflected by attenuation plates 4 and 6 is measured. To make the optical path length invariable, two additional plates 2 and 7 made from the same material as prisms 3 and 5 of an equivalent optical thickness are inserted into the system. That system conversion factor k_s is determined as the ratio of two readings detector of 8 at constant intensity of radiation. Knowing the reflectance difference Δ

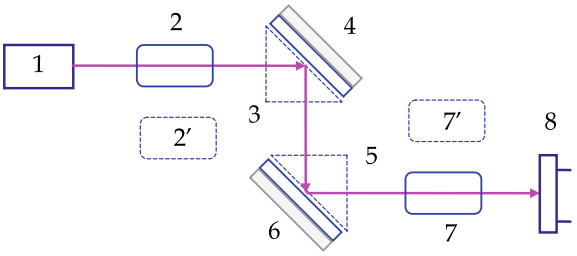

Fig. 4.3 Quasi-unselective attenuation of intense laser radiation

between $\rho_{\perp}{}^2$ and $\rho_{\|}{}^2$, one can determine the specific alignment of prisms compensating for fabrication errors by converging a given polarization status of the incident beam into the orthogonal state.

A similar degree of attenuation can be achieved by deploying a set of neutral glass plates or thin-netted attenuators installed in transmitted light. No such optical elements can be fully spectrally neutral; therefore, each attenuation factor needs to be measured as that of the prism pair. The higher is the attenuation factor required, the higher the auxiliary measurement uncertainty becomes. An increase of the optical density of a glass plate itself leads to a lower damage threshold for intensive laser radiation. Implementation of several attenuators in a set increases the optical path length, likely increasing the respective spot size on the system's detector, and could lead to interference of beams reflected by plate surfaces, causing higher random errors of measurement. Netted attenuators do not function in sets because of evident screening and diffraction effects.

If a very high attenuation is needed, a twin-prism attenuator (Fig. 4.4), being common for the millimeter wave range, may be used [4.7]. Its principle is based upon the phenomenon of frustrated total internal reflection [1.1]. For a distance b between two prisms much greater than wavelength λ, attenuation $\alpha_{\|}$ (in decibels) of light polarized in the plane of incidence depends linearly on b:

$$\alpha_{\|} = 54.58\beta(b/\lambda) - 20\log_{10}\left\{4n\beta\cos\Theta \Big/ \left[\left(n^2-1\right)\sqrt{n^2\sin^2\Theta - \cos^2\Theta}\right]\right\}, \quad (4.3)$$

where n is the relative refractive index of both prisms, Θ is the angle of internal incidence in the air gap, and $\beta = \sqrt{n^2\sin^2\Theta - 1}$. In the approximation of long distance b and therefore high attenuation, the attenuation factor α changes linearly with air gap b. If the electric vector of the incoming beam is parallel to the plane of incidence, no additional reflection losses occur on the prism surfaces of total internal reflection. In that arrangement at $\lambda = 10.6$ μm, some linear motion of two triangular prisms was applied in a direction nearly parallel to the opposing prism surfaces controlled interferometrically by a He–Ne laser [4.7]. The actual attenuation range reached 4–80 dB for values of $b \geq 0.5\lambda$, but lower factors of attenuation were not realized owing to probable deviation from parallelism of opposing prism surfaces, since the mechanical tolerance and temperature control of that application were not sufficiently adequate.

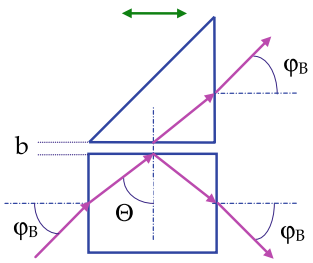

Fig. 4.4 Variable beam attenuator

4.1.2 *Diffuse Attenuators*

One obvious difficulty in making reliable measurements of energy or power extents of laser radiation consists in preserving some uniform measurement reaction for a spatially and temporarily nonuniform distribution of laser light. The reflective and transparent attenuators reviewed earlier do not minimize the initial nonuniform spatial distribution of incident light beams and can even increase directional uncertainty. That constraint can be reversed if diffuse attenuators averaging spatial distributions of laser or spontaneous radiation are used.

Figure 4.5 shows a parallel orientation of diffuse emitter E and detector D separated by distance ℓ and inscribed in a sphere of radius R. Emitter E as disk 1 is seen by detector D as the totality of single point sources located at increasing distance ℓ_R from the center from the point of disk 2. The closer are emitting and sensing disks E and D (compare Fig. 2.28), the greater is the prospect of nonuniform irradiation even with high radiance and uniform scattering indicatrix of the diffuser.

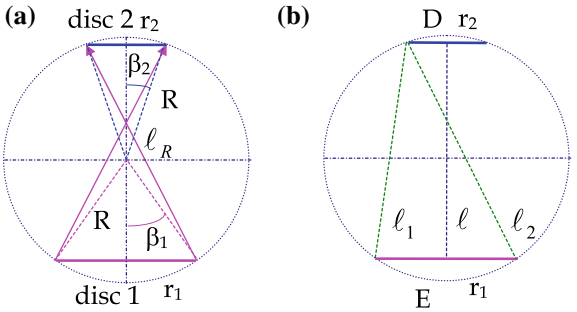

Fig. 4.5 Direct connectivity of radiating and irradiated surfaces: **a** inscribed disks 1, 2; **b** increase of point source distance 1, 2

As reviewed in Sect. 2.4 (see also [4.51–4.53]), any integrating sphere with a diffuse-reflecting internal surface is a more effective spatial integrator than a single diffuser, since after the first reflection of light by a sphere wall, each following irradiance distribution of the internal sphere surface is uniform. Even if the effective reflectance ρ'_0 of the internal sphere surface is only approximately 0.9, not fewer than ten effective sphere reflections take place, increasing uniformity of the sphere irradiance tenfold. Figure 4.6 illustrates the optical system [4.5] combining the simplicity of use of an attenuator with the spatial uniformity of the integrating sphere to measure the power extents of laser light.

The intensity of radiation entering the system is initially attenuated by an extra set of absorbing plates 1, preliminarily measured at operating wavelengths. The measurements can be performed by the radiometric system itself, for nonuniformity of each plate transmission averaged by the integrating sphere, presuming that the plates' attenuation factors are independent of the beam structure. Objective 2, via a fairly small aperture 3, causes a parallel incident beam to be expanded over sphere wall 4, reducing the first sphere irradiance to prevent laser radiation damage of its

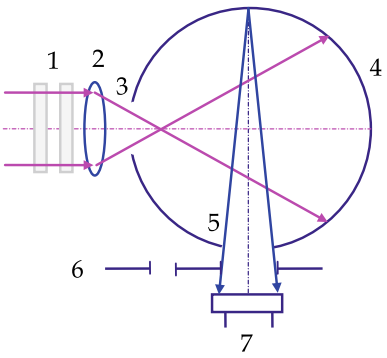

Fig. 4.6 Integrating-sphere-based radiometer

surface. Uniformly diffused light, emerging from aperture 5 onto detector 7, can be attenuated by a set of net attenuators or apertures 6. Spectral filters, selecting the measurement wavelengths, can be installed in any part of the light path. These elements can be combined with attenuators 1 to reduce background noise and preselect testing sources.

The attenuation factor k of any integrating sphere fundamentally depends on the effective spectral reflectance ρ'_0 (see Sect. 2.4) of the internal sphere surface of the total area A_0 and on the relative area A_{out} of its output port or ports: $k = (A_{out}/A_0)/(1 - \rho'_0)$. Therefore, the output port aperture (6 in Fig. 4.6) may serve as the compensator of wavelength-dependent changes: $\rho'_0 = \rho'_0(\lambda)$. One major disadvantage of an optical radiometer with an integrating sphere is due to the relatively high and fixed basic attenuation. For effective reflectance $\rho'_0 = 0.9$ and diameters of sphere 4 and aperture 6 of 70 and 7 mm, respectively, the sphere attenuation is 0.025, decreasing with reflectance. Yet, with an electrically calibrated pyroelectric detector, as high as the −50 to +30 dBm dynamic range is obtainable in the 1250–1650-nm wavelength range [4.53].

One of the first clear-cut fairly accurate laser calibration techniques was deployed not using diffuse transmission, but using diffuse reflection [4.8]. Since the diffuse reflectance of highly reflective white diffusers is close to 1.0 as for the perfect diffuser (see Chaps. 1 and 2), the laser-calibration concept could be based on conformance to the inverse-square law, presuming a uniform distribution of light reflected by the diffuser. If a small detector at distance ℓ to the diffuser is irradiated by the reflected radiation at nearly normal incidence, the ratio of detected and incident power is given by the areas of the detector and an imaginary hemisphere of radius ℓ : $\Phi/\Phi_0 = A\rho \cos\Theta/(2\pi\ell^2)$. Here the reflected radiation is assumed to be uniformly distributed over the hemisphere, and Θ and ρ are the angle of the actual incidence and the diffuser reflectance, which are supposed to be 0° and 1.0, respectively.

A more compact and universal measurement system with a likely broader dynamic range of spectral attenuation involves diffuse transmission of light via a layer

or sequence of layers of an appropriate thickness, but diffusely transmitting opal glass of sufficiently high scattering factor [4.9]. The first front attenuator consists of a translucent single or combined diffuser having one superpolished input surface to increase its laser damage threshold. Added diffusers, apertures, and a detector are separated by air gaps. The added diffusers can be likewise placed in reflected light. The uniform diffuser can be considered as the equivalent point source; thus, the diffuser transformation factor at a given wavelength in the far-field zone is (see Chaps. 1 and 2) [1.12, 1.15]:

$$\Phi_{\tau,\rho} = \tau_d \Phi_0 \Omega_{d,\tau}/\pi = \rho_d \Phi_0 \Omega_{d,\rho}/\pi, \tag{4.4}$$

where Φ_0 is the radiant flux emitted by the uniform diffuser as the point source, τ_d and ρ_d are the diffuse transmittance and the diffuse reflectance of the diffuser, and $\Omega_{d,\tau}$ and $\Omega_{d,\rho}$ are the solid angles in reflection and transmission at which the detector centered via the normal to the beam axis is seen from the center of the diffuser. For uneven scattering distributions of transmitted or reflected light:

$$\begin{aligned} \Phi_{\tau,\rho} &= \tau_d \Phi_0 \int\limits_{\Omega_d} f_\tau(\Theta)\, d\Omega/\Omega_{e,\tau} \\ &= \rho_d \Phi_0 \int\limits_{\Omega_d} f_\rho(\Theta)\, d\Omega/\Omega_{e,\rho}. \end{aligned} \tag{4.5}$$

Here $f_\rho(\Theta), f_\tau(\Theta), \Omega_{e,\rho}$, and $\Omega_{e,\tau}$ are the scattering indicatrixes and the equivalent solid angles in reflection or transmission, and Θ_i is the observation angle for solid angle Ω_i (see (Eq. 1.55)).

If a diffuser cannot be viewed as a point source (see Fig. 4.5), the transformation factor can be obtained via the coupling efficiency $\psi_{1,2}$ between diffuse emitting surfaces in a sphere [0.7, 0.11]. The coupling efficiency for two parallel uniformly diffuse radiating disks is given by:

$$\psi_{1,2} = \left(\frac{L_2 - L_1}{2r_1}\right)^2 = \frac{1 - \cos\beta_2}{1 + \cos\beta_1}. \tag{4.6}$$

Here β_1 and β_2 are the angles defining the views of the diffuse emitter and receiver radii from the center of their common circumference (see Fig. 4.5). Equation (4.6) assumes uniformly radiating diffusers and is only applied to the section being irradiated, not to an entire opening. If a section is part of an entrance diffuser irradiated by a beam whose power or energy is measured, the diameter of the full entrance aperture opening characterizes the maximum coupling efficiency.

Figure 4.7 depicts one example of a combined optical system for broadband laser radiometers with the goal of increasing the dynamic range of measurements by adding optical elements with attenuation factors lower than the intrinsic dynamic range of the registration system. Input section 1 consists of field aperture 2 and a spectral filter or low-attenuating diffuser or absorbing glass 3 mounted on a metal

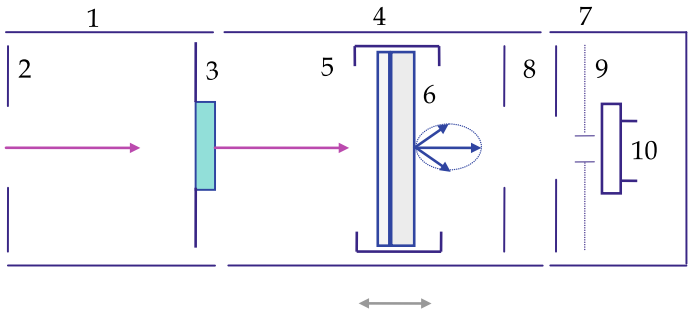

Fig. 4.7 Radiometer combining spatial averaging and attenuation tuning

baffle—each serves to avoid potentially high laser irradiance, which could damage the following dense diffuser. Optical head 4 incorporates either single or dual combination diffuser 6 mounted inside insert 5, establishing the main attenuation of the system for the flux or energy of radiation measured. Apertures 8 and 9 sequentially limit the initial irradiance of sensitive head 7, including system detector 10. Several additional apertures 8 protect the detector's surface from beams retroreflected by mounts and walls.

Either section 1 or section 4 can be attached to sensitive head 7, having attenuation factor F_1 or F_4 adjusted by changing either the distance from the diffuser to detector 10 or to a following diffuser. To make continuous laser power or energy measurements within one expanded dynamic range of the entire system, every attenuation factor must be lower than the maximal linear dynamic range D of detector 10. If the maximum I_{max} and minimum I_{min} of either linearly registered power or linearly registered energy relates as: $I_{max}/I_{min} = D \cong F_1 \cong F_4$, the dynamic range of the combined system D_Σ must be $D_\Sigma = 3D$. That range lessens from 3D to 2D if both heads 1 and 4 are installed, and from 2D to D and from D to the detector's initial level if only head 4 is operated and detector 10 directly measures incident laser radiation. This way, all of the system's attenuators can be self-calibrated in any given spectral region, while being implemented in the system as a transmission object to be studied. Small aperture or apertures 9 serve as additional attenuators if a diffuser is present in section 1 or section 4 [4.10].

As emphasized when deriving Eqs. (4.3)–(4.5), a single or combined diffuser results in spatial integration for nonuniform beams of light if the diffuser irradiates a subsequent detector as the secondary point source and the relative displacements of its effective emitting area are not high. Its attenuation factor is constant if the diffuser performs as a uniform diffusely emitting plane and intermediate device elements are irradiated by uniformly scattered light. If beam displacements do not allow a diffuser to perform as the point source, some additional measures must be taken to establish uniform irradiation. As seen in Chap. 2, the source does not perform as a material point if during observation from the center of a detector to its various emitting areas any visible changes of observation angle θ lead its edge emittance to be lower than that of the source center.

An alternative design illustrated by Fig. 4.8 provides a more balancing attenuation by a lens-shaped transmitting diffuser via the gradient of its optical thickness,

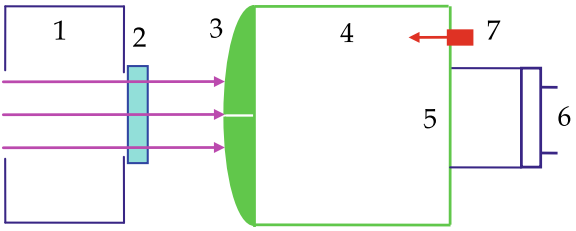

Fig. 4.8 Optical radiometer with lens-shaped diffuser: 1 - aperture; 2 - filter; 3-5 - diffusers; 6 - detector; light diode

as the inverse function of the cosine of the angle of observation: $\cos\Theta$ [4.11]. Such a measure allows one to increase the diameter of incoming beams so they are approximately twice the diameter of the detector: from 14 to 30 mm with a spectral attenuation factor about 200. The cross section of either primary or secondary diffuser 3 and 5 is nearly 40% larger than that of the input aperture. Moreover, the diffusers are enclosed in one container 4 of identical diffusing material to increase the system's integration action, maintaining the uniform diffused transmission for shorter distances between diffusers 3 and 5. The tested spatial nonuniformity of a detector was reduced from ±5 to ±0.3% for a 6-mm-diameter probe laser beam. Light emitting diode 7 was used for control and calibration purposes. The lens-shaped diffuser depicted in Fig. 4.8 allowed the input aperture diameter to be increased from 9 mm to almost 15 mm for an attenuation factor of about 1000. The attenuation factor remained variable from approximately 3000 to 150 at approximately 70–40 mm distances from the diffuser to the detector.

The reviewed designs of the radiometers and photometers for power and energy measurement were targeted at increasing the upper limits of the respective detector's dynamic range for optical-to-electrical signal conversion. The diffuser-based attenuators also improve the spatial or angular uniformity of individual detectors. However, if the detectors themselves are eminently uniform and insensitive to spatial and angular beam displacements of incoming light beams, there is no need for optical elements homogenizing spatial light distributions. A uniformly sensitive detector with a high damage threshold and a broad dynamic range only requires spectral selection and stray-light elimination. A high-threshold thermal detector needs an air- or water-cooling arrangement to maintaining its stable thermal settings. Still, the concept of increasing the intrinsic dynamic range for a radiometric measurement can be used independently of the need for the spatial averaging while measuring parameters of optical radiation. The advantages of using diffusers are also associated with the relatively high damage threshold for most commercial opal glasses, reaching 10^9–10^{10} W/cm^2 without notable nonlinear effects. Such a threshold is usually much higher than the equivalent threshold for absorbing glasses and spectral filters [4.12, 4.13].

4.1.3 Radiometric and Photometric Energy and Power Scales

The transfer (calibration) of a given unit of measurement to a specific radiometer or photometer can be realized by a comparison of the light action and the respective

power or energy dissipation of a known physical process. Such a transfer of a measurement unit is usually established by a thermal detector that functions as the effective blackbody radiator. To measure any energy or power extent of an incoming light beam, additional knowledge of the beam's spectral, spatial, and temporal distribution is likely required. Accordingly, a unique system of calibration standards and calibration outlines is developed for each radiant, luminous, or reduced parameter of light to be measured, such as radiant power, luminous flux, radiant energy, radiant intensity, and irradiance. Consequently, spectral, spatial, and temporal distributions, along with the coherence properties of all measured radiation beams, must be known.

Two evident measurement approaches provide viable solutions to the calibration concepts. According to the first one, the optical response measurement for a radiometer to be calibrated is performed directly by using a beam of radiation carrying a measure of the power or the energy of the transferring unit of measurement. In the second approach, two or more measurements of radiant or luminous intensity of a steady beam of light of known spectral content are sequentially made by a standard radiometer, being the absolute transformer of a given unit, and by the radiometer to be calibrated. The first method is used to make the calibration via measuring the irradiance distribution according to the inverse-square law from a blackbody at any known temperature and distance with the calibrated radiometer placed perpendicularly to a direction of the blackbody emission. The second approach compares the reactions of a standard thermal detector or a standard photodiode, each calibrated in the transferring unit, and a test radiometer.

Most of the conceptual methods for power and energy measurement were reviewed in Chaps. 1 and 2. Each method considers transfer of a radiant or luminous unit by an incoherent light beam of a known spectral, luminous, and effectively reduced spectral or visual efficiency. Conversions for space or time derivatives of power or energy units can be made according to their definitions. Figure 4.9 illustrates relationships among power and energy parameters of optical radiation [4.14].

Certain precautions must be taken when dealing with coherent laser radiation in narrow spectral intervals. Owing to the implicitly high degree of coherence and specific lasing conditions of laser light (see Chap. 3), laser radiation, especially partially coherent pulsed and pulse-modulated beams in comparatively broad spectral domains, may exhibit excessive spatial or temporal fluctuations.

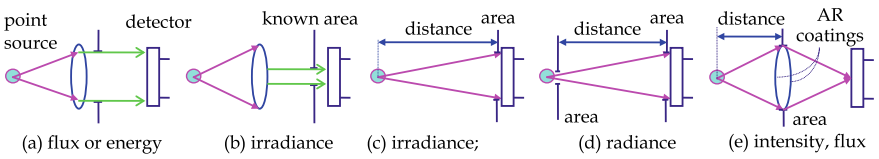

Fig. 4.9 Measurements of power and energy derivatives in confined beams of optical radiation: AR – antireflection

One common procedure for a transfer of the absolute radiometric scale of either the power or the energy to a beam of laser radiation, presumed to be stable and continuous, can be fulfilled by an electrically calibrated thermal detector or self-calibrated photodiode of uniform spatial distribution of its sensitivity across an entrance aperture, adequately larger than the beam's cross section not to necessitate diffraction corrections (see Sect. 3.4). The power or energy of the beam is measured in watts or joules, respectively, while maintaining spectral fluctuations of laser emission not to exceed a threshold of spectral sensitivity for the detector. A similar approach can be realized by measuring pulsed laser light for the maximum power reached by a pulse [0.19].

Figure 4.10 depicts adding a precision modulator 3 and synchronization device 6 for absolute power–energy scale conversion in continuous laser light. When the average power of laser light is measured, modulator 3 is in the open position. When the energy of a pulse is measured, modulator 3 rotates and detector 5 receives laser light during a time interval τ for modulator 3 to be open and create the light pulse. The second, high-speed detector is needed to measure the pulse form and obtain corrections for the actual pulse shape from a perfectly rectangular form. As the speed of the modulator rotation increases, fewer corrections are required for the slow thermal detector. The top modulator speeds are limited by the detector time constant, restricting the intervals required to measure the power of laser radiation pulses. For the specific calibration standard [0.18], the systematic error of the Joule energy scale was $\pm 3.5\%$, adding $\pm 1.5\%$ of random error. For semiconductor lasers with wavelength $\lambda = 0.85$ μm, light modulation was realized internally, reducing the systematic error for transformation of the energy unit to $\pm 1.5\%$ with $\pm 2\%$ random error. Other spectral coordinates can be added via various sources.

Further transformation of each radiometric power or energy scale from one standard to test and reference radiometers may be made by analogy. Depending on the transformation task, the emitting part of the standard, either the laser source or the modulator, can be used to calibrate the detector of a lower-level standard or measurement device. A blackbody-based thermodetector may be used to calibrate a source. Even transitions to scales for the radiant intensity, irradiance, and radiance can be accomplished. Any additional elements, such as calibration apertures for the

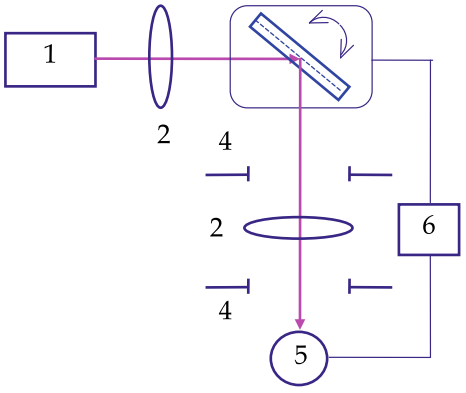

Fig. 4.10 Conversion of energy and power scales

radiant intensity and irradiance, as well as aperture sets at known distances for the radiance calibration, can be used for further transformation based on the primary power-energy standard.

The optical-power measurement standard at the National Institute of Standards and Technology (NIST) is based on the NIST cryogenic radiometer [4.26]. Measurement and electrical calibration procedures for the radiometer are made at cryogenic temperatures around 5 K. The low temperatures allow for substantial reduction of radiative effects due to thermal emission caused by the equilibrium temperature variations of a blackbody cavity. The ability to use superconducting wires permits elimination of a likely nonequivalence of optical and electrical heating, since heat practically does not dissipate in such wires. Reduction of copper's heat capacity at 5 K temperature lets utilize a large blackbody cavity without increasing its time constant. The relative 3σ uncertainty of measurements achieved by that cryogenic radiometer reached 0.021% at 0.8-mW power level [4.26]. For on-chip fiber-coupled cryogenic micro radiometer, the power levels measured reached 50 femto-W to 20 nW at $\pm 0.3\%$ repeatability and NEP (noise equivalent power) of $\sim 5 \times 10^{-15}$ $\mathrm{W}/\sqrt{\mathrm{Hz}}$ at 2-Hz modulation frequency using a 9-micron core SMF fiber [4.89].

4.1.4 Absolute Calibration of Photoelectric Radiometers

An evident way of calibrating sensitive photoelectric-detector-based radiometers is in transferring either a power or an energy scale directly from the source of radiation, possessing the power or the energy calibrated in the unit of a transferring scale, to a radiometer under calibration. The challenge consists in a likely mismatch of the power or energy of a source, such as a cw or pulsed laser, and either the sensitivity or damage threshold of the radiometer's thermodetector or photodetector. That challenge can be resolved by implementing attenuators of known attenuation. In turn, the evaluation process for the attenuator's transformation factors must be done, first, for given source wavelengths, and, second, within the accuracy of calibration. If attenuation reaches several decades, measurement accuracy can be limited by particular radiometer limitations to the linear dynamic range of the detector and the changes in its spatial sensitivity due to expansion of the beam by the attenuator.

Figure 4.11 illustrates the absolute-scale transfer method for indirect calibration of two detectors of distinctly different sensitivity. A sufficiently powerful laser source 1 of radiation at a wavelength of calibration λ irradiates low-sensitivity thermal detector 3 via either antireflection-coated or wedge-shaped beam splitter 2 to avoid interference effects. The absorption and scattering losses of the splitter need to be lower than the measurement errors. For the coated splitter, this means that low absorptance and scattering for both surfaces – one reflective, the other one with the antireflection coating. For the wedge beam splitter, its thickness and wedge must separate the retroreflected beams so they do not interfere within the detector's entrance aperture.

First, two measurements of the power emitted by source 1 with and without the beam splitter are made by the standardized, power-scale-preserving detector 3. For

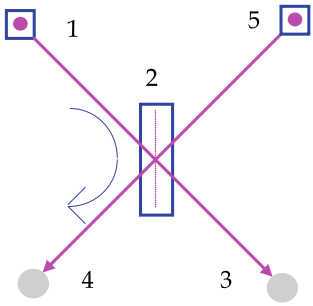

Fig. 4.11 Wide-range power-energy comparison

the wedge-shaped splitter, calibration equations defining the ratios of the fluxes transmitted and reflected by its surface Φ_0 and $\Phi_{\tau.}$ are:

$$\begin{aligned} \Phi_\tau &= \Phi_0\tau_{sp} = \Phi_0(1-\rho_{surf})^2; \quad (1-\sqrt{\tau_{sp}}) = \rho_{surf}; \\ \Phi_\rho &= \Phi_0\rho_{surf} = \Phi_0(1-\sqrt{\tau_{sp}}) = \Phi_0(1-\sqrt{\Phi_\tau/\Phi_0}). \end{aligned} \tag{4.7}$$

If the splitter is a plane-parallel plate, coated in such a way that the reflectance and transmittance of its first and second surfaces are, respectively, $\rho_1 = 1 - \tau_1$ and $\tau_2 \equiv 1, \rho_2 \to 0$, equations (4.7) become:

$$\begin{aligned} \Phi_\tau &= \Phi_0\tau_1 = \Phi_0(1-\rho_1); \\ \Phi_\rho &= \Phi_0\rho_1 = \Phi_0(1-\tau_1) = \Phi_0(1-\Phi_\tau/\Phi_0). \end{aligned} \tag{4.8}$$

After calibration of the beam splitter, the scale transformation from detector 3 to photodetector 4 is made either by Eqs. (4.7) or by Eqs. (4.8). For a wedged glass beam splitter, the power reflected by its single surface is about 25 times lower than that emitted by the source. If the power is still too high to be directly measured by sensitive photodetector 4, stronger attenuation may be achieved by a low-reflectivity coating. The advantage of such a sequential graduation consists in unchanged calibration conditions: properties of the splitter are measured at actual angles of incidence and reflection and can be reexamined at any time. Afterwards, a source less powerful than laser 1, such as a spontaneous emitter for the same wavelength λ, could be calibrated further by already calibrated radiometer 4.

The following indirect procedure for power-to-energy scale transfer is depicted in Fig. 4.12 and is based on a high-frequency power-modulation scheme [4.15] realizing a single-pulse energy scale via the pulse power and its duration. The procedure is undertaken by measuring the average power of a sequence of steady pulses, but controlling the duration of an individual pulse and thus knowing the particular energy of each pulse within such a sequence. When a given light source 1 emits a steady string of pulses at frequency *f*, and when the time constant τ of thermal detector 4—upon which the transferring power scale is based – considerably exceeds the pulse-string period $T = 1/f$ of the string, the response of inertial thermal detector 4 equals the response of the detector receiving the same power of cw radiation.

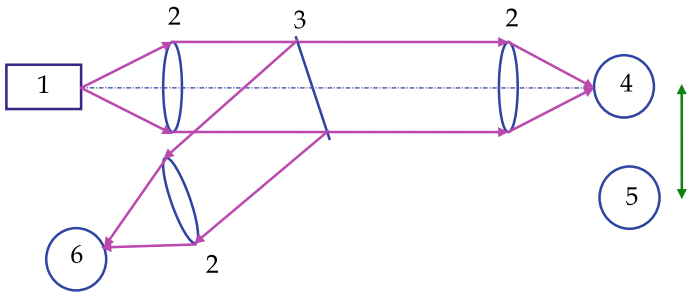

Fig. 4.12 Transformation of power into energy scale via the time domain

In Fig. 4.12, three front objectives 2 form two beams via splitter 3. One irradiates slow power-scale thermal detector 4 or fast radiometer 5 being calibrated in the energy scale. Beam splitter 3 separates a small part of source light so it irradiates fast reference detector 6. The respective time responses τ_5 and τ_6 of radiometer 5 and detector 6 are faster than the pulse string period T but slower than the time duration t of each single pulse emitted by source 1. Thus, when a string of light pulses from source 1 irradiates slow detector 4, only the average power of transforming radiation is measured. For irradiation of fast radiometer 5 by the same string, the energy of each pulse is registered. In any case, if the initial frequency f of the pulse string is changed, reference detector 6 detects the relative variation of energy in a single pulse. As a result, the transformation of the radiometric power scale from the average power of pulse-modulated light to the energy of each pulse in the string sequence is given by:

$$Q = \overline{Q}\left(U_{\text{single}}/U_{freq}\right) = \left(\overline{P}/f\right)\left(U_{\text{single}}/U_{freq}\right). \tag{4.9}$$

Here Q is the single-pulse energy measured, $\overline{Q} = \overline{P}/f$ is the average energy in the sequence of pulses at frequency f, $\overline{P}$ is the mean (average) power of the beam registered by thermal detector 4, and U_{single} and U_{freq} are the respective signals of reference detector 6 for the measurement of energy of the single pulse at frequency f and for the calibration of radiometer 5. As follows from Eq. (4.9), the higher is frequency f of the pulse string, the lower is, at constant average power $\overline{P}$, the energy of a single pulse in the sequence. The higher is the temporal resolution of a radiometer to be calibrated, the lower is the energy for the power-to-energy scale transfer to be granted [4.15].

4.1.5 Detector-Based Spectroradiometric and Photometric Scales

The preceding considerations for calibration of photometers and radiometers were based on referencing a power–energy scale to either an absolute source or a detector. For sensitive instruments, using the blackbody radiator or the absolute

calorimeter leads to obvious dynamic-range mismatch. Meanwhile, the definition of the candela adopted in 1979 (see Chap. 1) is encouraging broader usage of spectrally selective and unselective sources or detectors of monochromatic radiation. That encouragement has opened up prospects for calibration of absolute-scale radiometers based on photodiodes and pyroelectric detectors, which are much more sensitive than any similar thermopile calorimeters.

The advantage of using a pyroelectric detector for absolute calibration is due to the dependence of the detector's response to rate-of-time changes of the detector temperature's, opposite to thermopiles and bolometers, the outputs of which are proportional to temperature gradients. Reaction of a pyroelectric detector to the power or energy of incident light depends on a temperature-induced change of the state of its permanent electric polarization. Radiation absorbed by the pyroelectric crystal is converted to heat, which induces a charge, registered by electrodes on the opposite surfaces of that crystal. If the crystal's polarization linearly depends on temperature, its mean output current becomes [4.16]:

$$J = A(dP/dT)\left(d\overline{T}/dt\right), \tag{4.10}$$

where A is the area of the contacted crystal surfaces, $d\overline{T}/dt$ is the volume average of the rate of the crystal's temperature change over time, and dP/dT is the average change of the dipole moment at a temperature presumed to be uniform. For a light beam of intensity I_0 steadily modulated at frequency ω the current is:

$$J = \varsigma(A/\ell)[(dP/dT)/C_v]\mathrm{I}_0 \exp(i\omega t)\gamma(\omega), \tag{4.11}$$

where ζ is the absorbed fraction of the incident power of light, ℓ is the distance between contacted electrodes, C_v is the heat capacity per unit volume of pyroelectric, and γ(ω) is the complex function of the modulation frequency at a given boundary condition. Unfortunately, γ(ω) is not a constant, especially for low frequencies. At relatively high frequencies, the function approaches a permanent value, most likely not equal to 1.0. Instability of the temperature coefficient for the crystal's responsivity could be a source of inaccuracy, to overcome which a null-type procedure [4.17] is often applied maintaining a consistent reference to some thermal source. Typically, the light beam is modulated by a waveform-independent chopper, having its blades larger than the cross section of the incident light beam [4.18]. When the chopper blades fully screen the beam, any electrical heating of the detector is continually balanced against the radiant heating of the detector.

Another physical approach is more appropriate for absolute calibration of such a spectrally selective detector as a photodiode, relaying on complete photo-to-electric conversion efficiency for ideally manufactured photodiodes [4.19]. That technique is independent of the conventional methods based on thermal emission of a blackbody or an electrical-substitution radiometer. The electrical self-calibration procedure defines the absolute reflectivity and the quantum efficiency for the perfect photodiode. Application of the reverse electrical bias to the photodiode structure, which saturates the electrical current, created by a beam of monochromatic

radiation incident on such a photodiode, allows one to determine its absolute response. To introduce the electrical bias while detecting the power or energy of the beam, a removable transparent electrode, such as a weak aqueous solution of boric acid, not contaminating the diode, can be used. The diode quantum efficiency $\xi(\lambda)$ at wavelength λ of radiation is determined by the direct and reversed magnitudes of the electrical bias. The direct value $\xi_0(\lambda)$ is measured as the ratio of the photocurrent, obtained with zero bias, to the one at the actual bias, which saturates the photocurrent generated by the given light beam. The reversed bias voltage produces the conforming reverse magnitude $\xi_R(\lambda)$. Assuming that $\xi_0(\lambda)$ and $\xi_R(\lambda)$ represent all recombination mechanisms in the diode, the entire quantum efficiency at wavelength λ of incident light is:

$$\xi(\lambda) = \xi_0(\lambda)\xi_R(\lambda)/\{1 - [1 - \xi_0(\lambda)][1 - \xi_R(\lambda)]\}. \tag{4.12}$$

The absolute response $S(\lambda)$ of the photodiode is defined by its reflectivity and spectral dependence of the quantum efficiency $\xi(\lambda)$:

$$S(\lambda) = [1 - \rho_\Sigma(\lambda)] \cdot \xi(\lambda) \cdot \lambda/K, \tag{4.13}$$

where $\rho_\Sigma(\lambda)$ is the total specular and diffuse reflectance of the photodiode and $K = 1.23985\ \mu m \cdot W \cdot A^{-1}$. Since the diffuse-reflectance component for a silicon photodiode is quite low, only the specular-reflection spectrum is controlled for the calibration, making sure the photodiode antireflection coating is sufficiently effective. Multiple experimental comparisons for the self-calibrated photodiodes and absolute electrical substitution radiometers confirmed the adequate match of the two absolute power scales [4.19, 4.22, 4.23].

Absolute detectors are advantageous for transformation of spectrally selective scales, such as spectroradiometric and photometric power and energy scales. The spectral radiance $L_s(\lambda)$ of a thermal source can be approximated using theoretical spectral-radiance function $L_{\lambda,b}(T_c)$ for a blackbody: $L_s(\lambda) = B'(\lambda)L_{\lambda,b}(T_c)$, while applying individual corrections $B'(\lambda)$ when the source and blackbody emit at a given equivalent color temperature T_c. For a tungsten lamp, light emission can be estimated by the third-degree polynomial for the lamp's radiant intensity $I(\lambda)$ given as [4.20]:

$$I(\lambda) = \left(b_0 + b_1\lambda + b_2\lambda^2 + b_3\lambda^3\right)\left(c_1/\lambda^5\right)[\exp(c_2/\lambda T_c) - 1]^{-1}. \tag{4.14}$$

Owing to the smooth spectral distribution and high stability of the tungsten lamp emission, its spectrum, within a narrow spectral region that could be approximated by a single wavelength λ_i selected via a spectral filter or monochromator, can be assumed to be independent of λ:

$$I(\lambda_i) = \left(b_0 + b_1\lambda_i + b_2\lambda_i^2 + b_3\lambda_i^3\right) \int L_{\lambda_i}(T_c)\, dA_s \int \tau_i(\lambda)\, d\lambda, \tag{4.15}$$

where A_s is the source area and τ_i is the transmittance of the spectral selector. At a distance r from the lamp, if it may be considered as a point source, the normal irradiance at the calibrating detector is $E(\lambda_i) = I(\lambda_i)/r^2$. The detector's output created by that irradiance is proportional to its absolute spectral response $S(\lambda) : J_i = \int E(\lambda)S(\lambda)\tau_i(\lambda)\,d\lambda$. Consequently, presuming a constant $E(\lambda_i)$ within λ_i:

$$\begin{aligned} B'(\lambda) &= b_0 + b_1\lambda_i + b_2\lambda_i^2 + b_3\lambda_i^3 \\ &= E(\lambda_i)r^2 \Big/ \left(\int L_{\lambda_i}(T_c)dA_s \int \tau_i(\lambda)d\lambda \int S(\lambda)\tau_i(\lambda)d\lambda \right). \end{aligned} \tag{4.16}$$

Sensing irradiance at four wavelengths resolves all coefficients of the third-degree polynomial [4.20].

A luminous photometric scale for luminous flux $\Phi_v(\lambda)$ can be derived via the spectral distribution of radiant flux $\Phi_e(\lambda)$ emitted by the standard source according to Eq. (1.16) (see Chap. 1):

$$\Phi_v = K_{\max} \int \Phi_e(\lambda)V(\lambda)\,d\lambda. \tag{4.17}$$

Here $V(\lambda)$ is the visual response function defined and tabulated by the International Commission on Illumination (CIE); $K_{\max} = 683\ \text{lm} \cdot \text{W}^{-1}$. The current J of a scale-calibrating detector for radiant flux Φ_e is:

$$J = \int_{\lambda} \Phi_e(\lambda)s(\lambda)\,d\lambda = \int_{\lambda} \Phi_e(\lambda)s(555)s_n(\lambda)\,d\lambda, \tag{4.18}$$

where $s(\lambda)$ and $s_n(\lambda)$ are the detector's absolute and relative spectral sensitivities; $s(555\ \text{nm}) = 1.0$ at wavelength $\lambda = 555$ nm. The luminous responsivity $s(v)$ of any luminous photometer which can be designed on the basis of such a scale-calibrating photodetector can be expressed via a spectral mismatch factor F_v [4.21, 4.22]:

$$s_v = \frac{J}{\Phi_v} = \frac{s(555)}{K_{\max}} \frac{\int_{\lambda} \Phi_e(\lambda)s_n(\lambda)\,d\lambda}{\int_{\lambda} \Phi_e(\lambda)V(\lambda)\,d\lambda} = \frac{s(555)}{K_{\max}} F_v. \tag{4.19}$$

Supposing the relative sensitivity of the photodetector to be corrected exactly as matching the standard visual response function $V(\lambda)$, Eq. (4.19) leads to $s_v(\lambda) = V(\lambda)$. Thus, for $F_v \equiv 1$ the photodetector becomes the perfect visual photometer. From Eq. (4.15) it follows that for the point source its luminous intensity as the illuminance at distance r over any preset area A_d is:

$$I_v[kd] = K_{\max}[lm/W]F_v[sr^{-1}]J[A]r^2[m^2]/\{s(555)[A/W]A_d[m^2]\}, \tag{4.20}$$

where angle brackets designate the units of measurements. Accordingly, the spectral calibration requires evaluating the mismatch of a correction function for the calibrating photometer [4.22].

4.1.6 *Optical Elements of Radiometric and Photometric Standards*

Any practical realization of an absolute unit-scale-carrying system involves high accuracy and repeatability of calibration measurements, thus requiring special measures to be implemented in designs of radiometric and photometric standards. Unaccounted losses of radiation, systematic errors, and/or nonlinearities are among the major causes of calibration errors, as well as various noise components combined into a random error. Let us review some examples of realization of optical elements which might serve in the radiometric and photometric standards.

Figure 4.13 shows a practical example of a fully quantum efficient photodiode assembly in providing the absolute calibration by Eqs. (4.12) and (4.13). Four photodiodes serve as a complete light-trapping assembly for incident radiation to be definitively absorbed within seven interactions over windowless SiO_2-diode structures [4.23]. The trap efficiency, measured as only the first-diode signal I_1, with others cut by the shutter (dotted line in Fig. 4.13), versus the total signal I_Σ:

$$\rho_d \cong 1 - \left(1 - \rho_d^7\right) I_1 / I_\Sigma \cong 1 - I_1 / I_\Sigma, \tag{4.21}$$

reached 0.999 for almost the entire visible range of near 400–800 nm, even at low power levels as approximately 2 mW; in (4.21) ρ_d is the remaining spectral reflectivity of each diode with an antireflection coating applied to its top surface, presuming that $\rho_{d,0^\circ} \approx \rho_{d,45^\circ}$ is a nearly sufficient assumption for low-reflectivity levels.

A similar light-trapping concept is adopted for the absolute spectral response scale at NIST [4.28]. Figure 4.14 depicts the light-trapping detector assembly for five, instead of seven, reflections to accommodate the system's independence of radiation polarization for the optical signal. Incident light comes at 45° to plates 1 and 2, oriented in orthogonal to each other's planes, reflects by the wave normal from plate 3, and thus exits the same way as it enters the light trap.

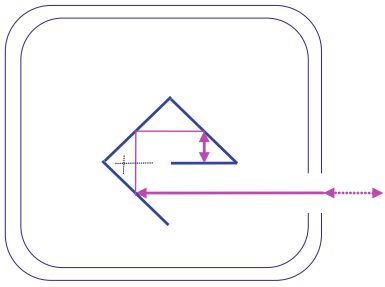

Fig. 4.13 Collinear assembly of four additive photodiodes

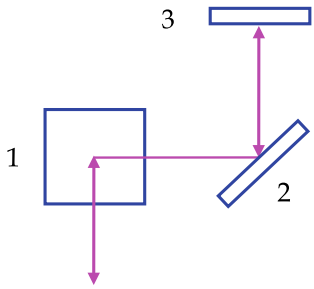

Fig. 4.14 Light-trapping detectors

The arrangement of plates 1 and 2 provides for the first and fifth reflections to be in the orthogonal planes to the second and the fourth ones – all at 45°, with the third reflection at 0°. The full trap detector's assembly is aligned for the reflected and the incident beam directions to be within 0.01 rad of each other. The entire assembly is positioned on one translation stage, setting the light-trapping detector in the middle between points of ±80% of the signal's maximum. Each front surface of the photodiodes has a thermally grown SiO_2 layer as an antireflection coating, reducing the remaining reflectance below 0.4% for most of the 406–920-nm wavelength range. Owing to low reflectance, the responsivity of the light-trapping detector assembly was nearly insensitive to reflectance changes as a result of variations in the quantity of absorbed water vapor for each photodiode (see Part II for details on the low-reflectance and trace-absorption measurements) [4.28].

For an absolute calibration measurement performed by a thermal detector, a cone-shaped cavity, similar to the one in Fig. 4.2, is widely used [4.25]. Figure 4.15 illustrates a broadband receiver assembly designed as a 45° cone for the incident beam to have at least four internal reflections before being absorbed with overall absorptance $\alpha \geq 0.99\%$. The cone with a 3.2-cm diameter aperture is constructed of oxygen-free high-conductivity copper with 0.13-mm-thick walls blazed to a 0.05-mm-thick and 30.4-mm-long stainless steel cylinder as an intermediary heat sink connected to the main one. The inner surface of the cone is

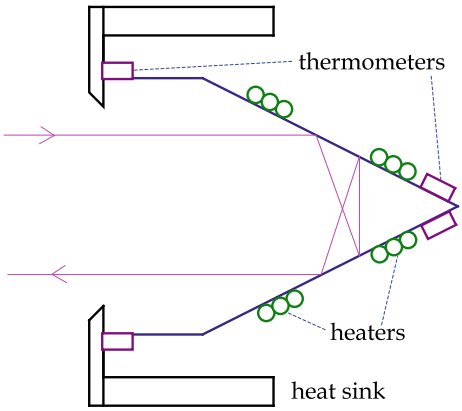

Fig. 4.15 Thermal detector assembly

coated with specularly reflective carbon black paint and the outer surface is attached to the resistance thermometers and heaters. The measured specular reflectance of the cone ranged from 5 to 10.5% for 0.3–40-μm wavelengths with diffuse component of less than 1%, leading to a calculated absorptance above 99%. The testing performed by an expanded He–Ne laser beam at 633 nm confirmed 99.8 ± 0.1% absorptance [4.25]. Implementation of an absorbing cone into a radiometer involves external systems of stray light baffling and temperature stabilization, quite elaborated in optical and mechanical design [4.26].

A typical system for the radiometric comparison of various standards or the transfer of a unit of measurement consists of a source of radiation of any wavelength of comparison and a system for swapping the comparing devices into identical positions of receptions for the source's radiation. Figure 4.16 depicts a laser system for comparing scales of a thermal-cone detector and photodiode-trap detector, dedicated for the NIST high-accuracy cryogenic radiometer [4.26]. Owing to the cryogenic temperatures utilized in the standard, first developed at National Physical Laboratory [4.29], the relative standard uncertainties for optical power measurements are within ±0.01%. To compare or transfer the optical power scale at that level for the broadband thermal detector and narrow-band photodiode, the laser's wavelength bandwidth is also maintained within ±0.01%, as is the geometry and positioning of an optical beam formed by the system's spatial filter.

A polarized beam of radiation from the laser is power-controlled by the stabilizer operated via the feedback monitor, receiving the signal reflected from the wedged window placed at the far end of the system to accommodate alignments for most of its elements. The beam geometry is defined by a 25-μm spatial filter positioned at focal points of two microscope objectives. Only the central spot of the Airy diffraction pattern between two minima passes through, thus minimizing diffraction or edge scattering errors. The polarizer filters birefringence errors in the wedged window and maintains the light polarization perpendicular to the plane of incidence at the mirror. The shutter blocks the laser light during the electrical calibration of the thermal detector.

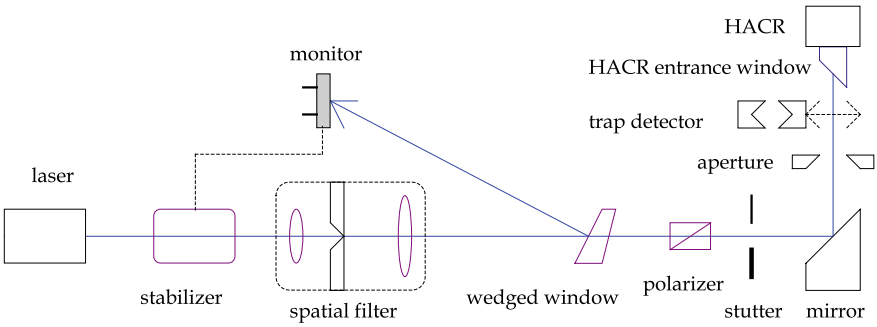

Fig. 4.16 Laser-based radiometric comparison scheme for optical-power transfer measurements

4.1.7 Radiometric and Photometric Scales for Spectral Irradiance and Luminous Intensity

Since the CIE accepted the definition of the candela via the spectral radiant intensity (see Chap. 1), any conversion of a radiometric or photometric scale became adoptable to spectroradiometric means of a given choice. Calibrating the scales of radiant or luminous intensity via the scale of spectral irradiance is particularly advantageous owing to the availability of blackbodies, producing practically a Planckian radiation distribution at precise temperatures, and owing to straightforward conversion of irradiance into radiant intensity at a precisely known distance to the source (see Fig. 4.9). As one example of scale conversion, Fig. 4.17 depicts the scheme for spectral-irradiance calibration via blackbody radiation of the standard source at NIST [4.28].

The radiance scale is set by a high temperature blackbody source via its output aperture, and is then converted to the scale of irradiance or illuminance for the calibrating radiometer or photometer with its aperture and NIST standardized spectroradiometer, as a radiance-to-irradiance/illuminance scale transformer [4.30]. Application of the high-temperature blackbody source operating at temperature $T \geq 3000$ K versus a similar gold-freezing source is driven by the need to increase the spectral output $W_\lambda(T)$ of the source radiation in accordance with Wien's law:

$$W_\lambda(T) = \left(c_1/\lambda^5\right) \exp(-c_2/\lambda T). \tag{4.22}$$

Here $c_1 = 3.74177118 \cdot 10^{-16}$ W · m^2 and $c_2 = 1.4387752 \cdot 10^{-2}$ m · K are the first and second radiation constants.

By comparing the responses of the standard and calibrating spectroradiometer and photometer, one can transform the irradiance scale, while also identifying the

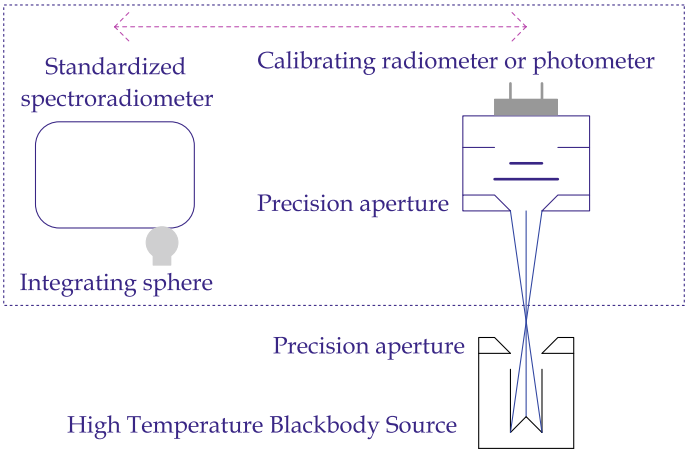

Fig. 4.17 Spectral irradiance or illuminance calibration scheme

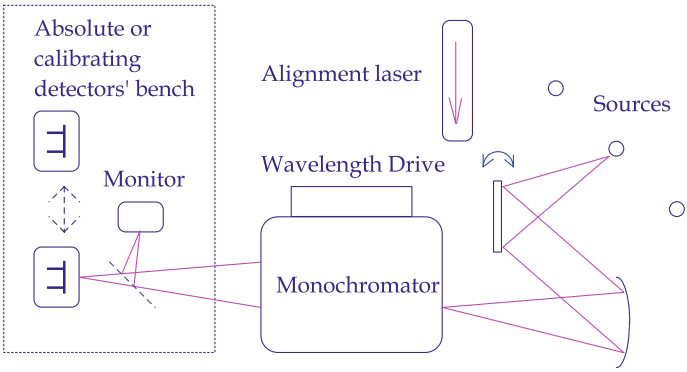

Fig. 4.18 Spectral calibration of photometric response

temperature of the blackbody radiation being used for the transformation. A comparable approach is applied to transformation of the luminous intensity scale via the absolute detectors and standardized sources versus each other for a spectral reaction (Fig. 4.18).

Similarly to Fig. 4.17, each calibrating photometer is fitted with a precision aperture while measuring the illuminance. The absolute and calibrating detectors substitute each other on the photometric bench via standardized sources calibrated by blackbodies, while Eqs. (4.12)–(4.20) are utilized for the conversion of the radiant to luminous intensity [4.30].

During spectral calibration measurements it is useful to attest the relative spectral distributions of power Φ_λ and sensitivity R_λ for respective sources and detectors, when dealing with reduced, such as photometric, quantities or scales:

$$\varphi_\lambda(\lambda) = \Phi_\lambda(\lambda)/\Phi_\lambda\left(\lambda_{peak}\right);\ r_\lambda(\lambda) = R_\lambda(\lambda)/R_\lambda(\lambda_{\max}), \tag{4.23}$$

where λ_{peak} and λ_{max} are the peak and the maximum wavelengths for source radiation and detector sensitivity, respectively. The detector-integrated sensitivity R_Σ as a spectrally reduced quantity is:

$$R_\Sigma = \int_0^\infty \Phi_\lambda(\lambda) R(\lambda)\, d\lambda \Big/ \int_0^\infty \Phi_\lambda(\lambda)\, d\lambda \ \ [A/W]\,. \tag{4.24}$$

Utilizing the designations of Eq. (4.23), the normalized detector's sensitivity becomes [4.31]:

$$R_\Sigma = R_{\lambda\max} \int_0^\infty \varphi_\lambda(\lambda) r(\lambda) d\lambda \Big/ \int_0^\infty \varphi_\lambda(\lambda) d\lambda\ [A/W]. \tag{4.25}$$

4.2 Attenuation and Color Photometers and Spectrophotometers

4.2.1 Measurements of Direct Transmittance and Specular Reflectance

Common design concepts for broadband and while-light photometers, as well as spectrally selective radiometers and spectrophotometers, often implement the methods of attenuation measurements discussed in Chap. 2. Realization of a given method in a specific device requires certain broad precautions to be used. For example, all attenuation photometers, and spectrophotometers especially, must prevent negative effects of radiation-beam displacements and instabilities of source power or energy on the measurement results. The reasons for variations may be varied, but preventive actions are universal.

Introduction into a light path of a substance of length ℓ and refractive index n_s not equal to the refractive index n_0 of the surroundings changes the length of that path by $\Delta\ell = \ell(n_s - n_0)$. The path-changing effect does not mean much for the attenuation under study by itself, though, owing to expected divergence 2Θ of the incident light beam, any position changes as functions of both 2Θ and $\Delta\ell$, including the sign of displacement $\Delta\ell$ (Fig. 4.19), may alter the reaction of the system's detector. Retroreflections among sample surfaces of refractive index n_s and an optical element with index n_i (see Chaps. 1 and 2 and Fig. 4.19c) could lead to random changes in the detector's response. A certain design elegance for any attenuation photometer would consist in establishing the stability of the detector's spatial sensitivity not exceeding the random error of the photometer's measurement. The balance can be established by the detector itself or can be aimed at via additional spatial integrators.

The ways to reduce spatial nonuniformity in power measurements were reviewed with the analysis of optical radiometers in Sect. 4.1. In attenuation studies the beam displacements are relatively small and it is often sufficient to install the single diffusing plate in front of a detector. Integrating spheres are rarely used since even one diffuser distant from the detector can decrease the effects of measured beam spatial fluctuations without significantly increasing beam attenuation (Fig. 4.19a). An alternative solution is shown in Fig. 4.19b. The negative lens

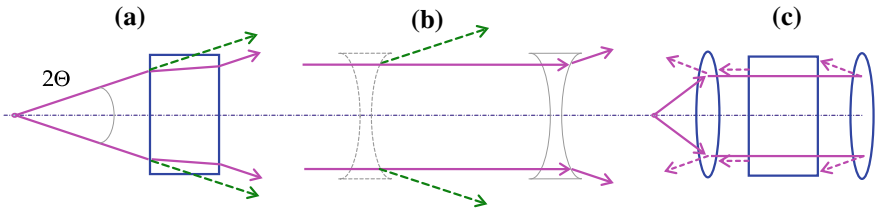

Fig. 4.19 Beam cross-section transformation (**a**), its compensation (**b**), and some retroreflection effects (**c**)

slightly widens the beam if a test sample is present (dotted lines in Fig. 4.19b), and narrows the beam when the sample is absent (solid lines in Fig. 4.19b). A lens can also serve to measure the detector's spatial sensitivity to beam diameter change.

In contrast to the features of the single-sample transmittance study seen in Fig. 4.19, specular reflectance measurements are not altered by changes in the cross section of the reflected bean. However, the beam exposure on the surface of most detectors is very sensitive to its position and inclination angle. Each displacement made by relative dislodging of an optical axis of the beam may cause one or another modification of the detector's output. Corrective measures for a given reflectometer could provide an unwavering transformation of the propagation direction for the incident beam or maintain some extra optical compensation for a substantial displacement of the reflected beam.

Figure 4.20 illustrates two examples of conventional compensation measures. Without test mirror 3, each compensation element—spherical mirror in Fig. 4.20a and transparent plate in Fig. 4.20b—is in initial position 4. When studied reflector 3 is implemented, mirror 4 is moved to position 4′, but plate 4 is taken out of its optical path, with the beam splitter swapped from position 2 into 2′. A suitable compensation in the first case [4.32] is achieved by moving test reflector 3 around a geometrical center of spherical mirror 4 at the mirror's focal length much longer than the displacement. In the second case, the compensation is ensured by the thickness and position of compensation plate 4, which neutralizes parallel beam displacements by beam splitter 2 during the transmission–reflection measurement cycle. Typically, reflectometers with compensators require preliminary nonuniformity testing since spatial changes of reflectance of the spherical mirror as a function of the beam cross section and the position of the mirror axis affect the results of reflectance measurements.

Let us review one scheme of the two-beam stabilized attenuation photometer and/or spectrophotometer for the measurements of specular and mixed reflectance and transmittance depicted in Fig. 4.21. This design was explicitly used for a pulsed-radiation spectrophotometer, though the design involves common stabilization concepts [4.33, 4.34]. A given light source 1 emitting spatially and temporary unstable radiation in pulsed or cw mode irradiates thin opal glass 2. Diffuser

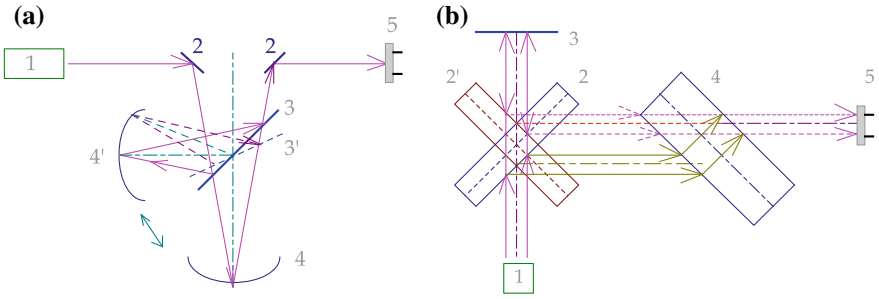

Fig. 4.20 Regular reflectance measurements with compensations of beam displacements: 1 - light source; 2 - supplemental mirrors and beamsplitter; 3 - mirror under test; 4 - displacement compensator; 5 - detector

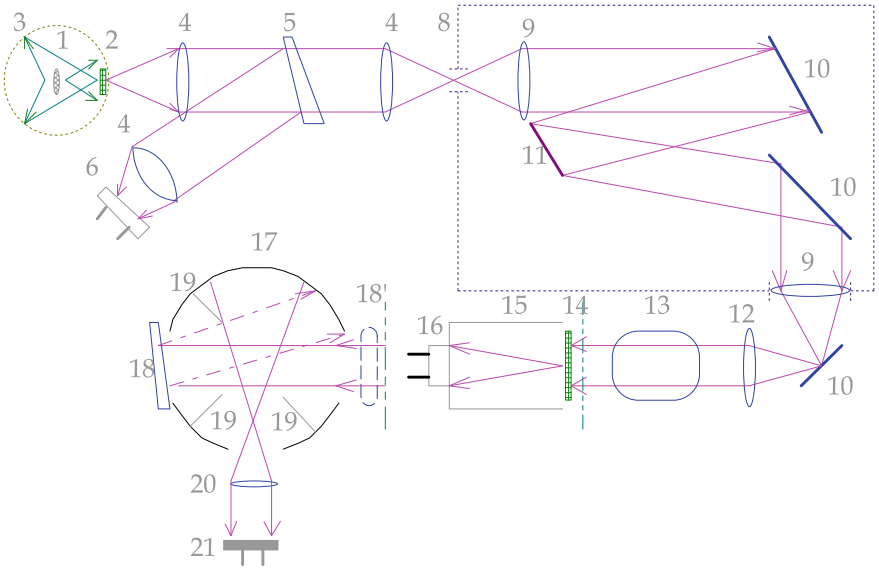

Fig. 4.21 Dual-channel attenuation photometer

2 serves to smooth the spatial distribution of that emittance, but it causes some additional attenuation. If the distance between source 1 and diffuser 2 is small, the extent of such attenuation is low. For a flashlamp with translucent emitting plasma, added integrating sphere 3 with either diffuse or specular reflectance of its wall could be more effective (see Chaps. 2 and 3), since it makes the emittance of source 1 spatially uniform and also increases the throughput of light emitted back by the source. That action is not effective for halogen lamps with opaque emitters.

Two objectives 4 form an image of thin diffuser 2 functioning as a secondary light source in front of the entrance pupil of spectral selector 8. Part of its output beam is directed via low-reflectivity beam splitter 5 to reference detector 6. Depending on the measurement task being performed, either a monochromator or a set of interference filters serves as spectral selector 8. Diffraction grating 11 and a not shown extra set of intensity filters or spectral filters are placed in the parallel path formed by objectives 9 and mirrors 10, providing steady quasi-normal incidence of radiation on each spectral selector: either a monochromator or a filter. Objective 12 shapes a parallel beam of light irradiating transparent object 13 under study. The beam of transmitted light is received by the second spatial integrator 14, decreasing the influence of beam displacements and reirradiating detector 16 spaced from integrator 14 by blackened cylinder 15, reducing stray light. For measurements of diffuse reflectance and diffuse transmittance, integrating sphere 17 is placed in the same parallel beam path as for any transmission study. Reflective sample 18 is irradiated at a relatively small angle of incidence of 4° or less, directing reflected light onto the sphere wall. Baffles 19 preserve the viewed-by-detector sphere wall and output aperture from being irradiated by radiation directly scattered by sample 18. Objective 20 forms a diffuse-scattering beam, irradiating internal detector 21. Translucent sample 18′ is installed before an entrance opening, and an aperture for reflecting samples is then substituted by the detachable cap of the integrating-sphere wall. Depending on the

measurement task to be performed, a variety of the measurement methods analyzed in Chap. 2 can be used.

4.2.2 *Polychromatic and Spectrophotometric Systems*

When studying optical properties of a fast process having sharp features in broad spectral domains, one obvious shortcoming of the optical schemes reviewed above is defined by the relatively long time intervals needed to register a quickly changing property, while a monochromator provides any sequential wavelength scanning over a broad spectral interval. From the standpoint of simultaneous registration, a polychromator registering an entire source spectrum at once becomes advantageous for fairly fast phenomena.

Figure 4.22 illustrates the integrating-sphere polychromator designed for transmitted, reflected, and scattered light in broad spectral domains. Incident light is diffusely transmitted or reflected by samples 1 or 1′ (dotted line) and registered inside integrating sphere 2 by set 3 of either different spectral detectors or similar receivers, seen via individual spectral filters 4. A 100% line is measured concurrently for all these detectors when the output aperture of sphere 2 is filled in by the undisturbed spherical cap 5, reflecting incident radiation as the sphere surface with no inclusions. For high sensitivity of each detector, the sphere diameter and consequently the number of detectors can be high enough to cover any broad spectral domain. For low reflectivity of that sphere, its effectiveness might not be sufficient. If the power or energy of the light source is unstable, one of these detectors would serve as the reference detector. That measure establishes a stable ratio of each spectral selection either to spectrally unresolved radiation or to any given spectral line [4.35]. Certain restrictions apply to such a method and to its spectral resolution. Besides, the accuracy of measurements in the integrating sphere with lots of inclusions may not be adequately high (see Sect. 2.4).

Conventional measurements of internal sample bulk transmittance are commonly performed by dual-beam spectrophotometers. Two samples of contrasting lengths of the test substance are installed in sequence in the main beam or at once in

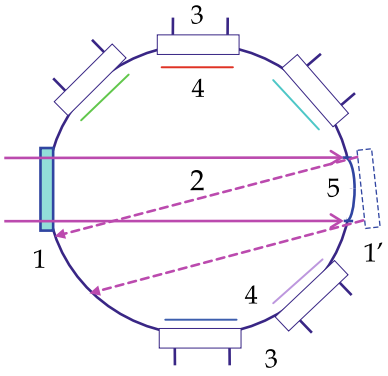

Fig. 4.22 Polychromatic integrating sphere

the main and reference beams. If all four surfaces of these two samples are equivalent to each other, the internal transmittance τ of the test substance is determined by Eqs. (2.41) and (2.47) as the ratio of two sample transmittances. In such a case, the requirements for the four surfaces to be assumed equivalent are not exceptionally strong. For example, a relative change of the total sample transmittance at a given wavelength λ : $\tau_{s,\lambda} = (1-\rho)^2$, due to reflectance change Δρ of any single surface without accounting for internal multiple reflections is:

$$\Delta\tau_{s,\lambda}/\tau_{s,\lambda} = \pm 2\Delta\rho/(1-\rho) \underset{\tau=1-\rho}{=} \pm 2\Delta\rho/\tau\,. \tag{4.26}$$

For n = 1.5 and Δn = ± 0.001, the magnitude of the total reflectance change for the entire sample $\rho = [(n-1)/(n+1)]^2$ becomes $\Delta\rho = \pm 0.25\%$, but the relative transmittance error remains small: $\Delta\tau_s/\tau_s = \pm 2 \cdot 10^{-4}/0.96 \cong 0.02\%$. The sample's internal transmittance, counting multiple reflections, is $\tau_s' = (1-\rho)^2/(1-\rho^2)$, with uncertainties $\Delta\tau_s'/\tau_s' = \pm 2.08 \cdot 10^{-4}$. Thus, the bulk transmittance measurement for comparable samples may be made without knowing the exact surface reflectances.

The layout of a common dual-beam spectrophotometer with an optical-null element is shown in Fig. 4.23. The main challenge of instrument design is in maintaining equivalent attenuation of light for the main and reference beams. In this arrangement, channel equivalence is maintained via additivity of the transmittance and reflectance of beam splitters 5 and 5′, $\tau_5 + \rho_{5'} \cong \rho_5 + \tau_{5'}$, assumed to be identical and expecting equivalence of the reflectance values of mirrors 6 and 6′. Providing the equivalence of both channels is established, the measured difference in attenuation of light for samples 9 and 10 is defined only by inequality of their optical densities. When electronics identify a noticeable difference in two sample densities, wedge 7 and subwedge 8 provide compensation for the difference noticed. When the measurement is made by maintaining equal attenuations in the

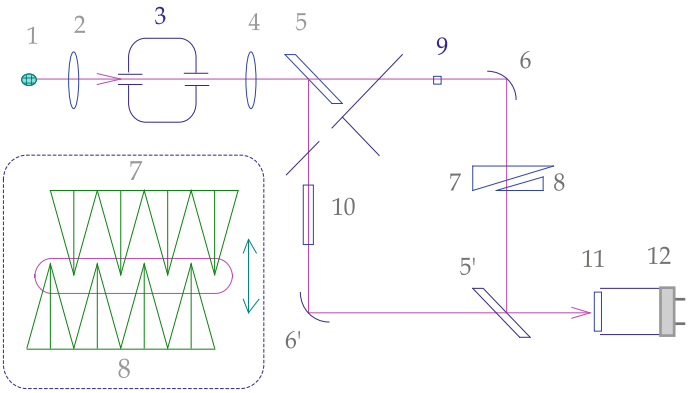

Fig. 4.23 Structure of a dual-beam spectrophotometer: 1 - stabilized light source; 2, 4 - objectives; 3 - spectral selector (monochromator); 5 - beam-splitters; 6 - mirrors; 7–8 - null element: wedge and sub-wedge; 9, 10 - short and long samples; 11 - spatial integrator; 12 - detector

beams being compared, sector attenuators substitute optical wedges (dotted insert in Fig. 4.17) to equalize for extra attenuation created by the long sample. Preceding calibration of attenuators at least by their light-shading geometry (see Sect. 4.3) identifies the attenuation by relative positions of the wedges. The factual equality of the measuring and reference beams needs to be verified for each measurement, which defines the achievable accuracy for that method [4.36].

Figure 4.24a depicts an optical structure of a registering spectrophotometer providing simultaneous reflectance and transmittance measurements by having a

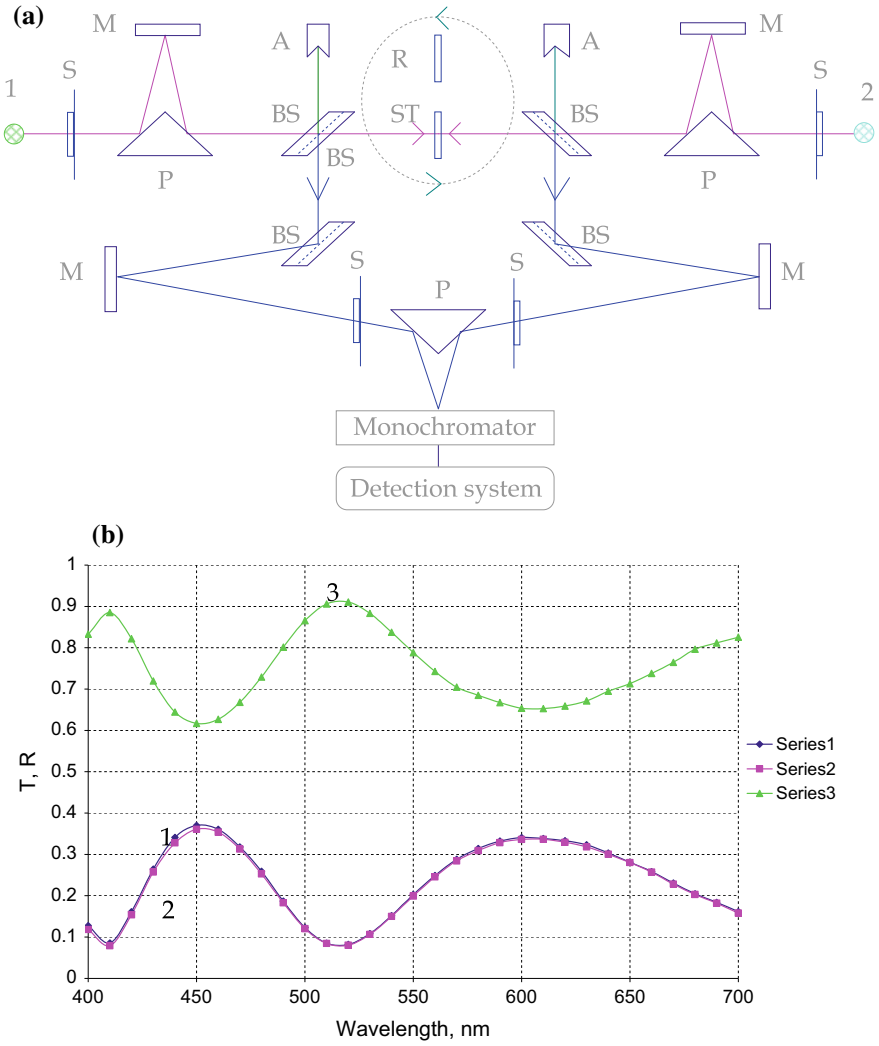

Fig. 4.24 Optical structure of a dual-purpose symmetrical reflection–transmission spectrophotometer (**a**) and experimentally measured transmittance: series 3, and front and back reflectance: series 1 and 2, of a ZnS sample (**b**)

symmetrical dual-beam optical design [4.37]. As analyzed in Chap. 2, when complementary attenuation factors of a sample, such as reflectance and transmittance, are concurrently determined at a given spectral coordinate, its scattering and absorption losses can be obtained more accurately than when making separate transmittance and reflectance measurements. Here two light beams from 100-W tungsten-halogen lamps 1 and 2 irradiate a reference or a studied sample marked RE and ST via nondispersive mirror optics consisting of prisms P and concave mirrors M. Extra absorbers A reduce the intensities of beams reflected back to the system from beam splitters BS. Four shutters S sequentially isolate every pair of transmitted and reflected beams, evenly transformed to an entrance slit of the monochromator. The simultaneous measurements of transmittance and reflectance from two opposite directions were performed by tuning the beam splitters individually [4.37]. Since the transmittances in both directions must have been equal, the measured difference confirmed the systematic error of approximately 1% (see Fig. 4.24b).

4.2.3 Reference Transmission Spectrophotometers

Most reference spectrophotometers applied for standardization purposes are required to maintain measurement accuracy near the ±0.01% level. Especially tight requirements for each aspect of a spectral transmittance measurement procedure should be implemented to achieve or exceed that level of accuracy (see Chaps. 1, 2 and 3 and Part II and Chap. 5, in particular, for further details). In this section let us review the concepts of two versions for such a reference spectrophotometer, deployed at NIST and NRCC [4.44, 4.45], respectively, with each based on the single-beam measurement method schematically shown in Fig. 4.25. Every version deploys normal

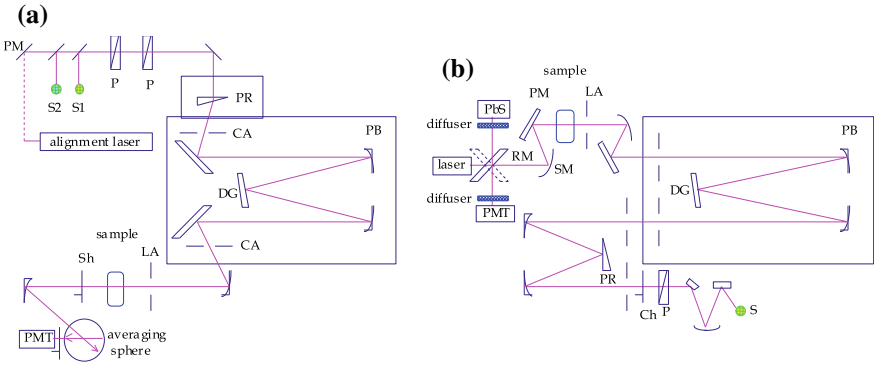

Fig. 4.25 Reference transmission spectrophotometers: S - source; PMT - photomultiplier; PM, SM - plane and spherical mirror; PB - off-axis parabolic mirror; PR - prism pre-dispenser; DG - diffraction-grating based monochromator; P - polarizer; Sh - shutter; Ch - chopper; RM - rotating mirror; PbS, PMT - detectors; LA, CA - limiting and circular aperture

incidence of light on a plane-parallel slab as the reference sample, avoiding measurement discrepancies due to inconsistent angles of incidence or propagation, but not spatially separating the multiple reflections between two sample surfaces themselves and other normal to the beam elements, therefore adding the potential complexity of the coherence-induced phenomena associated with the spectral studies.

Figure 4.26 depicts the arrangement of spectral irradiation of a sample for spectrophotometric imaging. The monochromator's exit slit serves as a secondary source of spectrally narrow radiation, which is imaged by the objectives on the detector. Coherence properties of such a source could contribute to interference and diffraction effects caused by partial coherence of the source (see Chaps. 3, 6 and 10 for details). According to the Van Cittert–Zernike theorem [1.1] (see Sect. 3.1), the image of the monochromator slit carrying the properties of the sample being studied would have a section of size $D' = 0.16 \cdot \lambda/\varphi$ illuminated almost coherently by a quasi-monochromatic uniform incoherent source of angular radius $\varphi = r/R$, where r is the source radius and R is its distance to the image.

Thus, within the accuracy of geometrical optics, an incoherent quasi-homogeneous uniform source of light creates a section within the exit pupil of the coherently illuminated area of size:

$$D'_{coh} \cong 0.16 \cdot \bar{\lambda}_0/(n' \sin \varphi') = 0.16 \cdot \bar{\lambda}/(\sin \varphi'), \tag{4.27}$$

where $\bar{\lambda} = \bar{\lambda}_0/n'$ is the mean wavelength of radiation in the image space. The size of this coherent image can be evaluated by observing either the interference pattern or the diffraction pattern and measuring the radius of the first Airy ring, $r_A = 0.61\bar{\lambda}_0/NA'$, where NA′ is the numerical aperture of the image [1.1, 4.44]:

$$D'_{coh} \cong 0.26a' r_A'/r'. \tag{4.28}$$

Here a' is the size of the exit pupil or exit slit in Fig. 4.26 and r′ is the size of the geometrical image of the exit slit of monochromator serving as the secondary light source for coherently irradiated spot D'_{coh}. If $D'_{coh} \geq 2a'$, the image space is irradiated coherently, causing the creation of visible interference or diffraction patterns owing to nonuniformity of irradiation or sample properties (Fig. 4.26, spots 1, 2).

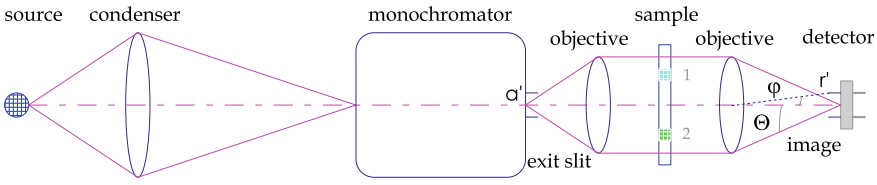

Fig. 4.26 Irradiation of a sample in a spectrophotometer

Considering the occurrence of a final-size area of source coherence during spectrophotometric measurements of transmittance, certain measures need to be taken to limit the size of that area and to provide sufficient spatial and temporal averaging of potential interference and diffraction patterns created during the sample study. For example, schemes of light focused on the sample are particularly sensitive to such effects, and thus should not be used for measurements. Each reference-spectrophotometer design shown in Fig. 4.25 addresses various aspects of accurate spectral measurements of transmittance – preserving the light-beam uniformity and divergence, parallelism of sample surfaces, elimination of multiple reflections within the sample and among sample and system's elements, reducing interference and diffraction effects, and accounting for light detector nonlinearities (see Sect. 4.3). Instead of lens objectives for sample irradiation, off-axis parabolic mirrors are used, having their optical axes on opposite sides of the system axis. The alignment laser serves for setting optical elements and sample surfaces at normal incidence. The main polarizer sets the defined state of polarization for the grating monochromator and the second one is used for linearity verification. Any stray-light level is minimized using dual monochromators with lens predispensers, maintaining 1-nm-level spectral resolution for 2–3 mm-wide exit slits to minimize interference. The design in Fig. 4.25a uses the averaging integrating sphere to prevent detector-homogeneity error due to beam displacements by the sample; the system in Fig. 4.25b is sufficiently uniform with a diffuser placed in front of each detector. Repeatability of transmittance measurement in both systems for neutral filters without steep spectral slopes was maintained within $\pm(1–4) \cdot 10^{-5}$ for systematic errors estimated not to exceed $\pm(1–2) \cdot 10^{-4}$ [4.44, 4.45].

4.2.4 Specialty Spectrophotometers

If the spatial uniformity of an object needs to be studied with submillimeter resolution or the samples themselves are of miniature sizes, the spectrophotometer's design may evolve to accommodate these tasks. Figure 4.27 depicts a fiber-based system for transmission and reflection measurements of optical components for wavelength division multiplexing [4.52]. Addressing, to a certain extent, the coherence issues discussed above, the design involves channel splitting and combining in white light spectrally resolving signals just prior to detection. White light from the source is coupled into a 200-μm-core optical fiber, the output of which is magnified and focused into a set of pinhole apertures via variable attenuators to establish beam sizes from 0.1 to 2 mm. The input beam is split to the reference detector and the main part is refocused on the reflective and transmissive sample via semitransparent mirrors. Transmitted light and reflected light via two 400-μm intermediate fibers are delivered in sequence by the moving mirror into the 600-μm-core fiber and the spectrum analyzer. Since owing to the design requirement the system focuses light into sample and pinhole apertures, diffraction and coherence-induced phenomena should play a

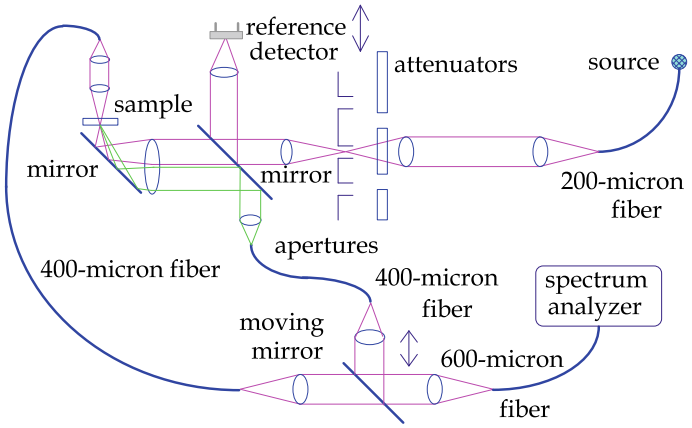

Fig. 4.27 Sub-millimeter beam size spectrophotometer

role in affecting the measured transmittance and reflectance. Comparison of the designed system and a PerkinElmer Lambda 18 spectrophotometer revealed near 1.5% discrepancy between the loss measurements performed with the two instruments despite ±(0.01–0.1)% repeatability of the individual studies [4.52].

Figure 4.28 shows a system for spectral transmittance and reflectance measurements of powder substances to be dispersed within a clear immersion fluid [4.54]. The outgoing beam from the spectral selector of the spectrophotometer is guided via optical fibers into main and reference channels, synchronously modulated by chopper Ch, and received by detectors D_M and D_R. Two configurations are used: configuration *a* for transmittance and configuration *b* for refractive-index measurements. The 60°-sapphire Dove prism DP is used for each measurement. A thin layer of immersion fluid with isotropic powder-substance particles is defined by moving window W via the null reading when touching the prism's window. The prism itself is immersed in purified water to reduce front and back surface reflections, and apertures A_1 and A_2 in front of polarizer P and main detector D_M serve to reduce the overall scattered light, though they can contribute to unobserved diffraction phenomena. S-polarized light was used for the studies at a given wavelength and varying the angle of incidence by the stepper motor [4.54]. For waveguide applications the

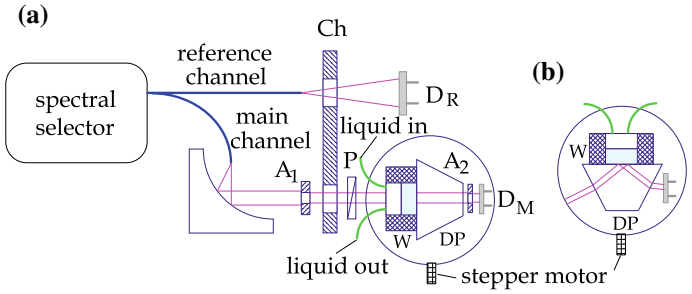

Fig. 4.28 Immersion spectrophotometer: **a** transmittance; **b** reflectance

spectrometers themselves can be miniaturized using on-chip technologies by deploying microring and microdonut resonators and diffraction grating arrays in silicon-on-insulator or other CMOS-compatible platforms to reach sub-nanometer resolutions in narrow operating bandwidths [4.76, 4.77].

4.2.5 *Systems of Multiple-Beam Interactions*

As follows from Eq. (2.41), for dual-beam comparison, the larger is the difference of the lengths for two measured samples: $\Delta\ell = \ell_{long} - \ell_{short}$, the smaller are the bulk losses that can be detected, with linear attenuation coefficient μ of the samples' bulk:

$$\mu = \left(\ln \tau_{sh} - \ln \tau_{lg}\right) / \left(\ell_{lg} - \ell_{sh}\right). \tag{4.29}$$

The smallest difference of the two logarithms in expression (4.29) to be distinguished is defined by the resolving power $\delta N = 1 - \tau_{lg}/\tau_{sh}$ of a given measurement system. The longest possible length of any test sample is restricted by the permissible dimensions of a measurement system and the possibilities of fabricating a particular material. To have high sensitivity with limited resolving capacity, a high effective but not necessarily actual sample-length contrast of a test substance needs to be achieved.

Two typical layouts designed to increase a number of light interactions with an object to be measured are depicted in Fig. 4.29: the dual-transmission measurement system [4.38] and the dual-interaction cavity for the reflectance study [0.6, 4.32, 4.39]. In each system light interacts twice with test sample 3: once directly and again by backreflection from supplemental mirror 4.

The prism and mirror dual-pass cavity for the measurement of transmittance is formed via prism 2 and mirror 4. For all reflectance studies, the dual-interaction cavity is made via mirrors 2 and 4. The initial 100% line in Fig. 4.29a is registered with the moving mirror in initial position 4′, which is then moved to measurement location 4, defined by the length and index of refraction of sample 3 maintaining the

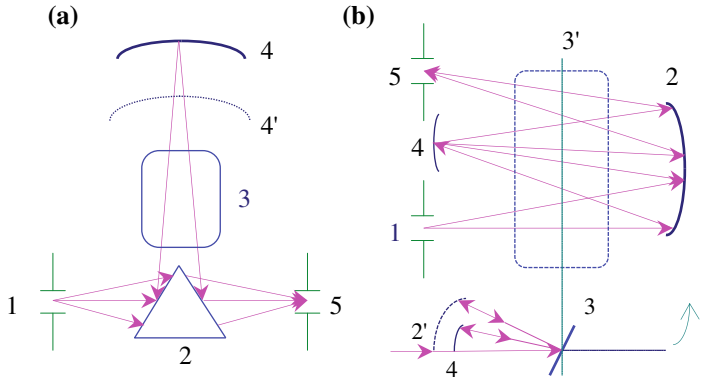

Fig. 4.29 Dual interaction with objects to be studied: 1 - source; 2 - prism or mirror; 3 - object under test; 4 - mirror; 5 - detector

beam cross-section unchanged. To insert mirror sample 3 in Fig. 4.29b spherical mirror 2 is swapped around the sample's axis (lower view) into new position 2′, not changing the direction of light propagation and therefore doubling the number of light interactions with the test mirror.

Both settings result in 2 times higher sensitivity to total attenuation of the entire test object, though spatially averaged by two beam passes and two angles of incidence. As a result, the increase of the measurements sensitivity coincides with the decrease of locality. In addition, for the transmission system, two light interactions with a transparent object double the number of surface reflections. Therefore, the measurement resolving power for the internal sample loss is limited by uncertainties not of dual magnitude of the surface reflectance (see Eq. (4.26)), but by its fourfold value. Consequently, the achieved twofold increase of sensitivity to internal optical density $D = \mu\Delta\ell$ coincides with the same increase of random error for these measurements. Accordingly, such dual-pass measurements are adequately accurate only when they are simultaneously supported by equally higher stability of all four surface reflectances for two samples to be compared.

If multiple reflections are created for an object with no intermediate medium (face surface), the sensitivity of the measurement to the object's attenuation factor κ is expanded by the number m of reflections:

$$\frac{N_n}{N_0} = \kappa^m \; or \; \frac{\Delta\kappa}{\kappa} = \frac{1}{m}\left(\frac{\Delta N_m}{N_m} + \frac{\Delta N_0}{N_0}\right), \tag{4.30}$$

where N_m and N_0 are the system reflection numbers after the m^{th} light interaction with and without the object, respectively. Consequently, if inside the measurement system shown in Fig. 4.29 the gap between two retroreflectors is filled by a gaseous substance under study, the sensitivity to the average linear attenuation coefficient μ is doubled in comparison with single light propagation, while the spatial averaging assists in decreasing the effects of gas-density fluctuations. By analogy with studies of reflectance at normal light incidence (Chap. 2, Figs. 2.13 and 2.14), the semi-transparent beam splitter is an efficient light coupler in measurements of the averaged and local optical properties. Figure 4.30 depicts exemplary schematics for normal-incidence measurement at beam splitter BS separating the incident and reflected beams. In Fig. 4.30a, detector D is calibrated via reflectance from nearly

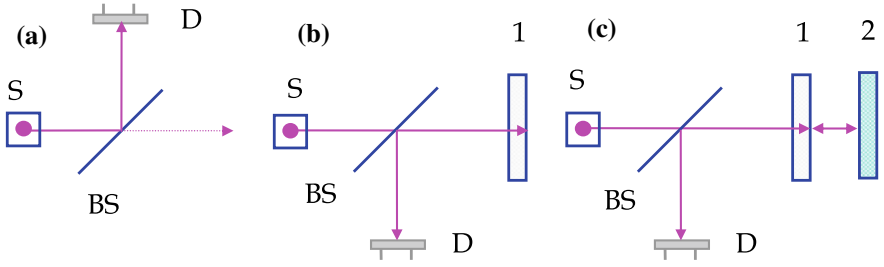

Fig. 4.30 Dual-interaction reflection measurements at normal incidence

50:50 beam splitter BS; in Fig. 4.30b, the reflectance of output coupler 1, being also presumably 50% reflecting and 50% transmitting but not noticeably absorbing and scattering, is measured; and in Fig. 4.30c, the resonator formed from output coupler 1 and mirror 2 is assembled for testing. For semitransparent output coupler 1 and highly reflecting mirror 2, the measurement sensitivity to local reflectance of the resonator is doubled when testing mirror 2 at precalibrated coupler 1 (see Part II for details on measurement methods and settings for multiple beam interactions).

4.2.6 Measurements at Intensive Irradiation

High levels of power for the laser and pulsed sources used in measurement systems may cause not only the appearance of nonlinear effects, complicating measurements under presumption of linear attenuation factors, but may also expand the dynamic range of measurements. An increase of the detecting power or the energy of the radiation itself does not allow one to extend the contributing dynamic range of measurements restricted by a particular detection system. An actual range extension can be achieved as a result of the combination of several measurement actions. Let us examine potential ways of measuring an attenuation factor κ by a detection system with linear dynamic range D. Let us set range D to be smaller than the inverse attenuation factor $1/\kappa$, being limited by the upper Φ_{max} and lower Φ_{min} boundaries for the linear reaction of the measurement system to the radiation flux Φ_0, while having first power Φ_0 higher than Φ_{max}.

To provide linear attenuation measurements at high flux power Φ_0 above the upper level of the system's linear threshold, the power must be attenuated to fit the $\Phi_{max} - \Phi_{min} = D$ range of the linear system reaction, correlating to the additivity principle (see Chap. 1). By using at least two attenuators with unknown transmittance τ_{a1} and τ_{a2} and reflectance ρ_{a1} and ρ_{a2} that both reduce flux Φ_0 to fit into the linear range D, the measurement sequence to evaluate the parameter of the attenuators and provide power measurements consists of the reaction of the detection system to four fluxes of radiation – the radiation fluxes transmitted (reflected) by the first attenuator, the second attenuator, the first and second attenuators, and the test sample:

$$\begin{aligned} N_{a1} &= \text{const} \cdot \tau_{a1}\Phi_0, \quad & N_\Sigma &= \text{const} \cdot \tau_{a1}\tau_{a2}\Phi_0; \\ N_{a2} &= \text{const} \cdot \tau_{a2}\Phi_0, \quad & N_s &= \text{const} \cdot \tau_{sample}\Phi_0. \end{aligned} \tag{4.31}$$

The first three equations in 4.31 give the attenuation factors of two attenuators, $\tau_{a1} = N_\Sigma/N_{a1}$ and $\tau_{a2} = N_\Sigma/N_{a2}$, and all four equations identify sample transmittance $\tau_{sample} = (N_s/N_{a2})(N_\Sigma/N_{a1})$. The actual optical properties of attenuators and the limited levels of radiation power must satisfy the inequalities:

$$\begin{aligned} &\tau_{a1}, \tau_{a2} \le \Phi_{max}/\Phi_0; \\ &\tau_{a1} \cdot \tau_{a2}, \tau_{sample} \ge \Phi_{min}/\Phi_0. \end{aligned} \tag{4.32}$$

In the example above, two measurement procedures by the N_{a1} and N_{a2} pair of equations (4.31) can be omitted if attenuators of known attenuation factors at a

given wavelength are available. Considering the attenuation measurements, a broad range of methods may be developed if the twofold error of measurements associated with extra evaluation of the attenuation factors is acceptable. An overpowering level of radiation also allows one to determine thresholds of nonlinear phenomena affecting measurements of attenuation factors for direct irradiation of samples and attenuators. To adjust a prohibitively high level of irradiation by observing likely nonlinearities for changing magnitudes of a linear attenuation factor, an extra measurement can be made as:

$$\tau_{\Sigma,1}/\tau_{\Sigma,2} = \Phi_{0,1}(\tau_a \cdot \tau_s)_1/\Phi_{0,2}(\tau_a \cdot \tau_s)_2. \tag{4.33}$$

If the ratio of the attenuation factors $k_{\Sigma,2}/k_{\Sigma,1} = \tau_{\Sigma,2}/\tau_{\Sigma,1}$ measured at unequal levels of irradiance is reliably recognized by the measurement system as being different from unity, the nonlinear effects are initiated. It is clear that both high-power nonlinear phenomena and the noise level of small-signal detection restrict the upper and lower thresholds of the linear dynamic range for attenuation measurements.

4.2.7 Studies of Integrated Scattering

If the dependence upon the direction of observation for scattering factors to be measured can be ignored, there is no need for a complex goniometric study, and an integrating sphere can integrate light scattered by a test sample. An additional advantage would be realized for capturing the scattering light in directions close to 0° and to 180° from the direction of incident light, which is not effortlessly achievable by relatively large goniometers [4.48–4.50].

Let us also note that multiple reflections in an integrating sphere can increase its sensitivity to low scattering, since a highly reflecting sphere not only integrates but also magnifies the detector's reaction via summing scattered by the sample light over various directions by factor:

$$K = \left(A_{dt}/4\pi R^2\right)\left[1/\left(1-\rho_0{}'\right)\right]. \tag{4.34}$$

Here R is the sphere radius, A_{dt} is the area of spherical segment substituted by a flat detector out of the internal sphere surface, and $\rho_0{}'$ is the effective reflectance of the sphere (formulae (2.104), (2.105)). If in such a sphere having internal surface of area A_0 only the entrance aperture and the detector opening of areas A_{en} and A_{dt} have zero reflectance, Eq. (4.34) converts to:

$$\begin{aligned} K &= \frac{1}{\frac{A_0}{A_{dt}}}\frac{1}{\left[1-\rho_0\left(1-\frac{A_{en}}{A_0}-\frac{A_{dt}}{A_0}\right)\right]} = \frac{1}{\frac{A_0}{A_{dt}}-\rho_0\left(\frac{A_0}{A_{dt}}-\frac{A_{en}}{A_{dt}}-1\right)} \\ &= \frac{1}{\frac{A_0}{A_{dt}}(1-\rho_0)+\rho_0\left(1+\frac{A_{en}}{A_{dt}}\right)}. \end{aligned} \tag{4.35}$$

Expression (4.35) clearly reveals that the increase of both ratios A_{dt}/A_0 and A_{dt}/A_{en} extends the positive effect of multiple reflections, while errors of both substitution and comparison methods enlarge with the higher number of sphere imperfections. Thus, some balance must be reached for every specific situation depending on the required sensitivity and accuracy of the study.

The integrating sphere seen in Fig. 4.21 depicts an easily accessible though highly sensitive attachment, utilizing the simplest substitution method for integrating sphere measurements. Its simplicity is given by direct sequential irradiation of a sample under study and the substitution standard at equivalent angles of incidence. Such a measurement procedure does not require switching of the direction of the incident beam. The absence of additional apertures for the sample of comparison minimizes the sphere losses into sphere openings and allows the use of a comparatively small integrating sphere. The disadvantages of substitution measurements are given by comparatively large systematic errors, depending on the difference of the magnitudes for scattering factors of substitution samples and the dimensions of the sphere, samples, and apertures (see Chap. 2).

Expression (2.118) for spherical samples, which do not disturb the sphere geometry, and expression (2.121) for flat samples permit one to implement correction factors based on the assumption of identical characters of the scattering mechanisms for all objects to be substituted. This applies to the measurement of uniform diffuse scattering, specular reflectance, and regular transmittance. Samples with a mixed scattering indicatrix may be represented by the sum of uniformly diffused and specular components. Since systematic error of integrating sphere measurements is absent for light specularly reflected by a spherical sample and directed to diffusely reflecting sphere wall, one can draw the conclusion that the correction factor for the sample with close-to-uniform scattering is equivalent to that obtained for the sample of mixed reflectance, as well as of mixed transmittance. The error of the diffuse, specular, and mixed reflectance measurement by the attenuation photometer in Fig. 4.21 for the substitution integrating sphere did not exceed ±0.2–0.3% [4.34] even for single-surface reflecting samples of reflectance as low as $\rho \cong 0.04$ when using correction factors for the actual sphere design. The errors of the direct transmittance measurement by the attenuation photometer without the integrating sphere were practically the same within ±0.1–0.2% [4.33].

Figure 4.31 shows a widely used integrating-sphere design for comparison measurements in a dual-beam spectrophotometer [4.36]. Light from source 1 is split into two beams via Nicol (2, 4) and Wollaston (3) prisms, entering integrating sphere 6 via mirrors 5 and 5′ via separate apertures. Diffuse and specular reflecting samples – test sample 7 and comparison sample 8 – are placed at respective output ports. Either a transparent or a translucent sample is placed at position 7′ of the entrance port for the measurement beam. To enable the absolute reflectance and transmittance studies, comparison reference sample 8 is made as the cap of the sphere wall at the same radius of curvature as the sphere and is placed in the output port of the reference beam. For the absolute measurement purposes, light diffusely reflected or transmitted from either test sample 7 or 7′, but not from comparison sample 8, must be baffled from detector 9 by opaque baffle 10 or 10′. Within the

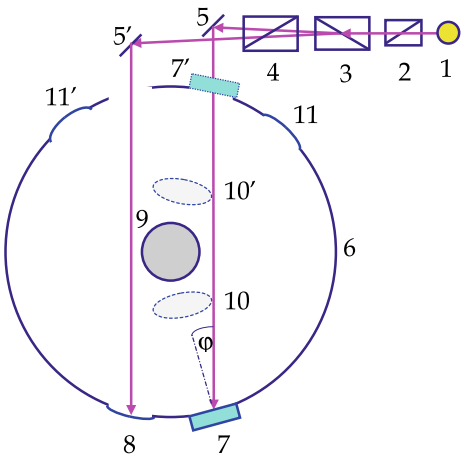

Fig. 4.31 Comparison dual-beam sphere

zones of expected specular reflectance, removable sphere cap 11′ is taken out or placed back to remove or keep the specularly reflected light inside. The angle of incidence φ at each sample is a constant of a given sphere design and is commonly larger than 4°–5° (compare with the ones in Figs. 2.36 and 2.37).

Let us note that for a compact design of an integrating sphere, aiming for high sensitivity, the existence of several sphere ports contributes to increasing the amount of stray light entering such a sphere, which is especially noticeable for measurements of low scattering factors if specularly reflected light must leave the sphere via additional exit apertures (see Fig. 4.32). One way of measuring stray-light intensity consists in opening and closing each port, such as using the sphere-wall cap to close the port and fully absorbing cone as the light trap to open it [4.34]. Applying Eqs. (2.118)–(2.122) to a sphere of known port sizes, one can evaluate and correct the samples' reflectivity range and curvatures and the intensity of stray light, respectively [4.34, 4.43].

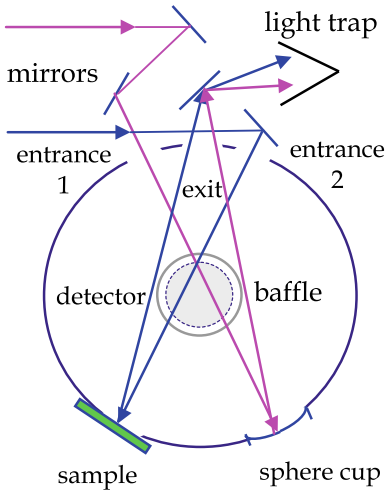

Fig. 4.32 Multi-port integrating sphere

For the absolute measurement methodology to offset the systematic error of the integrating sphere measurement the intensity of radiation directly scattered by the test sample and reaching any detector mounted on the sphere wall must satisfy Eq. (2.126). Following the discussions in Sect. 2.4, an alteration of radiation intensity may be provided by making the sphere baffle transmittance or the intensity of incident light irradiating the sphere wall satisfy Eqs. (2.126)–(2.128) for the test sample or for the comparison measurement, respectively. The corresponding baffle transmittance can be obtained using transparent or translucent materials, as well as by making a small corresponding aperture of area ΔA in the baffle, which relates to its total area A as $(\rho_0 - \rho_0')/(1 - \rho_0')$ (equation (2.144)). Baffle choices are confined by the spectral characteristics of the internal sphere surface and available materials. The relationship between the surface areas of the aperture and the baffle is surely not spectrally selective and it may not compensate for any spectral dependence of the sphere reflectance on light wavelengths. Making the sphere and baffle from materials having identical spectral characteristics could compensate for the spectral asymmetries in Eq. (2.143). If the baffle acts as a uniform diffuser in transmitted light, preventing nonuniformity for direct irradiation of the sample studied, the entire portion of light transmitted by the baffle becomes uniformly diffused. Therefore, following Eq. (4.6), the baffle diffuse transmittance τ_d should satisfy:

$$\tau_d \frac{1 - \cos\beta_2}{1 + \cos\beta_1} = \frac{\rho_0 - \rho_0'}{1 - \rho_0'}, \tag{4.36}$$

where the angle designations are given in Fig. 4.33. If the sphere and baffle are both made of any identical translucent material, only having different thicknesses to obtain the high reflectance and high transmittance, respectively, for the sphere and baffle, the optical properties should have a somewhat similar spectral behavior. Other advantages of applying low-absorbing translucent material are associated with low optical losses inside the integrating sphere itself, resulting in the higher effective reflectance of the full-sphere enclosure.

Figure 4.33 depicts the comparison integrating sphere for a single-beam application having one shifting baffle [4.41]. Integrating sphere 3 has only a single entrance aperture. Swing mirror 1 transfers irradiating light from test sample 2 to

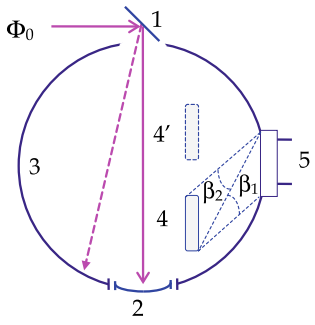

Fig. 4.33 Swing-mirror integrating sphere having a translucent baffle

the sphere wall with no inclusions. To compensate for absolute measurement error [2.60], translucent baffle 4 instead of the reflective one protects detector 5 from irradiation by light directly scattered by sample 2. In the absolute-reflectance study when a sphere wall spot is irradiated, the baffle is shifted to position 4′, thus not blocking reflected light. The sphere design is convenient, but has two significant side effects. The angle of light incidence on the sphere wall does not remain constant over the beam cross section and is not equal to the angle of light incidence on the sample. Besides, for other conditions being equal even to the ones of substitution spheres, the sphere entrance aperture must be larger than in previous designs to maintain beam shifts and balance, thus varying the angles of incidence on the sphere wall and the sample.

Another design that excludes wide apertures in the integrating sphere, but adds internal elements [4.42], is depicted in Fig. 4.34. Such an approach restrains the need of using protection baffles by placing the sample and the detector in one plane. Swing opaque mirror 2 is installed in this comparison measurement sphere instead of the protecting baffle (Fig. 4.34a). That internal mirror 2 sequentially positions the incident light spot onto test sample 3, and then onto inner-sphere wall section 5 by swapping orthogonal mirror positions in sphere 1. Expressions (2.145) and (2.146) show that two flat sphere elements with sample 3 and detector 4 (Fig. 4.34a) create substantial systematic errors even for the comparison-method measurements. Reduction of the flat section (Fig. 4.34b) by installing detector 4 onto the sphere surface, being baffled by opaque mirror 2, allows one to compensate for some systematic error. Irradiation of a small compensation part ΔA of the sensitive surface A of the detector by radiation directly scattered by the sample (see Sect. 2.4) diminishes any error of absolute measurements similarly to the layout in Fig. 4.33. The design in Fig. 4.34 by definition assumes the sphere-wall reflectance at different angles φ_i of radiation incidence is unchanged (arrows in Fig. 4.34b), while obstructing any sphere measurement of diffuse transmittance due to scattered light irradiating the detector.

As pointed out by Table 1.1, when the sample under study is irradiated by a direct beam at an angle of incidence Θ, the uniform diffuse reflectance of such a

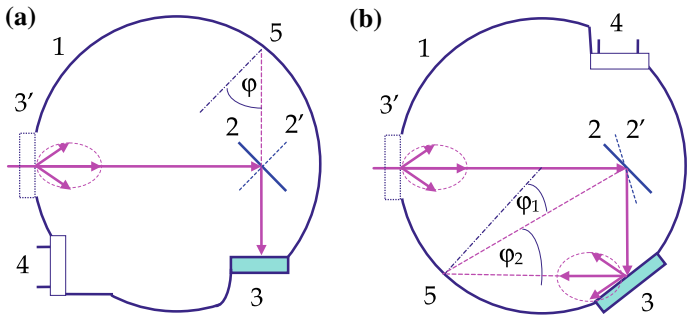

Fig. 4.34 Integrating spheres having the internal swing mirror

sample into the hemispherical angle 2π can be substituted by its irradiance factor in the reciprocal irradiation and observation directions Eq. (1.137). Besides, a practically uniform irradiation within the approximately 2π hemisphere can be realized by implementing a number of light sources inside half of the uniformly diffuse reflecting sphere (Fig. 4.35a). However, as shown in Chap. 2, the main advantage of the integrating sphere consists in the uniform irradiance distribution produced by reflection from its spherical surface. Thus, the disadvantage of multiple inclusions is multiplied by every implementation of a not diffuse reflector in the sphere. Figure 4.35b depicts the likely prospect of utilizing the translucent sphere (see Fig. 2.5) for determination of the radiance factor. One or several light sources 1 irradiate translucent sphere 2 made of a low-absorbing diffuser, the properties of which satisfy Eq. (2.21). Complete equality among all radiant fluxes emitted by every source of radiation is not required, since test sample 3 is directly compared with the assumed perfect diffuser $3'$. Each sample is located fully inside the translucent integrating sphere 2 for the cycle of comparison measurements. Objective 4 forms a stable observation geometry for light scattered by measured sample 3 or comparison sample $3'$ and viewed by detector 5 in direction Θ within solid angle Ω. The precise locations of samples 3 and $3'$ are obtained in the sphere's geometrical center, maintaining hemispherical irradiation. Such hemispherical irradiation obtained inside the translucent sphere has the dual advantage of directing radiation from the outside sources into the sphere and keeping it within the sphere.

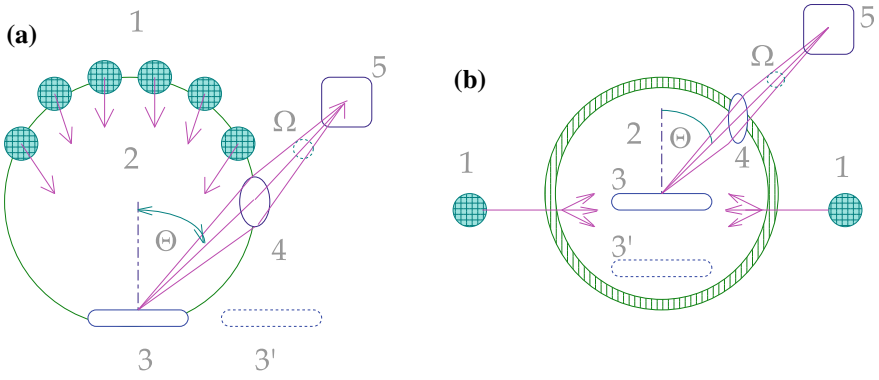

Fig. 4.35 Determination of sample's scattering properties via the radiance factor

Certain drawbacks of the preceding integrating sphere layouts can be linked to some inability of the sphere designs to capture radiation reflected via the entrance apertures for the directly irradiated spheres. One design layout allowing simultaneous measurements of the sum of the specular and diffuse-reflectance or transmittance of a test sample is depicted in Fig. 4.36. It provides absolute comparison studies at normal incidence of radiation on either a reflecting or a transmitting sample and on the error-equalizing comparison spherical cap, representing in its properties the effective internal sphere wall [2.55]. As reviewed in detail in Sect. 2.4, the sphere cap is the comparison reference sample, with both sphere cap 6 and

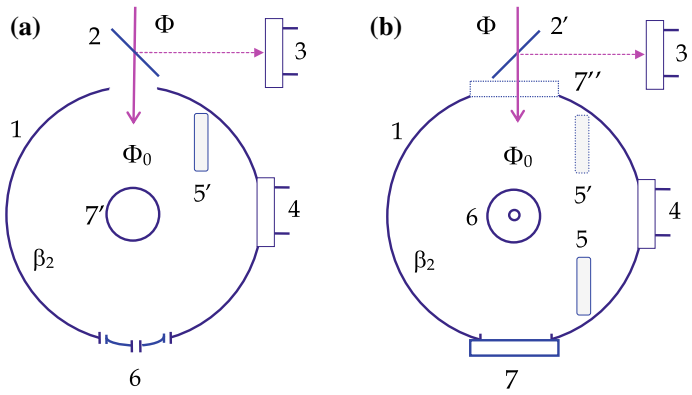

Fig. 4.36 Diffuse- and specular-reflectance measurement sphere

studied sample 7 always remaining inside the sphere and being sequentially inserted into the incident beam of light. Equalizing sphere cap 6 also has the small balance-opening port, the area of which compensates for the systematic error of the absolute measurements by Eq. (2.144). In Fig. 4.36a, the sphere cap is directly irradiated at location 6, the sample is set to position 7′, while the opaque baffle is turned out of the beam into location 5′. Figure 4.36b depicts direct irradiation of the reflecting sample at position 7, while the equalizing cap and the baffle are placed in opposite locations 6′ and 5, respectively. When any translucent sample is studied at position 7″, opaque baffle 5 is returned to spot 5′ and the sphere extra cap is placed at spot 6″ to cover the sample port of the sphere. Nonabsorbing beam splitter 2 and additional detector 3, identical to detector 4 of the sphere, serve to determine the specularly reflected components of incident radiation.

Two initial readings of detectors 3 and 4 registered in positions depicted in Fig. 4.36a, are:

$$N_{3,0} = \kappa_3 \Phi \rho_{spl}; \quad N_{4,0} = \kappa_4 \Phi \tau_{spl} \rho_0' \left(1 - \rho_0'\right)^{-1}, \tag{4.37}$$

where κ_3 and κ_4 are the proportionality factors, Φ is the total flux of the source beam, ρ_{spl} and τ_{spl} are the reflectance and the transmittance of splitter 2, and ρ_0' is the effective reflectance of equalizing sphere cap 6, which is made equal to the effective reflectance of the entire internal sphere surface (see Eqs. (2.144), (2.148)). For sphere elements being in new positions as in Fig. 4.36b, each detector signal becomes:

$$N_3 = \kappa_3 \Phi \rho_{spl} \rho_r \rho_{spl}; \; N_{4,\rho} = \kappa_4 \Phi \tau_{spl} \rho_d \rho_0' \left(1 - \rho_0'\right)^{-1}; \; N_{4,\tau} = \kappa_4 \Phi \tau_{spl} \tau_{r+d} \rho_0' \left(1 - \rho_0'\right)^{-1}, \tag{4.38}$$

where τ_{r+d} is the mixed transmittance for translucent sample 7″. Another signal N′ is measured by sphere detector 4 with no splitter 2 in either arrangement shown in Fig. 4.36 to determine all optical properties:

$$N'_{4,\rho} = \kappa_4 \Phi \rho_d \rho'_0 \left(1 - \rho'_0\right)^{-1}. \tag{4.39}$$

The factors characterizing all properties of reflective or translucent samples are resolved as:

$$\rho_d = \frac{N_{4,\rho}}{N_{4,0}};\ \tau_d = \frac{N_{4,\tau}}{N_{4,0}};\ \rho_r = \frac{N_3}{N_{3,0}} \frac{N'_{4,\rho}}{N_{4,\rho}}. \tag{4.40}$$

Let us note that the dynamic range for diffuse-scattering measurements by detector 4 in that integrating sphere is restricted by the factual transmittance of incident radiation via extra beam splitter 2. Thus, the transparent beam splitter with one of its surfaces having an antireflection coating is the most effective. This is based on much higher attenuation inside the sphere, being:

$$\Phi_4 = \Phi_0 \frac{A_{\text{det}}}{A_{sph}} \frac{\rho'_0}{1 - \rho'_0}, \tag{4.41}$$

where Φ_0 is the flux entering the sphere, and A_{det} and A_{sph} are the areas of the detector and the internal sphere surface. In contrast, flux $\Phi_{0,3,\max}$ to detector 3 is defined by incident flux Φ_0 and reflectance ρ_{spl} of splitter 2.

One more version of an integrating sphere design for measurements of the scattering factor that does not introduce systematic error of determining diffuse reflectance and transmittance of spherical samples is seen in Fig. 4.37a. Versus the internal translucent sphere layout, illustrated in Fig. 2.35, this design deploys the translucent nonabsorbing sphere 5, which is external to main integrating sphere 1. Error corrections in that version are only for imbedding flat inclusions into main sphere 1 and for changing its effective reflectance via added sphere 5 in its entrance port 2. First, the reflective test sample 6 is irradiated by the direct beam from a light source via entrance port 2 with sphere 5 being out of the beam and internal detector 4 protected from light scattered from sample 6 by conventional opaque slightly

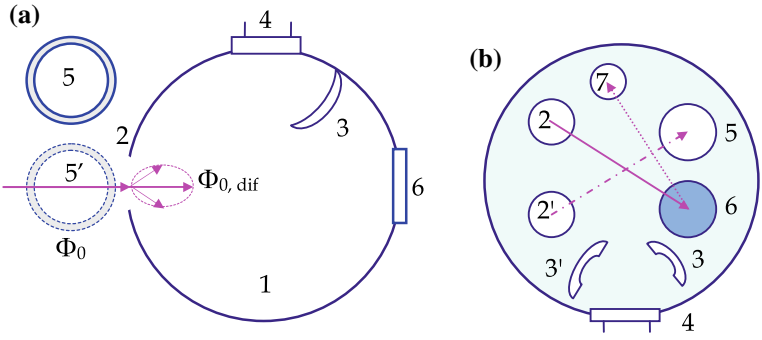

Fig. 4.37 Comparison spheres: true-diffuse illuminating (**a**) and specular-excluding (**b**)

curved baffle 3. Then, an entire inner surface of sphere 1 including the sample and detector 4 is irradiated by uniformly diffused flux Φ_0 of the incident beam via translucent sphere 5 of a nonabsorbing translucent material, in position 5′ (see Chap. 2). The ratio of all inner surface of sphere 5 to its spherical surface fitted to port 2 of sphere 1: A_5 and A_2, define the attenuation factor of translucent sphere $\rho_{\text{sample-6}} = (N/N_0)(A_2/A_5)$. The assumption for zero absorptance of translucent sphere 5 defines the measurement accuracy.

Figure 4.37b depicts a comparison integrating sphere of spectrophotometer Cary 5000, which is equipped with specular-reflectance excluding port 7 and curved detector baffles 3, 3′. The main beam irradiates sample 6 via port 2 and the reference one is directed to sphere-matching reference reflector 5. That sphere was used for measuring of powder samples behind a transparent quartz window [4.81], which attenuated the sample beam and contributed to multiple reflections of the sphere, thus numerical-fitting models were needed for empirical corrections to sample's spectral reflectance. Empirical-based modeling is also required for small samples using large-beam off-the-shelf systems, while deploying sample masks, reshaping beams, or altering specimen [4.82–4.84].

4.2.8 *Specialty Applications of Integrating Spheres for Optical Calibrations and Measurements*

Exceptional averaging and depolarization properties of integrating spheres [2.47–2.88, 4.40–4.53] can be used for absolute calibration of light sources [2.3, 2.7]. When radiant or luminous fluxes emitted by standard and test sources are sequentially compared in a sphere, only the spectral-correction factor of the sphere, but not its internal reflectance, needs to be known and should be a sphere constant for comparison of light sources. However, if only the flux from a test source is being integrated by the sphere (Fig. 4.38), the sphere's spectral conversion factor also needs to be known. A numerical solution for a particular calibration task can be developed by solving the integral equation for the sphere's irradiance (see Sects. 2.1, 2.4) in view of screening factors $B_i(A, A')$ for the sphere's internal baffles and specific position factors $P_i(A, A')$ of various inclusions or ports at each i^{th} reflection [2.6]:

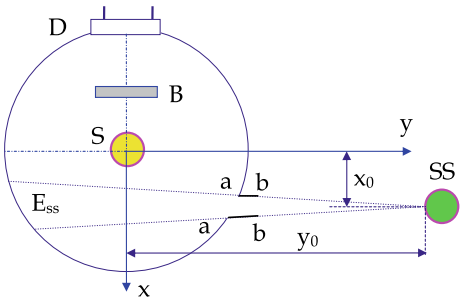

Fig. 4.38 Comparison of fluxes via integrating sphere

$$E_i(A) = \iint \rho(A')E_{i-1}(A')B_i(A,A')P_i(A,A')dA'. \tag{4.42}$$

Here ρ(A) is the uniform diffuse reflectance of the sphere wall within i^{th} area A_i, irradiated from A′. For each setting, the optimal sphere configuration defines the positions of windows and baffles. In a practical implementation [4.47], illustrated in Fig. 4.38, versus the original implementation [4.46] shown in Fig. 2.4, the open-port screening baffle was removed to reduce sphere nonuniformity caused by added objects inside. In this case, the size of the spherical port *a–a* was controlled by the extra flat diaphragm *b–b*, establishing correction factors for loss of light into the port for test source S versus standard SS.

Another role of an integrating sphere is associated with its ability to uniformly irradiate spherical or elliptical objects with uniformly diffused light. This uniform irradiance can be formed inside a reflective integrating or diffusely transmitting sphere of negligible absorptance α of its wall at wavelengths under study Eq. (2.20). The inaccuracy χ of the assumption made in that relation is: $\chi \leq \Delta\Phi/\Phi = \Delta\tau = \alpha$. For opal glasses with absorption coefficients α of 0.001–0.0001 for visible to near-IR wavelengths, low glass absorptance enables diffuse sample irradiation via direct irradiation of the translucent sphere. In the absence of notable absorption, any sphere formed by diffuse reflecting and diffuse transmitting material balances all incident radiation into the surrounding space without adding or diminishing the total amount of that radiation; thus flux Φ_0 incident onto a translucent sphere remains located within imaginary spheres, coincident with the main sphere (see Fig. 2.5). If the test sample, made as the sphere of radius *r* smaller than the internal radius *R* of translucent sphere, is placed inside the translucent sphere irradiated by a probe beam with flux Φ_0, then instant irradiation of the sphere will next irradiate the entire outer surface of the sample (which in turn can be investigated for its surface defects such as material or structural small-area cracks or flaws) with the flux density of Φ_0/S, where S is the area of the sample's outer surface $4\pi R^2$. The sensitivity of such defect detection will be defined by the relative area of defects, changing the reflectivity of the sample measured and skewing the 4π scattering distribution of the spherical irradiance in the translucent sphere.

Depending on the properties of the sample's surface, the measurement sensitivity may need to be improved to recognize surface defects, and for that purpose, that sample itself may be used as a semitransparent resonator for the wavelength of irradiation for which the sample's absorptance becomes sufficiently low, enhancing propagation of radiation through the sample. Owing to multiple reflections inside the sample in the translucent sphere (Fig. 4.39), for sample reflectance ρ_λ, bulk absorptance α_λ, and diameter D, the spectral flux $\Phi_{\Sigma\lambda}$ within the sphere at wavelength λ is:

$$\begin{aligned}\Phi_{\Sigma\lambda} &= \Phi_\lambda\rho_\lambda + \Phi_\lambda(1-\rho_\lambda)^2\alpha_\lambda + \cdots + \Phi_\lambda(1-\rho_\lambda)^2\alpha_\lambda\rho_\lambda^2\alpha_\lambda^2 \\ &= \Phi_\lambda\left(\rho_\lambda + \frac{(1-\rho_\lambda)^2\alpha_\lambda}{1-\rho_\lambda^2\alpha_\lambda^2}\right).\end{aligned} \tag{4.43}$$

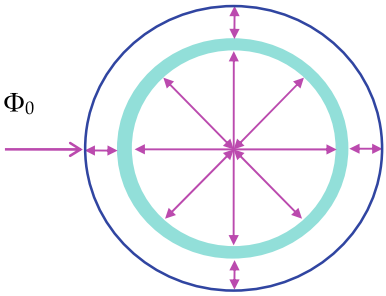

Fig. 4.39 Specular sphere inside a diffuse sphere

If the sample's spectral bulk absorptance α_λ is low and is presumed to be $\alpha_\lambda = 0$, Eq. (4.43), differentiated versus the flux $\Phi_{\rho,\lambda} = \Phi_\lambda \rho_\lambda$ reflected from the sample, becomes:

$$\begin{aligned} \Phi_{\Sigma,\lambda} &\underset{\alpha_\lambda \to 0}{=} \Phi_\lambda(\rho_\lambda + (1-\rho_\lambda)/(1+\rho_\lambda)); \\ \Phi_\Delta = \Phi_{\Sigma,\lambda} - \Phi_\lambda \rho_\lambda &\underset{\alpha_\lambda \to 0}{=} \Phi_\lambda(1-\rho_\lambda)/(1+\rho_\lambda). \end{aligned} \tag{4.44}$$

For studies in spectral regions of negligibly low bulk absorptance of the sample itself, as well of the translucent integrating sphere, the only sample's loss to be taken into account is its surface spectral scattering μ_λ; therefore, Eqs. (4.43) and (4.44) convert to [4.75]:

$$\begin{aligned} \Phi_{\Sigma,\lambda} &= \Phi_\lambda(\rho_\lambda + \mu_\lambda) + \Phi_\lambda(1-\rho_\lambda-\mu_\lambda)^2\left[1 + (\rho_\lambda+\mu_\lambda)^2 + \cdots\right] \\ &= \Phi_\lambda\left[(\rho_\lambda+\mu_\lambda) + \frac{(1-\rho_\lambda-\mu_\lambda)^2}{1-(\rho_\lambda+\mu_\lambda)^2}\right]; \end{aligned} \tag{4.45}$$

$$\frac{\Phi_{\Sigma,\lambda}}{\Phi_\lambda} \underset{\alpha_\lambda \to 0}{=} \left(\rho_\lambda + \mu_\lambda + \frac{1-\rho_\lambda-\mu_\lambda}{1+\rho_\lambda+\mu_\lambda}\right). \tag{4.46}$$

This derivation presumes identical 2π-scattering losses μ_λ into upper and lower semispheres of the sample's surface in semitransparent resonator measurements, which retains its sensitivity for low and high spectral reflectance of the sample. Resonator studies also double the measurement sensitivity to likely changes of spectral reflectance of surface, as well as to reflectance defects by Eq. (4.44) for Φ_Δ, enhancing sensitivity via the multiple reflectance product $(1-\rho)/(1+\rho)$, analogously to Eqs. (1.106), (10.42) (see Chaps. 1 and 10). Further enhancements can be made via spectral tuning of the translucent-sphere to diffuse properties of expected samples, choosing a matching diffuse material for its wall and optimizing the wall thickness, to improve sensitivity of measurements as diffuse properties vary (see [4.85–4.87]).

4.2.9 Color-Coordinate Measurements

Surface defects, such as ones in the silicon nitride rolling elements, as an example [4.55], can be sensed similarly to label-free bio molecule or tissue identifications [4.88] by comparing color changes due to those defects versus the likely uniform color of defect-free surface, in which a color change of the sintered silicon nitride surface facilitates identification of pores, chips, or versus foreign-matter defects of different colors being formed at the surface (see Sect. 2.3). The color stimulus is best determined by measuring the absolute but not relative transmission or reflection spectrum of the object for any standardized radiation bandwidth (see Chap. 2). Using measured data obtained from the object, its tristimulus coordinates would be identified [2.45] by converting the spectrum measured as the mathematical model for the product of the emission spectrum of a standardized source, the spectrum of the object measured, and the tristimulus values $\bar{x}(\lambda), \bar{y}(\lambda), \bar{z}(\lambda)$ for one of CIE-identified standard observers. The anticipated measurement [4.75] of the spectral transmission or reflection of the object should be obtained by means of an absolute spectral measurement via any absolute color spectrophotometer, satisfying the conditions of illumination and observation defined by the CIE and reproducing the precise wavelengths but not necessarily the intensities of illumination and observation spectrums of a standardized CIE source and of a standardized observer. The limits of potential sensitivity for such measurements are only restricted by discrimination confinements for the measured color difference, being determined by the vector variance of two color stimuli that are discriminable, as long as the spectrum of optical radiation defining a given color discrimination is measurable.

Figure 4.40 illustrates the direct-diffuse illumination and observation geometry for absolute measurements of color defined by the CIE [2.33]. Figures 4.41 and 4.42 give examples of the experimental confirmation of color sensitivity of the absolute technique (Chap. 2) for measuring the color coordinates of two transparent

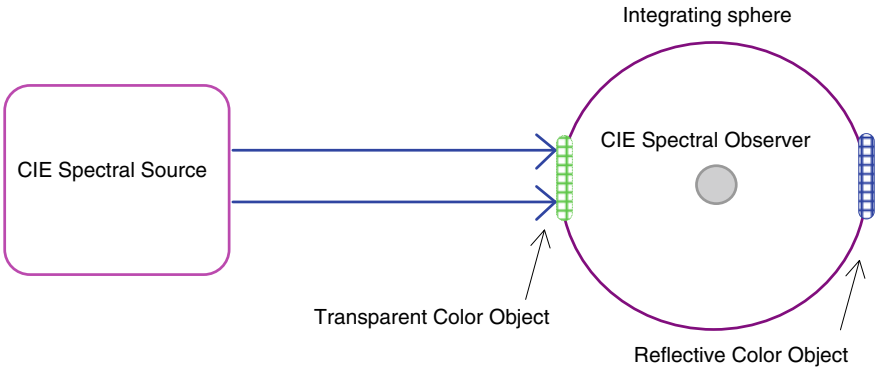

Fig. 4.40 Absolute transmission or reflection color measurement in direct-diffuse configuration

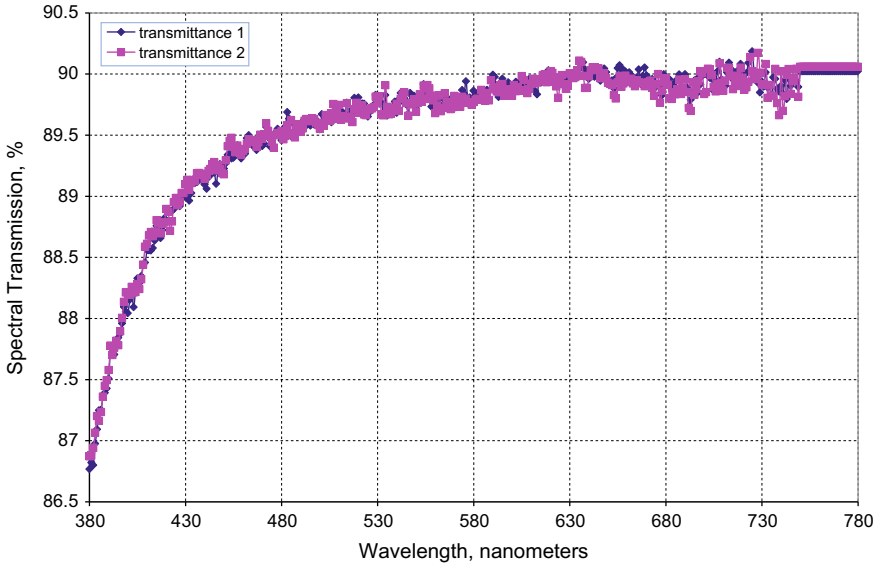

Fig. 4.41 Expanded transmission spectrums of studied transparent polymer samples No. 1 and No. 2

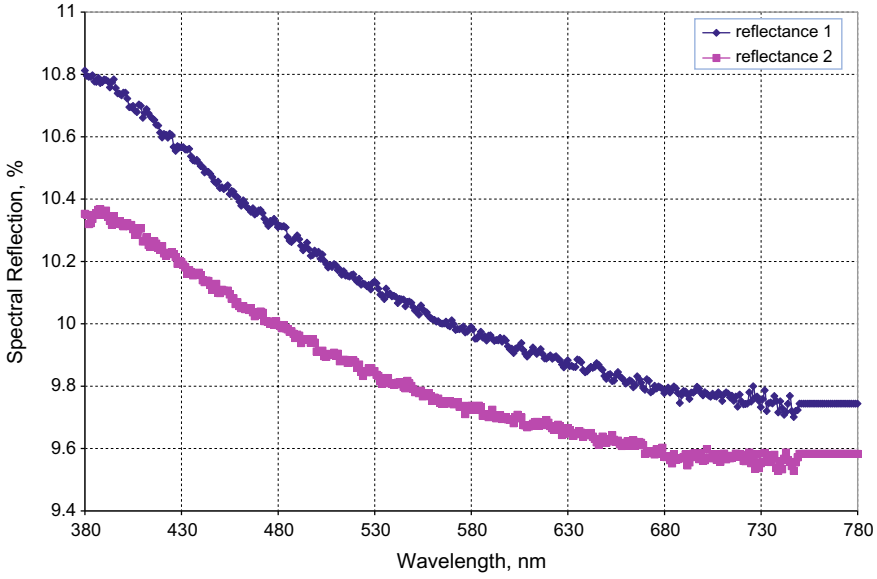

Fig. 4.42 Reflection spectrums of two studied polymer samples No. 1 and No. 2

materials in the CIE-specified spectral domain of 380–780 nm and calculating the yellowness index according to ASTM E 313-00 [4.80] by Eq. (2.73) as:

$$YI = 100 \cdot \frac{C_x x - C_z z}{y} = 100 \cdot \frac{1.2985x - 1.1335z}{y} [\%], \tag{4.47}$$

where the ASTM-defined coefficients for the D65 CIE source applied are $C_x = 1.2985$ and $C_z = 1.1335$. The whiteness index in reflected light is defined by Eq. (2.74) at $x_n = 0.333334$ and $y_n = 0.333331$:

$$WI = Y + 800(x_n - x) + 1700(y_n - y). \tag{4.48}$$

Figure 4.41 identifies the transmittance spectrums for two samples of some unknown history, made by a deliberately untraced, but established process, which were identified by that process as color-identical and seemingly confirmed as such by the indistinguishable transmission charts.

Figure 4.42 shows reflectance spectrums of both samples remeasured at identical illumination and observation geometries in reflected light with following absorption spectrums (not shown) computed as the difference: $\alpha(\lambda_i) = 1 - \tau(\lambda_i) - \rho(\lambda_i)$, where α, τ, and ρ are the absorption, transmission, and reflection at λ_i (see [0.50] for more details). As seen from the reflectance spectrum, samples 1 and 2 are not equal to one another, but conventional color measurements in transmission do not reveal the distinction (Table 4.1).

As it is seen, the sensitivity of that absolute color coordinate measurement technique is at least on the level of $\pm 5 \cdot 10^{-5}$ for color indices X and Y, and at least near $\pm 1 \cdot 10^{-4}$ ($\pm 0.01\%$) for the yellowness index and the whiteness index, nonetheless the photometric accuracy of spectrophotometer used for the measurements was at usual $\pm 0.1\%$, while regular color detection methods do not normally distinguish color differences below 0.1%.

The well-known high sensitivity of color-coordinate measurements enables color-based studies even for the light-path difference as low as $\lambda/8$ or lower [4.72–4.74]. Aside from phase-detection techniques further discussed in Sect. 8.5, let us briefly review one more option for a color-sensing phase measurement [8.28]. Recalling Fig. 3.15 and Eqs. (3.147)–(3.162), among which is Eq. (3.151) for the

Table 4.1 Differences of color coordinates and yellowness and whiteness indices

Transmission	*YI*	*X*	*Y*	*Z*
Sample 1 t	0.675037	0.3133	0.329758	0.356942
Sample 2 t	0.625845	0.313263	0.329695	0.357043
Delta measured	0.049192	3.73E-05	6.34E-05	−0.0001
Reflection	*WI*	*X*	*Y*	*Z*
Sample 1 r	20.9235	0.308507	0.324665	0.366828
Sample 2 r	18.6529	0.309311	0.325467	0.365222
Delta measured	2.270597	−0.0008	−0.0008	0.001606

radiation intensity, $I_{\perp} = I_0 \sin^2(\delta/2)$, transmitted via the crossed polarizer and analyzer is the most commonly used, one can construct a functional dependence for the phase difference: $\delta = \delta_0 + \delta_\lambda$, versus the initial difference δ_0 at the wavelength λ_0, called the sensitive color [4.69, 4.73]. Then, using any one of the Eqs. (2.78)–(2.100) for the tristimulus values X, Y, Z of the measured intensity of polarized polychromatic light between the arbitrarily oriented polarizer and analyzer versus the beam phase in transmission, one may construct color coordinates $x + y + z \equiv 1$, all as functions of the phase difference $\delta = \delta(\lambda)$. Sensing color-coordinate changes versus the phase difference, one could build a matrix system of quadratic equations for the one-to-one correspondence of color and phase [4.74].

4.3 Photometric Accuracy and Verification of Linearity

Every radiometric or photometric consideration requires making one or another measurement of the power or energy extent of radiation. If a given optical property – transmittance, reflectance, scattering, or absorptance – is measured, the change of intensity of the incident beam of light before and after interaction of that beam with the object under study must be detected. If any power-driven parameter of light, such as power, energy, or radiance, is measured, an extra calibration measurement via an emission or reception standard must be performed for the absolute measurement. As a result, the limits of photometric accuracy are actually explored or tested in each photometric or radiometric test, being identified by double error of single-versus-reference measurement of light power or energy and by the nonlinearity of a given radiometer for its inadequate reaction R_i to linear changes of light intensity I_i, as $R_1/R_2 \neq I_1/I_2$. Methods for evaluation of deviations from linear radiometric reactions on radiation actions and of unresolved remainders of systematic errors used for any compensation of nonlinearities are examined below.

One example in which any manifestation of nonlinearity is deliberately obscured is shown in Fig. 4.43. This compensation method is widely utilized in recording spectrophotometers in such a way that internal detector 7 performs just as an intensity equalizer for two fluxes to be compared. In Fig. 4.43, a beam from source 1 is divided after monochromator 2 by a mirror-chopper or identical device 3 into two differential beams. If one of the two beams interacts with the sample under study 4, the intensity of the second beam is attenuated by matching wedge 5 and subwedge 6; detector 7 equalizes the intensities of the two beams. The result of that measurement is determined by the actual distance of the motion for wedge 5 with

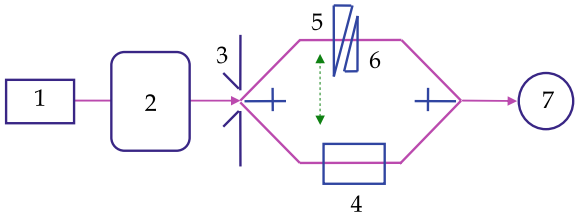

Fig. 4.43 Schematic illustration of compensation measurements

reference to a fixed position of subwedge 6. This compensating method prevents a nonlinearity of the photometer from manifesting itself. To calibrate the combined motion of wedges, another linear measurement tool is required, therefore creating auxiliary error of calibration due to unequal propagation of light via two diverse paths and complicating the measurement procedure for the spectrophotometer as having residual errors, without resolving the potential nonlinearity itself.

The very unique difference for any methodology of the photometric-accuracy measurement from a procedure that detects, for example, spatial nonuniformity or inhomogeneity, is evident. If the sensitivity of a radiometer or photometer to position changes of a beam is measured, there is no need to detect the intensity of the beam itself. When nonlinearity is being measured, the transformation behavior of the studied radiometer to foreseeable changes of intensity of optical radiation must be determined. The choices of optimum procedures are provided by given measurement tasks and the conditions under which they are performed. Measurements using unstable laser or pulsed light can substantially differ from those in uniform spontaneous light. Detecting linear behavior in a wide dynamic range is quite different from testing highly linear responses for small intensity changes.

4.3.1 Measurements with Fixed Attenuation

Any study of photometric accuracy must determine the function for conversion of light intensity into a respective detection signal or its deviation from a linear conversion. The function can be detected by an action, governed by a linear law, such as the change of irradiance or illuminance dependent on the square distance to a point source or a reduction of radiant or luminous intensity in proportion to the density of the attenuating substance or angle of rotation of a polarization prism. In any case, the nonlinearity is nonconformance of a reaction of the system to a defined linear action, governed by a validated physical dependence.

A well-defined method for detection of photometric accuracy is associated with confirmation of a photometric or radiometric reaction of a test radiometer to alteration of the irradiance or illuminance generated by a point source of light according to the inverse-square-distance law [0.4, 0.6, 0.12] (Sect. 1.2). Equations (2.28) and (2.29) identify the sensitivity of such a measurement as a smallest distance change which transforms irradiance into the minimal reaction of the radiometer. The actual dynamic range of such a measurement method is defined by limits $\ell_{\min}$ and $\ell_{\max}$ at which a light source may be confirmed as the point source and at which the test radiometer may detect irradiance. The main assumptions of the inverse-square law need to be preserved: transmittance of a medium between sources and detectors should not depend on distance. In air the assumption holds true only within certain limits. For example, at a temperature 25 °C and humidity of 65%, the internal transmittance: $\tau_{\text{int}} = \exp[-\mu_{\lambda}(\ell_{\max} - \ell_{\min})]$, of a 5-m air gap differs from 1.0 by 0.06% at $\lambda = 1.06$ μm, but by 0.09% at $\lambda = 530$ nm. Such errors may restrict the applicability limits for most accurate measurements.

The bigger is the magnitude of $\ell_{\min}$, allowing a source to be considered as the point source, the longer is the respective distance $\ell_{\max}$ at which the expected change of source irradiance actually takes place:

$$E_{\min}/E_{\max} = [(\ell_{\min} + \ell_{\max})/\ell_{\max}]^2. \tag{4.49}$$

Therefore, longer $\ell_{\min}$ distance leads to narrower limits for evaluation of photometric accuracy. In spite of restrictions and inconvenience, either a decrease or an increase of irradiance established by the inverse-square law is predictable for any sources or detectors. This means the actual behavior of a test device can be evaluated in terms of the function $E = E(\ell^{-2})$ at any point of its dynamic range.

More convenient are the measurement procedures relying on sets of precalibrated or preestimated attenuators inserted into a beam of light directly propagating from a source to a test radiometer. There are several possibilities for making the linearity measurements. One possibility is that every attenuator, as well as the entire set of attenuators, if needed, is precalibrated by a system already identified as being linear, though having identification error as a result. Another possibility is that attenuation is provided by methods not requiring precalibration. Yet another possibility is that measurements are made by attenuators whose properties, as well as absolute reactions to them by test radiometers, do not need to be known.

The measurement procedures of nonlinearity tests with precalibrated attenuators are the most apparent and only require establishment of conditions matching those of the calibration process. Settings include equivalent radiation in spatial, temporal, and spectral domains and mode distributions, similar light divergence or surface density, and prevention of multiple reflections among singularly calibrated attenuators. Convenient methods for nonlinearity measurements not requiring any preceding calibration use geometrical vignetting for a spatially and temporary homogeneous distribution of radiation. One known example is a measurement technique with net attenuators made either as sets of relatively small apertures in any opaque substrate or motorized choppers and shutters, having an open sector or sectors in a steady screening matrix instead of apertures.

The net attenuators have a number of clear apertures; flux Φ_τ transmitted by the apertures is defined as the surface density E_λ of a given beam of light multiplied by the area A_0 of the apertures: $\Phi_\tau = A_0 \cdot E_\lambda$. Therefore, the bounds of applicability for the net-measurement method are the light-beam surface density and diffraction limit. For fixed flux Φ_0 of the incident beam, the upper threshold level obtainable by a net attenuator is defined by the beam's cross section, and the lower one is restricted by diffraction of wavelength λ on the smallest net aperture. The upper and the lower measurement limits of the method's linear dynamic range are $\Phi_{\max} = \Phi_0 A_{i\Sigma}/A_0$ and $\Phi_{\min} = \Phi_0 A_i/A_0$, where A_0 is the beam's cross section and A_i and $A_{i\Sigma}$ are the areas of the i^{th} smallest aperture and of the largest number of combined apertures in the beam.

The use of motorized choppers for linearity measurement is limited by the ratio of the maximum possible rotation frequency $f_{\max}$ to the inverse time constant τ of the radiometer being tested. When: $\tau \gg f_{\max}{}^{-1} = T$, the test radiometer reacts to the

mean power of light transmitted by the chopper during its period of rotation T; thus, each open sector acts as the δ-pulse existing at the instant of time $\Delta t \ll T \ll \tau$. Such a sector transmits incident flux Φ_0 due to the ratio $\Delta\tau/T$ of two δ-pulses:

$$\Phi_{choper} = \Phi_0 \Delta t / T = \Phi_0 \omega_{\text{sec}} / 2\pi. \tag{4.50}$$

Here ω_{sec} is the central angle of the disk open sector. If $\tau \leq T$, the radiometer to be tested may react to every rotation circle as to the pulse, the amplitude of which changes from zero to Φ_0 and then back to zero. In a system with synchronous detection, the modulation frequency *f* of light has to be at least 1 order of magnitude higher than that of the disk rotation [4.56]. When time intervals t_1 and t_2 corresponding to central angles ω_1 and ω_2 obey $t_{1,2} < \tau < T$, nonlinearity studies can be made by measuring the energies of pulses produced by sectors rotating at constant velocity *v*:

$$W_1/W_2 = \Phi_0 t_1 / \Phi_0 t_2 \underset{v=const}{=} t_1/t_2. \tag{4.51}$$

The practical limitations for chopper-based studies are similar to those for net attenuators, restricting the upper and lower limits of applicability for motorized-chopper measurements. In both cases, a shared operation of several attenuators is prohibited, since it could cause a coincident opening and closing of a single beam of radiation, and the total action of such a set would not be additive.

One apparent advantage of the net or chopper attenuator is due to simplicity of calibration: just by geometries of transparent and screening areas – presuming noticeable diffraction effects are prevented. Spectrally selective attenuators are more complex to use. Even considering that the spectral properties of absorbing or scattering glasses are generally known, a calibration process requires one to obtain consistent spectral measurements, being especially intricate, if high accuracy of linearity studies is required. Routinely it is much easier to measure spectral transmittance (or reflectance) of a glass plate as a whole, and to use the data for nonlinearity testing. By contrast with aperture-based attenuators, while taking strict measures preventing multiple-beam interference, one can use glass plates in attenuation sets. The concept of simultaneous studies provides the basis for so-called *methods of addition of light* that provide numerous measurement possibilities.

The ability to deploy a combination of various attenuators concurrently placed into a beam of light allows one not only to resolve the major disadvantage of using singularly calibrated objects, but also to reject any needs for absolute linearity-scale calibration at all. Nonlinearity measurements applying unknown single actions rely on the additivity principle, under the presumption of the absence of any noticeable interference, diffraction, or radiation-induced nonlinearity. The linear system's radiometric reaction to the sum of two single actions should be equal to the aggregate of the reactions to these actions occurring independently. Here the light-addition nonlinearities are for all possible radiation-induced effects, as well as for the multiple reflections among single elements. Reflections must be counted separately, since they break the independence of individual actions for every individual

attenuator as the basis of the additivity principle. Every consecutive procedure of light addition with attenuators is expected to start from any vertex of the dynamic range to be studied—when such a range is established, a light-addition test could be performed in reverse order. First, the initial signal N_0 corresponding to the highest radiant flux Φ_0 is measured. Then, two attenuators with unknown attenuations K_1 and K_2 are brought in turn into the incident beam of light, having presumed to be constant flux Φ_0, and each individual reaction N_1 and N_2 to the attenuator action is recorded. Finally, both attenuators are deployed at once, and reaction N_Σ to their total action is measured. The difference $\Delta = |N_\Sigma - (N_1 + N_2)|$ identifies the absolute deviation from linearity, and the ratio $\delta = \Delta/(N_1 + N_2)$ gives its relative magnitude. Since the dynamic range of linear measurements by a test radiometer is unknown even within initial magnitudes $N_0 - N_1$ and $N_0 - N_2$, the optical density D of each attenuator needs to be as small as possible for the procedure to have the smallest measurement steps.

There are a few ways to continue the process from the point $N_1 + N_2$. The initial flux Φ_0 can be attenuated any possible way to the sum signal $N_\Sigma = N_1 + N_2$. Then, the cycle of two attenuator actions is repeated to the next attenuation point, etc. The method can be used with various alterations, but the results obtained might not always be correct for the entire dynamic range studied: $D = m \cdot N_\Sigma$, where *m* is the number of measurement cycles. One example of a nonlinear transformation consists of an unresolved chain of nonlinear sections fitted to a nonlinear dependence, caused by the exponential – instead of liner – reaction, as shown in Fig. 4.44.

The step function in Fig. 4.44 could be mistaken as being quasi-linear if repeatability of the measurement is not sufficient to resolve small variations as of the nonlinear deviation for one step. At sufficiently high sensitivity and accuracy, only a procedure starting each measurement step from the point of initiation is capably of fully resolving the actual nonlinearity. It is always accurate to start every new step from the first point of any given dynamic range. To continue from the first to the second step, the action must begin again from the start with another pair of attenuators of higher optical density. The light action of the second pair of attenuators needs to coincide with the total attenuation N_Σ of the first pair at point $2N_\Sigma$ to

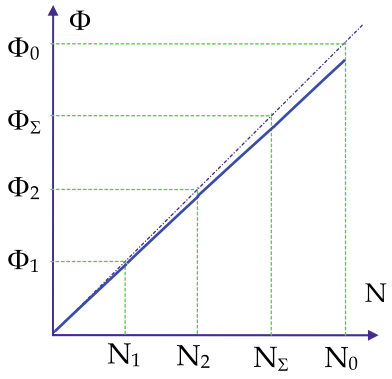

Fig. 4.44 Measured quasi-linear steps fitted to a relatively-nonlinear transformation curve

be measured next. The process continues until a consistent deviation from linearity is reached. Consequently, the intensity interval between the first and the preceding point until the nonlinearity has occurred represents the dynamic range of linear photometric response.

Elimination of diffraction phenomena is a required measure for linearity measurements using net attenuators, but multiple reflections among two or more elements must be prevented during every method of light addition. Since such prevention concerns only light reaching a radiometer under test, exclusion of multiple reflections can be achieved via wedge-shaped elements, antireflection coatings, or by immersing all reflective surfaces. Adding uncalibrated transmission attenuators such as wedge plates should be restricted owing to unequal angles of incidence on the element and set. Antireflection coatings are more effective (see Chap. 3), but the effectiveness of a coating depends on the spectral range of application; thus, immersing the set is the simplest action minimizing effects of multiple reflection to under the sensitivity limit.

Chart 4.1 demonstrates the actual efficiency of such a not precisely matching immersion as immersion of glass attenuators in purified water. Related experiments [3.37] were performed using unstable pulsed laser light when the multiple reflections could be very apparent owing to spectral instability of laser emission. The measurement setup was shown in Fig. 3.20. Attenuation factors $K_i = 1/\tau_i$ for three plane-parallel neutral-glass plates P_i at $\lambda = 1.06$ μm were evaluated separately in water and in air by one radiometer and then combined in all aggregations among them. Repeatability of measurements characterized by the margin of error at 95% confidence for each individual measurement of radiation intensity with filters in water was improved by an order of magnitude – to 0.1–0.9% from 4.4 to 8.0%. The factual random errors of series of the individual intensity measurements with sets of attenuators present in the light beam were correlating to reductions of the surface reflectance—from $\rho \cong 0.04$ for a glass of refractive index $n = 1.5$ in the air to respective $\rho \cong 0.005$ for the glass immersed in purified water with index of refraction $n_w \cong 1.3$ ($n_{im} = 1.33299$ at $\lambda = 589.3$ nm).

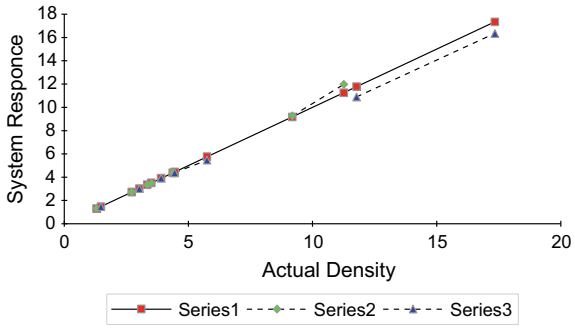

Chart 4.1 Effectiveness of nonprecise immersion: a - linear responce; b - filters in water; c - filters in air

4.3.2 Dual-Aperture and Superposition Methods

Usually, a technique for photometric accuracy measurements will start from the highest level of radiation intensity and finish at the lowest level: for example, from the smallest to the largest distance from a point source of light or without and with the attenuators. The opposite way – starting from the lowest intensity level – could be very productive as well: adding to a main light source an auxiliary one with equivalent spatial, temporal, and spectral parameters of its radiation, and superposing them together over the same section of an entrance aperture of a radiometer or photometer under test. Successive measurement steps remain the same – sequentially adding more sources of equal parameters or increasing the intensity of each source twofold, moving to double intensity and allowing measurement with no calibration. This superposition scheme was suggested centuries ago – two candles or kerosene lamps being added to each other as light sources [4.57].

There are several methods for addition and removal of extra light sources – either actual or effective, to irradiate a test object from different directions. Doing so, one has to evaluate each action for its individual effectiveness considering possible changes of the spatial and directional sensitivity of the test detector if positions of the source images vary. Of course, the safest way is to accommodate each source in a virtually mixed beam of light irradiating the radiometer under test. There are a few methods for that accommodation. One consists in implementation of several real sources in a reflective cell or in an averaging sphere having a single output aperture collimated into the radiometer to be tested. Another way is associated with effectively or actually small light sources, such as light-emitting diodes, projected onto the test radiometer by a beam, forming a shared image, spatially averaging individual positions, and also fitting the detector's aperture.

As net attenuators open and close various sections of an incident light beam, the notion of open regions under similar restrictions to diffraction limits can be used to add multiple light sources equivalent to each other in their spectral, spatial, and temporal domains. By forming m apertures in an opaque matrix, inscribed into any incoming beam, and then sequentially closing and opening each aperture, one makes the m-factorial action of light on the radiometer under test. The structures defining the *superposition* and *double-aperture* methods [4.38–4.45] are shown schematically in Fig. 4.45. Revolving disks 1 and 2 in Fig. 4.45a have m identical openings. Any openings, fitting inside cross section 3 of an incident beam, denote two sections of the light beam passing through. For any uniform irradiance across the light beam and unchanged sensitivity of radiometer 4 being tested two selections of summed beam sections, the ratio of open areas in the light beam gives the change ratio of the light action applied. First, any two nearly identical apertures in disks 1 and 2 are inserted into the light beam sequentially producing respective signals $N_{i,1}$ and $N_{i,2}$. Second, both apertures are inserted simultaneously, and the difference ΔN_Σ of the two-aperture signal $N_{i,\Sigma}$ from the expected sum: $N_{i,1} + N_{i,2}$, is measured. When as with attenuators, if the areas of openings are made proportional to 2^m, where $m = 1, 2, 3\ldots$, the intensity for each subsequent open aperture is doubled that for the previous one: $A_{i+1} = 2A_i$; $A_{i+2} = 4A_i$, etc. The entire area of circle 3 defines the

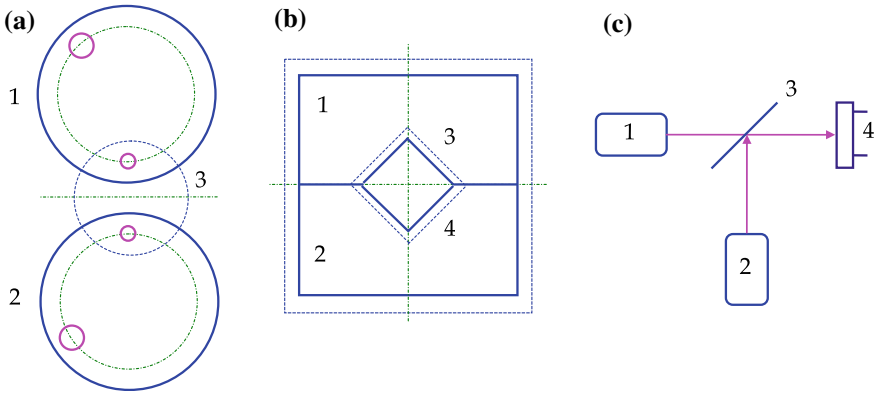

Fig. 4.45 Measurements of photometric accuracy by superposition (**a**), double-aperture (**b**), and supplemental-light (**c**) techniques

upper limit, representing the beam's cross section for the uniform irradiance distribution of incident light. If adequate correlations among the areas of single apertures are known, the process is quick even for small steps among every action. Any desired sequence can be achieved. Typical formulae for continuance from the initial two equal steps are $i - 1 \rightarrow 1{:}1{:}2{:}3{:}4{:}5\ldots$, or $(i - 1) + (i - 2) \rightarrow 1{:}1{:}2{:}3{:}5{:}8\ldots$, where i is the number of steps starting from $i = 3$.

If the relationships among the areas of all apertures are unknown, or if properties of a given light source do not allow making uniform distribution of irradiance in a beam, the superposition procedure has to be realized by measuring every photometric reaction to a singular light action. Every $(i + 1)^{th}$ step is made nearly equal to the sum of the previous two i steps, making $\mathrm{i} + 1 = 2\mathrm{i}$. The final action is made by the superposition of light beams corresponding to the sum of all openings. Equality of the sum for individual actions to the doubled light action confirms that the radiometer studied linearly transforms the intensity of light between points corresponding to each single opening and to the sum of two opening. This procedure performed by combined adaptable individual light actions governed by the 2^m law is called the *double-aperture* method.

In the layout in Fig. 4.45b, two m-aperture disks from Fig. 4.45a are replaced by two sliding sectors as adaptable rhombs 1 and 2 of triangular or any other suitable profile in opaque matrixes 3 and 4. First, with only sector 1 open the smallest light action producing signal $N_{1,min}$ is measured. Second, for the closed first sector the nearly same signal $N_{2,min}$ of presumably identical light action is registered with sector 2 open. Then, both sectors in the first two positions are opened simultaneously and the combined signal $N_{min,\Sigma}$ must be the sum of the first two signals: $N_{1,min} + N_{2,min}$, if the detection system performs linearly. Each light action for the next pair of actions to be summed is nearly equal to the sum of the two previous actions, and so forth. The same concept may be realized with two independent variable sources 1 and 2 irradiating any test radiometer 4 via semitransparent beam splitter 3 (Fig. 4.45c). The ability to diversify initial and intermediate actions is one

advantage of such measurements, though some restrictions of the method are associated with the possibilities of quasi-nonlinear transformations, as depicted in Fig. 4.44. In other words, the higher is the intensity of a single light action, the smaller is the relative sensitivity to any deviation from the linear behavior. A trustworthy procedure must provide the least single light action in all the dynamic range of the expectedly linear behavior.

Somewhat broader potentials can be realized by the so-called *supplemental-light* method, deploying any number n of spectrally, spatially, and temporally identical light sources, though being able to vary any discretization step; for example, several light-emitting diodes, emitting out of the integrating sphere, or a matrix of n apertures implemented in a beam of a single variable source of radiation, capable of being turned on and off independently. Each action or combination of them can be counted separately since the photometric reaction to every light action gives one independent discretization step. If the total action for the entirety of effective sources fits the linear behavior of the radiometer or photometer under test, the number of such supplemental sources, or the discretization step, or the emittance of a single, but variable light source, should be increased further to identify the highest point of the linear dynamic range of the photometric reaction tested.

4.3.3 Pulsed Measurements

The capability to tune not only the power but also the energy or duration of light action of radiation may advance measurement prospects by expanding all the methods of photometric accuracy measurements considered. Distinction of measurements for pulsed radiation can be expressed via variable relations of time constants for irradiation and reception. Other aspects are similar to those in continuous light, but the limitations are greater. Analogously to nonlinearity factor K_Φ of an averaged reaction $\mathrm{J_{i,avj}}$ of a test radiometer to a mean power $\Phi_{\mathrm{i,avj}}$ of cw radiation:

$$\mathrm{K}_\Phi = \left(J_{1,avj}/\Phi_{1,avj}\right)/\left(J_{2,avj}/\Phi_{2,avj}\right), \tag{4.52}$$

similar factor K_W can be used for reaction to energy $\mathrm{W_i}$ of any pulse, integral radiant intensity Θ_i, radiant exposure $\mathrm{H_i}$, as the spatial integral of irradiance Ξ, or other pulse extents (see Chap. 1):

$$\begin{aligned}\mathrm{K}_W &= \frac{J_1}{W_1}\Big/\frac{J_2}{W_2} = \frac{J_{1,j}}{H_{1,i}}\Big/\frac{J_{2,j}}{H_{2,i}} = \frac{\int\limits_{\tau_r} J_{1,j}\,dt}{\int\limits_{\tau_p} \Phi_{1,i}\,dt}\cdot\frac{\int\limits_{\tau_p} \Phi_{2,i}\,dt}{\int\limits_{\tau_r} J_{2,j}\,dt} \\ &= \frac{\int\limits_{\tau_r} J_{1,j}\,dt}{\iint\limits_{S,\tau_p} \Xi_{1,i}\,dtds}\cdot\frac{\iint\limits_{S,\tau_p} \Xi_{2,i}\,dtds}{\int\limits_{\tau_r} J_{2,j}\,dt}.\end{aligned} \tag{4.53}$$

Here indices $_{1,\ 2;\ p,\ r;\ i,\ j}$ are respectively related to the first and the second pulse reaction, to the incident pulse p and to the temporal response r of the radiometer, to the i^{th} and j^{th} instant of time.

The fact that the sensitivity $S_{\lambda,const}$ of a detector to a continuous light action of flux power Φ and the sensitivity $S_{\lambda,pulse}$ to a δ-pulse carrying maximum power $\Phi_{max} = P_{max}$ in the same spectral domain is the detector constant gives the correlation for the sensitivities to continuous and pulsed radiation:

$$s_{\lambda,cont} = U_R/(R\Phi) = s_{\lambda,pulse} = CU_C/W, \tag{4.54}$$

where W is the energy of the δ-pulse, R and C are the internal resistance and the capacity of the detector, and U_R and U_C are the maximum detector signal amplitudes in continuous and pulsed modes [4.65]. To make the sensitivity correlation, parameters R and C of the detector must be accurately determined. That is not a trivial task since both parameters depend on the intensity of irradiation. When they are unknown at a time of measurement, the load of the test radiometer has to have resistance and capacity higher than those of its detector [0.16]: $R_l, C_l \gg R_d, C_d$. Such pulsed measurements, as ones in continuous light, are obtained for the integrals of each i^{th} factor during the time t of observation:

$$K_W = \int_t \Phi_i K_{\Phi,i}\, dt \,/ \int_t \Phi_i\, dt. \tag{4.55}$$

The characteristics for measurements of photometric accuracy in pulsed radiation are defined by the requirements of individual methods of such measurements themselves. For example, when conformity of a pulse response to a change in any radiant or luminous exposure in inverse proportion to the square distance from a pulsed source is studied, the likely spatial fluctuations of the locality of the source's pulse discharge could have a weighty influence on the relevant uncontrollable changes of exposure. Accordingly, photometric accuracy measurements in such a case are expected to be made with spatial integration, dispersing respective intensity fluctuations of unstable light pulses.

The accuracy of pulsed measurements for the double-aperture or supplemental-light method is likely limited by spatial pulse-to-pulse fluctuations and temporal dissynchronization among pulses. Inappropriate spatial changes of the light intensity between separate pulses will cause unequivocal single actions even by apertures with equal areas. Any asynchronous time behavior of distinct pulsed sources, concurrently applied for addition or supplemental actions, may not be tolerable by a relatively fast detector, reacting to power distributions of pulses as the actions of divergent intensities. In contrast to power measurements, a radiometer with a slow pulse response (see Sect. 3.2 for terms) can integrate different actions in such a way that its time-integrated reaction will remain additive to the sum of all light beams accepted in unequal time intervals. This opens up possibilities not only for the spatial but also for the temporal addition or supplement of light pulses.

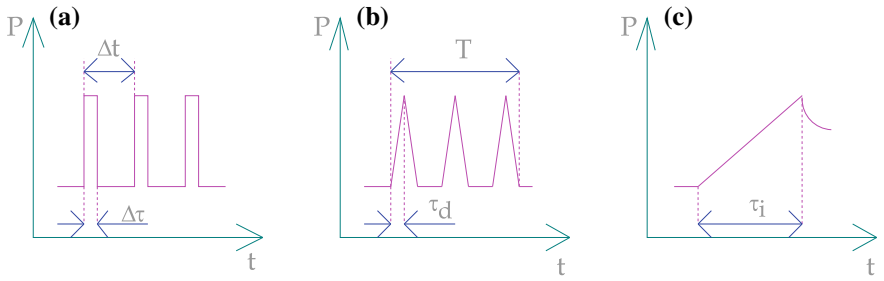

Fig. 4.46 Transformation of short pulses by a fast detector and an integrator

Figure 4.46 shows one method for the temporal light supplement, where the actual summation of individual radiometric actions is realized in the time domain via a detection system with time constant τ_i positively larger than total time period T of an entire sequence of pulses (Fig. 4.46c). If the time constant τ_d of the system's detector is compatible with the duration $\Delta\tau$ of pulses, it may modify the shape of the pulses processed (Fig. 4.46b), not processing the maximum power P of the incident pulse (Fig. 4.46a). Nevertheless, the reaction of an integration system such as that in Fig. 4.46c is proportional to the total number of single pulses emitted by a source. Such a procedure allows action back and forth, while determining likely deviations from linearity simply by variation of the number of emitted light pulses. If the repetition rate $f = 1/\Delta t$ of a pulse sequence is greater than the cut-off frequency $1/\tau_d$ for the detector itself the test may be applied for the detector only, or for the entire radiometer with the detector. Measurements for this method of the *temporal supplement of light* by a sequence of pulses with constant amplitude can be quite simple. Every single pulse in a string determines the discretization step and the amplitude of each single action, and the total number of pulses defines the limits of the dynamic range of measurement, and a correlation between constants $\Delta\tau$ and τ_d sets respective boundaries on the potential applicability of a given method for a particular detector or the entire pulse radiometer or photometer, including its electrical circuits.

Certain combinations of temporal and spatial light supplement can be arranged via short light pulses, the duration of which precludes overlapping of multiple reflections at longer round trip times (see Chaps. 1 and 3, Fig. 1.8). Such techniques [4.71] become quite applicable with ultrashort pulses from terahertz sources in the 0.1–4-THz bandwidth range where silicon has negligible absorption and silicon-plate loss can be attributed strictly to Fresnel surface-reflection losses. For picosecond light pulses, using millimeter-thick plates with the same air gaps ensures intersurface round trip times of tens of picoseconds, thus avoiding pulse overlapping with intensity attenuation steps:

$$I_N/I_0 = \left((1-\rho)^2\right)^N, \tag{4.56}$$

where N is the number of plates with surface reflectance ρ. For silicon plates of refractive index $n = 3.41$ and $\rho = 0.2986$, each single-plate attenuation step on sole-pulse detection gives $I_1/I_0 = 0.4919 \approx 0.5$ [4.71]. The deviations from linear responses for photodetectors caused by harmonic distortions are investigated adding two or more heterodyned laser sources, emitting on slightly offset wavelengths to generate an RF tone, or combining RF-modulated sources for multiple-tone studies [4.78, 4.79].

4.3.4 *Arrangements for Light Addition Studies*

Figure 4.47 illustrates the typical layout for double-aperture measurement of photometric accuracy. The arrangement shown resembles Young's dual-slit interference experiment [1.1], having potential interference errors due to diffraction and the following interference (see Chap. 3). The visibility of the dual-beam interference pattern on the optical axis created by light of wavelength λ diffracted by two apertures of width w separated by distance d can be expressed as [1.1, 4.62]:

$$V = |\sin(2\pi d\varphi/\lambda)/(2\pi d\varphi/\lambda)|, \tag{4.57}$$

where φ and Θ are the angular radii of the source and detector apertures for the angular distribution of flux dΦ on the detector being $\left(\sin^2(\pi d\Theta/\lambda)/(\pi d\Theta/\lambda)^2\right)d\Theta$ if only one of two apertures is open. As follows from Eq. (4.57), the smaller are the separations between apertures and the angular sizes of the source and detector, the lower is the visibility of the interference pattern that may be achieved. Appropriate precautionary measures should be taken to either avoid a highly visible interference or to provide spatial and temporal integration of as many fringes as possible, making sure any redistribution of radiation intensity caused by the diffraction and interference is averaged out.

Spatial fluctuations of light emission, typical for pulsed radiation, can affect but will not exclude the capabilities to obtain photometric nonlinearity measurements by addition of light. Suitable spatial integration over a cross section of a beam of pulsed light may be sought while implementing a chosen method of pulse measurements. One practical realization for obtaining a sufficient-enough spatial integration in partially coherent radiation emitted by a relatively unstable pulsed laser source 1 is illustrated in Fig. 4.48 [3.37]. Static opaque light-addition matrix 5 and cover plates 6

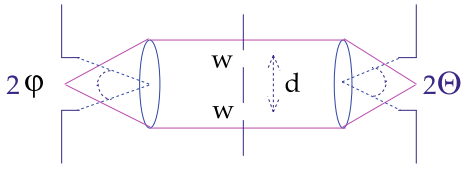

Fig. 4.47 Double-aperture diffraction

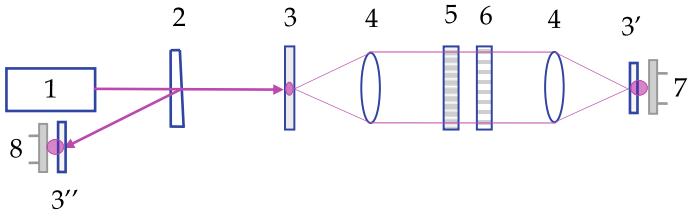

Fig. 4.48 Testing photometric accuracy in pulsed light

and telescope objectives 4 were placed after spatial integrator 3, as an opal glass diffuser. The intensities of added light pulses were measured by test radiometer 7 and reference detector 8 via splitter 2, all behind diffusers 3′ and 3″. An even number m of apertures were made in permanent matrix 5, and removable cover plates 6 concurrently opened up any n out of m apertures in matrix 5. The number ratio m/n defined the actual number of plates 6 opening all m apertures sequentially. Accordingly, the ratio $m/2n$ defined the limited number of plates needed to uncover only $2n$ apertures, only $4n$, and so forth. Eventually all matrix apertures were uncovered at once by removing every cover plate. A nonlinearity δ_{lin} for every single point of the dynamic range under study, defined by the particular cover plate used, was identified by the sum of reactions onto $i = k$ plates chosen: $\delta_{\text{lin}} = (\Phi_0 - \Sigma_{i=1}^{k}\Phi_i)/\Phi_0$. Here Φ_i is the flux transmitted by the i^{th} cover plate. Despite the increased number of single measurements required at every point of the dynamic range, the technique did not rely on any assumptions, leading to systematic errors.

Figure 4.49 depicts a 16-aperture opaque matrix for independent light supplement. The first eight cover plates open two apertures at once (sets *a*), four cover plates open four apertures (sets *b*), and two cover plates open eight random apertures. Thus, deviations from linear behavior of a test radiometer may be measured eight times at the $0.125\Phi_0$ intensity point, four times at the $0.25\Phi_0$ point, and twice at the $0.5\Phi_0$ middle point. In the experiment conducted [3.37], two pulsed light

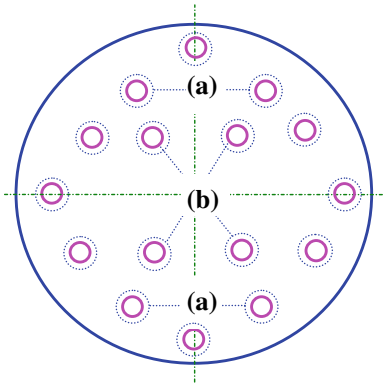

Fig. 4.49 Independent light supplement

sources were utilized: a Nd:YAG laser in Q-switch mode at $\lambda = 1.06$ μm, and a halogen flashlamp emitting radiation in the 400–700-nm wavelength range. In each case, the beam diameter in the parallel path was 14 mm. The diameters of the permanent apertures in the matrix and cover plates were 1.2 and 1.8 mm, respectively. All laser measurements were made via an opal glass integrator with diffuse transmittance $\tau_d \approx 0.5$. The margin of error at 95% confidence of every single pulse measurement even for a nonstabilized laser was only ±0.2%. The same error due to spatial and temporal fluctuations among different apertures with a flashlamp, a monochromator, and a less dense spatial integrator was ±0.05%.

Two measurement arrangements are outlined in Fig. 4.50. The layout in Fig. 4.50a is based on the double-aperture linearity tester for the NIST reference transmittance spectrophotometer, developed to perform measurements with a standard deviation of $\pm 4 \cdot 10^{-5}$ [4.44] (see Fig. 4.25a for spectrophotometer design). For linearity measurements the source emission was varied by changing the current of the tungsten lamp and using a neutral-density wedge. The repeatability of least-squares-fitted measurements for at least 20 readings was within $\pm 2 \cdot 10^{-5}$. The largest correction factors for nonlinearities of the reference spectrophotometer were near $(2.7–2.8) \cdot 10^{-4}$ at the middle point of each decade. Similar cascaded double-aperture measurements, further expanded using two quartz surface reflections, confirmed an over eight-decade linear dynamic range for unbiased (photovoltaic) silicon diodes [4.63].

Figure 4.50b illustrates a version of the linearity tester in the quasi-parallel beam of light for the NRCC reference spectrophotometer (see the design in Fig. 4.25b) [4.68]. The dual-aperture technique was realized via the adaptable-rhomb scheme shown in Fig. 4.45b. The area of the opening for every sequential aperture was defined by moving two steel blades by linear actuators. Dark signals with closed

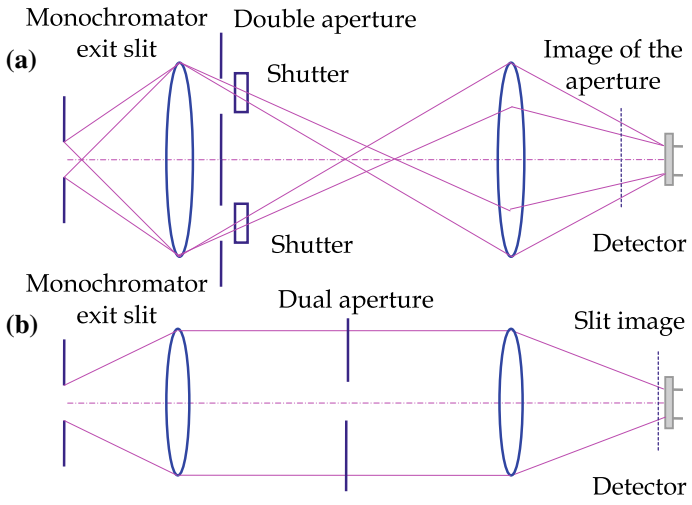

Fig. 4.50 One realization of double-aperture technique

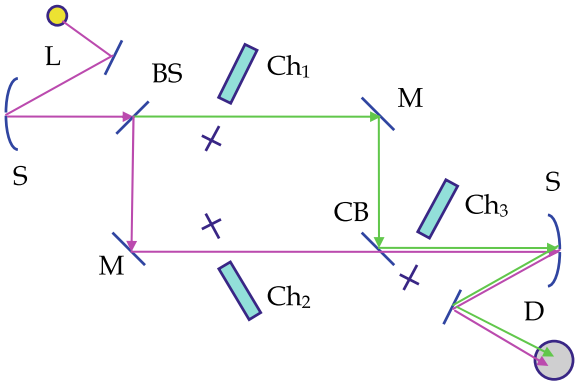

Fig 4.51 Automated beam splitter-cojoiner linearity study

blades were subtracted from the test results. The reliability of performed linearity measurements verified versus a known highly linear silicon photodiode was $\pm(1–3) \cdot 10^4$ over a 3400:1 dynamic range at a 97% confidence level.

Attempts can be made to perform automated testing of photometric accuracy (see [4.66–4.70]). Figure 4.51 depicts the beam cojoiner, which splits and recombines a single light source onto a detector, attenuating two single and one combined beam in automated steps with 125 combinations [4.67]. White light from lamp L is collimated by spherical mirror S, split into two beams by beam splitter BS and recombined by combiner CB, bringing it to focus on detector D without any superposition to avoid interference. Each chopper Ch_1–Ch_3 has five blade-mounted attenuators for 125 possible combinations executed successively with dark-current measurements at $\pm 0.1\%$ accuracy.

The experimental results for all double-aperture and supplemental-light methods of photometric accuracy measurements confirm that by achieving high accuracy of individual measurements, one can detect most linearity deviations by making identified increments of light intensity from any point of the dynamic range of a photometer or radiometer under test.

Part II
Measurements of Optical Losses

II.1. Features of Low-Loss Assessments

By definition, the notion of *optical loss* characterizes the amount of wasted power or energy being transferred by the light beam under consideration and lost as a result of a given interaction of the beam with the object studied. Independently of the character of such an action, the transmission loss χ_τ designating the ratio of the flux incident on the object Φ_0 to the lost flux Φ_χ is (Eq. 1.93):

$$\chi_\tau = \frac{\Phi_\chi}{\Phi_0} = 1 - \frac{\Phi_\tau}{\Phi_0} = 1 - \tau_\Sigma = \frac{\Phi_0 - \Phi_\tau}{\Phi_0}. \tag{II.1}$$

Here, τ_Σ is the total transmittance of the object and Φ_τ is the transmitted flux. Depending on the task to be performed, reflection χ_ρ, scattering χ_σ, or absorption χ_α loss can be similarly recognized as an informative loss. With respect to reflected Φ_ρ, scattered Φ_σ, or absorbed Φ_α flux, the loss is:

$$\begin{aligned} &\chi_\rho = 1 - \rho = \left(\Phi_0 - \Phi_\rho\right)/\Phi_0;\ \chi_\sigma = 1 - \sigma = (\Phi_0 - \Phi_\sigma)/\Phi_0\,; \\ &\chi_\alpha = 1 - \alpha = (\Phi_0 - \Phi_\alpha)/\Phi_0\,. \end{aligned} \tag{II.2}$$

If only one event: transmission, reflection, scattering, or absorption, is imperative, every loss is:

$$\chi_\tau = \rho + \sigma + \alpha; \quad \chi_\rho = \tau + \sigma + \alpha; \quad \chi_\sigma = \tau + \rho + \alpha; \quad \chi_\alpha = \tau + \rho + \alpha. \tag{II.3}$$

The relative sensitivity δ_χ to optical loss χ under indirect study of flux Φ_i can be identified as:

$$\delta_\chi = \frac{\Delta\chi}{\chi} = \frac{2\Delta\Phi}{\Phi_0 - \Phi_i} - \frac{\Delta\Phi}{\Phi_0} = \frac{\Delta\Phi}{\Phi_0} \cdot \frac{\Phi_0 + \Phi_i}{\Phi_0 - \Phi_i}, \tag{II.4}$$

where $\Delta\Phi$ is the error of each i^{th} measurement of the flux of radiation. From expression (II.4) one obvious conclusion can be observed: the smaller is the loss under study, i.e., the closer is flux Φ_i measured to the initial flux Φ_0 incident on the object, the bigger is the error of indirect measurement. At the $\Phi_i \rightarrow \Phi_0$ limit, the highest sensitivity to be achieved while indirectly determining any particular type of loss tends to double the error of the flux measurements related not to the flux, but to the loss itself:

$$\Delta\chi/\chi \underset{\chi\rightarrow 0}{=} 2\Delta\Phi/\chi, \tag{II.5}$$

while at any direct study: $\xi = \Phi_\xi / \Phi_0$, by measuring Φ_ξ and Φ_0 the error is $\Delta\xi = \Delta\Phi_\xi / \Phi_\xi + \Delta\Phi_0 / \Phi_0$.

Analysis of attenuation of optical radiation by a given substance under investigation, until recently, was the natural prerogative of practical spectrophotometry. However, exceptional attributes of optical instruments based on multiple interactions of light – lasers, high resolution interferometers, long optical fibers, and planar waveguides – have increased tremendously the sensitivity required to detect very low variations of the optical properties of their elements. Specific limitations to existing measurement devices and newly developed optical elements resulted in the surfacing of vast novel and ultrasensitive methods of measurements, though highlighting the need for establishing verifiable correlations among various measurement concepts. For example, laser generation needs to be stipulated by the gain coefficient b_0 of the active medium, which exceeds the passive loss μ of a resonator enclosed by two mirrors with reflectance ρ_1 and ρ_2 for stable emission of laser light to be sustained [II.1, II.5, II.8]:

$$(\rho_1 \cdot \rho_2)^{-1} = \exp\left(\ell\left(\sqrt{b_0 \cdot \mu} - \mu\right)\right), \tag{II.6}$$

where ℓ is the length of the laser resonator. For example, to support operation of a compact diode-pumped laser with $\ell = 1$ cm, $b_0 = 0.01$ cm^{-1}, and $\mu \leq 0.05$ cm^{-1}, the value of the $\rho_1 \cdot \rho_2$ product must not be less than 0.99; thus each single mirror reflectance must exceed 0.999. The necessity to reach such a high reflectance substantially limits the allowance for errors acceptable for a suitable measurement method or equipment controlling cavity mirrors or transmission elements inside that resonator.

The optical element's absorption, which may be negligible for conventional applications, could for intensive laser radiation cause thermal deformation and following wavefront distortion, then overheating or even potential damage of the absorbing element. Furthermore, even when studying a spatially integrated optical property of any absorber, it may be essential to detect irregularities of the absorber's local properties concurrently with having a high spatial resolution. Even higher resolution must be reached when studying optical fibers or planar waveguides. To maintain low losses in a communication line below a few decibels per kilometer, the linear attenuation coefficient in such a fiber line in most cases should be kept below 10^{-5} cm^{-1} (10^{-5} cm^{-1} = 4.343 dB/km). Such parity follows from the definition of fiber

or waveguide loss μ, expressed in decibels per kilometer via output Φ and input Φ_0 fluxes as:

$$\mu\ell\,[dB/km\cdot km] \rightarrow 10\log_{10}(\Phi/\Phi_0) = 10\lg\{\exp(-\mu\ell\,[cm^{-1}\cdot cm])\}. \quad \text{(II.7)}$$

Another distinction defined by given applications of optical elements and often overlooked necessitates the need for equivalency of operation of elements and measurement conditions. As seen in Chaps. 2 and 4, apparent difficulties complicate measurements of specular reflectance at normal incidence of light. In many actual cases, these measurements may be realized not at normal incidence, but at close-to-normal incidence, though with some exceptions. If light interacts with the test surface by its normal, the surface specular or so-called coherent reflectance [II.2] can be expressed as

$$\rho = \rho_p \exp\left[-(4\pi R_a/\lambda)^2\right], \quad \text{(II.8)}$$

where ρ_p is the specular reflectance of a perfectly flat surface, R_a is the root mean square height of surface roughness, simply, *rms roughness*, and λ is the wavelength of light irradiating the surface.

For the same light incident at oblique angle Θ, the surface reflectance ρ_Θ transforms into:

$$\rho_\Theta = \rho_p(\Theta) \exp\left[-(4\pi R_a \cos\Theta/\lambda)^2\right]. \quad \text{(II.9)}$$

With increase of the angle of incidence, the effective surface roughness: $R_a \cos\Theta/\lambda$, decreases and the component of coherent reflectance increases. Therefore, a surface conforming to the reflectance test in the measurement with oblique incidence of light can fail the test during irradiation at the normal, particularly for some laser applications. Even at $\Theta = 4°$ and $R_a = 0.03\lambda$, the ratio ρ_Θ/ρ is 1.0007 and becomes 1.002 at $\Theta = 6°$ and $R_a = 0.03\lambda$ or at $\Theta = 4°$ and $R_a = 0.05\lambda$. Accordingly, the measurements should not be made at oblique incidence if the reflectance must be higher than 0.999.

One aspect of low-loss measurements is determined by the lack of choices for prudent standards of reflection, transmission, scattering, or absorption with customized optical properties. Practically, every metal in contact with air tends to produce oxides and even sulfides. Glass surfaces undergo similar processes, and even under a vacuum thin-film formations are realized very quickly. The exact magnitude of the refractive index of a transformation layer on a glass substrate can be defined by many factors: such as physical and chemical properties of the contacting medium, patches of applied abrasive, and some local stresses produced in the polishing process, as well as by the conceivable presence of light-absorbing films. Problems of implementation and conservation of sufficient standards with postulated optical properties denote another technical problem, which can be solved by developing methods of absolute, but not standard-dependent measurements.

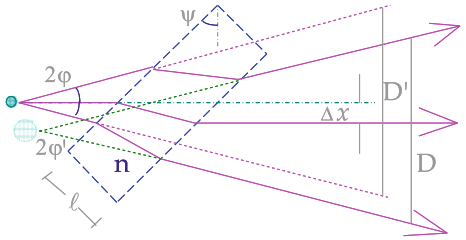

Fig. II.1 Transformation of a light beam

Absolute methods do not rely on comparison samples and provide results with respect to power or energy extents of light entering the measurement system and interacting with the object being studied.

Developments of absolute and relative methods for optical measurements could follow any reasonable trend of particular applications, such as the ones discussed in Chaps. 2 and 4 of Part I. Prior to considering specific measurements procedures, let us look at some restrictions, limiting practically all intensity measurements. Figure II.1 shows straightforward results of implementation in a light-beam path of a common plane-parallel plate of thickness ℓ and relative refractive index n. The plate, if tilted by any angle ψ, changes by ΔX the initial position of the optical axis of that beam and the diameter D of its cross section. Depending on the beam divergence, given by angle 2φ at the beam vertex, the transformation factor for a circular beam becomes:

$$\Delta D = 2\ell(\tan\varphi - \tan\varphi') = 2\ell\{\tan\varphi - \tan[\arcsin(\sin\varphi/n)]\}. \tag{II.10}$$

The displacement of the optical axis of the beam is

$$\Delta X = \ell \sin(\psi - \psi')/\cos\psi', \tag{II.11}$$

where ψ' is the increase of the angle of refraction created by the inclination of the plate. The beam transmitted via the plate becomes polarized with the ratio of orthogonally polarized components:

$$I_\perp/I_{||} = \cos^2(\phi - \phi'). \tag{II.12}$$

Even a quite often-made approximation for a totality of internal losses of a transmission sample such as a plane-parallel plate of a material under study defining Bouguer's law (Eq. 1.74):

$$\Phi = \Phi_0 \exp(-\mu\ell) = \Phi_0 \exp(-(\alpha + \sigma)\ell), \tag{II.13}$$

when replacing it with only the first two terms of the Taylor series retained, is only valid for the tending to zero internal attenuation coefficient of the sample $\mu \to 0$ which is not always the case:

$$\Phi \underset{\mu\to 0}{\cong} \Phi_0(1-\mu\ell);\ \mu\ell \underset{\mu\to 0}{\cong} (\Phi_0-\Phi)/\Phi_0. \tag{II.14}$$

Here μ, α, and σ are the linear attenuation, absorption, and scattering coefficients (see Sect. 1.3).

Combining errors and taking into account every possible change of the initial intensity of light entering a measurement system, as well as all factors that could influence light transformation into a signal to be registered, the generalized optical property ζ of a plane-parallel sample becomes:

$$\varsigma = N_\varsigma/N_0 = \delta_{N_\varsigma}\delta_{N_0}\delta_C\delta_L\delta_S \cdot I_\varsigma/I_0, \tag{II.15}$$

where N_ζ and N_0 are the detection system readouts with and without the sample under such a test, I_0 and I_ζ are the intensities of the light beam before and after interaction with a test sample, δ_C is the detector's sensitivity change as a function of the coordinates of incident beam, δ_L is the nonlinearity function of the detection system in the $N_\zeta - N_0$ range, and δ_S is the unbalance of light source intensities or detector sensitivity changes from either source or detector substitution. The total relative error is:

$$\begin{aligned}\Delta\varsigma/\varsigma = \Delta N_\varsigma/N_\varsigma + \Delta N_0/N_0 = \Delta I_\varsigma/I_\varsigma + \Delta I_0/I_0 + \Delta\delta_{I_\varsigma}/\delta_{I_\varsigma} + \Delta\delta_{I_0}/\delta_{I_0} \\ + \Delta\delta_C/\delta_C + \Delta\delta_L/\delta_L + \Delta\delta_S/\delta_S.\end{aligned} \tag{II.16}$$

Since for low-loss measurements the light intensity before and after the interaction with the object under study does not change much, the combined relative error of low-loss measurement could be estimated as [II.43–II.45]:

$$\Delta\varsigma/\varsigma = 2\Delta N/N = 2\Delta I/I + \sum_{i=1}^{m}\Delta\delta_i/\delta_i, \tag{II.17}$$

where $\Delta N/N$ and $\Delta I/I$ are the normalized fluctuations of the registered electric signals and of the respective intensities of light, $\Delta\delta_i/\delta_i$ is the normalized component of the i^{th} error of measurement, and m is the number of uncorrected components for the total error of the entire measurement series. From Eq. (II.17) it follows that the highest possible sensitivity the low optical loss is limited, first, by the twofold magnitude of the relative error of one measurement of radiation intensity. Another essential limit is defined by the sum of remainders of not excluded systematic errors of a given measurement method, being compensated for one or another way.

Depending on the measurement task to be performed and the conditions for the implementation of the measurement method chosen, likely systematic errors of measurements could contain temporal, spatial, and spectral (wavelength-dependent) components, or could be eliminated in their entirety. The accuracy of the following conversion of measured radiation into an electrical or another signal to be registered

is defined by the signal-to-noise ratio of specific detectors and electric circuits and is identified by noises of different nature. Even in the absence of any added noise components, thermal noise caused by accidental motions of charge carriers at the detector's thermal equilibrium with its surroundings always maintains some limit for any measurement device of electric nature. Consequently, the rational selection of a suitable measurement system with well-defined parameters for a specific low-loss measurement task to be performed should lead to the optimal concept that realizes the system sensitivity and accuracy to be as close to the fundamental limits as possible while producing the highest signal-to-noise ratio. As a result, every feasible task of measurement of a low optical loss under study should be considered from the standpoint of achievable sensitivity, obtainable accuracy, and the absence of systematic errors for the desired conditions of irradiation and observation of light [II.1–II.45].

Chapter 5
Conventional Loss-Measurement Techniques

5.1 Internal Transmittance and Attenuation Coefficient

When measuring relative changes of the intensity of radiation transmitted by a layer of a substance under study, one can identify, to a certain extent, practically any type of optical loss: reflectance of the substance borders with the surroundings, scattering and absorption factors of the entire irradiated object itself, etc. However, there are only a limited number of practical ways for measuring an internal substance loss. Likely procedures include detection of the front and back surface attenuation factors of the substance layer and subtracting these factors from the entire layer transmittance or exclusion of surface losses by comparing several samples of that substance presuming equal surface losses for the distinct samples and identifying the total internal bulk attenuation of the substance via the length difference of the samples measured.

Any conventional spectrophotometric technique (see Part I) for the measurement of internal transmittance of a plane-parallel sample at two perfectly polished surfaces relies on preliminary knowledge of the sample's relative refractive index with the surroundings. Presuming that both boundary surfaces of the sample have equal random deviations $\Delta\rho$ from identical and ideally specular reflectance ρ, defined by relative index n of refraction for the sample substance, and counting internal multiple reflections by Eq. (1.106), the relative error $\Delta\tau/\tau$ of the internal bulk transmittance measurement (cf. Eq. (4.26)) is given by:

$$\Delta\tau/\tau = (-\Delta\rho)/(1-\rho) - (\Delta\rho)/(1+\rho) = -2\Delta\rho/\left(1-\rho^2\right). \tag{5.1}$$

Here the minus sign defines opposite direction of changes. In turn, the error $\Delta\rho/\rho$ of the reflectance study for every surface is proportional to the quadruple magnitude of the refraction uncertainty Δn:

$$\Delta\rho/\rho = 4\Delta n/\left(n^2-1\right). \tag{5.2}$$

M. Bukshtab, *Photometry, Radiometry, and Measurements of Optical Losses*, Springer Series in Optical Sciences 209,
https://doi.org/10.1007/978-981-10-7745-6_5

As a result, the actual measurement error of internal transmittance of a given sample under study is defined by the fourfold value of the uncertainty for a single-surface reflectance either due to random changes of the sample surface properties or inaccuracy of the surface-refraction measurements. Any small refraction change $\Delta n/n = \pm 0.001$ for $n = 1.5$ leads to reflectance error $\Delta\rho = \pm 1.3 \cdot 10^{-4}$. This miscalculation causes the error of the internal attenuation factor measured by a conventional spectrophotometer to be within uncertainty $\Delta\tau/\tau = \pm 2.6 \cdot 10^{-4}$. If the expected internal loss is lower, its actual magnitude cannot be distinguished under these circumstances.

As seen in Chaps. 1 and 2, to determine the internal-bulk transmittance, $\tau_{int} = \exp(-\mu\ell)$, of a solid-state sample for a single light pass, either the angle of light incidence onto the sample must sufficiently deviate from the sample's surface normal or sample surfaces should not be parallel (see Fig. 1.7). For normal incidence of light on a sample made as a plane-parallel plate, when the beams internally retroreflected by the plate cannot be separated from each other, a quadratic equation as a function of sample's bulk transmittance needs to be solved (see Eq. (1.104)):

$$\tau_{\Sigma,0} = \frac{(1-\rho_0)^2\tau_{int}}{1-\rho_0^2\tau_{int}^2}. \tag{5.3a}$$

By resolving the equation via Napierian optical density: $D_N = \mu\ell$, one obtains:

$$\mu\ell = \ln\rho - \ln\left\{\sqrt{\frac{(1-\rho)^4}{4\rho^2\tau_{\Sigma,0}^2}+1} - \frac{(1-\rho)^2}{2\rho\tau_{\Sigma,0}}\right\}, \tag{5.3b}$$

where $\tau_{\Sigma,0}$ is the sample transmittance at normal incidence of light. Differences from true $\mu\ell$ values and those calculated without multiple reflections: $\mu\ell_{sngl} = \ln\left((1-\rho)^2 \Big/ \tau_{\Sigma,0}\right)$, are seen in Table 5.1.

Table 5.1 Internal transmittance with and without disregarding internal multiple reflections

Index of refraction, n	1.5	1.5	2.0	2.0
Total transmittance, $\tau_{\Sigma,0}$	0.9	0.92	0.8	0.782
Optical density, $\mu\ell$	0.0252	0.0033	0.00004	0.025
Single-pass density, $\mu\ell_{sngl}$	0.0237	0.0017	−0.01	0.025
$\mu\ell - \mu\ell_{sngl}$	0.0015	0.0016	0.01004	0.012

Table 5.1 illustrates that by ignoring the effects of internal multiple reflections in a sample, any low bulk optical losses to be studied can be artificially reduced, resulting in incorrect results.

Equations (2.41)–(2.47) demonstrate that two comparison measurements of the total bulk-plus-surface transmittance of two plane-parallel samples of the same substance with difference $\Delta\ell$ between their lengths practically allow one in many cases to dismiss influences of multiple reflections for a low internal attenuation to be distinguished. However, the two-sample concept of measurement does not allow complete disregard of the outcome of possible fluctuations for surface properties of the two samples measured, which become higher owing to four instead of two surfaces being involved. Depending on each particular circumstance, one or another factor is more or less significant. Assuming four sample surfaces to have one indistinguishable reflectance, the ratio of long and short sample transmittances is:

$$\frac{\tau_{\mathrm{lg}}}{\tau_{\mathrm{sh}}} = \exp[-\mu(\ell_{\mathrm{lg}} - \ell_{\mathrm{sh}})]\frac{1-\rho^2\exp(-2\mu\ell_{sh})}{1-\rho^2\exp(-2\mu\ell_{\mathrm{lg}})} = \kappa\cdot\exp[-\mu(\ell_{\mathrm{lg}} - \ell_{\mathrm{sh}})], \qquad (5.4)$$

where κ is the multiple reflection factor. The magnitudes of κ as functions of n and μ at $\Delta\ell = 20$ cm are as follows:

κ	μ = 0.01	μ = 0.001	μ = 0.0001
n = 1.45	1.0003	1.00005	1.000005
n = 2.0	1.004	1.0005	1.00005

Since the relative effects of multiple reflections for two comparative samples of a substance of relatively low refractive index are not that crucial, the linear attenuation coefficient μ of the substance may be effectively measured as for one test sample of differential length $\Delta\ell$. If the calibration signal N_0 of a photometer or spectrophotometer is measured for light transmitted via the short sample and the main signal N_1 is taken with the long sample, the linear attenuation coefficient μ is:

$$\mu = (\ln N_1 - \ln N_0)/(\Delta\ell). \qquad (5.5)$$

The way of increasing the sensitivity of measurements of low bulk losses by expanding the efficient optical length of light interaction with the object under study follows from Eq. (5.5). It may not be necessarily a material length of the substrate under study, but may be the distance of light's interaction.

If the factual differences of the products of two sample-surface reflectances are small enough, at not extensive bulk attenuation: $\mu(\ell_{\mathrm{lg}} - \ell_{sh}) \to 0$, the measurement comparison of two samples allows one to omit the negligibly low multiple-reflection factor in relation (2.41):

$$\tau_{\text{diff}} \underset{\rho_{1,\text{lg}}\rho_{2,\text{lg}} \approx \rho_{1,\text{sh}}\rho_{2,\text{sh}};\, \mu\Delta\ell \to 0}{\cong} \frac{\tau_{\text{lg}}}{\tau_{\text{sh}}} = \frac{(1-\rho_{1,\text{lg}})(1-\rho_{2,\text{lg}})}{(1-\rho_{1,\text{sh}})(1-\rho_{2,\text{sh}})} \exp[-\mu(\ell_{\text{lg}} - \ell_{\text{sh}})]. \quad (5.6)$$

Presuming all four surfaces to have low absorption and scattering at $\Delta\tau/\tau = \Delta\rho/(1-\rho) = \Delta\rho/\tau$, the relative change of differential transmittance for these samples is $\Delta\tau_{diff}/\tau_{diff} = 4\Delta\rho/\tau$. Thus, with measures ensuring the absence of systematic inequalities and for normally distributed random fluctuations of the optical properties of these surfaces, the error of bulk transmittance measurements for two samples of unequal length depends on the mean uncertainty of the sample-surface reflectance:

$$\Delta\tau_{diff}/\tau_{diff} = \sqrt{\sum_{i=1}^{4} (\Delta\tau_i/\tau_i)^2} = \frac{2\Delta\bar{\rho}}{\bar{\tau}}. \quad (5.7)$$

Equation (5.7) confirms that for all conditions being equal differential measurements of internal transmittance of two samples have identical surface-fluctuation errors as single-sample studies. Here $\bar{\rho}, \bar{\tau}$ are mean reflectance and transmittance values.

Figure 5.1 shows a schematic diagram of a single-beam precision spectrophotometer measuring exceptionally low optical losses in high-purity glass samples by the differential-length method [5.1]. Tungsten-halogen lamp 1 via triplet lens 2 irradiates the entrance slit of dual monochromator 3, resolving 20-nm spectral intervals and having low background scattering light within the 500–1000-nm spectral domain. Differential samples 4 and 4′ reaching up to 300 mm in length were positioned on one sliding table and sequentially placed in two equivalent light paths. In an intermediate position, both samples were removed from their respective beams to verify or control the stability of all parameters of such a single-detector registering system. To diminish spatial nonuniformity of photomultipliers 7 and 8, consequently used in the 500–800 and 800–1000-nm spectral domains, diffuser plate 5 was set in front of each detector inside cylindrical tube 6 having a highly specular reflecting inner surface. Tuning the distance from the plate to each detector allowed slight adjustments to be made reaching acceptably low attenuation and high spatial uniformity of the detection system. Alteration of the light-beam diameter from 2 to 6 mm, which corresponded to

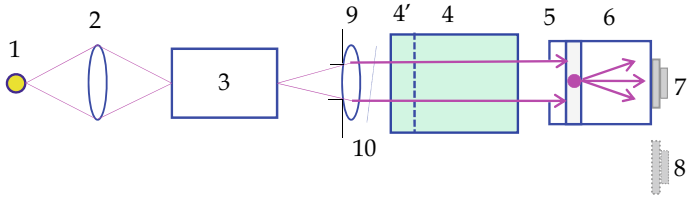

Fig. 5.1 Single-beam spectrophotometer for low-loss measurement

the change from the long to the short sample, produced tolerable enough ±0.1% nonuniformity for that system.

The long and the short sample selected for low-loss measurements were both cut out of a single rod of one low-loss glass specimen under study. Each end surface of the short and the long sample was polished simultaneously to better than λ/20 and to parallelism with deviation of less than 10 arc seconds. Preceding every measurement cycle, both samples were treated in a liquid detergent, then rinsed in deionized water, dried, and placed for nearly 1 h into an acetone evaporator. An added polarization ellipsometer was utilized to yield only samples which had all surface refractive indices equivalent within ±0.001 magnitude. To exclude systematic errors created by multiple reflections between each sample and collimator lens 9, neutral density filter 10 with transmittance $\tau = 0.2$ was implemented at a small angle to the system axis. That measure suppressed the transmission of the main beams by 5 times, but the reflected beams were attenuated by 25 times owing to their double propagation, and thus having the dual-pass transmittance $\tau^2_{\text{d.refl}} = 0.2^2 = 0.04$. The random error of each measurement did not exceed $\pm 2 \cdot 10^{-4}$. Owing to high measurement accuracy, it was proven for the first time that bulk losses in flint and fluoride crown glasses within the 750–1000-nm wavelength band could be as low as $(3–5) \cdot 10^{-4}$ cm^{-1} [5.1].

The dual-beam balancing configurations are widely used in specialty spectrophotometers as well owing to the benefits of lock-in amplification of channel signals therefore reducing low-frequency noise of the measurement system. Following the concept in Fig. 4.23, two other dual-channel orientations – with simultaneous and consecutive irradiation of samples – are shown in Fig. 5.2. In Fig. 5.2a two reflecting modulators M_d act out of phase, while detector D sequentially measures light transmitted from source S via monochromator M through long and short samples installed simultaneously in two diverse light paths. In Fig. 5.2b similar modulator M_d opens and closes the path for beams propagating, first, via the reference channel with optical compensator C and then via the measurement channel with the test samples installed sequentially. The second layout represents a typical design for the IR spectral region, having spectral selector M placed after optical elements that are irradiated to avoid direct thermal emission from every sample to the detector.

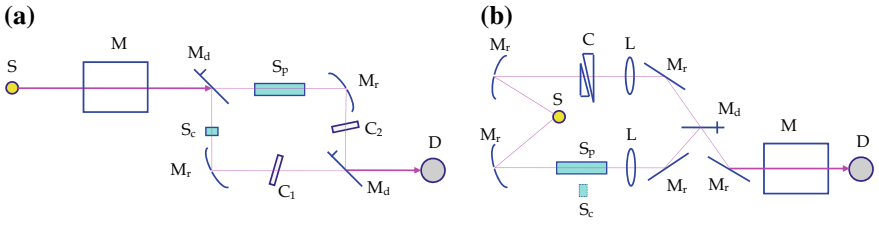

Fig. 5.2 Common schematics for conventional spectrophotometers: S - source; D - detector; M - monochromator; M_d - modulator; M_r - mirror; S_p - sample; S_c - comparison sample; C - compensator(s); L - lens

A common weakness of these optical structures consists in unequal path lengths of optical channels, measuring samples of uneven lengths, thus having distinct shapes of the beams reaching the detectors while not compensating for optical-path reduction or magnification due to either test sample. Two specific schematics of dual-beam and dual-channel spectrophotometers with lock-in amplifiers specifically designed for accurate low-loss measurement are shown in Fig. 5.3. In the dual-beam photometer in Fig. 5.3a, precise equalization of channel intensities due to imperfect beam splitting by the modulator and other asymmetries was compensated for in several steps: via selecting and tilting attenuator 7 and balancing the lock-in amplifier gain or tuning photomultiplier resistors. Keeping the stability of the tungsten-iodine filament lamp voltage and of the motor speed of the dual-blade chopper at $1 \cdot 10^{-4}$ and $2 \cdot 10^{-4}$ allowed $\pm 1 \cdot 10^{-5}$ short-term stability of the system balance to be achieved. Balancing measures, along with avoidance of multiple reflections and clean-sample preparation and control identically to the system in Fig. 5.1, including the spatial integrator and detector assembly, ensured transmittance measurement repeatability of $\pm 2 \cdot 10^{-4}$, mainly due to sample displacement and beam expansion from the long to the short sample. Since the setup was expanded to accept a sample up to 25 cm long, with 20-cm two-sample differential length, the overall system accuracy reached $1 \cdot 10^{-5}$, permitting internal losses down to $1 \cdot 10^{-4}$ cm^{-1} in 10-nm spectral intervals to be measured [5.2].

In the dual-channel arrangement in Fig. 5.3b, the photomultipliers were replaced with p-i-n photodiodes, increasing the signal-to-noise ratio to nearly 1: $5 \cdot 10^{-6}$ in the 500–1000-nm spectral domain. Alignment of the setup was made by a He–Ne laser also utilized to control sample stress-induced birefringence. In the initial version of the system, a pair of twin fused-silica plates 8 balanced the differences in the densities of two light beams without changing the optical paths, eventually allowing a sensitivity near 10 dB/km to be reached and approximately 100 dB/km

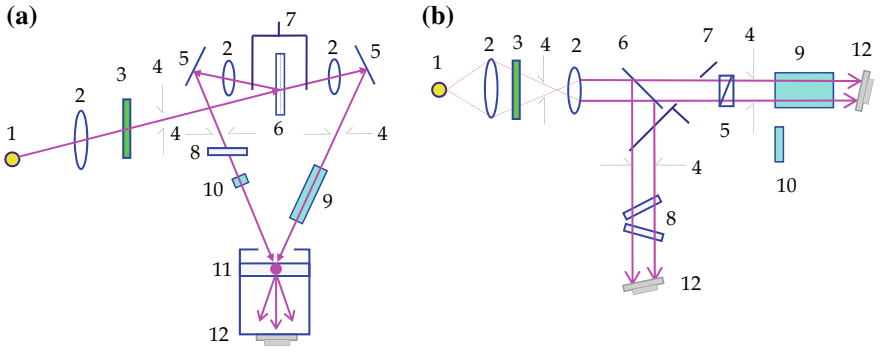

Fig. 5.3 Dual-beam (**a**) and dual-channel (**b**) spectral-selective photometers for low-loss measurements: 1 - source; 2 - objectives; 3 - spectral filters; 4 - apertures (baffles); 5 - mirror (**a**) and depolarizer (**b**); 6 - beam-splitter; 7 - reflecting-transmitting modulator; 8 - attenuator (**a**) and variable-attenuator based equalizer (**b**); 9 and 10 - long and short samples; 11 - spatial integrators; 12 - detectors

losses in F2 and F7 glasses to be registered in the 750–805-nm region [5.3]. The final version of the low-loss spectral photometer in Fig. 5.3b was assembled with a halogen lamp, two p-i-n diodes having ±0.1° temperature stabilization, and with depolarizer 6 diminishing birefringence effects. Tilting both detector surfaces was reducing stray light from the beams retroreflected within the system. The reaction of each detector changed by ±(0.02–0.05)% for expansion of the beam diameter from 3 to 4.5 cm. Minimized-signal fluctuations were nearly $1 \cdot 10^{-4}$, corresponding at $\Delta\ell = 25$ cm to approximately 2 dB/km optical-loss sensitivity. The lowest detected linear attenuation coefficient of the sample bulk difference in the 0.75–0.85-μm spectral domain was around 75 dB/km at nearly 50 dB/km of bulk scattering. Calorimetrically verified internal linear absorption coefficients in the samples studied at wavelength $\lambda = 1.06$ μm did not exceed ~4 dB/km (see Chap. 9 for details). The spectrophotometric measurements also detected changes of measured attenuation for repolished sample surfaces of ±2.7 dB/km at $\lambda = 0.9$ μm and ±(4.6–6.3) dB/km at $\lambda = 0.5$–0.75 μm. All linear attenuation coefficients were measured at a differential sample length of $\Delta\ell = 25$ cm [5.3].

One specific disadvantage of measurements of internal optical loss in transmission, such as unknown surface factors even when making comparison measurements, necessitates controlling the status of all sample surfaces by a supplemental technique. Therefore, there is a time delay between measurement and control procedures, limiting the attainable confidence of the low internal loss studies. Potentially, the random portion of systematic error created by undetermined surface conditions can be reduced in square-root proportion to the number of samples measured. To reduce that number and to save the material under test, only one sample may be made, for example, as an isosceles triangle prism [5.4]. Such a prism needs to be irradiated in a direction parallel to its base, while the prism itself is put in several positions along a bisectrix of its refraction angle φ (Fig. 5.4). Any round beam of light entering such a prism becomes elliptical; therefore the transmittance τ measured along the direction *x,* which coincides with the major semiaxis *a* of the ellipse, is:

$$\tau = (1-\rho)^2 \left\{ \frac{2}{\pi a^2} \int_{-a}^{+a} \sqrt{a^2 - x^2} \exp\left[-\frac{2}{n \tan(\varphi/2)} \right] \right\} \exp(-\mu \ell_x). \tag{5.8}$$

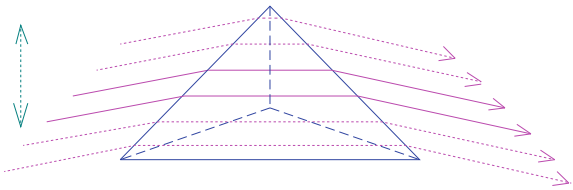

Fig. 5.4 Light transmissions through prismatic sample

Here ρ is the averaged transmitted-surface reflectance. Since the angles of incidence and refraction for the isosceles prism are equal, the factor in brackets in relation Eq. (5.8) does not change for parallel beam displacements. With that constancy and in the absence of dispersion in the prism's material, the ratio of two sequential prism transmittances should depend only on the difference in the path lengths.

There is no increase of sensitivity to low losses in the sample bulk in the prism transmission technique since any increase of the number of light passes via the sample surfaces reduces only the random portion of measurement error caused by accidental changes of a prism-surface reflectance caused by uncontrollable pollution or stains on prism surfaces. The technique does not distinguish variations of surface reflectances, but does average their variations. The sensitivity to the internal loss of the prism method even decreases near the prism's vertex where $\ell \to 0$. For the experimental verification of achievable measurement accuracy, one surface of a fused-silica prism was spattered with magnesia to give about 4% spatial nonuniformity [5.4]. The dependence of observed transmittances in the function of $\ell \to 0$ was linear only for light passes via remaining nonsprinkled surfaces. The transmittance values obtained via the shattered surface approximately fit a straight line only within $\pm(1\text{–}2) \cdot 10^{-3}$ margins. Nevertheless, the measured average magnitude for the bulk linear attenuation coefficients, evaluated via all three prism surfaces, $5.2 \cdot 10^{-4}$, $37.9 \cdot 10^{-4}$, and $20.5 \cdot 10^{-4}$, was only different from the equivalently detected average coefficient before the shattering by $1.2 \cdot 10^{-5}$. The repeatability limit for the measurement with multiple prism paths was near $\pm 6 \cdot 10^{-5} = \pm 26$ dB/km, being not better than that for all considered comparison spectrophotometric measurements of two: long and short, samples of one material under study.

One valuable alternative for elimination of a relatively large loss due to surface reflectance of a glass sample when measuring its internal attenuation coefficient is associated with incidence at the Brewster angle [5.23–5.28]. Ideally, a border of two dialectics irradiated by light polarized in the plane of incidence reflects no light at the Brewster angle φ_B Eq. (1.85). Equations (1.102) and (1.103) define the transmittance and reflectance of a plane-parallel plate of thickness ℓ irradiated at angle φ when all the plate's internal retroreflections can be collected by semispace large detectors. In the case of irradiation near the Brewster angle, one can expect very low residual reflectance and practically no multiple reflections. Hence, Eqs. (1.102) and (1.103) can be efficiently approximated as:

$$\rho_{B,2} = \rho_B\Big(1 + (1 - \rho_B)^2 \exp\big(-2\mu\ell/\cos\varphi_{B,r}\big)\Big); \tag{5.9}$$

$$\tau_{B,2} = (1 - \rho_B)^2 \exp\big(-\mu\ell/\cos\varphi_{B,r}\big), \tag{5.10}$$

where ρ_{B2} and τ_{B2} are the plate's reflectance and transmittance at Brewster angle φ_B, and $\varphi_{B,r} = 90° - \varphi_B$ is the angle of refraction. Owing to practical limitations – surface nonparallelism and nonflatness, as well as nonzero divergence of irradiation

– the whole-plate reflectivity at the Brewster angle is never zero, but it reaches the feasible minimum, allowing pseudo-Brewster angle techniques to be used for determination of refractive indices and extinction coefficients of absorbing materials Eqs. (1.86)–(1.90).

From a practical standpoint, the process of determining the minimum intensity of a beam of light while tuning the angle of incidence can be quite elaborate; it is more practical to make relative intensity measurements – looking for the effective minimum of the ratio of the sample surface reflectances and simultaneously measuring the ratio of same surface transmittances for two orthogonal states of polarization. From Eqs. (1.26), (1.82), (1.83), and (1.85):

$$\begin{aligned}\rho_{||/\perp} &= \frac{\rho_{||}}{\rho_{\perp}} = \left(\frac{\cos\varphi_1 \cdot \cos\varphi_2 - \sin\varphi_1 \cdot \sin\varphi_2}{\cos\varphi_1 \cdot \cos\varphi_2 + \sin\varphi_1 \cdot \sin\varphi_2}\right)^2 \\ &= \left(\frac{n_2 \cdot \cos\varphi_1 \cdot \cos\varphi_2 - n_1 \cdot \sin^2\varphi_1}{n_2 \cdot \cos\varphi_1 \cdot \cos\varphi_2 + n_1 \cdot \sin^2\varphi_1}\right)^2;\end{aligned} \tag{5.11}$$

$$\begin{aligned}\tau_{||/\perp} &= \frac{\tau_{||}}{\tau_{\perp}} = \cos^2(\varphi_1 - \varphi_2) = \cos^2[-(90^\circ - 2\varphi_1)] \\ &= \sin^2(2\varphi_1) = \left(\frac{2\tan\varphi_1}{1 + \tan^2\varphi_1}\right)^2 = \left(\frac{2n}{1+n^2}\right)^2.\end{aligned} \tag{5.12}$$

For a plain border of a conducting medium of complex dielectric constant: $\hat{\varepsilon} = (\mathrm{n} - \mathrm{i}\cdot\mathrm{k})^2$ (Eq. 1.86), irradiated in a vacuum at angle φ, the expressions for $\rho_{\|/\perp}$ and $\rho_{\perp}$ can be converted to [5.23]:

$$\rho_{||/\perp} = \rho_{||} \Big/ \rho_{\perp} = \Big((a - \sin\varphi\tan\varphi)^2 + b^2\Big) \Big/ \Big((a + \sin\varphi\tan\varphi)^2 + b^2\Big); \tag{5.13}$$

$$\rho_{\perp} = \Big((a - \cos\varphi)^2 + b^2\Big) \Big/ \Big((a + \cos\varphi)^2 + b^2\Big), \tag{5.14}$$

where $(\mathrm{a} - \mathrm{i}\cdot\mathrm{b}) = \sqrt{(\varepsilon - \sin^2\varphi)}$. Measuring ratios by Eqs. (5.12) and (5.13) at two angles of incidence near the pseudo-Brewster angle resolves unknown constants a and b, enabling calculation of $\rho_{\perp}$, n, and k.

Another technique for study of dielectric constants n and k can be realized by measuring only $\rho_{\|/\perp}$ and $\rho_{\|-\perp/\|+\perp}$ reflectance ratios [5.25, 5.26]. Figure 5.5 illustrates the method for direct measurements in reflected radiation of difference-to-sum ratios by detecting modulated AC and unmodulated DC intensity components of reflected light, rotating the state of polarization of the incident light beam and causing the light intensity modulation of the AC signal to be proportional to $\rho_{\|} - \rho_{\perp}$ and that of the DC signal be proportional to $\rho_{\|} + \rho_{\perp}$ [5.25]. An extra reference-intensity measurement of $\mathrm{I}_{\rho,0}$ is made for $\varphi = 180^\circ$ with no sample present, while with the sample it is $\mathrm{I}_{\rho,\varphi} = \mathrm{I}_{\mathrm{ac}}/\mathrm{I}_{\mathrm{dc}}$, yielding the $\rho_{||-\perp/||+\perp}$ ratio as [5.26]:

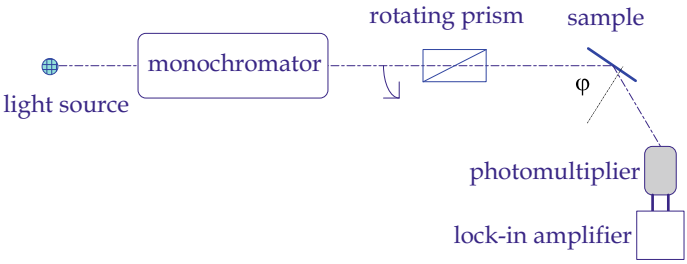

Fig. 5.5 Rotational measurement of reflected components

$$\rho_{\|-\perp/\|+\perp} = \left(I_{\rho,\varphi} - I_{\rho,0}\right) \Big/ \left(1 - \sqrt{I_{\rho,\varphi}/I_{\rho,0}}\right). \tag{5.15}$$

A similar concept may be applied to measuring internal absorption and scattering losses near the Brewster angle (Fig. 5.6) – the pseudo-Brewster angle itself is identified by detecting the position of the minimum and then a transmission-loss measurement is made at the angle determined [5.28]. The system zero-degree reading is established from the first position of sample's rotation for its reflection to coincide with an incident laser beam propagating via an added half-wave plate circulator preventing oscillations into the laser resonator. Then, the pseudo-Brewster angle's position is detected via the minimum of the reflectance in Eq. (5.9), prompting calculation of the approximate value of the refractive index n by Eq. (1.85). Finally, the internal sample-bulk loss μ is measured at that angle φ_B via the transmittance maximum per Eq. (5.10). The challenge is in detecting the precise position of the Brewster angle, especially for small refractive indices. At $n = 1.5$ (see Fig. 5.7), it requires nearly 1° from the Brewster angle to reach 0.01% of the surface reflectance. At the same time, measuring internal losses near the Brewster angle does not require one to account for the multiple reflections due to low surface reflectances (Fig. 5.8). With sufficient angular accuracy of rotation, the pseudo-Brewster angle transmission loss measurements are sensitive enough to resolve losses at 10^{-3}–10^{-4} cm^{-1} level and lower: for example, $1.37 \cdot 10^{-3}$ reflectivity, corresponding to refractive index $n = 1.444$ versus expected value of 1.449, and $7.33 \cdot 10^{-3}$ cm^{-1} internal loss, equivalent to 0.032 dB/cm, were experimentally confirmed [5.28].

Fig. 5.6 Brewster angle transmission-loss study

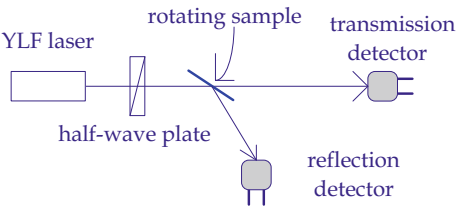

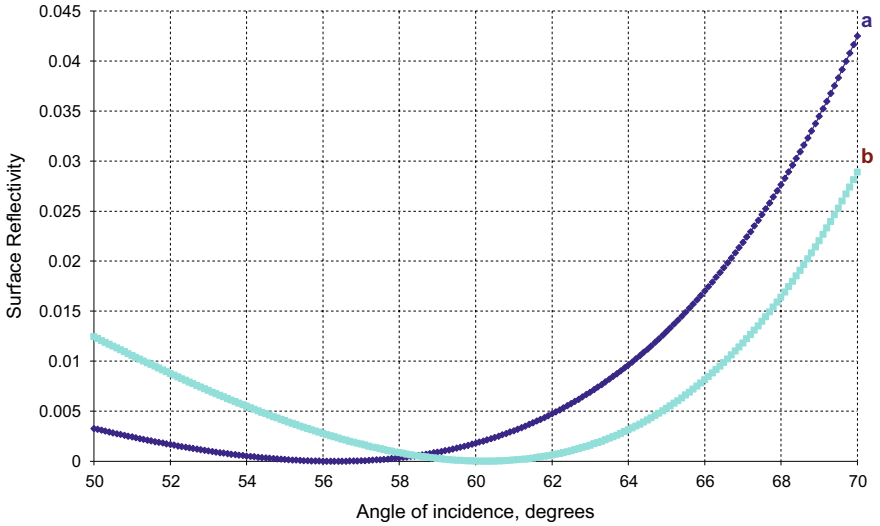

Fig. 5.7 Single-surface reflectivity at Brewster angle for relative refractive index 1.5 (**a**) and 1.75 (**b**)

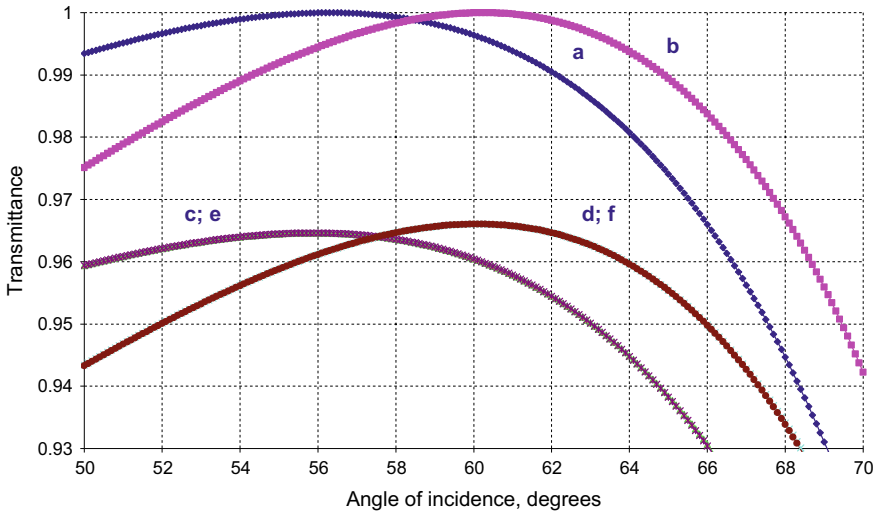

Fig. 5.8 Transmittance of 2-mm plate near Brewster angle: a, b - ideal plate; c–f - bulk attenuation coefficient 0.01; a, c, e - refractive index: 1.5; b, d, f - 1.75; c, d - multiple reflections; e, f - single pass

5.2 Specular Reflectance

Since one obvious distinction of reflectance measurements compared with transmittance ones consists in opposite irradiation and observation directions, most difficulties in reflection studies arise at normal incidence of light onto specularly reflecting objects for a reflected beam directed back into a light source. To circumvent the complexities, the angle of incidence is often maintained close to the normal, nevertheless treating the respective result as being obtained at normal irradiation. At a small angle of incidence φ, for which the reflectivity does not deviate beyond expectations, such a method can be acceptable. However, the limits of the normal-incidence assumption should not be based on an unrelated-to-loss study supposition: $\sin^2\varphi \to \tan^2\varphi \to 0$, if angle φ tends to zero.

Let us consider the change of specular reflectance of a dielectric at small angle φ of incidence caused by discrepancies of the state of polarization for any incident beam due to roughness of a single test surface. The relative differences of reflectance ρ only due to the state of polarization are:

$$\begin{aligned}\delta_\perp &= \frac{\rho_\perp}{\rho_0} = \frac{\tan^2[\varphi - \arcsin(\sin\varphi/n)]}{\tan^2[\varphi + \arcsin(\sin\varphi/n)]} \cdot \left(\frac{n+1}{n-1}\right)^2; \\ \delta_{||} &= \frac{\rho_{||}}{\rho_0} = \frac{\sin^2[\varphi - \arcsin(\sin\varphi/n)]}{\sin^2[\varphi + \arcsin(\sin\varphi/n)]} \cdot \left(\frac{n+1}{n-1}\right)^2.\end{aligned} \tag{5.16}$$

The reflectance ratio δ via incidence angle φ due to surface roughness R_a Eqs. ([II.8], [II.9]) is:

$$\delta = \frac{\rho_{sm,\varphi}}{\rho_{sm,o}} \exp\left[\left(\frac{4\pi R_a}{\lambda}\right)^2 - \left(\frac{4\pi R_a \cos\varphi}{\lambda}\right)^2\right]. \tag{5.17a}$$

Here $\rho_{sm,\varphi}$ and $\rho_{sm,0}$ are the reflectances of an ideally smooth surface at angle φ and at normal incidence. If surface roughness is comparable to radiation wavelengths, Eq. (5.17a) must be modified to include the root mean square slope m of the surface profile and the deviation $\Delta\varphi$ of surface irradiation angle φ [II.3, II.4]:

$$\delta = \frac{\rho_{sm,\varphi}}{\rho_{sm,o}} \left\{ \exp\left[\left(\frac{4\pi R_a}{\lambda}\right)^2 - \left(\frac{4\pi R_a \cos\varphi}{\lambda}\right)^2\right] + \frac{2^5\pi^4}{m^2}\frac{R_a^4}{\lambda^4}\cos^3\varphi \cdot \Delta\varphi \right\}. \tag{5.17b}$$

Figure 5.9 illustrates changes of reflectance values at normal and close-to-normal incidence. In view of actual changes of reflectance, but not transmittance, the evident distinction within parts per thousand takes place even for angle variations within a few degrees from normal incidence. Surface roughness of λ/100 or lower levels does not create much of a difference for small angles, though larger surface imperfections, as λ/50 roughness in Fig. 5.9, produce enough scattering to increase the total reflectance by 0.74% at 20° incidence. Therefore, the

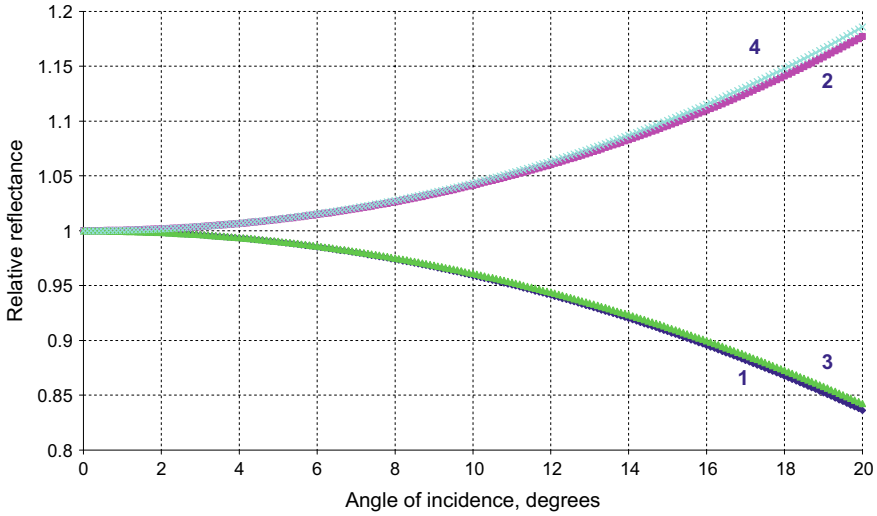

Fig. 5.9 Relative reflectance changes versus angle of incidence at parallel (1,3) and perpendicular state (2,4) or rough (3,4) surfaces: n = 1.5; roughness-wavelength/50

actual surface properties and margins of desired accuracy both limit deviations from normal incidence in reflectance studies.

Conventional specular reflectance measurements at near-normal incidence are in general performed in reference to a fairly well known or presumed to be known standard. The schematic of the characteristic reflectance-measurement attachment for a two-beam spectrophotometer is depicted in Fig. 5.10 [5.5]. For any single-beam spectrophotometer, one extra measurement step is required versus the two-beam settings: one for the standard and another for the test sample. A common three-point pin holder and an alignment system (not shown) can be used to perform measurements on spherical mirrors with identical curvatures.

The concept of direct reflectance measurements at normal incidence via a semitransparent beam splitter was analyzed in Chap. 2 (see Figs. 2.13 and 2.15).

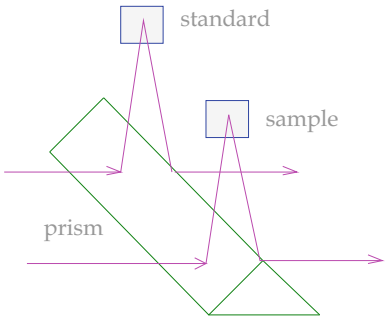

Fig. 5.10 Near-normal reflectance study

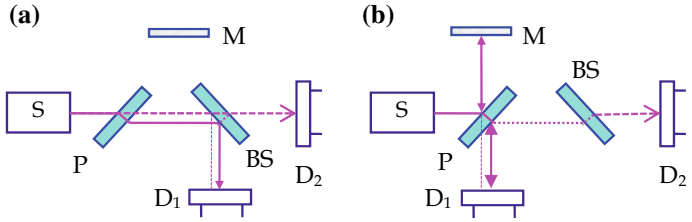

Fig. 5.11 Compensation measurements of specular reflectance: S - source, BS - beam splitter, M - test mirror, P - plate, D - detector

Figure 5.11 illustrates a system for similar laser source-based reflectance studies with the auxiliary plate P compensating for the displacement of the beam path and for the transmittance of the splitter as well [5.6]. Two detectors D_1 and D_2 creating reflection and transmission arms are used to evaluate multiple reflections occurring between a test mirror and the laser resonator at normal incidence. For two readings in Fig. 5.11a no multiple reflections occur between the output coupler of the laser source and both detectors if the detectors are placed at slight angles:

$$N_{1,a} = \kappa I_0 \tau_p \rho_{sp}; \tag{5.18a}$$

$$N_{2,a} = \kappa I_0 \tau_p \tau_{sp}, \tag{5.18b}$$

where τ_{sp} and ρ_{sp} are the transmittance and reflectance of the beam splitter and τ_p is the transmittance of compensating plate P. In Fig. 5.11b detector D_1 is irradiated via mirror M with plate P taken out:

$$N_{1,b} = \kappa I_0 \tau_{sp} \rho \rho_{sp} \frac{1}{1 - \rho \rho_{sp}^2 \rho_s}; \tag{5.19a}$$

$$N_{2,b} = \kappa I_0 \tau_{sp} \tau_p \frac{1}{1 - \rho \rho_{sp}^2 \rho_s}, \tag{5.19b}$$

where ρ is the reflectance of test mirror M and ρ_s is the laser reflectance, whose output coupler is resonant to mirror M, set for normal incidence of light. If transmittances τ_{sp} and τ_p cannot be distinguished by the measurement system, then the ratios *a/b* in Eqs. (5.18a, b) and (5.19a, b) give:

$$N_{1,a}/N_{2,a} = \rho_{sp}/\tau_{sp}; \; N_{1,b}/N_{2,b} = \rho \rho_{sp}/\tau_p; \tag{5.20}$$

$$\rho \underset{\tau_{sp} \equiv \tau_p}{=} \frac{N_{2,a} N_{1,b}}{N_{2,b} N_{1,a}}. \tag{5.21}$$

The availability of two detectors also simplifies the calibration process of the measurement system. Differences in the reflectances and transmittances of two plates in the beam splitter's position can be evaluated by detector D_2 in its main position and when it substitutes mirror M. The sensitivities of the two detectors may be verified by swapping beam splitter BS in the 90°-inverse position to the position in Fig. 5.11a and checking the detectors' responses in radiation reflected from the beam splitter with detector D_2 in place of mirror M.

Another system for measurements at normal incidence using the splitter-combiner concept analyzed in Chap. 2 (see Fig. 2.14), is shown in Fig. 5.12. The system utilizes the integrating sphere to overcome likely nonuniformity of a single detector to be irradiated from opposite directions. A polarizer PL is used for system alignment with samples placed on a rotary table (dotted line). First, thick fused-silica flats P_1 and P_2 are aligned at the same angles to the direction of beam propagation by a He–Ne laser and the ratio $R = \rho_{\perp}/\rho_{||}$ of sample reflectance values for S and P states of polarization are measured via rotation of polarizer PL, verifying that alignment:

$$R = \frac{\rho_{\perp,S}(\Delta\varphi)}{\rho_{||,S}(\Delta\varphi)} \frac{\rho_{\perp,P_1}(\varphi_1)\rho_{\perp,P_2}(\varphi_2)}{\rho_{||,P_2}(\varphi_2)\rho_{||,P_1}(\varphi_1)}, \tag{5.22}$$

where ρ_i is the reflectance of each respective element and $\Delta\varphi$ is the angle of likely deviation from normal incidence onto the sample. For small misalignment errors (see the plots in Fig. 5.9), the sample's reflectance should not change, and equality $R \equiv 1.0$ for normal incidence gives the exact positions of the plates. Measurements were performed at near ±0.2% accuracy for specular reflectance values ranging between 0.03 and 1.0, and the repeatability of the results obtained was maintained within ±0.001 [5.7].

As is seen from the methods reviewed, the ability to perform a precise measurement of specular reflectance at normal incidence of light on a test object requires a lot of care to be taken for alignment and positioning errors and reduction of multiple reflections, and use of multiple extra elements, whose properties must

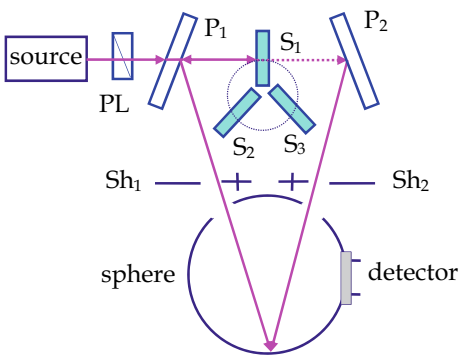

Fig. 5.12 Reflectometer for normal incidence of light

be known. For all splitter-based reflectance measurements, the intensities of the reflected beams are reduced proportionally to the product of the splitter's reflectance and transmittance. If an increase of sensitivity at normal incidence needs to be achieved, even more complicated structures with multiple reflections must be used (see further chapters). Let us thus take another look at measurements of specular reflectance at close-to-normal incidence.

Similarly to transmission studies of transparent and not excessively dense objects, for low-loss measurements in reflected light the sensitivity to local interactions of light with a smooth surface of a mirror can be increased by multiple interactions with that mirror surface, providing all retroreflected light beams are collected onto a single detector. Likewise, the increase $\Delta\ell$ of the effective optical path length of the light beam via a transmitting object can be represented as: $\Delta\ell = \ell_2/\ell_1 = m \cdot \ell$, where m is the multiplicity factor of the effective length, and m-interactive reflection action can therefore be given as:

$$N_m/N_0 = \rho^m \text{ or } \rho = \sqrt[m]{N_m/N_0}, \tag{5.23}$$

where N_0 and N_m are the signals of one detector reacting to an incident beam and to a beam undergoing all m interactions. The potential inaccuracy of the multiple-interactive measurement is:

$$\frac{\Delta\rho}{\rho} = \pm\frac{1}{m}\left(\frac{\Delta N_0}{N_0} + \frac{\Delta N_m}{N_m}\right). \tag{5.24}$$

Here the relative error $\Delta\rho/\rho$ of the multipass reflectance study is inversely proportional to the number of reflections, bouncing measured light from a test object. This would not hold true if the reflectance is so low that interactions make any final retroreflected components indistinguishable to the detector.

A classic procedure [0.6] for surface-averaged measurement of absolute specular reflectance at constant angle Θ of incidence is seen in Fig. 5.13a [4.32] (see also Figs. 2.11 and 4.29). During the initial reference cycle of 100%-line setting without a test object, swapping mirror SW is on top of the system. When test mirror M is inserted, swapping mirror SW is transposed down (dotted lines). All light interactions are kept at the parallel transitions of the test mirror and at constant angle Θ of incidence, but the procedure has not only the twofold increase of measurement sensitivity to the reflectance changes, but also the matching decrease of spatial resolution, since initiated beam interactions are dispersed over a larger area of the test mirror. Thus, the reflectance is measured as a spatially averaged factor. The additional disadvantage is associated with high sensitivity of the attachment's alignment to incorrect positioning of the mirror studied and the swapping mirror. Placement of the detector inside the integrating sphere lessens its sensitivity to any changes of the directions of reflected beams though significantly decreasing irradiance and thus the sensitivity of the detector.

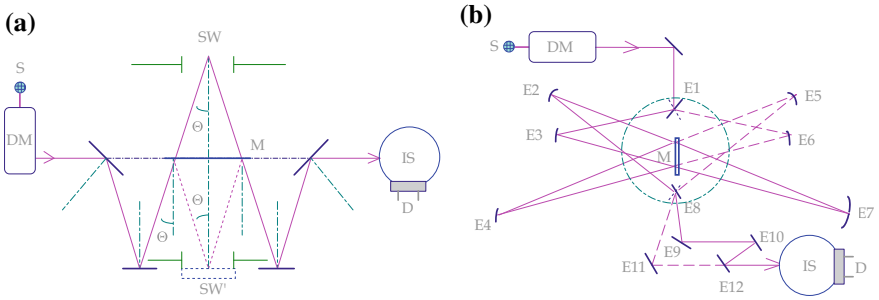

Fig. 5.13 Double reflection attachments: S - source; DM - dual monochromator; M - mirror under test; D - detector; SW, E - mirrors

The expansion of that established methodology was seen in Fig. 4.20a for flat test mirror M placed near the center of curvature of a spherical swaying-mirror system. Such a position balances the intensity variations of the output beam due to implied misalignments, although it does not maintain a strictly invariable angle of incidence onto the mirror under study [4.32]. Figure 5.13b illustrates two actual optical paths for the improving-technique reflectometer at approximately 5° average angle of incidence, accomplished by rotating the sample holder 180° with mirrors E_1–E_8 (see dotted cycle). Absolute reflectance readings are obtained for fourfold reflectance of sample M. First, the 100% line is measured via mirror E_7. With sample mirror M in the first position, light goes via mirrors E_2–E_4. The second mirror measurement is made via swayable mirrors E_1 and E_8 and mirrors E_4 and E_5–E_7. The equivalence of two reflectance values for mirrors E_4 and E_7 must be maintained. Other variables may be detected during repeated 100% readings. The random error of the entire measurement procedure was near ±0.02%.

Symmetrical dual-reflection measurements can be achieved by unwavering propagation of radiation via the swaying-mirror measurement system with and without a wide mirror under study (Fig. 5.14) [5.8]. Light emitted by source S and reflected from flat mirror 1 emerges via an exit slit of dual monochromator M into the double-reflection cavity. Spherical mirror 2 sends the monochromator's exit-slit image to flat mirrors 3 and 10 (Fig. 5.14a). Mirror 8 forms an irradiation zone of $6 \cdot 10\text{-mm}^2$ cross section on test object O. The angle of incidence φ for the axial beam reaches 2° at aperture ratio 1:1.6. Spherical mirror 9 returns radiation reflected by object O back to the object. After participating in sequential reflections by mirrors 7, 11, and 12, light reaches detector D for signal N_1. To measure reference signal N_2, the object's carrier is elevated and light is reflected by mirror 6, similar to mirror 9, having no interaction with mirror 9, and further propagates in the same way, as being reflected from the object. The ratio of the measurement to the reference signals becomes:

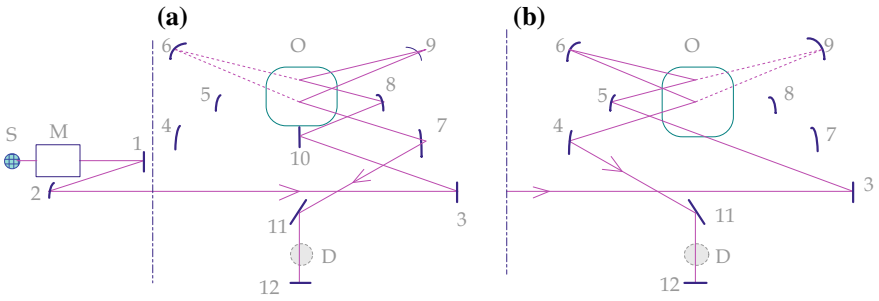

Fig. 5.14 Reflectometer for absolute double-reflection measurements at quisi-normal light incidence

$$N_1/N_2 = \rho^2\rho_6/\rho_9 \underset{\rho_6=\rho_9}{=} \rho^2, \tag{5.25}$$

where ρ, ρ_6, and ρ_9 are the reflectances of the test object and mirrors 6 and 9, which in typical arrangements are presumed to be equal.

Instead of the presumption that the reflectances of mirrors 6 and 9 are equal, the design allows one to reorient the system by 180°, having intermediate mirror 10 no longer in the system (Fig. 5.14b). Then, incident light reaches object O after reflection from mirror 5, and returns via mirrors 6, 5, and 4 onto swayable mirror 11, and finally to the detector. Reference mirror 9 is utilized when the second reference signal is measured with no objects inside the dual-reflection cavity, for the ratio of two measured signals to become: $N_3/N_4 = \rho^2\rho_9/\rho_6$. As a result, four measured signals provide fourfold reflectance of studying object without added assumptions:

$$(N_1/N_2)\cdot(N_3/N_4) = \rho^4. \tag{5.26}$$

As a consequence of the fact that this determination of the fourfold magnitude of specular reflectance requires four measurements, the sensitivity of such a low-loss measurement is the same as for the double-reflection study when measuring only two signals. Nevertheless, that procedure represents a truly absolute measurement of a spatially averaged reflectance since no equality assumption for auxiliary mirror reflectances needs to be made. Since the optical system is only made of mirrors, measurements are performed without any chromatic aberration, and the desired spectral domain of the study is solely identified by the sources and detectors applied.

Earlier analyzed methods presumed some fixed angle of incidence onto the mirror under study. Figure 5.15 depicts an absolute specular reflectometer for measuring specular reflectance from near normal to 90° incidence. Tracking mirrors 1 and 2 (cf. Fig. 2.12), as well as an integrating sphere, having an internal detector, make two nearly even light paths. Without a sample, the tracking mirror–integrating sphere assembly is turned to accept incident light via the sample path in position 2

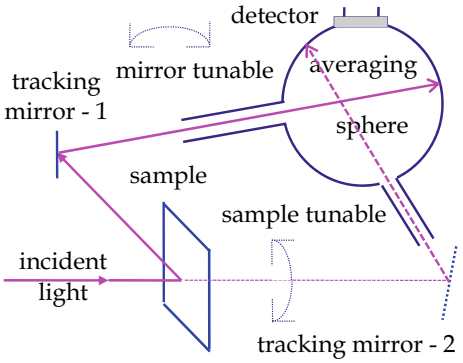

Fig. 5.15 Absolute specular reflectometer

and in position 1 for the specular sample installed [5.9]. In experiments the sphere was coated with a fluorocarbon powder having the highest reflectivity for 250–2500 nm. Uncertainties for the specular reflectance measurements were estimated to be near ±0.2% of measured values.

Figure 5.16 illustrates the absolute reflectometer realizing variable-angle measurements of the twofold reflectance via normal incidence onto an auxiliary mirror (similarly to that in Fig. 2.13). Auxiliary mirror M_1 here is made spherical to compensate for the light beam divergence Mirror M_2 serves for the reflectance reference via beam splitter BS, referring intensity deviations of the monochromator or white-light source to detector D by opening or closing mirror M_1 via chopper Ch. When a polarization-dependent loss of sample M_1 was detected via polarizer P at angles of incidence from 6° to 70°, the measurement reproducibility was within ±0.2% [5.10].

Considering one more time the reflectance measurement at normal incidence when sending and receiving radiation by one element, a somewhat unexpected transceiver-type setting could be invoked in the terahertz time-domain spectrometry [5.30]. A femtosecond pump and probe pulse using picosecond time separation enables partition of incident and reflected light beams to be sent and received by a single emitter–transmitter element as a birefringent organic 4-N,N-dimethylamino-4-N-methylstilbazolium tosylate (DAST) crystal (Fig. 5.17). The beam from an

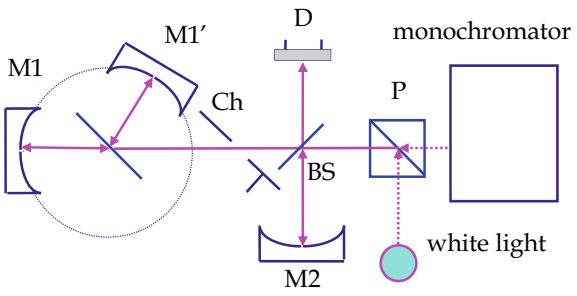

Fig. 5.16 Variable-angle dual-path reflectometer

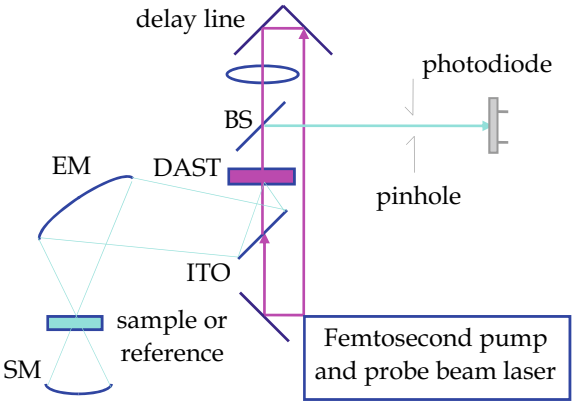

Fig. 5.17 Time-domain reflection-transmission photometer

erbium-doped fiber laser emitting 70-fs pulses at 100 MHz in the 1560-nm domain is split into pump and probe beams, and excites a DAST crystal, generating terahertz radiation. The terahertz-induced thermal lensing (see Chap. 9) in the same crystal, triggered by reflection from a sample or a reference mirror, or reflected and transmitted twice by the sample and reflected from spherical mirror SM, causes deflection of the delayed probe beam and is selected by the pinhole to be detected by the photodiode. An indium tin oxide splitter–combiner ITO transmits and reflects pump and probe light, but reflects terahertz radiation. A germanium spectral filter rejects further propagation of pump light to off-axis elliptical mirror EM, allowing simultaneous measurement of sample terahertz reflection and dual-pass transmission and obtaining the absorption-plus-scattering loss or the refractive index and absorption coefficient [5.30].

Summarizing the reviewed methods of straightforward reflectance measurements, let us make an extra note on the effects of multiple reflections for transparent specularly reflecting samples. By analogy with transmission studies Eq. (5.4), specular reflectance studies can be made by varying the number of light interactions – in this case reflections – with the sample, but multiple reflections adversely affect the measurement results if are not fully accounted for. For example, owing to aging of sample surfaces, a series of measurements of reflectance ρ and transmittance τ of a given sample may identify the presence of absorption or scattering layers, detecting difference $\Delta = 1 - (\tau + \rho)$. Transparent optical coatings can serve as practical standards of direct transmittance and specular reflectance for many measurement tasks because of very low scattering and absorption, negligible thickness, and the convenience of applications in both transmitted and reflected light [5.11]. If the reflectance and the transmittance of any internally transparent sample with different first and second surfaces are measured, each sample-surface transmittance and reflectance needs to be resolved via complete Eqs. (1.102) and (1.103). Considering the transmittance τ and reflectance ρ of the first and of the second surface: τ_f, ρ_f and τ_s, ρ_s, the total transmittance and the total reflectance of an unequal-surface sample become:

$$\begin{aligned}
\tau_{\Sigma,f-s} &\underset{\mu=0}{=} \frac{\tau_f\tau_s}{1-\rho_f'\rho_s'} \underset{\rho'=\rho}{=} \frac{\tau_f\tau_s}{1-\rho_f\rho_s};\\
\rho_{\Sigma,f-s} &\underset{\mu=0}{=} \rho_f + \frac{\tau_f\rho_s\tau_f}{1-\rho_f'\rho_s'} \underset{\rho'=\rho}{=} \rho_f + \frac{\tau_f^2\rho_s}{1-\rho_f\rho_s};\\
\tau_{\Sigma,s-f} &\underset{\mu=0,\rho'=\rho}{=} \frac{\tau_s\tau_f}{1-\rho_s\rho_f};\ \rho_{\Sigma,s-f} \underset{\mu=0,\rho'=\rho}{=} \rho_s + \frac{\tau_s^2\rho_f}{1-\rho_s\rho_f},
\end{aligned} \tag{5.27}$$

where the primes indicate reflections from inside the sample. For nonabsorbing surfaces: $\rho_i' = \rho_i$, thus, unequal reflectances in inverted positions give an indication of the presence of absorption layers on one or both surfaces. Expanding measurements via Eq. (5.27), alongside with Eqs. (1.106) and (1.107) for ideally polished and not coated substrates of identical surface reflectances ρ_0: $\tau_{\Sigma,0} = (1 - \rho_0)/(1 + \rho_0)$, $\rho_{\Sigma,0} = 2\rho_0/(1 + \rho_0)$, may allow to identify all unknown factors:

$$\begin{aligned}
\tau_{rel,f-0} &= \frac{\tau_{\Sigma,f-s}}{\tau_0} = \frac{\tau_f\tau_s(1+\rho_0)}{(1-\rho_f\rho_s)(1-\rho_0)};\\
\rho_{rel,f-0} &= \frac{\rho_{\Sigma,f-s}}{\rho_0} = \left(\rho_f + \frac{\tau_f^2\rho_s}{1-\rho_f\rho_s}\right)\frac{(1+\rho_0)}{2\rho_0};\\
\tau_{rel,s-0} &= \frac{\tau_{\Sigma,s-f}}{\tau_0} = \frac{\tau_s\tau_f(1+\rho_0)}{(1-\rho_s\rho_f)(1-\rho_0)};\\
\rho_{rel,s-0} &= \frac{\rho_{\Sigma,f-s}}{\rho_0} = \left(\rho_s + \frac{\tau_s^2\rho_f}{1-\rho_s\rho_f}\right)\frac{(1+\rho_0)}{2\rho_0},
\end{aligned} \tag{5.28}$$

by assuming no absorption or scattering in the sample surfaces and its bulk substrate, therefore permitting the substitutions: $\tau_f = 1 - \rho_f$, $\tau_s = 1 - \rho_s$. When one of the plate surfaces is uncoated, for example $\rho_f = \rho_0$, Eqs. (5.27) and (5.28) are easier to resolve via only two variables if $\tau_s = 1 - \rho_s$:

$$\tau_{\Sigma,0-s} \underset{\mu=0}{=} \frac{\tau_0\tau_s}{1-\rho_0\rho_s} \underset{\tau_0=1-\rho_0}{=} \frac{(1-\rho_s)(1-\rho_0)}{1-\rho_0\rho_s}, \tag{5.29a}$$

$$\rho_{\Sigma,0-s} \underset{\mu=0}{=} \rho_0 + \frac{\tau_0^2\rho_s}{1-\rho_0\rho_s} \underset{\tau_0=1-\rho_0}{=} \rho_0 + \frac{(1-\rho_0)^2\rho_s}{1-\rho_0\rho_s}, \tag{5.29b}$$

$$\tau_{rel,0-s-0} = \frac{\tau_{\Sigma,0-s}}{\tau_{\Sigma,0}} \underset{\tau_0=1-\rho_0}{=} \frac{(1-\rho_s)(1+\rho_0)}{(1-\rho_0\rho_s)}, \tag{5.29c}$$

$$\rho_{rel,0-s-0} = \frac{\rho_{\Sigma,0-s}}{\rho_{\Sigma,0}} \underset{\tau_0=1-\rho_0}{=} \left(1 + \frac{(1-\rho_0)^2}{1-\rho_0\rho_s}\frac{\rho_s}{\rho_0}\right)\frac{(1+\rho_0)}{2}. \tag{5.29d}$$

If no unexpected absorption and/or scattering layers are present on either surface of the sample, the law of conservation of energy allows to simplify the measurements by invoking the balance: $\tau_{\Sigma,i} + \rho_{\Sigma,i} = 1$.

Attempts could be also made to identify a reflectance and transmittance of a sample via certain known properties, such as using the spectral refractive index of a transparent medium [5.31] or modeling [5.32], if these means seem trustworthy for a task. When relying on refractive index n versus angle of incidence φ, Fresnel formulae for a given state of radiation polarization (1.34, 1.35, 1.82, 1.83) become:

$$\rho_{\parallel} = \left| \frac{n^2 \cos\varphi - \sqrt{n^2 - \sin^2\varphi}}{n^2 \cos\varphi + \sqrt{n^2 - \sin^2\varphi}} \right|^2 ; \; \rho_{\perp} = \left| \frac{\cos\varphi - \sqrt{n^2 - \sin^2\varphi}}{\cos\varphi + \sqrt{n^2 - \sin^2\varphi}} \right|^2 , \quad (5.30, \text{a, b})$$

$$\tau_{\parallel} = \left| \frac{2n \cos\varphi}{n^2 \cos\varphi + \sqrt{n^2 - \sin^2\varphi}} \right|^2 ; \; \tau_{\perp} = \left| \frac{2\cos\varphi}{\cos\varphi + \sqrt{n^2 - \sin^2\varphi}} \right|^2 . \quad (5.30, \text{c, d})$$

5.3 Scattering Factor

If a specific measurement task requires recognition of the optical loss only in transmitted or in reflected radiation, the total amount of absorption-plus-scattering loss for any object being studied can be evaluated as a single factor, since either event leads to light being lost. Considering this specificity, the distinction from 1.0 for the sum of direct transmittance τ_d and specular reflectance ρ_r represents the total loss on absorption α, diffuse transmission τ_d, and diffuse reflection ρ_d, as:

$$a + \tau_d + \rho_d = a + \sigma \equiv \eta = 1 - (\tau_r + \rho_r), \quad (5.31)$$

where σ and η are the respective factors for 360° scattering and for total attenuation. If the loss is identified via transmission and reflection, the relative sensitivity $\Delta\eta/\eta$ to attenuation factor η is:

$$\frac{\Delta\eta}{\eta} = \frac{\Delta\tau_r + \Delta\rho_r}{1 - (\tau_r + \rho_r)} = \frac{\Delta\tau_r + \Delta\rho_r}{\eta} . \quad (5.32)$$

Inaccuracy of such an indirect determination summarizes the errors of transmittance and reflectance measurements related to the low loss to be detected. In particular, for $\tau_r + \rho_r = 0.99$ and $\Delta\tau_d = \Delta\rho_r = \pm 0.5\%$, as well as for $\tau_r + \rho_r = 0.999$ and $\Delta\tau_r = \Delta\rho_r = \pm 0.05\%$, the uncertainty becomes $\Delta\eta/\eta = \pm 100\%$. Therefore, the approach of measuring factors of total scattering and absorption via transmittance and reflectance should be fairly informative. The loss estimation can be used to sense measurement correctness for the sum of specular reflectance and direct transmittance of any transparent object.

A method for scattering-factor measurement based on detecting the amount of radiation diverging from the directions of direct transmittance and specular reflectance requires detailed identification of such spatial variables as radiation direction φ or solid angle Ω of observation, making the scattering factor σ:

$$\sigma(\varphi,\Omega)=\int_{\Omega} I_{\varphi}d\Omega/I_0=\tau\int_{\Omega} I_{\varphi}d\Omega/I_{\tau}=\rho\int_{\Omega} I_{\varphi}d\Omega/I_{\rho}. \tag{5.33}$$

Light components scattered within directions of the direct transmission and specular reflection can be evaluated by scanning the solid angle of observation around every direction in sequence:

$$\begin{aligned} &I_1=I_{\rho(\tau)}+I_{\eta 1};I_2=I_{\rho(\tau)}+I_{\eta 2};\\ &\Delta I_{\sigma}=I_1-I_2=\int_{\Delta\Omega} I_{\varphi}d\Omega;\ \eta_{\rho(\tau)}=\Delta I_{\eta}\Omega_{\rho(\tau)}/\Delta\Omega. \end{aligned} \tag{5.34}$$

Any scattering factor measurement can also be considered as one realization of a specified reflection or indirect transmission at some particular angle φ_i of observation not coinciding with the direction of either direct transmission or specular reflection (see Table 2.1). If there is a need to know the detailed distribution of the measured scattering factor within the entire 360° or 4π space, the scattering analysis can be performed with a goniophotometer scanning the radiation-scattering spectral domain over a given space. The essential distinction of such a measurement is defined by the extremely small angular density for uniformly scattered light. To have high spatial resolution, the solid angle Ω of reception needs to be much smaller than the spatial domain of scattering: accordingly, the spatial component of scattering to be detected becomes a diminutive part of the total amount of scattered light.

Typically, goniophotometers are intended to measure the relative distribution of the scattering factor of an object to be studied with respect to some absolute standard, presumed to perform as a perfect diffuser (see Chap. 1). However, if the linear dynamic range of envisioned reception for scattered light is adequately extended, the scattering factor can be determined as the light flux reflected or transmitted into a direction φ and a solid angle Ω_m related to the flux which directly propagates from a source within solid angle Ω_0 and is incident on the scattering object. Such a procedure establishes the process for absolute measurement of the scattering factor when for both intensity measurements the detector utilized is steadily oriented to the normal to the receiving beam and when for a small deviation from that normal incidence its sensitivity does not change.

In the setup in Fig. 5.18, integrating sphere 5 of internal detector 6 integrates flux $d\Phi$ of radiation over solid angle $d\Omega$ scattered by object 2 to direction φ in 2π space [0.12]. Opaque baffle 7 screens detector 6 from direct irradiation by nonuniformly scattered light. Objective 3 and iris aperture 4 identify a fairly small

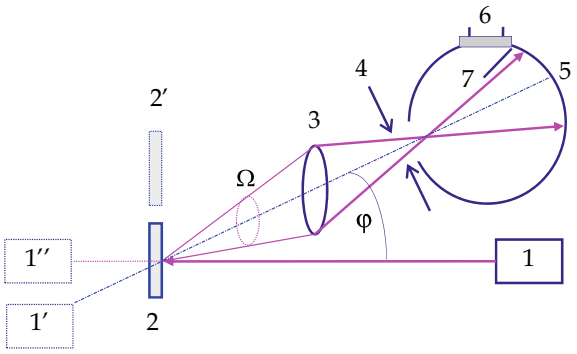

Fig. 5.18 Scattering-factor measurements at given angle φ

spot of an emitting zone of object 2, which is entirely irradiated by source 1. The indicatrixes of radiance and of radiant intensity can also be determined, respectively, at the smallest and largest openings of iris 4. Standard 2′, presumed to serve as the perfect diffuser, can substitute object 2 for verification of its scattering indicatrix. Absolute reflectance measurements may be realized by taking object 2 out to position 2′ and moving source 1 to position 1′. If the dynamic range of the system is not sufficient to measure the source intensity directly, an attenuator of transmittance $\tau_a(\lambda)$ can be placed instead of the sample being normal to the beam axis. Rather than taking scattering measurements in reflected light, one can reset the system for transmission studies by moving the source into position 1″.

If the scattering factor needs to be measured at a fixed observation angle, the goniometer is not necessarily required. Figure 5.19 illustrates a system for measurements of the backscattering factor of a highly reflecting mirror of a ring laser in which the appearance of any backscattered light is strictly prohibited. This technique compares the mirror backscattering factor σ with the regular reflectance ρ_r of another mirror at normal incidence [5.12]. If the scattering factor is low: $\sigma \ll \rho_r$, at $\rho_r \to 1$, high accuracy of ρ_r measurement is not required since:

$$N_\sigma / N_\rho = \sigma/\rho_r \cong (\sigma \pm \Delta\sigma)/(\rho_r + \rho_d + a) \underset{\rho_r \to 1}{=} \sigma \pm \Delta\sigma/\rho_r. \tag{5.35}$$

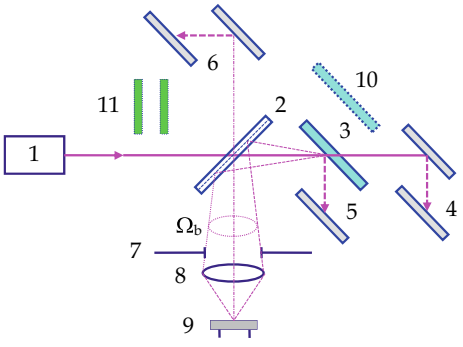

Fig. 5.19 Measurements of backscattering factor

Here ρ_d and α are the diffuse reflectance and absorptance of the high reflecting mirror of comparison and $\Delta\sigma$ is the systematic error of scattering measurements. For $\rho_r = 0.99$ and $\rho_d + \alpha \rightarrow \Delta\sigma = 0.01$, the factual measurement systematic error $\Delta\sigma/\rho_r$ translated to low scattering σ of the mirror studied is only 1%.

When measuring the backscattering factor using the apparatus described above, a light beam emitted by laser source 1, passed by beam splitter 2, and scattered back at 180° to the direction of incidence is captured by objective 8 and detector 9 within solid angle Ω_b, defined by round aperture 7. The beam, specularly reflected by mirror under study 3 and by other elements of the system, is attenuated to an insignificant level by a set of absorbers 5 consisting of two superpolished neutral glass plates (see Fig. 4.3). Calibration of the measurement scale is made via any high specularly reflecting sample mirror 10 implemented at normal incidence in the beam path instead of sample 3. Set 11 of precalibrated attenuators is used together with mirror 10, thus limiting the linear dynamic range needed to compare the contrasting signals, as from these high reflecting and low scattering optical elements. The actual level of background scattering noise, exposing detector 9 in the absence of mirrors 3 and 10 and being referred to specularly reflected radiation, defines the lowest backscattering factor to be practically measured by such a system.

If the light-scattering features of a medium interacting with radiation are substantially smaller than a subset of wavelengths for a beam of that radiation, the angular distribution of scattered light is uniform with a constant radiance. Rayleigh scattering, at the small features circumference, still much larger than light wavelength λ: $2\pi r_s \gg \lambda$, average intensities of two orthogonally polarized waves of observation for spherical polar coordinates of vector $|\vec{p}|$ and scattering angles φ, Θ are [1.1]:

$$\bar{I}^s_\theta = I^s_{||} \cos^2 \varphi;\ \bar{I}^s_\varphi = I^s_\perp \sin^2 \varphi, \tag{5.36}$$

having the degree of polarization P of scattered light versus angle θ of observation for Rayleigh scattering phenomena:

$$P(\Theta) = \left| \left(I^s_\perp - I^s_{||} \right) / \left(I^s_\perp + I^s_{||} \right) \right| = \sin^2 \Theta / \left(1 + \cos^2 \Theta \right). \tag{5.37}$$

As a result, in direction $\Theta = 90°$ the polarization is near complete and scattered light is polarized perpendicularly to the plane of observation. For natural daylight, light intensities averaged over all directions of observation and states of polarization, since $\overline{sin^2\varphi} = \overline{sin^2\varphi} = 1/2$, respectively are:

$$\bar{I}^s_{\Theta,nat} = I^s_{||}/2;\ \bar{I}^s_{\varphi,nat} = I^s_\perp/2. \tag{5.38}$$

Since measurements of the absolute scattering factor within small solid angle $\Delta\Omega$ for low losses are restricted by a quite diminutive intensity of measured radiation: $I_\Omega = I_0 \sigma \Delta\Omega / 4\pi$, measurements can be performed at a fixed observation direction Θ in comparison with some reference standard. Providing only Rayleigh scattering phenomena are of interest, demanding intensity versus scattering angle studies may

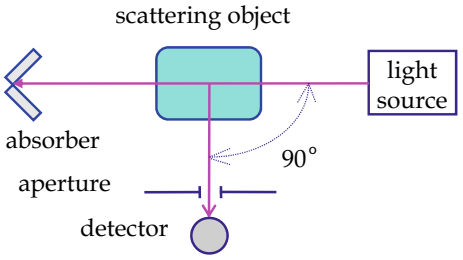

Fig. 5.20 Measurement of Rayleigh scattering

be reduced to a single measurement of the relative intensity of radiation scattered into 90° angle versus the intensity of the incident beam. For that stationary condition, it is certainly easier to reach the highest possible sensitivity to the low-scattering loss. From equations (5.36) it follows [1.1] that if a scattering object is irradiated by polarized light in opposite states of polarization and the intensity of scattered light is observed at 90°, the maximum and the minimum, respectively, of the state of radiation polarization for scattering light would be achieved. A simplified layout of a photometer for measurements of low uniform scattering observed at 90° angle in directly irradiated samples is depicted in Fig. 5.20 [5.13]. The photometer allowed investigating density fluctuations in scattering mediums along with deviations from the Rayleigh scattering phenomena.

As much as bulk optical properties of an object can be analyzed via scattering in a certain direction, integrated scattering-factor measurements may be used to identify rms roughness for irradiated optical surfaces (see relations [II.8], [II.9]) [II.2–II.4]. Since light scattering from any polished optical surface is fairly low, the so-called Coblentz hemisphere may be used instead of the integrating sphere to enhance the overall sensitivity, especially at IR wavelengths when sensitivity is at a premium (Fig. 5.21). The apparatus shown consists of aluminized semisphere 1 of a single aperture 2 for light incident on sample 3 and specularly reflected from the semisphere. Scattered light is focused by semisphere 1 on detector 4. Specularly reflected light is viewed by inclining sample 3, but light scattered at skewed angles (dotted lines) is guided out of the semisphere and should be counted. The total scattering factor of mirror 3 is defined and measured via ratio of the diffuse reflectance to the specular plus diffuse reflectance [5.14].

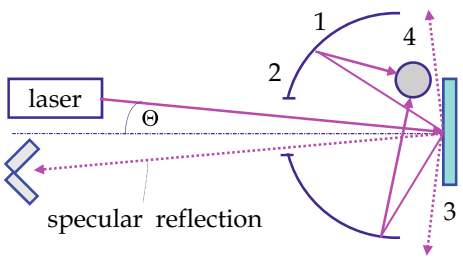

Fig. 5.21 Layout of Coblentz-sphere measurements

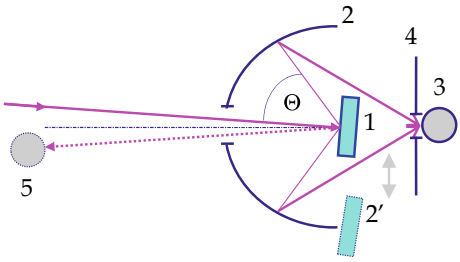

Fig. 5.22 Integration of scattering by spheroid mirror

Substitution of the hemispherical mirror by a spheroid further increases the signal-to-noise ratio for detection of total sample scattering. In the system shown in Fig. 5.22, light scattered by object 1 placed near the first focus of spheroid mirror 2 is reflected into a relatively large solid angle of observation, defined by the surface of the spheroid, and is focused to the second focal spot occupied by detector 3. For absolute calibration of the system, auxiliary flat mirror 2′, with coating equivalent as much as possible to that of spheroid mirror 2, is set instead of test sample 1 at another angle allowing to directly irradiate detector 3 via light specularly reflected by mirrors 2 and 2′. The same detector moved into position 5 can measure specular reflectance of mirror 2′. For known reflectances of mirrors 2 and 2′ of low own scattering and sufficient dynamic range of the detector, such a calibration process is fairly accurate and allows estimation of the rms roughness Ra via the total scattering factor σ_Σ [5.15]:

$$R_a = \lambda \times \sigma_\Sigma / (4\pi \cdot \cos \Theta). \tag{5.39}$$

Integration of hemisphere-distributed 2π scattering can also be done using a cavity-shaped detector [5.16]. To serve as a collector of 2π-scattered light, the detector should, first, be evenly sensitive within the full-hemispherical solid angle, and, second, have its absorptance equal to unity over the entire wavelength range of measurements. Otherwise, diverse corrective factors need to be implemented for its sensitivity, also accounting for multiple reflections between sample and detector surfaces. Figure 5.23 shows an assembled pyroelectric detector as the spatial integrator of hemispherical scattering [5.16]. This angular form of the cavity-shaped detector was merely chosen to simplify its fabrication. An outer electrode of a polyvinyl fluoride (PVF) pyroelectric film was formed by a brass shim. The inner detecting

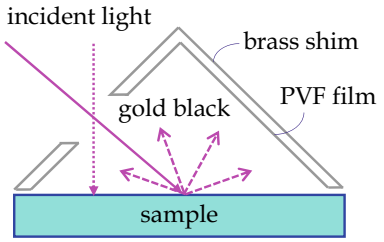

Fig. 5.23 Cavity-shaped detector

pyroelectric was made as a layer of gold black coating serving as the inner electrode and its effective thickness optimized for scattering measurements in the 5–10-μm spectral range was found to be near 40 μm at 30-Hz modulation frequency of the incident beam. The sensitivity of the detector reached approximately $2 \cdot 10^7$ cm $Hz^{1/2}$ W^{-1} with ±3% detection error for the 6–13-μm spectral region [5.16].

In some cases, such as in laser welding, the use of integrating spheres is prohibitive owing to splashing of molten metal on pulsed laser exposure and limited-angle goniophotometry at discrete angles allows light-scattering intensity to be sensed in available directions for the following estimation of integrated scattering [5.18]. Other obstacles to precise and sensitive goniophotometric studies on laser irradiation are due to object inhomogeneity and speckle phenomena (see [II.26] for details), besides respective limitations of the measurement and detection systems. An example of a directional-reflectance characterization setup designed for three laser wavelengths to accuracy of ±0.002 or less to be reached at the 1σ confidence interval having targeted 360°-detection capability, 0.001° resolution, and repeatability is illustrated in Fig. 5.24.

The respective light sources in such a measurement facility [5.19] were three lasers: 442-nm He–Cd laser, 632.8-nm He–Ne laser, and 859.9-nm GaAlAs semiconductor laser, requiring enhanced collimation, plus circulation and spatial filtering. All optical elements of the system were antireflection-coated to minimize scattering and beam depolarization at every wavelength. A refracting telescope, consisting of objectives O1 and O2 and pinhole A5, was used for filtration of higher-order spatial frequencies for light diffracted by pinhole apertures A1–A8. Similar telescopes, consisting of notch filter F, lens L, aperture stop AS, scattering baffle SB, and field stop FS, were placed in front of imaging detector D2 and reference detector D1 (Fig. 5.24b). Attenuation of the ambient background was 40 dB with a 10-nm-wide notch filter (see also Figs. 4.7 and 4.8). To minimize speckle, spatial resolution for light reflected by sample S did not exceed 2° for 1-in. irradiation diameter at angles of incidence of 30°, 45°, and 60° or a maximum emittance angle of ±70°. The reference channel was formed by λ/2 wave plate W

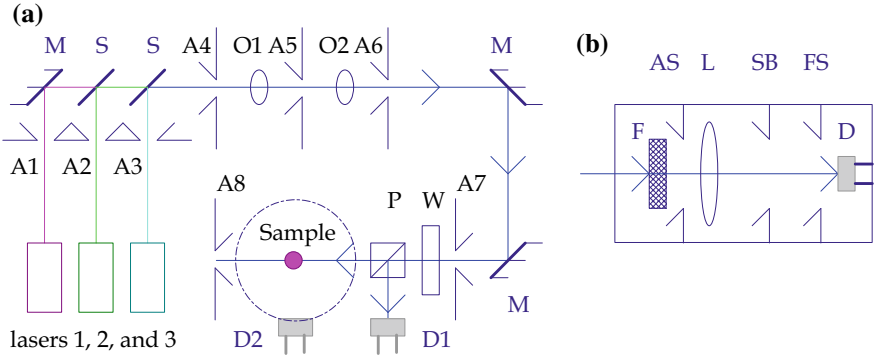

Fig. 5.24 Bidirectional reflectance measurements (**a**) and detector assembly (**b**)

and polarization beam splitter P at an extinction ratio of 500:1 or greater. Optical signals were registered by $10 \cdot 10$ mm^2 silicon photodiodes with a noise-equivalent power of $1.8 \cdot 10^{-14}\,\mathrm{W}/\sqrt{\mathrm{Hz}}$. Further amplification and ratio measurements were provided via transimpedance and phase-sensitive 5–100-kHz lock-in amplifiers for synchronous detection of two channel signals with the ratio repeatability within ±0.2%, but ±0.4% over all disassemblies and several-day runs. The overall precision for the bidirectional reflectance measurements was ±0.002 at the 1σ confidence interval with angular repeatability being identical to the 0.001°-resolution reached [5.19].

For any reflectance measurements in partially coherent laser radiation the high resolution in angular scattering detection causes the occurrence of speckle phenomena resulting from interference patterns due to interaction of beams reflected by surface and volume irregularities larger than the wavelength λ of radiation. The interference pattern can be treated as due to an ensemble of secondary point sources with random distribution profile, creating diffraction in the far field of observation [II.22]. The resulting patterns consist of individual lobes of angular diameter ψ defined by the diffraction limit, $\psi = 2\lambda/D$, for a test object of diameter D. Angular movements of the observation detector over the lobe diameter cause various sets of speckle lobes to be observed, while temperature and other drifts lead to similar instabilities of a given beam intensity being detected. From the standpoint of speckle averaging, the higher is the requirement for angular resolution, spreading further apart the object and detector, the larger is the observation diameter required for efficient speckle-pattern integration. For the measurement system in Fig. 5.24, the speckle-lobe diameter at 30-cm separation of detector D1 for $\lambda = 859.9$ nm was 0.042 mm, making a 10-mm clear aperture lens sufficient for averaging [5.19].

Although the overall sensitivity of a goniophotometric study can be lower than that of integrated detection for hemispherically integrated scattering, spectral goniophotometry permits plotting of the spatial distribution of scattered light allowing to obtain the roughness spectrum of a micropolish of a test surface, thus rewarding efforts to increase the sensitivity of spectrogoniophotometric studies. Figure 5.25 shows an insert to a sensitive spectrogoniophotometer, detecting the sample's angular scattering via a bidirectional reflectance measurement [5.17]. Scattered light is measured at the state of polarization of an incident beam for angles φ and Θ of incidence and observation. Bidirectional reflectance $\rho(\Theta,\varphi)$ is sensed as:

$$\rho(\Theta, \varphi, ||/\perp) \cdot |\cos\Theta| = \Delta\Phi_{scat}/(\Phi_0 \Delta\Omega), \tag{5.40}$$

where Φ_0 and $\Delta\Phi_{scat}$ are the incident and the reflected or scattered flux/intensity of a respective light beam and ΔΩ is the solid angle of observation. In an evaluation experiment, irradiation of the sample was made by a He–Ne laser at $\varphi = 1°30'$ presuming its negligibly small divergence. Every beam intensity was measured by a photomultiplier within solid angle $\Delta\Omega = 6.8 \cdot 10^{-5}$ sr. The relative sensitivity of each individual integrated scattering measurement limited by stray light reached $1 \cdot 10^{-6}$ [5.17].

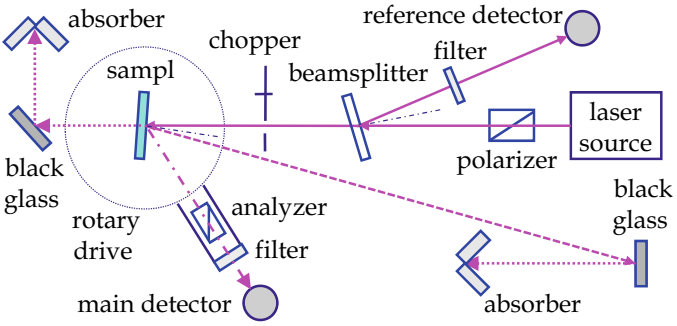

Fig. 5.25 Goniometric measurement of angular scattering

In cases when integrating spheres are permissible, but relatively low loss measurements are expected, straightforward dual-channel spectrophotometry can be accomplished via an auxiliary sphere as a reference standard, following the concept of coupled integrating spheres shown in Fig. 4.37. The initial realization of such a sphere [5.20] was not intended for low-loss measurements, nevertheless the added sphere attenuation implies using the detriment as an advantage. This second diffuse reflecting integrating sphere (Fig. 5.26) placed into the reference port of a dual-beam spectrophotometer establishes the much lower-level 100% line for weakly reflecting samples. Instead of the common high reflecting comparison sample as the sphere cap (see Chaps. 2 and 4) in the reference port of integrating sphere 2, auxiliary sphere 3 and test sample 4 are in this case sequentially irradiated by monochromator 1 and viewed by detector 5. Applying the law of conservation of energy, the effective reflectivity ρ_p of the common port for main and auxiliary spheres of relative area A_p inserted into the sphere with wall reflectivity ρ_0 and spherical surface area A_0 becomes:

$$\rho_p = \frac{A_p}{A_0 - A_p} \frac{\rho_0}{1 - \rho_0}. \tag{5.41}$$

Since the two-channel ratio for samples S and C, with other factors being equal, is $Q = \text{const} \cdot \rho_s/\rho_c$, the attenuation factor of auxiliary sphere 3 versus a sphere-wall spherical comparison sample of ρ_0 becomes:

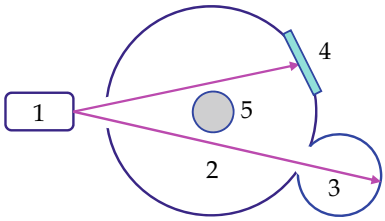

Fig. 5.26 Integrating and reference spheres

$$Q_a = \frac{A_p}{(A_0 - A_p)(1 - \rho_0)} = \frac{A_p/A_0}{(1 - A_p/A_0)(1 - \rho_0)} \equiv \frac{A_{p/0}}{(1 - A_{p/0})(1 - \rho_0)}. \quad (5.42)$$

For reference port relative surface area $A_p = 0.01A_0$ and $\rho_0 = 0.95$, the ratio $Q_a \approx 0.01/0.05 = 0.2$ causes a 20% downshift of the 100% reference line or a 10% downshift for $\rho_0 = 0.9$ and $A_{p/0} = 0.01$ or $\rho_0 = 0.95$ and $A_{p/0} = 0.005$.

Somewhat combined, to an extent, scattering measurements can be realized for a fairly complex object such as biological tissue [5.29]. Figure 5.27 depicts the system for step-scanning of forward light scattering by tissue from 3° to 23° in 100 steps via motorized iris aperture IA for direct irradiation by He–Ne laser 1 and detection by integrating sphere 6. The setup also collects 0°-scattered light via the 45°-polished end of tilted optical fiber 5. The laser beam is expanded to 2.75 mm in diameter and split into beams which go to reference detector 2 and irradiate sample tissue 3. Light forward scattered by tissue is collected by achromatic lens 4 at intermediate focus in the plane of iris IA, while 1.3-mm-diameter fiber 5 collects 0° scattering, also blocking it from entering the sphere with main detector 7, which detects the remainder of radiation scattering given by angle Θ of the iris-opening step. The measured ratio of detector signals is averaged and normalized via the system settings calibrated for incomplete light blocking and via objects of known scattering properties – size-standardized polystyrene microspheres or other reference objects.

Let us also note that the dual lock-in amplification technique, as one example of sensitive detection approach for weak scattering phenomena, can be deployed to detect extremely low intensities of bidirectionally scattered light, along with even lower levels of time-delayed luminescence, often accompanying common events of minute laser scattering [5.21]. Figure 5.28a depicts two phase-locked choppers set at 180° phase difference, which should completely block any stray light from the light source. Consequently, when measuring fluorescence with a time delay greater than the period of modulation, the intensity of the steady background radiation should be blocked by several orders of magnitude from the signal. This technique may be used with any pulse-modulated light source having pulse width 50% or less

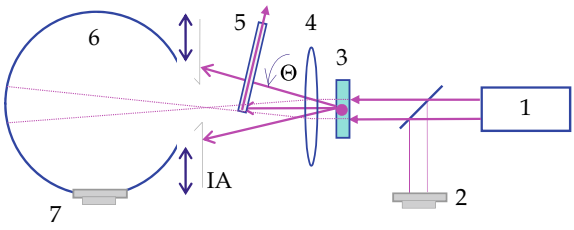

Fig. 5.27 Combined study of integrated and direct scattering

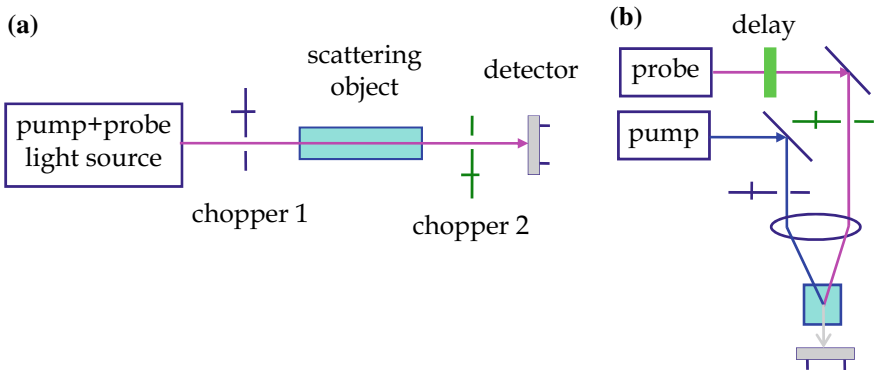

Fig. 5.28 Direct (**a**) and delayed (**b**) phase-locked scattering measurements

lower than the chopping frequency period. That way no light from the source will directly reach the detector. A somewhat different arrangement is seen in Fig. 5.28b, where diverse pump and probe sources of light are deployed, and the time delay between the irradiating and the measuring light pulses establishes the essence of the time-delay study.

A straightforward approach for sensing only specular reflectance but measuring the sum of scattering and absorption losses ξ of opaque mirror M is depicted in Fig. 5.29. The concept presumes one type of loss being negligible and another as being of main interest, and involves swapping mirror M and detector D, which uniformity defines the applicability of the technique [5.22]. In Fig. 5.29a, two sequential measurements 1 and 2 (dotted line) are formed by beams, first, specularly reflected by referencing coupler C and, second, directly transmitted by coupler C and reflected by test mirror M. In Fig. 5.29b, measurements 3 and 4 are taken via beams specularly reflected by coupler C and reflected by mirror M, and then directly transmitted by coupler C only (dotted line). The incidence angles θ and φ for all measurement positions are presumed to be unchanged and identical. Intensities I_1 and I_2 for beams of radiation viewed by detector D in Fig. 5.29a are obtained via single specular reflectance from coupler C and via its direct transmittance plus specular reflectance of mirror M. Signals 3 and 4 relate to coupler-plus-mirror specular reflectance and to the coupler transmittance. In the factual system, coupler C was formed by a mirror modulator, which was opening and closing each path, making the ratios:

$$I_1/I_2 = \rho_c/(\tau_c\rho_m); \quad I_3/I_4 = \rho_c\rho_m/(\tau_c), \tag{5.43}$$

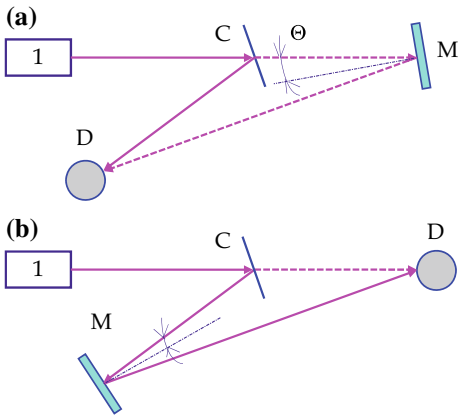

Fig. 5.29 Measurement of losses on scattering plus absorption

where ρ and τ are the specular reflectance and direct transmittance, and subscripts *c* and *m* relate to the coupler and the mirror. Taking the ratio of the two relations Eqs. (5.43) and then making mirror M serve as coupler C and vice versa gives the following relations after four pairs of intensity measurement:

$$(I_1 I_3 / I_2 I_4)_c = (\rho_c / \tau_c)^2; \quad (I_1 I_3 / I_2 I_4)_m = (\rho_m / \tau_m)^2. \tag{5.44}$$

The actually measured reflectance–transmittance ratios for the coupler and the mirror can be verified by the law of conservation energy in transmitted and reflected light: $\tau = 1 - \rho$, with no absorption and thus $\xi \to 0$:

$$(I_1 I_3 / I_2 I_4)_c \xrightarrow[\tau=1-\rho]{} \rho_c^2/(1-\rho_c)^2; \quad (I_1 I_3 / I_2 I_4)_m \xrightarrow[\tau=1-\rho]{} \rho_m^2/(1-\rho_m)^2. \tag{5.45}$$

The practical uncertainty of these measurements was identified by comparing the total loss for every mirror measured with the combined loss experienced by mirror pairs assembled as Fabry–Perot resonators. The results of two compared measurement methods were within ±0.05% margins of the uncertainty for each technique, with the repeatability of the loss measurements near ±0.005% [5.22].

Chapter 6
Systems of Multiple Reflections

6.1 Flat-Mirror and Prism Reflector Cells

As seen in Chaps. 2 and 5, expanding the effective optical path length or the number of light interactions with the object under study increases the sensitivity to the optical properties of the object. Therefore, it is prevalent to desire as many interactions as possible when looking for the highest sensitivity to optical losses. However, if the object's refractive index n is different from that of its surroundings (see relations (1.102), (1.103)), the losses at two boundaries can overcome the loss being measured by their uncertainty. For any transparent object of length ℓ, linear attenuation coefficient μ, and relative refractive index n, the bulk-plus-surface transmittance τ for m light passes via the object is:

$$\tau = \left[1 - \left(\frac{n-1}{n+1}\right)^2\right]^{2m} \exp\left(-\mu m \ell n\right) = \left[\frac{4n}{(n+1)^2}\right]^{2m} \exp\left(-\mu m \ell n\right). \tag{6.1}$$

The relative error $\Delta\tau/\tau$ of that transmission study as a function of object's surface reflectance ρ is:

$$\frac{\Delta\tau}{\tau} = \pm\left(\frac{2m\Delta\rho}{1-\rho} + \Delta\mu\ell nm\right) = \pm\left[2m\left(\frac{\Delta n}{n} + \frac{2\Delta n}{n+1}\right) + \Delta\mu\ell nm\right]. \tag{6.2}$$

Consequently, the uncertainty $\Delta\mu$ of the resolved linear attenuation coefficient μ of the object's bulk becomes:

$$\Delta\mu = \pm\frac{1}{\ell n}\left(\frac{2\Delta\rho}{1-\rho} + \frac{\Delta\tau}{m\tau}\right) = \pm\frac{1}{\ell n}\left(\frac{2\Delta n}{n} + \frac{4\Delta n}{n+1} + \frac{\Delta\tau}{m\tau}\right). \tag{6.3}$$

Equation (6.3) confirms that increase of the number of light interactions with an object whose refractive index is different from that of its surroundings increases the measurement's sensitivity only to the combined bulk-plus-surface optical losses.

M. Bukshtab, *Photometry, Radiometry, and Measurements of Optical Losses*, Springer Series in Optical Sciences 209,
https://doi.org/10.1007/978-981-10-7745-6_6

Uncertainties of the object's surface properties manifest themselves to exactly the same extent as in any single-pass study. At the same time, increase of the number of passes creates a respective decrease of the intensity of light transmitted via the object in proportion to double surface losses: $(1-\rho)^{2m}$, decreasing the overall sensitivity of the measurement. As a result, the multipass reflection system is efficient only for low-density substances, such as gases inside a multiple-reflection cavity or for studies of optical properties of specularly reflecting mirrors either inserted into a cavity in reflected light or shaping the cavity themselves. To increase the effectiveness of the bulk transmission measurements of solid objects, surface reflections must be eliminated by applying antireflection coatings, by immersing the object's boundaries within a multipass cell, or by utilizing linearly polarized light propagating via the borders at the Brewster angle (see Chap. 10 for details).

Systems of multiple reflections can be created by parallel prolongation of the double-reflection cavity analyzed earlier for reflectance measurements at oblique incidence (see Fig. 5.13). The number of reflection pairs can be changed as a function of the spacing between two parallel flat mirrors 1 and 2 [6.1], and via angle Θ of incidence (Fig. 6.1). For opposite incidence and propagation directions (Fig. 6.1a) of the input and the output beam given by 2Θ angle, the cross sections of the beams and of the mirrors identify the number of reflections that can be obtained by altering the distance ℓ between the mirrors without any beam overlap. If one only fixes the mirror positions at which the direction of the beam emerging from the system is parallel to the direction of the incident beam (see Fig. 6.1b), the total number m of reflections is a multiple of 2: $m = 2^j$, $j = 1, 2, 3, \ldots$. At every intermediate position, the distance ℓ between mirrors of width L for m reflections becomes:

$$L/m \leqslant \ell \tan\Theta \leqslant \ell/(m-1). \tag{6.4}$$

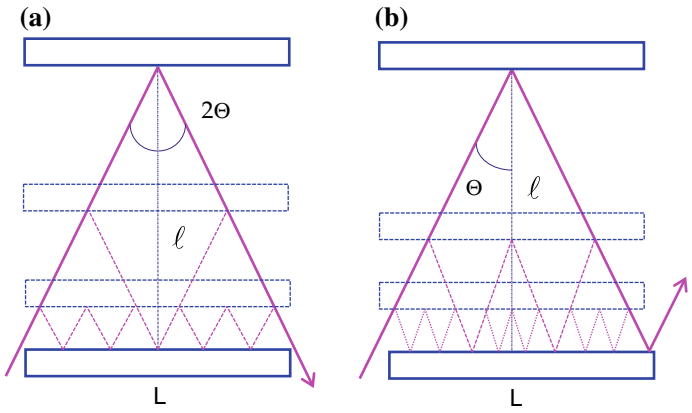

Fig. 6.1 Creation of multiple reflections via translation of parallel mirrors

If it is necessary to maintain angle 2Θ between the directions of the emerging and incident beams (Fig. 6.1a), the number of reflections is $m = 2^j - 1$ and the distance ℓ between cavity mirrors becomes:

$$L/(m+1) \leqslant \ell \tan \Theta \leqslant \ell/m. \tag{6.5}$$

The m times reduction of mirror separation distance ℓ for $m = 2^j$ equivalently increases the even number $2m - 1$ of additional reflections, occurring within a cavity created by these two mirrors, if the directions of the emerging and incident beams remain parallel to each other.

The intensity I_0 of a beam retroreflected in the cavity decreases after each dual-reflection cycle as $I_2 = I_0\rho_1\rho_2$, where ρ_1 and ρ_2 are actual reflectances for the light spots on the first and the second mirror. After m reflection cycles, the decrement of the incident beam intensity is proportional to the product of the average reflectances of both mirrors and the number of cavity reflections: $I_2 = I_0(\bar{\rho}_1\bar{\rho}_2)^m$. The mean reflectance of two cavity mirrors $\bar{\rho}$ averaged over irradiated mirror surfaces inside the cavity is:

$$\sqrt{\bar{\rho}_1\bar{\rho}_2} \equiv \bar{\rho} = (I_m/I_0)^{1/2m} = (I_m/I_0)^{1/i}, \tag{6.6}$$

where $i = 2m$ is the total number of reflections inside the cavity, and I_0 and I_m are the intensities of the beam entering the cavity and exiting it after participating in m dual reflections. Consequently, the mean reflectance can be determined by comparing the intensities for any intermediate states of the cavity:

$$\bar{\rho} = (I_m/I_1)^{1/2(m-1)} = (I_m/I_k)^{1/2(m-k)}, \tag{6.7}$$

where I_m and I_k are the intensities of beams corresponding to the m^{th} and k^{th} reflection cycles, respectively, starting from $k = 1$. The parallel-prolongation technique described presumes one is dealing with nondivergent beams if expecting $m \to \infty$, whereas actual divergence increases beam spot sizes and limits the numbers of reflections obtained [6.1].

The method of scaling reflections highlights two essential points of view for low-loss measurements. The first one deals with the ability of a particular measurement technique to provide multiple evaluations of a presumably unchanging factor or coefficient, allowing one to distinguish systematic errors, such as variations of measured magnitude versus a coordinate, and nonlinearities of detectors or other elements. The transformation of the distance ℓ between mirrors described above gives a sequence of ratios: $\bar{\rho}^4/\bar{\rho}^2, \bar{\rho}^8/\bar{\rho}^2$ *or* $\bar{\rho}^8/\bar{\rho}^4$, etc., allowing one to resolve the difference among the intermediate results, averaged by distinct zones of both mirrors. The second vital point deals with the measurement resolution. When measuring extremely low loss $\mu \to 0$ at high reflectance $\bar{\rho} \to 1$ and fixed resolution, only a sufficiently elevated difference of reflections between states m and k can resolve I_m and I_k signals.

To distinguish optical properties of unequal, but reciprocal multireflection cavity elements by detecting changes of the radiation intensity interacting with such a cavity, at least three of these contrasting elements are required. In other words, to resolve two unequal reflectances of similar mirrors ρ_1 and ρ_2 in addition to two measurement cycles by Eq. (6.6), one related cycle must be made with a third mirror combined with either of the first two, presuming its reflectance ρ_3 is different from that of the other two. Three measurement cycles give the equations for reflectance products:

$$\bar{\rho}_1\bar{\rho}_2 = \left(I_{1,2}/I_0\right)^{1/2} \equiv A, \quad \bar{\rho}_1\bar{\rho}_3 = \left(I_{1,3}/I_0\right)^{1/2} \equiv B, \quad \bar{\rho}_3\bar{\rho}_2 = \left(I_{3,2}/I_0\right)^{1/2} \equiv C. \tag{6.8}$$

The solution is:

$$\bar{\rho}_1 = \sqrt{AB/C}, \quad \bar{\rho}_2 = \sqrt{AC/B}, \quad \bar{\rho}_3 = \sqrt{BC/A}. \tag{6.9}$$

Each individual reflectance error combines the total errors of all measurement cycles: $\Delta\bar{\rho}_{i,ind} \cong \sqrt{3}\Delta\bar{\rho}$.

Illustrated by Fig. 6.1, the method for creating multiple reflection demonstrates trade-offs between sensitivity and resolution for intracavity measurements. Any method creating multiple reflections with the oblique incidence of light on a pair of cavity mirrors increases its sensitivity by adding reflections, along with decreasing its spatial resolution. Besides, the larger is the number m of intracavity reflections, the higher are the requirements for parallelism of cavity mirrors and the lower is the output beam intensity $I_m = I_0\bar{\rho}^{2m}$. If the light intensity decreases below the detector's sensitivity, there is no sense in making the increase. Figure 6.2 depicts a similar concept of spreading multiple reflections by several separate and equivalently manufactured optical elements of a test substance instead of dispersing reflections over a large-surface cavity mirror. In this example, prisms I–IV with the coating to be studied on their faces are installed at some fixed angle of incidence φ. Figure 6.2a shows the 100%-line setting. In Fig. 6.2b, sliding mirror M_2 is moved into position M_2' for a reading on the sample test set. The ratio of readings gives the fourfold prisms' reflectance averaged over all four examined surface coatings sputtered over prisms I–IV [6.2]. As in a parallel-mirror cavity, the alignment of

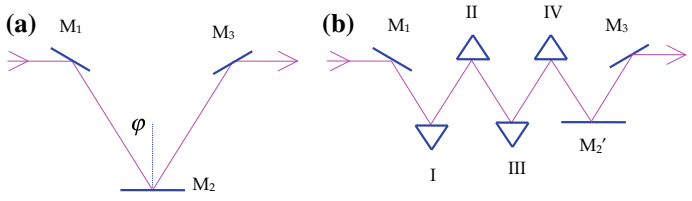

Fig. 6.2 Multiple interactions with a sample set: M – mirrors; I–IV – prisms

each element is critical since the optical path-length variation with and without the test objects creates additional error.

Figure 6.3 illustrates a similar technique for reflectance measurement with a cavity-preset angle of incidence for two parallel mirrors concurrently irradiated by a beam of light [6.3]. Top mirror 5 of a reflecting cavity and detector 8 are placed on a sliding table. When mirror 5 is moved out of the beam path into position 5′, detector 8 is relocated to position 8′ to be directly irradiated by laser source 1. Such a rearrangement allows one to measure the initial intensity I_0 of the incident beam before its interaction with mirrors. Autocollimator 9 or He–Ne laser 3 are utilized to align the cavity mirrors, maintain the number of reflections, and set the angle of incidence. The cross sections of the incident and output beams can be adjusted by the input and output apertures 4 and 7.

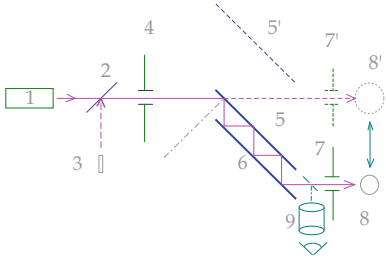

Fig. 6.3 Measurements at a fixed angle of incidence

Any given number of internal reflections in a multiple reflection cavity can be increased almost twice by placing the cavity not in transmitted but in reflected light (Fig. 6.4). The concept is realized by changing the wedge angle φ between cavity mirrors. The initial angle of incidence Θ for the first mirror at the cavity entrance can be tuned to the reverse beam propagation direction at the cavity's exit [6.4]. Thus, the size of cavity mirrors needed for a desired number of reflections is practically twice as small as for a parallel-mirror cavity in transmitted light. However, the angle of incidence of such a cavity design does not remain constant, changing from its maximum at the cavity entrance to close-to-normal incidence at the cavity end, where beam direction is reversed. This concept of the returning beam is very much identical to the ray tracing in the light pipe made as a hollow cone with a coated circumference or as a glass one for the total internal reflectance of light entering it and eventually coming back in its entirety at the right angle. Such geometrical light pipes are widely used in illumination engineering [0.48, 0.49].

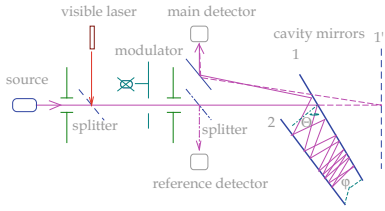

Fig. 6.4 Averaging study of flat mirrors in a wedged cavity

The total number j of reflections inside that wedge cavity is given by the ratio of incidence to wedge angles: $j = 2\Theta/\varphi + 1$, with the number of reflection cycles $m = \Theta/\varphi$. These numbers are high for $\Theta >> \varphi$. The total number j = 2 m + 1 of reflections inside such a cavity is an odd number owing to one extra reflection at the first cavity mirror. The intensity I_{out} of the output cavity beam versus the intensity I_0 of the input beam averaged over surfaces of mirrors 1 and 2 represented by mean reflectance values is:

$$I_{out} = I_{1,2} = I_0 \bar{\rho}_1^{m+1} \bar{\rho}_2^{m}. \tag{6.10}$$

To neutralize one additional interaction with the first mirror, a reference measurement is made not versus the incident but versus the beam having a single reflection from mirror 1. For that purpose mirror 1 is moved to position $1'$, where the beam reflected by it reaches the same primary detector as via multiple reflections. Since $I_1 = I_0\rho_1$, the product of reflectances can be resolved by Eq. (6.6): $(\bar{\rho}_1\bar{\rho}_2)^m = I_{1,2}/I_1$. Using third mirror 3 and making three measurement cycles in the combinations 1, 2, 1, 3, and 2, 3, the surface-averaged reflectance of the first mirror is measured as:

$$\bar{\rho}_1 = \left[\left(I_{1,2}/I_1\right)\left(I_{1,3}/I_1\right)\left(I_{2,3}/I_2\right)\right]^{1/(j-1)}. \tag{6.11}$$

Here the total number j of reflections in the cavity and the number m of reflection cycles are related as $j = 2m + 1$.

An experimental verification of measurements using a wedge cavity made of gold mirror coatings on plane-parallel substrates having surface roughness of $\lambda/10$ was done in the 9.1–11.3-μm spectral region of CO_2 laser emission [6.4]. Differential signals from the main and reference thermal detectors were registered with about ±1% accuracy when using 0.65-Hz modulation frequency of the external modulator (Fig. 6.4). At the maximum number j = 39 of intracavity reflections, the initial 1-mm beam diameter, set by factual system apertures, was correspondingly increased from 1 to 8 mm. By respectively altering wedge angle φ, the lowest (11) and the highest (39) numbers of total cavity reflections were realized. Figure 6.5 illustrates the relative distribution of the reflectance magnitudes averaged over two surfaces of cavity mirrors. The graph shows the dependence of the average reflectance on the angle of incidence, giving a conceptual indication of the repeatability of the measurement performed. The mean-reflectance value obtained averaged over all intermediate measurements was $\bar{\rho}_a = 0.9889$ with the

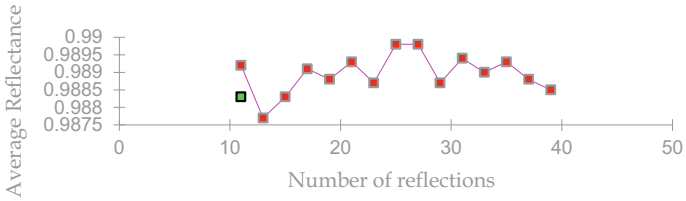

Fig. 6.5 Reflectance distribution of a gold mirror surface at 10.6 μm

root-mean-square deviation of the double-averaged reflectance being $2\sigma = \sqrt{\sum_{i=1}^{\eta} (\bar{\rho}_a - \bar{\rho}_i)/[\eta(\eta - 1)]} = 0.0003$.

Owing to the main distinction of the wedge-shaped cavity of returning incident light via the entering optical path, that cavity was applied as a virtual mirror in a displacement-sensing Michelson interferometer (Fig. 6.6) with one cavity mirror attached to a piezoelectric transducer (PZT) [6.5]. Rewriting the wedge-cavity equation for the total number m of reflection cycles or the same number of reflections per mirror and considering that at an automatic fringe detector reacts to a full-wavelength λ path change:

$$k\lambda = 2n\Delta d \sin(m\varphi)/\sin\varphi, \tag{6.12}$$

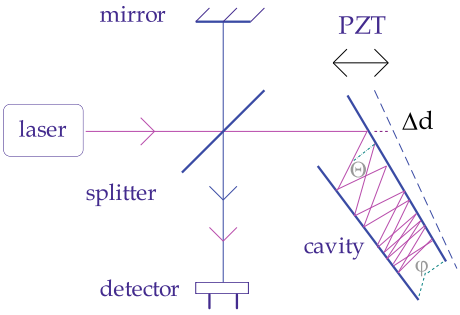

Fig. 6.6 Wedge-cavity as interferometer mirror

enhanced by multiple reflections at wedge angle φ and displacement Δd in a media of refractive index n. Relating to the number k of full detector cycles, the sensitivity of displacement becomes [6.5]:

$$S_{disp} = \Delta d/k = (\lambda/2n)/\sin(m\varphi)/\sin\varphi \underset{\theta,\varphi\to 0}{\cong} \lambda/(2nm). \tag{6.13}$$

As a result, the displacement sensitivity of the original interferometer can be increased by the number of reflection cycles in the wedge-shaped cavity, with additional penalties concerning angular-displacement sensitivity and a loss of the detector's signal due to multiple reflections.

A more elaborate design of a two-element multipass cavity involves corner-cube retroreflectors of unequal dimensions that are half-way enclosed by one right-angle prism [6.7] in an arrangement similar to a four-element Fabry–Perot interferometer consisting of two retroreflectors and beam splitters facing each other [6.6]. The conceptual idea (see Fig. 6.7) for positioning the corner-cube reflectors, oppositely

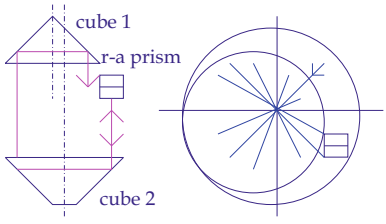

Fig. 6.7 Corner-cubes plus right-angle prism cavity (beam spots and passes are drawn illustratively)

arranged with their optical axes parallel to each other, but corners shifted, is with parallel propagating beams though not in the plane containing the axes. For both corner cubes, having identical dihedral angles with the same angle error ε, the resulting deviation angle ψ of an entrance beam parallel to the cell axis after n reflections with no beam overlap is:

$$\psi = \varepsilon\sqrt{10n}, \tag{6.14}$$

defining – along with the beam-waist size and the respective diffraction of the beam after each reflection – the actual limits for the system design. The modeled illustrative cell [6.7] based on dissimilar corner-cube retroreflectors and a supplemental right-angle prism was capable of accommodating up to 24 total cell passes as the light path reentering the cell via the prism after 12 reflections with parallel beam propagation paths inside the cavity, fitting the space tightly and homogeneously (see also Chap. 12 for applications of corner-cube reflectors).

6.2 Multipass Cavities

The dual-reflection attachments for conventional spectrophotometers reviewed earlier (Figs. 5.13 and 5.14) highlighted ways to reduce the uncertainty of a test sample alignment by substitution of a supplementary flat mirror by a spherical one. By analogy, a multiple-reflection cavity of curved mirrors may simplify the alignment of the system and thus create a greater number of cavity reflections. Various combinations of reflector arrangements and curvatures for a spherical-mirror cavity may allow one to increase the spatial density of radiation, while concurrently maintaining a steady direction of the light beam existing the cavity. This is greatly important for analysis of weak optical phenomena, such as low-loss multiphoton absorption and nonlinear scattering, especially in gaseous substances.

The confocal cavity (Fig. 6.8) consisting of three mirrors having equal radii of curvature is the device of choice for weak-interaction studies [6.8]. The first two

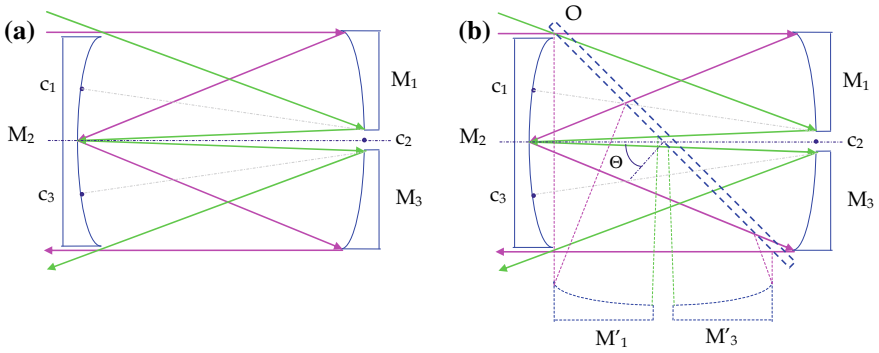

Fig. 6.8 Three-mirror confocal White cavity

mirrors M_1 and M_3 form one side of the highly reflecting cavity, while the third mirror M_2 forms the opposite side of the cavity. The centers of curvature of mirrors M_1 and M_3 coincide with the reflecting surface of mirror M_2 at distances C_1 and C_3 from the median of both the cavity and mirror M_2 (see the dash-dotted line). Usually distances C_1 and C_2 are equidistant from the cavity median. The center of curvature C_2 for third mirror M_2 coincides with the median of the protraction of mirrors M_1 and M_3. The advantage of the horizontal arrangement of in–out images, despite them being curved, is that any beam of radiation entering the cavity at angle φ to the median exits at opposite angle $-\varphi$ independently of the length of its optical path. The number of cavity passes is a multiple of 4, and the closer centers C_1 and C_3 are to the median, the more the number is increased. Since the cavity consists of only concave mirrors, the largest conceivable number of reflections is less limited by radiation divergence. The image of a light source filling the entrance aperture on the generatrix of surface M_2 is reproduced after every reflection on one of the mirror surfaces or at the exit aperture symmetrical with the entrance aperture.

At the same time, any increase of the number of reflection cycles in such a confocal White cavity, having convenient horizontal positions of the entrance and exit apertures, likely causes relatively high astigmatism of the source image owing to increases of the angles of incidence for all mirrors [6.9]. Even for a point source, the meridional or the sagittal astigmatic elongation is:

$$\begin{aligned}\Delta h \cong 2h \sin\varphi \tan\varphi &= \frac{2hb^2}{R^2}\left[\left(\frac{N/2-1}{N}\right)^2 + \cdots + \left(\frac{3}{N}\right)^2 + \left(\frac{1}{N}\right)^2\right] \\ &= \frac{hb^2}{12R^2}\left(N - \frac{N}{4}\right),\end{aligned} \tag{6.15}$$

where h is the height or width of each mirror in the corresponding computation of the meridional or sagittal lengthening, b is the distance between entrance and exit apertures, R is the radius of all curvatures, and N is the total number of cavity passes. For a combination of the cavity with a slit monochromator of vertical entrance and exit slits, the least horizontal separation of slit images at $h \to b$ has to coincide with the smallest elongation. For the best result, the slits are grooved at the opposite edges of mirrors and intermediate images are separated in a vertical plane, doubling the number of cavity passes for a constant cavity size and without increasing the angles of incidence.

To examine a flat mirror in a White cavity, the entire system is transformed into its bent position by analogy with the double-reflection attachments seen in Figs. 5.13 and 5.14. Mirror O under study is introduced into the cavity in its vertical

plane (thick dotted lines in Fig. 6.8b) at angle Θ to the cavity axis of symmetry, crossing center C_2 and splitting centers C_1 and C_3 by the cavity median, and mirrors M_1 and M_3 are turned around into new positions M_1' and M_3' (thin dotted lines in Fig. 6.8b) corresponding to the specular reflection from test mirror O [6.10]. The minimum and maximum angles of incidence in the meridional and sagittal planes are defined by the cavity's cross section, dependent on the exact locations of centers C_1 and C_3 and slit heights.

The number of cavity reflections N is directly proportional to the distance b between the entrance and exit apertures and is inversely proportional to the separation of the centers of curvature: $N = b/(C_1 + C_3)$. The magnitudes of C_1 and C_3 are determined by taking into account type-of-direction signs: plus sign when the mirror and the curvature center are both situated on one side of the cavity's symmetry plane, and minus sign for the opposite position. If the sum $C_1 + C_3$ is negative, the intermediate images are distributed over the surface of mirror M_2 further away from the symmetry plane than the positions of the source images being collimated into the entrance and exit apertures. When the sum $C_1 + C_3 = 0$, the beam of incident light is projected into the exit aperture directly after the first reflection. For a large separation of the source images, the astigmatic elongation of each image increases, hence, usually $C_1 + C_3 > 0$.

Without an object under study, the intensity of a parallel beam of light entering the triple-mirror White cavity through its entrance aperture and leaving the cavity via the exit aperture is:

$$I = I_0\left(\bar{\rho}_1\bar{\rho}_2^2\bar{\rho}_3\right)^m/\bar{\rho}_2, \tag{6.16}$$

where I_0 is the intensity of light entering the cavity, $\bar{\rho}_i$ is the average reflectance of the element marked by a given index, and $m = N/4$ is the number of four-reflection cycles. Denoting the average reflectance of the entire cavity as $\bar{\rho} = \sqrt[4]{\bar{\rho}_1\bar{\rho}_2^2\bar{\rho}_3}$, Eq. (6.10) for the intensity transforms to:

$$I = I_0\bar{\rho}^N/\bar{\rho}_2, \quad or \quad \log I = \log I(\bar{\rho}, N) = N\,\log\bar{\rho} + const. \tag{6.17}$$

If a test object of surface-averaged reflectance $\bar{\rho}_x$ is placed inside the bent cavity, the intensity becomes:

$$I_x = I_0\rho_{x,1}\,\rho_{1,1}\,\rho_{x,2}\,\rho_{2,1}\,\rho_{x,3}\,\rho_{3,1} + \ldots = I_0(\bar{\rho}_x\,\bar{\rho})^N/\bar{\rho}_2 = I_0\bar{\rho}_x^N. \tag{6.18}$$

Expressing all the results either on the direct or on the logarithmic scale, the reflectance under study, averaged over the object's surface or bulk and over the variety of angles of incidence, is:

$$\bar{\rho}_x = \sqrt[N]{I_x/I}, \quad or \quad \log \bar{\rho}_x = (\log I_x - \log I)/N. \tag{6.19}$$

Extending the number of light interactions with a test object in a spherical-mirror cell allows one to increase the measurement sensitivity to small losses resolved not only for narrowly directed radiation, but also for strongly diverted light. In the verification experiments [6.10, 6.11], the practically realized numbers of internal reflections were varied from 4 to 16 and up to 32. When studying a mirror with $\bar{\rho}_x \geq 0.995$, the reproducibility of the observed readings was maintained at ± 0.0003 with estimated random error $\Delta\bar{\rho}_x = \pm 0.0005$ [6.11].

Figure 6.9 illustrates the observed changes of surface-averaged specular reflectance for a dielectric mirror coating versus the state of polarization (S or P) of incident light and its angle of incidence (1 or 2). The high-reflecting mirror coating tested was made by alternating 27 layers of silicon dioxide and tantalum pentaoxide, deposited on a fused-silica superpolished substrate. The measured magnitudes and fitted curves represent reflectance values at two angles of incidence in the meridional plane for $\Theta = 8°$ and $\Theta = 30°$, marked 1 and 2, respectively, and at two states of polarization: one for each incidence angle – random and S polarization states at $\Theta = 8°$ (dotted lines), and random and P polarization states at $\Theta = 30°$ (solid lines). The resultant spectral narrowing for observed regions of high specular reflectance corresponds to detected interchange of phase thicknesses of coating layers at a greater average angle of light incidence (sagittal angles were not distinguished). The highest mean reflectance, 0.9996 ± 0.0002, at $\lambda = 520$ nm, was registered for the coating with 33 layers of Ta_2O_5/SiO_2 at the smallest angle $\Theta = 8°$ in the meridional plane. The study in the confocal White cavity of Fig. 6.8 of direct transmittance for a triple-layer antireflection coating on a glass slab provided the highest magnitude of the acquired transmittance, near the 0.985–0.990 level [6.11].

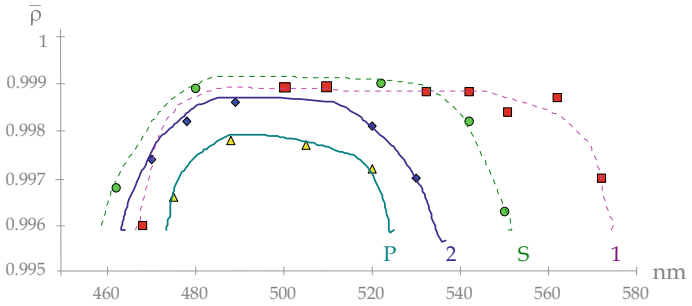

Fig. 6.9 Averaged values of spectral reflectance $\bar{\rho}$ for a multilayer coated mirror versus the wavelength in nm, state of polarization, and angle of incidence

6.2.1 *Long-Path Matrix Cells*

Owing to the focusing feature of the White cavity and its ability to tightly situate intermediate confocal spots among adjacent retroreflections, vast variations of the

cavity design for long optical paths are found applications for detecting atmospheric pollutants [6.12–6.25]. Simulating conditions of the upper atmosphere, cavities often operate at cryogenic temperatures and involve Dewar assemblies maintaining kilometer-long optical paths when needed [6.12, 6.13]. One example of prolonged White cavity with a 2-km path is shown in Fig. 6.10 [6.13]. Compared with the typical three-mirror design in Fig. 6.8, extra corner-mirror set M_4 is added, being formed from the plane lower and spherical upper mirrors, further forming an almost vignetting-free image of the first half of all reflection series, doubling the number of intracavity passes, and allowing one to form four rows of vertically displaced images on intermediate mirror M_2, suitable for matrix-detector arrays. The total cavity path length [6.13] was adjustable in 80-m increments from 60 m to 2540 m, but the maximum path length used was 1980 m, limited by vibration noise and stray light of nearly 1%.

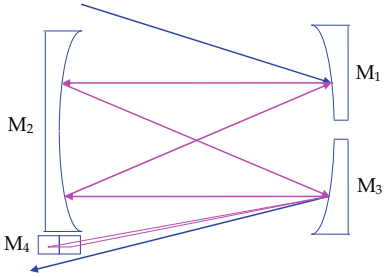

Fig. 6.10 Four-mirror modified White cavity (beam paths drawn are strictly illustrative)

Another aspect of creating the long-optical-path cell relates to the ability to discriminate among adjacent multiple reflections by setting focal points in horizontal and vertical lines and allowing the use of matrix detectors. Figure 6.11 depicts one version of such a design, generating a square lattice of light-source images while adding to the three-mirror version a focusing rooftop prism [6.15] instead of the mirror assembly in Fig. 6.10. This matrix approach is versatile in making a multireflection cavity function as a tapped delay line, with each tap setting an equidistant increment between neighboring reflection spots, allowing one to use measureable ratios of intensity among them for system calibration, determining the average cell-mirror reflectance, and providing absolute measurements (see

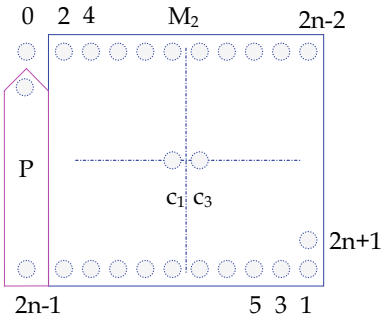

Fig. 6.11 Formation of focal-point lattice

Sect. 6.1). Figure 6.11 depicts focal light spots on the vertical projection of central cavity mirror M_2 and focal points c_1 and c_2 of mirrors M_1 and M_3 (see Fig. 6.8). The first two rows of 2n points are seen with the third row starting from the point $2n + 1$ created after the $2n^{th}$ reflection from lens-shaped rooftop prism P forming one vertical line of points $2n - 1$ and n, while the prism apex line is positioned in the plane of mirror M_2, all having the advantage of foci points not overlapping with each other [6.15].

An alternative approach with the goal of doubling the total number of intracavity reflections without the complexity of adding additional focusing mirrors while using a tunable laser source for outside air pollution detection is shown in Fig. 6.12 [6.16]. Mirrors M_1–M_3 of a three-mirror White cavity have 10-m radius of curvature and are made on quartz substrates dielectrically coated to 0.995 reflectivity in two wavelength regions: 616 nm of an argon laser and at 308 nm as its doubled frequency. Such a cavity design allowed up to 50 reflections in a laboratory environment, but an appreciably lower number in open air owing to turbulence. Corner mirror M_4 is used here to strictly retrace an outgoing light beam for the same cavity path to be measured via beam splitter BS, creating measurement and reference channels. A beam splitter of reduced size was used to limit beam wandering in the atmosphere by vignetting beam offsets but inducing an extra 75% loss of power. Nonuniformity of beams in the main and reference channels was further mitigated by placing detectors D_1 and D_2 inside integrating spheres S_1 and S_2. The spheres minimized the effects of interference noise due to multiple reflections in filters F_1 and F_2 placed in front of the respective detectors irradiated in each sphere by diffuse light. Third detector D_3 measured light transmitted by Reference Cell of the OH

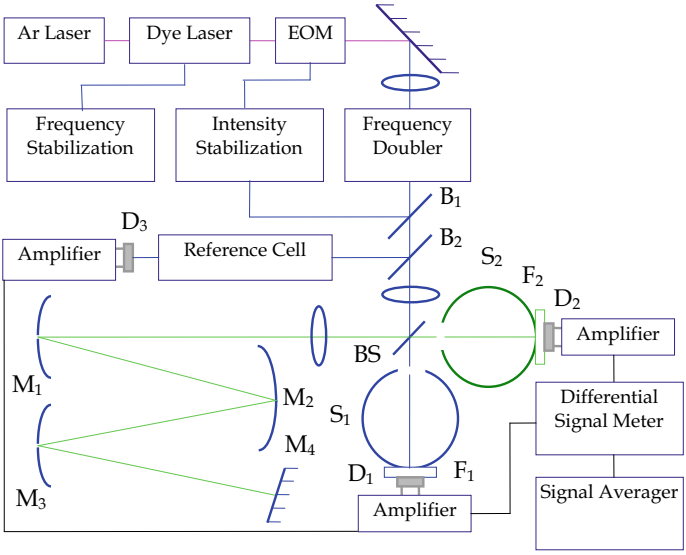

Fig. 6.12 Dual-path White multipass cell at light spot integration

content via splitter B_2, which with splitter B_1 was used for beam-intensity stabilization and concentration-sensitivity verifications. In the system's internal calibration, the differential signal between measurement and reference detectors, wired at opposite polarity, was initially zeroed by aligning the position of each detector on its sphere wall; therefore the specimen-induced signal was detected as the channels' differential imbalance, further amplified and averaged. One channel of the signal averager was used for the differential signal of detectors D_1 and D_2 and another was used for the reference cell channel containing a vapor-calibrated concentration of OH molecules. The detection sensitivity to OH absorption losses reached $3 \cdot 10^{-6}$ in a laboratory environment even with a 1-m-long absorption pass in the cavity, but was reduced to near $6 \cdot 10^{-5}$ for outside air for a multipass cavity absorption length of about 1 km [6.16].

Fourier-transform spectrometer-based system with a three-mirror confocal cavity having its measurement sensitivity enhanced by a scanning Michelson interferometer allowing time-multiplexing detection of all spectral components at a fixed resolution is depicted in Fig. 6.13 [6.17]. It used either a 2.25 or an 8.7-m base-cavity path, formed from four transverse passes each, with the small cavity providing a path of up to 81 m for 36 total-cell passes and the large one providing a path of 700 m for 80 cell passes. Each of the cells was sequentially used to measure the cavity reference signal when the cavity was filled with clean air and the same cavity signal for a pollution sample. The scanning IR Michelson interferometer consisted of spherical mirror MS focusing light from source S onto stable mirror MT in transmission, and onto scanning mirror SM in reflection from beam splitter BS, all paired with a White cavity of mirrors M_1–M_3. During one scan of interferometer mirror SM, creating a sine-wave modulation in the kilohertz range, the detected signal was digitized at the spectral resolution desired, with every scan repeated until the best signal-to-noise ratio was reached for the averaged scan result, providing the combined signal interferogram of the spectrum measured.

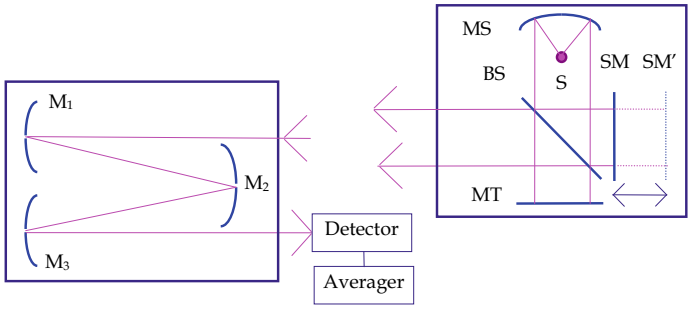

Fig. 6.13 Interferometer-based IR scanning system

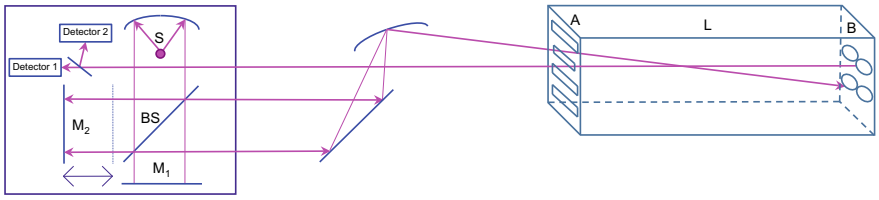

Fig. 6.14 Expanded-cavity interferometric IR scanning system

Another expanded-cell version of a Fourier-transform interferometer-based system with a large multipass cavity of eight mirrors is illustrated in Fig. 6.14 [6.14, 6.18]. In-focus side A of expanded cavity LC consisted of four rectangular mirrors (all 6.4 cm wide – three 32-cm long, one 28-cm long), accommodating entrance and exit beam apertures. The collecting side B of the cavity had four round mirrors 30 cm in diameter positioned 22.5 m from the mirrors on side A, which were gold-coated for high IR reflectivity, yielding the total cavity light path in kilometers. Such a large cell was used to detect reactive pollutants, allowing efficient separation of interference spectrums from water vapor, while for detection of nonreactive polluting species a 3-cm^3 volume cavity with a 115-cm-long path was deployed. Each cell was combined with a Michelson interferometer of 0.5-cm^{-1} spectral resolution and liquid-nitrogen-cooled detectors: InSb and HgCdTe for 2000–3900-cm^{-1} and 600–2000-cm^{-1} spectral regions, respectively. The effective detection sensitivity to trace pollutants in air was approximately $2 \cdot 10^{-11}$ [6.18].

Commonly in pollution-detection spectroscopy two identical cells are attached to a dual-beam spectrophotometer – to be filled with a pollutant in the measurement channel and with clean air in reference channel (see Chap. 4 for specific examples). When a large multipass cavity is used, especially with its light path to be stabilized and environmentally protected, it is practically beneficial to reuse a single cell in various configurations, thus allowing to make comparison measurements. Instead of referencing the pollutant-based reading to the clean-air one, referencing of the multipass signal can be made to the signal of a single pass of the same cavity via a tunable-mirror cavity for path-differencing [6.20]. Similarly to creating multiple reflections between variably spaced mirrors (see Fig. 6.1), the White cell can be tuned to have a single cavity path, consisting of four cavity steps among three mirrors, and to other multiples of 4 (Fig. 6.15). For the single cavity path, mirror

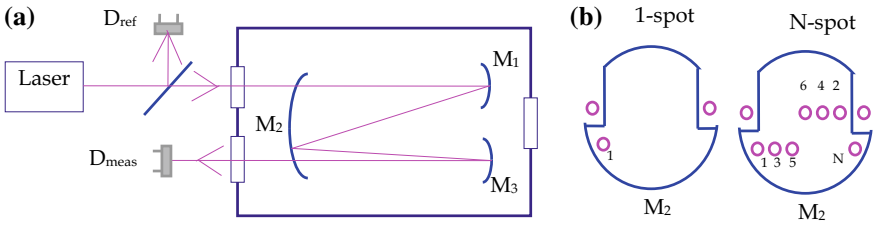

Fig. 6.15 Path-differencing in the standard three-mirror White cavity

M_3 is tuned to forward the incoming beam on exiting the cavity right after the first four passes in the three-mirror cavity space, making one focal spot on central mirror M_2 (Fig. 6.15a). Another position of mirror M_3 is tuned for the N-spot optical path for $2(N + 1)$ single passes via a cavity of length L (Fig. 6.15b). The ratio of the output beam intensity in the cavity of one and N light spots gives the total internal attenuation for the species under study via the optical-path difference: $\Delta L = 2\,(N-1)L$. Such a path-differencing technique utilizing a T-shape form of center mirror M_2 by cutting out the input and the output sections and also splitting intracavity images into two rows, which was first proposed in earlier work [6.19], was tested with a deuterium fluoride (DF) pulsed laser at 2631-cm^{-1} wavelength and 0.3-Hz pulse-repetition rate via a 25-spot multipass cavity capable of being repositioned into one-spot alignment with ±1-mm tolerance in 1-min intervals, resulting in 1% repositioning error. For the empty three-mirror cavity, the 25:1 path ratio provided 0.314 ± 0.003 average-reflectivity value for 24-path transversal of the cavity, having 10% intensity fluctuations for the beam focused on mirror M_2. To avoid focusing on mirror surfaces, the cavity was readjusted for middle-space collimation, reducing the outcome of intensity oscillations and respective system noise to within ±1% [6.20].

Another alternative design for expanding a matrix-forming multipass cavity is shown in Fig. 6.16, in which the cavity expansion is accomplished by combining two three-mirror cavities via another three-mirror cell and having a common mirror for all three cavities [6.21]. The first cell contains concave mirrors M_1, M_3 and M_2, the second cell contains similar mirrors M_3, M_5 and M_4, the third cell contains central mirror M_3 and two diagonally placed ones – M_6 and M_7. Mirrors M_6 and M_7 have the combined focal length of the other mirrors. Reflectors M_1 and M_3 and M_3 and M_5, being double mirrors for the standard design, are offset against each other to provide connectivity with diagonal mirrors M_6 and M_7 of the connecting cell. As in the three-mirror White cavity, the images in the expanded cell are formed on the surfaces of respective central mirrors M_2 and M_4, but after half of the total transverse path via the cavity, diagonal mirrors M_6 and M_7 turn the light path to mirror M_3, which returns it back on the same path, but from the opposite direction. Similar trajectories can be repeated by realigning the third-cavity set of mirrors [6.21].

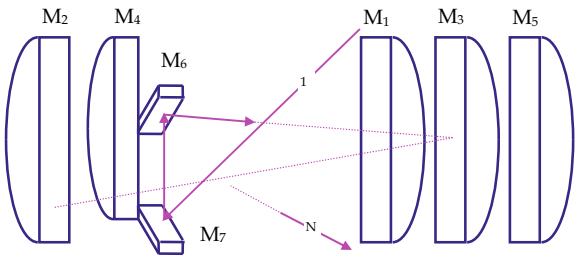

Fig. 6.16 Three interconnecting-cell based multipass cavity

The even number N of four-path cavity transversals depends on positioning of the middle mirror M_3 and diagonal mirrors M_6 and M_7, as well as on the ratio of the cavity and light-beam diameters D/d:

$$N = (D/d)^3/\sqrt{2} - \sqrt{2}/d + 2. \tag{6.20}$$

The largest attainable number of total cavity reflections is limited by the astigmatic elongation of intermediate images in every subcavity (Eq. (6.15)). To deal with broadening, a further cavity expansion can be done by replacing each of the two diagonal mirrors M_6 and M_7 by the set of three mirrors rotating the intermediate image by 90° every time light passes them [6.21].

The multimirror and matrix-imaging upgrades of the White cavity, while increasing the size and substantially lengthening the intracavity light path, lead to the related decrease of output image stability and higher aberrations due to the astigmatic image elongation. A compact approach [6.22] to advancing the multipass cavity involving a few large-aperture concave mirrors densely packaged on adjustable stages is illustrated by Fig. 6.17. One corner or rooftop mirror (see Figs. 6.9 and 6.10) is replaced by individually aligned narrow-field mirror M_4 of the same radius of curvature as center field mirror M_2, while another concave mirror objective M_5 is added to the opposite side of the cavity, along with dual mirror objectives M_1 and M_3. As in the confocal three-cavity White design, conjugated mirrors M_1 and M_3 are set at such an angle to each other that the separation distance between focal spots on the surface of mirror M_2 is half of the distance between adjacent images. The initial formation of images in this expanded cavity (Fig. 6.17a) is also identical to that in the original White cell, until the first two rows of the input spot images are formed, and the light beam reaches additional mirror M_4, from which it is redirected to auxiliary mirror M_5, reflected back to M_4, and forwarded to mirror M_1 as coming from another inlet window forming a secondary pair of rows. One version of the design adds two auxiliary mirror objectives M_5 and M_6 instead of one (Fig. 6.17b). These objectives may not necessarily have identical dimensions or focal distances as the main cavity mirrors and are conjugated in pairs, such as M_1 and M_6 and M_3 and M_5, but commonly all mirrors have the same radii of curvature [6.22].

The design of a two-field and three-objective mirror system was intended to improve the stability of images while keeping low image distortions with number $N_3 = 2(mk - 1)$ of transverse light passes, where $m = 1, 2, 3\ldots$ is the number of columns and $k = 2, 4, 6\ldots$ is the number of row pairs in the image matrix. The

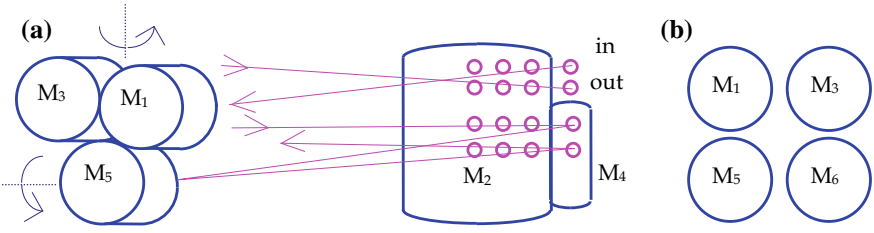

Fig. 6.17 Matrix-imaging three- and four-objective multipass cells

four-objective matrix system in Fig. 6.17b was designed to increase the energy density in the cavity via image superposition for number of passes $N_4 = (k - 1)(4m - 2)$, with double superposition of images occurring for $k \geq 4$, $m \geq 2$ when retracing the same matrix backward, assuming consequent interference noise can be disregarded. The largest number of targeted passes depends on the accuracy of mirror positioning, such as rotating and tilting the angles of mirror objectives (marked by arrows in Fig. 6.17), and constancy of angular steps, as well as factual variations of mirror curvatures and profiles. Other limitations for the number of sustainable passes come from aberration tolerances. For the exemplary cell in Fig. 6.17a, having radius of curvature of the mirrors $r = 1000$ mm, dimensions of field mirrors M_2 and M_4 of 100×100 mm^2 and 90×10 mm^2, respectively, and all three objectives M_1, M_3, and M_5 being 60 mm in diameter, the system tolerated nearly 100 passes for a 150×10 μm^2 input image with estimated astigmatic elongation on the periphery of the images not exceeding 0.8 mm for 218 passes analyzed [6.22].

One approach for tightening the internal multipass-cavity space utilizes flat field mirrors instead of concave ones (Fig. 6.18). The design [6.23] precedes the White cavity arrangement and uses four mirrors (concave M_2 and plane M_1, M_3 and M_4), while the later set is placed at the center of curvature of mirror M_2. Incident light focused on input mirror M_1 is reflected to mirrors M_2, M_3 and M_4 and again to mirrors M_2, M_3, and M_4, forming a pipe, until exiting in between right-angle-positioned mirrors M_3 and M_4. The cavity is aligned for the longest internal path when the right angle is tuned under 90° for the light path from M_3 to M_4 being parallel to horizontal positioning of mirror objective M_2, accommodating a high relative aperture, but with high losses due to vignetting by mirrors M_3 and M_4.

The concept of utilizing the V-shaped cavity approach with two concave and two flat mirrors which are spaced at 1.5-focal distance versus the common 2f- or so-called curvature-spacing is depicted in Fig. 6.19. The shorter spacing permits one to convert a four-single-pass cavity transversal into a six-pass path from the

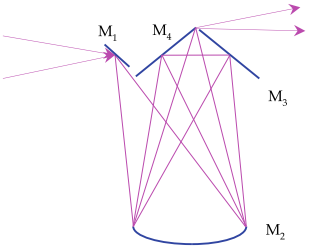

Fig. 6.18 V-shape four-mirror multipass cavity

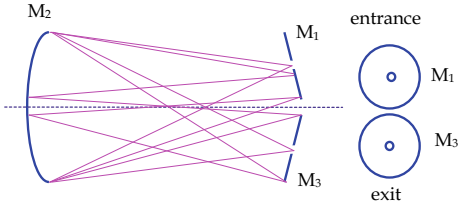

Fig. 6.19 Three-mirror V-shape six light-pass cavity

entrance to the exit via central holes in mirrors M_3 and M_4, obtaining the largest relative aperture reaching f/3.7 [6.24]. First three cavity passes via reflections from mirrors M_2 and M_3 form a twofold magnified image of the entrance spot on concave mirror objective M_2. The next three cell passes and reflections from mirrors M_1 and M_2 further direct the input light beam to exit via mirror M_3. On this six-pass trajectory, reflections from mirror M_3 produce radiation losses via the exit hole, requiring its relative area to be sufficiently small.

As the V-shaped cavity was designed to match high-resolution systems of large f-numbers, the three-mirror White cavity (Fig. 6.20) could be fitted into the parallel-beam compartment of a spectrometer [6.25]. The diverging light beam exiting output aperture 1 of spectrometer S is coupled by mirror-pair A, B into the cavity of mirrors M_1, M_2, M_3. The matching mirror-pair C, D, retaining the spectrometer throughput, forms the light beam emerging out of the cavity to detector D via slit 2. Such a parallel-beam propagating cavity was tested in eighteen-pass configuration with an FTIR spectrometer detecting air exhausts respectively at 6-, 9-, 100- and 4-ppm sensitivity to NO, NO_2, CO_2, and CO traces.

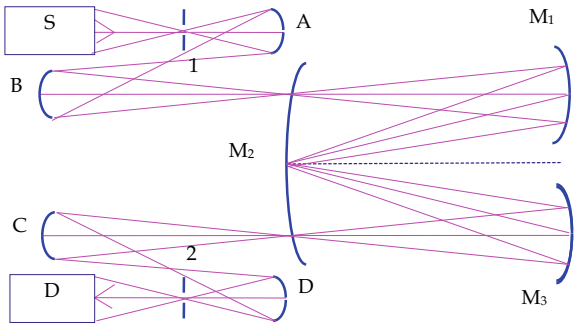

Fig. 6.20 Parallel-beam coupling of White cell

A version of the White cavity, almost eliminating astigmatic elongation for a single point of a chosen image with optimized settings of the image rows and columns [6.26] is illustrated in Fig. 6.21. The round entrance beam comes atop of mirror M_2

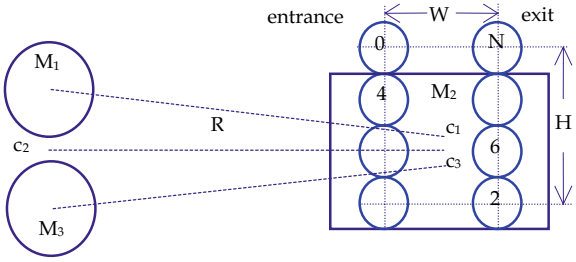

Fig. 6.21 Astigmatism-optimized setting of a White cell

(0 spot) and leaves after N transits over the cavity space, allowing for separation W of two image rows on the surface of mirror M_2. For the center of output image N, astigmatism should vanish for the optimized ratio of the row width W to height H:

$$W/H = \sqrt{(N+2)/3(N-2)}. \tag{6.21}$$

Balancing astigmatism for the inside and outside edges of the output image of radius r_{im} requires width $W = r_{im}\sqrt{(N^2-52)/48}$, therefore converting the image width-height ratio requirement to [6.26, 6.27]:

$$W/H = \sqrt{(N^2-52)/3\,(N-2)^2}, \tag{6.22}$$

where $H = 2r_{im}(N-2)/4$ is the row height. With the astigmatism balanced to have opposite signs at the inside and the outside edges of image N, the astigmatic elongation of images with row separation W by Eq. (6.22) versus rows packed at $W_d = 2r_{im}$ was about 5 times less for 82 passes [6.26].

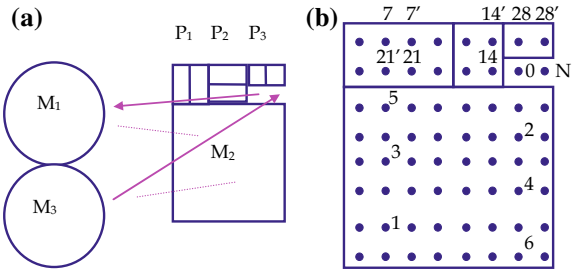

Fig. 6.22 Prisms-enhanced three-mirror cavity

To restrict image instabilities due to extended optical paths (see Figs. 6.10, 6.14 and 6.16), a White cavity may be enhanced by prism reflectors [6.28], similarly to the corner-cube reflector-based cell shown in Fig. 6.7. The confocal three-mirror (M_1–M_3) cavity is enhanced by three prism reflectors P_1–P_3 with light entering and leaving the cell under prism P_3 (Fig. 6.22a). Figure 6.22b depicts the positions of images from 0 to N, showing the shift within prism P_1 from point 7 to point 7′, for 56 focal spots on mirror M_2 for a total of 112 cavity passes for a 672-m-long light path for 6-m mirror spacing. An offset similar to that for prism P_1 (point 7 to 7′) is formed by prism P_2 (point 14 to 14′) and prism P_1 (point 21 to 21′), and switching to prism P_3 for points 28 to 28′, at which the beam returns parallel to the incoming beam and the cycle repeats, until at N = 56 the entered light leaves the cavity. Such a stabilized cell allowed to reach a nearly 3 ppb trace-sensitivity level for Fourier-transform IR spectroscopy [6.28]. The function of the prisms in such a design is to compensate for an angular displacement caused by a mirror misalignment, after which each progressive reflection deviates the beam further from its optical path. In the conjugated points, such as 7-7′, the beam is reflected in the same direction, but at the opposite angle, compensating for the angular offset in the prism plane, and repeating it in other prisms.

A drawback of angular-error compensation by prisms is associated with factual divergence of a light beam entering the cavity, which can eventually lead to much higher attenuation than predicted for the paraxial beam. An enhancement of the prism-based design can be made using multiple-facet reflectors as schematically illustrated in Fig. 6.23 for each of two reflectors behaving like four different prisms [6.29]. Two reflectors could replace prisms P_1 and P_2 in Fig. 6.22, if they satisfy the constraints for retaining the beam inside the cavity. Ultimately, introduction of plane surfaces into any White cavity requires detailed ray tracing to be performed for the entire cell not to have extreme throughput losses or aberration distortions.

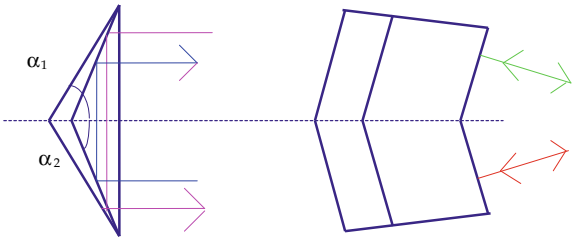

Fig. 6.23 Multiple-facet prism reflectors

Figure 6.24 depicts a modified and experimentally verified version of the all-concave two-field mirror and three-objective mirror cavity, shown in Fig. 6.17 [6.31], upgraded to primarily separate input and output beams to opposite sides of the narrow field mirror, instead of having them adjacent to each other [6.30]. One radius of curvature set for all mirrors defines the cavity length, with the center of curvature for main field mirror F_1 located between main objective reflectors O_1 and O_2 as in the three-mirror design (Fig. 6.8), while that for the added narrow field mirror F_2 is between O_1 and O_3 in the plane, bisecting them in the same way as does the center of F_1. In the setting illustrated in Fig. 6.24, the 36 images on field mirrors correspond to 72 transverse passes of the cavity, identified as optimal from signal-to-noise ratio considerations for a total light path of approximately 128.5 m and average reflectivity of all five mirrors around the $\bar{\rho} = 0.9865$ level, allowing for that cavity, attached to a Fourier-transform IR spectrometer, to reach 20–30 ppb by volume (ppbv) short-term sensitivity, and nearly 50–80 ppbv with the system fan turned on [6.31].

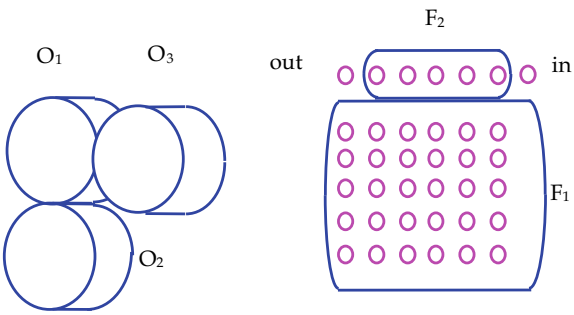

Fig. 6.24 Modified three-objective multipass cell

6.3 Mirror Waveguides

With the three-mirror cell approach, a beam of light enters and exits the multipass cavity along its opening section and the lowest achieved angles of incidence are limited by the cross section of the cavity and the beam. To reduce the angles of incidence, the cavity entrance and exit are made on opposite sides of the single mirror. To enhance handling of diverging light beams at the narrowest separation possible, a system of multiple reflections can be constructed as an open resonator formed by two concave mirrors. From the standpoint of transformation of radiation energy, a coaxial pair of mirrors of the same radius of curvature R is similar to a symmetrical lens waveguide [6.32]. For an off-axis point on one mirror of that waveguide cavity with coordinates X_0, Y_0, any paraxial beam incident at such a point in a direction making angles Θ, Ψ to the cavity axis in meridional and sagittal planes after N reflections has coordinates [6.32]:

$$X_N = X_0 \cos N\varphi + \sqrt{\frac{d}{4f-d}}\,(X_0 + 2f\ \tan\Theta)\sin N\varphi;$$
$$Y_N = Y_0 \cos N\varphi + \sqrt{\frac{d}{4f-d}}\,(Y_0 + 2f\ \tan\Psi)\sin N\varphi, \qquad (6.23)$$

where d is the period of the waveguide or the distance between its elements, $f = R/2$ is the focal length of the cell mirrors, and φ is the polar angle of an intermediate source image: $\cos\varphi = 1 - d/2f$.

Any transitional image is located inside the cavity while the polar angle φ remains real and thus $|\cos\varphi| \leqslant 1$ and $0 \leq d \leq 2R$. In the configuration illustrated by Fig. 6.25, beam intersections with each of two mirrors form an ellipse of the respective coordinates [6.32, 6.34]:

$$X_N = A\sin(N\varphi + \alpha), \quad Y_N = B\sin(N\varphi + \beta). \qquad (6.24)$$

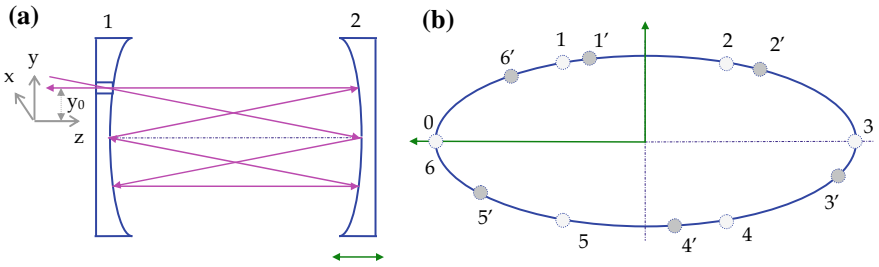

Fig. 6.25 Light path inside two-mirror waveguide (**a**) and transformation of image positions versus waveguide length (**b**)

Semiaxes A and B of each ellipse and ellipse orientation parameters α and β are identified as [6.32]:

$$\begin{aligned} A^2 &= [4f/(4f-d)]\left(X_0^2 + d\,X_0 \tan\Theta + d f \tan^2\Theta\right), \\ B^2 &= [4f/(4f-d)]\left(Y_0^2 + d\,Y_0 \tan\Theta + d f \tan^2\Psi\right); \\ \alpha &= \arctan\left\{\sqrt{(4f/d)-1}\,[1/(1+2f\,\tan\Theta/X_0)]\right\}, \\ \beta &= \arctan\left\{\sqrt{(4f/d)-1}\,[1/(1+2f\tan\Psi/Y_0)]\right\}. \end{aligned} \tag{6.25}$$

A beam of light entering such a resonator through a penetrating aperture or an unreflective zone E in one of the mirrors reaches the same entrance region after an N/2 complete passes or after N single passes of the resonator at: $2N\varphi = 2\kappa\pi$, where $\kappa = 1, 2, 3\ldots$ The ellipse turns into a circle if both semiaxes A and B are equal for the angular constants differing exactly by π/2: $\alpha = \beta \pm \pi/2$. The maximum realized number of reflections on each mirror is then defined by the beam diameter D and by its circumference: $L = 2\pi A$. For example, at $\Psi = 0$, a circle of radius A is formed at $Y_0^2 = X_0^2[(4f/d) - 1]$; $A^2 = X_0^2 + Y_0^2 = X_0^2 4f/d$; $\tan\Theta = -2X_0/d = -A/\sqrt{f\,d}$. After the first N reflections which are formed on the ellipse or circle, the spots repeat the round. That causes interference of crossing light beams, restricting the number of attainable reflections for most laser applications.

Alteration of the number of reflections within each closed cycle for light to leave the cell via the entrance aperture can be realized by changing the distance *d* between two mirrors. In the concentric configuration d = f, $\varphi = \pi/3$; thus, there are six waveguide passes before a light beam exits through the cell entrance opening (Fig. 6.25). The displacement of one of two mirrors into confocal setting d = 2f ensures coincidence of entrance and output images after each four passes corresponding to three mirror reflections. The total number of passes N and the azimuth angle φ between adjacent intersection points providing the beam closure condition: $N\varphi = 2i\pi$, are:

$$N = 2(2i+1); \quad \varphi = 2i\,\pi/N = [(N-2)/(2N)]\pi, \tag{6.26}$$

where i = 1, 2, 3…. Since $\cos\varphi = 1 - d/(2f)$, the distance d_N related to any closed-cycle (reentrant) optical path of N light passes in such a spherical mirror waveguide becomes:

$$d_N = 2f\left[1 - \cos\left(\frac{N-2}{2N}\pi\right)\right]. \tag{6.27}$$

Here the closed-path distance d_N asymptotically tends to the mentioned confocal configuration at the limit $N \to \infty$. If d = 2f, the ellipse is closed at N = 4, requiring one turn of the light spots.

The number of light passes via the cavity needed to reach a specific sensitivity of the loss measurement is defined by the optical losses to be resolved. Assuming that

every action of light entering or exiting via an opening is maintained with no additional losses, the total attenuation factor for the filled cavity becomes $\gamma = \bar{\rho}^N = (1 - \bar{\chi})^N$. Here $\bar{\chi}$ is the average loss for a given wavelength for a single reflection or for a single pass having the medium under study inside the waveguide. Hence, the cavity's relative sensitivity to the total optical loss studied is equivalent to:

$$\frac{\Delta\bar{\chi}}{1-\bar{\chi}} = \frac{1}{N}\frac{d\gamma}{\gamma}; \quad \frac{\Delta\bar{\chi}}{\bar{\chi}} = \pm\frac{\Delta\gamma}{\gamma}\frac{1}{N}\left(\frac{1}{\bar{\chi}} - 1\right). \tag{6.28}$$

To reach attenuation $\Delta\gamma/\gamma = 10\%$ at $\bar{\chi} = 1 - \bar{\rho} = 0.005$, near 199 reflections are required, leading to average cavity-reflection loss or inserted-loss sensitivity $\Delta\bar{\chi} = N^{-1}\Delta\gamma/\gamma = 0.1 \cdot 0.005 = 0.05\%$.

As for other cavities, the higher is the number of cavity passes, the greater is the sensitivity not only to losses, but also to cavity misalignments. From Eqs. (6.23) and (6.27), the relevant errors are:

$$\Delta X_N = -\frac{N^2}{2}\frac{X_0}{2df - f^2}(\Delta d)^2; \quad \Delta Y_N = \frac{NY_0}{2f - d}\Delta d. \tag{6.29}$$

For working distances $f \leq d \leq 2f$, the absolute magnitudes of errors are given by [6.32–6.34]:

$$|\Delta X_N| \leqslant \frac{N^2 X_0}{6f^2}(\Delta d)^2; \quad |\Delta Y_N| \leqslant \frac{NY_0}{2f}|\Delta d|. \tag{6.30}$$

If a light beam enters and leaves the cavity after the N^{th} pass via the opening, it can be shown [6.33] that the positions of the images for the first and the $(N-1)^{th}$ transformation by cavity mirrors are independent of the number of passes. Thus, $x'_{N-1} = x_0/f + x'_0$ and $y'_{N-1} = y_0/f + y'_0$. For the simplest confocal match: $d = 2f$, these two images are turned by $\pi/2$ in the x-y plane, the entering and exiting spots on mirror 2 are symmetrical: $x'_0 = -x_0/2f$, $y'_0 = y_0/2f$; $x'_{N-1} = x_0/2f$, and $y'_{N-1} = x_0/2f$, and the spot displacement $\Delta\ell$ depends on the length ℓ of the optical part inside such a cavity [6.34]:

$$\ell = Nd + \frac{X_0^2}{4f - d}\left[\sum_{m=1}^{N}\sin^2 m\varphi + \sum_{m=1}^{N}\sin^2(m-1)\varphi\right]_{\substack{2f \cong d; \\ \varphi \approx \pi/2}} Nd + \frac{NX_0^2}{4f - d}. \tag{6.31}$$

Here the displacements are considered to be relatively small and are approximated as $\Delta\ell \cong N\Delta d$.

Interference among consecutive reflection cycles can be prevented, while also increasing the number of cavity passes, if after each loop the ellipse is displaced

around the cavity axis. A purposely created astigmatism in one or both mirrors [6.33] via unequal focal points: $f_x \neq f_y$, in x–y orthogonal planes causes inequality for *x-y* spatial frequencies and precessing of the ellipses:

$$\cos\varphi_x = 1 - d/(2f_x); \quad \cos\varphi_y = 1 - d/(2f_y). \tag{6.32}$$

As a result, subsequent spots of light intersection with the mirrors precess across the cavity's cross section, not only preventing interference, but also significantly increasing the path length, as long as each intermediate spot does not overlap with the entrance and the exit ports of the cavity. Actual transformation of every light beam projection onto the orthogonal $x-y$ plane depends on the way the perturbing mirror deviates the beam, as well as on the specific f_x/f_y ratio and parameters of the beam and the waveguide. A similar effect can be achieved by inserting into the waveguide an auxiliary mirror, deflecting the light beam and rotating the precessing ellipse around the cavity axis [6.33]. Subsequent experiments in a cell made of 3-m-spaced, 7.5-cm-diameter, 10-m-radius mirrors on 1.25-cm-thick fused-silica substrates initiated a 1000-pass folded line, traversing a 3-km path length with 10-μs delay at 10-dB power loss in the entire waveguide [6.33]. Reflectance measurements in the waveguide of two gold-coated 100-mm-diameter, 497-mm focal length mirrors via a least-squares fit of logarithmically plotted pulse averages of a grating-tuned deuterium-fluoride (DF) laser at $\lambda = 3.9843$ nm versus the number of passes resulted in an average reflectance of 0.9839 for $N_{i,j} = 10$, 50 and of 0.9844 for $N_{i,j} = 14$, 154 [6.34]. Other versions of multipass cavity may include a single toroid-mirror cell, which optical pathlength is given by its incidence angle [6.86], a confocal [6.87] or aberrated cell [6.88].

Another advantage of either an astigmatic-mirror cavity or an auxiliary-mirror cavity for rotating a precessing ellipse of images is in filling the cavity space more tightly, with evenly and wider spaced images, and realizing a higher volume density than in a regular three-mirror White cavity, though requiring extreme precision in mirror manufacturing tolerances. One way of compensating for mirror tolerances is in adjusting the cavity spacing and rotating one mirror versus the other [6.35, 6.36]. Errors in mirror radii for a given set of astigmatic mirrors may be compensated for by a combination of rotation and separation of two mirrors reaching various reentrant patterns identified by the light trajectories. A central-input 3.2-liter (l) cell was made of astigmatic 7.6-cm-wide aluminum octagon mirrors as an 8.655 cm^2 cylinder of 1.4-l illuminated volume for a 5-cm-wide beam and 100-m pass length via 182 total passes. The cell was coupled to a tunable rapid-sweep diode laser, operating in the 4.5- and 7.5-μm wavelength regions at 30-Hz data acquisition. A visible-trace coaligned laser was utilized to realign the cell for reentrant patterns at 90, 182, 274, 366, and 454 passes measuring the cell's transmittance: the 182-pass transmittance was 20%, yielding 99.2% average mirror reflectivity [6.36].

In view of rather tight tolerances for astigmatic mirror cells, even with rotation and variable-spacing capabilities, by limiting the number of the attainable reentrant conditions for the central-input type cells, one can use somewhat less demanding cylindrical mirror pairs [6.37] or cylindrical–spherical mirrors in the near reentrant

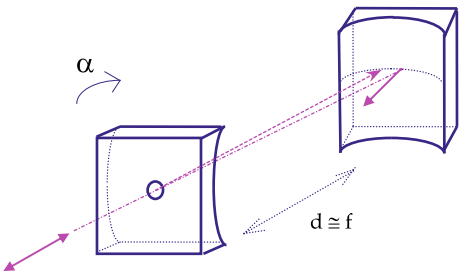

Fig. 6.26 Near re-entrant mirror waveguide cell

cavity configurations [6.38]. Figure 6.26 depicts the design of a cylindrical-mirror cavity in which each mirror principal axis is orthogonal to another at unequal focal lengths $f_1 \neq f_2 \approx f$. This way, the x and y cavity axes contain one curved and one flat surface at $f_x \neq f_y$. Dense Lissajous patterns may be formed for small mirror reflection spots, but for a limited number of reentrant solutions, which essentially are not required for photoacoustic loss measurements (see Chap. 9) since light intensity is not measured, thus allowing for more cavity passes [6.37]. Waveguides of two 5-cm square cylindrical mirrors – a set having 64.8-mm focal length with 4.7-mm-diameter central hole in the input mirror – and either unequal cylinders of $f_1 = 64.8$ and $f_2 = 51.9$ mm or a cylindrical–spherical set with $f_c = 64.8$ mm and $f_s = 100$ mm were tested with a He–Ne laser at 632.8 nm [6.38]. For not rotated mirrors, the 26-pass spot pattern was obtained at the mirror distance $d/f = 0.88$, and rotation of the input mirror by $\alpha \approx 9°$ led to $N = 122$ passes.

For certain waveguide configurations, it is desired to convert the ellipses of light spots into circles, allowing use of the cavity volume for adding tools, such as cylindrical electrodes in Stark-modulation spectroscopy [6.39]. Rewriting the reentrant conditions of Eqs. (6.26) and (6.27) in the form: $N\varphi = 2\pi M$, $\varphi = 2\pi M/N$, for $M = 1, 2, 3\ldots$, the reentrant number of passes becomes: $N = 4\,M \pm K$ for $K = \pm 2, \pm 4\ldots$, where positive K corresponds to $d < 2f$ and negative K corresponds to $2f < d < 4f$ [6.37, 6.38]. Given that at confocal setting $d = 2f$ and $K = 0$, the input beam entering the cell at coordinates $x_0 = 0$, $y_0 = 1$ with slopes $\Theta = \Psi = 45$ makes the first spot at $x_0 = 1$, $y_0 = 0$ and leaves the cell after four internal passes. Obviously, only sets of the lowest N numbers are of use in various N, M configurations before light exists the waveguide. For relatively large slopes, $d < 2f$ configurations can lead to large beam spots and walk-offs on mirror edges, but for small angular displacements and large focal lengths, high values of N with small numbers of spot orbits may be reached. For $f = 5500$ mm at $d = 466.4$ mm, a 32.5-mm-radius spot circle was realized at $N = 86$ and $M = 4$ by injecting light at $\Theta = 1.13°$ and $\Psi = -0.19°$ via a 4.5-mm hole, having approximately 40-m total cavity light path at 4.6-mm spot separation [6.39].

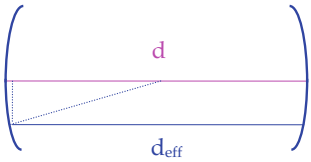

Fig. 6.27 Effective distance in a cell

For waveguides assembled from highly curved spherical mirrors having light reflection spots placed distantly from the optical axis as in Fig. 6.27, the paraxial approximation of light propagation via the waveguide cell is invalid since the effective distance d_{eff} between mirrors becomes shorter, owing to the circle of spots being positioned on the effective radius: $R_{eff}^2 = R^2 - R_{circle}^2$. Substituting for d_{eff} at $d/f = d_{eff}/f_{eff}$ in Eq. (6.32) leads to [6.40]:

$$d_{eff} = d - 2\left(R - \sqrt{R^2 - R_{circle}^2}\right);$$
$$R = 2f = \frac{8d + (d/f - 4)\sqrt{\left(4d^2 + R_{circle}^2 d/f(d/f - 8)\right)}}{d/f(8 - d/f)}. \tag{6.33}$$

Equation (6.33) accounts for a finite spot-circle radius letting one to set the d/f ratio via N, M, and R_{circle}. For the cell allowing multiple concentric spots to coexist and thus permitting studies of various species without readjustment of that radially symmetric cell requires the cell mirrors to be elliptic with surface profile z(r) being a function of the elliptical surface radius r satisfying the following equation [6.40]:

$$z(r) = 0.5\left(d - \sqrt{d^2 - (d/f)r^2}\right). \tag{6.34}$$

6.4 Raman Scattering: Enhancement of Sensitivity and Mitigation of Fluorescence

The Raman and Brillouin phenomena of weak molecular scattering, caused by interaction of light with molecules in quasi-transparent media – absorbed and reemitted at Raman frequencies, elastically scattered by individual molecules, or inelastically diffracted on ultrasonic oscillations due to acoustic perturbations of molecules as one ensemble, by the nature of each effect dictates using a multiplication schematic to measure the intensity of light scattered by each phenomenon. Laser irradiation is practically always required to excite a detectable signal, Stocks-shifted to Raman or Brillouin frequency of emission or diffraction along with the highest possible wavelengths resolution, separating a minute spectral shift at the Stocks or anti-Stokes frequency from Raleigh scattering at the excitation wavelength plus from broad-spectrum fluorescence in Raman studies and from otherwise negligibly-low amplified spontaneous emission of the laser used in Brillouin spectroscopy (see paragraph 12.2).

6.4.1 Multiplication Schemes

In Raman spectroscopy expanding a number of multiple passes of light in a multipass cavity allows to substantially enhance the sensitivity of measurements to such intracavity losses as scattering and absorption, while sensing the intensity of the light interacting with the cavity mirrors and its interior. In distinguishing the Raman signal the enhancement needs to be made not only by multiplying the radiation scattered in 4π space, which could be done via an integrating sphere, but also to each single interaction of pumping laser radiation with Raman-scattering substance. The two-mirror waveguide reviewed earlier, combined with a surrounding set of multiple detectors for the radiation scattered into 2π angle, illustrates the approach (Fig. 6.28). The total scattering factor is measured by interpolating adjacent detected scattering signals to spatial regions not viewed by the detectors or via adding a scanning capability [6.41]. Another enhancement when using the waveguide cavity for Raman scattering is due to refocusing of the probe beam helping to enhance the Raman gain [6.42, 6.43].

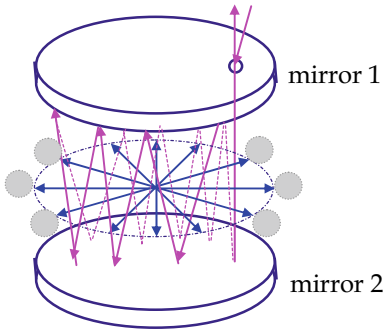

Fig. 6.28 Enhancement of scattering signal

The symmetrical waveguide depicted in Fig. 6.28 was itself capable of changing the cavity length d from f to near $2f$, with the number of reflections successfully maintained between six to 170 [6.34]. Sulfur dioxide in a gas mixture of SO_2 at $37.1 \cdot 10^3$ Pa and of N_2 at $96 \cdot 10^3$ Pa was studied in that cavity. A beam of light from a DF excimer laser at $\lambda = 3.9843$ μm entered the cell via a 2-mm-diameter entrance aperture, being displaced by $X_0 = 42.5$ mm from the cavity axis. The cavity consisted of gold-coated off-axis paraboloids with focal length $f = 0.5$ m. Each detector registered an average power of 20 laser pulses with nearly ±0.5% random error. The average two-mirror reflectance ρ and linear absorption coefficient α of a gas mixture were determined via the slope of the logarithmic dependence of the average reflectance $\bar{\rho}$ upon a number of reflections (see Eqs. (6.16)–(6.19)). That number changed between ten and 50 at corresponding distances ℓ of 10.99 m and 46.78 m. The measured magnitudes of ρ and α were, respectively, $\bar{\rho} = 0.9844 \pm 0.0002$ and $\bar{\alpha} = (0.0866 \pm 0.0004)$ m^{-1}. Displacement of light spots did not exceed ±0.1 mm even for 102 reflections and $\ell \cong 102$ m. In the cavity made with spherical mirrors having 100-mm radii of curvature, the number of reflections reached 66 for images of diameter 1.5 mm and for $\Delta\ell = \pm 0.2$ mm [6.34]. Multilayer dielectric ZnS–cryolite ($NaALF_6$) mirrors having radii of

curvature of 10 m and diameters of 75 cm were also measured in an astigmatic waveguide [6.33]. An enforced $f_x - f_y$ foci difference within a few $\lambda = 633$ nm wavelengths of a He–Ne laser was sufficient to maintain 168 reflections inside that waveguide with distance $d = 3$ m between mirrors. The highest measured average reflectance approached 0.998 ± 0.0005 [6.41].

Figure 6.29 illustrates a laser system for Raman-scattering detection which uses spectrally resolved polarized laser light at orthogonal excitation–observation directions, with Dove prism P_2 rotating the Raman scattering plane out of the excitation and Rayleigh scattering plane set by prism P_1 [6.45]. The concept represents a straightforward approach of increasing the sensitivity to Raman scattering by raising the incident power density of light excitation directly via a source inside a resonator of a laser [6.45] or via a multireflection cell of mirrors M_1, M_2 directing a focused retroreflected beam to pass by the observation region multiple times [6.46].

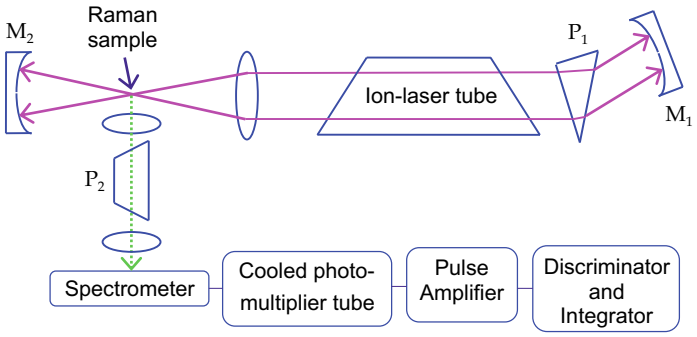

Fig. 6.29 Intraresonator excitation for Raman scattering

A version of Raman-scattered signal enhancement is depicted in Fig. 6.30, having linearly polarized light passing via a cavity consisting of a two-concave-mirror cell and a four-concave-mirror cell – with the excitation in one direction and Raman scattering viewed in the transverse direction [6.45]. Crossing states of polarization of incident laser light and the observed scattered light allow one to minimize Rayleigh scattering, which along with stray light could be intense.

The laser excitation beam enters and exits the waveguide cell of mirrors 1 and 2 via Brewster-angle windows BW, experiencing several interactions with a gas

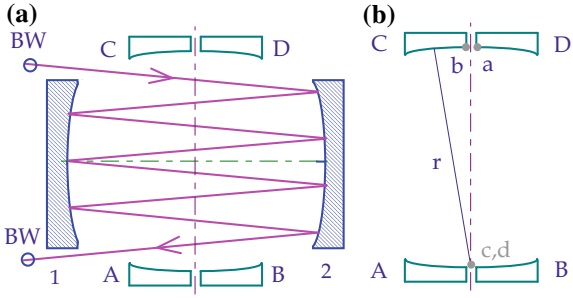

Fig. 6.30 Orthogonal excitation and observation of Raman scattering

filling the cell. Another side of the cavity is formed by the cell of mirrors A, B, C, and D, all of radius r, while mirrors C and D have a common center c,d forming one spherical surface, but the centers of curvature a and b of mirrors A and B are crossed, letting one reaching sufficient sensitivity to observe Raman scattering excited by cw laser light. A more efficient concept of focusing excitation light and collecting Raman scattering can be realized in multireflection cells using elliptical mirrors [6.47]. First, a two-mirror cell, consisting of identical on-axis ellipsoids, therefore letting a beam of exciting laser radiation enter the cavity at the maximum divergence angle φ and exit after a number of internal reflections sequentially focused by cell mirrors with foci f_1 and f_2, is shown in Fig. 6.31a. A light beam incident on mirror 2 via its focus f_2 at radius r_2 reaches mirror 1 via the second focus f_1 at radius $r_1 = r_2(1 - e)/(1 + e)$, where $e = c/a$ is the ellipse's eccentricity. The maximum angular aperture φ, as the difference of the maximum and minimum angles φ_0 and φ_1, and f number F are related as $1/2 \cdot \tan(\varphi/2)$ [6.47]:

$$\tan\varphi = 2ar_2e\left(1-e^2\right)/\left(a^2(1-e^2)^2 - r_2^2e^2\right); \quad F = a\left(1-e^2\right)/2r_2e. \tag{6.35}$$

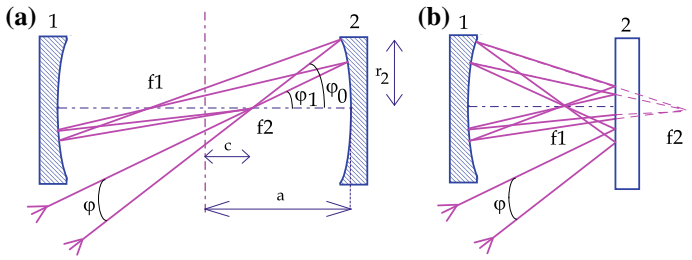

Fig. 6.31 Multiple reflection cell for Raman scattering

For the width of the first image of the incident beam focused at f_2 defined by the Airy diffraction circle of diameter $d_0 = 2.44\lambda F$ [1.1], the second image in focus f_1 has diameter $d_1 = d_0M$, where M is the ellipse's magnification: $M = (1 + e)/(1 - e)$. Subsequently, the diameter of the N^{th} image is defined by a progression:

$$d_N = d_0M^N, \; N = 0, 1, 2, \ldots, \tag{6.36}$$

with the number N (integer) of internal passes experienced by a beam entering the cell given as:

$$N = INT[\ln(d_N/d_0)/\ln M]. \tag{6.37}$$

If the N^{th} image is larger than $D = 4c \cdot \tan\varphi_1$, light escapes the cell as a cone at half-base angle φ_0:

$$D = 4c \cdot \tan\varphi_1 = 4cr_2/\left(c + a\sqrt{1 - r_2^2/(a^2 - c^2)}\right). \tag{6.38}$$

Figure 6.31b illustrates a single-focus ellipsoid mirror-based system with a flat second mirror imaging the second focus of the ellipsoid in reflection to coincide with the first one. Owing to the relatively small image sizes of the retroreflected light spots for eccentricity e below 0.1–0.2, the system allows reaching a sufficiently high number of reflections – 32 in an experimentally confirmed cavity, despite ellipsoid-mirror systems being susceptible to coma aberrations [6.47]. Figure 6.32 shows the dependencies of the image diameters and N and F versus eccentricity e.

Specific difficulties of using the ellipsoid-mirror systems are defined by the very low eccentricity e at which high numbers of intracavity reflections are achieved, and

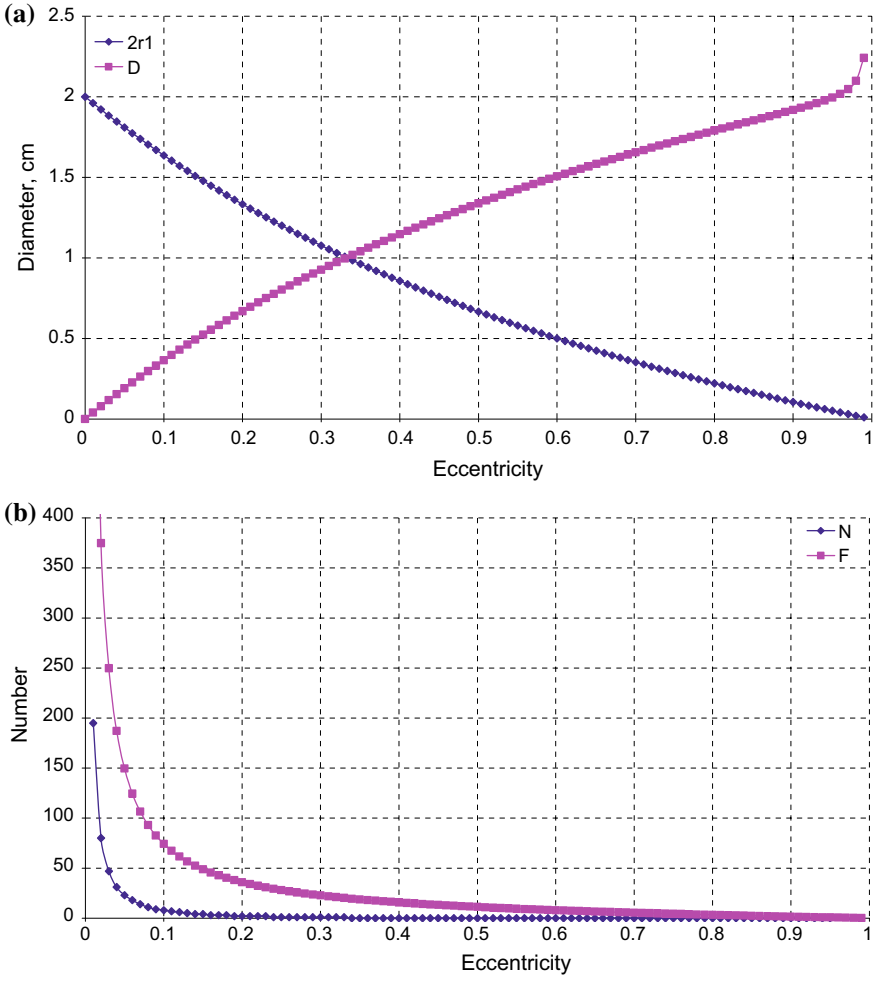

Fig. 6.32 **a** Diameters of the reflected $2r_1$ and escaping D beams in ellipsoid-mirror cavity at $r_2 = 1$ cm. **b** Number of reflections N and f/number F in ellipsoid-mirror cavity at semiaxis a = 15 cm

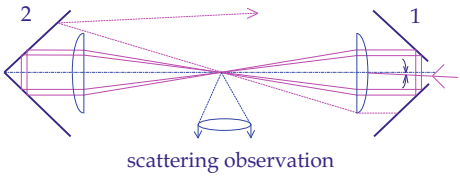

Fig. 6.33 Focusing light-trap with on-axis and off-axis mirror sets

not necessarily high spatial resolution. Another design of the focusing light-trap cell, giving higher resolution at a lower intensity gain, is shown in Fig. 6.33 [6.48]. The cell consists of two corner-cube mirror assemblies – one on-axis and another slightly off-axis – combined with a pair of focusing lenses.

On-axis mirror pair 1 is assembled having one circular opening for the laser beam to enter the cavity and experience multiple reflections, while exiting the cell over its traverse side (dotted line). Mirror set 2 is assembled to be off-axis – focusing and refocusing the beam after four reflections and the same number of transmissions via each surface of two plano-convex lenses, reducing latent spherical aberrations. After the series of reflections and transmissions the beam intensity I_0 transforms to:

$$I = I_0\left(\tau^2 + \tau^6\rho^2 + \tau^{10}\rho^4 + \ldots\right) = I_0\tau^2\left(1 - \rho^{2m}\tau^{4m}\right)/\left(1 - \rho^2\tau^4\right), \qquad (6.39)$$

where τ and ρ are the single surface transmittance and the single mirror reflectance of each lens and mirror, respectively; $m = 1, 2, \ldots$ is the number of intracavity reflection–transmission cycles. In the derivation of Eq. (6.39), each lens is presumed to be thin with no scattering or absorption losses.

Figure 6.34 exemplifies the intensity gain to be achieved in the lens–mirror light trap versus the cavity losses due to imperfect mean mirror reflectance ρ and lens

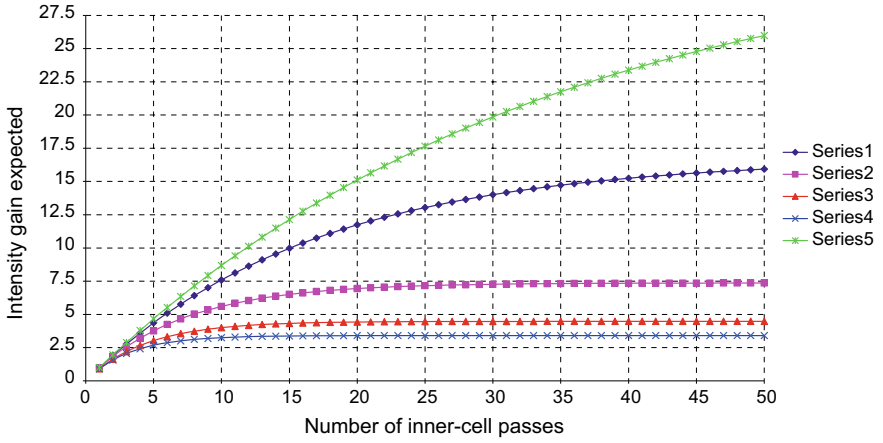

Fig. 6.34 Intensity gain in mirror-lens cell: 1 − r = t = 0.99; 2 − r = 0.95, t = 0.99; 3 − r = 0.99, t = 0.95; 4 − r = t = 0.95; 5 − r = t = 0.995

surface transmittance τ. An intensity gain near 20 was realized in a 1.1·0.3·0.3-mm^3 focal volume utilizing continuous-wave (cw) light and high-reflectivity for mirrors and antireflection coatings for lens surfaces with $\rho \approx \tau \approx 0.998$ at $\lambda = 514.5$ nm [6.48]. Experimental verification with a pulsed cavity-damped argon-ion laser provided a signal-to-noise ratio improvement of near 30, though the mirror–lens cell intensity gain was limited to 15 [6.49].

One obvious disadvantage of the mirror–lens combinational cell designs seen in Fig. 6.33 is in placing the lens surfaces inside the multiple reflection cavity, that can cause uncontrollable losses, limiting the sensitivity to Raman scattering, as illustrated by Fig. 6.34, especially if the surface quality deteriorates, when there is contact with gases inside the cell. Figures 6.35, 6.36, 6.37, 6.38, 6.39 and 6.40, showing adaptations of a configurable and tunable multipass cavity design, reveal other design versions for measurements of Raman scattering and absorption-plus-scattering losses inside the cavity [6.50]. Every design version provides for reconfiguration and resonant tuning, as well as for pulsed- or cw-light excitation during Raman scattering measurements. The first version of the design in Fig. 6.35 combines corner-cube like mirrors and confocal lenses with semitransparent mirror coupler C and high-reflectance mirror M forming the cell, serving as a semitransparent resonator in reflected light (see Sect. 8.4 for the functionality of such a resonator). Coupler C and mirror M provide coupling of the beam and reconfiguration for the entire cell by rotating the mirror positions around the axes (see the dashed lines) the cell is uncoupled for background testing, coupled for Raman scattering measurements, or recoupled for intra-absorption testing.

Configuration *a* in Fig. 6.35 has the coupler C and mirror M tuned for the laser probe beam to make only one single pass via the cell, and for any background radiation level to be detected (the beams are shown as the dashed lines).

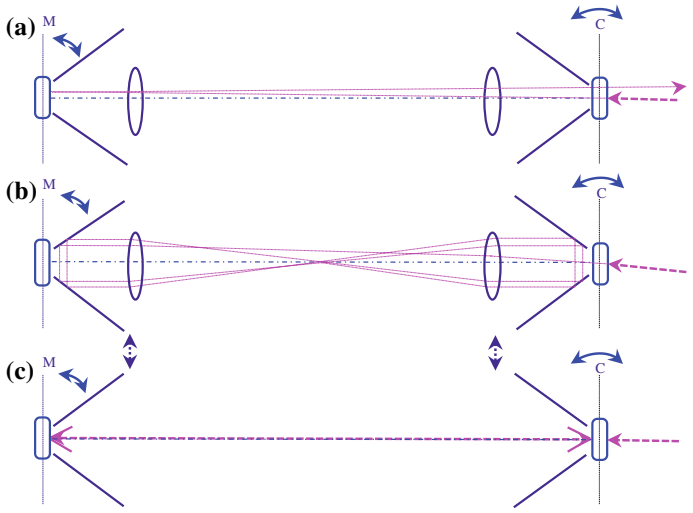

Fig. 6.35 Lens-fitting reconfigurable and tunable multipass scattering cell

Configuration *b* in Fig. 6.35 has coupler C and mirror M tuned for the cell having a focusing multipass propagation via the center region containing, for example, Raman scattering species under study. Configuration Fig. 6.35c has coupler C and mirror M tuned for the cell resonance in absorption measurements, and the confocal lenses for focusing the probing laser beam into scattering species have been removed.

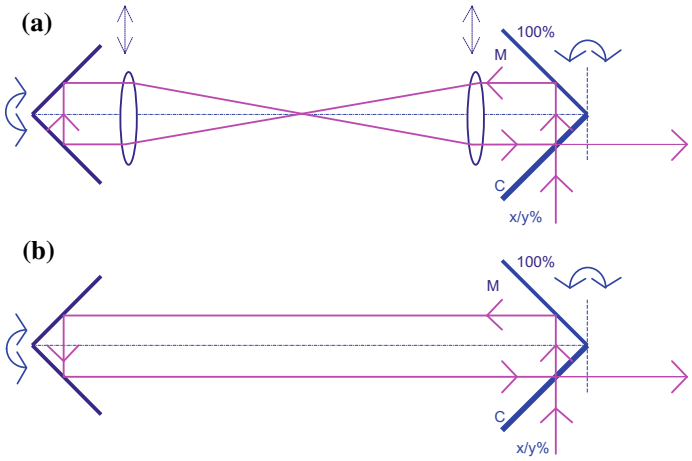

Fig. 6.36 Asymmetric reconfigurable-tunable mirror multipass cell

Figure 6.36 depicts an asymmetric-cell design, in which semitransparent coupler C serves as a one-side mirror of the corner cube and the second corner-cube mirror is the resonator mirror M. The beam enters the cell via coupler C, either coupled or decoupled with mirror M, configuring the resonator into every configuration of Fig. 6.35 and keeping the measurement concept intact.

Figure 6.37 illustrates another cell design with flat mirror coupler C replacing one assembly of corner cube mirrors. Another corner cube serves as resonator

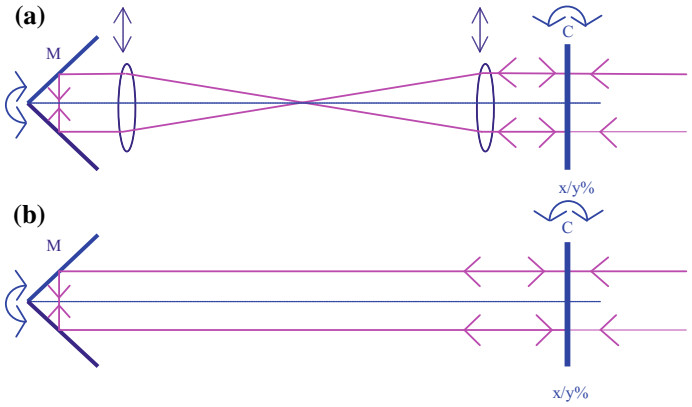

Fig. 6.37 Open-sided reconfigurable tunable mirror multipass cavity

mirror M, making either resonant coupling or decoupling, with the remainder of the system functionality unchanged.

Figure 6.38a illustrates one more version of the focusing-plus-detuning resonator, whereas Fig. 6.38b depicts the flat resonator of the mirror M and the partially transparent coupler C for the main beam with focusing mirrors M_1–M_4 serving as the collection cell for Raman scattering.

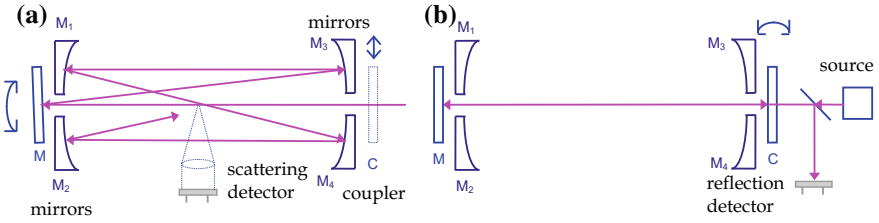

Fig. 6.38 Reconfigurable and tunable mirror multipass cell for measurements of Raman scattering (**a**) and of inner-cell optical loss (**b**)

The configuration of Fig. 6.38 could be made with spherical, parabolic, or elliptical mirrors instead of the corner cube mirrors and confocal lenses of Fig. 6.37, therefore decreasing intracell losses. Such a combinational-cell configuration is enhancing sensitivity to Raman scattering by setting simultaneous or sequential measurements of the scattering itself and the inner-cell loss. In view (*a*), coupler C (dotted lines) is taken out, and the cavity is configured for the maximum number of inner-cell reflections. In view (*b*), the coupler and the flat high-reflectance mirror are aligned and misaligned, allowing for resonant and reference measurements (see Sect. 8.4). This version of the design incorporates the same coupling-decoupling setting for coupler C and for mirror M as in Fig. 6.37. The design could be challenging owing to more elaborate profiles of the cell mirrors M_1–M_4, which may be required to avoid astigmatism, coma, or other aberrations.

Other versions of multipass cells can provide added enhancements for Raman spectroscopy via off-axis excitation of a windowless Herriott cavity [6.89], utilizing a resonant Fabry-Perot cell, at a resonance continually tuned to a wavelength of laser excitation by a piezo actuator mounted on one of its mirrors [6.90], using a Fourier-transform imaging spectrometer (see Sect. 12.1 for details) and a Sagnac interferometer at broad light-sheet illumination and high-acceptance angle of observation [6.91], and/or via the intense excitation by a probe pulse, forcing a deep crater in a powdered substance under study, while using the crater created for a multiple-reflection gain of subsequent Raman scattering observed for a weak probe pulse of the same laser source [6.92].

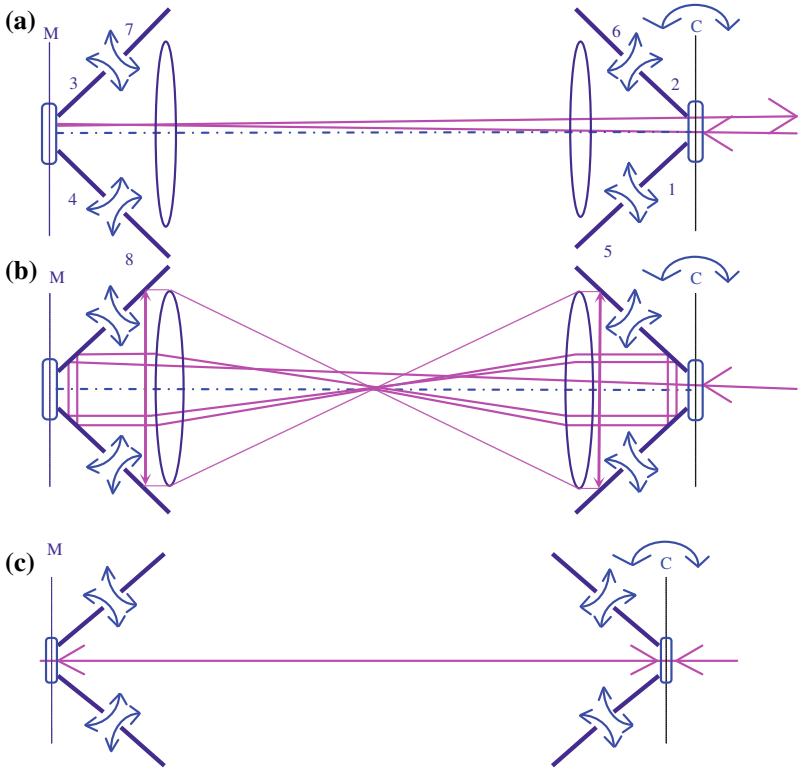

Fig. 6.39 Sectional reconfigurable and tunable mirror multipass cell

Figure 6.39 shows a fully tunable design approach of the reconfigurable cell. This approach has two sublevels of the cell configuration. The first one for tunable mirrors 1–4 keeps laser-probe light retroreflected in the fashion similar to that of Fig. 6.38. The second one is created by mirrors 5–8 being tuned separately from mirrors 1–4 to recycle the beam of light back into the cavity. The configurations seen in Fig. 6.39 match those in Figs. 6.37 and 6.38 for the measurement concept.

Figure 6.40 illustrates the most flexible version of the reconfigurable and tunable multipass cell, in which each single 90° corner mirror is replaced by a double independently aligned set of four self-adjustable mirrors tuning the angle between the mirrors for the first pair to be exactly 90°, and for the second pair to be either lower than 90° or higher than 90°. Every corner section consists of four mirrors – ach pair is aligned at a given angle to a pair mate with two windows for mirror M and coupler C. Other settings for a detection of Raman scattering remain intact while providing both configurable and tunable measurement of the intra-cell absorption and scattering loss (see [0.50] for more details).

Let us also note that simply maximizing the number of light passes via the multipass cell may not necessarily increase the effectiveness of measurements, since

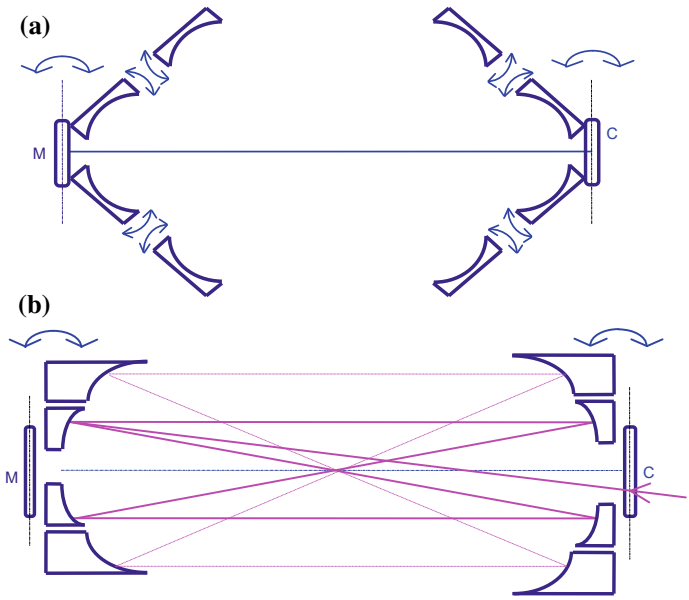

Fig. 6.40 Sectional, focusing, configurable, and tunable mirror multipass cell

the level of noise may increase along with the signal gain. The signal-to-noise ratio in a cw or a pulsed laser system for Raman versus Rayleigh scattering in a multipass cavity reaches its maximum at some optimal number of passes improving the single-pass efficiency, but overlapping of pulses might be nearly as effective for the signal gain [6.51]. Such a cell (Fig. 6.41) capable of high-throughput efficiency while enhancing path-length uniformity without beam overlapping and minimizing off-axis lateral shift for input and output beams could be made by combining two coupled off-axis paraboloid mirrors and two right-angle reflectors with light source S and detector D placed at focal spots of paraboloids at the distance: $f = 1/(2n \cdot \sin\varphi)$ [6.52].

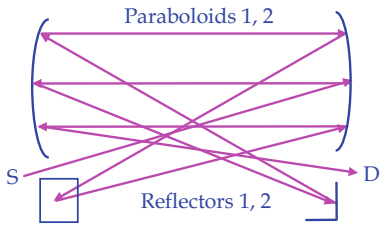

Fig. 6.41 High-throughput cell

6.4.2 *Mitigation of Fluorescence and Background Emission*

In Raman spectroscopy, the inelastic spontaneous scattering of light, caused by the molecular disturbance in an electric field, exhibits a low vibrational cross-section, defined by the molecular polarizability, is extremely difficult to separate from accompanying Raleigh scattering, fluorescence, and interference of a background emission. Various schemes that may be deployed to distinguish the Raman scattering of interest from other phenomena resemble in many ways methods for differentiating of low optical losses.

6.4.2.1 Polarization Discrimination

A polarization-discrimination scheme was naturally deployed for one of first laser-bound Raman spectroscopy systems in Ar-ion laser resonator (see Fig. 6.29) by rising the laser excitation power via multiple-path inner resonator reflections and observing Raman spectrums in a plane of a state of polarization of the laser beam. Presuming for purely rotational Raman lines the depolarization ratio to be 0.75, that polarization-observation scheme should have led to about 50% loss of Raman intensity. Nonetheless, as a result of the extinction effort blocking unpolarized light both the background stray light and fluorescence were almost completely removed, although the level of scattering inside the resonator was quite high [6.45].

Another way of polarization discrimination is in accomplishing a polarization modulation [6.53]. A rotating polarizer selects predominantly polarized Raman spectrum from unpolarized fluorescence or luminescence, while its rotation is synchronized with a lock-in amplifier via an additional polarized light source defining an initial position of the chopper polarizer (Fig. 6.42). A resulting spectrum of the synchronized detection for polarized Raman scattering is clear of

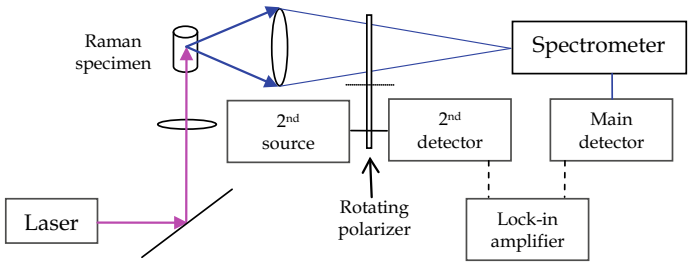

Fig. 6.42 Polarization modulation scheme for suppression of fluorescence

fluorescence light contained in the orthogonal to laser state of polarization. In an experimental arrangement of the system illustrated by Fig. 6.42, the rotating polarizer was followed by a polarization scrambler added to compensate effects of spurious extra polarization caused by spectrometer's grating, although altering relative intensities of the Raman lines [6.53].

A step further in measuring fluorescence-independent Raman spectra relies on comparing Raman signals in the planes perpendicular and parallel to the polarization state of the polarized laser excitation beam [6.54]. Presuming a fluorescence to be unpolarized and spatially uniform, by subtracting two responses, the first measured in the state of excitation with the Raman signal remained in the same plane plus one half of fluorescence and the second in the orthogonal state containing another half of uniformly distributed fluorescence, one could obtain only the Raman signal, free of fluorescence or background light, but under presumption of uniform distribution. In case of nonuniform fluorescence, respective measurement exposures could also be correlated.

An additional advantage of applying the polarization subtraction technique is in the ability to reduce other noise components of a detector, such as the fixed-structure noise of a CCD array applied for the spectral differentiation of Raman components versus excitation and background signals [6.55]. Since CCD shot noise is reduced by minimizing the total amount of accumulated photons, a recommendation for the Raman measurements is in providing the subtraction at the maximum exposure time, not yet saturating the CCD by the accumulated fluorescence, and then repeating the measurement cycle multiple times to enhance the signal-to-noise ratio, while only removing by subtraction a fixed-structure noise component along with the fluorescence emission.

Experimental results seen in Fig. 6.43 illustrate the effectiveness of polarization subtraction [6.56]. The graph of Fig. 6.43a, shows a mixed-fluid carbohydrate specimen, measured without and with a polarizer in two orthogonal orientations at diminishing levels of fluorescence, but at no clear distinction of the Raman peak. In the experiments, the state of laser polarization and of the additionally deployed polarizer were not aligned, because of exceedingly high fluorescence, masking traces of the Raman peak and revealing only the water absorption band. The following view (Fig. 6.43b), clearly demonstrates the advantages not only of polarization subtraction, but also of tuning the exposure time of CCD-detector array from 100 to 900 ms to enhance the signal-to-noise ratio, while keeping the same mixed-fluid sample with added ~40 millimolls of methane. That nine-fold increase in CCD exposure in view b, helped maintaining the same, if not lower level of fluorescence, while adding the polarizer in one the two orientations have reduced inputs of fluorescence − compare the left side of blue line of the unpolarized signal, and also enhanced polarized inputs representing peaks of methane and water − right side of the same blue line, and allowed to visualize the Raman peak over the unmitigated fluorescence [6.56].

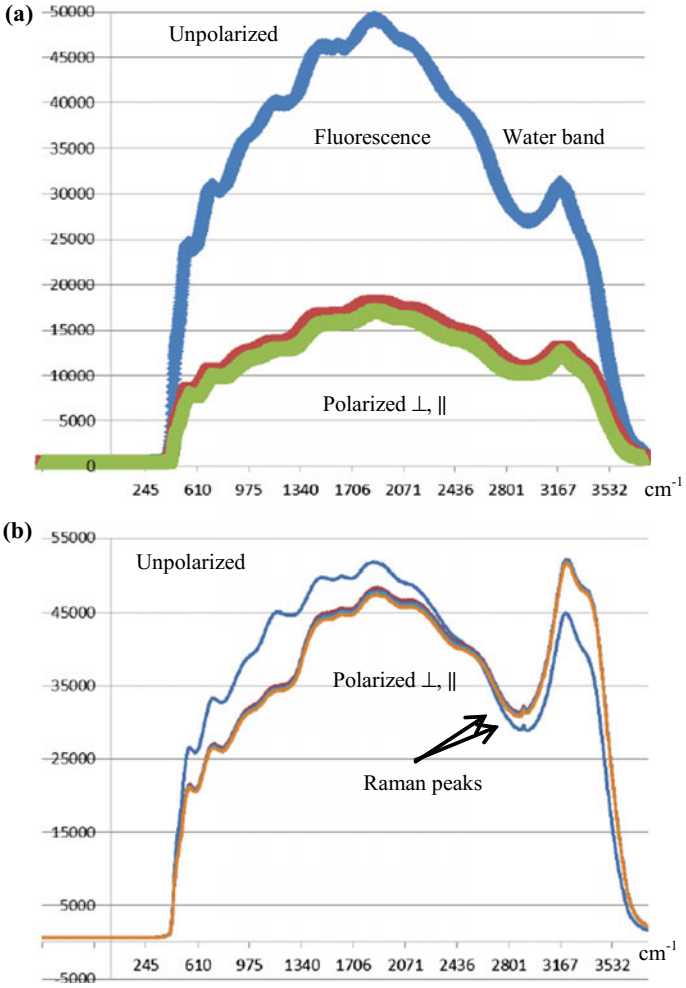

Fig. 6.43 Enhancing Raman signal versus fluorescence

6.4.2.2 Time Discrimination: Pulsed and Phase-Modulation Techniques

A way to part out the Raman-scattering from a fluorescence relates to the time scale, as Raman response is moderately instantaneous to its excitation versus prolonged fluorescence [6.85]. One of first implementations of pulse-based discrimination used Q-switched second-harmonic Nd:YAG laser, generating 100 ns pulses at 10 mW of average power at 532 nm, and a photon-counting detection via an uncooled photomultiplier tube [6.57]. Such a pulse based system allowed

discriminating 125-microsecond lifetime fluorescence reducing it by about 60-fold while using 1-microsecond detection interval for Mn-doped ZnSe sample studied.

Similar means of fluorescence suppression may be accomplished using intensity-modulated laser excitation followed by a phase-sensitive demodulation correlated to the laser's modulator. By registering two spectra at the phases $\varphi_0 \pm \varphi$, separated from laser-sampling phase φ_0, phase-uncorrelated fluorescence is subtracted from the Raman signal that promptly follows the laser pulses [6.58]. In experiments, the sinusoidal frequency modulation was provided by a Pockels-cell with the second acousto-optic modulator operating at $\sim$15 MHz, making the laser intensity modulation at a 30-MHz fundamental frequency. One extra pulse generator allowed tuning the phase delay to either 90 or 180°, making sure the fluorescence suppression is maximized. Up to 150 MHz high-frequency sinusoidal modulation was further deployed for phase-resolved spectroscopy of a weak Raman scattering at intense fluorescence of rhodamine B in water [6.59].

An obvious approach of enhancing time-resolved spectroscopy is in using the fastest tools, such as fast-gated intensified CCD cameras pushing the time resolution into picoseconds [6.60]. Using Ti:Sapphire laser excitation at 785 nm with 300 mW average power at a repetition rate of up to 110 MHz allowed fast-gated detection of Raman light at the temporal resolution of about 150 ps. In the experiments, two highly fluorescent samples were used − crystalline $CaWO_4$ with Nd^{3+} impurities and Hexobenzocoronane powder as a transparent and a heterogeneous sample, respectively. Obtaining the gated-camera signals at 100 ps time intervals with 200 ps gate width allowed distinguishing Raman signals not only from fluorescence (luminescence), but also from even stronger Rayleigh scattering signals coinciding in time with laser's excitation pulses [6.60].

Further advances of the time-gating could be made via blocking any arrival of fluorescence by a Kerr modulator, placed in between two crossed polarizers and functioning as a switchable $\lambda/4$ waveplate, hence letting only a Raman pulse to go through − at some expense of incomplete polarization rotation in a Kerr medium in open and closed states [6.61]. Added losses accounted for about 15% and 0.005% in the subsequent experiments with a mode-locked Ti-Sapphire laser. One-picosecond gating time was realized in the system deploying collinear design utilizing low peak power pulses operating at high repetition rates, instead of a high peak-power lasers at low repetition rates as a potential nonthermal ablation is to be avoided for biological samples [6.62]. Transform-limited 140 fs, 30 nJ pump pulses at 808 nm by a mode-locked Ti:Sapphire laser at 80 MHz rate were used for second-harmonic generation of Raman-excitation at 404 nm, along with polarization tuning and spectral filtering of pump and excitation beams from Raman spectrum.

An implementation of time-resolved miniaturized Raman spectroscopy system, suppressing interference of fluorescence via a single-photon avalanche diode array, allowed achieving a sub-nanosecond time resolution with 532-nm pulsed micro-chip laser and sub-ns pulse gating [6.84]. A passively Q-switched diode-pumped solid state laser, generating $\sim$1.5 μJ, 600 ps, 0.1-nm wide spectral pulses at 40-kHz repetition rate, was split into a main channel and a reference triggering photodiode. A grating spectrometer operating in the 50–2200 cm^{-1} wavenumber range at 6 cm^{-1} of spectral resolution and a dichroic-edge 532-nm

filter were used to process signals detected by the 1024×8 pixel single-photon avalanche diode array operated at 1-ns gating. Experimental data confirmed 16 ns as inadequate to gate out short-lifetime fluorescence versus the 1-ns gate [6.84].

6.4.2.3 Spectral Discrimination

One of the clearest advantages of Raman spectroscopy versus the spectral measurement of absorption is in spectral separation of excitation and Raman-scattering wavelengths, while the excitation could be made at a wavelength of choice, allowing to position the Raman wavelength at the desired spectral region of optimal detector sensitivity, such as of a CCD camera. However, this feature of Raman spectrometers would not necessarily separate the measured signal from background fluorescence, existing in the same spectral domain, although saturation phenomena for CCD-based spectrometers should be significantly reduced, if Raman scattering measurements are performed only in some narrow spectral intervals of interest [6.63]. The cited implementation incorporated multiple Volume Bragg Grating-based spectral selectors, used for (a) stabilizing the chosen emission-excitation wavelength from a diode laser, (b) filtering out Rayleigh scattering/fluorescence, and (c) selecting only a desired set of Raman wavelengths via incorporating several ultra-narrow notch spectral filters – all in one 3-dimensional substrate.

Shifted Excitation: Wavelength (Frequency) Modulation

Conceptually, signal-modulation spectroscopy was first implemented for mitigation of scattered light, then subsequently applied to fluorescence suppression in Raman studies and other applications of derivative spectroscopy [6.64]. When vibrating a scanning mirror in the Littrow-design spectrometer via a small angle in the plane perpendicular to a plane of spectral selection, while synchronizing its movement via a lock-in amplifier, the spectrometer spectral output continued to be proportional to the intensity of optical radiation at the selected wavelength even as the intensity of stray light, in that case of UV scattering, remained several times greater as it was not modulated on amplifier's frequency. Wavelength-modulation Raman spectroscopy measurements may be conducted similarly [6.65]. Under the presumption that a small change of an excitation wavelength does not alter intensity or profile of fluorescence, subtracting two spectra obtained at close excitation lines removes the unchanged fluorescence, revealing the differential spectrum of Raman lines. Experimentally, an emission wavelength of a cw dye laser, externally pumped by an Argon laser, was wavelength-modulated within 0.5 nm inside its cavity by a vibrating Fabry-Perot etalon, with its movement synchronized via a reference output of a lock-in amplifier. The modulated dye-laser beam was transmitted by the etalon to a reflective diffraction grating selecting the modulation wavelength within a free spectral range of the etalon and to a test sample via a movable slit. The

differential transmission spectrum processed by dual-monochromator spectrometer contained pronounced Raman peaks above and beyond the unmodulated fluorescence background. Further integration that enhanced the signal to noise ratio added known difficulties of finding a true measurement baseline as well as correcting for baseline-drift distortions and temporal deviations, accordingly only three of the four peaks obtained were fully resolved as not being excessively noisy [6.65].

The first wavelength-modulation experiments confirmed that, if a modulation wavelength only changes within a small frequency or wavelength interval, the level of intrinsic fluorescence emission remains mostly unchanged, enabling progression of the technique to less-complicated differential shifted-excitation studies without temporal modulation and or lock-in amplification reducing the process to obtaining a combined spectrum at two adjacent, but spectrally resolved wavelengths [6.66], or to recurrently changing an excitation wavelength via a tunable source or other spectral means and measuring spectrums at various discrete points for better background correction [6.67–6.73]. Presuming the fluorescence level to remain unaltered at the shift among adjacent excitation frequencies, the difference of measured spectra should provide a differential Raman spectrum with the detriment of doubled system noise for twofold spectral measurements.

The resultant spectrum may be represented as the difference of Raman lines at frequencies or wavenumbers ν_1 and ν_2 – which symmetric shift from the median frequency ν_0 is negligibly small. Consequently, acquired two spectra $S_1(\nu_1)$, $S_2(\nu_2)$ provide a differential Raman spectrum:

$$\begin{aligned}\Delta S &= S_1(\nu_1) - S_2(\nu_2) = S_1(\nu_0 + (\nu_1 - \nu_0)/2) - S_2(\nu_0 - (\nu_2 - \nu_0)/2) \\ &= S_0(\nu_0 + \Delta\nu/2) - S_0(\nu_0 - \Delta\nu/2) \cong \Delta\nu[\partial S_0(\nu_0)] = \Delta\nu[\partial S_{\text{Raman}}(\nu_0)].\end{aligned} \tag{6.40}$$

Since noise signals of each of two measurement contributing to the differential acquisition add up, the weakest Raman lines are buried in doubled signal noise of the difference measurement:

$$\Delta S = \Delta\nu[\partial S_{\text{Raman}}(\nu_0)] + 2S_{\text{Noise}}. \tag{6.41}$$

This shot noise associated with the intense fluorescence background photons can not be simply removed by subtraction and demands implementation of other approaches, such as quenching fluorescence, shifting excitation to wavelengths not causing the high luminescence, or utilizing highly-efficient multi-channel detectors allowing to accumulate a sufficient Raman signal, even in the presence of fluorescence making sure the dominant noise source is contained [6.75–6.77].

To help extract a spectral profile of Raman lines from a differential spectrum, a polynomial fitting of the differential curve is typically required via one of available nonlinear least-squares algorithms to permit distinguishing Raman peaks from combined noise. Combinations of multi polynomial methods, enhanced statistics, Fast-Fourier Transform (FFT) filtering techniques are deployed for automated removal of noise to enable the differential Raman studies [6.68–6.73].

Since the noise removal essentially is the enabling tool in providing a differential measurement, extensive efforts had been undertaken in validating algorithms of the fluorescence suppression, seemingly identifying the Least Squares Fitting and Principal Component Analysis to be among the best processing algorithms, and Standard-Deviation or Fourier-Filtering as the worst, due to observed distortions of reconstructed Raman lines, while having asymmetric Raman picks since the spectrum, processed by latter methodologies, do not seem to maintain a constant ratio [6.80].

An extra enhancement of shifting-wavelength excitation scheme involves quasi-continuous multi-frequency shift with a recurring sampling at a given time interval or using multiple light sources utilizing the two-wavelengths technique – presuming all wavelengths to be unchanged within the time interval of sampling for a center wavelength, averaging a domain. Such a multi-wavelength technique treats every spectral measurement in a series of excitation frequencies as independent Poisson trials, analyzed via various iterative-analysis techniques to reconstruct the most probable Raman and fluorescence spectrums [6.77–6.83]. As for other inverse problems in spectroscopy utilizing probability methods for a restoration of the noisy degraded images [6.75], in which a small spectral signal is hidden by increased noise from another large signal, some noise components such as Poisson shot noise, may be removed from the spectrum using a maximum-likelihood approach [6.76]. Using eight independent laser sources while correcting the obtained Raman spectra via the shifting-excitation technique and obtaining one fluorescence spectrum by averaging all measured ones permitted isolating the shift-variant Raman signals from the broad fluorescent background via that multi-excitation algorithm. For 2, 4, and 8 lasers, the RMS error of spectra estimation decreased from 0.12 to 0.08 while progressing from 2 to 4 to 8 lasers [6.78].

Other versions of wavelength shifting [6.74, 6.81] deployed a continuous modulation of the excitation wavelength via multichannel lock-in detection of differential signals, under the same presumption of unchanged fluorescence spectra at a wavelength modulation. In the first system [6.74] the concept was studied via 2-mm polystyrene beads suspended in a fluorescent dye with the signal-to-noise ratio of Raman signals at 0.4-Hz modulation three times better than for two-wavelength measurements. In another setting [6.81], the wavelength modulation was tested via fiber-probe approach for biomedical studies of highly-scattering tissues, causing Raman signals to experience multiple scattering or photon migration, leading to high-fluorescence background superimposed by optical-fiber material luminescence, especially in the fingerprint region of 400–2000 cm^{-1} wavenumbers. Using a tunable 785-nm diode laser with 1-W maximum power and tuning range of $\Delta\nu = 160$ GHz or $\Delta\lambda = 0.32$ nm of the wavelength shift, experiments comprised of acquiring Raman spectra over 5-s time intervals in discrete steps varying each wavelength at a symmetric trapezoidal pattern over 30 s, corresponding to 6 spectra acquired. Every Raman spectrum was detected by an enhanced CCD-based spectrometer at a full vertical binning. A 200-μm diameter multimode fiber was delivering a laser excitation beam with seven matching fibers collecting Raman signals. Adding twenty spectrums, at 30-s accumulation time each, has been sufficient for the SNR enhancement to an order of magnitude in best cases [6.81].

Chapter 7
Laser Spectroscopy

7.1 Active Intracavity Measurements

Practically every method of multiple interaction of light with a test object considered so far enhances the sensitivity to a given low optical loss via the enhanced measured signal owing to an increased number of light interactions. Among other phenomena, generation of laser light in any active medium with a low gain factor is stipulated by the very same multiple reflections in an open laser resonator with a high quality factor. Since the power and energy parameters of stimulated emission are defined by correlations of laser gain and attenuation, corresponding to every pass via that open laser resonator, one can expect high sensitivity of laser emission to the presence in its resonant cavity of any embedded optical loss. Such excessive sensitivity can be manifested via changes of the laser power or energy output in a broad spectral domain of its active medium amplification or as spectrally selective optical losses in narrow spectral intervals.

Placing into a laser cavity a substance which does not cause laser generation suppression by its optical loss $\mu_x \ell_x$ makes the relative output intensity I/I_0 of laser radiation change as [II.1]:

$$\frac{I}{I_0} = \frac{\mu_a \ell_a}{\mu_x \ell_x}\left(1 - \frac{I}{I_0}\right) - \frac{\mu_a}{b_0 - \mu_a}. \tag{7.1}$$

Here I_0 is the intensity of the initial output of the laser when the substance under study is not in the resonator, μ_a and ℓ_a are the linear attenuation coefficient and the length of the active laser medium, and b_0 is the unsaturated gain coefficient. Direct resolution of resonator loss $\mu_x \ell_x$ by Eq. (7.1) is hindered by the presence of unknown factors μ_a and b_0, which can be measured by implementing in the resonator a calibrated transmission specimen and by varying the laser gain parameters.

Because of these calibration requirements, intra-resonator laser measurements are mainly performed as relative procedures providing extra compensation of

M. Bukshtab, *Photometry, Radiometry, and Measurements of Optical Losses*, Springer Series in Optical Sciences 209,
https://doi.org/10.1007/978-981-10-7745-6_7

implemented optical loss by diminishing another loss caused by a calibration element or by forming an advanced calibration scale for the entire laser. The most practical laser calibrator used is a relatively thick and transparent glass plate, installed at near the Brewster angle φ_B for its material. Any deviation of the actual angle of incidence φ_A from the Brewster angle defines changes for the plate reflectance $\Delta\rho$ and for the resultant output of laser intensity ΔI. The extra attenuation $\Delta\rho$ due to the plate's presence is defined by:

$$\Delta\rho = 2\frac{\tan^2[(\varphi_B + \varphi_A) - \varphi_R]}{\tan^2[(\varphi_B + \varphi_A) + \varphi_R]}. \tag{7.2}$$

Here φ_R is the angle of refraction and φ_A is the increment of the angle of incidence, counted from the Brewster angle direction. A sufficiently large plate thickness is needed to prevent intersections and interference between beams reflected from opposite surfaces of the plate. Similarly to the reflectance measurements at normal incidence, the displacement of a beam transmitted through the Brewster compensator can be attuned by the identical second plate placed at the opposite orientation to the first one as revealed in Chap. 5 (see Fig. 5.11 and [7.2]).

In the initial calibration of straight-cell sensitivity to intracavity loss, mirror object 5 (Fig. 7.1a) is outside the laser cavity to be calibrated. For the high-reflecting rear mirror at position 3, the loss scale to be measured is verified by tilting main calibration plate 4 from the Brewster angle. When measured mirror 5 is brought to its position at angle of incidence Θ, the resonator is bent to mirror position 3′ and calibrator 4 is again tuned in from the Brewster angle. The accuracy of measurements is limited by factual inequality of diffraction losses at straight and bent resonator settings and misalignment errors. The experimentally measured reflectances only reached 0.998 with a repeatability ±0.2% [7.1, 7.2].

A similar resonator design (see Fig. 7.1b) was also used to experimentally evaluate the sensitivity of different pulsed lasers: He–Ne and Nd:YAG, to intracavity optical loss associated with a high-temperature plasma [7.3]. During the initial plot for each laser pulse of 3–5 ms in duration, the uninterrupted intensity I_0 level for the laser beam was recorded by main detector 7. At the moment when plasma was burned in test capillary 5, which was registered by a signal of reference detector 8 obtained via splitter 6, the second level of intensity I_x was measured. As

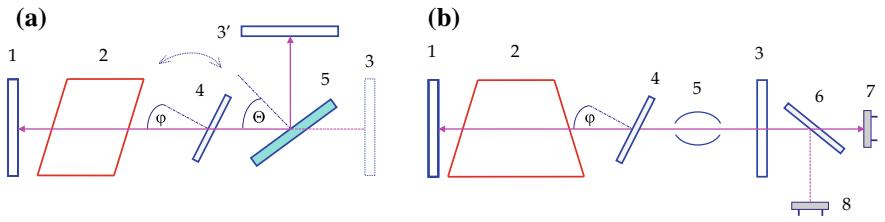

Fig. 7.1 Laser intra-cavity loss measurements: 1, 3 – cavity mirrors, 2 – active element, 4 – calibration plate; 5 – test capillary; 6 – splitter, 7 – main detector, 8 – reference detector

in the mirror reflectance study, the actual sensitivity to transmission loss inside that laser resonator was limited by competition of emitted modes and pumping or generation instabilities. The lowest detected internal attenuation factor $\exp(-\mu_x \ell_x)$ was between 0.08 and 0.10 at a plasma temperature of 5800–6500 K and at a concentration of the plasma electrons of $5 \cdot 10^{16}$ cm^{-3} [7.3].

An auxiliary resonator can be used to separate the influence of a low loss to be studied from the calibrated one [7.3]. For this purpose, laser active element 2 and under test low-loss object 5 are situated in main cavity 1-3 with aperture 4, while calibration element 6 is separated into its own adjacent resonator 3-6-7 (see Fig. 7.2). The second resonator may be considered as a single composite mirror 3-6-7, set to the maximum of interference for laser light, having reflectance ρ:

$$\rho_\Sigma = \left[\left(\sqrt{\rho_a} + \tau_c \sqrt{\rho_b}\right) / \left(1 + \tau_c \sqrt{\rho_a \rho_b}\right)\right]^2. \tag{7.3}$$

Here ρ_a, ρ_b, and τ_c are the reflectances of left and right mirrors and the transmittance of calibrator 6.

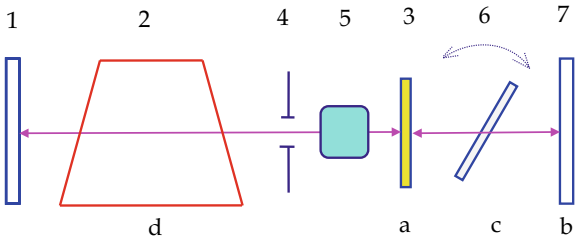

Fig. 7.2 Dual resonator separating intra-cavity calibration and testing

Application of the calibrating cavity of elements 3, 6, and 7 allows one to compare of a variety of divergent losses via unequal weight factors. Therefore, even the potential inaccuracy of imprecise estimation of the calibrator's Fresnel surface losses has a smaller influence on the results of such intracavity studies. Practical measurements with the dual-cavity laser were provided by equalizing the output laser energy with and without test objects and verifying internal losses in the calibration resonator as $K = \ln(\rho_{\text{eff.0}}/\rho_{\text{eff}})$. Experimentally observed correlations between the internal resonator loss of the laser to be resolved $\mu_x \ell_x$ and that implemented in the calibration resonator were evaluated as:

$$\mu_x \ell_x = \ln\left[\frac{\left(\sqrt{\rho_b} + \tau_a \sqrt{\rho_a}\right)\left(1 + \tau_a \tau_c \sqrt{\rho_a \rho_b}\right)}{\left(1 + \tau_a \sqrt{\rho_a \rho_b}\right)\left(\sqrt{\rho_b} + \tau_a \tau_c \sqrt{\rho_a}\right)}\right]. \tag{7.4}$$

Here the indices for reflectance ρ and transmittance τ are designated in Fig. 7.2 and the transmittance τ_d of the active element having the Brewster-angle windows is taken as unity. The actual sensitivity of measurements with a supplemental resonator at $\rho_b = 0.999$ and $\rho_a = 0.998$, using calibrated solutions of $CuSO_4$ applied at various concentrations, was increased to $(2-4) \cdot 10^{-4}$ cm^{-1} at $\lambda = 632.8$ nm [7.3].

More advanced prospects of increasing the accuracy and sensitivity of active laser measurement are associated with sharp magnifications of all internal resonator factors when the threshold of the laser generation is achieved [3.32, II.1]. The threshold condition is reached for internal factors of attenuation and amplification balancing each other on every dual pass of an open laser resonator:

$$\rho_1 \rho_2 \exp[(g - a)2\ell_a - \mu_x 2\ell_x] = 1, \tag{7.5}$$

where α is the linear absorption coefficient, usually characterizing all of the dissipative losses in the inverted laser medium per unit of its length ℓ_a, μ_x is the linear attenuation coefficient, ℓ_x is the length of the object studied placed inside the laser resonator, and ρ_1 and ρ_2 are the reflectances of the cavity mirrors. Seeking some generation suppression by implementing in the resonator diverse calibration losses with and without a test object, one can not only raise the sensitivity and accuracy of measurements, but can also stabilize and exclude from the final results the influence of the resonator's instability factors, such as varying diffraction losses due to placement of the object. That is especially valuable for nonlinearities of stimulated emission of light and bares some analogy with the comparison measurements analyzed in Chap. 5. Equation (7.5) demonstrates that when sensing a low loss under the gain-saturation condition, the smaller is the gain coefficient, the lower is the loss that may be sensed, taking advantage of having the added second resonator with a higher loss.

A Brewster angle calibrator is generally used to detect intracavity losses by capturing the instance of saturation of laser gain (Fig. 7.3a). In a resonator of mirror M, active element AE, and output coupler OC, calibrator C is set at the Brewster angle with and without the sample under study O. Gain saturation is measured by detector D at two opposite orientations – φ_{left} and φ_{right} – of calibrator C, inducing equal reflectance losses $\rho_{\|,\text{l-r}}$ for light polarized in the plane of incidence:

$$\begin{aligned}\rho_{\|,l} &= \frac{\tan^2\{(\varphi_B + \varphi_{left}) - \arcsin(\sin(\varphi_B + \varphi_{left})/n)\}}{\tan^2\{(\varphi_B + \varphi_{left}) + \arcsin(\sin(\varphi_B + \varphi_{left})/n)\}} \\ &\equiv \frac{\tan^2\{(\varphi_B + \varphi_{right}) - \arcsin(\sin(\varphi_B + \varphi_{right})/n)\}}{\tan^2\{(\varphi_B + \varphi_{right}) + \arcsin(\sin(\varphi_B + \varphi_{right})/n)\}} = \rho_{\|,r}.\end{aligned} \tag{7.6}$$

The larger is the calibrator deflection when lasing is terminated, the broader is the separation of left and right calibrator position: $\Delta\varphi = \varphi_{\text{left}} - \varphi_{\text{right}}$. Therefore, this

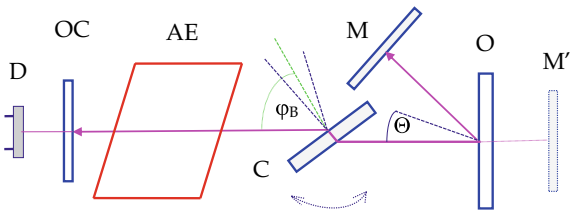

Fig. 7.3 Layout for threshold-sensing intracavity loss measurement

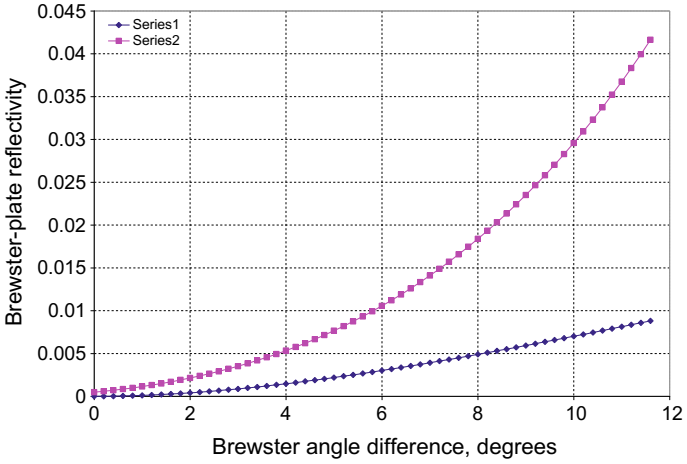

Fig. 7.4 Relative change of reflectance of a plane-parallel glass plate in the vicinity of the Brewster angle: the angle of the plate's inclination is below (series 1) and above (series 2) the Brewester angle

higher deflection range relates to lower dependency of the sensed intracavity loss on the discrepancy of left and right angular positions due to fluctuations of the refractive index and Brewster angle of the calibrator material. Besides, as seen from Fig. 7.4, the relationships between the calibrator rotation positions and its reflectance magnitudes near the Brewster angle are not linear. Only by increasing the difference between φ_{left} and φ_{right}, can virtually linear increments of the reflection losses be concurrent with a close-to-linear change of the calibrator's position. Figure 7.4 reveals that with $\Delta\varphi$ increasing, unequal angles for left and right rotations relate to one reflectance, causing changing diffraction losses and systematic errors. For intracavity experiments with a stabilized He–Ne laser at $\lambda = 0.633$ μm, the $\Delta\varphi$ angle reached 22–25° at ±17 min of arc uncertainty of the calibrator's position. Such a deviation, due to the system's response of around 0.17% per degree, corresponded to random error of the reflectance measurement at about the ±0.0001 level [7.4].

Similarly to utilizing a Brewster-angle plate for quantitative calibration of intracavity losses when the bigger is the dynamic range of the inclination, the higher is the sensitivity to a small optical loss that can be realized, another apparent way for loss calibration of a laser cavity is via polarization modulation of radiation emission. According to the Malus law: $I = I_0\cos^2\delta$, the intensity I_0 of polarized light propagating via an analyzer can be altered to any desired phase status δ, and thus attenuated to any magnitude with well-known and predictable behavior. Realizations of this concept depend on the measurement tasks and may adopt a rotatable phase retarder, turning around the direction of light propagation to obtain the desired phase shift, or a magneto-optic or electro-optic modulator, whose optical birefringence is induced by an external electromagnetic field, etc.

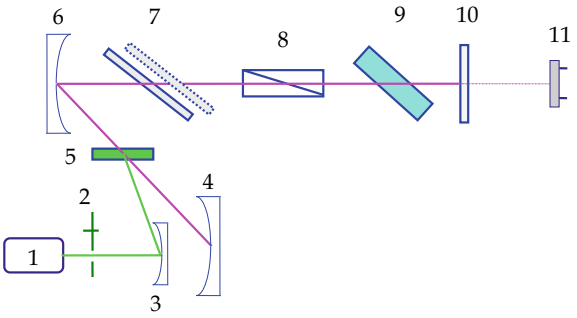

Fig. 7.5 Laser spectrometer utilizing loss-calibration via modulation of polarization

Figure 7.5 depicts an intracavity laser spectrometer with polarization modulation of laser-light intensity inside the resonator for measuring low optical losses in liquids or solids [7.5]. A crystal with a not quadratic but linear Pockels' effect is used to sense small changes of modifying phase angle δ, realizing high sensitivity to intracavity loss via detector 11. Phase angle $\delta = \pi\left(U/U_{\lambda/2}\right)$ and thus the internal resonator loss calibrated are defined by the ratio of applied U and semiwave $U_{\lambda/2}$ voltage for that specific modulator [7.5]. In the experiments a dye laser with a set 7 of interference filters was used as the wavelength-defining spectral selector. Stabilized light of argon laser 1, modulated by chopper 2 at a low frequency, irradiated cuvette 5 with a lasing dye via mirror 3. Low-frequency beam modulation served to prevent excited molecules from being accumulated in the triplet state, which increases active medium absorption. To prevent thermal lens effects and excitation of axial modes except the TEM_{00} mode, the dye was constantly cooled by distilled water near 4 °C, maintaining as little turbulence as possible. All elements of the laser cavity between mirrors 4, 6, and 10, including test cavity 9 containing the liquid under study, but excluding modulator 8, were placed at the respective Brewster angle.

Attenuation χ_0 by a polarization modulator complexly depends on the state of polarization of laser radiation and is affected by resonator elements on opposite sides of the modulator [7.5]:

$$\chi_0 = \frac{2}{[(1+P_L)(1+P_R)]^2} \times \left[\begin{array}{l} P_R(1+P_L)^2 + P_L(1+P_R)^2 - 2P_LP_R(1+\cos\delta) + \sin^2\delta - \\ -(\cos\delta + P_LP_R)\sqrt{P_L^2 + P_R^2 + 2P_LP_R\cos\delta - \sin^2\delta} \end{array} \right]. \quad (7.7)$$

Here P_L and P_R are the polarization exchange factors for respective elements on the left and the right side of the Pockels modulator. For $\chi_0 \ll 1$, it may be assumed that $P_L + P_R \cong 1$ and $\delta^2 \ll P_L + P_R$; thus, Eq. (7.7) can be simplified to $\chi_0 = \delta^2/(P_L + P_R)$. The measured attenuation factor χ can be identified by relative changes of modulator voltage U with and without the test object:

$$\chi = \frac{\pi^2\left(U_0^2 - U_x^2\right)}{2 \cdot 2.303 \cdot U_{\kappa/2}^2 (P_L + P_R)}. \tag{7.8}$$

The polarization-exchange factor P_R of the empty test cavity was determined as: $P_R = [(1-\tau)/(1+\tau)]^2$ at $\tau = [2n/(1+n^2)]^2$, giving for the fused silica cavity windows at the Brewster angle $P_R = 0.139$. The phase shift caused by the cuvette, interference filters, and the inverted dye molecules was not determined due to its complexity and $P_L = 0.781$ was obtained via properties of standardized solutions of $CoSO_4$. The linear attenuation coefficient χ in a mixture of rhodamine 6G, computed by Eq. (7.8), differed from the exact magnitude obtained by relation (7.7) by $1 \cdot 10^{-5}$ cm^{-1}. The intracavity measurements at voltage miscalculations $\Delta U \leq 5\%$ were characterized by random errors near $\pm 2 \cdot 10^{-5}$ cm^{-1} with about $\pm 5 \cdot 10^{-5}$ cm^{-1} reproducibility [7.5].

7.2 Comparison of Intracavity Methods

Considering any active laser intracavity measurement and comparing its relative sensitivity with that of a conventional study using a spectrophotometer, one can simplify Eq. (7.1) as in [7.6]:

$$I_x = const(G - \chi_x - \chi)\frac{\chi}{\chi_x + \chi}. \tag{7.9}$$

Here G is the gain factor of the active laser medium, χ_x is the passive loss on the beam's way via internal propagation of the laser resonator, and χ is the loss at an exit mirror. Identifying the internal loss χ_x as a linear coefficient and looking for its effect on the relative change dI/I of the output intensity of the laser gives:

$$\frac{dI_x}{I_x} = \frac{d(G - \chi_x - \chi)}{G - \chi_x - \chi} + \frac{d\chi}{\chi} + \frac{d(\chi_x + \chi)}{(\chi_x + \chi)}. \tag{7.10a}$$

Treating G and χ as constants for finite increments of $\Delta I/I$, expression (7.10a) transforms to:

$$\frac{\Delta I_x}{I_x} = \frac{\Delta\chi_x}{G - \chi_x - \chi} + \frac{\Delta\chi_x}{\chi_x + \chi} = \frac{\Delta\chi_x}{(1 - \chi_x/G - \chi/G)(\chi_x + \chi)}. \tag{7.10b}$$

Consequently, the lower are the losses to be measured, the smaller should be the gain and loss factors of the resonator, confirming the concept of compensation measurement discussed above.

Relations (7.9) and (7.10) allow one to compare changes of the laser output intensity needed to sense a low optical loss to be implemented into the cavity. Figure 7.6 illustrates results computed by expression (7.10b) and results obtained in the experiments [7.7] at G = 5%, $\chi_x = 2.3\%$, and $\chi = 1\%$. The comparison was made for a CO solution of a constant concentration in cells of 2- and 10-cm length (respective lines 1 and 2 in Fig. 7.6b) using a cw He–Ne laser at $\lambda = 632.8$ nm and

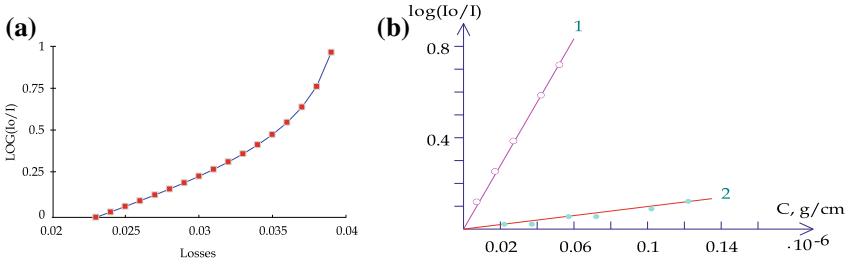

Fig. 7.6 Layout for threshold-based intra-cavity measurements (**a**) and reflectance changes around the Brewster angle (**b**)

a spectrophotometer. The laser cavity windows were at the Brewster angle of the effective length near 2.4 cm: 0.5% concentration change caused a 38.7% increase of intensity viewed as 116 times gain of sensitivity per unit length.

For a laser medium of relatively high gain factor and quasi-homogeneous line broadening of its stimulated transition, the output intensity I with the accuracy of a constant can be defined as [7.8]:

$$I = const\left[b_0 - \frac{\ln(\rho_1\rho_2)^{-1}}{\ell_0}\right]\frac{1-\rho_2}{(1-\rho_2)+(1-\rho_1)\sqrt{\rho_2/\rho_1}}, \tag{7.11}$$

where b_0 and ℓ_0 are the linear gain coefficient and the length of the laser's active medium, and ρ_1 and ρ_2 are the reflectance values of the rear mirror and the output coupler. Owing to the high laser amplification, stimulated emission can be initiated even with a low quality factor of the laser resonator. In that case, the number of intraresonator reflection cycles is low. Thus, active low loss measurements in a high-gain medium become inadequately effective when the object in question is placed in the resonator away from the active medium either to the rear mirror or the output coupler. Comparing with loss measurements in transmitted light evaluated as: $I = I_0\tau = I_0\exp(-\mu\ell) \underset{\mu\to 0}{\cong} I_0(1-\chi)$, and substituting in Eq. (7.11) for the effects of implemented losses: $\rho_2 \equiv (1-\chi)^2\rho_2; \rho_1 \equiv (1-\chi)^2\rho_1$, one obtains:

$$\begin{aligned} \mathrm{K}_1 &\equiv \frac{I_0 - I_1}{\chi I_0} = \frac{1}{b_0\ell_0 + \ln\sqrt{\rho_2}} + \frac{1+\rho_2}{1-\rho_2}; \\ \mathrm{K}_2 &\equiv \frac{I_0 - I_2}{\chi I_0} = \frac{1}{b_0\ell_0 + \ln\sqrt{\rho_2}} + \frac{2\sqrt{\rho_2}}{1-\rho_2}. \end{aligned} \tag{7.12}$$

Here, for simplification, the rear mirror reflectance is assumed to be that of a perfect mirror $\rho \equiv 1.0$. As expected from earlier analysis, with low gain factors: $G \cong b_0\ell_0$, any notable sensitivity increase can be realized independently of the relative positioning of the low-loss object, simultaneously with having a high quality factor of the resonator: $\mathrm{Q} = \rho_1 \cdot \rho_2$ (Fig. 7.7, curves 1, 2). Within regions of $\rho_2 \cong \exp(-2b_0\ell_0)$,

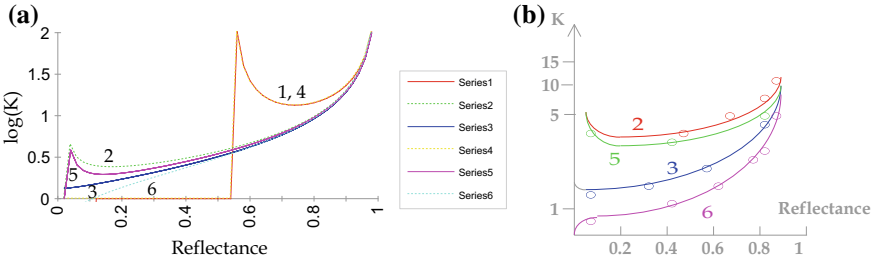

Fig. 7.7 Comparative sensitivity of a high-gain laser versus direct measurement – computed (**a**) and factually realized (**b**) for a loss object at the output coupler (1–3) and at the rear mirror (4–6): 1, 4 – G = 0.3; 2, 5 – G = 1.9, 3, 6 – G = 5.3

corresponding to near-threshold operation (lines 2, 4), a slight increase not very dependent on the object's location can also be achieved. If the laser's gain is high, the optimum loss-element placement is dependent on the quality factor of the laser resonator. Results of computation also point out that intracavity active-laser studies in certain situations instead of being more effective can be even less effective than conventional direct measurements, since the likely nonlinear character of stimulated transitions, leading to lasing near the gain saturation of such a laser, can easily diminish the outcome of implementing the added loss under study.

Experimental arrangements leading to results illustrated in Fig. 7.7b were made using a He–Ne laser at $\lambda = 3.3922$ μm. Owing to the high sensitivity of stimulated emission near gain saturation to unexpected random factors and the low efficiency of active studies, predicted by the calculations above, sufficient increase of relative sensitivity was achieved only for a highly reflective resonator with $\rho_1\rho_2 \cong 0.9$. The actual sensitivity to the intracavity losses was about 10 times higher: $\sim$0.01 or less – and nearly independent of the left or the right relative placement of calibrated mixtures of methanol measured [7.9].

Since the relative increase in sensitivity to internal resonator losses in lasers with high gain factors is not as great, it is reasonable to consider placing into a resonator an extra multiple reflection cell, increasing the number of interactions only with a test substance (Fig. 7.8a). For such a measurement, compared with the active study without multiple interactions, Eq. (7.10) for the intensity of the stimulated light emission with the multiple-reflection cell becomes:

$$I = const \cdot (G_0 - \chi_0) / \left[(1 - \rho_2\tau_0) + (1 - \rho_N\tau_0)\sqrt{\rho_2/\rho_N} \right], \tag{7.13}$$

where $G_0 = b_0\ell_0$, $\chi = \ln\sqrt{\rho_N\rho_2\tau_0^2}$ is the optical loss for a single pass of the entire laser cavity, τ_0 is the transmittance of the active element, and $\rho_N = \bar{\rho}^{N-1}(1 - \chi_x)^N$ is the effective reflectance of the multiple-reflection cell with internal loss χ_x of the object to be studied on N light passes via the cell (see Chap. 6). Separating the small loss under study χ_x for a single cavity pass from the total loss χ and the attenuation loss χ_0 for the entire resonator, and assuming all factors to be small,

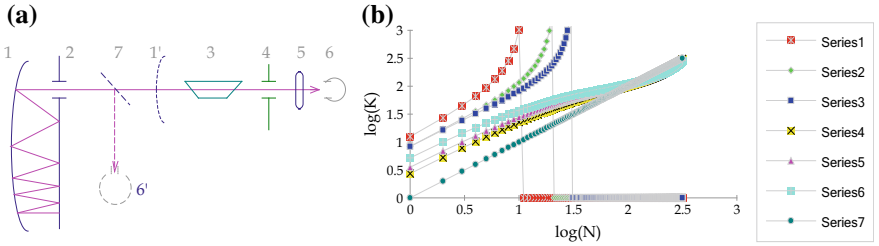

Fig. 7.8 **a** Layout for internal and external (dotted line) placement of multiple-reflection cell for a laser resonator: 1,1′ – rear mirror; 2 – cell; 3 – active element; 4 – aperture; 5 – output coupler; 6,6′ – detector; 7 – splitter. **b** Multiple reflections cell inside (Series 1–6) and outside (Series 7) of laser cavity: Series 1, 2, 3 – G = 0.25; Series 4, 5, 6 – G = 2.5; Series 1, 4 – Q = 0.7; Series 2, 5 – Q = 0.8; Series 3, 6 – Q = 0.9

thus: $\chi - \chi_0 = N\chi_x/2 \ll \chi, \chi_0$, one can express the relative measurement sensitivity by analogy with Eq. (7.12) in the form [7.10]:

$$\mathrm{K} \equiv \frac{I_0 - I}{\chi_x I_0} = N\left[\frac{1}{2(G_0 - \chi_0)} + \frac{1}{2\chi_0}\right], \tag{7.14}$$

where $2\chi_0 = (1 - \rho_2) + (N - 1)(1 - \rho_1) + 2(1 - \tau_0)$.

The sensitivity behavior of dual light interactions within that combined double laser cavity, having low gain coefficients, can be seen from either Eq. (7.10a) or Eq. (7.10b). The smaller is the difference between the laser gain amplification and the total cavity loss, increasing as a function of the number of multiple reflections in the additional cell, the sooner gain saturation occurs and the higher the loss sensitivity becomes (curves 1–3 in Fig. 7.8b). With respect to the added cavity of multiple reflections, the internal sensitivity increases as the cavity loss decreases, following the gain amplification. For high laser gain factors, when generation suppression does not occur, sensitivity to the intracavity loss is lower than that at the threshold condition (curves 4–6 in Fig. 7.8b). It is actually elevated in comparison with external multiple reflection studies only for the first few interaction cycles and does not remain efficiently high when the number of reflections increases.

One alternative for active intracavity loss measurements is to observe the peak-to-dip ratio for light transmitted and reflected by the laser resonator, consecutively tuning the laser cavity to the resonance for either the generated or the inserted wavelength [7.17]. Figure 7.9 illustrates two typical configurations: an open laser resonator (Fig. 7.9a) and a ring-laser gyroscope cavity (Fig. 7.9b). The latter design generally requires having concurrently a low resonator loss and a high gain-to-noise ratio. In both configurations one resonator mirror is attached to a motion controller so the light path length in the resonator can be periodically swapped around the light wavelength resonance.

In each setting, the law of conservation of energy via detectors D1 and D2 detecting transmitted and reflected light for a cavity consisting of mirrors 1 and 2 irradiated by laser source S via beam splitter BS is:

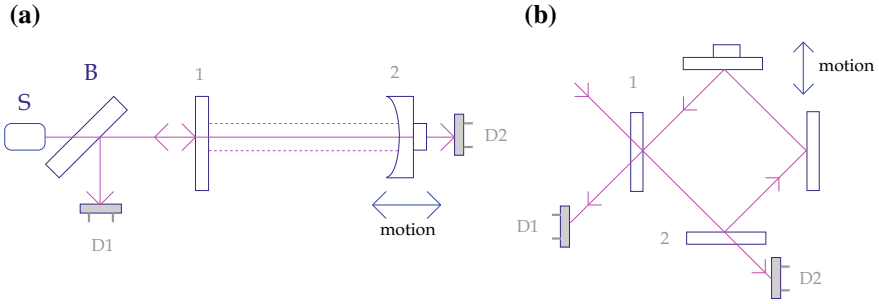

Fig. 7.9 Peak-to-deep resonator loss measurements

$$I_0 = I_L + I_{D1} + I_{D2} = I_L + I_\rho + I\tau_2; \tag{7.15a}$$

$$I_L = I_C \cdot \chi - I_C \cdot \tau_1 - I_C \cdot \tau_2. \tag{7.15b}$$

Here I_0 and I_C are the intensity of light incident on and inside the resonator and I_L, I_ρ, and I_τ are the intensity of lost, reflected, and transmitted light. Combining Eqs. (7.15a, b) for $I_\tau = I_C\tau$ gives:

$$I_0 = I_\rho + I\tau_2 + I_C \cdot \chi - I\tau_1 - I\tau_2 = I_\rho + I_C \cdot (\chi - \tau_1), \tag{7.16}$$

where χ and τ_1 and τ_2 are the attenuation factor of the internal resonator and the transmittances of mirrors 1 and 2. When a piezoelectric drive of the motion controller sweeps the resonator's path length approaching the cavity resonance, the signal transmitted via mirror 2, detected by detector D2, experiences a peak P, and therefore the reflected signal detected by detector D1 sees a dip D:

$$P = I_C \cdot \tau_2; \quad D = I_0 - I_\rho = I_C \cdot (\chi - \tau_1). \tag{7.17}$$

For detectors D_1 and D_2 synchronized by the motion controller, the measured dip-to-peak ratio is:

$$D/P = (\chi - \tau_1)/\tau_2. \tag{7.18}$$

As a result, the internal resonator loss χ can be determined from Eq. (7.18) as the relation:

$$\chi = \tau_1(D/P) + \tau_2. \tag{7.19}$$

For equivalent transmittance $\tau_1 = \tau_2$ of resonator mirrors 1 and 2, the dip-to-peak detection provides:

$$\chi = \tau \cdot [(D/P) + 1], \tag{7.20}$$

which in addition to the dip-to-peak ratio requires measuring the transmittance of every mirror of the resonator.

Owing to distinct path lengths of the resonator for s and p polarizations caused by the phase shift experienced by each component of incident radiation at every mirror reflection, measurements were made separately for s and p polarization states. The observed dip-to-peak ratios for s-mode were much higher than those for p-mode, having sharper s-mode resonances [7.17]. When the active element was placed into the emitting laser resonator, the factual gain G was measured as the difference of the effective and the actual loss: $L_{eff} = L - G$, with laser generation being on and off.

7.3 Intracavity and Ringdown Spectroscopy

Correlations of the fundamentally linear structure of stimulated laser emission in the presence of spectrally dependent losses in an open laser resonator identify the prospects for detection of an ultimately small content of an object to be tested. As first found for lasers with inhomogeneous line broadening [II.1, II.8, 7.11], insertion into a laser cavity of a spectrally dependent transmission loss τ:

$$1/\tau(\omega) = 1/\tau_0 - \Delta(1/\tau) \cdot \cos(2\pi\omega/\Delta\omega), \tag{7.21}$$

causes spike suppression ΔI of a quasi-infinite laser spectrum at intensity I_0:

$$\frac{\Delta I(\omega)}{I_0} = \frac{\Delta(1/\tau)}{1/\tau_0}\left[\frac{p\tau_0}{I_0} + \frac{I_0}{\Phi\tau_0}\exp\left(-\frac{2\pi\gamma}{\Delta\omega}\right)\right]^{-1}. \tag{7.22}$$

Here τ_0 and τ are the initial and interrupted spectral transmittance of the laser cavity, p and Φ are the power of the spontaneous noise and the pumping light, and γ is the dispersion bandwidth for the homogeneous line broadening. In this case and when the spectral bandwidth Δω of any loss inserted into the laser cavity is much narrower than the dispersion bandwidth γ, the second component in relation (7.22) becomes much smaller than the first one. As a result, the measurement sensitivity to a low absorption loss becomes defined by the ratio $p\tau_0/I_0$ of spontaneous to stimulated emission of radiation. For a broad inhomogeneous transition, the respectively expanded spectral ratio should result in extremely high sensitivity to the absorption loss implemented in such a laser cavity.

Even in one of the first experiments conducted [7.11], the magnitudes of the detected linear absorption coefficient α inside the open resonator of a Nd:glass laser with spectral bandwidth $\gamma = 20\ cm^{-1}$ and $p\tau_0/I_0 = 10^{-4}$–10^{-6} were in the range $\alpha = 10^{-7}$–$10^{-8}\ cm^{-1}$. To verify such high sensitivity, a Fabry–Perot interferometer made as a glass cavity with Brewster-angle windows was implemented in an indiscriminating open laser resonator. The reflectance ρ of the border between the glass cavity and the filling-in liquid was changed by varying the benzol concentration in a chlorine–benzol solution. While the remaining specimen reflectance declined to $2 \cdot 10^{-7}$, certain pulse modulations, having a relative depth of about

10%, were still observed. However, such an internal laser spectrograph does not react linearly to any changes of the inserted losses: the lower is the actual loss $\Delta(1/\tau)$, the longer should be the time t of its conceivable action; therefore, one must have: $\Delta(1/\tau) \cdot t \rightarrow 1$.

Occupancy of a laser cavity by an absorbing substance changes the correlation between gain and loss factors during each individual generation act of laser stimulated emission. Hence, the intensity of laser emission at angular frequency ω as a function of time t changes according to:

$$I(\omega) = I_0(\omega) \exp[b_0(\omega) - \mu(\omega)ct], \tag{7.23}$$

where $b_0(\omega)$ and $\mu(\omega)$ are the gain and loss coefficients at angular frequency ω and ct is the optical path length of emitted light wave. Disregarding spontaneous noise compared with stimulated emission for any steady-state transition, the laser gain is almost equal to the entire internal loss averaged over the generated frequency scale, and the intensity of forced spike suppression in a limited dynamic range can be assumed to be dependent only on the additional diminutive absorption loss $\alpha(\omega)$ under study:

$$I(\omega) = I_0(\omega) \exp[-\Delta a(\omega)ct]. \tag{7.24}$$

The ratio of the entire exposure of emission at the absorption frequency to that near the absorption frequency:

$$H(\omega_0)/H_0 = [1 - \exp(a_0 ct)]/(a_0 ct). \tag{7.25}$$

Relation (7.25) shows that the sensitivity of active intracavity laser spectroscopy is proportional to the time interval of the steady-state phase of the laser's stimulated emission, though any increase of sensitivity along with a pulse-length increase of a solid-state laser is limited by the negative effects of spontaneous emission and deviations from the linear transition of intensity with the spectral coordinate of the loss matching its intensity spike. In experiments with a pulse length of about 20 ms in an indiscriminating open resonator of a Nd:glass laser, the sustained linear measurement process was limited to times $t \geq$ 10–12 ms by the small dynamic range of the photographic registration applied [7.12], but not by the spontaneous emission. In the approximation of nearly rectangular shape of all laser pulses, being true at $a_0 ct < 10$, the measured losses computed by Eq. (7.25) were near $(7 - 12) \cdot 10^{-9}$ cm^{-1}.

To maintain a constant gain factor of a laser with the inhomogeneous line broadening required for any quantitative low-loss measurements, nonuniform saturation behavior has to be realized over its broad frequency spectrum containing, for example, 10^4 longitudinal modes. A dye laser exhibits homogeneous line broadening with relatively wide amplification regions. That allows one to isolate the relatively broad spectral bandwidth γ of a nearly constant amplification factor, and to consequently realize high sensitivity of spectral loss detection in a narrow

frequency interval $\Delta\omega$, as it can be seen from Eq. (7.22). In experiments with a pulsed rhodamine 6G dye laser with $t = 2$ μs and $\gamma = 578$–582 nm, a law-governed dip in the spectral intensity was observed via small changes of the initial optical density of salt solutions with absorption line width of $\Delta\lambda = 0.1$ nm [7.13]. With the spectral range of the laser's spontaneous emission extended to $\Delta\gamma = 30$ nm, the actual sensitivity to a low optical loss inserted in the cavity was increased to $1 \cdot 10^{-4}$. At the same time, any alteration of the Q factor of the laser cavity from 0.9 to 0.6 as well as modulation of laser's pumping power by ±20% had practically no effect on the results obtained in these measurements.

The reproducibility of intracavity laser spectroscopy using a dye laser depends on the stability of the laser gain factor and can be improved by reducing the spectral range of laser emission with selective spectral transition of its population inversion in the active medium, using mode beating, and by thermal effects or hidden inclusions in the active dye. Likely uncertainties are restrained to some degree when a thin dye is activated in a ring resonator. With use of a dye ring laser with a 0.2-mm-thick flat layer of a free-flowing solution of rhodamine 6G in ethylene glycol at the Brewster angle, the reproducibility of the laser amplification factor at $\Delta\gamma = 100$ nm was sustained near $\pm 10^{-5}$ [7.14]. The dye was placed in the center of a concentric cavity of highly reflecting mirrors on relatively thick wedged substrates with $\rho_{1,2} = 0.996$–0.990. For a registration time of the steady-state emission maintained at $t \cong 3 \cdot 10^{-2}$ s, the sensitivity to intracavity absorption losses was extended to 10^{-9} cm^{-1}.

Any temporal dependence of laser exposure, computed by expression (7.25), has to be linear with the slope defined by the linear absorption coefficient studied. However, even for the steady-state phase status of stimulated emission, laser mode competition, causing spectral line broadening and the successive high sensitivity being sought, subsequently results in a nonlinear intensity profile. If relative depths of actually observed absorption spikes are low, the intensity of laser emission detected in experiments does not change and the nearly linear character of the absorption peaks can be maintained in a small temporal domain, inversely proportional to the intensity level over a lasing threshold. As seen from Fig. 7.10, even for an approximately 5% increase of intensity [7.15], the deviations from linearity started to appear at 1.5–1.7 ms. To maintain the highest temporal resolution possible avoiding feasible nonlinearities of photographic registration needed for the

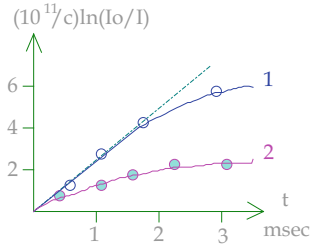

Fig. 7.10 Dependence of lasing intensity on time: $1 - I_0/I = 1.05$; $1 - I_0/I = 1.075$

detection, a vidicon detector was used as the preferred choice for making measurements of ultralow optical losses.

With use of a ring traveling-wave dye laser operating near the lasing threshold (Fig. 7.11), the detection noise was reduced to 10^{-10} cm^{-1}, allowing sensing of optical losses as low as 10^{-9} cm^{-1}. Intracavity 3-μm-thick glass etalon 7 selected spectral width $\Delta\lambda \leq 10^{-9}$ nm of the absorption lines studied within spectral domain of loss registration $\Delta\gamma = 0.24$ nm for a laser pulse duration near $t = 1.15$ ms [7.15]. All internal laser resonator elements were installed at Brewster angles. Faraday rotator 8 and meticulous alignment of the laser mirrors produced traveling-wave emission with the thermostabilized and filtered active dye.

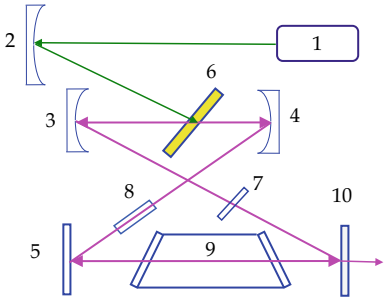

Fig. 7.11 Intra-cavity laser spectrometer: 1 – argon pump; 2–5 – mirrors; 6 – dye; 7 – etalon; 8 – Faraday rotator; 9 – cell; 10 – output coupler

Another intracavity laser spectrometer, functioning as a traditional spectrograph, is shown in Fig. 7.12. Fabry–Perot interferometer 6 having a free spectral range of 200 GHz and a spectral resolution of 2.5 GHz was used as the main scanning element in addition to wedged glass etalon 7 in a dispersing resonator of the dye laser. No mode competition was noticed in the cavity; therefore, the sensitivity of such a laser spectrometer was relatively low, but its practical dynamic range was sufficiently large. A linear absorption coefficient as low as approximately $5 \cdot 10^{-7}$ cm^{-1} for a registration time of 30 s was recorded [7.16].

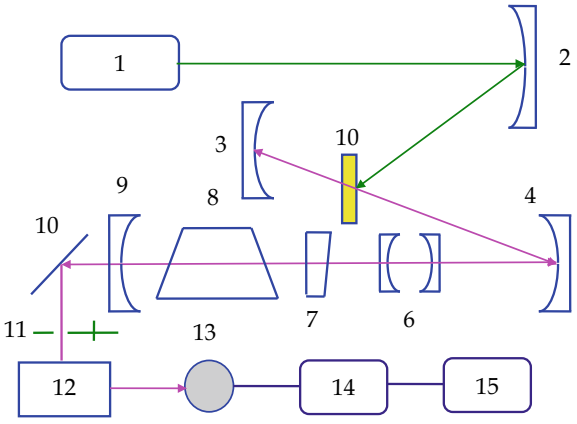

Fig. 7.12 Scanning intra-cavity laser spectrometer: 1 – pump laser; 2, 3, 4, 5 – mirrors; 6 – scanning interferometer; 7 – wedged etalon; 8 – Brewster cell; 9 – output coupler; 10 – dye flow; 11 – modulator; 12 – monochromator; 13 – detector; 14 – lock-in amplifier; 15 – plotter

7.3.1 Sensitivity Limitations of Intracavity Laser Spectroscopy

The previously reviewed sensitivity gains of active intracavity laser spectroscopy to optical losses were accomplished for laser spectrometers being not exactly measurement devices, but mostly detection instruments. The main reason for that is defined by either the complex or the fundamentally unknown dependency of the measured intensity spike depth upon the relative laser intensity, also being a function of other parameters, and changing with time. Consequently, any credible spectrophotometric scale for a specific intracavity spectroscopy measurement is only reproducible in a relatively small dynamic range of an individual type of optical loss, for the substance under study, and for the particular laser resonator involved.

In the analysis above the concept for increased sensitivity to the loss inserted into an active laser resonator was primarily attributed to temporal competition between the resonator modes and to quenching of the modes explicit for a relatively narrow bandwidth of the absorber under study versus the spectral profile of the laser gain. For the steady-state condition of laser generation or when very few modes exist in a resonator, no sensitivity enhancement should be observed. On the basis of that, a single-mode dye laser should exhibit no sensitivity gains to an intracavity loss versus a broadband multimode laser. However, the time evolution of the entire laser spectral profile was observed instead of narrow absorption lines due to resonator losses, and the sensitivity reached a limit long before the steady-state phase [7.22]. Moreover, the factually observed sensitivity of intracavity spectroscopy was a function of the laser's pumping power and bandwidth [7.20–7.22].

Let us summarize the sensitivity limitations of intracavity laser spectroscopy in two cases: for a relatively narrow spectral profile of laser generation compared with that of the absorber, and for a broadband spectrum of spontaneous emission with Gaussian distribution, being lased having a narrowband absorber inserted into that laser resonator. In the first case, intensity changes of a broadband argon-pumped dye laser can be presumed to linearly depend on the ratio of unsaturated gain to intracavity loss:

$$\mathrm{dI/I} = [(\mathrm{g}/\gamma)(\mathrm{g} - \gamma)^{-1}]\mathrm{d}\gamma, \tag{7.26}$$

where the dye laser is generating single-mode radiation at gain g and intracavity loss γ, and its relative intensity dI/I is proportional to intracavity loss change $d\gamma$ [7.18, 7.21, 3.32]. Relation (7.26) approaches $1/\gamma$ at $g \gg \gamma$ and the intensity enhancement is due to multiple reflections in the laser resonator. The enhancement should be infinitely large, $\mathrm{dI/I} \to \infty$ at $\mathrm{g} \to \gamma$, though this simplified supposition could not be confirmed experimentally, and a high sensitivity gain is only achieved using broadband lasers [7.21, 7.22]. The spectral and temporal intensity distribution of dye laser broadband generation with no wavelength-dependent cavity absorption is given by [7.3, 7.20, 7.22]:

$$I(\kappa, t) = (I_0/\Delta\kappa_0)\sqrt{\gamma_c \tau_g/\pi}\exp\left\{-\left[\left(\kappa_g - \kappa_0\right)/\Delta\kappa_0\right]^2 \gamma_c \tau_g\right\}, \tag{7.27}$$

where I_0 is the total intensity of laser generation, τ_g and κ_g are the generation time to the observation instant and the spectral wave number, κ_0 and $\Delta\kappa_0$ are the central wave number of the laser gain profile (cm^{-1}) and the lasing bandwidth related to the number of cavity modes generated, and γ_c is the total cavity loss. With no cavity absorber, the laser-generation spectrum should have a Gaussian shape or some superposition of Gaussian shapes for individual lasing modes, and its intensity should increase and its bandwidth should decrease proportionally to $\sqrt{\tau_g}$, until lasing reaches the single-mode state.

However, experimentally, the predictions of Eq. (7.27) for spectral width $\Delta\kappa_0$ of laser generation decreasing over time τ_g and relative intensity I/I_0 increasing, along with the sensitivity of intracavity absorption, are confirmed only until the lasing approaches the steady-state condition, while the sensitivity reaches its plateau, with multiple modes present in laser generation [7.22]. A high spatial nonuniformity of the optical path length in a dye laser cavity must be responsible for temporal fluctuations, which destroy the time correlation for the mode structure in the laser cavity and the predictions of Eq. (7.27), limiting the factual sensitivity of intracavity spectroscopy.

With a relatively narrowband absorber inside a dye laser cavity, Eq. (7.27) becomes:

$$I(\kappa,t) = (I_0/\Delta\kappa_0)\sqrt{\gamma_c\tau_g/\pi}\exp\left\{-\left[\left(\kappa_g-\kappa_0\right)/\Delta\kappa_0\right]^2\gamma_c\tau_g - \chi(k)(\ell/L)c\tau_g\right\}. \tag{7.28}$$

Here $\chi(\kappa)$ is the wavelength-dependent absorber loss (absorption plus scattering), ℓ/L is the relative length of the absorber versus the cavity length, and c is the light velocity. The lasing is presumed to be broadband compared with the absorption spectrum for weak intracavity losses: $\chi(k)(\ell/L)c\tau_g \leq 1$. Equation (7.28) was experimentally confirmed for the central region of a laser spectrum [7.20–7.22], with the sensitivity enhancement of intracavity spectroscopy being analogous to that for the intracavity multiple-reflection measurement in a passive resonator. In summary, the sensitivity enhancement of intracavity laser spectroscopy is mostly effective via stabilizing laser generation parameters, controlling the stability of the laser cavity path length, and operating near the lasing threshold.

7.3.2 *Cavity Ringdown Spectroscopy*

The highest sensitivity of intracavity absorption spectroscopy is reached at extremes of time-dependent events in laser resonators. Even higher sensitivity can be reached in a passive multipass cavity excited by pulsed laser light, inherently exhibiting much shorter coherence lengths than identical cw radiation, therefore reducing first-order etalon effects. Although pulsed methods are analyzed in the next chapter, let us review the conceptual aspects of *laser cavity ringdown spectroscopy* mainly targeting detection of very low concentrations of gaseous substances in resonant multiple-reflection cavities and evaluation of high reflectance of mirrors themselves. Such a methodology, which in its diverse application aspects is reviewed in Sect. 8.3, is based on creating a high-reflectivity Fabry–Perot cavity in transmitted

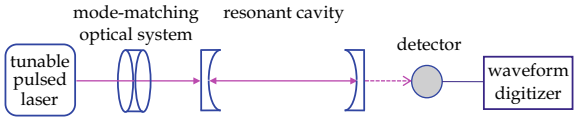

Fig. 7.13 Cavity ring-down waveform spectrometer

radiation at resonances matching the light wavelength. Since that cavity becomes transparent for the resonant wave, passing decaying light can be observed by an outer detector with relatively high sensitivity to the intracavity loss [7.23]. An example of decay-digitizing ringdown-rate spectrometer is illustrated in Fig. 7.13. A wavelength-selective cavity (either empty or filled with a test substance) is probed by short pulsed radiation (in comparison with the cavity round trip time) at the tuning resonant wavelength, and the temporal behavior of such multiple-reflection cell transmittance is registered. Maxima of transmittance occur for the cell resonance modes tuned to multiples of the emitted wavelengths. The shorter is the laser pulse, the wider is its spectral width, and the shorter is the coherence length for multiple reflections to add stochastically, limiting interference noise (see Sects. 3.3 and 7.4) due to overlapping of partially coherent light beams.

Providing that even a short laser pulse is much longer than the round trip time $\tau_c = 2L_c/c$ in the open resonator, the light pulse amplitudes a_i and frequencies ν_i [7.23]:

$$E(\nu) = \frac{1}{2\pi}\int_{-\infty}^{\infty} dt \cdot E(t)\mathrm{e}^{-i2\pi\nu t} = \sum_i a_i s(\nu - \nu_i). \tag{7.29}$$

For a ringdown resonant cell, the Airy formulae in transmission (Eqs. (3.121), (3.122)) can be rewritten for the cell acceptance function $C(\nu)$ of frequency ν as:

$$C(\nu) = \left((1-\rho)^2 e^{i2\varphi}\right)/\left(2ie^{i\varphi}\sin\varphi + \left(1-\rho^2\right)\right) \cong \sum_m c(\nu - \nu_m), \tag{7.30}$$

where $(1 - \rho)$ and ρ are the transmittance and reflectance of mirrors making a cavity of length L_c, $\varphi = 2\pi\nu L_c/c$, $\nu_m = ic/2L_c$, and $\nu_i = ic/2L_s$. The cavity-coupled pulse energy W is proportional to the square product of the pulse amplitude $E(\nu)$ and the cavity acceptance function $C(\nu)$ integrated over frequency:

$$\begin{aligned} W &\propto \int |E(\nu)C(\nu)|^2 d\nu \\ &= \int d\nu \sum_{i,j} a_i a_j^* s(\nu - \nu_i)s^*\left(\nu - \nu_j\right) \sum_{m,n} c(\nu - \nu_m)c^*(\nu - \nu_n). \end{aligned} \tag{7.31}$$

Presuming the cavity modes are well separated, disregarding terms with $i \neq j$ and $m \neq n$, and ignoring any variation of the laser spectrum across the cavity acceptance function C, one may approximate the mode function $c^2(\nu - \nu_m)$, which is much narrower than other frequency structures, as a delta function, thus:

$$W \propto \sum_{i,m} |a_i|^2 |s(\nu_m - \nu_i)|^2 \equiv \sum_{i,m} A_i S(\nu_m - \nu_i). \tag{7.32}$$

When ringdown measurements are based on signal averaging and numerical fitting of the loss rate, pulse-to-pulse fluctuation and in-pulse fluctuation of the pulse energy in the detection time must be known. For Gaussian pulse form $S(\nu_m - \nu_i) \sim \exp[-2\pi^2\tau_p^2(\nu_m - \nu_i)]$ and pulse width τ_p, the rms fluctuations of relative energy in a ringdown cavity, creating noise and limiting the sensitivity of measurement, become [7.23]:

$$W_{rms}/\overline{W} \leq \left(1\Big/\sqrt{N}\right)\sqrt{\sqrt{\pi}/P - 1} \cong 1\Big/\sqrt{NP}, \tag{7.33}$$

where $P = 2L_c/c\tau_p \leq 1$ is the number of cavity modes fitting within every laser mode, total of N. Relation (7.33) underlines an intuitive averaging conclusion: the coupled-energy instability due to etalon effects is inversely proportional to the number of longitudinal modes in the ringdown cavity.

To narrow the cavity bandwidth and keep fluctuations low, the laser spectrometer in Fig. 7.13 had a 1-m ringdown cavity with a total loss per pass $\chi_p = (1 - \rho^2) = 1.2 \cdot 10^{-4}$ excited by 15-ns pulses with 0.05-nm bandwidth generated in a 0.25-m-long dye laser resonator. Ringdown cavity modes viewed as one delta function were 18 kHz wide, separated by 150 MHz. The source lased 62 longitudinal modes 70 MHz wide, broadly separated by approximately 600 MHz. Fluctuations of less than 15% were computed to occur, whereas the experimentally observed fluctuations were approximately 10%. For cavity ringdown measurement, decay-rate information with and without a test substance in the cavity was accumulated via the end mirror and digitized, numerically fitting the loss rate obtained to a single-exponential waveform:

$$\begin{aligned} F(t)_i &= A_i + B_i \exp\left(-(t - t_0)/\tau_{c,empty}\right); \\ F(t)_j &= A_j + B_j \exp\left(-(t - t_0)/\tau_{c,test}\right), \end{aligned} \tag{7.34}$$

where $A_{i,j}$ and $B_{i,j}$ are measurement constants. The detected absorption peaks were near the hundreds of parts per million level for a cavity round trip of 200 cm, converting to absorption coefficients near or better than 1 ppm [7.23].

The prior analysis presumed certain spectrally uniform characteristics of ringdown cavities themselves. The mean cavity mirror reflectance ρ and intracavity absorption or scattering loss χ define the ringdown time: $\tau_0 = L_c/[c(|\ln(\rho)|)]$; $\tau_\chi = L_c/[c(|\ln(\rho - \chi)|)]$, becoming $\tau_0 \approx L_c/[c(1 - \rho)]$ at $\rho \to 1.0$. In the case of a spectrally selective cavity with an absorbing and scattering substance, the intensity *I(t)* of the coupled light decays exponentially in time, presuming that absorption follows Beer's law:

$$I(t) \propto \int_0^\infty I(\lambda) \exp[-1/\tau(\lambda)] \cdot t \cdot d\lambda. \tag{7.35}$$

Here I(λ) is the pulse spectral intensity distribution and τ(λ) is the integrated decay time [7.24]:

$$\tau(\lambda) = L_c / \left\{ c \left[|\ln \rho(\lambda)| + \sum_i \mu_i(\lambda) \int_0^{L_c} N_i(x) dx \right] \right\}, \tag{7.36}$$

where $\mu_i(\lambda)$ is the attenuation cross section, $N_i(x)$ is the number density, and $\mu_i N_i(\lambda, x)$ is the total attenuation coefficient accounting for the absorption and scattering losses, presumed to be time-independent, for a source spectral line width negligible in comparison with absorption features.

To overcome the difficulties associated with a broad bandwidth, nonuniform spectral-intensity distribution, and intensity fluctuations, when sensing short pulses in ringdown measurements, a combination of a ringdown spectrometer and an interferometer, concurrently sensing temporal and spectral characteristics of probing pulses, can be used [7.24]. Combining a cavity ringdown spectrometer and a Michelson interferometer, thus increasing the spectral resolution, resulted in ringdown time dependencies being found by Fourier-transforming the spectrally integrated cell response versus the path-length difference of two interferometer arms. The intensity I of radiation transmitted via such a resonant setting is a function of the frequency ν and the path-length difference Δ of the interferometer arms:

$$I(\Delta) = \int_0^\infty I(\nu) \cos^2(\pi \nu \Delta) d\nu \quad or \quad I(\nu) = \int_{-\infty}^\infty I(\Delta) \exp(i 2\pi \nu \Delta) d\Delta. \tag{7.37}$$

Intensity changes could be observed in time as the ringdown transient per frequency interval:

$$I(\nu, t) = I(\nu, 0) \exp[-t/\tau(\nu)], \tag{7.38}$$

where $I(\nu, 0)$ is the normalized intensity of light entering the empty cavity. Thus, the absorption-dependent intensity could be obtained by the product of two normalized intensities, one at time t for all values of optical path difference Δ and another for the start of time versus Δ:

$$\mathrm{I}(\Delta, \mathrm{t}) = \mathrm{I}_{\mathrm{norm}}(\Delta, \mathrm{t}) \mathrm{I}(\Delta, 0), \tag{7.39}$$

meaning that source's spectral intensity distribution must be known and stable during the test.

In the system in Fig. 7.14, a symmetric ringdown cavity was formed by two 25-mm-diameter plano-concave mirrors, having 25-cm radius of curvature and placed 45 cm apart. Both mirrors were coated to effective reflectance 0.9992 near the 763-nm wavelength of the experiments. Pulsed light from a dye laser was coupled into the cavity via one mirror, and radiation leaking via another mirror was focused onto a 200-μm core fiber and transferred into a Bruker IFS66v spectrometer; the measured pulses were digitized and fit to a single exponential

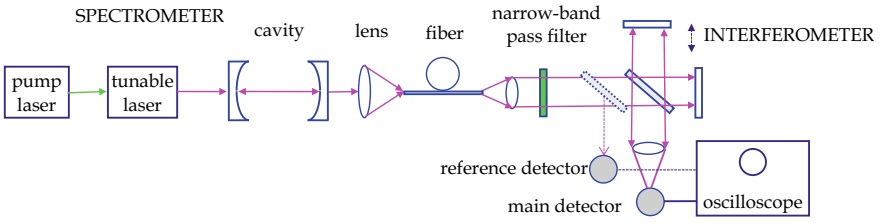

Fig. 7.14 Ring-down interferometer-spectrometer

waveform for the ringdown time to be determined. Light exiting the cell was also split to a photomultiplier-tube reference detector for intensity calibration. Measurements with broad (400-cm^{-1} wide) and narrow (1.1-cm^{-1} wide) pulses were performed for intensity distributions analyzed during the first 100 ns, corresponding to a 30-m path length of the cavity. The absorption losses were measured at 2 μs, or approximately 600 m cell path length. The noise-equivalent detection limit, estimated for normalized absolute absorption measurements, was estimated at $2.5 \cdot 10^{-7}$ cm^{-1}, or 40 km of $1/e$ absorption length [7.24].

An approach to increase the sensitivity of ring-down measurements by stacking a train of short pulses and thus overcoming the limitations of narrow cavity bandwidth is shown in Fig. 7.15 [8.18]. The technique presumes individual pulses in the train to remain mode-matching and resonant with ringdown cavity transverse and longitudinal modes, and the length of coherence of the pulse train to extend over the time expected for the cavity to be filled by radiation with negligible dispersion. The resultant combined pulse become spectrally broad, and may be further resolved at lower sensitivity by adding Fourier-transform, as in Fig. 7.14, or dispersing spectrometry for the stacked pulse. In Fig. 7.15, the train consists of 1-μJ

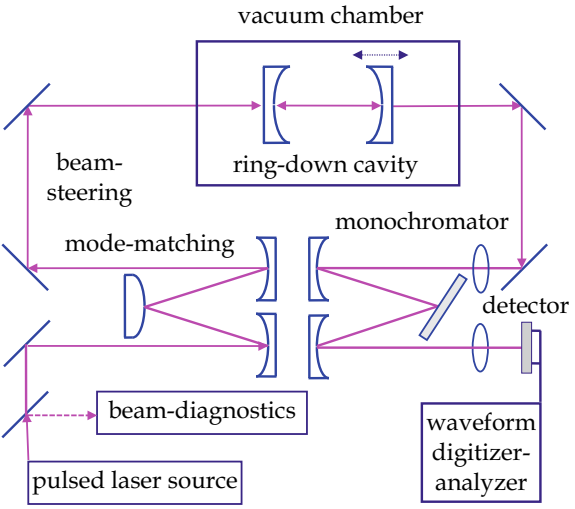

Fig. 7.15 Pulse-stacking ring-down spectrometry

picosecond pulses repeating at 11.818 MHz to up to several milliseconds with the repetition rate having a 5% duty cycle. Radiation approached the respective transform and diffraction limits at 30 μm and 2 μrad of rms positioning and pointing stability with a pulse-train center wavelength stabilized to ±0.0001. A three-mirror telescope was used for mode matching on beam steering and alignment, provided by visible He–Ne laser light via pinholes. A 2.115-m-long symmetric ringdown cell was assembled from two high-reflectivity plano-convex multilayer mirrors on silica substrates and placed in a vacuum chamber. The cell's output was coupled to a monochromator having a grating with a 150 lines per millimeter, blazed for 5-μm wavelength. Pulse stacking allowed the signal-to-noise ratio to be improved from the single-pulse level and an increase of the decay constant to 10.5 μs from 7.5 μs, related to the average-mirror loss of 940 ppm, thus correcting the loss value to 650 ppm for 5.38-μm center wavelength. The noise-level sensitivity, corresponding to ±20-ns variation of the measured 10.5-μs decay time, was estimated to be nearly $2 \cdot 10^{-9}$ cm^{-1} [8.18].

To a certain extent, the practical limits of sensitivity for ringdown measurements are defined by the interference effects [7.23–7.32]. If there is no sample in a ringdown cavity, the intensity I of cavity-coupled light decreases for each round trip time t_c by the squared mirror reflectance: $I(t + t_c) = \rho^2 I(t)$. After n round trips, respective signal S becomes:

$$S(t + nt_c) = \exp(2n \ln \rho) S(t) \cong \exp[-2n(1 - \rho)] S(t). \tag{7.40}$$

In the cavity with a sample of frequency-dependent absorption coefficient $\alpha(\nu)$, signal S is [7.25]:

$$S(t + nt_c, \alpha) \cong \exp\{-n[2(1 - \rho) + \alpha(\nu) L_c]\} S(t). \tag{7.41}$$

Since the ringdown time τ is inversely proportional to the loss coefficient μ of the cavity: $\tau_0 = t_c/\mu_0$, $\tau = tc/\mu$, where $\mu_0 = 2(1 - \rho_1\rho_2)$, $\mu_0 = 2[(1 - \rho_1\rho_2) + \alpha(\nu)L_c]$, loss α is given by the change $\Delta\tau$ of the ringdown time:

$$\alpha(\nu) L_c = (1 - \rho_1\rho_2)(\tau - \tau_0)/\tau = (1 - \rho_1\rho_2)(\Delta\tau/\tau). \tag{7.42}$$

Presuming $\rho_{1,2} = 0.9999$ and $\Delta\tau/\tau = 0.001$, the sensitivity of ringdown spectroscopy would be limited to near $2 \cdot 10^{-7}$, though practical limitations could be even tighter, since the reflectivity of a coated mirror has a tendency to degrade significantly over time, particularly under exposure to laser or other radiation [II.20, 8.16].

Multibeam interference in a ringdown Fabry–Perot cavity excited by coherent light in its fundamental mode is defined by Airy response functions (Eqs. (3.122)–(3.125)). In view of the linear superposition principle of interference phenomena, occurring independently for different frequency components (see Chaps. 1, 3, 6 and 8), the complex optical-response function $\widetilde{H}_{qmn}(\omega)$, expressing correlations among input and output cavity fields [1.1, 7.26]: $\tilde{e}_{qmn}(\omega) = \widetilde{H}_{qmn}(\omega)\tilde{e}_i(\omega_{qmn})$, at frequency ω_{qmn}

for longitudinal q and transverse m, n modes versus laser angular frequency ω_c, is identified by the sum of responses [7.27]:

$$\widetilde{\mathrm{H}}_{mn}(\omega) = \sum_{q} \widetilde{\mathrm{H}}_{qmn}(\omega) = \frac{-2}{\ln(1-\mu_{mn})(2-\mu_{mn})} \times \sum_{\Delta q=-\infty}^{+\infty} \Gamma_{mn}^2 \left\{ \frac{1-(1-\mu_{mn})\exp\left[\left(i\omega-\omega_{qmn}-\Delta q\omega_c\right)t_c\right]}{\Gamma_{mn}^2+\left(\omega-\omega_{qmn}-\Delta q\omega_c\right)^2} \right\}. \quad (7.43)$$

Here eigenfrequencies ν_{qmn} and function $\widetilde{\mathrm{H}}_{mn}(\omega)$ of the empty and stable resonator are [II.5, II.42]: $\nu_{qmn} = \dfrac{\omega_{qmn}}{2\pi} = \dfrac{c}{2\ell}\left[q + \dfrac{2}{\pi}\arctan\left(\dfrac{\ell}{\sqrt{\ell(2r-\ell)}}\right)(m+n+1)\right]$; $\widetilde{\mathrm{H}}_{mn}(\omega) = \dfrac{\mu_{mn}}{1-(1-\mu_{mn})\cdot\exp\left[i\left(\omega-\omega_{qmn}\right)t_r\right]}$, Γ_{mn} is the cavity linewidth; $t_c = 2\ell/c$; μ_{mn} is the cavity single-pass loss, counting diffraction loss σ_{mn}, and ℓ is the cavity length. The linewidth Γ_{mn}, loss μ_{mn}, and time decay constant τ_{mn} for each mode relate as: $\Gamma_{mn} = 1/(2\tau_{mn}) = -\ln(1-\mu_{mn})/t_c$. For frequencies $\left|\left(\omega-\omega_{qmn}\right)\right|t_c \ll 1$ near cavity resonance and small losses $\mu_{mn} \ll 1$, Eq. (7.43) may be closely approximated by the dispersion function:

$$\widetilde{\mathrm{H}}_{qmn}(\omega) \approx \Gamma_{mn}/\left[\Gamma_{mn} - i\left(\omega-\omega_{qmn}\right)\right]. \quad (7.44)$$

If amplitude and phase variations of the excited spectrum are broader than the relative width of the cavity modes, the intensity of light transmitted via a cavity output mirror in the time domain is:

$$I(t) = 2\sqrt{\varepsilon_0/\mu_0}\sum_{qmn}\sum_{q'm'n'} a_i\left(\omega_{qmn}-\omega_l\right)a_i\left(\omega_{qmn}-\omega_l\right)\Gamma_{qmn}\Gamma_{q'm'n'} \times \exp\left(-\Gamma_{qmn}t\right)\exp\left(-\Gamma_{q'm'n'}t\right)\cos\left[\left(\omega_{qmn}-\omega_l\right)t + \varphi_i\left(\omega_{qmn}-\omega_l\right) - \varphi_i\left(\omega_{q'm'n'}-\omega_l\right)\right]C_{mn}C^*_{m'n'}\iint \psi_{mn}(x,y,L_c/2)\psi^*_{m'n'}(x,y,L_c/2)dxdy, \quad (7.45)$$

where ε_0 and μ_0 are the free space permittivity and permeability, ω_ℓ is the laser's angular frequency, $\alpha_{\mathrm{i}}(\omega - \omega_\ell)$ and $\varphi_{\mathrm{i}}(\omega - \omega_\ell)$ are field's spectral amplitude and phase, and C_{mn} is the spatial coupling coefficient of transverse cavity eigenmodes, given by Gauss–Hermite polynomials $\psi_{\mathrm{mn}}(x, y, z)$ as [7.27]:

$$\widetilde{E}(x,y,z,\omega) = \sum_{q}\sum_{mn} C_{mn}\psi_{mn}(x,y,z)\tilde{e}_{qmn}(\omega);$$

$$C_{mn} = \int_{-\infty}^{\infty}\int_{-\infty}^{\infty} u_i(x,y,L_c/2)\psi^*_{mn}(x,y,L_c/2)dxdy. \tag{7.46}$$

Excitation of cavity modes by a narrow Gaussian pulse with linear frequency modulation β gives:

$$I(t) = 2\sqrt{\frac{\varepsilon_0 E_0^2\pi}{\mu_0\sigma_{eff}^2}}\sum_{mn}|C_{mn}|^2\sum_{q=q_{\min}}^{q_{\max}}\times$$
$$\left\{\begin{array}{l}\Gamma_{mn}^2\exp\left(-\left(\omega_{qmn}-\omega_\ell\right)^2\Big/2\sigma_{eff}^2\right)\exp(-2\Gamma_{mn}t)+\\ +2\sum\limits_{q=q_{\min}}^{q_{\max-1}}\sum\limits_{q'=q+1}^{q_{\max}}\left[\begin{array}{l}\Gamma_{mn}^2\exp\left(-\left(\omega_{qmn}-\omega_\ell\right)^2\Big/2\sigma_{eff}^2\right)\exp\left(-\left(\omega_{q'mn}-\omega_\ell\right)^2\Big/2\sigma_{eff}^2\right)\\ \cdot\exp(-2\Gamma_{mn}t)\cos\left(\left(\omega_{qmn}-\omega_{q'mn}\right)t+\varphi\left(\omega_{qmn}-\omega_\ell\right)-\varphi\left(\omega_{qmn}-\omega_\ell\right)\right)\end{array}\right]\end{array}\right\},$$
(7.47)

where σ_{eff} is the effective half-width of the excitation spectrum for input field $e_i(t) = e_0\exp(-\gamma t^2 + i\beta t^2)$. Integration via a cavity exit plane for all frequencies defines its transmittance $T(\omega_\ell) = W(\omega_\ell)/W_{\text{in}}$:

$$T(\omega_\ell) = \frac{1}{W_{in}}\int_0^{\infty}\frac{\sqrt{\varepsilon_0/\mu_0}}{\pi}\sum_{mn}|C_{mn}|^2$$
$$\times\frac{{\mu_{mn}}^2|\mathfrak{a}_i(\omega-\omega_\ell)|^2}{1+(1-\mu_{mn})^2-2(1-\mu_{mn})\cos\left[(\omega-\omega_{qmn})t_c\right]}d\omega. \tag{7.48}$$

Equation (7.48) confirms the cavity transmittance T is dependent on the ratio of the source linewidth to the longitudinal mode spacing of the cavity, causing any pulse chirp to modulate a decaying signal by longitudinal and transverse mode beats. Equation (7.47) predicts the output cavity signal to be the sum of weighted exponential decays modulated by sinusoidal beats at a cavity eigenfrequency spacing as a linear frequency modulation of laser emission with chirp β: $\omega(t) = \omega_\ell - 2\beta t$, with changes in the optical path length $\delta\ell$ shifting the cavity eigenfrequencies: $\delta\omega \cong -(\delta\ell/(\lambda/2))\omega_c$. In experiments performed with relatively long and short decay cavities pumped by either a pulsed Nd^{3+}:YAG laser at 840 nm, $\Delta t \cong 4.8$ ns, and $\Delta\nu \cong 100$ MHz, or a Ti:Al_2O_3 laser at 760 nm, $\Delta t \cong 3.3$ ns, and $\Delta\nu \cong 135$MHz, the measured ringdown signals, at a given laser carrier frequency, were integrated up to five times over the ringdown time constant e^{-1} of the cavity. From a 13.39-cm long to an 180-cm long empty cavity, the excitation of only transverse modes and longitudinal and transverse modes with deep modulation of the signal at maxima separated by the free spectral range of the cavity was observed [7.27], confirming the predictions of Eqs. (7.47) and (7.48). Mode beatings vanished for low-order transverse modes for a wide cross-section cavity. The modeled and experiential evidence of longitudinal and transverse spectral-mode beatings highlights the fact that without explicit time averaging,

a ringdown cavity can be inherently spectrally selective, causing distortion of an exponential decay due to mode-beating noise [7.26, 7.27].

Multimode Versus Single-Mode Studies

For short-pulse laser light irradiating a matching ringdown cavity, the light coupling occurs for multiple longitudinal modes, as well as for some transverse modes. The longitudinal mode beating leads to a recurring fast series of decay pulses matching the cavity and to transverse mode beatings for cavity-mode mismatch. Any ringdown signal should be electronically filtered, removing faster beatings from slower decays; however, a decaying pulse envelope may become a multiexponential function, since exited modes will have different cavity losses, leading to the necessity to perform deconvolution of excited cavity modes, adding processing noise and compromising the sensitivity of the ringdown study [7.25, 7.30].

For a cavity excitation pulse of a finite frequency bandwidth, the time-dependent intensity $I(t)$ of the cavity ringdown signal integrated over the entire bandwidth of frequencies ν is [7.28, 7.25]:

$$I(t) = \exp[-t \cdot c \cdot (1 - \rho_1\rho_2)/\ell] \int_{-\infty}^{\infty} I(\nu - \nu_\ell) \cdot \exp[-t \cdot c \cdot \alpha(\nu - \nu_0)/\ell] \cdot d\nu. \tag{7.49}$$

Here the measured absorptance $\alpha(\nu - \nu_0)$ and the beam intensity $I(\nu - \nu_0)$ are both functions of frequency, while α is the integral-normalized absorption line shape centered at ν_0 but I is the individual spectral intensity I_ν integrated over frequency and centered at ν_ℓ. Each frequency in Eq. (7.49) decays with its time constant τ_ν and the integrated signal is the weighted summation of frequency components coupled into the cavity of length ℓ. When $I(\nu)$ is a delta function and the $\alpha(\nu)$ value does not significantly change over $\Delta\nu$, the ringdown signal decays as a single exponential, but since the lased frequency components commonly fluctuate from one pulse to another, the signal becomes the convoluted time function (see Sect. 3.2).

As common practice, the ringdown function is measured by digitizing the output signal I(t) when fitting data to a single-exponential function while determining the cavity absorption loss. The digitization is associated with time window Δt, over which the data are fit. Hypothetically, the window should be as short as possible: $\Delta t \to 0$, also starting at the beginning of the ringdown signal $t \to 0$. However, such a sampling would lead to indistinguishable signal probes and increased fluctuations owing to finite digitization rates and noise created by scattered and diffracted light. A nearly fourfold variation of the time window led to 50% changes in experimentally measured losses caused by a wider bandwidth of a dye laser versus an absorber: 1.5 GHz versus 450 MHz [7.28]. Equation (7.49) points out that when ringdown losses near and away from the absorption band center are dominated, respectively, by the absorber and cavity mirrors, the ringdown time related to the absorber can become relatively low, causing the single-exponential decay approximation to vanish.

For a pulsed laser generating multiple longitudinal modes of fluctuating wavelengths and amplitudes, radiation injected into and transmitted by a matching ringdown cavity of length ℓ, longer than the pulse length of duration τ, will consist of a series of pulses, separated by time $t_c = 2\ell/c$ with relative pulse-to-pulse intensity variation $dI/I = (1 - \rho_1\rho_2)dt/t_c$. For an input pulse of amplitude A, having k modes $A_k(t)$ at phase $\psi_k = 4\pi\ell/\lambda_k$, since diverse modes do not interfere, the total intensity I_n is [7.29]:

$$I_n = \rho^{2n}(1-\rho)^2 \sum_k \left[\sum_{m=0}^{\infty} A_k(t - mt_c)\rho^m \exp(im\psi_k)\right]^2. \tag{7.50}$$

Here only discrete instances of time $t = n \cdot t_c$ are considered for $t < mt_c$ at identical cavity mirrors, starting at $t \cong 0$, when input light is turned off to initiate the ringdown process. Equation (7.50) shows that a ρ^{2n}-factored exponential decay is common for all modes, and fluctuations affect only the intensity of light initially stored in the cavity, but the decaying intensity can be affected if $\psi_k \neq$ const.

Interference effects due to cavity length changes ΔL can be modeled via the cavity mirror oscillation in sinusoidal motions of period T longer than decay time τ for a uniform movement of velocity $v = 2\pi\Delta L/T$. For each mirror reflection, light frequency ω_i is altered by the Doppler effect: $\omega_d = \omega_i(1 - v/c)(1 + v/c) \approx (1 - v/c)\omega_i \equiv \beta\omega_i$, for cavity length ℓ concurrently modified by $1/\beta$. The Doppler shift and the cavity length changes affect the amplitude Fourier spectrum $A(t) = \int A(\omega)\exp(i\omega t)d\omega$ of the light pulse of the source frequency spectrum $A(\omega)$ at the cavity exit before it is switched off:

$$A(t) = \int_{-\infty}^{\infty} \exp(i\omega t) \sum_{m=0}^{\infty} (\beta\rho)^m A(\beta^m\omega) \exp\left[(-i\omega\ell/c)\left(2m + 1 - 2m^2 v/c\right)\right] d\omega. \tag{7.51}$$

The Gaussian-shape pulse $A(\omega) = \exp\left(-((\omega - \omega_0)/\Delta\omega)^2\right)$ at temporal resolution higher than the wavelength period allowing one to replace time integration by summation leads to intensity I_n [7.29]:

$$I_n = (\beta\rho)^{2n} \int_{-\infty}^{\infty} \left[\sum_{m=0}^{\infty} (\beta\rho)^m \exp\left(-\left(\omega\beta^{n+m} - \omega_0\right)^2/\Delta\omega^2\right) \exp(i\psi)\right]^2 d\omega$$
$$\underset{\beta\to 1}{=} \rho^{2n} F(n) = \rho^{2n} \sum_k F_k(n), \tag{7.52}$$

where $\psi = (2\omega\ell/c)(m - (m^2 + 2nm)v/c)$. At velocity: $v \ll c$, the time dependent intensity I_n is a product of exponential decay ρ^{2n} and time function $F(n)$ of pulse linewidth $\Delta\psi$, cavity mirror reflectivity ρ, and cavity length ℓ, with $F(n)$ fluctuating

erratically at pulse-to-pulse instabilities, showing up as noise in the main exponential decay ρ^{2n} and changing the average decay time τ. Therefore, a time averaging among repetitive pulses is essential, but is only efficient for a large number of modes [7.29].

Single-mode ringdown spectroscopy addresses the convolution problem of Eq. (7.49), as well as interference effects of pulse frequency fluctuation among various longitudinal modes, by sweep-tuning the ringdown cavity length and scanning the loss spectrum under study [7.30, 7.31]. By choosing the ringdown cavity length to have a free spectral range of $c/2\ell$, a much larger spectrum than the frequency-stabilized narrow spectrum of incident radiation allows one to excite a single cavity mode and eliminates the need for spectral deconvolution with no transverse-mode beating. The ringdown signal for a transform-limited Gaussian light pulse tuned to a single-mode cavity is [7.27, 7.30]:

$$I(t,\omega) \sim I_0(m,n)\left(\sqrt{2\pi}/\Delta\omega\right)\left(c(1-\rho)/2\ell\right)^2 \exp(-t/\tau(\omega)) + noise + straylight, \tag{7.53}$$

where $I_0(m, n)$ is the initial light intensity coupled into a given cavity transverse mode m, n, and τ(ω) is the ringdown time constant, which varies along the absorption line profile of the test substance:

$$\tau(\omega) = \ell/(c[(1-\rho)+\alpha(\omega)\ell]). \tag{7.54a}$$

Making measurements with the empty and filled cavity, the absorption coefficient α(ω) is:

$$\alpha(\omega) = \left(\tau_{empty} - \tau(\omega)\right)/\left(c\tau_{empty}\tau(\omega)\right). \tag{7.54b}$$

The empty-cavity measurement can be substituted with the respective measurement at the spectral coordinate corresponding to $\alpha(\omega_i) \equiv 0$.

Noise-floor sensitivity, given as the relative standard deviation of ringdown time uncertainty, can be limited by domination of either shot noise or technical noise, being sampling-rate-dependent:

$$\begin{aligned} \sigma_\tau/\tau(\omega) &\underset{\substack{shot\\noise}}{=} [2\ell/c(1-\rho)]\sqrt{\sigma_\omega h\omega/\left[\sqrt{2\pi}I_0(m,n)\tau(\omega)\right]}; \\ \sigma_\tau/\tau(\omega) &\underset{\substack{tech\\noise}}{=} [2\sigma_{tech}/I(t=0,\omega)]\sqrt{2\Delta t/\tau(\omega)}. \end{aligned} \tag{7.55}$$

Here, for shot-noise domination, the relative standard deviation is proportional to the reciprocal of the number of decaying cavity photons $I_0(m,n)/hw$ and for statistically independent technical-noise domination it is proportional to the relative uncertainty of the ringdown time $\Delta t/\tau(\omega)$ [7.30].

For a pulse excitation casing essentially multiexponential decay via multiple-mode excited cavity, the ringdown study can be accomplished by fitting to

the monoexponential decay if effectively stabilized broadband laser radiation is coupled to any mode-separating cell, such as White or waveguide cavity, when multiexponential character is not distinguished or the cavity is set to have equal losses for every transverse mode [7.31, 7.32]. Only for the monoexponential decay character $I = I_{offset} + I_0 \exp(-t/\tau)$, can the intracavity loss α_Σ be appropriately estimated from the aggregate decay rate $\beta = 1/\tau_\Sigma$:

$$\alpha_\Sigma = \beta/c - |\ln \rho|/\ell = 1/(c\tau_\Sigma) - |\ln \rho|/\ell. \tag{7.56}$$

Alternatively to using Eqs. (7.35) and (7.36), relying on integration of the total ringdown decay:

$$I_\Sigma \tau_\Sigma = \int_0^\infty I_0 \exp(-t/\tau_\Sigma) dt, \tag{7.57}$$

one can analyze the should-be monoexponential decay as fitting to general form: $I(t) = I_{offset} + I_0 \exp(-\beta t)$, while the decay is measured in successive time windows of equivalent width t_w at delay $\Delta t > t_w$:

$$I_A = \int_{t_w(A)} I(t) dt; \quad I_B = \int_{t_w(B)} I(t) dt; \quad I_O = \int_{t_w(O)} I_{\text{intensity}-\text{offset}}(t) dt. \tag{7.58}$$

For it to be eliminated, the intensity offset I_O needs to be measured at the same time interval t_w as for two time windows A and B, converting the general decay equation: $1/\tau_\Sigma = \ln(I_A/I_B)/(\Delta t)$, to an offset-enhanced one:

$$1/\tau_\Sigma = (1/\Delta t) \ln[(I_A - I_O)/(I_B - I_O)]. \tag{7.59}$$

In a pulsed single-mode experiments performed with a frequency-stabilized parametric laser coupled into a 10-cm-long ringdown cavity, the noise-equivalent intracavity-loss sensitivity level reached approximately $5 \cdot 10^{-10} \text{cm}^{-1}\text{Hz}^{-0.5}$, with 0.3% standard deviation of individual measurement repeatability [7.30]. Multimode measurements based on nonlinear least-squares analysis accounting for signal offset when detecting ringdown decay rates experimentally confirmed the monoexponential decays effectively reached in a stable, steadily aligned resonant cavity under multimode excitation [7.32]. The ringdown high-finesse fiber resonator studies attained near $5 \cdot 10^{-4}$ sensitivity to induced fiber losses [7.33].

Continuous-Wave Ringdown Spectrometers

Continuous-wave (cw) ringdown spectroscopy has tight requirements for matching the narrow linewidth of a single-mode cw laser, such as about 1 MHz, with the narrow bandwidth of a high-reflectivity cavity of finesse larger than 10^4. Equations (7.50)–(7.52) confirm that small thermal drifts of the cavity length or

vibrations easily cause the cavity to be out of resonance. Addressing the cavity-matching issue, one can slowly scan the cavity length to achieve high-efficiency coupling to a beam of incident light and then abruptly switch the beam off, initiating its decay [7.34]. The high-finesse cavity can be stabilized by one polarization component of radiation while creating a decay signal using the orthogonal state of polarization [7.35]. Cavity finesse can be changed in a relatively short wavelength range, permitting cavity stabilization, and some combination of the above techniques may also be used [7.36–7.41].

Following Eqs. (7.49)–(7.52) for a high-finesse ringdown cavity, which length is slowly changed with velocity v, the intensity I(t) of a continuous monochromatic wave at frequency ω could be approximated by summing all multiply reflected wave components inside the cavity: $I_0^M(t) = (1-\rho)^2 I_0^M |\sum \rho^m \exp(i\kappa v t_c m\,(2k-m))|^2$ for $m = k + \delta(\omega)$. For the Lorentzian line shape of a single-mode laser used for cavity excitation, being spectrally broadened by Gaussian white noise and coupled into a high-finesse ringdown cavity, the combined intensity I_Σ of decaying modes could be identified as a sum of all spectral component of the excitation line shape [7.36]:

$$I_\Sigma(t) = \frac{1}{\pi}\int_0^\infty (1-\rho_{1,2})^2 \rho_{1,2}^{2(k+\delta(\omega))} \left| \sum_{m=-(k+\delta(\omega))}^{\infty} \rho_{1,2}^m \exp\left[-i\omega t_c (v/c) m^2\right] \right|^2 \times \frac{I_0 \cdot \Delta\omega \cdot d\omega}{(\omega-\omega_0)^2 + (\Delta\omega/2)^2}. \tag{7.60}$$

Here discrete time instances are viewed in terms of cavity round-trip time $t = k_i \cdot t_c$ much smaller than decay time τ_c of that cavity, ω_0 and $\Delta\omega$ are the line-center frequency and full width at half-maximum of a Lorentzian spectral line, $\delta(\omega)$ is the frequency change, but is an integer for summation: $\delta(\omega) \to |(c/2\pi)(\omega-\omega_0)/\omega_0|$.

When detecting the absorption spectrum of the sample being studied by measuring the ringdown cavity decay time and consecutively scanning the frequency ν_i, where $i = 1, 2, 3, \ldots$ of a cw source coupled to the resonant cavity, one can represent the uncertainties of decay-time measurement of the sample absorption coefficient α_i for concentration C_i via the spectral line shape function $g(\nu_i)$ of emission [II.40, 7.37]:

$$\alpha_i = C_i S_i(T) g(\nu_i)/\sqrt{\pi}, \tag{7.61}$$

where $S_i(T)$ is the strength of absorption line at temperature T and $\sqrt{\pi}$ is the factor normalizing $g(\nu_i)$. Summation over the entire frequency domain of measurement leads to integrated absorption A_Σ:

$$A_\Sigma \equiv C_\Sigma \sum_i S_i(T) = \sqrt{\pi} \sum_i \alpha_i / \sum_i g(\nu_i). \tag{7.62}$$

The relative uncertainty in detecting the concentration of absorbing molecules becomes [7.37]:

$$u(C_\Sigma)^2/C_\Sigma^2 = u(A_\Sigma)^2/A_\Sigma^2 + u(S_\Sigma(T))^2/S_\Sigma(T)^2, \tag{7.63}$$

where the relative uncertainty $u(A_\Sigma)^2/A_\Sigma^2$ is determined by errors of fitting the measured spectrum to a known function: Gaussian or Lorentzian, etc. If α_i and $g(\nu_i)$ are measured independently:

$$u(A_\Sigma)^2/A_\Sigma^2 = \pi \sum_i u(\alpha_i)^2 \Big/ \left(\sum_i \alpha_i\right)^2 + \left(\sqrt{\pi}\Big/\sum_i g(\nu_i)\right)^2 \times \sum_i (\partial g(\nu_i)/\partial \nu_i)^2 u(\nu_i)^2. \tag{7.64}$$

If uncertainties of the measured absorption coefficient $u(\alpha_i)^2$ and of the emitted laser frequencies $u(\nu_i)^2$ are known for sufficiently large sampling data, Eq. (7.64) can be evaluated for any given line function by replacing the summation with integration over the total frequency range [7.37].

Figure 7.16 illustrates the intensity distribution of intracavity transmission for a Fabry–Perot cavity consisting of two mirrors with reflectivity estimated as 0.9999 for 700-nm center wavelength resonant to cw laser emission. One cavity mirror is assumed to be on a piezoelectric transducer sweeping the cavity length and allowing radiation to be accumulated in a resonant mode until it is sharply switched off to start the decay process, which corresponds to 105 ms, $k_i t_c = 0$, in Fig. 7.16. Both the bandwidth of coupled laser modes and the scanning speed affect the ringdown signal by increasing the bandwidth and superimposing several modulation peaks for the decay signal, therefore complicating the fitting to a single exponential function. At the same time, the superposition of multiple frequency

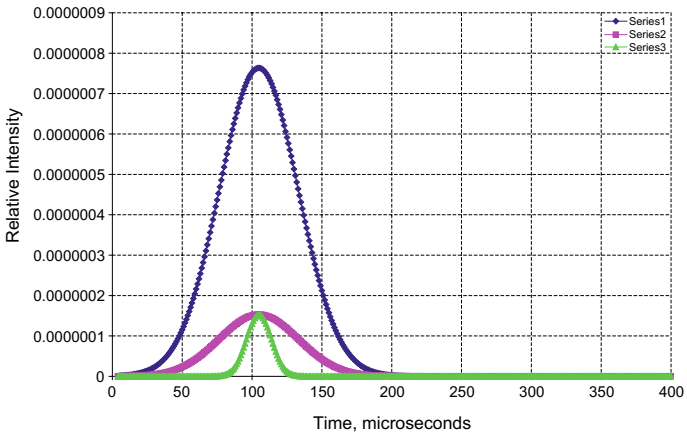

Fig. 7.16 Relative intensity of the ringdown signal in a 30-cm cavity for 700-nm cw laser light at 500 and 100 kHz bandwidth scanned at 4 microseconds/wave (series 1 and 2) and at 100 kHz, 40 microseconds/wave (series 3)

components and the randomness of the phases of light components multiply reflected in the cavity flatten any high-frequency signal modulation.

Active laser-frequency stabilization via an added stable Fabry–Perot interferometer during cw ringdown studies helps increase the sensitivity of decay-cell resonance measurements using radio-frequency phase modulation with optical heterodyne detection of modulation sidebands [7.42]. Concurrently, testing systems with cavity-lock acquisition, which tune a cavity length to frequently pass via resonances, led to the observation of oscillation transients seen even at low mirror velocities with the transients being dependent on the cavity finesses and length and the mirror velocity [7.42, 7.43]. These field transients, the rates of which always increase with time, causing a chirplike behavior, are due to the accumulated Doppler shift with relaxation time of the oscillations equal to the storage time of a high-finesse cavity [7.44]. When the moving mirror passes a cavity resonance, damped oscillations occur, amplifying the Doppler shift and causing modulation of the cavity field.

Cavity-Enhanced Broadband Spectroscopy

If spectral information about loss features is to be taken simultaneously over an extended range of wavelengths while enhancing measurement sensitivity to optical losses, the ringdown technique could utilize a broadband radiation source. Several approaches are capable of accumulating an obviously low-intensity spectral signal of the cavity transmission to be sufficient for registration [7.45–7.47]. One straightforward way for the broadband ringdown spectroscopy is to couple white light into the relatively high-finesse cavity and analyze its output by any spectrograph equipped with a detector array. The multitude of its detectors would simultaneously register time-integrated intensities over a range of wavelengths and fit each of them to a single exponential function obtaining the specimen spectral absorption function by comparing signals in the empty and the filled cavity. Another way is to modulate an incoming beam of cw light or a string of pulses registering an individual wavelength-dependent phase shift caused by each specific time-decay in a given ringdown cavity. Certain combinations of the reviewed techniques could also be used, as seen in Fig. 7.14 and shown in Fig. 7.17 [7.46].

An unstabilized short-arc xenon lamp is used as the main light source with an added neon-lamp for the wavelength calibration of a monochromator. An interference filter narrowed white light source emission into centered at 628-nm spectral region for the highest reflectivity of both cavity mirrors reaching $\rho = 0.9999$. For the 45-cm long cavity spacing and purposely incoherent light source, transmittance $\tau = (1-\rho)^2/(1-\rho^2)$ of that optically stable resonator of two identical mirrors is only $5 \cdot 10^{-5}$ without a specimen, hence requiring to utilize a cooled intensified low noise photodiode-array detector at its noise signal equivalent to having $\rho \approx 10^{-5}$.

Performing measurements of a time integrated intensity of the empty versus one filled by a specie: $I_\tau(t) = I_0(1-\rho)/(1+\rho)$, and by estimating its absorption coefficient as of a low-loss medium $\alpha \approx \ell^{-1}(I_\tau/I_0 - 1)(1-\rho)$ for a resonator of

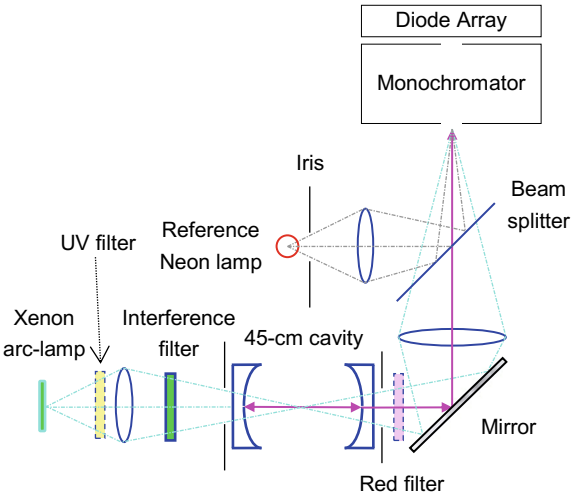

Fig. 7.17 Ring-down cavity enhanced broadband spectrometer

length ℓ (see Chap. 8 for more detail), the resolution capability of a particular system is limited by the density of eigenmodes in a ringdown cavity of a given length and the resolving power of a monochromator. Experimentally reached resolution 0.66 cm^{-1} or 0.026 nm around 628-nm region allowed to resolve weak atmospheric transitions in molecular oxygen at 1 bar and gaseous azulene at its vapor pressure at room temperature when averaging five spectra, taken at 5-s exposure time each with 25 s of the total exposure time [7.46].

From the standpoint of increasing an attainable spectral range of the wavelengths coupled into a chosen high-finesse cavity for ringdown studies, a total-internal-reflection-based resonator could be realized (Fig. 7.18) via illumination of especially low divergence [7.48]. Seen Brewster-angle retroreflector prisms make the broadband multiple-reflection resonator, being bandwidth limited by expected low spectral losses of the prism material and its dispersion, which affects the efficiency of radiation coupling into the cavity for a specifically defined prism spacing. Application of that resonator design are associated with the supercontinuum light sources [7.47] or mode-locked lasers [7.48].

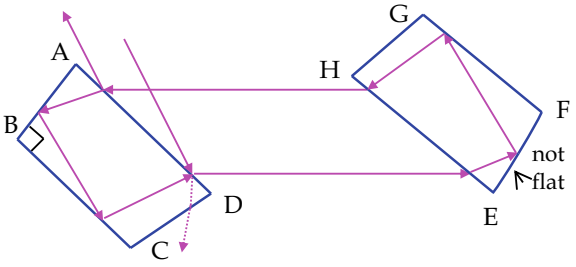

Fig. 7.18 Brewster angle prism-based resonant cavity

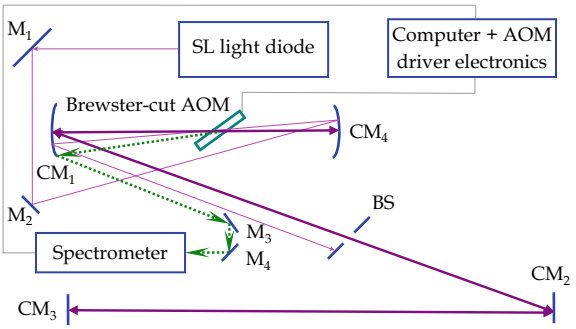

Fig. 7.19 Ring-down cavity-dump spectroscopy setup

Another approach using a broadband, but not necessarily laser, source is shown in Fig. 7.19 [7.49]. The concept is to couple light in and out of a resonant cavity not via a cavity mirror, but via an acousto-optic modulator (AOM) deflecting broadband radiation from a superluminescent (SL) diode to an external spectrometer, without a need of waiting for the cavity energy to reach the systems' detection threshold because of an extra AOM loss. A beam of radiation from *SL* light diode is guided into the main resonator CM_1–CM_4 via mirrors M_1, M_2 and are damped down by beam stop BS as AOM is switched off. The beam is coupled to the resonant mode as AOM is turned on. The stored inside energy is coupled out by mirrors $M_{3,4}$ to spectrometer's detector when AOM is switched off while fast detection is not required, leaving the timing to system electronics. However, the main advantage of ringdown measurement to be made within one pulse decay is no longer valid, requiring controlling pulse intensity fluctuation, plus placement of AOM inside the cavity causes an extra diffraction loss while it is switched on.

To increase the length of a ringdown cavity a V-shape configuration may be deployed [7.63], enabling to reduce back-reflection feedback with a resonator of the excitation laser (Fig. 7.20). By modulating the cavity length using 0.003 cm^{-1} minimal-scan step, $1 - \sigma$ noise-equivalent absorption coefficient of $\sim 2.6 \cdot 10^{-8}$ cm^{-1} $Hz^{-1/2}$ was reached at 0.003 cm^{-1} spectral resolution in 1.2 cm^{-1} spectral span for 2.8-km long absorption path length [7.63]. Differential measurements could be utilized to reduce residual etalon effects (see the next paragraph) via on-off testing for two laser beams at both scan frequencies, enabling a difference spectrum [7.64]. Parallel studies of transmittance-reflectance of a ringdown cavity, synchronized with simultaneous tuning of a cavity length and laser frequency [7.65], plus measurements of a spectral width of a cavity mode [7.66] via frequency-locking and stabilization of cavity's length [7.67], and transmission-reflection ratios or extinctions [7.68–7.72] can be made.

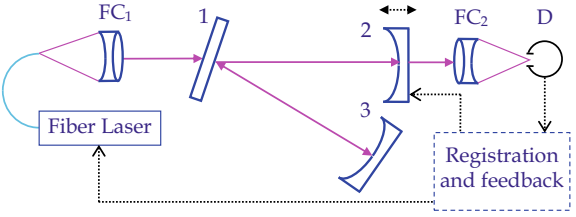

Fig. 7.20 V-shaped ringdown cavity with variable-resonant length

7.4 Reduction of Interference Fringes in Multipass and Derivative Spectroscopy

Nearly every multiple reflection scheme analyzed in this chapter enhances, in one way or another, multiple interactions of radiation with highly reflecting mirrors, that way initiating the basis for multipath interference, if not for specularly reflected beam themselves, but at least for light scattered by mirrors for interference-fringe spacing matching the free spectral range of the cell. Furthermore, any effort to maximize the beam-path length by increasing the number of cell passes leads to likely beam overlapping caused by tighter spacing of adjacent beams and increased interference manifestation, exhibiting itself as intensity noise (see Chap. 3). The appearance of cavity-length matching fringes is highly manifested in various measurement techniques involving multipass cavities or other resonator derivatives – frequency, wavelength, and modulation spectroscopy, wavelength tuning, or spectral scanning (see Chaps. 8 and 10) – owing to changing the frequencies or wavelengths of interfering beams. Since the use of high-finesse cavities is essential for these methods, undesirable interference cannot be completely suppressed, but can be reduced to an acceptable level by one or another form of integration – spatial or temporal modulation, intensity or position dithering, pattern averaging, and electronic filtering, except in "smart" designs guiding each beam to its own optical path and thus avoiding the overlapping [7.50–7.61].

Interference fringes due to etalon effects in high-reflection cavities can especially obscure the results of any multiwavelength measurements, particularly if a cavity is spectrally scanned using a tunable source and the observed interference extremes matching its free spectral range are confused with either the spectral features being investigated or the harmonics of frequency and wavelength modulation in derivative spectroscopy [7.50, 7.51]. During a multipass cavity scan, the observed fringe intensity characteristically goes to the maxima and the minima of interference, corresponding to the cavity spacing, similarly to the interference changes shown in Figs. 3.17 and 3.18, as the fringe amplitudes increase at maxima and decrease at minima of either dual-path or multipath interference. Since cell-related fringes inherently exist in high-finesse cells, to separate them from the spectral features under observation one can ultimately use one or another form of added signal modulation to integrate the fringe amplitudes over the free spectral range of the cavity, averaging interference patterns in space or time, and accumulating the measured signal. The modulation can be applied either to light itself or to the optical-path-length difference responsible for interference fringes created by light beams existing in the cell.

Considering changes of intensity in transmitted and reflected light caused by the multipath interference, Eqs. (3.119) and (3.122) for the equal reflectances $\rho_1 = \rho_2 = \rho$, $\tau_{int} = 1$ and $\tau + \rho = 1$ become:

$$I_\rho = I_0 \frac{4\rho \sin^2(\delta/2)}{(1-\rho)^2 + 4\rho \sin^2(\delta/2)} \equiv I_0 \frac{F \sin^2(\delta/2)}{1 + F \sin^2(\delta/2)}, \tag{7.65}$$

$$I_\tau = I_0 \frac{(1-\rho)^2}{(1-\rho)^2 + 4\rho \sin^2(\delta/2)} \equiv I_0 \frac{1}{1 + F \sin^2(\delta/2)}. \tag{7.66}$$

Here for absent internal losses: $\tau_{\text{int}} = 1$, the finesse parameter: $F = 4\sqrt{\rho_1\rho_2}/(1-\sqrt{\rho_1\rho_2})^2 = 4\rho/(1-\rho)^2$ at $\rho_1 = \rho_2$, identifies the intensity depth of fringes seen in the cell. The fringe sharpness is measured by the fringe half-width ε for the half intensity, identified at half maximum: $\delta = 2m\pi \pm \varepsilon/2$, thus:

$$\frac{I_\tau}{I_0} = \frac{1}{1 + F \sin^2(\delta/2)} \underset{\delta=\varepsilon/2}{=} \frac{1}{1 + F \sin^2(\varepsilon/4)} \underset{\varepsilon\to 0}{=} \frac{1}{1 + F(\varepsilon/4)^2} = \frac{1}{2};$$

$$\varepsilon \to \frac{4}{\sqrt{F}} = \frac{2(1-\rho)}{\sqrt{\rho}}. \tag{7.67}$$

Defining finesse $\Im$ as the fringe separation per 2π phase change [1.1] or as the free spectral range of the cavity related to the half-intensity width ε of the fringes observed, the finesse equation is:

$$\Im \equiv 2\pi/\varepsilon = \pi\sqrt{F}/2 = \pi\sqrt{\sqrt{\rho_1\rho_2}}\Big/\left(1-\sqrt{\rho_1\rho_2}\right) \underset{\tau_{\text{int}}=1;\rho_1=\rho_2=\rho}{=} \pi\sqrt{\rho}/(1-\rho). \tag{7.68}$$

For equal to 0.5% diffuse component of the mirror reflectivity caused by uniform scattering, the peak-to-peak modulation of the transmission intensity has finesse $\Im = 0.223$, thus making such a fringe visibility quite noticeable even for a low mirror-edge diffraction with no beam overlaps, if the radiation specularly reflected by one high quality mirror at reflectance $\rho_{1s} = 0.999975$ interacts with diffuse reflected light from another mirror at $\rho_{2d} = 0.000025$ for effective average reflectance $\rho_{1,2} = 0.005$. The latter interference pattern is imposed over the much higher relative intensity of radiation and may become visible only if accumulated on many transversals of a multipass cell.

Another aspect of a fringe structure superimposed over the intensity of radiation used for the measurement in a multipass cavity is associated with thermally induced drifts of the cavity mirror separation distance, limiting the sensitivity of the loss measurement to be performed, especially since the fringe removal by integration over time inherently relies on some stable fringe pattern. Besides the temperature drifts, short-term fluctuations of cavity gas specimen pressure or particular gas-flow process will cause similar limitations to the measurement sensitivity, particularly for small optical densities corresponding to the lowest optical loss to be detected. Potential fluctuations of the specimen's refractive index at the long path lengths attained in multipass cavities translate into tight requirements for stability of the cavity, as well as phase variability of the laser radiation utilized for the sensitive

measurement. For example, experiments with a 62.5-cm-long White cell maintaining 30-mbar inner-gas pressure confirmed that 80-μbar pressure deviations were limiting the measurement sensitivity to optical density of $7 \cdot 10^{-7}$, with turbulence limitations due to $1/f$ noise at integration times being above 30 s [7.52].

Similar sensitivity-limiting experiments [7.50, 7.51] demonstrated the validity of time integration for the fringe-affected intensity of radiation observed in a 1-m-long White cavity. Measurements were made in 1600-cm^{-1} spectral band via a tunable diode laser referencing the optical sensitivity of the studies via a calibration cell with the loss level equivalent to 80 ppb of NO_2 in air. The cell was set to have 40-m total path length, and exhibited various fringes with relative intensities near 10^{-4}–10^{-2} for spacing related to 0.0025-cm^{-1} free spectral range of a 1-m cavity, being observed despite careful mirror alignment. The most pronounced fringe spacing corresponded to interference between adjacent light spots on the White cell field mirror (see Sect. 6.2), measured as 75.3 ± 2 MHz versus nominal 75 MHz or 0.0025 cm^{-1}. Most intensity fluctuations due to fringes were averaged by imposing a modulation jitter over the tuning laser-diode current at 300–500 Hz frequency with a relatively small amplitude compared with the main signal modulation used for spectral tuning and detection, sweeping a laser wavelength back and forth over at least one fringe period. A measurement sensitivity of 0.1 ppb for trace detection of NO_2 in air was achieved [7.50]. For second and higher harmonic detection, the jitter modulation frequency and phase optimization allowed minimization of fringe noise, while maintaining a sufficiently high harmonic-absorption signal, which is typically decreased owing to jitter [7.51].

Another way of averaging fringe-prone intensity modulation of radiation transmitted via a multipass cavity is by modulating the cavity path length in such a manner that the resonant length deviates between any adjacent maximum and minimum of interference (see Chap. 3). Since transitions from maxima to minima require a phase change of $\Delta\delta = \pi/2$ or a wavelength change of $\Delta\lambda = \lambda_0/4$ for interfering waves, the minimum path-length change inducing interference-fringe averaging is:

$$\Delta L_{min} = \Delta\delta\left(\frac{\lambda_0}{2\pi}\right) = \frac{\lambda_0}{4}. \tag{7.69}$$

Possibilities of inducing optical path-length changes in a multipass cell include one or another path-length spoiler: a piezoelectric transducer changing the mirror's position, an oscillating Brewster-angle plate, and/or a cell-pressure modulator - all varying the cell path length among interference extremes likely a few times over the free spectral range of the cell for a given wavelength.

A Brewster-angle plate, as a common tool in laser spectroscopy (see Sect. 7.1) broadly used for laser-generation suppression or intracavity loss calibration, may be utilized as an interference-fringe spoiler, rotated about the Brewster angle to offset the cavity path length over at least half of its free spectral range [7.53]. The constraint for using a rotating Brewster plate is in the necessity to polarize light in the plane of its incidence, otherwise interference for orthogonal components would obscure the fringe-reduction effort. For unpolarized radiation, a normal-incidence

plate with two-face antireflection coatings matching wavelength λ_0 should be easier to implement. The plate also needs to be thick enough to induce larger than $\lambda_0/4$ path-length changes when rotated $\pm\varphi$ from either the Brewster angle or normal incidence. In its experimental implementation, a Brewster-plate spoiler (1-mm-thick, 25-mm-diameter Irtran window used in the 7.5-μm wavelength range) was scanned over $\pm 2°$ using a triangular-wave modulator providing about equal-time oscillations over plate positions. An angle of 2° was sufficient for fringe-pattern averaging, but it also changed 1.2-kHz laser-diode modulation waveform and modulated a beam center position, thus producing residual noise at turning points even at a low oscillation frequency of 47 Hz [7.53].

Compared with White cavities, mostly requiring careful mirror alignment not to induce beam overlapping, Herriott waveguides (Sect. 6.3) are quite insensitive to alignment, thus not being appreciably affected by perturbations of mirror movements caused by a piezoelectric transducer modulating the cavity path length as desired [7.54]. To prove such independence, a single mirror of a 22-pass cavity having 950.7-cm optical path length was traversed over approximately 40 μm at 23-Hz frequency, with a respective ±20-μm excursion from the nominal cavity length maintaining the 22-pass configuration. The second-harmonic measurements of NO_2 absorption traces were obtained via a 1-kHz laser-diode current modulation, as in fringe-removing tests by jitter modulation described earlier in this section [7.51]. From approximately 0.3% absorption-equivalent intensity of the multipath fringes observed, the mirror-movement oscillation reduced the residual-fringe amplitude to 0.1% with a sawtooth waveform of the transducer modulation; multipath fringes were also absent for six-path cavity transversal [7.54].

A pressure-modulation technique for reducing interference fringes was tested in a White cavity [7.55], in which transducer-based modulation of its field mirror was not sufficient to remove all fringes observed, being seen as four-cell and two-cell path interference, with the latter likely present due to the reflection–scattering interaction reviewed above. Measurements of CO traces, corresponding to a center-line absorptance of $1.3 \cdot 10^{-5}$ in the 2000-cm^{-1} spectral range, were initially masked by larger-intensity fringes, which were removed by applying pressure modulation to CO gas from 15 to 35 or ±10 Torr corresponding to one-fringe period. That pressure modulation changed the measured center-line frequency by ± 0.0084 cm^{-1}, and also decreased the intensity of the pressure-modulated signal and decreased the reproducibility of measurements with random pressure variations.

As seen in Sect. 6.3, reentrant numbers of passes via two-mirror waveguide $N = 4M \pm K$ define families of N–M spot modes for such a waveguide. The propagation properties of these modes can be explored to minimize interference noise due to fringes associated with each propagation mode [7.56]. On the basis of estimation of the path-length difference between beam spots adjacent to an entrance–exit opening, the $N = 4M \pm 4$ spot family was found to have the longest path differential, equal to $N/2 \pm 2$, compared with just 4 and N–4 for the $N = 4M \pm 2$ family or the evolved difference $N/3 \pm 4/3$, $2N/3 \pm 4/3$ for the $N = 4M \pm 6$ family, thus creating the narrowest fringes for the highest-order free spectral range. Experimental observations of the interference fringes associated

with spot families were performed in a small-volume 42-cm^3 cell consisting of 2.5-cm-diameter mirrors, both with 15-cm curvature radius, having 70 passes and 10-m optical path length. Owing to tight image-spot spacing and some beam overlapping, the relative intensity of fringes approached approximately $5 \cdot 10^{-3}$ of the He–Ne laser power in the 3.39-μm wavelength region. Pressure modulation of the air in the cell allowed interference fringes to be spectrally scanned for the spot family N–M = 62 − 16 with N = 4M − 2 reflections and for the spot family N–M = 64 − 15 with N = 4M + 4 reflections, with the observed fringe periods corresponding to a four-pass and a 32-pass optical-path difference, respectively. In the latter case, much narrower and much more closely spaced fringes with lower amplitudes were seen, which should be easier to remove by electronic filtering and signal averaging at suitable modulation frequencies [7.56].

In frequency-modulation spectroscopy (see Sect. 10.2), where the spectral derivative of a measured absorption line is detected using high-frequency modulated laser light, the frequency filtration of cavity-prone interference fringes can be realized in the time domain as a Fourier expansion of the signal by applying a secondary frequency modulation [7.57]. Relations (7.65) and (7.66) could be rewritten by representing the phase difference δ via the frequency ratio:

$$I_\rho = I_0 \frac{4\rho \sin^2(\delta/2)}{(1-\rho)^2 + 4\rho \sin^2(\delta/2)} = I_0 \frac{4\rho \sin^2(\nu/\nu_c)}{(1-\rho)^2 + 4\rho \sin^2(\nu/\nu_c)}; \tag{7.70}$$

$$I_\tau = I_0 \frac{(1-\rho)^2}{(1-\rho)^2 + 4\rho \sin^2(\delta/2)} = I_0 \frac{(1-\rho)^2}{(1-\rho)^2 + 4\rho \sin^2(\nu/\nu_c)}, \tag{7.71}$$

where ν is the frequency of radiation and ν_c is the free spectral range of the cell in the frequency domain. For the frequency-scanned cell at $\rho \to 0$, the first derivative of intensity of a light beam reflected by the cell becomes:

$$\left(I_\rho / I_0\right)' = A'(\nu) \underset{\rho \to 0}{\sim} (4\pi\rho/\nu_c) \sin(2\pi\nu/\nu_c). \tag{7.72}$$

By symmetrical triangular-wave modulation at additional frequency ω, the derivative signal can be expressed via a Fourier nth-cosine series with further linear mapping to Fourier integrals [7.57]:

$$\left(I_\rho / I_0\right)' \to \sum_n \left(V_n'(\nu_{las}) + A_n'(\nu_{las}) + RAM_n'(\nu_{las})\right) \cos(n\omega t), \tag{7.73}$$

where ν_{las} is the laser center frequency at which measurements are to be performed, modulated by the triangular wave with frequency swing ν_s and amplitude T, giving: $\nu = \nu_{las} + \nu_s T(\omega, t)$; V is the combined Gaussian and Lorentzian – or Voigt – spectral profile of an absorption line to be measured and RAM is any residual amplitude modulation due to the original and additional frequency modulations applied. As a result of that dual modulation, both the absorption signal and the

interference fringes are Fourier-transformed, with their respective functions having relative peaks and falling to zero within finite pass bands, while only the fringe function is periodic with reoccurring zeros, but the signal function is not, thus allowing one to differentiate and optimize the signal-to-fringe noise ratio. The wider the separation between the modulation and additional frequencies in these measurements, the higher is the rejection of the fringes that should be achieved [7.57].

Examples of an electronic filtering of spatial frequency-modulated interference fringes with no need for additional modulation due to the frequency separation of the measured signal and fringes are found in frequency-modulation spectroscopy [7.58, 7.59]. Figure 7.21 illustrates the optical settings of the measurement system (see Chap. 10 for details), filtering the interference-fringe-related signal from two-tone-modulated radiation of a diode laser, guided by off-axis paraboloids P1 and P2 via a Brewster-angled cavity having absorption species inside. The laser beam was additionally chopped at 500 Hz by modulator M to facilitate lock-in detection. The detection frequency-modulated signal was current-ramped at 1-kHz frequency, having up to 10-kHz Fourier components in frequency space, and was filtered from the interference fringe signal, which had spatial components at much higher frequencies, by a 10-kHz low-pass filter. A noise-level sensitivity of approximately $1.5 \cdot 10^{-5}$ averaged over 4096 frequency scans was achieved with nearly no fringes.

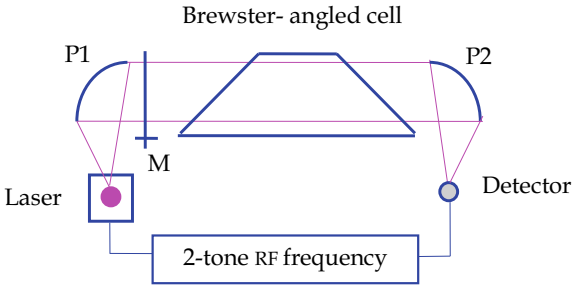

Fig. 7.21 Frequency-modulation optics

In applications where the means for averaging, integration, and/or separation of etalon-induced interference fringes reviewed cannot be applied, either predetection or postdetection techniques can provide some ways to identify the fringes before spectral-loss measurements are made or to separate a loss contribution of Gaussian, Lorentzian, or Voigt form from a sinusoidal fringe pattern. Nevertheless, many cases remain – for example, weak-etalon effects in antireflection-coated elements in high-power laser lines [7.61, 7.62] – when the need for removing interference fringes necessitates finding some means for decreasing the visibility of interference patterns themselves, as well as requiring implementation of specific practical ways for spatial and/or temporal separation of the measured spectral data from the interference pattern and, as a result, from interference fringes associated with that pattern and caused by the modulation noise of the fringes (see Chap. 3 for more

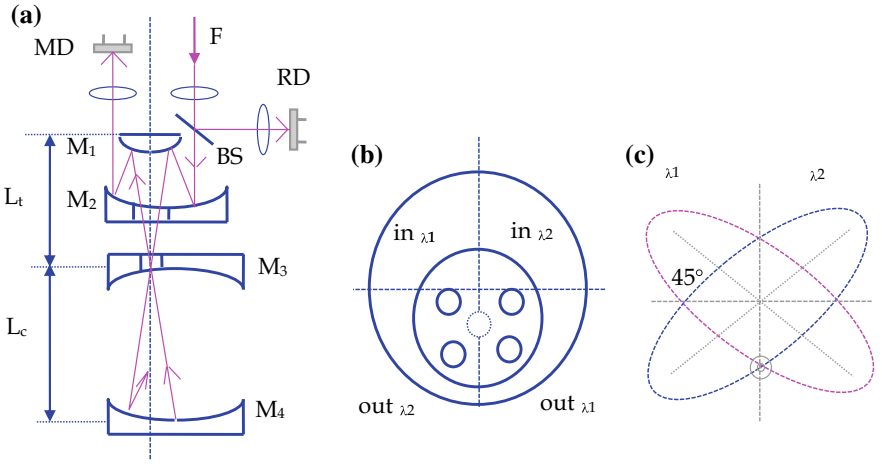

Fig. 7.22 Herriott-type waveguide with beam-separating Cassegrain telescope

details on the fringe visibility analysis in transmitted–reflected light and the combined visibility).

One example of forthright separation of likely overlapping focusing spots and reduction of mirror scattering or edge diffraction, likely causing weakly observable background interference, is shown in Fig. 7.22 [7.60]. A Cassegrain-type telescope consisting of mirrors M_1 and M_2 was deployed to separate input and output beams for the mirror waveguide M_3 and M_4, positioning the light source (in this case fiber end F), and main detector MD by the side of waveguide mirror M_3. Reference detector RD provided differential balanced detection of the signals compared (see Sect. 10.3). Two tunable laser diodes were orthogonally coupled into the waveguide cell (Fig. 7.22b, c). The cell-mirror spacing was chosen for a reentrant number of passes for this two-mirror waveguide of $N = 4M \pm 4 = 56$ with $M = 13$ and distance $L_c \approx 1$ m at $L_t \approx 20$ cm to ensure creation of the narrowest fringes for the highest-order free-spectral range (see above and [7.56]). Both waveguide mirrors were of 100-mm diameter with maximum 80-mm extension for each elliptical pattern of λ_1 and λ_2 with an 8-mm input hole in mirror M3. Telecommunication InGaAsP laser diodes for 1.65-μm and 1.39-μm spectral regions were used as the spectral sources for methane and water-vapor detection. Laser beams were collected by 20-mm diameter, 50-mm focus lenses and sensed by 1-mm-diameter InGaAs photodiodes in titanium mountings for the micron-level alignment. The lens surfaces were antireflection-coated and the light beams were coupled into lens objectives via spliced optical fibers to prevent accidental retroreflections with highly polished mirror substrates having surface smoothness under 0.5-nm rms. As a result, in the targeted $1 \cdot 10^{-5}$ dynamic range of absorption detection, measurements in that experimentally tested system confirmed no accidental fringing without any added effort [7.60].

Chapter 8
Measurements in Passive Resonators

8.1 Pulse-Separation Techniques

The ability of any optical element to operate in a laser cavity is defined by a positive balance of active and passive losses for the cavity with that element. Reflective objects create transmission, scattering, and absorption losses; transmission ones create reflection, scattering, and absorption losses, etc. It is critical for the loss under study to be measured at a specific spatial, spectral, and temporal condition of light emission providing adequate measurement arrangements. Let us consider two methods for passive intracavity measurements of a high specular reflectance: $\rho_r \to 1$, of a mirror. Such a reflectance may be measured directly or by sensing the difference from unity of the sum of its scattering loss, absorptance, and transmittance, considering a mirror substrate as a vital part.

The relative errors of these opposing methods – one involving direct evaluation of high reflectance ρ_r, and the other involving measurements of losses, additive to reflection loss $\chi_\Sigma = \tau + \sigma + \alpha = 1 - \rho_r$ – are correlated:

$$\frac{\Delta\rho_r}{\rho_r} = -\frac{\Delta\chi_\Sigma}{1-\chi_\Sigma} = -\frac{\Delta\chi_\Sigma}{\rho_r}, \tag{8.1}$$

where the minus sign indicates opposite directions of increments. Equation (8.1) points out that the higher is the reflectance ρ_r studied, the higher is the accuracy of the indirect measurement via loss χ. If N multiple reflections accompany any direct or indirect measurement, the relative error is:

$$\left(\frac{\Delta\rho_r}{\rho_r}\right)_{mul} = -\frac{1}{N}\frac{\Delta\chi_\Sigma}{\rho_r}. \tag{8.2}$$

Consequently, indirect measurement of a high specular reflectance is more accurate than an indirect determination of low scattering or absorption, as made via

M. Bukshtab, *Photometry, Radiometry, and Measurements of Optical Losses*, Springer Series in Optical Sciences 209,
https://doi.org/10.1007/978-981-10-7745-6_8

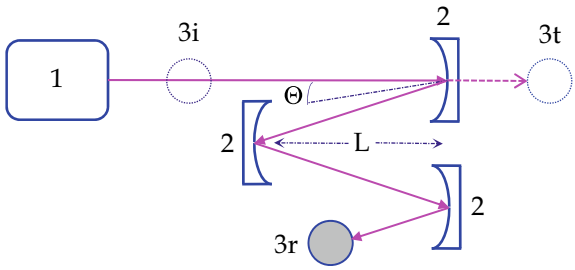

Fig. 8.1 Detection of the mean-mirror waveguide loss: *1* source; *2* mirror; *3* detector at positions *r*, *i*, and *t*, detecting reflectance, initial intensity, and transmittance

a low-loss factor related to a high reflectance instead of the reverse ratio for a weak scattering or absorption (Eq. (5.32)). Figure 8.1 illustrates a layout for indirect measurements in a chain of highly reflecting mirrors [8.1]. The partially shown waveguide is assembled from m identical mirrors under test, allocated at identical distances L and irradiated at angle of incidence Θ. The light intensity I_m transmitted by the waveguide to the intensity I_0 of laser source 1 is:

$$\frac{I_m}{I_0} = 1 - \tau_1 - \alpha_1 - \eta_1 - \sigma_1 - \sum_{i=2}^{m} (\tau_i + \alpha_i + \eta_i + \sigma_i) \prod_{j=1}^{i-1} (1 - \tau_j - \alpha_j - \eta_j - \sigma_j), \tag{8.3}$$

where i and j are the numbers of multiplication and summation, τ_i and α_i are the transmittance and the absorptance of the i^{th} mirror, and η_i and σ_i are the diffraction and the scattering loss. In experiments [8.1], mirror scattering losses were the subject of measurements, and the line diffraction loss η_i was computed via the Fresnel number: $N_{Fi} = r^2/L\lambda$, as $\chi_i = 10.9 \cdot 10^{-4.94 N_{Fi}}$ [8.1, II.5]. The direct transmittance measurement for each mirror, except any opaque metal mirrors, was performed directly via the detector at position 3t, while every mirror absorptance was detected by a thermocouple (see Sect. 10.1 for calorimetric loss measurement techniques). Since no other factors, except those defined by Eq. (8.3), identify extra optical losses in such a waveguide, the measurement procedure was based on determination of all factors, excluding the scattering loss, which was the final target of the measurements. That particular method is not especially accurate, but provides a conceptual basis for practically sufficient methods of loss measurements.

The low-loss detection technique illustrated in Fig. 8.1, as well as the multiple-reflection studies reviewed in Chap. 6, were developed to measure the mean loss averaged over the number of samples or a large sample surface. To evaluate the local attenuation factor or coefficient, the multiple-reflection cell needs to be maintained at normal incidence of radiation on the surface or the bulk under study (Fig. 8.2). For a resonator of output coupler 1 and highly reflecting mirror 2, the transmitted flux Φ is:

$$\Phi_\tau = \Phi_0 \tau_1 \tau_2 \left(1 + \rho_1 \rho_2 + \cdots + \rho_1^m \rho_2^m\right) \underset{m \to \infty}{=} \Phi_0 \frac{\tau_1 \tau_2}{1 - \rho_1 \rho_2}. \tag{8.4}$$

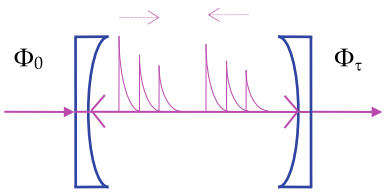

Fig. 8.2 Propagation of continuous or pulsed light via a test-mirror cavity

Here m is a tending-to-infinity number of reflections in a steady-state resonator, and Φ_0 and Φ_τ are the incident and transmitted fluxes. For the purpose of analyzing measurement accuracy, the element's absorptance and scattering may be presumed to be negligible: $\tau_1 = \tau_2 = \tau = 1 - \rho$; therefore, as a result:

$$\Phi_\tau = \Phi_0 \frac{1-\rho}{1+\rho} \underset{\rho \to 1}{\to} 0; \qquad \frac{\Delta\Phi}{\Phi} = \frac{\Delta\Phi_0}{\Phi_0} + \frac{\Delta\rho}{1-\rho} + \frac{\Delta\rho}{1+\rho} \underset{\rho \to 1}{\to} \infty. \tag{8.5}$$

For a high Q-factor of the resonator for $\rho_{1,2} = \rho \to 1$, continuous-wave (cw) measurement via light transmitted by the resonator does not allow one to distinguish the optical properties of the resonator components.

Instead of spatial separation of retroreflected components, each internal reflection cycle may be distinguished via its existence in the cavity. A pulse of radiation having duration t_p smaller than time interval $t_p < 2\ell/c$ needed for light having its vacuum speed c to traverse a cavity of length ℓ twice allows one to separate each cycle of the multiple interactions in such a cavity. Any single amplitude in a sequence of pulses reflected or transmitted by the cavity with repetition period $T = 2\ell/c$ decreases as: $A_i = A_{i-1}\rho_1\rho_2 \equiv A_{i-1}\bar{\rho}^2$. The highest number m of the intracavity reflections which can be registered by a high-speed detector resolving every pulse in this time sequence establishes the minimal flux $\Phi_{\min}$ capable of being measured:

$$\Phi_{\min} = \Phi_0 \tau_1 \tau_2 (\rho_1 \rho_2)^m \equiv \Phi_0 \bar{\tau}^2 \bar{\rho}^{2m}, \tag{8.6}$$

where the sign $\equiv$ denotes implementation of new designations for the mean factors: $\bar{\tau} = \tau_1\tau_2$; $\bar{\rho} = \rho_1\rho_2$.

Illustrated by Fig. 8.2 pulsed-measurement technique is not complicated at all and could be made even at routine temporal resolution settled by an accessible space between cavity mirrors. Such a study was one of the first ever accomplished for any highly reflecting mirror waveguide using a cw He–Ne laser and the confocal resonator of spherical mirrors with a radii of curvature $R_{1,2} = \ell = 100\,\text{m}$. The incident sequence of light pulses: $t_p = 0.4$ μs, was formed by a chopper via a continuous beam at radiation wavelength $\lambda = 632.8$ nm. The mirror reflectances, estimated by a spectrophotometer, were equal to about 0.995. The total measured 'pulsed' loss accounted for 1% at each mirror. The Fresnel number: $N_{F_i} = 2$, for the cavity matched the mirror diffraction loss of 0.5%. The average scattering factor for the single mirror was considered of another 0.5% [8.2].

Any measurement of cavity-averaged reflectance for a set of two mirrors forming the cavity may be done by measuring a ratio of amplitudes of two consecutive pulses in any time sequence:

$$W_{i+m} = W_i \bar{\rho}^{2m}; \qquad \bar{\rho} = \sqrt[2m]{W_{i+m}/W_i}, \tag{8.7}$$

where m is now the number of cycles between two chosen pulses, being measured. At the limit of the mean or average cavity reflectance $\bar{\rho} \to 1$, the optical loss conversion can be written as follows:

$$\ln(\bar{\rho}) = \frac{1}{2m}\ln(W_{i+m}/W_i) = \ln(1-\bar{\chi}) \underset{1-\bar{\chi}=\bar{\rho}\to 1}{\cong} -\bar{\chi} - \bar{\chi}^2/2 \cong \frac{\bar{\rho}-1}{\sqrt{\bar{\rho}}}, \tag{8.8}$$

where $\bar{\chi}$ is the mean loss factor at each reflection. By disregarding a difference of $\bar{\rho}$ from 1.0, i.e., assuming measurement error $\Delta\bar{\rho} = \pm\bar{\chi}^2/2$, the mean optical loss $\bar{\chi}$ for the resonant mirror pair is:

$$\bar{\chi} \cong -[\ln(W_{i+m}/W_i)]/(2m), \tag{8.9}$$

and can be resolved via the slope of logarithmic dependence $\ln(W_{i+m}/W_i) = f(m)$ on an oscilloscope.

To determine resonator losses more precisely, simultaneous measurements of two variables of every pulse – the energy or power and the pulse number – need to be made. Knowledge of the exact pulse number allows one to distinguish the loss as a function of the number of reflections and to increase the sensitivity of measurements. Figure 8.3 depicts one example of a measurement system [8.3]. An output signal from main detector 6 is selected by discriminator 7 with upper level W_i, which starts the summation of the transmitted pulses. The energy amplitude U_0 of a given pulse is measured by voltmeter 11 and stored by processor 12. Simultaneously, U_0 is detected by comparator 9 and counter 10, registering the first measured pulse. That sequence is continued until the magnitude U_{m+1} of the $(m+1)^{th}$ pulse energy (power) becomes smaller than a preset reference voltage, defined by the detector's energy or power sensitivity limit (see Eq. (8.6)).

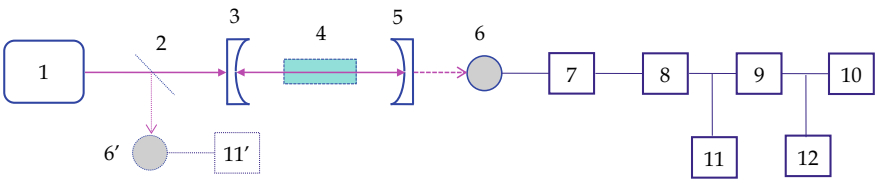

Fig. 8.3 Pulsed measurement system detecting total optical losses in an open resonator: *1* source; *2* splitter; *3, 5* mirrors; *4* transmitting object; *6, 6′* detectors; *7* discriminator; *8* amplifier; *9* comparator; *10* counter; *11, 11′* voltmeters; *12* processor

The ratio of the last U_m to the first U_0 pulse amplitudes, for which the scale of the maximum to the minimum depends on the linear dynamic range of the detector, establishes the maximum number m of computing reflections and therefore determines the highest achievable sensitivity to optical loss $\bar{\chi}_S$ under test:

$$\ln(\bar{\rho}\tau) = (1/2m)\ln(U_m/U_0) \cong -\bar{\chi}_S \cong (\bar{\rho}\tau - 1)/\bar{\rho}\tau. \tag{8.10}$$

Here τ is the transmittance of the cavity itself or object 4 inside it. By analogy with the spatially averaging systems of multiple reflections (Sect. 6.1), studies using similar ratios $(1/2j)\ln(U_j/U_0)$, obtained for any intermediate number j of pulses, can provide auxiliary sets of averaging results of the study. Such a test also verifies the linearity of the entire procedure (see Chaps. 4 and 6).

The technique considered can be slightly simplified to evaluate only the highest and the lowest pulse amplitudes [8.4] when the number of cavity pulses separating these two extrema is also counted. For such a purpose, voltmeter 11 serves to measure only the highest magnitude of the first pulse U_0. The potential divergence of energies of the other pulses is controlled by the second detector $6'$ and by additional voltmeter $11'$ using beam splitter 2. Each pulse voltage is referred to the voltage of the first pulse: U'_j/U'_0. The final number of pulses to be counted is recognized by comparator 9, which detects the lowest magnitude corresponding to its preset voltage U_c. If the last pulse signal $U_m \cong U_c$, the cavity loss is given by:

$$W_m/W_0 \cong (U_c/U_0)(U'_0/U'_m). \tag{8.11}$$

The range of the comparator uncertainty, $\Delta U_c = U_c - U_m$, suggested by the assumption $U_c \cong U_m$ defines not only the actual error of measurement, but also the limit of the lowest loss detectable by the method. If the difference of amplitudes $\Delta = U_j - U_{j+1}$ for any two consecutive pulses is larger than ΔU_c, i.e., the dual-pass loss is higher than the measurement uncertainty of the discriminator, the existence of every pulse should be detected. If $\Delta = U_j - U_{j+1} < \Delta U_c$, two or more pulses can pass by the discriminator undistinguished, leading to computation error of the pulse number. Therefore, the $\Delta U_n \approx \Delta U_c$ assumption limits the sensitivity of such a low-loss measurement.

Any of the reviewed methods of resonator-based measurements allow one to determine a low mirror loss, which is averaged over both mirrors of the cavity. At normal incidence of light on a flat mirror, alterations of its surface reflectance can be detected by a transverse shift of the mirror across a light beam. To distinguish absolute reflectance of one resonator element, a third mirror may be used (see Eqs. (6.8) and (6.9)). Instead, two consecutive measurements via parallel sequences of relatively short pulses in light transmitted and reflected by the resonator, consisting of the elements under study, allows one to identify the loss contributed by a single mirror in the cavity [8.5].

By keeping the pulse duration to resolve the intracavity space: $t_p \leq 2\ell n/v$ (where ℓ, n, and v are, respectively, the cavity length, its internal index of refraction, and the speed of light for the light pulses within the cavity), one can make two series of

measurements – one in transmission and another in reflection (Fig. 8.4), by adding a transparent beam splitter 2 and a reflection detector 6 to light source 1, two cavity mirrors 3 and 4, and transmission detector 5. Instead of parallel transmission and reflection measurements, consecutive transmittance–reflectance study can be performed by two detectors registering pulses in transmission and in reflection or by moving one detector 5 into position 6. Considering Eqs. (8.7)–(8.9), if the cavity mirror substrates have finite thickness: $d \leq v n_s t_p$, each pulse in transmitted and reflected sequences becomes a sum of reflections by two surfaces of a single cavity component. For a larger substrate thickness, satellites of every pulse can appear, and, for resonant cavity measurements, every substrate must be either wedged or antireflection (AR)-coated. For back surfaces of wedged AR-coated substrates, one may set $\rho_b \cong 0$.

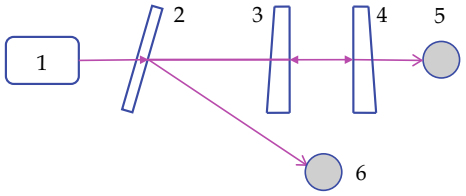

Fig. 8.4 Measurements of transmitted and reflected pulses: *1* source, *2* splitter; *3, 4* wedged mirrors; *5, 6* detectors

The energy of every consecutive pulse in reflected light conforms to the following sequence:

$$W_0 = \tau_2\rho_2\rho_3; W_1 = \tau_2\rho_2(1-\rho_3)^2\rho_4; W_2 = \tau_2\rho_2(1-\rho_3)^2\rho_4\rho_3\rho_4;$$
$$W_m = \tau_2\rho_2(1-\rho_3)^2\rho_3^{m-1}\rho_4^m.$$

Hence, *m*-bound ratios of the energy W_m of the m^{th} pulse to the energy W_1 of the first pulse or the $(i + m)^{th}$ to i^{th} pulse energies and the ratio of m^{th} to 0^{th} pulse energies in reflected light become:

$$(W_m/W_1)_\rho = (\rho_3\rho_4)^{m-1}\ ; \quad (W_m/W_0)_\rho = (1-\rho_3)^2\rho_3^{m-2}\rho_4^m. \tag{8.12}$$

Only the ratio of the pulse energy to that reflected from the cavity input mirror 3 unequally depends on the properties of each element forming the cavity. Oppositely, the *m*-bound ratio for transmitted light is:

$$(W_{i+m}/W_i)_\tau = (\rho_3\rho_4)^m. \tag{8.13}$$

The reflectance of each cavity mirror 3 and 4 can be resolved either in reflected or in reflected and in transmitted light:

$$\rho_4 = (W_m/W_1)_\rho^{1/m-1}/\rho_3; \qquad \rho_4 = (W_{i+m}/W_i)_\tau^{1/m}/\rho_3;$$
$$(1-\rho_3)^2/\rho_3^2 = (W_m/W_0)_\rho/(W_m/W_1)_\rho^{m/m-1}; \quad (1-\rho_3)^2/\rho_3^2 = (W_m/W_0)_\rho/(W_{i+m}/W_i)_\tau. \tag{8.14}$$

The overall sensitivity of such a method is reduced by the requirement to implement additional beam splitter 2. Since the cavity transmittance $\tau_{cav} = (1 - \rho_3)(1 - \rho_4)$ is given by the properties of output coupler 3 and high-reflectance mirror 4, being very low, the beam splitter transmittance τ_2 should be as high as possible. For $\tau_2 = 0.995$, $\tau_2\rho_2 = 0.005$ and also for $\rho_3 = 0.5$, $\rho_4 = 0.995$, the reflected and transmitted pulse intensities are identical from each pulse to the next, preserving the sensitivity. Of course, the procedure of alternating or additive transmittance and reflectance measurements in the arrangement described requires solving quadratic or higher-order equations and may not be easily implemented, though it could provide some conceptual insights for further methods for distinguishable measurements in asymmetric resonators (see Sects. 8.4, 10.4, and 10.5).

Concluding our analysis of straightforward pulsed low-loss measurement methods (see also Sects. 8.3 and 8.4), let us note one common obstacle of the reviewed techniques. Owing to very short time intervals between any two consecutive retroreflected pulses, for example, 10 ns for cavity length ℓ = 1.5 m, they require a combination of high temporal resolution and a long optical path inside the cavity. At a result, containing beam divergence could become the restricting factor for a long resonator consisting of two flat mirrors. Hence, a certain compromise has to be made between the spatial and the temporal resolution for a given measurement. Use of concentric resonators for imaging of widened light spots (see Chap. 6) allows one to correlate spatial and temporal properties of multiple reflections, since their ability to keep a light beam focused permits the creation of additional internal cycles of retroreflected radiation pulses to be measured. If every pulse escapes such a resonator after N added internal reflections, the main time interval t_N between exiting pulses $t_N = 2N\ell/c$ becomes N times higher, and the temporal resolution or the length of the cavity can be respectively lower.

A cell of concentric mirrors prolonging the intracavity reflection cycle is shown in Fig. 8.5. A beam from source 1 is launched by mirror 2 into waveguide 3–4 and back to detector 6 via window 5 with transmittance τ_w and reflectance ρ_w. The magnitudes of τ_w and ρ_w define the intensity of the output pulses and the time interval between pulses after a cycle of internal reflections, progressing in the following sequence: $I_i = I_0\tau_w^2\bar{\rho}^{2N-1}; I_{i+2N} = I_0\tau_w^2\rho_w\bar{\rho}^{2(2N-1)}$. As a result, the equation for the average mirror loss $\bar{\chi} = 1 - \bar{\rho}$ in the cavity between two consecutive output pulses resolved by detector 6 becomes:

$$I_{i+2N}/I_i = \rho_w\bar{\rho}^{2N-1}\,. \tag{8.15}$$

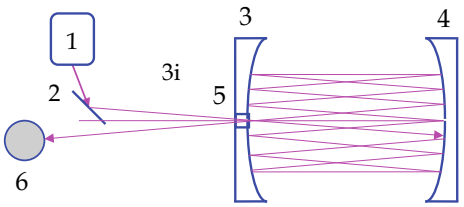

Fig. 8.5 Delayed-pulse loss measurements

This delay-based technique not only increases the time interval between any two consecutive pulses, but also expands the measurable difference for the pulse amplitudes. As a result, the number of reflection cycles in the cavity does not need to be highly enhanced to realize higher sensitivity, though it would help to do so if needed. The elevated number of reflections for every successive pulse allows, for example, periodic inquiries of test substances occupying the intracavity space, as well as examination of time-dependent processes, such as absorption and saturation [8.5].

A variation of the pulse-delay technique can also be used in modulated cw radiation measurements, such as applying frequency modulation to provide a relatively fast wavelength tuning and multiple-reflection delay in an off-axis optical cavity [8.31, 8.32] (see Chap. 6). The designed system (Fig. 8.6) targeted high-resolution real-time spectrally resolved measurements of ethane-gas absorption using a single, cryogenically cooled lead-salt laser diode, emitting cw radiation near 3.4-μm wavelength. A pulse-modulated beam at 8 kHz from laser 1 irradiates delay-line absorption cavity 2, whose output reaches main-channel detector 3. Added detector 4 controls the reference channel with calibration cell 5 via beam splitter 6. Two modes of operations are deployed. In the first, scanning mode, the wavelength of laser emission is tuned within nearly 0.4-cm^{-1} bandwidth over the ethane transition of approximately 0.05-cm^{-1} width at 2990.09-cm^{-1} frequency. In line-locking mode, the system tracks the wavelength of the ethane transition by first-derivative demodulation of the reference signal from detector 4. He–Ne laser 7 and computerized motion controllers keep the alignment of all system components. In the scanning mode using curve-fitting calibration of the ethane-reference standard, this portable modulation spectroscopy system reached nearly 0.1-ppb sensitivity with 1-s scan sampling rate and 0.2-ppb with 0.8-s frequency and line-locking continuous performance [8.31].

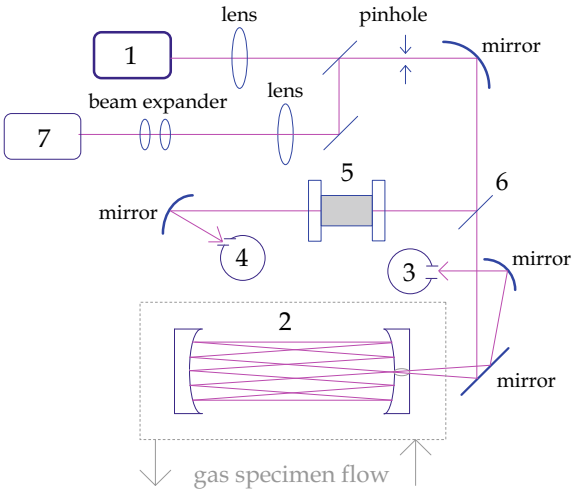

Fig. 8.6 Frequency modulated cavity-delayed measurements

8.2 Interferometric Analysis

Similarly as short pulsing decomposes the continuity for multiple reflections of radiation in a retroreflecting cavity, multiple-beam interference intensifies spatial and temporal separation owing to coherent correlation of interacting beams. For monochromatic light of wavelength λ coupled into a resonant cavity of high-reflecting mirrors at an angle Θ with a coherence length longer than the dual optical path of the cavity, the intensity of radiation existing in the cavity depends on the phase shift gained on the dual cavity path: $\delta = 4\pi\ell n \cos\Theta/\lambda$. If a resonant cavity is made of nonabsorbing and nonscattering dielectric mirrors of reflectances ρ_1 and ρ_2 deposited on an intermediate substance with transmittance τ, the total intensity of light in transmission is:

$$I_{\tau,\lambda} = I_{0,\lambda} \frac{(1-\rho_1)\tau(1-\rho_2)}{\left(1-\tau\sqrt{\rho_1\rho_2}\right)^2 + 4\tau\sqrt{\rho_1\rho_2}\sin^2(\delta_\lambda/2)}, \tag{8.16}$$

where I_0 is the initial intensity of radiation entering the cavity. Relating the output intensity to the intensity of the first cavity transmission: $(1-\rho_1)\tau(1-\rho_2)$, one can rewrite the distribution as:

$$\left(I_\tau/I_{\tau,1}\right)_\lambda = \left(1+\left[4\tau\sqrt{\rho_1\rho_2}\Big/\left(1-\tau\sqrt{\rho_1\rho_2}\right)^2\right]\sin^2(\delta_\lambda/2)\right)^{-1}. \tag{8.17}$$

Maintaining stable normal incidence of light onto both cavity mirrors at wavelength λ and varying the inter-mirror distance ℓ to measure the ratio of the maximum and the minimum intensities of the multipath interference pattern in transmission reveals the product $\rho_1\rho_2$ of the two cavity mirror reflectances and of the intra-cavity transmittance τ via the intensity contrast:

$$\left(\frac{I_{\tau,\max}}{I_{\tau,\min}}\right)_\ell = \left[\frac{1+\tau\sqrt{\rho_1\rho_2}}{1-\tau\sqrt{\rho_1\rho_2}}\right]^2 \underset{\rho_1=\rho_2}{=} \left(\frac{1+\tau\rho}{1-\tau\rho}\right)^2. \tag{8.18}$$

This distributes the mean intensity $\bar{I}$ of transmitted light along its path with fringe visibility:

$$V_\tau = \frac{I_{\tau,\max}-I_{\tau,\min}}{I_{\tau,\max}+I_{\tau,\min}} = \frac{2\tau\sqrt{\rho_1\rho_2}}{1+\tau^2\rho_1\rho_2} \underset{\rho_1=\rho_2}{=} \frac{2\tau\rho}{1+\tau^2\rho^2}. \tag{8.19}$$

The finesse $\Im$ of the interference fringes obtained, corresponding to a half-intensity width (see Eq. (7.68)), is:

$$\begin{aligned} \Im &= (\pi/2)\sqrt{4\tau\sqrt{\rho_1\rho_2}/\left(1-\tau\sqrt{\rho_1\rho_2}\right)^2} \\ &\equiv (\pi/2)\sqrt{\Re} \underset{\tau=1;\rho_1=\rho_2=\rho}{=} \pi\sqrt{\rho}/(1-\rho) = (\pi/2)\sqrt{F}, \end{aligned} \tag{8.20}$$

for asymmetric-cavity finesse parameter $\Re = 4\tau(\rho_1\rho_2)^{1/2}/(1-\tau(\rho_1\rho_2)^{1/2})^2$, which becomes $F = 4\tau\rho/(1-\tau\rho)^2$ at $\rho_1{=}\rho_2$ and defines the multiplication strength of cavity multiple reflections (see Sects. 3.3 and 7.4).

The higher is the finesse $\Im$ of multiple-beam interference fringes, the sharper are the transmission maxima and the more sensitive is the light intensity distribution to the resonator spacing. Thus, one measurement procedure can consist in measuring the transmission maxima versus the distance between mirrors. Figure 8.7 schematically illustrates an oblique pathway in a Fabry–Perot interferometer and the layout for a low-loss measurement system using the linear motion of an interferometer mirror [8.6]. A linear vibration of the mirror's position at frequency f with velocity $v = \Delta d_0/\Delta t \ll c$ within space region $\Delta\ell$ covering extremes of cavity transmission causes coordinated modulation of the intensity of output radiation (Fig. 8.7b). For a pulse detector coupled to an oscilloscope of angular sweep rate $\beta = 2\pi(\Delta f/\Delta t)$, being synchronized with that linear motion, its output senses the distributed-in-time interference pattern for all axial modes of light emitted by the source and reaching the detector. If the source emits quasi-monochromatic waves, the intensity distribution, for the high finesse parameter $\Re(F)$ of the cavity of not necessarily identical mirrors, represents a pattern of narrow maxima and broad minima.

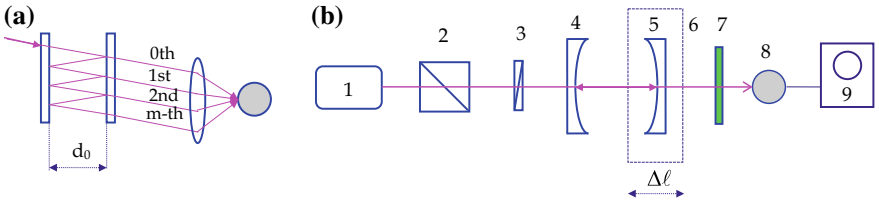

Fig. 8.7 Separation of light pulses (**a**) and oscillating interferometer for low-loss measurements (**b**): *1* laser source; *2* polarizer; *3* quarter-wave plate; *4, 5* spherical mirrors; *6* modulator; *7* bandpass filter; *8* detector; *9* oscilloscope

At steady mirror spacing d_0, the time delay of the m^{th} beam is $\tau_m = 2md_0/c$, and the cavity delay of the directly transmitted beam is $\tau_0 = d_0/c$. For the frequency input $\omega = \omega_0 - \beta t$, the m^{th} output phase becomes:

$$\delta_m = \omega_0 t - \beta t^2/2 = \omega_0[t - 2md_0/c - d_0/c] - (\beta/2)[t - 2md_0/c - d_0/c]^2. \tag{8.21}$$

The amplitude of the m^{th} output component is: $E_m = E_o\tau_{res}\rho_{res}\exp(-j\delta_m)$, and the total intensity of all retroreflected beams compared with the intensity of the directly transmitted beam is [8.6]:

$$E_\Sigma = \sum_{m=0}^{\infty} \tau_{res}\rho_{res}\exp\left\{-j(2md_0/c)[\omega_0 - \beta(t - d_0/c)] - j2\beta m^2(d_0/c)^2\right\}. \tag{8.22}$$

The intensity of a beam having internal multiple reflections within time decay: $\Delta\tau = \tau_m - \tau_{0,}$ obtained by processing of the slow motion of the interferometer mirror, may be approximated as:

$$I_\tau \cong \tau(1-\rho_1)(1-\rho_2)\left\{\left[\sum_{m=0}^{\infty}\left(\tau\sqrt{\rho_1\rho_2}\right)^m \cos\left(\psi m + \varphi m^2\right)\right]^2 + \left[\sum_{m=0}^{\infty}\left(\tau\sqrt{\rho_1\rho_2}\right)^m \sin\left(\psi m + \varphi m^2\right)\right]^2\right\}, \tag{8.23}$$

where $\varphi = 4\pi v d_0/(\lambda c)$ and $\psi = -4\pi v t/\lambda$ are the respective parameters of the slow scanning with velocity v. The inaccuracy of that approach: $\Delta \cong 2\exp\left[-m\left(1-\tau\sqrt{\rho_1\rho_2}\right)\right]$, is defined by the closeness of the number m for all detected reflection components to infinity. For $\tau\sqrt{\rho_1\rho_2} = 0.9975$ and m = 3040, the Δ value is 0.1%. At the same time, the motion reduces the intensity of every maximum (see expressions (3.123)) and changes the spatial orientation as a function of velocity v and of the total loss $\left(1-\tau\sqrt{\rho_1\rho_2}\right)$. The greater is the swiftness, the bigger is the error, but the higher is the resonator loss, the lower is the cavity finesse parameter F and the relative output intensity: I_{out}/I_0; therefore, the wider is the extreme bandwidth and the lower is the effect of the mirror motion. The first-order motion effect of a single moving mirror is experimentally found [8.6] to be near:

$$\frac{\Delta I_{out,\max}}{I_{0,\max}} = \frac{\Delta t_p}{t_p} \cong \sqrt{1 + 13.8\frac{\varphi^2}{\left(1-\tau\sqrt{\rho_1\rho_2}\right)^4}}. \tag{8.24}$$

Here t_p is the half-power output pulse width for the detector resolving the intensity maximum.

As follows from Eq. (8.24), the lower is the total magnitude of the loss which needs to be detected, the lower should be the velocity of the mirror motion (see Fig. 8.8). For instance, the ratio $\varphi/\left(1-\tau\sqrt{\rho_1\rho_2}\right)^2 \le 0.04$ at $\varphi = 10^{-6}$ and $\tau\sqrt{\rho_1\rho_2} = 0.995$ leads to error $\Delta t_p/t_p \le 1\%$, but at $\tau\sqrt{\rho_1\rho_2} = 0.9975$, the error $\Delta t_p/t_p$ of

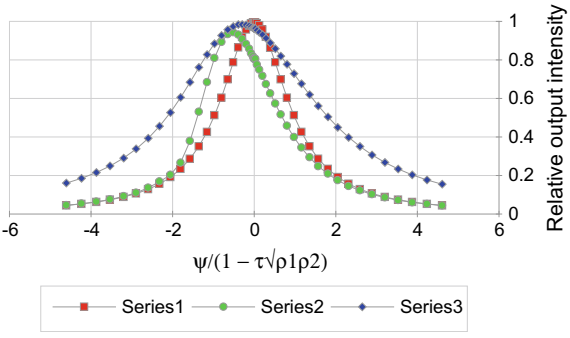

Fig. 8.8 Temporal response of an interferometer affected by a mirror motion

maxima-position detection rises to 5%. Figure 8.8 depicts the relative intensity I_τ/I_0 as a function of the ratio $\psi/\left(1-\tau\sqrt{\rho_1\rho_2}\right)^2$ given by Eq. (8.23) under the following conditions – for series 1 : $\varphi = 10^{-6}$ and $\tau\sqrt{\rho_1\rho_2} = 0.9975$, for series 2 : $\varphi = 0$, $\tau\sqrt{\rho_1\rho_2} = 0.9975$, and for series 3 : $\varphi = 10^{-6}$ and $\tau\sqrt{\rho_1\rho_2} = 0.995$. The moving-mirror velocity being not equal to zero not only reduces the intensity of all maxima, but also makes the output response of the cavity be asymmetrical, especially for the low magnitudes of the optical losses studied.

By disregarding mirror movement, one can transform Eq. (8.22) into Eq. (8.16), and since finesse parameter $\Re$ at $\rho_1 = \rho_2 = \rho = 1 - \tau$ equals $F = 4\rho/(1-\rho)^2$, Eq. (8.17) becomes:

$$I_{\tau,\lambda} = I_0 \frac{(1-\rho_1)\tau(1-\rho_2)}{\left(1-\tau\sqrt{\rho_1\rho_2}\right)^2} \frac{1}{1+F\,\sin^2(\delta_\lambda/2)}. \tag{8.25}$$

If finesse parameter F remains high, the finesse of the resultant cavity fringes is enhanced, keeping the relative width t of all maxima for time-resolved oscillations low: $t_{max} \ll t_2\pi$ (see Eq. (8.23)). Hence, factoring only the first-order terms, one can resolve the optical loss in the resonator via the relative sharpness $t_p/t_{2\pi}$ of temporal fringes compared with the time constant of vibrations $t_{2\pi}$:

$$\tau\sqrt{\rho_1\rho_2} \cong 1 - \left(\pi t_p/t_{2\pi}\right) + (1/2)\left(\pi t_p/t_{2\pi}\right)^2 + \ldots. \tag{8.26}$$

Since Eq. (8.26) is directly obtained via the definition of finesse $\Im$ (see relation (7.68)): $\Im = \delta_{max}/(2\pi) = (\pi/2)\sqrt{\Re} \underset{\rho_1=\rho_2}{=} (\pi/2)\sqrt{F} = t_p/t_{2\pi}$, and since time instance $t_{2\pi}$ is fully determined by the phase status of the mirror oscillation, only one parameter t_p identified by Eq. (8.26) depends on the resonator properties. Thus, contradiction for any of the assumptions made, for example, inequality of cavity mirror reflectances, leads to a measurement error. Accordingly, the maxima to be registered are shifted and decreased, but the time constant of a sequence does not change.

To obtain low optical losses by measuring the light intensity profile of a temporal interference pattern, an intensity detector needs to trace variations of the function $I_\tau \cong I_{\tau,max}/\left(1+4t^2/t_p^2\right)$, which in the associated frequency domain becomes: $f(\omega) = (\pi/2)t_p I_{\tau,max}\exp\left(-\left(t_p/2\right)|\omega|\right)$. While having constant scanning parameters at $t_P = 30$ μs and 1% total losses, the required frequency band $f(\omega)$ for maintaining measurement distortion error below 1% must be: $f(\omega) \geq 50$ kHz, but at $\tau\sqrt{\rho_1\rho_2} = 0.9975$, it must be: $f(\omega) \geq 200$ kHz. Owing to a great number of interactions in a resonator of highly reflecting mirrors, indirect measurements of the product $\tau\sqrt{\rho_1\rho_2}$, identifying the total resonator loss: $\chi_\Sigma = 1 - \tau\sqrt{\rho_1\rho_2}$, are fairly accurate (see Eqs. (8.1), (8.2)). Even the large number of assumptions made does not significantly affect the result. As follows from Eq. (8.26), even 10% error of $t_p/t_{2\pi}$ measurement leads to inaccuracy $\Delta(\tau\sqrt{\rho_1\rho_2}) \leq 0.5\%$ at $\tau\sqrt{\rho_1\rho_2} \geq 0.995$, and to $\Delta(\tau\sqrt{\rho_1\rho_2}) \leq 0.1\%$ at $\tau\sqrt{\rho_1\rho_2} \geq 0.999$. In experiments [8.6], each measurement of the average reflectance $\bar{\rho}$ of the cavity of either flat or spherical mirrors with under 2-m radius of curvature at $\bar{\rho} = 0.997 - 0.940$ was characterized

by ±0.1% reproducibility. When measuring individual reflectances via the three-mirror substitution technique (see Eq. (6.9)), the error increased to ±0.2%. A He–Ne laser and an interference filter having 20-nm half-bandwidth in the vibration-isolated system shown in Fig. 8.3 were used for measurements. The transmission loss of a polished blank fused-silica plate, inserted into the resonator at the Brewster angle, was equivalent to 0.0025 for 7.5-mm thickness. This loss corresponds to a bulk linear attenuation coefficient of 0.002 ± 0.0005 or to about 1 dB/m.

The mirror-oscillation method relies on making measurements of the relative sharpness of interference maxima, which are sensitive to finesse parameter $\Re$ or F of a resonator. The same objective can be achieved by measuring changes of the light intensity in interference extrema I_{max} and I_{min}, namely, the contrast of that pattern. For quasi-monochromatic light, transmitted via any open resonator under study with equivalent mirrors, having average reflectance $\bar{\rho} = \rho_1 = \rho_2$ and total transmittance $\tau_{int} = 1$ of internal space, Eq. (8.18) for the interference contrast becomes:

$$I_{\tau\,max}/I_{\tau\,min} = [(1-\bar{\rho})/(1+\bar{\rho})]^2. \tag{8.27}$$

Since Eqs. (8.18) and (8.27) are obtained with no restrictions, the mean mirror reflectance $\bar{\rho}$, as well as the product $\tau\sqrt{\rho_1\rho_2}$ which substitutes $\bar{\rho}$ for not identical mirrors and $\tau \neq 1$, may be conceptually measured more accurately by Eq. (8.27) rather than (8.24). However, the required for such a measurement linear dynamic range needs to be doubled in comparison with the study via extrema, being either the maxima or the minima, which are referred to the average intensity. For example, at $\tau\sqrt{\rho_1\rho_2} = 0.995$ or 0.999, the range needs to be higher than $1.5\cdot10^6$ or $5\cdot10^6$. Nevertheless, the requirements of distortion accuracy of the registration system for the comparison of two intensities are less critical than when measuring the sharpness of fringes.

In fact, not only fluctuations of beam locality but also reduction of the magnitudes of extremes due to always-existing conditional vibrations are the main cause of errors when measuring beam intensities (see Fig. 8.8). Mirror misalignment and mismatch of the light beam propagation direction to the dominant resonance mode of a cavity produce about equivalent inaccuracy. For example, an intensity change $I_{\tau\,max}/I_{\tau\,min}$ from $4\cdot10^6$ to $1\cdot10^6$ leads to 0.001 decrease of the magnitude measured for $\bar{\rho}$. One-minute angular misalignment creates $\pm2\cdot10^4$ error of the average reflectance. During experimental verification, with use of several high-reflectivity mirrors in intensity-discrimination measurements, respectively $\pm1\cdot10^{-4}$ sensitivity and $\pm5\cdot10^{-4}$ repeatability levels were reached [8.7].

8.2.1 Elimination of Interference

Previously, slow oscillations of a single resonator mirror served to convert a spatial profile of the interference pattern for a resonator into some intensity parameter designating the resonator quality factor. A similar motion may serve to achieve such a contrary task as elimination of any distinguishable interference pattern for beams transmitted by a resonant cavity. For that purpose, instead of measuring intensity

changes in transmission, a detector should integrate a flux transformed by the resonator at a time interval considerably longer than the duration of oscillation motion. That means the velocity of the specific longitudinal mirror motion is expected to be so high that the durations of the maxima overlap the time period of oscillations $t_p \cong t_{2\pi}$. Full destruction of the constant phase shift among interfering beams allows the interaction of the coherent radiation components to become a virtually additive transformation and to disregard the respective interference terms in the superposition of multiply reflected beams.

To facilitate additive superposition of interacting light beams in a mirror waveguide (see Sect. 6.3), the visibility of interference can be reduced to be undetectable by displacing the incident light beam after each reflection on one of the cavity mirrors [8.8]. Instead of the cavity opening as in Fig. 6.24, the transmitting-plus-reflecting coupling window 7 having $\tau_c = 1 - \rho_c$ is used (Fig. 8.9). After N passes of the waveguide inner space or after 2N − 1 single reflections, light leaves the waveguide via window 7 in the direction of specular reflection from the first waveguide mirror. An internal beam reflected by the window makes another N passes and leaves the cavity; the cycle repeats itself with factors τ_c and ρ_c. Integrating detector 5, with the prolonged time constant $\tau_d \geq \tau_{2\pi}$, registers the totality of all components that emerge:

$$I_\rho = I_0\left(\rho_c + \tau_c^2\bar{\rho}^{2N-1} + \tau_c^2\bar{\rho}^{2N-1}\rho_c\bar{\rho}^{2N-1} + \cdots\right) = I_0\left[\rho_c + \frac{(1-\rho_c)^2\bar{\rho}^{2N-1}}{1-\rho_c\bar{\rho}^{2N-1}}\right]. \tag{8.28}$$

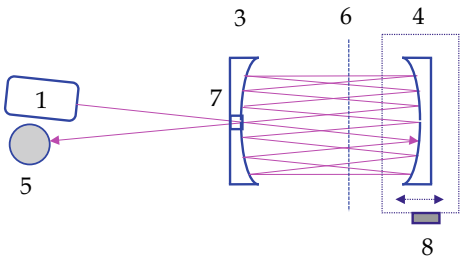

Fig. 8.9 Multiple-reflection waveguide with interference suppression via mirror vibration

The reflective and transmitting window transforms the loss-related sensitivity of the waveguide in such a way that at $\rho_c \to 1$ the system does not respond to any exchange of internal parameters, but at $\rho_c \to 0$, the intensity alteration $I_\rho/I_0 = \bar{\rho}^{2N-1}$ depends only on the average reflectance or on the number of passes in the single cycle, as with an open (fully transparent) opening. The maximum cavity sensitivity to an internal optical loss in the waveguide is reached at $\tau_c = \rho_c = 0.5$, when the window's effect on the intensity ratio I_ρ/I_0 reaches its minimum. Such a minimum follows from the conversion:

$$\frac{I_\rho}{I_0} = f(\rho_c) = \left[\frac{\rho_c + (1-2\rho_c)\bar{\rho}^{2N-1}}{1-\rho_c\bar{\rho}^{2N-1}}\right] \underset{\rho_c=0.5;\bar{\rho}\to 1}{\to} \frac{\rho_c}{1-\rho_c} = 1. \tag{8.29}$$

The relative intensity change, as a function of reflectance $\Delta\rho_c$ related variation, has its minimum at $\rho_c = 0.5$, since at that point the product $\rho_c(1 - \rho_c) = 0.25$ has its maximum. The relative change is:

$$\delta\left(\frac{I_\rho}{I_0}\right) = \frac{\Delta\left(I_\rho/I_0\right)}{\left(I_\rho/I_0\right)} = \frac{\Delta\rho_c}{\rho_c} + \frac{\Delta\rho_c}{1-\rho_c} = \frac{\Delta\rho_c}{\rho_c(1-\rho_c)}. \tag{8.30}$$

To reach maximum sensitivity to internal optical losses, the outcome of multiple reflections may be seen as a relative increase of I_ρ above I_0. Converting Eq. (8.28) by the relative difference:

$$\frac{I_\rho - I_0}{I_0} = \left[\frac{(1-\rho_c)^2}{\rho_c^2}\frac{\rho_c\bar{\rho}^{2N-1}}{1-\rho_c\bar{\rho}^{2N-1}}\right], \tag{8.31}$$

and substituting ρ_c by its equal to 0.5 magnitude for the semitransparent window, one obtains:

$$M \equiv \left(I_\rho - I_0\right)/I_0 = \bar{\rho}^{2N-1}\left(2 - \bar{\rho}^{2N-1}\right). \tag{8.32}$$

After differentiation, expression (8.32) is transformed to the sensitivity for the optical difference:

$$\frac{\Delta M}{M} = (2N-1)\frac{\Delta\bar{\rho}}{\bar{\rho}} + \frac{(2N-1)\Delta\bar{\rho}}{2-\bar{\rho}^{2N-1}} \underset{\bar{\rho}\to 1}{=} 2(2N-1)\frac{\Delta\bar{\rho}}{\bar{\rho}}. \tag{8.33}$$

The number of reflections and the relative sensitivity of the measurement by additive multiple reflections via a semitransparent window are twice as high as the ones in the open waveguide in Fig. 6.24.

To perform measurements with unnoticeable interference effects, one of the cavity mirrors can be placed onto a vibrating stand, similarly to one seen in Fig. 8.7. In the experiment [8.8], the cavity alignment in Fig. 8.9 was maintained by the sharpest interference fringes for He–Ne laser source 1 while turning off piezoelectric modulator 8. Light specularly reflected from semitransparent window 7 in mirror 3 was sensed by detector 5 at inserted baffle 6. The mean reflectance of paraboloids 3 and 4 reaching $\bar{\rho} = 0.9925$, obtained at $2N - 1 = 33, \lambda = 632.8$ nm, and window reflectance $\rho_c = 0.711 \pm 0.002$, was characterized by random error $\pm 5 \cdot 10^{-4}$. At $\rho_c = 0.35 \pm 0.01$ and $\lambda = 3.51$ μm of a Xe laser with higher power fluctuations, the average magnitude $\bar{\rho} = 0.9905$ was measured with ± 0.001 error.

An obvious way for minimizing interference relates to making measurements in incoherent radiation. One widely used example is optical time-domain or low-coherence reflectometry (see Chap. 11), utilizing limited coherence of isotropically scattered radiation [1.10] for millimeter-level resolution among scattering centers [11.40]. Combining high-speed interferometer-mirror motion and the wide-frequency spectrum Δf of a light source, the system's spatial resolution: $\Delta x \cong v/2\Delta f$, in reflected light should be low enough not to resolve interference (see Fig. 8.8). In other words, when the interferometer arm-length difference becomes

larger than the coherence length of the source, and phase information for interfering beams is intentionally uncontrolled, such an interferometer can be used as a reflectometer [II.39]. Another version of the noninterfering arrangement relates to having orthogonal states of polarization in two interferometer arms, which can also be sensed separately, with a polarization-independent sum for polarization-insensitive reflectometry [11.41].

Spectral reflectance and wavelength dispersion (see Sect. 8.5) of sharply wavelength selective reflectors can be measured using low-coherence interferometry–reflectometry [8.32]. By tracking the reference-arm length via a supplemental He–Ne laser, a measured sample's IR Fourier-transform interferogram as the convolution product of the broadband source spectrum and the complex reflection coefficient of the sample, such as a fiber Bragg grating, was measured. By normalizing the power spectrum of the source itself, the measured square field amplitude yielded the fiber Bragg grating's reflectance, from which the spectral dispersion of the grating was computed using zero-padded interferograms, reaching 1.5-ps birefringence resolution and spatially resolving down to 25 pm in the wavelength detection for the grating spectral-reflectance measurements performed [8.32]. The measurement results were immune to errors due to temperature variations or instrumental drift.

8.3 Resonant Phase-Shift and Decay-Time Studies

Previously, space and time averaging of light in a resonator or linear vibration of its cavity mirror served to integrate phase contrasts among retroreflected light components during their interactions with a resonant cavity. On the other hand, in the preceding section we saw how a frequency or a spatial modulation had a law-governed impact on the phase of a registered signal needed to distinguish an interference impression of multiple-beam interactions with the cavity studied. Similarly, observation of an integrated phase shift for frequency-modulated and apparently incoherent laser radiation transmitted via a high-finesse cavity allows one to measure the intracavity loss when detecting the photon lifetime, or in other words the decay rate for photon existence in the cavity.

Consider amplitude-modulated polarized quasi-monochromatic radiation entering a cavity formed by highly reflecting mirrors at distance ℓ (Fig. 8.10). If the light

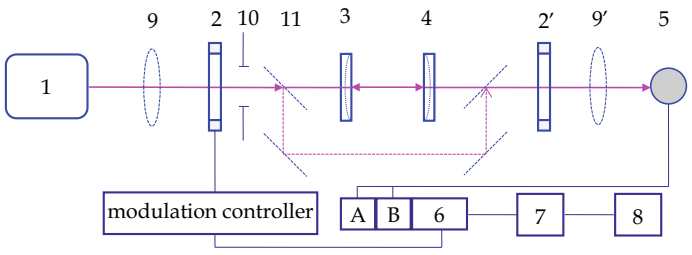

Fig. 8.10 Photon lifetime measurements of inner-resonator losses

intensity is time-modulated at frequency f and initial phase φ_0 as $\sin^2(2\pi ft \pm \varphi_0)$, the phase shift δ of light traversing the cavity is a function of the total time τ_Σ that radiation exists inside the cavity: $\tan\delta = 4\pi f\tau_\Sigma$ [8.9]. The lifetime τ_Σ depends on the number m of dual cavity passes at cavity round-trip time τ_c to attain π-phase: $\pi = m\tau_c = m2\ell/c$ (see also Sect. 7.3). Defining the effective photon lifetime τ_Σ in the cavity as the time $\tau_\Sigma = \tau_e$ needed for the photon energy of this radiation to be dissipated to $I_0\exp(-1) \cong 0.34I_0$, any change of the photon time constant τ_c after the photon has propagated the resonator resolves the mean-squared reflectance $\bar{\rho}^2$ of its mirrors:

$$\bar{\rho}^2 = \rho_3\rho_4 = \exp(-\tau_c/\tau_\Sigma) = \exp(-1/m). \tag{8.34}$$

Light transmitted by the resonator represents the sum of different phase components, modulated at one frequency f, having their intensities declining proportionally to the product of two cavity mirror reflectances: $(\rho_3\rho_4)^m$. Every component can interfere unless the width of the spatial modulation exceeds the coherence length of laser source 1. If the time constant of phase-sensitive detector 5 is larger than the modulation period $T = 1/f$, its output is the additive sum of all terms of interference for the seemingly incoherent radiation components being summarized.

The additive sum I of intensity terms (relation (8.23)) modulated as $I(t) = I_0\cos(4\pi ft + \varphi_0)$ is:

$$I = I_0(1-\rho_3)(1-\rho_4)\sum_{m=0}^{\infty}(\rho_3\rho_4)^m\sin[\omega(t-m\tau_0)+\varphi_0], \tag{8.35}$$

where $\omega = 4\pi f$ and $\tau_0 = 2\ell/c$. Since the mirror-reflectivity product $\rho_3\rho_4 < 1$, Eq. (8.35) at $\varphi_0 = 0$ becomes:

$$I = I_0(1-\rho_3)(1-\rho_4)\sin(\omega t+\varphi)\Big/\sqrt{1-2\rho_3\rho_4\cos(\omega\tau_0)+(\rho_3\rho_4)^2}. \tag{8.36}$$

Here $\varphi = arctan\{[-\rho_3\rho_4\sin(\omega\tau_0)]/[1-\rho_3\rho_4\cos(\tau t_0)]\}$. Maintaining the frequency ω and duration τ_0 under $\omega\tau_0 \ll 1$, terms sin $\omega\tau_0$ and cos ωt_0 can be replaced by ωt_0 and 1, and for a relatively small number of passes $1 < m < 100$ phase φ becomes [8.9]:

$$\tan\varphi = -\frac{\rho_3\rho_4}{1-\rho_3\rho_4}\sin(\omega\tau_0) \underset{1<m<100}{\cong} -m\tau t_0, \tag{8.37}$$

where $m = \rho_3\rho_4/(1-\rho_3\rho_4)$ is the effective number of reflections in the high-reflectivity resonator under test. The reflectance product, or the mean-squared reflectance, for large number of passes $m \gg 1$ at $\omega\tau_0 \ll 1$ can be closely approximated as:

$$\rho_3\rho_4 = \bar{\rho}^2 \cong m/(m+1). \tag{8.38}$$

In Fig. 8.10, polarized cw radiation from single-mode laser 1 is modulated by a birefringence piezo-optic modulator or photoelastic modulator 2 before such a light beam enters the steady resonator consisting of mirrors 3 and 4 under test. Every retroreflected component, transmitted by the resonator formed by mirrors 3 and 4 and

registered by detector 5, is converted by two-channel selective amplifier 6, synchronized with the modulation signal at modulation frequency f, and is further measured by ratio meter 7, connected to recorder 8. The initial phase status φ_0 is determined by default settings of the modulator at position 2′ behind the resonator or via bypassing the cavity using four extra mirrors 11. Since mirrors 11 do not change the phase of light, the unknown total reflectance of these extra mirrors does not affect the phase judgment. The choice of extra mirror reflectances is only limited by the linear dynamic range of the detection system used. Additional lenses 9 and 9′ or field stop 10 can also be used. When the initial status φ_0 is measured, the phase scale for first channel A of amplifier 6 is set to zero, but the scale for channel B is set to 90°. Therefore, the A/B ratio directly gives the magnitude of *tan* φ. After the loss in the resonator formed by mirrors 3 and 4 has been measured, a new element X for study can be inserted into the cavity at any angle Θ, as seen in Fig. 8.11. Obviously, the alignment of cavity mirrors 3 and 4 with third mirror X needs to be preserved for the main cavity-mirror reflectance product to be unchanged. Nevertheless, the diffraction loss in the bent resonator will be different (see Chap. 7 and Fig. 7.1a).

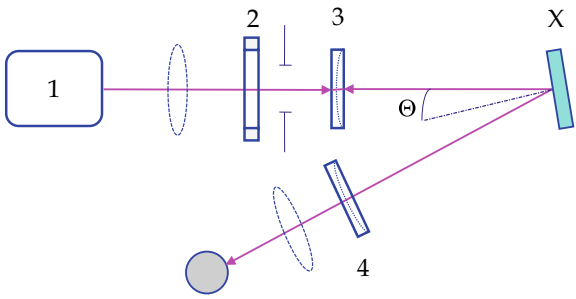

Fig. 8.11 Bent-resonator study of additional mirror at angle Θ

An additional advantage of internal resonator mirror loss measurements is determined by the twofold increase of the sensitivity to the optical losses under study. As it was set earlier by Eqs. (8.16)–(8.20), any attenuation, additionally implemented by mirror *X*, has twice as high an influence on the output intensity of light compared with the attenuation by a single resonator element. That effect is created by the double pass between resonant mirrors at every cycle of multiple reflections. Therefore, any change of reflectance of the bending mirror causes an identical intensity exchange as for the entire resonator: $\Delta\rho_X = \Delta\sqrt{\rho_3\rho_4}$. By having $\rho_3\rho_4$ substituted via $\rho_3\rho_\Theta^2\rho_4$, relation (8.37) for the phase angle φ of a bent resonator is converted into:

$$\tan\varphi = 4\pi f(2\ell/c)\rho_3\rho_\Theta^2\rho_4/\left(1-\rho_3\rho_\Theta^2\rho_4\right). \tag{8.39}$$

The higher is the ρ_Θ^2 magnitude, the stronger is the detector response to its possible deviation.

Experimental high-reflectance studies by the photon-lifetime measurement technique, also called a *phase-shift method*, were made in the visible and near-to-mid IR spectral regions [8.10, 8.11]. For a single measurement of a pair of highly reflecting

mirrors having $\rho_3 \cong \rho_4 \geq 0.999$, spaced at ℓ from 10 to 110 cm, and at $f = 50$ kHz and $\tan\varphi$ from 0.3 to 3.0, the repeatability of readings ranged from $\pm 5 \cdot 10^{-4}$ at $\lambda = 528.8$ nm to $\pm 1 \cdot 10^{-4}$ at $\lambda = 632.8$ nm. Additional comparison was made between the active intracavity and the phase measurements. A ring resonator mirror, valued by the system as having 0.9989 reflectance at $\Theta = 0°$, was first measured by the setup depicted in Fig. 7.3, and its reflectance at $\Theta = 45°$ was measured as being 0.9995. Then, the mirror was remeasured in the bent resonator shown in Fig. 8.11 at $\Theta = 45°$. The acquired reflectance had exactly the same high 0.9995 value. The highest magnitude of specular reflectance, 0.99975 ± 0.00005 at $\lambda = 874.2$ nm, was reached for mirror made by the deposition of coating layers onto a superpolished substrate [8.10]. Using a HF/DF laser at $\lambda = 2.6$–4.2 μm and 1-MHz modulation frequency, the repeatability of phase-shift measurements in a dispersive cavity declined to $\pm 1 \cdot 10^{-3}$ owing to less stable sources and detectors in the IR region and to thermal jitter of the cavity length, which was dynamically matched to lasing modes on the microsecond timescale with 0.1-s averaged phase detection [8.11].

8.3.1 Interference Safeguards

As noted in the preceding section, the phase-shift measurement concept is based on the presumption that light components retroreflected in the test resonator do not interfere. The implementation of that was warranted by the level of spatial modulation of light, exceeding the coherence length of the source used, with a large enough time constant of the light detector, securing additive summation of intensities of multireflected components. Probable limitations to these assumptions can be measured by comparing the actual time intervals of temporal averages with correlation times of intensity fluctuations (see Chap. 3). If the amplitude of light entering the resonant cavity is modulated at center frequency ω_0: $A_{in}(t) = A_{mod}\sin(\omega t) = A_0\cos(\omega_0 t + \varphi_0)\sin(\omega t)$, and if its initial phase shift φ_0 can be disregarded, the entire amplitude of the electromagnetic field in the cavity is given by the sum of differential and supplementary radiation components [II.43]:

$$A_{out}(t) = \tau_{a1}\tau_{a2}\frac{A_0}{2}\sum_{m=0}^{\infty}(\rho_{a1}\rho_{a2})^m\{\sin[(\omega+\omega_0)(t-m\delta_0)] + \sin[(\omega-\omega_0)(t-m\delta_0)]\}, \tag{8.40}$$

where $\tau_{a1}, \tau_{a2}, \rho_{a1}$, and ρ_{a2} are the amplitude transmittances and reflectances of cavity mirrors, ω is the frequency of radiation, and $\delta_0 = 2\ell/c$ is the cavity round-trip time. Instead of Eqs. (8.36) and (8.37), obtained by additive summation of intensities, deriving the output versus the input intensity by totaling amplitudes of component superposition gives [8.9, 7.26]:

$$I_{out} = I_0 \frac{\tau_1\tau_2 \cos(2\omega_0 t - \varphi)}{\sqrt{\left(1+\rho_1\rho_2 - 2\sqrt{\rho_1\rho_2}\cos(\omega+\omega_0)\delta_0\right)\left(1+\rho_1\rho_2 - 2\sqrt{\rho_1\rho_2}\cos(\omega-\omega_0)\delta_0\right)}}; \tag{8.41}$$

$$\tan\varphi = \frac{2\sqrt{\rho_1\rho_2}\sin\omega\delta_0\cos\omega_0\delta_0 - \rho_1\rho_2\sin 2\omega_0\delta_0}{1 - 2\sqrt{\rho_1\rho_2}\cos\omega\delta_0\cos\omega_0\delta_0 + \rho_1\rho_2\cos 2\omega_0\delta_0}, \tag{8.42}$$

where τ_i, ρ_i are the respective factors for light intensities; I_0 is the intensity of incoming light.

In view of optical phase $\varphi_{opt} = 2\pi\nu\ell/c = \omega\delta_0/2$ at $\rho_1\rho_2 = \bar{\rho}$, Eqs. (8.41) and (8.42) convert to Airy formulae (see expressions (3.119–3.123) and [7.26]):

$$I_\tau = \frac{I_0}{(1-\rho)^2\left(1+\frac{4\rho}{(1-\rho)^2}\sin^2\varphi_{opt}\right)};\ \tan\varphi = \frac{2\omega_0\delta_0\rho\left(1-\rho-2\sin^2\varphi_{opt}\right)}{(1-\rho)^2\left(1+\frac{4\rho}{(1-\rho)^2}\sin^2\varphi_{opt}\right)}. \tag{8.43}$$

The conversion indicates that the phase shift is dependent not only on the optical loss, but also on the phase product: $\omega_0\delta_0$. The lower are the modulation frequency and the cavity length, the higher are the fluctuations and likely inaccuracy of the measurement results. Hence, prevention measures could be made for phase-shift studies as for other procedures affected by interference: by averaging of interfering spatial and temporal spectral components at each measurement step.

Considering the weak-modulation effect at phase: $\omega_0\delta_0 \ll \pi$, Eq. (8.41) transforms to:

$$\frac{I_{out}(t)}{I_0\bar{\tau}^2} = \frac{(1 - 2\bar{\rho}\cos 2\varphi + \bar{\rho}^2)\cos 2\omega_0 t + 2\omega_0\delta_0\bar{\rho}(\cos 2\varphi - \bar{\rho})\sin 2\omega_0 t}{(1 - 2\bar{\rho}\cos 2\varphi + \bar{\rho}^2)^2}. \tag{8.44}$$

From the averaging standpoint, the output of a Fabry-Perot interferometer needs to be measured over at least one free spectral range of that interferometer: $\varphi_1 = (\kappa - 0.5)\pi < \varphi < (\kappa + 0.5)\pi = \varphi_2$, where κ is an integer. Accounting for phase fluctuations between two neighboring maxima at $\varphi = \kappa\pi$ and considering that the phase is uniformly distributed within one free spectral range $\varphi_1 = \pi(\kappa - 1/2) \le \varphi \le \pi(\kappa + 1/2) = \varphi_2$:

$$\langle\tan\varphi\rangle = \frac{2\omega_0\delta_0\bar{\rho}}{\varphi_2 - \varphi_1}\int_{\varphi_1}^{\varphi_2}\frac{\cos 2\varphi - \bar{\rho}}{1 - 2\bar{\rho}\cos 2\varphi + \bar{\rho}^2}d\varphi \equiv 0. \tag{8.45}$$

Relation (8.45) points out that to obtain correct results by measuring light signals proportional to *sin φ or cos φ*, the averaging process needs to be done prior to the computation of the phase function and obtaining as a result [7.25, 7.26]:

$$\begin{aligned}
\langle I_0 \sin\varphi\rangle &= \frac{2\omega_0\delta_0\bar{\rho}}{\varphi_2-\varphi_1}\int\limits_{\varphi_1}^{\varphi_2}\frac{\cos 2\varphi-\bar{\rho}}{(1-2\bar{\rho}\,\cos 2\varphi+\bar{\rho}^2)^2}d\varphi \\
&= \frac{\omega_0\delta_0\bar{\rho}}{\varphi_2-\varphi_1}\left|\frac{\sin 2\varphi}{(1-\bar{\rho}^2)(1+\bar{\rho}^2-2\bar{\rho}\,\cos 2\varphi)}+\frac{2\bar{\rho}}{(1-\bar{\rho}^2)^2}\arctan\left[\frac{(1+\bar{\rho})^2\tan\varphi}{(1-\bar{\rho}^2)}\right]\right|_{\varphi_1}^{\varphi_2}; \\
\langle I_0 \cos\varphi\rangle &= \frac{1}{\varphi_2-\varphi_1}\int\limits_{\varphi_1}^{\varphi_2}\frac{d\varphi}{1-2\bar{\rho}\,\cos 2\varphi+\bar{\rho}^2}=\frac{1}{(\varphi_2-\varphi_1)(1-\bar{\rho}^2)} \\
&\times\left|\arctan\left[\frac{(1+\bar{\rho})^2\tan\varphi}{(1-\bar{\rho}^2)}\right]\right|_{\varphi_1}^{\varphi_2}.
\end{aligned} \tag{8.46}$$

Integration over one free spectral range gives: $\delta(\sin 2\varphi)\equiv 0$, and the ratio of averaged terms becomes:

$$\tan\varphi=\frac{\langle I_0\sin\varphi\rangle}{\langle I_0\cos\varphi\rangle}=\frac{2(\rho_1\rho_2)^2\omega_0\delta_0}{1-(\rho_1\rho_2)^2}, \tag{8.47}$$

being equivalent to Eq. (8.37), derived by assuming the additive summation of intensities of incoherent components of interfering radiation at the infinitely small-phase shift [8.9, 7.25, 7.26].

On the basis of the analysis above, certain measures needs to be taken as main precautions for the phase-shift measurement: ensuring a uniform distribution of phase shift φ over one free spectral range of the resonator under study; individual averaging of the sine and cosine signals; providing spatial and spectral stabilization of the light emission of the laser source, as well as ensuring repeatable and stable alignment of the resonant cavity (see Sect. 7.4 for details). The verification experiments [8.13] detected very high fluctuations of both He–Ne and argon laser signals with a relatively low modulation frequency of approximately 1 kHz. Relatively long averaging times of a few tens of seconds were required to equalize otherwise nonuniform distributions of the phase shift within ±10% error. The averaging performed for the separate sine and cosine signal partitions via Eqs. (8.46) made several times over the free spectral range of the cavity provided the results always yielding lower losses than obtained by the averaging of $\tan\varphi$ via Eq. (8.45).

The choice of the light source is also relevant for the phase-shift measurement technique. Low-coherence thermal sources have a large spatial divergence, which is highly efficient for the averaging. Indeed, the novel synchrotron radiation with extremely low angular divergence, but a very broad spectral emission, has desirable optical properties for the phase-shift studies – high directness and low coherence length. The results of phase-shift measurements with cw lasers are very much dependent on the average linewidths and fluctuations among longitudinal laser modes in the cavity. Even integration over very long time terms may not limit fluctuations to a desired level. Since thermal and acoustic sources add noise due to cavity length variations, the overall variability of phase-shift measurements would be improved by a reasonable increase of the integration time constant and by making a significant and thus easy-to-measure phase shift.

8.3.2 Decay-Time Measurements

Analyzing the prospects of pulsed measurements at the beginning of this chapter, we saw how the intensity of a pulse entering a resonant cavity decreases in proportion to the product of the reflectances of the cavity mirrors and the squared transmittance of its internal space. It was also presumed that the duration of each pulse is shorter than the resonator round-trip time, meaning that the short pulse is distinguishable on every separate reflection and no interference among retro-reflected pulses occurs. It is evident that a virtually similar effect can be achieved while obtaining a decaying wave front via a quick turning off of a continuously propagating beam [8.12, 8.13]. Any radiation energy accumulated in the cavity would decline exactly as the energy of an inserted pulse, with the only difference being that the effective length of a continuously formed pulse would be precisely equal to the length of the cavity experiencing transitional process.

From Eqs. (3.108)–(3.111) it follows that to fill the internal space of a highly reflecting optical cavity with light, the spectrum of emitted waves has to be in resonance with the cavity. Consider monochromatic light at frequency ω entering a resonator of highly reflecting mirrors. The total output electric field transmitted by the cavity can be represented as (see Sect. 3.1):

$$\begin{aligned} E_{out,\Sigma}(t) &= E_{out}\exp(-i\omega t) \\ &= E_{ins}\exp(-i\omega t)C_{mnq}\sqrt{\tau_1\tau_{\text{int}}\tau_2}\big/\big(1-\tau_{\text{int}}\sqrt{\rho_1\rho_2}\exp(i\delta)\big), \end{aligned} \tag{8.48}$$

where C_{mnq} is the mode-matching factor for the coupling efficiency of the cavity and the source emission at frequency ω, δ is the round-trip phase shift in the cavity: $\delta = 2\omega\ell/c + \varphi_x + \varphi_y$, and phases φ_x and φ_y specify the transverse mode geometry in the cavity. Near the cavity resonance with phase $\delta \cong 2\pi$, the field amplitude can be resolved via the frequency difference $\Delta\omega = \omega_{mnq} - \omega$ as [II.5]:

$$\begin{aligned} E_{out} &\cong E_{ins}\frac{C_{mnq}\sqrt{\tau_1\tau_{\text{int}}\tau_2}}{1-\tau_{\text{int}}\sqrt{\rho_1\rho_2}\Big[1-i(\Delta\omega 2\ell/c)-(1/2)(\Delta\omega 2\ell/c)^2\Big]} \\ &\approx E_{ins}C_{mnq}\frac{c}{2\ell}\frac{\tau_1\tau_{\text{int}}\tau_2}{1-\tau_{\text{int}}\sqrt{\rho_1\rho_2}\big(1-i\Delta\omega\frac{2\ell}{c}\big)} \\ &= E_{ins}C_{mnq}\sqrt{\frac{\tau_1\tau_{\text{int}}\tau_2}{\rho_1\rho_2}}\frac{c}{2\ell}\left(\frac{c}{2\ell}\frac{1-\tau_{\text{int}}\sqrt{\rho_1\rho_2}}{\tau_{\text{int}}\sqrt{\rho_1\rho_2}}+i\Delta\omega\right)^{-1} \\ &= E_{ins}A_{mnq}\frac{c}{2\ell}(\gamma_c+i\Delta\omega)^{-1}. \end{aligned} \tag{8.49}$$

For two conditions of the internal optical field near its resonance – steady-state mode status: $E_{ins}(t) = E_s\exp(-i\omega_s t)$ at $t < 0$, and transient status: $E_{ins}(t) = E_s\exp[-(\gamma_s + i\omega_s)t]$, when the source's E_s and ω_s are turned off at an instant $t > 0$ – the Laplace transform in cavity-output space gives [8.12]:

$$E_{ins}(t) \underset{t<0}{=} E_s A_{mnq} \frac{c/2\ell}{\gamma_c + i\Delta\omega} \exp(-i\omega_s t), \tag{8.50}$$

$$E_{ins}(t) \underset{t>0}{=} E_s A_{mnq} \left\{ \frac{c/2\ell}{\gamma_c - \gamma_s + i\Delta\omega} \exp[-(\gamma_s + i\omega_s)t] + \frac{c/2\ell}{(1 - \gamma_c/\gamma_s - i\Delta\omega/\gamma_s)(\gamma_c + i\Delta\omega)} \exp[-(\gamma_c + i\omega_c)t] \right\}. \tag{8.51}$$

Equation (8.51) for t > 0 distinguishes contrasting states of unequal complex frequency responses γ_c and γ_s of the cavity and the source. For the source turned off slowly and $\gamma_c \gg \gamma_s$, the first equation term dominates and the cavity properties do not become apparent from the decay curve. But, if the light is switched off sharply: $\gamma_s \gg \gamma_c$, the first term vanishes and at resonance cavity frequency ω_c:

$$E_{ins}(t) \underset{\gamma_s \gg \gamma_c}{=} E_s A_{mnq} \frac{c/2\ell}{\gamma_c + i\Delta\omega} \exp[-(\gamma_c + i\,\omega_c)t]. \tag{8.52}$$

The physical meaning of relation (8.52) is identical to the requirement for a pulsed source to have its pulse duration shorter than the cavity round-trip time. Otherwise, interference between declining and incident signals leads to error in decay measurement. At decay rate γ_c, the subsequent characteristic decay time $t_c = 1/2\gamma_c$ defines the decline of beam intensity by an equation equivalent to (8.8):

$$I(t) = I_0 \exp(-t/t_c) = I_0 \exp(-2\gamma_c t). \tag{8.53}$$

After substitution of variables from Eq. (8.49) and introducing decay length $\ell_{decay} = ct_c$:

$$\frac{\tau_{\text{int}}\sqrt{\rho_1\rho_2}}{1 - \tau_{\text{int}}\sqrt{\rho_1\rho_2}} = \frac{ct_c}{\ell} \quad or \quad \tau_{\text{int}}\sqrt{\rho_1\rho_2} = \bar{\rho} = \frac{ct_c}{l + ct_c} \equiv \frac{\ell_{decay}}{\ell + \ell_{decay}}. \tag{8.54}$$

Equation (8.54) confirms that the lower is the optical loss in the cavity, the higher is the effective length ℓ_{decay} of propagation at wavelength λ for its intensity exponentially decreasing by e times.

As was seen when examining pulse and interferometric measurements, the relationships among intensities of the components of radiation existing in the cavity, identifying the decay time constant, are factually determined by the effective number of intracavity reflections. Accordingly, Eqs. (8.8) and (8.53) can be rewritten as:

$$\begin{aligned} \ln(\bar{\rho}) &= \frac{1}{2n}\ln(W_{i+n}/W_i) = \frac{\bar{\rho} - 1}{\sqrt{\bar{\rho}}}; \\ \ln(I_t/I_0) &= -\frac{t_0}{t_c} = \ln\bar{\rho}^2 = -2\frac{1 - \bar{\rho}}{\bar{\rho}} \underset{\bar{\rho}\to 1}{\cong} -2\bar{\chi}. \end{aligned} \tag{8.55}$$

Here $t_0 = 2\ell/c$ is the cavity round-trip time and $\bar{\chi}$ is the average loss over one single cavity mirror for the cavity having identical or otherwise indistinguishable mirrors. As a result:

$$t_c = t_0\sqrt{\bar{\rho}}/2\bar{\chi} = \ell\sqrt{\bar{\rho}}/c\bar{\chi} \underset{\bar{\rho}\to 1}{\cong} \ell/(c\bar{\chi}). \tag{8.56a}$$

Since at $\bar{\rho} \to 1$ the magnitude of $\sqrt{\bar{\rho}}$ also tends to unity, the decay time can be directly resolved by way of each cavity mirror average-loss measurement. On the other hand, the decay time t_c can be expressed via finesse of cavity resonances. Substituting $\bar{\rho} = \tau\sqrt{\rho_1\rho_2}$ in Eq. (8.20) at $\tau = 1.0$ gives:

$$\begin{aligned} t_c &= (\ell/c)\bar{\rho}/(1-\bar{\rho}) = (\ell/c)\left(\sqrt{\bar{\rho}}/\pi\right)\Im \ \ or \\ \Im &= (ct_c/\ell)\left(\pi/\sqrt{\bar{\rho}}\right) \underset{\bar{\rho}\to 1}{=} \left(\ell_{decay}/\ell\right)\pi. \end{aligned} \tag{8.56b}$$

A schematic of the mirror reflectometer for decay-time measurement [8.12] is seen in Fig. 8.12. A light beam from a single-frequency argon-ion laser at $\lambda = 514.5$ nm is transmitted via crossed polarizers, a Pockels cell, a mode-matching lens, and either a mirror ring or a Fabry–Perot cavity, respectively, consisting of four or two mirrors, to finally reach a fast detector. The signal triggers electronic switches (not shown) and the comparator. An internal clock sets up the threshold to compensate for the delay between the action of the Pockels cell and the impact of the light-beam [8.12]. The factually measured switch-off time due to the cavity reaction was near 25 ns. The measured decay times for two unlike pairs of flat and curved mirrors in a 10-m-long cell were, respectively, 185 μs ± 1.4% and 26.24 μs ± 0.2%, all averaged over 20 readings. The highest measured products of two-mirror reflectance were estimated as reaching 0.999820 ± 3 ppm and 0.999820 ± 7 ppm, making nearly 60 ppm for the total of the absorption and scattering losses for each separate mirror.

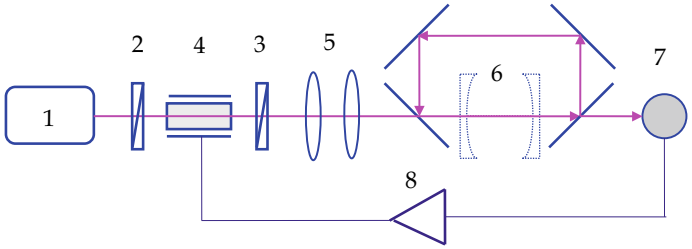

Fig. 8.12 Decay-time mirror interferometer: *1* laser source; *2* and *3* polarizers; Pockels cell; *5* mode matching lens; *6* decay cavity; *7* detector; *8* comparator

A typical setup for decay-time measurements performed in a relatively short cavity, whose length is tuned on and off via a piezoelectric transducer (PZT) and which is excited by cw-laser light coupled into such a cavity via an acousto-optic modulator, is depicted in Fig. 8.13 [8.14].

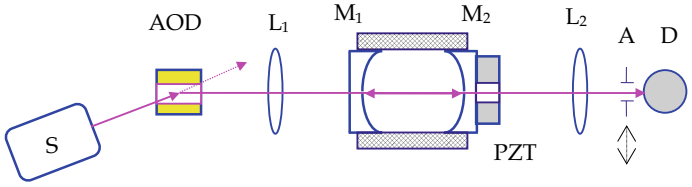

Fig. 8.13 Decay-time measurements of cavity loss and finesse

Multilayer Ta_2O_5/SiO_2 mirrors M_1 and M_2, deposited on superpolished substrates mounted in a clean-room environment on a sealed Teflon spacer, formed a nearly 4-mm long cavity. The cavity was excited by a cw Ti: sapphire laser via acousto-optic deflector (AOD) and mode matching lens L_1. Small changes of the cavity length of 4 ± 0.2 mm were caused by pushing on one of substrates by a PZT, compressing slightly the Teflon spacer. Lens L_2 imaged the beam traversing the cavity to photomultiplier tube detector D via circular aperture A. To measure the ringdown time, the cavity was slowly scanned until its resonance with the laser wavelength. When the preset intensity threshold was achieved, the detector triggered the acousto-optic deflector switch, which after a delay of about 300 ns turned off the beam in 45 ns. Two sets of mirrors with radii of curvature of 173 mm and 1 m were studied. The highest detected decay time was 8.2 μs. Based on Eq. (8.56a), the total loss for the best mirror pair was measured to be about 1.6 ppm at $\lambda = 850$ nm with the single mirror reflectivity near 0.999996 at 830–880 nm [8.14].

In spite of the relatively high sensitivity of decay-time loss measurements, certain attention should be paid to the fact that experimental results are taken by a great deal of averaging over many diverse readings. For example, Fig. 8.14 resembles an actual noisy decay curve averaged over 100 single decays [8.14]. One reason for that noise was temporal instability of the source spectrum and thermal cavity drifts (see Chap. 3), but it was also directly related to fractional errors of fitting experimental data into a single exponential function (see ringdown spectroscopy considerations in Sect. 7.3). Since the fractional detection error is set by the integer-defined decay time: $\pm\ell/(2c)$, regardless of the processing speed [8.12], this leads at round-trip number $k = t_c c/\ell$ to the fractional limit of the decay measurement being $\pm\left(1 - \tau_{\text{int}}\sqrt{\rho_1\rho_2}\right)$ or to $\pm 1/2k = \ell/(2ct_c) = Loss/2$, which, in turn, leads to indistinguishable reflectivity $\pm(\bar{\rho} - \sqrt[4]{\bar{\rho}})/2$ at $\bar{\rho}^2 = \rho_1\rho_2$. For $(\rho_1\rho_2)_a = 0.99$ or $(\rho_1\rho_{2b})_b = 0.9999$ and corresponding individual reflectances $\bar{\rho}_a = 0.995$ or $\bar{\rho}_b = 0.99995$, the irresolvable fractional error is $1.25 \cdot 10^{-3}$ or $1.25 \cdot 10^{-5}$. To measure optical losses below 100 ppm, some extra stabilization of the equilibrium temperature for the cavity, specimen, and cavity surroundings may be needed (see Chap. 10).

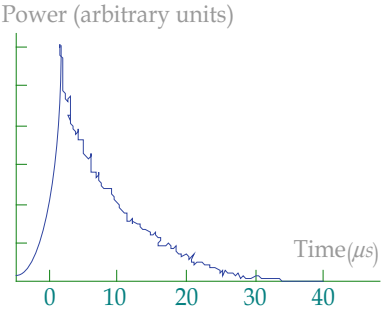

Fig. 8.14 Illustration of an averaged decay

More efficient operations of a ringdown scanning spectrometer can be achieved by slowly sweeping the cavity length via a PZT as in Fig. 8.13, coupling the cavity modes to a tuning wavelength of a cw laser, and fast-triggering the cavity off when the coupled-light intensity reaches a preset threshold [7.36]. In the system shown in Fig. 8.15, photodiode D with trigger circuit T records the matching intensity of cavity-coupled light and sets the cavity off its resonance within a few nanoseconds after a transistor is triggered to decrease the signal to the PZT. The same PZT also compensates for thermal drifts of the cavity, tracking the cavity length via the laser-tuning wavelength. In the experiments, the cavity mirrors had 0.9999 reflectivity and were set 30 cm apart while approximately $3 \cdot 10^{-9}$-cm^{-1} noise-level absorption coefficient sensitivity was obtained for measured ringdown acetylene overtone signals with ±3% signal-baseline oscillations due to observed etalon effects in mirror substrates (see Sect. 7.4). By minimizing cw laser jitter on spectral scanning and cavity tuning, and by stabilizing the temperature of the mirror cavity or monitoring the drift of actual temperature, the relative ringdown detection sensitivity ranged from 10^{-3} to 10^{-7}, allowing up to $8.63 \cdot 10^{-27}$ strength of the PQ(35) transition line of oxygen to be sensed within ±0.4% uncertainty [7.36, 7.37].

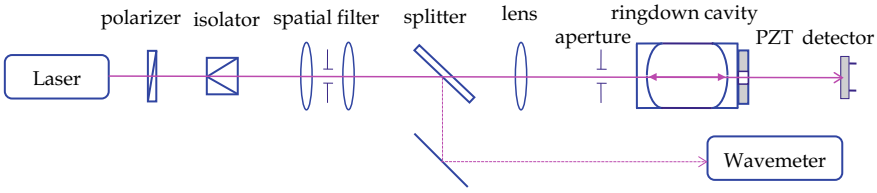

Fig. 8.15 Wavelength-sweeping ringdown spectrometer

Another approach to achieving high stability of a resonant cavity minimizing sweep-induced oscillations of the cavity extrema or ringing effects [8.40] and increasing the sensitivity of ringdown decay studies is in locking a single-frequency laser wavelength to a resonance cavity mode [II.41, 8.29]. In Fig. 8.16, a diode-pumped Nd:YAG continuous-wave laser tunable to 0.14 nm in the 1064-nm range, is servo-locked to radiation transmitted by and reflected from the three-mirror ringdown cavity via an added analog detection circuit, enabling 500 MHz/s laser frequency scans at tens of kilohertz in signal acquisition mode. The frequency-locking scheme is realized via electro-optic modulator EOM placing frequency-modulation sidebands on light passing from the laser. Polarization-cube beam-splitters PBS divide modulated radiation into s and p components and recombine them on photodetectors PD1–PD3. Acousto-optic modulator AOM provides rapid switching of incoming light on and off the ringdown cavity, as well as

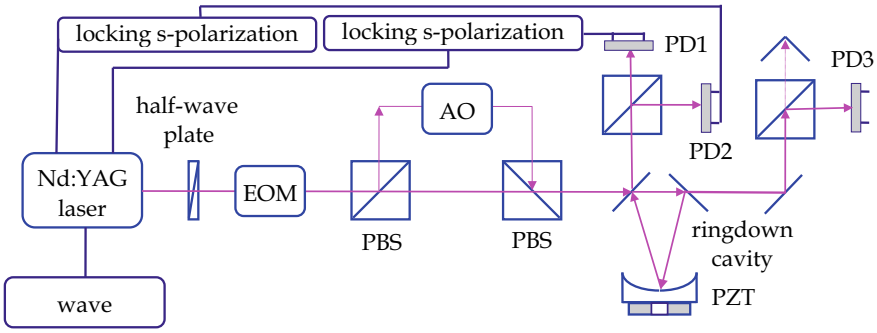

Fig. 8.16 Frequency-modulation locked laser ringdown spectrometer

frequency shifting the s-polarization component to the longitudinal mode of the cavity being adjacent to one to which the p-component is locked in, allowing both components to be resonant with the cavity. The three-mirror cell consists of two flat mirrors, attached to one spacer, and a plano-concave mirror mounted on a PZT, making a 42-cm-long cavity path and an empty cavity ringdown time of 2.8 μs. Experimentally measured absorption spectrums were obtained in 10 s at 75-kHz spectral resolution. The system's long-term and short-term sensitivity was estimated to be $(8.8-1.0)\cdot 10^{-12}$-cm^{-1} Hz$^{-1/2}$ [8.29]. A similar scheme of cavity-locking, for more precise control of the laser-emission wavelength [8.41], used an extra He–Ne-laser-stabilized transfer resonant cell actively locking the CO_2 laser frequency. An alternative solution for repetitive cavity locking and unlocking is illustrated in Fig. 8.17, which applies rapid reacquisition of cavity mode-locking state after detection of each ringdown signal, thus reducing launching of high-order transverse cavity modes by rejecting feedback to external-cavity diode laser ECDL utilized for measurements [7.40]. Radiation from the external-cavity diode laser is coupled into

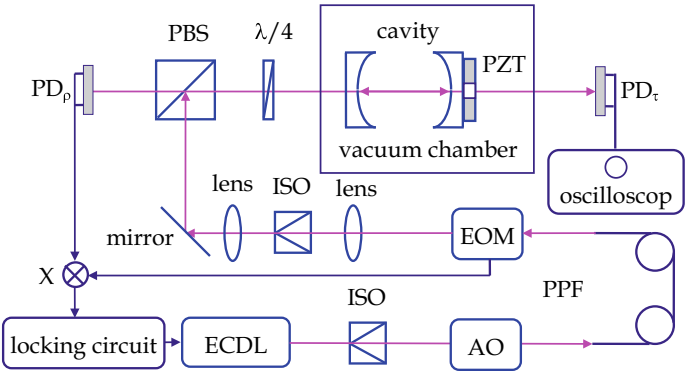

Fig. 8.17 Periodically locked continuous-wave laser ringdown spectrometer: *ISO* – optical isolator; *λ*/4 – quarter-wave plate, *X* – double-balanced RF mixer

the ringdown cavity via acousto-optic modulator AOM and is frequency-locked to the TEM_{00} cavity mode via the polarization scheme shown in Fig. 8.16. The frequency of the external-cavity diode laser does not drift when the acousto-optic modulator is switched off, initiating the cavity ringdown signal, thus allowing the system to quickly regain the cavity lock with the acousto-optic modulator being turned on again. Mode-matching of the resonant cavity to laser light is done via single-mode polarization-preserving fiber PPF and lens optics, suppressing below 3% high-order transverse modes versus TEM_{00} mode intensity. High-speed amplified photodiodes PD_τ and PD_ρ, which signals were demodulated via a double balanced mixer X at 15 MHz, detected the decay of radiation being transmitted by the cavity and the error signal caused by reflected light being reduced to zero on ringdown events, since frequency-modulation sidebands are not initiated when light leaves the cavity, and frequency stabilization is placed on hold with the acousto-optic modulator in the "off" position. The noise level of absorption loss for single-shot sensitivity reached $7.5 \cdot 10^{-8}$ cm^{-1} when 13,000 events were averaged within 2 h or $4.7 \cdot 10^{-8}$ cm^{-9} for the average of 256 ringdown events acquired at 1.5-Hz rate for each average having $\pm 1.4 \cdot 10^{-8}$ cm^{-1} standard-deviation noise for the residuals of the Voigt fit to the absorption features being measured [7.40].

A system for rapid spectral ringdown detection of backward propagating light [8.43] is seen in Fig. 8.18. External-cavity diode laser ECDL serving as a source of coherent radiation for optical-heterodyne reception of a beam reflected from the ringdown cavity is set at a fixed (slowly varying) frequency for a path-tuned cavity or is frequency-swept itself. A three-port optical circulator separates light reflected back by the cavity from light emitted by the external-cavity diode laser. Both reflected- and transmitted-radiation detectors PD_τ and PD_ρ sense ringdown signals, with higher sensitivity in reflected light to intracavity interference, exhibiting full-wave oscillations over the decaying ringdown signal envelope (see also Sects. 3.3 and 7.4). In experiments [8.43], all system element surfaces were tilted to prevent occurrence of multiple-reflection interference noise with cavity mirrors made on wedged substrates, establishing the linear measurement dynamic range from 0 to $2 \cdot 10^{-5}$ cm^{-1}. Comparable resonant pulse-stacking of ultrashort high-repetition rate pulses [8.18] and rapidly swept and fast-tuning systems with

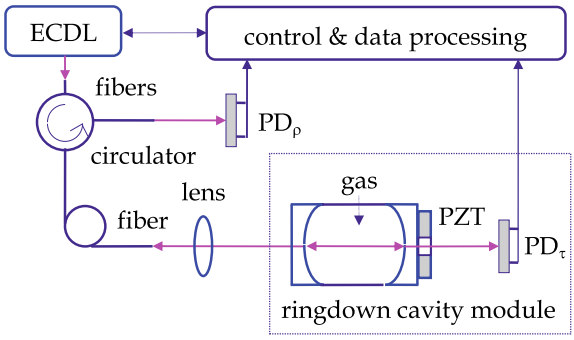

Fig. 8.18 Rapidly sweeping reflecting ringdown spectrometer

reference cavities and/or off-axis injection of light into ringdown cavities and mirror waveguides (see Chaps. 6 and 7) can be used [8.42–8.45].

If ringdown time measurements are applied to detection of optical losses in solid or perhaps liquid substances, thermal and other changes of the cavity's refractive index also need to be evaluated. Rewriting Eq. (8.54) for an intracavity material of length ℓ and refractive index n_c, one would have:

$$t_c = \frac{\ell_c}{c}\frac{\tau_{\text{int}}\sqrt{\rho_1\rho_2}}{1-\tau_{\text{int}}\sqrt{\rho_1\rho_2}} = \frac{\ell n_c}{c}\frac{\tau_{\text{int}}\bar{\rho}}{1-\tau_{\text{int}}\bar{\rho}} = \frac{\ell n_c}{c}\frac{(1-\mu)\bar{\rho}}{1-(1-\mu)\bar{\rho}}, \tag{8.57a}$$

where $\bar{\rho}$ is the average reflectivity of cavity mirrors and $\mu = 1 - \tau_{\text{int}}$ is the intracavity loss determined via transmittance $\tau_{\text{int}} \neq 1$. Identifying the relative decay-measurement sensitivity as change $\Delta t_c/t_c$:

$$\begin{aligned}\frac{\Delta t_c}{t_c} &= \frac{\Delta\ell}{\ell} + \frac{\Delta n_c}{n_c} + \frac{\Delta((1-\mu)\bar{\rho})}{(1-\mu)\bar{\rho}} - \frac{\Delta(1-(1-\mu)\bar{\rho})}{1-(1-\mu)\bar{\rho}} \\ &\underset{\substack{\mu\to 0\\ \rho\to 1}}{\cong} \frac{\Delta\ell}{\ell} + \frac{\Delta n_c}{n_c} + \frac{\Delta(1-\mu)}{1-\mu} - \frac{\Delta(1-\bar{\rho})}{1-\bar{\rho}},\end{aligned} \tag{8.57b}$$

one could see that the higher is the reflectivity of each cavity mirror and the lower is the cavity loss sensed, the higher the sensitivity becomes. Conversely, because of the opposite-sign contributions, intracavity and mirror losses can compensate for each other, reducing the overall sensitivity if every type of loss is not separately resolved (see Sect. 8.4). Measurements in a fiber-based cavity [3.84], despite the loss sensitivity reaching approximately $5 \cdot 10^{-4}$ dB, confirmed the challenges for the solid-state cavity ringdown studies, such as the uncertainties in reflection locality on the fiber core-cladding interface leading to resonator leakages.

Figure 8.19 illustrates the schematic for a decay-time study of the scattering plus absorption loss in a microphotonic whispering-gallery mode disk resonator [8.38]. Tunable laser S, emitting less than 300 kHz linewidth in the 1420–1498-nm spectral region, was coupled to microdisk resonator C via polarization controller P and two variable attenuators A_1, A_2, maintaining a constant signal on detector D. The laser wavelength was tuned via double-dip mode-coupling resonances for clockwise and counterclockwise propagation via the 10-μm-radius disk formed in Si–SiO_2 layers. To separate linear and nonlinear contributions of the disk absorption, the resonance wavelength and on-resonance transmittance values of the microdisk modes were monitored as functions of input power, identifying a relative amount of linear absorption and the scattering loss contribution within the resonator. A nearly 0.25 dB/cm linear absorption coefficient had been detected leading to the measured decay rate $\gamma_c = 0.57 \pm 0.03$.

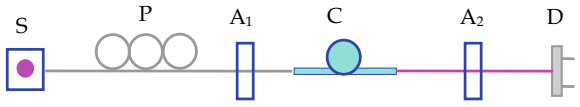

Fig. 8.19 Micro-cavity decay measurement

As small-size microring resonators are useful for bio-sensing, the phase-shift measurements of ringdown time in a microcavity (relation 8.37) via detecting a ratio of in-phase to out-of-phase components make studies independent of laser-light intensity fluctuations [8.54]. Part-per-billion levels of sensitivity could be reached by measuring evanescent-field absorption in silicon nitride microring disks coated with a functionalized sorbent to enable analysis of differential absorption spectra by observing shapes of disk resonance lines [8.56]. The as low as $2.7 \cdot 10^{-12}$ cm^2 absorption cross-section detection sensitivity was reached for the phase-shift ringdown studies of Rayleigh backscattering in a silica microsphere resonator, measured simultaneously with the transmission of the microsphere via a tapered fiber coupler [8.57]. Polarization-sensitive surface studies could be also realized by enabling a phase-shift evanescent ringdown ellipsometric spectroscopy [8.55].

8.4 Quality-Factor Transfer Method and Asymmetric-Cavity Measurements

Every method of measurements in a resonant cavity needs to provide a temporal or spatial modulation of some kind for radiation interacting with the resonator, and then demodulate the resultant spectrum to resolve the optical loss exhibited by the cavity. Consider the prospect of a measurement procedure which is capable of using any waveform of optical radiation: pulsed or continuous and also time- or frequency-modulated. Since pulsed laser light induce considerable power action, often causing thermal and nonlinear effects, the data obtained with pulsed versus continuous irradiation may be essentially different. Accordingly, it is quite reasonable to seek a procedure not related to an explicit type of light source to be used. That task requires excluding side effects coincident with such uncertainties as irregular temporal or spectral beam structure, intensity fluctuations and undesired interference phenomena of light interacting with the cavity.

As we recall from Eqs. (8.4) and (8.5), any direct transmission measurements of light intensity via a resonator of highly reflective elements does not provide highly sensitive output to small losses in resonant elements. However, this fact holds true only in comparison with the radiant flux Φ_0 which is incident onto the resonator. Consider that after some determination of transmitted intensity Φ_τ by Eq. (8.4), the beam passing via two equivalent mirrors under test can be measured without multiple reflections as $\Phi_{\tau,0} = \Phi_0 \tau_1 \tau_2$. The ratio of the two fluxes is:

$$\Phi_\tau / \Phi_{\tau,0} = 1/\left(1 - \bar{\rho}^2\right). \tag{8.58}$$

Here the sensitivity is essentially increased in proportion to the average reflectance $\bar{\rho}^2$ or to the product of the reflectances of the two mirrors. Such a ratio rises to 10 at $\bar{\rho}^2 = 0.949$ and to 100 at $\bar{\rho}^2 = 0.995$.

Since Eq. (8.4) is obtained under the assumption of a near-infinite number m of intra-resonator multiple reflections, being added incoherently as having a short length of coherence:

$$\Phi_{\tau,\infty} = \kappa\Phi_0\tau_1\tau_2\frac{1-(\rho_1\rho_2)^m}{1-\rho_1\rho_2} \underset{\rho_1\rho_2<1;m\to\infty}{=} \kappa\Phi_0\frac{\tau_1\tau_2}{1-\rho_1\rho_2}, \tag{8.59}$$

for its validity, the totality of all components retroreflected in the cavity must be integrated by a detector in space or time. The sum of remaining terms, exhibiting more than m reflections, and contributions of residual interference should be lower than the acceptable measurement error Δ:

$$\left|\left(\Phi_\tau - \Phi_{\tau,\infty}\right)/\Phi_\tau\right| = \left|(\rho_1\rho_2)^m\right| \le \Delta. \tag{8.60}$$

If a detector is capable of distinguishing a ±0.1% change of the signal to be measured, no fewer than 687 reflections must reach the detector at $\rho_1\rho_2 = 0.99$ to have $\Delta \le 0.001$. The number of reflections is reduced to 135 and to 66 at $\rho_1\rho_2 = 0.95$ and $\rho_1\rho_2 = 0.9$, respectively. Typically, three mirrors in pairs of two are measured to resolve Eq. (8.58) via a single-mirror reflectance. Instead, observation of resonator properties in reflected light allows identifying reflectances of cavity mirrors by swapping their positions while substantially suppressing residual interference.

Figure 8.20 illustrates implementation of two virtually semitransparent elements X and Y, forming the test cavity, in the path of a beam of incident light. Beam splitter 2 serves to irradiate reference detector 3 tracking the intensity of laser source 1. Splitter 4 transfers light reflected by the wave normal from elements X and Y to main detector 5, with field stop 6 reducing stray light. The ratio $N_5/N_3 = M$ of the main-to-reference detector signals provides one reading of the measurement system. The intensity M of light reflected from elements X and Y, considered at the moment as having nonabsorbing and nonscattering substrates with respective reflectances and transmittances $\tau_x = 1 - \rho_x$ and $\tau_y = 1 - \rho_y$, is:

$$M = \kappa\Phi_0\tau_i\tau_2\tau_4\rho_4\left[\rho_x + \rho_y(1-\rho_x)^2/\left(1-\rho_x\rho_y\right)\right]. \tag{8.61}$$

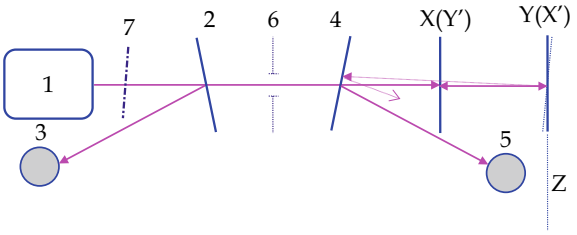

Fig. 8.20 Intracavity resonator-tuning measurements

Here τ_i is the transmittance of filter or isolator 7, serving to exclude any optical feedback between the resonator formed from mirrors X and Y studied and laser cavity 1. A few techniques can be used to distinguish radiation reflected from either mirror X or mirror Y with and without the participation of multiple reflections. One may even use the baffle depicted in Fig. 8.9 or replace mirror Y by any nonreflecting absorber and/or completely remove mirror Y. The easiest way to cause multiple reflections to vanish is by misalignment of mirror Y away from a wave normal to the incident light beam, making even the first reflection component miss detector 5 (dashed lines in Fig. 8.20). Since the intensity of radiation reflected by the mirror X is: $M_0 = \kappa\Phi_0\tau_i\tau_2\tau_4\rho_4\rho_x$, the combination of two detector readings for two measurements of X–Y and X intensities gives:

$$\mathrm{K}_1 \equiv \frac{M - M_0}{M_0} = \frac{\rho_y(1-\rho_x)^2}{\rho_x\left(1-\rho_x\rho_y\right)}. \tag{8.62}$$

The inverted ratio is measured with mirrors X and Y substituting each other while repeating the two readings, in this case Y–X and Y:

$$\mathrm{K}_2 \equiv \frac{M' - M'_0}{M'_0} = \frac{\rho_x\left(1-\rho_y\right)^2}{\rho_y\left(1-\rho_x\rho_y\right)}. \tag{8.63}$$

Multiplying and splitting Eqs. (8.62) and (8.63) into one another, after new designations:

$$\begin{aligned} A &\equiv \sqrt{\mathrm{K}_1\mathrm{K}_2} = (1-\rho_x)\left(1-\rho_y\right)/\left(1-\rho_x\rho_y\right); \\ B &\equiv \sqrt{\mathrm{K}_1/\mathrm{K}_2} = \rho_y(1-\rho_x)/(\rho_x(1-\rho_x)), \end{aligned} \tag{8.64}$$

we obtain the solution for the two measurement combinations performed via the ρ_x and ρ_y pair:

$$\begin{aligned} \rho_x = &\left[(1+AB+1-A)+\sqrt{(1+AB+1-A)^2-4(1+AB)(1-A)}\right]\Big/ \\ &\left[2(1+AB)\right];\ \rho_y = (\rho_x B)/\left[1+\rho_x(B-1)\right]. \end{aligned} \tag{8.65}$$

The solution obtained corresponds to the plus sign before the square root; the minus sign gives the trivial 0 and 1 pair of X–Y mirror reflectivities and, hence, such a result is obviously omitted.

Owing to inevitability of interchanging mirrors X and Y for two initial measurements, the reflectance of any opaque reflector Z can be obtained afterward by replacing the second cavity mirror and using one of either mirror X or mirror Y at position X, making only two normal-incidence measurements in the configuration X–Z by tuning the cavity in and out to obtain the reflectance ρ_z via Eq. (8.62). A more effective measurement may be obtained by bending the initially assembled

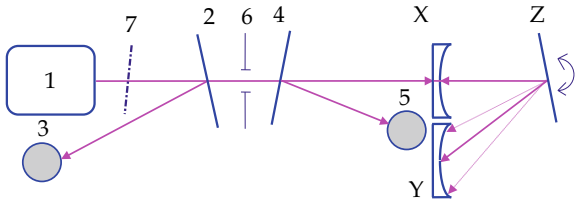

Fig. 8.21 Internal resonator mirror study plus Y-mirror surface scanning

and already known X–Y mirror resonator, as seen earlier in Fig. 8.11. In the bent cavity, the reflectance ρ_z of highly reflecting mirror Z is measured at any fixed angle of incidence, as noted in the previous section, with the reflectance sensitivity of the bent-resonator measurements being twice as high. The bent-resonator settings also allow the spatial examination to be performed over a relatively large mirror Y surface, which may not be necessarily flat, when the added mirror Z is installed on any rotary table (Fig. 8.21).

Measurement Eq. (8.62) with element Z installed inside the cavity is transferred to:

$$\frac{M_\Sigma - M_0}{M_0} = \frac{\rho_y \rho_z^2 (1-\rho_x)^2}{\rho_x (1-\rho_z^2 \rho_x \rho_y)}. \tag{8.66}$$

Obviously relation (8.66) also holds true for any transparent component installed in the cavity with already measured mirror reflectances. Despite the fact that the error of the measurement increases with the number of tests required, the doubled sensitivity to any low loss of the third mirror or a transparent object overcomes that drawback. Another advantage of the method described is associated with the shift of its photometric scale from the point corresponding to 100% reading to 50% mid-scale point for reflectance ρ_x. That effect increases the sensitivity of multiple reflections not only for high reflectivities but also for low reflectivities of test elements. For example, one may see that even at low $\rho_x = \rho_y = 0.1$, the $5 \cdot 10^{-4}$ increase of the reflectivity of any one of these mirrors would extend the detector's photometric reaction by $5 \cdot 10^{-3}$, i.e., by an order of higher magnitude.

Previous considerations for the applicability of this *quality-factor transfer method* were based on the assumption of nonscattering and nonabsorbing substances, such as any thin-film coating layers and substrates for the resonator forming the mirror pair. Let us determine the conditions for accurate measurements of the reflectivity of mirror Z, while allowing for some imperfections in the resonator mirror pair X–Y. Representing the absorptance and scattering factors of mirrors X and Y by a total loss factor α, both formed on substrates of near equal thicknesses, Eqs. (8.62) and (8.63) may be transformed to the identities for new mirror reflectances ρ_x' and ρ_y':

$$K_1 = \frac{\rho_y (1-\rho_x)^2}{\rho_x (1-\rho_x \rho_y)} \equiv \frac{\rho_y' (1-\rho_x'-\alpha)^2}{\rho_x' (1-\rho_x' \rho_y')}; \quad K_2 = \frac{\rho_x (1-\rho_y)^2}{\rho_y (1-\rho_x \rho_y)} \equiv \frac{\rho_x' (1-\rho_y'-\alpha)^2}{\rho_y' (1-\rho_x' \rho_y')}. \tag{8.67}$$

Let us determine the conditions to be maintained to have $\rho_x' = \rho_x - \alpha$ and $\rho_y' = \rho_y - \alpha$. For ρ_x, as for ρ_y:

$$\rho_x' = \rho_x \frac{\rho_y'(1-\rho_y)}{\rho_y(1-\rho_y'-\alpha)} \frac{(1-\rho_x'-\alpha)}{(1-\rho_x)} = \rho_x \frac{(\rho_y-\alpha)(1-\rho_y)(1-\rho_x+\alpha-\alpha)}{\rho_y(1-\rho_y+\alpha-\alpha)(1-\rho_x)}$$
$$= \rho_x - \frac{\rho_x}{\rho_y}\alpha. \tag{8.68}$$

These conditions hold true at $\rho_x' \cong \rho_y'$. Combining the semitransparent but partially absorbing and scattering element X with the high reflector Z, we obtain at $\rho_x' \cong \rho_x - \alpha$, $\rho_z \to 1$, and $\rho_x \cong 0.5$:

$$\frac{\rho_z(1-\rho_x)^2}{\rho_x(1-\rho_x\rho_z)} \equiv \frac{\rho_z'(1-\rho_x'-\alpha)^2}{\rho_x'(1-\rho_x'\rho_z')};$$
$$\rho_z' = \rho_z \frac{\left[\rho_x(1-\rho_x\rho_z') - \rho_z'\alpha^2\right]}{\rho_x(1-\rho_x\rho_z)} = \rho_z(1-2\alpha^2). \tag{8.69}$$

Consequently, application of two nearly semitransparent reflectors for the absolute calibration of the initial resonator reduces the effects of absorption or scattering to one lower order of negligibility.

Completing the analysis of low-loss measurements for the tuning resonator made of highly transparent, semitransparent, or highly reflective objects, one can define the sensitivity of the study as:

$$\frac{\Delta K}{K} = \frac{\Delta\rho_x}{\rho_x} + \frac{\Delta\rho_z}{\rho_z} + 2\frac{\Delta\rho_x}{1-\rho_x} + \frac{\Delta\rho_x\Delta\rho_z}{1-\rho_x\rho_z}. \tag{8.70}$$

The general Eq. (8.70) covers any combinations of optical properties for a semitransparent output coupler X or for highly-reflecting mirror Z measured. With $\rho_x \to \rho_z \to 1$, it transforms to:

$$\Delta K_{HR}/K_{HR} = \Delta\rho_x + \Delta\rho_z + 2\Delta\rho_x/\tau_x + \left(\Delta\rho_x\Delta\rho_z\right)^m, \tag{8.71}$$

where m is the effective number of the resonator's reflections. For the opposite case of $\rho_x \to \rho_z \to 0$:

$$\Delta K_{AR}/K_{AR} = 2\Delta\rho_x + \Delta\rho_x\Delta\rho_z + \Delta\rho_x/\rho_x + \Delta\rho_z/\rho_z. \tag{8.72}$$

Two extrema of the optical properties to be measured are characterized by the highest sensitivity of the technique: in the first case due to a large number of multiple reflections, and in the second due to relatively high intensity conversion via rapid alteration of the reflected radiation emerging from the aligned and the misaligned resonator. For the intermediate case of $\rho_x \cong \rho_y \to 0.5$ and $\rho_z = 1.0 =$ const: $\Delta K/K \to 7\Delta\rho_x$. At $\rho_x \cong 0.5 =$ const and $\rho_z \to 0$: $\Delta K/K = 2\Delta\rho_z$, but at $\rho_x \cong 0.95 =$ const, we have: $\Delta K/K = 21\Delta\rho_z$. Although the rise of sensitivity to

the low optical loss in the highly reflective cavity follows the increase of the effective number of internal reflections, high accuracy of the measurements can be achieved even with the twofold increase of sensitivity. At the same time, for any sensitivity increase, all disturbing factors associated with such an increase which may contribute to measurement noise must remain negligibly low.

As presumed in the analysis, certain measures are taken to prevent changes of the intensity measured for the light components retroreflected inside the resonator due to interference. An essential factor, coincident with the measurements in reflected light, concerns the conceivable suppression of interference phenomena in reflection. As revealed in Chap. 3, the decrease of residual fringe visibility in reflected radiation is directly proportional to the difference of the reflectivities of irradiated resonant mirrors. For a two-mirror resonator with no internal loss: $\tau_{in} = 1$, Eq. (3.126):

$$V_{\rho}\underset{\tau_{in}\equiv 1.0}{=}\frac{2\sqrt{\rho_x\rho_z}(1-\rho_x)(1-\rho_z)}{\rho_x(1-\rho_z)^2+\rho_z(1-\rho_x)^2}, \tag{8.73}$$

indicates that application of any single high reflector with reflectance $\rho_z = 1.0$ in reflected light diminishes the visibility V_ρ of the interference pattern in reflection to zero, independently of the reflectance of another element. Correspondingly, by observing the total intensity of a multiply reflected beam in reflected, instead of transmitted light, one makes all interference phenomena being suppressed altogether without any additional measures and being virtually independent on coherence properties of the source of radiation. As a result, at $\rho_x \cong 0.5$ and $\rho_z = 0.99$ the fringe visibility is reduced to 0.01 and to 0.001 at $\rho_z = 0.999$, even at $\rho_x \cong 0.95$ and $\rho_z = 0.999$ the visibility is less than 0.04. Concurrently, V_τ in all these cases ranges from 0.94 to 0.9997 (see Eq. (3.127)).

8.4.1 Measurements in Tuning Resonators

To verify the capabilities of resonator-tuning method in providing accurate and sensitive measurements not only for highly reflective, but also for semitransparent or even low-reflectivity resonators in reflected light, a custom Nd:glass pulsed laser at $\lambda = 1.053$ μm having an effectively mode-locking resonator was developed. To reduce negative effects of polarization-related fluctuations of the measurement system's transmission (Fig. 8.22), the angles of incidence on beam splitters 2 and 4 as

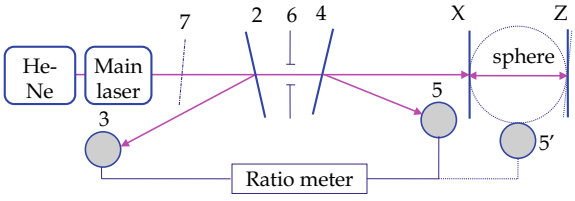

Fig. 8.22 Pulsed-measurement system in tuning resonator

the only elements turned out of the normal to passing beams were less than 2.5–3°. To provide the highest possible isolation of the laser and the resonator being analyzed, both splitters transmitted 25% and reflected 75% of radiation intensity. The total optical density for the two splitters and added optical isolator 7 was near 3.5 (Eq. (1.77)). Alignment of both resonators was made by an auxiliary coaxial He–Ne laser and/or an autocollimator [2.55].

Any change of distance between the two resonator mirrors from 30 to 150 mm did not change the ratio measured. The total energies of pulses reflected by beam splitters 2 and 4 were registered by thermostabilized photodiodes 3 and 5. A five-decade digital ratio meter processed the ratio of signals for main and reference detectors. The photometric accuracy of the entire double-channel measurement system verified by a version of pulsed supplemental-light technique (see Chap. 4) was indistinguishable from the noise-level sensitivity: ±0.05%, of such a supplemental-light method [3.37].

Commonly, the pulse-to-pulse spectral distribution of a pulsed laser emission is not highly reproducible even for steady-state averaged power or energy studies (see Sects. 3.3 and 7.3). Thus, respective resonant measurements in fluctuating radiation are very sensitive to temporal reproducibility of emitted light pulses. Stability in the experiments was achieved by removing spectral-selective elements from the laser resonator, making it mode-locking emission capable. The optimum laser cavity consisted of paired 90 and 100% reflecting mirrors, deposited on plane substrates of fused silica, having AR-coated second surfaces, additionally equipped with apertures selecting the TEM_{00} longitudinal mode. The 2σ repeatability of any single reflectance measurement by that dual-channel system was $2\sigma \leq \pm 0.05\%$.

Characteristic properties of two of the group of resonator mirrors are given in the Table 8.1. The first and second sets of data belong to mirrors made, respectively, by depositing zirconium dioxide and silicon, and titanium and silicon as the quarter-wave layers formed on identical superpolished plane blanks of fused silica. The first row gives reflectance magnitudes obtained by measurements of

Table 8.1 Measured properties

Property	Mirror 1	Mirror 2
$\rho = 1 - \tau_{sph}$	0.995	0.995
τ_{las}	0.0005	0.0005
ρ_r	0.9925	0.9990
σ	0.0060	0.0000_5
$\tau_{las} + \rho + \sigma$	0.9990	0.9995

transmittance: $\rho = 1 - \tau_{sph}$ using a spectrophotometer, and the second row gives results of the direct transmittance measurements τ_{las} obtained by this system. Both series did not distinguish any difference between the two mirrors. Measurements by the quality-factor transfer method performed in X-Y cavity via beforehand-measured mirror X with reflectance $\rho_x = \rho_r = 0.5165 \pm 0.0005$ are given in the third row. Studies of mirrors diffuse scattering σ were made by inserting a 35-mm-diameter integrating sphere between mirrors X and Y of the cavity and relocating detector 5 to the new position 5′ in Fig. 8.22.

To increase the effectiveness of the integrating sphere, the dimensions of its openings were minimized according to the considerations provided in Sects. 2.4 and 4.2. The entire sphere was made from two thin copper sheets, coated by several layers of white $BaSO_4$ diffuser. Since the effectiveness of integration for scattered light by a sphere may be increased by raising the ratio of the area of its internal detector to the area of the sphere itself (see relation (4.35)), the sphere detector and entrance ports were 8-mm-diameter openings, ensuring unblocked propagation of incident and reflected beams. To compensate for the systematic error of absolute measurements for the diffuse reflectance and transmittance, the shifting baffle was made with a commensurate compensating aperture (see Sect. 2.4) approximately 1.2 mm in diameter. The baffle was secured in its two swapping positions to protect the internal sphere detector at position 5′ from light directly scattered by reflecting and by transmitting samples, while detecting the diffuse reflectance or the diffuse transmittance of mirrors X or Y.

All the results obtained in the variable-length tuning resonator were consistent within $\pm(2\text{–}5) \cdot 10^{-4}$ during the test time of several days. Despite that the initial high reflectance of the second mirror in Table 8.1 above made by chemical deposition degraded during the first few days, it eventually stabilized near $\rho_2 \cong 0.9940$. Nevertheless, the first mirror in Table 8.1, chosen as being the best in the thin-film coating run of several samples for its measured reflectance in the 0.9835–0.9925 range, performed very steadily during the entire time span, consistently exhibiting position-tracking reflectance within ± 0.0001. Moreover, only with that mirror was consistent lasing of a custom diode-pumped Nd: YAG microlaser experimentally accomplished. The transmittance properties for additionally measured samples made of plane-parallel fused-silica plates corresponded to the magnitudes calculated by their refractive indices within absolute limits of $\pm(2\text{–}7) \cdot 10^{-4}$ [8.15].

The sequence of measurement results in Table 8.1 demonstrates the continuance of the latter intra-resonator approach to low-loss measurement. According to the routine spectrophotometric study (row 1), the presumably equal transmittance and undistinguishable losses on absorption and scattering were assigned to two selected mirrors out of five in a coating run. A higher direct resolution for local transmittance via a laser beam, increasing the repeatability of measurements to $\pm 0.1\%$, barely distinguished two better mirrors in row 2. The high sensitive resonator-tuning quality-factor conversion method in reflection (row 3) positively identified the best mirror of the study, which was further confirmed by a subsequent lasing experiment. Supplementary studies of scattering factors (row 4) and observed closeness to

unity for every sum of optical properties (row 5) confirmed the high accuracy and high sensitivity for the entire measurement procedure.

8.4.2 *Quality-Factor Transition Between Two Resonator Eigenstates*

Expanding the method of quality-factor conversion for a spectrally broadband resonant cavity, one can envision a few approaches to tuning the cavity on and off its multiple-reflection path: modulating the path length in any desired way, including polarization-sensitive degeneracy for two orthogonal eigenstates in the resonator. Such a method could include a path-deflection modulator to guide cavity-mirror reflection in and out of the normal-incidence path, as in Fig. 8.23, versus tuning the mirror in Fig. 8.20. Otherwise, the resonator-tuning technique remains unchanged for an X-Y mirror cavity or mirror Z. Since intracavity loss would include a dual magnitude of modulator transmittance for modulator M being inside, it could be straightforwardly counted off by cavity calibration prior to inserting high-reflectance mirror Z.

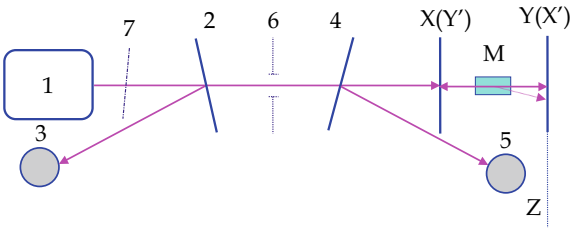

Fig. 8.23 Resonator-based measurement by deflection

For measurements in transmission, quality-factor transition may be accomplished between eigenstates of a cavity, containing a quarter-wave birefringence plate, for studying the residual reflectivity of an AR coating (like in [8.16]). A quarter-wave plate in reflection mitigates among maxima and minima of the resonator's eigenstates, making $\lambda/4+\lambda/4$ phase shift via orthogonal birefringence axes oriented at $\pm 45^\circ$ to the longitudinal cavity axis and the input state of polarization. For the maxima and minima of cavity transmission, or in other words resonance and antiresonance, Eqs. (3.123) for a quarter-wave plate as a Fabry–Perot interferometer are:

$$\frac{I_{\tau\max}}{I_0} = T_{p-r} = \frac{(1-\rho_1)\tau(1-\rho_2)}{\left(1-\tau\sqrt{\rho_1\rho_2}\right)^2} \underset{\substack{\rho_1=\rho_2=\rho_p;\\ \tau=(1-\chi_s)}}{=} \frac{\left(1-\rho_p\right)^2(1-\chi_s)}{\left(1-\rho_p(1-\chi_s)\right)^2};$$

$$\frac{I_{\tau\min}}{I_0} = T_{p-a} = \frac{\left(1-\rho_p\right)^2(1-\chi_s)}{\left(1+\rho_p(1-\chi_s)\right)^2}, \tag{8.74}$$

where ρ_p is the reflectivity of each plate's surface, presumed identical and χ_s is the plate's substrate total scattering and absorption loss. For a transparent substrate: $\chi \to 0$, and for plate's surfaces being AR-coated with low residual reflectivity: $\rho_p^2 \to 0$, and Eqs. (8.74) for plate's transmittance T_{p-r} and T_{p-a} become:

$$T_{p-r} = \frac{(1-\rho_p)^2(1-\chi_s)}{(1+\rho_p(1-\chi_s))^2}\frac{(1+\rho_p(1-\chi_s))^2}{(1-\rho_p(1-\chi_s))^2} \underset{\chi_s\to 0}{\cong} T_{p-a}\left(\frac{1+\rho_p}{1-\rho_p}\right)^2$$
$$\underset{\rho^2\to 0}{\cong} T_{p-a}(1+4\rho_p); \quad T_{p-a} \underset{\substack{\rho^2=0;\\ \chi_s=0}}{=} T_{p-r}(1-4\rho_p). \tag{8.75}$$

If an AR-coated quarter-wave plate is inside the cavity and the plate's rotations allow the cavity state to be transferred into resonant and antiresonant modes, the ratio K of respective resonator transmittances is:

$$K \equiv \frac{T_{c-r}}{T_{c-a}} = \frac{(1-\rho_c)^2 T_{p-r}}{(1-\rho_c T_{p-r})^2}\cdot\frac{(1-\rho_c T_{p-a})^2}{(1-\rho_c)^2 T_{p-a}} = \frac{T_{p-r}}{T_{p-a}}\cdot\left(\frac{1-\rho_c T_{p-a}}{1-\rho_c T_{p-r}}\right)^2$$
$$= (1+4\rho_p)\left(1+\frac{4\rho_c\rho_p}{1-\rho_c T_{p-r}}\right)^2. \tag{8.76}$$

Considering Eq. (8.20) for the resonant cavity finesse, and assuming the quarter-wave plate's transmittance in the resonant state as unity, we can rewrite Eq. (8.76) via cavity finesse parameter F_r (see Eqs. (3.119) to (3.125) and (7.65) to (7.68)):

$$K = \frac{(1+4\rho_p)}{T_{p-r}}\left(T_{p-r}+\frac{4(\rho_c T_{p-r})\rho_p}{1-\rho_c T_{p-r}}\right)^2$$
$$= \frac{(1+4\rho_p)}{T_{p-r}}\left(T_{p-r}+\frac{4F_r\rho_p}{\pi}\right)^2 \underset{T_{p-r}=1}{\cong}(1+4\rho_p)\left(1+\frac{4F_r\rho_p}{\pi}\right)^2. \tag{8.77}$$

Equation (8.77) encourages increasing the resonator's finesse to improve the sensitivity of measurements to residual surface reflectance ρ_p, which, in turn, decreases the resonator's effectiveness when $\rho_p \neq 0$. Owing to quadratic dependence of the intensity ratio K on the residual reflectivity ρ_p, a solution should be sought similarly to Eqs. (8.62) and (8.63) via distinguishing the reflectivities of the first face and second face of the plate and making two series of measurements swapping the positions of the plate surfaces. On another hand, using the approximation of $\sqrt{(1+4\rho_p)} \to 1$ allows one to obtain a linear solution with the systematic error $\pm 2\sqrt{\rho_p}$ simplifying the measurement procedure [8.16]:

$$\rho_p \underset{2\sqrt{\rho_p}\to 0}{\cong} (\pi/(4F_r))\left(\sqrt{K}-1\right). \tag{8.78}$$

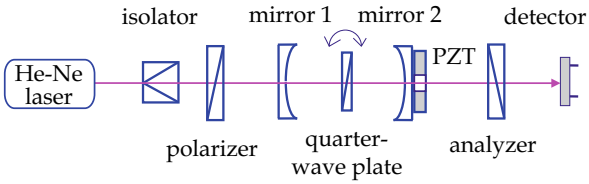

Fig. 8.24 Resonant and anti-resonant cavity studies

Figure 8.24 shows an experimental system for two eigenstate-based measurements in a high-finesse cavity [8.16]. Single-frequency He–Ne laser light is coupled into a Fabry–Perot scanning interferometer via a polarizer–analyzer pair. One cavity mirror placed on a PZT made a low-frequency scan with interferometer's free spectral range being set at $c/2\ell$ but the quarter-wave plate added two nondegenerated orthogonal eigenstates frequency-spaced at $c/4\ell$. Tilting of the wave plate to the ordinary and extraordinary cavity axes positioned $\pm 45°$ to the input-light state of polarization caused the cavity to be switched on and off between resonant and antiresonant states. To compensate for errors of $\pm 45°$ orientation of the wave-plate's axes, two series of measurements were always performed by rotating the plate twice around its crystalline axis and having $K = \sqrt{(K_1 \cdot K_2)}$. At a cavity finesse of approximately 100, the measurement sensitivity was approximately 100 ppm [8.16], though owing to the systematic error $\pm 2\sqrt{\rho}$ of obtaining the results by inexact Eq. (8.78) being of the order of the measured residual reflectance, making multiple averages may have not produced any sensitivity increase.

8.4.3 *Nonresonant, Off-Axis Techniques*

Similarly to suppressing the interference phenomena by making resonator measurements in reflected light and removing superposition of radiation by spreading the multiple reflections in space or time, both ring-down and cavity-decay studies reviewed in Sects. 7.3 and 8.3 could benefit from setting the cavity off its sharpest on-axis resonance [8.30, 8.44] into an expanded-length propagation pass any off-axis irradiation system (Sect. 6.3). Off-axis irradiation provides spatial separations of multiple reflections on each consecutive path, until a reentrant coordinate is reached (see Fig. 6.8), except for the entrance of radiation into the Fabry–Perot cavity like one illustrated in Fig. 8.24. Each beam-spot rotation is defined by the cavity geometry: $\cos\varphi = 1 - d/R$ (see Eq. (6.17)), and on a number N of single cavity passes: $2N\varphi = 2\kappa\pi$, $\kappa = 1, 2, 3 \ldots$ (Eq. (6.19)), the beam reenters its path. For a spherical-mirror cavity of radiuses R_1 and R_2 and mirror spacing d, the cavity path is stable at $0 < (1 - R_1)(1 - R_2) < 1$. Depending on the polar angle φ of entering light, a reentrance may occur after many reflection cycles, effectively making the cavity N times longer and thus decreasing its free spectral range ($\Delta\lambda$), which defines the separation $\Delta\lambda$ between the adjacent interference maxima: $\Delta\lambda = \lambda_i - \lambda_j$.

As for other ring-down measurements (see Sects. 7.3 and 8.3), the time-rate equation for the power decay of cw radiation coupled into a cavity of two identical

mirrors with reflectance ρ and transmittance τ and travelling in each propagation direction owing to intracavity multiple reflections is [7.26, 8.30, 8.31]:

$$\mathrm{d}I/\mathrm{d}t = (c/2\ell)\big(C_{mnq}\tau I_0 - 2I(1-\rho)\big). \tag{8.79}$$

Here C_{mnq} is the coupling factor, I_0 and I are the incident and the intracavity power of radiation, and the factor of 2 accounts for radiation leaving the cavity via both mirrors but entering via just one. For lossless cavity mirrors: $\tau + \rho = 1$, and a stable light source, the empty-cavity solution is:

$$I_e = \big(C_{mnq}I_0/2\big)(1 - \exp(-t/t_c)), \tag{8.80}$$

with a steady-state solution reached at $I_{left} = I_{right} = I_0C_{mnq}/2$. Here t_c is the ring-up or ringdown constant: $t_{c,e} = \ell/(c(1-\rho))$. If the cavity is filled with a gaseous substance of frequency-dependent absorptance α(ν): $t_{c,\alpha} = \ell/(c((1-\rho)+\alpha(\nu)\ell))$, the effective reflectance of each cavity mirror becomes: $\rho_\alpha = \rho\,\exp(-\alpha(\nu)\ell)$, and instead of using the decay ratio: $\alpha(\nu) = \big(1/\tau_{c,\alpha} - 1/\tau_{c,e}\big)/c$, one can express the relative intensity changes: ΔI/I, for the steady-state cavity radiation output as [8.30]:

$$\begin{aligned}(I_\alpha - I_e)/I_e = (1 - \exp(-\alpha(\nu)\ell)) \cdot (\rho/(1-\rho))/(1 + (1 - \exp(-\alpha(\nu)\ell))\\ \cdot (\rho/(1-\rho)) \equiv G \cdot A/(1 + G \cdot A)),\end{aligned} \tag{8.81}$$

with new designations: $A = 1 - \exp(-\alpha(\nu)\ell)$ and $G = \rho/(1-\rho)$, where factor $G \approx \tau_c c/\ell \approx F/\pi$ defines the cavity multiple-reflection gain.

Opposite to either single-mode or multimode ring-down study, multipath propagation and subsequent reduction of the cavity free spectral range to be narrower than the source bandwidth makes the fringe contrast ratio approach 1.0 independently of the wavelength of laser emission, not requiring single-mode resonances to occur. Owing to multipath propagation, a 0.5-m-long cavity with approximately 300 MHz free spectral range effectively becomes a 6-MHz cavity via a path increased by 50 round trips (Fig. 8.25). Each cavity mirror may be also

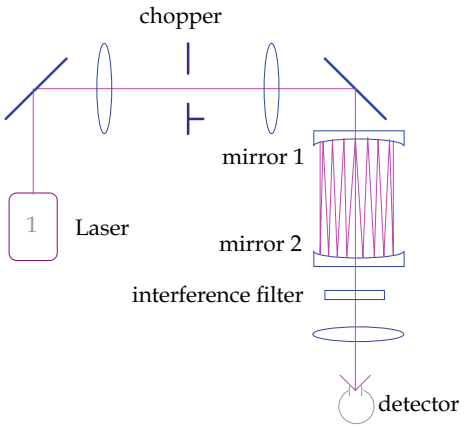

Fig. 8.25 Off-axis ringdown cavity measurements

astigmatized (see Sect. 6.3), forcing Lissajous patterns of precessing light spots on every mirror, further increasing the cavity optical path [8.30]. In the experiments, identical 6-m-radius, 1-in.-diameter mirrors were spaced 67-cm apart forming the cavity and while astigmatized it held 400 passes with 500-kHz effective free spectral range. An external-cavity 630-nm diode laser source tuned at 2 cm^{-1}/s was coupled into the cavity, scanning one free spectral range per cavity ring-down time, suppressing resonant energy storage in the cavity and stabilizing cavity output. The chopper at the focal point of two telescope lenses modulated incident light with 50% duty cycle and 3-kHz repetition rate, setting a 0.5-μs shut-off time for ring-down measurements. Despite a relatively high cavity loss: $m \cdot (1 - \rho)/2$, over every m-reflection reentrance, the rms noise-level absorption sensitivity of ring-down measurements averaged over 100 sweeps reached $1.5 \cdot 10^{-9}$ cm^{-1} $Hz^{-1/2}$ for the cavity build-up time defined by the chopper 3 kHz frequency. Alternative integrated-cavity output measurements were provided via laser tuning at over a 2-cm^{-1} frequency interval for the effective 200 MHz frequency resolution integrating many times over the free spectral range with $\sim 1 \cdot 10^{-7}$ per-pass noise and reaching $\sim 2 \cdot 10^{-10}$ cm^{-1} $Hz^{-1/2}$ noise-level sensitivity at 100 sweeps [8.30].

8.4.4 *Resonant Asymmetric-Cavity Techniques*

The quality-factor transfer method, opening this paragraph, was developed to suppress interference in reflected light, allowing any mirror of the asymmetric two-mirror cavity under test to be measured in nonresonant settings for broadband radiation, such as pulsed laser light. In laser resonator applications of microresonant cavities in which maxima for any resonant wavelength are definitively distinguished in either transmitted or reflected light, a close-to-1.0 mirror reflectance must be achieved for the laser generation [II.1, II.8, II.11, II.28]. If an asymmetric mirror cavity is viewed in reflected light, a reflectance of each mirror in nonresonant settings can be identified via Eqs. (8.61)–(8.66). In resonant settings, Eqs. (3.120) and (3.123) define the maximum and the minimum intensities in reflection and transmission for a resonant mirror cavity of reflectivities ρ_1 and ρ_2 separated by transmittance τ.

If the mirrors of reflectance ρ_1 and ρ_2, transmittance τ_1 and τ_2, and scattering-plus-absorption losses μ_1 and μ_2 are separated in clean air or a vacuum, the optical properties of every mirror in the asymmetric two-mirror cavity can be identified via opposite irradiation directions as illustrated in Fig. 8.26. Owing to asymmetry, cavity reflectivity changes on left–right irradiation, but not transmission. Following Eq. (3.119), the left $E_{\rho 12}$ and right $E_{\rho 21}$ wave amplitudes in reflection are:

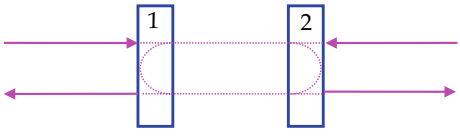

Fig. 8.26 Asymmetric cavity left-right irradiation

$$E_{\rho 12} = E_0 \frac{\rho_{1a} + \rho_{1a}^2 \rho'_{2a} e^{i\delta} + \tau_{1a}\tau'_{1a}\rho'_{2a} e^{i\delta}}{1 - \rho'_{1a}\rho'_{2a} e^{i\delta}} = E_0 \frac{\rho_{1a} - \rho_{2a}(\rho_{1a}^2 + \tau_{1a}^2) e^{i\delta}}{1 - \rho_{1a}\rho_{2a} e^{i\delta}}$$

$$= E_0 \frac{\rho_{1a} - \rho_{2a}(1 - \mu_{1a}) e^{i\delta}}{1 - \rho_{1a}\rho_{2a} e^{i\delta}}; \tag{8.82a}$$

$$E_{\rho 21} = E_0 \frac{\rho_{2a} + \rho_{2a}^2 \rho'_{1a} e^{i\delta} + \tau_{2a}\tau' 2_{1a}\rho'_{1a} e^{i\delta}}{1 - \rho'_{2a}\rho'_{1a} e^{i\delta}} = E_0 \frac{\rho_{2a} - \rho_{1a}(\rho_{2a}^2 + \tau_{2a}^2) e^{i\delta}}{1 - \rho_{2a}\rho_{1a} e^{i\delta}}$$

$$= E_0 \frac{\rho_{2a} - \rho_{1a}(1 - \mu_{2a}) e^{i\delta}}{1 - \rho_{1a}\rho_{2a} e^{i\delta}}. \tag{8.82b}$$

Transformations invoke the law of conservation of energy for each mirror: $\rho_i + \tau_i + \mu_i = 1$. When amplitudes are converged to intensities (see Sect. 3.3), and since the cavity transmission is insensitive to the direction of irradiation, Eqs. (8.82a, b) and (3.122) become, respectively:

$$I_{\rho,ij} = E_\rho E_\rho{}^* = I_0 \frac{\left(\sqrt{\rho_i} - (1 - \mu_i)\sqrt{\rho_j}\right)^2 + 4\sqrt{\rho_i \rho_j}\sin^2(\delta/2)}{\left(1 - \sqrt{\rho_i \rho_j}\right)^2 + 4\sqrt{\rho_i \rho_j}\sin^2(\delta/2)}; \tag{8.83}$$

$$I_{\tau,ij} = E_\tau E_\tau{}^* = I_0(1 - \rho_i - \mu_i)(1 - \rho_j - \mu_j)/$$
$$\left(\left(1 - \sqrt{\rho_i \rho_i}\right)^2 + 4\sqrt{\rho_i \rho_i}\sin^2(\delta/2)\right). \tag{8.84}$$

When the asymmetric cavity is studied via stable irradiation, allowing for observation of the steady-state maxima and minima of interference, Eqs. (8.83) and (8.84) are converted to:

$$I_{\rho\,\max,ij} = I_0 \left(\frac{\sqrt{\rho_i} + (1 - \mu_i)\sqrt{\rho_j}}{1 + \sqrt{\rho_i \rho_j}}\right)^2. \quad I_{\rho\,\min,ij} = I_0 \left(\frac{\sqrt{\rho_i} - (1 - \mu_i)\sqrt{\rho_j}}{1 - \sqrt{\rho_i \rho_j}}\right)^2. \tag{8.85}$$

$$I_{\tau\,\max,ij} = I_0 \frac{(1 - \rho_i - \mu_i)(1 - \rho_j - \mu_j)}{\left(1 - \sqrt{\rho_i \rho_j}\right)^2}. \quad I_{\tau\,\min,ij} = I_0 \frac{(1 - \rho_i - \mu_i)(1 - \rho_j - \mu_j)}{\left(1 + \sqrt{\rho_i \rho_j}\right)^2}. \tag{8.86}$$

Figure 8.27 illustrates the tendencies of the maxima and minima for the two complementary interference patterns in transmission and reflection: $I_{\rho max}$ corresponding to $I_{\tau min}$, and vice versa. The intensity changes are plotted versus reflectance rising from 0.01 to 1.00 in 0.01 steps. Since these interference patterns are supplemental to each other owing to redistribution and losses of incident radiation: $I_0 = I_\rho + I_\tau + I_\mu$, ratios $I_{\rho max}/I_{\tau min}$ and $I_{\rho min}/I_{\tau max}$ can be measured simultaneously:

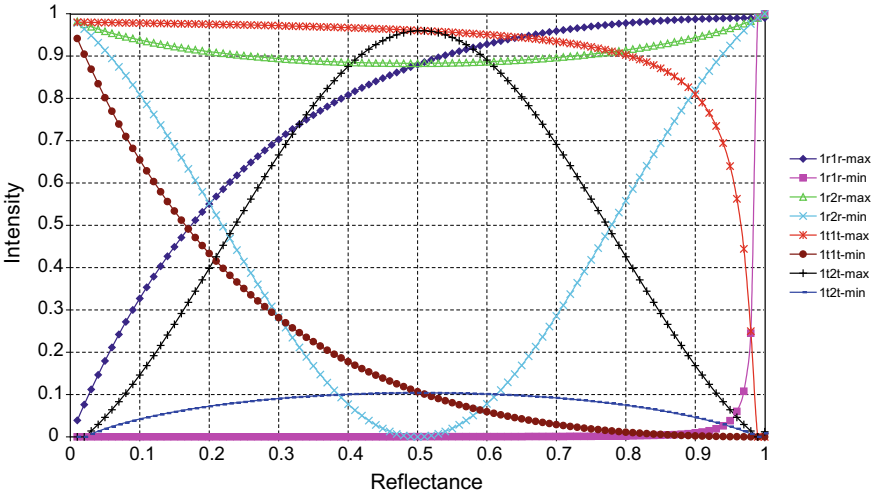

Fig. 8.27 Maxima and minima of reflectance and transmittance for asymmetric resonant cavity: *r* stands for reflectance, *t* stands for transmittance; *11* – equal mirror reflectances from 0 to 1; *12* – first mirror reflectance from 0 to 1, second from 1 to 0

$$\frac{I_{\rho\max,ij}}{I_{\tau\min,ij}} = \frac{\left(\sqrt{\rho_i} + (1-\mu_i)\sqrt{\rho_j}\right)^2}{(1-\rho_i-\mu_i)(1-\rho_j-\mu_j)}. \quad \frac{I_{\rho\min,ij}}{I_{\tau\max,ij}} = \frac{\left(\sqrt{\rho_i} - (1-\mu_i)\sqrt{\rho_j}\right)^2}{(1-\rho_i-\mu_i)(1-\rho_j-\mu_j)}. \tag{8.87}$$

Ratios $(I_{\rho\,max}/I_{\rho\,min})_{12}$ and $(I_{\rho\,max}/I_{\rho\,min})_{21}$ can be measured by cavity retuning to the maximum and the minimum:

$$\frac{I_{\rho\max,12}}{I_{\rho\min,12}} = \left(\frac{\sqrt{\rho_1} + (1-\mu_1)\sqrt{\rho_2}}{\sqrt{\rho_1} - (1-\mu_1)\sqrt{\rho_2}}\right)^2 \left(\frac{1-\sqrt{\rho_1\rho_2}}{1+\sqrt{\rho_1\rho_2}}\right)^2.$$
$$\frac{I_{\rho\max,21}}{I_{\rho\min,21}} = \left(\frac{\sqrt{\rho_2} + (1-\mu_2)\sqrt{\rho_1}}{\sqrt{\rho_2} - (1-\mu_2)\sqrt{\rho_1}}\right)^2 \left(\frac{1-\sqrt{\rho_1\rho_2}}{1+\sqrt{\rho_1\rho_2}}\right)^2. \tag{8.88}$$

Measurements in transmission of the $I_{\tau\,max}/I_{\tau\,min}$ ratio from either direction allow the reflectance product $\rho_1\rho_2$ to be determined:

$$I_{\tau\max,12}/I_{\tau\min,12} = \left(\left(1+\sqrt{\rho_1\rho_2}\right)/\left(1-\sqrt{\rho_1\rho_2}\right)\right)^2. \tag{8.89}$$

Figure 8.28 illustrates the dependencies of the ratios computed according to Eqs. (8.87)–(8.89) for the settings of Fig. 8.27.

Equations (8.87) for the i, j sequence surely converge to the mirrored equations for the j, i sequence. To determine all unknown mirror parameters of a cavity: ρ_1, μ_1 and ρ_2, μ_2 or ρ_1, τ_1 and ρ_2, τ_2, four independent measurement equations need to be obtained. Such a measurement cycle can be performed via combination measurements of reflected and transmitted intensity maxima and minima versus the input

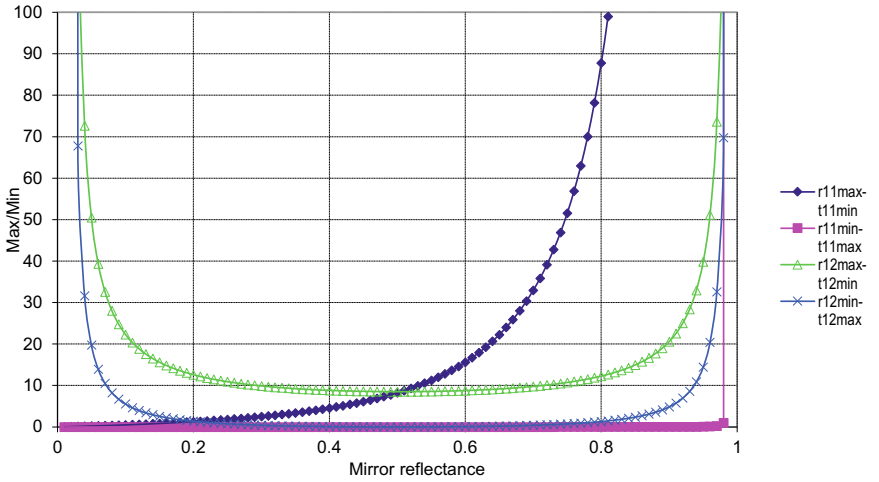

Fig. 8.28 Maximum/minimum and minimum/maximum reflectance/transmittance ratios (percentage): r11, t11-mirror reflectances from 0 to 1, transmittances from 1 to 0; r12, t12-first mirror reflectance from 0 to 1, second mirror reflectance from 1 to 0

intensity of a mirror pair via opposite directions. Since for a cavity having at least one highly reflective mirror either the reflection or the transmission minima are practically indistinguishable from the incident radiation or measurement noise (see curves *1r1r*-min and *1t1t*-min in Fig. 8.27), these measurements are the most difficult to perform versus the reflection minimum and the transmission maximum (curves *1r1r*-max and *1t1t*-max or *1r2r*-max and *1t2t*-max):

$$\frac{I_{\rho\,\max,12}}{I_{\tau\,\min,12}} = \frac{\rho_1 + 2(1-\mu_1)\sqrt{\rho_1\rho_2} + \rho_2}{(1-\rho_1-\mu_1)(1-\rho_2-\mu_2)}; \tag{8.90}$$

$$\frac{I_{\rho\,\min,12}}{I_{\tau\,\max,12}} = \frac{\rho_1 - 2(1-\mu_1)\sqrt{\rho_1\rho_2} + \rho_2}{(1-\rho_1-\mu_1)(1-\rho_2-\mu_2)}; \tag{8.91}$$

$$\frac{I_{\rho\,\max,21}}{I_{\tau\,\min,21}} = \frac{\rho_2 + 2(1-\mu_2)\sqrt{\rho_1\rho_2} + \rho_1}{(1-\rho_1-\mu_1)(1-\rho_2-\mu_2)}; \tag{8.92}$$

$$\frac{I_{\rho\,\min,21}}{I_{\tau\,\max,21}} = \frac{\rho_2 - 2(1-\mu_2)\sqrt{\rho_1\rho_2} + \rho_1}{(1-\rho_1-\mu_1)(1-\rho_2-\mu_2)}. \tag{8.93}$$

If only reflected or only transmitted light is accessible, the ratios of the intensity maxima to the intensity minima in reflection resolve two mirror reflectivities via Eqs. (8.88), but three pairs of mirrors: 12, 13, and 23, via Eqs. (8.89) need to be measured in transmitted light:

$$\frac{I_{\tau\max,12}}{I_{\tau\min,12}} = \left(\frac{1+\sqrt{\rho_1\rho_2}}{1-\sqrt{\rho_1\rho_2}}\right)^2; \quad \frac{I_{\tau\max,13}}{I_{\tau\min,13}} = \left(\frac{1+\sqrt{\rho_1\rho_3}}{1-\sqrt{\rho_1\rho_3}}\right)^2;$$
$$\frac{I_{\tau\max,23}}{I_{\tau\min,23}} = \left(\frac{1+\sqrt{\rho_2\rho_3}}{1-\sqrt{\rho_2\rho_3}}\right)^2. \tag{8.94}$$

Adding to the challenges of measurements via interference extrema, a single TEM_{00} mode cavity coupling requires to remove all high-order modes, which could make the cavity look "lossless" necessitating parallel cavity-finesse measurements to confirm reaching the extrema [8.34–8.37]. Other techniques, such as a quantitative assessment of the main cavity coupling to unavoidable etalons of the system components, effectively enhancing the cavity finesse, or utilizing a differential multiple-frequency shifting process [7.64] could also be deployed (see Sect. 7.4 for more details).

Figure 8.29 depicts an asymmetric-cavity measurement setup for the reflection-minima plus transmission-maxima studies in opposite directions [8.37]. Reflectance and transmittance values for the resonant cavity were calculated while approximating full Eqs. (8.85)–(8.93) by truncated expressions for left and right propagation: $\left((\sqrt{\rho_1}-\sqrt{\rho_2}+\tau_1\sqrt{\rho_2})/(1-\sqrt{\rho_1\rho_2})\right)^2_{left}$; $\left((\sqrt{\rho_2}-\sqrt{\rho_1}+\tau_2\sqrt{\rho_1})/(1-\sqrt{\rho_1\rho_2})\right)^2_{right}$. Coupling linearly polarized 852-nm light to a 43.9-μm-spaced 10-cm-radius supermirror cavity was done via polarizing beam splitter 1, half-wave plate 2, polarization rotator 3, and objective 4. By measuring mode matching aspects from opposite directions of light propagation and converting the measured asymmetric cavity losses while making corrections for ideal mode-matching of the cavity, the estimated factors were $\rho_1 = 0.9999619$, $\tau_1 = 5.0$ ppm, $\mu_1 = 33.2$ ppm, $\rho_2 = 0.9999501$, $\tau_2 = 4.5$ ppm, and $\mu_2 = 45.4$ ppm [8.37]. Similar cavity-decay measurements in extremely small volumes at relatively long effective-absorption pathlengths could be made in whispering-gallery mode microresonators tuned in and out of resonance by stretching [8.39].

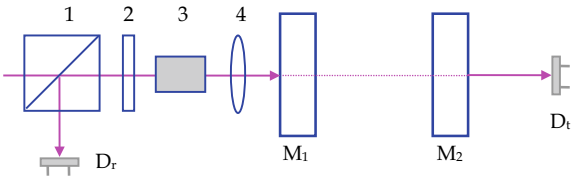

Fig. 8.29 Polarization coupling for a resonant cavity

8.5 Evaluation of Loss Dichroism and Phase Dispersion

The already reviewed examples of sensitivity expansion for an intracavity study to the phase status of multiply reflected light not only allows one to resolve the reflectivity difference of resonant mirrors, but even to distinguish the phase

dispersion and phase retardance of radiation in a cavity. Such a feature is increasingly valuable for evaluation of homogeneity and spectral performance of multilayer laser mirrors, since reflection of light even by a border of two perfect dielectrics is an anisotropic process (see Eqs. (1.34), (1.35), (1.82) and (1.83)). If radiation interacts with a mirror made as a stack of quarter-wave or other phase layers of low and high refractive indices, the phase shift δ between orthogonally polarized components increases linearly with the light wavelength and its angle of incidence. It also depends on the particular thickness of every layer.

If a linear full-wave or half-wave retarder such as a crystal/polymer wave plate is inserted into a highly reflective resonator and is observed in reflection, its phase retardance on the double pass is a multiple of π, thus not making a distinguishable phase effect. The quarter-wave plate, introducing a λ/4 and π/2 phase shift in transmission and in reflection, produces a very noticeable phase change for design wavelength λ. A quarter-wave plate in a resonator aligned to the maximum in one polarization eigenstate and the minimum in another becomes a low-reflectivity Fabry–Perot interferometer or etalon of surface reflections $\rho_s \approx \rho_p \approx \rho$. For a transparent plate with $\tau_{int} = 1$, the absolute intensity maximum in reflected light and the maximum to minimum relative intensity ratio in transmitted light are (due to relations (3.124, 3.125)):

$$I_{\rho\max}/I_0 = 4\rho/(1+\rho)^2; \tag{8.95a}$$

$$I_{\tau\max}/I_{\tau\min} = (1+\rho)^2/(1-\rho)^2. \tag{8.95b}$$

By making measurements of either the absolute maximum intensity in reflection or the relative maximum-to-minimum intensity ratio in transmission, we can resolve the residual surface reflectivity ρ (see preceding Sect. 8.4 for more details):

$$I_{\rho\max}/I_0 \underset{\rho^2\to 0}{\cong} 4\rho/(1+2\rho) \underset{\rho\to 0}{\cong} 4\rho; \tag{8.96a}$$

$$I_{\tau\max}/I_{\tau\min} \underset{\rho^2\to 0}{\cong} (1+2\rho)/(1-2\rho) \underset{\rho\to 0}{\cong} 1+4\rho. \tag{8.96b}$$

From relations (3.125), the maximum–minimum intensity difference in transmitted versus incident light is:

$$(I_{\tau\max} - I_{\tau\min})/I_0 = 1 - (1-\rho)^2/(1+\rho)^2 = 4\rho/(1+\rho)^2. \tag{8.97}$$

The relative maximum and minimum intensity difference in transmission defines the indirect plate dichroism ΔT in two resonant states and for incident light intensity $I_0 = 1$ can be approximated as:

$$\begin{aligned}\Delta T &= T_r - T_a = I_{\max} - I_{\min} \\ &= I_0\left(1 - (1-\rho)^2/(1+\rho)^2\right) \underset{I_0=1.0}{=} 4\rho/(1+\rho)^2 \underset{\rho\to 0}{\approx} 4\rho.\end{aligned} \tag{8.98}$$

Considering the interdependence of the quarter-wave plate's dichroism on its residual surface reflectivity, one can measure parameters of resonant-cavity decay [8.27] using Eqs. (8.98) and (8.53) as:

$$Loss_r = (1 - \rho_c T_r) \cong \ell/\left(c\tau_{c,r}\right); \quad Loss_a = (1 - \rho_c T_a) \cong \ell/\left(c\tau_{c,a}\right), \tag{8.99}$$

where T_r and T_a are the wave-plate resonant and antiresonant transmittance (see Sect. 8.4) and ρ_c is the mirror reflectivity for the cavity decay. Making cavity ringdown measurements of extreme decay times for a quarter-wave plate in the cavity (see Sects. 7.3 and 8.3), the plate dichroism is:

$$\Delta T \approx 4\rho \cong [\ell/(c)]\left(\tau_{c,r}^{-1} - \tau_{c,a}^{-1}\right) = [\ell/(c)]\left(\tau_{c,S}^{-1} - \tau_{c,P}^{-1}\right). \tag{8.100}$$

The cavity layout for decay-time ringdown dichroism studies is similar to that seen in Fig. 8.24, where resonant and antiresonant directions are aligned along birefringent S and P axes of the quarter-wave plate in a ringdown cavity. In the experimental arrangement [8.27], a 632.8-nm AR-coated quarter-wave multiple-order plate was set in a Fox–Smith interferometer. Low-frequency 10-Hz scan was used for acquisition of data with continuous control of the mode-matching status of the cavity with a monomode He–Ne laser. The decay times measured by averages of 30 readings were 0.83 and 0.36 μs, leading to 1.08% and 2.48% S-P cavity loss, and to 1.40% dichroism. While nearly identical 1.39% dichroism was registered in an active-laser cavity in atomic system studies [8.27], the measurement sensitivity could have been limited by the approximations of converting the exact Eq. (8.97) to lesser accurate expressions (8.88), (8.99).

By further advancing pulsed or decay-time approaches to the intracavity loss measurement (see earlier paragraphs and Eqs. (8.8), (8.53)–(8.57)), a low loss in a resonant cell of highly reflecting mirrors in two eigenstates, and respective dichroism, can be detected via integrated output intensities of light at time delays t_s and t_p after an incident polarized pulse has entered the resonator:

$$I(t) = I_0\left(\rho_1\rho_2\rho^2\right)^{t/\delta_0} \cong I_0 \exp\left[-\frac{(\chi_1 + \chi_2 + 2\chi)}{\delta_0}t\right]. \tag{8.101}$$

Here $\delta_0 = 2\ell/c$ is the phase shift (phase retardance) for the round trip in the cavity of length ℓ in a vacuum and ρ_1, χ_1 and ρ_2, χ_2 are the reflectances and losses of the first and second cavity mirrors. The third mirror of reflectivity ρ and loss χ is inserted at incidence angle Θ as in Figs. 8.11 and 8.21. By making two sequential ringdown measurements of τ_e for s and p polarization in empty cavity: $\tau_e = \delta/(\chi_1 + \chi_2 + 2\chi)$, linear dichroism χ_Σ of the inserted third mirror is determined as: $\chi_\Sigma = \chi_s + \chi_p$.

If incident-light polarization makes a 45° angle with the orthogonal directions of a phase-birefringent resonator, this results in two equivalent projections, thus providing a differential evaluation of the phase retardance examined. When analyzing an output beam via any linear polarizer placed at ±45° to s and p polarization, its intermediate intensity I(t) after the delay time t is [8.17]:

$$I(t) = (I_0/4)\{\exp(-t/\tau_p) + \exp(-t/\tau_p) \pm 2\exp[-(1/\tau_p + 1/\tau_s)t/2]\cos(\delta t/\delta_0)\}. \quad (8.102)$$

Equation (8.102) emphasizes the output intensity oscillations between two exponential decays of the orthogonal birefringent directions. The time interval of oscillations is identified by the phase retardance of the internal cavity enclosure. If there is no retardance, all oscillations should be completely restrained. The threshold of observation for such a restrain is identified by at least a half period of the oscillation that could be observed at retardance: $|\delta| \geq \pi\delta_0/\tau_i = \pi(\chi_1 + \chi_2 + 2\chi)$, where τ_i is the decay for the vibration direction with the lowest total loss, either χ_s or χ_p. A loss of about 500 ppm corresponds to the detection limit of the retardance being studied: $|\delta| \geq 0.2°$. The higher is the loss, the lower is the sensitivity of the ringdown decay-time measurement (see Eq. (8.56)). In experiments with a tunable pulsed dye laser pumped by a 10-ns nitrogen laser, oscillations were clearly absent, allowing measurements of the linear phase retardance of the mirrors tested at $\lambda = 629.1$ nm with a precision of $\pm 0.05°$ with angular sensitivity limits for the phase retardance better than 0.1° [8.17].

8.5.1 Recognition of Phase Dispersion

For all the measurements considered earlier, either the high reflectance or the high transmittance of a single element or a pair of elements was considered from the standpoint of the best performance in a resonant cavity made of these elements. At the same time, when building an exceptionally short pulse laser, such as a femtosecond or an attosecond one, a relevantly flattened wavelength dispersion of the laser cavity is essential. Accordingly, a sensitive measurement of the phase dispersion created by a specific laser element serves as an increasingly valuable tool for evaluation of any mutual compatibility of all individual resonant elements when assembling a laser cavity.

Consider a quasi-monochromatic wave group having a medium frequency ω_0 transmitted via an optical element causing group delay $\tau_g(\omega_0)$. The phase shift produced by that action is: $\exp[-i\omega_0\tau_g(\omega_0)]$. The wavelength dependence of the optical group delay may be distinguished by any spectrally sensitive phase measurement. An interferometer sensitive to the change of the optical path length can be created from any reflective element and the element under test. The entire cavity to be studied can also be used for the phase-sensitive arrangement. A Michelson interferometer with an element inserted into its sample arm is an example of an instrument for a test [8.19]. The Fourier transform of the electric field transmitted by the sample and reference arms of the interferometer as a product of their complex transmittances is: $S_\tau(\omega) = T_s(\omega)\,T_{s,0}\,(\omega)\,T^*_{ref}\,(\omega)\,U(\omega)$ [8.20]. Here $T_s(\omega)$, $T_{s,0}(\omega)$, and $T^*_{ref}(\omega)$ are complex transmittances of the sample arm, of the empty sample arm, and of the reference arm for the dual pass via the cavity, and U is the power spectrum. The phase of that transform: $\varphi(\omega) = \varphi_s(\omega) + \varphi_{bias}(\omega) - \omega\tau_0$, is determined by the phase shift $\varphi_s(\omega)$ caused by the element, in contrast to a

specific interferometer bias, $\varphi_{bias}(\omega)$, which causes an imbalance between $T_{s,0}(\omega)$ and $T_{ref}(\omega)$. The term τ_0 identifies, in this case, the uncertainty for the zero-delay settings of the interferometer used. As a result, the entire group delay is:

$$\tau_g(\omega) = d\varphi(\omega)/d\omega - \tau_{bias}(\omega) + \tau_0. \tag{8.103}$$

Figure 8.30 depicts a simplified structure of the phase- and intensity-compensating white-light Michelson interferometer [8.19]. A collimated beam with less than 1° divergence from the white-light source S propagates via two beam splitters (main beam splitter 1 and compensating beam splitter 2) into optically equalized sample and reference arms. Interference filter IF tunable within 10–15-nm bandwidth selects light in spectrally recombined sample and reference beams. To have white-light fringes for a few desired femtoseconds of temporal resolution, splitters were made as identical INCONEL-metal-coated glass plates step-coated in optical-density gradations of 0.1. Each optical scan of the interferometer was made via precise motion of the reference-arm mirror in 45-nm steps, providing 0.3-fs time extension. The relative group delay for each frequency was defined via conversion of the propagation time from an allocated center of the observed interference pattern. That time center was identified as the 50% rise point of the wave packet. The center of every pattern for the phase-compensated interferometer obtained before measuring the group delays varied by ±1 fs over the 400–700-nm range [8.19].

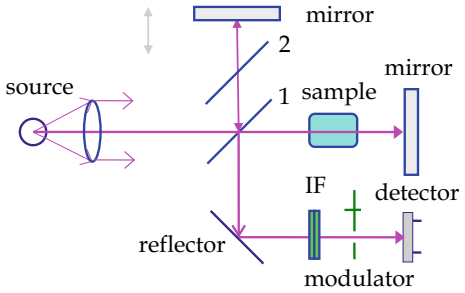

Fig. 8.30 White-light dispersion-sensing interferometer

The method described above directly measures a phase variation of a cross-correlated wave group as a function of the center wavelength of a quasi-monochromatic band filtered by a spectral filter. It creates an obvious difficulty, especially if the transmission bandwidth becomes narrower and its contour becomes wider. An improved design for direct registration of the phase status via Fourier components of an interferometric signal is shown in Fig. 8.31 [8.20]. A He–Ne laser beam traveling along a parallel trajectory to white light, whose spatial coherence is improved via a single-mode fiber, is used for subwavelength calibration of the optical path difference. Owing to dual propagation via a λ/8 wave plate in the interferometer's reference channel, perpendicularly polarized components for the main and reference channels are split via polarizing beam splitter PBS to separate photodiodes. The trigger generator detects the direction and the magnitude of the realized path difference stored in a designated wave memory. White-light interference signal of the main detector is sampled by the quarter-wave phase change at $\lambda = 632.8$ nm. A Fourier-transformed phase-correlation spectrum

is obtained by measuring an optically resonant cavity formed from two test mirrors, positioned in the main arm, dividing the result by four. Owing to the double-interferometric scheme applied, in which one of the two interferometers is set to detect length changes in the test cavity, the cross-correlation signal was measured free of fluctuations [8.20].

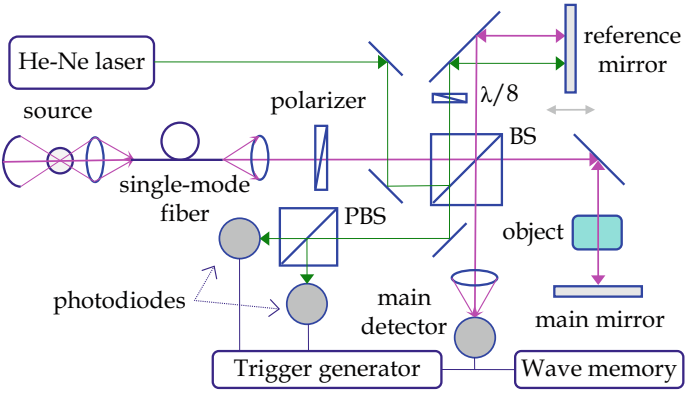

Fig. 8.31 White-light Fourier transform interferometer

One alternative approach to white-light interferometry is spectrally resolving frequency-dependent group-delay interferometry with a high-resolution CCD camera as depicted in Fig. 8.32 [8.21]. Michelson interferometer arms are formed by a gold mirror assumed to provide a constant group delay and the test mirror. One of the two mirrors is tilted around its horizontal axis to make fringes of even thickness for every spectral component of white light, further separated by the entrance slit. A transmission diffraction grating with 200 grooves per millimeter and an achromatic lens create the spectrally dispersed vertical-cut image of the superimposed white fringes on the CCD camera, with wavelength-dependent fringes dispersed in the horizontal direction. The two-beam interference pattern changes intensity along the exit slit with a phase term defined by the phase shift and tilt angle φ of each mirror. The measured intensity distribution at every wavelength was fitted to a cosinusoidal function, while the inaccuracy of curve fitting and the concealed optical path difference in the beam splitter limited the actual sensitivity, although allowing resolution of a ±0.2-fs delay at λ = 670–870 nm [8.21].

Fig. 8.32 Spectrally resolving white-light interferometer

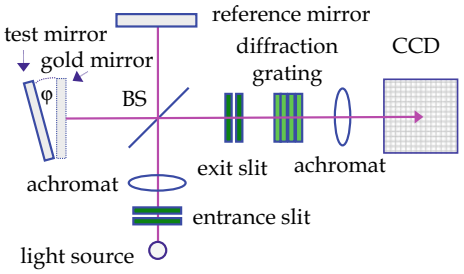

8.5.2 In Situ Laser-Based Measurements

Measuring the dispersion spectrum of the laser cavity in its actual operating condition in a laser can be done by using the laser concurrently as a light source and as an interferometer. Since the laser mode-locking condition results in a group of pulses at a repetition rate twice the cavity's transition time [3.32], the output of the laser as a function of its wave frequency evaluates the frequency-dependent time delay of the laser cavity. A continuously pumped and widely tunable femtosecond laser maintained at intensity-independent and therefore linear conditions is the clear choice for the measurement procedure [8.22, 8.23].

Consider the resonant laser cavity under study with low susceptibility to nonlinear effects consisting of two high-reflectivity mirrors spaced in a vacuum by distance ℓ and of a block of dispersive material of length ℓ_m placed between the mirrors. The round-trip phase φ gained by a quasi-monochromatic wave packet, emitted by a laser source, propagating in such a cavity is:

$$\varphi(\omega) = (2\omega/c)\{\ell + [n(\omega) - 1]\ell_m\}. \tag{8.104}$$

Differentiating over frequency, one can obtain a frequency-dependent cavity round-trip time t_c:

$$t_c = \frac{d\varphi}{d\omega} = \frac{2(\ell - \ell_m)}{c} + 2\ell_m \frac{\partial}{\partial\omega}\left[n(\omega)\frac{\omega}{c}\right] = \frac{2(\ell - \ell_m)}{c} + \frac{2\ell_m}{v_g}, \tag{8.105}$$

where v_g is the group velocity of the given quasi-monochromatic wave packet. If any feedback of the cavity path-length variation on the laser's spectral emission and all intensity-dependent nonlinear phase effects are prevented, the wavelength derivative of the cavity round-trip time is the cavity group-delay dispersion D_Σ, as the sum of the dispersions D_i of its elements [8.23]:

$$\frac{\partial t_c}{\partial\lambda} = 2\ell_\Sigma \frac{\partial}{\partial\lambda}\left(\frac{1}{v_g}\right) = 2\ell_\Sigma D_\Sigma = 2\sum_i \ell_i D_i. \tag{8.106}$$

The layout for an in situ frequency-domain measurement system of dispersion in a tunable-laser cavity is depicted in Fig. 8.33. The pulse train from a mode-locked

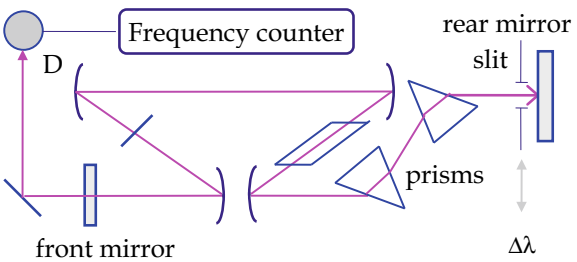

Fig. 8.33 Operating laser-based dispersion measurement

Ti: sapphire laser is observed by a low-noise digital frequency counter. Spectral scans are made by computer-controlled motion of the slit placed between the rear mirror of the cavity and two Brewster-angle prisms serving for dispersion compensation. Alterations of the round-trip group delay being measured in the experiments were made via transformation of small frequency changes converted to the time domain: $\Delta t_c = -\Delta\nu/\nu_0^2$, related to the ones for central frequency ν_0. The observed stable mode-locking conditions were found to correspond to a negative wavelength dispersion of approximately 1.5 and 10.5 fs/nm. All nonlinear contributions to the measured dispersions were evaluated to be quite small since the results were effectively independent of the laser pulse width, which was purposely changed to 80 and 300 fs from the basic width of 100 fs [8.22].

One universal way to perform an in situ dispersion measurement is associated with letting amplified spontaneous emission out of the active laser resonator under study [8.24]. To test the concept while preventing the effects of temperature fluctuations of the cavity round-trip time, especially noticeable for femtosecond semiconductor lasers having relatively short resonators, the system in Fig. 8.31 is replaced by two Michelson interferometers sharing a common beam splitter BS and end mirror M attached to a PZT (Fig. 8.34a). Concluding the light path of the first interferometer is steady-state mirror M_1 deployed to monitor the cavity-length change. The second cavity has a movable matching mirror M_2, utilized to detect derivative signals of phase correlations themselves. Measurements were provided via the system's femtosecond laser, with its birefringent filter removed with the pumping power kept under a lasing threshold, therefore making the laser-amplified spontaneous emission as broad as possible. The reverse wavelength group-delay dispersion curves of the laser entire resonator and its laser rod only are illustrated by curves *1* and *2* in Fig. 8.34b. The measurement accuracy for the group delay, obtained as the standard deviation among forty eight individual spectrum scans, was near ±(0.5–2.0) fs [8.24].

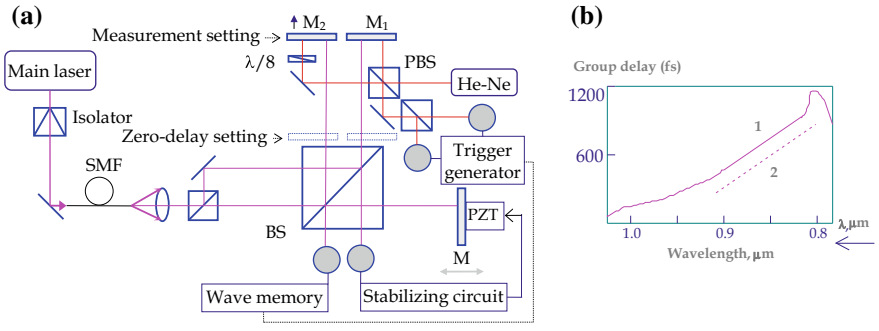

Fig. 8.34 Dual Michelson-interferometer system (**a**) and an example of phase-dispersion curves (**b**): SMF is the single-mode fiber (see Fig. 8.31)

8.5.3 Spectrophotometric Study of Phase Dispersion

When considering detecting the wavelength dependence of the spectral transmittance in correlation to the phase dispersion δ of a resonant cavity, one can analyze the propagation of a beam of polychromatic light via a resonant cavity consisting of highly reflecting or transparent elements. There are two possibilities for concluding such a study. First, the cross-correlated spectrum of the cavity transmission is compared with the incident spectrum of the light source. Second, the resonant-cavity spectrum is matched with the spectrum of a cavity set out of resonance, similarly to the resonator-tuning technique reviewed in Sect. 8.4, but utilizing an identical arrangement in transmitted instead of reflected light (see Fig. 8.20). For the first approach, the relative intensity I for the multiple-beam interference in transmission (see expression (3.122)) becomes:

$$I_\tau / I_0 = \frac{(1-\rho_1)(1-\rho_2)\tau}{\left(1-\tau\sqrt{\rho_1\rho_2}\right)^2 + 4\tau\sqrt{\rho_1\rho_2}\sin^2(\delta/2)}, \tag{8.107}$$

where ρ_1, ρ_2, and τ are the reflectances of the cavity mirrors and the transmittance of the empty or filled cavity. In the second case, the multipath interference-bound beam relates to the beam transmitted without retroreflections:

$$I_{\tau mult} / I_{\tau\,\mathrm{sing}} = \frac{1}{\left(1-\tau\sqrt{\rho_1\rho_2}\right)^2 + 4\tau\sqrt{\rho_1\rho_2}\sin^2(\delta/2)}. \tag{8.108}$$

The ratio in Eq. (8.107) depends on the cavity phase shift δ and cannot exceed 1.0, but can be very low. Equation (8.108) predicts very high transmission maxima, with minima reaching 0.25 for τ, $\rho \to 1$ [8.25]. Both equations provide for wavelength dependence of phase dispersion $\delta(\lambda)$ when functions $\rho_1(\lambda)$, $\rho_2(\lambda)$, and $\tau(\lambda)$ are predetermined. The phase sensitivity for each of these two methods [8.26] is:

$$\frac{\partial(I_\tau/I_0)}{\partial\lambda} = \mp \frac{4(1-\rho_1)(1-\rho_2)\tau\sqrt{\rho_1\rho_2}\sin\delta}{\left[\left(1-\tau\sqrt{\rho_1\rho_2}\right)^2 + 4\tau\sqrt{\rho_1\rho_2}\sin^2(\delta/2)\right]^2}\frac{\partial\delta}{\partial\lambda}; \tag{8.109}$$

$$\frac{\partial\left(I_{\tau mult}/I_{\tau\,\mathrm{sing}}\right)}{\partial\lambda} = \mp \frac{4\tau\sqrt{\rho_1\rho_2}\sin\delta}{\left[\left(1-\tau\sqrt{\rho_1\rho_2}\right)^2 + 4\tau\sqrt{\rho_1\rho_2}\sin^2(\delta/2)\right]^2}\frac{\partial\delta}{\partial\lambda}. \tag{8.110}$$

The only disadvantage of measurements in transmitted light is that to establish the wavelength dependence of the phase dispersion for the total resonator, it becomes necessary to determine independently two reflection spectrums: $\rho_1(\lambda)$ and $\rho_2(\lambda)$, and one transmission spectrum: $\tau(\lambda)$, of both resonator mirrors even if the cavity is empty, making sure their substrates are transparent.

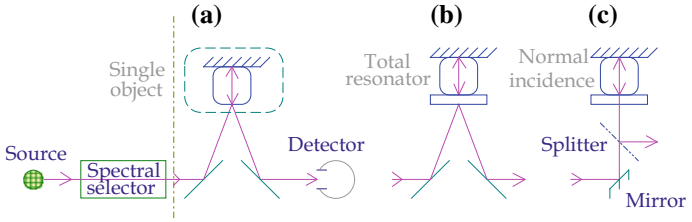

Fig. 8.35 Reflection-based measurements for spectral distribution of phase dispersion transmitted by the plane-parallel dielectric plate

Dispersion measurements in reflected light can be performed in a straightforward manner (Fig. 8.35). First, reflectance magnitudes $\rho_1(\lambda)$ and $\rho_2(\lambda)$ of an output coupler and a rear mirror of the laser cavity under test are measured in reflected light separately (Fig. 8.35, configuration *a*). For the measurement, the rear mirror can be installed in its position with any active element in place for direct determination of the product of its squared transmittance and mirror reflectance $\tau^2\rho_2$. Second, the reflection spectrum of the entire two-piece or three-piece laser resonator is measured (Fig. 8.35, configurations *b or c*). Precautions must be taken not to widen the retroreflected beams in the resonator and any optics between the source and the detector and accumulate as many of the retroreflected light components as possible. The error due to the limited number of terms in the summation of the multiply-reflected light components is provided by Eqs. (8.59) and (8.60) (see preceding Sect. 8.4). The relative intensity I_ρ of the beam reflected by the entire resonator compared with the intensity I_0 of the incident beam is given by (see Eq. (3.119)):

$$\frac{I_\rho(\lambda,\delta)}{I_0} \hat{=} \rho_\Sigma(\lambda,\delta) = \frac{\left[\sqrt{\rho_1(\lambda)} - \sqrt{\tau^2\rho_2(\lambda)}\right]^2 + 4\sqrt{\rho_1(\lambda)\tau^2\rho_2(\lambda)}\sin^2(\delta/2)}{\left[1 - \sqrt{\rho_1(\lambda)\tau^2\rho_2(\lambda)}\right]^2 + 4\sqrt{\rho_1(\lambda)\tau^2\rho_2(\lambda)}\sin^2(\delta/2)}. \tag{8.111}$$

Knowing the total $\rho_\Sigma(\lambda,\delta)$ and single $\rho_1(\lambda);\tau^2\rho_2(\lambda)$ reflectances, the phase dispersion δ becomes:

$$\delta(\lambda) = \arccos\left\{1 - 2\frac{\rho_\Sigma(\lambda)\left[1 - \sqrt{\rho_1(\lambda)\tau^2\rho_2(\lambda)}\right]^2 - \left[\sqrt{\rho_1(\lambda)} - \sqrt{\tau^2\rho_2(\lambda)}\right]^2}{1 - \rho_\Sigma(\lambda)}\right\}. \tag{8.112}$$

By analogy to Eqs. (8.106) and (8.107), the relative sensitivity to phase dispersion in reflected light is:

$$\frac{\partial\left(I_{\rho,\Sigma}/I_0\right)}{\partial\lambda} = \pm\frac{4\sqrt{\rho_1(\lambda)\tau^2\rho_2(\lambda)}\left\{\left[\sqrt{\rho_1(\lambda)}-\sqrt{\tau^2\rho_2(\lambda)}\right]^2+\left[1-\sqrt{\rho_1(\lambda)\tau^2\rho_2(\lambda)}\right]^2\right\}\sin\delta}{\left\{\left[1-\sqrt{\rho_1(\lambda)\tau^2\rho_2(\lambda)}\right]^2+4\sqrt{\rho_1(\lambda)\tau^2\rho_2(\lambda)}\sin^2(\delta/2)\right\}^2}\frac{\partial\delta}{\partial\lambda}. \tag{8.113}$$

For identical mirror reflectances and no transmission losses, Eqs. (8.109) and (8.113) become:

$$\frac{\partial\left(I_{\rho,\Sigma}/I_0\right)}{\partial\lambda} = \frac{\partial\left(I_{\tau,\Sigma}/I_0\right)}{\partial\lambda} = \pm\frac{4\rho(\lambda)[1-\rho(\lambda)]^2\sin\delta}{\left[[1-\rho(\lambda)]^2+4\rho(\lambda)\sin^2(\delta/2)\right]^2}\frac{\partial\delta}{\partial\lambda}. \tag{8.114}$$

Therefore, the unbounded sensitivity of the resonant technique in reflection is the same as that of similar intracavity, interferometric, and/or Fourier-transform measurement in transmission.

The most noticeable difference of phase measurements in reflected radiation is associated with the considerably higher sensitivity to optical properties at low reflectances of the elements forming the resonator. From Eqs. (8.109) and (8.113) it follows that at $\rho_1 = 0.05$, $\rho_2 = 0.9$, $\tau = 1$, and $\sin(\delta/2) = 0$, the relative sensitivity to wavelength dispersion in transmitted radiation: $\partial(I_\tau/I_0)/\partial\lambda \cong \mp 0.42\partial\delta/\partial\lambda$, is a full order of magnitude lower than that in reflected radiation, $\partial\left(I_\rho/I_0\right)/\partial\lambda = \pm 5.05\partial\delta/\partial\lambda$. That is why phase dispersion even of a single cavity element may be measured in reflected light by creating an open resonator consisting of that element having low surface reflectivity and being also low dispersive, such as a polished glass or fused silica. At the same time, wavelength dispersion in reflection of the single silica surface or of an entire silica plate can be presumed to be unchanged over a relatively wide spectral range. The only restriction for any reflected-light technique relates to the inability to make any nonresonant measurements in the resonator of a highly reflective output coupler, as practically no light will reflected back from inside the resonator unless such a resonator is in its maximum of reflection. Furthermore, in contrast to the Fabry–Perot cavity in transmitted light, every resonator viewed in reflected light does not change any given spectral resolution of its primary spectral selector.

Figure 8.36 shows spectral dependencies of the phase sensitivity for the transmission and reflection intensity measurements obtained by relations (8.109) and (8.113). The data are for a nearly semitransparent resonator with $\rho_1 = 0.5$ and $\rho_2 = 0.99$ and for a high-reflectivity resonator with $\rho_1 = 0.95$ and $\rho_2 = 0.99$. At $\rho_1 = 0.95$ and $\rho_2 = 0.9999$, the sensitivity in reflection for the low-phase changes near $\delta = 0°$, 360° is close to its maximum and almost 100 times higher than the respective spectral phase change $\partial\delta/\partial\lambda$ (see the insert in Fig. 8.36). At $\rho_1 \geq 0.99$ and $\rho_2 \to 1.0$, the integrated reflection sensitivity is lower than the transmitted one since in that case light is coming out of the cavity only at the spectral maxima of radiation interference. By rewriting Eq. (8.112) as: $\cos\delta = 1 - A/B$, the sensitivity

to phase changes in reflected light becomes: $d\delta = cot\,\delta \cdot [dB/B - d(B - A)/(B - A)]$, clarifying why measurements in reflected or transmitted light for phase: $\delta = \pm 90°, \pm 270°$, are not sensitive to spectral changes of the cavity optical-path length.

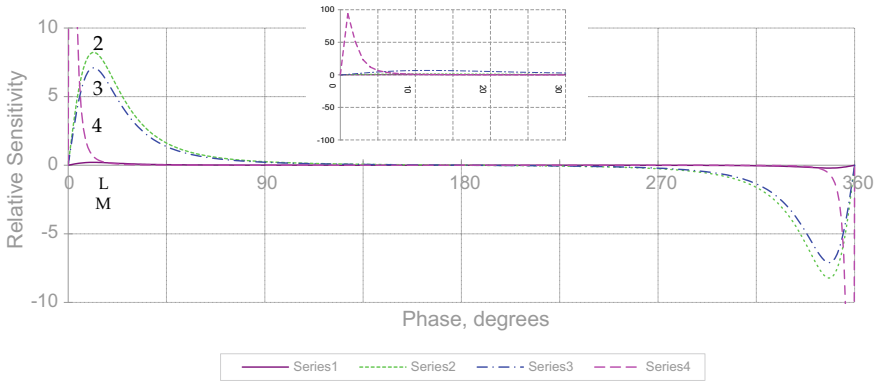

Fig. 8.36 Computed dependencies of relative phase sensitivity $\partial(I_{\tau,\rho}/I_0)/\partial\lambda$ measured in transmitted (1, 2) and in reflected (3, 4) radiation for semitransparent (1, 3) and for high-reflectivity (2, 4) resonators versus $\partial\delta/\partial\lambda$. The insert illustrates the out-of-scale magnitude for the near 100% maximum of transmittance in curve 4

Commensurate experiments were performed using a PerkinElmer 330 spectrophotometer and its reflection attachment, as illustrated in Fig. 8.37a, b. [8.26]. The experiments targeted examining the reflective measurement method and evaluating, during the fabrication of optical coatings, the potential impacts of dispersive elements of the laser cavity under test, such as the output coupler, the rear mirror, and the active element. Since at the time of the study no active element was available, measurements were performed with a flat spacer (see Fig. 8.37). First, the reflectance of each element was measured with its coating face up. Second, a resonator was created by spacing the reflecting surfaces with a 9.5 mm-thick silica spacer identical to a mirror single substrate. Thus, when any phase spectrum was computed by relations (8.101) and (8.102), dual transmittance values of the first substrate and of the spacer were automatically subtracted from the final result, and every total spectrum was measured for the resonator, consisting of the particular

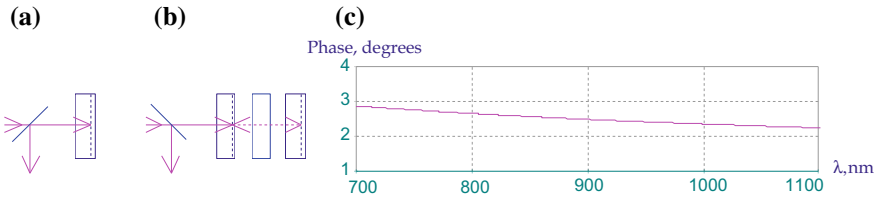

Fig. 8.37 The layout for dispersion measurements (**a**, **b**) and a phase delay within a 19-mm thick silica substrate (**c**)

output coupler, the silica spacer, and the rear mirror. There was no need to align the test resonator, because the spacer and substrates were made to 5-second parallelism. The phase delay difference between any measured identical substrates made of fused silica and sapphire, forming a silica-spaced resonator in the spectral range of all measurements performed, did not exceed 1.2° out of a possible 360° phase change being investigated [8.26] (see Fig. 8.37c).

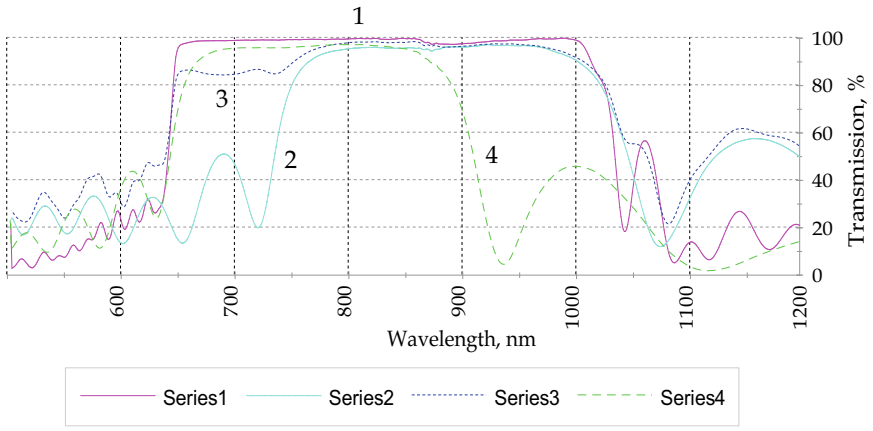

Fig. 8.38 Reflectance of a high-reflectivity (HR) mirror (series 1), of a uniform output coupler (series 2), of the cavity formed from the two of them with a silica spacer in between (series 3), and of a dispersive coupler (series 4)

Raw data for measured reflection spectrums of all components measured via Eq. (8.112) are shown in Fig. 8.38. The spectrums of two output couplers and a dielectric high-reflectivity multiple-layer mirror for the Ti:sapphire laser are in Fig. 8.39. The spectrum of each element was measured in reference to the spectrum of the silica spacer, whose reflectance was unchanged within $4 \cdot 10^{-6}$ from 500 to 1200 nm. The measured spectrums of the output couplers and the rear high-reflectivity mirror are given in Fig. 8.40a–c. The spectrum in Fig. 8.40d was obtained for a Fabry–Perot resonator formed from a "uniform" output coupler, a silica

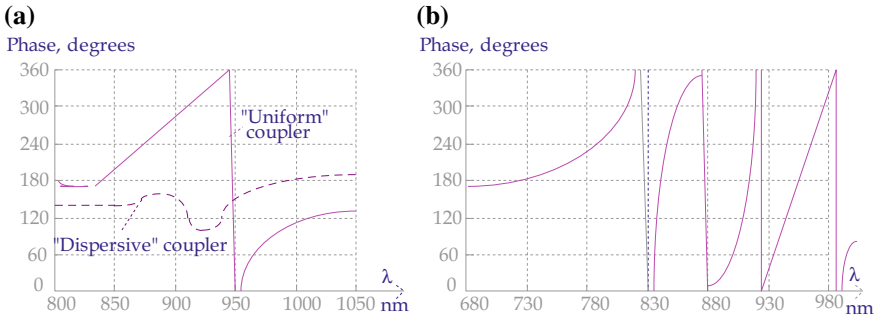

Fig. 8.39 Characteristic design outcomes for two output couplers (**a**) and a high-reflectivity mirror (**b**)

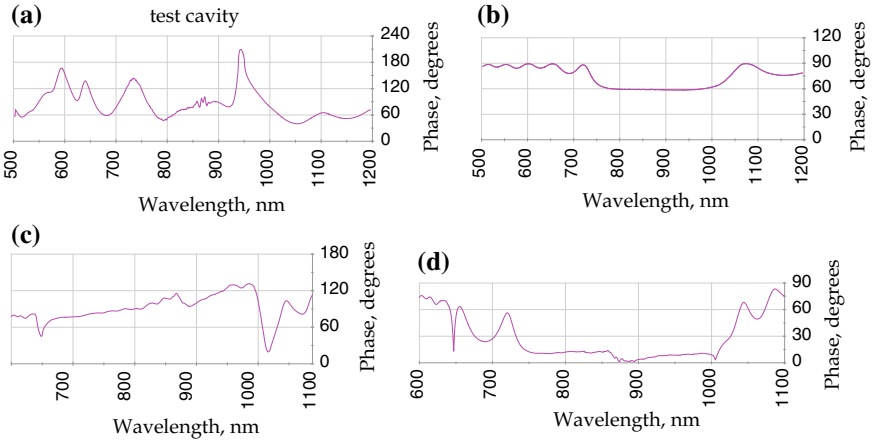

Fig. 8.40 **a** Phase status of the "dispersive" Ti:sapphire output coupler. **b** Measured phase dispersion of the "uniform" output coupler for a Ti:sapphire laser. **c** Measured phase dispersion of the HR rear mirror for a Ti:sapphire laser. **d** Measured phase dispersion of the entire resonator for a Ti:sapphire laser: "uniform" output coupler, silica spacer, and HR mirror

spacer, and a high-reflective mirror. Every phase delay was computed by averaging the results of five to ten spectral points detected at 0.1-nm spectral resolution, reducing the noise of each single phase measurement. The spectrum in Fig. 8.41 was obtained via substituting the high-reflectivity mirror by a high-reflectivity aluminum coating, assumed to have zero dispersion, closely matching the uniform middle section of the spectrum in Fig. 8.40b.

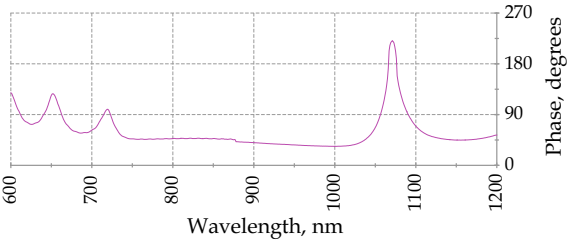

Fig. 8.41 Measured phase dispersion of the "uniform" output coupler for a Ti:sapphire laser obtained versus HR aluminum coating

The reflection experiment demonstrated high sensitivity to phase dispersion for every resonant element, especially for a small phase change. The spectrums for the low- and high-reflectivity cavities for the fused silica and the aluminum coating confirmed the high repeatability of the reflection-based measurement and phase accuracy, conforming to 3°–5° or less. Similarly to the phase-delay data obtained by the frequency-domain and the cross-correlation measurements described above, the reflection spectrums of wavelength phase dispersion of femtosecond laser cavities give likely statistics averaged by all layers, elements, and substrates involved, and by the spectral resolution of the spectrometers used. To prevent contacts between the coatings and silica surfaces, the spacer can have a drilled hole having cross section

larger than the beam size. Such a measure and possibly higher spectral resolution will separate individual phase spectrums. The true normal incidence of the reflection phase studies should also provide access to the longer cavities of actual lasers. Likewise, high sensitivity of a spectrophotometric color measurement at normal incidence in transmission enabled a refractive index study of uncoated wafers by detecting interference fringes via an FTIR spectrometer [8.53].

8.5.4 Colorimetric Approach to Phase Recognition

As seen in Part I, quite sensitive optical measurements can be accomplished when analyzing color coordinates and detecting spectral distributions of phase retardance (see Sects. 2.3 and 3.3). A combination of the approaches can also be used for phase evaluation during birefringence studies [8.28]. If a beam of polarized light is transmitted via a birefringent plate positioned in between a polarizer and an analyzer, whose optical axes are crossed, while the plate optical axis is oriented at ±45° to the polarizer and analyzer axes (Fig. 3.15, Eq. (3.151)), transmittance $T_\perp$ of the beam is a function of the optical phase difference δ:

$$\begin{aligned} T_\perp &= I_{\tau,\perp}(e,o,\lambda)/I_0 = \sin^2(\delta(e,o,\lambda))/2 = \sin^2(2\pi\ell(e,o,\lambda)/\lambda)/2 \\ &= \sin^2(\pi\ell(e,o,\lambda)/\lambda), \end{aligned} \tag{8.115}$$

where $\delta = (2\pi/\lambda)\ell$ is the phase difference for path difference ℓ via ordinary and extraordinary axes ***o*** and ***e***. Since tristimulus values for the radiation intensity at a given point with assigned color coordinates (*o, e*) can be expressed according to Eq. (2.101) for incident flux Φ_0(o, e, λ), reference stimuli X, Y, Z for normalized tristimulus values $\bar{x}(\lambda)$, $\bar{y}(\lambda)$, $\bar{z}(\lambda)$ with monochromatic inputs $0 \le \lambda_i \le \infty$ are:

$$\begin{aligned} X(o,e) &= k \int_\lambda \Phi_0(o,e,\lambda) \cdot T_\perp(o,e,\lambda) \cdot \bar{x}(\lambda)\, d\lambda; \\ Y(o,e) &= k \int_\lambda \Phi_0(o,e,\lambda) \cdot T_\perp(o,e,\lambda) \cdot \bar{y}(\lambda)\, d\lambda; \\ Z(o,e) &= k \int_\lambda \Phi_0(o,e,\lambda) \cdot T_\perp(o,e,\lambda) \cdot \bar{z}(\lambda)\, d\lambda, \end{aligned} \tag{8.116}$$

while tristimulus coordinates x(o, e) and y(o, e) of radiation at the point (o, e) are (z = 1 − x − y):

$$\begin{aligned} x(o,e) &= X(o,e)/(X(o,e) + Y(o,e) + Z(o,e)); \\ y(o,e) &= Y(o,e)/(X(o,e) + Y(o,e) + Z(o,e)). \end{aligned} \tag{8.117}$$

The challenge in determining the color coordinates is in figuring out the optical path-length dependence on wavelength: $\ell = \ell_0 + \ell_\Delta(o, e, \lambda)$, where ℓ_0 and ℓ_Δ are the constant initial and the gained path difference, with the later being dependent the changes of color coordinates (o, e) and of wavelength λ. In many cases path difference ℓ_Δ may be represented as a quadratic function of wavelength λ: $\ell_\Delta(o,e,\lambda) = A(o,e) + B(o,e)\lambda + C(o,e)\lambda^2$, with coefficients A, B, and C depending on color coordinates. For small changes in the gained path difference $\ell_\Delta \ll \ell_0$, relation (8.117) approximates to [8.28]:

$$\begin{aligned}\sin^2(\pi\ell/\lambda) = \sin^2(\pi(\ell_0+\ell_\Delta)/\lambda) &\underset{\ell_\Delta \ll \ell_0}{\approx} \sin^2(\pi\ell_0/\lambda) + (\pi\ell_\Delta/\lambda)\sin(2\pi\ell_0/\lambda) \\ &+ (\pi\ell_\Delta/\lambda)^2\cos(2\pi\ell_0/\lambda) = \sin^2(\pi\ell_0/\lambda) \\ &+ (\pi(\mathrm{A}/\lambda + \mathrm{B} + \mathrm{C}\lambda)/\lambda)\sin(2\pi\ell_0/\lambda) \\ &+ \pi^2(\mathrm{A}/\lambda + \mathrm{B} + \mathrm{C}\lambda)^2\cos(2\pi\ell_0/\lambda) = \mathrm{T}(o,e,\lambda). \end{aligned} \tag{8.118}$$

To prevent dealing with nonlinear equations, when the quadratic term in the optical path-length dependence on wavelength is disregarded by approximating transmission T as a linear function: $\mathrm{T}(o,e,\lambda) \cong \sin^2(\pi\ell_0/\lambda) + (\pi(\mathrm{A}/\lambda + \mathrm{B} + \mathrm{C}\lambda)/\lambda)\sin(2\pi\ell_0/\lambda)$, the tristimulus values become:

$$\begin{aligned} X(o,e) &= k\int_\lambda \Phi_0(o,e\lambda) \\ &\cdot\left(\sin^2(\pi\ell_0/\lambda) + (\pi(A/\lambda + B + C\lambda)/\lambda)\sin(2\pi\ell_0/\lambda)\right)\cdot\bar{x}(\lambda)\mathrm{d}\lambda; \\ Y(o,e) &= k\int_\lambda \Phi_0(o,e\lambda) \\ &\cdot\left(\sin^2(\pi\ell_0/\lambda) + (\pi(A/\lambda + B + C\lambda)/\lambda)\sin(2\pi\ell_0/\lambda)\right)\cdot\bar{y}(\lambda)\mathrm{d}\lambda; \\ Z(o,e) &= k\int_\lambda \Phi_0(o,e\lambda) \\ &\cdot\left(\sin^2(\pi\ell_0/\lambda) + (\pi(A/\lambda + B + C\lambda)/\lambda)\sin(2\pi\ell_0/\lambda)\right)\cdot\bar{z}(\lambda)\mathrm{d}\lambda. \end{aligned} \tag{8.119}$$

If the initial light path ℓ_0 and the spectral distribution Φ_0(o, e, λ) are known, a solution of Eq. (8.119) with unknown path-difference coefficients A(o, e), B(o, e), and C(o, e) can be sought as a matrix: **Ha = b**, of three equations, each with three unknowns, in the form [8.28]:

$$\mathbf{H} = \begin{bmatrix} X_1 & X_2 & X_3 \\ Y_1 & Y_2 & Y_3 \\ Z_1 & Z_2 & Z_3 \end{bmatrix}, \quad \mathbf{a} = \begin{pmatrix} A \\ B \\ C \end{pmatrix}, \quad \mathbf{b} = \begin{pmatrix} X - X_0 \\ Y - Y_0 \\ Z - Z_0 \end{pmatrix}. \tag{8.120}$$

All X, Y, and Z elements of matrices (8.120) can be determined similarly to only X functions:

$$X_0 = k\int_{\lambda} \Phi_0(\lambda)\cdot \sin^2(\pi\ell_0/\lambda)\cdot \bar{x}(\lambda)d\lambda;$$
$$X_1 = k\int_{\lambda} \Phi_0(\lambda)\cdot (\sin(2\pi\ell_0/\lambda))/\lambda\cdot \bar{x}(\lambda)d\lambda;$$
$$X_2 = k\int_{\lambda} \Phi_0(\lambda)\cdot \sin(2\pi\ell_0/\lambda)\cdot \bar{x}(\lambda)d\lambda;$$
$$X_3 = k\int_{\lambda} \Phi_0(\lambda)\cdot \sin^2(2\pi\ell_0/\lambda)\cdot \lambda\cdot \bar{x}(\lambda)d\lambda, \qquad (8.121)$$

with a solution sought via inverse matrix at a pre-set initial optical path length ℓ_0 [8.28] with a solution as a linear function of a pre-set optical path length being sought via inverse matrix $\mathbf{H^{-1}}$: $\mathbf{a = H^{-1}b}$, for constants X_0, Y_0, and Z_0 (a full solution for the unaltered quadratic function via Eq. (8.118) could also be found analytically and more likely solved numerically [8.28]).

8.5.5 *Spatial-Spectral Interferometry*

The previously reviewed phase- and dispersion-measurement techniques highlighted the advantages of using reference radiation for verification of the phase status of light pulses under test (see Figs. 8.31 and 8.34). From a general standpoint, one can consider applying a reference-light pulse of sufficient energy, whose amplitude and phase parameters are known and to which a measured pulse is referred, for any linear-measurement method, where the frequency components of the reference and measured pulse must overlap for stationary interference to occur [8.48]. In time-stationary linear measurement, time-integrated detection is used, and the system's response is linearly proportional to the power of the sensing light field (see Eq. (1.10)). In linear interferometry, such as Fourier-transform interferometry, the output is a function of the time delay τ between interferometer arms, and even the time-integrating detector is sensitive to the power spectrum of the sum of interfering electromagnetic fields, including the cross-correlated terms of two fields $E_0^*(\omega)E(\omega)$, one of which: $E(\omega)$, is unknown and the other: $E_0(\omega)$, is the reference one. In this case, as in homodyne and heterodyne detection (see Chaps. 9, 12), an unknown weak pulse can be detected with enhanced sensitivity if it is referenced to a high-power (energy) reference pulse.

A generalized schematic of linear spectral interferometry recording the phase difference $\varphi(\omega)$ of signal $E(\omega)$ versus reference $E_0(\omega)$ in the total frequency domain $\Sigma\omega$ defined by an extra spectrometer [8.48] is shown in Fig. 8.42. Reference and

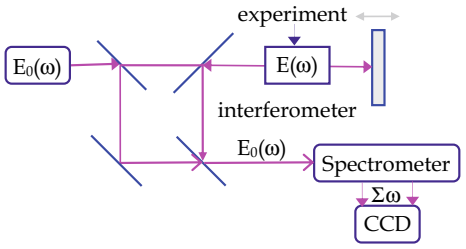

Fig. 8.42 Generalized spectral interferometry

affected-by-experiment pulses interfere, causing corresponding spectral fringes to be recorded simultaneously by a multichannel detector, such as a CCD array (see Fig. 8.32). One advantage of that system versus the time-domain scanning interferometer in Fig. 8.30 is that small fluctuations of the path-length difference affect all frequencies and measured phase $\Delta\varphi$, thus reducing the fringe pattern's contrast, though effectively measuring only phase differences for maxima of interference at discrete frequencies for $\Delta\varphi = 2\pi$. To measure any pulse delay smaller than 2π and to improve spectral resolution as a result, an extra time delay τ is introduced for a measured pulse versus the reference one, effectively adding $\omega\tau$ linear phase to the reference signal and yielding spectral phase difference: $\Delta\varphi = \varphi(\omega) - \varphi_0(\omega) - \omega\tau$ [8.46]. Since both reference and measured pulses are derived from the same source as in Fig. 8.42, any spectral phase difference between the pulses should be attributed to the phase dispersion being studied.

To obtain the phase as a continuous function of frequency for every pulse measured, spectrally and spatially resolved interferometry can be used as a two-dimensional technique by detecting both states of radiation polarization or by separating the spectral components of radiation in space either to simultaneously determine cosine plus sine functions of the phase and to spectrally unwrap the cosine term, removing its sign ambiguity, or invoke the sine term instead [8.46–8.51]. Figure 8.43 illustrates upgrading the concept shown in Fig. 8.42 by adding phase sensitivity to each pulse measurement using polarization multiplexing [8.48]. Embedding crossed polarizers LP into the interferometer's arms makes the polarization of the reference field to be in quadrature with the measured field, allowing sine and cosine quadratures to be registered at the same time. Linearly polarized light of reference field $E_0(\omega)$ is circularly polarized by quarter-wave plate $\lambda/4$, allowing two perpendicular polarization components to be analyzed independently via Wollaston prism WP, both being spectrally resolved into separate detector-array tracks of the two-dimensional CCD.

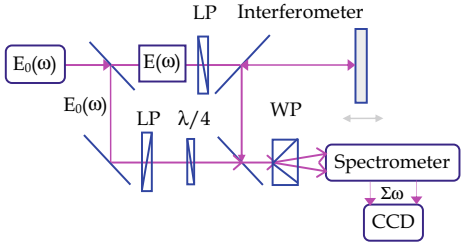

Fig. 8.43 Dual-quadrature spectral interferometry

An example of a spatially resolved spectral interference measurement system [8.49] is shown in Fig. 8.44. Two-dimensional spatial and spectral interference occurs between white-light reference and signal fields interacting at angle 2Θ to each other, and the fringes that occur produce a sinusoidal pattern in one direction, being shifted in the orthogonal direction by the spectral phase difference between the two spectral components of the reference and signal fields at 2π fringe spacing. Interfering frequency components are angularly dispersed by the prism and are recombined at the focal plane of the cylindrical lens to be registered by the two-dimensional CCD array. For a stationary spectral distortion of a test object, the

difference between reference and test fields should remain constant, with delay τ functioning as the carrier frequency for the spectral encoding. The system in Fig. 8.44 involves uneven propagation of white light via a 50:50 beam splitter made as one broadband coating layer on BK7 substrate, with three substrate passes for the signal and one for the reference beam, hence requiring one extra calibration measurement compensating for the material dispersion. To obtain spectral phase differences via measured spatial distributions, power spectrums of reference and signal fields were subtracted from interference signals to account for nonuniformity of the white source, with inverse Fourier transform to the time domain to filter negative and zero-time terms, Fourier transforming the results back to the frequency domain, to be multiplied by a linear phase exponent factor of delay τ [8.49].

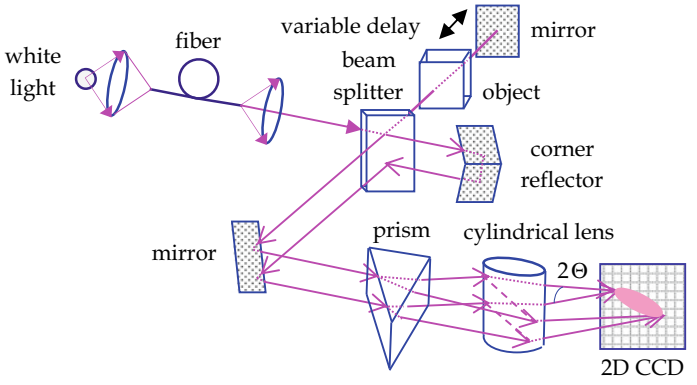

Fig. 8.44 Spatially-resolved spectral interferometry

The spectrally and spatially resolved interferometer depicted in Fig. 8.45 [8.51] measures the two-dimensional fringe pattern for a seeding reference field and a test field leaking out of a high-finesse femtosecond laser enhancement cavity. Measuring the two-dimensional pattern in combination with individual spectrums of the interferometer arms is sufficient to identify the complex wave function of the

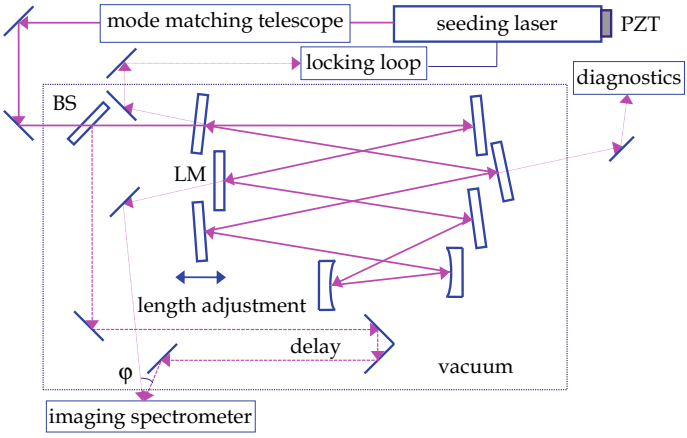

Fig. 8.45 Resonant dispersion measurements via spatial-spectral interferometer

intracavity field related to the seeding one. The enhanced cavity under study is an eight-mirror ring resonator, whose round-trip time is tuned to the inverse of the seeding laser repetition rate. The cavity is set in a vacuum chamber to minimize losses and group-delay dispersion. The seeding laser resonator is locked to the cavity via a PZT-mounted mirror, with transverse-mode matching by the telescope. The interferometer's reference arm is formed by 4% surface reflectance of beam splitter BS via the delay line. The beam passing the splitter enters the cavity and a part of it leaks via mirror LM with 1.65-ppm transmittance, forming the test arm of the interferometer. The two beams are recombined in the imaging spectrometer at separation angle φ. The reference arm delay line serves to adjust the time delay τ between interferometer arms, being calibrated by taking the test cavity off resonance. When the cavity reaches the steady state, single-pulse acquisition is sufficient for determination of the cavity's response function. Measurements of single-round-trip group-delay dispersion of the tested resonant cavity were made with 1-fs^2 reproducibility [8.51].

Similar sensitivity to group-delay dispersion could be reached via a one-dimensional linear measurement technique in a passive high-finesse cavity, referenced by an equidistant frequency comb [8.33], enabling detection of the spectrally resolved cavity dispersion simultaneously with measurements of the cavity finesse and losses [8.52]. Each of two systems in Fig. 8.46 enabled a 1-2 fs^2 accuracy to group-delay dispersion in the respective passive cavity. Chromatic dispersion testing of a birefringent hollow-core photonic crystal fiber deploying Fourier-transform spectral interferometry (see Chap. 12) in Mach-Zehnder configuration at 0.2-nm resolution spectrometer revealed rather small dependencies of differential group delay and polarization mode dispersion measured on the placement and the length of a commercial up to 0.97-m long fiber studied [8.58].

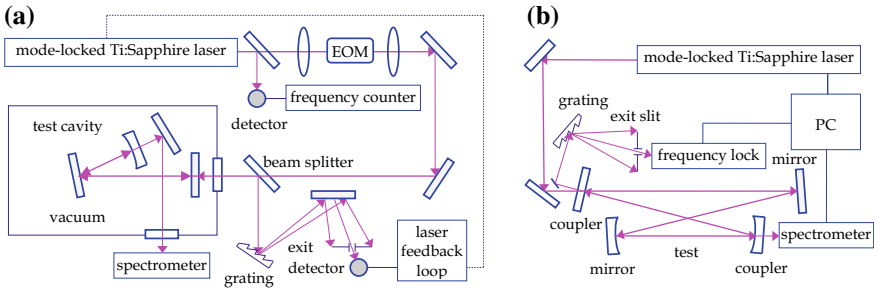

Fig. 8.46 Spectrally resolved dispersion (**a**) and dispersion-plus-finesse (**b**) measurements referenced to frequency comb: *EOM* electro-optic modulator

Chapter 9
Determination of Absorption Losses

9.1 Laser Calorimetry

As much as scattering of radiation propagating via a medium under study allows one to evaluate internal inclusions and optical density fluctuations in such matter, the internal absorption of that matter gives a sense of radiant transformation into other forms of energy and essentially distinguishes any obscure regions absorbing radiation in the otherwise transparent medium. Absorbed light can be directly measured via the transformation of its radiant energy into heat when detecting a respective increase of the temperature of the irradiated substrate. The attenuation of radiation by the bulk of an irradiated substance is resolved by the Bouguer–Lambert–Beer law (see Eqs. (1.71)–(1.79)). For radiation transmission through a highly transparent substance, the exponential function of attenuation for flux Φ_0 of radiation incident onto that substance of refractive index n can be substituted by the first two factoring terms as:

$$\Phi_{\mathrm{a}} = \Phi_{\mathrm{int}} - \Phi_{\tau} = \mathrm{a}\Phi = e^{-\alpha\ell}\Phi \underset{\alpha\ell\to 0}{\cong} \alpha\ell\,\Phi, \tag{9.1}$$

where Φ_{a} is the radiant flux absorbed in a sample of length ℓ, Φ_{int} is the flux entered the sample's bulk via its front surface and transmitted into the section from which the temperature rise is determined: $\Phi_{\mathrm{int}} = \Phi_0\left(4\mathrm{n}/(\mathrm{n}+1)^2\right)$ (see Eqs. (1.84)); a is the absorption factor, α is the linear bulk absorption coefficient, and Φ_{τ} is the flux transmitted by the sample bulk of length ℓ.

The temperature rise $\Delta\mathrm{T}$ identified by an increase of the internal energy of a relatively thin and long sample in its isothermal condition creates a homogeneous flow of heat to its surroundings. Thermal flux Φ'_{a} can be defined via the outer-surface heat transfer coefficient h for external area A_{Σ}:

M. Bukshtab, *Photometry, Radiometry, and Measurements of Optical Losses*, Springer Series in Optical Sciences 209,
https://doi.org/10.1007/978-981-10-7745-6_9

$$\Phi'_{\alpha} = hA_{\Sigma}\Delta T. \tag{9.2}$$

Since at thermal equilibrium: $\Phi'_{\alpha} = \Phi_{\alpha}$, the sample's linear absorption coefficient $\alpha = \alpha/\ell$ is:

$$\alpha = hA_{\Sigma}\Delta T_0/(\ell\Phi_0). \tag{9.3}$$

A steady-state rise ΔT_0 of the sample's temperature resolved by either a differential thermocouple or a thermistor attached to its lateral surface defines the sample's absorptance or its absorption loss α.

At the instant termination of irradiation, the sample's temperature T starts declining as [9.1, 9.2]:

$$hA_{\Sigma}\Delta T = -(\partial/\partial T)(CV\Delta T). \tag{9.4}$$

The resultant decrease of the measured sample's surface temperature versus time t is given by:

$$\Delta T = T_0 \exp\{-[hA_{\Sigma}/(CV)]t\}, \tag{9.5}$$

where V and C are the volume and the heat capacity of the sample and $[hA_{\Sigma}/(CV)]^{-1} = t_0$ is the time constant of either the heating or the cooling curve for e times decline of temperature T of the irradiated sample. Equations (9.3) and (9.5) for any infinitely long, thin, and low-absorbing sample of area A_s of its entire external surface allow one to distinguish the sample's linear absorption coefficient α:

$$\alpha = CV\Delta T_0/(t_0\ell\Phi_0) = CA_s\Delta T_0/(t_0\Phi_0). \tag{9.6}$$

The linear absorption coefficient α can be analogously determined by an adiabatic process, increasing the temperature of a sample at thermal equilibrium with its surroundings inside a totally absorbing enclosure. If the sample is formed as a long cylinder or a parallelepiped for the substance studied of negligible thermal conductivity along its optical axis, at the beginning of irradiation of the sample the temperature rise in the middle of the sample's generatrix becomes a linear function of time [9.3]:

$$\partial T/\partial t = \Phi\ell/(CV) = \Phi/\left(A\rho_p c_p\right), \tag{9.7}$$

where ρ_p and c_p are the density and the specific heat of the substance. When the temperature is substantially raised over that of the surroundings, the generated heat overflows into the sample background. As a result, the differential equation (9.7) for the total process of irradiation and heat transfer gives:

$$T = (\Phi_a/B + T_0)\{1 - \exp(-Bt/(A\rho_p c_p))\}, \tag{9.8}$$

where B is the velocity of the radiative heat transfer and T_0 is the temperature of the initial equilibrium.

As it follows from Eq. (9.8), to determine the linear absorption coefficient α, the radiant flux entering the absorbing region and all parameters of heat transfer must be known. The heat transfer parameters could be velocity B and time constant t_0, both identified in the vicinities of the linear rise or the same linear decline of temperature. Sample properties ρ_p and c_p also have to be known. Ordinarily, two similar samples, one to be measured and the other acting as a reference, are placed in a passive thermostat to achieve thermal equilibrium of the process and to exclude any convective heat transfer. Since the temperature change ΔT for any low-absorbing material cannot be high, the entire calorimeter should be in a relatively high vacuum or filled with a pure gas of known thermal conductivity. Two factors not yet considered could notably distort the reading of a heat detector, as a differential thermocouple, and the linear dependence of temperature on time. The first one is the light scattered by the bulk and surfaces of the irradiated sample that could directly expose the thermocouple. The second factor is the likely nonzero thermal conductivity of the sample, causing unpredictable effects on readings for the heat absorbed by sample surfaces.

Some time partition of bulk and surface actions is a natural measure to distinguish between local and distributed absorptance and scattering for a light beam incident on a sample made as a long rod. If the radius r of such a sample with the thermocouple in the center of its periphery is much shorter than half of its length $\ell/2$, the time instants of the heat transfer from the sample bulk and its front and back surfaces to the detector should be well separated. Besides, light scattered by sample surfaces directly exposes the detector much earlier than the heat transferred by the sample. That fact allows three terms of the heat-transfer equation [9.4] to be resolved as follows:

$$T - T_0 = \Phi_0\left\{\kappa(2\sigma) + (mc_p)^{-1}\left[\alpha\ell\left(t - \frac{r^2\rho_p c_p}{8\lambda_T}\right) + 2a\left(t - \frac{r^2\rho_p c_p}{4\lambda_T} - \frac{\ell^2}{4}\frac{\rho_p c_p}{6\lambda_T}\right)\right]\right\}, \tag{9.9}$$

where Φ_0 is the incident flux, identified via the transmitted by the entire rod flux $\Phi_{\tau,\Sigma}$, measured accumulating all multiple reflections: $\Phi_{\tau,\Sigma} = \Phi_0 2n/(n^2+1)$; κ is the uniformity factor, depending on homogeneity of the detector's sensitivity and the sample's indicatrix of scattering; σ and α are the scattering and the absorptance of sample surfaces; and m, n, and λ_T are the mass, the refractive index, and the thermal diffusion length of the sample at its thermal conductivity $K_T = \lambda_T \rho_p c_p$. When the distinguishing time interval $t_2 = r^2\rho_p c_p/(8\lambda_T)$ is shorter than time $t_3 = (\ell/2)^2\rho_p c_p/(6\lambda_T)$ and when the magnitude of σ is lower than the magnitudes of $2a$ and $\alpha\ell$, there are three separated in time temperature-transformation

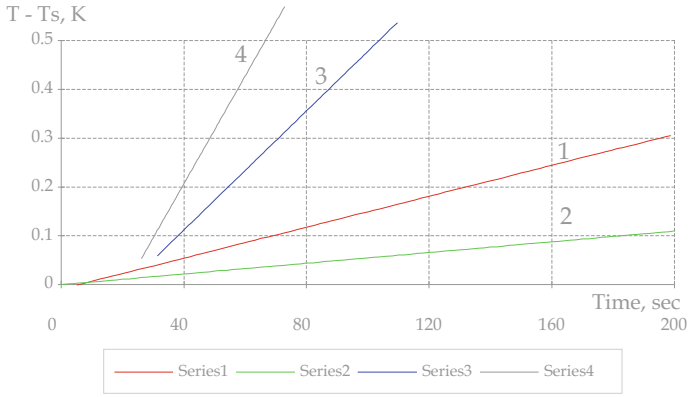

Fig. 9.1 Calculated thermal rise curves for a long KCl rod with bulk to surface absorptance ratios of: 1:1 – 1; 1:0 – 2; 1:5 – 3; and 1:10 – 4

processes. In the first short time interval t_1, the initial rise of the temperature is influenced only by the direct light scattering. For the second term t_2, the linear increase: $\Delta T = T(t) - T_0$, discerning only the sample's bulk absorption appears as [9.5]:

$$T - T_0 = \Phi \alpha t / \left(A \rho_p c_p\right) \quad \text{at} \quad t_1 < t < t_2. \tag{9.10}$$

Finally, the linear phase transforms to the joint time action t_3 of bulk and surface absorption:

$$T - T_0 = \frac{\Phi}{V \rho_p c_p} (\alpha \ell + 2\mathsf{a}) \left(t - \frac{2\mathsf{a}}{\alpha \ell + 2\mathsf{a}} \cdot \frac{\ell^2}{4} \cdot \frac{\rho_p c_p}{6 \lambda_T} \right) \quad \text{at} \quad t > t_2. \tag{9.11}$$

As is seen from all equations, any separation of time intervals t_1 and t_2 is identified not only by the sample geometry and its thermal diffusivity $\lambda_T/\rho_p c_p$, but also by the ratio of bulk and surface losses $\alpha\ell/(2\mathsf{a})$ (see Fig. 9.1). If the magnitudes of $\alpha\ell$ and $2\mathsf{a}$ are close enough, two time domains in relations (9.10) and (9.11) are practically indistinguishable from each other, and the lower is the loss to be sensed, the higher should be the temperature resolution of measurements, approaching 10^{-2}–10^{-3} K. If single-surface loss is considerably larger than the bulk loss, the linear temperature interval (see Fig. 9.2) is drastically decreased and may even not be resolved. In a corresponding experiment [9.4] at the characteristic time of about 50 s, which definitively separated two regions of bulk and bulk-plus-surface absorption loss, the observed ratio of the surface to bulk absorption was 1.1. The exact solution for the three-dimensional heat-transfer equation without disregarding heat losses with the temperature rise made ratio $2\mathsf{a}/\alpha$ nearly 20% higher, approaching 1.3 [9.4].

Three-slope-type behavior can be evenly observed for samples with low losses and low thermal diffusivity. For greater-absorbing silicate glasses or crystals such as ZnSe of higher thermal diffusivity, the process is less clear and not well fitted to

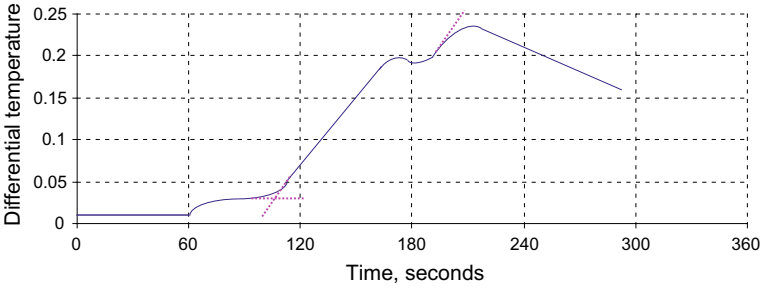

Fig. 9.2 Illustration of experimental temperature rise for KCL sample: size – 1.3 × 1.3 × 7.73 cm^3; weight – 26.43 g; laser power – 13.5 W [9.4]

difference or sum-slope equations. In such cases, better time resolution of optical losses may be achieved by local-temperature control at various points of the sample [9.5]. Since the center of a lateral sample surface and the transverse sides are the opposite areas of the highest sensitivity to the bulk and surface loss, at these points each characteristic time constant of the separate slopes becomes notably decreased or increased.

For accurate separate evaluation of bulk and surface losses one must know the heat-transfer equation describing the status of a test sample inside an actual measurement system [9.6, 9.7]:

$$\lambda_T \nabla^2 T(\mathbf{r},t) + g(\mathbf{r},t) = \rho_p c_p \partial T(\mathbf{r},t)/\partial t. \tag{9.12}$$

Its solution is obtained by setting the initial: $T(\mathbf{r},t) = T_0$, and limiting: $\lambda_T \partial T(\mathbf{r},t)/d\mathbf{n} + q\nabla T = 0$, conditions. Here $T(\mathbf{r},t)$ is the temperature of an arbitrary point of the sample at coordinate r and at time instant t; $g(\mathbf{r},t)$ is the density of all heat sources inside the sample under study; q is the convective heat transfer coefficient, considered for simplicity as being independent of time or coordinate; and $\mathbf{n}$ is the vector of the outer normal in the direction $\mathbf{r}$. Spatial variations of absorptance can be obtained by solving the equation for different temperature distributions across the sample and along its axis.

Apparent difficulties in obtaining a full-fledged solution can be simplified by reducing the three-dimensional equation to a one-dimensional one. The simplest realization having the ability to resolve absorption losses along the long sample axis z can be achieved by establishing a steady-state temperature profile in a uniform sample after the initial transitions have been completed. Three thermocouples placed on a sample's lateral surface near its center and at two end surfaces determine the primary heat profile (Fig. 9.3). The uniform temperature distribution T_c

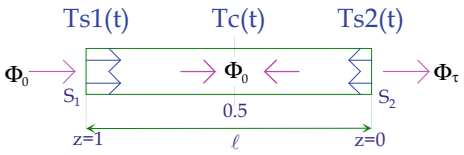

Fig. 9.3 Bulk and surface heat sources

conditioned by a generally uniform bulk absorption is broken by the temperature increments caused by surface heat fluxes Q_1 and Q_2: $\Delta T_{l1} = T_{l1} - T_c$; $\Delta T_{l2} = T_{l2} - T_c$. When there is no distortion by scattered light of any heating curve obtained, the lateral heat flow and its transition in a well-isolated calorimeter can be disregarded or assumed to be uniform, and the one-dimensional solution for a sufficiently long sample pole, such as of length-to-width ratio 5 or greater, gives [9.8]:

$$T_\infty(z) = T_c + \frac{Q_{s2}\ell}{2\lambda_T A}(1-2z) + \frac{\Phi_0 \alpha \ell^2}{2\lambda_T A}\left(0.25 - z^2\right), \quad at \quad 0 < z < 0.5;$$
$$T_\infty(z) = T_c + \frac{Q_{s1}\ell}{2\lambda_T A}(1-2z) + \frac{\Phi_0 \alpha \ell^2}{2\lambda_T A}\left[0.25 - (z-1)^2\right], \quad at \quad 0.5 < z < 1. \tag{9.13}$$

For the ideal case in a vacuum of zero heat losses to the surroundings, two measurements of the temperature differences $(\Delta T_{l1}, \Delta T_{l2})$ are adequate to determine both surface heat sources as:

$$Q_{s1} = (3\Delta T_{l1} + \Delta T_{l2})(\lambda_T A/\ell); \quad Q_{s2} = (\Delta T_{l1} + 3\Delta T_{l2})(\lambda_T A/\ell). \tag{9.14}$$

At the steady-state condition, when impermanent terms of the heat equation are negligible, the temperature distribution along a sample pole should rise equivalently according to the following equation:

$$\frac{dT}{dt} = \frac{1}{V\rho_p c_p}\left(Q_{s1} + Q_{s2} + \alpha\ell\Phi_\tau \frac{1+n^2}{2n}\right), \tag{9.15}$$

where n is the relative refractive index of the sample. The static parabolic temperature profile is:

$$T_{par}(z) = \frac{(Q_{s1} + Q_{s2})\ell}{2\lambda_T A}\left[\left(z - \frac{q}{1+q}\right)^2 - \frac{q^2 - q + 1}{3(1+q)^2}\right], \tag{9.16}$$

where $q = Q_{s2}/Q_{s1}$ is the ratio of heat fluxes at front and back surfaces Q_{s1} and Q_{s2}. If the sample's properties vary along its length as $\alpha(z) = \bar{\alpha} + \tilde{\alpha}(z)$, the nonparabolic term in the temperature-distribution profile becomes [9.8]:

$$\tilde{\alpha}(z) = \left(\lambda_T A/\Phi_\tau\right)\left(2n/(1+n^2)\right)\left(\partial^2 T_{par}/\partial z^2\right).$$

The heat-transfer equations examined assume simultaneous measurements of the temperature changes along with radiant fluxes incident on and transmitted by a test sample. In studies of low bulk absorption losses, both end surfaces of the sample should be left uncoated since additional layers could affect properties of the heat distribution. To identify the internal flux of radiation Φ_a existing inside the test

sample for which the bulk absorption loss is studied, multiple reflections on its light-reflecting surfaces must be resolved for both adverse directions (see Fig. 9.3). The bidirectional internal flux Φ_Σ inside the plane-parallel sample with an equal surface reflectance ρ is given by:

$$\Phi_\Sigma = \Phi_0(1-\rho-\mathrm{a})\left(1+\alpha\ell\rho+(\alpha\ell\rho)^2+\cdots+(\alpha\ell\rho)^i\right), \tag{9.17}$$

where i is the tending-to-infinity number of reflections. Since interference in that case may only cause a spatial redistribution of the intensity profile, the bidirectional integrated flux $\bar{\Phi}$ in the sample is:

$$\bar{\Phi}_\Sigma = \frac{\Phi_0(1-\rho-\mathrm{a})\left(1-(\alpha\ell\rho)^i\right)}{1-\alpha\ell\rho} \underset{i\to\infty}{=} \frac{\Phi_0(1-\rho-\mathrm{a})}{1-\alpha\ell\rho} \underset{\alpha,a\to 0}{=} \Phi_0. \tag{9.18}$$

Similarly to relation (2.10) for the total flux inside a negligibly low absorbing translucent sphere, Eq. (9.18) does not contradict the law of conservation of energy. The equality underscores the sum of the averaged flux of all incident radiation redistributed inside such a nonabsorbing medium.

When measuring the flux Φ_τ transmitted by the test sample: $\Phi_\tau = \Phi_0(1-\rho)/(1+\rho)$ (see Eq. (1.106)), the total radiant flow consolidated within the bulk of the sample is:

$$\bar{\Phi}_\mathrm{a} = \Phi_0 = \Phi_\tau(1+\rho)/(1-\rho) = \Phi_\tau\left(1+\mathrm{n}^2\right)/(2\mathrm{n}). \tag{9.19}$$

The flux irradiating the first surface remains: $\Phi_1 = \Phi_0$, but the flux localized via the output surface is:

$$\begin{aligned}\bar{\Phi}_2 &= \Phi_0(1-\rho)+\Phi_0(1-\rho)\rho^2+\cdots = \Phi_0/(1+\rho)\\ &= (\Phi_0/2)(\mathrm{n}+1)^2/\left(\mathrm{n}^2+1\right) = \Phi_\tau(1+\mathrm{n})^2/(4\mathrm{n}).\end{aligned} \tag{9.20}$$

As a result, considering only a nonresonant length of the sample and not counting the interference redistribution of radiant intensity, the ratio of uneven energies of light at opposite sample ends is [9.2]:

$$\mathrm{Q_{s1}}/\mathrm{Q_{s2}} = 2\left(1+\mathrm{n}^2\right)/(1+\mathrm{n})^2. \tag{9.21}$$

Interference of coherent waves inside the sample of a resonant length makes the redistribution even sharper. Similarly to relation (3.122), the internal radiant flux for equal surface reflectances is:

$$\Phi_\Sigma = \Phi_0\frac{(1-\rho)}{1+\rho^2-2\rho\,\cos\,\delta} = \Phi_0\frac{(1-\rho)}{(1-\rho)^2+4\rho\,\sin^2(\delta/2)}. \tag{9.22}$$

The maximum and minimum magnitudes related to the incident and transmitted fluxes are:

$$\Phi_{\alpha,\max} = \Phi_0 \frac{1}{1-\rho} = \Phi_0 \frac{(1+n)^2}{4n} = \Phi_\tau \frac{(1+n^2)(1+n)^2}{8n^2};$$
$$\Phi_{\alpha,\min} = \Phi_0 \frac{1-\rho}{(1+\rho)^2} = \Phi_0 \frac{2n}{1+n^2} = \Phi_\tau. \tag{9.23}$$

For typical refractive index $n = 1.5$, the relationship between effective thermal sources, created by uniform bulk absorptance for nonresonant waves at two opposite sample surfaces, becomes: $\Phi_1 = \Phi_0 = \Phi_\tau\ 6.5/6; \Phi_2 = \Phi_\tau\ 6.25/6$. In the case when reflected waves are resonant, the maximum ratio for the glass sample having two identical surfaces is: $\Phi_{\alpha,\max}/\Phi_\tau \cong 9/8$. Therefore, a static temperature profile is always asymmetric around the center of an irradiated homogeneous sample and all the techniques analyzed likely require certain curve fitting to the entire transient process, predicted to be at the center of the sample rod, as well as verification of the temperature distribution along its axis.

An advanced system for calorimetric measurements of low absorption losses is depicted in Fig. 9.4. Three samples of the substance under test are placed in vacuum calorimeter 2 together [9.7]. The central sample is exposed by source 1, the second serves as a reference sample, and the third has a certified wire inside for calibration of all thermocouples: measurement couple 3 and reference couple 4. Using calorimeter 2 adds some complexity but allows one to reduce heat losses, while anticipating the presence of the surface absorption films. The time constants for the scattering and for the bulk and surface-bulk absorption can be changed from minutes to hours by the keeping camera observing the samples under a vacuum, or by injecting a gas, for example, pure helium. Such an interchange helps identify the best fit for the results obtained, making essential corrections for the thermal constants, used for computations of low absorption losses being measured. Utilizing a 100-mW laser at $\lambda = 647$ nm with the temperature in the vacuum calorimeter stabilized near ± 5 mK, the noise-level sensitivity to absorption losses was

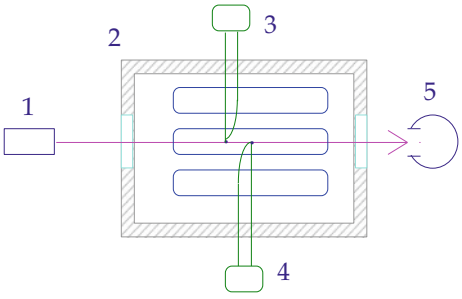

Fig. 9.4 Absorption-measurement setting: 1 – laser; 2 – calorimeter; 3,4 – thermocouples; 5 – photodetector

consistently maintained within ±2 dB/km. The measured absorption coefficients in two similar fused-quartz and synthetic-quartz rods were near 55 and 16 dB/km with approximately 10% error [9.7].

To achieve higher sensitivity to absorption losses, the sample under study can be positioned inside a laser cavity with a high Q-factor, where the internally circulating power could exceed the external one by a few orders of magnitude. If a sample with uncoated plane-parallel surfaces is inserted into such an active laser resonator, the correction factor for the internally absorbed power is still defined by Eq. (9.19), but is now related to the power that circulates inside the resonator. The effective number of reflections inside the entire laser cavity $m = 1/[1 - (1 - \rho - \mathsf{a})^2\rho_1 2\alpha\ell\rho_2]$ cannot be very high even for a close-to-unity product $\rho_1\rho_2$ of resonator mirror reflectances and low absorption losses a and $2\alpha\ell$ owing to the not eliminated surface reflectivity $\rho \cong 0.04$ of an uncoated glass or silica sample. Nevertheless, in one of the first calorimetric low-loss measurement experiments conducted inside a Nd:YAG laser cavity at $\lambda = 1.06$ μm, the absorption-loss sensitivity was estimated as reaching ±0.5 dB/km [9.2]. The lowest linear absorption coefficient for a Suprasil W1 fused silica sample, measured via the cooling curve (Eq. (9.6)) inside the laser resonator at P = 115 W, was nearly 2.3 ± 0.5 dB/km (see Fig. 9.5).

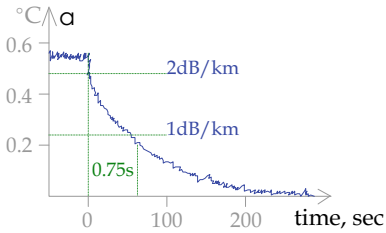

Fig. 9.5 An example of a temperature decline

Another way to increase the power density for bulk exposure is to focus a laser beam into a small region of the sample under test. The focusing decreases the negative effects of absorption losses and of the scattering for the sample surfaces situated in unfocused radiation, enabling the measurements to be performed in a small region of the sample bulk and thus the absorption coefficient to be sensed locally. When evaluating the initial thermal rise ΔT(t), the focusing reduces the requirements to long-term stability of the calorimeter. For the short-term stability on the level of ±0.001 K/min, the sensitivity to a low linear bulk absorption coefficient may reach 10^{-5}–10^{-6} cm^{-1} [9.7–9.9]. When the rising temperature slope illustrated in Fig. 9.6 was measured, the mean absorption coefficient in NaCl samples was resolved as being about $7 \cdot 10^{-6}$ cm^{-1} [9.9].

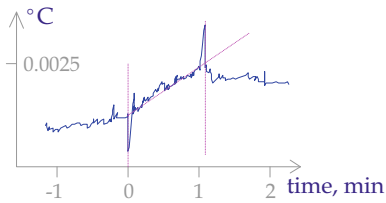

Fig. 9.6 An example of a rising temperature slope

Owing to certain difficulty in partitioning the surface and bulk losses when measuring absorption coefficients of low-loss materials, one may attempt to decisively isolate the contrary heat fluxes of the surfaces and of the bulk of the sample [9.10]. However, efforts such as thermal cooling of opposite sample surfaces, intended to eliminate both surface thermal sources Q_{s1} and Q_{s2} (see Eq. (9.13)), could cause unintended distortion of the measured temperature by creating a high thermal flow along the sample axis. Using a metal foil or blackening the sample's lateral surface prevents the extra influence of scattering, but increases the contrast of the measured and computed temperatures and complicates the measurement process.

A combination of adiabatic and isothermal techniques can also be utilized to provide the essential comparison between loss measurements in a relatively short glass preform and in a considerably longer fiber being drawn from it [9.11]. The adiabatic technique allows one to separate the bulk absorption from the surface absorption by maintaining a high ratio between the sample length and its diameter: usually $\gamma \geq 10{:}1$. Since that ratio for any fiber is commonly much higher, such as much more than 100:1, the heating process along this fiber axis becomes strongly nonlinear, and the adiabatic technique will not be applicable. Indeed, the long length of the fiber in the isothermal technique helps to isolate bulk and surface losses. In confirming experiments, a preform of a silver halide crystal and fiber a drawn from it were placed in a calorimeter as one shown in Fig. 9.4. Every sample was irradiated by a continuous-wave (cw) CO_2 laser beam focused into its central point. The magnitude of the lowest detected bulk absorption coefficient for the preform was affected by a given molar composition, reaching nearly $1 \cdot 10^{-4}$ cm^{-1} at $\lambda = 10.6$ μm. The impact of the surface absorption was highly influenced by the surface quality of a given sample. After chemical etching of appropriately polished surfaces, the magnitude of the bulk absorptance for the same preform decreased to about $5 \cdot 10^{-5}$ cm^{-1}. The values of the absorption coefficients of the drawn fibers tested were significantly higher, owing to likely crystal lattice defects and imperfections during the fiber extrusion process used [9.11].

A low-loss fiber designed for mid-IR radiation can be used by itself as a transfer medium for noncontact calorimetry [9.18], as owing to Kirchhoff's law at thermal equilibrium the absorptance of a sample being measured equals its emissivity. One difficulty is that the small temperature increase due to low absorptance results in efficient emittance in the 8–12-μm wavelength range. In the conforming experiments [9.18], one polished end face of a silver halide fiber of 0.45-mm diameter at 55° effective collection angle was placed 0.5 mm or less from a quartz rod, which also had a calibrated thermocouple attached to its surface, all enclosed in a calorimeter. The experimentally detected thermal rise–decay curves obtained via the fiber and the thermocouple were quite similar with the measured absorption factor being $4 \cdot 10^{-3}$.

9.1.1 Local Absorptance

The techniques for local absorptance measurements are virtually similar to those used for detection of the linear absorption coefficient of a sample bulk. The only exception consists in the contrasting thermal properties of the massive bulk and any thin layer under study, as a purely unknown substance. Equations (9.9)–(9.13) are also applicable to the notion of separation of losses from opposite sample surfaces and a substrate in between. A schematic layout for space-resolving measurements for the local absorption loss is shown in Fig. 9.7a. Three thermodetectors are attached to the lateral surface of a sample – first, near its front surface with the thin film studied at the middle of the surface, the second, to the center, and the third, to another surface. When the absorptance of the bulk and two surfaces are not equivalent: $a_1 \neq a_2 \neq \alpha\ell$, each measured temperature profile is different for each thermocouple.

Figure 9.7b exemplifies differentiation of typical time decays [9.12]. During an initial time frame t, when the laser radiation heating is started and abruptly turned off: $t_1 < t < t_2$ (Eqs. (9.10), (9.11)), the first thermocouple reacts only to the thermal energy absorbed in the coating and in the front surface of the sample. The second thermocouple separates the sequential thermal flows, respectively proportional to: $\alpha\ell$, and then to: $a_1 + \alpha\ell + a_2$. The third thermodetector distinguishes three consecutive terms: from the coating on the front surface, from the bulk, which in the instance illustrated is lower than the thermal fluxes from surfaces, and from the back surface. The temperature changes were measured for a $20 \cdot 20 \cdot 130$ mm^3 KCl sample, having on its first surface a quarter-wave thick PbF_2 film for test wavelength $\lambda = 5.3$ μm. The bulk absorption coefficient determined was $5 \cdot 10^{-6}$ cm^{-1}, the absorptance factor of the uncoated sample surface was $3 \cdot 10^{-3}$ cm^{-1}, and the absorptance of the coated surface was $0.9 \cdot 10^{-3}$ cm^{-1} [9.12].

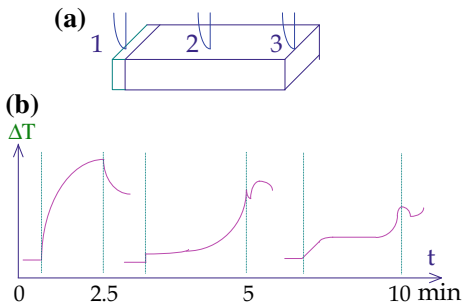

Fig. 9.7 Longitudinal profile of sample-temperature change

In contrast, when determining the local absorptance of a thin dielectric film deposited on a transparent substrate prepared as a large disk with a radius about 8–10 times greater than its thickness, the temperature distribution across that disk is certainly nonuniform. The reaction of a thermocouple placed on the sample's lateral surface is proportional to the distance between the points of irradiation and measurement. The nonidentity factor of the two absorptances: $\kappa = a_{\text{true}}/a_{\text{calk}}$, as a ratio of the true and the actually measured absorption factors, depends on the temperature

conductivity of the substrate and of the surroundings, and on the distribution of radiation energy in a cross section of the incident beam. When measuring a substance having low temperature conductivity, while withstanding an intensive heat interchange with the surroundings, the true-to-measured difference can be quite significant [9.13].

To reduce a potential nonidentity of the measured and true values of absorptance, an increase of temperature conductivity between distant points of irradiation and measurement may be required. A thin metal film deposited onto the coating to be analyzed around its irradiation zone and used as a thermistor can serve the purpose. A temperature gradient caused by absorption in the coating exposes a high-conducting film and changes its conductivity R to $\Delta R = \Delta T \cdot K_T \cdot R$, where K_T is the temperature factor for the resistance. If the electric current is measured via the resistor, making it concurrently a thermometer, the heat-flow equation for the sample at thermal equilibrium is [9.14]:

$$C(\partial T/\partial t) + G\Delta T = \Phi_0 \alpha + (\partial P/\partial t)\Delta T. \tag{9.24}$$

Here G is the effective thermal conductance of dielectric coating–metal film; $P = J^2R = G(T_e - T_0)$ is the power dissipated by the electric current which heated the film up from initial temperature T_0 to final temperature T_e, and α is the local absorptance of the sample to be determined. Taking into account the transition of the thermal conductance: $G_e = G_0 - (\partial P/\partial t)$, one can transform Eq. (9.24) to:

$$\Delta T = (\Phi_0 \alpha / G_e)[1 - \exp(-t \cdot G_e / G_0)]. \tag{9.25}$$

The measured temperature conductivity of the ZnS–ThF_4 film system was predetermined as the half-period magnitude $G_e = C \cdot \ln(2/t_{0.5})$ of the temperature changes from T_0 to $T_0 + \Delta T$ by a known electric current [9.14]. The total absorptance of both layers studied was considered to be:

$$\alpha = 2\pi n_0 (\kappa_1 + \kappa_2) / (n_1^2 - n_2^2), \tag{9.26}$$

where $n_1 - ik_1$ and $n_2 - ik_2$ are the complex refractive indices of respective layers (see Eqs. (1.86a,b)) and n_0 is the refractive index of the substrate. The extinction coefficient and absorptance in ZnS, measured in a vacuum by a thin gold resistor assuming a negligible loss in ThF_4, were nearly $k = 1 \cdot 10^{-4}$ and $\alpha = 13$ cm^{-1}.

Applying a similar measurement technique and using a compensating thermometer, one can make extra corrections for temperature fluctuations (Fig. 9.8). An additional thermometer is deployed similarly to a regular resistance thermometer, but is placed onto the test substrate without any metal electrode film. An extra bridge circuit between thermal detectors minimizes temperature drifts and heating effects of the bias current. The lowest recorded temperature rise of a fused-silica substrate being measured at 0.001 °C temperature resolution in a $1 \cdot 10^{-3}$-mbar vacuum was 0.014 °C. That temperature rise corresponds to the absorption coefficient near 0.032 cm^{-1} [9.15].

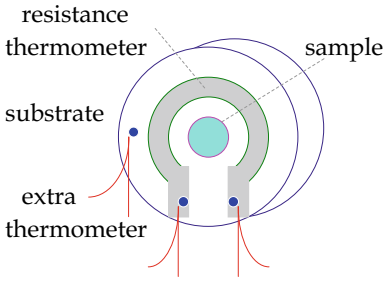

Fig. 9.8 Layout of the dual thermometer

Another way to reduce potential dissimilarity of the true and the measured temperature is to use a compensation technique isolating a nonuniformly heated sample from its environment [9.16]. For the isolation the sample in an isolated camera was placed in a high vacuum. The temperature of the camera was regulated via negative feedback to changing temperature of the sample substrate. Since the temperature gradient with these measures was minimal, the influence of temperature conductivity of the sample and substrate was eliminated without extra correction factors. At $\Delta T \leq 2$ mK detectable temperature difference and $6.7 \cdot 10^{-5}$-Pa pressure, the technique's repeatability was about 10^{-4}–10^{-5} [9.16]. The lowest value of measured absorptance corresponding to traces of water in the substrate's surfaces and bulk reached $(1-4) \cdot 10^{-4}$.

For measurements of absorptance in metals, a uniform temperature distribution across the irradiated sample is achieved much more quickly owing to the high thermal conductivity of a metal. Thus, if an electrically calibrated resistor is used as a matching thermal source inserted into or contacting the sample, calibration of the calorimeter becomes quite simple (Fig. 9.9). The measurement process consists of two steps. First, the sample is directly exposed to incident flux Φ_0 and the measurement of absorbed flux Φ_a by a thermocouple thermometer coupled to the sample is made. Then, electrical dissipation of the same power: $P = \Phi_a$, is accomplished via a calibrated resistor, matching the first thermometer reading. The ratio of the two readings at a constant temperature: $(P/\Phi_0)_{T=const}$, provides the factual mirror absorptance [9.17].

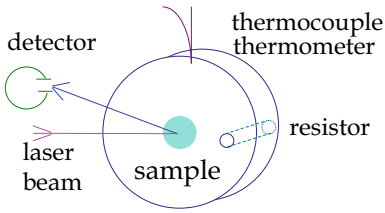

Fig. 9.9 Absorption study for a metal sample

Since metal mirrors are opaque, only reflected and scattered, but not transmitted radiation can be measured simultaneously with the mirror temperature. For a low-scattering mirror, the scattered flux Φ_σ cannot be easily counted without specific

scattering measurements. With the assumption of low scattering: $\Phi_\sigma \to 0$, determination of the total power Φ_0 incident on the mirror can be made by registering the reflected Φ_ρ and absorbed Φ_a fluxes with the accuracy of omitted scattering factor Φ_σ. When the reflected flux Φ_ρ is measured by a blackbody thermodetector of known absorptance factor α_b, the mirror absorptance α to be measured becomes:

$$\alpha = \frac{\Phi_a}{\Phi_b(1/a_b) + \Phi_a} = \frac{P}{\Phi_\rho a_b^{-1} + P}, \tag{9.27}$$

where the factor $1/a_b$ relates to the actual absorptivity of the blackbody detector, being $a_b \neq 1.0$. When any practical heat flow from the irradiated sample into its surroundings is prevented by using a well-insulated vacuum chamber with near $\pm 10^{-3}$ K temperature stability, the prospective sensitivity to the low absorptance of some comparatively small metal mirror in such a chamber is very similar to the sensitivity to the absorptance being measured for a linear bulk absorption coefficient $\alpha\ell$ in a transparent crystal. The factual sensitivity to the local absorptance in the experiments performed was approximately 1% of the laser power used, with the minimum change of the detector signal being near 0.4% [9.17].

Finally, when measuring absorptance in tissues, none of calorimetric techniques may be appropriate; therefore, reflection, rather than transmission, spectroscopy can be used instead, such as low-coherence interferometry [9.112]. Similarly to the scanning-mirror interferometry (Chap. 8) and optical coherence tomography systems (see Sect. 9.2), a combination of the scanning Michelson interferometer with a supercontinuum light source having 455–680-nm bandwidth was utilized. A tissue sample and a scanning interferometer mirror were on two motorized stages controlling the penetration depth of sample irradiation: 0–2 mm, in 27-μm steps. Absorption spectrums were derived from the measured scattering-plus-absorption ones versus the spectrums of only scattering by polystyrene spheres with $\pm 0.5\text{-mm}^{-1}$ accuracy [9.122]. Contributions of bulk-absorption and surface-scattering losses can be resolved calorimetrically by measuring multiple samples of varying length, presuming scattering losses not to change [9.123].

9.2 Thermal-Lensing, Photothermal, and Photoacoustic Techniques

The analyzed calorimetric methods for measurements of absorption loss are based on correlated long-term temperature changes of an irradiated sample under test. Such methods cannot be equally applied to liquids and gases since their mobility diminishes the characteristic time intervals of the temperature changes to very short periods of time. That unstable predicament of liquids and gases also causes the subsequent appearance of convectional heat fluxes and acoustic waves. To localize phenomena of short-term energy transitions conditioned by absorption losses observable within short periods of time, one may apply instantaneous optical

methods for detection of fast phenomena, which should have much quicker response times than the thermal techniques.

Any steady-state rise of temperature of a homogeneous object irradiated by radiation which is absorbed should resemble the distribution profile for the intensity of incident light. That profile modifies the refractive index of the object. As a result, commensurate changes of refraction can be functionally linked to a linear absorption coefficient of the substance of which the irradiated object is formed. The light-distorted refraction can cause multiple effects: angular deflection of an oblique beam from its propagation direction, phase shift for a beam of radiation transmitted by the object by a wave normal owing to changes of its path length, and even light-induced birefringence in the irradiated substrate. These effects may be sensed by measuring the deflection of light beams and disregarding the subsequent, but delayed heat transfer. However, in such cases the procedures for measurements of absorption losses become indirect, since not the absorption coefficient but the alteration of the object's refraction, created by the absorbed energy and power, is registered. Consequently, for any quantitative measurements of the absorptance, some reference substance with a definitively known linear absorption coefficient similar to the substance under study is required. These secondary thermo-optic effects induced by radiation can be primarily observed in solids or liquids, but the temperature coefficient of the refractive index as the coefficient of expansion is higher in liquids than in solids, and thus thermally induced effects are broadly used for liquid specimens as well as for solid ones [9.19].

9.2.1 Thermal Lensing

If a laser beam with a Gaussian intensity distribution profile: $I(\mathbf{r}) = I_0 \exp(-r^2/r_0^2)$, irradiates a sample of refractive index n_0 and unequal-to-zero bulk linear absorption coefficient α along its length ℓ, the dissipation of the thermal energy absorbed by the sample is (see Sect. 9.1):

$$\mathrm{Q}(\mathbf{r})\mathrm{dr} = \frac{2\alpha\ell\Phi_{int}}{\pi r_0^2} \exp\left(-\frac{2\mathrm{r}^2}{\mathrm{r}_0^2}\right) 2\pi\mathbf{r}dr. \tag{9.28}$$

Here Φ_{int} is the flux incident on the sample and r_0 is the effective radius of the amplitude for the irradiating field decreasing e times from its maximum value across the beam axis. For a liquid sample in a transparent cuvette, the physical path length of light propagation does not change owing to heating since fluids expand transversely; hence, the resultant temperature gradient ΔT for transverse coordinate r of the sample bulk is [9.21]:

$$\Delta T \cong \frac{const_1 \cdot \alpha\ell\Phi_{int}}{\pi\lambda_T}\left(const_2 - \frac{2r^2}{r_0^2}\right), \tag{9.29}$$

causing near-parabolic distortion of refractive index n as a time function of the temperature gradient:

$$n(\mathbf{r},t) = n_0 + (\partial n/\partial T)\Delta T(\mathbf{r},t). \tag{9.30}$$

The density profile formed by incident radiation changes the direction of transmitted light, acting as a divergent lens with focal length F. The optical power F^{-1} of the lens at absorbed flux $\Phi_\alpha \cong \alpha\ell\Phi_{\mathrm{int}}$ is inversely proportional to the thermal conductivity λ_T of the liquid substance and to the effective cross section of the beam [9.19]:

$$1/F = \Phi_\alpha(\partial n/\partial T)/\left\{\pi r_0^2\lambda_T n_0[1 + t_c/(2t)]\right\}, \tag{9.31}$$

where $t_c = r_0^2\rho_p c_p/(4\lambda_T)$ is the characteristic time interval for the liquid thermal lens to appear.

At distances $\mathrm{z} \gg \mathrm{z}_0$ in the far-field zone, the thermal lens converts the radius $r(\mathrm{z})$ of the effective cross section of the beam and the curvature R of its wave front by dependencies [2.1]:

$$r_0(z) = r_{o,\min}^2\left(1 + z^2/z_0^2\right); \quad R = z\left(1 + z_0^2/z^2\right). \tag{9.32}$$

Both parameters are defined by the minimal radius $r_{o,\min}^2$ of the caustic region and the distance $z_0 = \pi r_{o,\min}^2 n/\lambda$ to the caustic plane at the initial coordinate $z = 0$. As experimentally confirmed in [9.20], in the far-field zone a change of the beam radius $r_0 = \lambda z/(\pi r_{0\min} n)$ is instantly correlated to its divergence $\Theta_{1/2} \cong \lambda/(\pi r_{0\min} n)$ and, thus, to the respective redistribution of the sample density:

$$\Delta r_0/r_0 = -\Delta\Theta/\{2[1 + t_c/(2t)]\} = -\Phi_\alpha(\partial n/\partial T)/[(\lambda\lambda_T)(2 + t_c/t)]. \tag{9.33}$$

The decrease or increase of the beam's cross section due to thermal lensing causes an inversely proportional change of the irradiance created by a divergent astigmatic laser beam according to Eq. (3.71). At $\Delta\Theta \ll \pi$ and $\mathrm{r}_0 \gg \mathrm{r}_{0\min}$, the on-axis beam intensity becomes approximately:

$$I_0(t = 0)/I_0(t = \infty) = 1 - \Delta\Theta + \Delta\Theta^2/2. \tag{9.34}$$

As a result, the absorption coefficient of the liquid substance under study can be identified as:

$$\alpha = -[\Delta I_0/I_0(t = \infty)](\lambda\lambda_T)/[\Phi_{int}\ell(\partial n/\partial T)], \tag{9.35}$$

where $\Delta I_0 = I_0(t = 0) - I_0(t = \infty)$ is the maximum exchange of the beam intensity from the start of laser action to full relaxation. The temporal dependence of the beam intensity may be expressed as [9.20]:

$$I_0(t) = I_0(t=0)\Big/\left\{1 - \Theta\Big/[1 + t_c/(2t)] + (\Theta^2/2)\Big/[1 + t_c/(2t)]^2\right\}. \quad (9.36)$$

The validity of Eqs. (9.34)–(9.36), derived specifically for liquids, is conditioned, first, by the absence of heat transfer due to convection. That holds true at $\alpha\ell\Phi_{\text{int}} \ll 32K_1\lambda_T^2/\left(K_2 g C r_0^3\right)$, where K_1, K_2, and C are the viscosity, the thermal expansion, and the heat capacity of the liquid and g is the free fall acceleration. If $\Phi_{\text{int}} \leq 100$ mW, the convection is prevented for magnitudes of $\alpha\ell < 10^{-1}$. A stronger restriction is set by likely diffraction of radiation on density fluctuations arising at the time of measurements. Therefore, all changes of $\Delta\Theta$ should not exceed the diffraction limit, identified by the minimal radius of a Gaussian laser beam: $\Delta\Theta_{\min} \cong \Phi_\alpha(\partial n/\partial T)/(1.6\pi\lambda_T r_0) < \lambda/(\pi r_{0\min})$. In other words, any change of the optical path length caused by the center or the edge of the thermal lens:

$$\Delta\ell = [\Phi_\alpha(\partial n/\partial T)/(2\pi\lambda_T)] \int_0^{r_0} \left[1 - \exp\left(-2r^2/r_0^2\right)\right](dr/r), \quad (9.37)$$

must be smaller than the diffraction limit: 0.22λ, for wavelength λ which evaluates such a profile.

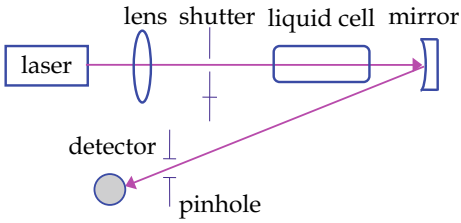

Fig. 9.10 Absorption-loss measurement in liquids

The typical layout of absorption measurement by this *thermo-optic technique* is illustrated in Fig. 9.10. The test liquid in the cell of length $\ell \gg z_0$ and the lens are placed at confocal distances $z = \pi r_{0,\min}^2/\lambda$ around the caustic region of coordinate z_0. A detector behind a 0.1-mm pinhole is installed in the far-field zone. The system's sensitivity to absorption losses depends on the properties of the liquid and fluctuations of the power of radiation: $\alpha_{\min} \cong \Delta\Phi\lambda\lambda_T/[\ell(\partial n/\partial T)]$. The time functions depicted in Fig. 9.11 are demonstrative of $\Delta\Theta = -0.01$ for the solid line and $\Delta\Theta = -0.3$ for the dotted one, both for low-absorptivity carbon tetrachloride CCl_4. The latter line represents the measured absorptance $\alpha_{CCl_4} = 5.7 \cdot 10^{-5}$ cm^{-1}. The lowest detected absorption coefficient for carbon tetrachloride liquid was $\alpha = 5.5 \cdot 10^{-6}$ cm^{-1} at $\lambda = 632.8$ nm, $\Phi_0 = 0.01$ W, and $\ell = 0.1$ m [9.20].

Similarly, a thermal lens can be induced inside an active laser resonator to enhance the measurement sensitivity to intracavity absorption losses via multiple light interactions. The loss sensitivity becomes proportional to the focal length of the thermal lens at a given power sensed as spot diameters at two resonator mirrors of the propagating beam whose divergence is caused by the lens [9.19, 9.22].

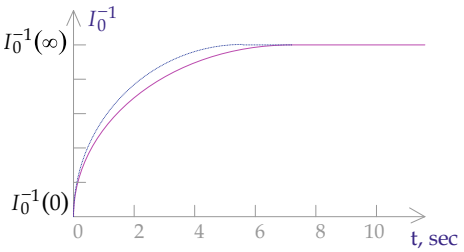

Fig. 9.11 Example of thermooptic refraction in liquid

A schematic for the active-resonator technique is shown in Fig. 9.12. The active laser resonator with a test sample inside oscillates in its fundamental longitudinal mode via irises I_1 and I_2 with the power in each spot section modified by thermal lens TL on every resonator mirror being measured by power meter PM via scanning system SS. On the initiation of a single thermal lens in the resonator, the thermal phenomena that occur may be treated as a two-lens plus two-mirror set with a thin thermal lens making a pair of two mirrors and lenses [9.22]. For the empty resonator of two spherical mirrors with finite apertures, the major resonator parameters: diffraction losses, resonant frequencies, and mode diameters – are given by the Fresnel number N_{Fi} and stability factors G_1 and G_2 [II.5]:

$$N_{\mathrm{Fi}} = (a_1 a_2)/(\lambda d); \quad G_1 = (1 - d/r_1)(a_1/a_2); \quad G_2 = (1 - d/r_2)(a_2/a_1). \quad (9.38)$$

For symmetrical lenses L_1 and L_2 of focal lengths f_1 and f_2 placed in the resonator, as shown in Fig. 9.12:

$$\begin{aligned} N_{\mathrm{Fi}} &= (a_1 a_2)/(\lambda d_{12}) \approx (a_1 a_2)/(\lambda d); \\ G_1 &\approx (1 - (d/r_1)(1 + r_1/f_1))(a_1/a_2); \\ G_2 &\approx (1 - (d/r_2)(1 + r_2/f_2))(a_2/a_1), \end{aligned} \quad (9.39)$$

the radii of waists ω_1 and ω_2 of the respective lasing beam spots on two mirrors of diameters $2a_1$ and $2a_2$ become:

$$\omega_1 \omega_2 = (d\lambda/\pi)/\sqrt{1 - G_1 G_2}; \quad \omega_1/\omega_2 = (a_1/a_2)\sqrt{G_2/G_1}. \quad (9.40)$$

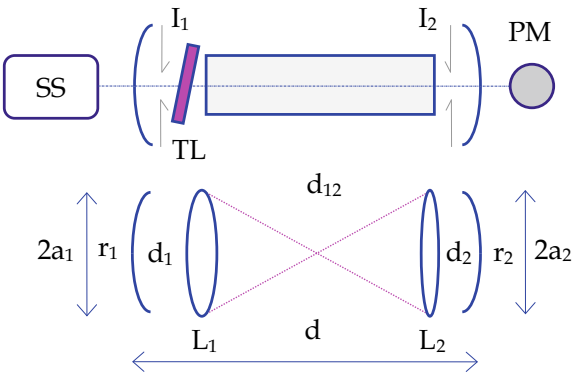

Fig. 9.12 Thermal lens inside an active laser resonator

For a laser cavity having a thin thermal lens L_3 in a liquid inside the resonator between two lenses L_1 and L_2, located in the liquid cell walls, Eqs. (9.39) with the thermal lens located near one of two existing lenses converge to [9.22]:

$$N \cong (a_1 a_2)/(\lambda d); \quad G_1 \cong (1 - (d/r_1)(1 + r_1/f_{12}))(a_1/a_2);$$
$$G_2 \cong (1 - (d/r_2)(1 + r_2/f_3))(a_2/a_1), \tag{9.41}$$

where f_3 is the focal length of thermal lens L_3, and focal length f_{12} is given by: $(1/f_{12}) = (1/f_1) + (1/f_2) - d_{12}/(f_1 f_2)$. Hence, for the lenses in cell windows the measurements of spot sizes ω_1 and ω_2 need to be obtained at both resonator mirrors, solving the system of Eqs. (9.41) and determining focal length f_3. The procedure is more convenient when the thermal lens is the only lens in the cavity, requiring spot-size detection only on one mirror (Fig. 9.13). Lens power f_{TL}^{-1} can be acquired from the location of mirror image r_1':

$$1/f_{TL} \approx 1/(d_{TL} - r_1) + 1/(r_1' - d_{TL}), \tag{9.42}$$

if curvature radius r_1' is measured via minimal image size $2\omega_0$ at distance z_1 from the beam's waist:

$$\omega_0 = \omega_2 \Big/ \sqrt{1 + (\pi\omega_2^2/\lambda r_2)^2}; \quad z_1 = d - r_2 \Big/ \left(1 + \left(\lambda r_2/\pi\omega_2^2\right)\right). \tag{9.43}$$

The measurement sensitivity for spot size ω_2 versus thermal lens power f_{TL}^{-1} is defined as [II.5, 9.22]:

$$\omega_2^2 = const \cdot \sqrt{(G_1 - r_1/f_1)/G_2}; \quad \left(\partial\omega_2^2/\partial(1/f_1)\right) = const \cdot \sqrt{G_2(G_1 - r_1/f_1)}, \tag{9.44}$$

with a tendency to become largest for the resonator confocal geometry at $G_2 \to 0$ or $G_1 \to r_1/f_1$. However, improving the sensitivity to thermal lensing enhances other active cavity factors affecting measurement results, such as optical inhomogeneity in a laser gaseous discharge, thermal lenses in windows and walls of a liquid cell, a laser tube guiding, and retroreflections of propagating radiation, especially for higher-order modes and resonator apertures – which are all lower at a far-from-confocal configuration. Furthermore, the approximation of the perfect parabolic refractive-index distribution describes the thermal lens behavior, but is

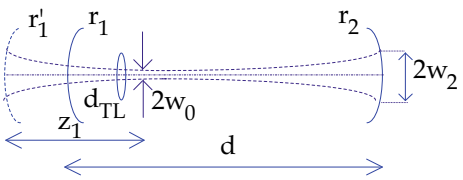

Fig. 9.13 Thin thermal lens detection

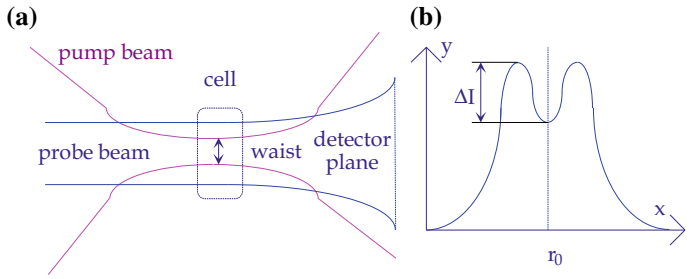

Fig. 9.14 Fresnel diffraction on a pulsed thermal lens

not quantitatively accurate without counting the imperfect lens profile, as well as the resulting aberrations and lens- and pinhole-induced diffraction [9.23–9.25].

A combined dual-beam sensing approach is based on near-field diffraction on a thermal lens enforced by a pulsed pump beam creating a spatial phase modulation, further detected as a dip in the radial intensity profile of an also pulsed probe beam [9.26]. Figure 9.14 depicts the pumping and probing concept, and illustrates an example of the resulting dip in the probe-intensity profile. In Fig. 9.14a, the pump beam is tightly focused into a cell, filled with a liquid sample under study, initiating the thermal lens, whose radial dimensions are near 1 order of magnitude smaller than those of the probe beam. As a result, the probe beam is defocused while having a dip (Fig. 9.14b) centered by the thermal lens with dip intensity I proportional to the liquid's absorptance $\alpha\ell$:

$$\alpha\ell \rightarrow \Delta I(t)/I(t) = \left(I_{r=0,t=\infty} - I_{r=0,t}\right)/I_{r=0,t=\infty}. \tag{9.45}$$

Here α and ℓ are the linear absorption coefficient of the liquid sample and the length of the cell (see Eq. (II.14)), r is the radial coordinate, and the time instance $t = \infty$ corresponds to the time when the thermal gradient has completely vanished after the pulsed excitation when the focal length of the lens is equal to infinity. The maximal thermal lens is obtained at the time instance $t = 0$ right after the excitation, since the dissipated thermal energy takes time to diffuse from the center spot. Such a pulsed thermal lens detection technique is based on the transient intensity measurements and does not require far-field observation, thus being less susceptible to alignment instabilities or model imperfections [9.26].

9.2.2 Photothermal Deflection

When pumping-laser light is absorbed by a medium in the presence of fast-quenching collisions, most of the light energy is converted to translational–rotational modes of the medium's molecules and the laser-irradiated region is heated. This results in a change in the refractive index of that region, which can be

monitored by weaker-intensity laser probe light. In fluids, when the medium's refractive index expands in one direction, having a nonzero curvature, the liquid acts as a lens, changing the shape of the transmitted probe beam. As seen in the previous section, that effect can be detected as a change of the intensity of a probe beam passing via a thermal distortion. A resultant nonuniform refractive index for pump-beam absorption may be detected by a photothermal deflection of a probe beam interacting with the medium or its surroundings. A photothermal outcome can also be sensed by placing the medium in an interferometer or a multiple-reflection cavity. The refractive index change would cause a fringe shift to be sensed as an intensity change of the central fringe, creating a photothermal phase-shift or phase variation. A nonuniform sample expansion can also be detected via its thermally induced birefringence.

Photothermal deflection spectroscopy can be also used as a collinear technique when the refraction gradient is created and probed via the absorbing sample, and as a transverse method when the probing is made via a thin layer adjacent to the sample, also called mirage technique; the latter can be used for any opaque materials or samples of pure optical quality [9.27, 9.28]. Figure 9.15 illustrates excitation by a pump laser beam, causing a change of refractive index in the heated region of an absorbing sample, and also depicts the collinear probe beam deflection, as well as some relatively oblique deflection for the transverse probe beam, sensing a gradient for modified index of refraction in the thin border-layer adjacent to the sample surface.

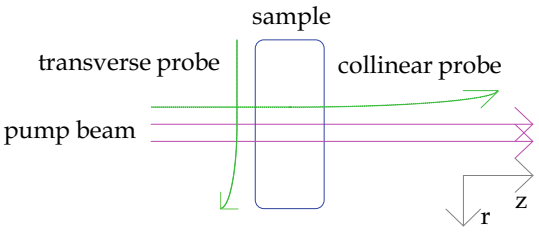

Fig. 9.15 Photothermal deflection

Considering the absorbing sample being an infinitely wide in the radial direction to irradiation with the probe beam focused in a smaller spot than the pump beam, oscillating at frequency ω in the absorbing medium, and while neglecting the acoustic-wave effects and presuming thermal conductivity of the sample to be low, the propagation-integrated temperature rise T above ambient for infinitely-wide sample at distance r, separating the maxima intensity of the pump and probe beams, becomes [9.28, 9.55]:

$$\int_0^{\ell} dz T_{sample}(\vec{r},t) = \left(\Phi_0(1-\exp(-\alpha\ell))\Big/\left(2\pi^2 r_0^2 i\omega\left(\rho_p c_p\right)_{sample}\right)\right) \times \exp\left(-2r^2/r_0^2\right)\exp(i\omega t) + const. \tag{9.46}$$

For the thermal conductivity or the thermal diffusion length λ_T (see Sect. 9.1) being much smaller than the probe-beam radius r_0, the temperature distribution follows the beam profile, as predicted by Eq. (9.46), owing to absent thermal diffusion. If the thermal diffusion length λ_T is much greater than the beam's waist $2r_0$, the temperature gradient reduces to [9.28]:

$$\int_0^{\ell} dzT_{sample}(\vec{r},t) = \left(\Phi_0(1-\exp(-\alpha\ell))/\left(2\pi^2 r\lambda_{T,sample}\right)\right)\left(1-\exp\left(-2r^2/r_0^2\right)\right) \times \exp(i\omega t) + const, \tag{9.47}$$

and that temperature distribution expands beyond the pump beam's profile at low modulation frequencies, since at high frequencies the on-axis temperature decreases as 1/ω. Equations (9.46) and (9.47) highlight the fact that a thermal deflection study probes the gradient of temperature, opposite to conventional thermal lensing techniques, which probe the gradient of curvatures.

As described by Eqs. (9.46) and (9.47), when a thin sample is irradiated by either intensity-modulated or position-modulated pump light, time- or frequency-dependent changes of the temperature of the sample's medium, registered by a sensitive synchronous spatial detector, can be distinguished at two limits: high-frequency modulation in a low-thermal-conductivity medium and low-frequency modulation in a high-thermal-conductivity medium. If the thermal diffusion length λ_T in the medium is much smaller than the radius r_0 of the cross section of a Gaussian pump laser beam, the time-modulated deflection angle φ of the probe beam at an angular modulation frequency ω of pumping light becomes [9.27]:

$$\varphi \underset{\lambda_T \ll r_0}{=} (dn/dT)\left(\Phi/\omega\rho_p c_p \pi^2 r_0^2\right)[1-\exp(-\alpha\ell)]\left[-2\left(x_m/r_0^2\right)\exp\left(-x_m^2/r_0^2\right)\right]. \tag{9.48}$$

Here x_m is the separation length of the intensity maxima for the pump and probe beams and Φ is the pump-beam power. For a low sample absorptance: $\alpha\ell \leq 2$, the deflection is proportional to the total loss $\alpha\ell$ and to pump power Φ, and is inversely proportional to modulation frequency ω. If the thermal diffusion length λ_T is much larger than the beam radius r_0 and if the modulation frequency ω is relatively low, the magnitude of the deflection angle φ is virtually independent of ω and is close to:

$$\varphi \underset{\lambda_T \gg r_0}{=} (dn/dT)\left(\Phi/\lambda_T \pi^2 x_m\right)[1-\exp(-\alpha\ell)]\left[1-\exp\left(-x_m^2/r_0^2\right)\right]. \tag{9.49}$$

One version of the collinear technique for probing of radial deflection of radiation [9.29] is shown in Fig. 9.16. A pump beam from a tunable dye laser 1 is intensity-modulated by acousto-optic modulator AOM and focused into thin layer 4 of a low-absorbing coating stack made on a presumably nonabsorbing substrate. The probe beam of He–Ne laser 2 is directly focused to an area of the maximum

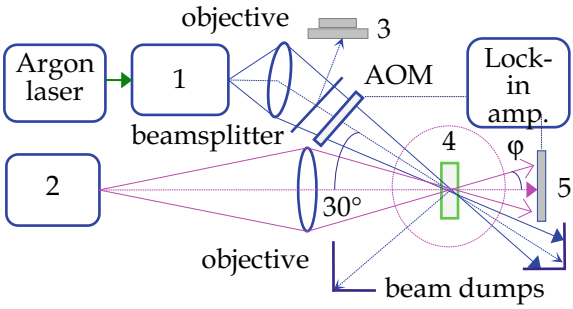

Fig. 9.16 Sensing transverse photothermal deflection

thermal gradient. Position sensor 5 and power meter 3 sense the power parameters of polarized pump and probe beams. Depending on the lock-in correlation of the thermal conductivities of the coating and the substrate as functions of the modulation frequency ω, one can optimize the area of the heated region to correlate with the absorption coefficient of the sample being studied. The estimated highest noise-level sensitivity of the system was near $2 \cdot 10^{-7}$. Experimentally determined [9.28] absorption coefficients with transverse probing for a 0.7% solution of benzene in CCl_4 were between $2.7 \cdot 10^{-3}$ and $1.5 \cdot 10^{-4}$ with a threshold of $1 \cdot 10^{-5}$. For the collinear probing depicted in Fig. 9.16, designed to increase sensitivity and simplify alignment, the repeatability of measurements for the absorption coefficients studied in various optical coatings and ranging from $6 \cdot 10^{-3}$ to 10^{-1} was not better than ±20% at the estimated $1.10 \cdot 10^{-6}$ noise level for 50 mW of pump power. Since every photothermal deflection result was obtained by measuring the deflection angle φ, while presuming proportionality of angle to absorptance $\alpha = \text{const} \cdot \varphi$, which depends on many factors (alignment and geometry of the beams, modulation frequency, optical and thermal properties of the substrate and coating layers), every substrate was calibrated by direct spectrophotometric measurements. With use of a 100-mW dye laser at $\lambda = 570 - 640$ nm for a stable high-purity glass sample, the repeatability of absorption mapping of a deeply polished glass surface reached $(4 - 6) \cdot 10^{-5}$ [9.29]. The technique is applicable for relative absorption mapping, reaching nearly $1 \cdot 10^{-6}$ sensitivity [9.29, 9.32].

As follows from Eqs. (9.46) and (9.47), enhancements in measurement sensitivity can be gained by position-modulated pumping at relatively low frequency ω when the probe beam is deflected on density gradients created by frequency-dependent changes of the temperature, and thus of the refractive index in the absorbing substance. The aim of such an approach is to increase the sensitivity to thermal deflection by synchronous detection of density modulations occurring in the proximity of a small irradiated spot either in the sample of a low-absorbing substance itself or in any adjacent layer. By observing alterations of the beam location on a sensitive spatial detector, one can relate the beam deflection amplitude to the sample's linear absorption coefficient. Temperature and refractive index gradients in coatings, gases, solids, and liquids are substantial enough to expect high sensitivity to absorption losses.

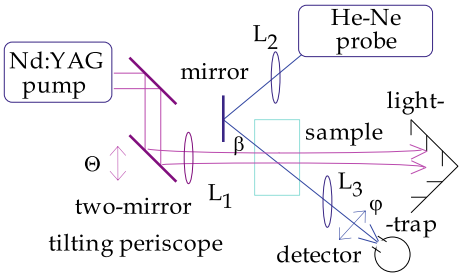

Fig. 9.17 Position-modulated deflection

A nearly twofold improvement in sensitivity may be achieved by the position modulation of the pump beam at a constant power versus the low-frequency amplitude modulation [9.33]. In the system of Fig. 9.17, a tilting periscope creates a spatially modulated thermal strain in the sample, while any probe beam deflection registers a nonuniform increase of temperature due to bulk absorption in the sample. The lateral pump-beam displacement angle θ driven by a piezo actuator on one of two periscope mirrors is independent of the modulation frequency ω given by beam's waist $2r_0$ and the focal length f of the input lens L_1: $\theta \approx 1.2r_0/f$. At a sufficiently high angular frequency: $\omega \gg \lambda_T/r_0^2$, and a small propagation length of heat waves in the sample, $d = \sqrt{(2\lambda_T/\rho_p c_p \omega)} \ll 2r_0$, the deflection angle φ becomes proportional to the displacement $g(x)$ and separation x for the probe and pump beams:

$$\varphi \underset{\lambda_T \gg 2r_0}{\sim} (-1/n)(dn/dT)(\alpha\Phi/\lambda_T)(1/\sin\beta)\left(\lambda_T/\rho_p c_p \omega\right) g(x). \tag{9.50}$$

The complex displacement function $g(x)$ for the position-modulated (p-m) and the amplitude-modulated (a-m) beam could be respectively characterized as [9.33]:

$$\begin{aligned} g(x)_{p-m} &= i\frac{8}{r_0^3}\exp\left(\frac{-2x^2}{r_0^2}\right)\exp\left(\frac{-x_0^2}{r_0^2}\right)\sum_{p=0}^{\infty}(-1)^p\left(I_p\left(\frac{x_0^2}{r_0^2}\right) - I_{p+1}\left(\frac{x_0^2}{r_0^2}\right)\right) \\ &\quad\times\left(x_0 I_{2p}\left(\frac{4x_0 x}{r_0^2}\right) - 2xI_{2p+1}\left(\frac{4x_0 x}{r_0^2}\right) + x_0 I_{2p+2}\left(\frac{4x_0 x}{r_0^2}\right)\right); \\ g(x)_{a-m} &= i\left(-\frac{8x}{r_0^3}\right)\exp\left(\frac{-2x^2}{r_0^2}\right), \end{aligned} \tag{9.51}$$

where I_{ip} are modified Bessel functions and x_0 is the lateral displacement of the pump beam. As seen from Eq. (9.50), the deflection angle φ decreases at a fairly high angular modulation frequency ω, but beam-wander-induced turbulence also decreases, defining limiting noise. An experimentally tuned 130-Hz optimal frequency resulted in equivalent noise of approximately 0.1 ppm/cm, but uncertainties

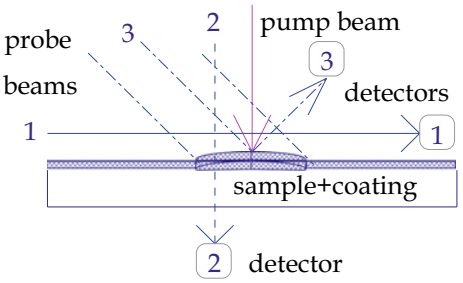

Fig. 9.18 Deflection studies of coatings

of angles of incidence and beam waists, thermal conductivities and diffusivities of the samples, and continuous stray light produced by the pump beam kept the repeatability of measurements at approximately ±20% [9.33].

Several configurations may be applied to investigate optical coatings via thermal deflection [9.30–9.32]. Figure 9.18 illustrates three main configurations – lateral (1), collinear (2), and reflected light (3) for beam probing – at the pump-beam position defining irradiated spot parameters for a total system of the optical coating under study and the sample substrate, each contributing to the sample's refractive index gradient and thermal deformation. The near-field-diffraction pulsed thermal lensing technique depicted in Fig. 9.14, with reflected-light detector configuration 3 in Fig. 9.18 and forward excitation by a pump beam into a coating spot and wide-beam probing, was used to detect the spatial dip in the center of the intensity profile [9.34]. The experiment revealed a time- and power-dependent absorption behavior of coatings at damaged surface spots. A similar mode-mismatch, wide-probe pulsed thermal lensing approach was sufficient to detect absorption levels for fluence magnitudes far below the coating damage threshold, allowing detection of surface displacements near 0.002 nm for single-coating layers and nonlinear (power-dependent) absorption in a quartz substrate at $(2.8 \pm 0.5) \cdot 10^{-9}$ cm^{-1}/W, presuming the quartz linear absorption coefficient of $\alpha \approx 0.03$ cm^{-1} at 193-nm wavelength [9.35].

Another approach is to sense spectral detuning of a coating due to photothermal deflection [9.36–9.40]. The approach is based on a dry–wet reversible spectral shift in the transmission–reflection properties of multilayer coatings, initially detected for a stack of TiO_2/SiO_2 or HfO_2/SiO_2 layers [9.36]. The spectral shift or photothermal detuning is sensed in response to an absorption-induced temperature rise of the coating exposed to a pumping laser and probed in transmitted or reflected light [9.37, 9.40]. Each intensity change $I_{t-t}(\rho)$ and $I_{t-t}(\tau)$ is defined by the temperature profile $\Delta T(\rho, \tau)$:

$$I_{t-t}(\rho) = (d\rho/dT)(1/\rho)\Delta T(\rho); \quad I_{t-t}(\tau) = (d\tau/dT)(1/\tau)\Delta T(\tau), \tag{9.52}$$

and is measured as the difference between a modulated thermally induced and a constant signal. In the arrangement depicted in Fig. 9.19, the pump and probe beams are focused into nearly one spot on a test coating, while their relative positions are adjusted by transverse alignment of the pump lens. The experimentally

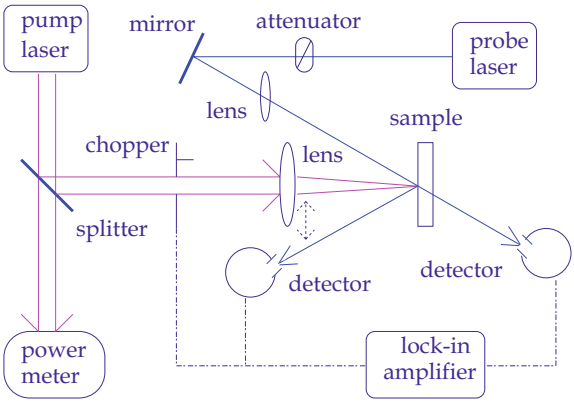

Fig. 9.19 Photothermal detuning measurements

detected temperature coefficient of reflectivity for a 99.8% high-reflectivity coating designed for 0° incidence was near $1.27 \cdot 10^{-3}$ K^{-1} at the normal incidence for the pump beam and 27° incidence for the probe beam at $\lambda_{probe}/\lambda_{pump} = 632.8/530$ nm [9.40]. The thermal-detuning technique is also sensitive to temperature variations inside the coating and the heat-conduction properties of the coating stack, being somewhat limited to coatings having a relatively large temperature coefficient of the refractive index in reflection or transmission where the detector is placed, but a relatively low thermal expansion coefficient.

One obvious deficiency of reviewed thermal-lensing deflection techniques for determining absolute magnitudes of the linear absorption coefficient measured can be to some extent addressed by combining photothermal and calorimetry studies within a single laser pulse, providing determination of the absorption coefficient itself and making absorption mapping [9.41]. Figure 9.20 shows a combined calorimetric and near-field mode-mismatch thermal-lens system. A pulsed excimer laser at 193 nm with homogenizing beam-steering optics was used to create a uniform top-hat intensity profile for the pump beam [9.42], creating a 0.70-mm-diameter spot on a sample at 2 mJ per pulse and 520 mJ/cm^2 sample

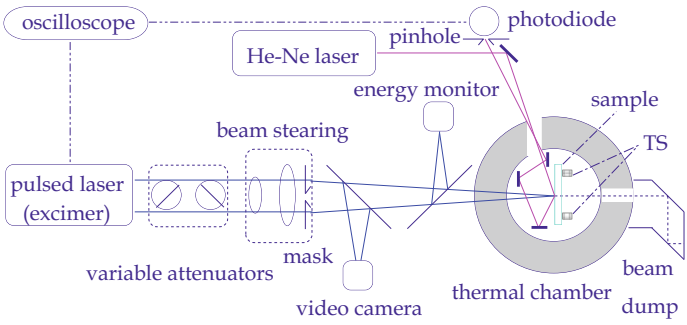

Fig. 9.20 Simultaneous calorimetric and photothermal studies

irradiance. The probe beam of a He–Ne laser operating in cw mode irradiated a sample placed in a thermally isolated chamber at 5° angle via the side window. A photodiode behind a 0.5-mm-diameter pinhole registered the central-dip thermal deflection (see Fig. 9.14). Negative temperature-coefficient sensors TS attached to the back surface of the sample detected irradiation-induced temperature changes (see Sect. 9.1). The noise-limited levels of sensitivity were $6 \cdot 10^{-5}$ for thermal deflection and $3 \cdot 10^{-5}$ for laser calorimetry, with the higher noise for deflection due to strong electromagnetic emission of the excimer laser and system instabilities, and the assessed value of $6.3 \cdot 10^{-4}$ for the measured absolute absorptance [9.41]. One also needs to be aware of the absorption-saturation effect in pulsed photothermal studies, which makes this technique sensitive to a laser excitation pulse profile and its broadening [9.43]. Occurrence of thermal lensing may also be sensed via detection of second order eigenmodes in a resonant cavity [9.124].

9.2.3 Photothermal Interferometry

An interferometric-bound measurement should provide for higher sensitivity to absorption losses, though with stronger requirements for both power and frequency stability of the probing laser beam and for the dynamic range of registration [9.21]. Commonly, interferometric procedures are based not on deflection of a beam due to absorption in a sample, but on the optical path length alteration caused by the sample-density modification created by the absorbed energy (Fig. 9.21). A parallel light beam of laser 1 propagates via plane-parallel plates 2 and 4 without any notable attenuation. At a transmitted beam power: $\Phi_\tau = \Phi_0(1-\rho)^2$, higher than the thermo-optic threshold for liquid sample 3, the phase of propagating light is altered in proportion to the optical path length:

$$\Delta\varphi = 2\pi\ell\Delta n/\lambda = 2\pi\frac{\partial n}{\partial T}\frac{\ell}{\lambda}\Delta T, \tag{9.53}$$

where ℓ is the constant length of the liquid being studied, defined by its cell. Since each successive component of retroreflected light is attenuated by ρ^2, detector 7 may only distinguish interference between first two beams – one transmitted and the other reflected twice by surfaces of plates 2 and 4. The directly transmitted beam is diverted by mirror 5 to auxiliary detector 6, serving to account for fluctuations of radiant power.

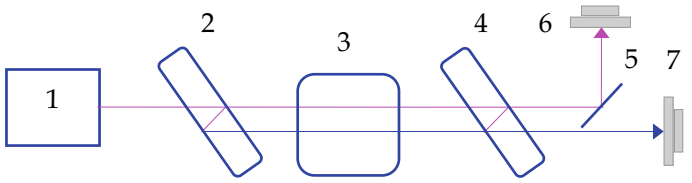

Fig. 9.21 Dual-beam interferometer sensing path-length alteration

Under the condition of presumably equivalent optical properties of both interferometric plates 2 and 4 and of the front and back surfaces of the glass cell, total transmitted flux Φ_Σ at the two-beam interference of fluxes Φ_1 and Φ_2 becomes [1.1]:

$$\Phi_\Sigma = \Phi_1 + \Phi_2 + 2\sqrt{\Phi_1\Phi_2}\cos\varphi_{1,2} \underset{\Phi_1=\Phi_2=\Phi_0}{=} 2\Phi_0(1-\rho)^6[\exp(-\alpha\ell)]\rho^2[1+\cos(\varphi_0+\Delta\varphi)]. \tag{9.54}$$

Since even the combined power of two dual-reflected beams is much lower than that of the incident beam, a higher sensitivity of detector 7 is required to register simultaneously the maximum and minimum of interference. At the maximum sensitivity of the two-beam interferometer for $\varphi_0 = \pi/2$, the registered flux is $\Phi_{\Sigma,\max} \cong 5\cdot10^{-4}\ \Phi_0$. Despite the restricted dynamic range of such interferometric registration, internal system noise does not notably affect the results obtained, since both interfering beams are passed by the same sample under study: the upper beam, for example, traces the sample's spot irradiated by the incident beam, affected by the absorption, and the second one is passed by the unaffected spot, or vice versa.

For a liquid under study extending only in its transverse direction and being irradiated by a Gaussian-shaped beam, the temperature distribution profile during irradiation can be written as [9.21]:

$$\Delta T(r,t) \cong \frac{\alpha\ell\Phi_\tau}{4\pi\lambda_T}\left[\ln\left(1+\frac{8\lambda_T t}{\rho_p c_p r_0^2}\right) - \frac{1}{\rho_p c_p r_0^2/8\lambda_T t+1}\frac{2r^2}{r_0^2}\right]. \tag{9.55}$$

The integrated magnitude of changed temperature ΔT registered in a caustic region designated by radius $r = r_0$ in a time interval shorter than the characteristic time $t \ll t_c = \rho_p c_p r_0^2/4$ becomes:

$$\Delta T(r,t) \cong [\alpha\ell\Phi_\tau/(4\pi\lambda_T)](2t/t_c). \tag{9.56a}$$

For $t \gg t_c$ and a cross-sectional temperature distribution not depending on r, this changes to:

$$\Delta T(r,t) \cong [\alpha\ell\Phi_\tau/(4\pi\lambda_T)]\ln(2t/t_c). \tag{9.56b}$$

Equation (9.53) for a sample such as carbon tetrachloride with $\alpha = 10^{-4}$ cm^{-1} predicts t_c to be near 3.2 s at $\Phi_0 = 0.01$ W and $r_0 = 1$ mm. At $t = t_c$ the temperature rise is $\Delta T = 7\cdot10^{-5}$ K, which at $\ell = 12$ cm, $\lambda = 632.8$ nm, and $\partial n/\partial T = -5\cdot10^{-4}\,K^{-1}$ corresponds to $\Delta\varphi = 0.045$ rad, and the power change (see Eq. (9.54)) is $\Delta\Phi_\Sigma = \cos^2(\Delta\varphi/2) \cong 1.5\cdot10^{-3}\ \Phi_{0,\Sigma} \cong 7.5\cdot10^{-7}\ \Phi_0 \approx 10^{-8}$ W. The lowest linear absorption coefficient α detected by the system of Fig. 9.13 was limited by the sensitivity of the detectors used and reached $2\cdot10^{-5}$ cm^{-1} [9.21].

In a similar study of solid samples whose length expansion is not limited and changes as a function of the temperature, Eq. (9.53) for the thermal deflection transforms into one for the thermal expansion [9.21]:

$$\Delta\varphi = \frac{2\pi}{\lambda}\left(n\frac{\partial \ell}{\partial T} + \ell\frac{\partial n}{\partial T}\right)\Delta T = \frac{2\pi}{\lambda}\ell\left(\frac{1}{3}nk_{lin} + \frac{\partial n}{\partial T}\right)\Delta T. \tag{9.57}$$

Here k_{lin} is the volume expansion coefficient. Since for the vast majority of optical materials k_{lin} is near $|-\partial n/\partial T|$, light-induced changes of the optical and actual length of the irradiated sample should compensate each other, reducing the interferometric sensitivity to absorption-induced path-length changes in a solids. When a solid sample is studied, the intensity of laser irradiation needs to be increased and the temporal response of the detector must be faster, preventing extension to a nonlinear deformation stage. With a He–Ne laser probe beam, thermal-bump and high-coherence interferometry as well as absorption-induced polarimetry can be used, even testing adhesion of the thin-film coatings during an intense laser beam exposure [9.44–9.50].

Transverse changes of the refractive index of a long cylindrical sample in direction r under uniform heating along its axis may be expressed as a function of universal medium constants P and Q [II.11]:

$$n_{||,\perp}(r) = n_0 + (P \pm Q)[T(r) - T_0] \pm Q[T_{med}(r) - T_0], \tag{9.58}$$

where

$$P = \frac{\partial n}{\partial T} - \frac{k_{lin}E}{2(1-\sigma_p)}(C_{||} + 3C_{\perp});\ Q = \frac{k_{lin}E}{2(1-\sigma_p)}(C_{||} - C_{\perp}). \tag{9.59}$$

Here $n_{||}, n_{\perp}, C_{||}$, and $C_{\perp}$ are the refractive indices and photoelastic constants for light components polarized in, respectively, parallel and perpendicular planes to the plane of incidence; T_0 and n_0 are the sample steady-state temperature T and refractive index corresponding to the T value; T_{med} is the steady-state temperature of the sample's surroundings at the sample radius r, and E and σ_p are Young's modules and Poisson's ratio. The first constant: P, designates changes of the mean refractive index for the opposite states of polarization caused by the intensive probe laser beam. The second constant: Q, is proportional to the difference of two photoelastic constants for these states of polarization and characterizes the birefringence of the medium being induced by thermal expansion.

For solid-state optical materials such as glasses, the difference of these photoelastic constants is not very high. Radiation-induced deformation can be reduced to a flat deformation if the temperature change in the prolonged irradiated region is orders of magnitude higher than the sample's temperature, and if the cross section of that region is small in comparison with its length. That happens when a beam is focused by a long-focal-length lens. The change of the mean refractive index of a heated cylindrical sample along its axis does not depend on the state of light polarization; thus the mean refraction $\bar{n}$ is:

$$\bar{n} = \Delta n_{||} = \Delta n_{\perp} = P\Delta T_0. \tag{9.60}$$

The respective strain ε arising from bulk absorption in an isotropic sample of unlimited dimensions at distance r from the center of a Gaussian laser beam at duration t_a is [9.45]:

$$\varepsilon \cong \frac{\alpha \ell \Phi_{\text{int}} k_{lin} t}{2\pi \rho_p c_p r^2} \left(\frac{1+\sigma_p}{1-\sigma_p} \right), \tag{9.61}$$

where Φ_{int} is the radiant flux (power) propagating within the sample's bulk, c_p and ρ_p are the specific heat and the sample density, and t is the observation time. Equation (9.61) is valid for the balancing conditions: $r^2 \gg r_0^2, r^2 \gg \left[\sqrt{t}\lambda_T/(\rho_p c_p)\right]^2$, $\left[\lambda_T/\sqrt{r}(\rho_p c_p)\right]^2 \gg v_s$, or $t \gg t_a$, where v_s is the sound velocity, $\left[\sqrt{t}\lambda_T/(\rho_p c_p)\right]^2$ is the characteristic length of thermal diffusion, and r_0 is the radius of spot of the focused beam – confirming the absence of transverse waves. Hence, solid-state absorption measurements should be performed at a sufficient distance from the beam and later than the instant action of radiation happens. As a result, it can be presumed that a temperature gradient in the irradiated sample's cross section produces only longitudinal waves of deformation.

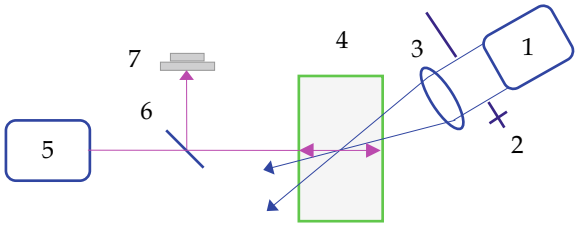

Fig. 9.22 Sensing of radiation-induced sample refraction

A typical structure for interferometric measurements of bulk absorption in solid samples is depicted in Fig. 9.22. A beam from pump laser 1 at absorbing wavelength λ is modulated by chopper 2 with its half period equal to t_a and is focused by lens 3 into the bulk of sample 4. The sample surfaces are made flat and parallel, thus making for the Fabry–Perot interferometer in reflected light [9.45]. The probe beam emitted by high-coherence laser 5 with wavelength λ_{ref} as retroreflected by sample surfaces is registered by detector 7 via beam splitter 6. Owing to a dual pass of the irradiated region, Eq. (9.57) converts to:

$$\frac{\partial \Phi_\rho / \partial T}{\Phi_\rho} \frac{\Delta \varphi}{\Delta T} = \frac{4\pi}{\lambda} \left(n \frac{\partial \ell}{\partial T} + \ell \frac{\partial n}{\partial T} \right). \tag{9.62}$$

Assuming that 10^{-7} sensitivity to reflected fluxes $\partial\Phi_\rho/\Phi_\rho$ can be reached and at the $\Delta T \approx 10^{-7}$ K temperature sensitivity limit, bulk absorption coefficients close to $1 \cdot 10^{-6}$ cm^{-1} can be essentially measured [9.26]. However, to obtain such elevated sensitivity, the power stability of the probe beam must also be at that level.

Figure 9.23 depicts an interferometer providing the loss measurement, with the sample substituted by its holographic image to study the sample's bulk absorptance at arbitrary configuration of its surfaces [9.46]. First, hologram 4 of sample 3 to be irradiated by pump laser 1 is made via a probe beam of laser 2. Then, the hologram is used to compare absorption-induced changes of irradiated sample 3 versus its image 4. Detector 5 compares the reconstructed wave front with one thermally distorted by sample absorption. The smallest bulk linear absorption coefficient measured at $\lambda = 10.6$ μm reached $(1.0 \pm 0.2) \cdot 10^{-3}$ cm^{-1} at the same level of estimated surface losses.

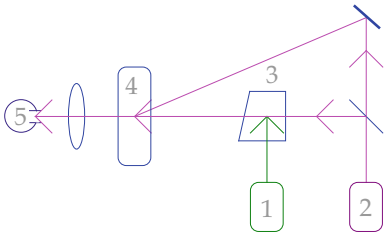

Fig. 9.23 Interferometry of a holographic image

Owing to high sensitivity to optical path length changes, interferometric measurements are more susceptible to acoustic noise. If the pump beam is modulated at a relatively low frequency $f < 1/t_a$, the acoustic signal caused by sample deformations under the intensive light action (see Eq. (9.59)) needs to be either isolated or compensated. Compensation may be made using the interferometer with a second reference arm, similarly to one in Fig. 9.21. For that purpose, sample irradiation in Fig. 9.23 was done by a sequence of pulses with duration $t_a < r_0/v_s$ and frequency $f_a < v_s/(2r)$ [9.46]. The reference signal of the not shown second detector provided an auxiliary feedback compensating the initial phase status of the interferometer. An identical compensation may be made by using a piezoelectric transducer, whose signal would preserve constancy of the optical path length in the apparatus. For measurements obtained using a Jamin interferometer at $\lambda = 1.06$ μm and at a surface density of irradiating pulses near 100 KJ/cm^2, the lowest magnitude of the linear bulk absorption coefficient measured in pure fused silica reached approximately $3 \cdot 10^{-6}$ cm^{-1} [9.46].

A realization of the Jamin interferometer for a loss measurement is shown in Fig. 9.24. A pump laser beam induces a thermal reaction to absorption in the

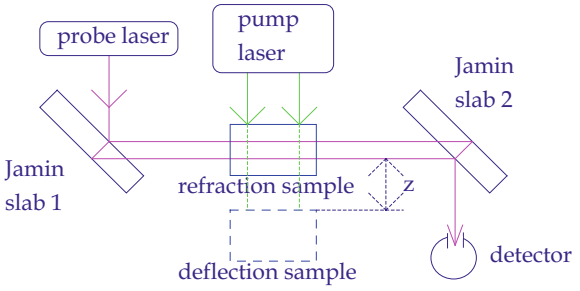

Fig. 9.24 Jamin interferometer for photothermal detection

refractive or beam-deflecting sample; the former is probed directly and the latter is probed at distance z from sample's front surface, making the mirage effect. Since the interferometer detects any thermally induced beam deflection as a phase change but not a refractive index change versus alteration of the temperature, in contrast to thermal-deflection methods, its response to the same variation of the deflection angle is more sensitive. The interferometer's response is not a linear function of the thermal gradient, which could be advantageous to deducing any sample-driven signal from noise, but the signal is sensitive to the probe-beam displacement and distance z from the sample's surface [9.48].

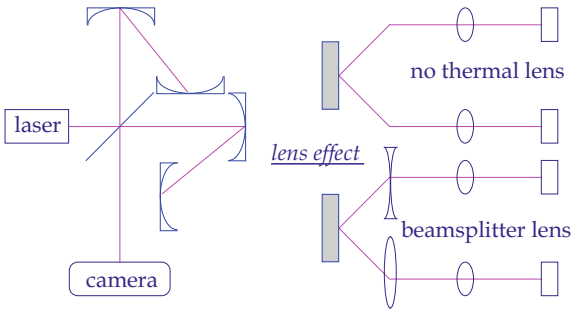

Fig. 9.25 Thermal-lens effect in an interferometer

Another version of the interferometric technique was used with a Michelson interferometer (Fig. 9.25). The absorptance of the interferometer's beam splitter was detected by comparing readings at a low and a high power of radiation, with the latter generating a thermal lens in the splitter [9.49]. The path difference $\Delta\ell$ that occurred along the beam axis was measured at the $1/e^2$ level of intensity as:

$$\Delta\ell = 1.3(\partial n/\partial T)(4\pi\lambda_T)^{-1}(\alpha\ell)\Phi_\lambda, \tag{9.63}$$

where λ_T is the thermal conductivity (thermal diffusion length), Φ_λ is the radiation power at wavelength λ, α is the linear absorption coefficient, and ℓ is the thickness of the beam splitter. For waist radius ω at the beam splitter and a thermal lens with focal length $f_{therm} = \omega^2/2\Delta\ell$, it converts to:

$$\alpha = (4\pi/2.6)\left(\omega^2\lambda_T\right)/((\partial n/\partial T)\Phi_\lambda f_{therm}\ell). \tag{9.64}$$

Equation (9.64) assumes that the splitter's expansion and absorption in its coating have negligible effects in comparison with the bulk absorption of the splitter. The derived magnitude of the linear absorption coefficient measured using this interferometric technique at $\lambda = 1064$ nm in the bulk of a Suprasil 311 SV fused-silica beam splitter was estimated to be as low as 0.25 ± 0.10 ppm/cm [9.49] on the basis of the tabulated ratio of the known temperature dependence of the index of refraction $\partial n/\partial T$ and thermal conductivity λ_T of Suprasil: $(\partial n/\partial T)(\lambda_T)^{-1} \cong 10^{-5}\, m/W$.

As an alternative, an absorption-induced thermal lens can be detected via the spot size change on any CCD detector array for a light beam affected by such a lens [9.50]. For certain sufficiently large beam spot size ω_{in}, the observed output beam radius ω_{out} becomes a function of array-matrix parameters A and B and of beam curvature R induced by the thermal lens:

$$\omega_{out} \sim \omega_{in}(B/R + A). \tag{9.65}$$

For N cycles of beam propagation via the thermal lens: $1/R = 1/R_{cold} + N/f_{therm}$, the thermal lens can be detected via the spot size change for the respectively hot and cold optical elements as:

$$f_{therm} = BN\omega_{in}/(\omega_{hot} - \omega_{cold}). \tag{9.66}$$

The measured thermal-lens-induced absorptance in Michelson interferometer mirrors, assuming lower absorption levels for other elements, was near 15–5.7 ppm with approximately 1.3 ppm sensitivity [9.50].

The methods of interferometric measurements of linear absorption coefficients in solid samples analyzed above were based on irradiation conditions imposed by Eqs. (9.58) and (9.59), which require equality of the azimuth and radial temperature gradients in the sample. That is why the beam of light must be shaped as a long thin cylinder, creating a virtually planar deformation and isotropic changes of the refractive index versus temperature $\partial n/\partial T$. Instead, focusing a beam of intensive radiation as a wide cone into an absorbing specimen creates some uneven distribution of its bulk temperature. Observable birefringence B for a transparent material could appear in a zone of sharp temperature changes as noticeable inequality $\Delta\ell$ of optical path lengths for light beams with opposite states of polarization propagating in direction z along the sample length ℓ:

$$B = \Delta\ell_{||,\perp} = \int_0^{\ell} \left| n_{||} - n_{\perp} \right| dz. \tag{9.67}$$

As a result, propagation of a polarized probe beam via a strained region in the direction of the absorption-sampling beam allows one to correlate alterations for the initial phase of the probe beam with the induced thermal birefringence in the irradiated sample and, thus, its linear absorption. As follows from Eqs. (9.46) and (9.47), the initial orientation of the main axes of such a stress birefringence depends on the optical properties of the test substance and the wavelength and intensity distribution of the intense pump beam. Therefore, a quantitative measurement requires one to define not only amplitudes, but also effective positions of orthogonal optical axes of the resulting ellipticity in the irradiated test sample. If one axis of the induced birefringence is formed by the polarizer, determining the initial state of polarization for the probe beam, and the second is formed by the crossed analyzer, the irradiated sample performs as a common linear retarder with the thermally

induced birefringence (see Sect. 3.3). If the surface reflections are disregarded for that simplest case, the probe beam of radiation propagating along with an initial intensity I_{ref} distinguishes the light-induced phase shift $\Delta\varphi$ as:

$$I_{\max} \sim I_{ref}\left(1 + \cos^2 \Delta\varphi\right); \quad I_{\min} \sim I_{ref}\left(1 - \cos^2 \Delta\varphi\right);$$
$$\Delta\varphi = \arccos \sqrt{(I_{\max} - I_{\min})/(I_{\max} + I_{\min})}. \tag{9.68}$$

If the preset orientation of radiation-induced birefringence is unchanged during the entire process, the analyzer's plane – perpendicular or parallel to the reference polarization – defines the subsequent intensity transformation ΔI of probe beam for the respective phase shift $\Delta\varphi$ as:

$$\Delta I \sim \sin^2(\Delta\varphi/2) = I_0 \sin^2\left(\pi\Delta\ell_{||,\perp}/\lambda\right). \tag{9.69}$$

Within constraints of a relatively weak thermal action at a low bulk absorptance of the sample studied: $\pi\Delta\ell_{||,\perp}/\lambda \ll 1$, the thermally induced birefringence is proportional to the square power for the product of linear absorption coefficient α of the sample bulk and energy W of the pump beam:

$$\Delta I_{ref} \sim (\alpha\ell_{irr}\mathrm{W})^2, \tag{9.70}$$

where ℓ_{irr} is the length of the irradiated region in the weakly absorbing substance of the test sample.

Figure 9.26 depicts the system for absorption measurements via laser-induced birefringence [9.51]. While making the pump and probe beams of lasers 1 and 2 collinear, interference filter 6, beam splitter 4, and analyzer 7 select only the polarized probe beam to reach intensity detector 8. Spectrally selective beam splitter 4 has high transmittance for pump light and high reflectance for probe light. The temporal resolution is set to skip a fast pump action and only react to slow birefringence changes traced by the probe beam. Testing many similar samples of various absorption properties at an unchanged beam geometry allows the correctness for the above assumption of linear thermal behavior to be confirmed via the proportionality of the absorption coefficients and the light pulse energies measured: $\alpha_i = \alpha_j\left(W_{j,pump}/W_{i,pump}\right)\sqrt{I_{j,ref}/I_{i,ref}}$. Here $W_{i,j}$ are the energies of pump pulses and

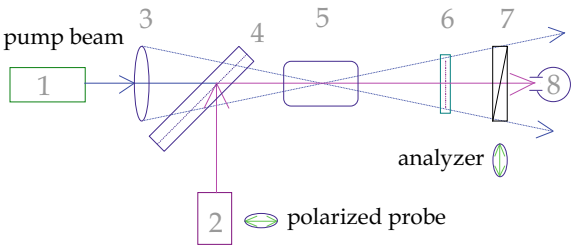

Fig. 9.26 Evaluation of light induced birefringence

$I_{i,j,ref}$ are the corresponding signals for probe pulses on detector 8. Such a measurement method was used to evaluate compound low-loss glasses of compatible optical properties. In experiments using a Nd:glass pump laser at $\lambda = 1.06$ μm with pulse duration $t_{pulse} = 1-3$ ms, the required quadratic dependence according to the Malus's law (see Eqs. (9.68) and (9.69)) for $I_{j,ref}/I_{i,ref}$ was observed with pump energies up to tens of joules [9.51]. The lowest detected absorption coefficients were near 20–70 dB/km. The durations of birefringence-induced probe pulses transmitted by the analyzer for the time–energy settings above were near 50 ms.

Regarding the analyzed interferometric absorption measurement techniques, let us point to the apparent difficulty of detecting small changes in the interferometer's pass length for a slow thermal transition – susceptibility of a fridge pattern to vibration noise. Particularly for differential-type studies, such as in Fig. 9.21, if two interferometer arms are used for measuring a thermo-optic signal, implementation of the vibration-compensation technique seems difficult. Using a folded Jamin interferometer, owing to its low sensitivity to vibrations, allows one to stabilize the mutual fringe pattern for differential measurements while separating arm signals and nulling the occurring background fringe shifts via a reference fringe pattern [9.52]. For that purpose (see Fig. 9.27) two He–Ne laser beams were used: one for detecting the probe-beam-induced absorption and another for referencing the fringe pattern, while the intensities of the beams were equalized by neutral-density filter N. Dual-coating mirrors M1 and M2 for 515-nm pump and 632.8-nm probe wavelengths superimposed the beam pairs. The pump beam intensities were adjusted by a thin reflecting glass plate P, while two wedges W were providing parallelism of interfering beams, making sure the both beams, which recombined on the second Jamin interferometer plate JP2, were collinear. Diffraction grating DG separated pump and probe beams after sample cell S and reference cell C. The He–Ne beams via plane mirrors PM1 and PM2 passed via galvanometer-driven compensator GC, which was part of a closed-feedback loop stabilizing the fringe pattern and modulating it for phase-sensitive detection, and via manual compensator MC. Photodiodes D1 and D2 behind pinhole screens sensed $\pm 200/\lambda$ fringe shifts due to optical path length changes, allowing detection of CCl_4-level for linear absorption

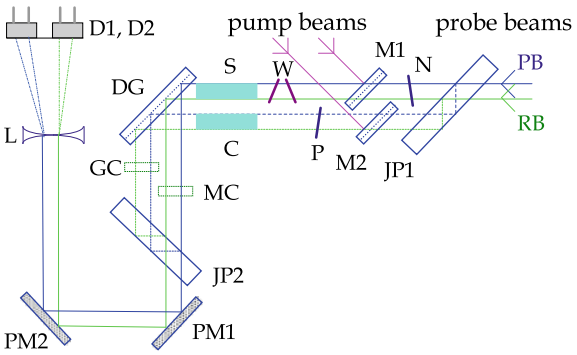

Fig. 9.27 Differential interferometric measurements

coefficients of $1.2 \cdot 10^{-5}\,\mathrm{cm}^{-1}$ or lower [9.52]. Beam-deflection studies may be enhanced using a high-quality Hermite-Gaussian mode for the excitation beam pattern to be preserved when propagating an increased field gradient [9.125].

9.2.4 Photoacoustic Spectroscopy

As assessed above, nonemissive transformation of radiation energy absorbed in a solid sample irradiated by an intense pump pulse creates a temperature gradient which induces sample's thermal expansion. The subsequent elastic strain (see Eq. (9.61)) not only changes the initial density, size, and refractive index of the irradiated sample, but also creates a dynamic pressure and a corresponding acoustic wave. The resultant acoustic signal can be registered directly on the surface of the solid sample or via a gaseous substance, since, if the gas is nonabsorbing for pump light, its properties are not affected by the sample's density and dimensional changes when placed in contact with the irradiated solid. As a result, the detection sensitivity of such a photoacoustic study of bulk absorption of light in solids is as high as for other absorption-induced techniques, except those performed at low irradiances.

The exposure of a solid sample of absorptance a by continuous, synchronously modulated, or pulsed radiation with pulse duration t_p, frequency ν, and intensity: $I(t) = I\big(1 - \exp\big(-t/t_p\big)\big)$, leads to a corresponding periodic modulation of the sample temperature T via the dependence [9.44, 9.53–9.56]:

$$\nabla^2 T + \mathsf{a}\frac{2I(t)}{\pi r^2}\exp\left(-\frac{2r^2}{r_0^2}\right) = \frac{\rho_p c_p}{\lambda_T}\frac{\partial T}{\partial t}. \tag{9.71}$$

Such modulation creates the radial $\varepsilon_r = \partial^2 P/\partial t^2$ and the azimuth $\varepsilon_a = (r)^{-1}(\partial P/\partial t)$ strain, both defined by constant P (see Eqs. (9.58), (9.59)), known as *the replacement potential*:

$$\nabla^2 P - \frac{1}{\nu^2}\frac{\partial^2 P}{\partial t^2} = \frac{1+\sigma_P}{1-\sigma_P}k_{lin}T. \tag{9.72}$$

As referred to earlier, if the sample is irradiated by a thin cylindrical beam with a narrow cross section of radius r_0 and the observation is made at time $t \gg t_\mathrm{p}$ in the $r \gg r_0$ region, the thermal strain in the sample is planar, and is defined by Eq. (9.61). Then, the acoustic signal is proportional to the total absorptance $\mathsf{a} = \alpha\ell$ of the sample bulk of length ℓ and to the pump energy: $W_p = \int \Phi_p(t)dt$, where Φ_p is the time dependent power of the pulse.

One exception needs to be made for highly absorbing substances. A high initial attenuation of the pump power by the front section of a highly absorbing sample reduces the light energy absorbed per unit length toward the sample's end, and thus the created elastic strain. To count the total absorptance $\alpha\ell$ for the full sample length, the totality of unequal signals needs to be integrated using a transducer for the length of the sample. If a cw beam modulated at chopping frequency ω is used, the absorbed flux $\Delta\Phi$ in a sample of length ℓ with surface reflectance ρ may be expressed as [9.54]:

$$\Delta\Phi \underset{\alpha\ell\sim 1}{=} (\Phi_\tau/2(1-\rho))\omega[\exp(\alpha\ell) - (1-\rho) - \rho\exp(-\alpha\ell)], \tag{9.73}$$

where Φ_τ is the transmitted radiant power. At a low absorption loss: $\alpha\ell \ll 1$, it becomes:

$$\Delta\Phi \underset{\alpha\ell\ll 1}{=} \frac{\Phi_\tau}{2}\frac{(1+\rho)}{(1-\rho)f}\alpha\ell\left(1+\frac{1}{2}\alpha\ell\frac{(1+\rho)}{(1-\rho)}\right). \tag{9.74}$$

A photoacoustic measurement layout is illustrated in Fig. 9.28. Either pulsed or modulated cw light from laser 1 via chopper 2 irradiates solid sample 3 with attached upper 4 and lower 5 piezoelectric transducers. Power meter 6 and lock-in-amplified detector 7 measure the beam power and the induced acoustic signal, respectively. Similarly to thermocouple calorimetry (see Sect. 9.1), two transducers separate the surface and bulk absorption signals, allowing one to detect the sample scattering coefficient. One transducer is directly attached to the sample surface and the other one is set symmetrically to the first but without any acoustic contact – to register only radiation directly scattered to the transducer. Each sample calibration is made by relevant spectrophotometric measurement at the wavelengths of the highest absorptance to determine the optimal transverse location of the sample in reference to the incident laser beam. With use of Ar, CO_2, and CO lasers, near $1\cdot10^{-4}\,\mathrm{cm}^{-1}$ absorption coefficients were measured, maintaining scattering light below levels corresponding to losses of about $1\cdot10^{-5}\,\mathrm{cm}^{-1}$ [9.54].

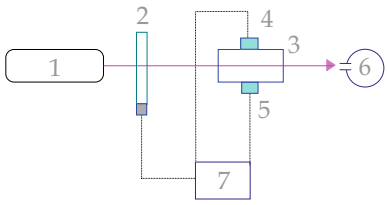

Fig. 9.28 Photoacoustic absorption measurements

Applications of relatively short light pulses allow one to separate bulk losses from surface ones using only one transducer on the sample's surface [9.58]. The concept of loss separation is based on the fact that the efficiency of acoustic-wave generation reaches its maximum when the time interval of the sound propagation across the sample is greater than the duration t_p of the exiting light pulse itself. Under that condition, the acoustic wave does not exit the sample bulk during the entire time interval of the pump light action, and its amplitude is formed by the entire radiant energy of the optical pulse. For sound velocity $5\cdot10^{-5}\,\mathrm{cm/s}$ in the medium studied and the beam transverse dimensions of $1\cdot1\,\mathrm{mm}^2$, the speed assumption above holds true for $t_p \leq 2\cdot10^{-7}$ s pulses. If the sample's elastic strain is kept to be planar by focusing light as a long thin cylinder (expression (9.61)), the photoacoustic signal still oscillates at frequency ν, depending on the system resonance, but the intensity of the first pulse is directly identified by the absorption loss of the bulk portion of the sample under study. At $t_p = 10^{-8}$ s and modulation frequency $f = 2$ MHz for $\lambda = 1.06$ μm and $\lambda = 0.532$ μm, the resolved

magnitudes of the absorption coefficient in $50 \cdot 10 \cdot 1\ \mathrm{mm}^3$ potassium titanyl phosphate (KTP) crystals were nearly $(1-5)\cdot 10^{-3}\ \mathrm{cm}^{-1}$ [9.58].

Another way of separating the acoustic signals from a solid sample bulk and its two surfaces is by keeping a transducer in the far-field of the acoustic reception zone: $r_\mathrm{f} \gg t \cdot v_\mathrm{s}$; here v_s is the sound velocity. If light scattering by sample surfaces is sufficiently reduced by a matching fluid or a thin baffle between the sample and the transducer, the far-field acoustic signal is resolved as [9.59]:

$$\mathrm{U} \approx \mathrm{const} \cdot \left(\mathrm{k_{lin}} v_\mathrm{s} / \mathrm{c_p}\right) \mathrm{a} \mathrm{W}_0, \tag{9.75}$$

where W_0 is the pump energy and $\mathrm{a} = \alpha\ell$ is the total sample absorptance. Therefore, the signal power for a Gaussian intensity distribution does not depend on the pulse duration: $t_\mathrm{p} \ll \mathrm{r_f}/v_\mathrm{s}$, or the geometry of the narrow pump beam. At pulse energies $\mathrm{W}_0 \leq$ 60–70 mJ of laser light focused as narrow cylindrical beams of 1-mm diameter, every change of the acoustic signals was observed only as a linear function of pulse energy variations for the smallest absorption coefficient near $1.5 \cdot 10^{-4}\ \mathrm{cm}^{-1}$ [9.59].

More conventional absorptance measurements in photoacoustic spectroscopy are based on analysis of the acoustic oscillations in a resonant cavity having a sample – irradiated by a beam of modulated light – being inside the resonant cell with a nonabsorbing gas, filling in the cavity space between one of sample surfaces and a single or multiple transducers [9.55, 9.56]. The acoustic wave is detected via the internal pressure gradient in the cell as a function of the varying temperature of the gas contacting the sample while the amplitude of the acoustic signal, being related only to the absorptance in sample's boundary layer ℓ_T, is identified by the sample thermal diffusion length λ_T:

$$\ell_T = \sqrt{2\lambda_T / \left(\rho_p c_p \omega\right)}. \tag{9.76}$$

The boundary layer expansion depends on the characteristic absorption length $\ell_a = 1/\mathrm{a}$ of the sample – here reassigning the surface absorptance as α, the bulk length ℓ, linear absorption coefficient a, thermal conductivity λ_T (see Sect. 9.1), and on the angular modulation frequency ω of the incident light beam.

The acoustic-cell signal as a time function of the pressure gradient $\Delta\mathrm{P}(t)$, proportional to the respective temperature modulation $\Delta\mathrm{T}(t)$ of the sample surface, directly contacting the cell gas, is defined by [9.53]:

$$\Delta\mathrm{P}(t) = \frac{\left(\mathrm{c_p}/\mathrm{c_v}\right)\mathrm{P_{g,0}}\lambda_\mathrm{T}\Delta\mathrm{T}}{\sqrt{2}\ell_g \mathrm{T_{g,0}}} \exp[i(\omega\mathrm{t} - \pi/4)], \tag{9.77}$$

where $\mathrm{P_{g,0}}$ and $\mathrm{T_{g,0}}$ are the ambient pressure and temperature of the gas, $\mathrm{c_p}$ and $\mathrm{c_v}$ are the specific heat of the gas at the constant pressure P or volume V, ℓ_g is the gas cell length, and $\ell_{T,g}, \lambda_\mathrm{T,g}$ are the full- and the effective thermal-diffusion length of a gas layer in contact with the sample being exposed to temperature changes. Presuming $\varepsilon\ell_g \ll 1$ and $\mathrm{a}, \alpha \ll 1$ for the low strain and low-loss bulk plus low surface losses of the sample, the amplitude $\Delta\mathrm{P}$ and the phase $\Delta\varphi$ of modulated acoustic signal, could be converted to [9.60]:

$$\Delta P = \frac{(c_p/c_v)P_{g,0}\lambda_{T,g}\Phi_0 a\ell_T}{\sqrt{2}\ell_g T_{g,0}\{4\lambda_T[1+\lambda_{T,g}\ell_T/(\lambda_T\ell_{T,g})]\}}\sqrt{2\alpha^2+2\alpha a\ell_T+(a\ell_T)^2};$$
$$\Delta\varphi = \frac{\pi}{4} - arctan(1+a\ell_T/\alpha). \tag{9.78}$$

The last two equations demonstrate that both the amplitude and the phase of the acoustic signal are identified not only by the surface and bulk absorption of the sample, but also by internal properties of the cell. Thus, absolute calibrations and referencing of resonant cells are always required for quantitative measurements of absorptance in photoacoustic spectroscopy, while combined measurements of the amplitude and phase can provide useful references [9.57].

Another concept for distinguishing bulk and surface absorption losses in photoacoustic spectroscopy is associated with the dependence of the length ℓ_T of the effective absorbing layer on the radiation-modulation frequency ω. If only surface absorption exists, the relative acoustic signal is approximately proportional to the inverse frequency ω^{-1}, but is proportional to $\omega^{-3/2}$ for the bulk loss only. In these opposite cases, the phase changes are 90° and 45°, respectively (9.61). Utilizing the system in Fig. 9.28 and identifying each particular dependency as $\omega^{-0.9}$ for surface absorptance and $\omega^{-1.7}$ for bulk absorptance in the 10–100-Hz frequency range resulted in the experimentally measured bulk-to-surface: $a\ell_T/\alpha$, ratio in a KCl crystal at $\lambda = 10.6$ μm being 1:1.5. When the holographic interferometer in Fig. 9.23 was used, the surface and the bulk absorption losses detected for the same test sample were reversed to $\alpha = 1.1\cdot10^{-3}$ cm^{-1} and $a\ell_T = 5\cdot10^{-3}$ cm^{-1} [9.61].

To increase the sensitivity of photoacoustic spectroscopy only for the surface under study, a pump beam can be surface-focused as a pattern of thin lines generating a firm surface acoustic wave [9.62]. Accordingly, a matching pressure transducer can be made as a narrow-bandwidth interdigitated detector, with its structure resembling an irradiating pattern to enhance sensitivity. In a confirming experiment, a respective intense signal produced by scattered light was filtered in the time domain by setting up a matching delay corresponding to the acoustic transit time from an absorbing sample region to the detector. The absolute referencing of the entire measurement structure was made by inserting a thin aluminum film on the edge of each sample, which absorbed nearly 10%. The linear absorption coefficients of two thin-film coatings measured were $3\cdot10^{-4}$ and $6\cdot10^{-4}$ cm^{-1}, with the surface absorptance of one not even antireflection-coated fused-silica sample as low as $3\cdot10^{-7}$ cm^{-1}, varying from 10^{-6} to 10^{-7} cm^{-1} for various samples.

9.2.5 *In Situ and Remote Photoacoustic Spectroscopies*

Applications of nonresonant and resonant photoacoustic cells for in situ or remote pollution detection may enhance the loss-measurement sensitivity to the absorption loss in various test specimen irradiated by intensity- or frequency-modulated radiation [9.63–9.66]. Ether an intensity-modulated or a frequency-modulated beam of potent laser light at wavelength λ of interest (Fig. 9.29) irradiates, via a window or a focusing lens, a cavity filled with a gaseous test substance whose absorption is measured. The

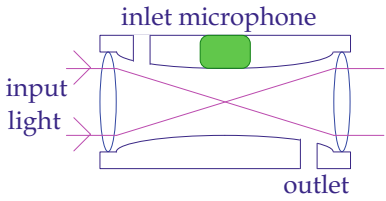

Fig. 9.29 Photoacoustic cell design

rms value of the pressure variation occurring in such an acoustically resonant or a nonresonant cavity is detected by a pressure transducer (microphone) and compared with the average power Φ of radiation, which for single-cell propagation is:

$$\bar{\Phi} = \Phi_{in}(1 - \exp(-(\alpha N + \sigma)\ell))/((\alpha N + \sigma)\ell). \tag{9.79}$$

Here Φ_{in} is the flux of incident light, N is the mean density of homogeneously distributed absorbing gas molecules, and α and σ are the linear absorption coefficient and the scattering loss of the gaseous substance under study filling the cavity of length ℓ [9.65].

Even in one of the first experiments with a pulsed ruby laser and a cw CO_2 laser via 45.5-cm-long and 20-cm-long single-path acoustic cells, the measurement sensitivity to spectral absorption reached $3 \cdot 10^{-6}$ for air saturated by water vapor and $1.2 \cdot 10^{-7}$ cm^{-1} for a CO_2–NO_2 mixture at 694.3-nm and 9.6-μm wavelengths, respectively [9.63]. Radiation energy absorbed at room temperature in the respective cell and transferred to thermal motion of gas molecules of the test composition was registered by a low-frequency differential-pressure transducer owing to the gas pressure rise. For the pulsed laser, the pressure observation time was limited by the heat diffusion length of the cell walls and for the cw laser its intensity modulation rate was slow enough for heat conduction to establish a steady temperature distribution. The response time for the differential pressure of the cell, measured by a capacitance manometer, was less than 10 μs, while the minimum pressure rise of the gas exceeded thermal agitation noise levels of the air mixture by many decibels [9.63]. Gas absorption measurements in a high-pressure acoustic cell can be masked by $\sqrt{p_o}$ noise, where p_o is the intracavity cell pressure, due to diffusion processes in the gas mixture or the presence of thin absorption layers on the cell windows, even when the gas itself does not absorb light [9.64].

Similar measurements in a gas-filled acoustic cell can be performed on condensed samples [9.66]. A solid, powder, or liquid sample can be placed vertically in a cylindrical quartz cup, resting on an output cavity window, coaxial to the cell for irradiation by focused-downward and modulated light (Fig. 9.30). In this case, a

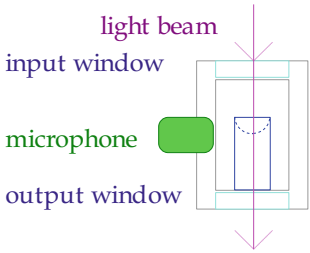

Fig. 9.30 Condensed-sample cell

nonresonant cell is made as a small-volume vertical cylinder, enhancing the amplitudes of the pressure oscillations measured via a radial-port microphone membrane of that sealed cell by a lock-in amplifier. The heat from the sample flows into a surrounding transparent gas, causing synchronous modulation of its pressure, the magnitude of which is calibrated via a blackbody absorber, allowing spectral features of the cell to be removed and enabling quantitative detection of the absorption coefficient of the sample. To provide measurements that are relatively free of systematic errors, the actual cell response needs to be calibrated versus the dependence of its signal on the chopper frequency, which is usually inversely proportional to it. In addition, it must be calibrated for the system's noise at low absorptivity of the sample, when the cell window and walls' absorption and scattered light, which are dependent on the sample reflectivity and its surface morphology, contribute to establishing the noise-dependent limits to the measurement's sensitivity.

A gated-pulse measurement technique may be used for absorption studies of liquids [9.67], when not amplitude-modulated or phase-modulated, but rather a time-resolved transient ultrasonic signal is detected, allowing one to discriminate ballistic sound propagation from an irradiated liquid versus the sound from cell windows or walls (Fig. 9.31). If that acoustic cell, filled with a low-absorbing expanding liquid forming a narrow cylindrical volume of length ℓ and radius r, is irradiated by a pulse of radiation of energy E_0 and duration t_d, its energy-transformation equation becomes:

$$E_0(1-\exp(\alpha\ell)) \underset{\alpha\to 0}{\approx} E_0\alpha\ell = c_p\rho_p V\Delta T. \tag{9.80}$$

Equation (9.80) is justified under the assumption of isobaric adiabatic liquid expansion, where ρ_p and c_p are the density and the specific heat of the liquid at constant pressure; $V = \pi r^2\ell$ is the irradiated volume, and ΔT is the temperature rise within pulse period t_p. Heating causes thermal expansion of the liquid with expansion coefficient β for radius r of its column to increase by small fraction $r' \ll r$ and:

$$\pi(r+r')^2\ell - \pi r^2\ell \underset{r'\ll r}{\cong} 2\pi r r'\ell = \beta V\Delta T. \tag{9.81}$$

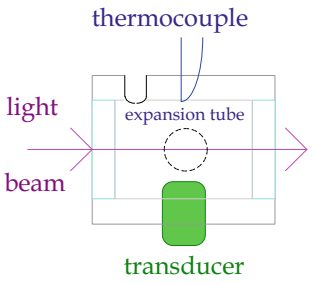

Fig. 9.31 Expanding-liquid cell

As a result, the linear absorption coefficient α measured by gated-pulse photoacoustic spectroscopy is [9.67]:

$$\alpha = 2\pi r r' c_p \rho_p V \Delta T / \beta E_0. \tag{9.82}$$

The use of a submersed piezoelectric transducer as in Fig. 9.31 allows narrowband acoustic impedance matching with fast rise time and reduced ambient mechanical and electrical noises. With a boxcar integrator measuring the compression pulse amplitude of duration t_d (approximately 1 μs in the experiments provided), the absorption coefficients of the light and the heavy water were from $1.77 \cdot 10^{-4}$ to $52.6 \cdot 10^{-4}$ cm^{-1} at wavelengths from 446.3 to 694.2 nm [9.67].

An even higher signal-to-noise ratio may be achieved when registering the second and higher acoustic harmonics, owing to further isolation of the signal due to background noise by the cell windows and walls. If the intensity of the light beam irradiating an absorbing gas in an acoustic cell (Fig. 9.32) is sufficient for the absorbed energy to generate high harmonics of cw (continuous-wave) modulation or pulse rate, the sensitivity of the absorption measurement at the acoustic harmonics is enhanced since the background acoustic response due to cell windows and walls remains linear [9.68]. For example, in an experiment with a tunable pulsed dye laser at 30-Hz repetition rate, the highest signal-to-noise ratio was reached for the fifth harmonic using 150-Hz detection frequency [9.69].

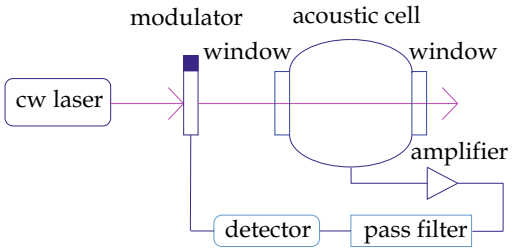

Fig. 9.32 Second-harmonic absorption cell

In each acoustically nonresonant cell reviewed, a relatively high sensitivity was maintained by keeping a small volume and especially a small cross section of the acoustic detector. When a sample gas must be flowed in and out of an acoustic cell, a larger volume is needed, diminishing the detector's efficiency. By making the cell acoustically resonant to a modulation frequency, one can compensate for the loss of detector sensitivity at a high Q-factor of the resonant cell [9.70]. An advantage of an acoustically resonant cell is in no need to keep a constant cell pressure, thus allowing continuous monitoring of flowing-in gasses and also saturating absorption of cell walls, while positioning the outer gas inlet and outlet in areas where a standing acoustic wave has a node. The enhanced selectivity of the resonant cell allows detection of gas mixtures using multiwavelength or tunable lasers [9.71, 9.72]. The drawbacks of acoustically resonant detectors are their slow reaction to

absorption changes in large cell volumes, dependency of the resonant frequency on temperature and gas composition in the cell, and the rapidly changing phase of the acoustic-pressure signal near the resonance [9.65]. The sensitivity of photoacoustic techniques – whether resonant or nonresonant, modulated cw or pulse, in situ or remote measurement – approaches parts-per-billion and nearly 10^{-8}-cm^{-1} linear absorption coefficients [9.73–9.75].

9.2.6 *Trace-Gas Photoacoustic Analysis*

From the standpoint of low-loss measurements for trace gas detection in a resonant acoustic cell, only a single-frequency resonance is needed, permitting one to narrow down the acoustic resonance profile by increasing the cell's Q-factor, which for cw-based techniques may lead to difficulties in synchronizing the resonance and modulation frequencies versus temporal drifts of temperature, composition, and pressure, slowing the system down for in situ or remote monitoring. Pulsed laser measurements in a cell with a high Q-factor allow one to obtain the entire excited acoustic-mode resonance spectrum by Fourier transformation of the time-resolved signal for the cell's response to just a single light pulse, reducing susceptibility to slow drifts of the resonant frequency [9.76]. The time evolution of a single-pulse microphone signal can be detected by a boxcar integrator or transient detector and averaged over a series of pulses to suppress noises originating from the environment. To enhance cell sensitivity, even windowless cells may be fitted with acoustic filters restraining cell-wall resonances caused by reflected or scattered light [9.77].

Figure 9.33 schematically illustrates a high-Q resonant photoacoustic cell setting with either closed or open windows [9.78]. In this case, the resonator itself is a stainless steel cylinder with polished inside surfaces, enhancing its Q-factor, which for the 10.3-cm long and equal-diameter cylinder was measured being near 820 in N_2. The transverse beam placement versus the on-cell axis was varied to access multiple nodal points of its acoustic modes with a sensitive condenser microphone connected to a selective low-noise preamplifier attached halfway on cylinder's surface. Acoustic filters and buffer volumes, tuned to suppress outside noise, were positioned at each end of the cell. To obtain 2-Hz spectral resolution, a Fourier transform of a 0.5-s time signal at 16.67-kHz sampling rate for each 100-pulse train

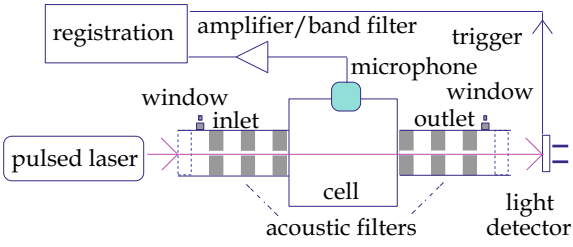

Fig. 9.33 High-Q resonant photoacoustic cell

was averaged over 8192 points, curve-fitted via Lorentzian series. The estimated absorption coefficient detection limits were $(6–9) \cdot 10^{-8}$ cm^{-1} [9.78].

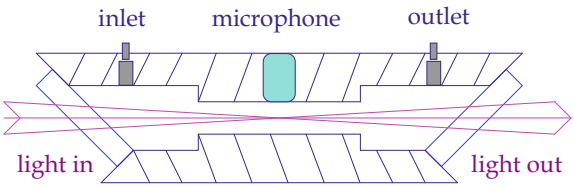

Fig. 9.34 Long Brewster-window-based cell

A long Brewster-window cell configuration for pulsed photoacoustic measurement is shown in Fig. 9.34. The small-radius cell is irradiated by a tightly focused, long-cylinder-shaped laser beam, enhancing the sensitivity by close positioning a microphone to the beam; it has stretched-out windows, positioned at the Brewster angle for time separation of retroreflections and of the pressure pulse itself. Spectral absorption studies in the cell were made via 9–11-μm radiation at 0.2-Hz repetition rate from a high-pressure CO_2 laser which was continuously tunable within the 76-cm^{-1} band, being practically a single-pulse technique [9.79]. The measurements were performed assuming direct proportionality for absorbed versus incident energy for narrow-beam irradiation (Eq. (9.80)). For slow relaxation processes in test gas compositions, for which all perturbations of gas thermal equilibrium due to absorbed energy of the incident pulse are relaxed via collision-induced vibrational-to-translational energy transfers, inducing pressure-pulse responses, the pressure-pulse temporal evolution becomes [9.65, 9.79]:

$$P(t) \sim (1 - \exp(-t/t_{n-r})) \cdot \exp(-t/t_t). \tag{9.83}$$

Here t_t is the conduction decay time due to thermal diffusivity: $\lambda_T/\rho_p c_p$ (see Sect. 9.1), of the test gas and t_{n-r} is the nonradiative relaxation time, which is inversely proportional to the pressure built up by the light pulse focused into the test gas. The t_{n-r} value characterizes the simultaneous local increase of the temperature and pressure. In turn, the pressure wave is defined by the acoustic relaxation time constant: $t_{a-p} = \omega/v_s$, which determines the dissipation of the thermal diffusion wave: $t_{a-p} = \omega^2 \rho_p c_p / 8\lambda_T$. Here ω is the radius of the Gaussian-beam waist and v_s is the sound velocity. The actual time of vibrational-to-translational energy transfer separates regions of slow: $t_{n-r} \sim t_{a-p}$, and fast: $t_{n-r} \gg t_{a-p}$, processes.

Figure 9.35 illustrates the temporal evolution of a pressure-driven photoacoustic pulse versus time constants t_{n-r} and t_t. The evolution consists of the exponential rise due to the energy relaxation with time constant t_{n-r} and the exponential decay due to thermal conduction with time constant t_t. Decay curves 1 and 2 correspond to relatively fast vibrational-to-translational energy transfers under 100 μs; decays 3 and 4 relate to slow transfers above 100 μs. In the experiments conducted [9.79], the sensitivity to low absorption coefficients reached nearly 10^{-6} cm^{-1}. Despite there being 4 orders of magnitude in linearity for photoacoustic signals versus the

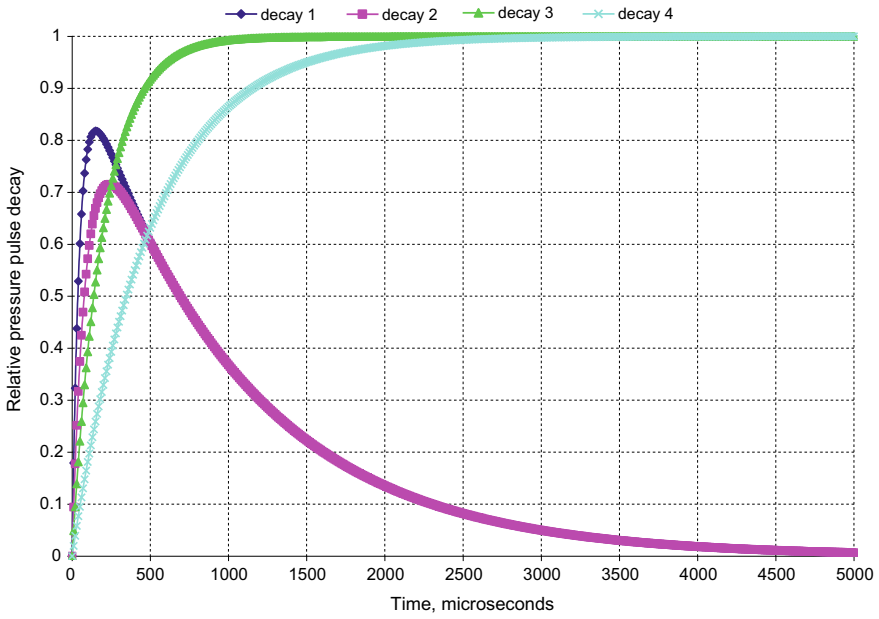

Fig. 9.35 Temporal pulse evolution at t = 10 ms and t_{n-r} = 50, 100, 200, and 500 μsec for decays 1–4

concentration of absorbing species, some noticeable nonlinearities due to either saturation of pulse energy or energy-dependent absorption loss were also observed.

One more sensitivity enhancement for pulsed photoacoustic measurements is the Helmholtz configuration of an acoustic cell: two resonant cavities connected by a duct, initially adopted for cw-modulated techniques, taking advantage of narrow-band resonances of two coupled volumes – one for the sample, the other for a microphone, which can be connected via a differential scheme [9.80]. Applications of Helmholtz resonators in combination with cryogenic temperatures can increase the photoacoustic signal amplitude in chopper-modulated measurements up to $T^{-2.75}$ [9.81]. Pulsed measurements using a Helmholtz cell configuration in the arrangement shown in Fig. 9.33, made at CO_2 laser wavelengths, reached near 10% absolute-value match for 3.25 cm^{-1} absorption coefficient, measured within 0.3 cm^{-1} versus the published 2.98 cm^{-1} value obtained via cw-based measurements [9.82]. The result by itself confirms a good agreement of distinctive absorption data points, though not fulfilling the high expectations for the factual accuracy and the sensitivity of indirect linear absorption coefficient measurements.

A dual-resonator cell designed for relatively fast – 10 s or less response time – pulsed photoacoustic detection is shown in Fig. 9.36 [9.83]. The cell is symmetric and contains acoustic resonators 1 and 2 sandwiched between acoustic filters as in Fig. 9.34, with identical microphones 1 and 2 positioned near the center of each resonator (out of the irradiation plane), having their signals collected via the

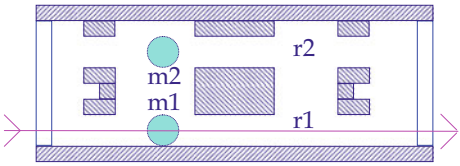

Fig. 9.36 Dual acoustic resonator cell: m – microphone, r – resonator

differential output to reduce the system's gas-flow noise. In the experiments, the repetition rate of a 1064-nm laser was tuned to match the 4100-Hz acoustic resonant frequency of the cell for the low Q-factor (Q = 17), making the full width at half-maximum of every resonance be near 235 Hz. The resonator tube and filter-to-inlet volumes were near 2 and 17 cm^3 for a design-limited response time of approximately 4 s, with the actually measured time being near 10 s. The smallest evaluated methane concentration was estimated as 1.2 ppbv, leading to the expected minimum detectable absorption coefficient $\alpha \approx 3.3 \cdot 10^{-8}\,cm^{-1}$ [9.83].

A dual nonresonant differential arrangement of a photoacoustic cell is illustrated in Fig. 9.37 [9.84]. Two small-volume acoustic cells of near 1 cm^3 having approximately 5 cm^2 surface area with an electret microphone coupled to a field-effect transistor preamplifier were used for photoacoustic measurements with a single-mode, single-spectral-line CO_2 laser in the 10.6-μm band, tunable over ±200 MHz, at 800-Hz pulse repetition rate generating 10-μs-long pulses at 25-W peak power. The actual sensitivity for 50-ppm concentration of NH_3 in N_2 was estimated to be $1.3 \cdot 10^{-8}\ (W \cdot cm^{-1})/Hz^{1/2}$, versus the lowest resonant-cell sensitivity: $1.6 \cdot 10^{-8}\ (W \cdot cm^{-1})/Hz^{1/2}$, obtained using the detection system shown in Fig. 9.33 [9.78]. These estimates were made for less than 2:1 signal-to-nose ratio, based on the registered rms noise fluctuations of the differential-output acoustic signal for active cells with no NH_3, assuming the absence of acoustic noise owing to absorption–desorption processes on cell surfaces [9.85, 9.86].

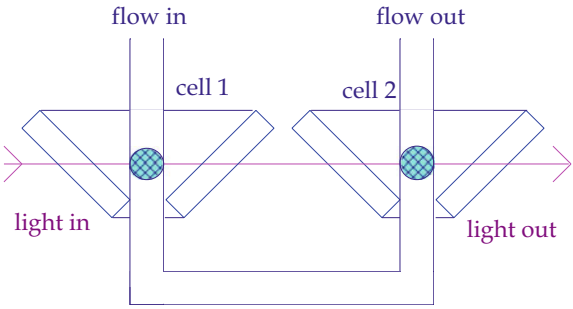

Fig. 9.37 Differential nonresonant cells

Some enhancement in the power density of incoming radiation and, as a result, in the sensitivity of photoacoustic measurements was achieved by combining a tunable diode laser operating at near 1530 nm and an erbium-doped fiber amplifier (EDFA) [9.87]. A directly modulated tunable diode laser (Fig. 9.38), providing

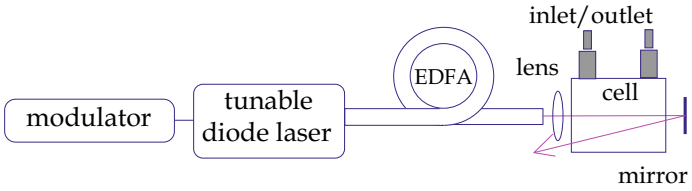

Fig. 9.38 Photoacoustic sensor based on an EDFA

20 mW of power in cw mode, was slowly scanned at 1–10 MHz in wavelength, equal to half the resonant frequency of the photoacoustic cell, saturating the coupled erbium-doped fiber amplifier, and thus ensuring a constant 500 mW of output light power, was collimated into the cell with dual propagation via a mirror. The 1σ based, noise-limited sensitivity for detection of NH_3 in N_2 was estimated as being near 6 ppb, making the calculated level of the absorption density limit: $\alpha_{min}\ell = 1.8 \cdot 10^{-8}$ at path length ℓ of 18.4 cm, and the minimum absorption coefficient $\alpha_{min} = 1.5 \cdot 10^{-9}\,(W \cdot cm^{-1})/Hz^{1/2}$, normalized by the power-to-bandwidth ratio at 19 mm for the dual cell path [9.87].

In addition to gas-filled resonators, accumulating the energy of absorbed radiation detected by microphones as acoustic sensors, a quartz tuning fork made of piezoelectric crystal quartz can be used to both accumulate and sense the energy of absorbed light [9.113]. The advantage of this approach is in lower susceptibility to environmental acoustic noise for analyzing small volumes in nonresonant cells. Figure 9.39 depicts the schematics for the direct irradiation of the fork along its prongs (Fig. 9.39a) and for the combined fork and acoustic resonator settings with a shorter in-fork optical path, being enhanced by two resonant tubes (Fig. 5.39b). For the quartz fork in a cell, as in any acoustic cavity (see Eqs. (9.80)–(9.82)), the pressure-induced resonant signal S_a due to the energy absorbed in the gas-filled cell via the loss factor $\alpha\ell$ is directly proportional to the light power P and the resonator quality factor Q, but is inversely affected by the resonant frequency f_0 and the resonant volume V: $S_a \sim \alpha\ell P/f_0 V$. Quartz forks are available in small sizes with

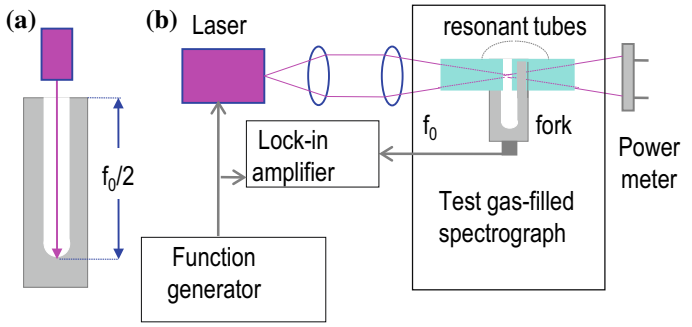

Fig. 9.39 Quartz-tuning fork enhanced measurements

high Q factors: nearly 20,000 if the fork is encapsulated in a vacuum and 8000 at normal atmospheric pressure, both at standardized resonant frequency $f_0 = 2^{15}$ Hz. Combinations of the resonant fork and the resonance-enhanced acoustic cells (see Fig. 9.39b) allow reaching 10^{-9}–10^{-10} cm^{-1} W/$\sqrt{\text{Hz}}$ noise-level sensitivity [9.114–9.118]. Interferometric cantilevers and compact electromechanical acoustic cavities with differential resonators for noise removal allow similar sensitivity levels to be realized [9.119, 9.120].

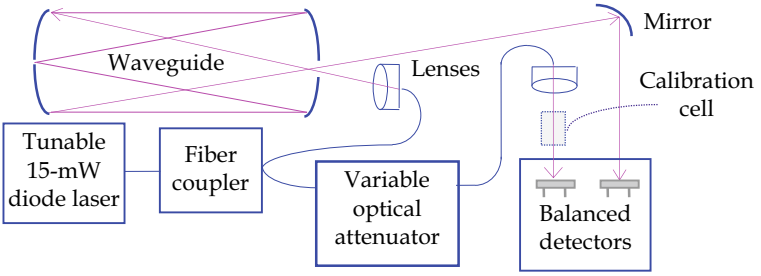

Fig. 9.40 Tunable-diode multipath loss-detection insert

In terms of the absolute sensitivity, photoacoustic detection is not inevitably better than other low-loss detection techniques. For example, a comparative study of photoacoustic and direct absorption measurement methods revealed quite similar sub-parts-per-million levels of minimal detectable concentrations for NH_3 in N_2 [9.88]. The study employed two measurement cells: a multipass waveguide absorption cell as in Fig. 6.24 and a photoacoustic cell similar to that in Fig. 9.33, each excited by a fiber-coupled distributed feedback laser and each emitting at 1.53-μm wavelength −15 mW for calorimetric and temperature-stabilized sensing and 5 mW for photoacoustic sensing (Fig. 9.40). The Herriott cell had a 36-m-long effective optical path and 0.27-l volume, and was heated to 40°C; the photoacoustic stainless steel cell had a volume near 50 cm^3 and a 40-mm-long and 4-mm-diameter central resonator excited at 4-kHz modulation frequency to match the resonance of the acoustic cavity. The estimated minimal-detectable concentrations of NH_3 in N_2 were 0.7 and 0.6 ppm [9.88] for the multipass absorption and the photoacoustic measurement techniques for 1 and 3-min response times, respectively.

9.2.7 *Optical Spectroscopy of Ultrasonic Waves*

An extremely sensitive detection of wavefront distortions due to low absorption losses can be accomplished by probing acoustic deformations via an interferometer, while using either a Hartmann–Shack or a similar wavefront-deformation sensor [9.121, 9.122]. Figure 9.41 illustrates the concept of spatial separation for the irradiation and observation directions to split the bulk from surface absorption loss contributions. A collimated ArF excimer laser beam with a flat-top circular profile

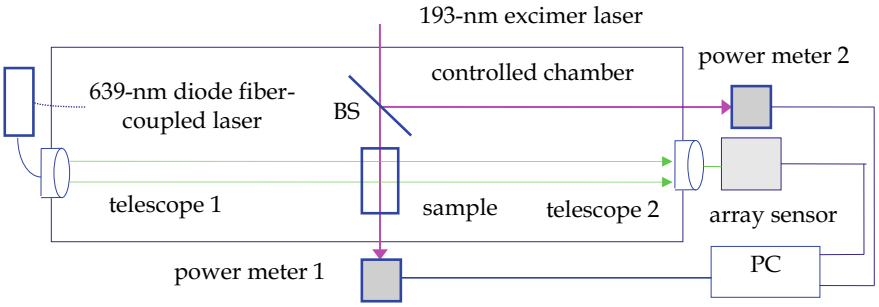

Fig. 9.41 Detection of laser-induced wavefront deformation

collinearly propagates through a test sample and the expanded beam of a fiber-coupled red diode laser crosses it perpendicularly. The laser-induced wavefront deformation is sensed by a two-dimensional 1280 × 1024 pixel sensor array via a CCD camera, reaching quite overwhelming λ/10,000 rms sensitivity at $\lambda = 193$ nm. Camera readings and two optical power-meter signals – split via beam splitter BS with one meter measuring the power of light beam propagating via the sample and another referencing the input laser power – are managed by a PC, controlling the excimer laser shutter for variable sample heating and cooling intervals and respective pressure monitoring.

Another approach for remote interferometric sensing of the photoacoustic waves generated by mid-IR radiation of a quantum cascade laser, absorbed in a sample [9.126] and registered via a fiber-based Mach-Zehnder interferometer, is depicted in Fig. 9.42. Quantum cascade laser QCL was tunable from 8.12 to 9.71 μm focusing a 40-ns light pulse on Sample, another side of which was probed by fiber laser *FL* at 1549.9 nm via respective fiber collimators FC_1, FC_2. Fiber circulator CR with erbium-doped fiber amplifier EDFA and balanced photodetectors PD_1, PD_2 concluded the interferometer, stabilized via a piezo-electric phase shifter. The measurement scan taking 7.3 s within the range of *QCL* tunability showed nearly $1 \cdot 10^3\ m^{-1}$ absorption sensitivity [9.126]. Pairs of orthogonally mounted Fabry-Perot interferometers may be used as sensors of ultrasonic vibrations for photoacoustic imaging of tissue [9.127]. A relative comparison of the achievable sensitivity for the photothermal and photoacoustic absorption measurements on three distinct

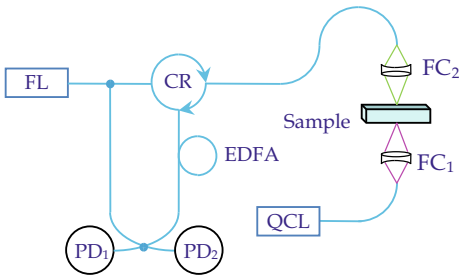

Fig. 9.42 Remote sensing of photoacoustic waves

systems: photoacoustic and photothermal common-path spectrometers, plus a whispering-gallery resonator interferometer – revealed reasonable agreements in 390–3800 nm spectral range at absorption coefficients ranging from $\sim 10^{-4}$ cm^{-1} to 2 cm^{-1} complementing results obtained by a standard-grating spectrometer and an FTIR (see Sect. 12.1) instrument [9.128].

9.3 Emissive Spectroscopy

Each technique reviewed in this chapter – diffraction, interferometric, photoacoustic – is sensitive, though indirectly, in detecting the absorption factor and linear absorption coefficient, since sensing absorbed energy or power without calibration and with no quantitative means of knowing the absorptance itself does not provide quantization. Emission spectroscopy gives the advantage of absolute determination of absorbed or emitted power according to Kirchhoff's law and Planck's law. The spectral emissivity ε_λ of the ideal blackbody, kept at thermal equilibrium, is exactly equal to the spectral absorptance α_λ : $\varepsilon_\lambda \equiv \alpha_\lambda = 1$. At the same equilibrium, graybody emissivity: $\varepsilon_\lambda \equiv \alpha_\lambda = 1 - \rho_{\lambda,\Sigma}$, is affected by its reflectivity $\rho_{\lambda\Sigma}$ at wavelength λ. For a transparent object the balance includes the specular-plus-diffuse and the direct-plus-diffuse components of light emission or absorption: $\varepsilon_\lambda \equiv \alpha_\lambda = 1 - \rho_{\lambda,\Sigma} - \tau_{\lambda,\Sigma}$, where $\rho_{\lambda\Sigma}$ and $\tau_{\lambda\Sigma}$ are the total reflectance and the total transmittance, respectively (see Chap. 1).

An intuitive transformation of Kirchhoff's law for reflective and transmissive objects can be seen via the illustration in Fig. 9.43 [9.89]. If in a plane-parallel transparent slab of thickness *d*, an inner layer *dx* emits radiation into 4π space with spectral emittance M(λ,T) at wavelength λ + dλ and equilibrium temperature T, then from unit surface area A in small solid angle dΩ the light intensity is: $dI = (1/4\pi)M(\lambda,T)dxd\Omega$. After propagation via the slab with linear attenuation coefficient μ, the intensity at either slab surface (see Eq. (1.87)) becomes: $dI_{surf} = (1/4\pi)M(\lambda,T)e^{-\mu(\lambda,T)x}dxd\Omega$. Since $\exp(-\mu(\lambda,T)x) = \tau(\lambda,T)$ is the internal slab transmittance, its integrated normal emittance E is:

$$E(\lambda,T) = (1/4\pi)M(\lambda,T)d\Omega \int_0^d \exp(-\mu(\lambda,T))dx$$

$$= \frac{M(\lambda,T)}{4\pi\mu(\lambda,T)}(1-\tau(\lambda,T))d\Omega. \tag{9.84}$$

The total amount of internally emitted radiation leaving the slab surface of reflectivity ρ(λ,T) is:

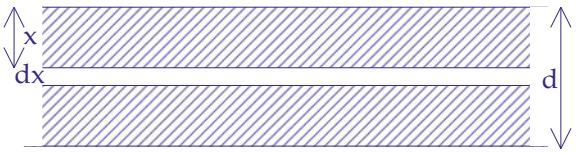

Fig. 9.43 Light emission by transparent layer

$$E(\lambda,T)_{external} = (1-\rho(\lambda,T))\frac{M(\lambda,T)}{4\pi\mu(\lambda,T)}(1-\tau(\lambda,T))d\Omega. \tag{9.85}$$

Considering the slab's emission only into 2π space as for a blackbody with full absorption [9.89]:

$$E(\lambda,T)_{external} = (1-\rho(\lambda,T))\frac{M_b(\lambda,T)}{2\pi}(1-\tau(\lambda,T))d\Omega, \tag{9.86}$$

one obtains counting multiple reflections for a plane-parallel transparent plate (Eq. (1.104)):

$$M(\lambda,T) = \frac{(1-\rho(\lambda,T))(1-\tau(\lambda,T))}{1-\rho(\lambda,T)\tau(\lambda,T)}M_b(\lambda,T), \tag{9.87}$$

where $M_b(\lambda,T)$ is the emittance of the ideal blackbody, fully absorbing radiation with factors: $\mu(\lambda,T) = \alpha(\lambda,T) = 1$.

Following Eq. (9.87) and the specifics of the emissivity of transparent objects, the measurement concept for absorptance-via-emittance measurement, maintaining the thermal equilibrium, may look straightforward (Fig. 9.44), though it could require certain finesse at the low optical losses [9.91]. Conceptually, the frequency- or wavelength-dependency $L_{e,\nu}$ or $L_{e,\nu}$ for spectral radiance obeys Planck's law inside an isothermal enclosure as an ideal blackbody at temperature T:

$$L_{e,\nu} = \left(2h\nu^3/c^2\right)/\left(e^{h\nu/kT}-1\right);\ L_{e,\lambda} = \left(2hc^2/\lambda^5\right)\Big/\left(e^{hc/\lambda kT}-1\right), \tag{9.88}$$

for light wavelength λ and frequency ν, where h and k are the Planck and Boltzmann constants, and where the blackbody enclosure emits radiation by Eq. (1.46) as an ideally Lambertian object. That enclosure should be large to accommodate the specimen and maintain blackbody properties.

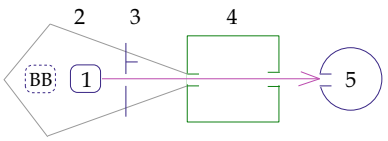

Fig. 9.44 Measurements of emittance

When sample 1 for absorption study at temperature T_s is inside enclosure 2 at temperature T_c, emitting radiation via chopper 3 to monochromator 4 and detector 5, the detector's signal becomes an aggregate of the sample emittance via internal reflections of cavity walls minus the emittance of the chopper blades, presuming the cavity walls and the chopper blades are at the same temperature T_c as the entire

isothermal enclosure, except the sample. The total energy of light transmitted via monochromator 4 makes the combined signal E of detector 5 [9.90, 9.91]:

$$E_s = const \cdot (\varepsilon_\lambda W_0 + \rho_\lambda W_c + \tau_\lambda W_c - W_c). \tag{9.89}$$

Here W_0 and W_c are the spectral energy densities, emitted by the test sample and the cavity. Sample emittance ε, in view of its absorptance via reflectance and transmittance: $\varepsilon_\lambda = \alpha_\lambda = 1 - \rho_\lambda - \tau_\lambda$, is:

$$\begin{aligned} E_s &= const \cdot (\varepsilon_\lambda W_0 - \varepsilon_\lambda W_c + (\varepsilon_\lambda + \rho_\lambda + \tau_\lambda) W_c - W_c) \\ &\underset{\varepsilon_\lambda + \rho_\lambda + \tau_\lambda = 1}{=} const \cdot \varepsilon_\lambda (W_0 - W_c). \end{aligned} \tag{9.90}$$

To make an absolute calibration of the system, blackbody radiator BB at the same temperature T_0 is installed instead of sample 1. Since for a blackbody $\varepsilon_{bb} = 1$; $\rho_{bb} = 0$, the respective signal is [9.91]:

$$E_{bb} = const \cdot (\varepsilon_{bb} W_0 + \rho_{bb} W_c + \tau_{bb} W_c - W_c) = const \cdot (W_0 - W_c); \quad E_s / E_{bb} = \varepsilon_\lambda. \tag{9.91}$$

The combination measurement with the blackbody behind the sample of transmittance τ gives:

$$\begin{aligned} &E_{s+bb} = const \cdot (\varepsilon_\lambda W_0 + \rho_\lambda W_c + \tau_\lambda W_0 - W_c) = const \cdot (\varepsilon_\lambda + \tau_\lambda)(W_0 - W_c); \\ &E_{s+bb} / E_{bb} = \varepsilon_\lambda + \tau_\lambda. \end{aligned} \tag{9.92}$$

Equations (9.90)–(9.92) confirm that to increase the measurement sensitivity for low absorption losses and consequently for low emissivity of a test object, the temperature contrast between temperatures of the object and the background must be increased as much as possible. Fluctuations of the temperature contrast between the sample and the cavity, as well as the temperature of the chopper blades, directly affect the accuracy of such a measurement. For example, at room temperature near 20 °C, a potential 0.5 °C change of T_b displaces the apparent position of the maximum-emitting spectral line in the mid-IR region by nearly 5 μm [9.90]. Applying the revealed emission measurement technique, while keeping samples at liquid-nitrogen temperatures, and also utilizing a Fourier spectrometer, providing the highest possible throughput in the IR spectral range, enabled an absorption coefficient in the 10^{-5}-cm^{-1} range to be measured with a spectral resolution of approximately 1 cm^{-1} [9.44].

In the emissivity measurement, as well as in other procedures involving uncoated surfaces, protective measures may need to be taken to avoid the internal multiple reflections in all plane-parallel plates. Transformation to the effective coefficients ε_λ', α_λ', ρ'_λ, and τ'_λ counting multiple reflections could be done via following relations (see Chap. 1):

$$\varepsilon_\lambda = \alpha_\lambda = (1-\rho_\lambda)\left[1-\exp(-\alpha\ell)\right]/\left[1-\rho_\lambda\exp(-\alpha\ell)\right];$$
$$\tau_\lambda = (1-\rho_\lambda)^2\exp(-\alpha\ell)/\left[1-\rho_\lambda^2\exp(-2\alpha\ell)\right];$$
$$\rho_\lambda = \rho_\lambda\left[1+\exp(-2\alpha\ell)(1-2\rho_\lambda)\right]/\left[1-\rho_\lambda^2\exp(-2\alpha\ell)\right]. \tag{9.93}$$

As a result, the effective linear absorption coefficient α' of the internal bulk of a substance under study is being defined not only by the measured emissivity, but also by the surface reflectance ρ_λ from the following relationships [9.91]:

$$\alpha_\lambda = \varepsilon_\lambda = \left(1-\rho_\lambda^2\right)\left(1-\exp\left(-\alpha'\ell\right)\right)/\left(1-\rho_\lambda^2\exp\left(-\alpha'\ell\right)\right);$$
$$\alpha'\ell = \ln\left[\left(1-\rho_\lambda^2\varepsilon_\lambda-\rho_\lambda^2\right)/\left(1-\rho_\lambda^2-\varepsilon_\lambda\right)\right]. \tag{9.94}$$

Consequently, any linear absorption coefficient measurement for a reflecting substance requires having at least two test samples with the correspondingly distinguished lengths to be compared.

Applying Kirchhoff's law, one can obtain the emittance and the absorptance of an expected blackbody via bidirectional: ψ, θ, spectral reflectance measurements of the blackbody's cavity:

$$\rho_\lambda(\psi,\theta) = \Phi_{\rho,\lambda}(\theta)/\Phi_{0,\lambda}(\psi);$$
$$\alpha_\lambda(\psi,\theta) = 1-\rho_\lambda(\psi,\theta) = \left(\Phi_{0,\lambda}(\psi)-\Phi_{\rho,\lambda}(\theta)\right)/\Phi_{0,\lambda}(\psi); \tag{9.95}$$
$$\varepsilon_\lambda(\psi,\theta) \underset{\varepsilon_\lambda=\alpha_\lambda}{=} 1-\rho_\lambda(\psi,\theta),$$

where Φ_0 and Φ_ρ are the incident and the reflected flux of radiation at the angle of incidence ψ and the angle of observation θ (see Fig. 9.45). Owing to low residual reflectivity for a close-to-ideal blackbody cavity, the emissivity errors made while expecting close-to-zero reflectivity can be low: $\Delta\varepsilon_\lambda = \Delta\rho_\lambda = \rho_\lambda\Delta\rho_\lambda/\rho_\lambda$. At $\rho_\lambda = 0.0005$ and 10% reflectivity measurement error, the emittance ε and absorptance ρ are $\varepsilon_\lambda = \rho_\lambda = 0.9995 \pm 0.00005$.

Emittance measurements, performed via bidirectional reflectance detection by equations (9.95), have distinguished a particular off-axis cavity at $\varphi = 10°$, D = 1 cm, and length-to-aperture ratio L/D = 12.45 (Fig. 9.45a) as having the highest emittance [9.93]: $\varepsilon_\lambda = 0.99999$ at $\lambda = 10.6$-μm wavelength of a CO_2 laser, among various cavities tested while all of them were coated with same diffusing black paint. Measurements were made via an integrating hemiellipsoid as the blackbody cavity (Fig. 9.45b) having the sample and a light detector at two focal points of the ellipsoid with the incident laser beam entering the test cavity along its

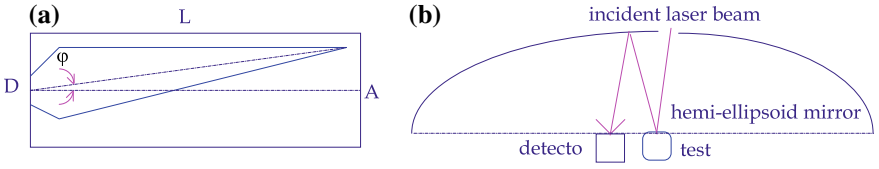

Fig. 9.45 Off-axis blackbody cavity (**a**) and hemi-ellipsoid collection of radiation emission (**b**)

axis *A* (Fig. 9.45a). The laser beam was chopped at 5–35-Hz frequency, delivering 99.975% of laser light to the cavity in an evaporated-aluminum hemiellipsoid, focusing the cavity emittance to a thermopile detector connected to a lock-in amplifier [9.92]. The comparison of the emittance and calorimetric studies revealed reasonable matches of absorption values near 10^{-4} cm^{-1} for polished KCl samples [9.93]. Calibrations of blackbodies for emissivity measurements are often made via a Fourier-transform spectrometer (see Sect. 12.1), especially at IR wavelengths and low temperatures [9.125–9.127].

9.4 Integrating Spheres as Multiple-Reflection Cavities

9.4.1 Integrating-Cavity Absorption Measurements

Utilization of integrating spheres, as seen in Chap. 2 (Eqs. (2.5), (2.6)), enables accurate and sensitive measurements of diffuse and direct reflectance or transmittance at thermal equilibrium of radiation in a sphere [0.2–0.7, 0.12]. Following the law of conservation of energy for detection of attenuation coefficients in reflected and transmitted radiation, any internal sphere absorptance completes the total sphere internal loss to unity. Thus, for perfect geometry of the integrating sphere and infinitely small apertures for light beams entering and exiting such a sphere for irradiation and detection of irradiance of the inner sphere surface, the wall absorptance α can be determined by measuring two sphere irradiances: one irradiated only by the sphere's internal reflections E_0, and the other irradiated by the sphere reflections E_0 and direct input E_d, accomplished via selective baffling or viewing:

$$E_0/(E_0 + E_d) = \rho; \rightarrow 1 - \rho = 1 - E_0/(E_0 + E_d); \rightarrow \alpha = 1 - \rho = E_d/(E_0 + E_d). \tag{9.96}$$

Equation (9.96) resembles relation (2.131) for the absolute reflectance measurements [2.46–2.48].

Another way of detecting the integrating cavity absorptance is by comparing the irradiance while altering its inner-surface area [9.94, 9.95]. For flux Φ_0 entering the sphere via an infinitely small aperture, the sphere equilibrium is maintained via light reflected and absorbed by sphere walls:

$$\begin{aligned}\Phi_0 &= \Phi_0(1-\rho) + \Phi_0\rho(1-\rho) + \Phi_0\rho^2(1-\rho) + \cdots \\ &= \Phi_0(1-\rho) + \Phi_0\rho(1-\rho)/(1-\rho) = \Phi_0(1-\rho) + \Phi_0\rho.\end{aligned} \tag{9.97}$$

If an infinitely small detector senses internal irradiance E_0 of the sphere, Eq. (9.97) becomes:

$$\Phi_0 = \Phi_0(1-\rho) + \Phi_0 A_0\rho(1-\rho)/(A(1-\rho)) = \Phi_0(1-\rho) + E_0 A_0\rho(1-\rho). \tag{9.98}$$

Here A_0 is the internal sphere surface. When an auxiliary aperture of area A is opened into the sphere, its internal irradiance is reduced to E_A and the sphere equilibrium for flux Φ_0 equals to:

$$\Phi_0 = \Phi_0(1-\rho) + E_A(A_0 - A)\rho(1-\rho) + E_A A. \tag{9.99}$$

Via Eqs. (9.98) and (9.99) for known areas A_0 and A and irradiances E_0 and E_A, the sphere absorptance α is:

$$\alpha = (1-\rho) = E_A A/(E_0 A_0/A - E_A(A_0/A - 1)). \tag{9.100}$$

As a result, one can use an integrating sphere for direct absorptance measurements: since radiation scattered inside such a sphere is completely recycled via multiple sphere reflections, the true spatially integrated absorption coefficient α of the entire sphere surface is determined as $\alpha = 1 - \rho$, as long as the internal surface of the sphere is a uniform diffuser with unchanging diffuse reflectance $\rho = \rho_d$ and the infinitely small inclusions (see Chap. 2). First, let us recall Eqs. (1.71–1.73) leading to the Bouguer–Beer–Lambert law. If an incident beam of light with energy E_0 is transmitted via a homogeneous plane-parallel sample of linear absorption coefficient α, the energy E_a absorbed by the sample material is:

$$dE_a = -E\cdot\alpha\cdot dx = -E\cdot\alpha\cdot d(t\cdot v) = -E\cdot\alpha\cdot d(t\cdot c/n), \tag{9.101}$$

where E is the energy of incident light traveling at speed v via such a sample of thickness x and refractive index n. Converting to absorbed power P via the volume density E_v of incident light:

$$P = dE_a/dt = E\cdot\alpha\cdot v = E_v\cdot V\cdot\alpha\cdot c/n, \tag{9.102}$$

one can express the light flux Φ_a absorbed by volume V of a spherically irradiated or, another words, 4π-irradiated sample (9.96) as:

$$\Phi_a = (E_v V)\alpha c/n. \tag{9.103}$$

Relation (9.103) can be obtained via irradiance vector $\vec{\Xi}$ representing the spherical energy density E_v of spectral irradiation at a given point in volume dV [0.5, 1.1] (see Chaps. 1 and 2):

$$E_v(c/n) = \int_\Omega L d\Omega, \quad where \quad \vec{\Xi} = \int_\Omega \vec{L}(\vec{r},\vec{s}) d\Omega, \tag{9.104}$$

and where **r** and **s** are the unit vectors of the irradiance and direction. From the equation of radiative transfer [1.1, II.24], integrating the divergence of irradiance vector $\vec{\Xi}$ over volume V gives [9.97]:

$$-\nabla\cdot\vec{\Xi} = (\alpha c/n)E_v \;\rightarrow\; -\int_{\vec{s}} \vec{\Xi}\cdot\vec{S} = (\alpha c/n)\int_V E_v dV. \tag{9.105}$$

Presuming the integral in Eq. (9.105) accounts for the light energy, entering the spherical sample and being lost due to absorption only, the power of radiation absorbed in volume V is:

$$\mathrm{P_a} = (\mathrm{E}_v\mathrm{V})\alpha c/n. \tag{9.106}$$

For any uniform diffuse irradiation of the spherical surface, the normal component of the inner vector irradiance Ξ_n can be expressed via outward radiance L (Eq. (1.47)): $\Xi_\mathrm{n} = \pi\mathrm{L}$; thus:

$$\mathrm{E}_v = 4\pi\mathrm{nL/c} = 4\mathrm{n}\Xi_\mathrm{n}/\mathrm{c}. \tag{9.107}$$

From Eqs. (9.106) and (9.107), the outward normal irradiance Ξ_n defines the absorbed power $\mathrm{P_a}$ (9.97):

$$\mathrm{P_a} = 4\alpha\mathrm{V}\Xi_\mathrm{n}. \tag{9.108}$$

Concisely, detection of the linear absorption coefficient in the uniformly integrating sphere can be reduced to determination of the power of incident uniform light absorbed by the sample and the normal irradiance created in that spherical sample under study occupying a known volume.

Multiplication-factor alteration of the reflective surface of the integrating sphere via Eq. (9.100) may not be an effective measurement technique. Enlarging the openings modifies the sphere's reflectivity by impeding its ability to uniformly integrate light (see Sect. 2.4). An alternative approach via openings relies on changing the internal sphere reflectivity by adding an object of spherical geometry but unknown reflectivity for reference-measurement series to be made. The reference technique is illustrated in Figs. 2.5 and 2.35 and is described by Eqs. (2.20)–(2.27) and (2.167)–(2.169) – insertion of a translucent sphere inside an integrating sphere allows keeping uniform irradiation inside either sphere [2.8]. Exactly the same approach can be used to measure the absorptivity of any sample, which requires enabling the uniform-diffuse irradiation for Eq. (9.108) to be applicable for such a measurement.

One example of the reflectivity-alteration technique described above is illustrated in Fig. 9.46 [9.97]. Opaque integrating sphere 1 has the thickest wall for the highest diffuse reflectivity ρ_1. Internal translucent sphere 2 with diffuse reflectivity ρ_2 and transmissivity τ_2 creates volumes 0 and 3 in sphere 1. Radiation from the light source or sources S-a and S-b is transmitted via optical fibers to volume 3 and then guided out to detectors D-0 and D-4 for irradiance measurements inside intermediate spherical cavities 0 and 3 and the walls of spheres 1 and 2 with the use of the fiber, minimizing openings in both spheres. Translucent sphere 2 serves a

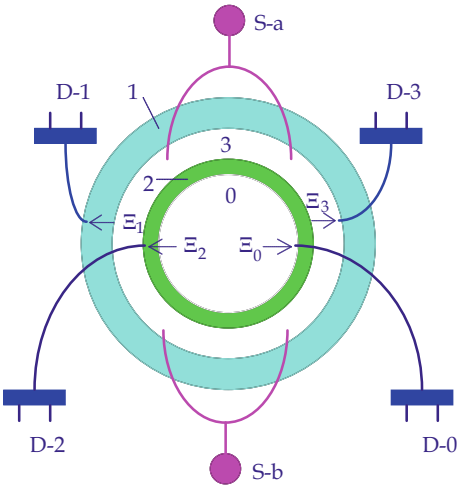

Fig. 9.46 Integrating-sphere sandwich

twofold purpose – it calibrates irradiance in sphere 1 and holds a gaseous or liquid test medium.

When sphere 2 is absent, the balance of energy in sphere 1 measured via irradiance Ξ_3 of light exposing the sphere wall and irradiance Ξ_3 of light leaving the sphere wall (see Fig. 9.46) is:

$$\Xi_1 A_1(1-\rho_1) = \Xi_3 A_3(1-\rho_1) + \Xi_3 A_{in} + \Xi_3 A_{out} + 4\alpha_1 V_3 \Xi_3, \tag{9.109}$$

where α_1 is the inner sphere absorptance; ρ_1 and A_1 are the reflectance and the internal area of sphere 1 minus its inclusions; A_{in} and A_{out} are the areas occupied by the input and output ports, respectively. The sphere balance equation makes the law of conservation of energy – the total power entering the cavity is equal to the power absorbed by its walls and inclusions plus the power leaving the cavity. With sphere 2 having inner sphere absorptance α_2 being inside sphere 1, altered irradiance Ξ'_3 provides a calibration reading of detector D_3 via output area A_{out}:

$$\Xi_1 A_1(1-\rho_1) = \Xi'_3 A_3(1-\rho_1) + \Xi'_3 A_{in} + \Xi'_3 A_{out} + 4(\alpha_1+\alpha_2) V_3 \Xi'_3. \tag{9.110}$$

Similar balance equations can be written for translucent sphere 2 via irradiance values Ξ_2 and Ξ_0 when the enclosure of sphere 2 is empty and when it is filled with the specimen under study.

Under the presumption of a negligible spectral absorptance inside each sphere: $\alpha_1 \to 0$, $\alpha_2 \to 0$, Eq. (9.110) for a sample of absorptance α_λ filling the enclosure of sphere 2 becomes:

$$\Xi_2 A_0(1-\rho_2) = \Xi_0 A_0(1-\rho_0) + \Xi_0 A_{D\text{-}0} + 4\alpha_\lambda V_0 \Xi_0. \tag{9.111}$$

Equation (9.111) accounts for the internal reflectivity ρ_0 of sphere 2 being filled by any liquid sample under study with refractive index $n_\lambda \neq 1.0$ and is therefore different from the outer-wall reflectivity ρ_2. The difference of course vanished for a gaseous sample. For irradiance values Ξ_2 and Ξ_0 proportional to the readings of detectors D-2 and D-0, the sample absorptance α_λ may be determined via known spectral reflectivities ρ_2 and ρ_0 of the inner and outer sphere surfaces:

$$\alpha_\lambda(\lambda) = (A_0(1-\rho_2)/4V_0)(\Xi_2/\Xi_0) - ((A_{\text{D-0}} + A_0(1-\rho_0))/4V_0). \tag{9.112}$$

Whereas $\rho_2 = \rho_0$ for the gaseous sample or presuming that spectral reflectivities ρ_2 and ρ_0 can be predetermined as components of calibration factors K of spheres 1 and 2 with the liquid sample:

$$\alpha_\lambda(\lambda) = K_1(\Xi_2/\Xi_0) - K_2, \tag{9.113}$$

which involves measurement of spectral refractive indices $n_{i\lambda}$ of the sphere and the sample, affecting values of irradiance Ξ_0 and of absorptance $\alpha_\lambda(\lambda)$ being measured, one can generally measure the calibration parameters using two samples of known properties [9.98]. Equation (9.111) can also be resolved via the irradiance ratio Ξ_2/Ξ_0 to be measured or calibrated:

$$\begin{aligned}(\Xi_2/\Xi_0) &= (1-\rho_0)/(1-\rho_2) - (4r\alpha_\lambda(\lambda)/(3(1-\rho_2))) \\ &= (1+4r\alpha_\lambda(\lambda)/3)/(1-\rho_2) - \rho_0/((1-\rho_2)),\end{aligned} \tag{9.114}$$

where r is the radius of internal translucent sphere 2 with a negligible area A_D versus $A_0 = 3V/4r$.

Practical realizations of absorption measurement in liquids or gases (see below for specifics of integrating sphere studies with gaseous substances) filling the translucent integrating sphere implies spectral calibration of an empty and a filled sphere, determining factors K_1 and K_2. For liquid solutions or water pollutants, a pure water sample and a calibration solvent of known absorption coefficients α_w and α_s can be consequently measured for Eq. (9.113) to become, respectively:

$$\begin{aligned}\alpha_w(\lambda) + \alpha_s(\lambda) &= K_{1,\lambda}\left(\Xi_{2,\lambda}/\Xi_{0,\lambda}\right) - K_{2,\lambda}; \\ \alpha_s(\lambda) &= K_{1,\lambda}\left(\Xi_{2,\lambda}/\Xi_{0,\lambda}\right) - \left(K_{2,\lambda} + \alpha_w(\lambda)\right).\end{aligned} \tag{9.115}$$

Here subscript λ designates wavelength-specific parameters to be determined by the calibration process. In addition to having spectral dependencies, sphere calibration factors are perturbed by leakage of radiation via entrance and exit apertures and by the refractive index differences of an empty and filled, especially partially filled, sphere for the volume-dependent calibration to be made [9.98]. Besides, the irradiance of the filled-by-sample sphere is affected by the sample's absorption to be determined.

Furthermore, even if spectral calibrations are made to determine the absorption coefficient of an internal medium, the average number of collisions and path lengths of light in the cavity must be known [9.99]. As radiation enters any integrating

sphere (see Chap. 2), it bounces off the sphere walls with reflection coefficient ρ, and multiple diffuse reflections make the sphere irradiance Ξ (equation (2.5)) for an effective number of internal reflections $(1 - \rho)^{-1} = L_e$, being the empty-sphere photon lifetime:

$$\Xi_{in} = (\Phi_{in}/A_{in})/(1 - \rho) = (\Xi_{in} V_{in}/A_{in})/(1 - \rho) = \Phi_0 \tau (4r/3) L_e, \qquad (9.116)$$

where Φ_0 is the flux uniformly distributed in 4π space entering the sphere via translucent walls of transmittance τ, and Ξ_{sp}, V_{sp}, and A_{sp} are the spherical irradiance, sphere volume, and surface area of the sphere of radius r. Equation (9.116) can be rigorously derived via the probabilities of the photon distribution in a sphere, which defines the average path length $\bar{\ell}$ in the sphere per entering photon [9.99] that is also valid independently of a shape of the integrating cavity [9.110]:

$$\ell_{empty} = 4V_{sp}/A_{sp}(1 - \rho) = 4r/3(1 - \rho), \qquad (9.117)$$

where the probability of a photon to survive a wall reflection is ρ and the probability of it being lost is 1 − ρ.

Similarly, the respective probabilities P_α and P_s of a photon being absorbed and surviving a transit across the internal sphere volume filled by a test medium are related as $P_\alpha = 1 - P_s$. Since the path length of a photon emitted or incident at angle φ is: $\ell(\varphi) = 2r \cos\varphi$ (see Fig. 2.28), Eq. (1.73) respectively becomes:

$$Q_a/Q_0 = P_s = \exp(-\alpha \ell(\varphi)) = \exp(-2\alpha r \cos\varphi). \qquad (9.118)$$

Conversion to light emitted at angle φ versus the total flux Φ_0 follows via subsequent relations (see Chap. 1): $I(\varphi) = I_0 \cos\varphi$, $d\Phi(\varphi) = I(\varphi) 2\pi \sin\varphi d\varphi = I_0 2\pi \sin\varphi \cos\varphi d\varphi$, and $\Phi_{2\pi} = \pi I_0$. Considering the probability P of the photon not being absorbed in the medium while propagating at angle φ: $P(\varphi) = P_s \Phi(\varphi)/\Phi_{2\pi}$, the integration over all angles of incidence for photon flights from the wall leads to the following probabilities for the photon to survive or be absorbed [9.99]:

$$P_s = 2 \int_0^{\pi/2} \sin\varphi \cos\varphi \exp(-2\alpha r \cos\varphi) d\varphi = \frac{1 - \exp(-2\alpha r)(2\alpha r + 1)}{2\alpha^2 r^2};$$
$$P_\alpha = 1 - \frac{1 - \exp(-2\alpha r)(2\alpha r + 1)}{2\alpha^2 r^2}. \qquad (9.119)$$

In addition to any straight-line propagation described by Eqs. (9.118) and (9.119), in absorbing and in scattering mediums the sphere photon trajectories may not be straight lines owing to scattering. Since the probability of a photon surviving a wall reflection is ρ and the probability of it surviving intracavity flight is P_s, the combined probability for the first reflection and flight is ρP_s, and is $(\rho P_s)^{n-1}$ for n − 1 reflection collisions plus flights. Combining the direct photon flight with survival probability P_s with sphere-wall reflection probability ρP_s, the average photon lifetime L_f in an integrating sphere filled by an absorbing medium becomes:

$$L_f = P_s + P_s\rho P_s + P_s\rho^2 P_s^2 + \cdots = \frac{P_s}{1-\rho P_s}. \tag{9.120}$$

The average path length ℓ_a of photons absorbed in the sphere can be expressed via the linear absorption coefficient as: $\ell_a = 1/\alpha$. The proportions of surviving and being absorbed photons are $\exp(-\alpha\ell_i)$ and $1 - \exp(-\alpha\ell_i)$, respectively, making the total proportion of photons absorbed before reaching the sphere wall be P_α/α. The path length ℓ_f of surviving photons and the path length ℓ_a of photons absorbed in the filled cavity are:

$$\begin{aligned} &\ell_{a,i} = (1 - \exp(-\alpha\ell_i));\ \ell_a = \sum_i \ell_i = \frac{P_\alpha}{\alpha}; \\ &\ell_f = \frac{1}{\alpha}\frac{(1-P_s)}{(1-\rho P_s)} = \frac{1}{\alpha}\frac{(1-\rho P_s - P_s(1-\rho))}{(1-\rho P_s)} = \frac{1}{\alpha}\left(1 - \frac{L_f}{L_e}\right). \end{aligned} \tag{9.121}$$

As $P_s = 1 - P_\alpha$ and $(1 - \rho) = 1/L_e$, the probability P_α of a photon being absorbed on reflection plus passage is $1 - \rho P_s$. By comparing the flow of photons in and out of the inner translucent sphere: $\Xi_{in} = \Xi_2 A_0(1 - \rho_2)$, $\Xi_0 = L_f\Xi_2 A_0(1 - \rho_2)/A_0$ (see Fig. 9.46, Eqs. (9.111)–(9.114)), one can express the ratio of inward to outward irradiance as:

$$\Xi_{in}/\Xi_{out} = 1/(L_f(1-\rho_2)) = (1 - \rho_0 P_s)/(P_s(1-\rho_2)). \tag{9.122}$$

Equations (9.121) and (9.122) can be rearranged, emphasizing each factor for cavity-path length $\bar{\ell}$:

$$\frac{\ell_f}{\bar{\ell}} = \frac{1}{a\bar{\ell}}\left(1 - \frac{L_f}{L_e}\right);\ \frac{\Xi_{in}}{\Xi_{out}} = \frac{1}{P_s}\left(\frac{1}{1-\rho_2}\right) - \left(\frac{\rho}{1-\rho_2}\right), \tag{9.123}$$

and be converted to Eq. (9.114) with the P_s value by Eq. (9.119): $1/P_s \cong 1 + 4\alpha r/3$, for $\alpha r \ll 1$ [9.99]. Similar irradiance measurements as those done by Eq. (9.114) in the empty and filled sphere for empty-sphere and filled-sphere photon lifetimes of $L_e = (1 - \rho)^{-1}$ and $L_f = P_s/(1 - \rho P_s)$, respectively, are made by the ratio:

$$\Xi_0{}^e/\Xi_0{}^f = L_e/L_f = (1 - \rho P_s)/(P_s(1-\rho)). \tag{9.124}$$

Instead of Eq. (9.115) measurements of water samples versus pure water can be made as:

$$\Xi_0{}^w/\Xi_0{}^s = L_f{}^w/L_f{}^s = (P_s{}^w(1 - \rho P_s))/(P_s(1 - \rho P_s{}^w)). \tag{9.125}$$

Analysis of the integrating cavity "sandwich" may be extended to a cylindrical cavity with inner path length $\bar{\ell}$ being the mean-chord length or the distance between opposite surfaces [9.100].

Instead of two integrating spheres combined into a sandwich, making radiation interchange dependent on the parameters of both spheres, a single integrating sphere enables measurements of absorption in a filling-in liquid or gas sample in a similar manner if the spherical irradiation is delivered via a sphere-centered uniform diffuse emitting source [9.101]. The survival probability P_c of emitted photons propagating from the center of a sphere with radius r to the outer wall is $\exp(-\alpha r)$, and for reflected photons is $\rho \exp(-\alpha r)$. Then, the postreflection photon-survival process is derived by Eq. (9.120); as a result:

$$L_f = \exp(-\alpha r) + \rho \exp(-\alpha r) \frac{P_s}{1 - \rho P_s} = \exp(-\alpha r) \left(1 + \frac{\rho P_s}{1 - \rho P_s}\right) = \frac{\exp(-\alpha r)}{1 - \rho P_s} = \frac{P_c}{1 - \rho P_s}. \tag{9.126}$$

For absorption probability $P_\alpha = 1 - P_s = (1 - \exp(-\alpha r))$ the average path length of absorption becomes $\ell_f = (1/\alpha)(1 - \exp(-\alpha r)(\alpha r + 1))$, making the average path length for the whole population of photons that are absorbed in the first flight, on reflection as a function of $(1 - \rho)$, and after the wall reflection, already given by Eq. (9.121) for an inner sphere in a cavity sandwich, be [9.101]:

$$L_{f,\Sigma} = (1/\alpha)(1 - \exp(-\alpha r)(2 - \rho((1 - P_s)/(1 - \rho P_s))) + \exp(-2\alpha r)(\alpha r + 1)). \tag{9.127}$$

Despite simplification versus a dual-sphere cavity, the central uniform diffuse emitting source-based cavity absorption study is quite involved if the absolute value of the absorption coefficient of a liquid needs to be determined. Instead, comparison measurements versus pure water can be performed via Eq. (9.126) for L_w and L_s:

$$T_{s/w} = \frac{L_{f,s}}{L_{f,w}} = \frac{\exp(-\alpha_s r)(1 - \rho P_w)}{\exp(-\alpha_w r)(1 - \rho P_s)} = \exp(-(\alpha_s - \alpha_w) r) \frac{1 - \rho P_w}{1 - \rho P_s}, \tag{9.128}$$

where $T_{s/w}$ is the relative transmission coefficient of a liquid sample versus pure water. In cases of unknown sphere reflectivity, which happens every time when the sample's refractive index is not unity, additional measurements of known liquids are needed to identify spectral reflectivity values of the sphere itself. Furthermore, additional scattering in the sample affects the effective path length of radiation propagation by decreasing the $\exp(-(\alpha + \mu)r)$ factor proportionally to scattering coefficient μ, and also changing the average path length for photons reflected from the sphere wall. Therefore, unknown sample scattering sets limits on the applicability of measurement by relation (9.128), as well as practical uniformity deviations of the presumably uniform diffuse emittance for the centrally located source, which requires verification [9.102].

In any practical consideration, Eq. (9.128) needs to be solved via spectrally dependent parameters of the sphere with the sample and the independently verified pure-water specimen. Expanding the probabilities of photon survival versus absorption coefficients of the pure water and sample via Eq. (9.119), relation (9.128) provides straight absorption–reflection dependence:

$$T_{s/w} = \frac{\exp(-\alpha_s r)}{\exp(-\alpha_w r)} \left(\frac{\alpha_w^2}{\alpha_s^2}\right) \frac{2(\alpha_s r)^2 - \rho(1 - (2\alpha_s r + 1)\exp(-2\alpha_s r))}{2(\alpha_w r)^2 - \rho(1 - (2\alpha_w r + 1)\exp(-2\alpha_w r))}. \quad (9.129)$$

Owing to quadratic terms for the contrasting absorption coefficients, the relative sphere measurements by Eq. (9.129) are especially sensitive to absorption or scattering properties, but are indifferent to relative variation of sphere-wall reflectivity. Figures 9.47, 9.48 and 9.49 depict changes in spectral transmission for absorption measurements of emulated water samples by numerical simulation of the published absorption measurement data (such as in [9.103]) versus equivalently diverging sphere wall reflectivity numbers. The relatively high sensitivity for the reference comparison measurement imposes strict requirements on the accuracy of reference data and the absence of scattering, as illustrated by Figs. 9.47, 9.48, and 9.49, when a very small absorption coefficient increment of 0.001 cm^{-1} was added to the tabulated spectral values of pure water, changing transmission values nearly

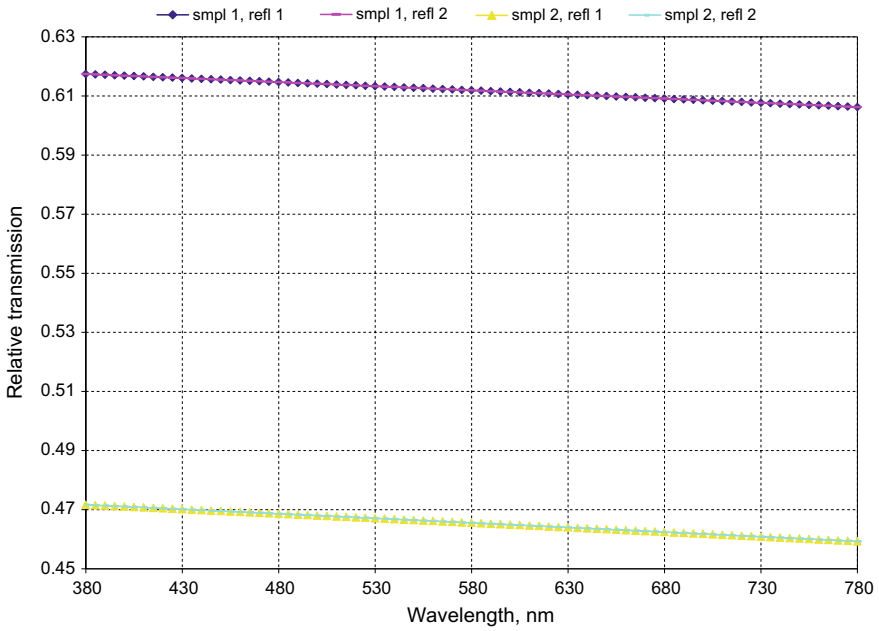

Fig. 9.47 Relative transmission of emulated water samples versus pure water in 1-cm radius sphere

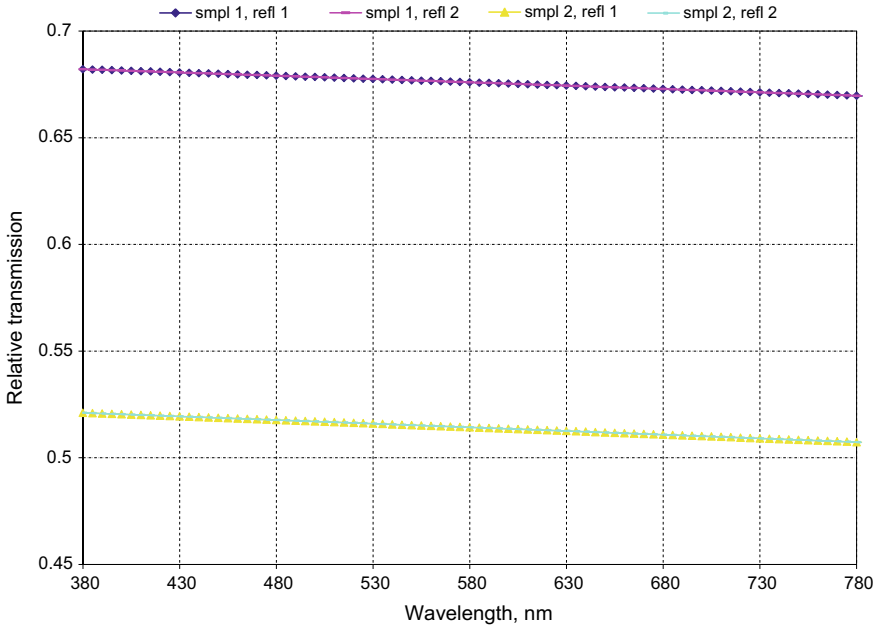

Fig. 9.48 Relative transmission of water samples versus 0.001 cm^{-1} absorbing water in 1-cm sphere

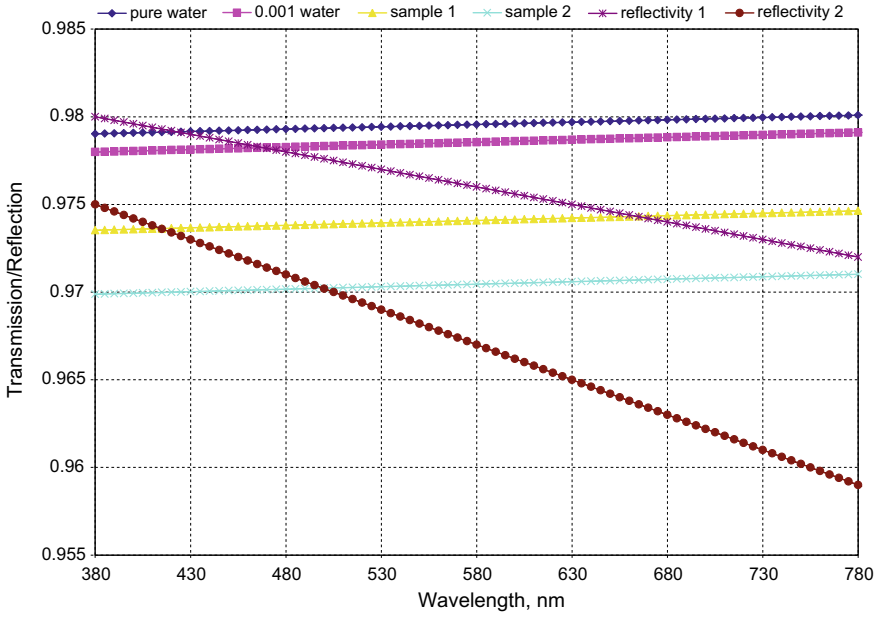

Fig. 9.49 Spectral transmission and reflection of water samples for spheres in Figs. 9.47 and 9.48

10% for samples referenced to pure water with a bit smaller in magnitudes, but more spectrally divergent changes for reflectance values. Thus, most considerations on designing the flow-through and central-source integrating absorption meters require detailed analytical or numerically modeling and thorough experimental confirmations [2.85, 9.104–9.106, 9.111].

9.4.2 *Integrating Spheres as Absorption Cells for Gaseous Substances*

Since it is fairly convenient to fill a sphere with a gas having the attenuation, or scattering, or absorption coefficient in question, low-loss measurements can be obtained by comparing readings of the empty and filled sphere. Considering the high reflectivity of the sphere wall in low-loss measurements, assuring an approaching infinity number of cavity-volume passes by the radiation of interest, the average cavity length $\bar{\ell}$ per path is defined by the ratio of the perfect-sphere volume to its surface – being 4r/3 for radius r – multiplied by the wall magnification factor $(1 - \rho)^{-1}$ accounting for the totality of all multiple reflections, where ρ is the sphere wall reflectivity.

For element dA_1 receiving radiation at angle θ from an elementary sector dA_2 of the sphere wall with emittance L and the flux $d^2\Phi = LdA_1dA_2(\cos\theta/r_{1,2})^2$ is (Fig. 9.50, Eqs. (1.25)–(1.60) and (2.154)):

$$d^2\Phi = 2\pi L \cos\Theta \sin\Theta d\Theta dA_1 \ , \tag{9.130}$$

leading the combined flux $d^2\Phi_0$, irradiating the elementary platform dA_1 by the entire-sphere uniform diffuse emitting surface of the equivalent solid angle π Eq. (1.31), to be:

$$d^2\Phi_0 = \pi L dA_1. \tag{9.131}$$

If the sphere is filled with an attenuating substance with attenuation – absorption α plus scattering σ – coefficient μ(λ), the flux becomes:

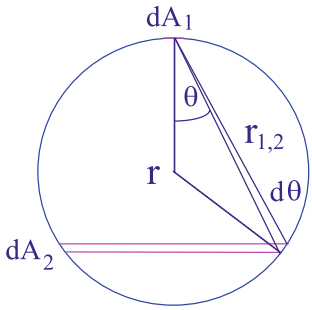

Fig. 9.50 Irradiation of a sphere wall

$$d^2\Phi(\mu) = d^2\Phi \exp\left(-\mu(\lambda)\bar{\ell}\right) = 2\pi L \exp\left(-\mu(\lambda)\bar{\ell}\right)\cos\Theta \sin\Theta d\Theta dA. \quad (9.132)$$

The flux Φ reaching surface dA_1 integrated over the full sphere nonlinearly depends on $\mu(\alpha)$ [9.107]:

$$d^2\Phi(\mu) = 2\pi LdA \int_0^{\pi/2} \exp(-2r\mu(\lambda)\cos\Theta)\cos\Theta \sin\Theta d\Theta d\theta$$
$$= \frac{2\pi LdA}{(2r\mu(\lambda))^2}(1 - (1 + 2r\mu(\lambda)\exp(-2r\mu(\lambda)))). \quad (9.133)$$

Approximating the exponent by the first two terms for a low-loss substance, Eq. (9.133) becomes:

$$d^2\Phi(\mu) = \pi LdA\left(1 - 4\mu(\lambda)r_{1,2}/3\right), \quad (9.134)$$

per the Bouguer–Lambert–Beer's law for a sphere filled with a low-loss gas versus an empty sphere: $\Phi_\mu = \Phi_0\exp(-\mu(\lambda)r_{1,2})$, which may also be expressed via the fractional flux $\Delta\Phi = \Phi_0 - \Phi_\mu$ attenuated by the inner sphere volume:

$$\left(\Phi_0 - \Phi_\mu\right)/\Phi_0 = \Delta\Phi/\Phi_0 = \mu(\lambda)\bar{\ell} = 4\mu(\lambda)r/3. \quad (9.135)$$

Further extending the not attenuated flux Φ_0 magnified by the internal sphere reflections for effective wall reflectance ρ_0' (Eq. (2.108)) versus the uniformly diffused flux $\Phi_0(d)$ entering the sphere:

$$\frac{(\Phi_0(d) - \Phi_0)}{\Phi_0(d)} = \frac{\Delta\Phi_{ent}}{\Phi_0(d)} = \mu(\lambda)\bar{\ell}_{mult} = \frac{(4\mu(\lambda)r/3)}{1 - \rho'_0}$$
$$= \frac{\ln\rho}{\ln\rho - \mu(\lambda)\bar{\ell}_{mult}} \underset{\rho'_0 \to \rho_0}{\to} \frac{\ln\rho}{\ln\rho - 4\mu(\lambda)r/3}, \quad (9.136)$$

which shows the absorption of the gas-filled sphere to be enhanced by effective path length $\bar{\ell}_{mult} = 4r/(3(1 - \rho'_0))$.

An alternative method for path-length identification of radiation in the integrating sphere is to estimate the completed sphere transits and their variance using the geometric probability distribution of completed sphere transits [2.49, 9.108]. Since in the sphere of a Lambertian diffuser (see Fig. 2.28, Eq. (2.103)) its irradiance E_0 is constant, the flux Φ_0 emitted by element dA into the sphere is defined by the full sphere surface: $\Phi_0 = 4\pi r_0^2 E_0$, and the flux Φ_{pt} leaving a port becomes $\Phi_0 = A_{pt}E_0$, where A_{pt} is the spherical surface removed by the port (Fig. 9.51). For a circular port of radius r: $A_{pt} = 2\pi r_0 h = 2\pi r_0(r_0 - \sqrt{(r_0^2 - r^2)})$. As a result, the fraction f of the flux Φ_0 leaving the sphere via port i of radius r: $f_i = 0.5 - \sqrt{0.25 - r^2/4r_0^2}$, is simply defined by the sphere geometry. On the basis of geometry, the effective sphere

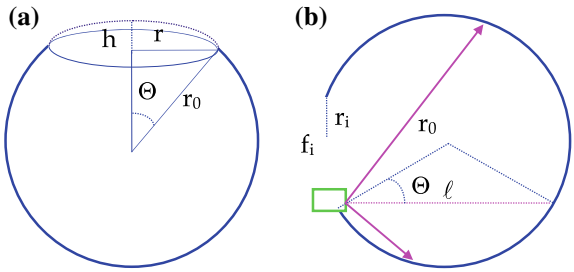

Fig. 9.51 The open port of an integrating sphere (**a**) and the meaning of a protected first-sphere irradiation (**b**)

reflectance can be identified via the summation of specific port reflectivities and geometrical fractions of these ports taken out of the complete spherical surface A_0 [2.49]. The average reflectance ρ_Σ of the sphere wall with n openings, each of reflectance ρ_i and fraction f_i, is:

$$\rho_\Sigma = \sum_1^n \rho_i f_i + \rho_0 \left(1 - \sum_1^n f_i\right), \tag{9.137}$$

where ρ_0 is the reflectance of the wall unaffected by inclusions. If flux Φ_0 is incident on the unaffected wall, the reflected flux is $\Phi_0\rho_0$, with flux $\Sigma f_i\Phi_0\rho_0$ leaving via openings and $(1 - \Sigma f_i)\Phi_0\rho_0$ remaining. As a result, with the second sphere-wall reflection the flux remaining in the sphere becomes $\rho_\Sigma\Phi_0\rho_0$, and with the n^{th} sphere-wall reflection the flux remaining is $\rho\Sigma^{n-1}\Phi_0\rho_0$. Similarly, the sphere efficiency factor changes from $\rho_0/(1 - \rho_0)$ to $\rho_0/(1 - \rho'_0)$ (see Sect. 2.4) for the efficiency F:

$$\begin{aligned} &\Phi_\rho = \Phi_0\rho_0/(1 - \rho_\Sigma) \equiv \Phi_0 F_\Sigma; \\ &F_\Sigma = \Phi_\rho/\Phi_0 = \rho_0 \Big/ \left(1 - \rho_0\left(1 - \sum_1^n f_i\right) - \sum_1^n \rho_i f_i\right). \end{aligned} \tag{9.138}$$

Likewise, the efficiency F_i identifies the fraction of radiation exiting the i^{th} port: $F_i = f_i F_\Sigma = f_i\rho_0/(1 - \rho_\Sigma)$ [2.49].

Following the geometrical-series approach above, one may identify internal sphere losses via mean and mean-square single-reflection path lengths of an average photon in the sphere [9.108]. For a sphere filled with a low-loss substance of attenuation (absorption) coefficient α_λ, the incoming flux Φ_0 is first attenuated on propagating the mean path length $\langle l \rangle$: $\Phi_0\langle l\rangle\alpha_\lambda$, and is then attenuated with the first unaffected-by-inclusions wall reflectance: $\Phi_1 = \Phi_0(1 - \langle l\rangle\alpha_\lambda)(1 - \rho_\lambda)$. After the first wall reflection: $\Phi_{1\rho} = \Phi_0(1 - \langle l\rangle\alpha_\lambda)\rho_\lambda$, and after the i^{th} reflection: $\Phi_{\rho i} = \Phi_{i-1}\rho_\lambda(1 - \langle l\rangle\alpha_\lambda)(1 - \Sigma f_i) \equiv \Phi_{i-1}\rho_{\lambda\Sigma}$. Summing all retroreflections as a geometric series similarly to Eqs. (9.137) and (9.138) with denominator: $(1 - \rho_{\lambda\Sigma}) = (1 - \rho_{\Sigma\lambda}(1 - \langle l\rangle\alpha_\lambda)(1 - \Sigma f_i))$, one may obtain the total sphere flux and partial attenuation ratios $A_i = \Phi_i/\Phi_0$ for any sphere substance A_s, wall A_w, and openings A_o [9.108]:

$$\Phi_{\Sigma\rho} = \sum_{1}^{\infty} \Phi_{i\rho} = \frac{\rho_\lambda(1 - \langle l\rangle\alpha_\lambda)}{1 - \rho_{\Sigma\lambda}(1 - \sum f_i)(1 - \langle l\rangle\alpha_\lambda)}; \tag{9.139}$$

$$A_s = \langle l\rangle\alpha_\lambda\left(\Phi_0 + \Phi_{\Sigma\rho}\right) = \frac{\langle l\rangle\alpha_\lambda(1 - \rho_{\Sigma\lambda}\sum f_i(1 - \langle l\rangle\alpha_\lambda))}{1 - \rho_{\Sigma\lambda}(1 - \sum f_i)(1 - \langle l\rangle\alpha_\lambda)}; \tag{9.140}$$

$$A_w = \Phi_{\Sigma\rho}(1 - \rho_{\Sigma\lambda})/\rho_{\Sigma\lambda} = \frac{(1 - \rho_{\Sigma\lambda})(1 - \langle l\rangle\alpha_\lambda)}{1 - \rho_{\Sigma\lambda}(1 - \sum f_i)(1 - \langle l\rangle\alpha_\lambda)}; \tag{9.141}$$

$$A_o = \Phi_{\Sigma\rho}(1 - \langle l\rangle\alpha_\lambda)\sum f_i = \frac{\rho_{\Sigma\lambda}\sum f_i(1 - \langle l\rangle\alpha_\lambda)^2}{1 - \rho_{\Sigma\lambda}(1 - \sum f_i)(1 - \langle l\rangle\alpha_\lambda)}. \tag{9.142}$$

For the Lambertian scattering distribution defined by Eq. (1.46) $I = I_0 \cos\Theta$, the mean optical path length $\langle l\rangle$ (see Fig. 9.51a, b), being integrated and weighted via the intensity I, becomes:

$$\langle l\rangle = \int_0^{\pi/2} 2r_0 \cos\Theta I \cos\Theta 2\pi \sin\Theta d\Theta \Big/ \int_0^{\pi/2} I \cos\Theta 2\pi \sin\Theta d\Theta = \frac{4r_0}{3} = \bar{\ell}, \tag{9.143}$$

as in relations (9.130)–(9.135). The mean-square single-reflection path length is:

$$\left\langle l^2\right\rangle = \int_0^{\pi/2} (2r_0 \cos\Theta)^2 I \cos\Theta 2\pi \sin\Theta d\Theta \Big/ \int_0^{\pi/2} I \cos\Theta 2\pi \sin\Theta d\Theta = 2r_0^2, \tag{9.144}$$

with variance [II.43, II.44]: ${\sigma_1}^2 = \left\langle l^2\right\rangle - \langle l\rangle^2 = 2{r_0}^2/9$, and the probabilities of photon disappearance, being absorbed in internal sphere substance: $p_\alpha = \langle l\rangle\alpha_\lambda$, in its wall: $p_w = (1 - \langle l\rangle\alpha_\lambda)(1 - \rho_{\Sigma\lambda})$, or lost in openings: $p_o = (1 - \langle l\rangle\alpha_\lambda)\Sigma f_i$, and of the photon surviving: $p_{srv} = (1 - \langle l\rangle\alpha_\lambda)(1 - \rho_{\Sigma\lambda})(1 - \Sigma f_i)$. Partial transits of light not completing a full-sphere path and vanishing must also be evaluated, fairly complicating the analysis [9.108].

One aspect of integrating-sphere absorption-cell functionality relates to the temporal response, for which the time constant t_{decay} of a diffusely reflecting cavity needs to be assessed [9.109–9.111]. Ranging from 0 to 2r, the average path length $\bar{\ell}$ leads to the average time for successive reflection cycles: $\bar{t} = \bar{\ell}/v = \bar{\ell}/(nc)$. Since radiation that entered the sphere makes the internal irradiance Ξ_0 decay exponentially with time, the sphere irradiance after the input and first wall reflection becomes:

$$\Xi_{ent.} = \Xi_0 \exp\left(-t/t_{decay}\right); \quad \Xi_{refl.} = \rho\Xi_0 \exp\left(-t/t_{decay}\right). \tag{9.145}$$

Counting the time for the decay at the first reflection $t = t_{\text{decay}}$ and after the m^{th} and $(m + 1)^{\text{th}}$ reflections:

$$\begin{aligned} &\Xi_{refl,0} = \rho\Xi_0 e^{-1}; \quad \Xi_{refl,m} = \rho^{m+1}\Xi_{refl,0}; \quad m \to -1/\ln\rho; \\ &t_{decay} = (-1/\ln\rho)\left(\bar{\ell}/(nc)\right). \end{aligned} \tag{9.146}$$

As the average-time assumption in relations (9.146) estimates various arrival times for diffuse internal sphere reflections, Monte Carlo analysis of radiation decays in various scenarios can be performed to estimate the temporal versus the cw response of the spherical cavity [2.86, 9.110, 9.111]. Another way is to analyze the probability density function $\Psi(\ell)$ of the path length, which defines the proportion of path lengths that lie within the interval $\ell + d\ell$ by normalizing the integral $\int_0^\infty \Psi(\ell)d\ell \equiv 1$ to the total sphere irradiance seen by the internal detector in absence of an absorber. Considering the Bouguer–Lambert–Beer's law (Eq. (1.73)), the attenuated flux $\Phi(\mu)$ in the absorber-filled sphere is:

$$\Phi(\mu) = \Phi_0 \int_0^\infty \Psi(\ell)\, \exp(-\mu(\lambda)\ell)d\ell. \tag{9.147}$$

Applying Eqs. (9.145) and (9.146) for irradiance as a function of time for the mean path length $\bar{\ell} = 4r/3$ at the decay time $t_{decay} = (-1/\ln\rho)\left(\bar{\ell}/(nc)\right)$ in the sphere and transforming to distance $\ell = ct$, the sphere irradiance becomes: $E(\ell) = E_0 \cdot \exp(-t/t_{decay}) = E_0 \cdot \exp(-\ln\, \rho \cdot \ell/\bar{\ell})$. For simplicity, one can view the normalized probability density function $\Psi(\ell)$ of the sphere's light attenuation as complying with the Bouguer–Lambert–Beer's law [9.111]:

$$\Psi(x) = \Psi_0 \exp(-\ln\rho \cdot \ell/\bar{\ell}). \tag{9.148}$$

Here Ψ_0 is the normalization constant obtained for a nonattenuating sphere. Transforming the probabilities from Eqs. (9.147) to (9.148) to proportionality relations for attenuated and nonattenuated fluxes:

$$\begin{aligned} \Phi_0(\ell) &= const \int_0^\infty \exp\left(\ln\rho \cdot \ell/\bar{\ell}\right)d\ell; \\ \Phi_0(\mu) &= const \int_0^\infty \exp\left(\ln\rho \cdot \ell/\bar{\ell} - \mu(\lambda)\ell\right)d\ell. \end{aligned} \tag{9.149}$$

Following relations (9.149) and normalizing the attenuating sphere to an empty one [9.111], while applying Eq. (9.136), the attenuating-sphere irradiance versus the empty-sphere irradiance becomes:

$$\frac{E(\mu)}{E_0} = \exp\left(-\mu(\lambda)\bar{\ell}\right)\frac{\ln\rho}{\ln\rho - \mu(\lambda)\bar{\ell}_{mult}} \underset{\rho'_0\to\rho_0}{\to} \exp\left(-\mu(\lambda)\bar{\ell}\right)\frac{\ln\rho}{\ln\rho - \mu(\lambda)\bar{\ell}}. \quad (9.150)$$

For experimental verification of absorption measurement capabilities in a high-reflectivity integrating sphere cavity [9.111], the analytical expressions were compared with the numerical models accounting for the specific sphere design, such as a direction of the first irradiation and a restricted field of view of a detector utilized, including the discrepancies between the models used, analytical approximations applied, and particular species studied. The designed 50-mm-diameter sphere was calibrated by changing the concentrations of a known specimen and fitting the correction factors obtained, allowing the absorption of gaseous methane to be measured for 1561-nm wavelength in 0–2.5 vol% concentration range, corresponding to the absorptance from 0 to 0.01 cm^{-1}, with the random component of measurement error in the experiments being below 1%.

The ringdown cavity technique (see Chaps. 7 and 8) could also be used for integrating-sphere based absorption studies [9.132]. Figure 9.52a shows the system with a cylindrical integrator (view *b*) made of a fumed silica as layers of air–glass interfaces of a quartz powder, having 20–40 nm diameter particles and at 12,000 layers or 2.5-cm thickness approaching $\sim$0.999 diffuse reflectance.

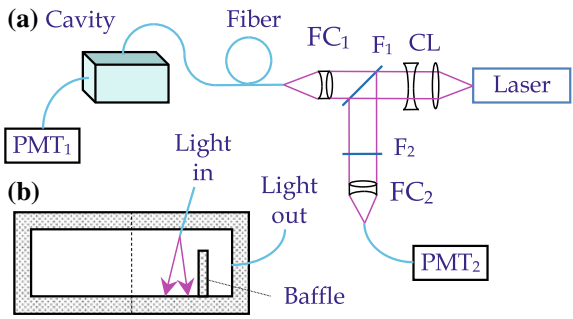

Fig. 9.52 Integrating-cavity ringdown system (**a**); cavity insert (**b**)

An input pulse from 532-nm *Laser* at 10–15 ns duration and 10-Hz repetition rate coupled by collimator *CL* via glass filters F_1, F_2 and fiber collimators FC_1, FC_2 to multimode fibers were measured in *Cavity* and referenced by photo-multipliers PMT_1, PMT_2. The ringdown time measured included a wall-time addition due to light penetration to the stack of layers, identified as 3.5 ± 2.6 ps for an average cavity reflectivity of 0.99904 ± 0.00003 [9.132]. A multiple path input–output could be used to preserve integrating-cavity walls from impacts of contamination [9.133].

Chapter 10
Direct Attenuation Measurements

10.1 Differential, Ratio, and Single-Channel Systems

The actual means to increase the sensitivity of a given method for optical loss measurement are not necessarily restrained by limitations to the maximum number of light interactions with the object. For example, the ratio of the highest optical power not inducing damage or optical nonlinearity in the given object to the lowest optical signal definitively distinguished from noise without the need to count photons reaches at least ten or more decades of optical density when applied to optical measurements. If using any feasible method, one converts the high sensitivity to the power or energy of light into high susceptibility to small changes of that power or energy by observing a low optical loss, doing it concurrently with assuring an adequate linear dynamic range of measurements, spatial stability, and temporal stability, the low-loss measurement task would be instantly solved.

A well-known way for increasing the relative sensitivity to a measured loss for a limited dynamic range involves implementing a differential registration of two optical beams: one interacting with an object and the other beam serving as a reference. A common dual-beam spectrophotometer is designed with this concept in mind. It normally has measurement and reference channels and optical or electronic compensation of the difference between channel signals [0.6, 10.1] (see Fig. 4.23). Considering spatial separation of two channels in transmitted and reflected light by way of a beam splitter with transmittance τ_s and reflectance ρ_s, the differential-signal channel reaction is:

$$M_{\Delta,identical} = \kappa_r \rho_s I_0 - \kappa_m \tau_s I_0 \tau \underset{\substack{k_r = k_m = k_1 \\ \rho_s = \tau_s = k_2}}{=} \kappa_1 \kappa_2 I_0 (1 - \tau)$$

$$\equiv const_1 \cdot I_0 (1 - \tau) \underset{\tau \to 1}{\to} 0. \tag{10.1}$$

Here I_0 is the intensity of the light source used, and κ_m and κ_r are the transformation factors of the measurement and reference channels, accounting for distinctive optical properties of two channel elements or unequal detector sensitivities. Since

M. Bukshtab, *Photometry, Radiometry, and Measurements of Optical Losses*, Springer Series in Optical Sciences 209,
https://doi.org/10.1007/978-981-10-7745-6_10

the purpose of implementing such a differential technique is to compensate for every potential fluctuation of light emission and for variations of the properties of individual channel elements, let us evaluate the spectrophotometer reaction $M_{\Delta,d}$ to fluctuation ΔI of the source intensity I_0 at distinct channels and not approaching unity sample transmittance τ. The difference for the new signals affected by intensity fluctuations becomes:

$$M_{\Delta,\mathrm{d}} = k_r\rho_s(I_0 \pm \Delta I) - k_m\tau_s(I_0 \pm \Delta I)\tau = (I_0 \pm \Delta I)(k_r\rho_s - k_m\tau_s\tau);$$
$$M^{=}_{\Delta,\mathrm{d}} \xrightarrow[k_r\rho_s = k_m\tau_s]{} (I_0 \pm \Delta I)(1-\tau); \quad M^{\neq}_{\Delta,\mathrm{d}} \xrightarrow[k_r\rho_s \neq k_m\tau_s]{} (I_0 \pm \Delta I)(k_a - k_b\tau). \qquad (10.2)$$

As a result, the signal fluctuations are not fully compensated by controlling only the difference of two comparing signals, if the sample is not totally transparent and the channels are not identical: $\kappa_m\tau_s = k_b \neq k_a = \kappa_r\rho_s$.

The latter obstacle in compensating for intensity or sensitivity fluctuations could be the key in understanding the practical reasons why differentiation-compensating techniques do not better the designs of most-precise spectrophotometers [10.2, 10.3]. Besides, to maintain beam compensation in differential photometers, spectral attenuation at each wavelength must be provided equally in two channels. Any deviation of the optical transmission factor or the electronic gain of a single element in one channel needs to be equivalent to that in the other channel. That is why a 100%-line calibration is a must procedure for every differential measurement, and even if it is successfully achieved, changes of a single parameter while the measurement is performed, such as variations of the light-propagation direction in one of the channels, would lead to the realized high sensitivity not being necessarily transformed to high accuracy of optical-loss measurement.

One fundamental solution to the differential-measurement task is to make measurements of ratios of signals in the main and reference channels. At either constant transmittance and/or reflectance within any single channel, not necessarily equal to that of another one, the ratio of channel signals correctly distinguishes and compensates for any single-channel fluctuation, providing the reference signal remains stable, as:

$$M = \frac{M_m}{M_r} = \frac{\kappa_m\tau_s(I_0 \pm \Delta I)\tau}{\kappa_r\rho_s(I_0 \pm \Delta I)} = \frac{\kappa_m\tau_s}{\kappa_r\rho_s}\tau \equiv const \cdot \tau. \qquad (10.3)$$

Following from Eq. (II.15), the optical sensitivity of a direct loss measurement via ratio (10.3) is limited by the twofold magnitude of the inverse signal-to-noise ratio in every single channel. When all systematic errors are eliminated and noise in each channel is equally random, limiting errors of ratio measurements can be expressed by double magnitudes of equivalent noise-to-signal ratios in the measurement and reference channels:

$$\delta_{\lim} = \pm(\Delta I_m/I_m + \Delta I_r/I_r) \underset{\Delta I_m \approx \Delta I_r; I_m \approx I_r}{=} \pm 2\Delta I/I. \qquad (10.4)$$

One can see that when having a photodiode with a linear dynamic range of 10^5–10^6 decades, 10^{-9}–10^{-10} A dark current, and 0.1–0.5 A/W sensitivity, being connected to a transimpedance preamplifier linearly converting a current to voltage within 5 to 6 decades of dynamic range [10.4], the actual sensitivity of the optical-loss measurement may reach ±1 ppm or higher; nonetheless specific realizations of such a direct approach may prove difficult.

One example of a difference-to-sum system, designed to increase the sensitivity of the transmittance and reflectance measurements, was shown in Fig. 2.12 [2.10]. A light beam from an exit slit of a spectrometer is sent via modulator M onto toroidal mirrors M_1, M_2, and M_3 and plain mirrors M_4 and M_5 to detector D. A rotating sample holder takes sample S in and out of the beam at a modulation frequency of 25 Hz sensing the difference of the 100% signal and the sample's transmittance τ or reflectance ρ signal, related to the sum of two signals: $(1-\tau)/(1+\tau)$ or $(1-\rho)/(1+\rho)$, and the ratio for both τ and ρ evaluating the total sample loss $\chi = 1-\tau-\rho$ as: $(1-\tau-\rho)/(1+\tau+\rho) = \chi/(2-\chi)$. Such a system doubles its sensitivity to the sample's optical properties at the expense of certain alignment difficulties, even if optical path differences are correctly compensated (see Fig. 4.20).

A split-pulse laser system with two samples of differential length ℓ_{1-2} in the sample and reference arms of an uneven-leg Michelson interferometer arrangement in reflection, can sense the difference of reflected by each arm signals being measured by a sufficiently fast detector, resolving arrivals of two 10-ns long pulse signals in the time domain. Owing to measurements in reflected light, the loss sensitivity to the difference in sample length's attenuation is doubled: $\chi = \ln(A/B)/(2\ell_{1-2})$, where A and B are the magnitudes of arm's signals in reflection. Similarly to the two-beam spectrometer system, the experimental loss difference study of diverse samples in pulsed laser light of short coherence length were made at ~8–13% absolute-scale accuracy [10.5].

If differential-bound detection is of essence, it needs to be enhanced by ratio measurements of registering signals to achieve high sensitivity. The differential-division system layout applied for the low-loss measurement is illustrated in Fig. 10.1 [10.6]. Pulse generator 1 produces a desired sequence of radiation pulses from light-emitting diode 2 at a low frequency near 1 Hz or higher. Lens 3 forms two correlating signals via semitransparent beam splitter 4. Each channel incorporates similar adjustable diffuse-glass attenuators 5 and 6, photodiodes 7 and 8, preamplifiers 9 and 10, and digital voltmeters 11 and 12. The measurement results are obtained via intensity difference M between the reference and measurement

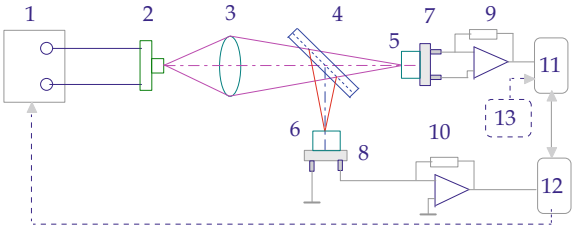

Fig. 10.1 Difference-ratio measurements of low optical losses

signals in radiation reflected and transmitted by the splitter divided by the reference signal. Without a sample:

$$M_1 = (U_2 - U_1)/U_2 = (\kappa_2 I_0 \rho_s - \kappa_1 I_0 \tau_s)/\kappa_2 I_0 \rho_s = 1 - \kappa_1 \tau_s / \kappa_2 \rho_s. \quad (10.5)$$

If a test sample is inserted in the measurement channel in transmitted light, M_1 changes to M_2:

$$M_2 = \frac{U_2' - U_1'}{U_2'} = \frac{\kappa_2 I_0' \rho_s - \kappa_1 I_0' \tau_s \tau}{\kappa_2 I_0' \rho_s} = 1 - \tau \frac{\kappa_1 \tau_s}{\kappa_2 \rho_s}. \quad (10.6)$$

As a result, the transmittance τ of the transparent sample is determined by a differential ratio [10.6]:

$$\tau = (1 - M_2)/(1 - M_1). \quad (10.7)$$

As seen from Eqs. (10.5)–(10.7), the differential-division procedure does not produce extra systematic errors, as could happen in unbalanced differential studies. However, noise limitation is higher with differential-ratio registration, since at least three signals instead of two as in equivalent direct two-channel division studies are utilized at every measurement point. Thus, the total noise signal $\sqrt{2}\Delta I_{noise}$ is slightly higher: $\sqrt{3}\Delta I_{noise}$, where ΔI_{noise} is the equivalent noise power in each channel. For radiation wavelength of 0.9 μm and 50-ms duration of light-emitting diode pulses, even with the almost tripled noise the differential-division system shown maintained a $\pm 2 \cdot 10^{-4}$ noise limit of differential-ratio measurement in 1 h and a $\pm 4 \cdot 10^{-5}$ limit in 10 min.

One obvious disadvantage of the differential measurement is higher noise compared to the single-channel and direct-ratio systems. A compromise attaining high sensitivity of differential studies and higher accuracy of ratio measurements may be achieved by using an added, but stable calibrated signal of an auxiliary source [10.7]. To confirm such a concept, the system in Fig. 10.1 was upgraded to maintain the electric signal in the measurement channel, which was subtracted from a stabilized power of calibrated electric source 13. During each measurement only a small variable part of the measurement signal, defined by the low loss to be studied, was recorded by a sensitive scale of voltmeter 11. The signal measured in the reference channel was used as the negative feedback to the current of pulse generator 1 stabilizing light output of light-emitting diode 2 (dotted lines in Fig. 10.1). The drift for the reference differential measurement signal at wavelengths of emission was reduced to $\pm 1 \cdot 10^{-4}$ within 1 h and to $\pm 2 \cdot 10^{-5}$ within 10 min.

Attenuation-difference measurements of various sorts find applicability for remote sensing and trace detection, such as differential absorption spectroscopy [10.8–10.22]. The main concept of the technique is in sensing returns of lidar-like signals for two or more collinear waves – one of which is a resonant line for

absorption by a species and the other is not [10.9] – via a relatively long incremental remote path length sufficient for the detectable sensitivity to a differential loss. If the wavelengths to be compared are spectrally close for similar scattering losses and a nonresonant wavelength is not absorbed by a species, the differential (sum) loss equation becomes:

$$\begin{aligned} I_{sum} &= k_R I_{0,R}\ \exp(-\mathsf{a}(\lambda_R)N\Delta\ell) + k_{NR} I_{0,NR}\ \exp(-\mathsf{a}(\lambda_R)N\Delta\ell) \\ &\underset{\substack{\mathsf{a}(\lambda_{NR})\to 0 \\ k_R = k_{NR}}}{=} I_{0,R}\ \exp(-\mathsf{a}(\lambda_R)N\Delta\ell) + I_{0,NR}, \end{aligned} \tag{10.8}$$

where a and N are the absorption cross section and the concentration of the species to be detected, while indices R and NR relate to the resonant and nonresonant wavelengths at respective initial light intensities $I_{0,R}$ and $I_{0,NR}$ propagating along differential path length $\Delta\ell$. Unvarying intensity $I_{0,NR}$ gives:

$$\mathsf{a}(\lambda_R)N\Delta\ell = -\ln\left(I_{sum}/I_{0,R} - I_{0,NR}/I_{0,R}\right). \tag{10.9}$$

Here factors k_R and k_{NR}, describing additional influences for the broadband radiation in the atmosphere at resonant and nonresonant wavelengths, including reflections from the ground, are presumed to be equal.

Differential-spectroscopy measurements are performed by fast scanning in relatively broad spectral domains exceeding the spectral features of the absorption spectrums to be detected [10.11]. Multichannel detection techniques with pixel arrays or spectrally dedicated channels are used [10.12] to reduce reference signal fluctuations due to atmospheric turbulence and increase the signal-to-noise ratio. Similarly as fluorescence and scattering provide added measurement signals [10.10], the differential-wavelength technique can be used for multichannel scattering at various angles of observation [10.13]. Narrowband spectral referencing to a known atmospheric water vapor wavelength helps establish rapid transition from the resonant to nonresonant waves, which can also be combined via polarization modulation in a single detector for difference-ratio measurements (Eqs. (10.5)–(10.7)) at various signal and reference wavelengths [10.14].

Likewise, differential-absorption measurements can be applied to split-channel detection via test and reference optical paths to balance the channel noise contribution (see also Sect. 10.2) and stabilize the initial differential-beam intensity [10.15]. An example of a differential setup for two-channel, two-wavelength, polarization-multiplexed absorption measurements [10.16] is shown in Fig. 10.2. Two laser sources, generating light at resonant and nonresonant wavelengths, ac-modulated out of phase with each other and multiplexed into one combined beam via mirror 1 and wedge plate 2 to maximize the intensity of the highly absorbed resonant wave and make the nonresonant wave intensity sufficient for detection, maintained collinear propagation of beam components. Lenses 3 and single-mode fiber 4 delivered two multiplexed wavelengths to a hole in parabolic mirror 5 and rotating mirror 6 on step-height retroreflector 7, which was immersed

in the liquid under study. Light back-reflected by each step was imaged by mirror 5 onto detector 8 and a lock-in amplifier sensing beam oscillations at a chosen modulation frequency, which was proportional to the intensity difference between resonant and nonresonant waves and nullified at equal intensities. The system in Fig. 10.2 measured down to 1% difference in concentrations of liquid oxygen with 3-μs time constant [10.16]; similarly, the split-channel balanced system reached 35-ppm sensitivity [10.15].

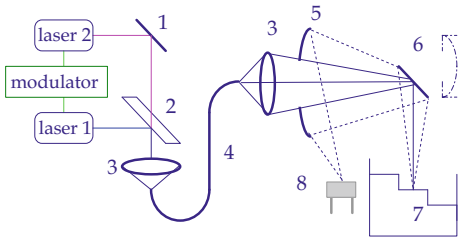

Fig. 10.2 Differential optical-loss balancing study

Figure 10.3 illustrates the differential-absorption detection setting for NO_2 or NO_3 concentration studies in the atmosphere based on light-emitting diodes. Temperature-stabilized light-emitting diode 1 for NO_2 or for NO_3 remote measurement at the 450 or 630 nm wavelength band is placed in the focus of a Newtonian telescope, whose main mirror 3 formed a 20-mm-diameter parallel beam onto retroreflectors 4, returning a beam of nearly 30-cm diameter. Beam-forming mirrors 2 and 5 and stepper motors direct the returning beam into mode-mixing multimode fiber 8, further irradiating Czerny–Turner spectrograph 6 and detector array 7. The total light path was 6090 m allowing up to parts-per-billion or parts-per-trillion atmosphere concentration of NO_2 and NO_3 to be traced, respectively, in the 450- and 630-nm spectral domains [10.18].

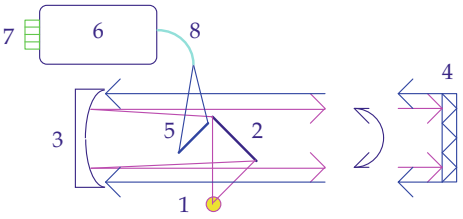

Fig. 10.3 Long-path differential absorption setting

Considering to obtain any quantitative data from remote differential-absorption spectroscopy studies, one needs to keep in mind extensive efforts necessary to analyze measurement results at various wavelengths and account for concentration-dependent extinction, solar radiation scattering, stray light, etc., as a result necessitating specific computation formalisms to be used in avoiding systematic errors [10.19, 10.20]. The added efforts are required when applying the polarization-based differential techniques to measure absorbing and scattering characteristics of dense biological aerosols and of human tissue [10.21, 10.22]. All-wavelength single-pulse spectral measurements could be utilized with supercontinuum sources reaching near 1 ppm·m mid-IR absorption sensitivity equivalent to ∼0.5–0.2% absorptance [10.83].

Analyzing rational challenges of later techniques, one may expect the lowest measurement noise and the highest accuracy to be rather obtained by direct single-channel light detection with independent stabilization of radiation emitters and detectors or by tracking fluctuations of the radiation emission by some added feedback to the light emitter or detector. Simultaneous stabilization of both the source and the detector, satisfying a specific limit required for any given low-loss measurement process, eliminates the need for other improvements. Such advanced measures for the Beckman DU-8B spectrophotometer allowed a noise-to-signal ratio of $\pm 5 \cdot 10^{-5}$ to be reached within 0.5-Hz frequency bandwidth and 0.5-nm spectral resolution at $\lambda = 0.19 - 0.9$ μm. Photometric accuracy of $\pm 3 \cdot 10^{-5}$ was realized in transmission studies of highly transparent objects [10.3]. Equally high photometric accuracy at the $\pm 4 \cdot 10^{-5}$ level was realized for transmittance measurements in a single-beam research spectrophotometer optimized by the National Institute of Standards and Technology (NIST) [4.44]. A notably higher dynamic range of measurements – reaching 3400:1 with $(1 - 3) \cdot 10^{-4}$ absolute accuracy – was carried out with a National Research Council of Canada single-beam spectrophotometer additionally detecting deviations from linearity [4.45].

The accuracy and sensitivity of optical loss measurements discussed above were related to total attenuation factors for radiation interacting with test objects. If, as in most actual cases, the task consists in detecting an internal sample loss, measured intensity changes due to bulk properties must be distinguished from those induced by surfaces or surface losses must be fully eliminated. Since for monochromatic polarized light incident on the border of two dielectrics at the Brewster angle the border reflection vanishes [1.1], Brewster-angle measurements can be used to nearly eliminate or partition the bulk and surface losses. Since no real light beam is fully polarized or monochromatic, the degree of polarization and the angle of incidence accounting for the beam divergence need to be optimized for the Brewster-angle procedure. The intensity $I_\perp$ of the not fully nullified orthogonal light component polarized perpendicularly to the plane of incidence and the extinction ratio $\delta = (I_\parallel - I_\perp)/(I_\parallel + I_\perp)$ of the polarized beam components must be related as:

$$2\rho_\perp I_\perp \underset{I_\parallel \to 1}{\cong} 2\rho_\perp I_\perp / I_\parallel = 2\rho_\perp (1 - \delta)/(1 + \delta) \ll \exp(-\mu\ell), \tag{10.10}$$

where $\rho_\perp$ is the reflectance of a single sample surface for perpendicularly polarized light and μ is the linear attenuation coefficient of the substance under study. If loss as low as 10^{-5} must be evaluated for residual reflectivity $\rho_\perp = 0.15$ near the Brewster angle, the extinction ratio δ of the beam polarized in the plane of incidence must not exceed 0.00007 or must be below the 0.0007 level to detect loss $\mu\ell = 10^{-4}$.

The main advantage of performing direct bulk-loss measurements at the Brewster angle consists in the much lower sensitivity of two-surface reflected light to fluctuations of the refractive index of each single reflective surface [10.23]. For example, the transmittance of a material at $n = 1.5$ at normal incidence $\tau_0 = 0.923$ (see Eq. (1.106)) changes within $\pm 3 \cdot 10^{-3}$ with $\Delta n = \pm 0.01$. For measurements at the

Brewster angle: $\varphi_{B,n=1,5} = 56.3°$, light incident at the given angle upon a surface of $n = 1.51$ and at a different angle of $\varphi_{B,n=1,51} = 56.49°$ would create reflectance $\rho_{\|} = 4 \cdot 10^{-6}$. This corresponds to transmittance changes that are 3 orders of magnitude lower than at normal incidence. However, the requirement to maintain incidence of radiation at the Brewster angle is much stronger. When targeting 10^{-6} sensitivity to internal bulk losses, the deviations from the correct angle at $n \approx 1.5$ must be less than $\pm 0.1°$ for both surfaces to give $\Delta_{\tau,\|} = 1 - (1 - \rho_{\|})^2 \leq 10^{-6}$, and must be less than $\pm 0.2°$ for $\Delta_{\tau,\|} \cong 10^{-5}$.

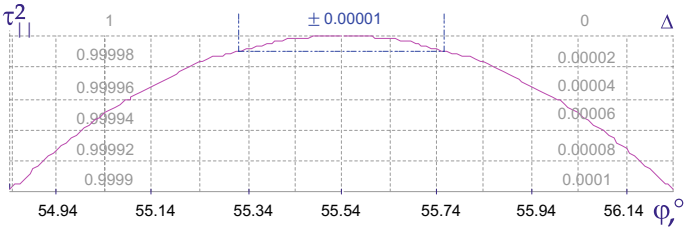

Fig. 10.4 Transmittance of a plane-parallel silica plate near the Brewster angle

The actual transmission spectrum of a plane-parallel fused-silica plate is illustrated in Fig. 10.4, which shows the measurement error per unaccounted surface reflectance for a perfectly aligned parallel beam of light, fully polarized in the plane of incidence. Figure 10.5 schematically depicts a low-loss apparatus for bulk transmission measurements at the Brewster angle. The beam intensity and plate transmittance are sensed by detector 5 (5') while both-surfaces reflectance detector 6 controls the residual reflectivity from the plate's surfaces and also helps to evaluate nonparallelism of the plate surfaces. Third detector 7 attached to a more sensitive radiometer than the first two detects scattering of radiation by two surfaces. Spontaneous light emitted by halogen lamp 1 with its current stabilized to the $\pm 10^{-5}$ level was formed by objectives 2 via pinhole 9 to make a parallel light beam of at least 2 times smaller diameter than plate 4, keeping the plate edges away from the beam not to create any stray light. Glan–Thompson polarizer 8 has provided better than 10^{-6} extinction ratio. Transmission measurements were made in the 633–850-nm wavelength spectral domain, selected by set 3 of interference filters: each with 10 nm spectral half-width. All three silicon p-i-n detectors used had 6-cm^2 sensitive area with very low spatial nonuniformity and equivalent noise of approximately 10^{-12} W: two decades lower than the 10^{-10} W level needed for 10^5

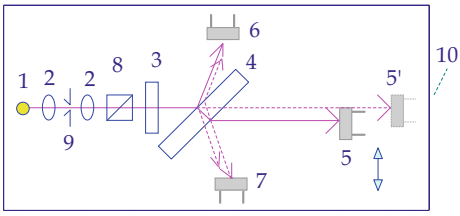

Fig. 10.5 Bulk-loss measurements at the Brewster angle

resolution at an incident beam power of approximately 10^{-5} W. The system was enclosed in thermostat 10 at ±0.1 K with 1 h temperature stability. The signals detected in the channels were registered at $7 \cdot 10^{-6}$ amplitude resolution. As a result of all measures, the thermal drift of the measured signals did not exceed $1 \cdot 10^{-5}$ during the 1-min time interval needed to move the sample in and out of a beam. The minimal detected level of internal losses in 3-cm-thick fused Suprasil W1 samples was 12–13 dB/km $(3 \cdot 10^{-5}\ \mathrm{cm}^{-1})$ for sensed surface-scattering loss of freshly cleaned quartz surface equivalent to 0.3 dB/km [10.23].

Another distinct prospect of excluding a surface loss is associated with immersing the entire test sample in a refractive-index-matching fluid filling a transparent cuvette made of material similar to the sample. The method of internal-loss measurement for a plane-parallel sample immersed in a matching liquid, and therefore not substantially changing the light-propagation direction, is illustrated in Fig. 10.6 [10.24]. A test sample of length ℓ having internal attenuation coefficient μ is steadily situated inside the matching-material cell of length ℓ_c filled with a fluid with attenuation coefficient μ_{fl}. In the cell, the sample could be moved in and out of the parallel light beam, with radiant flux Φ_0, created by a lamp–two objectives–pinhole system similar to that in Fig. 10.5. In Fig. 10.6a, the total flux Φ_a transmitted by the fluid-filled cell with windows of total surface reflectance ρ, counting the border with the fluid, is:

$$\Phi_a = \Phi_0(1-\rho)\left[\exp\left(-\mu_{fl}\ell_c\right)\right](1-\rho). \tag{10.11}$$

In Fig. 10.6b, the transmitted flux via the new cell path now including the sample is reduced to:

$$\Phi_b = \Phi_0(1-\rho)\left\{\exp\left[-\mu_{fl}(\ell_c-\ell)\right]\right\}[\exp(-\mu\ell)](1-\rho). \tag{10.12}$$

As a result of the assumption made that the sample–fluid border reflectivity is negligibly low:

$$\exp(-\mu\ell) = (\Phi_b/\Phi_a)\exp\left(-\mu_{fl}\ell\right) \quad \text{or} \quad \mu = \mu_{fl} - (\ln\Phi_b - \ln\Phi_a)/\ell. \tag{10.13}$$

The suppositions and the accuracy of the index-matching technique for the sample–fluid border being nonreflective are based on several factors: reflection losses at sample–liquid borders being zero, stability of fluid properties for the entire

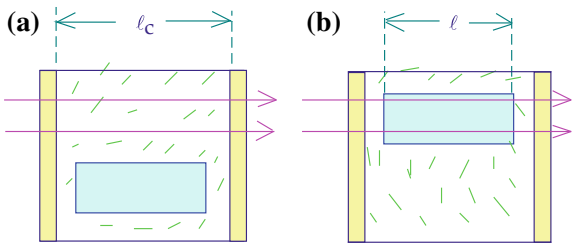

Fig. 10.6 Study of internal losses in immersion fluid

measurement cycle, and closeness of liquid losses to the sample losses being measured, since even temperature fluctuations of any large liquid loss could screen out a smaller loss under study. To have the total reflectance of a plane-parallel sample:

$$\rho_{\Sigma} = 1 - \tau_{\Sigma} = 1 - \left(1 - \rho_{s-fl}\right)/\left(1 + \rho_{s-fl}\right) = 2\rho_{s-fl}/\left(1 + \rho_{s-fl}\right), \qquad (10.14)$$

lower than 10^{-5}, the actual reflectance of each sample–liquid surface should be less than $5 \cdot 10^{-6}$. For a sample of refractive index $n = 1.46$, the latter requirement corresponds to $\Delta n \leq 0.006$. One fluid with properties matching immersed fused-silica samples is carbon tetrachloride (CCl_4), whose refractive index is less than 0.001 different from that of fused silica in the spectral domain of $0.5-1.1$ μm at $T = 21.8\,°C$, with an attenuation coefficient as low as $2 \cdot 10^{-5}$ cm^{-1} at $\lambda = 633$ nm.

For fluid-matching measurements in CCl_4 of 3-cm-thick Suprasil W1–Suprasil 1 fused-silica samples, as studied at Brewster-angle incidence and with registration equipment as in Fig. 10.5, the actual intensity fluctuations of a parallel light beam transmitted by the cell did not exceed $\pm 3 \cdot 10^{-5}$ with short-term temperature stability of ±0.3 K. The bulk losses in the fused-silica samples measured were about 50–5 dB/km in the respective wavelength range of $\lambda = 400-750$ nm [10.24], with the values of lowest bulk losses detected at 9.0 and 6.0 dB/km while having ±0.5 dB/km reproducibility and ±1.0 dB/km estimated overall accuracy. Subsequent immersion-fluid attachments to commercial spectrophotometers (see Chap. 4, Fig. 4.28) allowed the realization of down to 10^{-4} sensitivity for transmission and reflection factors with corresponding refractive index measurements for the samples [4.54], and detection of the particle size distribution and concentration for particles suspended in water via nonlinearly inverted spectral transmission measurements by adding a pinhole spatial filter to shield low-angle scattered radiation from reaching the detector [10.25].

10.2 Derivative Frequency Spectroscopy

Equally as frequency modulation is advantageous relative to amplitude modulation in terms of noise reduction, though requiring a substantially higher bandwidth for its implementation, wavelength- and frequency-modulation techniques may be beneficial versus amplitude-modulation schemes in noisy environments, especially with fast-varying parameters of the measurements to be performed. The main notion for wavelength- or frequency-modulation is to detect a change of the transmission or reflection spectrum being measured that is enhanced by modulation, and to distinguish the change versus stable and potentially intense background emission, which is responsible for overwhelming stray light in conventional measurements. These techniques are primarily useful for enhancing weak spectral features, mainly in overlapping conditions requiring improvements in spectral resolution [II.19].

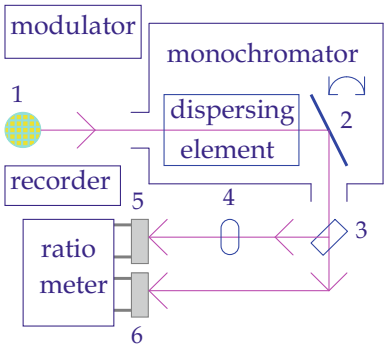

Fig. 10.7 Wavelength-modulation spectroscopy

Figure 10.7 illustrates the concept for wavelength-modulation spectroscopy [10.26]. A beam of radiation from source 1 via a dispersing element of a monochromator is modulated by vibrating chopper mirror 2 altering the output wavelength λ in the modulation range $\Delta\lambda$. The beam is divided by reflective splitter 3, sending the not attenuated portion to reference detector 6, while the main beam passes through sample 4 to be studied, reaching main detector 5. Owing to the wavelength modulation, the spectrum of the sample contains the modulation profile of depth proportional to the derivative of its attenuation versus wavelength. Continuous monitoring of the logarithmic ratio of consecutive detector readings removes spectral dependency of the source intensity, monochromator transmission, and two detector responses, but the sample attenuation spectrum contains wavelength derivatives, and noise subtraction takes place only for frequencies lower than the chopping frequencies, leaving high-frequency components intact.

The respective errors of wavelength and temporal distortion due to two-detector-matching and the slow-moving mirror can be eliminated by using a tunable-wavelength source, dividing its beam into two channels and recombining the beams on one detector [10.27]. Figure 10.8 illustrates a setting for differential wavelength-modulation spectroscopy [10.28]. Tunable-wavelength light λ_0 of laser 1 modulated at carrier frequency ω_m is split into sample and reference channels by splitters 3 and mirrors 4, chopped at higher frequency ω_c out of phase with each other for in-phase and quadrature components, and recombined on detector 6

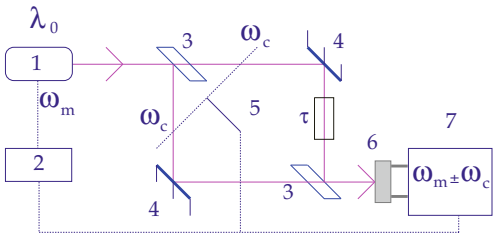

Fig. 10.8 Wavelength tuning and modulation

connected to lock-in amplifier 7 of bandwidth $\omega_c \pm \omega_m$, synchronized by modulator driver 2. The output contains in-phase and quadrature components displaced by $\pm 90°$ out of phase and separated into the sample and reference channels by the phase settings of the lock-in amplifier. Owing to wavelength modulation, the respective channel signals become:

$$S_S = I_0 \tau R_d + \left(\frac{dI_0}{d\lambda} \tau R_d + I_0 \tau \frac{dR_d}{d\lambda} + I_0 \frac{d\tau}{d\lambda} R_d \right) \Delta\lambda(t);$$
$$S_R = I_0 R_d + \left(\frac{dI_0}{d\lambda} R_d + I_0 \frac{dR_d}{d\lambda} \right) \Delta\lambda(t), \tag{10.15}$$

where τ is the sample transmittance, I_0 and R_d are the source intensity and the detector responsivity, S_S and S_R are the sample and reference signals, and $\Delta\lambda$ is the wavelength modulation depth at carrier frequency ω_c caused by relatively large index modulation: $\omega_m < \omega_c/2$. The first components in relations (10.15) represent dc contributions, which are to be normalized for differential registration to take place:

$$\frac{S_S}{I_0 \tau R_d} = 1 + \left(\frac{1}{I_0} \frac{dI_0}{d\lambda} + \frac{1}{R_d} \frac{dR_d}{d\lambda} + \frac{1}{\tau} \frac{d\tau}{d\lambda} \right) \Delta\lambda(t);$$
$$\frac{S_R}{I_0 R_d} = 1 + \left(\frac{1}{I_0} \frac{dI_0}{d\lambda} + \frac{1}{R_d} \frac{dR_d}{d\lambda} \right) \Delta\lambda(t). \tag{10.16}$$

Measuring the difference of normalized signals in Eqs. (10.16) at modulation frequency ω_m subtracts dc noise for frequency components: $\omega < \omega_c/2$, making the differential signal proportional to the normalized derivative of attenuation. The attenuation or absorption coefficient itself can be roughly determined by integrating the derivative measured. Performing spectral summation and correcting for an unbalanced wavelength-dependent zero-level deviation, which scaled linearly with the modulation depth, allowed sensing of the attenuation coefficient of benzene of approximately $7 \cdot 10^{-4}$ cm^{-1} [10.28].

Another detection approach is associated with high-frequency, but low-index modulation interference between reference and sample waves, forming the basis for frequency-modulation spectroscopy [10.36–10.53]. In the wavelength-modulation technique, the aim is to modulate a single-wavelength laser (see Fig. 10.7) at low chopping ω_c and modulation ω_m frequencies, also within a low detector bandwidth $\omega_c \pm \omega_m$, lower than the spectral width of the attenuation (absorption) band to be measured. The frequency-modulation technique uses high-frequency phase modulation of a beam of a single-frequency laser, exceeding the bandwidth of a measured absorption line and thus spreading its high and low radio-frequency modulation sidebands of sinusoidal phase modulation, but letting only one of the two weak sidebands of a strong carrier signal interact with an absorption feature of interest, being reduced inversely proportional to frequency to become inevitably below the laser technical noise and detector's shot noise. Accordingly, to distinguish that weak frequency-modulation signal from noise in such a broadband radio-frequency

detection approach either optical heterodyning or homodyning of the beam to be split and recombined on a signal detector – one beam interacting with a test sample and another providing a reference signal – is required [10.29–10.35, 10.52].

Owing to the necessity for a relatively broadband reception and, respectively, the higher noise of frequency-modulation spectroscopy, making direct detection unrealistic, coherent detection techniques are essential for accomplishing measurements with near quantum-limited sensitivity, providing the interfering sample and reference fields are perfectly matched [10.30–10.34]. The advantage of coherent optical detection is that the detectability of the measured signal is independent of either the presence of thermal radiation or the noise background with an adequately strong reference signal [10.30, 10.32]. The sufficiently strong reference field makes radiation power and its shot noise dominate the system noise, leading to the approachable limit of the time-averaged signal-to-noise ratio at equal time-varying intermediate frequency of interfering signal and reference fields:

$$SNR_{i.f.} = \eta P_{signal}/(h\nu B), \tag{10.17}$$

where P_{sig} is the radiation signal power, η and B are the quantum efficiency and noise bandwidth of the detector, and h and ν are the Plank constant and the radiation frequency [10.31]. Imperfect matching of signal and reference fields, which for laser radiation likely have a Gaussian and not a plane profile as assumed in Eq. (10.17), lowers the theoretical signal-to noise ratio limit given above, but can be compensated in part by increasing the beam size for the reference field [10.33]. Quantum fluctuations as well as access noise of the reference signal field further decrease the actual signal-to noise ratio from its limit [10.34].

Figure 10.9 depicts a coherent-subtraction technique, which is similar to the differential spectroscopy systems described earlier, widely used for a differential-absorption lidar sensor to distinguish low signals from noisy background [10.35]. Input and reference signals are combined via a 50:50 beam splitter capable of compensating for both quantum and access noise of the reference signal [10.34] and directing measured and reference laser beams equally to two detectors, substantiating coherent interference beats on both. Another splitter separates the coherent laser light into signal and reference beams in the proportion desired. For a sufficiently strong reference input, only sample-signal quadrature fluctuations remain unaltered, but reference-signal noise terms can be abolished by coherent subtraction of inputs phase-shifted against each other to equivalent light detectors, making only sample-signal fluctuations limit coherent-receiver sensitivity [10.34].

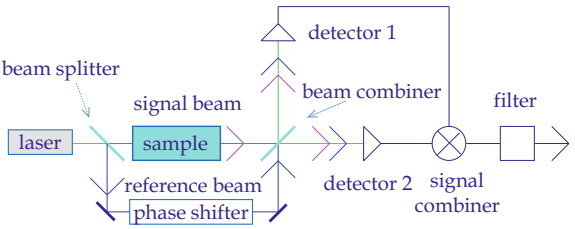

Fig. 10.9 Coherent beating and noise subtraction

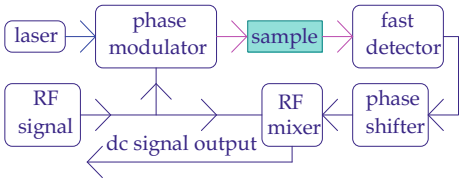

Fig. 10.10 Frequency-modulation technique

Frequency-modulation spectroscopy, as a high-rate expansion of the wavelength-modulation technique, applies high-frequency modulation to coherent single-frequency light, which spreads two mirrored modulation side lobes wider than the test spectral feature, thus allowing it to be probed by one of the side lobes (Fig. 10.10). An external phase modulator modulates an optical carrier signal at frequency ω_c by high frequency ω_m passing via a sample under test to a fast photodetector [10.36]. Owing to the sinusoidal modulation, the initial field of laser radiation: $E = 0.5E_0\exp(i\omega_c t)$, further carries the frequency spectrum:

$$E_f = 0.5E_0 \sum_{k=-\infty}^{\infty} J_k(M)\exp(i(\omega_c + k\omega_m)t) + const., \tag{10.18}$$

where M is the modulation index, being deliberately low, and J_k are the Bessel functions of order k. For $M \ll 1$, only two first functions remain: $J_0 \approx 1$ and $J_{\pm 1} = \pm M/2$, and other terms vanish, thus the spectrum includes a strong central frequency and weak side lobes at frequencies $\omega_c \pm \omega_m$. For frequency-dependent absorptance $\alpha(\omega)$ and refractive index $n(\omega)$, the transmitted amplitude E is:

$$\begin{aligned} E_T = (E_0/2)\Big(&\exp(-A_0 - i\varphi_0)e^{i\omega_c t} + \exp(-A_{+1} - i\varphi_{+1})(M/2)e^{i(\omega_c+\omega_m)t} \\ &- \exp(-A_{-1} - i\varphi_{-1})(M/2)e^{i(\omega_c-\omega_m)t}\Big). \end{aligned} \tag{10.19}$$

Here $A_k = \exp(-\alpha_k(\omega)\ell)$ is the attenuation and $\phi_k = i\ell(\omega_c + k\omega_m)n_k(\omega)/c$ is the phase shift for a sample of length ℓ for k = 0, 1, −1. The slowly varying photodetector intensity envelope, if M^2 terms are disregarded:

$$I_\omega(t) \sim \left(cE_0^2/8\pi\right)e^{-2A_0}\begin{pmatrix} 1 + (e^{A_0-A_1}\cos(\varphi_1 - \varphi_0) - e^{A_0-A_{-1}}\cos(\varphi_0 - \varphi_{-1}))M\cos(\omega_m t) + \\ + (e^{A_0-A_1}\sin(\varphi_1 - \varphi_0) - e^{A_0-A_{-1}}\sin(\varphi_0 - \varphi_{-1}))M\sin(\omega_m t) \end{pmatrix}, \tag{10.20}$$

contains distinguished-from-zero bit signal at frequency ω_m if either A_k or φ_k terms are different.

If the absorption loss and the phase difference induced by the sample at the side lobes are larger than at the central frequency ω_c: $|A_0 - A_1|$, $|A_0 - A_{-1}|$, $|\varphi_0 - \varphi_1|$, $|\varphi_0 - \varphi_{-1}| \to 0$, the beat-signal quadrature component ($\cos \omega_m t$) is proportional to

the loss difference between upper and lower sidebands, while the in-phase beat component (sin $\omega_m t$) is proportional to the phase-shift difference encountered by the carrier and the average phase shift encountered by the sidebands:

$$I_\omega(t) = I_0(c/8\pi)e^{-2A_0}(1 + (A_1 - A_{-1})M\cos(\omega_m t) + (\varphi_1 + \varphi_{-1} - 2\varphi_0)M\sin(\omega_m t)). \tag{10.21}$$

When $\omega_m = 2\pi\nu_m$ is high enough to separate upper and lower sidebands wider than the spectral feature to be tested but the feature itself is wider than one sideband, fine-tuning of either the carrier ω_c or the modulation ω_m frequency allows the feature to be scanned by one of the sidebands. If the carrier-frequency signal is also narrow enough not to overlap with both sidebands, and the loss A_B and phase φ_B due to the background can be considered constant, measurements of relative sample loss: $\Delta A_1 = A_1 - A_B$, $\Delta A_{-1} = A_{-1} - A_B$, and phase: $\Delta\varphi_1 = \varphi_1 - \varphi_B$, $\Delta\varphi_{-1} = \varphi_{-1} - \varphi_B$, simplify Eq. (10.21) to:

$$\Delta I_\omega(t) = I_0 e^{-2\bar{A}_0}\left(1 + \Delta\bar{A}_{1,-1}M\cos(\omega_m t) + \left(\Delta\bar{\varphi}_{1,-1} - 2\varphi_0\right)M\sin(\omega_m t)\right). \tag{10.22}$$

Factual realizations of frequency-modulation spectroscopy are done by the heterodyning of both modulation sidebands and the carrier frequency, which cancels the beatings against the carrier signal when no sample is present, inducing signals proportional to sample loss and phase shift as results of disturbance of the cancellation. Ideally, the absolute value of the loss and phase shift can be determined by comparing ac and dc portions of the heterodyne signal intensity, while practical measurements are rather limited by fluctuations of background signal intensity [10.36]. Since the heterodyne signal intensity is proportional to the geometrical product of the carrier and sideband intensities, the natural tendency is to increase the modulation index M, though in this case higher-order harmonics of modulation could disturb the validity of the equations derived. Another limiting factor for high sensitivity of frequency-modulation spectroscopy is the residual amplitude modulation, requiring compensation for the intensity changes induced [10.46].

More precise calculations of radiation intensity in frequency-modulation spectroscopy deal with beatings at higher than first order sidebands, still presuming a small difference of absorption and dispersion at adjacent sidebands: $|A_n - A_{n+1}|$, $|\varphi_n - \varphi_{n+1}| \ll 1$, and weak interaction of the sample with radiation: $|A_0 - A_n|$, $|\varphi_0 - \varphi_n| \ll 1$ [10.46]. As a result, Eq. (10.20) transforms to:

$$I_\omega(t) = I_0^2\exp(-2A_0)\begin{pmatrix} 1 + 2\cos\omega_m t\sum_{k=0}^{\infty} J_k J_{k+1}(A_{-k} - A_k + A_{-k-1} - A_{k+1}) \\ + 2\sin\omega_m t\sum_{k=0}^{\infty} J_k J_{k+1}\left(\varphi_{-k} - \varphi_k + \varphi_{-k-1} - \varphi_{k+1}\right) \end{pmatrix}, \tag{10.23}$$

where $J_k = J_k(M)$. For the limiting case of weak modulation index $M \ll 1$, $J_k(M)$ becomes negligibly low at $k > 1$, giving: $J_k(M) \rightarrow M^k/2^k k!$, and as a result Eq. (10.23) simplifies to relation (10.22).

Other versions of frequency-modulation spectroscopy use tone-burst and double-frequency [10.41, 10.43] as well as two-tone [10.42] modulation techniques, with higher sensitivity being realized for the latter owing to the much narrower detector bandwidth of the measurements required versus single-tone schemes, such as one shown in Fig. 10.10. Two-tone modulation remodulates the ω_1 signal at angular frequency ω_2:

$$E_1(t) = E_0 \exp(i\omega_0 t) \sum_{k_1=-\infty}^{\infty} J_{k_1}(M_1) \exp(ik_1\omega_1 t);$$
$$E_2(t) = E_1(t) \sum_{k_2=-\infty}^{\infty} J_{k_2}(M_2) \exp(ik_2\omega_2 t), \tag{10.24}$$

where E_0 and ω_0 are the optical beam amplitude and angular frequency (carrier frequency, Eq. (10.18)). Consequently, the amplitude of the two-tone modulated single-frequency beam is [10.44]:

$$E_2(t) = E_0 \exp(i\omega_0 t) \sum_{k_1,k_2} J_{k_1}(M_1) J_{k_2}(M_2) \exp(i(k_1\omega_1 + k_2\omega_2)t). \tag{10.25}$$

Equation (10.25) simplifies for both modulations realized with equal small modulation index $M = M_1 = M_2 \ll 1$, allowing one to consider only the central: $J_0(M) \sim 1$, and sideband: $J_{\pm 1}(M) \sim \pm M/2$, signals:

$$E_2(t) \approx E_0 \exp(i\omega_0 t)(1 + 0.5M \exp(i\omega_1 t) - 0.5M \exp(i\omega_1 t))(1 + 0.5M \exp(i\omega_2 t) - 0.5M \exp(i\omega_2 t)). \tag{10.26}$$

The specificity of the two-tone method is in modulating at two frequencies separated by a small shift Ω: $\omega_1 = \omega_m + \Omega/2$; $\omega_2 = \omega_m - \Omega/2$. Extracting the beat signal at the narrow frequency Ω at a photodetector gives the output intensity I_Ω proportional to the product of $c(E_i E_i^*)/8\pi$:

$$I_\Omega(t) = I_0\left(cM^2/16\pi\right)(\exp(-2A_1) + \exp(-2A_{-1}) - 2\exp(-2A_0))\cos(\Omega t) + const. \tag{10.27a}$$

If each frequency-dependent loss is low: $A_i \rightarrow 0$, the two-tone frequency signal of a low-loss sample could be approximated as:

$$I_\Omega(t) \sim I_0(c/8)M^2(2A_0 - A_{+1} - A_{-1})\cos(\Omega t). \tag{10.27b}$$

As a result of two-tone frequency modulation and signal detection with a narrow difference frequency Ω, the tuning of a single-frequency laser make signals at

frequencies ω_1, ω_0, and ω_{-1} consequently becoming nonzero, thus making the sample attenuation (absorption) spectrum consisting of the central peak and the doubled at two tones negative and positive symmetrical side lobes with no more than half of the central intensity [10.44].

Most applications for single-tone and two-tone frequency modulation techniques utilize widely tunable diode lasers, whose current can be directly modulated at various modulation indices, being especially suitable for IR molecular spectroscopy [10.45–10.50]. However, junction current modulation causes simultaneous frequency and amplitude (power) modulation of a diode laser, while amplitude modulation, during frequency-modulation measurements, imposes sideband beat noise even in the absence of a test sample, removing the advantage of relative detection versus zero baseline. If an amplitude modulation is imposed over frequency-modulated field $E_F(t)$, its amplitude becomes: $E_{A\text{-}F}(t) = [1 + M_A \sin(\omega_m t)]E_F(t)$, where M_A is the amplitude-modulation index.

Only if both modulation indices M_F and M_A are small (M_A is likely be at least an order of magnitude smaller than M_F), Eq. (10.21) for the detector signal intensity becomes [10.47]:

$$I_{A-F}(t) \sim I_0(c/8\pi)\begin{pmatrix} 1 + M_F(A_1 - A_{-1})\cos(\omega_m t) + M_A(\varphi_1 + \varphi_{-1})\cos(\omega_m t + \psi) + \\ M_F(\varphi_1 + \varphi_{-1} - 2\varphi_0)\sin(\omega_m t) + M_A(2 - A_1 + A_{-1} - 2A_0)\sin(\omega_m t + \psi) \end{pmatrix}. \tag{10.28}$$

Pure frequency modulation converts Eq. (10.28) to (10.21) removing the background signal:

$$I_{FM}(t) = I_0(\omega_m)M_{FM}((A_1 - A_{-1})\cos(\omega_m t) + (\varphi_1 + \varphi_{-1} - 2\varphi_0)\sin(\omega_m t)), \tag{10.29}$$

while pure amplitude modulation at $M_{FM} = 0$, similarly to wavelength-modulation spectroscopy, returns a no-zero background even for the time-varying portion at ω_m, changing Eq. (10.28) to:

$$\begin{aligned} I_{AM}(t) = I_0(\omega_m)M_{AM}((2 - 2A_0 - A_1 - A_{-1})\sin(\omega_m t + \psi) \\ + (\varphi_1 + \varphi_{-1})\cos(\omega_m t + \psi)). \end{aligned} \tag{10.30}$$

The presence of dual frequency modulation-amplitude modulation modifies the two-tone signal amplitude to [10.48]:

$$\begin{aligned} E_{F-A}^{t-t}(t) \sim\ & e^{i\omega_0 t}(1 + M_{A1}\exp(\omega_1 t + \psi_1))(1 + M_{A2}\exp(\omega_2 t + \psi_2)) \\ & \times \exp(iM_{F1}\sin(\omega_1 t))\exp(iM_{F2}\sin(\omega_2 t)). \end{aligned} \tag{10.31a}$$

If the difference $\Delta\omega$ of two modulation frequencies ω_1 and ω_2 is much lower than the full width at half-maximum Γ_{FWHM} of the measured spectral feature: $\Delta\omega \ll \Gamma_{FWHM}$, and also if the frequency-modulation and amplitude-modulation indices are small: $M_A \ll M_F \ll 1$, the two-tone signal intensity of the detector is [10.46]:

$$I_\Omega(t) \sim I_0(c/8\pi)\begin{bmatrix} 2M^2 + 2A_0\left(M_F^2 - M_A^2\right) - A_1\left(M_F^2 + 2M_A M_F \sin\psi + M_A^2\right) \\ -A_{-1}\left(M_F^2 - 2M_A M_F \sin\psi + M_A^2\right) \end{bmatrix} \cos(\Omega t), \tag{10.31b}$$

which converts to Eq. (10.27) at $M_A \to 0$, where ψ is a not remaining constant phase difference between frequency and amplitude modulation, also depending on wavelength. The obvious goal of frequency-modulation measurements is in removing any residual amplitude modulation that leads to nonzero background signal and accompanied beat noise, ultimately reducing sensitivity, which can be especially severe for directly modulated diode lasers having the full-noise spectrum.

Possible residual amplitude modulation for a frequency-modulated heterodyne signal, which exists even when the sample under test is not present, can be assessed by setting the differential sample loss: $\Delta A = A_1 - A_{-1}$, and the phase shift: $\Delta\varphi = \varphi_1 - \varphi_{-1}$, induced by the sample to zero: $\Delta A = \Delta\varphi = 0$. From Eqs. (10.28) and (10.31), the intensities of residual amplitude-modulation are [10.49]:

$$I_{RAM}^{S-T}(t) = I_0(c/8\pi)2M(\sin\psi\ \cos(\omega_m t) + \cos\psi\ \sin(\omega_m t)); \tag{10.32}$$

$$I_{RAM}^{T-T}(t) = I_0(c/8\pi)2M^2\cos(\Omega t). \tag{10.33}$$

If the modulation index M is low: $M \ll 1$, any nonzero residual amplitude modulation should produce lower background noise in two-tone modulation schemes, not being affected by the phase difference ψ between frequency and amplitude modulations, although being not in a linear but in the M^2 dependence. This is in contrast to the single-tone background signal, which is dependent on the not-constant ψ shift and is proportional to 2M.

In a technique-demonstrating experiment (see Fig. 10.10) for single-mode, single-frequency radiation of a ring dye laser tunable from 530 to 630 nm, modulated by a $LiTaO_3$ electro-optic modulator at up to 1.5-GHz frequency, the background-level sensitivity verified by a Fabry–Perot resonator (5-GHz free spectral range and 16.8 finesse) in reflection was approximately $6 \cdot 10^{-4}$ at 25% peak for measuring spectral-line absorption with an estimated $5 \cdot 10^{-5}$ limit if the background remained constant on a single line scan [10.36]. Figure 10.11 depicts experimental arrangements for pulsed measurements (Fig. 10.11a) allowing down to microsecond spectral changes to be observed [10.37] and for the two-tone technique (Fig. 10.11b) offering higher sensitivity at a high (gigahertz) modulation

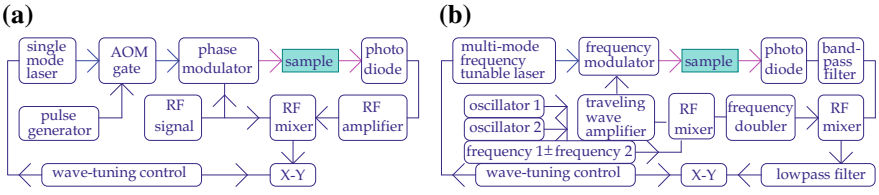

Fig. 10.11 Expermental systems for single-tone pulsed (**a**) and two-tone (**b**) frequency-modulation spectroscopy

frequency with relatively narrow bandwidth detectors [10.44]. The pulsed scheme used two modulators: acousto-optic modulator AOM as a pulse gate, trimming 1-μs-long low-duty pulses from a continuous-wave (cw) tunable ring dye laser with 1–2-MHz spectral width, and a $LiTaO_3$ phase modulator, further modulating the laser pulses at 50–100-MHz radio frequencies. The two-tone scheme provided sum and difference frequencies of 16 GHz ± 6 MHz via one $LiTaO_3$ frequency modulator applied to a multimode dye laser beam. Light transmitted by the sample was detected by a fast photodiode and filtered out at 12-MHz differential dual-modulation frequency, with the laser modulation bandwidth reaching approximately 10 GHz for 50 mW of rhodamine 6G lasing power. The respective sensitivity limits to differential absorption versus the background for the pulsed single-tone system and between two side lobes in the two-tone system were estimated as $2 \cdot 10^{-4}$ and $1 \cdot 10^{-5}$, respectively [10.37, 10.44].

In practical implementations another limiting factor for frequency-modulation spectroscopy is the accompanying optical noise of any high-sensitivity heterodyning owing to etalon effects among reflecting surfaces of transmitting elements, causing fluctuating background signals and distorting line shapes of the spectrums measured [10.49–10.53]. Since even 0.1% antireflection (AR)-coated surface reflections create equivalent-absorption signals above 10^{-5} levels with spectral widths similar to the linewidths measured, active fringe-suppressing measures are needed for quantum-noise-limited sensitivity (see Sects. 3.3 and 7.4 for interference-relieving approaches). In highly reflecting mirror cavities or waveguides, interference fringes can appear as a slowly varying baseline in a given cell transmission being studied, owing to superposition of images retroreflected in the cavity, as well as image walk-offs on mirror edges or cell misalignments. When intermediate images cannot be completely separated, any desired reduction of dual-path or multipath interference fringes requires some signal integration and averaging, which can be provided in space and time by combining high-frequency and low-frequency filtering, supplemental signal dithering, and single-tone and two-tone modulation – all leading to added averaging of the interference pattern (see Sect. 7.4 for details). While analyzing the derivatives of measured spectra, various algorithms and signal-processing optimization and multiplicative corrections, as well as small-window differentiation techniques along with highest spectral resolution of original spectra help enhancing measurement accuracy [10.84, 10.85].

10.3 Wavelength Tuning and Balanced Detection

Sensitive optical measurements in laser radiation do not necessarily require high-power lasers to be used even for remote monitoring of trace species. In contrast, eye-safe environments require the laser power to be contained under safe-exposure limits. In such cases, high sensitivity of measurements can be attained by other means, such as deploying remote reflectors aligned to tunable diode lasers for atmosphere-pollution

monitoring and/or utilizing multipass cavities sensing gaseous species to be detected in controlled volumes via extended optical path lengths. Alternatively, high-sensitivity detection techniques allow long-distance heterodyne, homodyne, or balanced measurements of trace amounts of species at extremely low concentrations.

10.3.1 Tunable Diode Systems

The direct-transmission measurement method, detecting resonant absorption by spectrally scanning a wavelength or frequency of interest, remains a technique of choice often owing to broad availability of current-tuned diode lasers (see preceding sections). If a turbulent medium containing a polluting species is directly scanned in transmission, and radiation sent is returned via a remote retroreflector of ideal reflectivity $\rho_r = 1.0$, the return-signal intensity is:

$$I_r = I_0 \exp\left(-\alpha(\nu) N \ell_\Sigma\right) \exp(-\beta(t)). \tag{10.34}$$

Here β is the time-dependent extinction and scattering coefficient for turbulent atmosphere over the extended optical path length ℓ_Σ (see Eq. (10.8) for other designations). If the laser frequency ν is tuned over the spectral range of interest and if the intensity change of received light is sensed as its frequency derivative, the equation becomes [10.54]:

$$dI_r/d\nu = -I_0 N \ell_\Sigma \exp(-\alpha(\nu) N \ell_\Sigma) \exp(-\beta(t)) d\alpha(\nu)/d\nu. \tag{10.35}$$

Referring the derivative signal $\Delta I/\Delta\nu$ to the initial intensity I_r, and considering a most likely Lorentzian (natural) broadening in the form: $a(\nu) = \alpha_0 \Big/ \left(1 + (\Delta\nu/\gamma)^2\right)$, where α_0 is the attenuation (absorption) coefficient in the center and γ is the half width at half-maximum of the line measured, the ratio of signals is:

$$(dI_r/d\nu)/I_r = (2a_0 N \ell_\Sigma)(\nu - \nu_0) \Big/ \left(\gamma^2 \left(1 + (\nu - \nu_0)^2/\gamma^2\right)^2\right), \tag{10.36}$$

making such a derivative ratio insensitive to turbulence or scattering fluctuation of the received signal intensity via length ℓ_Σ being sufficient for detection with an appropriate confidence level.

Figure 10.12 illustrates the long-range direct monitoring concept via a remote retroreflector [10.54]. In one realization, a tunable $PbS_{0.82}Se_{0.18}$ semiconductor

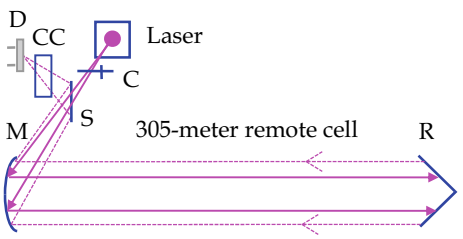

Fig. 10.12 Retroreflector long-path monitoring

diode laser generating eye-safe radiation near 1-mW power within the 4.7-μm spectral band of the fundamental absorption line for CO traces was used for current tuning around 2145-cm^{-1} wavelength. A closed-cycle cryogenic cooler maintained 10 K operating temperature of the laser chip. Off-axis aluminum-coated parabolic mirror M and matching corner-cube remote retroreflector R provided 610-m of total cell length being monitored. Extra calibration cell CC via germanium beam splitter S in conjunction with nitrogen-cooled InSb detector D was used for absorption coefficient calibration, using reference gas mixtures of known concentrations. Derivatives of optical absorption spectrums were obtained by modulating the laser current at 10 kHz with 20-mA peak-to-peak depth from the nominal current of 400 mA. A lock-in amplifier tuned to 170-Hz frequency of beam chopper C directly measured the transmittance–reflectance of the cell, whose signal I_r (Eq. (10.36)) referenced the derivative spectrum. Noise-level CO-contaminant sensitivity approached approximately 5 ppb with 1-s integration time [10.54].

The approach based on a multipass cell is depicted in Fig. 10.13 [10.55, 10.56]. In that system, two White cells were concurrently utilized – a 5-m-long one, adjustable from 20 to 500-m path length, and a 0.5-m cell for up to 30-m path length. A $Pb_{1-x}S_xSe$ tunable diode laser for SO_2 trace detection at atmospheric concentrations was used at cryogenic-helium temperatures, maintaining single-mode operation at low powers of 100–200 μW. Both cells 1 and 2 were attached to vacuum pumps for low-pressure studies and were used for sample-concentration calibrations, as well as for verification of the measurement accuracy and fringe-related noise, since tunable diode laser spectroscopy lacks absolute means of verifying the tuning wavelength, except by referencing to known absorption lines – in this setup NO_2 was used. In the operating range of 1050–1150 cm^{-1} the diode laser wavelength was tuned over 1 cm^{-1} via current modulation and temperature control, traceable to approximately 0.01 cm^{-1} by calibration to NO_2 wavenumbers. Initially, diode laser light was mechanically chopped at 150 Hz to be synchronously detected by a HgCdTe detector via a lock-in amplifier, which proved too noisy for low-loss measurements and was replaced by adding low-current diode modulation at 1 kHz provided by wavelength-tuning laser modulation. A series of interference fringes, identified as primarily due to AR-coated lens surfaces or cell mirrors, accompanied the spectral scans at an effective reflectivity of approximately $1 \cdot 10^{-3}$ especially with a long-path cell; nevertheless, near $2 \cdot 10^{-5}$ absorption sensitivity was attained [10.56].

During testing, the system in Fig. 10.13 was found to have the lowest noise for second harmonic detection, since not only the transmitted signal but even the first harmonic signal was susceptible to laser-power fluctuation, which allowed

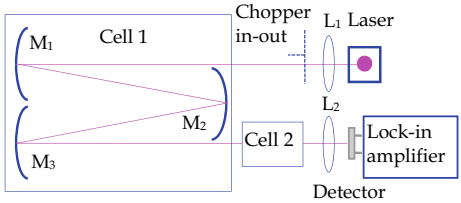

Fig. 10.13 Detection system based on a multipass cell

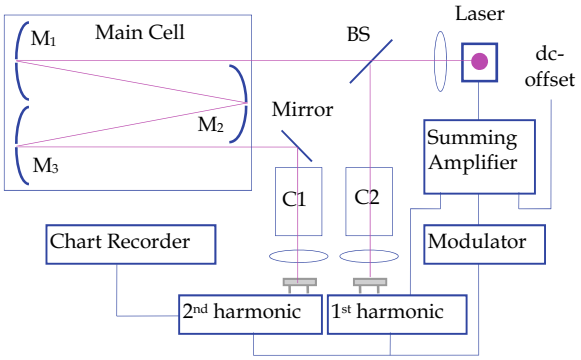

Fig. 10.14 Wave lock-in multipass-cells detection system

detection of the weakest absorption lines with the smallest DC offset. An improved system is shown in Fig. 10.14. It used a smaller main White cell with sevenfold path length reduction, but led to only 2 times lower sensitivity of near $3 \cdot 10^{-8}$ m^{-1} or about 1–0.1 ppb of noise-level concentration detection limit with added short cell C1 for locking laser wavelengths [10.57]. Second cell C2 was used via beam splitter BS and contained ammonia, to the absorption line of which the laser wavelength was locked. A slow dc offset was also introduced to ramp the feedback loop by slowly scanning an absorption line from one edge to the other. That extra cell C2 allowed air references to be made versus the absorption lines tested in the main cell and in C1, avoiding species interferences.

One major difficulty of tunable diode laser spectroscopy is associated with the reproducibility of tuning wavelengths, since current modulation leads to fluctuations of the laser junction temperature and instabilities of recorded spectrums, especially if they are integrated over time to improve sensitivity. When a wavelength scale is calibrated by a Fabry–Perot etalon, its high path-length sensitivity, leading to temperature-induced free spectral range changes and transit-angle errors, affects the accuracy of calibration [10.58, 10.59]. The design in Fig. 10.15 incorporates dual-beam measurement, places the etalon before any dispersive elements

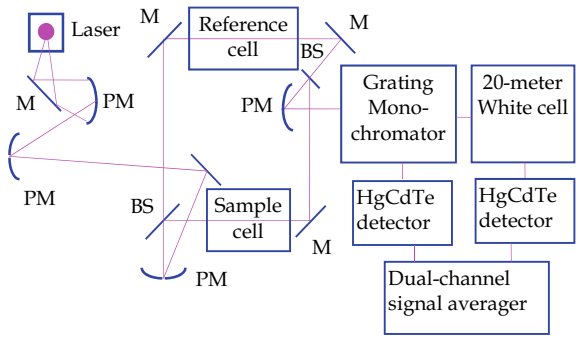

Fig. 10.15 Diode-laser dual-beam spectrometer

preventing deviations in free spectral range due to path-angle changes, and adds a grating monochromator as a spectral selector [10.60]. IR radiation in the 1202–1263-cm^{-1} wavenumber range is imaged via reflective optics: plane M and off-axis paraboloid PM mirrors, into the dual-beam monochromator, a 20-m White cell, HgCdTe detectors, and a dual-channel averager. The design places the sample and reference beams entering the monochromator atop of each other, hence avoiding 50% loss of a combining beam splitter. The signal averager provides concurrent two-beam integration over the laser 20-Hz frequency sweep, which is phase-locked to the averager, allowing it to integrate all measured spectral points simultaneously and to average multiple scans over time for sufficient noise reduction. Such integration over 2 min for 2660 sweeps decreased the average level of accumulated noise to near $2.5 \cdot 10^{-4}$ of the laser beam intensity [10.60].

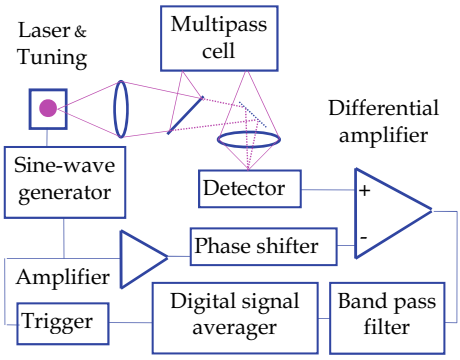

Fig. 10.16 Diode-laser sweep integration

The extension of the sweep-integration approach illustrated in Fig. 10.16 is made by increasing the sweep frequency to 200 Hz, using a 1024-point averager with 5-μs integration time per point [10.61]. To control the steep intensity modulation of the diode laser due to the relatively fast sweep, the system also incorporates an amplifier plus a phase shifter to null laser-power changes by compensating the detector signal via a differential amplifier. A band-pass filter is used to cut out low-frequency laser noise, processing the detecting spectrum with relatively small distortions, which along with sinusoidal instead of sawtooth modulation sufficient to make a relatively linear sweep allowed detection of absorption features approaching $1 \cdot 10^{-5}$ for a 200-m-long path length in the 0.2–0.4-cm^{-1} wavenumber region [10.61]. Since the second-derivative signal is affected by intensity changes due to laser modulation, the ratio measurements of sample and reference channels were performed to correct for changes [10.62].

A tunable diode laser source, sine-wave-modulated at an optimal frequency of 5 kHz, allowed the system design to be simplified using high-power single-mode light [10.63]. In Fig. 10.17, a 1.5-μm-wavelength beam from a distributed-feedback

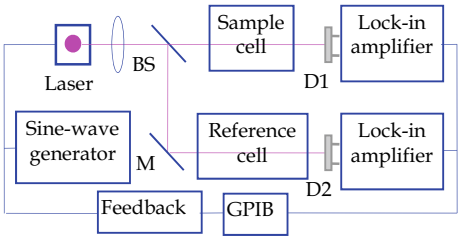

Fig. 10.17 Two-channel tunable laser system

laser mounted on a Peltier cooler was regulated via a commercial controller and split in 90:10 ratio into sample and reference cells, 100 and 30 cm long, respectively, containing the pollutant to be detected and a control species. Second-derivative detection was applied to the measurement of absorption, but the third derivative was applied for laser-wavelength locking, owing to the strong dependence of laser power on current changes making first-derivative detection inadequate. The minimal detectable concentration of ammonia measured at the noise-equivalent level was near $2 \cdot 10^{-6}$ [10.63].

Taking advantage of single-mode tunable sources, one can use diode laser spectroscopy for direct-absorption measurement, such as depicted in Fig. 10.18. The system implements the wavelength-modulation approach instead of frequency modulation, which requires mathematically heavy conversion or knowledge of the spectral line shape to be detected; thus, it is mostly applicable for central-line detection of trace species [10.64]. To provide direct-attenuation measurement, the differential-ratio technique (see Sect. 10.1) via Eq. (10.3) but not (10.2) is deployed for quantitative detection of water vapor by tuning the wavelength of a single-mode laser across the spectral lines to be detected and measuring the direct absorption spectrums expressed as the $(I_2 - I_1)/I_2$ ratio; here I_1 and I_2 are the signal intensities reaching detectors D1 and D2. In the implemented system, a InGaAsP laser emitting 5 mW at nominal 1384-nm wavelength was modulated at low 80-Hz frequency – hence not to decrease its tuning range and maintain it sufficiently large to resolve spectral lines measured in a single wavelength sweep. The signals of detectors D1 and D2 were optically balanced via the angles of two-channel beam splitters BS. Third detector D3 detected changes in the relative emission wavelength during each

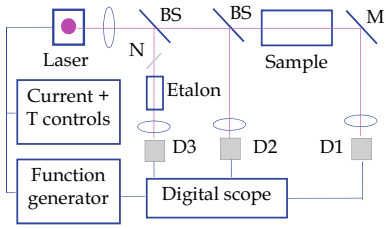

Fig. 10.18 Triple-channel detection system

tuning sweep via a low-finesse etalon, the reflections from which back to the laser were attenuated by neutral filter N. The absorption coefficients for measured spectral lines of water vapor were near $3.8 \cdot 10^{-3}$ cm^{-1} for a 1-cm^{-1} tuning range [10.64]. A similar technique with 5–10-kHz modulation frequency with a fourth channel added for Doppler-shit tracing in high-speed gas flows was capable of trace detection of water vapor in flight [10.65]; the 80-nm tuning range, with $5 \cdot 10^{-6}$ sensitivity at the 95% confidence level, was reached using a multiple quantum-well asymmetric InGaAsP laser in an external cavity for CO_2-line spectroscopy [10.66].

Diode and other tunable lasers can be utilized in multipass cavity-enhanced wavelength-modulation or frequency-modulation spectroscopy, such as shown in Fig. 6.11 (see Chap. 6). An analogous approach, developed for fast-scanning OH laser spectroscopy [10.67], is depicted in Fig. 10.19. A modified dual-path White cell, following those in Figs. 6.11 and 6.12 with beam splitter BS to separate the beam entering the cell from the beam exiting the cell, increasing the beam's size 4 times and reducing its shift, was used with a total multipath length reaching 1.2 km for a 6-m-long cell. A free-running cw ring dye laser, modified for fast-scanning capability and stabilized output power, generated the main 616-nm wavelength radiation frequency, doubled to 308-nm light via second-harmonic-generating crystal SHG. A near 10-cm^{-1} wide spectrum was scanned at 5-kHz repetition rate in just 100 μs. Four-crystal electro-optic modulator EOM compensated for its piezoelectric effect and its own birefringence, was used for power stabilization via polarizer P and a feedback loop – for comparing a reference photodiode signal with a stabilized voltage in the error amplifier. Fast scanning of dye laser wavelengths was realized via angle-tuning of a 0.5-mm-thick etalon by a galvanometer drive. The spectral locking of the laser was obtained via the absorption line of the OH, using a bypass beam and another etalon via the first-derivative signal to a delaying master trigger. The resultant peak-to-peak noise of the stabilized system was near $8 \cdot 10^{-4}$ for a single scan with noise-level sensitivity of $1 \cdot 10^{-5}$ in the UV–visible spectrum with 1-min integration time [10.67].

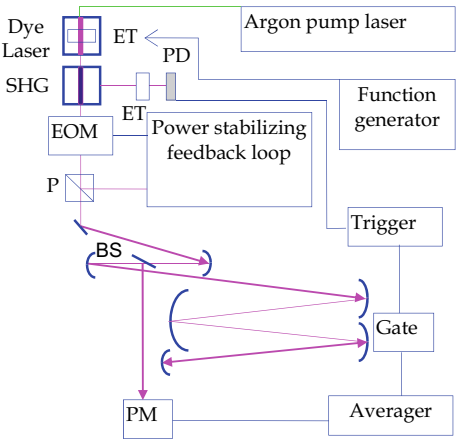

Fig. 10.19 Dual-path fast-scanning spectrometer: *ET*-etalon, *PD*-photodiode, *PM*-photomultiplier

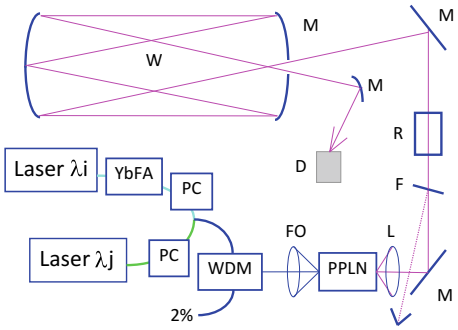

Fig. 10.20 Continuously-tunable scanning: YbFA – Yb fiber amplifier

Figure 10.20 illustrates a waveguide-cavity-enhanced system using a continuously tunable laser based on fiber-coupled pump lasers, frequency-converted to 3.3–4.4 μm via a periodically polled lithium niobate crystal [10.68]. The first pump laser was an external-cavity tunable diode laser at 814–870 nm, while the second one was an Yb-fiber-amplified diode laser generating 1083-nm wavelength: both lasers were fiber-coupled, delivering, respectively, 8 and 15 mW of power via two polarization controllers PC to wavelength-division-multiplexer WDM, of which 2% tap was used for power monitoring and its main leg led into fiber-pigtailed achromatic objective FO. The wavelength conversion was accomplished in 19-mm-long temperature-controlled periodically polled niobate crystal PPLN with AR coatings mounted on a step-motor-controlled stage for differential quasi-phase-matching. The output 2.9-μW beam tunable between 3.37 and 3.70 μm with 40-MHz spectral resolution was focused by CaF_2 lens L via a germanium filter, blocking unconverted pump radiation into the main waveguide cavity W, also passing through a supplemental set of reference cavities R. The multipass 30-cm cell with 18- or 36-m total length was similar to that in Fig. 6.25, with cell-mirror astigmatism compensated via adjusted cell spacing and mutual mirror rotation [6.36] (see Sect. 6.3). The overall system sensitivity was limited to $2 \cdot 10^{-4}$ relative to the output power because of occurrence of interference fringes due to optical element retroreflections while reaching 0.5-ppm noise-limited sensitivity for the 18-m optical path in the cavity [10.68].

A less elaborate system based on a fiber-pigtailed tunable distributed-feedback laser for overtone absorption spectroscopy in the 1530-nm wavelength domain is illustrated in Fig. 10.21 [10.69]. The same waveguide as in Fig. 10.20 set for 36-m configuration was irradiated by the named current-tuned, temperature-controlled laser via objective O_1 and output light was detected via parabolic mirror M by one of two autobalanced two-channel detectors. Another fiber channel was split for objective O_2 and the second detector via variable optical attenuator VOA balancing the channel for attenuation in waveguide W. The fiber laser, delivering 15 mW of power at 1531.7 nm with less than 10-MHz linewidth, was spliced to the splitter and variable optical attenuator VOA and after 182 cell passes approximately 17 μW

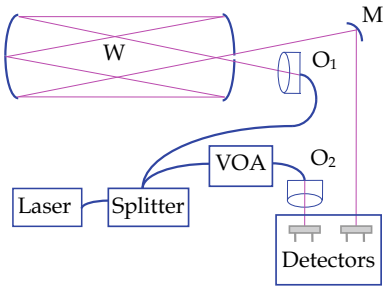

Fig. 10.21 Tunable-diode balanced setting

remained with 0.17% throughput efficiency, corresponding to 0.967 average cell-mirror reflectivity – degraded from the original 0.980 value. The attenuation level of variable optical attenuator VOA was set to below 25 dB for reference power $P_{reference} = 2.2 \cdot P_{signal}$, owing to the occurrence of interference fringes likely caused by fiber-to-fiber etalon effects in the attenuator, which affected the signals registered at higher powers. Within less than 30 s of the processing time, the sensitivity of this system to ammonia reached 0.7 ppm at 3:1 signal-to-noise ratio, with simultaneous CO_2 detection capability within a single diode laser scan of 0.3 cm^{-1} [10.69]. For every concentration measurement cycle, either the autobalance mode or the linear mode of the dual-beam balanced InGaAs detectors was used with, respectively, 500 and 1000 spectral scans, recorded and averaged for the signal-to-noise performance stated (see below for more details).

10.3.2 Balanced Detection

As much as the differential, as well as homodyning and heterodyning techniques allow compensation of dominated noise components of detected optical signals for the measurement techniques reviewed in Sects. 10.1 and 10.2 earlier, balanced-detection methods apply the same principals by matching the properties of identical photodetectors receiving at least two signals to be compared. One experimental-demonstration setting for noise reduction due to balanced detection is illustrated in Fig. 10.22 and was realized in heterodyne-radiometry experiments with a tunable

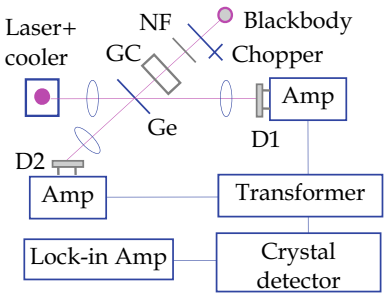

Fig. 10.22 Balanced heterodyne detection: *Amp* – amplifier

diode laser as a local oscillator [10.70]. A blackbody emitter at 900 °C and a 10-μm tunable PbSnSe diode laser kept in a cryogenic cooler at 12–30 K, with 920–980-cm^{-1} tuning, were heterodyned via a 50% germanium beam splitter. HgCdTe photodiodes with 1.5-GHz bandwidth and 0.45 effective heterodyne quantum efficiency photomixed two beams, providing radio-frequency signals amplified by low-noise amplifiers, square-law detected, and lock-in-amplified with a wide-band transformer adding signals together. The signal-to-noise ratio attained via double-balanced detection was 1.85 times better compared with single-detector heterodyning of the laser versus blackbody light filtered by notch filter NF and gas cell GC.

Figure 10.23 shows the balanced-homodyning system for frequency-modulation loss measurements, aimed at improving sensitivity and suppressing residual amplitude modulation and supplemental laser-excess and interference-fringe noises [10.71]. Radiation from a tunable diode laser is equally split into sample and reference channels by 50:50 nonpolarizing beam splitter BS. Low-aberration aspheric lenses L were deployed to maintain equivalency of light power within 1%. Optical isolator OI and AR coatings of all optical surfaces, as well as electronic filtering, maintained low interference-fringe noise. With use of such a dual-beam balanced-homodyne detection scheme with different lasers having 5.4- and 1.3-μm wavelengths, the differential-absorption magnitudes measured were $1 \cdot 10^{-6}$ and $7 \cdot 10^{-7}$, respectively, with noise-level sensitivity values estimated as $1 \cdot 10^{-7}$ and $2 \cdot 10^{-7}$ at each wavelength [10.71].

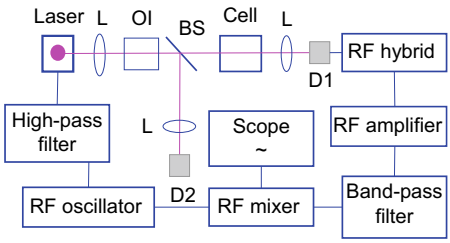

Fig. 10.23 Homodyne frequency spectroscopy

When high sensitivity to an optical loss under study needs to be achieved only for threshold detection, such as the occurrence of nonlinear phenomena as a result of an abrupt transition from very low loss to a detectable loss, the direct differential measurement settings described in Sect. 10.1 may be used for balanced detection attempting to improve the sensitivity to just-above-threshold loss [10.72]. Figure 10.24 illustrates the differential-balanced technique utilized for detection of

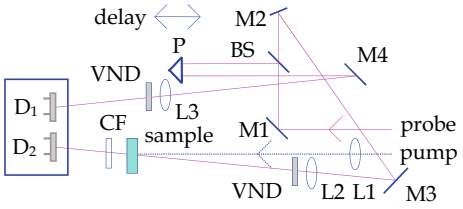

Fig. 10.24 Balanced differential pump-probe system

nonlinear pump–probe transmission loss in a highly transparent sample irradiated by pulsed laser light. The pumping and probing was accomplished by two dye lasers with 3-ns pulse width for 435-nm pump and 470–520-nm probe wavelengths separated by color filter CF. The system was to sense 0.1% transmittance changes by nulling the difference signal between main and reference detectors D_1 and D_2. In addition to equalizing channel paths and matching the properties of the detectors to synchronize the maximal amplitudes of the pump and the probe light pulses within 0.1%, channel path lengths were controlled to 14 mm or less for under 3-ns time delay. Pulse timing was synchronized by adjusting the distance between prism P and mirrors M4 and M1–M3; the power of each channel was matched via variable neutral-density filters VND.

Owing to differential measurements, any imbalance of photodetector currents will produce a constant offset in both measured and reference channels; this can be subtracted, but that offset could limit small-loss sensitivity and should not saturate the detectors and balance circuits. A boxcar integrator was utilized to reduce shot-to-shot noise variations by averaging the difference signal over many laser pulses to within $\pm 5 \cdot 10^{-4}$. Unavoidable noise was due to spatial-sensitivity deviations of the two photodiodes affected by fluctuations of the spatial intensity distribution for probe laser pulses, which was partially compensated by neutral-density filters equalizing the average fluence in each laser beam. During experiments the pump beam was focused to a 400-μm-diameter spot and the probe beam was focused to a 200-μm-diameter spot within the pumped region on a sample with above 99% transmittance. Transmission nonlinearities with $1 \cdot 10^{-3}$ sensitivity were observed with 10-ns time resolution [10.72].

To improve optical-channel balancing, a continuously adjusted matching of the photodiode currents via negative feedback outside the main-signal path can be used [10.73, 10.80]. The matching requires an electronically variable current splitter, not degrading an existing proportionality for main and reference signals in making the balance be preset in the electronic circuitry. Another requirement is to make the reference signal stronger than the measured signal, splitting its current via two paths to a pair of bipolar junction transistors linearly processing either signal or noise as dc, while not affecting noise cancellation as reference-signal excess is dumped to ground. The signal difference is further processed by a transresistance amplifier, electronically balanced via adjusting the base-emitter voltage of the transistor pair. By zeroing the transresistance amplifier current, the circuit provides excess noise cancellation, since it is handled as a dc component, while zero balance is maintained by an additional integrating amplifier, whose output voltage V_{out} [10.73]:

$$V_{out} = G \cdot \ln\left(I_{ref}/I_{signal} - 1\right), \tag{10.37}$$

is defined by the logarithmic ratio of reference to signal current I_{ref}/I_{signal} and by amplifier gain G. The approach can be seen as ratio balancing for ideal zero balance, reached at derivative output $\Delta V/V$:

$$\Delta V/V \rightarrow \left(I_{ref}/I_{signal} - 1\right) \rightarrow 0 \quad \text{at} \quad I_{ref} \rightarrow I_{signal}, \tag{10.38}$$

not making an absolute signal measurement, but establishing equilibrium with the reference.

An advantage of the ratio-balancing over the direct-division technique by the two-channel ratio is the likely wider noise-suppression bandwidth, since dividers can be relatively slow, although the optical ratio divider method remains a direct, absolute, sensitive low-loss technique that cancels drift, modulation noise, and excess noise, but extracts the signal and shot noise for the majority of measurement task having the main goal of reaching the highest assessable accuracy.

Experimental free-space and fiber-optic setups for the noise-cancelling balance detection reviewed are shown in Fig. 10.25 [10.74]. In the experimental verification, the signal-balancing method was applied via frequency-modulation spectroscopy by scanning single-mode laser light across a spectral absorption line of interest (see Sect. 10.2). A balance signal during each scan experienced certain monotonic variations which appeared as stable, and therefore were counted out via precalibration. The free-space and fiber-coupled versions of the system were compared to establish sensitivity limits of the measurements, since the fiber-based setup seemed prone to interference-fringe noise (see Sect. 7.4), with wavelength-dependent reflectivity changes of the fiber components and space-to-fiber coupling elements (Fig. 10.25b). For the free-space setup (Fig. 10.25a), a single-mode AlGaAs diode laser emitting the 763-nm wavelength band was tuned over approximately 3 cm^{-1} in 100 ms. Collimated laser radiation was split via AR-coated beam splitter BS and gold-coated mirror M into measurement and reference beams detected by similar detectors D1 and D2 of the balancing system. Absorption-path difference AP for two channels in air was set by varying the distance between mirror M and splitter BS. The balanced output was amplified, band-pass-filtered within 0.1–1000 Hz, and digitized, making 100 sweep averages of each scan. The open-air measured peak absorptance and noise-level sensitivity limits were $5 \cdot 10^{-5}$ and approximately $5 \cdot 10^{-7}$ – both calculated using simulated Voigt line profiles and approximating a linear laser current tuning rate. Further measurements were performed via a 25-cm absorption cell in path AP filled with pure O_2 at 1-Torr pressure. Not analyzing noise sources of measurements, partially due to wavelength-dependent properties of polarizing beam splitter BS or added fringe noise caused by cell windows, the low-loss absorption pick and

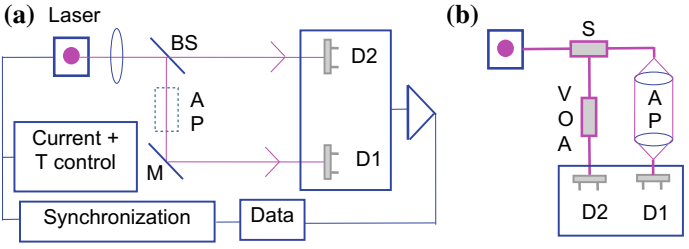

Fig. 10.25 Noise-canceling balanced detection: free-space (**a**), fiber (**b**)

background noise detected were at $2 \cdot 10^{-4}$ and $6 \cdot 10^{-6}$ levels, respectively. The same cell was used for measurements in a fiber-coupled system, deploying angled connectors utilizing an index-matching gel, and comparing several tunable InGaAsP lasers with 1.31-μm wavelength. The observed 50-cm spacing of interference-fringe noise corresponded to the dual path of the absorption cell. Averaged over 100 scans, the water vapor line peak absorptance and background noise were at $2 \cdot 10^{-3}$ and $2 \cdot 10^{-5}$ levels, while the lowest peak, measured using a 1.39-μm laser, was near $8 \cdot 10^{-4}$ at $5 \cdot 10^{-5}$ noise level. Small laser gains were also measured, reaching $2 \cdot 10^{-5}$ cm^{-1} in a 3-cm dye cell [10.74].

Similar balanced measurements were conducted for trace detection of NO_2 absorption in a 0.5-m-long absorption cell with 2°-angled and AR-coated fused-silica windows (Fig. 10.26) using two single-mode AlGaInP diode lasers in 640- and 670-nm wavelength bands [10.75].

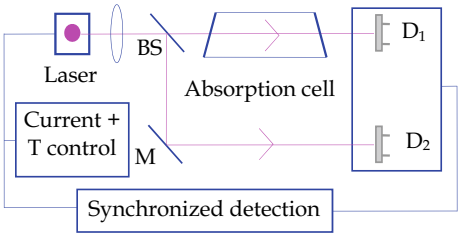

Fig. 10.26 Balanced frequency-modulation setup

Nonpolarizing beam splitter BS directed light onto main D_1 and reference D_2 photodiodes via the cell and mirror M. The sampling rate of data acquisition was 25 kHz at 40 μs per data point with 1375 points for 20 Hz of spectrum-processing rate, providing $2.5 \cdot 10^{-4}$ cm^{-1} per point of spectral resolution, sufficient for at least 100 points for a $2.5 \cdot 10^{-2}$-cm^{-1} wide line. The minimal detected absorptance peak was $(7 \pm 2) \cdot 10^{-7}$ at 640-nm wavelength for 200 averaged scans in 10 s at 20-Hz frequency, 1-m optical path, and $7 \cdot 10^{-8}$ noise-level sensitivity [10.75].

Another extension of the balanced-detection technique was made utilizing distributed-feedback pulsed quantum-cascade lasers operating in the 5.4-μm spectral band. The lasers were temperature- and current-tuned at 0.13 cm^{-1}/K with injection currents of 10^{-2} cm^{-1}/mA, mostly operating at 1-MHz pulse-train frequency and 10-ns pulse width. The scheme in Fig. 10.26 with angled and AR-coated germanium cell windows was used for measurements with the reference light path shortened, removing mirror M, and purging the air between the absorption cell and detector D_1 and also between beam splitter BS and detector D_2. The best balanced-detection two-channel sensitivity was reached for monitoring NO, nearly two times better than for NO_2, with 50-ns pulse width and 5-kHz repetition rate, detecting 0.0385 peak of absorption at noise-level sensitivity corresponding to $9 \cdot 10^{-4}$ background absorptance [10.76]; near 12-dB signal-to-noise ratio for a DC/AC-coupled detector at 0–54-MHz frequencies was also reached [10.82]. Further advantages for differential and autobalanced detection schemes could be provided via continuous monitoring the ratio of signal and reference beams, added RF-current perturbations and reducing mode structure of cavity

enhanced studies, plus absolute-frequency referencing of molecular transitions to an extra frequency comb of laser pump and signal beams [10.86–10.88].

10.4 Separation of Bulk and Surface Losses

Uncertainties in the actual conditions of sample surfaces exposed to radiation transmission and reflection may severely restrict the sensitivity of any internal optical-loss detection, when measuring the bulk properties of a given sample. The Brewster-angle and surface-immersing techniques are intended to fully eliminate reflections at sample surfaces, when distinguishing its bulk properties. Let us consider a somewhat opposing concept for independent detection of each surface loss, realized for every single optical measurement of the internal bulk loss to be determined. As already reviewed in Sect. 8.4, resonator-based arrangements in reflected light allow one to distinguish every surface loss by interchanging the relative positions of two mirrors creating the resonator. Similar measurements in light reflected from a cavity formed by two elements of a low-loss and low-reflectivity substance can also help identifying the bulk property.

10.4.1 Distinction of Surface Losses

One can separate specular reflections from two surfaces, keeping normal incidence of light at one of them, by making a small wedge between these surfaces. That wedge angle needed for the spatial separation of the beam reflected by the surface is defined by a particular configuration of the optical system. Internal attenuation experienced by radiation propagating in a given substance can be evaluated in reflected light by comparing similarly wedged substance samples of a distinguished length using a technique equivalent to transmission-based studies analyzed in Sect. 5.1, except for broader choices. This wedge angle of the samples being compared should not notably obscure normal incidence at all borders involved and the internal optical path lengths (see Sect. 8.1, Fig. 8.4). If such prospective measurements are made by detecting the intensities of reflected beams, the sample substance acts twice, increasing the sensitivity to detection of internal bulk loss twofold [10.77].

Let us first consider a method for the absolute measurement of every single surface reflectance of a long and a short sample of a given substance under study. A layout of such a technique in reflected light is depicted in Fig. 10.27. Instead of conventional transmission measurements, two samples are studied by measuring the intensities of the beams reflected from every single surface and from a low-reflectivity resonator formed by any two parallel surfaces of these samples. To measure the reflectance at normal incidence, semitransparent beam splitter BS is used. Light passed by that splitter irradiates short and long samples of one substance at the normal to either its first or second surface. Light reflected from a surface and the splitter reaches photodetector D. Every optical path and all sample wedges should be configured to prevent interference, except for resonant faces.

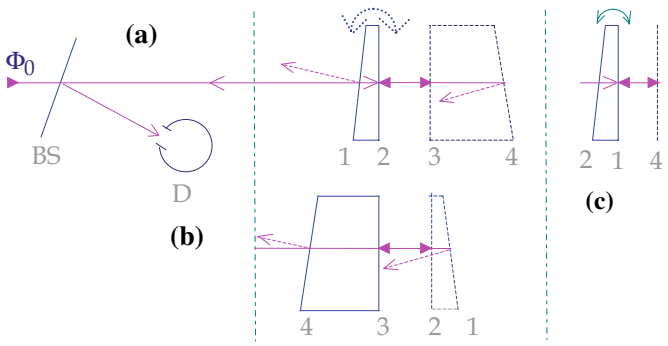

Fig. 10.27 Internal loss measurements via separating surface reflections

Evidently, the relative reflectance of a single surface versus another surface can be directly measured by substituting two surfaces into one position, aligned by the normal to incident light. If these surfaces belong to one sample, the sample has to be turned around by 180°. If the surfaces belong to different samples, the normal surface should be irradiated first, thus not to uneven bulk thicknesses in the beam path. The next step is to distinguish unequal reflectances and double single-beam sensitivity to the internal optical loss. For that, the short sample in configuration (*a*) in Fig. 10.27 is turned in such a way that not its first but its second surface 2 is normal to the beam (see the round arrows in Fig. 10.27). The response N_1 for detector D of sensitivity k becomes:

$$N_1 = k\Phi_0\tau_s(1-\rho_1)^2[\exp(-2\mu\ell_{sh})]\rho_2\rho_s, \tag{10.39}$$

where Φ_0 is the flux of incoming source radiation, τ_s and ρ_s are the transmittance and the reflectance of splitter BS, and τ_i and ρ_i are the properties of the i^{th} surface. For a following measurement, the long sample (see the dotted lines in Fig. 10.27) is placed in the light path at the normal to first surface 3. Since surfaces 2 and 3 resonate, any measures reviewed in Chaps. 3, 6 and 8 using essential temporal and spatial integration and diminishing the visibility of interference in reflected and transmitted light could be used to prevent disturbing interference effects in a given system. Hence, the total additive flux retroreflected by two now-resonating surfaces and reaching the detector becomes:

$$\begin{aligned} N_\Sigma = {} & k\Phi_0\tau_s\rho_s\{(1-\rho_1)^2[\exp(-2\mu\ell_{sh})]\rho_2 + (1-\rho_1)^2[\exp(-2\mu\ell_{sh})]\cdot \\ & \cdot(1-\rho_2)^2\rho_3 + (1-\rho_1)^2[\exp(-2\mu\ell_{sh})]\cdot \\ & \cdot(1-\rho_2)^2\rho_3\rho_2\rho_3 + \cdots\} = k\Phi_0\tau_s\rho_s(1-\rho_1)^2[\exp(-2\mu\ell_{sh})]\cdot \\ & \cdot[\rho_2 + (1-\rho_2)^2\rho_3/(1-\rho_2\rho_3)]. \end{aligned} \tag{10.40}$$

By comparing last two equations, one can see that the first term in relation (10.40) equals the total flux by Eq. (10.39). To eliminate any uninformative part of the second flux and to exclude such an undetermined factor as the detector's sensitivity, let us express the result as the difference of Eqs. (10.40) and (10.39), related to (10.39). Designating $N_\Sigma - N_1$ as N_2, we obtain:

$$N_2/N_1 = (1-\rho_2)^2\rho_3/[\rho_2(1-\rho_2\rho_3)]. \tag{10.41}$$

If all sample surfaces are fabricated in one manufacturing cycle and kept at the same condition, and if the measurement task is to determine the average surface reflectance ρ, Eq. (10.41) transforms to:

$$N_2/N_1 = (1-\rho)^2/\left(1-\rho^2\right) = (1-\rho)/(1+\rho). \tag{10.42}$$

That form reminds us of well-known Eq. (1.106) for normal transmittance of any transparent sample, assuming the absence of its bulk attenuation. From Fig. 10.27 it can be seen that this method is designed for measurements of air-sample transmittance with surface reflectances ρ_2 and ρ_3.

The relative sensitivity of such a measurement method to a change δ in the average reflectance ρ is:

$$\partial(N_2/N_1)/(N_2/N_1) = -\partial\rho/(1-\rho) - \partial\rho/(1+\rho). \tag{10.43}$$

For a substance with low surface reflections: $\rho \ll 1$, conceivable fluctuations Δρ of the measured reflectance are twice as small as the fluctuations ΔN of two registered detector signals:

$$\Delta\rho = \pm 0.5\Delta(N_2/N_1)/(N_2/N_1). \tag{10.44}$$

As a result, even doubling individual error of a single intensity reading at two measurements taken to 0.02%, for example, versus 0.01%, the resultant actual sensitivity to every reflectance loss will be twice as low, approaching $1 \cdot 10^{-4}$ magnitude.

Another factor that could affect the results obtained is the instability $\Delta\rho_i$, within a time of a measurement, of each specific reflectance of a surface exposed to radiation further transmitted into the sample bulk and then leaving the sample. Writing Eq. (10.40) in the form:

$$N_\Sigma = const \cdot \left[\bar{\rho} + (1-\bar{\rho})^2\bar{\rho}/\left(1-\bar{\rho}^2\right)\right], \tag{10.45}$$

and substituting: $(1-\bar{\rho}) = \bar{\tau}$, while omitting terms of the second power for $\bar{\rho} \ll 1$, one obtains:

$$\Delta\bar{\rho} = \Delta N_\Sigma/2 + 2\Delta\bar{\rho}/\bar{\tau}. \tag{10.46}$$

Equation (10.46) demonstrates that any unresolved changes of surface reflectances affect the results of the resonator reflection measurement analogously to transmission ones (see Sect. 5.1, Eq. (5.7)), being related not to the low reflectance, but to the high transmittance. At the same time, these resonator reflection measurements are 2 times less affected by the noise of the detection system. For example, if every reflectance fluctuation is equal to $\Delta N \approx \Delta\rho \approx \pm 1 \cdot 10^{-4}$, the total error of the measured reflectance for a substance of refractive index $n \cong 1.5$ is: $\Delta\bar{\rho} = \pm(0.00005 + 2 \cdot \Delta 0.0001 \cdot 0.4/0.96) = \pm 5.8 \cdot 10^{-5}$. As a result, the accuracy of measurements of low reflectance in reflected light is limited by the signal-to-noise ratio of the detectors used, and to a lower degree by the stability of sample surfaces, since it is well known that the short-term instability of the refractive index of deeply polished glass or a silica surface does not exceed a few parts per million.

The reflected-light measurement technique implemented as an internal-transmittance study of the air sample has the advantage of distinguishing absolute reflectance values of sample surfaces, for which the long and short samples are swapped (Fig. 10.27, configuration *b*). The opposite sample surfaces 2 and 3 swap their positions. After an identical measurement cycle giving a new set of measured intensities M_1, M_Σ, and M_2 registered by the same detector, Eq. (10.42) converts to:

$$M_2/M_1 = (1 - \rho_3)^2 \rho_2 / [\rho_3 (1 - \rho_3 \rho_2)]. \tag{10.47}$$

Equations (10.42) and (10.47) define a single solution for reflectances ρ_2 and ρ_3 (compare with the quality-factor transfer measurement method analyzed in Sect. 8.4). If one intends to identify reflectances of opposite surfaces 1 and 4, the samples are turned around by 180° (configuration *c* in Fig. 10.27), and an equal measurement cycle concludes, distinguishing the remaining optical properties of the samples studied.

10.4.2 Resolving Internal Properties

When all four surface reflections of the short and long samples of a substance under study are measured, the linear attenuation coefficient of the internal bulk can be directly resolved. Figure 10.28 depicts the complete optical system for resonator-reflection

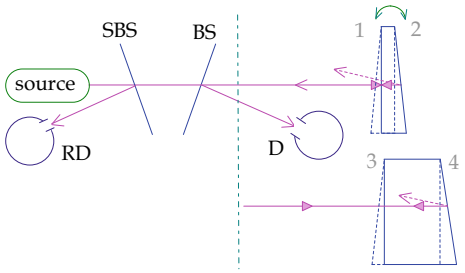

Fig. 10.28 Measurement of internal bulk loss in reflected light

studies, only a part of which was shown in Fig. 10.27. In addition to main beam splitter BS and detector D, it has additional reference detector RD tracking intensity changes for the beam reflected by auxiliary beam splitter SBS. As a result, intensity fluctuations and instabilities are accounted for by measuring the ratio of the main and reference detector signals (see Sect. 10.1). Respectively, let us further consider every signal of main detector D as being related to the signal of reference detector RD, and, therefore, the incident flux Φ_0 to be a constant of the measurement system.

First, a short sample of the substance studied, with the surface reflectances predetermined by the measurement procedure illustrated in Fig. 10.27, is placed into the optical path shown in Fig. 10.28 for its front surface having reflectance ρ_1 to be normal to incident light. The ratio-bound detector reading of the system is:

$$N_1 = k\Phi_0\tau_{SBS}\tau_{BS}\rho_{BS}\rho_1 = const \cdot \rho_1. \tag{10.48}$$

For the second measurement the sample being measured is turned around the optical axis into a wedge-angle tilted position making its second surface 2 perpendicular to the direction of propagating light; thus:

$$N_2 = const \cdot (1-\rho_1)^2[\exp(-2\mu\ell_{sh})]\rho_2. \tag{10.49}$$

Here μ and ℓ_{sh} are the sample-bulk attenuation coefficient and length. The ratio of these equations gives:

$$\exp(-2\mu\ell_{sh}) = (N_2/N_1)(\rho_1/\rho_2)(1-\rho_1)^{-2}. \tag{10.50}$$

Since the preceding measurements revealed the reflectance magnitude of every surface, let us for now omit ratio ρ_1/ρ_2 from Eq. (1.23) as an already-identified constant. This condition is equivalent to considering the sample surfaces as equal to each other within the accuracy of detected signals N_1 and N_2. Hence, in view of known or equal reflectances, Eq. (10.50) transforms to:

$$\exp(-2\mu\ell_{sh}) = (N_2/N_1)(1-\rho_1)^{-2} \underset{\mu\to 0}{\cong} (1-2\mu\ell_{sh}). \tag{10.51}$$

Two equivalent measurements of one long sample, oriented similarly, create signals N_3 and N_4, and provide analogous expressions for the dual-length attenuation $2\mu\ell_{lg}$ of the long sample:

$$\exp\left(-2\mu\ell_{lg}\right) = (N_4/N_3)(\rho_3/\rho_4)(1-\rho_3)^{-2}. \tag{10.52}$$

Finally, complete expressions (10.50) and (10.52), accounting for every surface reflectance, provide:

$$\exp\left[-2\mu\left(\ell_{lg}-\ell_{sh}\right)\right] = (N_4/N_3)(N_1/N_2)(\rho_3/\rho_4)(\rho_2/\rho_1)[(1-\rho_1)/(1-\rho_3)]^2. \tag{10.53}$$

Assuming every surface reflectance ρ_i and transmittance $\tau_i = 1 - \rho_i$ to be already determined, and substituting each factor $\rho_{1\leftrightarrow 4} = \rho$ and $\tau_1 = \tau_3 = \tau$, the attenuation on dual-difference of the sample lengths is:

$$\exp\left[-2\mu\left(\ell_{lg} - \ell_{sh}\right)\right] \underset{\rho_{1\leftrightarrow 4}=\rho}{=} (N_4/N_3)(N_1/N_2)[(1-\rho_1)/(1-\rho_3)]^2 \underset{\tau_1=\tau_3}{=} (N_4/N_3)(N_1/N_2). \tag{10.54}$$

In deriving Eqs. (10.49)–(10.54), we supposed that propagation of light via all surfaces and every bulk was made via a beam normal. For a wedged sample this means that its internal transmittance should not be a function of wedge angle φ. As follows from Fresnel's formulae (see expressions (1.82), (1.83)), in order to have the squared transmittance for any state of polarization: $(1 - \rho_\perp)^2$ or $(1 - \rho_\parallel)^2$, be less than $1 \cdot 10^{-4}$ different from that at normal incidence, the angle of light incidence onto the sample with $n = 1.5$ in air needs to be $\varphi \leq 0.5°$. This requirement corresponds to the maximum wedge angle of the sample in refraction: $\varphi' \leq 20'$ [10.79].

When compared with equally performed length-differential studies of samples in transmission (see Chap. 5), the method discussed should have 2 times higher sensitivity to internal bulk loss for equivalent twofold propagation of one entrance surface instead of the single propagation of every, front and back, surface. The only difference is in adding a single reflection from two mostly unequal back surfaces of long and short samples. By establishing the described ability to distinguish actual differences for these surface reflectances or by neutralizing the difference by providing an additional treatment of unequally reflecting surfaces, one can account for any surface inequality or reduce it to the appropriate level when both reflectances are measured as equal.

Similarly to studies in transmission, reflection-based analysis can be done under conditions eliminating surface reflectances (see Sect. 10.1). As depicted in Fig. 10.29, the test sample can be fabricated as a half length of a common twin-Brewster-cut element used in transmission with one normal-to-surface cut and another surface to be formed at the angle $\varphi' = \arccos\left(1 \Big/ \sqrt{1 + n_\lambda^2}\right)$. Owing to such an angle, at a specific wavelength λ corresponding to a given index of refraction n_λ, light incident on the front face at angle φ propagates inside by the

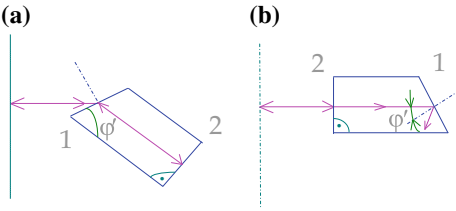

Fig. 10.29 Loss studies in reflected light at the Brewster angle

normal to the back surface (Fig. 10.29a). After second-surface reflection, the entered light goes back the same way, and signal N_1 of the system identical to that in Fig. 10.28 becomes:

$$N_1 = k \cdot \Phi_{0,||} \exp(-\mu\ell)\rho_2 \exp(-\mu\ell). \tag{10.55}$$

The second measurement is made with the sample surfaces reversed and keeping surface 2 at the normal to radiation, giving: $N_2 = k \cdot \Phi_{0,||}\rho_2$. Since both times light is reflected from one surface, the internal bulk attenuation on the doubled in reflection length ℓ of the sample is:

$$\exp(-2\mu\ell) = N_1/N_2. \tag{10.56}$$

Because all measurements are performed in reflected light, the full bulk loss is measured as the loss of a sample twice as long as the actual sample. At the same time, all other measurement conditions remain the same as in the relevant transmission study. For example, the inaccuracy of confirming the precise Brewster angle of light incidence on the front surface has the same effect as was seen in Fig. 10.4, due to dual pass of radiation via that front surface. Any error in forming angle φ is in that case converted into a deviation from normal incidence at the back surface of the sample. The related error of surface-reflectance measurement for out-of-normal versus normal incidence can be seen in Fig. 5.7, keeping Snell's law in mind when converting errors from the incidence to the refraction angles.

The procedure for measurements of internal sample loss shown in Fig. 10.29 can be further simplified if the reflectances of all surfaces of the compared samples are identified to be equivalent within acceptable error of these measurements. In that case the measurement process consists of just two steps (see Fig. 10.30). Light from source 1 via beam splitter 2 directing a portion of that light onto reference detector 3 is incident on the front surface of long wedge sample 4 at small angle ψ, which could be greater than sample wedge angle φ. For the first reading, radiation reflected from front surface M of long wedge sample 4 propagates via short wedge sample 5 of the same substance under study at the same angle of incidence ψ and in the second step, short sample 5 is taken out of the optical path by sliding table 7 and long sample 4 is rotated over its wedge angle φ, guiding the beam reflected by back surface N of sample 4 to reach detector 6. The ratio of main-to-reference detector signals is:

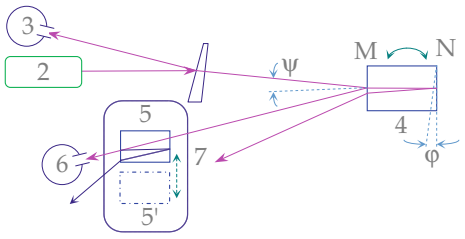

Fig. 10.30 Reflectance–transmittance study of bulk attenuation

$$\left(N_{main}/N_{ref}\right)_1 = const \cdot \rho(1-\rho)[\exp(-\mu\ell_{sh})](1-\rho); \tag{10.57}$$

$$\left(N_{main}/N_{ref}\right)_2 = const \cdot (1-\rho)\left[\exp\left(-\mu\ell_{lg}\right)\right]\rho\left[\exp\left(-\mu\ell_{lg}\right)\right](1-\rho). \tag{10.58}$$

Since in each case light is reflected once, also adding the dual transmission, the intensity ratio is:

$$\exp\left[-\mu\left(2\ell_{lg}-\ell_{sh}\right)\right] = \left(N_{main}/N_{ref}\right)_2\left(N_{main}/N_{ref}\right)_1. \tag{10.59}$$

In this case the slightly oblique incidence serves a few purposes. First, it eliminates the need for beam splitter BS as in Fig. 10.28. Second, it provides for dual propagation of reflected light via the long sample and only a single pass of transmitted light via the short one. Therefore, the dual optical path via the substance under test is in effect increased by the added length of the short sample.

Prior to describing any experimental confirmation of the method discussed, let us pay attention to the added difficulty of internal-loss measurement in reflected light. A challenge is due to the approximately 20 times lower power of light reflected from a single glass surface in comparison with light incident from the light source. In most cases that circumstance leads to the necessity of using a powerful source, such as a laser. From any application standpoint, this is quite reasonable, since most objects having low optical losses are anyway designed for one or another laser application. However, the use of lasers during measurements is also allied with a somewhat higher level of intensity fluctuations. Even the two-channel ratio-measurement system requires additional synchronization measures for evaluating long-term and short-term fluctuation terms.

Figure 10.31 illustrates a layout of the internal loss measurement system in reflected light utilizing radiometers 4 and 5. Synchronization of registration cycles for identical radiometers was provided by relay 6. High-resolution digital ratio meter 7 measured the ratios of output voltages [10.79, 0.21]. A cw He–Ne or a pulsed Nd:YAG laser was used as light source 1. Long 3 and short 3′ fused-silica samples were irradiated at a fixed angle of incidence from 4.5° to 45°. Photometers [4.10] (see Chap. 4) with ±0.1% standard deviation were applied as meters 4 and 5.

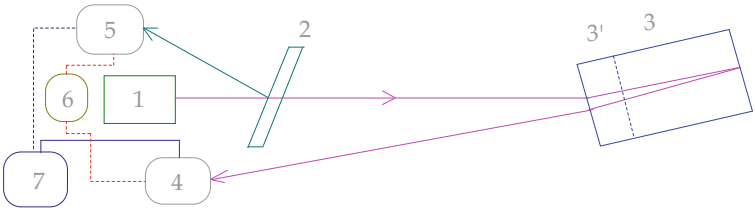

Fig. 10.31 Simplified schematic of a loss measurement system in reflected light

Coexisting readings of signals in two channels were synchronized by relay 6 within ±5 ms. That synchronization reduced the standard deviation of every measurement by ratio meter 7 to ±(0.02–0.03)%. Samples 3 and 3′ of a fused-silica glass were sequentially installed in one identical position. Small changes of the angle of incidence, since it was a constant for each sample, did not alter the magnitude of bulk loss. The initially measured linear attenuation coefficient was approximately $5 \cdot 10^{-4}$ for each 10–15 mm of the dual-length difference of the long sample and short sample [10.79]. When the sample temperature was stabilized to 0.1 °C, the attenuation declined to $(1.2-2.5) \cdot 10^{-4}$ cm^{-1} [0.21].

10.5 Reflection Spectrophotometry

As conventionally established, the standard spectrophotometric practice for determination of an internal optical loss in a sample bulk is based on measurement of the total attenuation by a plane-parallel sample, from which the dual magnitude of the average surface loss of the sample is subtracted, being either estimated or measured by a supplemental method. The sensitivity of such a transmission measurement can be increased by multiplying the number of light interactions with the entire sample, but the number of interactions at border surfaces is multiplied also, increasing the uncertainty of surface losses. As seen in the previous section, the surface loss can be resolved concurrently with the bulk loss, doubling the sensitivity to the internal attenuation of sample's bulk.

Let us conceptually analyze the options for spectrophotometric study of each optical loss under investigation: surface and bulk, by further extending the reflection-based procedure, having no need to create an optical resonator, which increases the measurement sensitivity and complicates the realization of measurement. Consider a beam of radiation from a laser or other source 1 (Fig. 10.32) incident at a relatively small angle φ on a plane-parallel sample 2, having two equally fabricated surfaces of the substance under study with a linear attenuation coefficient μ and index of refraction n. In the position illustrated in Fig. 10.32a, detector 3 measures the intensity of light that is entered the sample via the first surface, transmitted by its bulk over length ℓ, reflected internally from the second surface at angle $\varphi' = \arcsin(\sin\varphi/n)$, transmitted back via the bulk and again the same length ℓ, and is exited through the first surface. The detector's reaction N_1 can be represented as:

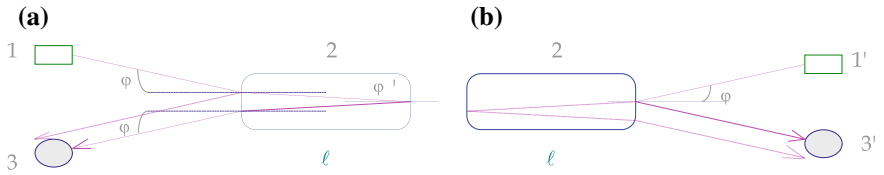

Fig. 10.32 Dual transmission via a single entrance–exit surface and sample bulk in reflected light

$$N_1 = \kappa(1-\rho)\exp(-\mu\ell)\rho\exp(-\mu\ell)(1-\rho). \tag{10.60}$$

Here κ is the proportionality factor and $\rho \equiv \rho_\varphi$ is the reflectance of likewise-fabricated surfaces for angle φ.

For the second configuration (Fig. 10.32b), the incident beam, at angle φ corresponding to φ′ for outside incidence of light, is directly reflected from precisely the same spot as light was internally reflected in Fig. 10.32a. The second signal becomes: $N_2 = \kappa\rho$, and therefore:

$$N_1/N_2 = \kappa(1-\rho)^2\exp(-2\mu\ell). \tag{10.61}$$

Accordingly, such a reflection-type measurement procedure is equivalent to a similar transmission study, but for a dual-length test sample. No additional sample is required for the reflection measurement. This way, the reflection-type measurement becomes a twofold sensitive technique, having one surface of the sample studied functioning as an effective surface mirror (Fig. 10.33).

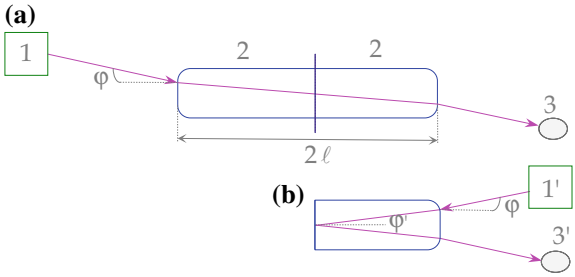

Fig. 10.33 Dual-transmission and single-reflection measurement

This particular reflection-based measurement method, while increasing the sensitivity in comparison with the traditional transmission studies for the internal optical attenuation of a studied sample, illustrates the measurement approach, which also carries apparent disadvantages. The primary one consists in the necessity to interchange the positions of all sources and detectors, which is not always convenient. It is certainly easier, from the standpoint of unchanged arrangement of optical elements, to slightly tilt the sample under study and maintain the propagation conditions of the beam virtually unchanged. Let us reexamine one more time certain conceptual advantages and drawbacks of optical-loss measurements in transmitted and reflected radiation.

Following Chap. 2, comparison-based measurements of internal transmittance at normal incidence of light on two identical samples of contrasting lengths is less sensitive to the influence of multiple reflections than single-sample study. A similar concept can be realized in reflected radiation. For that purpose, either additional mirrors or the back surfaces of two samples being compared may be used (Fig. 10.34). If additional mirrors are placed behind each sample, the transmittance

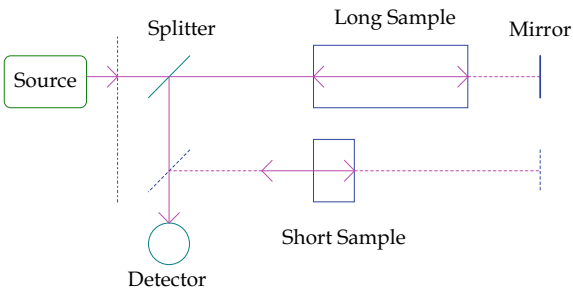

Fig. 10.34 Comparison study in reflected light at normal incidence

of each face can be considered equal as in other transmission measurements. If the back surfaces of the long and short samples are used to retroreflect the beam, the potential relative difference of surface reflectances needs to be evaluated. The ratio of these two surface reflectances will directly influence the results of the internal loss determination. If the ratio of the surface reflectances is accurately measured, the sensitivity of the measurement becomes twofold higher than in a direct transmission study, owing to the double pass of each sample bulk.

A similar concept of providing consecutive measurements of each single surface reflectance for one sample and its internal transmittance with doubled sensitivity is depicted in Fig. 10.35. The layout shows an absolute internal-loss measurement technique for radiation reflected from slightly wedged short and long samples of one material being studied at the practically normal incidence of light.

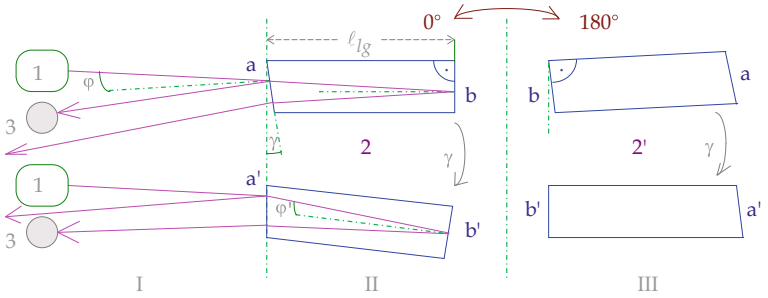

Fig. 10.35 Absolute loss-measurement technique in reflected light (only the long sample is shown)

The method provides an experimentally proven technique of comparing long and short samples, having different path lengths: $\ell_{lg} - \ell_{sh} = \Delta\ell$, and made of one material under study. To separate light beams reflected from the front and back surfaces, the samples are fabricated with an equal small wedge angle γ. To eliminate extra losses introduced by a beam splitter, the incidence of light is made slightly away from the normal to each surface. Source 1 of collimated radiation, in which capacity a laser is most effective, and detector 3 are located at such distances along light paths of the incident and the reflected beams that the angles of incidence φ and φ' on both surfaces of the sample do not change the transmittance and

reflectance values of the sample surfaces under any variations of these angles. One approach to identify sufficiently small angles involves separation of beams reflected by the first and second surfaces of the sample across an entrance aperture of the detector in such a way that when one reflected beam is detected, another one misses the aperture.

In configuration I in Fig. 10.35, only the beam reflected by the first surface of long sample 2 is sensed by detector 3. Reading N_1 of the measurement system having sensitivity factor κ is:

$$N_{1,lg} = \kappa \Phi_0 \rho_{a,lg}. \tag{10.62}$$

Here Φ_0 is the flux irradiated by source 1 and $\rho_{a,lg}$ is the reflectance of surface a of the long sample. In configuration II in Fig. 10.35 sample 2 is turned over its wedge angle γ for incident light to pass its first surface and bulk, be internally reflected at angle φ' by face b, and reach detector 3 via the second pass. Thus:

$$N_{2,lg} = \kappa \Phi_0 \left(1 - \rho_{a,lg}\right)^2 \exp(-2\mu \ell_{lg}) \rho_{b,lg}, \tag{10.63}$$

where μ is the linear attenuation coefficient of long sample 2, representing a uniform substance under study from which both long and short samples are made, and $\rho_{b,lg}$ is the reflectance of surface b of sample 2.

In configuration III in Fig. 10.35, sample 2 is rotated around 180°, converting the measurement system to identical irradiation settings, but from the opposite side (after the center line in Fig. 10.35). In this configuration the measurements are made at two sample positions identical to the configuration II, while faces a and b are substituting each other:

$$M_{1,lg} = \kappa \Phi_0 \rho_{b,lg}, \tag{10.64}$$

$$M_{2,lg} = \kappa \Phi_0 \left(1 - \rho_{b,lg}\right)^2 \exp(-2\mu \ell_{lg}) \rho_{a,lg}. \tag{10.65}$$

After this four-measurement cycle, long sample 2 is substituted by short sample 1 with a distinct length ℓ_{sh}, the same wedge angle γ, and being made from same material with linear attenuation coefficient μ to be determined. The identical second four-measurement cycle provides respective readings:

$$N_{1,sh} = \kappa \Phi_0 \rho_{a,sh}, \tag{10.66}$$

$$N_{2,sh} = \kappa \Phi_0 \left(1 - \rho_{a,sh}\right)^2 \exp(-2\mu \ell_{sh}) \rho_{b,sh}, \tag{10.67}$$

$$M_{1,sh} = \kappa \Phi_0 \rho_{b,sh}, \tag{10.68}$$

$$M_{2,sh} = \kappa\Phi_0\left(1-\rho_{b,sh}\right)^2\exp(-2\mu\ell_{sh})\rho_{a,sh}. \tag{10.69}$$

Before solving the system of equations obtained, let us consider surface instabilities among four surfaces of each sample. As seen from Eq. (2.44), relative changes in transmittance of a nonabsorbing surface of a transparent sample are due to uncertainty of the refractive index of that surface: $\Delta\tau/\tau = (\Delta n/n)[(n-1)/(n+1)]$. The equivalent uncertainty of the reflectance magnitude of the same surface at defined quasi-normal incidence of radiation follows from the Fresnel formulae:

$$\Delta\rho/\rho = (4\Delta n)/\left(n^2-1\right). \tag{10.70}$$

Consequently, fluctuations of refraction induce higher perturbations on the surface reflectance than on the transmittance for the surface of the transparent sample. The ratio of these factors is given by:

$$(\Delta\rho/\rho)/(\Delta\tau/\tau) = \tau/\rho = 4n/(n-1)^2. \tag{10.71}$$

Even for one surface transmitted twice in an equivalent transmittance measurement, the surface-bound sensitivity in reflected light remains much higher. Therefore, if the change of relative reflectance: $\Delta\rho/\rho$, for a given surface is constant or slightly deviates during a given measurement cycle, the corresponding changes of $\Delta\tau/\tau$ ratio for that surface can be considered negligible, proving the surface transmittance is unchanged within the measurement uncertainty.

The differences between all four surface reflectances can be identified by the following relationships:

$$\begin{aligned}
&\rho_{a,lg}/\rho_{a,sh} = N_{1,lg}/N_{1,sh};\quad \rho_{a,lg}/\rho_{b,sh} = N_{1,lg}/M_{1,sh};\\
&\rho_{b,lg}/\rho_{a,sh} = M_{1,lg}/N_{1,sh};\quad \rho_{b,lg}/\rho_{b,sh} = M_{1,lg}/M_{1,sh}.
\end{aligned} \tag{10.72}$$

If after all measurements have been performed, Eqs. (10.72) confirm that the actual differences between the reflectances of any four surfaces of both samples are below the sensitivity limit of the particular measurement apparatus to changes of incident radiant flux Φ_0, then the differences between the square transmittances of these surfaces are lower than the sensitivity of the particular detection system and can certainly be disregarded. Consequently, in that case one would obtain a system of four equations for the magnitudes of the linear attenuation coefficient μ of both samples in two orientations:

$$\begin{aligned}
\exp\left(-2\mu\left(\ell_{lg}-\ell_{sh}\right)\right) &= \left(N_{2,lg}/N_{2,sh}\right)\left(\rho_{b,sh}/\rho_{b,lg}\right);\\
\exp\left(-2\mu\left(\ell_{lg}-\ell_{sh}\right)\right) &= \left(N_{2,lg}/M_{2,sh}\right)\left(\rho_{a,sh}/\rho_{b,lg}\right);\\
\exp\left(-2\mu\left(\ell_{lg}-\ell_{sh}\right)\right) &= \left(M_{2,lg}/N_{2,sh}\right)\left(\rho_{b,sh}/\rho_{a,lg}\right);\\
\exp\left(-2\mu\left(\ell_{lg}-\ell_{sh}\right)\right) &= \left(M_{2,lg}/M_{2,sh}\right)\left(\rho_{a,sh}/\rho_{ab,lg}\right).
\end{aligned} \tag{10.73}$$

The magnitude of the linear attenuation coefficient μ of the substance studied may be resolved as the arithmetic average of all magnitudes: $\bar{\mu} = (\mu_1 + \mu_2 + \mu_3 + \mu_4)/4$. Each consequent magnitude is:

$$\begin{aligned}
\mu_1 &= \left(\ln N_{2,sh} + \ln M_{1,lg} - \ln N_{2,lg} - \ln M_{1,sh}\right) / \left[2(\ell_{lg} - \ell_{sh})\right]; \\
\mu_2 &= \left(\ln M_{2,sh} + \ln M_{1,lg} - \ln N_{2,lg} - \ln N_{1,sh}\right) / \left[2(\ell_{lg} - \ell_{sh})\right]; \\
\mu_3 &= \left(\ln N_{2,sh} + \ln N_{1,lg} - \ln M_{2,lg} - \ln M_{1,sh}\right) / \left[2(\ell_{lg} - \ell_{sh})\right]; \\
\mu_4 &= \left(\ln M_{2,sh} + \ln N_{1,lg} - \ln M_{2,lg} - \ln N_{1,sh}\right) / \left[2(\ell_{lg} - \ell_{sh})\right].
\end{aligned} \tag{10.74}$$

As can be seen from Eq. (10.74), three quarters of all actions of rotating and swapping samples can be omitted, since only two measurements of each sample transmittance in reflected light are needed to distinguish the internal loss of the sample material by dual differential length. Two other measurements are needed to distinguish the difference in back-face reflectances of short and long samples. Nevertheless, for the examined measurement method, all eight readouts give four values of the same linear attenuation coefficient under study. Considering potential additional errors to the final outcome, these four results via eight readouts are equivalent to four pairs of independent studies of one sample transmittance. Thus, this technique does not increase the errors of measurements for the average $\bar{\mu}$ value. The mean magnitude $\bar{\mu}$ identifies the linear attenuation coefficient of the substance under study more precisely taking into account any deviations of bulk optical properties from one sample to another and from one slice of the sample to the other, etc. Even if the surface reflectances of opposite sides of the samples being compared are very different from each other, the particular surfaces can be refabricated to satisfy the given measurement requirements.

Since the measurement method is realized by transmission of light via every sample in two opposite directions, it permits one to evaluate the appearance on the sample surfaces of such formations as uncontrollable absorption layers, unacceptable roughness, or scattering centers. Let us represent one irradiating surface as a complex structure, having some absorbing and/or scattering layers with a completely unknown individual transmittance τ_i (Fig. 10.36). Let us presume that the layers do not affect the reflectance of a single surface, since no changes were noted in comparison with other surface reflectances. Hence, the opposite-direction pairs of Eqs. (10.62)–(10.69) for either of two samples under study are:

Fig. 10.36 Layers on both sample surfaces

$$
\begin{aligned}
N_{1,i} &= \kappa\Phi_0{\tau_{1,i}}^2\rho_1;\\
N_{2,i} &= \kappa\Phi_0{\tau_{1,i}}^2(1-\rho_1)^2\exp(-2\mu\ell)\rho_2;\\
M_{1,i} &= \kappa\Phi_0{\tau_{2,i}}^2\rho_2;\\
M_{2,i} &= \kappa\Phi_0{\tau_{2,i}}^2(1-\rho_2)^2\exp(-2\mu\ell)\rho_1.
\end{aligned}
\tag{10.75}
$$

From which:

$$
\begin{aligned}
\frac{N_{2,i}}{M_{1,i}} &= \frac{{\tau_{1,i}}^2}{{\tau_{2,i}}^2}(1-\rho_1)^2\exp(-2\mu\ell) \equiv \tau_{left};\\
\frac{M_{2,i}}{N_{1,i}} &= \frac{{\tau_{2,i}}^2}{{\tau_{1,i}}^2}(1-\rho_2)^2\exp(-2\mu\ell) \equiv \tau_{right}.
\end{aligned}
\tag{10.76}
$$

Equations (10.76) validate that if these films that are invisible in reflected light on two surfaces of a single sample are dissimilar, they must be accounted for by Eqs. (10.74) as the difference in the values of two linear attenuation coefficients $\mu_{i,j}$ obtained from opposite sides of the sample. Consequently, any factual inequality of surface-plus-internal bulk transmittance magnitudes μ_{left} and μ_{right} of a single sample with surface reflectances that are measured to be equal, and as a result having the equivalent Fresnel surface transmittances, points to the necessary presence of absorbing and scattering layers on the surfaces. Therefore, any changes of environmental conditions or additional repolishing of these surfaces, which could lead to perception of the measured internal factor as being changed, demonstrate factual surface-bound uncertainties that can be eliminated. When $\Delta\mu_{left,right}$ is smaller than the random error of the particular measurement procedure, it may be presumed that no uncontrollable substances contaminating the sample surfaces exist, and therefore the averaged magnitude $\bar{\mu} = 0.5(\mu_{left} + \mu_{right})$ provides truthful optical characterization of the substance under study.

If for any reason the actual dimensions of the measurement system depicted in Fig. 10.35 cannot be extended as required to maintain quasi-normal incidence on each sample surface, the technique can be performed at normal incidence of light. Two common layouts can be implemented. The first one, with two beam splitters 2 and 4, is depicted in Fig. 10.37a. The second layout, having only one beam splitter 7,

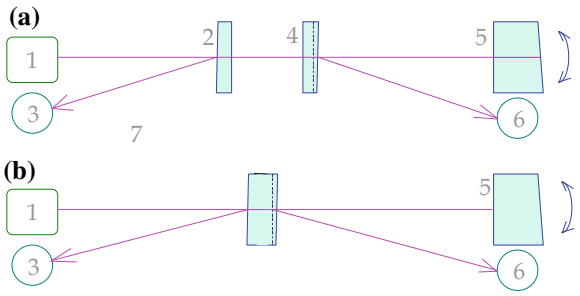

Fig. 10.37 Reflection spectrophotometry at normal incidence of radiation

is shown in Fig. 10.37b. The optimum ratio for splitting the beam into main detector 6 is 50:50 – by a semitransparent splitter, matching the highest τ·ρ product and maximum-intensity output (see Chap. 2). Splitting to reference detector 3 only serves to compensate for power fluctuations of source 1 – the same as for the method shown in Fig. 10.35.

If a solid sample high-transmittance measurement is to be made concurrently with a similar reflectance one, that measurement system could be likewise rearranged as illustrated in Fig. 10.38, with a previously measured sample of known bulk-surface properties serving as output coupler 3.

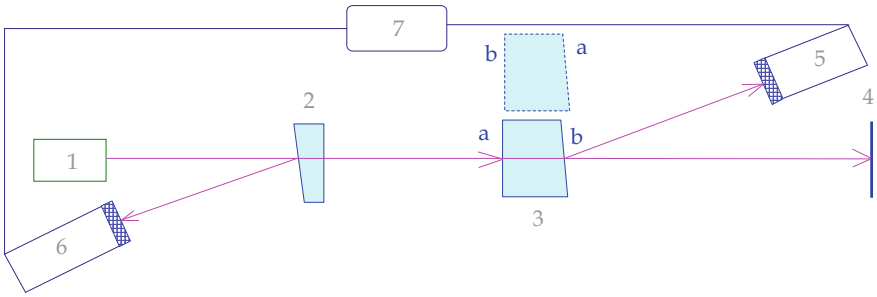

Fig. 10.38 Reflection–transmission based measurements, *1* source; *2* splitter; *3* output coupler; *4* mirror; *5*, *6* detectors; *7* digital readout

The reflectance ρ_4 of mirror 4 can be measured via output coupler 3, sequentially placed in two positions inverted by 180° (see the dotted lines in Fig. 10.38), with surface reflectances ρ_4 and $\rho_{3,a–b}$, and transmittances $\tau_{3,a–b}$, and bulk attenuation μl of coupler 3:

$$\begin{aligned} R_1 &= \kappa\Phi_0\tau_{2\Sigma}\tau_{3,a}\exp(-\mu\ell)\tau_{3,b}\rho_4\rho_{3,b}; \\ R_2 &= \kappa\Phi_0\tau_{2\Sigma}\tau_{3,b}\exp(-\mu\ell)\tau_{3,a}\rho_4\rho_{3,a}. \end{aligned} \tag{10.77}$$

Using previously performed measurements of output coupler surface reflectances by Eqs. (10.72) and (10.74) or (10.75) and (10.76) from inside the bulk or providing them once more, one obtains:

$$\begin{aligned} T_1 &= \kappa\Phi_0\tau_{2\Sigma}\tau_{3,a}\exp(-\mu\ell)\rho_{3,b}\exp(-\mu\ell)\tau_{3,a}; \\ T_2 &= \kappa\Phi_0\tau_{2\Sigma}\tau_{3,b}\exp(-\mu\ell)\rho_{3,a}\exp(-\mu\ell)\tau_{3,b}. \end{aligned} \tag{10.78}$$

The ratio of the respective products of the first and second equations of the system (10.77) and (10.78) is:

$$\frac{R_1 \cdot R_2}{T_1 \cdot T_2} = \frac{\rho_4^2}{\exp(-2\mu\ell)}. \tag{10.79}$$

From which:

$$\rho_4 = \exp(-\mu\ell)\sqrt{\frac{R_1 \cdot R_2}{T_1 \cdot T_2}}. \tag{10.80}$$

Obviously disregarding any negative square-root value, the positive value of mirror reflectance ρ_4 is obtained using the known internal transmittance $\mu\ell$ of intermediate sample 3, serving as a low-reflective output coupler of the system with mirror 4 under study. The squared mirror reflectance is determined using four measurements, with measurement error the same as that of two single-reflectance tests.

10.5.1 Reflected-Light Measurements

The measurement arrangements reviewed above for evaluations of sample bulk and surface losses include a stable and narrowly directed light source, in other words a laser. The laser source should exhibit small relative changes of spectral intensity $\Delta I_0/I_0$ of light within a measurement cycle, allowing the detection system to resolve any impact of attenuation by the sample's bulk from both reflections of its first and second surfaces or to resolve the difference of two bulk-transmittance values when switching from the long to the short sample. The stability of laser radiation measured is affected by both amplitude and phase noise, with the latter primarily via interference terms, which if eliminated may not dramatically affect the measurement results. Either a cw or a stabilized-pulse laser is applicable for providing accurate measurements.

Dual-channel measurement intensity-stabilization techniques, compensating for variations of power or energy derivatives of laser light, were discussed in Chap. 3 and previous paragraphs. The system described below was optimized for two-channel synchronized measurements of cw laser power. One primary reason for the necessity and expediency of having the second channel synchronized with the main one for power-based studies is conditioned by specific thermal laser noise at close-to-zero frequencies. Low-frequency noise inevitably causes a drift of the measured extents of radiation and sets limits on the true sensitivity of a measurement system to the optical losses to be detected. Synchronization of measurement moments in two channels within a mismatch time $\Delta\tau$, being much smaller than the thermal drift time t_d, stabilizes the ratio of signals in channels even for any residual drift that is mostly suppressed by a band-pass filter of the detection system.

Figure 10.39 depicts a flexible two-channel system for evaluation of low optical losses at a given laser wavelength for synchronized-channel measurements [10.80]. The particular spectral domain for the study is provided by chosen sources and detectors, while the specific measurement structure is defined by the optical property to be studied. For measurements of losses of the internal bulk and each surface of a transparent substance, the layouts in Figs. 10.36 and 10.37 are applicable. For high-reflectance measurements, the arrangement in Fig. 10.38 is suitable. To detect bulk or surface scattering factors, an integrating sphere may be added to the light path before, after, or around a test sample.

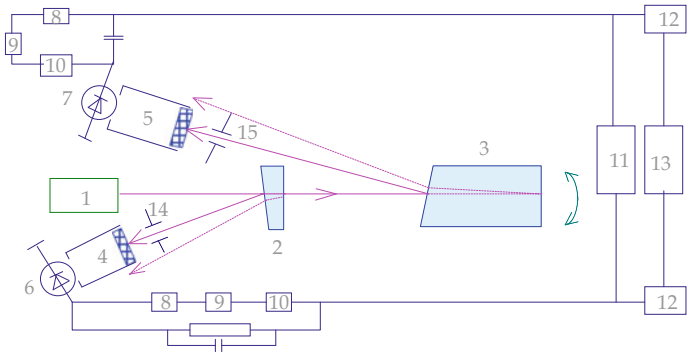

Fig. 10.39 Layout of a low-loss bulk attenuation measurement setting in reflected light

In every orientation of such a measurement system, the incident flux Φ_0 from source 1 is transmitted and reflected by wedge-shaped beam splitter 2 with very low vertex angle $\gamma \cong 10-20$ arc minutes. Light reflected from its first surface is separated by input aperture 14 into diffuse opal-glass attenuator 4, irradiating detector 6 of the reference channel. Radiation reflected from each surface of sample 3 under study is separately measured via identical components 15, 5, and 7 in the measurement channel. The signals from both detectors are transformed by transimpedance preamplifiers 8, low frequency filters 9, and pulsed amplifiers 10 to digital voltmeters 12. Time synchronization of every simultaneous measurement moment is performed by generator 11. All measurement-to-reference signal ratios are stored in computerized ratio meter 13. When measurements of a high reflectance are to be performed, the optical arrangement is converted into the layout depicted in Fig. 10.38. The beam of radiation reflected by mirror 4 under study is guided into main detector 5 by the wedged surface of any previously characterized transparent sample 3, serving here as the reflection output coupler for mirror 4. Thus, the system's dynamic range is not traded off when converting from the transmission to the reflection layout [10.79].

In a series of reflection-based measurement experiments [10.80], dark currents in each separately temperature-stabilized channel were maintained at near $\pm 2 \cdot 10^{-5}$ level during any consecutive hour. The random error of each ratio measurement averaged over seven to ten readouts did not exceed $\pm 3 \cdot 10^{-5}$. The reflectance magnitudes of all superpolished and temperature-stabilized single surfaces of short and long fused-silica samples measured were maintained within $\pm 5 \cdot 10^{-5}$ within several hours. As a result, the overall sensitivity of the described measurement system to low internal optical loss of a sample was $\pm 2.5 \cdot 10^{-6}$ cm^{-1} or ± 1 dB/km for the length difference of the two samples equal to or exceeding 10 cm. The highest reflectance under study could have potentially reached 0.99995, though such a high value was not observed during these studies. The lowest linear attenuation coefficient actually measured at He–Ne laser wavelength $\lambda = 632.8$ nm in a vapor-deposited fused-silica sample with numerical aperture 0.006 was 16 ± 0.6 dB/km. The magnitude of such a loss in fused silica represents aggregate attenuation, concurrently created by combination of both absorption and scattering losses within a nearly not divergent laser beam if compare with a fiber. Respective linear attenuation

coefficients measured in silica-core and silica-cladding fibers at much higher numerical apertures (0.1–0.2), actually drawn from some of fused-silica samples studied by the measurement system, were on an order of magnitude lower apparently owing to the impact of scattering modes guided by the fiber [10.80].

10.5.2 Sensitivity Comparison

Considering the factual sensitivity for any absolute measurement of the total attenuation of a low-loss sample, several ratio-based and differential-ratio-based systems, such as those described in Sect. 10.1 and this section, seem capable of identifying $\pm(1-2)\cdot 10^{-5}$ level of intensity changes with sufficient confidence to distinguish these changes from random noise. Typically, balanced-detection-based techniques are designed to sense absorption or other losses under study, without necessarily absolute determination of the magnitude of the loss, but referenced via one or another method of absolute calibration versus the specimen identified by other means of measurement. Therefore, providing direct comparison of sensitivities is difficult, if not impossible, but the reference described below may help establish one standpoint of comparison.

The comparison of unbalanced-detection versus balanced-detection techniques, provided by the optical-coherence tomography system illustrated in Fig. 10.40, establishes a certain reference due to the high sensitivity required for detection of scattered radiation and a similar two-channel layout as for loss-loss measurement [10.81]. The retina of the human eye serves as multilayer object 1 under study illuminated by superluminescent diode or mode-locked laser source 2 via a fiber-delivery system involving main 3 and secondary 4 couplers, connected to main 5 and balancing 6 detectors with translation mirror 7 or mirror cube 8 and focusing lenses La and Lb in the unbalanced configuration and with additional lens Lc in the balanced configuration. Both cases were analyzed to obtain the conditions for the maximum signal-to-noise ratio depending on fiber-end and object reflectivities ρ_f and ρ_{ob}, coupling fiber loss τ, system bandwidth B, radiation linewidth $\Delta\lambda$, and degree of polarization P for 50:50 couplers in the systems. The results obtained for balanced and unbalanced configurations are [10.81]:

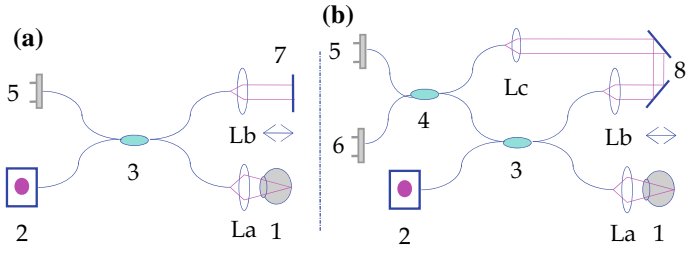

Fig. 10.40 Unbalanced (**a**) and balanced (**b**) coherence-tomography system

$$\left(\frac{S}{N}\right)_{unb,\max} = \frac{\rho_{ob}}{B}\frac{\Delta\lambda}{(1+P^2)}\frac{2\tau}{(\tau+\rho_f)^2};\quad \left(\frac{S}{N}\right)_{bal,\max} = \frac{\rho_{ob}}{\rho_f B}\frac{\Delta\lambda}{(1+P^2)}. \tag{10.81}$$

Setting for symmetrical comparison $\tau = \rho_f$, the maximums of balanced and unbalanced efficiency are:

$$\begin{aligned}(S/N)_{unb,\max} &= (\rho_{ob}/2\rho_f)(\Delta\lambda/B)(1+P^2)^{-1};\\ (S/N)_{bal,\max} &= (\rho_{ob}/\rho_f)(\Delta\lambda/B)(1+P^2)^{-1}.\end{aligned} \tag{10.82}$$

Corresponding Eqs. (10.81) and (10.82) for the maximal-achievable sensitivity in the balanced versus the unbalanced setting show the balanced arrangement is better only by a factor of 2, which could be easily affected by adding the extra coupler and by actual asymmetry of the balanced receiver. This confirms that signal-to-noise ratios in the direct and either ratio-based unbalanced or electronically balanced noise-compensating systems with no need for fast detection are quite compatible to those in balanced settings without the complexities of added components, unless making a fast measurement is of essence [10.81, 10.82].

Chapter 11
Propagation Losses in Fibers and Waveguides

11.1 Measurements of Internal Optical Attenuation for Guided Light

In view of the very small propagation losses for light guided via high-purity optical fibers drawn from highly transparent glasses with linear attenuation coefficients below 10^{-4}–10^{-5} cm^{-1}, one could think of the necessity to develop extremely sensitive measurement procedures detecting internal losses in such fibers. Nevertheless, especially high sensitivity is not be required since customary lengths of low-loss fibers, particularly for high-speed optical communication, are substantially longer than the corresponding lengths of the glass preforms from which these fibers are drawn. Even if at any specific propagation wavelength such a fiber has a linear attenuation coefficient $\mu = 1$ dB/km $= 2.3 \cdot 10^{-6}$ cm^{-1}, at a length of $\ell = 1$ km the total fiber attenuation $\mu\ell$ becomes low: 1 dB, but it is equivalent to light attenuation by nearly 26%. In a respective case of $\mu\ell = 0.1$ dB or $\mu\ell = 0.01$, the entire attenuation factor correspondingly drops to 2 and 0.2%. Only when an attempt is made to evaluate the amount of optical radiation absorbed or scattered by a short section of such a fiber should the sensitivity of that detection be substantially increased. This situation is essentially identical to any comparable detection method for similar extension of the measurement locality (see, e.g., Chaps. 8 and 9).

Particular methods of measurement for linear attenuation factors in optical fibers differ from those in bulk objects mainly by the irradiation and observation conditions, since the fiber core and cladding diameters are normally in range of 5–500 μm. Thus, to apply any earlier-described method of attenuation measurement for two identical fibers of different length, light has to be launched consistently into and out of a specific numerical aperture, matching the particular guiding modes of the fiber (see [II.33]). The fiber alignment becomes critical, since unrepeatable light launching causes excitations of different fiber modes and respective changes of measured attenuation as functions of the fiber's length and refractive index, which may diverge along distorted fiber paths [11.1]. Specific alignment

M. Bukshtab, *Photometry, Radiometry, and Measurements of Optical Losses*, Springer Series in Optical Sciences 209,
https://doi.org/10.1007/978-981-10-7745-6_11

uncertainty in a fiber measurement can be resolved only if all guided fiber modes corresponding to the steady-state mode distribution in the fiber or the fiber-preferred modes can be consistently selected for launching. Only under such a condition will the measurement be performed invariably.

The most common technique of fiber transmission measurement, called the cut-back method, is based on the matching comparison of two samples of different lengths as for any other transmission measurement, except that both the short and the long sample are made from the same fiber being studied (Fig. 11.1). Almost the entire fiber tested represents the long sample, but the short sample is formed from the beginning portion of that fiber, representing a so-called idle fiber, in which the steady-state mode distribution needs to be achieved for the light-launching conditions to be identical for both fiber sections compared. Radiation from a source is launched into an idle fiber or an idle part of the fiber being studied. The idle section serves for establishing the steady-state (static) radiation distribution for all guided fiber modes. Within such a fiber section, all potentially leaking light modes must be already guided out of that fiber. A so-called scrambling device or a matching liquid makes this process happen faster. If the mode distribution is steady, the intensity of a beam guided by the fiber virtually does not change for short distance variations. The characteristic length for the steady-state mode distribution to occur naturally depends on the fiber type, providing modes are not intentionally forced to leak. Such a length is ordinarily very long for a gradient fiber and short for a single-mode fiber [11.1, 11.2].

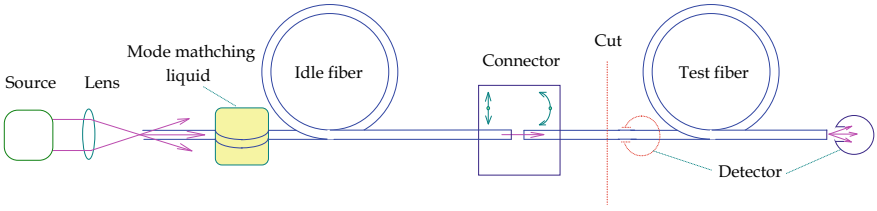

Fig. 11.1 Cutback technique for measurement of total internal-fiber loss

In the layout of Fig. 11.1, the source-idle fiber assembly functions as a stand alone light source designed to match the geometry of a fiber to be studied. If that test fiber is correctly aligned and coupled to the idle one, the loss measurement procedure consists in obtaining two transmission readings N_0 and N_{cut}, respectively, with the entire length of the fiber and with its short cut, establishing steady-state mode distribution (see the dotted lines in Fig. 11.1). If the optical properties along the fiber are uniform, the fiber linear attenuation coefficient μ is:

$$\begin{aligned} \mu &= 4.343 \times (\log_{10} N_0 - \log_{10} N_{cut})/(\ell_0 - \ell_{cut}) \\ &= 4.343 \times (\log_{10} N_0 - \log_{10} N_{cut})/\Delta\ell, \end{aligned} \tag{11.1}$$

where μ and the lengths $\ell_0 - \ell_{cut} = \Delta\ell$ of the fiber sections are in decibels per kilometer and in kilometers, respectively. The error of measurements is defined by

twofold inaccuracy of a single reading, instabilities and nonlinearities of the source and the detector, and the conditions of all the cleaved ends of the test fiber and its section, but even for ±5% single error and $\Delta\ell = 1$ km, the sensitivity to the internal loss is ±0.1 dB. The conversion from decibels per kilometer to inverse centimeters in relation (11.1) is based on the Bouguer–Lambert–Beer law (Eqs. (1.73) and (1.78)).

The concept of using the idle launching fiber, executing a steady-state mode distribution for the fiber to be studied, is extremely effective in fiber-attenuation measurements. Since factual losses in a short idle launching fiber are remarkably low, providing no leaking modes exist beyond the idle fiber, other optical losses, such as fiber nonuniformity, connection, and splice losses, can be confidently determined. For example, if the length of the fiber to be connected or spliced to an idle fiber is negligible, two transmission measurements of radiation exiting the idle fiber before the connection is made and with the connected short fiber of the same as idle type determine the connection loss. In certain fibers, such as ones designed for mid-IR wavelengths, it may take a long length of the fiber for the steady-state mode distribution to be established, plus a core refractive index becomes high enough to require accounting of multiple reflections [11.108].

Since cutting every fiber to be measured is not always convenient, the idle fiber, establishing the desired steady-state mode distribution in the given fiber type, allows an internal loss measurement even for a fiber connectorized at both ends. If the physical connections of the long and short fibers are repeatable within a margin of allowed connector loss, the process remains identical to that in Fig. 11.1 and the measuring loss relates to the differential length of the two fibers. If the fiber under study may not be taken out of a specific transmission system, the two-point procedure can be realized via light scattered out of a fiber cladding (Fig. 11.2). A short section of the fiber, having no jacket, can be surrounded by some immersion liquid, letting as much guided light out as possible. Any leaking radiation can be sensed by an integrating sphere or be directly side-measured by sensitive detector D, consistently detecting leaking of light by the section $\delta\ell$ for the measurement to be made at two points of the fiber of distances ℓ_1 and ℓ_2 [11.3]. Since detector D has no sensitivity to the direction of propagation, but light reflected by an open fiber end is inversely attenuated on its return, reflection of light from the far end of the fiber must be eliminated. Keeping the constant length $\delta\ell$ of the leaking section, irradiating one detector D used at both points, fluxes Φ_1 and Φ_2 to be registered at distances $\ell_{1,2} \rightarrow \ell_2 - \ell_1 = \Delta\ell$ are:

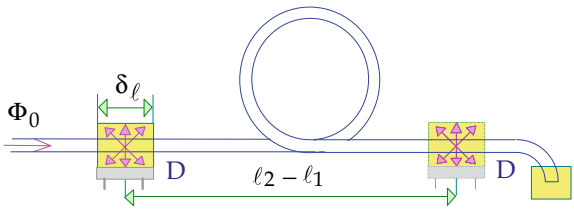

Fig. 11.2 Two-point measurement of inner-fiber loss

$$\Phi_1 \underset{\sigma\to 0;\mathrm{a}\to 0}{=} \text{const}\cdot\Phi_0\,(\sigma\delta\ell)\exp[-(\mathrm{a}+\sigma)\ell_1];$$
$$\Phi_2 = \text{const}\cdot\Phi_0\,(\sigma\delta\ell)\exp[-(\mathrm{a}+\sigma)(\ell_1+(\ell_2-\ell_1))], \tag{11.2}$$

where a and σ are the linear absorption and scattering coefficients of the fiber making its linear attenuation coefficient $\mu = \mathrm{a}+\sigma$. At a constant $\sigma\delta\ell$, the ratio of fluxes obtained equals the total loss: $\mu\delta\ell = (\mathrm{a}+\sigma)\delta\ell$, obtained in this case at differential length ℓ_2 of the fiber:

$$\Phi_2/\Phi_1 = \exp[-(\mathrm{a}+\sigma)\ell_2] \quad \text{or} \quad \mu\ell_2 = \ln\Phi_1 - \ln\Phi_2$$
$$= \text{power}_1[\text{dB}] - \text{power}_2[\text{dB}]. \tag{11.3}$$

Although such a procedure requires having a highly sensitive detector, its sensitivity to the internal attenuation is only limited by factual inaccuracy of the flux measurements and length separation $\Delta\ell \to \ell_2$.

If the amount of scattered light leaking out by the fiber cladding is low, such as in the case of single-mode fibers, it becomes difficult to perform a measurement with a flat detector. By implementing a light-leaking fiber coil in a highly reflecting integrating sphere, one can increase the measurement capability. The longer is the coil of the emitting fiber fitted into the sphere, and the smaller is the sphere versus its internal detector, the more power of radiation will be captured [2.5]. Another way of collecting scattered light is linked with using an aggregated detector made of sectional detectors enclosing the leaking-light zone. Figure 11.3 depicts a cube-detector layout, in which detectors form an integrating cube around the fiber section studied [11.4]. Two detectors have small apertures letting the fiber through such an assembly. Entire scattered light is measured simultaneously by all six detectors forming the integrating cube. To reduce dissimilarity of individual detectors, resistors in the detection circuits can be individually adjusted. By forming parallel registration circuits of six silicon detectors of $1\cdot 1\text{-cm}^2$ cross section and 8–11-kΩ resistors, the sensitivity to scattered light reached 10^{-10} W at $\lambda \cong 0.9$-μm light wavelength [11.4]. For the light power or its radiant flux of $\Phi_0 \approx 1$ mW, $\Delta\ell = 1$-cm length of light-leaking section, and fiber scattering coefficient $\sigma \cong 10^{-5}$, scattering losses were resolved at 1% accuracy at identical within ±5% sensitivity of the detectors.

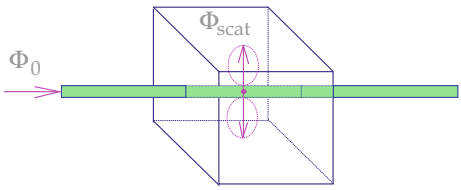

Fig. 11.3 Integrating-cube detector

Light scattered or leaked via the lateral surface of an optical fiber can also be successfully utilized to identify local inclusions or inhomogeneities of the fiber. When leaking light is identically measured before and after a point of inclusion or

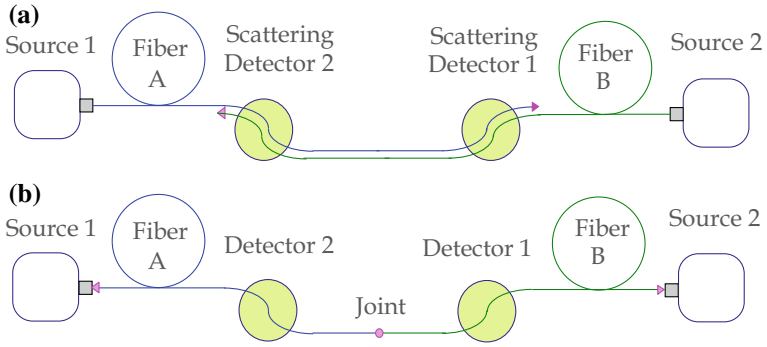

Fig. 11.4 Bidirectional measurements of splice or joint losses

internal degradation, as well as a splicing or connecting joint, the sensed intensity change equates the implemented loss [11.5]. Figure 11.4 illustrates a procedure for the measurement of any back-and-forth splicing loss for virtually all types of fibers. Two pairs of identical sources and detectors of light are used to measure attenuation in opposite directions of light propagation for fibers A and B. In the calibration step, radiation is launched into fibers placed into mode-stripping devices of two scattering detectors 1 and 2 (seen as curves); thus the first detector 1 reads the power launched by source 1, but detector 2 measures the power of source 2. Mode-stripping devices must leak as much light as possible for accurate readings and alignments of joined fibers. In the second step, fibers A and B are coupled or spliced without disconnecting them from their sources of light, while the detectors measure the respective changes of power transmitted into both sides of the joint.

The cutback and two-point attenuation measurement techniques considered above rely on having equivalent access to fiber ends and to fiber cladding. If the loss measurement is to be performed on a transmission system consisting of a number of interconnected but cabled fibers equipped with fiber connectors at both ends, any loss at each connector plug is added to the total attenuation of the entire transmission system. Since realistic lengths of communication fibers are rather large, each connector loss adds up and needs to either be evaluated via a short fiber, not attenuating by itself, or directly measured by other methods. One method of measurements of inserted losses while eliminating the extra attenuation at every connection point is depicted in Fig. 11.5 [11.6]. First, internal attenuation factors μ_a and μ_b of two launching fibers are measured via the direct and reverse path (Fig. 11.5a, b). Then, the device I under study, causing the local losses μ_I and μ_I' in the opposite directions, is connected by a test connector C_1 (Fig. 11.5c). In the positions in Fig. 11.5d, e, the system's loss is measured from opposite directions via similar connectors C_1 and C_2. Finally, measurement is made for the configuration in Fig. 11.5f. If losses μ_{C1} and μ_{C2} of connectors C_1 and C_2 are unchanged during the entire procedure and are also independent of the direction of light propagation, the detector readings become:

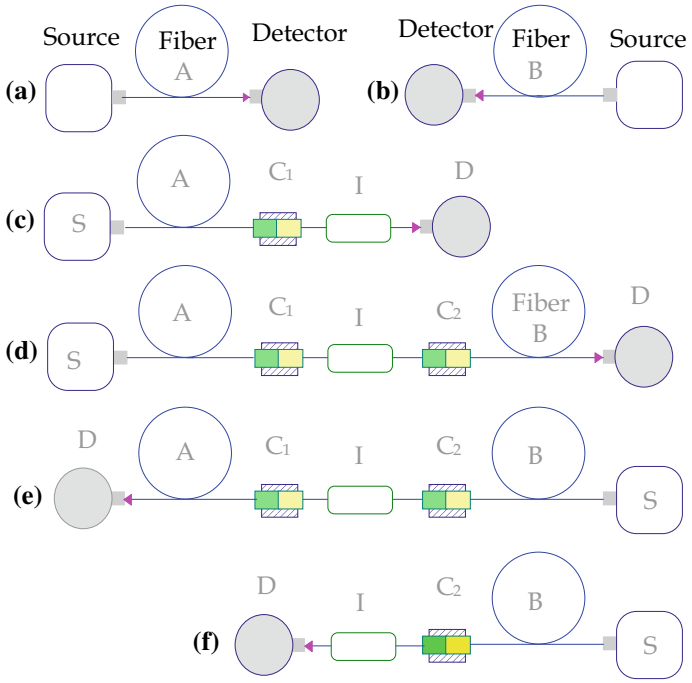

Fig. 11.5 Evaluation of local transmission-system losses

$$\begin{aligned} &N_c - N_a = \mu_{C1} + \mu_I;\ N_f - N_b = \mu_{C2} + \mu_I';\\ &N_d - N_a = \mu_{C1} + \mu_I + \mu_{C2};\ N_d - N_c = \mu_{C2};\\ &N_e - N_b = \mu_{C2} + \mu_I' + \mu_{C1};\ N_e - N_f = \mu_{C1}. \end{aligned} \tag{11.4a}$$

As a result, internal losses μ_I and μ_I', occurring in each direction by any local discontinuity, are:

$$\mu_I = N_c - N_a + N_f - N_e; \tag{11.4b}$$

$$\mu_I' = N_f - N_b + N_c - N_d. \tag{11.4c}$$

Owing to multiple steps required, repeatability of that measurement technique is not superior. It needs to resolve every local connection and each fiber loss as a function of propagation direction for the steady-state mode distribution in launching fibers. The measurement error averaged over ten trials for the mean local loss $(\mu_I + \mu_I')/2$ was reduced to ± 0.032 dB [11.6]. Under the steady state mode condition for single mode fibers the methodology may be used without connectors [11.106].

11.1.1 Integrated Waveguides

Studies of transmission losses in integrated planar waveguides, which are nondestructive, are usually provided via light-coupling techniques, approached similarly to cutback or steady-state mode distribution methods trying to maintain a constant coupling efficiency for launching light into and out of the waveguide. The most common is sliding-prism technique [11.96], in which the prism slides along the waveguide under test, measuring its loss dependence via the length of propagation (Fig. 11.6, configuration a).

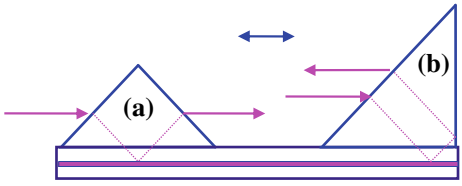

Fig. 11.6 Waveguide study via prism-coupling

Owing to difficulties in maintaining a constant coupling efficiency, several coupling prisms may be used or the loss-per-length dependence can be sensed via scattered light (see below). Other coupling approaches can be deployed: a glass-rod probe [11.97] or a prism [11.98] in reflection (Fig. 11.6, configuration b), which both frustrate the total internal reflection process on the upper boundary of the waveguide owing to coupling. Even a photographic-based technique could be considered [11.99].

Another approach is to study a waveguide as a whole, comparing its losses in transmission and reflection and the maxima and minima of reflectance and transmittance (see Sects. 3.3, 8.4). Figure 11.7 depicts a reflection–transmission arrangement for resonant waveguide-loss measurements via temperature-tuning the waveguide [11.101]. Light from source S is focused in and out by objectives O_1 and O_2 and measured by detectors D_t and D_r via beam splitter BS in transmitted and reflected radiation, respectively, while waveguide W is tuned by heater H to any

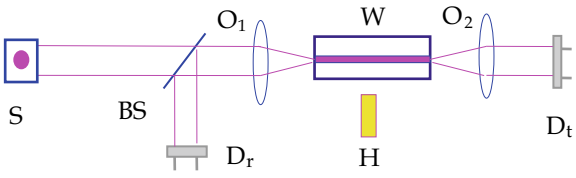

Fig. 11.7 Reflection-transmission waveguide study

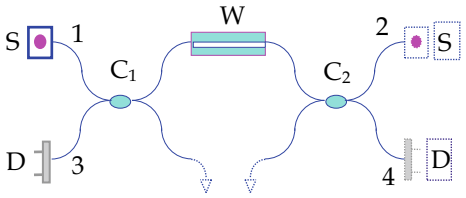

Fig. 11.8 Waveguide-cavity loss measurement

extrema. Figure 11.8 illustrates a reflection–transmission setup for waveguide measurements via two identical couplers C_1 and C_2 [11.102]. Radiation from source S at ports 1 and 2 is sensed by detector(s) D at ports 3 and 4 in opposite directions. The waveguide's reflectance ρ_w and transmittance τ_w as a Fabry–Perot resonator with mirror reflectivity ρ and transmittance τ_{int}, defined by Eqs. (3.124c) and (3.125c), is measured by launching light via fiber couplers C_1 and C_2:

$$\Phi_{\rho,S1-D3} = \frac{\Phi_{in}}{4}\tau_{c-w}(1-\rho)\rho_w(1-\rho)\tau_{w-c}; \quad \Phi_{\tau,S1-D4} = \frac{\Phi_{in}}{4}\tau_{c-w}(1-\rho) \cdot \tau_w(1-\rho)\tau_{w-c}; \quad \frac{\Phi_\rho}{\Phi_\tau} = \frac{\rho_w}{\tau_w}.$$

At perfect 50:50 coupling ratio of couplers C_1 and C_2, for a resonating waveguide cavity of reflectance ρ, the waveguide reflectivity ρ_w and transmissivity τ_w at its finesse F are (see Eqs. (3.119c) and (3.122c)):

$$\frac{I_\rho}{I_0} = \frac{\rho(1-\tau_{int})^2 + 4\rho\tau_{int}\sin^2(\delta/2)}{(1-\tau_{int}\rho)^2 + 4\rho\tau_{int}\sin^2(\delta/2)}; \quad \frac{I_\tau}{I_0} = \frac{\tau_{int}(1-\rho)^2}{(1-\tau_{int}\rho)^2 + 4\rho\tau_{int}\sin^2(\delta/2)};$$

$$\frac{I_\rho}{I_\tau} = \frac{\rho(1-\tau_{int})^2 + 4\rho\tau_{int}\sin^2(\delta/2)}{\tau_{int}(1-\rho)^2} = \frac{\rho(1-\tau_{int})^2/(1-\tau_{int}\rho)^2 + F\sin^2(\delta/2)}{\tau_{int}(1-\rho)^2/(1-\tau_{int}\rho)^2}. \tag{11.5a}$$

Tuning the incident-light wavelength to the waveguide maxima–minima in transmission–reflection and measuring the ratios of reflectance–transmittance extrema, one obtains from Eqs. (3.124c) and (3.125c):

$$\frac{(1+\tau_{int})}{(1-\tau_{int})} = \sqrt{\frac{I_{\rho,max}}{I_{\tau,min}}\frac{I_{\tau,max}}{I_{\rho,min}}} \equiv \sqrt{K}; \quad \tau_{int} = \exp(-\mu\ell) = \frac{\sqrt{K}-1}{\sqrt{K}+1}. \tag{11.5b}$$

If only transmitted radiation (similarly for reflected radiation) is assessable, the measurement ratios become:

$$\frac{I_{\tau,max}}{I_0} = \frac{\tau_{int}(1-\rho)^2}{(1-\tau_{int}\rho)^2}; \quad \frac{I_{\tau,min}}{I_0} = \frac{\tau_{int}(1-\rho)^2}{(1+\tau_{int}\rho)^2}; \quad \frac{I_{\tau,max}}{I_{\tau,min}} = \frac{(1+\tau_{int}\rho)^2}{(1-\tau_{int}\rho)^2};$$

$$\tau_{int} = \frac{1}{\rho}\frac{\sqrt{I_{\tau,max}/I_{\tau,min}}-1}{\sqrt{I_{\tau,max}/I_{\tau,min}}+1}. \tag{11.5c}$$

Maxima and minima ratio measurements only in reflected light lead to another solution via ratio R:

$$\frac{I_{\rho,\max}}{I_0}=\frac{\rho(1+\tau_{\text{int}})^2}{(1+\tau_{\text{int}}\rho)^2};\quad \frac{I_{\rho,\min}}{I_0}=\frac{\rho(1-\tau_{\text{int}})^2}{(1-\tau_{\text{int}}\rho)^2};\quad \frac{I_{\rho,\max}}{I_{\rho,\min}}=\frac{(1-\tau_{\text{int}}\rho)^2\,(1+\tau_{\text{int}})^2}{(1+\tau_{\text{int}}\rho)^2\,(1-\tau_{\text{int}})^2};$$
$$R\equiv I_{\rho,\max}/I_{\rho,\min};\quad \tau_{\text{int}}=\big((1+\tau_{\text{int}}\rho)\sqrt{R}-(1-\tau_{\text{int}}\rho)\big)$$
$$\big/\big((1+\tau_{\text{int}}\rho)\sqrt{R}+(1-\tau_{\text{int}}\rho)\big). \tag{11.5d}$$

Here one τ_{int} solution, at known ρ, is from the quadratic equation: $\tau_{\text{int}}^2\rho(1-\sqrt{\text{R}})+\tau_{\text{int}}(1-\rho)(1+\sqrt{\text{R}})+(1-\sqrt{\text{R}})=0$.

Any of Eqs. (11.5a)–(11.5d) allow one to determine the waveguide loss, avoiding the need to measure the input flux I_0 at known waveguide-surface reflectivity ρ. Measurements via the maximum and minimum of transmission or reflection minimize the uncertainty of the radiation phase status δ and its deviations. If the radiation wavelength is tuned to the maximum and to the minimum in transmission and the ratio: $\text{I}_{\tau,\max}/\text{I}_{\tau,\min}=\text{T}_\lambda$, is measured, the total internal loss μ of the waveguide studied is determined via Eq. (11.5c):

$$\exp(-\mu\ell)=\left(\sqrt{\text{I}_{\tau,\max}/\text{I}_{\tau,\min}}-1\right)\Big/\left(\rho\left(\sqrt{\text{I}_{\tau,\max}/\text{I}_{\tau,\min}}+1\right)\right);$$
$$-\mu\ell=\ln\left(\left(\sqrt{\text{T}_\lambda}-1\right)\Big/\left(\sqrt{\text{T}_\lambda}+1\right)\right)+\ln(1/\rho).$$

The results of experimental studies via Eqs. (11.5b) for a series of waveguide samples of different lengths matched the results of cutback- and other resonator-based measurements to ±1 dB for about 10 dB/cm loss [11.101]. Measurements using Eqs. (11.5a), which could have been difficult owing to unsettled δ settings, found average waveguide propagation losses from opposite directions at the 0.55 dB/cm level [11.102]. Similar transmission measurements via relation (11.5a) obtained using polarization coupling and wavelength tuning provided the waveguide spectral-loss function via spectral-curve fitting [11.103]. Nanophotonic waveguides allow studies to be made via nanocavities embedded along waveguides [11.107]. Backscattering waveguide measurements [11.104] could be performed similarly (see the following paragraphs).

11.1.2 Absorption and Scattering Losses

The presence of an internal absorption loss in an optical fiber or a waveguide changes the temperature the same way it does if radiation is propagating via equivalently transparent glass and/or a crystal (see Chap. 9 for specific details). One major difference consists in the contrasting border conditions for the two respective heat-flow equations. Owing to the considerably smaller thickness and the much greater length of a low-loss optical fiber, it is easier to separate fiber absorption and scattering losses during a calorimetric study, but it is surely harder to attach any thermodetector to the end or surface of the fiber in order to match the measured and the true temperature.

To perform calorimetric measurements of absorption losses in a fiber, the calorimeter design may be changed to accommodate a long fiber, deploying a set of individual thermodetectors to increase the calorimeter's sensitivity to a respectively small heat flow [9.10]. Large extensions of the distance from the thermal source may decrease the individual reaction of each detector, but could allow the time constants related to the scattering and absorption losses to be better distinguished. When the heat transfer is characterized by Eqs. (9.9)–(9.11), the characteristic time interval t_1 of the scattering action is longer than the time constant for an array of slow thermodetectors, and such a calorimeter would distinguish the scattering and absorption factors. Figure 11.9 depicts the characteristic intervals as a function of pressure [11.7]. A 20-s-long light pulse from a continuous-wave (cw) He–Ne laser was launched into a multimode fiber. The pulse's end matched the peak of thermal energy Q_σ due to scattered light. At atmospheric pressure (Fig. 11.9, signal a) and therefore at low thermal resistance of the fiber surroundings, the slow detectors did not divide the absorbed energy Q_α. In a deep vacuum (Fig. 11.9, signal b), only scattered light was sensed, but at the transitional pressure $P \cong 13$ kPa two sequential pulses of the radiation scattered and absorbed by the fiber were fully separated along time t_1 (Fig. 11.9, signal c) [11.7].

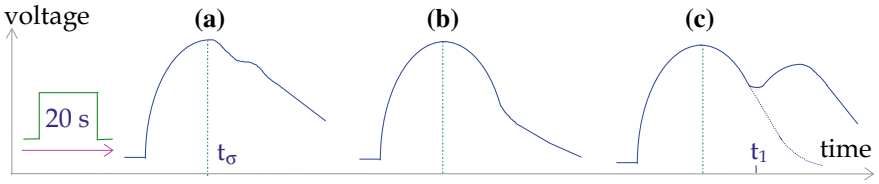

Fig. 11.9 Pressure-bound separation of thermal signals due to scattering and absorption

An alternative way to separate absorption and scattering phenomena instantly follows from Eqs. (9.9) and (9.11), considering that a radiometric reaction is inversely proportional to the distance ℓ between a point source and a detector (see Chaps. 1 and 2). Hence, a decrease of distance ℓ extends the thermal reaction, but reduces the characteristic time interval t_2 (see Sect. 9.1). That determines the actual sensitivity $\Delta T/t$ to the absorption portion of the loss in the fiber according to the following relation [9.7]:

$$\Delta T/t = (4/\pi)\,\Phi_\alpha/\left(\pi\ell^2\rho_p c_p\right), \tag{11.6}$$

where the factor $4/\pi$ denotes the finite dimension of the fiber sample. During exposure of a thin glass rod at $\ell = 0.66$ mm and $4/\pi\ell^2\rho_p c_p = 211$ K·cm/J by a laser pulse, the thermal-detection limit reached $2\cdot10^{-9}$ W/cm at $\Delta T = 1.8\cdot10^{-4}$ K and $t = 400$ s. In a calorimeter filled with pure helium, the actual absorbed level of power equivalent to noise was near $(\Phi_0\cdot\alpha)_{min} = 4\cdot10^{-9}$ W/cm at $\Delta T = 6\cdot10^{-5}$ K and $t = 100$ s [11.7].

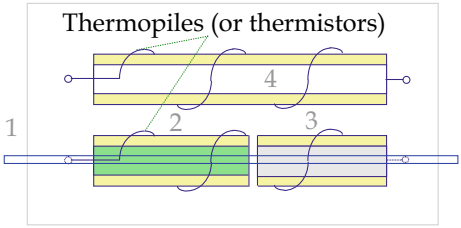

Fig. 11.10 Partition of absorption and scattering

Another contrasting way for separating absorption and scattering loss in a thin fiber guide is shown in Fig. 11.10. First, fiber 1 is placed into a hollow glass tube of a larger diameter than that of the fiber. Actual thermal separation of fiber losses is achieved via two collinear tubes 2 and 3 for the fiber and another tube 4 as the reference tube. Tube 2 is transparent to measure fiber absorption only, but tube 3 is blackened to detect fiber scattering. To prevent retroreflections of light scattered at low angles tube 2 is also filled with a transparent immersion liquid. The integrated absorbed and scattered fluxes, respectively, are [11.8]:

$$\Phi_\alpha = \int_{\ell}^{\ell+\Delta\ell} \partial\Phi_\alpha(\ell) = \Phi_0[(1+G)\alpha/\mu][1-\exp(-\mu\Delta\ell)]; \tag{11.7}$$

$$\Phi_\sigma = \int_{\ell}^{\ell+\Delta\ell} \partial\Phi_\sigma(\ell) = \Phi_0[(1-G)\sigma/\mu][1-\exp(-\mu\Delta\ell)], \tag{11.8}$$

where $G = \left(n_0^2 - n^2\right)/\left(4n_0^2\right) \cong \left(n_0^2 - n^2\right)/(2n_0)$ is the fiber geometric extent, denoting the guided part of scattered light, and n_0 and n are the refractive indices of the fiber core and cladding. Any rise ΔT_2 of the temperature of tube 3 is characterized by the action of the total flux: $\Phi_\Sigma = \Phi_{abs} + \Phi_{scat}$, and is given by:

$$\Phi_\Sigma = \Phi_0\{[(1+G)\alpha + (1-G)\sigma]/\mu\}[1-\exp(-\mu\Delta\ell)]. \tag{11.9}$$

Accordingly, the ratio of temperature rises in tubes 2 and 3 referred to that in tube 4 gives the loss quotient:

$$\Delta T_{black.tube}/\Delta T_{transp.tube} = 1 + (1-G)\sigma/[(1+G)\alpha], \tag{11.10}$$

where α and σ are the linear absorption and scattering coefficients of the fiber. Since for any silica fiber $n_0 - n \leq 0.02$ and $(1-G)/(1+G) \geq 0.985$, the plus–minus G factors can be omitted with approximately 1.5% error.

An additional possibility for increasing calorimetric sensitivity to the fiber loss relates to the fiber geometry. Owing to the virtual absence of the endface loss for a long single optical fiber, thin thermopiles (Fig. 11.10) may be replaced by a set of thermistors of larger surfaces. To compensate for the increase of direct radiation scattering caused by extra lateral surfaces [11.8], transparent tube 2 in Fig. 11.10 was sandblasted and blackened. For the system of fiber and thin tubes to behave as one system, tubes 2 and 3 were filled with an immersion liquid matching the thermal diffusivity of the tube glass. Since the amount of light emitted by any

heated body at thermal equilibrium is proportional to its lateral area and to the fourth power of its temperature T, the flux is $\Phi \sim A\left(T^4 - T_0^4\right) \cong A\,T^3(T - T_0)$. Presuming absence of the longitudinal flow and of the convection of heat in a deep vacuum, the radial thermal flux H becomes:

$$H_{therm} = 4\varepsilon_\lambda k T_0^3 2\pi r \Delta\ell \Delta T. \tag{11.11}$$

Here T_0 is the averaged ambient temperature, ε_λ is the spectral emissivity of the entire system of the fiber and tube, k is the Stefan–Boltzmann constant, ΔT is the difference of temperatures of heated and reference tubes, and r is the radius of the tube. A temperature rise creates imbalance voltage ΔU of the thermistor bridge:

$$\Delta U = U_0 \beta_T \Delta T \cdot R_{heat} R_{ref} \Big/ \left(R_{heat} + R_{ref}\right)^2, \tag{11.12}$$

where U_0 is the bridge balance voltage, β_T is the thermal coefficient of resistance, and R_{heat} and R_{ref} are the resistance of heated and reference thermistors. For a platinum thermistor with $\beta_T = 3.9 \cdot 10^{-3}$ K^{-1}, $T_0 = 295$ K, $r = 0.75$ mm, $U_0 = 0.5$ V, $R_{heat} = R_{ref}$, $\varepsilon_\lambda \cong 1$, and $\varsigma = 5.67 \cdot 10^{-12}$ W/(cm$^2 \cdot$K^4), the ratio $\Delta U/\Delta\ell$ is $2.3 \cdot 10^{-6}$ mV/cm. For $\Phi_0 = 1$ mW, $\alpha = 1$ dB/km, and $\Delta\ell = 20$ cm, imbalance $\Delta U \cong 4.1$ nV/(mW·dB/km).

During experiments with a 50-mW He–Ne laser at $\lambda = 633$ nm irradiating a fiber for about 1 min with a sequential 1-min delay, the level of equivalent-to-noise sensitivity was 0.1 dB/km. Absolute calibration was performed by substitution of the fiber by an electric wire. The imbalance of the bridge was $\Delta U = 4.0$ nV/(mW·dB/km) for a transparent silica tube with $\varepsilon_\lambda \cong 0.8$, and was $\Delta U = 4.0$ nV/(mW·dB/km) in the black-painted tube with $\varepsilon_\lambda \cong 0.9$. The linear absorption coefficient α measured at $\lambda = 633$ nm was near 1.4 dB/km, but the scattering coefficient σ reached 11.8 dB/km. Further measurements by the cube detector [11.8, 11.9] verified the scattering coefficient σ was 0.7 dB/km.

Similarly to the measurement of bulk absorptance (see Chap. 9), radiation absorbed inside a fiber situated inside a sound resonator filled with a resonating gas can be detected by a sensitive microphone [11.10]. Since 125-μm diameter of the silica fiber cladding practically equals the thermal diffusion length λ_T at low modulation frequency f (Eq. (9.60)), while the fiber's core and cladding thermal conductivities are practically identical, the temperature distribution in the fiber cross section A can be considered uniform. As a result, the thermal flux H from that low-absorbing fiber becomes:

$$H_{therm} = (\alpha\Phi/2A)\exp(ift). \tag{11.13}$$

Besides, the thin optical fiber can be substituted by a calibrating wire, heated by any alternating electric current of equivalent angular frequency $f/2$, more accurately than a bulk sample. Therefore, complex expressions (9.61) and (9.62) can be singled out as for only terms of the temperature distribution at frequency f. In a resonant cavity of much larger dimensions than λ_T, and, thus, with distant walls with negligible thermal influence, the radial temperature shift T_f, which makes air

pressure and acoustic waves, is proportional to the wave amplitude U_m: $T_f \sim U_m \lambda_T / f$. When the fiber is irradiated, amplitude U_{fiber} is:

$$U_{fiber} \sim \alpha \Phi / (2A\lambda_{T,fiber}). \tag{11.14}$$

When the alternating current I_a flows through a wire of conductance $1/R$ and of the size of the fiber, U_{wire} is:

$$U_{wire} \sim I_a^2 R / \left(2A^2 \lambda_{T,wire}\right). \tag{11.15}$$

At low modulation frequency f, the other factors in relations (9.61) and (9.62) are similar and [11.10]:

$$\alpha\Phi = I^2 R(\rho_p c_p)_{fiber} / [(\rho_p c_p)_{wire} A]. \tag{11.16}$$

The experimentally evaluated absorption coefficient α at $\lambda = 514.5$ μm was (9.3–9.2) ± 0.6 dB/km at $\Phi_0 \cong 240$ and 150 mW. The dependence of the signal amplitudes on frequency $f^{-1.6}$ was slightly different from that calculated for pure SiO_2 as $f^{-1.7}$, correcting the recalculated effect of aluminum cavity walls to ±1%. The mirage-effect measurement (see Sect. 9.3) estimated a fiber-absorption loss of 9–9.7 dB/km [11.10].

11.1.3 Analysis of Scattering Losses

One common assumption for most conventional light-scattering measurements in low-absorbing fibers presumes Rayleigh phenomenon for back-and-forward elastic scattering on small particles, being inversely proportional to the fourth power of the light wavelength: $\sigma_{Rayleigh} = \text{const}/\lambda^4$ ([II.20]). When this assumption holds true, it facilitates a scattering measurement by detecting light intensity at 90° to the incident beam [5.13]:

$$\sigma_{Rayleigh} = \frac{I_{90^\circ}}{I_0} \frac{\ell^2}{V} \frac{8\pi}{3} \frac{1 + 2I_{||}(\Theta)/I_{\perp}(\Theta)}{1 + I_{||}(\Theta)/I_{\perp}(\Theta)} = \frac{16\pi}{3} \frac{I_{90^\circ}}{I_0} \frac{\ell^2}{V}, \tag{11.17}$$

where I_0 and I_{90° are the intensities of incident radiation and radiation scattered at 90°, which is not polarized at isotropic Rayleigh scattering. However, if any impurity particles in the scattering fiber are not small in comparison with the radiation wavelength of interest, two other phenomena of light scattering could occur, such as a wavelength-independent effect and Mie scattering: $\sigma_{Mie} = \text{const}/\lambda^2$ [1.1]. The scattering loss in optical fibers can also be caused by large defects, such as fiber diameter fluctuations, leading to wavelength-independent scattering, as well as by crystallization or by other inhomogeneities or particle impurities. To identify plausible outcomes of these or other phenomena, developing absolute methods for scattering measurements may become essential if sensitivity versus bulk-loss studies can be improved, not to cause fiber nonlinearities at high power densities.

To measure complete 4π scattering, a fiber can be fitted, as any other object, into a highly reflecting integrating sphere. To distinguish scattering loss when integrating any long fiber length, high resolution to scattered light may not be required, since the entire fiber-length spool can be coiled into the sphere. Decreasing the sphere diameter would increase the sensitivity, since the internal sphere irradiance expands inversely to its squared radius as a straight fiber length reduces linearly. Since a cube detector limits the enclosed scattering zone of a fiber [11.4] (see Fig. 11.3), likewise the measurement of the sum of the absorption and scattering loss by Eqs. (11.2) and (11.3), the absolute measurement of the scattering loss σ can be made via the fiber transmittance as seen in Fig. 11.11:

$$\Phi_\sigma = \Phi_0 \sigma' \delta\ell \, \exp(-\mu\ell_\mathrm{i}); \quad \Phi_\tau = \Phi_0 \exp(-\mu\ell_\mathrm{total});$$
$$\sigma' = (\Phi_\sigma/\Phi_\tau \delta\ell) \exp(-\mu(\ell_\mathrm{total} - \ell_\mathrm{i})). \tag{11.18}$$

Here σ' stands for the effective fiber scattering coefficient, which excludes scattered light guided by the fiber at low propagation angles, $\delta\ell$ is the length of the scattering section, equal to the cube-detector length or to the diameter of the integrating sphere, in which the fiber fits straight, and ℓ_i and $\ell_\mathrm{total} = \ell_\mathrm{i} + \delta\ell$ are, respectively, the distance to the scattering section and the total length of the fiber, which owing to low fiber losses are presumed to be virtually equivalent. Comparison of the complete and 90° scattering distinguishes low-angle and wavelength-independent phenomena. If relation (11.18) is converted to logarithmic form, the total internal loss can be evaluated via the slope of its linear conversion by repositioning (dashed lines in Fig. 11.11) the cube detector or integrating sphere along the fiber [11.11]. Similarly [11.100], scattering and absorption losses may be deduced by simultaneous transmittance and scattering measurements.

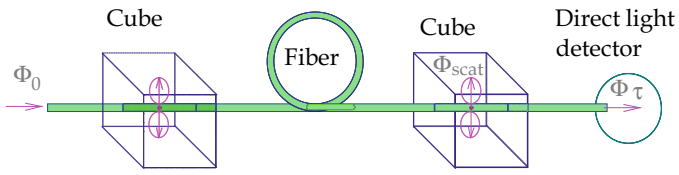

Fig. 11.11 Absolute measurement of fiber-propagation scattering loss

By contrast to the integrating-sphere placement, in which internal spherical 4π irradiance does not depend on the direction of first irradiation of its wall, cube detectors do not uniformly respond to oblique components of scattered light. The magnitudes of cube irradiance decrease proportionally to the cosine of the incidence angle. Therefore, cube detectors effectively estimate only Rayleigh but not low-angle components of scattering. To measure effectively the 4π scattering, cube readings must be corrected by the factor $\int \xi_i \cos\varphi_i dA/\overline{\xi}$, where ξ_i and $\overline{\xi}$ are the local and the average sensitivity for each detector surface of area A and φ_i is the angle of incidence. The quasi-sphere, made, for instance, of pentagonal detectors and proposed long ago [1.5], can more effectively evaluate fiber scattering. Other types of light concentrators can be used, as compound parabolic ones commonly utilized for light-emitting diodes [11.12].

A schematic representation of 4π scattering loss measurement in the integrating sphere is shown in Fig. 11.12 [11.13, 11.14]. The fiber jacket must be stripped from the fiber section inside the sphere. The steady-state distribution of fiber modes should prevent sensing of any leaking light modes. The fiber end can be put into the sphere to calibrate its internal detector 1. Detector 2 establishes the loss-calibration level by measuring the fiber transmission and is used to stabilize the source power output. As low as 0.025 dB/km scattering-loss level at $\lambda = 2.55\,\mu m$ was sensed [11.14].

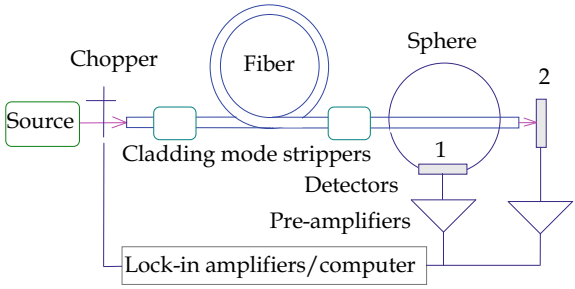

Fig. 11.12 Measurements of total fiber scattering

Obvious difficulties for the absolute measurements of low scattering losses in optical fibers are defined by 10^{-5}–10^{-6} lower intensity levels of scattering than of light transmitted via a low-loss fiber. It is not easy to achieve simultaneously high sensitivity and a high dynamic range of a detector, or to apply supplementary attenuators of known optical properties, especially in a broad spectral region. As noted in Chap. 2, an integrating sphere made of any low-absorbing translucent material can be utilized as a spectrally unselective attenuator, as well as a space integrator of diffusely reflected radiation [0.21, 2.8], providing the scattering indicatrix of the material chosen could be closely approximated by the cosine-law function (see also Chaps. 1, 2). Considering the applicability of such a sphere to measure the 4π scattering, Eqs. (2.12) and (2.13) confirm the uniform distribution of radiation incident upon the sphere inside and outside the sphere enclosure with the accuracy of approximation that there are no identifiable absorption losses in the sphere walls at $\rho_{wall} + \tau_{wall} \to 1$. The layout for a measurement procedure is schematically illustrated in Fig. 11.13 [2.5].

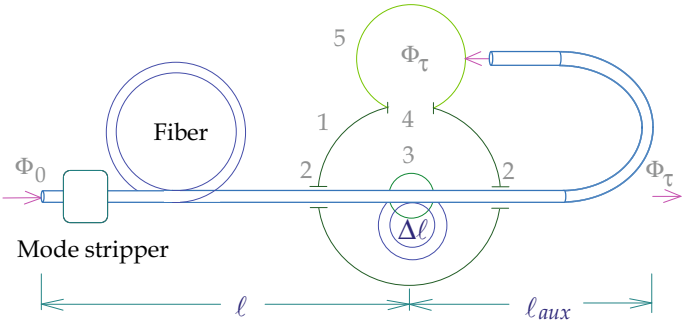

Fig. 11.13 Absolute measurements of ultralow fiber scattering

In the main integrating sphere 1 of a diffuse, highly reflecting material and optimized to be small dimensions for the low-scattering measurements, only four entrance–exit ports are made. The two smallest ports 2 hold a test fiber, third port of area A_d has detector 3, and fourth port 4 of area A_c couples translucent sphere 5.

When the flux Φ_0 of radiation is launched into a fiber of linear attenuation μ, combining respective scattering and absorption losses σ and α, the light flux Φ_{sc} is scattered into sphere 1:

$$\Phi_{sc} = \Phi_0(1 - \rho_f)\eta \exp(-\mu\ell), \tag{11.19}$$

where ρ_f is the reflectance of the fiber endface or connector and $\eta = \sigma\Delta\ell$ is the scattering factor of the fiber section of length $\Delta\ell$ inside integrating sphere 1. The reading of detector 3 in main sphere 1 is:

$$N_0 = const \cdot \Phi_0\left(1 - \rho_f\right) \exp(-\mu\ell) \frac{\sigma\Delta\ell}{1 - \rho_1'} \frac{A_d}{A_1}, \tag{11.20}$$

where ρ_1' and A_1 are the effective internal reflectance (see Sect. 2.4) and the inner surface area of sphere 1.

When the far end of the fiber of expanding length ℓ_{aux} is turned to irradiate the translucent sphere 5 (dotted line in Fig. 11.13) and since reflectance ρ and transmittance τ of that translucent sphere walls are: $\rho + \tau = 1$, reading N_Σ of detector 3 in response to flux Φ_{sc} plus flux Φ_τ of sphere 5 is:

$$N_\Sigma = const \cdot \Phi_0\left(1 - \rho_f\right)\{\exp(-\mu\ell)\sigma\Delta\ell + \exp[-\mu(\ell + \ell_{aux})](A_c/A_5)\} \cdot (1 - \rho_1')^{-1}(A_d/A_1). \tag{11.21}$$

Here A_5 is the area of the inner surface of sphere 5. At the negligibly small loss of the fiber far-end section: $\mu\ell_{aux}$, we have:

$$\sigma\Delta\ell = (N_0/(N_\Sigma - N_0))(A_c/A_5). \tag{11.22}$$

Such a technique does not require extra baffles in either sphere, since in that structure any seemingly low-leaking modes of the fiber cannot directly irradiate detector 3, while radiation, added from the translucent sphere, is uniformly scattered. Consequently, there are no systematic errors when making the absolute measurement of fiber scattering coefficients. The dynamic range for this measurement is reduced in proportion to the relative area A_c/A_5 of the coupling aperture between spheres. If the translucent sphere wall has a specular component of scattered radiation, the sphere irradiance E_5 should be evaluated by Eq. (2.161), which governs coupling of flux $\Phi_5 = A_cE_5$ into sphere 1.

For experimental arrangements [2.5], translucent sphere 5 was machined from a low-density opal glass with opening to inner sphere surface area of ratio A_c/A_5 = 26.46 dB. That ratio of direct radiation fluxes to radiation fluxes transmitted via sphere 3, measured with ±0.2 dB accuracy, was 26.6–26.8 dB at 0.9- and 1.06-μm wavelengths. A change within ±30° of the irradiation direction by the far end of the fiber for translucent sphere 5 did not alter detector readings. The test fiber designed for λ = 1.3 μm had total attenuation of 6.2 dB/km at $\lambda \cong 0.9\,\mu m$. The measured scattering-loss component at $\lambda \cong 0.9\,\mu m$ was 6.5 dB for multiple coils of fiber, giving a linear-scattering coefficient of 1.8 dB/km for the coiled fiber length $\Delta\ell = 280\,mm$.

11.1.4 Polarization Dependent Losses

Polarization-dependent loss (PDL) of a fiber is defined by the maximal transmission loss variation while the state of the input light polarization changes over 360°: $PDL = T_{max}/T_{min}$. Any loss measurement method can be applied to obtain PDL using a source of linearly polarized light scanning over all states of polarization. A combination of half- and quarter-wave plates rotating around the optical axis may also transform a fixed state of polarization for any specific wavelength into any desirable state. A common setup for the measurement is depicted in Fig. 11.14. A light beam from source 1 propagates by the idle fiber via spectral selector 2 and linear polarizer 3 to half-wave plate 4 and quarter-wave plate 5 rotating 360°, respectively, in 1.8° and 3.6° steps [11.15]. Light transmitted by fiber 6 under test via depolarizer 7 is measured by detector 8.

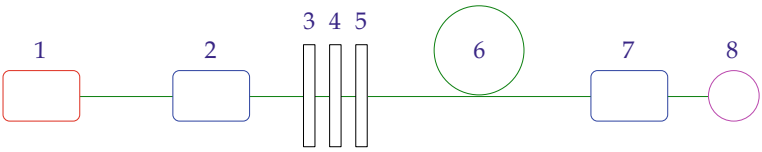

Fig. 11.14 Studies of polarization-dependent losses via rotating waveplates

For an 8°-beveled fiber, experimental PDL values matched the theoretical ones with ±0.002 dB accuracy. Also, instead of using a full 360° scan, one can measure PDL via a Jones matrices algorithm for only three input states of polarization [11.16]. For that purpose, the Jones matrix $\vec{T}$ of the device under test can be identified by the transmission responses of the test device to a linear stimulus parallel to a given axis (k_1), perpendicular to the axis (k_2), and parallel to bisector of the first two axes (k_3). The Jones matrix is:

$$\vec{T} = \beta \begin{bmatrix} k_1 k_4 & k_2 \\ k_4 & 1 \end{bmatrix}, \tag{11.23}$$

where β is a complex constant and $k_4 = (k_3 - k_2)/(k_1 - k_3)$. The maximum to the minimum polarization–transmission ratio, representing PDL, is given by a ratio of the squared Jones matrices [11.17]:

$$\mathrm{PDL} = \vec{\mathrm{T}}_{\max}/\vec{\mathrm{T}}_{\min} = s^2_{\max}(\mathrm{A})/s^2_{\min}(\mathrm{A}). \tag{11.24}$$

Here $s_{max}(A)$ and $s_{min}(A)$ are the single magnitudes of the respective Jones matrix of device A studied.

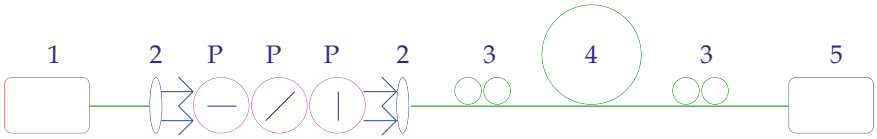

Fig. 11.15 Alternative polarization-dependent loss setup with rotating waveplates: *1*—source; *2*—lens; P-polarizer; *3*—polarization transformer; *4*—DUT; *5*—polarimeter

Figure 11.15 depicts the system for three-polarizer Jones matrix-based PDL testing [11.18]. Solenoid-mounted bulk polarizers P, positioned between objectives 2, define the state of polarization for the parallel beam of light from source 1 further coupled into the fiber under test 4 with its input and output connectors being the polarization transformers 3, whose losses do not depend on the state of polarization. Under the loss-independence assumption, the measured Jones matrix value is not changed by fiber connectors. Via random resets of the connectors' orientation, the single PDL readings were repeatable with ±0.05 dB consistency versus an averaged value [11.18].

For a long line of optical fibers or a network of fibers, connectors, isolators, etc., the total (global) PDL is the statistical sum of PDLs of concatenated elements as a function of the orientation for all optical elements' axes. Since the actual optical axis of a fiber, especially a single-mode one, fluctuates in time, a statistical description for the global PDL is required. Designating the fiber transmission at the depolarized input as: $T_{depol} = (T_{max} + T_{min})/2$, and representing PDL as a three-dimensional vector $\mathbf{\Gamma}$ of length: $\Gamma = (T_{max} - T_{min})/(T_{max} + T_{min})$, the transmission factor T of a single polarization state M_{in} becomes [11.19]:

$$T = T_{depol}(1 + \vec{M}_{in} \cdot \vec{\Gamma}). \tag{11.25}$$

When two concatenated elements, with PDL $\mathbf{\Gamma}_1$ and $\mathbf{\Gamma}_2$, respectively, follow one another, the global PDL $\mathbf{\Gamma}_{1,2}$ is:

$$\vec{\Gamma}_{1,2} = \frac{\sqrt{1-\vec{\Gamma}_2^2}}{1+\vec{\Gamma}_1\vec{\Gamma}_2}\vec{\Gamma}_1 + \frac{1+\vec{\Gamma}_1\vec{\Gamma}_2\left(1-\sqrt{1-\vec{\Gamma}_2^2}\right)\Big/\vec{\Gamma}_2^2}{1+\vec{\Gamma}_1\vec{\Gamma}_2}\vec{\Gamma}_2. \tag{11.26}$$

From Eq. (11.26), statistical data for $\mathbf{\Gamma}_{1,2}$, as the mean PDL or either as $\mathbf{\Gamma}_{1,2}$ minimum or maximum versus $\mathbf{\Gamma}_{1,2}$ or $\mathbf{\Gamma}_{1,2}$ can be obtained [11.20]. For more fiber-line polarization elements, the total PDL would likely be measured as depicted in Fig. 11.16. The orientation of each optical axis for a given fiber is simulated by polarization controllers 4. For up to five concatenated pieces, the agreements

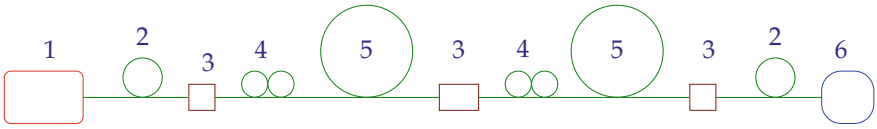

Fig. 11.16 Experimental setup for analysis of total polarization-dependent loss in a fiber network: *1*—source; *2*—idle fiber; *3*—connector; *4*—polarization controller; *5*—DUT; *6*—power meter

between the experimental and the theoretical mean and standard deviation for the PDL were repeatable within 0.01–0.005 dB [11.20].

A fiber transmission system with potential refractive index discontinuities can be degraded by phase-induced intensity noise caused by polarization interference, similarly to a system of bulk elements [11.65]. Certain specifics of phase-to-intensity noise conversion due to interference in fiber transmission systems are further reviewed in Sect. 11.4. Let us for now consider certain optimum propagation settings of a fiber-based system to have low interference noise via analyzing phase retardance of that fiber line, considering the performance of such a line as the noise filter [11.22].

For a substance of distributed birefringence, as a single-mode fiber, with random orientation of its optical axis, the contribution of interference noise can be computed by summing the interference patterns by fiber sections of equal and different numbers of reflections along each birefringent axis and then within a polarization direction. As seen in Sect. 3.3, multiple-path interference in birefringent substances can be represented via two processes for waves with equal and dissimilar numbers of reflections: the comparative and the cross-reference events (see Eq. (3.154)), while only light modes that contribute to the comparative interference have identical amplitudes [3.43]. Presuming arbitrary orientation of optical axis φ_i of a single fiber element i for randomly oriented birefringence axes, and since residual reflections for states of polarization ρ_o and ρ_e on two potential discontinuities in fiber networks are low, let us disregard the interference of waves separated by more than one dual-reflection pass in multiplicity m of all birefringent fiber elements. This means that the products of two squared reflection factors along ordinary and extraordinary axes are negligible in comparison with 1.0: $(\rho_{o1}\rho_{o2})^2 \ll 1, (\rho_{e1}\rho_{e2})^2 \ll 1$. As a result, relation (3.154) for the summarized phase shifts δ, δ_o, and δ_e becomes:

$$I_{\tau,\Sigma,m} = I_0\left[\frac{1-\rho_o}{\sqrt{(1-\rho_o)^2+4\rho_o\sin^2\delta_o}}\sum_{i=1}^{m}\cos\varphi_i\cos(\varphi_i-\gamma)+\frac{1-\rho_e}{\sqrt{(1-\rho_e)^2+4\rho_e\sin^2\delta_e}}\sum_{i=1}^{m}\sin\varphi_i\sin(\varphi_i-\gamma)\right]^2$$
$$-I_0\tau_o\tau_e\left\{\begin{array}{l}\sin^2\left(\frac{\delta}{2}\right)+\rho_o\rho_e\sin^2\left(\frac{3\delta}{2}\right)+\rho_o\sin^2\left(\delta_o+\frac{\delta}{2}\right)+\rho_e\sin^2\left(\delta_e+\frac{\delta}{2}\right)+\\ +\rho_o^2\rho_e\sin^2\left(2\delta_o+\frac{\delta}{2}\right)+\rho_o\rho_e^2\sin^2\left(2\delta_e+\frac{\delta}{2}\right)\end{array}\right\}\sum_{i=1}^{m}\sin 2\varphi_i\sin[2(\varphi_i-\gamma)]. \tag{11.27}$$

Expression (11.27) counts many multiple reflections for birefringent elements within a given fiber-communication line. Let us, only for simplicity, substitute these multiple fiber sections by one effective birefringent element of axis-angle φ_Σ. When

boundary reflectances are low, the number of accepting terms can be reduced via approximation of $\rho_{o1}\rho_{o2} \ll 1,\ \rho_{e1}\rho_{e2} \ll 1$ or $\rho_{o2} \ll 1,\ \rho_{e2} \ll 1$:

$$I_{\tau,\Sigma,s} = I_0\left[\frac{1-\rho_o}{\sqrt{(1-\rho_o)^2+4\rho_o\sin^2\delta_o}}\cos\varphi_\Sigma\cos(\varphi_\Sigma-\gamma)+\frac{1-\rho_e}{\sqrt{(1-\rho_e)^2+4\rho_e\sin^2\delta_e}}\sin\varphi_\Sigma\sin(\varphi_\Sigma-\gamma)\right]^2$$
$$-I_0\tau_o\tau_e\left\{\sin^2\left(\frac{\delta}{2}\right)+\rho_o\rho_e\sin^2\left(\frac{3\delta}{2}\right)+\rho_o\sin^2\left(\delta_o+\frac{\delta}{2}\right)+\rho_e\sin^2\left(\delta_e+\frac{\delta}{2}\right)\right\}\sin 2\varphi_\Sigma\sin[2(\varphi_\Sigma-\gamma)]. \tag{11.28}$$

For a limited coherence length of radiation for multiple wave components of orthogonal phase shifts δ_o and δ_e not to be interfering after some relatively distant propagation, we have:

$$I_{\tau,\Sigma,sgl,uncoher} = I_0\left[\sqrt{\frac{1-\rho_o}{1+\rho_o}}\cos\varphi_\Sigma\cos(\varphi_\Sigma-\gamma)+\sqrt{\frac{1-\rho_e}{1+\rho_e}}\sin\varphi_\Sigma\sin(\varphi_\Sigma-\gamma)\right]^2$$
$$-I_0(1-\rho_o)(1-\rho_e)\left\{\sin^2\left(\frac{\delta}{2}\right)+\rho_o\rho_e\sin^2\left(\frac{3\delta}{2}\right)\right\}\sin 2\varphi_\Sigma\sin[2(\varphi_\Sigma-\gamma)]. \tag{11.29}$$

Figure 11.17 illustrates the spectral transmittance of a quarter-wave retarder for the λ = 1555 nm with properties similar to those of fused silica, and whose optical axis is oriented at 30° to unchanging input–output polarization directions, making γ = 0° and φ = 30°. Computation is based on the presumption of 6% reflections for diamond polished single-mode fiber endfaces. The effects are computed by Eqs. (11.27)–(11.29) versus an ideal case of no reflections (Fig. 11.17, series 4). Although the characteristics of the curves are similar, the equations predict diverse

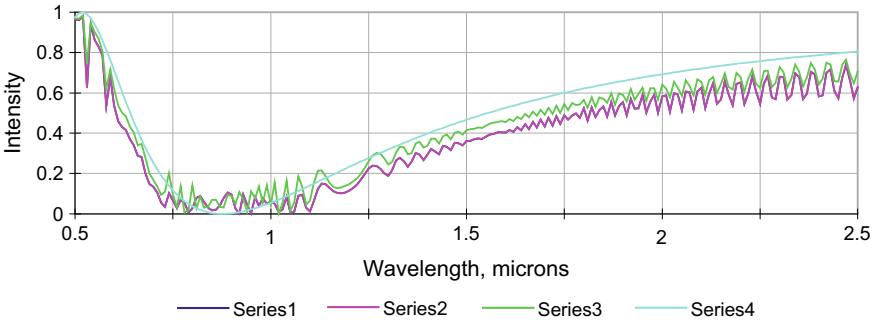

Fig. 11.17 Transmission curves of the quarter-wave retarder for 1555 nm placed between two air gaps: series 1—all effects are counted; series 2—only the first two dual-reflection cycles are included (the curves for series 1 and 2 coincide); series 3—only two-beam interference is computed; series 4—ideal case of no air-gap reflections

intensity noise seen as oscillations of mean intensities. At low reflectances, Eqs. (11.27) and (11.28) give similar results: the curves in Fig. 11.17 for series 1 and 2, with no need to consider all multiple reflections. Reduced Eq. (11.29) clearly gives incorrect transmission (Fig. 11.17, series 3). It is also seen that interference noise is elevated at high and low intensity of the radiation transmitted, being related to the phase retardance in multiples of π. It is different near the 50% intensity points, matching the ideally optimal $\delta_{opt} = \pi/2$. Counting all multiple reflections, the optimal phase shift δ_{opt} changes again, since the dual-path phase shift for each optical axis is not a multiple of π/2 anymore.

Let us consider identifying the optimal phase shift δ_{opt}, which be required to obtain the minimum stimulus for any spectral changes in radiation propagating via the fiber and the lowest interference noise in fiber transmission. Prospective spectral points matching the lowest interference changes of the observe intensity of light, and therefore likely minimal interference noise, correspond to zero magnitudes of second derivatives in transmission. These second derivatives are:

$$\frac{\partial^2\left(I_{\tau,\Sigma,dual}/I_0\right)}{\partial^2\delta} = -\frac{\tau_o\tau_e}{2}\left\{\begin{array}{l}\cos\delta + 9\rho_o\rho_e\cos 3\delta + \rho_o\cos(2\delta_o+\delta) + \rho_e\cos(2\delta_e+\delta) + \\ +\rho_o^2\rho_e\cos(4\delta_o+\delta) + \rho_o\rho_e^2\cos(4\delta_e+\delta)\end{array}\right\}\sin 2\varphi_\Sigma\sin[2(\varphi_\Sigma-\gamma)]. \tag{11.30}$$

$$\frac{\partial^2\left(I_{\tau,\Sigma,sgl}/I_0\right)}{\partial^2\delta} = -\frac{\tau_o\tau_e}{2}\{\cos\delta + 9\rho_o\rho_e\cos 3\delta + \rho_o\cos(2\delta_o+\delta) + \rho_e\cos(2\delta_e+\delta)\}\sin 2\varphi_\Sigma\sin[2(\varphi_\Sigma-\gamma)]. \tag{11.31}$$

$$\frac{\partial^2\left(I_{\tau,\Sigma,sgl,uncoher}/I_0\right)}{\partial^2\delta} = -\frac{(1-\rho_o)(1-\rho_e)}{2}\{\cos\delta + 9\rho_o\rho_e\cos 3\delta\}\cdot\sin 2\varphi_\Sigma\sin[2(\varphi_\Sigma-\gamma)]. \tag{11.32}$$

The second derivatives of the transmission factors in Eqs. (11.30)–(11.32) are shown in Fig. 11.18.

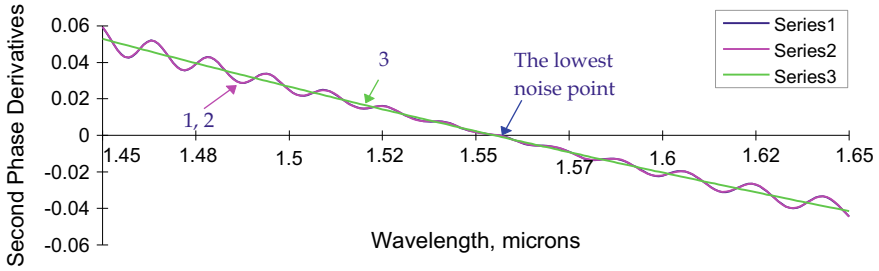

Fig. 11.18 Tuning the optimal wavelength, matching the optimal phase retardance and the point of lowest excessive noise: curves 1–3 were computed by Eqs. (11.30)–(11.32)

The analyzed reduction of birefringence-induced multiple-path interference noise can likely expand the options for designing the transmission and the measurement systems by incorporating fibers with an optimal birefringence for system-specific sections tuned to the optimal spectral transmission. For example, for actual fiber birefringence: $\beta = 2\pi\Delta n/\lambda$, as the inverse linear function of a local fiber beat length: $L_b = \lambda/\Delta n$, Eqs. (11.27)–(11.29) and (11.30)–(11.32) would be supportive in suppressing interference beat noise for a particular wavelength λ or a set of wavelengths propagating the fiber.

11.2 Analysis of Return Losses via Backscattered Radiation

Predominantly, the scattering of light identifies useless dissipation of energy. Although, in addition to making the sky blue, scattering may serve a very useful purpose, since capturing of uniformly scattered radiation by the core of a fiber allows analyzing a longitudinal distribution of internal loss for such a fiber [11.23–11.25]. The amount of light guided by a given fiber depends on numerical aperture NA (view c) in Fig. 11.19 below), matching the maximum acceptance angle Θ_m supporting total internal reflection at that fiber cladding with $\Theta_c = \sin^{-1}(n_c/n_0)$ since angle $\Theta'_c = 90°$. Here Θ_0, n_0 and Θ_c, n_c are the respective angles and refractive indices for core and cladding interfaces. Replacing refracted angle $\Theta'_m = \Theta_0$ via incidence angle Θ_c at core-cladding interface: $\sin\Theta'_m = \sin(90° - \Theta_c) = \cos\Theta_c$, and rewriting Snell's law for light entering the fiber: $(n^2/n_0^2)\sin^2\Theta_m = \cos^2\Theta_c = 1 - \sin^2\Theta_c = 1 - n_c^2/n_0^2$, while presuming the uniform Rayleigh scattering, one obtains [11.25]: $NA = n\sin\Theta_m = n\sqrt{1 - \sin^2\Theta_c} = \sqrt{n_0^2/n_c^2}$. Consequently, the fraction of scattered light guided back and forth by such a fiber is: $G = \Omega/4\pi \cong \pi(n\sin\Theta/n_0^2)^2/4\pi \cong (n_0^2 - n_c^2)/4n_0^2$.

The flux of radiation Φ carried out from a fiber by scattered light in two opposite directions of propagation initiated by incident light and light transmitted via a fiber section of length $\Delta\ell$ is:

$$\Phi = \Phi_0(1 - \rho_0)^2\exp(-\mu\ell_1)\cdot\sigma\Delta\ell G\cdot\exp(-\mu\ell_2), \tag{11.33}$$

where μ and σ are the attenuation and the scattering coefficients of the fixed backscattering fiber section $\Delta\ell$, and ℓ_1 and ℓ_2 are the distances to the points of launching light in and out of the fiber. Following Eq. (11.33), for evaluation of the total internal loss over fiber length $\ell_2 - \ell_1$, it is sufficient to localize the effective source of radiation scattered by the fiber within its section $\Delta\ell$, which must be certainly smaller than the distance difference $\ell_2 - \ell_1$. A few methods of localization are applicable. The most obvious one is done by launching a light pulse of duration $\Delta t = (\Delta\ell\cdot n_0)/c \ll (\ell_\Sigma\cdot n_0)/c$ into such a fiber. Here n_0 and ℓ_Σ are the effective index of refraction of the fiber core and the fiber length. The pulse time interval defines the effective length of the scattering source. As a result, the task for the detector is to resolve the pulse temporarily and to sense the scattering, additionally

attenuated by the length ℓ_Σ. The second method implies a frequency-modulation approach (see Chaps. 8–10). Launching into a fiber cw frequency-modulated light with its coherence length long enough to resolve the fiber's space or time interval provides frequency-dependent information. Consequently, such a frequency scan evaluates the interference pattern distributed along the fiber for reference and scattered radiation. The first procedure is optical time domain reflectometry [11.23–11.25], the second is optical frequency domain reflectometry [11.26–11.28].

For a length of the resolved space interval $\Delta\ell = (c/n_{0,g})\Delta t$, where $n_{0,g} = n_0[1 - (\lambda/n_0)\partial n_0/\partial\lambda]$ is the fiber-core group refractive index, the power P of guided backscattered light [11.23, 11.29–11.31] is:

$$P_{scat} = 0.5P_0\sigma v_{0,g}\Delta t\,\exp\left(-\mu v_{0,g}\Delta t\right)S. \tag{11.34}$$

Here P_0 is the power launched into the fiber, $v_{0,g}$ is the light group velocity: $\Delta t = \Delta\ell/v_{0,g}$, denoting a temporal pulse width, and S is the scattering factor identified by the fiber type:

$$S_{single\text{-}mode} \cong \frac{3/2}{(a_0/a)^2V^2}\frac{n_0^2 - n_c^2}{n_0^2};\; S_{step\text{-}index,\,mult.} \cong \frac{3}{8}\frac{n_0^2 - n_c^2}{n_0^2};$$
$$S_{square\text{-}law,\,mult.} \cong \frac{1}{4}\frac{n_0^2 - n_c^2}{n_0^2}, \tag{11.35}$$

where n_0 and n_c are the refractive indices of the fiber core and cladding: $V = (2\pi a/\lambda)\sqrt{n_0^2 - n_c^2}$ is the fiber normalized frequency, a_0 is the spot size (mode field diameter) of guided light, and a is the fiber core radius. In view of transient Eq. (11.33), backscattered-light loss μ in a homogenous fiber can be estimated in decibel (dB) via the shortened designation "lg" for $\log_{10}$ as:

$$D_{backscat} = -10\lg\frac{P_{scat}}{P_0} = 20\lg\frac{2n_0}{\sin\Theta} + 10\lg\frac{n_{0,g}}{c\Delta t\sigma} + 2\mu\ell\cdot 10\lg e. \tag{11.36}$$

Expressions (11.33)–(11.36) identify the backscattering signal as directly dependent on the geometry and the specific scattering factor of every scanned zone of the fiber under study. Hence, the accuracy of a backscattering measurement of the fiber loss is strongly dependent on the stability of these factors.

Since the light-scattering intensity guided via any fiber is very low, especially for a single-mode fiber, measurements of internal fiber loss via fiber-backscattering signal require exceptionally high detection sensitivity and are mainly based on extensive time integration of individual signals. The principal schematics for implementing the optical time domain reflectometry (OTDR) and optical frequency domain reflectometry (OFDR) techniques are shown in Fig. 11.19. In both systems, a light beam is launched into a test fiber using a mode-matching technique with any idle fiber or some lens objective matching the numerical aperture of the fiber under test. The optical time domain reflectometry technique utilizes a relatively short pulse source, a fast detector, and a boxcar integrator accumulating as many light

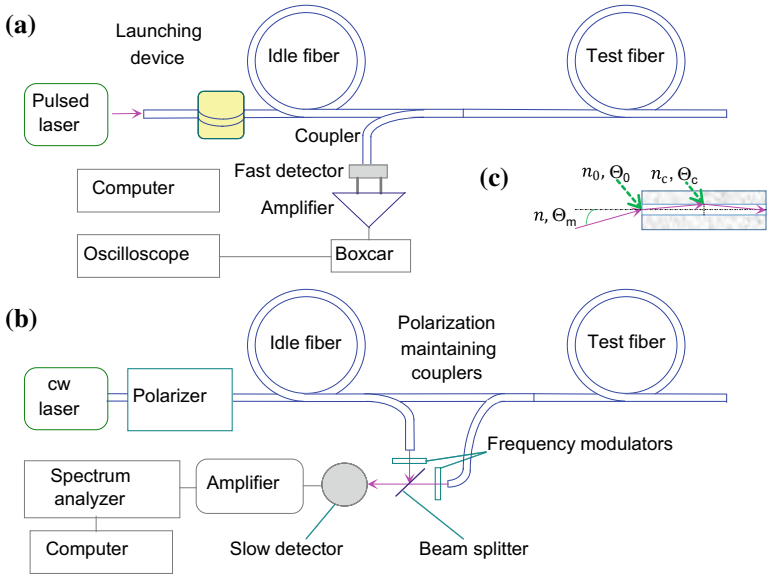

Fig. 11.19 The optical time domain (**a**) plus frequency domain (**b**) reflectometers and the full NA fiber-core launching schematics (**c**)

pulses as are required to reach the desired loss-measurement sensitivity for a not endlessly long time interval for the signal detection. Optical frequency domain reflectometry uses frequency-modulated cw radiation, a relatively slow, but especially low noise detector, and a spectrum analyzer synchronized to the modulation frequency of the optical frequency domain reflectometer, distinguishing two-beam interference of backscattered light with light, reflected from either a reference element or a reference channel and is inherently polarization-sensitive.

By comparing the pulse energy or the maximum power of the pulse for two wave envelopes scattered by equal spatial sections of the test fiber at distances ℓ_1 and ℓ_2, and thus setting the reflectometer to detect scattering signals recognizing a difference between them, the averaged loss $\bar{\mu}$ for length $\ell_1 - \ell_2$ becomes:

$$I_1/I_2 = \exp(-2\mu\ell_1)/\exp(-2\mu\ell_2) = \exp(-2\bar{\mu}\Delta\ell). \tag{11.37}$$

If the fiber length is measured in kilometers, the average attenuation $\bar{\mu}$ is computed in decibels per kilometer as the slope of the logarithmic display of an oscilloscope (OTDR) or spectrum analyzer (OFDR) for the reflectometer:

$$\bar{D}_{fiber} = \bar{\mu} \cdot 10 \lg e = [5 \lg(I_1/I_2)]/(\ell_2 - \ell_1). \tag{11.38}$$

When the linear attenuation coefficient μ of the fiber under study and its geometric extent G or the scattering factor S (see expressions (11.33), (11.35)) are not constant along the fiber length, it is necessary to account for the auxiliary terms: $10 \lg[\sigma_1 \Delta\ell_1/(\sigma_2 \Delta\ell_2)]$ or $10 \lg\left[(\sigma v_{0,g} \Delta t S)_1/(\sigma v_{0,g} \Delta t S)_2\right]$. Independently of the means of mode excitation via the idle fiber or another device, if light is launched into a test fiber with a steady-state mode distribution, a specific dead zone for backscattering measurements always exists, since scattering excites all fiber modes, some of which leak.

Similarly to studying the loss between two points of any fiber, the backscattering measurement can be used to assess the confined fiber loss. An abrupt fault of specular reflectance ρ sets loss D_ρ:

$$D_\rho = -10 \lg\left(P_\rho/P_0\right) = -10 \lg\left[\rho \exp\left(-2\bar{\mu}\ell_\rho\right)\right] = -10 \lg \rho + 2\bar{\mu}\ell_\rho 10 \lg e, \tag{11.39}$$

where P_ρ and P_0 are the reflected and launched power and ℓ_ρ is the distance to the fault of reflection ρ. The reflected signal may be compared with scattering from the nearest scattering point to the fault:

$$D_{\rho,\sigma} = -10 \lg\left(P_\rho/P_\sigma\right) = -10 \lg\left[(\rho/\sigma\Delta\ell G) \exp\left(-2\bar{\mu}\left(\ell_\rho - \ell_\sigma\right)\right)\right] \cong -10 \lg \rho + 10 \lg(\sigma\Delta\ell G), \tag{11.40}$$

where distances ℓ_ρ and ℓ_σ to the fault and to the scattering points are assumed to be equal. The likely nonreflecting fault, such as any splicing joint of unequal fibers, changes the fiber transmission with unequal factors τ_f and τ_b in forward and backward directions. Figure 11.20 depicts fault *J* in a fiber line seen via backscattered light between scattering signals from points A and B:

$$P_A = P_0 G_1 \sigma_1 \Delta\ell \exp(-2\mu_1 \ell_A);$$
$$P_B = P_0 \tau_1 \tau_2 G_2 \sigma_2 \Delta\ell \exp[-2(\mu_1 \ell_J + \mu_2(\ell_2 - \ell_J))],$$

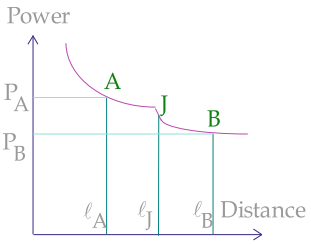

Fig. 11.20 Illustrative OTDR trace via an imperfect splice of two joined fibers

where the first and second fibers are defined by respective scattering and total losses σ_1, σ_2, μ_1, and μ_1. The average optical density D_J of the joint is:

$$D_J = 5\lg\left(\frac{1}{\tau_f \tau_b}\right) = \frac{D_f + D_b}{2} = 5\lg\frac{P_A}{P_B} + 5\lg\frac{\sigma_2 G_2}{\sigma_1 G_1} - D_{A,B}, \tag{11.41}$$

where $D_{A,B} = 10(\lg e)[\mu_1(\ell_J - \ell_A) + \mu_2(\ell_B - \ell_J)]$ is the total fiber-line loss in between points A and B. If the splicing fibers have similar geometry and scattering coefficients, relation (11.41) becomes:

$$D_J = 0.5\left(D_f + D_b\right) = 5\lg(P_A/P_B) - 10\,(\lg e)[\mu_1(\ell_J - \ell_A) + \mu_2(\ell_B - \ell_J)]. \tag{11.42}$$

Owing to the limited resolutions of optical time domain reflectometers and changes of the power distribution of radiation passed by imperfect fiber joints, local faults often look like longitudinal joints of loss decays (see Fig. 11.21). Thus, most reflectometers use curve-fitting techniques to evaluate linear attenuation coefficients μ_1 and μ_2 in two joined fibers, and the loss μ_J in a fiber joint is estimated as the difference of two logarithmic decays $\ell_2 - \ell_1$ and $\ell_4 - \ell_3$, extended to the middle point ℓ_J of such a fiber joint (see Fig. 11.21). Another way of approximating for actual splice loss μ_J can be made by an auxiliary detection of the average fiber-line loss $\hat{\mu}$ between any two distant points $\ell_1 - \ell_4$ [11.32]. By measuring the losses μ_1, μ_2, $\hat{\mu} = 0.5(\mu_1 + \mu_2)$, and μ_J from alike zones $\ell_2 - \ell_1 = \ell_4 - \ell_3 = \Delta\ell$ and $\ell_J - \ell_2 = \ell_3 - \ell_J = \Delta J$, the splice loss $\hat{\mu}_J$ averaged over all points is:

$$\hat{\mu}_J = \mu_J + [0.5(\mu_1 + \mu_2) - \hat{\mu}](\Delta\ell + \Delta J). \tag{11.43}$$

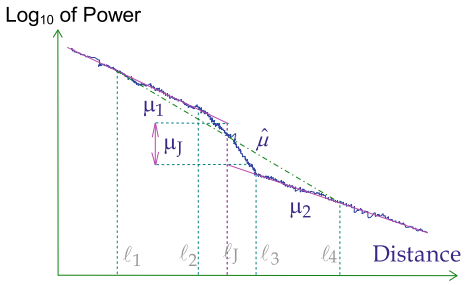

Fig. 11.21 Continuous trace of a fiber splice or joint

Owing to uneven mode excitation, backscattering measurements of optical losses in the fiber joints are more accurate if they are performed in two opposite directions of light propagation via one connecting fiber.

To advance the capabilities of time- and frequency-domain reflectometry, feasible development efforts primarily expand the dynamic range and spatial resolution of reflectometers. For conventional pulsed-echo OTDR this means increasing the peak power of the pulse limited by nonlinear effects, shortening the pulse width, and

applying single-photon and multiphoton counting techniques [11.33–11.38]. Another way of advancing the measurement capabilities is by automating the scattering-trace analysis, while presuming constancy of derivatives for the logarithmic scattering trace in a fiber not containing any discontinuities [11.39]. Setting up a meaningful threshold level for fluctuations of the fiber scattering losses, the discontinuity can be measured via the highest absolute value of the derivative (Fig. 11.22). The respective return of the derivative trace to the preset threshold characterizes the end of intermission within the limit of the OTDR pulse width. Any reflective faults initiate two opposite extremes (see the traces in Fig. 11.22). Therefore, a fiber end can be estimated by notable noise following fiber-end reflection [11.39]. Some practical realizations of automated reflectometers reached nearly 10^{-15}-W in sensitivity with the spatial resolution of a few nanometers [11.35, 11.36].

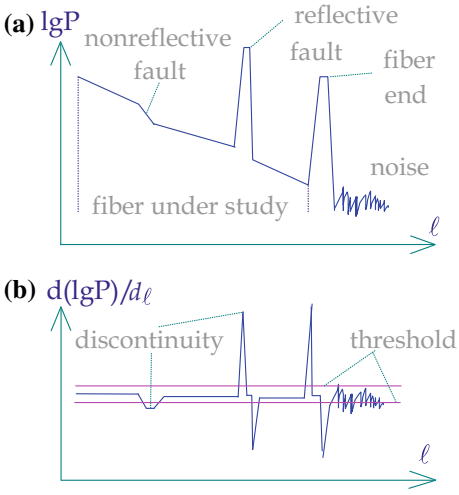

Fig. 11.22 Expanded OTDR loss trace (**a**) and loss-derivative trace (**b**)

Further progress in improving the sensitivity of OFDR measurements was made via low-coherence white-light interferometry [11.40–11.47]. The technique makes the frequency-domain reflectometer perform as an interferometer, spatially separating interfering scattered and modulated reference radiation, keeping the desired limits of the coherence length for any light source applied as low as possible [11.40, 11.41]. Two common structures for white-light low-coherence interferometers are illustrated in Fig. 11.23. In Fig. 11.23a the reflectometer functions as a Michelson interferometer, but is arranged with two unequally reflective arms [11.40], realizing the interference via a bidirectional coupler as:

$$P(t) = P_0 K(1-K)\left[1 + S_i^2 R_i + 2S_i\sqrt{R_i}\left|\gamma_{1,2}(t)\right|\cos\Theta\right]. \qquad (11.44)$$

Here P_0 is the incident radiant power, K is the coupler splitting ratio; S_i^2 and R_i are, respectively, the powers of radiation scattered back and forth and of radiation reflected from the mirror's i^{th} component of light; $\Theta = 2\pi ft + \varphi_0$ is the phase

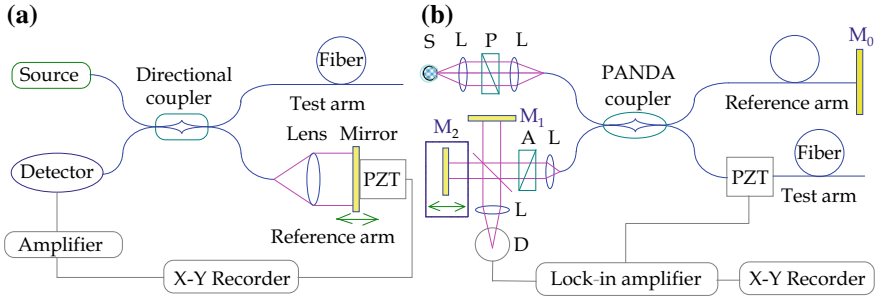

Fig. 11.23 White-light optical frequency domain reflectometers–interferometers

difference, $|\gamma|$ is the modulus of the normalized correlation function of radiation in each arm of the interferometer, and f is the modulation frequency. The intensity envelope of radiation registered by the interferogram is defined by a complex degree of spatial coherence of a quasi-monochromatic light source used via function $|\gamma|$ (see Sect. 3.3), with its width Δt inversely proportional to the spectral width Δf of the source. The visibility of the pattern is determined by the intensities of two interfering beams [11.40]:

$$V_i(t) = \frac{2S_i\sqrt{R_i}}{1+S_i^2R_i}\left|\gamma_{1,2}(t)\right| \;\; at \;\; \Delta t = \frac{4\ln 2}{\pi\Delta f}; \;\; \Delta\ell \cong \frac{v_g}{2\Delta f}. \tag{11.45}$$

Here the spectral distribution of radiation is presumed to be a Gaussian function, $\Delta\ell$ is the final linear resolution of the interferometer, and $v_{g,0}$ is the group velocity of radiation in the fiber. The resolution of the system is not directly affected by coupling ratio K, since it only redistributes light into two arms.

The reflectometer shown in Fig. 11.23a operated using a cw light-emitting diode having $\Delta\lambda \cong 130$ nm spectral bandwidth, centered at 1300 nm, injecting about 50 nW into the interferometer arms, made of two 1.5-m-long single-mode fibers. The reference arm mirror scanned over a 7.5-cm span at about 90-μm resolution. The interference signal modulated by translation was measured by an InGaAs detector in photovoltaic mode with a 1-Hz-wide passband, sufficient for less than 13 μm of spatial resolution of that system. Such a level of resolution allowed even tiny changes in the length of the test objects to be distinguished, such as the removal of material during polishing of a fiber end, in the test arm via the interference fringe shift: $\Delta\ell = m\lambda/2n$, where n is the refractive index of the fiber core and m is the number of shifted fringes. The measured derivative of the interferometer's propagation time over the stress applied to the fiber: $\mathrm{d}t/\mathrm{d}\sigma = 1/c\,(nd\ell/d\sigma + \ell dn/d\sigma)$ (cf. Eq. (9.46)), confirmed the stress sensitivity reaching 60 ps/km/MPa. The overall sensitivity to the group index of fiber refraction, as the ratio of fiber's optical length to its length in air $n = \ell_{air}/\ell_{optical}$, was estimated to be $5\cdot10^{-4}$ [11.40]. Such a high spatial resolution also permits sensing of local-loss distributions in waveguides [11.79].

Figure 11.23b depicts the scheme of a twofold interferometric reflectometer for spatial profile analysis via the auxiliary time delay in the reciprocally connected Michelson interferometer. Polarized light from source S via polarizer P and the polarization-maintaining PANDA coupler enters the main fiber-based Mach–Zehnder interferometer. The scattered-light profile in the measured fiber is compared with radiation in the reference arm, reflected by mirror M_0 and further selected by the PANDA coupler to free-space Michelson interferometer MI. Piezoelectric transducer PZT modulates radiation scattered by the fiber at frequency f to be registered by a lock-in amplifier. Two sections of a test fiber separated by the least distance $\Delta\ell$ could be resolved, if signals scattered by them do not produce any resolvable interference pattern because of insufficiently-small coherence length of the light source over a too short of a distance.

A typical interferogram resolved by a single interferometer, as one in Fig. 11.23a, is illustrated in Fig. 11.24 (interferogram a), representing the entire test fiber line. An adjustable additional delay, executed by the reference arm of the second interferometer via scanning mirror M_2, allowed allocation of sequential wave packets of backscattered radiation in a given vicinity and also avoidance of signals from needless sections of the fiber line studied (Fig. 11.24, interferogram b).

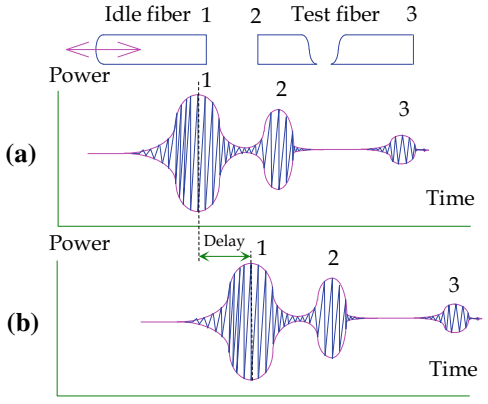

Fig. 11.24 Interference envelopes for radiation scattered within the fiber line

For verification of the spatial resolution attained by the twofold interferometric reflectometer in Fig. 11.23b, a calibrated 1.18-cm-long section of a single-mode fiber was used [11.41]. By utilizing a superluminescent light-emitting diode emitting λ = 830-nm center line with a coherence length $\ell \cong 50\,\mu$m modulated at frequency f = 6 kHz, the first limit of the spatial resolution was reached: $\ell/n_f = 17\ \mu$m, where n_f is the refractive index of the fiber. In further experiments [11.43–11.45], the lowest resolution limit was improved to 14 μm when using separate output couplers for the reference and measuring arms of the interferometer. To exclude the observed coherent jagging of light backscattered by the fiber, the measured signal was also guided in and out of each fiber by a polarization-insensitive coupler. Further improvement of optical resolution, including dead-zone removal, can be achieved via single-photon counting of spontaneous Stokes Raman

emission instead of Raleigh scattering [11.80–11.82]. Analogously, Brillouin scattering-distribution analysis along the fiber are used for OTDR/OFDR reflectometry [11.111–11.113], as well as the digital-range gating and other versions of time-gating techniques are applicable for enhancements of spatial and spectral resolution or sensitivity [11.109, 11.110].

11.3 Partition of Distributed Losses and Attenuation Factors in Reflected Light

The reviewed techniques of backscattering measurements of intrinsic fiber losses are intended to detect inherently low levels of radiation internally scattered by a fiber, guided backward toward a collocated source and a detector of radiation via one beam splitter. Owing to the capabilities for analyzing losses from one end of the fiber and the applicability of the techniques to virtually any distributed fiber sections, when various coupling losses are being sensed, backscattering reflectometers are irreplaceable for a variety of fiber-network testing. At the same time, reflection from the fiber endface due to Fresnel reflectance on a glass–air or silica–air interface is orders of magnitude more intense than that caused by Rayleigh scattering. Therefore, many efforts have been made to use Fresnel reflectance as a reference for absolute backscattering measurements via already available OTDRs and OFDRs [11.1, 11.48–11.57]. A mirror coupled to the far end of a fiber may presumably be a better reflectance standard than the silica–air fiber interface of an open connector, but its reflectance is 2 orders of magnitude higher. A high-reflection signal versus uniform scattering could affect the reflectometer's performance and make detection of the scattering itself impossible in fiber zones adjacent to the high reflectance. To prevent the occurrence of dead zones, most reflectometers have masking features, suppressing any Fresnel-reflectance regions which highly contradict fiber scattering from being captured [11.49].

An absolute calibration of return-loss scale can be provided via a close-to-unity reflectance of any mirror being measured similarly to a line fault by detecting back-propagation transmission loss [11.50]. Radiation reflected by a mirror propagates back, initiating corresponding scattering, which, in turn, travels in the forward direction to be finally reflected from the mirror one more time and considered by the reflectometer as propagating the existing fiber line. Hence, if the scattering loss is measured before and after the image of the mirror, any supplemental loss μ present in such a prolonged line is equal on logarithmic scale to a twofold mirror reflectance 2ρ, plus a dual loss on connection of that mirror to the fiber endface: 2χ. Consequently, a high reflectance of the mirror itself could be masked, adding intermediate reference points. If such a mirror reflectance is known, the absolute error of calibration is only doubled owing to dual propagation via the mirror: $\Delta\mu_{abs} = 2(\Delta\rho + \chi)$.

Another calibration scheme provides artificial 100% reflectance via a fiber loop [11.52]. First, an OTDR, connected to a loop coupler, summarizes two conversely transmitted light streams:

$$P_{\leftrightarrow} = 2P_0\tau^2{}_{cpl\leftrightarrow}\exp(-\mu_{lp}\ell_{lp})_{\leftrightarrow}, \tag{11.46}$$

where $\tau_{cpl\leftrightarrow}$ is the back plus the forward coupler transmittance, and μ_{lp} and ℓ_{lp} are the attenuation factor and the length of the loop (Fig. 11.25). In the second step, the loop is cut in the middle, and the two scattering signals from the symmetrical halves, functioning as a dual-scattering source, are measured together:

$$\begin{aligned} P_{two} &= P_0\tau^2_{spl,left}\sigma v_{0,g}\Delta tS[\exp(-\mu_{lp}\ell_{lp})_{left} + \tau^2_{spl,right}\exp(-\mu_{lp}\ell_{lp})_{right}] \\ &= P_0\tau^2_{spl,\leftrightarrow}\sigma v_{0,g}\Delta tS\exp(-\mu_{lp}\ell_{lp})_{\leftrightarrow}. \end{aligned} \tag{11.47}$$

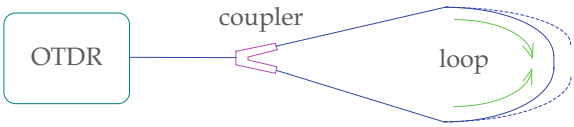

Fig. 11.25 Absolute calibration of fiber scattering losses

Assuming $\mu_{lp,left} = \mu_{lp,right}$, one can determine the fiber scattering factor σ at a given spatial resolution as:

$$F_{scat} = \sigma v_{0,g}\Delta tS = P_{two}/P_{\leftrightarrow}. \tag{11.48}$$

An attenuator can also be placed in the loop, reducing power $P_{at} = P_{\leftrightarrow}\tau_{at}$ by its attenuation: τ_{at}.

Practically every backscattering procedure, except for the two calibration techniques just discussed, struggles to extend its dynamic range and spatial resolution when applied to loss measurement, which is required to have some absolute loss scale. The ability to verify the absolute magnitude of a loss can only partially improve each procedure. At the same time, a correctly cleaved or polished fiber end which is easily accessible in any fiber line can be a reliable specular mirror with orders of magnitude higher reflectance than that of the scattering guided by a fiber. Under appropriate conditions [10.77–10.80] (see Sect. 10.5), any glass–air border reflectance is proven not to change within $\pm(1-2)\cdot10^{-4}$ or less for stable border surroundings. Since the level of fiber-end reflectance is much higher than the intensity of Rayleigh scattering guided by a fiber, the accuracy and spatial resolution of OTDRs or OFDRs could be accordingly improved by registering fiber-return loss using reflected light, keeping in mind that the backscattering method by itself has many useful advantages, which should be maintained – such as not requiring access to cleaved fiber ends. A joint backscattering plus reflection technique would be effective in providing sensitive and persistent measurements of return losses in fibers.

Prior to reviewing the techniques for backscattering and backreflection return-loss measurements, let us examine a method of optical cw reflectometry (OCWR) detection of loss [11.51]. That technique involves multiple steps, five to be exact, allowing a straightforward cw light source and power meter to be used (Fig. 11.26). If the intensity output I_0 of source S and the sensitivity K of detector D are unchanged for all five steps, the respective equations are:

$$I_a = kI_0\tau_{12}\tau_C; \quad I_b = kI_0\left(\tau_{13} + \tau_{12}\tau_{13}\tau_C^2\rho_X + \tau_{12}\tau_{13}\tau_C^2(1-\rho_X)^2\rho_{T1} + \tau_{14}\tau_{43}\rho_{T2}\right);$$
$$I_c = kI_0\left(\tau_{13} + \tau_{12}\tau_{23}\tau_C^2\rho_{T3} + \tau_{14}\tau_{43}\rho_{T2}\right); \quad I_d = kI_0\tau_C\tau_{23}; \quad I_e = kI_0. \tag{11.49}$$

Here τ_{ij} is the transmittance of four-port coupler O between two chosen ports i and j, and ρ_X, ρ_C, ρ_{T1}, ρ_{T2}, and ρ_{T3} are the measured, connecting, and terminating reflectance magnitudes, respectively. Providing that intensity I_0 and sensitivity K remain constant, and terminations ρ_{T1} and ρ_{T3} are equal, one can subtract intensity reading I_c from I_b, under the presumption of low reflectivity $\rho_X \to 0$, and therefore $(1 - \rho x)^2 \to 1.0$:

$$I_b - I_c = k\,I_0\left(\tau_{12}\tau_{13}\tau_C^2\rho_X + \tau_{12}\tau_{13}\tau_C^2(1-\rho_X)^2\rho_{T1} - \tau_{12}\tau_{13}\tau_C^2\rho_{T1}\right)$$
$$\underset{\rho_X\to 0}{=} kI_0\left(\tau_{12}\tau_{13}\tau_C^2\rho_X\right). \tag{11.50}$$

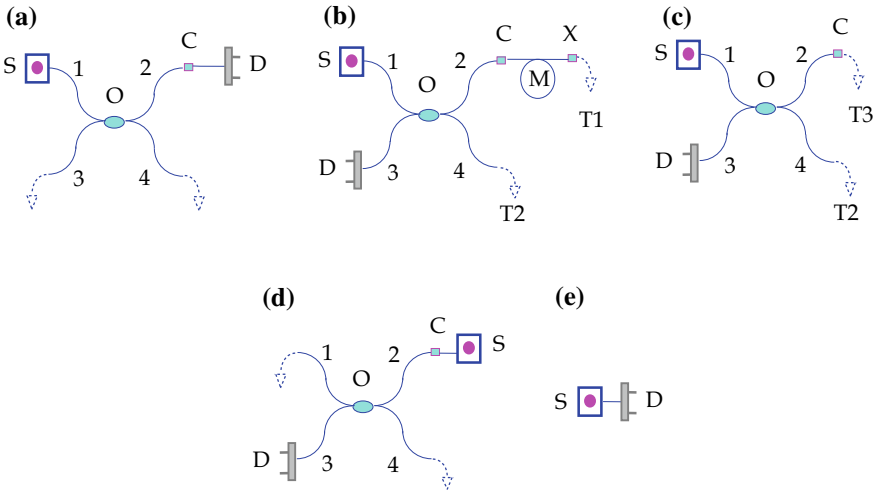

Fig. 11.26 Optical continuous-wave reflectometry measurement technique – steps (**a**) through (**e**)

Finally, the measured reflectivity ρ_X of low-reflectivity connector X under the presumption of stability is:

$$\rho_X = (I_b - I_c) \cdot I_e / (I_a \cdot I_d). \tag{11.51}$$

Considering the number of assumptions involved, the OCWR technique is more a performance verification for fiber–connector interfaces rather than a reflectance test. As a reflectance and transmittance measurement method for local discontinuities, one can rather sense loss-induced fiber or waveguide perturbations in an arm of a Michelson interferometer-reflectometer [11.103].

Instead of performing multiple OCWR reflectometry steps, not yet ensuring high accuracy for a reflectivity loss to be measured, owing to multitude of assumptions even if a fiber cutback method is used between steps b and c in Fig. 11.26, one can attempt to differentiate the contributions of distributed Raleigh backscattering and point-bounded reflectivity of a connector or a splice [11.51–11.53]. A concept for such separation is based on several assumptions which are quite difficult to quantify, such as the stability of the backscattering coefficient of the fiber at each reflection discontinuity, or a known form factor of a light pulse injected into the fiber and then backscattered and backreflected without any distortion, especially considering the extremely low magnitudes of Raleigh backscattering in fibers.

When performing measurements of diverse fiber losses by scattered and reflected light, it is valuable to separate the impact of every attenuation factor. Several conceivable concepts for measuring a reflectivity spike can be invoked via graphs shown in Fig. 11.27. If a joint of two fibers reflects incident light, the joint's scattering characteristics are masked by the impact of an intense broadened reflection. By detecting the average backscattering loss μ_1 and μ_2 for each joined fiber and approximating the length of loss lines to joint point J (Fig. 11.27a), one can roughly identify misalignment loss μ_J in the connection as $\mu_J = (\mu_1 - \mu_2)_J$. Reflection loss μ_R in the joint becomes: $\mu_R = (\mu_\Sigma - \mu_1)_J$, where μ_Σ corresponds to the sum of backreflection and backscattering. Another approach is based on

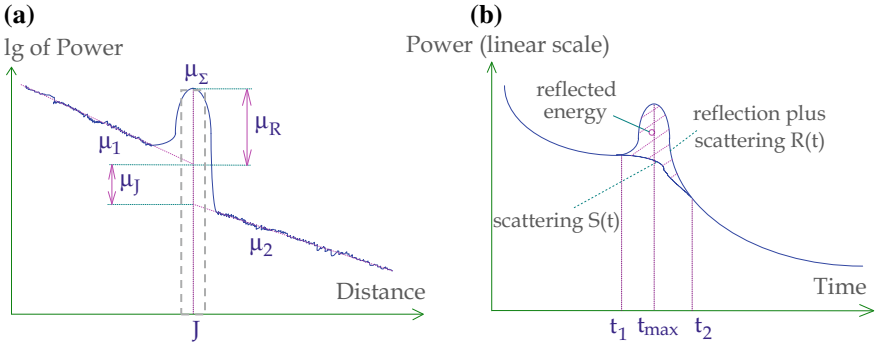

Fig. 11.27 Separation of end-reflection and scattering phenomena via substitution (**a**) and integration (**b**) of inner-fiber losses

approximating and identifying fiber discontinuities in reflection by rectangular pulses [11.51]. Substituting the energies of the backscattered and reflected pulses by rectangular areas under and above a continuation of Raleigh scattering, one may approximate the reflectivity at the detriment of ambiguity for a given pulse form and its duration (dotted area in Fig. 11.27a).

One more approach for partition of reflection and scattering joint losses is associated with step-by-step integration of the impact of a pulsed reflection (Fig. 11.27b) and subtraction of the scattering pulse S(t) portion from the total magnitude estimated from the properties of a given fiber [11.53]. Since time integration of a power stroke provides a scaled power measurement of the energy, integration of the entire impact gives the reflectance ρ as the difference: $\rho(t_1, t_2) = \text{const} \cdot \left[\int R(t_1, t_2)\, dt - \int S(t_1, t_2)\, dt\right]$ between total and scattered energies. Precautions must be taken when detecting time instances t_1 and t_2 for the beginning and the end of the impact of reflection. Since commonly an OTDR pulse response is not rectangular, the start and the end of integration can be gauged by symmetrical energy partition of each pulse into rise and decline zones. Either time pitch or time windowing of the reflected and backscattered light signals should permit one to detect and then extract additive noise added to the signal [11.53]. The iterative search may be also performed to locate the maximum of the reflectance-plus-scattering trace [11.83].

The analyzed measures for accurate examinations of the impacts of reflection of fiber ends and joints can be used to establish other measurement procedures, detecting internal fiber loss via only fiber-end reflection. That should be beneficial in a zone when light scattered by remote portions of a long fiber is not distinguishable from noise, but fiber-end reflectance produces the only accessible signal, or if the fiber under test is shorter than the effective pulse width of the OTDR used. Let us consider the possibility of obtaining absolute measurements of internal losses in a fiber by observing the intensities of pulses reflected from fiber endfaces. Let us initially set each endface to be either perfectly cleaved or included in a fiber connector, verified by other means as of sufficient surface quality [11.54].

One quite contrasting measurement method is similar to detection of internal bulk losses in reflected light (Sects. 10.4, 10.5). The main difference when applied to fibers (Fig. 11.28) is defined by the lack of options for using wedged samples to split two interfering sample-end reflection signals. Either pulsed or spatially modulated radiation will provide a separation of end reflections. A four-port instead of a

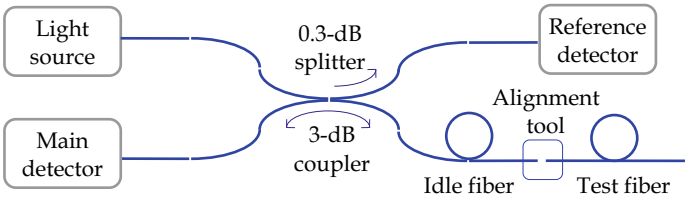

Fig. 11.28 Dual-beam reflection-scattering time-domain reflectometer

three-port directional coupler is utilized to compensate for fluctuations of either power or energy emitted by the source by way of low-loss coupling: 0.3 dB in the reference path and 3 dB of attenuation in the main return path, equivalently splitting light propagating back and forth. Since a reference path detector follows power or energy fluctuations of the source, any fluctuations will be further considered as absent within the margins of inaccuracy of the chosen ratio-based registering system.

For the first step of the measurement procedure, only a sufficiently long idle fiber exists in the measurement system as an integral part of it. Two main functions of the idle fiber are to provide the consistent reference reflectance from its output end and to retain the steady-state mode distribution on its double length for back-and-forth transmission of radiation which entered the fiber under study. Thus, during that first step, the reflectometer measures the signal reflected from the output end of the idle fiber:

$$N_i = const \cdot \exp(-2\mu_i \ell_i) \cdot \rho_i = const \cdot \exp(-2\mu_i \ell_i) \cdot [(n_i - 1)/(n_i + 1)]^2. \quad (11.52)$$

Here *const* stands the source power or energy, the main detector sensitivity, and the properties of the four-port coupler combined, and μ_i, ℓ_i, ρ_i, and n_i are the linear attenuation coefficient, length, reflectance, and group refractive index of the idle fiber. On the logarithmic scale counting the dual light path, the signal is:

$$\begin{aligned} P_i = const - 10\mu_i \ell_i \cdot \lg \mathrm{e} + 5 \lg \rho_i = const - 10\mu_i \ell_i \cdot \lg \mathrm{e} \\ + \ 10 \lg(n_i - 1) - 10 \lg(n_i + 1). \end{aligned} \quad (11.53)$$

This first step serves only for calibration of the measurement system and can be periodically repeated to verify its actual stability. In the second step, the fiber under study, similar to the idle fiber from the mode-coupling standpoint, is placed into the transmission–reflection path of the reflectometer. Let us first consider the fiber connection via an air gap, whose length $\Delta\ell_{air}$, intensified by multiple reflections, is much smaller than the reflectometer resolution: $\Delta\ell_{air}/(1 - \bar{\rho}^2) \ll \Delta\ell_{fiber}\bar{n}_{0,g}$. Here $\bar{\rho}$ and $\bar{n}_{0,g}$ are the mean reflectance and the group refractive index for the idle and test fibers. If both the output end of the idle fiber and the input end of the test fiber are similarly cleaved to be aligned perpendicularly to both fiber axes and they are aligned concentrically to each other, the new signal, for radiation multiply reflected from the entire gap on a linear and on a logarithmic scale, respectively, is:

$$\begin{aligned} N_{gap} = const \cdot \exp(-2\mu_i \ell_i) \cdot \left[\rho_i + \frac{(1 - \rho_i)(1 - \rho_f)}{1 - \rho_i \rho_f} \rho_f \right] = const \cdot \exp(-2\mu_i \ell_i) \cdot \\ \cdot \left[1 + \frac{1 - \rho}{1 + \rho} \right] \rho = const \cdot \exp(-2\mu_i \ell_i) \cdot \frac{2\rho}{1 + \rho}; \end{aligned} \quad (11.54)$$

$$P_{gap} = const - 10\mu_i\ell_i \cdot \lg e + 5\lg[2\rho/(1+\rho)] = const - 10\mu_i\ell_i \cdot \lg e + 10\lg(n-1) - 5\lg(n^2+1). \quad (11.55)$$

Here ρ_f is each fiber reflectance, and ρ and n are the average reflectance and refractive index of the idle and main fibers for the steady-state mode distribution. As the third, final step, light transmitted along the entire line and reflected from the far end of the test fiber is measured, keeping the alignment of the air gap:

$$N_f = const \cdot \exp(-2\mu_i\ell_i) \cdot \left[\frac{(1-\rho_i)(1-\rho_f)}{1-\rho_i\rho_f}\right]^2 \cdot \exp(-2\mu_f\ell_f) \cdot \rho_f = const \cdot \exp(-2\mu_i\ell_i) \cdot \left(\frac{1-\rho}{1+\rho}\right)^2 \cdot \exp(-2\mu_f\ell_f) \cdot \rho; \quad (11.56)$$

$$P_f = const - (\mu_i\ell_i + \mu_f\ell_f)10\lg e + 10\lg(2n) - 10\lg(n^2+1) + 10\lg(n-1) - 10\lg(n+1). \quad (11.57)$$

One can see that the difference of gap N_{gap} to idle N_i reflectivities related to N_i or $2\cdot(P_{gap} - P_i)$ is:

$$(N_{gap} - N_i)/N_i = (1-\rho)/(1+\rho) \quad \text{or} \quad 2(P_{gap} - P_i) = 10\lg[1 + (1-\rho)/(1+\rho)]. \quad (11.58)$$

As a result, comparing three signals – reflected from the end of the idle fiber, air gap, and end of the test fiber – gives:

$$\frac{N_f N_i}{(N_{gap} - N_i)^2} = \exp(-2\mu_f\ell_f) \quad or \quad \mu_f\ell_f[dB] = 0.23\{P_i - P_f + 10\lg[10^{0.2(P_{gap}-P_i)} - 1]\}. \quad (11.59)$$

As can be seen from relations (11.52)–(11.59), this technique of evaluating internal loss in a fiber is equivalent in its sensitivity to the internal bulk loss measurement in reflected light (Eq. (10.44)):

$$N_1/N_2 = (1-\rho)^2 \exp(-2\mu\ell), \quad (11.60)$$

where the first factor represents the double surface transmission. In such a fiber loss measurement, the air gap serves as an air-based plate, secured by endfaces of idle and test fibers. Fluctuations of the internal fiber loss evaluated in reflected light can be derived from Eqs. (11.59) and (11.60):

$$\Delta\mu_f\ell_f = \Delta\rho/(1-\rho) + \Delta P_f + \Delta P_i + \Delta(P_{gap} - \Delta P_i) \quad or \quad \Delta\mu_f = \Delta\rho/[(1-\rho)\ell_f] + 3\Delta P/\ell_f, \quad (11.61)$$

where ΔP is the mean error of a single power or energy measurement by the reflectometer. Accordingly, even the increased number of measurements by the procedure discussed does not significantly affect the measurement accuracy, since even at $\Delta\rho/\rho = \pm 5\%$ (0.21 dB), $\Delta P = 0.03$ dB, and $\Delta\rho/(1 - \rho) = \pm 0.01$ dB, the error is $\Delta\mu = \pm 0.1$ dB for 1-km fiber length and is ± 0.02 dB for 5 km. For shorter fiber lengths, the accuracy of signal detection by the reflectometer needs to be higher, or the procedure should be less complicated.

As seen from Eqs. (11.40)–(11.42), the air-gap reflection signal is almost 2 times higher than that for the single endface. Even such a small reflection signal can affect the performance of an OTDR, especially for an idle fiber that is long enough although highly transparent, not to noticeably reduce the dynamic range of the reflectivity study. The necessity to measure the intensities of signals reflected by air gaps is mainly dictated by a likely misalignment of joint fiber ends and potential imperfection of their reflectances. Also, a high air-gap reflection signal does not provide assurance for concentricity of two connected fibers, since the magnitude of reflectance does not change with tiny transverse misalignments of fiber cores for fiber ends parallel to each other. Therefore, even when measuring the reflectance of an air gap, one must maintain the alignments of the test fibers by reaching the relative maximum of reflectance from the farther endface of the fiber being aligned. The idle and test fiber alignment can also be simplified by evaluation of the surface quality of the endfaces of both fibers and their junctions.

Let us, once more, pay attention to the high sensitivity of reflection-based measurements to the optical status of fiber endfaces in reflected light. As was demonstrated by Eqs. (2.40) and (2.45), the relative sensitivity of any reflection versus transmission measurement of the optical status for a single glass–air border is orders of magnitude higher. As follows from Eqs. (11.41) and (11.42), for a measurement of the combined reflectance for two joined fiber endfaces forming an air gap, the actual sensitivity due to the $2\rho/(1+\rho)$ factor is nearly 2 times higher (compare the low-reflectivity resonators in Chaps. 8 and 10). Accordingly, the relatively high sensitivity of the reflection-based measurement method to changes in the optical properties of the joined fiber endfaces and their mutual alignment – even when the changes are realized far from the measuring device and are viewed remotely within the dynamic range of this system – can be utilized to evaluate the surface conditions of fiber endfaces, cleaved for any connection or a splice [11.55]. Conceivable measurement techniques consist of two sequential steps: measuring the face reflectance of the output end of an idle fiber, serving as a relative reflection standard, and measuring the reflectance of its gap with the endface under study (Fig. 11.29). Any likely procedure could measure the average group index of refraction $\bar{n}$ of joined fibers as:

$$\begin{aligned} N_{idle}/N_{gap} &= 2/(1+\bar{\rho}) = (\bar{n}+1)^2/(\bar{n}^2+1) \quad \text{or} \quad P_{idle} - P_{gap} \\ &= 10\lg(\bar{n}+1) - 5\lg(\bar{n}^2+1), \end{aligned} \tag{11.62}$$

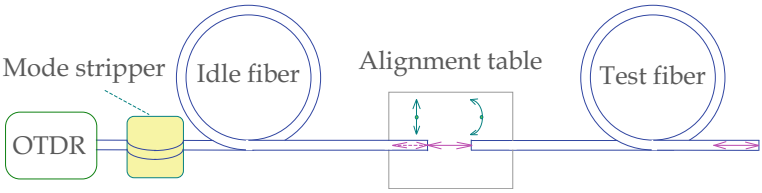

Fig. 11.29 Evaluation of fiber endface and connection losses

or could serve to compare the reflectance ρ_x of the studied fiber versus the known reflectance ρ_i of the idle fiber. In that case, transformation of Eqs. (11.49) and (11.51), in view of similar Eq. (8.61) for two unequal surfaces of reflective bulk samples, gives a quotient to be further resolved to obtain ρ_x:

$$(N_{idle}/N_{gap}) = 1 + (\rho_x/\rho_i)(1-\rho_x)^2/(1-\rho_i\rho_x), \text{ at } \rho_x \neq \rho_i. \tag{11.63}$$

An identical attempt can be made to evaluate splicing or connecting losses for two fibers, the first of which serves as the idle fiber for such a measurement method [11.56]. Three successive steps of reflectance measurements – from the output end of the first fiber, from the air gap of the joint for first and second fibers, and from the far end of the second fiber with the joint left unchanged – provide the loss measurement in the second fiber by relations (11.59). After the splice has been made, the only one measurement of reflection N_{spl} from the far end of the fiber has to be repeated. Its ratio with N_{idle} gives:

$$(N_{spl}/N_{idle}) = \tau_{spl,left}\cdot\tau_{spl,right}\cdot\exp(-2\mu\ell)_{sec.\,fiber} = \bar{\tau}^2_{spl}\exp(-2\mu\ell)_{sec.\,fiber}; \tag{11.64}$$

$$10\lg\bar{\tau} = P_{spl} - P_{idle} + 10\lg e\cdot(\mu\ell)_{sec.\,fiber}, \tag{11.65}$$

where $\bar{\tau}$ is the transmittance of the splice, averaged for the forward and backward propagation of the light guided by fibers. As a result, the total splice loss: $\chi_{spl} = 1 - \tau_{spl}$, is obtained by the equation:

$$\bar{\chi}_{spl} = 1 - \frac{N_{gap} - N_{idle}}{N_{idle}}\sqrt{\frac{N_{spl}}{N_{far\,end}}} = 1 - \exp(-\mu\ell)_{sec.\,fiber}\sqrt{\frac{N_{spl}}{N_{idle}}}. \tag{11.66}$$

Despite the relatively high sensitivity of these reflection measurements, the registration of the comparatively high air-gap reflection by a commercial reflectometer may not be suitable, particularly if the idle fiber is very short and even a single reflection from its output end may exceed the highest signal measured by the OTDR. To exclude the necessity of recording an air-gap reflectance, the technique could be simply based on the ability of OTDRs to measure fault losses [11.57]. Another factor allowing the intermediate measurement to be dropped is based on the low sensitivity in transmission (see Chap. 5) to optical conditions of a transparent glass surface,

which is affected by unknown formations: evaporated films, defects, or scattering centers. The main requirement is to upgrade an OTDR with an idle fiber and with a device for direct monitoring of fiber alignment and with high quality of fiber endfaces, which is required for further connection or splicing (see Fig. 11.30). The first step in obtaining a reflection from the output end of the idle fiber remains as identified by Eqs. (11.52) and (11.53). Second, the idle and test fibers are spliced or connected to each other with misalignment error $\Delta\bar{\tau}_{cnt}$, averaged for both directions of light propagation. If the idle fiber and the monitoring tool belong to one reflectometer, the value of $\Delta\bar{\tau}_{cnt}$ is just a fraction of the reflectometer's total measurement error. If the idle and test fibers have identical geometry, but altered refractive indices n_i and n_f, the extra loss in a faultless joint of fibers without any noticeable air gap is defined by the inequality $n_i \neq n_f$, and the equivalent signal reflected from the far end of the test fiber within $\pm\Delta\bar{\tau}_{cnt}$ error limit is:

$$\begin{aligned} N_f &= const\cdot\exp(-2\mu_i\ell_i)\cdot\left(1-\rho_{i,f}\right)^2\cdot\exp\left(-2\mu_f\ell_f\right)\cdot\rho_f \\ &= const\cdot\exp(-2\mu_i\ell_i)\cdot\frac{4n_in_f}{\left(n_i+n_f\right)^2}\cdot\exp\left(-2\mu_f\ell_f\right)\cdot\rho_f; \end{aligned} \tag{11.67}$$

$$\begin{aligned} P_f = const &- 10\left(\mu_i\ell_i+\mu_f\ell_f\right)\lg e + 5\lg\left(2n_i\right) + 5\lg\left(2n_f\right) - 10\lg\left(n_i+n_f\right) \\ &+ 10\lg\left(n_f-1\right) - 10\lg\left(n_f+1\right). \end{aligned} \tag{11.68}$$

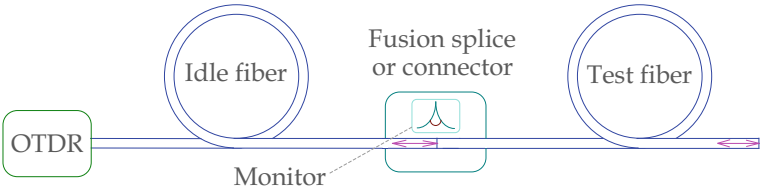

Fig. 11.30 Measurements of internal fiber loss via two endface reflections

Here the reflectance ρ of the fiber joint is approached as $\rho_{i,f} = [(n_i - n_f)/(n_i + n_f)]^2$. Relating these equations to Eqs. (11.52) and (11.53) for the reflection from the idle fiber with reflectance $[(n_i - 1/(n_i + 1)]^2$, one gets:

$$\exp\left(-2\mu_f\ell_f\right) = \frac{N_f}{N_i}\frac{\left(n_i+n_f\right)^2}{4n_in_f}\left(\frac{n_i-1}{n_f-1}\right)^2\left(\frac{n_f+1}{n_i+1}\right)^2; \tag{11.69}$$

$$\begin{aligned} \mu_f\ell_f = 0.23\Big[&\left(P_i-P_f\right) - 10\lg(n_i-1) \;+\; 10\lg(n_i+1) + 5\lg\left(4n_in_f\right) \\ &- 10\lg\left(n_i+n_f\right) \;+\; 10\lg\left(n_f-1\right) - 10\lg\left(n_f+1\right)\Big]. \end{aligned} \tag{11.70}$$

For fine fusion splices and junctions indirectly controlled the geometry error $\Delta\bar{\tau}_{cnt}$ is near (0.01–0.1) dB.

A similar procedure can be carried out for a joint with an air gap. In that case, Eqs. (11.67) and (11.68) are simply substituted by (11.59) and (11.60). By transposing different refractive indices, one has:

$$N_f = const\cdot\exp(-2\mu_i\ell_i)\cdot\left[4n_in_f/\left(n_i+n_f\right)\left(n_in_f+1\right)\right]^2 \cdot\exp\left(-2\mu_f\ell_f\right)\cdot\left[\left(n_f-1\right)/\left(n_f+1\right)\right]^2; \tag{11.71}$$

$$P_f = const - 10\left(\mu_i\ell_i+\mu_f\ell_f\right)\lg e + 10\lg\left(4n_in_f\right) - 10\lg\left(n_i+n_f\right) - 10\lg\left(n_in_f+1\right) + 10\lg\left(n_f-1\right) - 10\lg\left(n_f+1\right); \tag{11.72}$$

$$\exp\left(-2\mu_f\ell_f\right) = N_f/N_i\left[\left(n_i+n_f\right)\left(n_in_f+1\right)/4n_in_f\right]^2 \cdot\left[\left(n_f+1\right)/\left(n_f-1\right)\right]^2\left[\left(n_i-1\right)/\left(n_i+1\right)\right]^2; \tag{11.73}$$

$$\mu_f\ell_f = 0.23\left\{\left(P_i-P_f\right) - 10\lg\left[\left(n_i-1\right)/\left(n_i+1\right)\right] + 10\lg\left(4n_in_f\right) -10\lg\left[\left(n_i+n_f\right)\left(n_in_f+1\right)\right] \;+\; 10\lg\left[\left(n_f-1\right)/\left(n_f+1\right)\right]\right\}. \tag{11.74}$$

Furthermore, if the fibers are carefully aligned and test-fiber loss is measured via an air gap, and the fibers are either further spliced or connected via an immersion liquid, the resultant loss in the joint is:

$$\bar{\tau}_{spl} = \sqrt{N_{spl}/N_f}(1+\bar{\rho}_{end})/(1-\bar{\rho}_{end});$$
$$\bar{\mu}_{joint} = P_{spl} - P_f + 10\lg[(1-\bar{\rho}_{end})/(1+\bar{\rho}_{end})] = P_{spl} - P_f + \bar{\mu}_{gap}. \tag{11.75}$$

Here $\bar{\mu}_{gap}$ represents the average air-gap loss. For mean refraction $\bar{n} = 1.46$, the loss τ of the joint is 0.3 dB.

Finally, if there is any doubt that the actual misalignment error $\Delta\bar{\tau}_{cnt}$ is higher than expected, the procedure can be performed by measuring the entire joint loss in scattered light by Eqs. (11.39)–(11.43). Since the idle fiber cannot be infinitely long, the time resolution of the OTDR utilized (see Fig. 11.31) can be increased to

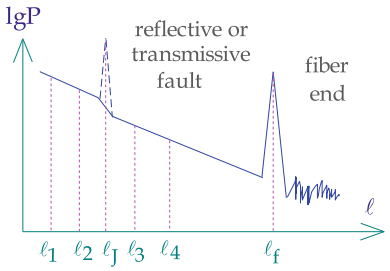

Fig. 11.31 Illustration of reflectance-plus-scattering fiber-loss contributions

resolve the joint with minimal prolongation (cf. Fig. 11.21). The directly measured total loss $\bar{\mu}_{joint}$ averaged by the dual pass is:

$$\bar{\mu}_{joint} = \frac{P_1 - P_2}{\ell_2 - \ell_1}(\ell_J - \ell_1) - \frac{P_3 - P_4}{\ell_4 - \ell_3}(\ell_4 - \ell_J). \tag{11.76}$$

Here powers P_1–P_4 are on the logarithmic scale for all particular points marked in Fig. 11.31. On the linear measurement scale, the entire joint loss matches the squared average transmittance $\bar{\tau}^2_{joint}$. Rewriting reflection Eqs. (11.52)–(11.57) for identical end reflectances of idle and test fibers:

$$\begin{aligned} N_i &= const \cdot \exp(-2\mu_i \ell_i) \cdot \bar{\rho}_{end}; \\ N_f &= const \cdot \exp(-2\mu_i \ell_i) \cdot \bar{\tau}^2_{joint} \cdot \exp\left(-2\mu_f \ell_f\right) \cdot \bar{\rho}_{end}; \end{aligned} \tag{11.77}$$

$$\begin{aligned} P_i &= const - 10\mu_i \ell_i \cdot \lg \mathrm{e} + 5 \lg \bar{\rho}_{end}; \\ P_f &= const - \left(\mu_i \ell_i + \mu_f \ell_f\right) 10 \lg \mathrm{e} - \bar{\mu}_{joint} 10 \lg \mathrm{e} + 5 \lg \bar{\rho}_{end}, \end{aligned} \tag{11.78}$$

the total loss in the test fiber described by relations (11.73) and (11.74) in each respective scale becomes:

$$\begin{aligned} \exp(-2\mu_f \ell_f) &= (N_f / N_i)(1/\tau_{joint,forward}\, \tau_{joint,backward}); \\ \exp(\mu_f \ell_f) &= \bar{\tau}_{joint} \sqrt{N_i / N_f}; \end{aligned} \tag{11.79}$$

$$\mu_f \ell_f = (P_i - P_f)/10 \lg \mathrm{e} - \bar{\mu}_{joint}. \tag{11.80}$$

Several backscattering reflectometers were tested for experimental confirmation of all the methods reviewed above for the direct measurements of fiber losses applicable to end-reflected and backscattered light [11.55–11.57]. One experimental reflectometer for the 900-μm spectral range was upgraded with 125-m-long idle fiber. The repeatability of the loss measurements in reflected light reached 0.5–0.7 dB with 12 dB of added dynamic range versus backscattering radiation. The fiber end-reflection technique at $\lambda \cong 1.3$ μm, verified using an ANDO AQ 1720 reflectometer via the air gap of equivalent fibers having $\bar{n} = 1.46$, measured 1.25-dB loss in a 2.36-km-long fiber line. The absolute-loss error in comparison with cutback measurement for these fibers (see Sect. 11.1) did not exceed ±0.15 dB. Reflectance testing of splice losses using an Anritsu-MW98A reflectometer gave the same results as the backscattering test within 0.05–0.1 dB.

11.4 Interference Noise and Crosstalk in Fiber Transmission Systems

Similarly as surface reflections stimulate interference-induced measurement noise in free-space optical elements, multiple refractive index discontinuities in fiber-optic transmission systems induce resembling effects. Air gaps in fiber connections make weak interferometers with fiber lengths matching air-gap pairs, thus contributing to system noise due to phase fluctuations inherent to the generating wavelength and actual-length stability of the light source and of each particular interferometer made, respectively (see Chap. 3, Fig. 3.5). In laser-based fiber communication, interferometric conversion of laser-phase noise to the respective signal-intensity noise can take place even if optical isolators are present [11.58, 11.65]. Interference effects caused by phase-to-intensity noise conversion were analyzed in Sects. 3.3 and 7.4 (see also [11.21, 11.95]). The following discussion considers certain quantitative aspects for detecting potential noise-induced power penalties in fiber-based optical communication systems and networks inflated by multiple reflections at fiber line discontinuities and via connectors and splices.

Commonly, any splice failures and improperly mated connectors are largely responsible for the refractive index discontinuities in optical-fiber transmission lines. If a physical contact between two spliced or connected fibers collapses, both backreflection and insertion-loss penalties can occur. A three-layer composition – silica–air–silica – created by the contact collapse is shown in Fig. 11.32. When radiation of wavelength λ traverses an air gap of phase thickness $\beta = (2\pi/\lambda)n_2 h cos\,\Theta_2$ between two fiber endfaces, the reflectance ρ and transmittance τ of the entire composition can be computed using the following equations [1.1]:

$$\rho = \left|\rho'^2\right| = \frac{\rho'^2_{12} + \rho'^2_{23} + 2\rho'^2_{12}\rho'^2_{23}\cos 2\beta}{1 + \rho'^2_{12}\rho'^2_{23} + 2\rho'^2_{12}\rho'^2_{23}\cos 2\beta}; \tag{11.81}$$

$$\tau = \left|\tau'^2\right| = \frac{n_3 \cos\Theta_3}{n_1 \cos\Theta_1} \frac{\tau'^2_{12}\,\tau'^2_{23}}{1 + \rho'^2_{12}\rho'^2_{23} + 2\rho'^2_{12}\rho'^2_{23}\cos 2\beta}, \tag{11.82}$$

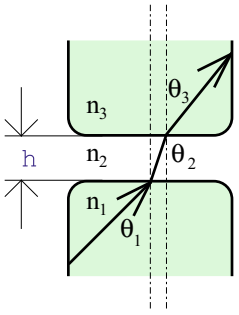

Fig. 11.32 Air-gap in fiber contact

where ρ' and τ' are the amplitude reflectance and amplitude transmittance, being $\rho' = (n_1 \cos\theta_1 - n_2 \cos\theta_2)/(n_1 \cos\theta_1 + n_2 \cos\theta_2)$ and $\tau' = 2n_1 \cos\theta_1/(n_1 \cos\theta_1 + n_2 \cos\theta_2)$; n_1, n_2, and n_3 are the respective refractive indices of the layers, and h is the physical thickness of the air gap (see also Sect. 3.3). Figure 11.33 illustrates changes of the total reflectance and the total transmittance versus air-gap thickness.

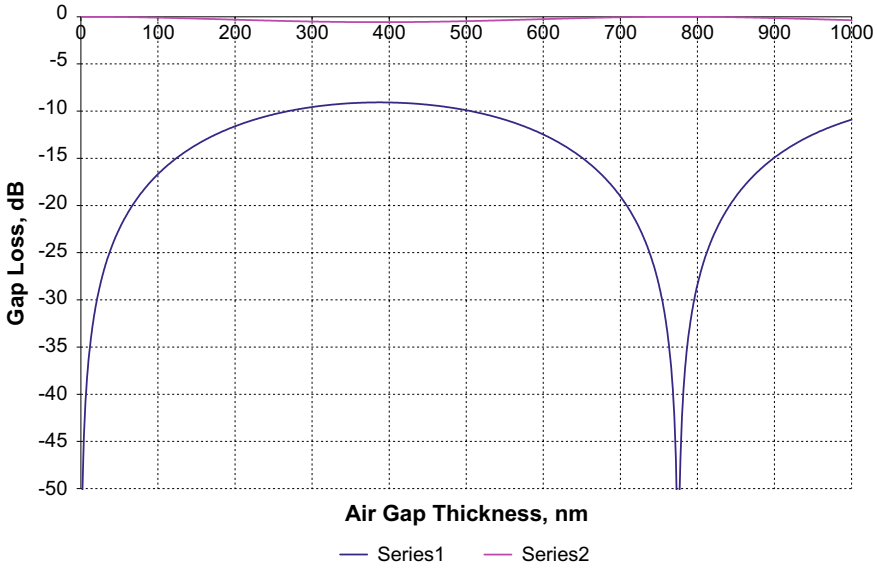

Fig. 11.33 Back reflection (1) and insertion loss (2) of two unmatted fiber ends versus thickness of the created air gap at 1550 nm (2-nm of air gap corresponds to −50 dB of gap's back reflection)

The graph reveals that the magnitude of back-reflectance due to an air gap between connecting fibers ranges from −100 dB at the half-wave gap, to −50 dB at nearly 2-nm gap, and to about −9 dB at the quarter-wave opening. These numbers indicate the probability of high back-reflectance of the joint occurring. For example, a scratch on a fiber surface does not lead to more than a 2-nm separation of the two fiber surfaces, and cannot create a noticeable reflectance spike. The potential grinding residue on connectorized fiber faces needs to be deeper than $\lambda/250$ to develop a higher than −40 dB back-reflectance or higher than 0.004 dB insertion-loss penalty, which is caused by the occurrence of the air gap.

To evaluate the inherent system penalties due to potential phase-to-intensity noise conversion, let us consider a dual concatenation of two-beam and multiple-beam interferometers being either a part of a fiber communication system or occurring as a result of connecting fiber-end mismatches. On its way, light propagates short- and long-length interferometers within one contact failure and among multiple contact combinations (Fig. 11.34). We will mainly consider only two-beam interference on adjacent discontinuities, since even for an erbium-doped fiber its core refractive index is not high enough to make noticeable multiple-beam

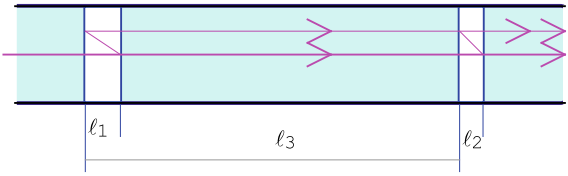

Fig. 11.34 Formation of two coupled-fiber interferometers

interference. However, the relatively high transmittance of every discontinuity allows each interfering beam to effectively propagate and, respectively, interact via break points of an entire fiber line. Depending on the particular optical lengths of interferometers made by discontinuities and the coherence length of the light source, certain interference effects may occur and contribute to coherent and incoherent summation.

In practice, interference effects responsible for the phase-to-intensity noise conversion of laser radiation are more easily modeled via the two-beam Mach–Zehnder interferometer broadly used for external modulation in fiber light-transmission systems (Fig. 11.35). Such an interferometer can be easily configured for any differential length for equal intensities of two interfering beams, and hence is a very practical tool in interference analysis.

Fig. 11.35 Propagation of radiation via a Mach–Zehnder interferometer

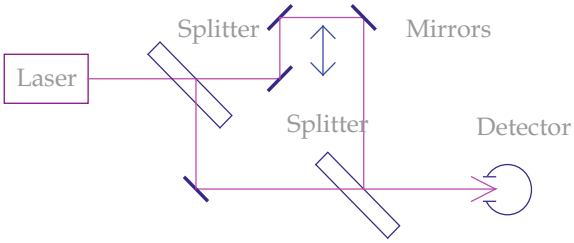

For an air-based Mach–Zehnder interferometer of length ℓ providing time delay $\tau = 2\ell/c$, the two-beam interference output *I(t)* for input amplitude $A = A_0 \cos[\omega_0 t + \varphi(t)]$ of monochromatic light is [1.1]:

$$I(t) = 2A_o^2\{1 + \cos[\varphi(t) - \varphi(t-\tau)]\}. \tag{11.83}$$

If the phase term $\Delta\varphi = \varphi(t) - \varphi(t-\tau)$ remains constant, the optical-intensity output of the interferometer does not change. However, if $\Delta\varphi$ randomly changes during time τ, the relative output intensity: $\iota(t) = I(t)/(2A_0^2)$, follows the trend of such a change. To predict any law-governing change, one needs to know the probability-density function P_i for integer ι in small interval $d\iota$ around ι. The spectral width $\Delta\nu$ of emission spectrums for any narrow-width semiconductor laser as a function of its phase noise φ_n can be defined by frequency fluctuation $\delta\nu$: $\varphi_n = 2\pi(\Delta L/c)\delta\nu$ [11.61, 11.76]. Thus, for such a semiconductor laser, the

mean-square phase error σ_φ^2 accumulated over time t depends on linewidth $\Delta\nu$ and vice versa:

$$\sigma_\varphi{}^2 = 2\pi \cdot \Delta\nu \cdot t. \tag{11.84}$$

A phase change of that laser exhibits a random-walk-type deviation with a Gaussian probability-density function. For time delay τ induced by a two-beam interferometer, P_i can be expressed as:

$$P_i(\Delta\varphi) = \frac{\exp\left[-(\Delta\varphi)^2/2\sigma^2(\tau)\right]}{\sqrt{2\pi\sigma^2(\tau)}}. \tag{11.85}$$

At the same time, the output-intensity distribution function of a two-beam interferometer even in the incoherent regime exhibits a non-Gaussian behavior, since its amplitude is limited to $\pm 2A_0^2$ (see Eq. (11.80)) in interference extremes [11.63]. Two-beam interferometer noise statistics can be acquired in a two-stage process [11.64]. First, Gaussian noise from a single-mode laser can be seen as:

$$E(t) = [E_0 + \alpha(t)] \exp[i\omega_0 t + i\varphi(t)]. \tag{11.86}$$

Then, the interferometer intensity I(t) as a function of the phase difference φ between its arms becomes:

$$\begin{aligned} I(t) &= 0.5E_0^2\{1 + \cos[\omega_0\tau + \varphi(t) - \varphi(t-\tau)]\} \\ &+ 0.5E_0[\alpha(t) - \alpha(t-\tau)][1 + \cos(\omega_0\tau)]. \end{aligned} \tag{11.87}$$

Here E_o and a_o are the mean field amplitude and instantaneous deviation from its value, ω_o is the mean angular frequency, τ is the differential delay in the interferometer, and $\varphi(t)$ is the instantaneous laser phase. In Eq. (11.87), the first term represents the source phase-induced intensity noise input and the second one gives the contribution of the intensity noise of that source. Disregarding the intensity-noise contribution [11.64], one can describe fluctuations by term Y_n, representing the normalized output-intensity phase noise of such an interferometer:

$$Y_n = \cos[\omega_0\tau + \varphi(t) - \varphi(t-\tau)]. \tag{11.88}$$

Statistics for the interferometer phase difference can be quite accurately modeled, since it is a zero-mean and Gaussian random-walk process [11.61]. Presuming insignificant intensity noise of a laser under consideration, a Gaussian distribution of the phase differences of interfering beams, and infinite detection bandwidth, the probability-density function P(i) of the interferometer's normalized output-intensity noise is [11.64]:

$$P(i) = \begin{cases} \dfrac{1}{\sqrt{2\pi D_\varphi(\tau)\left(1 - Y_n^2\right)}} \displaystyle\sum_{n=-\infty}^{\infty} \left\{ \exp\left\{ -\frac{\left[\arccos Y_n - \omega_0\tau + 2\pi n\right]^2}{2D_\varphi(\tau)} \right\} \right. \\ \left. + \exp\left\{ -\dfrac{\left[-\arccos Y_n - \omega_0\tau + 2\pi n\right]^2}{2D_\varphi(\tau)} \right\} \right\} \qquad \textit{while} \quad -1 < Y_n < 1, \\ 0 \qquad\qquad \textit{otherwise}. \end{cases} \tag{11.89}$$

Computed values of the probability-density function P(i) for the normalized signal of the Mach–Zehnder interferometer irradiated by incoherent and partially coherent radiation are shown in Fig. 11.36. Curve 1 depicts the intermediate state when $D_\varphi(\tau) = \pi$ and the interferometer beams are interfering in quadrature. Curves 2, 3, and 4 relate to incoherent interference for $D_\varphi(\tau) = 10\pi$, when the interferometer is aligned to minimum, quadrature, and maximum, respectively. In the totally coherent regime P(i), all magnitudes (too low to be visible) are much more dependent on the $\omega_0\tau$ product, with a local peak near $Y_n = \cos(\omega_0\tau)$. The interferometer's output intensity in quadrature is proportional to $\varphi(t) - \varphi(t - \tau)$, and the probability-density function of its intensity fluctuations is nearly Gaussian. Near the maximum and minimum settings in the coherent regime, the fluctuations become highly non-Gaussian. Further away from the coherence state, the effects of optical path variations are obscured by time-integrated phase variations, while the probability-density function P(i) of phase-induced intensity noise approaches nearly Gaussian behavior. In practice, all models and representations are masked by noise contributions due to thermal fluctuations of light source intensity and detector sensitivity.

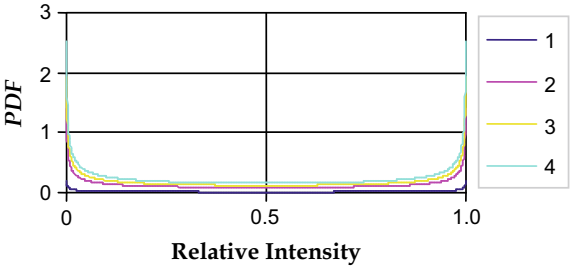

Fig. 11.36 Output of a dual-beam interferometer: *PDF* probability-density function

The effects of the interferometric-noise probability density function P(i) may be seen via mean-squared fluctuation $\Lambda = \left(\left\langle \imath^2 \right\rangle - \langle \imath \rangle^2\right) \Big/ \langle \imath \rangle^2$ of the interferometer's intensity $\langle \imath \rangle^2$ owing to phase noise $\left\langle \imath^2 \right\rangle$. Function Λ_d of a two-beam interferometer can be set via optical path length $2L$ to source coherence length ℓ ratio δ_τ [11.60]:

$$\Lambda_d = \frac{1}{2} \frac{1 + \exp(-4\delta_\tau) - 2\exp(-2\delta_\tau)}{1 + 2\exp(-\delta_\tau) + \exp(-2\delta_\tau)}. \tag{11.90}$$

At small δ_τ, the two-beam interference function approaches $\Lambda_d \approx 0.5(\delta_\tau)^2$. For multibeam interference, function Λ_m defines the statistical relative-intensity fluctuations of multibeam interferometers [11.60]:

$$\Lambda_m = \frac{2\rho^2}{[1+\rho\exp(-\delta_\tau)]^2}\left(\begin{array}{l}\dfrac{1-\rho\exp(-\delta_\tau)}{(1+\rho^2)(1-\rho^3\exp(-\delta_\tau))} \\ \cdot\left\{\begin{array}{l}\left[1+\dfrac{(1-\rho^2)\exp^4(-\delta_\tau)}{1-\rho^2\exp^4(-\delta_\tau)}\right]\left[\begin{array}{l}(1-\rho\exp(-\delta_\tau))(1-\rho^3\exp(-\delta_\tau)) \\ +2\rho\exp(-\delta_\tau)(1+\rho^2)\end{array}\right] \\ +4(\rho\exp(-\delta_\tau))^2\end{array}\right\} \\ -2\exp^2(-\delta_\tau)\end{array}\right). \tag{11.91}$$

At extrema of δ_τ, Λ_m becomes 0 at $\delta_\tau = 0$, $\Lambda_m = 2\rho^2/(1+\rho^2)$ at $\delta_\tau \to \infty$, and $\Lambda_m \approx \left((1+\rho^2)/3(1-\rho)^2\right)\delta_\tau$ at $\delta_\tau \ll 1$, where ρ is the reflectance of both interferometer mirrors. Equations (11.90) and (11.91) presume the lengths of the interferometer arms to set for the maximum transmission at every wavelength. At the $\delta_\tau = 0$ limit, the interferometer is short compared with wavelength λ, and fluctuations disappear. For a long interferometer at $\delta_\tau \to \infty$, fluctuations approach random Gaussian noise at $\rho \to 1$, but remain statistically non-Gaussian as long as $\rho \neq 1$, since phase change $\Delta\varphi$ forces the probability-density function P(ι) to spread out and be perceived as that of interfering beams with uniformly distributed phases [11.59].

Figure 11.37 illustrates Λ_d and Λ_m as functions of δ_τ and two-mirror reflectance for two-beam and multibeam interferometers. The two-beam solution counts

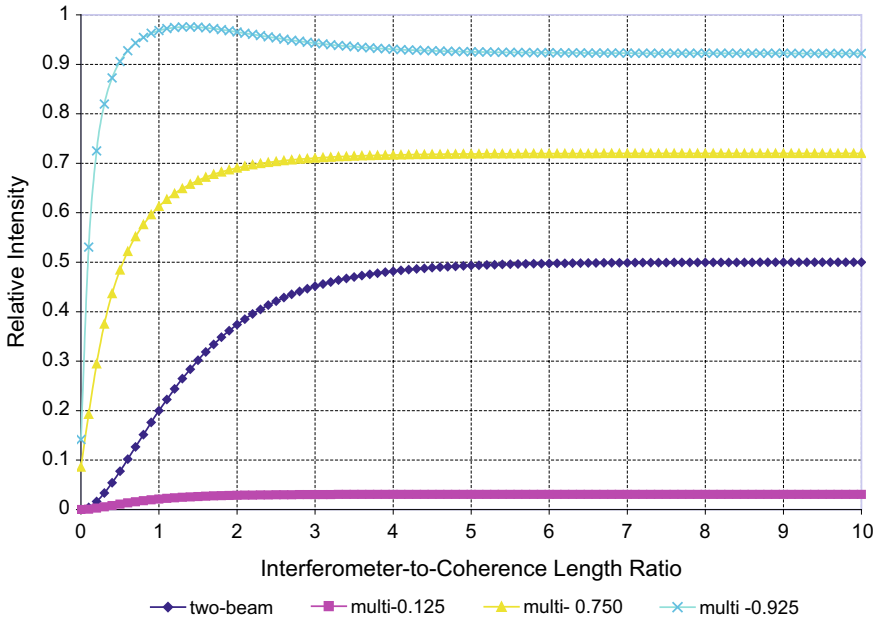

Fig. 11.37 Mean-squared intensity fluctuation function for the output of a two-beam interferometer having two identical mirrors and for the output of a multibeam interferometer versus the interferometer to coherence length ratio

interference of equal-amplitude beams; the multiple-beam solution identifies beams with changing amplitudes for consecutive interactions, but presumes equal reflectance of the interferometer mirrors accounting for reflected-light interference.

Signal fluctuations in fiber transmission lines result in concurrent photocurrent noise in a system's detector. Fourier transform of the autocorrelation function for the detector's photocurrent provides a power spectrum of photocurrent fluctuations due to signal phase noise [11.62]. With the designations of Eq. (11.80), the combined electrical field E(t) for the interferometer's output intensity can be written as:

$$E(t) \propto 0.5E_o\left\{e^{i[\omega t+\varphi(t)]}+e^{i[\omega(t+\tau)+\varphi(t+\tau)]}\right\}. \tag{11.92}$$

The magnitude of the resultant photocurrent i(t) versus the initial photocurrent i_0, which would have been observed without interference, relates as the square power of the respective electric field amplitude:

$$i(t) \propto (i_0/4)\left\{1+e^{i[\omega\tau+\varphi(t+\tau)-\varphi(t)]}\right\}. \tag{11.93}$$

For a Gaussian probability-density function of the two-beam interferometer described by Eq. (11.82) and a random phase variable for radiation power, defined by radiant flux $\Phi(\tau) = \varphi(t+\tau) - \varphi(t)$, the autocorrelation function of the detector's photocurrent at time intervals t can be expressed as [11.62]:

$$\Psi(t) = \frac{i_0^2\Omega}{8}\left\{\begin{array}{ll} e^{-\sigma^2(|t|)}\left[1+\cos(2\omega\tau)e^{-2\sigma^2(\tau-|t|)}\right], & |t|<\tau \\ e^{-\sigma^2(\tau)}[1+\cos(2\omega\tau)], & |t|>\tau \end{array}\right\}. \tag{11.94}$$

The power spectrum P(f) of photocurrent fluctuations versus radio frequency *f*, a conjugate variable to time t, can be obtained via Fourier transform of Eq. (11.94), assuming a Lorentzian line shape of the light source (see Eq. (11.84)). For the interferometer in quadrature and $\cos(2\omega\tau) = -1$, the power spectrum becomes [11.62]:

$$P_q(f) = \frac{i_o^2\Omega}{8\pi}\frac{\Delta\nu}{f^2+\Delta\nu^2}\left[1+e^{-4\pi\Delta\nu\tau}-2e^{-2\pi\Delta\nu\tau}\cos(2\pi f\tau)\right]. \tag{11.95}$$

Here Ω is the load resistance. When the interferometer path length corresponds to either maximum or minimum for an optical frequency ω, the interference term is $\cos(2\omega\tau) = +1$, and Eq. (11.95) transforms to:

$$P_m(f) = \frac{i_o^2\Omega}{8\pi}\frac{\Delta\nu}{f^2+\Delta\nu^2}\left[1-e^{-4\pi\Delta\nu\tau}-2e^{-2\pi\Delta\nu\tau}\frac{\Delta\nu}{f}\sin(2\pi f\tau)\right]. \tag{11.96}$$

If the interferometer's time delay τ becomes zero, both power spectrums vanish: $P_q = P_m = 0$. At the other extreme of $\tau \to \infty$, both spectrums are homodyne with the full width of each being the double of the laser linewidth.

When propagating via a two-beam Mach–Zehnder interferometer, the equally divided interfering beams should have identical amplitudes, creating the strongest interference term among two-beam interference patterns. For fiber systems, the multiple-beam Fabry–Perot interferometer is the likeliest to occur on any adjacent inner fiber discontinuities. Either an air gap in a connector or a splice would contribute to making such an interferometer (see Fig. 11.38). Two versions of the interferometer can be created: an air-based interferometer of length ℓ as the air gap itself and a fiber-based interferometer of fiber length L. The fiber-based interferometer can be made by any internal coupling of refractive index discontinuities.

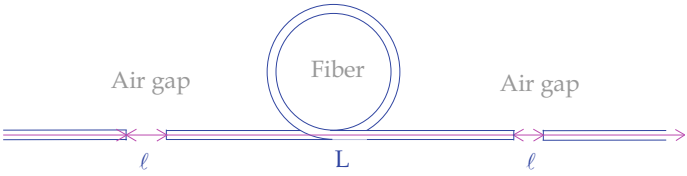

Fig. 11.38 Fiber-based Fabry–Perot interferometers

Owing to the relatively low refractive index of an optical fiber core, the intensity of radiation reflected twice in either the fiber-based or the air-fiber Fabry-Perot interferometer is nearly 2 orders of magnitude lower than the intensity of light propagating straight through. Therefore, for such an interferometer, another category of two-beam interference needs to be considered, which involves beams of very dissimilar amplitudes. In this case, the light intensity of the interferometer's optical output can be written in the form:

$$I(t) = const \cdot I_0 \left\{ 1 + 2\sqrt{\rho_1 \rho_2} \cos[\omega_0 \tau + \varphi(t) - \varphi(t - \tau)] \right\}. \tag{11.97}$$

Here the delayed and direct beams are presumed to interfere in quadrature: $\omega_0 \tau = (n + 0.5)\pi$, I_0 is the incident intensity, and ρ_1 and ρ_2 are the reflectivities of two discontinuities creating the interferometer. Relative intensity noise (RIN) for radiation propagating a fiber with sharp discontinuities creating the interferometer can be obtained via the normalized Fourier transform of Eq. (11.97) [11.62]:

$$RIN(f) = \frac{4\rho_1 \rho_2}{\pi} \frac{\Delta\nu}{f^2 + \Delta\nu^2} \left[1 + e^{-4\pi\Delta\nu\tau} - 2e^{-2\pi\Delta\nu\tau} \cos(2\pi f \tau) \right]. \tag{11.98}$$

For a more general case of a wavelength-mismatched interferometer, the RIN equation becomes [11.65]:

$$RIN(f) = \frac{4\rho_1 \rho_2}{\pi} \frac{\Delta\nu}{f^2 + \Delta\nu^2} \left\{ \begin{array}{l} \sin^2(\omega_0 \tau) \left[1 + e^{-4\pi\Delta\nu\tau} - 2e^{-2\pi\Delta\nu\tau} \cos(2\pi f \tau) \right] \\ + \cos^2(\omega_0 \tau) \left[1 - e^{-4\pi\Delta\nu\tau} - 2e^{-2\pi\Delta\nu\tau} \dfrac{\Delta\nu}{f} \sin(2\pi f \tau) \right] \end{array} \right\}. \tag{11.99}$$

Analysis of Eq. (11.99) points to the maximum conversion of phase to intensity noise for the interferometer in quadrature (Eq. (11.98)). If the delay τ is short and the spectral width ν is narrow: $2\pi\Delta\nu\tau \ll 1$, RIN approaches the small-phase fluctuation limit, which is proportional to the source's spectral width:

$$RIN(f)_{short} = \frac{16}{\pi}\rho_1\rho_2\Delta\nu\tau^2 sinc^2(ft). \tag{11.100}$$

If the interferometer created by two fiber discontinuities is much longer than the coherence length of the light source at $2\pi\Delta\nu\tau \gg 1$, the two interference terms combine incoherently and RIN(f) approaches:

$$RIN(f)_{long} \cong \frac{4\rho_1\rho_2}{\pi}\frac{\Delta\nu}{f^2+\Delta\nu^2}. \tag{11.101}$$

In the latter case, RIN(f) is independent of phase $\omega_0\tau$. The results of numerical simulations by Eqs. (11.94)–(11.98) for λ = 1.55 nm and two open connectors each with 6% reflectance coupled by a 2-m fiber jumper are shown in Fig. 11.39.

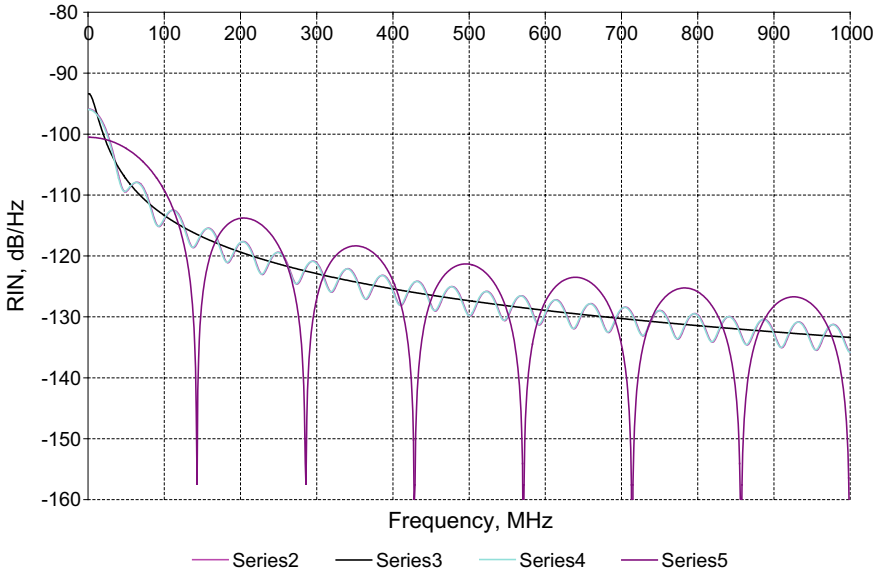

Fig. 11.39 Relative intensity noise (RIN) versus frequency for a 10-MHz-bandwidth laser and a 2-m fiber jumper. Series 2 and 4 represent approximate and exact solutions and series 3 and 5 represent incoherent and quadrature interference limits

Figure 11.40 provides an example of a RIN-versus-wavelength dependence at a radio frequency, clearly demonstrating the nonresonant character of wave extremes.

Since spectral function RIN(f) describes the radio-frequency dependence of system noise, a simpler way of determining system noise over the receiver's

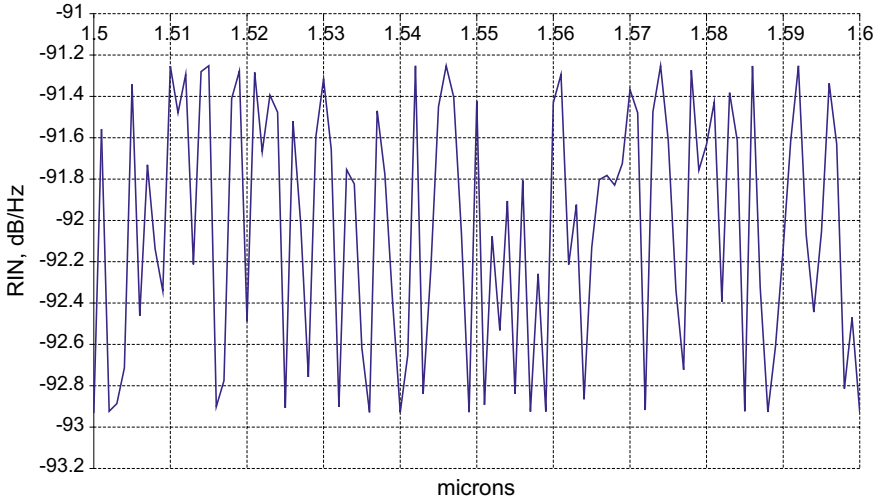

Fig. 11.40 RIN noise versus wavelength at 1-MHz frequency for 5-MHz source bandwidth (fiber jumper length is 7 m)

bandwidth is by integrating RIN(f) as a frequency function over the receiver's bandwidth. For a low-bit-rate system with a wide linewidth light source such as a light-emitting diode, the integral should remain inevitably small (see, e.g., relation (11.98)). For a high-bit-rate transport system with bandwidth $B \gg \Delta\nu$, the total RIN can be approximated as [11.65]:

$$RIN_{\Sigma} = 2\rho_1\rho_2 \left\{ \begin{array}{ll} 1 - e^{-4\pi\Delta\nu\tau}, & \omega_0\tau = (n+0.5)\,\pi \\ 1 + e^{-4\pi\Delta\nu\tau} - 2e^{-2\pi\Delta\nu\tau}, & \omega_0\tau = n\pi \end{array} \right\}. \tag{11.102}$$

If the number of reflections increases to more than two, and the interference terms combine incoherently (long interferometers), Eq. (11.99) for the reflectance products of all discontinuities involved gives:

$$RIN(f)_{long} \cong \frac{4}{\pi}\frac{\Delta\nu}{f^2 + \Delta\nu^2} \sum_{i=2}^{N} \sum_{j=1}^{i-2} \bar{\rho}_{i,j}. \tag{11.103}$$

Here $\bar{\rho}_{i,j}$ is the effective reflectance of discontinuities i and j incorporating inner-fiber transmittance τ:

$$\bar{\rho}_{i,j} = \left\langle \rho_i \rho_j (\tau_{i,j})^2 \right\rangle. \tag{11.104}$$

In relatively long fiber transmission lines, especially if optical amplifiers are deployed, multiple reflection noise can be generated not only at fiber discontinuities, but also owing to double Rayleigh backscattering in a fiber line. The effective reflection coefficient $\rho_{i,j}$ of a fiber line having an optical amplifier of gain G can be treated as a reflection product of the i^{th} and j^{th} scattering centers [11.66]:

$$\rho_{i,j} = G \cdot S \cdot \alpha_s \cdot \Delta\ell \cdot \exp\left(-\alpha\ell_i - \alpha\ell_j\right)\left(\vec{p}(t) \bullet \vec{p}_{i,j}\left(t - \tau_{i,j}\right)\right), \tag{11.105}$$

where α_s and α are the linear scattering and the absorption factors, S is the fraction of scattering power coupled into the fiber in the backward direction, $\Delta\ell$ is the mean interval of the fiber length over which the scattering occurs, and $\vec{p}$ and $\vec{p}_{i,j}$ are the unit polarization vectors related to the transmitted and double-reflected optical fields. For a non-polarization-maintaining fiber with randomly aligned polarization elements, the average polarization factor is $\left\langle\left(\vec{p} \bullet \vec{p}_{i,j}\right)^2\right\rangle = 0.5$. Integration of individual scattering center contributions by Eq. (11.105) gives backscattering reflectance ρ_{bs} from two fiber sides [11.66]:

$$\rho_{bs} = (S \cdot \alpha_s / 2\alpha)[1 - \exp(-2\alpha L)], \tag{11.106}$$

where L is the fiber length. For long fiber spans: $\rho_{bs} \to (S \cdot \alpha_s / 2\alpha)$, and Eq. (11.103) results in:

$$RIN(f) \cong \frac{2G^2\rho_{bs}^2}{\pi} \frac{\Delta\nu}{f^2 + \Delta\nu^2}. \tag{11.107}$$

Let us also consider the effect of residual birefringence of a fiber line connecting discontinuities. Keeping in Eq. (11.28) only first-order terms for low ordinary and extraordinary reflectances ρ_o and ρ_e and counting the total birefringence δ_Σ built up, the relative intensity I/I_0 of the two-beam pattern is:

$$\begin{aligned}\frac{I_{2beam}}{I_0} = &\left[\frac{1-\rho_o}{\sqrt{(1-\rho_o)^2 + 4\rho_o \sin^2\delta_o}} \cos\varphi_\Sigma \cos(\varphi_\Sigma - \gamma)\right. \\ &\left. + \frac{1-\rho_e}{\sqrt{(1-\rho_e)^2 + 4\rho_e \sin^2\delta_e}} \sin\varphi_\Sigma \sin(\varphi_\Sigma - \gamma)\right]^2 \\ &- I_0\tau_o\tau_e\left\{\sin^2\left(\frac{\delta}{2}\right) + \rho_o\rho_e \sin^2\left(\frac{3\delta}{2}\right)\right\} \sin 2\varphi_\Sigma \sin[2(\varphi_\Sigma - \gamma)].\end{aligned} \tag{11.108}$$

Since the task is to identify interference effects of light retroreflected on fiber discontinuities, we may consider fiber birefringence to be a constant of fiber transmission, and only identify it for a reflected path. Equations (11.99)–(11.101) for a birefringent fiber interferometer on two discontinuities become:

$$RIN(f) = \frac{4\rho_1\rho_2}{\pi}\left[1 - \sin^2\left(\frac{3\delta}{2}\right)\right]\frac{\Delta\nu}{f^2 + \Delta\nu^2} \cdot \left\{ \begin{array}{l} \sin^2(\omega_0\tau)\left[1 + e^{-4\pi\Delta\nu\tau} - 2e^{-2\pi\Delta\nu\tau}\cos(2\pi f\tau)\right] \\ + \cos^2(\omega_0\tau)\left[1 - e^{-4\pi\Delta\nu\tau} - 2e^{-2\pi\Delta\nu\tau}\dfrac{\Delta\nu}{f}\sin(2\pi f\tau)\right] \end{array} \right\}; \quad (11.109)$$

$$RIN(f)_{short} = \frac{16}{\pi}\rho_1\rho_2\left[1 - \sin^2\left(\frac{3\delta}{2}\right)\right]\Delta\nu\tau^2 sinc^2(ft); \quad (11.110)$$

$$RIN(f)_{long} \cong \frac{4\rho_1\rho_2}{\pi}\left[1 - \sin^2\left(\frac{3\delta}{2}\right)\right]\frac{\Delta\nu}{f^2 + \Delta\nu^2}. \quad (11.111)$$

The effect of 1/18th of light-wave birefringence in a fiber-based interferometer is shown in Fig. 11.41. It is evident, that intensity shifts of RIN (relative-intensity noise) correspond to extremes of birefringence, exhibited by fiber sections of propagation and can be decreased by appropriate fiber-phase matching.

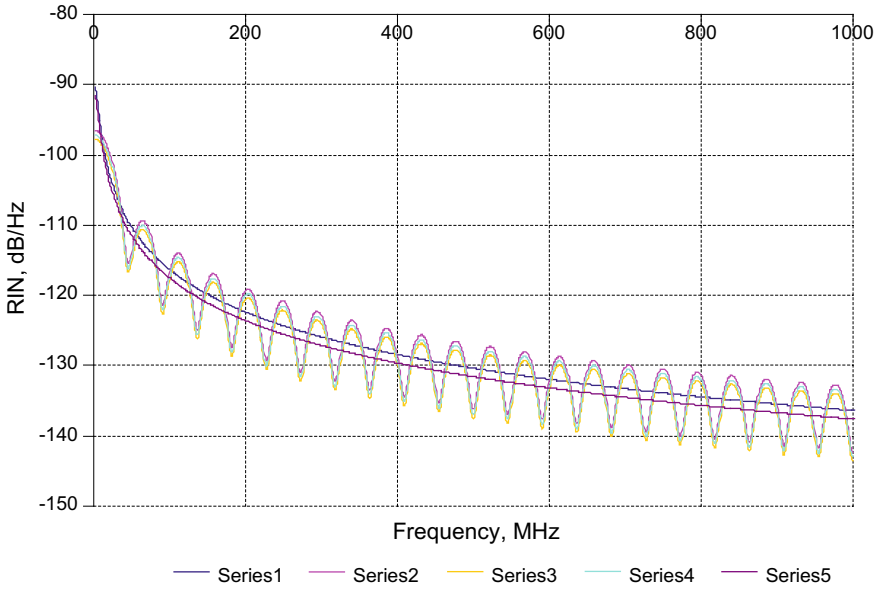

Fig. 11.41 RIN versus frequency for a 5-MHz source bandwitch with (series 3 and 5) and without (series 1 and 2) residual briefringence values at 1/24 (series 3) and 1/18 of a wave (series 4) in a 2-m jumper: coherent (series 2 and 3) and incoherent (series 1 and 5) interference

11.4.1 Crosstalk and Systems with Multiple Interferers

Most previously analyzed interference effects were caused by optical radiation from a single quasi-monochromatic source, while the wave components were retroreflected and imposed over each other via different propagation paths. In a multiwave and multisource optical system, spectral superpositions, such as coherent and incoherent interference or any combination of the two, can contribute to similar interference noise, called crosstalk noise or crosstalk. Crosstalk can be caused by imposing or by leaking diversely originated light components of close wavelengths into an optical path. Crosstalk penalty occurs not as a result of one-wavelength retroreflections, but as a consequence of interference of dissimilar wave components escaping from respective spectral filters via imperfect wavelength-separation elements. The effects of the latter interference noise on fiber transmission systems depend on any particular spectral contribution of various wavelength sources contributing to crosstalk within the receiver's bandwidth. Mainly, the number of wave modes emitted, their individual shapes, linewidths, and the spectral separation significantly contribute to crosstalk.

Consider two signals $P_1(t)$ and $P_2(t)$ modulated by intensity carrying messages $m_1(t)$ and $m_2(t)$ at frequencies $f_1(t)$ and $f_2(t)$ from optical carriers independently exciting electromagnetic waves $E_1(t)$ and $E_2(t)$. Each single field $\Xi_j(t)$ of modulated radiation is $\Xi_j(t) = \sqrt{P_j(t)}E_j(t)$, where $P_j(t) = 1 + m_j(t)\cos(2\pi f_j t)$. If both signals are combined on a photodetector reacting to intensity I(t) of combined electromagnetic field $\Xi_\Sigma(t)$, the detector's signal is defined by the low-frequency component of the squared modulus of the total field:

$$I(t) \propto \left\{|\Xi_\Sigma(t)|^2\right\} = \left\{\left|\sqrt{P_1(t)}E_1(t) + \sqrt{P_2(t)}E_2(t)\right|^2\right\}$$
$$= P_1(t) + P_2(t) + \left\{2\sqrt{P_1(t)P_2(t)}E_1(t)E_2(t)\right\}, \qquad (11.112)$$

where curly brackets define the low-frequency component. The interference term in brackets in Eq. (11.112) represents undesirable noise, originating from the mixture process of two combining signals, when its outcome fits into the frequency bandwidth of the signals received. Noise is given by convolution of two mixing frequency spectrums, and the interference spectrum is centered at frequency δf given by the frequency difference of optical sources, presuming the bandwidth of messages $E_1(t)$ and $E_2(t)$ defined by the detection process is much smaller than the linewidth $\Delta\lambda_j$ of optical source. Thus, the intensity of interference noise is proportional to the linewidths of the combined optical sources and their spectral separation δf.

Not accounting for broadening or reflections of two interfering signals, the signal to interference noise ratio (SNR_I) can be defined as the ratio of the signal intensity or the average power spectrum $0.5\langle m_{1,2}(t)^2\rangle$ for messages m_1 and m_2 to the average power spectrum for interference noise $N(\delta f)$ in the receiver's bandwidth B:

$$SNR_I = 10\log_{10}\left[\frac{0.5\left\langle m_{1,2}(t)^2\right\rangle}{N(\delta f)B}\right]. \tag{11.113}$$

Typically, a single-mode distributed-feedback laser emits a narrow spectrum with a linewidth resembling a Lorentzian function. Presuming no direct modulation of the source lasers at wavelengths λ_1 and λ_2, interference noise remains just about Lorentzian with spectral width Δf_L as a sum of bandwidths of the two sources at one center frequency: $\delta f = c(\lambda_1 - \lambda_2)/\lambda_1\lambda_2$, and the interference noise power spectrum is [11.67]:

$$N(\delta f)_L = \frac{8}{\pi\delta f}\left[1 + \left(\frac{2\delta f}{\Delta f_L}\right)^2\right]^{-1}. \tag{11.114}$$

Direct modulation of a distributed-feedback laser creates frequency chirp and excessive spectral broadening of a virtually Gaussian emission profile. The interference-noise spectrum resulting from mixing broadened sources at frequencies f_1 and f_2 approaches Gaussian behavior at the spectral linewidth: $\Delta f = \sqrt{\Delta f_1^2 + \Delta f_2^2}$. Since the linewidth of a message is much smaller than the carrier-modulation bandwidth and thus does not alter the carrier's spectral profile, the noise power spectrum for two interfering Gaussian sources is [11.67]:

$$N(\delta f)_G = \frac{13.33}{2\Delta f\sqrt{\pi}}\exp\left[-\left(\frac{2\delta f}{1.2\Delta f}\right)^2\right]. \tag{11.115}$$

From Eqs. (11.111) and (11.112) it follows (see Fig. 11.42) that the half width at half-maximum function of a detected electrical power spectrum equals the full

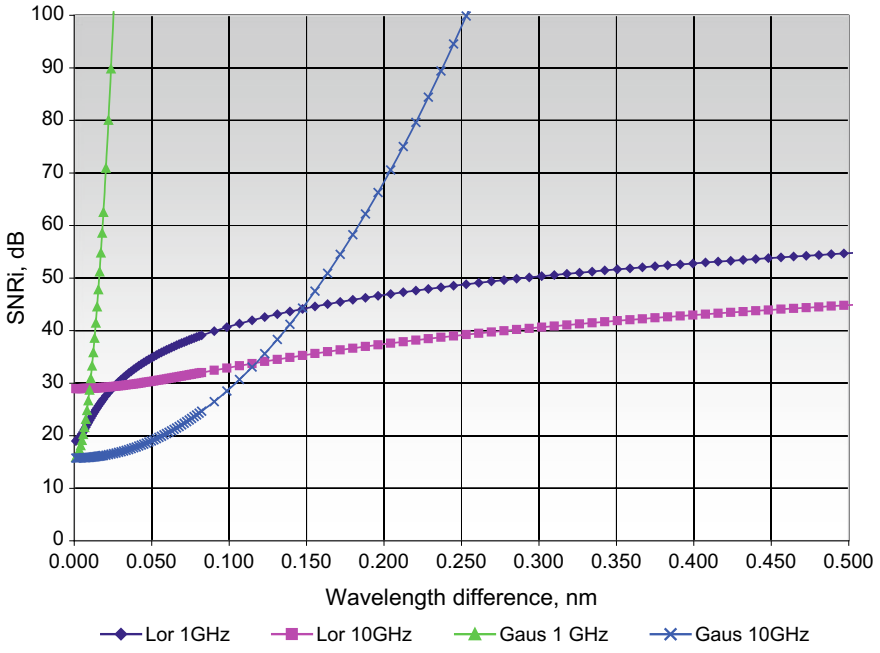

Fig. 11.42 Signal-to-Interference Noise ratio (SNRI) versus difference of wavelengths for two mixing optical sources: Lorentzain (Lor) - 1, 2; Gaissian (Gaus) - 3, 4

width at half-maximum function of the optical power spectrum of a Lorentzian source, with an extra $1/\sqrt{2}$ factor for a Gaussian source [11.68].

Consider two interferers of wavelengths λ_1 and λ_2, propagating to one detector via diverse optical paths coupled by one directional wave coupler, losslessly transmitting the wavelength of each path with isolation factor x for respectively crossing wavelengths. Equation (11.109) for receiving the intensity of the combined signal can be rewritten in the well-known two-beam interference form [1.1, 11.70]:

$$I_\Sigma(\lambda_1, \lambda_2) = I_1(1-x) + I_2 x + 2\sqrt{I_1 I_2 x(1-x)} \cos \Psi_{1,2}\, \vec{p}_1 \cdot \vec{p}_2. \tag{11.116}$$

Here I_1 and I_2 and p_1 and p_2 are the intensities and polarizations of the two interfering signals, respectively, and the wave coupler's transmittance for every passing wavelength is presumed to be $\tau = 1 - x$; Ψ is the phase of interfering waves. The three terms in Eq. (11.116) represent the signal, the crosstalk, and intensity noise caused by interference. The following classification may be used [11.70]: (a) coherent crosstalk; (b) incoherent noise-free crosstalk; and (c) incoherent beat-noise crosstalk. If the signal and crosstalk are coherent: $\Psi_a = \pi/2 - \Delta\varphi$, where $\Delta\varphi$ is the phase difference of the signal and of coupled crosstalk. Any incoherent waves of frequencies ω_1 and ω_2 and phases φ_1 and φ_2 couple independently in time: $\Psi_b = (\omega_1 - \omega_2)t + \varphi_1(t) + \varphi_2(t)$, but the beat frequency $\omega_1 - \omega_2$ can be filtered out if it exceeds the receiver's bandwidth. For incoherent beat-noise crosstalk, interfering signals originate either from closely wavelength matching sources if the beat frequency $\omega_1 - \omega_2$ falls into the receiver's bandwidth and phase noise φ is not filtered out to change phase Ψ_b, or from one source with differential delay τ: $\Psi_c = \omega\tau + \varphi(\tau) + \varphi(t - \tau)$.

In optical communication networks signal-leakage crosstalk may be accumulated if signals are transferred via imperfect wavelength-division and time-division elements such as multiplexers and demultiplexers. Defining the leakage factor ξ of an optical element as the ratio of leakage crosstalk to the power of the signal transferred by the element, the element's added power penalty to the communication-system penalty, presuming addition of the power of the crosstalk to the signal powers, becomes: $p = -10\log_{10}(1 - \xi)$ (dB). The additive law for summation of power holds true if the signal-to-crosstalk difference $\Delta\nu$ in frequency is much larger than the receiver's bandwidth (thus the frequency difference is filtered out) or if the signal and crosstalk states of polarization are orthogonal and no interference can occur. In any other case, signal-to-crosstalk interference does take place, but the signal and crosstalk powers do not combine additively. Considering the signal and the crosstalk as respective autonomous random binary functions d_s and d_c of either 0 or 1 magnitude, the electrical field transmitted by any leaking optical element becomes:

$$E_\Sigma(t) = E d_s(t) \cos[\omega_0 t + \psi_s(t)] + E\sqrt{\xi} d_c(t) \cos[\omega_0 t + \psi_c(t)]. \tag{11.117}$$

Here E is the normalized signal-field amplitude, and ψ_s and ψ_c are the phases of the signal and the crosstalk.

For a receiver response I as a convolution of the signal and receiver impulse-response functions and a signal as a combination of the signal itself, crosstalk, and receiver thermal noise, I(t) is [11.65]:

$$I(t) = \left\{ const \cdot |E|^2 \left[B(t) + 2\sqrt{B(t)\xi B(t-\tau)} \cos(\psi_s(t) - \psi_c(t)) \right] + N(t) \right\} * H(t). \quad (11.118)$$

Here B(t), B(t − τ), N(t), and H(t) are respective functions of the digital signal received, crosstalk, thermal noise, and receiver impulse response; B(t) = 1 for 0 < t < T, if T is the bit duration, and B(t) = 0 otherwise. Denoting the expectation values as μ_1 and μ_0 and noise variances as σ_1 and σ_0 of signal $I(t)$ for ones and zeroes, respectively, for Gaussian-distributed noise the probability of making a decision error becomes [11.65]:

$$P_e = \frac{1}{2} Q\left[\frac{\mu_1 - D}{\sigma_1}\right] + \frac{1}{2} Q\left[\frac{D - \mu_0}{\sigma_0}\right], \quad where\ Q(x) = \int_x^\infty \frac{1}{\sqrt{2\pi}} e^{-x^2/2} dx. \quad (11.119)$$

For p-i-n receivers, signal-related noise is usually absent and noise variances for ones and zeroes can be assumed to be the same, thus presuming there is no intersymbol interference: $\mu_0 = 0$, $\mu_1 = const|E|^2$, $D = \mu_1/2$, P_e is: $P_{e,p-i-n} = \frac{1}{2} Q\left[\frac{\mu_1}{2\sigma_0}\right] + \frac{1}{2} Q\left[\frac{\mu_1}{2\sigma_1}\right]$, *where as defined in* (11.114):

$$\sigma_1 = \langle I^2 \rangle - \langle I \rangle^2 = \sigma_0^2 + \mu_1^2 \left\langle \left(\sqrt{\xi}\right)^2 \right\rangle. \quad (11.120)$$

As a result, the power penalty P in decibels due to crosstalk-interference noise for zero shot noise is determined by analogy with noise due to reflectance (Eq. (11.104)) [11.65, 11.72]:

$$P_\rho = -5 \log_{10}\left[1 - 4q^2 \langle \bar{\rho}^2 \rangle\right]; \quad P_\xi = -5 \log_{10}\left[1 - 4q^2 10^{(\xi, dB/10)}\right], \quad (11.121)$$

Where $q \approx 5.9$ for the noise power $P = 10^{-9}$, leading to $0.5Q(q) = 10^{-9}$. For low-leaking optical elements: $\xi \ll 1$, the transmitted total power may be approximated as [11.71]:

$$P_\Sigma(t) = 0.5E^2 \left\{ d_s(t) + 2d_s(t)\sqrt{\xi} d_c(t) \cos[\psi_s(t) - \psi_c(t)] + \xi d_s(t) \right\} \underset{\xi \to 0}{\cong} 0.5E^2 \left\{ d_s(t) + 2d_s(t)\sqrt{\xi} d_c(t) \cos[\psi_s(t) - \psi_c(t)] \right\}, \quad (11.122)$$

where $0.5E^2$ is the normalized field power on the receiver. Equation (11.122) allows one to consider the crosstalk interference term versus the transmitted signal power in the small-crosstalk approximation. In this approximation, the receiver's power due to phase fluctuations of interfering waves is bounded as:

$$0.5E^2\left(1-2\sqrt{\xi}\right)\le P_\Sigma(t)_{\xi\to 0}\le 0.5E^2\left(1+2\sqrt{\xi}\right). \tag{11.123}$$

If the receiver's decision threshold is set in the middle between 1 and 0 of the power received: $P(t)=0.5[\langle P_1\rangle+\langle P_0\rangle]$, where $\langle P_1\rangle$ and $\langle P_0\rangle$ are the average power values corresponding to 1 and to 0, from relation (11.123) the resulting decision threshold D is in the $\left((E^2/4)\left(1-2\sqrt{\xi}\right)\le D\le(E^2/4)\left(1+2\sqrt{\xi}\right)\right)$ range. Considering DC- and AC-coupled receivers with decision threshold $D=E^2/4$ for DC-coupling, and assuming $\langle\cos[\psi_s(t)-\psi_c(t)]\rangle$ dependence for the worst and the best case for AC coupling, the associated crosstalk-induced optical power penalties of the digital communication system are [11.71]:

$$\mathrm{P_{DC}}=-10\log_{10}\left(1-4\cdot10^{(\xi,\mathrm{dB}/20)}\right);\mathrm{P_{AC-best}}=-10\log_{10}\left(1-2\cdot10^{(\xi,\mathrm{dB}/20)}\right);$$
$$\mathrm{P_{AC-worst}}=-10\log_{10}\left(1-6\cdot10^{(\xi,\mathrm{dB}/20)}\right). \tag{11.124}$$

Figure 11.43 illustrates the dependencies of the system's power penalty versus its crosstalk component in decibels.

Further impediments of crosstalk-induced penalties can occur if optical amplification is used, owing to beatings between crosstalk and amplified spontaneous

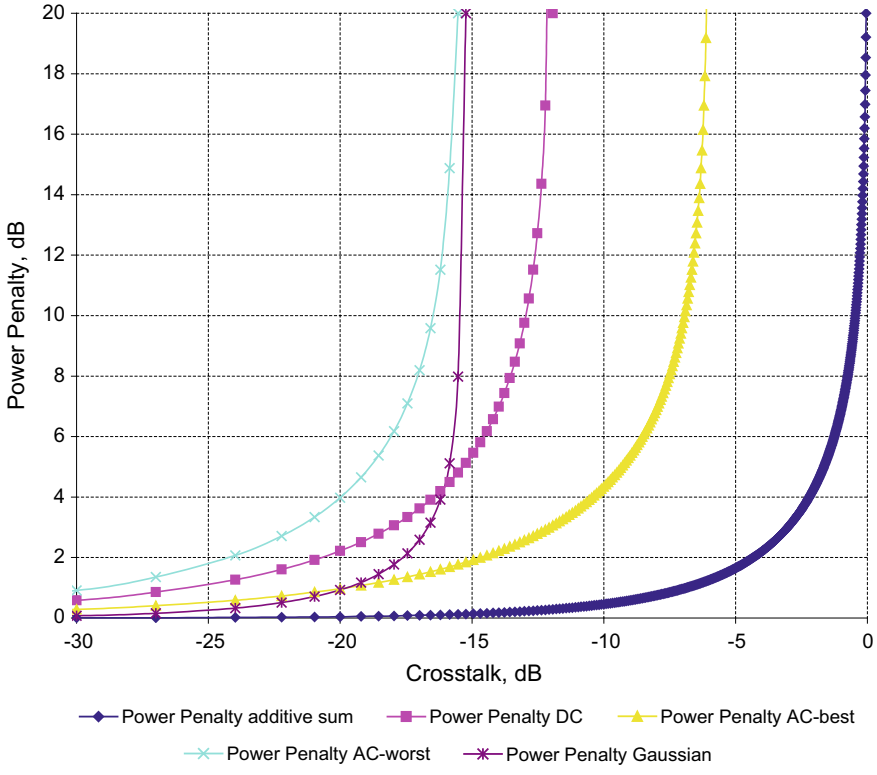

Fig. 11.43 Induced power penalties as functions of the system's crosstalk

emission (ASE) or owing to degradation of the extinction ratio [11.72–11.75, 11.93]. Considering arcsine statistics for the probability-density function of interferometric noise (Eq. (11.86)) and accounting for ASE generated in optical preamplifiers for p-i-n and avalanche photodiode receivers, one may compute the bit-error rate (BER) for combinations of interfering receiver bits [11.73]:

$$BER_{1,1} = \frac{1}{2\pi}\int_0^{\pi} erfc\left\{\sqrt{\left(\frac{1}{2}\right)\frac{P_1^2R_D^2G^2}{\sigma_1^2+(1+\xi)\sigma_{sg-sp}^2}}\left[1+\xi-D+2\sqrt{\xi}\,\cos(\Theta)\right]\right\}d\Theta;$$

$$BER_{0,1} = \frac{1}{2\pi}\int_0^{\pi} erfc\left\{\sqrt{\left(\frac{1}{2}\right)\frac{P_1^2R_D^2G^2}{\sigma_1^2+(1+r\xi)\sigma_{sg-sp}^2}}\left[1+r\xi-D+2\sqrt{r\xi}\,\cos(\Theta)\right]\right\}d\Theta;$$

$$BER_{1,0} = \frac{1}{2\pi}\int_0^{\pi} erfc\left\{\sqrt{\left(\frac{1}{2}\right)\frac{P_1^2R_D^2G^2}{\sigma_0^2+(r+\xi)\sigma_{sg-sp}^2}}\left[D-\xi-r+2\sqrt{r\xi}\,\cos(\Theta)\right]\right\}d\Theta;$$

$$BER_{0,0} = \frac{1}{2\pi}\int_0^{\pi} erfc\left\{\sqrt{\left(\frac{1}{2}\right)\frac{P_1^2R_D^2G^2}{\sigma_0^2+r(1+\xi)\sigma_{sg-sp}^2}}\left[D-r(1+\xi)+2r\sqrt{\xi}\,\cos(\Theta)\right]\right\}d\Theta, \tag{11.125}$$

where: $erfc(z) \equiv \frac{2}{\sqrt{\pi}}\int_z^{\infty} e^{-x^2}dx$; $erf(z) \equiv \frac{2}{\pi}\int_0^{z} e^{-x^2}dx$; P_1 is the power of a bit entering the amplifier; R_D is the responsivity of the receiver, G is the gain of the amplifier, σ_1 and σ_0 are the variances of one and of zero due to effects of thermal noise, ASE shot noise, and spontaneous-spontaneous bit noise, $\sigma_{sg\text{-}sp}$ is the variance due to signal-spontaneous bit noise with no crosstalk, and r is the extinction ratio: $0 \le r < 1$.

Finally, let us consider crosstalk interference in a birefringent communication fiber line, having ordinary refractive index n_o and extraordinary index n_e. Schematically, the occurrence of crosstalk can be represented as shown in Fig. 11.44. Two multiplexed wavelengths λ_A and λ_B with intensities $I_{A,0}$ and $I_{B,0}$ enter demultiplexer DM converting the two to transmitting wave A and leaking wave B, and reflecting wave B and leaking wave A. For simplicity, let us presume the initial intensity of every polarized signal $I_{A,0}$ and $I_{B,0}$ entering such a birefringent fiber to be equally split into orthogonal components along the ordinary and extraordinary axes of propagation; hence, they have intensities $I_{A,o} = I_{A,e} = 0.5I_{A,0}$ and $I_{B,o} = I_{B,e} = 0.5I_{B,0}$. As a result, in either the transmitting or the reflecting channel created by demultiplexer DM, two components of the main signal and two components of the leaking signal interfere

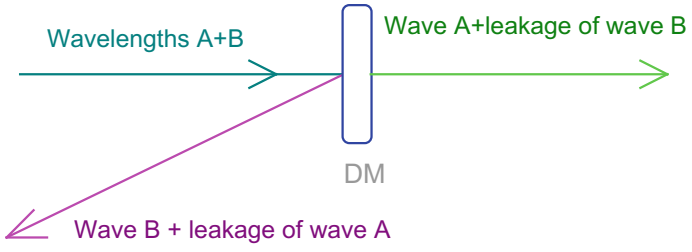

Fig. 11.44 Schematic representation of crosstalk interference

along each line of the birefringent fiber if any two selected waves of the four present are localized in one axis. The orthogonal waves have phase difference $\delta = 2\pi(n_e - n_o)(\Delta\ell/\lambda)$, while in-line-polarized waves have phase shift $\delta_e = 2\pi n_e(\Delta\ell/\lambda)$ or $\delta_o = 2\pi n_o(\Delta\ell/\lambda)$, where $\Delta\ell$ is the length-path divergence between the pair of any two interfering waves in the fiber transmission.

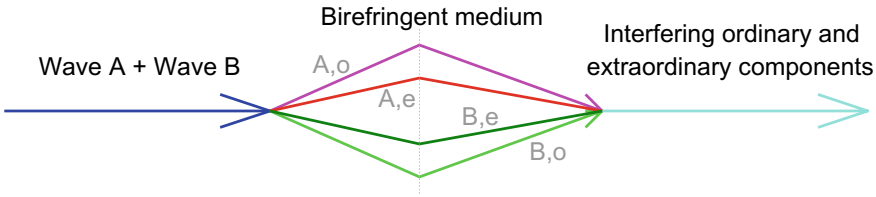

Fig. 11.45 Schematic conception of two-wave birefringence-induced interference

Figure 11.45 depicts two waves A and B entering a birefringent medium, such as a fiber line, if all four ordinary and extraordinary polarization components $A_{,o}$; $A_{,e}$; $B_{,o}$; and $B_{,e}$ experience respective phase shifts δ_o and δ_e, and all eventually interfere with each other while passing via the birefringent fiber. The total intensity I_Σ of transmitted optical signal A and leaking crosstalk B resulting from four-wave crosstalk-induced interference can be described as:

$$\begin{aligned}
I_{\Sigma,a} &= I_{A,o}(1-\xi) + I_{A,e}(1-\xi) + I_{B,o}\xi + I_{B,e}\xi + 2\sqrt{I_{A,o}I_{A,e}(1-\xi)^2}\cos\delta \\
&\quad + 2\sqrt{I_{B,o}I_{B,e}\xi^2}\cos\delta; \\
I_{\Sigma,b} &= I_{A,o}(1-\xi) + I_{A,e}(1-\xi) + I_{B,o}\xi + I_{B,e}\xi + 2\sqrt{I_{A,o}I_{B,o}\xi(1-\xi)}\cos\delta_o \\
&\quad + 2\sqrt{I_{A,e}I_{B,e}\xi(1-\xi)}\cos\delta_e; \\
I_{\Sigma,c} &= I_{A,o}(1-\xi) + I_{A,e}(1-\xi) + I_{B,o}\xi + I_{B,e}\xi \\
&\quad + 2\sqrt{I_{A,o}I_{B,e}\xi(1-\xi)}\cos(\delta+\delta_e) + 2\sqrt{I_{A,e}I_{B,o}\xi(1-\xi)}\cos(\delta+\delta_o).
\end{aligned} \tag{11.126}$$

For equal orthogonal intensities $I_{A,o} = I_{A,e} = 0.5I_{A,0} \equiv 0.5I_A$ and $I_{B,o} = I_{B,e} = 0.5I_{B,0} \equiv 0.5I_B$, Eq. (11.126) becomes:

$$\begin{aligned}
I_{\Sigma,a,Io=Ie} &\equiv I_A(1-\xi) + I_B\xi + I_A(1-\xi)\cos\delta + I_B\xi\cos\delta = I_A(1-\xi) \\
&\quad + [I_A(1-\xi) + I_B\xi]\cos\delta + I_B\xi; \\
I_{\Sigma,b,Io=Ie} &\equiv I_A(1-\xi) + \sqrt{I_A I_B\xi(1-\xi)}(\cos\delta_o + \cos\delta_e) + I_B\xi; \\
I_{\Sigma,c,Io=Ie} &\equiv I_A(1-\xi) + \sqrt{I_A I_B\xi(1-\xi)}[\cos(\delta+\delta_e) + \cos(\delta+\delta_o)] + I_B\xi.
\end{aligned} \tag{11.127}$$

Here every total intensity $I_{\Sigma a}$, $I_{\Sigma b}$, and $I_{\Sigma c}$ describes the result of interference for orthogonal, for in-plane, and for cross-plane radiation components as being singled

out for a given observation. Equations (11.126) and (11.127) define interactions for pairs of orthogonal or in-plane terms hypothetically presuming the wave separation into ordinary and extraordinary axes is made with no optical loss.

Figures 11.46–11.48 provide examples of interference patterns computed using Eq. (11.127). The numerical simulation is based on setting the fiber

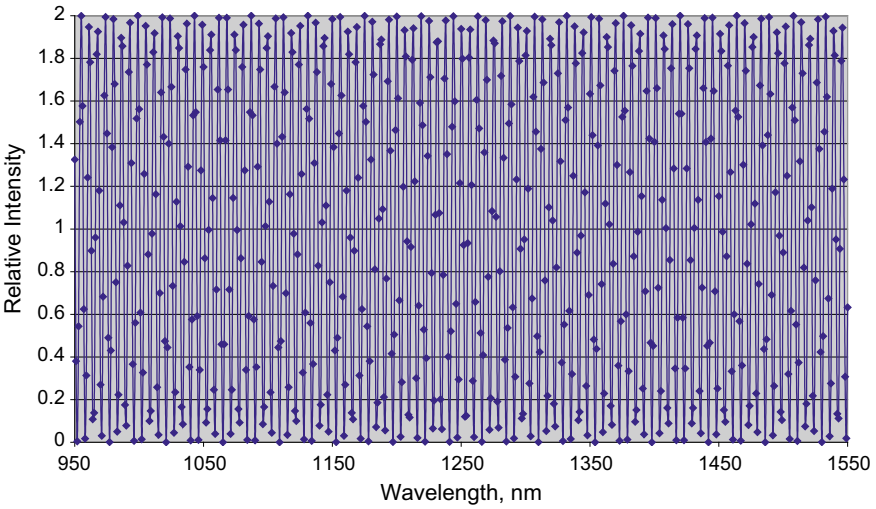

Fig. 11.46 Four-wave crosstalk-induced interference in a highly birefringent photonic crystal fiber: fiber length 1 m, leakage factor 0.01, orthogonal components of the signal and crosstalk are interfering

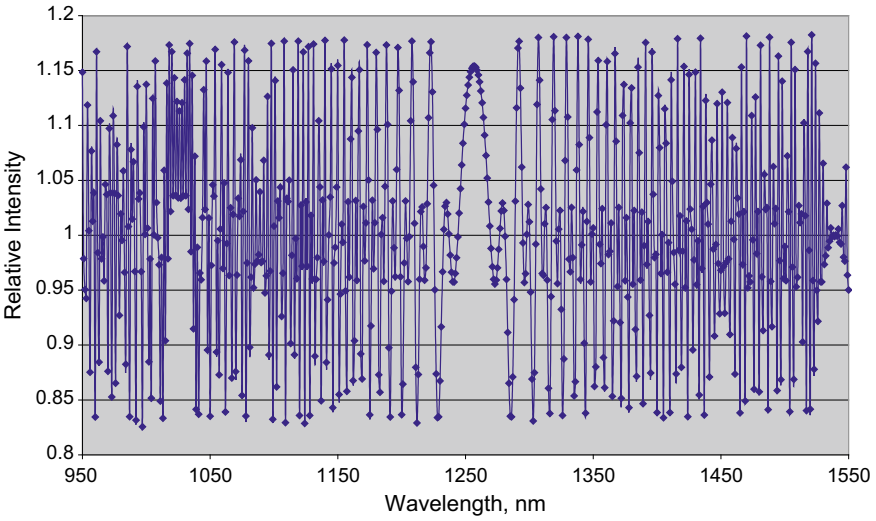

Fig. 11.47 Four-wave crosstalk-induced interference in a highly birefringent photonic crystal fiber: fiber length 1 m, leakage factor is 0.01, in-plane components of the signal and crosstalk are interfering

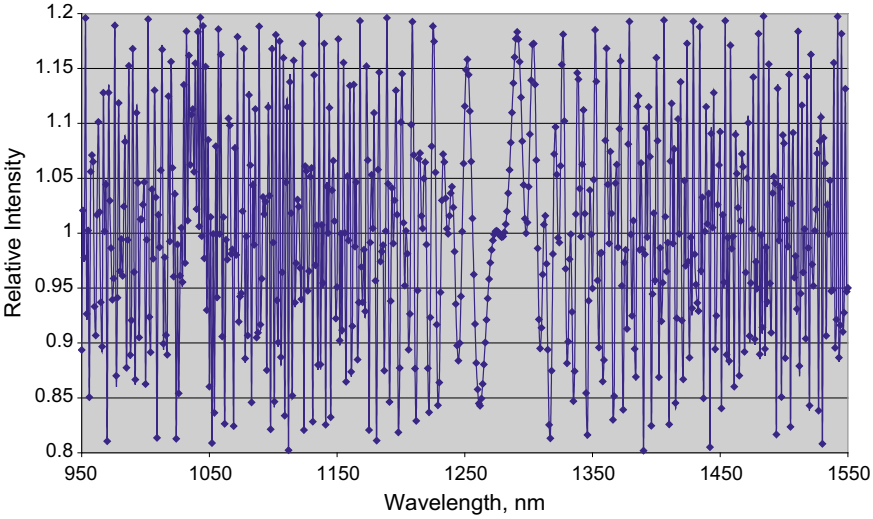

Fig. 11.48 Four-wave crosstalk-induced interference in a highly birefringent photonic crystal fiber: fiber length 1 m, leakage factor 0.01, cross-plane components of the signal and crosstalk are interfering

birefringence as $\Delta = n_e - n_o$, linearly changing from $1.25 \cdot 10^{-4}$ at 950 nm to $1.55 \cdot 10^{-4}$ at 1550 nm, loosely accommodating the properties of the photonic crystal fibers measured in [11.77]; the difference in the optical path lengths of the main and leaking signals via the demultiplexer is respectively set to 1 mm for the ordinary axis and to 2 mm for the extraordinary one.

If there is no birefringence, $\delta = 0, \delta_e \equiv \delta_o$, Eqs. (11.127) transform into an equation for the two-wave interference:

$$I_{\Sigma,\delta=0,\delta_e=\delta_o} = I_A(1-\xi) + 2\sqrt{I_A I_B \xi(1-\xi)}\cos\delta_o + I_B\xi. \tag{11.128}$$

The case of two-beam crosstalk-induced interference in a nonbirefringent fiber is seen in Fig. 11.49.

The actual beat-length properties of birefringent fibers can be obtained via modal-birefringence measurements either in radiation returned – backscattered or backreflected – or transmitted by the fiber utilizing polarization OTDRs, OFDRs, or any spectral-scan techniques (see Chaps. 3 and 10) [11.84–11.91]. Birefringence-dispersion measurement by wavelength-scanning via dual-beam interferometers (see also Chap. 8) allows for relatively high sensitivity, largely limited only by the spectral resolution of a given spectrometer [11.89–11.91]. Polarization-based measurements via backscattered radiation are inherently noisy owing to fiber inhomogeneities, especially due to the evolution of the state of polarization when

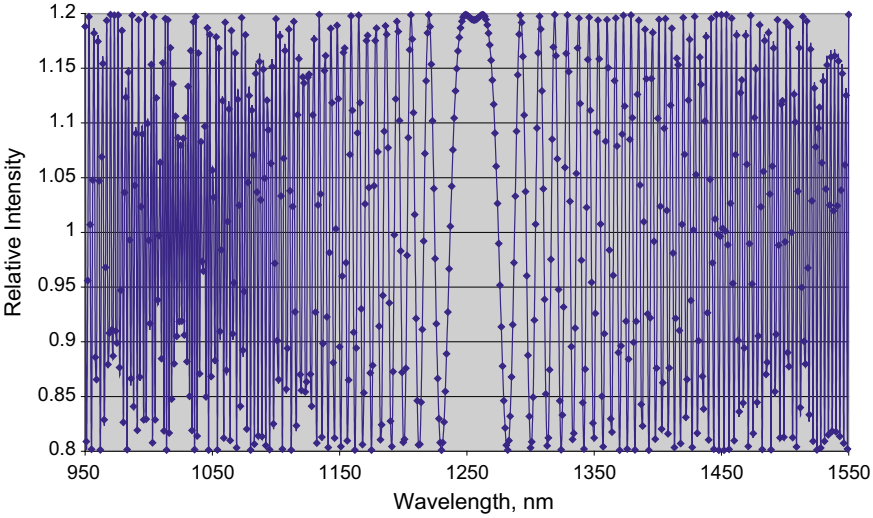

Fig. 11.49 Two-wave crosstalk-induced interference in a non-birefringent fiber: fiber length 1 m, leakage factor 0.01, ordinary refractive index as in Figs. 11.46–11.48

light propagates via a non-polarization-maintaining fiber, and therefore are limited in sensitivity and in spatial resolution, although they are capable of distinguishing mode-coupling characteristics: down to centimeters of polarization mode-beating lengths or degrees/meters in birefringence [11.85–11.88].

Chapter 12
Spectroscopic Interferometry and Laser-Excitation Spectroscopy

12.1 Fourier-Transform Spectroscopic Interferometry

The underlying Michelson-Morley experiment [12.1] was made possible in an interferometer designed by Michelson for atomic spectroscopy in his attempt to establish a new meter standard using a suitably narrow spectral line, the red-line singlet not doublet of cadmium, via measuring visibility of a resultant two-beam interference pattern (see Chap. 3): $V = (I_{max} - I_{min})/(I_{max} + I_{min})$. As pointed out by Rayleigh [12.2] that interferometer was not able to measure a unique spectral distribution from the visibility without a knowledge of the phase of its wavelength-modulating function [12.3]. Although, as concepts of Fourier transformation, of throughput advantage [12.4], and of multiplex gain [12.5] of the interferometer versus a scanning spectrometer were analyzed and developed, Fourier-Transform Infrared (FTIR) Spectroscopy emerged as an essential tool in overcoming relatively low spectral outputs of sources and high noise of detectors in the infrared.

12.1.1 Advantages of Fourier Transform Spectroscopy

Despite the renowned presence of Michelson interferometer, its widespread use for spectroscopic purposes had been on hold until theoretical rewards of the Fourier transform spectroscopy were understood and the advanced computation techniques, such as the Fast Fourier Transform (FFT), were fully developed. The throughput or Jacquinot advantage is the understanding that slit spectrophotometers limit the amounts of flux of radiation transmitted via its spectral-selection element by a width $\Delta\lambda$ of a resolution-defining slit [12.4]. Since the maximum transmission of the spectrometer at the resolving power R_λ, given by the widest of its two slits, is reached at the equal slit width, and thus presuming them both to be $\Delta\lambda = \varphi/D_\lambda$ for a given dispersion D_λ (see Fig. 4.26), the equation for the spectrometer's power could be written similarly to Eqs. (4.4) and (4.5) in the form of the flux-selecting geometry:

M. Bukshtab, *Photometry, Radiometry, and Measurements of Optical Losses*, Springer Series in Optical Sciences 209,
https://doi.org/10.1007/978-981-10-7745-6_12

$$\Phi_S = \tau L_\lambda S\Omega = \tau L_\lambda S\beta\varphi = \tau L_\lambda S\beta\Delta\lambda D_\lambda = \tau L_\lambda S\beta\lambda D_\lambda / R_\lambda, \tag{12.1}$$

where $R_\lambda = \lambda/\Delta\lambda$ is the spectrometer resolution; β, φ are the angular height and width of its slit; S is the normal area of the output beam; Ω is the solid angle subtended by the output slit and L_λ is the input source brightness at wavelength λ (see also Eqs. (1.31), (1.59) and Figs. 1.2, 1.4).

Equation (12.1), derived under a presumption of photometric interpretation and diffraction-limited slit widths (see Chap. 3 for more detail), prescribes the spectrometer throughput to be proportional to dimensions of its dispersive element, whether a prism or diffraction grating, and inversely proportional to its resolving power. The SD_λ product in Eq. (12.1) is given by the area of the base and dispersion for a prism and by the surface area and blaze angle for a grating in Littrow configuration, presuming the angular height and width of slits being identical [12.4].

In case of an interferometer, such as a Fabry-Perot etalon, being a relatively straightforward to consider the throughput for either transmitted or reflected light, is identified by the totality of wavelengths, existed within an input beam, satisfying its conditions of constructive interference (Eqs. (3.119), (3.122), (3.119c), (3.122c), and (8.16–8.20)). The resolving power of the etalon defines an angular width and separation of Airy fringes distinguishing neighboring rings [12.4]:

$$\partial(\cos\delta)/\cos\delta = \partial(\kappa)/\kappa = \partial(1/\lambda)/(1/\lambda) = 1/R_\lambda, \tag{12.2}$$

where $\kappa = 1/\lambda$ is the wavenumber of a monochromatic component of incident light as the angular width of each ring observed $\partial(\cos\delta)$ is defined by the finesse of the etalon (Eqs. (7.68) and (8.20)). Identifying the throughput as the flux transmitted by the etalon into a fringe ring selected by an annular aperture of its size at solid angle Ω subtended by it, from relations (3.122c), (7.66), (8.17):

$$\begin{aligned} \frac{I_\tau}{I_0} &= \left(1 + F\sin^2(\delta_\lambda/2)\right)^{-1} \\ &= \left(1 + \left[4\tau\rho\Big/(1-\tau\rho)^2\right]\sin^2(\delta_\lambda/2)\right)^{-1} \\ &\underset{\tau=1}{=} \frac{1}{1 + [4\rho/(1-\rho)^2]\sin^2(\delta_\lambda/2)}, \end{aligned} \tag{12.3}$$

where $F = 4\rho/(1-\rho)^2$ is the finesse parameter and τ is the inner transmittance of the etalon space.

Equation (12.2) leads to angle Ω, defined by a circular fringe ring of angular width $\partial(\cos\delta)$, being:

$$\Omega = 2\pi\partial(\cos\delta) = 2\pi\cos\delta/R_\lambda \cong 2\pi/R_\lambda. \tag{12.4}$$

Since the transmittance of the etalon within an individual fringe varies, therefore averaging cos δ out as $\pi/4$, the throughput of a Fabry-Perot etalon for a beam of radiance L and area S becomes:

$$\Phi_{F-P} = \tau L_\lambda S\Omega = 2\tau L_\lambda S\pi \cos\delta/R_\lambda = \tau L_\lambda S\pi^2/(2R_\lambda). \quad (12.5)$$

When comparing Eqs. (12.1), (12.5) for typical values of dispersion and resolving power of spectrometers and interferometers, the throughput advantage can reach tens or hundreds [12.4].

The multiplexing or Fellgett advantage [12.5] refers to the respective gain of the optical signal in spectroscopic interferometry, in which Fourier Transform performs the function of a dispersing system allowing the signal of all wavelengths to be collected simultaneously against single noise of detection—not being added up for every individually-registered wavelength. Essentially, the multiplex advantage comes from the absence of the exit slit, enabling the selection of individual wavelengths in dispersive spectrometry [12.42], thus resulting in $N^{0.5}$-less contribution of photon noise which adds up as a square root of combined signal noises: $N_\Sigma = \sqrt{(S_1 + S_i + ... + S_N)} = \sqrt{N} \cdot \sqrt{S}$.

Less-pronounced or rather provisional Connes' wavelength advantage relates to a common practice of using a He–Ne laser and its visible 632.8-nm wavelength for calibration of FTIR wave-number scale [12.7], since the very custom is routinely deployed in the dispersive spectroscopy. Although, the distance between two Michelson-interferometer mirrors in FTIR is more likely to remain stable and more reproducible when is continually calibrated by He–Ne laser wavelength versus a rotating grating in a dispersive spectrometer, especially for the infrared spectral region.

The emergence of corner-cube reflectors replacing flat mirrors in Michelson interferometer [12.8] became another vital development, enabling the quick spread of FTIR systems for spectroscopy. Let us note, these notional advantages of Fourier Transform Spectroscopy (FTS) relate to the direct comparison with the spectrum-scanning spectroscopy and mainly to simultaneous versus sequential measurements. There is no multiplexing or throughput gain versus any spectrometer with an instantaneous recording of spectrum via the same size opening, such as a spectrograph with a CCD array, if its pixel size could be considered infinitively small with no sensitivity gaps between two neighboring pixels. For example, the Hadamard spectrometer provides equivalent multiplexing of spectrums via multiple-slit Hadamard transform [12.11]. Moreover, considering the essence of Michelson-interferometer design (see Figs. 12.1 and 12.2), a half of its source

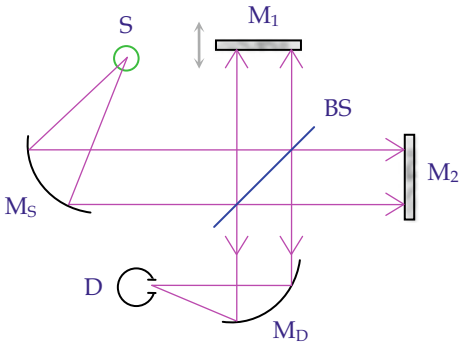

Fig. 12.1 Schematic of the Michelson interferometer

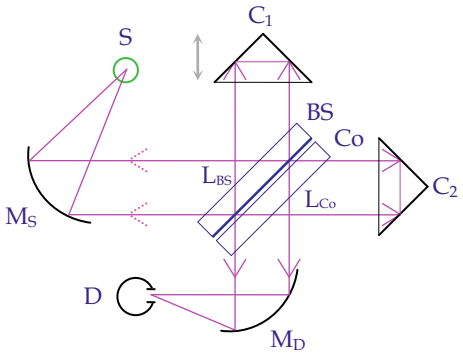

Fig. 12.2 Path-equalized FTIR spectrometer

radiation is lost on the beamsplitter, a half of the remainder is modulated, and only one half of the overall efficiency is retained in the sinusoidal modulation versus a square wave, consequently reducing the theoretical $\sqrt{N}$ advantage to $\sqrt{N/2^3} = \sqrt{N/8}$ [12.12].

12.1.2 Conceptual FTIR Interferometers

A common reflective layout of Michelson interferometer-based FTIR is pictured in Fig. 12.1. A parallel beam from point source S of infrared (IR) radiation, projected by off-axis parabolic mirror M_S to mirrors M_1, M_2 via semitransparent beamsplitter BS, is collimated by identical to M_S mirror M_D into detector D [12.10]. A relatively fast movement of mirror M_1 serves to first equalize a path-length difference of two arms of the interferometer and then discriminate the movable arm length within the coherence length of source S, as the spectrum is measured. The actual arm length difference is often calibrated via a 632.8-nm wavelength of a frequency stabilized He–Ne laser (not shown in Fig. 12.1). A physical source of IR light is never a point source, it becomes virtual one via its uniform radiance and a limited-size detector to also reduce noise and enhance sensitivity. Michelson interferometer fringes are observable as its arms difference does not exceed the coherence length of a source, but the path-length inequality of interferometer arms reduces the maximum visibility of interference fringes. When the source is of a finite size and interferometer's beam splitter is precisely positioned, while mirrors remain ideally parallel, concentric interference fringes (Haidinger rings) [12.13] are observed at infinity, plus linear fringes localized on mirror surfaces could become observable for cross-tilted mirrors.

Several solutions [12.3, 12.6] are available to keep a precisely equal path-length of two arms of Michelson interferometer, such as adding an extra compensator plate with its optical thickness equivalent to one of the beamsplitter, or deploying a beamsplitter cube, equalizing path lengths in glass. The corner-cube reflectors are used to prevent any misalignment associated with tilted mirrors, especially the moving one [12.8]. In practical applications, Michelson interferometer of Fig. 12.1 is enhanced to form equal path lengths in both arms (Fig. 12.2) where dotted arrows

show stray light coming back to source S via beamsplitter BS. The path length L in BS is equalized in extra compensator Co of the matching-bulk thickness. Identical corner cubes $C_{1,2}$ are formed by three metal mirrors, preserving one constant path difference over beam's cross-section during cube movements in one arm and keeping it independent of assembly rotations, if each mirror tilt is small and occurs near corner-cube center.

In essence, the movement of one of interferometer mirrors serves as a converter of detected unmodulated broadband radiation of a DC source into a modulated AC signal at frequency *f* of the mirror movement, also reducing detector noise caused by fluctuations of source intensity as the amplitude of white noise declines inversely to *f*. The resulting detector signal at frequency *f* becomes a function of path-lengths difference providing the Fourier transform of the intensity of the light source [0.46]. For a monochromatic oscillation at wavelength λ, the amplitude of a sum of two waves recombined by the interferometer arms at its detector is (see Chap. 3 and Fig. 3.9):

$$\begin{aligned} I_\Delta = \left|E_\rho E_\rho^*\right| = I_0(1+\cos\delta) = I_0(1+\cos((2\pi/\lambda)\Delta\ell)) \\ = I_0(1+\cos(2\pi\kappa\Delta\ell)), \end{aligned} \tag{12.6}$$

where $\Delta\ell = 2(\ell_1 - \ell_2)$ is the normal path-length difference of interferometer arms, δ is the phase difference for two interfering waves at the angle of incidence φ, and $\kappa = 1/\lambda$ is the spectroscopic wavenumber (vs. $\kappa_0 = 2\pi/\lambda$). The sum of monochromatic components of radiation becomes:

$$I_\Delta(\kappa) = \int_0^\infty I_{\tau,\rho}(\kappa)(1+\cos(2\pi\kappa\Delta\ell))\partial\kappa, \tag{12.7}$$

being constant-modified cosine form of Fourier transform for the spectral intensity of radiation, emitted by system's source, versus the path-length difference of Michelson interferometer arms. The constant term $I_{\tau,\rho} = I_0\tau(\kappa)\rho(\kappa)$ denotes the background radiation reflected and transmitted by the beamsplitter with reflectance ρ and transmittance τ, presuming ideal interferometer mirrors. Since the integral in relation (12.7) does not extend to infinity, but to path-length difference $\Delta\ell$, its Fourier transform over a finite length becomes an unapodized scanning function $S(\Delta\ell)$ [12.3]:

$$I(\Delta\ell) = \text{background} + \int_0^{\Delta\ell} I(\ell)\cos(2\pi\kappa\Delta\ell)\partial\ell, \quad S(\Delta\ell) = \Delta\ell\,\text{sinc}(2\pi\kappa\Delta\ell)\,. \tag{12.8}$$

The longer is the path difference, the sharper the scanning function becomes, enhancing the resolution of FTIR spectrometer but increasing requirements to mirror parallelism during scans.

Equations (12.7, 12.8) need further modifications to represent actual interfered light, collected by system's detector, as it receives only one half of it, recombined on beamsplitter BS by Michelson interferometer arms, while another half is returned back to source S (dashed arrows in Fig. 12.2). Recycled light scattered back to the system from source S, as well as from detector D, is nothing but noise and dealing with it represents a challenge to FTIR, especially for internally modulated Michelson interferometer [12.14]. Because of imperfections, including nonequivalent dispersions of interferometer arms, a measured phase component for a spectral intensity of the source could be obstructed by anomalous phase contributions for the intensity of the instrument itself [12.15].

Converting from source radiation to the spectral intensity of interferogram, received by the detector and summing-up varied phase contributions in FTIR spectrum, Eq. (12.7) turns to:

$$I_{\Delta,D}(\kappa) = \int_0^{\Delta\ell} \eta_{BS}(\kappa)\eta_0(\kappa)I_S(\kappa)\partial\kappa + \int_0^{\Delta\ell} \eta_{BS}(\kappa)\eta_0(\kappa)\eta_m(\kappa)I_S(\kappa)\cos(2\pi\kappa\Delta\ell)\partial\kappa, \tag{12.9}$$

where $I_S(\kappa)$ is the spectral intensity of the source; $\eta_{BS}(\kappa) = 0.5(4\rho\tau)$ is the efficiency of beamsplitter in the ideal case of $\rho(\kappa) = \tau(\kappa) = 0.5$ reaching 0.5; $\eta_m(\kappa)$ is the modulation efficiency, affecting only AC term and representing a zero delay modulation amplitude of balanced-arms input versus the interferogram baseline; and $\eta_0(\kappa)$ is the dispersion efficiency, which is 1.0 for perfectly optically-equal interferometer arms. Assigning effective spectrum's intensity $I_\eta(\kappa) = I_S(\kappa)\eta_{BS}(\kappa)\eta_m(\kappa)\eta_0(\kappa)$, optical path $\ell_o = n(\kappa)\ell$ and phase shift $\varphi_\kappa = \kappa\Delta\ell_o$, the interferogram equation becomes [12.15]:

$$\begin{aligned} I_D(\ell_o) &= \int_0^{\Delta\ell} I_\eta(\kappa)\cos(2\pi\kappa\ell_o - \varphi)\partial\kappa \\ &= \int_0^{\Delta\ell} I_\eta(\kappa)\cos\varphi\cos(2\pi\kappa\ell_o)\partial\kappa + \int_0^{\Delta\ell} I_\eta(\kappa)\sin\varphi\sin(2\pi\kappa\ell_o)\partial\kappa, \end{aligned} \tag{12.10}$$

defining spectral path-difference and dispersion-delay contributions, with the latter making the interferogram asymmetric, leading to a complex spectrum, and requiring a complex description. Furthermore, to extract a true spectrum from such a complex interferogram, a relevant complex calibration needs to be performed, removing erroneous contributions of the instrument, such as emissions of the beamsplitter, apertures, optics, and detector, which could produce a DC offset of the

signal or its modulation in a spectral domain of measurement. Assuming a superposition of all contributions to be linear, Fourier transform of a complex interferogram turns into [12.15]:

$$S_\Sigma(\kappa) = \int_0^{\Delta\ell} I(\ell_o)\exp(2\pi i\kappa\ell_o)d\ell_o = R_{det}(\kappa)[S_{true}(\kappa) + S_{erron}(\kappa)], \qquad (12.11)$$

where S_{true}, S_{erron} are the true and erroneous spectrums, and R_{det} is the detector spectral response as the wavenumber function. By independently measuring combinations of spectrally verifiable sources, such as a hot and cold blackbody, the complexity of FTIR spectrum should be resolved.

12.1.3 Enhanced FTIR Instruments

Since early developments of FTIR spectroscopy [12.9], a need to compensate for background emission of system's components led to various double-beaming schematics, one of which is seen in Fig. 12.3a [12.16]. The concept of double beaming is to have two beams out of phase with each other by making optical paths of the arms complimentary thus subtracting any background from the measured FTIR signal. In view (*a*) second beamsplitter BS_2 allows source's emission to pass via Cell containing an absorbing specimen and directly via the Michelson interferometer, which signal contains only modulation due to specimen's absorption. Connes-type interferometer [12.6] of view (*b*) demonstrates the double beaming at two detectors receiving reflected and transmitted via beamsplitter beams of equal intensity at 180°-phase shift.

Keeping Michelson interferometer mirrors parallel for every scan while extending its length proved difficult and various schemes were deployed to overcome the problem (see Fig. 12.3b, c). The corner-cube reflectors are most effective in narrow beams and the cat's eye ones are efficient in wide beams such as for stellar FTIR spectroscopy, since both schemes maintain independence of the

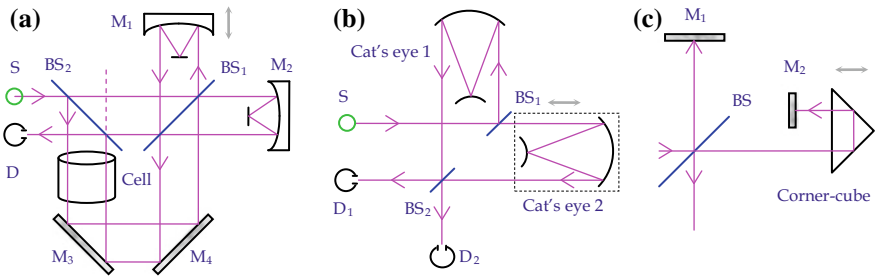

Fig. 12.3 Double background offsetting interferometers **a**, **b**, and uses of corner cube **c** and cat's eye retro reflectors **b**

direction of returning beam on a tilt of the mirror. Another approach is to compensate for mirror alignment imperfections via a two-arm balancing interferometer when a displacement in the one interferometer arm becomes complementary to that in another [12.17]. Such a concept is realized via double-sided mirror with each side participating in the first or second interferometer arm. As a result, the mirror tilt causes the same change as the succeeding rotation of one of the corner mirrors, using which it is compensated. In illustrated by Fig. 12.4 scheme, to uphold the 45° incidence mirrors M_1 and M_3 rotate a beam into vertical plane and M_2, M_4 provide the compensation for the tilt of DSM mirror [12.17].

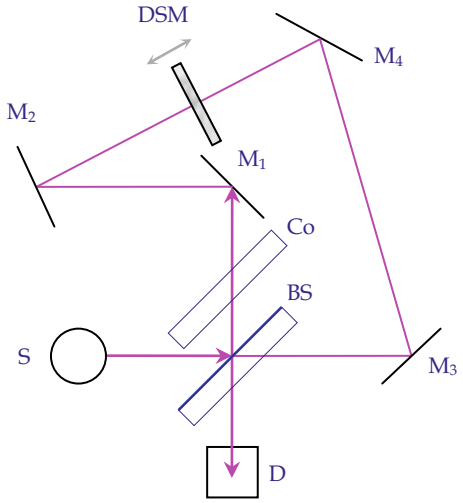

Fig. 12.4 Schematic of double-sided mirror balancing FTIR

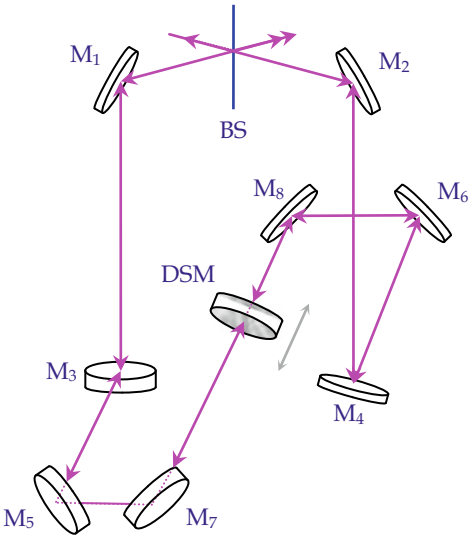

Fig. 12.5 Identical arms of Mobius band interferometer

One step further is provided by the design of Mobius band interferometer [12.18], which not only compensates for a tilt of the moving mirror but also for likely unequal rotations of the state of polarization. Although, Mobius interferometer requires adding mirrors enabling the identical polarization shift in every arm (Fig. 12.5). Figure 12.6 demonstrates dual-compensation concept for tilt error and lateral-movement distortion via pendulum mounting of the corner cube making its movement confined to one single plane during scanning [12.19]. The layout of Fig. 12.7 deploys identical corner cubes in symmetric interferometer arms, compensating for two-axis shearing error via integrated platform [12.20]. Combining double-sided mirror, the beamsplitter and added parallel mirror [12.20] in one arm with a corner cube in another arm (Fig. 12.8) makes an evident intensity imbalance in Michelson interferometer, thus while corner-cube movements quadruple the differential optical path, the corner-cube arm has one extra reflection versus the arm with the flat mirror similar to Fig. 12.6 reducing the modulation efficiency of two-beam interference. Any intensity deterioration ΔI in one arm in effect leads to a double drop in pattern visibility $\Delta V \approx 2\Delta I$ (see Chap. 3 for detail).

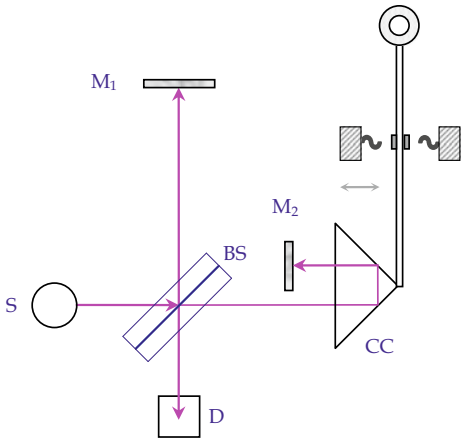

Fig. 12.6 Pendulum mounting of the corner cube in FTIR

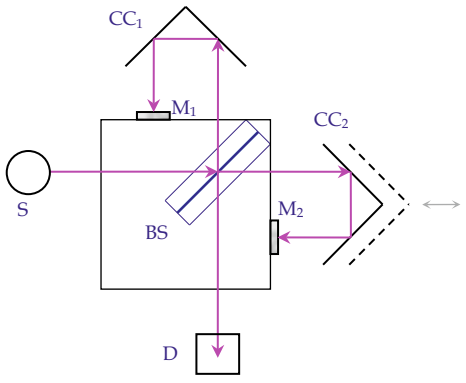

Fig. 12.7 Two-axis shear compensating modular FTIR

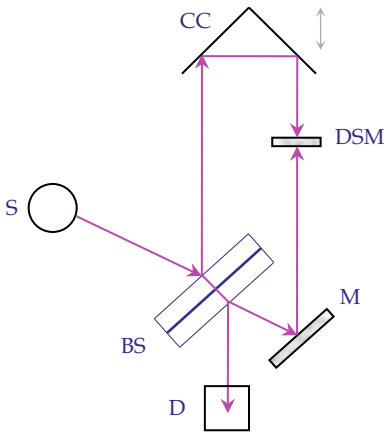

Fig. 12.8 Unbalanced FTIR with unified beamsplitter and mirror

One parameter limiting wider deployments of a moving corner cube is its relative bulkiness, especially when a fast scanning is required thus the moving mirror remains appealing for rapid-scan devices. Moreover, since tilt error of a moving element is measured via a wavenumber of a distorted fringe [12.22], it is highly pronounced at near infrared and visible wavelengths in FTIR utilized for biotech studies and, since a reciprocating motion of double-sided mirror generates four times the displacement in interferometer's differential path, it quadruples an uncompensated tilt error leading to ellipsoidal beam profile edged by displacements of mirror assembly in a moving articulator [12.23]. For near IR and visible radiation and white-light interferometry another error comes from the optical thickness of beamsplitter and compensator or halves of beamsplitter cube not precisely equal to each other, even for a matched pair and wedge-angle alignment [12.24, 12.25]. Since He–Ne laser tracking of each optical path length in FTIR interferometer is commonly done via especially designed optical paths for 632.8-nm beam, precise tracking of arm paths for an IR wavelength is best realized by known IR absorption lines or a copropagating optical path [12.26].

12.1.4 Comparison of FTIR Instrumentation

Following Eqs. (12.7), (12.8), the longer is the path length difference of interferometer arms the higher spectral resolution $\Delta\kappa$ can be obtained in a given FTIR instrument. Depending on instrument's apodization function, the instrumental resolution $\Delta\kappa_{\text{inst}}$ distorts theoretical limit $\Delta\kappa_{\text{theor}}$ by spectral function δ_{FWHM} of a peak observed [0.48]:

$$\Delta\kappa_{\text{inst}} = \Delta\kappa_{\text{theor}}/\delta_{\text{FWHM}} = (\Delta\ell\delta_{\text{FWHM}})^{-1}, \tag{12.12}$$

where δ_{FWHM} is the full-width-half-max function of the spectrum resolved by the interferometer. As FTIR instruments are compared, the theoretical limit being the inverse difference of the arms lengths is perceived as the highest attainable resolution assuming the sampling and apodization define an ideal instrument while the instrumental line shape of each spectrometer is equivalent. The theoretical limit

could also be seen phenomenologically from Rayleigh criterion of spectral resolution [1.1], as a path-length change between the principal maximum of interference and its first minimum. This straightforwardly translates to $\Delta\kappa = 1/2\Delta\ell_{max}$, if the concluding optical-path length $2\Delta\ell_{max}$ is not dispersive. When the path becomes dispersive (see Eqs. (12.9)–(12.11)), the wavenumber resolution $\Delta\kappa = (d\kappa/d\nu)\Delta\nu$ converts to frequency $\Delta\nu = \Delta\lambda/\lambda^2$ with wavelength terms:

$$\begin{aligned} \Delta\nu &= 0.5/(\Delta\ell_{max} + (\partial\Delta\ell_{max}/\partial\nu)\nu), \\ \Delta\lambda &= 0.5\lambda^2/(\Delta\ell_{max} - (\partial\Delta\ell_{max}/\partial\lambda)\lambda), \end{aligned} \tag{12.13}$$

where 0.5 factor increases to 0.603 for FWHM criterion or 0.886 at triangular apodization [12.27].

One obvious comparison of FTIR capabilities is versus a grating spectrometer, suitable for a measurement in the same spectral interval as FTIR's Michelson interferometer. Another one can be done via a lamellar-grating system, which concept relies on providing the path difference for two interferometer arms using a lamellar grating [12.28]. The lamellar-grating interferometer is based on substituting the articulator with a movable mirror in Michelson interferometer by one steady lamellar grating, being a version of surface-relief grating (see paragraph 3.4), and laying out the first interferometer arm via its steps, but second via its grooves in reflected light [12.29].

Figure 12.9 schematically depicts three types of IR spectrometers—one as diffraction-grating based monochromator and other two as lamellar-grating and Michelson interferometers, all built with the same source, detector, and identically accommodating collimating optics for a controlled test of relative merits in spectral resolution at frequencies (wavenumbers) from 10 to 150 cm^{-1} [12.30].

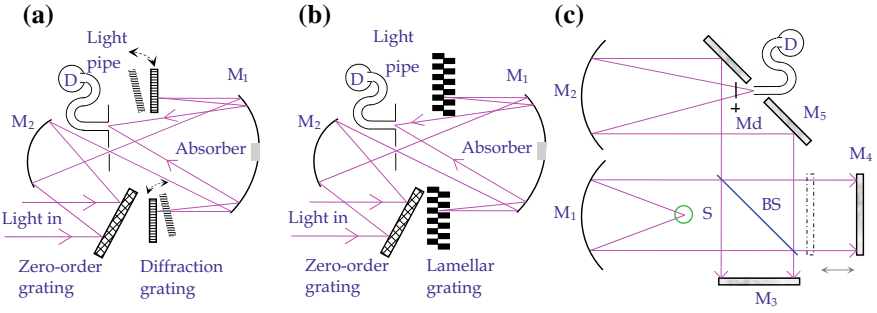

Fig. 12.9 Comparison of diffraction-grating monochromator **a** with lamellar-grating **b** and Michelson **c** interferometers: M_1, M_2 – paraboloid mirrors, M_3–M_5 – flat mirrors, S – source (not shown in views a, b), D – detector, Md – light modulator

All compared systems used the main beam of near 1.1-cm diameter with $f/1.5$ NA optics to have equal 0.5 steradian-cm^2 products of irradiated area and solid angle of irradiation, sufficient for small solid samples studied at cryogenic temperatures via a cooled detector and a metal light pipe. Other measures were also taken, such as matching the size of diffraction gratings with the interferometer mirrors and utilizing an absorber to prevent direct irradiation of the light pipe by the beam reflected from gratings to the center of mirror M_1 and to the pipe. The monochromator was equipped by two main 28 · 35-cm diffraction gratings with a 5 · 10-cm hole cut in their centers. The monochromator slits were fully open in interferometer configuration at two 30-cm^2 lamellar gratings, making its efficiency close to 100% for a limited frequency range below 100 cm^{-1} [12.29, 12.30]. Michelson interferometer was assembled with 1-mil Mylar beamsplitter for wavenumber-dependent modulation efficiency approaching 100% threshold in spectral intervals of reflectance-transmittance product near 0.25. That interferometer path length difference was variable from −0.5 to 20 cm. Three-way deep IR testing confirmed higher resolving power of interferometers versus the grating spectrometer: up to 0.1 cm^{-1} spectral resolution in 3–80 cm^{-1} frequency range [12.30].

To boost performance, Michelson interferometer can be build as a dual-beam spectrometer, splitting an incoming beam of IR radiation into sampling and reference paths – with Hi-Ne laser light propagating in between into a hole in one mirror. That design allowed to improve spectral resolution to 0.025 cm^{-1} in 10 cm^{-1} – 450 cm^{-1} wavenumber range and reach 0.0001 cm^{-1} frequency accuracy, at 7.2-cm maximum path difference [12.31]. In a conceptually similar design replacing flat mirrors with large corner-cube reflectors the highest resolution approached 0.001 cm^{-1} at 6.2-m of maximum optical-path difference of two interferometer arms [12.32]. Other means for enhancement involve time-resolved spectrum acquisition via step-scan or continuous recording – with the later transient spectrum synchronized by the interferogram sampling at an added phase correction of distortions in a changing optical path length for time-evolving events [12.33, 12.34], and combining a moving arm with a multiple reflection optical-path expanding cell [12.33–12.38].

Figure 12.10 provides examples of a resonant cavity embedded in an FTIR (see also Sect. 7.3 and Fig. 7.14). View (*a*) shows a step-scan interferometer with its

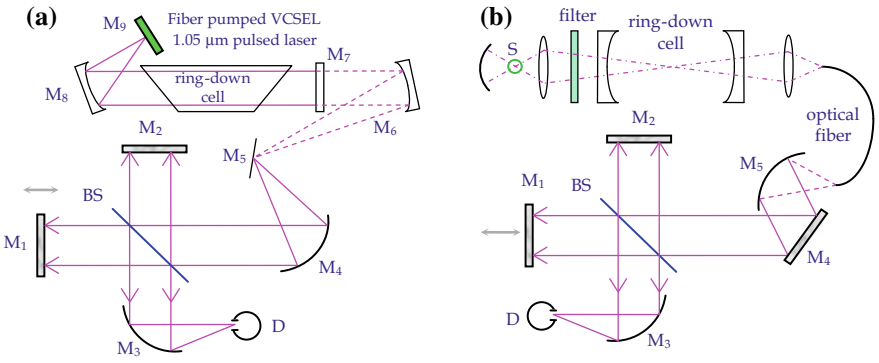

Fig. 12.10 Intracavity FTIR system embedding multiple reflection cell having step scan **a** and continuous **b** data acquisition

light source initially excited at a zero path-length difference and then moved to the next step for the subsequent time component of the interferogram to be sampled at its second excitation, etc. Each time component represents all path-difference steps of source emission and sample absorption [12.35]. The ringdown cavity is added to the moving arm of Michelson interferometer, for which an optically pumped VCSEL serves as a pulsed source with its output mirror M_9 and mirror M_7 defining standing-wave's cell with a gas sample under study. The system gathered 64–512 time components – each of 10,000 samples obtained at 32-ms acquisition time with the ringdown cavity adding 960-m optical path to every spectrum recorded, allowing to grow the path-length difference up to 130 km for $\sim 10^{-10}$ cm^{-1} Hz$^{-1/2}$ sensitivity at near 1-s averaging time and 30 min for all-points acquisition [12.36].

View (*b*) depicts a Fabry-Perot ringdown resonator coupled with a commercial FTIR (IFS 125 HR) via 3-m long 0.5-mm diameter multimode fiber having numerical aperture NA = 0.37 [12.38]. The system combines (*a*) the broadband-ringdown approach [7.46] (see Sect. 7.3.5), in which a ringdown resonator selects waves matching its stable longitudinal modes, and (*b*) the phase-shift cavity technique [8.12] (see Sect. 8.3), in which the wavelength dependent cavity delay shifts a phase of transmitted waves but ~100% efficiency coupling occurs for resonant eigenmodes. Here instead of measuring the ratio of in- to out-of-phase component it detects a spectrally diversified transmission of broadband light via a long unstabilized ringdown cavity by FTIR interferometer replacing the monochromator (compare Fig. 7.17). Since at non-resonant frequencies the signal intensities tend to be extremely low, 10-h long integration times were required to obtain 0.05 cm^{-1} linewidth-limited resolution for measured H_2O absorption in the vicinity of 13,850 cm^{-1} (722 nm) at no apodization [12.38]. When applying the phase shift-technique detecting $\sin\varphi$ and $\cos\varphi$ terms leading to tangent dependence of phase angle versus wavenumber (Eqs. (8.37, 8.47)) the 0.5 cm^{-1} resolution of IFS 66 FTIR spectrometer at 765 nm was reached in 15-min time [12.37].

12.1.5 Spatial Heterodyne Spectrometry

During initial phases, development of FTIR spectroscopy was progressing in varied directions partly due to Michelson interferometer unavoidable loss of light on a beamsplitter and stringent requirements for precision mirror movements restricting its wide-spread applicability. The lamellar-grating interferometer illustrated by Fig. 12.9b could be seen as the very first attempt to build a stationary Michelson interferometer using spatial Fourier transformation via interferometric modulations of diffracting by the lamellar grating wavefronts [12.29]. It can also be made, if interference fringes combined at an angle φ are holographically or photo-recorded orthogonally to a wavefront bisector [12.39], even for an incoherent light source per monochromatic wavelengths superpositions via Fourier-transform setting of coherent virtual sources. Another concept relates to substituting the beamsplitter with a diffraction grating [12.40], particularly with reflective one, suitable for a range of wavelengths from UV to VIS to IR [12.41].

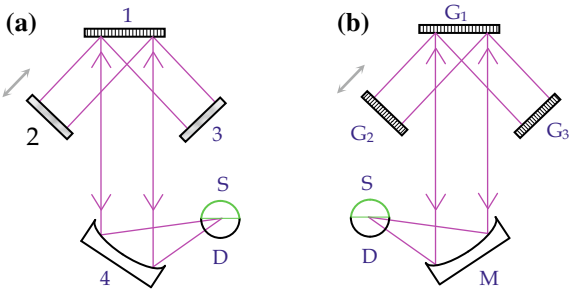

Fig. 12.11 Reflective FTIR with **a** diffraction grating replacing beam splitter and **b** three gratings

Two schematics of reflective FTIR systems are seen in Fig. 12.11. In view (*a*) single diffraction grating 1 bi-directs the incident beam of light, coinciding with the grating normal, to symmetrical paths of equal diffraction orders comprising interfering beams via normally placed mirrors 2, 3 returning both beams back to vertically tilted grating 1, to mirror 4, and detector D placed out of plane with source S. Mirror 2 is translated to change the optical path of its arm. However, such an interferometer is capable of resolving only narrow spectral lines of width $\Delta\lambda = \lambda/\delta$ defined by wavelength resolution δ of the grating, thus for broad-band interferometry not one, but three symmetric gratings are needed (view *b*) [12.41].

Even with three gratings, positions of diffracted beams change and the optical path difference is a nonlinear function of wavenumber, leading the beams to walk-off their nominal optical paths, limiting the interferometer passband and reducing its modulation efficiency. To overcome such limitations the spatial-heterodyne [12.6] and common-path [12.44] interferometers are deployed.

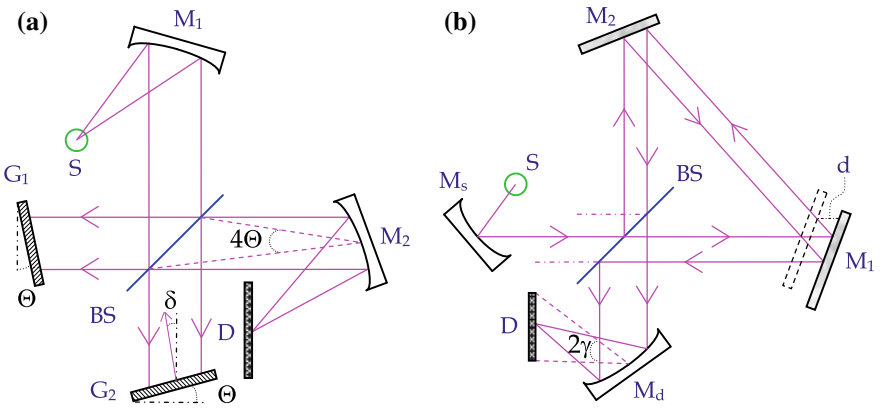

Fig. 12.12 Stationary spatial heterodyne **a** and triangular common path **b** FTIR interferometers

The concept of stationary heterodyne interferometry replacing arm's mirrors with diffraction gratings in a Littrow mode is depicted in Fig. 12.12a. As a result of the two-beam diffraction on gratings G_1 and G_2 the interference pattern on mirror M_3 or detector array D could be seen via an identical to diffraction-gratings equation with diffracting beams, merging at angle 4Θ in plane M_2:

$$2\kappa_0 \sin\Theta = m/p = \kappa[\sin\Theta + \sin(\Theta - \delta)], \tag{12.14}$$

where κ_n, κ are the wavenumbers of wavefronts at grating's normal and angle δ, p is the grating period, m is the diffraction order, and δ is the angle for the diffracted wavefront with the optical axis, while each grating normal is set at angle Θ to make angle 4Θ [12.43] (see paragraph 3.4 for detail). In selective-modulation common path Sagnac instrument seen in Fig. 12.12b interfering beams are formed via radiation propagating interferometer's arms in opposite directions, having the dotted line indicating the position of mirror M_1 for equal arm's distance. Offset d of two arms makes the beams collimated by mirror M_s tilt, interfering on photodiode array D via mirror M_d. The final spectral resolution for the first system is defined by a product of the order of diffraction by a total number of the grating lines, and by the maximum offset $\sqrt{2}d$ of two arms path length for the second—each doubled for the dual pass [12.43, 12.45].

The conversion of an image formed by tilted diffracting wavefronts into spatial frequencies in Fourier space comes from Huygens-Fresnel principle, defining the physics for transformation of image coordinates to spatial frequencies at a coherent summation of wave amplitudes [12.46]. Likewise, the division of radiation of a source for the common path interferometer to two virtual emitters could be seen as a version of the Young's two-pinhole experiment (see [1.1]), permitting to use a selective-modulation system with a spatial light modulator (not seen in Fig. 12.12b) and synchronous detection for the high throughput, without needs of Fourier transformation [12.47].

To compare the wavenumber resolution of a Michelson interferometer, a spatial-heterodyne and a common-path spectrometer, let us rewrite Eqs. (12.7), (12.8) for an equal arms' length:

$$I_\Delta(\kappa) = I_0/2 + \int_0^\infty I_{\tau,\rho}(\kappa)\cos(2\pi\kappa\Delta\ell)\partial\kappa, \tag{12.15}$$

where I_0 is the output at $\Delta\ell = 0$. The Fourier transform for the even function $I_\Delta(\kappa)$ gives [12.30]:

$$\begin{aligned} S(\Delta\ell) &= 4\int_0^\infty [I_\Delta(\kappa) - I_0/2]\cos(2\pi\kappa\Delta\ell)\partial\kappa \\ &= 4\int_0^\infty [I_\Delta(\kappa) - I_02]\cos(2\pi 2\kappa(\ell_1 - \ell_2))\partial\kappa, \end{aligned} \tag{12.16}$$

where $S(\kappa)$ is the frequency spectrum measured as a function of path-length difference. The intensity spectrum of spatial-heterodyne system (Fig. 12.12a) for diffracted beams at angle δ becomes:

$$I_\Delta(\kappa) = I_0/2 + \int_0^\infty I_{\tau,\rho}(\kappa)\cos(2\pi 2\kappa \sin(\delta)\Delta x)\partial\kappa. \tag{12.17}$$

Replacing $2\kappa \cdot \sin(\delta) = 4(\kappa - \kappa_0)\tan(\Theta)$ from Eq. (12.14) for the small angle δ and image size Δx:

$$I_\Delta(\kappa - \kappa_0) = I_{\delta=0}/2 + \int_0^\infty I_{\tau,\rho}(\kappa)\cos(2\pi 4(\kappa - \kappa_0)\tan(\Theta)\Delta x)\partial\kappa, \tag{12.18}$$

the intensity spectrum of heterodyne spectrometer is similar to one of Michelson interferometer:

$$S(\Delta x) = 4\int_0^\infty [I_\Delta(\kappa - k_0) - I_{\delta=0}/2]\cos(2\pi 4(\kappa - \kappa_0)\tan(\Theta)\Delta x)\partial\kappa, \tag{12.19}$$

at the reduced spatial frequency $4(\kappa - \kappa_0)\tan\Theta$ and as a function of interference-image size [12.43].

The theoretical resolving power of Michelson interferometer is the number of waves, fitting the path length difference $R_M = 2\kappa(\ell_1 - \ell_2) = 2\Delta L/\lambda$, its spatial frequency f_M. Comparing Eqs. (12.16), (12.19) for the same criteria, the resolving power of a spatial-heterodyne spectrometer is $R_H = 4W\kappa\sin\Theta$ or the total number of grooves imaged on a detector; here W is the grating's width and Θ is the Littrow angle. The optical path difference of triangular common-path spectrometer is set by the normal shift of mirror M_1 (see Fig. 12.12b) resulting in arms-length offset $\sqrt{2}d$, thus:

$$I_\Delta(\kappa) = I_0/2 + \int_0^\infty I_{\tau,\rho}(\kappa)\cos\left(2\pi 2\kappa \sin\gamma\sqrt{2}d\right)\partial\kappa, \tag{12.20}$$

where angle 2γ defines the total length of the interference pattern, providing the resolving power $R_C = 2\kappa\sqrt{2}d\sin\gamma$ with spatial frequency $f_C = \sqrt{8}\kappa d\sin\gamma$ versus $f_H = 2\kappa\sin\delta \approx 4(\kappa - \kappa_0)\tan\Theta$ [12.42–12.50]. Nonetheless, the actual resolving power of every FTIR spectrometer is a combination of the theoretical resolving power and its instrument-response function [12.10], obscured by system's noise or in other words its ability to accurately measure the interferogram function $I_0/2$ [12.48]. Plus, if the optical path length is wavelength dependent, since it almost always is, the resolving power $R_M = f_M = 2\Delta L/\lambda$ should account for wavelength dispersion of its path $R_M = 2(\Delta L + \partial L/\partial\lambda)/\lambda$. If apodization is used for side-lob suppression, a wavenumber/wavelength resolution becomes:

$$\Delta\kappa = \frac{0.5}{\Delta L + (\partial \Delta L/\partial \kappa)\kappa}; \Delta\lambda = \frac{0.5\lambda^2}{\Delta L - (\partial \Delta L/\partial \lambda)\lambda} \rightarrow \Delta\lambda_{\text{fwhm}}$$
$$= \frac{0.603\lambda^2}{\Delta L - (\partial \Delta L/\partial \lambda)\lambda} \rightarrow \Delta\lambda_{\text{trga}} = \frac{0.886\lambda^2}{\Delta L - (\partial \Delta L/\partial \lambda)\lambda}. \quad (12.21)$$

Here $\Delta\lambda$, $\Delta\lambda_{\text{fwhm}}$, $\Delta\lambda_{\text{trga}}$ are the theoretical resolution of Fourier-transform spectrometer, resolution measured at full-width-half-max of λ peak, and with the triangular-window apodization [12.51].

Another practical restraint is caused by Michelson interferometer's use of a collimated light source, which finite size causes off-axis distortions limiting its maximum path-length difference [12.45, 12.52]. Practical deviations from the point source concept lead to added blurring noise of the interferogram and translate to resolution limitations, alike the instrument function. Further, spatial-heterodyne spectrometers essentially could operate in uncollimated radiation, tolerating off-axis expansions of its source. Although, a so-called flat-fielding problem, associated with the expansion of detector across system's axis and the interferogram recording by such a detector of beams propagating via changing optical paths, necessitates a need for flat-fielding correction that is normally accomplished via verification measurements and wavefront-error corrections [12.53].

12.1.6 Polarization FTIR Interferometry

A major inefficiency of Michelson interferometer is due to its use of semitransparent beamsplitter, which creates equal-intensity beams to be interfering in its arms leading at even perfectly identical optical-arm paths to the loss of one half of light on every interaction with the beamsplitter. That eventually leads to $\sqrt{2^3} = \sqrt{8}$ reduction in system and modulation inefficiencies prior to interfering as noted in Advantages' section above [12.54]. However, the need for splitting the incoming beam into two interfering parts can be accomplished by other means, such as by deploying a polarizing beamsplitter, which besides having some beneficial reflection and transmission properties in a broad spectral domain, could provide the ability for 100% beam-splitting efficiency while using polarized light [12.55–12.65].

The beam-splitting inefficiency of Michelson interferometer FTIR exhibits itself by reducing signal-to-noise ratio both ways: limiting the intensity of signal and boosting background, which creates a random modulation of spectra measured. The notion of background-elimination concept led to inception of so-called Martin-Puplett architecture for the polarization FTIR interferometry [12.55]. Three conceptual versions based on wire-grid beamsplitter dividing light into two states of polarization and adding benefits of broad-band spectral transparency are shown in Fig. 12.13.

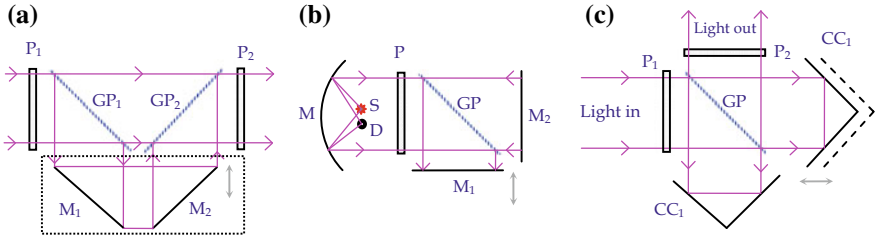

Fig. 12.13 Conceptual schematics of Martin-Puplett polarization FTIR

Figure 12.13a visualize the idea of polarization interferometry. A collimated beam of intensity I_0 is polarized by polarizer P_1, set at 45° to wire-grid polarizing beamsplitter GP_1, and evenly split into parallel and orthogonal states of polarization in reflection and transmission, then identically recombined by wire grid GP_2 becoming elliptically polarized—function of optical path difference ℓ, with intensity I_2 of beam transmitted by polarizer P_2 dependent on the path at wavenumber κ:

$$I_{2,||} = 0.5 \cdot I_0[1 + \cos(2\pi\kappa\Delta\ell)]; \quad I_{2,\perp} = 0.5 \cdot I_0[1 - \cos(2\pi\kappa\Delta\ell)]. \qquad (12.22)$$

This concept itself does not eliminate losses of light from an unpolarized source, as one half of it is cut by polarizer P_1 at added complexity and cost, but that half of unpolarized light may not be inevitably missing and could be used [12.58, 12.60]. Views *b*, *c* of Fig. 12.13 reveal more enhanced ways of implementation via mirrors as reflectors or corner cubes as polarization rotators [12.55].

Since a wire-grid beamsplitter reflects one state of polarization and transmits another, there would be more natural to use it addressing two optical ports (Fig. 12.14). The instrument [12.56] deploys second beamsplitter GP_D connecting auxiliary detectors D_1, D_2 to cover the adjacent spectral regions with the inevitable dc-background noise subtraction, using the main polarizing beamsplitter, having third GP_{in} connecting diverse specimen and the blackbody. Inputs 1, 2 are operated for comparative atmospheric studies versus reference radiation from the blackbody BB, for which entry wire grid polarizer GP_{in} is rotated 90°. This instrument alignment is verified via a relative 180° phase shift for the reflected against transmitted beam by central grid polarizer GP at zero path-length difference of two

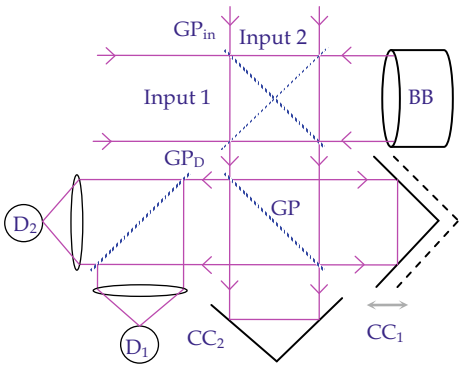

Fig. 12.14 Triple input, dual output polarization FTIR

arms—nevertheless, it is not always straightforward to align such a polarization interferometer while balancing varying lateral shears in its arms [12.57].

The next step of enhancing polarization FTIR is in enabling dual input-output capability of the polarizing beamsplitter [12.58], which is partially fulfilled for the twin-path interferometer of Fig. 12.15. That layout is realized using two identical inputs with switchable calibration sources $CS_{1–2}$, four wire-grid polarizers CC_1–CC_4 plus corner-cube reflectors GP_1–GP_4, utterly recovering the optical power lost on the input polarizer, as well as doubling the path length and enabling two synchronous interferometers running concurrently as a differential FTIR spectrometer, distinguishing low-level signals embedded in a background.

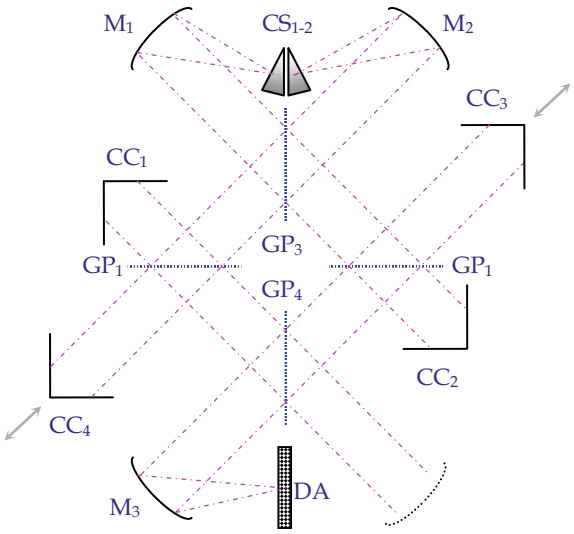

Fig. 12.15 Double optical path polarization FTIR interferometer

An ultimate enhancement would be to enable a doubled input-output setting analogously to a differential non-polarizing FTIR [12.60], adding a second detector via the unused optical port in Fig. 12.15 (dotted absent mirror identical to M_3). The concept of fully symmetric dual input-output polarization FTIR spectrometer-interferometer is shown in Fig. 12.16. The pairing of beamsplitters and mirrors of view (*a*) gives two channels for comparing either emission specimen as unpolarized light sources or absorption ones, embedded into the channels. A full version of view (*b*) quadruples optical paths similarly to Fig. 12.15 [12.61] enabling the full capability of two light sources and two specimen, being studied comparatively.

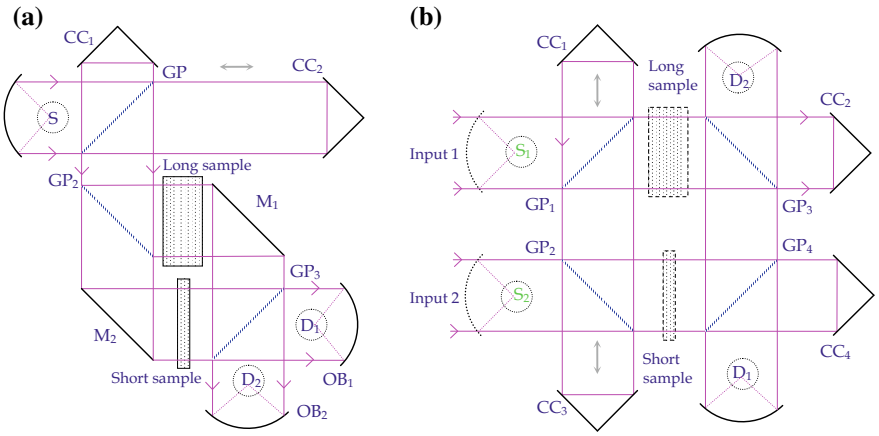

Fig. 12.16 Symmetric polarization FTIR interferometers deploying simplified dual beam (**a**) and quadruple path (**b**) architectures

12.1.7 Comparison of Some Experimental Results

Starting from 0.2 cm^{-1}–0.03 cm^{-1} for an apodized resolution at early stages of development [12.3, 12.30] and reaching 10^{-10} cm^{-1} $Hz^{1/2}$ sensitivity of measurement nowadays [12.36], Fourier transform infrared spectroscopy progressed in multiple forms and implementations: cw and pulsed, stationary, miniature, integrated, multichannel, etc. One of first realizations of enhanced FTIR interferometer design deploying double-beaming and lamellar-grating approaches (Figs. 12.3 and 12.9) resolved ± 0.008 cm^{-1} for strongly absorbing spectral lines at theoretical spectral resolution $\Delta\lambda/\lambda = 0.063$ cm^{-1} and at 16 cm of double-path difference on 8-cm lamellar step [12.66]. By embedding a He–Ne laser and tracking interferometer's arm length difference of only 7.2 cm ($\Delta\lambda/\lambda \approx 0.1$ cm^{-1}) the actual resolution reached ~ 0.025 cm^{-1} at a frequency accuracy of about 0.001 cm^{-1} [12.31]. An extension of FTIR techniques into visible and ultraviolet regions allowed reaching ± 0.001 cm^{-1} in wavenumber accuracy at signal-to-noise ratio ~ 15 while recording a broad spectrum of 10,000 cm^{-1} in one sweep at the resolving power of 10^{-5}–10^{-6} [12.67].

For a time resolved spectral observation, not restricted by a speed of the moving mirror, the step-scan technique is commonly used [12.68], displacing the mirror in sequential steps for time-related phenomena recorded at each path-length difference [12.69]. When using a setup similar to one of Fig. 12.10a but with the argon ion laser, ~ 5-μs of temporal resolution was obtained at 0.5 cm^{-1} of spectral resolution [12.33]. Although, simultaneous spectral and temporal measurements may require a precise wavelength calibration of the interferometer and vast frequency sampling, otherwise leading to phase distortions of such pulsed measurements [12.70, 12.71]. Conceptually the step scan technique was instigated in a Michelson interferometer equipped by 450-W Xe arc lamp to generate enough power for a nonresonant photoacoustic cell (see Chap. 9) deploying a TiO_2-coated fused silica beam splitter

to prevent its overheating and avoid wavefront distortions, though only 16 cm^{-1} resolution was achieved at a time in broad 0.36–3 μm spectral region [12.68].

Since Connes interferometer was created with the background compensating idea in mind at two-port output (see Fig. 12.3b), combining its scheme and step-scan notion limits requirements to detectors linearity along with background noise subtraction, enabling 0.001 cm^{-1} wavenumber resolution in a triple-pass system and 10^6 spectral elements spectrum collected in 5 h [12.72].

Nonetheless, stable and prolonged movement of FTIR-interferometer reflector permits reaching high spectral resolutions via traditional spectroscopic means, for example, enhancing sensitivity of its detector and increasing optical path-length from 7.2 cm to 6.2 m improved the unapodized resolution of double-beam interferometer (Fig. 12.3a) from 0.1 to nearly 0.001 cm^{-1} [12.31, 12.32].

Incorporating a multireflection cavity into one interferometer arms expands its optical path, which in combination with the step-scan technique enables substantial resolution benefits [12.33, 12.35]. As a result, intracavity FTIR spectroscopy permits reaching similar levels of wavenumber resolution for ultrashort optical pulses, concurrently probing the spectral and temporal domains. Using continuous-scan technique (see previous sections) substantiated by 1-μs pulse interleaving from an FTIR spectrometer IFS 120HR FT, irradiated by broad-spectrum 80-μs pulses of Ar^+ laser pumped Ti-Sapphire laser repeated with 60-μs delay and transmitted via 100-cm long absorption cavity, 0.05 cm^{-1} resolution at $\sim 2 \cdot 10^{-9}$ absorption level was reached by averaging 200 scans [12.34].

Even with interleaving the continuous-scan approach is limited to narrow spectral intervals, such as 12,450–12,700 cm^{-1} in the previous experiment. The step-scan format in a stepping mode equipped Connes interferometer resolved spectra in 5500–11,000 cm^{-1} range with an unapodized spectral resolution $14 \cdot 10^{-3}$ cm^{-1} and 1.6 μs time resolution [12.35]. Further upgrade [12.36] reached sensitivity of $1 \cdot 10^{-10}$ cm^{-1} $Hz^{1/2}$ with 10^4 simultaneously acquired spectral elements for absorption path-lengths near 130 km via an optically pumped vertical cavity surface-emitting laser (VCSEL) lasing 1050-nm wavelength. Alike, an intracavity heterodyned polarization interferometer setup [12.63] approached 4 pm/$Hz^{1/2}$ sensitivity for 5-kHz modulation frequency at 60 cavity reflections.

Figure 12.17a reveals a schematic of the preceding heterodyned polarization setting, made by adding the autocollimation multiple-reflection cavity of Fig. 6.4 (see Chap. 6 or [6.4] for detail). In this case [12.63] a heterodyne interferometer [12.39–12.45] is realized on polarizing beamsplitter cube PBS, splitting two orthogonally polarized beams into a reference and a variable-length path to recombine and generate a bit signal, proportional to the phase difference gained. A frequency stabilized He–Ne laser L is deployed to generate orthogonally polarized beams at 80 MHz frequency shift. A reference beat signal is created by light reflected from beamsplitter BS to detector D_1. In transmission, polarization beamsplitter PBS reflects one state of polarization to quarter waveplate WP and to mirror M transmitting another to a multiple reflection cavity of mirrors M_1, M_2. Depending on the mirrors tilt and separation, tuned by a piezo translator on a rotary stage, light experiences the total of $N + 1$ reflections in the cavity (paragraph 6.1, Eq. (6.10)) recombining with the orthogonal state on detector D_1, being reflected by PBS for the second beat signal of a phase difference $\Delta\varphi_{1-2} \sim \Delta\ell$.

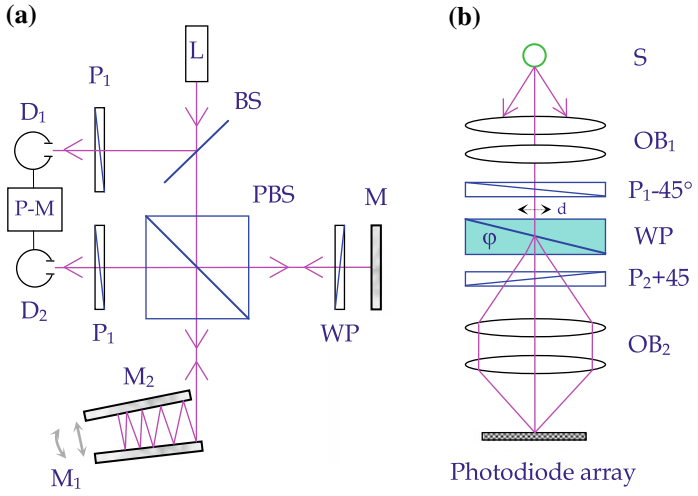

Fig. 12.17 Polarization heterodyne (**a**) and single pulse heterodyne (**b**) FTIR

Designs of spatial heterodyne interferometers target throughput and integration capabilities with the instantaneity of spectrally resolved single-exposure measurements and expect stepping up the wavelength resolution afterward. Figure 12.17b depicts a spatial heterodyne interferometer deploying a Wollaston prism as its heterodyning element [12.73]. On an optical axis of the prism a birefringence introduced by its first wedge to light transmitted by polarizer P_1 is compensated by the second, but for a lateral beam separated by distance d from the axis, the orthogonal states incur path difference $\Delta = 2d(n_0 - n_e) \tan \varphi$ (see paragraph 3.3). In proof-of-principle experiment at $\varphi = 3°$ the maximum path difference reached near 100 μm enabling spectral resolution of precisely 100 cm^{-1} (4 nm at 632.8 nm) for triangular apodization of interferogram recorded by 1024-element detector array [12.73]. A realization of lamellar grating via MEMs-actuated grating steps on static trenches led to a compact 100-mm^2 surface area design, having 15–20 cm^{-1} spectral resolution at 325-μm mechanical displacement and 5–100 ms measurement time, depending on averaging, in 625–4000 cm^{-1} wavenumber range [12.74]. An integrated FTIR without any beamsplitter for deep-UV applications from 140 nm down to 58 nm achieved 0.33 cm^{-1} of the measured spectral resolution at 29-nm optical path difference via the modified Fresnel-bimirror design created by tilting flat mirrors [12.75]. Another approach utilized the wavelength dependence of the optical arm length for $LiNbO_3$ waveguide Mach–Zehnder modulator, modulating two-path difference via the dispersion of its half-wave voltage [12.76]. Identifying a linear function for the nonlinear dependence of varying output intensity versus voltage to find the input power spectrum for the Fourier transform processing of interferograms presented a challenge. Using a halogen-tungsten lamp the system was capable of absorption measurements at low spectral resolution $\Delta\lambda \approx 100$ nm.

Replacing a regular beamsplitter with polarization one in Fig. 12.12b and adding a polarizer creates heterodyne interference fringes of orthogonal polarizations [12.77], interfering in a plane of polarizer P (Fig. 12.18a). That Sagnac interferometer is highly stable per counter-propagating waves in both directions, plus making measurements at two 90° spaced orientations of polarizer P allows full determination of polarization coordinates and intensities of orthogonal waves (see Chap. 3). A dispersive polarization interferometer at spatial-heterodyne offset originated via a polarization grating [12.78] is seen in Fig. 12.18b. Its design [12.79] aims sub-nanometer spectral resolution with broad-band source S and diffuser D for spatially incoherent irradiation of Wollaston prism *WP* that splits light in two linear polarization states and has an offset thickness *t*. Quarter-wave plate Q*WP* converts these states to circular ones matching $+1$ st and -1 st diffraction orders of polarization grating *PG* irradiated by afocal relay AR_1. Second afocal array AR_2 focuses resulting heterodyned interference pattern selected by the plane of analyzer *A* into focal plane array *FPA*.

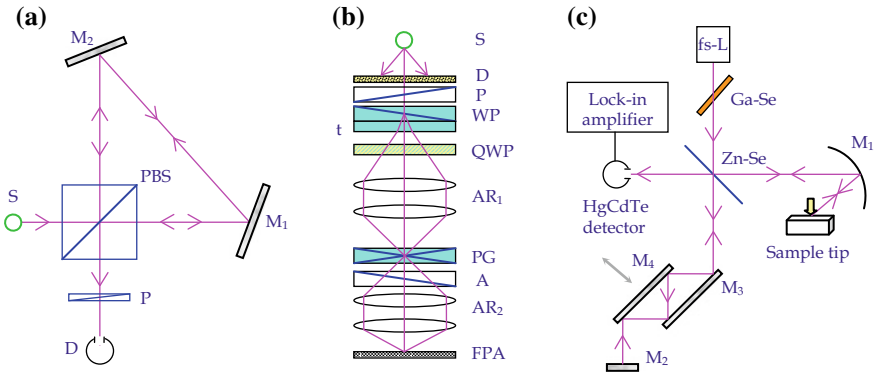

Fig. 12.18 Polarization Sagnac heterodyne interferometers: dispersive (**a**) spatial heterodyne (**b**), and dispersive near field (**c**)

Figure 12.18c shows a dispersive interferometer deploying the multipass cavity of two parallel mirrors at oblique incidence with a number of inner reflections depending on mirrors separation or the angle of incidence (see Figs. 6.1–6.3). The setup [12.80] used tip size limited scattering near-field microscopy of nanoscale spatial resolution and continuous heterodyne spectroscopy. Broad spectrum coherent pulses of 9–12 μm spectral band at 5 μW cw power from difference-frequency generation in 200-μm thick GaSe crystal irradiated by 10-fs Ti:Sapphire laser at 125 MHz, 500 mW were initiating Fourier-transform spectrums of tip's Rayleigh scattering. To reach 6 cm^{-1} spectral resolution in 2-s recording time at off-line resampling, frequent frequency calibrations of 1.7 mm long interferograms were made by 10.6-μm CO_2 laser and a step attenuator. Interferometer's 25-cm arm length was sufficiently short for hours-long stable phase calibration. Compressive sensing could help minimizing the number of sampling points for sparse signals or restore missing ones [12.152].

12.2 High-Dispersion Interferometers for Brillouin Spectroscopy

When a beam of coherent optical radiation interacts with an isotropic substance of a strong coupling bond among adjacent molecules, an absorbed fraction of the incident light beam causes initiation of the thermally excited acoustic waves. The interaction of incident light and coherently induced longitudinal sound waves activates inelastic Brillouin scattering, exhibiting itself in two satellite light components adjacent to a central intensity peak—due to elastic Rayleigh scattering on same molecules of studied substance, with the wavelength shifts according to Doppler effect:

$$\Delta_B = \pm 2n_{med}(V_{med}/\lambda_0)\sin(\beta/2), \tag{12.23}$$

where Δ_B is the Brillouin wavelength shift; n_{med} is the refractive index of a studying media; V_{med} is the media acoustic velocity; λ_0 is the wavelength of incident light, and β is the observation angle, firstly predicted [12.81] and observed afterwards [12.82]. Intensities of Rayleigh-scattering peak and the sum of Stokes and anti-Stokes terms of Brillouin scattering relates by the Landau–Placzek ratio [12.83]:

$$I_R/(I_{B^+} + I_{B^-}) = I_R/(2I_B) = (c_P - c_v)/c_v = (\zeta_T - \zeta_S)/\zeta_S = \gamma - 1, \tag{12.24}$$

where c_P and c_v are the specific heats at the constant pressure and constant volume; ζ_T, ζ_S are the isothermal and adiabatic compressibilities, and $\gamma = c_P/c_v$. Equation (12.24) should also account for the media dispersion and distinguish static Rayleigh versus dynamic Brillouin terms [II.21, 12.84].

12.2.1 Studies with Tunable, Single, and Multistage Fabry-Perot Etalons

Following from Eq. (12.23), the spectral separation of Brillouin satellite frequencies from the central Rayleigh peak is counted in sound waves and even for ultrasonic oscillations of high-viscosity molecules its scale is measured in low-nanometer and high-picometer wavelengths. Thus, searching for the highest spectral resolution a number of stabilizing and compounding schemes for the Fabry-Perot etalon were developed [12.85–12.100] as it enables one of highest resolution–throughput combinations in a limited free-spectral range, which is mostly anticipated in Brillouin-scattering spectroscopy.

A high resolution spectroscopic study necessitate a sufficiently stable interferometer to begin with and, since observing weak spectral lines takes a substantial amount of time for registration, its optical path lengths requires staying unchanged for a range of wavelengths to be observed or needs either passive or active dynamic stabilization, unless the etalon is stable by design or keeps tuning the resonant wavelength (see Chaps. 6–8). Considering the etalon as one plane-parallel plate of identical highly reflecting surfaces, transmitted light resonances occur for wavelength λ:

$$m\lambda = 2n_e\ell\cos\varphi_e = 2n_e\ell\cos(\arcsin(n_0\sin\varphi_0/n_e)), \tag{12.25}$$

where m is the order of interference; n_0, n_e are the refractive indices of a surrounding and of the etalon, respectively; φ_0, φ_e are the angles of incidence and of etalon refraction, and ℓ is the etalon thickness (see Eqs. (1.100), (3.115) and explanations thereof for detail). Interference maxima occur for wavelengths λ_i of a dual-path phase change: $\delta = 2\pi(2n_e\ell/\lambda_i)\cos\varphi_e \underset{\varphi=0}{=} 2\pi(2n_e\ell/\lambda_i) = 2m\pi$, while any individual etalon could be made as a single plate or two plates of surface reflectance ρ.

Similarly to a ringdown cavity and following Eqs. (7.65–7.68), the spectral resolution of a Fabry-Perot interferometer is defined by spectral linewidth $\Delta\lambda$ of its transmittance, which for an ideal interferometer at normal incidence is the instrumental linewidth. From Eq. (7.68), the etalon's resolving power $\lambda/\Delta\lambda$ or full-fringe phase difference related to half-intensity width:

$$\lambda/\Delta\lambda = \delta/\varepsilon = (2m\pi)/(2\pi/\Im) = m\Im, \tag{12.26}$$

is defined by its finesse $\Im$, as the free spectral range ratio related to the half-intensity width $2\pi/\varepsilon$, and the order of interference m [12.85]. Rewriting relation (12.26) via the finesse parameter F and substituting $\varepsilon = 4/\sqrt{F}$ from Eq. (7.67), it becomes $\lambda/\Delta\lambda = (\pi/2)m\sqrt{F}$. If radiation is not strictly monochromatic covering a small range of wavelength $\Delta\lambda$ represented by its mean wavelength $\bar{\lambda}$, and, if the phase spread $\Delta\delta$ of quasi-monochromatic light is much smaller than the half-width ε of a monochromatic fringe: $m\Im \ll \bar{\lambda}/\lambda$, the resultant intensity distribution remains the same [1.1].

Additional factors identifying applicability of an interferometer for a spectroscopic need are the maximum intensity of spectrally resolved light, being the maximum transmission for Fabry-Perot etalon, and the contrast factor C, defined as the ratio of maximum to minimum intensities. Following Eq. (7.66), the ratios via intensity I_0 of incident light and finesse parameter F are:

$$(I_\tau/I_0)_{max} = 1;\ (I_\tau/I_0)_{min} = (1+F)^{-1};\ I_{\tau\,max}/I_{\tau\,min} = 1+F. \tag{12.27}$$

Converting to finesse $\Im$ or mirror reflectivity ρ by Eq. (7.68), still neglecting any absorption:

$$C = I_{\tau\,max}/I_{\tau\,min} = 1 + 4\Im^2/\pi^2 = (1+\rho)^2/(1-\rho)^2, \tag{12.28}$$

etalon contrast C is identified by two mirrors reflectance ρ, as follows from Eqs. (3.125a, b).

Typical applications of a single etalon or a combination of multiple etalons use one of direct schematics seen in Figs. 1.8 and 1.9 (Chap. 1). A scanning Fabry-Perot interferometric spectrometer was first made of a two-plate tight enclosed-air etalon by continuously changing an air pressure and registering intensity changes in transmission for a central part of Haidinger-ring pattern via a photomultiplier tube [12.86]. Another approach, like a spherical etalon of Fig. 8.7, had one etalon mirror sweeping over $\lambda/2$ distance while synchronizing output of on-axis detector with a mirror oscillator [12.87]. The most stable two-plate etalon design utilizes a fixed spacer, such as two matching

quartz tubes sandwiched in between two mirrors. Using this concept, a tuning etalon can be made with a piezoelectric expandable ceramic spacer of the thickness varying versus a voltage applied to spacer electrodes [12.88]. A spherical-mirror etalon at a smaller axial-mode diameter may be made as well [12.89].

When the measurements entail an active stabilization of mirrors alignment and positioning, an output feedback system linked with a mostly-piezoelectric mirror drive is used [12.90, 12.91]. The former one involves scanning a mirror, while simultaneously stabilizing the parallelism via observing maxima of etalon fringes additionally created by several extra light sources. An example of the latter one deployed 1024-channel scaling of a piezoelectrically scanned Fabry-Perot interferometer via observing the maxima of Rayleigh scattering and correcting the spectral profile being observed.

The stability and parallelism of the first instrument versus a reference wavelength was $\sim\lambda/1000$, with an actual etalon parallelism limited by surface defects of flat mirrors [12.90]. Using analog-to-digital converter reduced a long term drift and nonlinearity of the second setup to 0.1% [12.91].

More advanced stabilization systems expected at high-resolution Brillouin scattering studies involve controlling spacing and alignment of etalon mirrors by observing not only the widths of maxima for elastic Rayleigh scattering, unavoidably accompanying inelastic one, but controlling the absolute peak intensity [12.92–12.94]. An actual measurement technique may consist of only tracking the maximum intensity of elastically scattered line versus the intensity of incident light [12.92], or observing the position and calculating the centroid of Rayleigh peak with continuous feedback until they match on the highest-resolution scale [12.93], or combining both processes by identifying positions of Rayleigh lines and frequency-correcting each individual spectrum [12.94].

While looking for an outmost contrast in high-resolution Brillouin scattering measurements even having any advanced single stage Fabry-Perot etalon could not be sufficient enough due to excessive Rayleigh scattering, overwhelming the Brillouin peaks by several orders of magnitude. Combining two etalons, one of a larger free spectral range and another of a high resolution, may provide a more powerful alternative, if the detection system has sufficient sensitivity to register much lower intensity minima, associated with incident light transmitting the tandem of etalons, as the combined set of Haidinger rings becomes very weak. If in this tandem, the extrema of the etalons at spacing L_1, L_2 are $\lambda_1 m_1 = 2L_1$ and $\lambda_2 m_2 = 2L_2$, the only wavelength to be transmitted has to satisfy both conditions, namely $\lambda_1 = \lambda_2$. The other extrema wavelengths for one etalon become suppressed by another, but ghosts of remaining orders contribute to overall noise of the tandem.

When two etalons are combined [12.95–12.100], there are potentially four sets of ghost rings besides even the suppressed maxima being caused by the surface reflections of two plates. If the supporting surfaces have anti-reflection coatings or the plane parallel plates are replaced by two wedges, retro-reflection ghosts may become weak or be moved away from the spectral region of interest. Moreover, crossed faint etalons of active surfaces S_1–S_3, S_1–S_4 and S_2–S_3, S_2–S_4, add more fringes that can be superimposed to the main interference pattern but only for the plane parallel plates, at the parallelism meeting geometric constraints for both

etalons of ≤1-arc second [12.95], while one of the etalons provides for a higher dispersion, another for a wider free spectral range.

The alternative way of doubling the etalon is in recycling transmitted light back either at a diverse angle via prisms or collinearly by polarization splitting, being straight and efficient as seen in Fig. 12.19 [12.96]. Polarizer P_1 selects the state of polarization for radiation from source S, reflected by polarizing beamsplitter PBS to the wedged-substrate etalon of mirrors M_1, M_2, becoming orthogonally polarized after retroreflection from mirror M while passing twice quarter-wave plate QP, to be further transmitted via PBS and polarizer P_2 to objective O_2 and collected on detector D. The initial setting used the nonpolarizing beamsplitter noting an increased contrast and enhanced resolution for the tandem versus one etalon but weaker fringes.

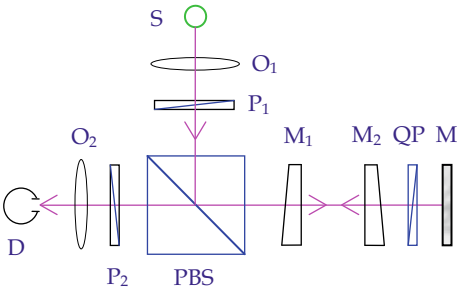

Fig. 12.19 Polarization doubling of Fabry-Perot etalon

A matching realization of two etalons in sequence for each scanned synchronously with the spacing as $\Delta d_1/\Delta d_2 = d_1/d_2$, permits removing ghosts while maintaining correlated scans [12.97, 12.98]. By making a sequential propagation of incident light in a sidewise-expanded etalon (Fig. 12.20) supplemented either by mirrors or corner cube prisms P_1, P_2 at pendulum mounting of the assembly (see Sect. 12.1), a triple-pass setting at 93% mirror reflectance and λ/100 flatness reached 70 in finesse at near 40% peak transmission with $\sim 10^8$ contract [12.99].

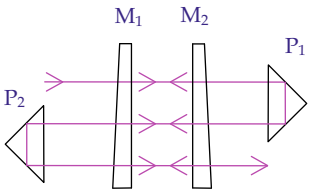

Fig. 12.20 Tripled Fabry Perot etalon

Added benefits could be realized at tandem operation in the bending double-pass schematic of Fig. 12.21 [12.100]. By keeping constant spacing $d_2 = d_1 \cos \varphi$, the

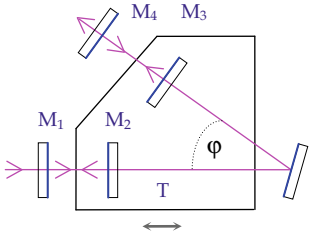

Fig. 12.21 Angled tandem of etalons

scan is made via translation stage T at angle φ unchanged, thus accomplishing a single-movement scan for the tandem of Fabry-Perot etalons. For the actual vernier-based spectrometer an added corner-cube prism and one extra return mirror were used to accomplish three passes via each single etalon [12.100].

12.2.2 Properties of Virtual Imaging Phase Arrays (VIPA)

Despite the extremely high contrast an interferometer of doubled or tripled Fabry-Perot etalon could provide, the challenge of detecting minima of interference leads to equally long recoding times even for photon counting. Attempts were always made to improve the etalon, such as by making a narrow window for light to enter the inner space without attenuation [12.101]. Only with emerging needs for wavelength division multiplexing in optical communications (see Chap. 11) these attempts materialized in the so-called Virtual Imaging Phase Array. The most common VIPA design is illustrated in Fig. 12.22 [12.102].

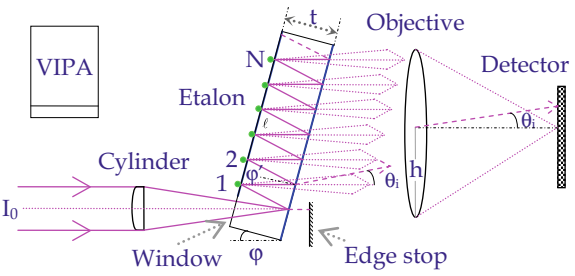

Fig. 12.22 Virtual imaging phase array interferometer

Its VIPA view shows the back face of the etalon with the transparent window at the bottom, which in the original design is irradiated by semi-Cylinder lens to fill the VIPA window at maximum power efficiency. Tilting of the etalon at a small angle φ allows an incident beam to enter and be retroreflected forward by high-reflectance coating of the front face not being stripped by the window to follow the multiple reflection path until bouncing off etalon's upper edge, for refracted resonant orders $m\lambda_i = 2\ell_i = 2d\cos\varphi_i'$ transmitting the back face and projected by Objective lens to Detector array. Dotted arrows illustrate light from virtual sources 1, 2, … N, marked

as green dots, creating multi-path interference equally to ones of Fabry-Perot etalon at intensities from $I_0(1-\rho)\rho^2$ to $I_0(1-\rho)\rho^{2N}$.

Since VIPA was originated for wavelength division multiplexing and the concept of virtual sources coupling into individual fibers [12.102], the incident beam passing the window and front-face coating at intensity $I_0(1-\rho)$, considering perfectly anti-reflection coated window, was useful. When using VIPA as an interferometer this first beam, passing length ℓ and not participating in constructive interference, creates background noise and is blocked by *E*dge stop in Fig. 12.22. The other source of noise can be created by the beam bouncing back from the etalon upper edge (the dotted line). Nonetheless, that returning back beam could be perfectly matching the rest of multiply reflected and resonating beams, if the edge meets same geometric tolerances as etalon faces with equivalent high-reflective coating [12.103]. Furthermore, as revealed in the following section, the needs for those measures could be completely eliminated by system design [12.104], with the benefit of realizing the highest resolution of a given VIPA at $\varphi \to 0$ (see Eq. (12.25)).

The particular distinction of VIPA versus Fabry-Perot etalon is due to its phase matching at angle φ, or φ' for a solid-state etalon, for wavelength λ_i being observed at added angle θ_i [12.106]. Considering high dispersion applications away from normal incidence of a VIPA versus a Fabry-Perot etalon and despite the two being identical at $\varphi = 0$, with the spectral resolution per Eq. (12.26), efforts were made to derive and verify an explicitly-VIPA dispersion law [12.105, 12.106]. The dispersion law for air-spaced VIPA and Fresnel paraxial approximation (see [1.1]) is [12.105]:

$$m\lambda = 2t\cos\varphi_i - (2t\sin\varphi_i)\theta_i - (t\cos\varphi_i)\theta_i^2, \tag{12.29}$$

which for the solid-state VIPA of relative refractive index n translates at $\sin\varphi = n_\lambda \sin\varphi'$ to [12.105]:

$$m\lambda = 2n_\lambda t\cos\varphi_i' - \left(2t\tan\varphi_i'\cos\varphi_i\right)\theta_i - \left(t\cos\varphi_i'\right)\theta_i^2/n_\lambda, \tag{12.30}$$

where φ_i' is the angle of incidence for light wavelength λ_i inside the etalon; θ_i is the viewing angle for λ_i. Equation (12.29) was derived applying Fresnel diffraction to the plurality of virtual sources via Objective to Fourier transform plane of detector array (Fig. 12.22). The result was later verified transforming $\cos\varphi_e$ in Eq. (12.25) by adding angle θ_i to etalon resonance at angle φ_i [12.106].

As for Fabry-Perot etalon, VIPA free spectral range (FSR) follows Eqs. (12.29), (12.30) [12.105]:

$$\begin{aligned} FSR_{n=0} &= \frac{c}{2t\cos\varphi_i - 2t\,\theta_i\sin\varphi_i - t\,\theta_i^2\cos\varphi_i}; \\ FSR &= \frac{c}{2n_\lambda t\cos\varphi_i' - \left(2t\tan\varphi_i'\cos\varphi_i\right)\theta_i - \left(t\cos\varphi_i'\right)\theta_i^2/n_\lambda}. \end{aligned} \tag{12.31}$$

For a particular wavelength λ_i at resonant condition $m\lambda_0 = 2t\cos\theta_i$ seen at observation angle θ_i, the VIPA angular dispersion factor $\Delta\theta/(\Delta\lambda/\lambda_0)$, with $\Delta\lambda = \lambda_i - \lambda_0$, for air and solid-state etalons become:

$$\begin{aligned}\Delta\theta/(\Delta\lambda/\lambda_0)_{n=0} &= -1/(\tan\varphi_i + \theta_i);\\ \Delta\theta/(\Delta\lambda/\lambda_0) &= \left[\sin(2\varphi_i)/\left(2\left(n_\lambda^2 - \sin^2\varphi_i\right)\right) + \theta_i/n_\lambda^2\right].\end{aligned} \tag{12.32}$$

Height h in Fig. 12.22 highlights another distinction of VIPA, causing a spatial separation of axes for outgoing versus incoming optical beams. Plus, since the images are formed by Cylinder and Objective lenses, a ratio of their foci define the resulting interference-pattern spacing. Finally, the cylinder lens is not a necessity, but an obstacle, and replacing it only benefits the system [12.107], as high-quality input objective is a better alternative, similarly to a tilted Fabry-Perot etalon [12.4].

Likewise for other interferometers and spectrometers, various cascading schemes for VIPA etalons can be used, with traditional spectroscopic instruments offering competitive throughput and resolution [12.108–12.115]. The Ebert grating monochromator [12.108] in the dual and triple pass schematics via vertically separated aberration-free curved circular slits due to its cylindrical symmetry, allowed reaching $5 \cdot 10^5$ resolving power at 7500-line/inch echelle gratings for the 11^{th} order of diffraction in 100-nm of covered wavelength range. The concept of a dual-pitch grating, adopted for lateral-shear interferometer creating the shear in orthogonal directions [12.109], may be seen as a prototype of the spatial heterodyne interferometer with crossed diffraction gratings.

For an enhanced double pass Fastie-Ebert spectrometer [12.110] its resolving power reached $7.5 \cdot 10^5$ having 0.024 cm^{-1} spectral resolution at 514.5 nm wavelength and resolution-independent spectral range of 2000 cm^{-1} at effective finesse of $\sim 7 \cdot 10^4$. A multiple-grating spectrometer upgrade [12.111] doubled the spectral resolution up to 1 GHz with $\sim 1 \cdot 10^{-10}$ contrast in the visible and UV range of spectrum. In a multiplexing application [12.112] the Fabry-Perot etalon was performing as a multi-pass Michelson interferometer (see paragraph 12.1), similarly to VIPA as in Fig. 12.23. By collimating an entirety of etalon interference fringes onto a spot-size detector each beam pass was acting as a single interferometer arm and its inner space was tuned from the lowest one at a maximum free spectral range to the highest at utmost resolution. At up to 20-cm long scan of the etalon spacing the actual spectral resolution obtained in an experiment was better than 0.003 cm^{-1}.

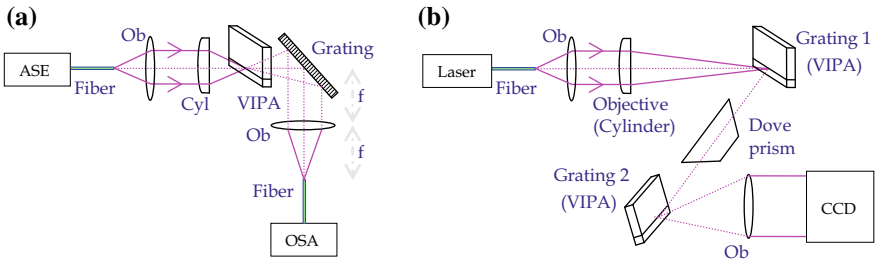

Fig. 12.23 Tandem VIPA spectrometers: VIPA with diffraction grating (**a**) and two cross cascaded VIPAs via Dove prism (**b**)

Figure 12.23 illustrates two schematics of spectral cross cascading-of a VIPA and a diffraction grating [12.113] and two VIPA as the diffraction gratings [12.114]. In Fig. 12.23a, the fiber source of 30-nm broad amplified spontaneous emission (ASE) was projected to a solid-state VIPA at 4.2° angle of incidence reaching Grating at 70° incidence with 50° diffraction angle, then collimated to single mode Fiber, being coupled to optical spectrum analyzer (OSA). The concept of dispersing light in a 2-D space adopted here used VIPA to separate resonant wavelengths in one dimension and diffraction Grating in another, enabling optical wavelength division multiplexing for 5 GHz (0.04 nm) channel spacing at 3-dB bandwidth of 1.75 GHz at channel isolations of 20 dB [12.113].

In Fig. 12.23b, instead of 90°-separation for two planes of dispersion, 45°-tilted Dove prism is deployed in between either two gratings or VIPAs enabling the diagonal rotation of a resulting pattern [12.114, 12.115]. Seemingly, that tilted dispersion could partition spatially dispersed and stray light beams, which are anyway spectrally dispersed for Brillouin shifts of intended studies. Further additions of a Dove prism and grating or a VIPA combination would enhance resolution of such an assembly with number N of spectral elements to $\sqrt{N}$, while decreasing its throughput.

Experimental results with VIPA spectrometers [12.115–12.125] demonstrated improvements in spectral resolution at relative compactness of Brillouin spectroscopy instrumentation. Adding spatial aperture masks for three-stage VIPA spectrometer with spherical lenses in between stages allowed a sub-GHz resolution at 80-dB extinction of Rayleigh peak at 33-GHz free spectral range, improving from 55 dB for two- and 30 dB for single-stage VIPA [12.115]. Nonetheless, the multistage Fabry-Perot etalons and single VIPA instruments reveal compatible spectral resolutions of GHz and sub-GHz levels. Such a triple-pass plane Fabry-Perot etalon based system resolved 0.05–0.3 GHz wide spectral lines of Brillouin scattering in optical glasses [12.116]. The Brillouin shift at 0.55-cm^{-1} level was observed for toluene at the spectral resolution below 0.1 cm^{-1} [12.117] while using Ebert system of [12.110] (see above). With the triple-pass tandem Fabry-Perot etalon setting (Fig. 12.21) 8°-incidence Brillouin spectra of a 10-μm AlGaAs epitaxial layer were resolved [12.118].

If the Fabry-Perot etalon is deployed in a nonscanning angular-dispersion system for all the dispersed by etalon beams projected to a sensitive CCD at no scanning with an extra requirement for the light source to be uniform and thus to produce even angular rings, the spectral resolution and sensitivity remain, as confirmed by originating experiments preceding VIPA developments [12.119]. For example, using a frequency-narrowed to 10 MHz argon-ion laser at 514 nm for 90°-scattering geometry, irradiating 20-mm diameter air-gap etalon with its 99%-reflectivity mirrors spaced at 4.99 mm with λ/150 flatness, the experimentally measured finesse reached 37.6 ± 1.5 at a contrast of up to 575 while approaching 1 GHz in spectral resolution at 1-s exposure time [12.120]. When using the same etalon paired with 532-nm Nd:YAG laser enabling 2-μm spatial resolution a deeper 0.05-GHz level of spectral resolution was reached, being equivalent to 10-m/s sound velocity [12.121].

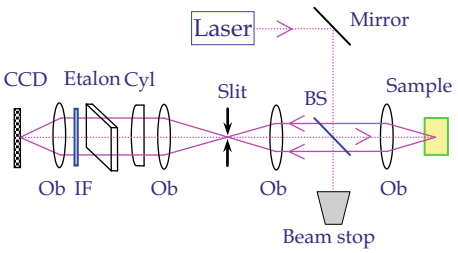

Fig. 12.24 Angle dispersion setting for Fabry-Perot etalon

Figure 12.24 illustrates the concept of angle-dispersive Fabry-Perot etalon spectroscopy [12.119–12.122] for 180°-backscattering geometry, which is of the highest intensity (see Eq. (12.23)). In the depicted system [12.121], Slit provided spatial filtering of Rayleigh scattering and of stray light in a confocal-microscope configuration, having Cylinder linearly dispersing backscattered by Sample distinct beams in air-spaced Fabry-Perot etalon. Interference filter IF was rejecting Raman scattering from Sample.

In the similar setting [12.122], with the solid-state etalon at 0.995-reflectivity mirror coatings and 90° scattering geometry, an area reducing aperture in front of the etalon helped enhancing the finesse via its flattest center section. The finesse level was improved from 100 at 10-mm aperture to 140 at 2 mm, with the contrast above 10^5 and a GHz-level of resolution at λ/100 mirror flatness. Another approach for background cleanup was realized using an Id-absorption cell as the notch filter in fiber-coupled system of similar to Fig. 12.24 backscattering setting with solid-state VIPA etalon, but replacing the cylinder lens with 2-inch diameter spherical optics to reduce scattering [12.123]. For 532 nm applications the iodine cell heated above 100 °C provided 50-dB suppression of elastic Rayleigh scattering for sub-GHz sensitivity either with a single etalon or VIPA tandem.

Alternatively, power-enhancing stimulated Brillouin scattering rises intensity of anti-Stokes shift in Rayleigh scattering-free zone of enhanced sensitivity [12.124] adding complexities of nonlinear phenomena. To another extent, diverging axes of incidence and observation to spatially separate Rayleigh and Brillouin scattering could be of help, such as viewing at $\sim 170°$ versus 180° [12.125].

12.2.3 Measurements of Brillouin Scattering in Biological Objects

A common distinction of most biological objects relates to a much lower transparency compared to optical elements as crystals, glasses, and liquids, for which the Brillouin scattering techniques reviewed prior were matured. Essentials of biological systems, attributing to specific fragility and short lab life of bio specimen, caused increased attention to faster concepts and methodologies for higher extinctions of elastic Rayleigh scattering and stray light, without complexities leading to retroreflections of a probing beam. Developments of Brillouin scattering measurement techniques for biological objects were progressing in parallel to other optical systems and with a similar trend of interferometers used, while extra care being taken

to preserve the natural state of high molecular mass substances like proteins and nuclear acids, which are almost always bathed and measured in an aqueous buffer.

From the standpoint of high extinction ratio – the peak of instrument transmission function to its transmission background, the multi-pass Fabry-Perot etalons seen in Figs. 12.19, 12.20 and 12.21 are among the most efficient instruments broadly deployed for biological purposes [12.126–12.128]. In one of the first distinguishing experiments maintaining a sample under study in surroundings resembling ones of a living organism, a triple-pass Fabry-Perot of $\sim 5 \cdot 10^6$ extinction with a finesse of about 45 continuously piezoelectrically tuned at 2 Hz frequency was utilized [12.128]. A single mode argon ion laser of up to 40 mW power at 488 nm was used as a light source at two spacing gaps of the etalon for spectral comparison: 6.19 mm at 24.25 GHz free spectral range and 7.90 mm at 19.00 GHz. Tested specimen were held as 50–100 μm thin films between microscope slides with quasi-index matching liquids, at Brillouin scattering measurements made for $90 \pm 1°$ observation angle β (Eq. (12.23)). Measured Brillouin shift ranged from 4.26 GHz for water, 6.36 GHz for polypeptide (caprylic acid), to 6.30–7.87 GHz for wet collagen at changing orientations of its axis.

Even a tandem VIPA setting can benefit from fine selectivity of a Fabry-Perot etalon [12.129]. Figure 12.25 shows one implementation of triple pass etalon as a tilt-tunable spectral filter in front of a cascaded VIPA spectrometer. That system had a side-mirror design of Fig. 12.20 with a low-finesse solid state etalon at 60%-mirrors reflectivity, 3 dB bandwidth, and 40% insertion loss per extra resonant cavities formed by mirrors.

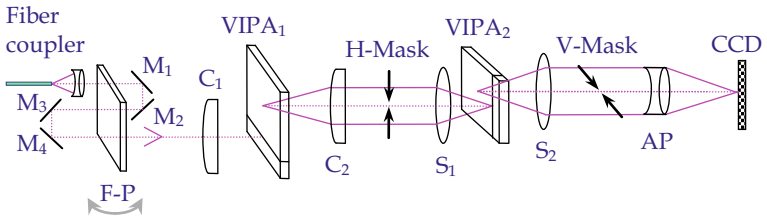

Fig. 12.25 Fiber coupled spectrometer: triple-pass Fabry-Perot and two-VIPA etalons

Following the proof of concept for Brillouin scattering in enabling reliable means to identify objects of biological significance, most sensitive measurements were performed for eye's cornea and lens, which strengths and dynamic elastic moduli remain unidentifiable by other techniques [12.130, 12.131]. Since cornea and crystalline-lens tissues are aqueous solutions of a high protein content, if these tissue specimen are placed in a cuvette or in between the microscope slides, the phase of light passing through is altered by an optical path-length change according to Eq. (9.53) as $\Delta\varphi = 2\pi\ell\Delta n/\lambda$, only due to refractive index changes since the length ℓ remains constant.

For a solid state sample intentionally focusing light as a wide cone instead of a long thin cylinder leads to an uneven temperature distribution, causing observable birefringence (Eq. (9.67)). Measuring stress-induced birefringence due to absorption in a non-uniformly irradiated sample such as via high-NA objective, at two

opposite states of polarization, or using crossed polarizers permits detection of low optical losses in transparent glasses as seen in Chap. 9. Furthermore, changes of refractive index of a transparent substance, such as a cornea or crystalline lens, could be observed via reflected light (see Chap. 10) at the time of Brillouin scattering measurements.

Given that the cornea and lens primarily consist of water and water-soluble proteins, at high frequencies of optical excitation eye's viscoelastic properties are caused by a volume elasticity or bulk (storage) modulus, a real part of complex longitudinal modulus M [12.126, 12.130–12.133] is:

$$\mathrm{M} = (\lambda_0 \Delta_\mathrm{B}/2\mathrm{n}_\mathrm{med}\sin(\beta/2))^2\sigma + \mathrm{i}\,\sigma\mathrm{v}_\mathrm{med}^2\delta_\mathrm{B}/\Delta_\mathrm{B} = \mathrm{M}' + \mathrm{iM}'', \tag{12.33}$$

where all designations are per Eq. (12.23) and δ_B is the line width of the Brillouin peak that is the reciprocal of lifetime of acoustic phonons, characterizing the sound attenuation coefficient α_sound in the medium; σ is the density of a medium where the excited longitudinal acoustic wave propagates. For a weakly attenuating medium $\delta_\mathrm{B} = \alpha_\mathrm{sound}\mathrm{v}_\mathrm{med}/\pi$ and the bulk modulus M' is [12.131]:

$$\mathrm{M}' = \mathrm{v}_\mathrm{med}^2\sigma = (\lambda_0\Delta_\mathrm{B}/2\mathrm{n}_\mathrm{med}\sin(\beta/2))^2\sigma, \tag{12.34}$$

defining the measured volume elasticity versus loss modulus M'', which identifies the lost energy.

The optical density of cornea or eye's lens could be determined by measuring the refractive index n_eye via reflectance ρ of light interacting with the eye on a border of two adjacent elements, while presuming the ratio of density σ and of refractive index n_eye being eye's element constant:

$$\begin{aligned}\mathrm{M}' &= (\lambda_0\Delta_\mathrm{B}/2\mathrm{n}_\mathrm{med}\sin(\beta/2))^2/\mathrm{n}_\mathrm{eye}\left(\sigma/\mathrm{n}_\mathrm{eye}\right)\\ &= \mathrm{const}_\mathrm{eye}(\lambda_0\Delta_\mathrm{B}/2\mathrm{n}_\mathrm{med}\sin(\beta/2))^2/\mathrm{n}_\mathrm{eye}.\end{aligned} \tag{12.35}$$

Two sets of optical measurements could be performed to detect viscoelastic properties of an eye element by Eq. (12.35), one of Brillouin shift $\Delta\mathrm{B}$ and another of relative refractive index n_eye, while expecting the ratio $\sigma/\mathrm{n}_\mathrm{eye}$ but not $\sigma/\mathrm{n}_\mathrm{eye}^2$ to be element's constant known as the Gladstone and Dale relationship $(n-1)/\sigma$ that has been proven to be valid for most common liquids [12.134].

For the earliest accurate measurements of Brillouin shifts of eye's lens and cornea specimen [12.130] the extinction of triple-pass Fabry-Perot etalon was enhanced to $2 \cdot 10^7$ with a finesse of $\sim$42 at $\lambda = 488$ nm of a single-mode argon laser, keeping its power below 25 mW to record a Brillouin shift as low as 4.5 GHz for a corneal material of the normal human eye available for experiments. The measurements were made at 90°-observation angle with an uncooled photomultiplier taking 10 min for each peak using 0.2-nm wide interference filter centered at 488 nm to eliminate broad-band and fluorescent light scattering. The excised pieces of eye lens specimen studied were held airtight in vacuum between two microscope slides. Depending on

specimen and a section measured, Brillouin shifts in a human and mammal cornea and lens ranged from 4.54 to 8.40 GHz having a width from 0.51 to 1.22 GHz with the lowest Brillouin shift of ∼4.50 GHz observed for a human cornea [12.131].

With the first implementation of a VIPA based Brillouin spectrometer (Fig. 12.26) the finesse was increased up to 56 at near 80% throughput and 33.3 GHz of VIPA free spectral range [12.132].Dual-axis confocal microscope [12.135] at 6° beam crossing angle was used to couple light from a single-frequency 532-nm Nd-YAG frequency-doubled polarized laser via achromatic objective *Ob* having 30-mm focal length and NA = 0.03. Horizontal cylinder HC and spherical lens S of 200-mm focal distance were deployed to match their transmission with VIPA free spectral range, focusing the specimen spectral image onto electron-magnified CCD in a narrow line via vertical cylinder VC of 38-mm focal distance. The Brillouin shifts and linewidths of 15.6 GHz and 0.26 GHz were measured for acrylic glass, 7.46 and 0.79 GHz for water, and 5.57 and 0.46 GHz for methanol, as the reference values. Studied in vivo properties of crystalline lens of a mouse eye exhibited Brillouin shifts from ∼11–15 GHz and from ∼7 to 10.5 GHz depending on the axis being scanned [12.132].

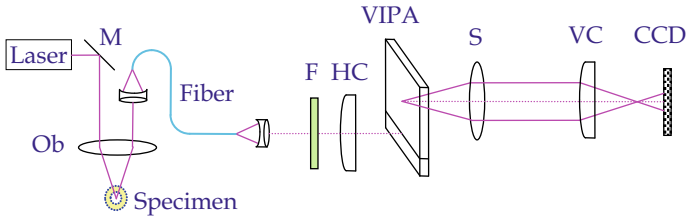

Fig. 12.26 Parallel dispersive 3-D Brillouin imaging VIPA spectrometer

Transitioning to in vivo testing of a human eye [12.136] the setup of Fig. 12.26 was upgraded with cross-axis dual VIPA spectrometer of Fig. 12.23b at eye-safe 780 nm wavelength and in the direct confocal setting via 10/90% beamsplitter seen in Fig. 12.24. Identical silica-substrate VIPA etalons with 99.9 and 95% front-, back-surface reflectivity cascaded for 45° axis tilt, 1.68° beam-entrance angle enabled ∼55 dB extinction of Rayleigh scattering. The axial eye scanning was done moving an objective at up to 80 μm/s recoding Brillouin spectra by EM-CCD camera at its frame integration time of 0.2–1 s and the fiber-coupled cw laser power at a specimen from 0.7 to 3 mW. Using axial scans of ∼60-μm resolution, Brillouin-scattering measurements resolved the anterior cortex of eye's lens at the shift varying from 5.25 to 5.85 GHz for an outer 300-μm layer. The Brillouin shifts of the corneal stroma tested from 100 to 400 μm in depths changed from 5.6 to 5.5 GHz and for the posterior region the shift declined from 5.5 to 5.25 GHz in over 200 μm [12.136].

For absolute-frequency calibration of the etalon, positions of spectrally-verifiable absorption lines of atomic vapor in a heated cell are often used [12.125, 12.133]. Likewise, strong absorption lines of alkali-metal and molecular-iodine vapors historically serve for a fine spectral filtering in dispersive spectroscopy and rejection of

laser light [12.137–12.139]. At modest cell temperatures a purified isotope vapor is near ideally-transparent filter for all wavelengths except its electronic transitions where high densities could be reached at centimeter lengths and Doppler-broadened linewidths. Depending on a wavelength of interest, I_2 for 514.5 to 532 nm and Rubidium D_2 lines for 720 to 780 nm of ^{87}Rb and ^{85}Rb isotopes or of their natural mixture, are useful. In addition, the least-square fitting algorithms can enhance absolute accuracy of Brillouin-frequency scale [12.140].

A variety of techniques could be deployed for spectral as well as spatial filtering of Brillouin scattering, such as inserting a knife edge or a slit as one or another spatial mask [12.101–12.140]. In particular, a range of wide to narrow slits could be tested to identify the most efficient spatial filter for a given angle of observation in a pattern [12.141]. The stray light destructive interference can also be applied for cleaning up the Rayleigh scattering background [12.142]. Figure 12.27 shows a Michelson-interferometer schematic for cancelling out the propagation of elastically scattered or retroreflected light from cuvette C filled with a liquid sample. A beam of linearly polarized light from single longitudinal mode laser L splits 50/50% by beamsplitter BS into the upper sample arm and lower reference one with continuously-varying neutral density filter CND and mirror M mounted on piezo-electric transducer PZT. The back scattered from the sample light is collected by fiber coupler FC and delivered to dual VIPA spectrometer Spr via single-mode Fiber. Controlling the position of PZT-mounted mirror within 50 nm allows precise tuning of the reference arm for stray-light destructing interference [12.142].

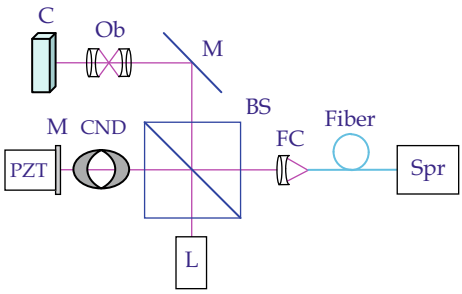

Fig. 12.27 Stray light destructive interference setting

Following the spatial filtering notion for separating directions of the highest reflectivity and scattering from the observation direction (see previous section and [12.125]), the annular beam-shaping [12.143] for the laser excitation of Brillouin scattering alternatively reduces background stray light due to residual specular reflections and elastic Rayleigh scattering [12.144]. Using the double cavity resonator in a single longitudinal mode laser enables creation of the annular beam irradiating a sample of interest off-axis while Brillouin scattering is collected via on-axis aperture.

From a standpoint of spectrally resolving the Stokes and anti-Stokes peaks of Brillouin scattering over well extinct Rayleigh maxima, multi-pass Fabry-Perot etalons offer a compatible resolution for extended exposure times. Using an off-shelf tandem etalon with 1 GHz of minimal frequency shift, detected at 50-μm lateral, 100-μm axial spot size and 5-s exposure, 514-nm measurements of Brillouin shifts performed on healthy human crystalline lenses in a 0.9% saline solution

revealed shifts from 7.8 GHz at the cortex outer to 9.0 GHz at 2.2 mm deep to anterior lens surface [12.145].

One missing yet factor of laser-based Brillouin scattering spectroscopy could be attributed to amplified spontaneous emission (ASE) of a laser source, which emission excites Brillouin-shifted peaks, since ASE of a single frequency laser is assumed negligibly low at 60–70 dB of extinction. Nonetheless, a total amount of integrated spectrally-distributed ASE over the free spectral range of an etalon even at 20 to 30 GHz spectral width is overwhelmingly noticeable versus orders-of-magnitude lower Brillouin peaks [12.133, 12.107]. Figure 12.28 depicts one example of the relative-intensity spectrum of Rayleigh scattering, brightest lines, and leaking 'white' ASE for 780 nm single-frequency laser.

Fig. 12.28 Unfiltered ASE spectrum directly dispersed by VIPA without an ASE suppression filter (reprinted with permission of SPIE)

Similarly to the technique in Raman spectroscopy making a Rayleigh scattering peak extinct by a narrow notch filter, such as of a volume holographic grating [12.146–12.149], ASE emission as well as stray-light background, which often includes the unnoticed ASE, may be dramatically suppressed via an ASE-suppression filter essentially removing needs for other spectral elements [12.107]. A conceptual schematic of single VIPA confocal microscope-interferometer is illustrated by Fig. 12.29. This approach unifies a confocal microscope and a VIPA spectrometer into a single unit connected with a single-frequency, atomic-transition stabilized laser via a single-mode fiber.

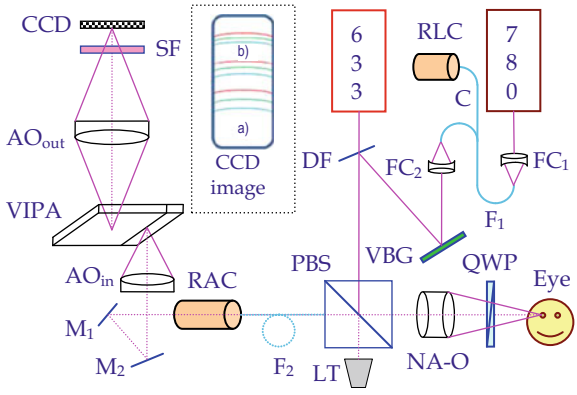

Fig. 12.29 One-stage high-extinction Brillouin scattering confocal virtual imaging phase array microscope spectrometer (CMS-VIPA)

Such a confocal-microscope-spectrometer is enabled while replacing a cylindrical lens at the VIPA input with a more superior achromatic microscope objective focusing light directly to VIPA. Instead of linear virtual light sources of Fig. 12.22, such a confocal spectrometer converts a multitude of point sources at its input, to become focused as resonant-wave circles of the outbound diffraction orders and sliced into the array of spherical segments by a rectangular sensor of EM-CCD camera ("CCD image" insert). Since a detector in a confocal microscope for Brillouin spectroscopy needs collecting light with the highest efficiency, while targeting the sample-depth discrimination via axial scanning, a relatively large pinhole or a single-mode fiber coupling can be safely used keeping the high lateral selectivity [12.150]. Plus, the axial confocality could be preserved at a small depth of focus of collecting high-NA objective.

In the system of Fig. 12.29, a fiber-coupled 780-nm diode laser was frequency locked to Rb-85 D_2 atomic line via Rubidium-vapor cell *RLC* and feedback coupler *C*. A single-frequency, single-longitudinal mode light beam was focused in and collimated out of polarization-maintaining fiber PM-SMF for $\lambda = 780$ nm via fiber collimators FC_1, FC_2. Volume Bragg grating ASE-suppression filter *VBG* was reflecting exiting the fiber beam into dichroic filter DF combining 780-nm light in reflection with 633-nm He–Ne laser beam in transmission, which served as the alignment axis for the entire system. A high-extinction ratio polarization beam-splitter PBS selected main polarization components of the beams at better than 200:1 extinction, experimentally verified via a 10,000:1 polarizer. A quarter-wave plate (780-nm, multiple order, quartz) established 180°-observation polarization-extinction scheme via $\lambda/2$ rotation on its double path for a Brillouin scattering object *Eye*, as which porcine eye specimen at epithelium stripped were used. Backward scattered light from *Eye*, passing PBS and 25-mm long trapezoidal Rb-85 D_2 absorption cell *RAC* heated to 100–175 °C, was centered by mirrors M_1, M_2 and short-focus objective AO_{in} on *VIPA* entrance window for the dispersed array being imaged by long-focus achromatic objective AO_{out} onto EMCCD of $200 \cdot 1600$ pixels, $16 \cdot 16$ micron each. Due to high-quality optics and precision system alignment, *VIPA*'s incidence angle verified by a following frequency calibration was minimized to 10 arc minutes, enabling linear dispersion $\Delta\lambda/\lambda_0$ and angular dispersion factor $\Delta\theta/(\Delta\lambda/\lambda_0)$ (Eq. (12.32)) to reach $0.6 \cdot 10^{-4}$ and 127.55 rad in the first order of diffraction, maintaining pixel resolution of 67–194 MHz/pixel from 1st to 5th order at 22.92-GHz free spectral range of 4.5 mm thick *VIPA* at 99.5 back- and 95% front-mirror reflectivity.

The insert in Fig. 12.29 schematically depicts spherical segments of spectral lines (b) on CCD screen (a) of centrally located green remainders of highly-extinct Rayleigh scattering, red Stokes, and blue anti-Stokes peaks (color on line). Since only positive diffraction orders are visible, the line sequence is always the anti-Stokes, Rayleigh, and Stokes of a given order – with a Rayleigh peak looking like a doublet as its central section is being extinct by Rb-85 D_2 line leaving two remaining satellites, broadened after propagation through a heated vapor cell [12.107]. The 0th order created by the incident beam is blocked by Edge Stop as in Fig. 12.22 with additional light trap *LT* right after *PBS* of Fig. 12.29.

Reaching as low as 10 arc-min incidence angle for *VIPA* was an enabling step in establishing single-etalon absolute frequency measurements of Brillouin-scattering. Calibrating the etalon in-situ confirmed to be the main step. The laser wavelength locked to Rb-85 D_2 absorption line at 780.241368271 nm [12.151] became a frequency comb of VIPA diffraction orders (Fig. 12.30). Such a CMS-VIPA wavelength-frequency scale was reproducible within ±30–50 MHz, re-established for each sample measured.

Fig. 12.30 Spectral grid of 780-nm Rb-D_2 line Rayleigh scattering for SMC-VIPA diffraction orders (reprinted with permission of SPIE)

For example, initially measured Brillouin shifts for water and methanol samples: 5.023 GHz and 3.795 GHz, changed only to 5.054 and 3.834 GHz remeasured another day for each test performed at a new calibration setting. Spectrums of calibration samples establishing references to published data at two exposure times are seen in Figs. 12.31 and 12.32. The statistically sound Brillouin shifts at 2σ standard deviation for CMS-VIPA measurements were 5.00 ± 0.10 GHz for water, 3.80 ± 0.08 GHz for methanol, and 10.50 ± 0.12 GHz for poly-methyl methacrylate (PMMA).

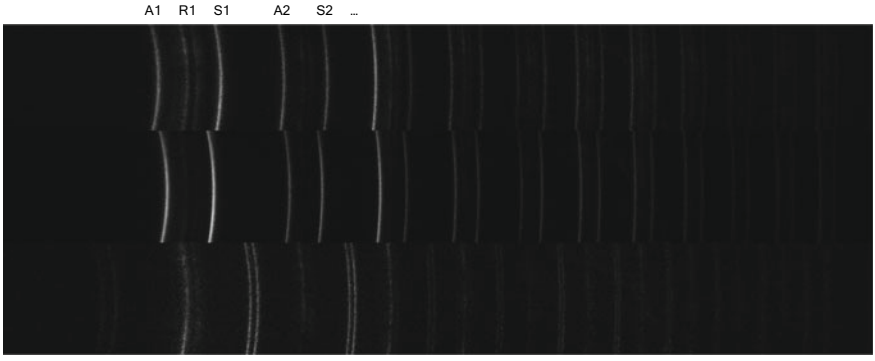

Fig. 12.31 Spectral orders 1, 2, … of Brillouin + Rayleigh scattering lines, 1-second exposure: up to bottom-water; methanol; PMMA; A1/S1 anti Stokes/Stokes Brillouin components of 1st order; R1—Rayleigh scattering 1st order, … (reprinted with permission of SPIE)

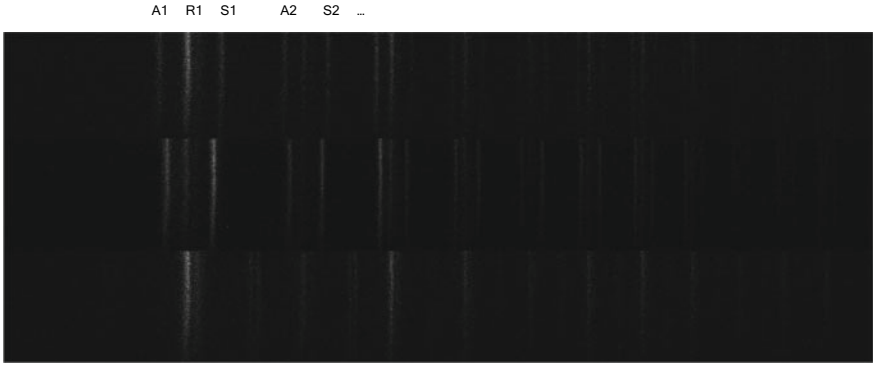

Fig. 12.32 Brillouin and Rayleigh scattering lines recorded at 10 microsecond single pixel exposure (reprinted with permission of SPIE)

The fact of seeing Brillouin-scattering peaks even at as fast exposure as the 10 microseconds points to sufficient sensitivity, resolution, and background extinction even with one single etalon when combined with other enhanced spectroscopic means as ASE suppression filter, atomic line absorption filter, and high-quality collimating optics. Even collecting Brillouin scattering with a relatively high NA = 0.45 objective didn't seem to broaden the Brillouin scattering lines observed.

Figure 12.33 shows spectrums of several cross-sections of porcine eye cornea obtained via axial scanning with 5–10 μm spatial resolution. At first, a specimen was moved into the focal point of objective *NA-O* by a motorized stage (not seen in Fig. 12.29) and its specular reflection spectrum was recorded verifying a frequency calibration via Rayleigh scattering lines prior to depth scans.

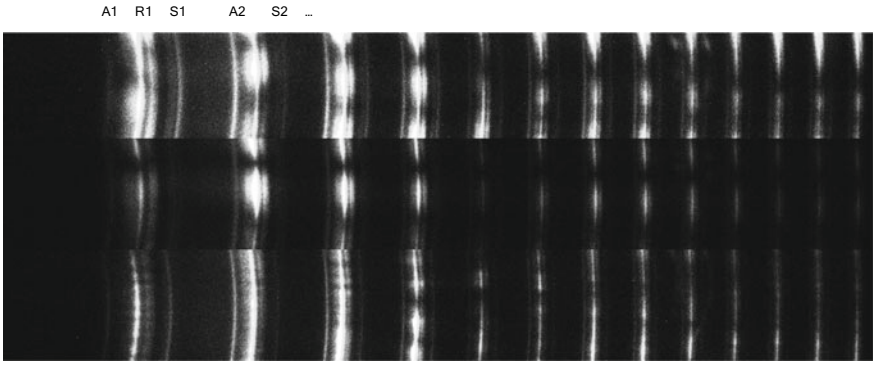

Fig. 12.33 Cross linked/untreated corneas: outer face 450-μm, untreated 50-μm deep (reprinted with permission of SPIE)

Despite an intense Rayleigh scattering from the outer cornea surface and temperature-enhanced broadening of Rayleigh lines expanding beyond the absorption line of Rb-85 D_2 vapor, Brillouin-shifted lines were highly visible starting right at the cornea surface. Figure 12.33 illustrates Brillouin scattering for riboflavin-treated versus untreated eye specimen. Measurements of untreated eyes at 22 °C compared to 37 °C did not seem to affect the shift measured, only dependent on a depth with 100–200 MHz higher Brillouin shifts in a middle of the cornea versus the anterior chamber. UV light-exposed and riboflavin-treated cornea specimen revealed steady 0.7–0.9 GHz increase of Brillouin shift to ~400 micron of depth penetration, matching its theoretical prediction [12.107].

12.3 Spectral Measurements with Frequency Combs

Numerous optical measurement techniques involving laser light rely on a precise reference to a frequency of laser excitation. For loss dichroism or dispersion studies (see Sect. 8.5) or for wavelength calibration of VIPA etalon in Brillouin scattering (Figs. 12.29 and 12.30), a frequency comb of recurring intensity peaks spanning over a broad spectrum turns into a resolute absolute scale, versus which the accurate measurements are made. Nowadays, wideband laser frequency combs expand from the ultraviolet and visible wavelengths into the deep infrared and terahertz regions of frequency spectrum establishing unparalleled levels of measurement precision for the scales of time and dimension and extending to a variety of laser measurements [12.153–12.155].

12.3.1 Frequency-Comb Scale

Separation of spectral modes of a frequency comb is identified by a repetition frequency f_R, being the inverse of period T of the sequence of pulses in the comb's time domain. Over time, a sequence of comb pulses is slipped by phase shift $\Delta\varphi$ caused by dispersion in a laser cavity. As a result, the entire frequency comb is shifted by offset frequency $f_0 = \Delta\varphi/2\pi T$:

$$f_{FC} = m \cdot f_R + f_0, \quad \text{where } m = \text{large integer}. \tag{12.36}$$

When the frequency comb described by Eq. (12.36) is compared to two distantly-separated frequencies being multiples or fractions of a known frequency f, the comb repetition frequency f_R could be itself measured. Plus, a beat signal between frequency f and a nearest comb line gives f_0.

As it was recognized early using lasers [12.156], beating laser frequencies against each other gives straightforward means to the optical frequency scale

(Fig. 12.34). In the performed experiment, resonators of He–Ne lasers 1, 2 were identical, at the length of one being slightly larger than another—with each of them tuned to a standing wave operation at $\lambda = 1.153$ μm, only for the first resonator having 148-MHz and the second 145-MHz modes spacing. Optically combining two laser beams on a photomultiplier tube PMT produced a clear beat signal at a frequency of ~ 5 MHz for the case of aligned states of polarization for both lasers and with the signal vanishing for the orthogonal orientation [12.156].

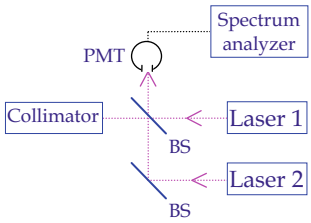

Fig. 12.34 Laser-beat frequency scale

Following the frequency-beat concept via various laser types, while comparing wavelengths of their emission to the Kr^{86} 6057-angstrom meter standard at a time, the factual speed of light was measured directly using methane stabilized He–Ne laser emitting at 3.39 μm as the product of its 88.376181627(50) THz frequency and 3.392231376(12) μm wavelength, yielding the speed of light $c = 299792456.2(1.1)$ m/s [12.157] versus the standardized[1] constant $c_0 = 299{,}792{,}458$. Further expanding the notion of combining laser frequencies [12.158], a direct comparison was made via a phase locking of an arithmetic average of two laser frequencies f_1, f_2 to the second harmonic $2f_3$ of the third laser, measuring $f_3 = (f_1 + f_2)/2$ as a result.

In the settings of Fig. 12.35, extended-cavity temperature stabilized 847-nm diode lasers were combined for second-harmonic generation in the phase-matched $KNbO_3$ crystal. Confocal cavities of each laser at 1.5-GHz free spectral range were tuned with a week feedback narrowing emission linewidths to ≤ 10 MHz of the frequency doubled lines. Beams were superimposed via beamsplitter BS at ~ 5-mW power, passing 35-dB Faraday isolator to be collinearly focused in 5-mm long $KNbO_3$ at the matching 5 mm confocal parameter. Keeping two frequencies within $f_1 - f_2 \leq 5$ THz enabled conversion of both harmonics f_1, f_2 and the $f_1 + f_2$ sum in a single $KNbO_3$ crystal. Blue filter BF and added 60° prism enabled phase-locking of each 10 nW, 424-nm blue beam for up to 50 nW of the sum [12.158].

[1]Resolution 1 of the 17th Conférence Générale des Poids et Mesures (CGPM), 1983.

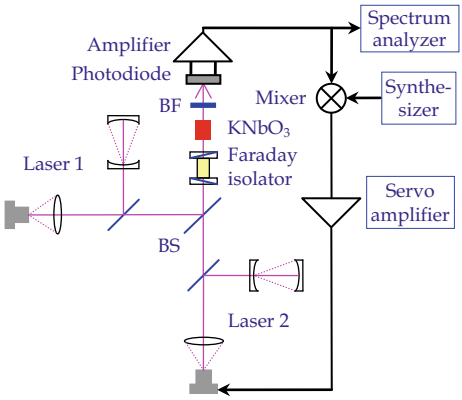

Fig. 12.35 Laser frequency conversion and summation-tuning

As the next step, uniformity and stability of femtosecond laser frequency combs were tested via two widely frequency-spaced diode lasers, phase-locked to frequency peaks of a commercial Ti-Sapphire laser [12.160]. Extended cavity diode lasers as shown in Fig. 12.35 were phase-locked to distinct modes of mode-locked femtosecond laser, while stabilizing the frequency beat signals to a reference radio-frequency of a local oscillator [12.159]. In addition, diffraction-grating based stabilization was deployed in extended cavities of both diode lasers, preventing a possible cycle-slipping event in each cavity via a phase-locked loop, referring the in-lock frequency to the local oscillator [12.160]. In a verification experiment, emissions at 822.8-nm and 870.9-nm of two laser diodes were phase-locked to two separated by 20 THz modes of the Ti:Sapphire laser. At the local oscillator frequencies ± 20 MHz and opposite offsets for two lasers, the third laser was locked 20-MHz below the center mode of Ti:Sapphire laser, if a number of modes between two frequencies was an odd number, or locked to the center mode for an even number. The uniform distribution of that 20-THz wide frequency comb modes was confirmed to be within $3 \cdot 10^{-17}$; that also verified the mode separation of the comb, being equal to the pulse repetition rate within $6.0 \cdot 10^{-16}$ [12.160].

The notion of sum- and difference-frequency generation with a frequency-interval bisection enables linking of optical and radio frequencies such as the sum of frequencies in visible and the difference in infrared and creating THz optical combs by inserting a radio frequency electro-optic modulator inside a low-loss optical cavity [12.159]. The later approach sharpens the modulation efficiency of a given carrier frequency of the modulator inside the resonant cavity (see Chap. 8 for detail) and effectiveness of consequently generated frequency sidebands, facilitating multiple-terahertz frequency combs to be created [12.161]. Effectively, a comb-feeding single-frequency cw laser is being locked to the resonance mode of the modulator cavity, having a free spectral range a multiple of the locking modulation frequency of laser radiation generating the frequency comb, which intensity profile I_k declines exponentially with order k of a generated side band as [12.159]:

$$I_k \approx I_0 \exp(-|k|\pi/\beta\Im), \tag{12.37}$$

where β is the modulator frequency-modulation index and ℑ is the finesse of the inserted cavity.

An example of a cw laser comb generator with inserted into a low-loss cavity electro-optic modulator EOM is shown in Fig. 12.36 [12.162]. A prototype Mg: Li-NbO_3 crystal modulator was embedded into a microwave-resonant cavity with 10.5 GHz resonance, 0.3 GHz bandwidth and the Q factor of 230, enabling 0.8 modulation index at 0.6 W microwave power. The main compound cavity consisted of lens substrate mirrors M_1–M_3 having HR-AR coatings on the flat-curved surfaces with M_1, M_2 forming a resonant cell at a 680 finesse and 20% transmittance of each mirror and M_2, M_3 making a filter cavity at a 400 finesse and 0.2 THz free spectral range for 30% efficiency. The first cavity lock was provided with M_1 on a piezoelectric transducer PZT at ~1/10 dither amplitude of the cavity linewidth. The PZT on mirror M_3 was tuning the filter-cavity bandpass frequency, enabling near 150 μW of polarization-stabilized He–Ne laser power to reach the comb generator, which created 1-THz spanning frequency comb at filter's cavity 5-GHz full-width half-max transmission, being sufficient enough to resolve the 10.5-GHz spaced individual sidebands. An external-cavity diode laser was used for the heterodyne detection and characterization of the frequency comb [12.162].

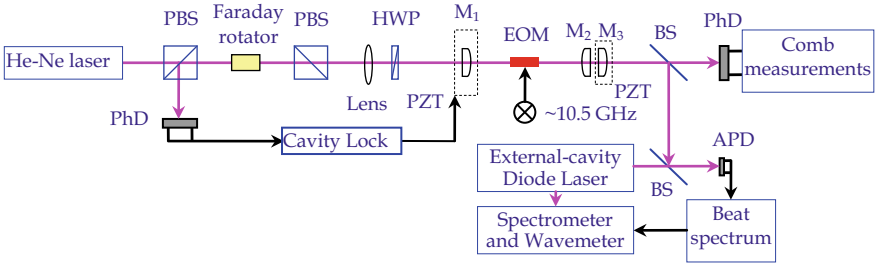

Fig. 12.36 CW laser frequency comb generator with embedded cavity EOM modulator

Broadening the multi-terahertz frequency comb and expanding it from UV-VIS to IR regions of optical spectrum takes a nonlinear medium, such as a telecom single-mode or microstructured fiber with a small-size core and large refractive-index difference, capable of guiding even tightly focused high intensity beams and readily reaching a nonlinearity threshold [12.163–12.165]. An accordingly designed microstructured fiber, as one of 1.7-mm diameter silica core surrounded by an array of 1.3 mm diameter air holes with the negative contribution of waveguide dispersion to group-velocity dispersion, could overcome dispersion limitations of standard single-mode fibers via anomalously-low total dispersion allowing to generate ultra-broadband continuums [12.164]. Such an octave spanning comb—expanding from at least 532 to 1064 nm, enables calibration of both frequencies as integer multiples of comb spacing Δf plus small frequency offsets f_1, f_2 being measured, and

verifying other frequencies in the octave, as 633-nm or 778-nm, via comb spacing Δf [12.165]. Locking comb's repetition rate to 10-MHz radio frequency reference while tuning pulse-to-pulse phase shift $\Delta\varphi$ to zero allowed stabilizing the Ti:Sapphire femtosecond comb to $5.1 \cdot 10^{-16}$ [12.166].

12.3.2 Frequency Comb Fourier-Transform Spectroscopy

Equally as coherent infrared time-domain technique is enacted by optical rectification of a femtosecond pulse (see Sect. 12.4), generating a Cherenkov cone of terahertz radiation in an electro-optic material – being collided with another femtosecond pulse synchronized and delayed to the first one [12.167], combining two frequency combs instigates static Fourier-domain spectroscopy of optical collision [12.168–12.170]. Enabling the trains of slightly delayed synchronized pulses could be facilitated by splitting one beam of a single comb or colliding independent frequency combs of unequal pulse repetition rates [12.168]. Figure 12.37 shows a system for splitting a comb into two beams generating difference frequencies at single and double frequencies of an octave spanning comb and eliminating frequency offset f_0.

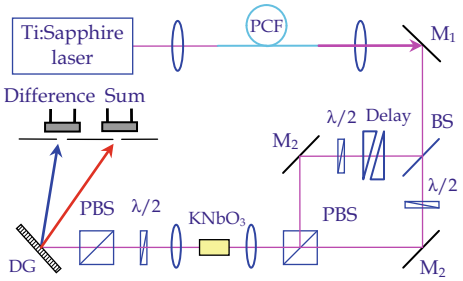

Fig. 12.37 Splitting and recombining one frequency comb

Since two beams are originated from one comb, a sum- and difference-frequency generation in a single nonlinear crystal are creating two groups of difference frequencies (see Eq. 12.35):

$$f_{FC1} - f_{FC2} = (m_1 \cdot f_R + f_0) - (m_2 \cdot f_R + f_0) = (m_1 - m_2) f_R. \qquad (12.38)$$

In the depicted setup, focusing 600-mW Ti:Sapphire laser beam of 25-femtosecond pulses at 750 MHz repetition rate to 5–30-cm long photonic crystal fiber PCF at 1.6-μm core diameter allowed generating frequency comb spanning from infrared 1049 nm wavelength to blue 439 nm light within 20-dB range of intensities. The center wavelengths for difference and sum frequencies were chosen at 946 and 473 nm with both processes in 5-mm long $KNbO_3$ crystal concurrently generating an offset-free comb near 946 nm.

The sum- and the difference-frequency generation processes were phase matched, with the sum comb having doubled offset frequency but the difference one at a zero offset. Both generated combs created beat nodes with the initial comb at

frequency offset f_0. The minimal power for the difference frequency signal per mode was estimated to be near 100 nW [12.169].

The concept of generating frequency-difference harmonics, enabling to cancel the frequency offset in a series of originating pulses, equally works for combining independent combs [12.168]. In two-channel schematic, similar to the laser beat frequency experiment of Fig. 12.34, by adding an optical rectification element to each channel the Fourier-transform spectrometer was realized statically via independent mode-locked lasers, emitting trains of 12- and 20-femtosecond pulses. The Ti:Sapphire lasers were generating 800-nm wavelength pulses with 78-MHz repetition rates being ~2-Hz apart. Optical rectification was accomplished by focusing laser beams to 0.5- and 1-mm thick GaSe crystal plates having mid-infrared second harmonics further collimated on GaSe combiner, thus forming coherent Fourier-transform spectrometer with no moving parts [12.170].

To advance the frequency-beating technique, enabling the multiheterodyne spectroscopy of frequency combs difference via essentially indistinguishable separation in repetition rates of the combined combs, both combs should be highly stable. As one of them serves as a local oscillator *LO* with the beat creating a radio-frequency (*rf*) comb: $\Delta f_R = f_{R,LO} - f_R$ at $f_{0,LO} - f_0 \to 0$ (see Eq. (12.38)), linewidths and the state of mutual coherence of two combs define the narrowness of each individual tooth in the resulting *rf* comb and signal-to-noise ratio versus *rf* noise of an individual beat. By combining emissions of fiber-based mode-locked lasers at relative linewidths below 1 Hz the phase and amplitude of 155,000 comb modes at 100-MHz spacing expanding over 15.5 THz from 1495 to 1620 nm were resolved and applied for broadband molecular spectroscopy [12.171].

A direct approach to Fourier transform spectroscopy with frequency combs relates to using high repetition rates of femtosecond lasers to radically reduce 1/*f* noise of an FTIR spectrometer performing at conventional 50–100 kHz modulation frequencies [12.172]. Synchronous detection of FTIR interferometer signals permits simultaneous in-phase and in-quadrature measurements (see Chaps. 8–10) for parallel absorption and dispersion studies as illustrated by Fig. 12.38. A modified Connes-type interferometer similar to one of Fig. 12.3b was combined with fast InGaAs detectors to sense 40-fs, 50 mW pulses of 140-MHz frequency comb in 1.5-μm fingerprint region.

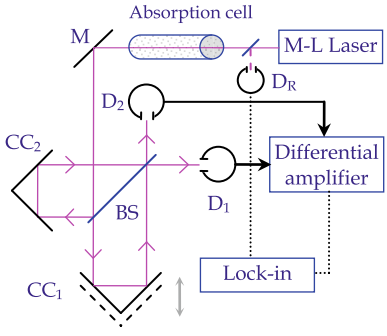

Fig. 12.38 Frequency comb synchronous FTIR spectrometer

In addition to main detectors D_1, D_2, reference detector D_R was used via $\sim 10\%$ extra beamsplitter for synchronization. M-L laser cavity contained a Cr^{4+}:YAG crystal pumped by 1064-nm Nd:YVO_4 laser with saturable-absorber mirror for mode locking and chirped resonator mirrors for dispersion compensation. Spectral resolution for acetylene in a 70-cm long single-path absorption cell reached 1.5 GHz at a 500:1 signal to noise ratio spanning 7200 resolved spectral elements with 280-s recording time [12.172].

12.3.3 Cavity-Enhanced Spectroscopy With Frequency Combs

As seen previously (Chap. 8 and Fig. 12.10), coupling a frequency comb into a multipass cavity could be advantageous for enhancing sensitivity of intracavity loss and dispersion measurements. It also assists characterizing optical parameters of the cavity [12.174], as well as enhancing comb stability [12.175] when concurrently controlling repetition frequency f_R of a pulse train and comb offset frequency f_0 (Eq. (12.38)). Subsequently, the frequency stabilized comb may be coherently coupled to the ringdown cavity to be resonant over an assembly of comb components enabling broadband spectroscopy [12.173].

Synchronous coupling of the entire comb train facilitates constructive interference of pulses in the ring-down cavity [12.172], thus improving overall sensitivity of intracavity measurements. To realize simultaneous coupling of comb components to a given set of ringdown-cavity modes, the repetition rate and offset frequency of a femtosecond comb generated by a Ti:Sapphire laser were independently controlled via a set of piezo motors and controllers adjusting the length and dispersion of a laser cavity [12.176]. Adopting 0.999 reflectivity mirrors for the entire 790–850 nm comb spectrum to maintain ≤ 10 fs^2 intracavity dispersion when tuning f_R to 4 MHz and setting f_0 by rotating one cavity mirror having $\pm 2 \cdot 10^{-4\circ}$ selectivity, 125,000 components of 10-fs comb at $f_R = 380$ MHz were coupled into the ringdown cavity with 10^{-8} integrated absorption sensitivity at 1-s long measurement in 100-nm band or with 0.8 cm^{-1} spectral resolution at 1.4-ms acquisition in 15 nm.

Similarly to efforts of broadening the frequency comb using a highly nonlinear crystal fiber, while a femtosecond comb is created by a mode locked fiber laser with a chirped pulse amplifier, the spectral domain of intra-cavity measurement could be expanded further [12.177]. Stretching femtosecond pulses in a linearly-chirped fiber amplifier due to fiber's group-velocity dispersion plus self-phase modulation avoids the self-focusing effect prior to pulses being compressed back by a double-grating compressor, if needed [12.178]. Figure 12.39 depicts a broad-bandwidth system for intra-cavity absorption measurements in 1.45–1.65 μm wavelength domain utilizing erbium-doped fiber amplifier generating 175-fs string at 40-mW average power and 100-MHz frequency.

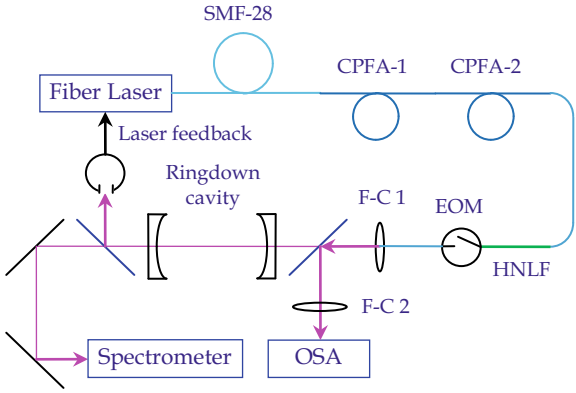

Fig. 12.39 Frequency-comb ringdown spectrometer

The mode-locked Fiber Laser operating in a normal dispersion mode was coupled to 15-m of anomalous dispersion fiber SMF-28, serving for pre-stretching pulses to 7 ps, followed by two 2-m long chirped-pulse highly doped erbium fiber amplifiers CPFA for 350 mW of output power of 6.7-ps stretched pulses. The highly nonlinear 40-cm long HNLF fiber broadened the pulse span to several hundred nanometers, while EOM switch enabled the cavity ringdown measurements. At 100-μW/nm of spectral power reaching the ringdown cavity, absorption studies of overtone spectra for CO, C_2H_2, and NH_3 were provided with nearly $2 \cdot 10^{-8}$ cm^{-1} $Hz^{-1/2}$ sensitivity [12.177].

By resolving individual modes of a frequency comb via high-resolution VIPA spectroscopy (Sect. 12.2) further enhancement of resolution for broadband ringdown absorption studies can be enabled [12.179]. The approach of Fig. 12.23 for the VIPA etalon cross-coupled to a diffraction grating [12.113] provides x-y spatial and spectral separation of comb peaks into two-dimensional array localized in the imaging plane of VIPA spectrometer. Depending on a given arrangement, each spectral element disperses the comb modes into x or y axis, such as VIPA diffraction orders in one and diffraction grating ones in another, that is tilted from 90° by orientation of the grating. By limiting measurement bandwidth to 10-nm region centered at 633 nm and filtering frequency comb modes from $3f_R$ to $14f_R$ via spherical Fabry-Perot cavity matching VIPA spectrometer, near 1.2-GHz resolution was reached for up to $75 \cdot 10^9$ resolvable peaks at 1-s integration time [12.179]. The detectable limit of $8 \cdot 10^{-8}$ cm^{-1} was reached for linear absorption coefficients in human-breath ringdown testing in 1.5–1.7 μm region with 800 MHz resolution at 200-nm spectral band [12.180]. A 2000-channel detection capability was demonstrated from 1.75 to 1.95 μm with single-channel sensitivity of $4 \cdot 10^{-8}$ cm^{-1} $Hz^{-1/2}$ in nitrogen and $4 \cdot 10^{-7}$ cm^{-1} $Hz^{-1/2}$ for water tracing in arsine [12.181].

Cross coupling of a VIPA etalon and a diffraction grating when adding a 2-D array detector enables lessening individual detector requirements of extended dynamic range and high signal-to-noise ratio for broadband frequency-comb measurements

[12.182]. Frequency-scanning of the resolved comb modes allows high-dispersion spectroscopy with resolution defined by the comb linewidth rather than by VIPA and with the enhanced sensitivity to multipath-cavity absorption.

Other special developments use heterodyne techniques via colliding power-leveled frequency combs initiated in continuous-wave (cw) lasers by dual-drive optical modulators [12.183–12.186].

Figure 12.40 visualizes the notion of utilizing the dual-drive Mach-Zehnder modulators MZT generating 24-KHz shifted frequency combs from one external-cavity cw diode laser. The first comb was used as a probe and another as local oscillator LO. The probe beam was split to 100-MHz shifted channels and to a multipass cavity. The dual modulator at 6-DB attenuation in the probe drive enabled the power leveling in the comb with spacings from near-dc frequencies up to 18 GHz while reaching noise-equivalent absorption $2 \cdot 10^{-5}$ cm^{-1} $Hz^{-1/2}$ per square root of a number of spectral elements [12.183].

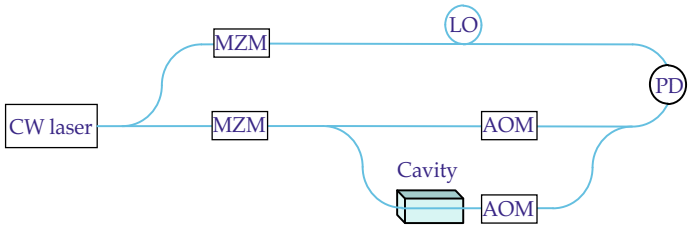

Fig. 12.40 CW-laser dual frequency comb multi-heterodyne spectrometer

Further progress could be reached by eliminating ringing effects in static Fourier-transform spectroscopy with frequency combs, due to each comb line oscillating m times within c/f_R delay (Eq. (12.36)). The elimination is achieved in a comb-based Fourier-transform spectrometer, if instrument's path-length difference is exactly matched to c/f_R of the comb, ultimately overcoming the instrumental-resolution limit [12.185]. Modulating the frequency comb, being coupled into a multipass cavity, to a multiple of the cavity free spectral range for phase-sensitive demodulation of its transmission enabled eradicating noise of frequency-to-amplitude conversion and reaching absorption sensitivity of $4.3 \cdot 10^{-10}$ cm^{-1} $Hz^{-1/2}$ per spectral element at 1575 nm [12.184]. With both techniques a tight cavity lock maintaining constant-power transmission is needed (see paragraph 7.3 and [7.42]) for implementing the Fourier-transform comb spectrometer, because of signal-line shape changing due to Doppler effect on a moving spectrometer mirror in one arm versus another while beating the comb lines with its sidebands, depending on the ratio of modulation frequency to molecular linewidth and requiring analytical modeling of likely ratios to be measured [12.186].

12.4 Time- and Frequency-Domain Terahertz Spectroscopy

A widespread availability of FTIR spectroscopy and an expansion of ultrafast lasers enabled progress of terahertz time-domain techniques for identifying molecular spectra [12.187–12.192]. A broad spectral content of a pico- or femto-second laser pulse enables frequency conversion into far infrared light due to coherent collisions of the pulse frequency components via one or another nonlinear process or via a photoconductive antenna [12.190]. Transmission, reflection, or imaging methodologies, performed in the frequency domain in conjunction with Fast Fourier or Wavelet Transform, are often used for either free-space or beam-confining vibrational fingerprint studies.

12.4.1 Time-Series Analysis of Transmittance and Reflectance

Frequency-bound measurements of optical properties of dispersive media necessitate shifting from conceptual interpretations of interaction of light and matter via transmittance or reflectance for weakly absorbing objects to dealing with polarizability and conductivity for objects of likely conductive properties. Vectors of electric **P** and of magnetic **M** polarization are commonly introduced to describe interactions of electromagnetic waves and matter (see paragraph 1.1), transforming material relations $\mathbf{D} = \varepsilon\mathbf{E}$, $\mathbf{B} = \mu\mathbf{H}$ to additive form [1.1]:

$$\mathbf{D} = \mathbf{E} + 4\pi\mathbf{P}, \quad \mathbf{B} = \mathbf{H} + 4\pi\mathbf{M}. \tag{12.39}$$

Defining electric and magnetic polarization via material relations: $\mathbf{P} = \eta\mathbf{E}$, $\mathbf{M} = \chi\mathbf{H}$, with η and χ as the dielectric and magnetic susceptibilities, dielectric permittivity and magnetic permeability:

$$\varepsilon = 1 + 4\pi\eta, \quad \mu = 1 + 4\pi\chi. \tag{12.40}$$

become also expressed additively. The connectivity of multiplicative and additive relations helps establishing correlations among optical properties of objects and vectors of electromagnetic fields.

Considering phenomenologically matter as a multitude of physical objects, such as molecules that become polarized by an applied electromagnetic field and gain electric and magnetic moments being linear functions of the field, the electric moment may be written as $\mathbf{p} = \zeta\mathbf{E}$, where ζ is the mean volume polarizability of each individual molecule averaged over all orientations. The total electric moment for N molecules per unit volume is $\mathbf{P} = N\zeta\mathbf{E}$ and, presuming a molecule inside an imaginary sphere isotropically inducing $(4\pi/3)\mathbf{P}$ polarization input, the Lorentz-Lorenz formulae follow [1.1]:

$$\eta = \frac{N\zeta}{1-(4\pi/3)N\zeta}; \quad \varepsilon = \frac{1+(8\pi/3)N\zeta}{1-(4\pi/3)N\zeta};$$
$$\zeta = \frac{3}{4\pi N}\frac{\varepsilon-1}{\varepsilon+2} = \frac{3}{4\pi N}\frac{n^2-1}{n^2+2}. \tag{12.41}$$

Since a medium refractive index $n = \sqrt{\varepsilon\mu}$ changes with frequency ω of electromagnetic waves interacting with it due to dispersion, relations (12.41) should account for dependence of dielectric permittivity $\varepsilon = n^2(\omega)$ on frequency. Assuming only one effective electron being polarized by the field in a medium molecule at resonance frequency ω_0, the mean medium polarizability becomes:

$$N\zeta = N\frac{e^2}{m\left(\omega_0^2-\omega^2\right)}. \tag{12.42}$$

The resultant frequency interdependency of dielectric permittivity ε(ω) and refractive index n(ω):

$$\frac{\varepsilon-1}{\varepsilon+2} = \frac{n^2-1}{n^2+2} = \frac{4\pi}{3}\frac{Ne^2}{m\left(\omega_0^2-\omega^2\right)}, \tag{12.43}$$

is not generally linear. Plus, as a molecular response to an electromagnetic field involves resisting forces, leading to damping of oscillations and extinction, medium polarizability ζ similarly to the refractive index of a conductor is the complex function of frequency with a multitude of resonant frequencies, resulting in a complex solution [12.193], and therefore transforming relations (12.42, 12.43) to:

$$N\zeta = N\frac{e^2}{m\left(\omega_0^2-\omega^2\right)-i\omega g};$$
$$\frac{4\pi}{3}N\zeta_k = \frac{n^2-1}{n^2+2} = \frac{4\pi}{3}\frac{Ne^2}{m}\sum_k \frac{f_k}{\left(\omega_0^2-\omega_k^2\right)-i\omega g_k}, \tag{12.44}$$

where g_k and Nf_k are the damping factor and the number of electrons for resonant frequency ω_k.

As radiation interacts with conductive mater, factors and coefficients of interaction become complex functions of frequency, including the dielectric constant, phase velocity, refractive index:

$$\hat{\varepsilon} = \varepsilon + i4\pi\sigma/\omega;\ \hat{v} = c/\sqrt{\mu\hat{\varepsilon}};\ \hat{n} = c/\hat{v} = \sqrt{\mu\hat{\varepsilon}} = (c/\omega)\hat{k},$$
$$\hat{k} = \omega\sqrt{(\varepsilon + i4\pi\sigma/\omega)}/c, \tag{12.45}$$

where $\hat{k}$ is the complex wave number and σ is the specific conductivity. The refractive index $\hat{n}$, the complex function of real index n and extinction coefficient κ, is dependent on frequency ω as:

$$\hat{n} = n(1 + i\kappa); \quad \hat{n}^2 = n^2\left(1 + 2i\kappa - \kappa^2\right); \quad \hat{n}^2 = \mu\hat{\varepsilon} = \mu(\varepsilon + i4\pi\sigma/\omega). \quad (12.46)$$

Equating real and imaginary parts of $\hat{n}^2$: $n^2(1-\kappa^2) = \mu\varepsilon; n^2\kappa = \mu\sigma/v$, leads to the solution [1.1]:

$$\begin{aligned} 2n^2 &= \sqrt{\mu^2\varepsilon^2 + 4\mu^2\sigma^2/v^2} + \mu\varepsilon; \\ 2n^2\kappa &= \sqrt{\mu^2\varepsilon^2 + 4\mu^2\sigma^2/v^2} - \mu\varepsilon. \end{aligned} \quad (12.47)$$

Despite n or k not being directly resolved, identifying $n^2(1-\kappa^2)$ and $n^2\kappa$ for optical frequencies where $\mu \to 1$ directly gives the dielectric constant ε and the ratio of conductivity to frequency σ/v.

In time, unobstructed movements of a free electron in a conductor may be described as [1.1]:

$$\boldsymbol{r} = \boldsymbol{r}_0 - (1/\beta)\boldsymbol{v}_0 exp(-\beta t). \quad (12.48)$$

Here the damping constant β characterizes the decay time $\tau_d = 1/\beta$ from the initial velocity $\boldsymbol{v}_0$ to $\boldsymbol{v}$. If a time-harmonic field $\mathbf{E} = \mathbf{E}_0\exp(-i\omega t)$ is applied, N electrons create a current of density $j = \sigma E$ at:

$$\sigma = Ne^2/(m(\beta - i\omega)). \quad (12.49)$$

The frequency dependence of complex refractive index $\hat{n}$ and dielectric constant $\hat{\varepsilon}$ is caused by free and bound electrons, but for small bound contributions and nonmagnetic media it turns to:

$$\begin{aligned} &\hat{\varepsilon} = \hat{n}^2 = 1 - \frac{4\pi Ne^2}{m\omega(\omega - i\beta)}; \quad n^2\left(1-\kappa^2\right) = 1 - \frac{4\pi Ne^2}{m\left(\omega^2 + \beta^2\right)}; \\ &2n^2\kappa = \frac{4\pi Ne^2/\beta}{m\omega\left(\omega^2 + \beta^2\right)}. \end{aligned} \quad (12.50)$$

Here the last two relations define real and imaginary parts of $\hat{n}^2$ (see Eq. (12.46) and [1.1]).

Subsequently to the introduction of complex material constants, the law of refraction for a metal bordering a dielectric could be expressed via its complex relative index $\hat{n}$, as in Snell's law:

$$\sin\varphi_{rf} = \frac{\sin\varphi_{in}}{\hat{n}} = \frac{\sin\varphi_{in}}{n(1+i\kappa)} = \frac{1-i\kappa}{n(1+\kappa^2)}\sin\varphi_{in}. \tag{12.51}$$

Here indices *in* and *rf* assign the incidence and refraction. Since per Eq. (12.51) the angle φ_{rf} becomes complex, the meaning of refraction angle changes, plus relations for the reflectance and transmittance even of boundaries of thin metal and dielectric films tend to be elaborate [1.1, 1.3, 12.193], but at normal incidence the reflectance is polarization independent (see Eq. (1.91)), with the absorption α and extinction κ coefficients and *1/e* distance d due to relations (1.87), (1.88).

Fresnel formulae for reflectance or transmittance of a border of a dielectric and a conductor remain intact for the real dielectric constant and refractive index changed to complex ones. The amplitude reflectance $r(\omega)$ and transmittance $t(\omega)$ of light incident on a border of dielectric d and conductor c remain:

$$\hat{r}(\omega) = |\hat{n}_c - \hat{n}_d|/|\hat{n}_c + \hat{n}_d|; \quad \hat{t}(\omega) = |1-\hat{\rho}(\omega)| = |2\hat{n}_d|/|\hat{n}_c + \hat{n}_d|, \tag{12.52}$$

under the presumption of no border absorption or scattering at $\hat{n}_d$, $\hat{n}_c$ being frequency dependent.

Equation (1.91) define complex reflectivity ρ_0 for a boundary of a conductor in air at normal incidence. While dealing with an actual sample in coherent light its multiple reflections and bulk attenuation of a likely used plane-parallel plate need to be taken into account (see Chaps. 3, 6, and 8). Consider a transparent slab of either a conductive or a dispersive medium of frequency-dependent refractive index $\hat{n}_c$ surrounded by a dielectric of index $\hat{n}_d$ irradiated as in Fig. 3.9, but at normal incidence. Following Eqs. (3.116, 3.119, 3.121, 3.122) let us express the slab total and surface reflectance and transmittance at equal front and back surfaces and the bulk extinction α as:

$$\begin{aligned} r &= \frac{E_\rho}{E_0} = \left[\rho_{sa} + \frac{\rho_{sa}\tau_s^2\tau_a^2 e^{i\delta}}{1-\rho_{sa}^2\tau_a^2 e^{i\delta}}\right]; \\ \hat{R} &= \frac{I_\rho}{I_0} = \hat{\rho}\frac{(1+\tau)^2 - 2\tau(1+\cos\delta)}{(1+\tau\hat{\rho})^2 - 2\tau\hat{\rho}(1+\cos\delta)}; \end{aligned} \tag{12.53}$$

$$\begin{aligned} t &= \frac{E_\tau}{E_0} = \frac{\tau_a\tau_s^2}{1-\hat{\rho}_s^2\tau_a^2 e^{i\delta}}; \\ \hat{T} &= \frac{I_\tau}{I_0} = \frac{(1-\hat{\rho})^2\tau}{1+\tau^2\hat{\rho}^2 - 2\tau\hat{\rho}\cos\delta} \\ &= \frac{(1-\hat{\rho})^2\tau/\hat{\rho}}{1/\hat{\rho}+\tau^2\hat{\rho} - 2\tau\cos\delta}, \end{aligned} \tag{12.54}$$

where $\hat{R}$, $\hat{T}$, ρ_s, τ_s are the slab total and surface reflectance and transmittance; δ is the phase angle for the slab of thickness ℓ and bulk transmittance τ_a. For surface reflectance $\hat{\rho} = |\hat{n}_c - \hat{n}_d|^2/|\hat{n}_c + \hat{n}_d|^2$ the relations turn to:

$$\begin{aligned}\hat{R} &= \frac{(1+\tau)^2 - 2\tau(1+\cos\delta)}{\left(\dfrac{|\hat{n}_c+\hat{n}_d|^2+\tau|\hat{n}_c-\hat{n}_d|^2}{|\hat{n}_c+\hat{n}_d||\hat{n}_c-\hat{n}_d|}\right)^2 - 2\tau(1+\cos\delta)} \\ &= \frac{1+\tau^2-2\tau\cos\delta}{\left|\dfrac{\hat{n}_c+\hat{n}_d}{\hat{n}_c-\hat{n}_d}\right|^2 + \tau^2\left|\dfrac{\hat{n}_c-\hat{n}_d}{\hat{n}_c+\hat{n}_d}\right|^2 - 2\tau\cos\delta};\end{aligned} \tag{12.55}$$

$$\begin{aligned}\hat{T} &= \frac{\left(\left|\dfrac{4\hat{n}_c\hat{n}_d}{|\hat{n}_c+\hat{n}_d|^2}\right|^2\right)\tau\left|\dfrac{\hat{n}_c+\hat{n}_d}{\hat{n}_c-\hat{n}_d}\right|^2}{\left(\left|\dfrac{\hat{n}_c+\hat{n}_d}{\hat{n}_c-\hat{n}_d}\right| + \tau\left|\dfrac{\hat{n}_c-\hat{n}_d}{\hat{n}_c+\hat{n}_d}\right|\right)^2 - 2\tau(1+\cos\delta)} \\ &= \frac{\tau\left|\dfrac{4\hat{n}_c\hat{n}_d}{\hat{n}_c^2-\hat{n}_d^2}\right|^2}{\left|\dfrac{\hat{n}_c+\hat{n}_d}{\hat{n}_c-\hat{n}_d}\right|^2 + \tau^2\left|\dfrac{\hat{n}_c-\hat{n}_d}{\hat{n}_c+\hat{n}_d}\right|^2 - 2\tau\cos\delta}.\end{aligned} \tag{12.56}$$

At not transparent bulk, $\tau = 0$, derived equations convert to $\hat{T} = 0$ and $\hat{R} = \hat{\rho}$, being the formula (1.91). Let us further assume the bulk transparency, $\tau = exp(-\alpha\ell) = 1.0$, and zero extinction $\alpha = 4\pi\kappa/\lambda = 0$. For the phase angle $\delta = \pm\pi/2$ the functions interference terms $\cos\delta = 0$ vanish, thus we could consider the reflectance and transmittance of a plane-parallel slab as mean, not integrated (compare Eqs. (1.106, 1.107, 3.129, and 3.130)), for the expressions (12.55), (12.56) to become:

$$\hat{R}_{mean} = \frac{2}{1/\hat{\rho}+\hat{\rho}} = \frac{2\hat{\rho}}{1+\hat{\rho}^2} = \frac{2|\hat{n}_c+\hat{n}_d|^2|\hat{n}_c+\hat{n}_d|^2}{|\hat{n}_c+\hat{n}_d|^4+|\hat{n}_c-\hat{n}_d|^4}; \tag{12.57}$$

$$\begin{aligned}\hat{T}_{mean} &= \frac{\hat{\rho}(1-\hat{\rho})^2}{1+\hat{\rho}^2} = \frac{|4\hat{n}_c\hat{n}_d|^2}{\left|\hat{n}_c^2-\hat{n}_d^2\right|^2}\,\frac{|\hat{n}_c-\hat{n}_d|^2|\hat{n}_c+\hat{n}_d|^2}{|\hat{n}_c+\hat{n}_d|^4+|\hat{n}_c-\hat{n}_d|^4} \\ &= \frac{16\hat{n}_c^2\hat{n}_d^2}{|\hat{n}_c+\hat{n}_d|^4+|\hat{n}_c-\hat{n}_d|^4}.\end{aligned} \tag{12.58}$$

The functions extrema come at $\cos\delta = \pm 1$, with complementary maxima and minima of $\hat{T}, \hat{R}$ being:

$$\hat{T}_{max} = \left|\frac{4\hat{n}_c\hat{n}_d}{|\hat{n}_c+\hat{n}_d|^2-|\hat{n}_c-\hat{n}_d|^2}\right|^2; \quad \hat{R}_{min} = \frac{1+1-2}{1/\hat{\rho}+\hat{\rho}-2} = 0; \tag{12.59}$$

$$\hat{T}_{min} = \left| \frac{4\hat{n}_c\hat{n}_d}{|\hat{n}_c + \hat{n}_d|^2 + |\hat{n}_c - \hat{n}_d|^2} \right|^2; \quad \hat{R}_{max} = \left| \frac{\hat{n}_c^2 - \hat{n}_d^2}{\hat{n}_c^2 - \hat{n}_d^2} \right|^2. \tag{12.60}$$

Figure 12.41 illustrates the dependencies of reflectance and transmittance of the slab versus angle δ for two sets of refractive indices $\hat{n}_c = 1.5$, $\hat{n}_d = 1$ and $\hat{n}_c = 2.85$, $\hat{n}_d = 1.25$. Four $\hat{R}$, $\hat{T}$ curves and lines are due to Eqs. (12.55), (12.56), and (12.57), (12.58). For studies in the air at $n_d = 1$, the extrema for relative refractive index $\hat{n} = n(1 + i\kappa)$ turn to:

$$\hat{R}_{min} = 0; \quad \hat{R}_{max} = \frac{|\hat{n}^2 - 1|^2}{|\hat{n}^2 + 1|^2} = \left(\frac{n^2(1+\kappa^2) - 1}{n^2(1+\kappa^2) + 1} \right)^2; \tag{12.61}$$

$$\begin{aligned} \hat{T}_{max} &= \left| \frac{4\hat{n}}{|\hat{n}+1|^2 - |\hat{n}-1|^2} \right|^2 = 1 + \kappa^2; \\ \hat{T}_{min} &= \left| \frac{4\hat{n}}{|\hat{n}+1|^2 + |\hat{n}-1|^2} \right|^2 = \frac{4n^2(1+\kappa^2)}{(n^2(1+\kappa^2)+1)^2}. \end{aligned} \tag{12.62}$$

Considerately, complementary extrema of $\hat{T}_{max} = 1 + \kappa^2$ and $\hat{R}_{min} = 0$ reveal the way to directly measure the $1 + k^2$ factor of extinction coefficient κ for a likely dispersive or conductive medium. For non-conducting media at no absorption: $\kappa \to 0$, $n_c \to n$, $n_d = 1$, the equations convert to formulae:

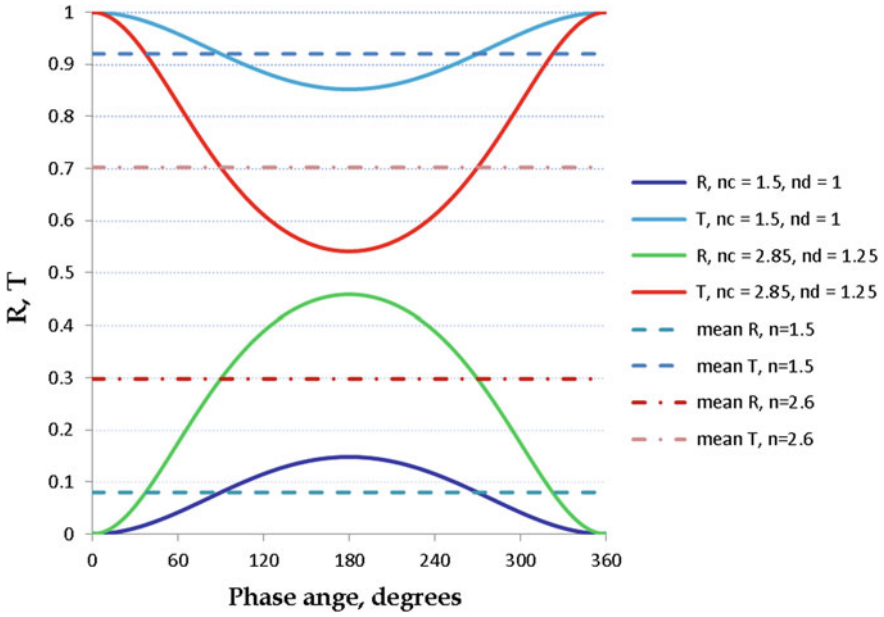

Fig. 12.41 Complex reflectance and transmittance versus phase angle

$$R_{mean} = \frac{(n^2-1)^2}{(n^2+1)^2+4n^2}; \quad R_{max} = \left(\frac{n^2-1}{n^2+1}\right)^2; \qquad R_{min} = 0; \tag{12.63}$$

$$T_{mean} = \frac{8n^2}{(n^2+1)^2+4n^2}; \quad T_{min} = \frac{4n^2}{(n^2+1)^2}. \quad T_{max} = 1; \tag{12.64}$$

Given complexities of determining properties of highly absorbing media, even via available Eqs. (12.55)–(12.62) for normal light incidence, the majority of prevailing techniques rely on scanning of object properties by varying frequencies or incidence angles to resolve Fresnel equations for a complex refraction and extinction. The frequency scanning studies use the Kramers-Kronig dispersion relations [12.194–12.197] quantitatively estimating the amplitude reflectivity $\hat{r}(\omega)$ and phase angle $\Theta(\omega)$:

$$\begin{aligned} \hat{r}(\omega) &= r(\omega)exp(i\Theta) = \frac{1-\hat{n}(\omega)}{1+\hat{n}(\omega)}; \\ \Theta(\omega_r) &= \frac{2\omega_r}{\pi}\int\limits_0^\infty \frac{ln\rho(\omega)}{\omega^2-\omega_r^2}d\omega; \\ \hat{n}(\omega_r) &= 1+\frac{c}{\pi}\lim_{x\to 0+}\int\limits_0^\infty \frac{\alpha(\omega)d\omega}{\omega^2-(\omega_r+ix)^2}. \end{aligned} \tag{12.65}$$

Here ω_r is the factual scan frequency while the angle $\Theta(\omega)$ in reflection is a function of reflectance at all frequencies from 0 to ∞. The angle-scan technique uses at least two distinct incidence angles φ to resolve a refraction index and absorption coefficient of the complex reflectance [12.198, 1.1]. The first technique is limited by a range of frequencies over which the practical integration could be accomplished, mainly for the upper range of frequencies, while both require numerical fitting.

Following Eqs. (12.52–12.54) for the frequency deconvolution analysis of time-domain spectra, the amplitude reflectance and transmittance of a plane-parallel slab at normal incidence having the complex relative refractive index $\hat{n}$ in air under the presumption of $\hat{n}_{air} = 1$ become:

$$\hat{r}_{slab}(\omega) = \left|\frac{\hat{n}-1}{\hat{n}+1}\right| + \frac{\left[4\hat{n}|\hat{n}-1|/(\hat{n}+1)^3\right]exp[-i2\hat{n}\omega\ell/c]}{1-[(\hat{n}-1)/(\hat{n}+1)]^2 exp[-i2\hat{n}\omega\ell/c]}; \tag{12.66}$$

$$\hat{t}_{slab}(\omega) = \frac{\left[4\hat{n}/(\hat{n}+1)^2\right]exp[-i(\hat{n}-1)\omega\ell/c]}{1-[(\hat{n}-1)/(\hat{n}+1)]^2 exp[-i2\hat{n}\omega\ell/c]}, \tag{12.67}$$

with a conversion: $\tau_{s1a}\tau_{s1a} = (1-\rho_{sa1})(1-\rho_{sa2}) = 2n_1 2n_2/(n_1+n_2)(n_2+n_1)$. Here the pulse waveform measurements are presumed to be made versus a reference sample in reflection and air in transmission, aiding the index n and extinction κ plus absorption coefficients $\alpha(\omega) = 2\kappa_\omega\omega/v = 2n\kappa_\omega\omega/c$.

12.4.2 Coherent Time-Domain Measurements Via Pulse Delays

Time-domain spectroscopy of far-infrared spectra has been originated using frequency conversion and optical rectification of pico- and femto-second coherent laser pulses [12.187–12.189]. The optical beating method, leading to a frequency conversion into a terahertz spectrum, utilizes FTIR measurements (see Sect. 12.1) via a Michelson or Fabry-Perot interferometer [12.188]. The coherent time-delay methodology relies on interlacing of two light pulses, one interacting with an object of interest and another delayed, while measuring object dispersive properties as distortions and broadening of an original pulse. Reflectance spectrum $\hat{\rho}(\omega)$ could be obtained via a reference object of the known properties $\hat{\rho}'$ and $\hat{\varepsilon}'$[12.189]:

$$\begin{aligned}\hat{\rho}(\omega) &= \hat{\rho}\,'(\omega)\int_{-\infty}^{+\infty}[I(t)/I'(t)]exp(i\omega t)\mathrm{d}t;\\ \hat{\rho}\,'(\omega) &= \frac{\cos\varphi_i - \sqrt{\hat{\varepsilon}_2'(\omega)/\varepsilon_1 - \sin^2\varphi_i}}{\cos\varphi_i + \sqrt{\hat{\varepsilon}_2'(\omega)/\varepsilon_1 - \sin^2\varphi_i}},\end{aligned} \tag{12.68}$$

where $\hat{\rho}'(\omega)$ is the reference reflectance, $\varphi_i$is the angle of incidence, and indices 1, 2 relate to the propagating and reflecting media with complex dielectric constant $\hat{\varepsilon}$ computed by the inversion:

$$\frac{\hat{\varepsilon}_2(\omega)}{\varepsilon_1} = \sin^2\varphi_i + \cos^2\varphi_i\left|\frac{1-\hat{\rho}(\omega)}{1+\hat{\rho}(\omega)}\right|^2. \tag{12.69}$$

With a multi-quantum-well superlattice slab of thickness ℓ, at front and back surface interfaces of reflectance $\hat{\rho}_{12}, \hat{\rho}_{23}$, numerical fitting was used to obtain index $\hat{n}_2$ from reflectivity $\hat{\rho}_s(\omega)$ [12.189]:

$$\hat{\rho}_s(\omega) = \frac{\hat{\rho}_{12} + \hat{\rho}_{23}exp\left(i2\ell\sqrt{\varepsilon_2}\cos\varphi_2\right)}{1 + \hat{\rho}_{12}\hat{\rho}_{23}exp\left(i2\ell\sqrt{\varepsilon_2}\cos\varphi_2\right)}. \tag{12.70}$$

Another approach to generating terahertz radiation by optical excitation relies on a Hertzian dipole being a fast dipole with dimensions much smaller than the radiating wavelengths [12.190]. A common setting for emission and delay-line detection of terahertz radiation is seen in Fig. 12.42 [12.191, 12.192]. A short femto- or picosecond pulse irradiates a silicon-on-sapphire dipole-emitting bipolar antenna, which excites a fast transient resulting in terahertz light source 1. Similar assembly 2 serves as the detector of a terahertz beam collimated to interact with *Sample* by *Parabolic* mirrors. The laser detection pulse is delayed via the excitation one to enable the time-domain spectroscopy at terahertz frequencies.

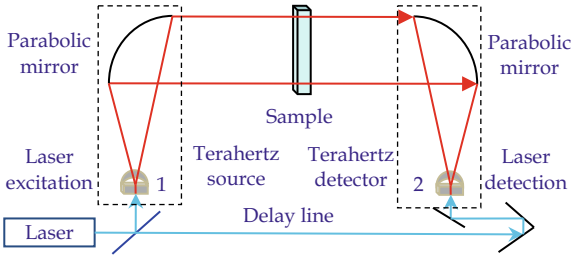

Fig. 12.42 Laser excitation and detection of terahertz radiation

In a variation of Fig. 12.42 system at two extra grating beamsplitters for pump-probe studies of samples in reflected light the relative phase angle Θ in reflection was measured at a 1-THz frequency with a 10-mrad sensitivity [12.200]. For these measurements a Drude-Lorentz model of conductivity [12.199], identifying complex dielectric permittivity $\hat{\varepsilon}$ as a sum of intra-band and inter-band functions was used:

$$\hat{r}(\omega) = |r| exp(i\,\omega t) = \frac{n(\omega) + i\kappa(\omega) - 1}{n(\omega) + i\kappa(\omega) + 1};$$
$$\hat{\varepsilon} = \varepsilon_{core} + \frac{4\pi i}{\omega}\frac{Ne^2\tau_d}{m(1 - i\omega\tau_d)} = \varepsilon_1 + i\varepsilon_2 = (\hat{n}_1 + i\hat{\kappa}_2)^2; \tag{12.71}$$

$$\hat{\varepsilon} = \varepsilon + i\,4\pi\sigma/\omega = (4\pi i/\omega)\hat{\sigma};$$
$$\hat{\sigma} = \sigma + \varepsilon\omega/4\pi i; \quad \varepsilon_1 = \hat{n}^2 - \hat{\kappa}^2; \quad \varepsilon_2 = 2\hat{n}\hat{\kappa}, \tag{12.72}$$

where ε_{core} relates to sample core (inter-band) carriers and Ne^2 to its intra-band free electron carriers (see Eqs. (12.45)–(12.50)) for designations). These equations may also be applied to testing conducting wafers and dopants [12.200].

In the systems like one of Fig. 5.17 (see Chap. 5) designed for simultaneous reflectance and transmittance studies at normal incidence while omitting beamsplitters, measuring the amplitude reflectance versus an ideal reference sample as of pure gold permits inverting Eq. (12.71) to:

$$n(\omega) = \frac{1 - r^2(\omega)}{1 + r^2(\omega) - 2|r|(\omega)\cos\Theta(\omega)}; \tag{12.73}$$

$$\alpha(\omega) = \frac{2\omega}{c}\frac{2r(\omega)\sin\Theta(\omega)}{1 + r^2(\omega) - 2|r|(\omega)\cos\Theta(\omega)}, \tag{12.74}$$

for refractive index $n(\omega)$ and absorption coefficient $\alpha(\omega) = \kappa(\omega)2\omega/v$ versus frequency, assuming $n_{air} \cong 1.0$. In that normal-reflectance time-of-flight setting the system is sensitive to a longitudinal sample displacements Δy, causing a phase error $\Delta\Theta = 2n_\omega\omega\Delta y/c$ and likely $n(\omega)$, $\alpha(\omega)$ errors [5.30]. At $r(\omega)\rightarrow 1$, $\Theta(\omega)\rightarrow 0$, measurements of $\alpha(\omega)$ could reach a few decades in dynamic range [12.201].

At strictly transmission studies of conductive materials having notably high reflectivity, multiple reflections result in exponentially declining echoes in time-domain spectra, overlapping for thin while separating for sufficiently thick samples. From a standpoint of amplitude transmission the propagation process for a slab of thickness ℓ sandwiched between windows in air can be seen as:

$$\begin{aligned} E_s(\omega) &\sim t_{1-s}(\omega)t_s(\omega)t_{s-2}(\omega)MR(\omega)E(\omega), \\ E_{ref}(\omega) &\sim t_{1-s}(\omega)t_s(\omega)t_{s-2}(\omega)E(\omega). \end{aligned} \tag{12.75}$$

Here MR is the multiple reflection factor; indices s, ref, 1, 2 are for the sample, the reference, front, and back window [12.202]. The complex relative amplitude transmittance $t_s(\omega) = \mathrm{E_s}/\mathrm{E_{ref}}$ (see Eq. (12.67)) becomes:

$$\hat{t}_s(\omega) = \frac{2\hat{n}_s(\hat{n}_1+\hat{n}_2)}{(\hat{n}_1+\hat{n}_s)(\hat{n}_s+\hat{n}_2)} \frac{exp[-i(\hat{n}_s-\hat{n}_{air})\omega\ell/c]}{1-\left|\frac{\hat{n}_s-\hat{n}_1}{\hat{n}_s+\hat{n}_1}\right|\left|\frac{\hat{n}_s-\hat{n}_2}{\hat{n}_s+\hat{n}_2}\right|exp[-i2\hat{n}_s\omega\ell/c]}. \tag{12.76}$$

Finding a solution to Eq. (12.76) which presumes no multiple reflections in two windows is challenging, but for thick samples at separated echoes it could be closely approximated if taking measurements of terahertz pulses transmitted directly plus at least of two echoes [12.202, 12.203].

If multiple reflections are neglected, while sample amplitude transmittance is approximated as proportional to $4\hat{n}_c\hat{n}_d/|\hat{n}_c+\hat{n}_d|^2$ (Eqs. (12.56, 12.67)) multiplied by the complex response of the slab material and functions of an actual measurement system, various approximation errors affect the results depending not only on a physical model of propagation, the angle of incidence and multiple reflections, but also on data extraction, time-frequency deconvolution, etc. [12.204]. When performing the Fourier deconvolution of spectra to extract material parameters measured, the sample thickness is expected to be precisely known, validating the exponential dependencies for the absorption coefficient and the phase delay. Since the accuracy of thickness determination directly contributes to errors of parameter measurements, a way to perform the analysis without knowledge of thickness is to rely on multiple-reflection echoes being measured in series [12.205].

A way of resolving ambiguity of identifying a unique $n(\omega)$, $\kappa(\omega)$ set via a numeric trials is in adding samples, and not varying angles of incidence or using bidirectional tests [12.206–12.210]. The measurement complexity multiplies, as various pairs of multiple reflectors add up for every extra sample (see Sect. 3.3.3 for polarization-interference contribution), but enables singularity.

At even more intricacy of adding a collinear difference-frequency generation converter based on a tunable parametric oscillator concurrent studies of $n(\omega)$ and $\alpha(\omega)$ could be enabled [12.211]. Due to its high nonlinearity, 4-dimethil-tosulate (DUST) crystal was used to generate wide-band THz light via two pump wavelengths λ_1, λ_2 for a shape of THz spectrum from the difference-frequency process revealing the frequency spectrums of $n(\omega)$ and $\alpha(\omega)$, while knowing λ_1, λ_2 and $\Delta\lambda = \lambda_1 - \lambda_2$.

The system of Fig. 12.43 illustrates a concept of direct simultaneous terahertz measurements of transmittance and reflectance while using, instead of a transceiver in Fig. 5.30, a beamsplitter and a second detector, letting 50% of terahertz emission to be lost while gaining confidence [12.212]. The added reflection-path silicon wafer beamsplitter BS_2 redirects terahertz radiation from Sample to detector 1 and detector 2 sees the transmitted part. The rest of the system is conceptually alike one of Fig. 12.42, with extra elements supporting the generation and detection of terahertz light. An alternative dual reflection-transmission study relates to sequential insertions of beamsplitter and/or mirror pairs guiding either a transmitted or reflected by sample beam onto one detector [12.214], while deploying broadband THz radiation from laser-induced filaments in air [12.213].

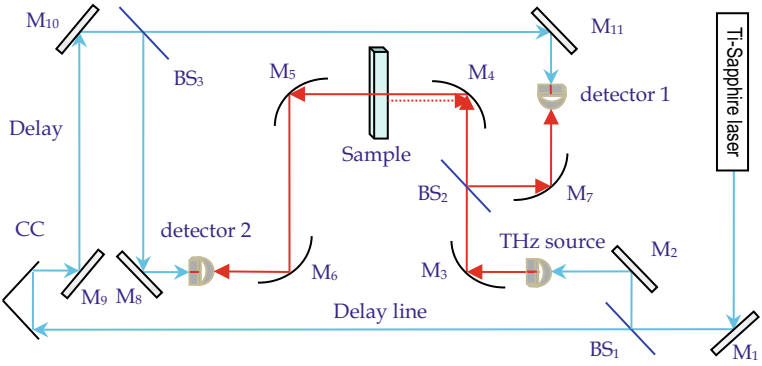

Fig. 12.43 Beamsplitter based setting for reflection-transmission terahertz studies

A time-domain terahertz measurement is effectively an optically-gated process with a pump pulse serving as an opening gate for the emitter and a delayed pulse becoming the detector gate, enabling many applications including terahertz imaging [12.115]. A similar pump-probe process with electro-optic sampling permits coherent studies at high frequencies via femtosecond probes [12.116]. A thin, such as 30-μm-thick ZnTe sensor serves as a detector of the pump and terahertz probe pulses for the electro-optic modulation creating Pockels effect sensed with a quarter-wave plate and Wollaston polarizer by two balanced photodetectors, as the terahertz beam modulates the copropagating pump one. The concept provides an alternative to photoconductive antennas enhancing the resolution at compatible sensitivity, especially toward higher frequencies [12.117].

While electro-optic sampling relies on rotation of polarization vector of a pump pulse, being modulated by a terahertz probe in ZnTe sensor and necessitating polarization-sensitive detection, quasi-phase matched crystals with nonlinear optical susceptibility can create THz-induced phase and amplitude changes, enabling direct energy measurements [12.118]. The probe-phase method retains the sensitivity advantage and probe-energy one gains its sensitivity at higher frequencies.

Adding spectral filtering of an electro-optic probe decreases shot noise of terahertz detection and its spectral depletion, while also extending the detection bandwidth into IR frequencies [12.119].

12.4.3 *Frequency-Domain Photomixing Terahertz Spectroscopy*

As time-domain techniques offer advantages of instantaneous spectrally-broad measurements in a single pulse, continuous-wave narrow linewidth lasers enable optical heterodyne conversion or photomixing for both coherent detection as well as generation of terahertz radiation [12.221–12.226]. The generation is enabled via electron-hole pairs instigated by difference-frequency radiation absorbed in low-temperature grown epitaxial layers of GaAs or InGaAs for photomixed cw-pump lasers. Two lasers irradiate a short gap between GaAs surface electrodes stimulating the difference frequency bound current that enables terahertz emission in a complimentary antenna [12.221]. The faster the process, the shorter the photoconductive lifetime in GaAs, the broader spectrum of a GHz or THz emission is accomplished [12.223]. Using distributed-Bragg-reflector (DBR) diode lasers with resonant optical feedback allows stabilizing laser center frequencies and narrowing the heterodyning linewidths.

Figure 12.44 depicts the concept of resonant frequency-difference generation for terahertz light. The diode lasers 1, 2 are paired with confocal external resonators Rz_1, Rz_2 for resonant-wavelength feedback via piezoelectric transducers PZT_1, tuning each inter-mirror distance to a desired wavelength, being phase optimized by transducers PZT_2 while reflected beams are blocked by apertures A_1, A_2 [12.225]. The external resonators permit to narrow the diode-laser linewidths and stabilize the outputs. Both outbound beams focused by objectives O_1, O_2 are merged by beamsplitters $BS_{1\text{-}2}$ and mirror-splitter pair M-BS via optical isolator ISO on THz photomixer – a low-temperature grown GaAs wafer, enabling coherent difference-frequency generation of terahertz radiation. The subsequent measurements of absorption spectrum at a 313-GHz conversion frequency made for acetonitrile (CH_3CN) in gas Cell by InSb bolometer D and spectrum analyzer SA were at $\sim 1 \cdot 10^{-4}$ $Hz^{1/2}$ detection limit [12.223].

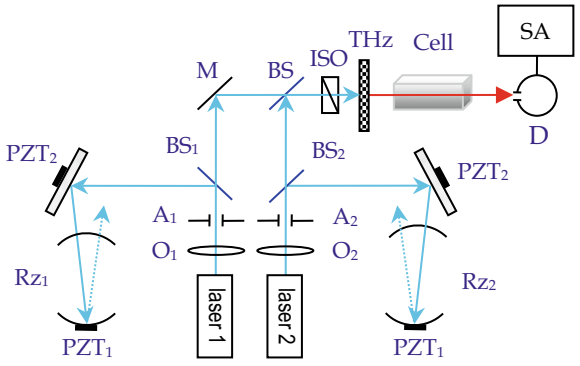

Fig. 12.44 Excitation of terahertz light by photomixing

For the difference-frequency mixing, as for two single-frequency laser beams with intensities I_1, I_2 at close frequencies ν_1, ν_2 – overlapping each other onto a photoconductive antenna such as of a low-temperature grown GaAs, the instant power I_Σ on the photomixer is modulated as [12.221]:

$$\begin{aligned} I_\Sigma &= I_{1,2} + 2\sqrt{mI_1I_2}[\cos 2\pi(\nu_2 - \nu_1)t + cos2\pi(\nu_1 + \nu_2)t] \\ &\sim I_{1,2} + 2\sqrt{mI_1I_2}\cos 2\pi|\nu_2 - \nu_1|t, \end{aligned} \tag{12.77}$$

where $I_{1,2}$ is the combined optical power of two beams. The approximation in Eq. (12.77) is taken at close to each other frequencies for the difference generating terahertz emission but sum to be high enough to make a negligible modulation contribution. If a bias voltage is applied, the time-dependent mixer conductance creates current J_Σ, modulated at the difference frequency [12.222]:

$$J_\Sigma = J_0\left[1 + 2\sqrt{mI_1I_2}\sin(\omega t + \varphi)/\left(I_{1,2}\sqrt{1+\omega^2\tau^2}\right)\right], \tag{12.78}$$

where J_0 is the dc current; τ, φ is the carrier photoconductive lifetime and added phase shift, and $\omega = 2\pi|\nu_2 - \nu_1|$, enabling modulated radiation at microwave or terahertz frequency ω as a result. If two photomixers are coupled together as a terahertz transceiver, photoconductive sampling in frequency domain enables narrow-linewidth homodyne detection to enhance resolution [12.224].

The frequency-domain coherent terahertz measurements are performed similarly to ones in time-domain (Fig. 12.45) by adding photomixing and synchronous-detection capabilities [12.225]. In the setting shown, a sufficiently broad emission of diode laser DL is enabled using its closely spaced wavelengths λ_{1-2} tuned via two resonators combining diffraction grating DG with mirrors M_1, M_2 [12.226]. Both selected wavelengths were focused on log-periodic terahertz antenna while monitoring the selections via optical spectrum analyzer SA with 0.5 nm resolution, supported by interferometer FP at 10 GHz free-spectral range and 50 MHz resolution. Modulator MD and silicon bolometer B cooled to 4 K with *Lock-in Amplifier* were used for studies of Sample terahertz transmission [12.226].

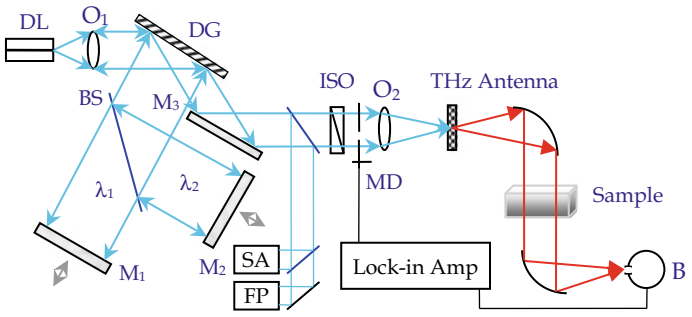

Fig. 12.45 Photomixing terahertz spectroscopy via dual-frequency laser

Multifrequency-heterodyning [12.170, 12.127] can be attained via terahertz frequency combs, one for terahertz light generated by a femtosecond laser inducing the photoconductive antenna, being time gated with a second comb lightly detuned from the original or both inducing optically rectified IR-THz beams enabling Fourier-transform spectroscopy of no moving parts (paragraph 12.1). Figure 12.46 schematically depicts the concept of multifrequency-comb heterodyning [12.228]. Two quantum-cascade lasers (QCL) integrated into low-dispersion cavities generating terahertz frequency combs via cavities-engineered nonlinearities were lens coupled and kept in enclosure 1 at 36K temperature. Each comb spectrum extended from ~250 GHz to 2.8 THz. Mirror *M* and beamsplitters BS were used to create Sample and Reference paths for balanced detectors 2, 3 – superconducting hot-electron bolometer and Schottky-mixer in signal and reference channels, respectively, with the latter being deployed to account for nonlinearities of the former. Since QCL lasers were operating in pulsed biasing modes to limit thermal constraints, phase and timing corrections were used to recover multiheterodyne lines from chirping instabilities [12.228].

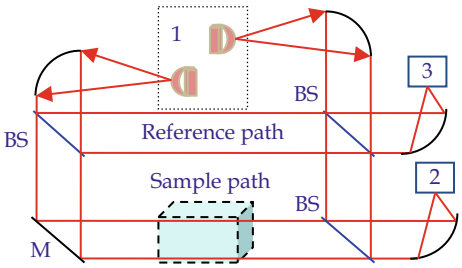

Fig. 12.46 Multifrequency-comb terahertz heterodyning

Unifying the time- and frequency-domain approaches, a single pulse electro-optic sampling can provide an instant alternative via terahertz frequency modulation of the probe pulse [12.229, 12.230]. When using a linearly-chirped optical probe a temporal waveform of the copropagating terahertz beam is encoded into the frequency spectrum of probe pulse and could be decoded by a spectrometer. A cross-coupled pair of diffraction gratings imaged by cylindrical lenses enabled frequency chirping of a probe beam to 20 ps and spatially resolving terahertz radiation in a CCD spectrometer with a 2100 lines/mm holographic grating while merging pump-probe pulses by a time-variable delay line [12.229]. For the single-pulse technique via a reflective stair-step echelon grating of 30-μm wide, 5-μm tall gold-coated steps, at 33-fs time delay between pulses and 17-ps time window, a 100-fs time resolution limited by 100-μm spatial resolution was reached [12.230].

References

Preface

0.1. P. Bouger, Traité d'Optique sur la Gradation de la Lumière, Académie Royale des Sciences, A. Paris, MDCCLX (1760)—see also: P. Bouger, Optical tractat on grading light, with commentaries by A.A. Gershun, translated from French to Russian by M.A. Tosltoy and P.P. Pheophilov under editorship of A.A. Gershun (Academy of Sciences of USSR, Leningrad, 1950)
0.2. J.H. Lambert, *Photometria sive de mensura et gradibus luminus, colorum et umbrae* (Klett, Augsburg, 1760)
0.3. A.J. Fresnel, *Oevres Complètes*, vol. 10 (Paris, 1866), pp. 640–648
0.4. C. Fabry, *Introduction Générale à la Photométrie, Editions de la revue d'optique théoretique et instrumentale* (Paris, 1927)
0.5. A.A. Gersun, *Svetovoe Pole* (GTTI, Moscow, 1936) (The Light Field, translated by P. Moon, G. Timoshenko, J. Math. Phys. **19**, 51, 1939)
0.6. J. Strong, *Procedures in Experimental Physics* (Prentice-Hall, Englewood Cliffs, 1942)
0.7. J.W.T. Walsh, *Photometry*, 3rd edn. (Constable, London, 1958; Dover, New York, 1965)
0.8. G. Bauer, *Strahlungsmessung im optichen Spektralbereich* (Vieeweg, Braunschweig, 1962) (Measurements of Optical Radiation, translated by K.S. Ankersmit, Focal Press, New York, 1965)
0.9. P.M. Tikhodeev, *Light Measurements (Photometria)* (Gosenergoizdat, Moscow, 1962)
0.10. A.A. Wolkenstein, *Visual Photometry of Low Luminance* (Energia, Moscow, 1965)
0.11. R.A. Sapoznikov, *Theoretical Photometry* (Energia, Moscow, 1967)
0.12. M.M. Gurevich, *Introduction to Photometry* (Energia, Leningrad, 1968; 2nd edn., 1983)
0.13. R.A. Smith, F.E. Jones, R.P. Chasmar, *The Detection and Measurement of Infrared Radiation*, 2nd edn. (Clarendon Press, Oxford, 1968)
0.14. H.A.A. Keitz, *Light Calculations and Measurements*, 2nd edn. (St. Martins Press, New York, 1971)
0.15. A. Stimson, *Photometry and Radiometry for Engineers* (Wiley, New York, 1974)
0.16. A.A. Wolkenstein, E.V. Kuvaldin, *Photoelectric Pulsed Photometry: Theory, Methods, and Instruments* (Mashinostroenie, Leningrad, 1975)
0.17. C.L. Wyatt, *Radiometric Calibration: Theory and Methods* (Academic Press, Orlando, 1978)
0.18. F. Grum, R.J. Becherer, *Optical Radiation Measurements, Radiometry*, vol. 1 (Academic Press, New York, 1979)

M. Bukshtab, *Photometry, Radiometry, and Measurements of Optical Losses*, Springer Series in Optical Sciences 209,
https://doi.org/10.1007/978-981-10-7745-6

0.19. A.F. Kotyuk (ed.), *Measurements of Energy Extents of Laser Radiation* (Radio-Sviaz, Moscow, 1981); A.F. Kotyuk, B.M. Stepanov (eds.), *Measurements of Spectral-Frequency and Correlation Parameters of Laser Radiation* (Radio-Sviaz, Moscow, 1982)
0.20. R.W. Boyd, *Radiometry and the Detection of Optical Radiation* (Wiley, New York, 1983)
0.21. M.A. Bukhshtab, *Measurements of Low Optical Losses* (Energoatomizdat, Leningrad, 1988)
0.22. F. Hengsberger (ed.), *Absolute Radiometry: Electrically Calibrated Thermal Detectors of Optical Radiation* (Academic Press, New York, 1989)
0.23. W.J. Smith, *Modern Optical Engineering*, 2nd edn. (McGraw-Hill, New York, 1990)
0.24. R. Frieden, *Probability, Statistical Optics and Data Testing: a Problem Solving Approach* (Springer, New York, 1991)
0.25. *Impulsnaya Photometria: Publications of Conferences for Pulsed Photometry and Radiometry*, vols. 1–9 (Mashinostroenie, Leningrad, 1969–1986)
0.26. A.T. Friberg (ed.), *Selected Papers on Coherence and Radiometry* (SPIE Optical Engineering Press, vol. MS 69, Bellingham, 1993)
0.27. H.P. Baltes (ed.), *Inverse Source Problems in Optics* (Springer, Berlin, New York, 1978)
0.28. Commission International de l'Éclairage, *The Basis of Physical Photometry*, 2nd edn., Publication No. 18.2 (Central Bureau of the CIE, Vienna, 1983)
0.29. C.L. Wyatt, *Radiometric System Design* (Macmillan, New York, 1987)
0.30. D.P. DeWitt, G.D. Nutter, *Theory and Practice of Radiation Thermometry* (Wiley, New York, 1988)
0.31. L.B. Wolff, S.A. Shafer, G.E. Healey (eds.), *Physics-Based Vision: Principles and Practice, Radiometry* (Jones and Bartlett, Boston, 1992)
0.32. W.R. McCluney, *Introduction to Radiometry and Photometry* (Artech House, Norwood, 1994)
0.33. M. Bass (ed.), *Handbook of Optics, Volume I: Fundamentals, Techniques, and Design; Volume II: Devices, Measurements, and Properties*, 22nd edn. (McGraw-Hill, New York, 1995)
0.34. E. Wolf (ed.), *Progress in Optics*, vol. XXXVI (Elsevier, Amsterdam, 1996)
0.35. E.L. Dereniak, G.D. Boreman, *Infrared Detectors and Systems* (Wiley, New York, 1996)
0.36. C. DeCusatis (ed.), *Handbook of Applied Photometry* (AIP Press, Woodbury, 1997)
0.37. W. L. Wolfe, *Introduction to Radiometry, Tutorials in Optical Engineering*, vol. TT29 (SPIE, 1998)
0.38. K.J. Gasvic, *Optical Metrology*, 3rd edn. (Wiley, New York, 2002)
0.39. G.H. Rieke, *Detection of Light: From the Ultraviolet to the Submillimeter* (Cambridge University Press, Cambridge, 1994; 2nd edn., 2003)
0.40. A.C. Parr, R.U. Datla, J.L. Gardner (eds.), *Optical Radiometry: Experimental Methods in the Physical Sciences* (Academic Press, San Diego, 2005)
0.41. A. Valberg, *Light Vision Color* (Wiley, Chichester, 2005)
0.42. R.G.W. Brown, J.P. Dakin (eds.), *Handbook of Optoelectronics* (Taylor & Francis, Abingdon, 2006)
0.43. H. Gross (ed.), *Handbook of Optical Systems, Volume 1*, *Fundamentals of Technical Optics* (Wiley, New York, 2005); H. Gross, F. Blechinger, B. Achtner (ed.), *Handbook of Optical Systems, Volume 4, Survey of Optical Instruments* (Wiley, New York, 2008)
0.44. J. Laane (ed.), *Frontiers of Molecular Spectroscopy* (Amsterdam, 2008)
0.45. J.M. Palmer, B.G. Grant, *The Art of Radiometry* (SPIE Press, Bellingham, 2009)
0.46. E. Hecht, *Optics*, 5th edn. (Pearson, London, 2016)
0.47. W. Demtröder, *Laser Spectroscopy 1, Basic Principles*, 4th edn. (Springer, Berlin, Heidelberg, 2014)

0.48. W.J. Smith, *Modern Optical Engineering, The Design of Optical Systems* (McGraw-Hill, New York, 2000)
0.49. A.V. Arecchi, T. Messadi, R.J. Koshel, *Field Guide to Illumination* (SPIE Press, Bellingham, 2007)
0.50. M. Bukshtab, *Applied Photometry, Radiometry, and Measurements of Optical Losses*, 1st edn. (Springer, Dordrecht, 2012)

Chapter 1

1.1. M. Born, E. Wolf, *Principles of Optics: Electromagnetic Theory of Propagation, Interference and Diffraction of Light*, 6th edn. (Pergamon, Oxford, 1984; 7th edn., Cambridge University Press, Cambridge, 2003)
1.2. G.V. Rosenberg, The light ray: contribution to the theory of the light field. Sov. Phys. Usp. **20**(1), 55–79 (1977)
1.3. A. Sommerfeld, *Optics* (Academic Press, New York, 1954)
1.4. A.A. Gershun, *Publications on Photometry and Light Measurements: Selected Papers on Photometry and Illumination Engineering* (Gostekhizdat, Moscow, 1958)
1.5. Principles of Light Measurements, CIE Publication No. 18, 1970; International Lighting Vocabulary, CIE Publication No. 17, 1970; International Electrotechnical Vocabulary, Chapter 845, Lightning, 1982
1.6. R.W. Ditchburn, *Light* (Wiley, New York, 1963)
1.7. F.A. Jenkins, H.E. White, *Fundamentals of Optics*, 4th edn. (McGraw-Hill, New York, 1976)
1.8. G.S. Landsberg, *Optics* (Nauka, Moscow, 1976)
1.9. G.G. Stokes, On the intensity of the light reflected from and transmitted through a pile of plates. Proc. R. Soc. Lond. **11**, 545–556 (1862)
1.10. Lord Rayleigh, On the reflection of light from regularly stratified medium. Proc. R. Soc. A. **93**, 565–577 (1917)
1.11. T. Smith, The treatment of reflection as a special case of refraction. Trans. Opt. Soc. **27**, 312–323 (1925)
1.12. M. Gurevich, Über eine Rationelle Klassifikation der Lichtenstreuenden Medien. Phys. Z **31**, 753 (1930)
1.13. F. Benford, Radiation in a diffusing medium. J. Opt. Soc. Am. **36**(9), 524–554 (1946)
1.14. L.B. Tuckerman, On the intensity of the light reflected from or transmitted through a pile of plates. J. Opt. Soc. Am. **37**(10), 818–825 (1947)
1.15. P. Kubelka, New contributions to the optics of intensely light scattering materials. Part 1, J. Opt. Soc. Am. **38**(5), 448–457 (1948); errata **38**, 1067
1.16. F. Abelés, Recherches sur la propagation des ondes électromagn'etiques sinusoïdales dans les milieux stratifiés. Applications aux couches minces, Ann. Phys. (Paris) **5**, 596–640 (1950)
1.17. A.F. Huxley, A theoretical treatment of the reflexion of light by multilayer structures. J. Exp. Biol. **48**, 227–245 (1968)
1.18. H.G. Olf, Stokes's pile of plates revisited. J. Opt. Soc. Am. A **5**(10), 1620–1625 (1988)
1.19. A. Perot, C. Fabry, Méthode interfirentielle pour la mesure des longeurs d'onde dans le spectre solaire. C. R. Acad. Sci. **131**, 700 (1900)
1.20. A. Kastler, Atomes a I'Interieur d'un Interferometre Perot-Fabry. Appl. Opt. **1**(1), 17–24 (1962)
1.21. F. Gires, P. Tournois, Interféromètre utilisable pour la compression d'impulsions lumineuses modulées en fréquence. C. R. Acad. Sci. **258**(6), 6112–6115 (1964)

1.22. F.E. Nicodemus, Directional reflectance and emissivity of an opaque surface. Appl. Opt. **4**(7), 767–773 (1965)
1.23. R.C. Jones, Terminology in photometry and radiometry. J. Opt. Soc. Am. **53**(11), 1314–1315 (1963)
1.24. D.B. Judd, Terms, definitions, and symbols in reflectometry. J. Opt. Soc. Am. **57**(4), 445–452 (1967)
1.25. W.H. Steel, Luminosity, throughput, or etendue? Appl. Opt. **13**(4), 704–705 (1974)

Chapter 2

2.1. H.G. Heard, *Laser Parameter Measurements Handbook* (Wiley, New York, 1968)
2.2. S.R. Gunn, Calorimetric measurements of laser energy and power. J. Phys. E **6**(2), 105–113 (1973)
2.3. R. Ulbricht, Die Bestimmung der mittleren räumlichen Lichtintensität durch nur eine Messung. Electrotech. Z. **21**, 595–597 (1900)
2.4. A.C. Hardy, O.W. Pineo, The errors due to the finite size of holes and sample in integrating spheres. J. Opt. Soc. Am. **21**(8), 504–506 (1931)
2.5. F. Rotter, View into the integrating sphere through the observation window. Appl. Opt. **10**(12), 2629–2638 (1971)
2.6. Y. Ohno, Integrating sphere simulation: application to total flux scale realization. Appl. Opt. **33**(13), 2637–2647 (1994)
2.7. Y. Ohno, Realization of NIST luminous flux scale using an integrating sphere with an external source, in *Proceedings of the 23nd Session of CIE (Commission Internationale de l'Éclairage)*, vol. 1, No. 1, Division 2, 1995, pp. 87–90
2.8. M.A. Bukhshtab, Method of determination of small scattering coefficients. J. Appl. Spectrosc. **46**(5), 523–528 (1987)
2.9. A.A. Wolkenstein, D.I. Andreev, B.I. Isaenko, Optical method of determining the light intensity, radiance and luminous flux. J. Tech. Phys. **22**(12), 2026–2037 (1952)
2.10. D. Beaglehole, A sensitive single beam device for continuous reflectance or transmittance measurements. Appl. Opt. **7**(11), 2218–2220 (1968)
2.11. G.E. Pride, A reflectance measuring attachment for the Beckman spectrophotometer. J. Opt. Soc. Am. **36**(9), 510–512 (1946)
2.12. R.F. Weeks, Simple wide range specular reflectometer. J. Opt. Soc. Am. **48**(11), 775–777 (1958)
2.13. J.E. Shaw, W.R. Blevin, Instrument for the absolute measurement of direct spectral reflectances at normal incidence. J. Opt. Soc. Am. **54**(3), 334–336 (1964)
2.14. J.T. Gier, R.V. Dunkle, J.T. Bevans, Measurement of absolute spectral reflectivity from 1.0 to 15 microns. J. Opt. Soc. Am. **44**(7), 558–562 (1954)
2.15. J.S. Preston, G.W. Gordon-Smith, A new determination of luminance factor of magnesium oxide. Proc. Phys. Soc. B **65**, 76 (1952)
2.16. J.C. Maxwell, On the theory of compound colours, and the relations of the colours of the spectrum. Proc. R. Soc. Lond. **10**, 404–409 (1859–1860)
2.17. H.E. Eves, A proposed standard method of colorimetry. J. Opt. Soc. Am. **5**(6), 469–478 (1921)
2.18. L.T. Troland, Report of committee on colorimetry for 1920–1921. J. Opt. Soc. Am. **6**(8), 527–596 (1922)
2.19. I.G. Priest, The computation of colorimetric purity. Part I, J. Opt. Soc. Am. **9**(5), 503–520 (1924); Part II, J. Opt. Soc. Am. **13**(2), 123–132 (1926)
2.20. D.B. Judd, A general formula for the computation of colorimetric purity. J. Opt. Soc. Am. **21**(11), 729–750 (1931)

2.21. D.B. Judd, Chromaticity sensitivity to stimulus differences. J. Opt. Soc. Am. **22**(2), 72–108 (1932)
2.22. D.B. Judd, The 1931 I. C. I. Standard observer and coordinate system for colorimetry. J. Opt. Soc. Am. **23**(10), 359–374 (1933)
2.23. A.C. Hardy, Method of and apparatus for comparing and recording of radian energy. U.S. Patent 1,806,198; 19 May 1931
2.24. E.Q. Adams, X-Z planes in the 1931 I. C. I. System of colorimetry. J. Opt. Soc. Am. **32**(3), 168–173 (1942)
2.25. R.S. Hunter, Photoelectric tristimulus colorimetry with three filters. J. Opt. Soc. Am. **32**(9), 509–538 (1942)
2.26. Committee on colorimetry: quantitative data and methods for colorimetry. J. Opt. Soc. Am. **44**(11), 633–688 (1944)
2.27. T. Young, *Lectures on Natural Philosophy*, vol. 2 (Johnson, London, 1807)
2.28. V.C. Smith, J. Pokorny, Spectral sensitivity of the foveal cone photopigments between 400 and 500 nm. Vis. Res. **15**, 161–171 (1975)
2.29. R.M. Boynton, Theory of color vision. J. Opt. Soc. Am. **50**(10), 929–944 (1960)
2.30. R.M. Boynton, *Human Color Vision, Holt* (Rinehart & Winston, New York, 1979)
2.31. R.M. Boynton, History and current status of a physiologically based system of photometry and colorimetry. J. Opt. Soc. Am. A **13**(8), 1609–1621 (1996)
2.32. G. Golz, D.I.A. MacLeod, Colorimetry for CRT displays. J. Opt. Soc. Am. A **20**(5), 769–781 (2003)
2.33. CIE Technical Report 15:2004, Colorimetry, 3rd edn. (Vienna, 2004)
2.34. D.B. Judd, G. Wyszecki, *Color in Business, Science, and Industry*, 3rd edn. (Wiley, New York, 1975)
2.35. G. Wyszecki, W. Stiles, *Color Science: Concepts and Methods, Quantitative Data and Formulae*, 2nd edn. (Wiley, New York, 2000)
2.36. D. Malacara, *Color Vision and Colorimetry: Theory and Applications* (SPIE, 2004)
2.37. A.R. Robertson, W.D. Wright, International comparison of working standards for colorimetry. J. Opt. Soc. Am. **55**(6), 694–706 (1965)
2.38. J.S. Christie, G. McConnell, A new flexible spectrophotometer for color measurements, in *"Color 77", the Third Congress of the International Colour Association*, ed. by F.W. Billmeyer, G. Wyszecki (1978); paper A38, p. 309
2.39. J. Campos, A. Pons, A. Corrons, Description of a precision colorimeter. J. Phys. E. **20**, 882–884 (1987)
2.40. I. Nimeroff, Propagation of errors in spectrophotometric colorimetry. J. Opt. Soc. Am. **43**(6), 531–533 (1953); Propagation of errors in tristimulus colorimetry. J. Opt. Soc. Am. **47**(8), 697–702 (1957)
2.41. L.D. Taylor, D. Slocum, Method and spectrophotometer for exchanging color measurement and diagnostic information over a network, US Patent Appl. No. 2004/0233429 A1, 25 Nov 2004
2.42. Y. Ohno, J. Hardis, Four-color matrix method for correction of tristimulus colorimeters, Parts 1, 2, in *Proceedings of 5*th*, 6th IS&T Color Imaging Conferences* (1997), pp. 301–305; (1998), pp. 65–68
2.43. G. Eppeldauer, Spectral response based calibration method of tristimulus colorimeters. J. Res. Natl. Inst. Stand. Technol. **103**(6), 615–619 (1998)
2.44. Y. Ohno, CIE fundamentals for color measurements, in *IS&T NIP16 Conference*, Vancouver, 2000
2.45. M.A. Bukshtab, Concept of absolute color measurements and absolute color spectrophotometry, 2007
2.46. A.H. Taylor, The measurement of the diffuse reflection factors and a new absolute reflectometer. J. Opt. Soc. Am. **4**(1), 9–23 (1920)
2.47. C.H. Sharp, W.F. Little, Measurements of reflection factors. Trans. Illum. Eng. Soc. **15**(9), 802 (1920)

2.48. E. Karrer, The use of the Ulbricht sphere in measuring reflection and transmission. J. Opt. Soc. Am. **5**(1), 96–120 (1921)
2.49. J.A. Jacquez, H.F. Kuppenheim, Theory of integrating sphere. J. Opt. Soc. Am. **45**(6), 460–470 (1955)
2.50. B.J. Hisdal, *Reflectance of perfect diffuse and specular samples in the integrating sphere*. J. Opt. Soc. Am. **55**(9), 1122–1128 (1965); Reflectance of nonperfect surfaces in the integrating sphere. J. Opt. Soc. Am. **55**(10), 1155–1160 (1965)
2.51. D.G. Goebel, Generalized integrating-sphere theory. Appl. Opt. **6**(1), 125–128 (1967)
2.52. M.W. Finkel, Integrating sphere theory. Opt. Commun. **2**(2), 25–28 (1970)
2.53. H.L. Tardy, Flat-sample and limited-field effects in integrating sphere measurements. J. Opt. Soc. Am. A **5**(2), 241–245 (1988)
2.54. H.L. Tardy, Matrix method for integrating-sphere calculations. J. Opt. Soc. Am. A **8**(9), 1411–1418 (1991)
2.55. M.A. Bukshtab, Measurement techniques for high reflectance and low scattering of laser mirrors, Ph.D. Dissertation, The Vavilov' State Optical Institute, Leningrad, 1983
2.56. Absolute methods for reflection measurements, CIE Publication TC-2.3, 1979, No. 44
2.57. D.K. Edwards, J.T. Gier, K.E. Nelson, B.D. Roddick, Integrating sphere for imperfectly diffuse samples. J. Opt. Soc. Am. **51**(11), 1279–1285 (1961)
2.58. V.P. Rvachev, M.Yu. Sakhnovskii, Theory and application of an integrating photometer for the study of objects with arbitrary scattering functions. Opt. Spectrosc. **18**(3), 274–278 (1965)
2.59. P.F. O'Brien, Network representation of the integrating sphere. J. Opt. Soc. Am. **45**(5), 343–345 (1956)
2.60. M.A. Bukhshtab, Improving the accuracy of absolute measurements in photometric sphere. Opt. Spectrosc. **54**(1), 90–93 (1983)
2.61. M.A. Bukshtab, Spectrally-nonselective method of absolute reflectance measurements, in *Impulsnaya Photometria*, vol. 7 (Mashinostroenie, Leningrad, 1981), pp. 22–24
2.62. M.A. Bukhshtab, G.M. Gorodinskii, Photometric sphere having constant ray paths. J. Opt. Technol. **49**(6), 396–397 (1982)
2.63. J.G. Symons, E.A. Christie, M.K. Peck, Integrating sphere for solar transmittance measurement of planar and nonplanar samples. Appl. Opt. **21**(15), 2827–2832 (1982)
2.64. J. Kessel, Transmittance measurements in the integrating sphere. Appl. Opt. **25**(16), 2752–2756 (1986)
2.65. A. Roos, C.G. Ribbing, Interpretation of integrating sphere signal output for non-Lambertian samples. Appl. Opt. **27**(18), 3833–3837 (1988)
2.66. A. Roos, Interpretation of integrating sphere signal output for nonideal transmitting samples. Appl. Opt. **30**(4), 468–474 (1991)
2.67. K. Grandin, A. Roos, Evaluation of correction factors for transmittance measurements in single beam integrating spheres. Appl. Opt. **33**(25), 6098–6104 (1994)
2.68. J.W. Pickering, C.J.M. Moes, H.J.C. Sterenborg, S.A. Prahl, M.J.C. van Gemert, Two integrating spheres with an intervening scattering sample. J. Opt. Soc. Am. A **9**(4), 621–631 (1992)
2.69. J.W. Pickering, S.A. Prahl, N. van Wieringen, J.F. Beek, H.J.C.M. Sterenborg, M.J.C. van Gemert, Double-integrating-sphere system for measuring of optical properties of tissue. Appl. Opt. **32**(4), 399–410 (1993)
2.70. A.H. Taylor, Errors in reflectometry. J. Opt. Soc. Am. **25**(2), 51–52 (1935)
2.71. H. Olson, D.A. Pontarelli, Asymmetry of an integrating sphere. Appl. Opt. **3**(6), 631–633 (1963)
2.72. W. Budde, Integrating sphere for the photometry of the sky. Appl. Opt. **3**(8), 939–941 (1964)
2.73. F.J.J. Clarke, J.A. Compton, Correction methods for integrating sphere measurement of hemispherical reflectance. Color Res. Appl. **11**(4), 253–262 (1986)

2.74. A. Roos, C.G. Ribbing, M. Bergkvist, Anomalies in integrating sphere measurements on structured samples. Appl. Opt. **27**(18), 3828–3832 (1988)
2.75. C.C. Habeger, Angular radiance variation in an integrating sphere. J. Opt. Soc. Am. A **11**(7), 2130–2136 (1994)
2.76. L. Levi, A screenless integrating sphere. Appl. Opt. **6**(6), 1138 (1967)
2.77. H.L. Tardy, Flux concentrators in integrating sphere experiments: potential for increased detector signal. Appl. Opt. **24**(22), 3914–3916 (1985)
2.78. K.A. Snail, L.M. Hanssen, Integrating sphere designs with isotropic throughput. Appl. Opt. **28**(10), 1793–1799 (1989)
2.79. D.B. Chenault, K.A. Snail, L.M. Hanssen, Improved integrating-sphere throughput with a lens and nonimaging concentrator. Appl. Opt. **34**(34), 7959–7964 (1995)
2.80. L.M. Hanssen, Effects of restricting the detector field of view when using integrating spheres. Appl. Opt. **28**(11), 2097–2103 (1989)
2.81. L.M. Hanssen, Effects of non-Lambertian surfaces on integrating sphere measurements. Appl. Opt. **35**(19), 3597–3606 (1996)
2.82. J.E. Clare, Comparison of four analytic methods for the calculation of irradiance in integrating spheres. J. Opt. Soc. Am. A **15**(12), 3086–3096 (1998)
2.83. B.G. Crowther, Computer modeling of integrating spheres. Appl. Opt. **35**(30), 5880–5886 (1996)
2.84. M. Szylowski, M. Mossman, D. Barclay, L. Whitehead, Novel fiber-based integrating sphere for luminous flux measurements. Rev. Sci. Instrum. **77**, Article 063102 (2006)
2.85. B. Rizk, Private life of an integrating sphere: the radiant homogeneity of the descent imager-spectral radiometer calibration sphere. Appl. Opt. **45**(13), 2095–2101 (2001)
2.86. A.V. Prokhorov, S.N. Mekhontsev, L. Hanssen, Monte Carlo modeling of an integrating sphere reflectometer. Appl. Opt. **42**(19), 3832–3842 (2003)
2.87. D. Hidović-Rowe, J.E. Rowe, M. Lualdi, Markov models of integrating spheres for hyperspectral imaging. Appl. Opt. **45**(21), 5248–5256 (2006)
2.88. C.K. Gatebe, J.J. Butler, J.W. Cooper, M. Kowalewski, M.D. King, Characterization of errors in the use of integrating-sphere systems in the calibration of scanning radiometers. Appl. Opt. **46**(31), 7640–7651 (2007)
2.89. R.L. Lucke, Lambertian radiance and transmission of an integrating sphere. Appl. Opt. **46**(28), 6966–6970 (2007)
2.90. S. Potvin, J. Genest, Reducing the effect of integrating sphere speckle when characterizing the instrument line shape of a Fourier-transform hyperspectral imager. Appl. Opt. **48**(30), 5849–5852 (2009)
2.91. R.L. Lucke, J. Grun, C. Manka, S. Nikitin, Specular integrating tube for scattered-light spectroscopy. Appl. Opt. **49**(21), 4063–4066 (2010)
2.92. S. Park, S.-N. Park, D.-H. Lee, Correction of self-screening effect in integrating sphere-based measurement of total luminous flux of large-area surface-emitting light sources. Appl. Opt. **49**(20), 3831–3839 (2010)
2.93. R. Daniel, R. Almog, Y. Sverdlov, S. Yagurkroll, S. Belkin, Y. Shacham-Diamand, Development of a quantitative optical biochip based on a double integrating sphere system that determines absolute photon number in bioluminescent solution: application to quantum yield scale realization. Appl. Opt. **48**(17), 3216–3224 (2009)
2.94. A.M. Nilsson, A. Jonsson, J.C. Jonsson, A. Roos, Method for more accurate transmittance measurements of low-angle scattering samples using an integrating sphere with an entry port beam diffuser. Appl. Opt. **50**(7), 999–1006 (2011)
2.95. P. Lemaillet, J.-P. Bouchard, D.W. Allen, Development of traceable measurement of the diffuse optical properties of solid reference standards for biomedical optics at National Institute of Standards and Technology. Appl. Opt. **54**(19), 6118–6127 (2015)
2.96. K. Agatsuma, D. Friedrich, S. Ballmer, G. DeSalvo, S. Sakata, E. Nishida, S. Kawamura, Precise measurement of laser power using an optomechanical system. Opt. Express **22**(2), 2013–2030 (2014)

2.97. S.K. Yang, J. Lee, S.-W. Kim, H.-Y. Lee, J.-A. Jeon, I.H. Park, J.-R. Yoon, Y.-S. Baek, Precision measurement of the photon detection efficiency of silicon photomultipliers using two integrating spheres. Opt. Express **22**(1), 716–726 (2014)
2.98. S. Bellini, R. Bendoula, E. Latrille, J.-M. Rogera, Potential of a spectroscopic measurement method using adding–doubling to retrieve the bulk optical properties of dense microalgal media. Appl. Spectrosc. **68**(10), 1154–1167 (2014)
2.99. N.P. Belov, V.N. Grisimov, P.V. Odnovorchenko, A.S. Sherstobitova, A.D. Yas'kov, Irradiance distribution in an integrating sphere with an internal screen. J. Opt. Technol. **83**(10), 610–612 (2016)

Chapter 3

3.1. E. Wolf, Coherence and radiometry. J. Opt. Soc. Am. **68**(1), 7–17 (1978)
3.2. E. Wolf, *Introduction to the theory of coherence and polarization of light* (Cambridge University Press, Cambridge, 2007)
3.3. M.J. Beran, G.B. Parrent Jr., *Theory of Partial Coherence* (Society of Photo-Optical Instrumentation Engineers, Bellingham, 1974)
3.4. L. Mandel, E. Wolf, Spectral coherence and the concept of cross-spectral purity. J. Opt. Soc. Am. **66**(6), 529–535 (1976)
3.5. E. Collett, E. Wolf, Is complete spatial coherence necessary for the generation of highly directional light beams? Opt. Lett. **2**(2), 27–29 (1978)
3.6. A. Walther, Radiometry and coherence. J. Opt. Soc. Am. part 1 **57**(9), 1256–1259 (1967); part 2 **63**(12), 1622–1623 (1973)
3.7. M.J. Bastiaans, Transport equation for the Wigner distribution function in an inhomogeneous dispersive medium. Opt. Acta **26**(11), 1333–1344 (1979)
3.8. L.A. Apresyan, Yu.A. Kravtsov, Photometry and coherence: wave aspects of the theory of radiation transport. Sov. Phys. Usp. **27**(4), 301–313 (1984)
3.9. L. Mandel, E. Wolf, Coherence properties of fields. Rev. Mod. Opt. **37**(4), 231–287 (1965)
3.10. E. Wolf, New theory of radiative energy transfer in free electromagnetic fields. Phys. Rev. D **13**(4), 869–886 (1976)
3.11. E.W. Marchand, E. Wolf, Radiometry with sources of any state of coherence. J. Opt. Soc. Am. **64**(9), 1219–1226 (1974)
3.12. A.T. Friberg, Effects of coherence in radiometry. Opt. Eng. **21**(6), 927–936 (1982); A.T. Friberg, T. Setala, Electromagnetic theory of optical coherence. J. Opt. Soc. Am. A **33**(12), 2431–2442 (2016)
3.13. E. Wolf, New theory of partial coherence in the space-frequency domain. Part I: spectra and cross spectra of steady-state sources. J. Opt. Soc. Am. **72**(3), 343–344 (1982); Part II: Steady-state fields and higher-order correlations. J. Opt. Soc. Am. A **3**(1), 76–85 (1986)
3.14. W.H. Carter, E. Wolf, Coherence properties of Lambertian and non-Lambertian sources. J. Opt. Soc. Am. **65**(9), 1067–1071 (1975)
3.15. W.H. Carter, E. Wolf, Coherence and radiometry with quasi-homogeneous planar sources. J. Opt. Soc. Am. **67**(6), 785–796 (1977)
3.16. R.G. Littlejohn, R. Winston, Correction to classical radiometry. J. Opt. Soc. Am. A **10**(9), 2024–2037 (1993)
3.17. E. Wolf, Radiometric model for propagation of coherence. Opt. Lett. **19**(23), 2024–2026 (1994)
3.18. L. Mandel, E. Wolf, *Optical Coherence and Quantum Optics* (Cambridge University Press, New York, 1995)
3.19. K. Yoshimori, K. Itoh, Interferometry and radiometry. J. Opt. Soc. Am. A **14**(12), 3379–3387 (1997)

3.20. K. Yoshimori, K. Itoh, On the generalized radiance function for a polychromatic field. J. Opt. Soc. Am. A **15**(10), 2786–2787 (1998)
3.21. K. Yoshimori, Radiometry and coherence in a nonstationary optical field. J. Opt. Soc. Am. A **15**(10), 2730–2734 (1998)
3.22. M.A. Alonso, Radiometry and wide-angle wave fields. J. Opt. Soc. Am. A: I. Coherent fields in two dimensions **18**(4), 902–909 (2001); II. Coherent fields in three dimensions **18**(4), 910–918 (2001); III. Partial coherence **18**(10), 2502–2511 (2001)
3.23. J. Turunen, Space-time coherence of polychromatic propagation-invariant fields. Opt. Express **16**(25), 20283–20294 (2008)
3.24. O.V. Angelsky, S.B. Yermolenko, C.Yu. Zenkova, A.O. Angelskaya, Polarization manifestations of correlation (intrinsic coherence) of optical fields. Appl. Opt. **47**(29), 5492–5499 (2008)
3.25. D.G. Fischer, S.A. Prahl, D.D. Duncan, Monte Carlo modeling of spatial coherence: free-space diffraction. J. Opt. Soc. Am. A **25**(10), 2571–2581 (2008)
3.26. M. Abramowitz, I.A. Stegun, *Handbook of Mathematical Functions* (Dover, New York, 1965)
3.27. D.C. O'Shea, W.R. Callen, W.T. Rhodes, *Introduction to Lasers and their Application* (Addison-Wesley, London, 1976)
3.28. J. Perina, *Coherence of Light*, 2nd edn. (Reidel Publishing Co., Dordrecht, 1985)
3.29. A.A. Sychev, Study of spectral emittance of solid-state lasers, in *Proceedings FIAN*, Nauka, Moscow, 1975, vol. 84, pp. 3–61
3.30. S.W. Director, R.A. Rohrer, *Introduction to Systems Theory* (McGraw-Hill, New York, 1971)
3.31. I.S. Marshak (ed.), *Pulsed Sources of Light* (Energia, Moscow, 1978)
3.32. A. Yariv, *Quantum Electronics*, 3rd edn. (Wiley, New York, 1989)
3.33. M.I. Gryaznov, Generalized parameters of pulsed radiation, in *Impulsnaya Photometria*, vol. 6 (Mashinostroenie, Leningrad, 1979), pp. 35–41
3.34. J.W. Goodman, *Statistical Optics* (Wiley, New York, 1985)
3.35. M.A. Bukhshtab, Restricting the interference noise in optical measuring systems. J. Opt. Technol. **49**(11), 677–678 (1982)
3.36. V.K. Nikolaev, Yu.V. Khimichev, *About Interference Losses in Transparent Dielectric Plates*, vol. 10 (Electronic Techniques (UKS), Moscow, 1972), pp. 78–82
3.37. M.A. Bukshtab, A.A. Wolkenstein, Interference errors of measurements using laser and pulsed quasi-monochromatic radiation and methods of their limitation, in *Impulsnaya Photometria*, vol. 8 (Mashinostroenie, Leningrad, 1984), pp. 5–15
3.38. D.R. Hall, P.E. Jackson (eds.), *The physics and technology of laser resonators* (IOP Publishing (Adam Hilger), Bristol, New York, 1989)
3.39. M.A. Bukshtab, Effects of spectral irregularities of radiation emitted by pulsed lamps in high-speed spectroradiometry, in *Impulsnaya Photometria*, vol. 9 (Mashinostroenie, Leningrad, 1986), pp. 77–84
3.40. J.G. Edwards, Some factors affecting the pumping efficiency of optically pumped lasers. Appl. Opt. **6**(5), 837–843 (1967)
3.41. A. Holmes, Exact theory of retardation plates. J. Opt. Soc. Am. **54**(9), 1115–1120 (1964)
3.42. N.G. Theofanous, A.T. Arapoyianni, Effect of multiple reflections on retardation-based electro-optic measurements. J. Opt. Soc. Am. A **8**(11), 1746–1754 (1991)
3.43. M. Bukhshtab, The influence of surface reflections on computation and measurement of retardance. Meas. Sci. Technol. **6**(7), 910–920 (1995); erratum: **7**, 1093 (1996)
3.44. E.D. Palik (ed.), *Handbook of Optical Constants of Solids*, vol. 1 (Academic Press, New York, 1985)
3.45. M.A. Bukhshtab, G.J. Mizell, Phase retardance and optical extinction symmetry measurements for some birefringent materials, in *Proceedings of SPIE*, vol. 1994, paper No. 12, 1993

3.46. E. Lommel, Die Beugungserscheinungen einer kreisrunden Oeffnung und eines kreisrunden Schirmschens theoretisch und experimentell Bearbeitet. Abh. Bayer. Akad. **15**, 233–328 (1885)
3.47. E. Wolf, Light distribution near focus in an error-free diffraction image, in *Proceedings of the Royal Society of London. Series A,* vol. 204, pp. 533–548, 1951
3.48. J. Focke, Total illumination in an aberration-free diffraction image. Opt. Acta **3**, 161–163 (1956)
3.49. E.W. Marchand, E. Wolf, Boundary diffraction wave in the domain of the Rayleigh-Kirchoff diffraction theory. J. Opt. Soc. Am. **52**(7), 761–767 (1962)
3.50. W.R. Blevin, Diffraction losses in radiometry and photometry. Metrologia **6**(4), 39–44 (1970)
3.51. W.H. Steel, M. De, J.A. Bell, Diffraction corrections in radiometry. J. Opt. Soc. Am. **62**(9), 1099–1103 (1972)
3.52. L.P. Boivin, Diffraction corrections in radiometry: comparison of two different methods of calculation. Appl. Opt. **14**(8), 2002–2009 (1975)
3.53. L.P. Boivin, Diffraction corrections in the radiometry of extended sources. Appl. Opt. **15**(5), 1204–1209 (1976)
3.54. L.P. Boivin, Radiometric errors caused by diffraction from circular apertures: edge effects. Appl. Opt. **16**(2), 377–384 (1976)
3.55. L.P. Boivin, Reduction of diffraction errors in radiometry by means of toothed apertures. Appl. Opt. **17**(20), 3323–3328 (1978)
3.56. E.L. Shirley, R.U. Datla, Optimally toothed apertures for reduced diffraction. J. Res. Natl. Inst. Stand. Technol. **101**(6), 745–753 (1996)
3.57. T. Gravelsaeter, J.J. Stamnes, Diffraction by circular apertures. 1: method of linear phase and amplitude approximation. Appl. Opt. **21**(20), 3644–3651 (1982)
3.58. D.J. Butler, R. Kohler, G.W. Forbes, Diffraction effects in the radiometry of coherent beams. Appl. Opt. **35**(13), 2162–2166 (1996)
3.59. E.L. Shirley, Revised formulas for diffraction effects with point and extended sources. Appl. Opt. **37**(28), 6581–6590 (1998)
3.60. P. Edwards, M. McCall, Diffraction loss in radiometry. Appl. Opt. **42**(25), 5024–5032 (2003)
3.61. E.L. Shirley, Diffraction effects on broadband radiation: formulation for computing total irradiance. Appl. Opt. **43**(13), 2609–2620 (2004)
3.62. E.L. Shirley, Diffraction corrections in radiometry: spectral and total power and asymptotic properties. J. Opt. Soc. Am. A **21**(10), 1895–1906 (2004)
3.63. S. Engman, P. Lindblom, Blaze characteristics of echelle gratings. Appl. Opt. **21**(23), 4356–4362 (1982)
3.64. J. Harvey, E. Nevis, Angular grating anomalies: effects of finite beam size on wide-angle diffraction phenomena. Appl. Opt. **31**(31), 6783–6788 (1992)
3.65. M. Rousseau, J. Mathieu, *Problems in Optics*, translated by J. Blaker (Pergamon Press, New York, 1973) pp. 178–183
3.66. M.G. Moharam, T.K. Gaylord, Diffraction analysis of dielectric surface-relief gratings. J. Opt. Soc. Am. **72**(10), 1385–1392 (1982); T.K Gaylord, M.G. Moharam, Analysis and applications of optical diffraction by gratings. Proc. IEEE. **73**(5), 894–937 (1985)
3.67. S.M. Al-Marzoug, R.J.W. Hodgson, Optimization of multilayer mirrors at 13.4-nm with more than two materials. Appl. Opt. **47**(12), 2155–2160 (2008)
3.68. D.M. Pai, K.A. Awada, Analysis of dielectric gratings of arbitrary profiles and thicknesses. Opt. Soc. Am. A **8**(5), 755–762 (1991)
3.69. T. Delort, D. Maystre, Finite-element method for gratings. J. Opt. Soc. Am. A **10**(12), 2592–2601 (1993)
3.70. M.A. Alonso, Exact description of free electromagnetic wave fields in terms of rays. Opt. Express **11**(23), 3128–3135 (2003)

3.71. J.-F. Lepage, N. McCarthy, Analysis of the diffractional properties of dual-period apodizing gratings: theoretical and experimental results. Appl. Opt. **43**(17), 3504–3512 (2004)
3.72. O. Mata-Mendez, J. Avendaño, F. Chavez-Rivas, Rigorous theory of the diffraction of Gaussian beams by finite gratings: TM polarization. J. Opt. Soc. Am. A **23**(8), 1889–1896 (2006)
3.73. D.C. Skigin, R.A. Depine, Diffraction by dual-period gratings. Appl. Opt. **46**(9), 1385–1391 (2007)
3.74. R. Tharaldsen, *Rigorous Coupled-Wave Analysis* (2008)
3.75. M.A. Bukshtab, Maxima-shifting anomaly for step-function diffraction gratings in reflected light (2008)
3.76. H. Kogelnick, Coupled wave theory for thick hologram gratings. Bell. Syst. Tech. J. **48**, 2909–2947 (1969)
3.77. C.B. Burcardt, Diffraction of a plane wave at a sinusoidally stratified dielectric grating. J. Opt. Soc. Am. **56**(11), 1502–1509 (1966)
3.78. C.B. Burcardt, Efficiency of a dielectric grating. J. Opt. Soc. Am. **57**(5), 601–603 (1967)
3.79. F.G. Kaspar, Diffraction by thick, periodically stratified gratings with complex dielectric constant. J. Opt. Soc. Am. **63**(1), 37–45 (1973)
3.80. K. Knop, Rigorous diffraction theory for transmission phase gratings with deep rectangular grooves. J. Opt. Soc. Am. **68**(9), 1206–1210 (1978)
3.81. K. Knop, Diffraction gratings for color filtering in the zero diffraction order. Appl. Opt. **17**(22), 3598–3603 (1978)
3.82. D.-K. Woo, K. Hane, S.-K. Lee, High order diffraction grating using v-shaped groove with refractive and reflective surfaces. Opt. Express **16**(25), 21004–21011 (2008)
3.83. T. von Lerber, M.W. Sigrist, Cavity-ring-down principle for fiber-optic resonators: experimental realization of bending loss and evanescent-field sensing. Appl. Opt. **41**(18), 3567–3575 (2002)
3.84. T. von Lerber, H. Ludvigsen, A. Romann, Resonator based measurement technique for quantification of minute birefringence. Opt. Express **12**(7), 1363–1371 (2004)
3.85. P. Hlubina, D. Ciprian, Spectral-domain measurement of phase modal birefringence in polarization-maintaining fiber. Opt. Express **15**(25), 17019–17024 (2007)
3.86. J.M. Miller, N. de Beaucoudrey, P. Chavel, J. Turunen, E. Cambril, Design and fabrication of slanted binary surface relief gratings for a planar optical interconnection. Appl. Opt. **36**(3), 5717–5727 (1997)
3.87. M. Burkhardt, K.G. Heinze, P. Schwille, Four-color fluorescence correlation spectroscopy realized in a grating-based detection platform. Opt. Lett. **360**(17), 2266–2268 (2005)
3.88. T. Levola, P. Laakkonen, Replicated slanted gratings with a high refractive index material for in and outcoupling of light. Opt. Express **15**(5), 2067–2074 (2007)
3.89. G.J.C. van der Horst, Fourier analysis and color discrimination. J. Opt. Soc. Am. **59**(12), 1670–1676 (1969)
3.90. S. Peterhansel, H. Laamanen, J. Lehtolahti, M. Kuittinen, W. Osten, J. Tervo, Human color vision provides nanoscale accuracy in thin-film thickness characterization. Optica **2**(7), 627–630 (2015)
3.91 M.A. Bukshtab, Cross-coupled transmission diffraction-gratings based color combiner (2017)

Chapter 4

4.1. S.R. Gunn, Volume-absorbing calorimeters for high-power laser pulses. Rev. Sci. Instrum. **45**(7), 936–943 (1974)
4.2. D.L. Franzen, L.B. Schmidt, Absolute reference calorimeter for measuring high power laser pulses. Appl. Opt. **15**(2), 3115–3122 (1976)

4.3. W.H. Reichelt, E.E. Stark Jr., T.E. Stratton, A gas calorimeter for use at 10.6 μm. Opt. Commun. **11**(3), 305–308 (1974)
4.4. V.N. Matweev, V.A. Rubsov, N.D. Ustinov, Improving accuracy of measurements by volume-absorbing calorimeters, in *Impulsnaya Photometria*, vol. 6 (Mashinostroenie, Leningrad, 1979), pp. 88–91
4.5. A.A. Wolkenstein, New commercial pulsed photometers; B.V. Byvshev, A.A. Wolkenstein, E.V. Kuvaldin, V.I. Popkov, New industrial pulsed photometers, in *Impulsnaya Photometria*, (Mashinostroenie, Leningrad, 1969), vol. 1, pp. 71–79; (1975), vol. 4, pp. 59–65
4.6. G.L. Voronkov, *Attenuators of Optical Radiation* (Mashinostroenie, Leningrad, 1980)
4.7. W. Leeb, Variable beam attenuator for the infrared. Appl. Opt. **13**(1), 17–19 (1974)
4.8. R.C.C. Leite, S.R.S. Porto, A simple method for calibration of ruby laser output. Proc. IEEE **51**(4), 606–607 (1963)
4.9. E.N. Anuchin, G.I. Kadaner, E.V. Kuvaldin, A study of elements of a pico-second pulsed photometer, in *Impulsnaya Photometria*, vol. 6 (Mashinostroenie, Leningrad, 1979), pp. 120–122
4.10. M.A. Bukhshtab, V.N. Maksimov, V.N. Rezchikov, A convenient radiometer for expanded cw and pulsed laser and light-diode power and energy measurement applications: ФПМ, in *Impulsnaya Photometria*, vol. 7 (Mashinostroenie, Leningrad, 1981), pp. 95–99
4.11. A.G. Biryukov, B.A. Maslov, B.I. Medvedev, V.G. Tyutyunnik, Digital and direct-reading pulsed radiometer for low-energy pulses making automatic dynamic range selection, in *Impulsnaya Photometria*, vol. 7 (Mashinostroenie, Leningrad, 1981), pp. 92–95
4.12. A.A. Wolkenstein, O.M. Mikhailov, Photometric studying of opal glasses. Svetotekhnika (2), 3–5 (1971)
4.13. A. Starke, A. Bernhardt, Laser damage threshold measurement according to ISO 11254: experimental realization at 1064 nm, in *Proceedings of SPIE*, vol. 2114, 1993
4.14. A.C. Doynikov, Photometer, in *Big Russian Encyclopedia*, 3rd edn. vol. 27 (Soviet Encyclopedia, Moscow, 1977), p. 585
4.15. Yu.P. Baranov, M.A. Bukhshtab, A.I. Glazov, S.V. Tikhomirov, A method of calibration of low-energy laser radiometers, in *Impulsnaya Photometria*, vol. 7 (Mashinostroenie, Leningrad, 1981), pp. 88–91
4.16. R.J. Phelan, A.R. Cook, Electrically calibrated pyroelectric optical-radiation detector. Appl. Opt. **12**(10), 2494–2500 (1973)
4.17. J. Geist, W.R. Blevin, Chopper-stabilized null radiometer based upon an electrically calibrated pyroelectric detector. Appl. Opt. **12**(11), 2532–2535 (1973)
4.18. J. Geist, Waveform-independent lock-in detections. Rev. Sci. Instrum. **43**(11), 1704–1705 (1972)
4.19. E.P. Zalewski, J. Geist, Silicone photodiode absolute response self-calibration. Appl. Opt. **19**(8), 1214–1216 (1980)
4.20. C. Carreras, A. Corrons, Absolute spectroradiometric and photometric scales based on an electrically calibrated pyroelectric radiometer. Appl. Opt. **20**(7), 1174–1177 (1981)
4.21. Methods of characterizing the performance of radiometers and photometers (CIE Publication 53, Paris, 1982)
4.22. C.L. Cromer, G. Eppeldauer, J.E. Harris, T.C. Larason, A.C. Parr, National Institute of Standards and Technology detector-based photometric scale. Appl. Opt. **32**(16), 2936–2948 (1993)
4.23. E.F. Zalewski, C.R. Duda, Silicon photodiode device with 100% external quantum efficiency. Appl. Opt. **22**(18), 2867–2873 (1983)
4.24. P.V. Foukal, C. Hoyt, H. Kochling, P. Miller, Cryogenic absolute radiometers as laboratory irradiance standards, remote sensing detectors, and pyroheliometers. Appl. Opt. **29**(7), 988–993 (1990)

4.25. R.U. Datla, K. Stock, A.C. Parr, C.C. Hoyt, P.J. Miller, P.V. Foukal, Characterization of an absolute cryogenic radiometer as a standard detector for radiant-power measurements. Appl. Opt. **31**(34), 7219–7225 (1992)
4.26. T.R. Gentile, J.M. Houston, J.E. Hardis, C.L. Cromer, A.C. Parr, National Institute of Standards and Technology high-accuracy cryogenic radiometer. Appl. Opt. **35**(7), 1056–1068 (1996)
4.27. T.C. Larason, S.S. Bruce, C.L. Cromer, The NIST high accuracy scale for absolute spectral response from 406 nm to 920 nm. J. Res. Natl. Inst. Stand. Technol. **101**(2), 133–140 (1996)
4.28. H.W. Yoon, C.E. Gibson, P.Y. Barnes, Realization of the National Institute of Standards and Technology detector-based spectral irradiance scale. Appl. Opt. **41**(28), 5879–5890 (2002)
4.29. T.J. Quinn, J.E. Martin, A radiometric determination of the Stefan-Boltzmann constant and thermodynamic temperatures between 240 °C and 1100 °C. Philos. Trans. R. Soc. Lond. Ser. A **316**, 85–189 (1985)
4.30. C.L. Cromer, G. Eppeldauer, J.E. Hardis, T.C. Larason, Y. Ohno, A.C. Parr, The NIST detector-based luminous intensity scale. J. Res. Natl. Inst. Stand. Technol. **101**(2), 109–132 (1996)
4.31. F.E. Nicodemus, Radiometry with spectrally selective sensors. Appl. Opt. **7**(8), 1649–1652 (1968)
4.32. H.E. Bennett, W.F. Koehler, Precision measurement of absolute specular reflectance with minimized systematic errors. J. Opt. Soc. Am. **50**(1), 1–6 (1960)
4.33. A.A. Wolkenstein, A.F. Kirillov, E.V. Kuvaldin, Spectrophotometry utilizing a pulsed light source, in *Impulsnaya Photometria*, vol. 1 (Mashinostroenie, Leningrad, 1969), pp. 102–109
4.34. G.M. Gorodinskii, M.A. Protsenko, O.M. Mikhailov, Measurement of reflection factors utilizing photometer ФМ-89. Meas. Tech. **21**(3), 30–32 (1978)
4.35. V.A. Soloviev, N.K. Kutliev, V.K. Volunschikov, V.P. Shabalov, A repeatability study of a spectral distribution of energy of pulses emitted by pulsed lamp ISK-25 activated in a sequence of pulses, in *Impulsnaya Photometria*, vol. 9 (Mashinostroenie, Leningrad, 1986), pp. 84–87
4.36. A.C. Hardy, A new recording spectrophotometer. J. Opt. Soc. Am. **25**(9), 305–311 (1935); J.L. Michadson, Construction of the general electric recording spectrophotometer. J. Opt. Soc. Am. **28**(10), 365–371 (1938)
4.37. P. Wu, P. Gu, J. Tang, Spectrophotometer for measuring spectral reflectance and transmittance. Appl. Opt. **33**(10), 1975–1979 (1994)
4.38. S.Yu. Gerasimov, O.N. Gusev, A.I. Koliadin, T.A. Krovko, A photometer for precision evaluation of spectral attenuation coefficients of highly transparent optical glasses. J. Opt. Technol. **51**(9), 18–19 (1983)
4.39. G.P. Semenova, V.G. Vorob'ev, Yu.D. Pushkin, Reflection attachment to spectrophotometer for measurement of high absolute reflections. J. Opt. Technol. **43**(4), 78–79 (1976)
4.40. E.A. Evans, S. Lowenthal, Moment generator: new role for the integrating sphere. J. Opt. Soc. Am. **62**(3), 411–415 (1972)
4.41. A.S. Toporets, An integrating sphere attachment to spectrophotometer SФ-8 for measurements of diffuse reflectance and transmittance. Opt. Spectrosc. **10**(4), 528–532 (1961)
4.42. V.L. Shipunov, T.N. Chernova, N.B. Berdnikov, N.I. Potapov, Photometer FO-1. J. Opt. Technol. **49**(5), 57–58 (1982)
4.43. D. Rönnow, A. Roos, Stray-light corrections in integrating-sphere measurements on low-scattering samples. Appl. Opt. **33**(25), 6092–6097 (1994)
4.44. K.D. Mielenz, K.L. Eckerle, R.P. Madden, J. Reader, New reference spectrophotometer. Appl. Opt. **12**(7), 1630–1641 (1973)

4.45. J.C. Zwinkels, D.S. Gignac, Design and testing of a new high-accuracy ultraviolet-visible-near-infrared spectrophotometer. Appl. Opt. **31**(10), 1557–1567 (1992)
4.46. Y. Ohno, C.L. Gromer, J.E. Harris, G. Eppeldauer, The detector-based candela scale and related photometric calibration procedures at NIST. J. IES **23**(1), 89–98 (1994)
4.47. M.L. Rastello, E. Miraldi, P. Pisoni, Luminous-flux measurements by an absolute integrating sphere. Appl. Opt. **35**(22), 4385–4391 (1996)
4.48. J. Bastie, B. Andasse, R. Foucart, Luminous flux measurements with a goniophotometer: study of time effects on data collection, in *Proceedings of the 22nd Session of CIE (Commission Internationale de l'Éclairage)*, vol. 1, No. 1, pp. 45–47, 1991
4.49. D. Sheffer, U.P. Oppenheim, A.D. Devir, Absolute reflectometer for the mid infrared region. Appl. Opt. **29**(1), 129–132 (1990); Absolute measurements of diffuse reflectance in the $\alpha°$/d configuration. Appl. Opt. **30**(22), 3181–3183 (1991)
4.50. L. Hanssen, Integrating sphere system and method for absolute measurement of transmittance, reflectance, and absorptance of specular samples. Appl. Opt. **40**(19), 3196–3204 (2001)
4.51. C.G. Venkatesh, R.S. Eng, A.W. Mantz, Tunable diode laser-integrating sphere systems: a study of their output intensity characteristics. Appl. Opt. **19**(10), 1704–1710 (1980)
4.52. L. Abel-Tiberini, F. Lemarquis, M. Lequime, Dedicated spectrophotometer for localized transmittance and reflectance measurements. Appl. Opt. **45**(7), 1386–1391 (2006)
4.53. A. Carrasco-Sanz, S. Martín-López, P. Corredera, M. González-Herráez, M.L. Hernanz, High-power and high-accuracy integrating sphere radiometer: design, characterization, and calibration. Appl. Opt. **45**(3), 511–518 (2006)
4.54. I. Niskanen, J. Räty, K.-E. Peiponen, Measurement of refractive index of isotropic particles by incorporating a multifunction spectrophotometer and immersion liquid method. Appl. Opt. **46**(22), 5404–5407 (2007); Complex refractive index of turbid liquids. Opt. Lett. **32**(7), 862–864 (2007)
4.55. T. Niwa, Sintered silicon nitride member and ceramic ball. U.S. Patent 6,472,075; 29 Oct 2002
4.56. L.N. Aksuitov, G.K. Kholopov, Methods of photometric accuracy measurements of radiation detectors. J. Opt. Technol. **46**(10), 42–47 (1979)
4.57. J. Elster, H. Geitel, Wied. Ann. **48**, 625 (1893); Phys. Z. **14**, 741 (1913)
4.58. C.L. Sanders, A photocell linearity tester. Appl. Opt. **1**(3), 207–211 (1962); Accurate measurements of and corrections for nonlinearities in radiometers. J. Res. Natl. Bur. Stand. Sect. A **76**, 437–453 (1972)
4.59. F. Rotter, Die Prüfung der Linearitet von Strahlungsempfänger. Z. Instrumentekd, B **73**(3), S. 66–71 (1965)
4.60. A. Reule, Testing spectrophotometer linearity. Appl. Opt. **7**(6), 1023–1028 (1968)
4.61. R.C. Hawes, Technique for measuring photometric accuracy. Appl. Opt. **10**(6), 1246–1253 (1971)
4.62. K.D. Mielenz, K.L. Eckerle, Spectrophotometer linearity testing using the double-aperture method. Appl. Opt. **11**(10), 2294–2303 (1972)
4.63. W. Budde, Multidecade linearity measurements on Si photodiodes. Appl. Opt. **18**(10), 1555–1558 (1979); Large-flux-ratio linearity measurements on Si photodiodes. Appl. Opt. **21**(20), 3699–3701 (1982)
4.64. A.R. Schaefer, E.F. Zalewski, J. Geist, Silicon detector nonlinearity and related effects. Appl. Opt. **22**(8), 1232–1236 (1983)
4.65. E.V. Kuvaldin, V.I. Popkov, Evaluation of photometric accuracy of photodetectors in a broad dynamic range, in *Impulsnaya Photometria*, vol. 4 (Mashinostroenie, Leningrad, 1975), pp. 169–170
4.66. L. Coslovi, F. Righini, Fast determination of the nonlinearity of photodetectors. Appl. Opt. **19**(18), 3200–3203 (1980)

4.67. R.D. Saunders, J.B. Shumaker, Automated radiometric linearity tester. Appl. Opt. **23**(20), 3504–3506 (1984)
4.68. J.C. Zwinkels, D.S. Gignak, Automated high precision variable aperture for spectrophotometer linearity testing. Appl. Opt. **30**(13), 1678–1687 (1991)
4.69. R.G. Frehlich, Estimation of the nonlinearity of a photodetector. Appl. Opt. **31**(28), 5926–5929 (1992)
4.70. E. Theocharous, J. Ishii, N.P. Fox, Absolute linearity measurements on HgCdTe detectors in the infrared. Appl. Opt. **43**(21), 4182–4188 (2004)
4.71. M. Naftaly, R. Dudley, Linearity calibration of amplitude and power measurements in terahertz systems and detectors. Opt. Lett. **34**(5), 674–676 (2009)
4.72. M. Francon, S. Mallick, *Polarization Interferometers: Applications in Microscopy and Macroscopy* (Wiley-Interscience, New York, 1971)
4.73. D. Malacara, *Optical Shop Testing*, 2nd edn. (Wiley, New York, 1992)
4.74. M. Francon, *Optical Interferometry* (Academic Press, New York, 1966)
4.75. M.A. Bukshtab, Nondestructive evaluation of silicon nitride rolling elements for bearings (2008)
4.76. B.B.C. Kyotoku, L. Chen, M. Lipson, Sub-nm resolution cavity enhanced microspectrometer. Opt. Express **18**(1), 102–107 (2009)
4.77. Z. Xia, A.A. Eftekhar, M. Soltani, B. Momeni, Q. Li, M. Chamanzar, S. Yegnanarayanan, A. Adibi, High resolution on-chip spectroscopy based on miniaturized microdonut resonators. Opt. Express **19**(13), 12356–12364 (2011)
4.78. T. Ozeki, E.H. Hara, Measurement of nonlinear distortion in photodiodes. Electron. Lett. **12**(3), 80–81 (1976)
4.79. M.N. Draa, A.S. Hastings, K.J. Williams, Comparison of photodiode nonlinearity measurement systems. Opt. Express **19**(13), 12635–12645 (2011)
4.80. ASTM E 313-00: Standard practice for calculating yellowness and whiteness indices from instrumentally measured color coordinates (2001)
4.81. T.J. Johnson, B.E. Bernacki, R.L. Redding, Y.-F. Su, C.S. Brauer, T.L. Myers, E.G. Stephan, Intensity-value corrections for integrating sphere measurements of solid samples measured behind glass. Appl. Spectrosc. **68**(11), 1224–1234 (2014)
4.82. S.D. Noble, T.G. Crowe, Sample holder and methodology for measuring the reflectance and transmittance of narrow-leaf samples. Appl. Opt. **46**(22), 4968–4976 (2007)
4.83. K.D. Jersnoj, S. Hassing, Analysis of reflectance and transmittance measurements on absorbing and scattering small samples using a modified integrating sphere setup. Appl. Spectrosc. **63**(8), 879–888 (2009)
4.84. W.B. Rogers, M. Corbett, S. Magkiriadou, P. Guarillof, V.N. Manoharan, Breaking trade-offs between translucency and diffusion in particle-doped films. Opt. Mat. Express **4**(12), 2621–12631 (2014)
4.85. D.F. Heath, G. Georgiev, Characteristics of a new type of Mie scattering volume diffuser and its use as a spectral albedo calibration standard for the solar reflective wavelength region, in *Proceedings of SPIE*, vol. 8153, Article 81530V-1 (2011)
4.86. C.P. Ball, A.P. Levick, E.R. Woolliams, P.D. Green, M.R. Dury, R. Winkler, A.J. Deadman, N.P. Fox, M.D. King, Effect of polytetrafluoroethylene (PTFE) phase transition at 19 °C on the use of Spectralon as a reference standard for reflectance. Appl. Opt. **52**(20), 4806–4812 (2013)
4.87. H. Zhang, Y. Yang, W. Jin, C. Liu, W. Hsu, Effects of Spectralon absorption on reflectance spectra of typical planetary surface analog materials. Opt. Express **22**(18), 21280–21291 (2014)
4.88. J.-H. Jung, K. Kim, H.-S. Yu, K.-R. Lee, S.-E. Lee, S.-H. Nahm, H.-J. Park, Y.-K. Park, Biomedical applications of holographic microspectroscopy. Appl. Opt. **53**(27), G111–G122 (2014)
4.89. N.A. Tomlin, J.H. Lehman, S. Nam, Towards a fiber-coupled picowatt cryogenic radiometer. Opt. Lett. **37**(12), 2346–2348 (2012)

Part II

II.1. B.I. Stepanov (ed.), *Method of Design Calculations for Optical Quantum Generators*, vol. 1 (Nauka & Technika, Minsk, 1966)
II.2. H.E. Bennett, J.M. Bennett, in *Physics of Thin Films*, ed. by G. Xass, R.E. Thun, vol. 4 (Academic, New York, 1967), pp. 41–57
II.3. H.E. Bennett, J.O. Porteus, Relation between surface roughness and specular reflectance at normal incidence. J. Opt. Soc. Am. **51**(2), 123–129 (1961)
II.4. C.A. Depew, R.D. Weir, Surface roughness determination by the measurement of reflectance. Appl. Opt. **10**(4), 969–970 (1971)
II.5. H.W. Kogelnik, T. Li, Laser beams and resonators. Appl. Opt. **5**(10), 1550–1567 (1966)
II.6. C.R. Locke, D. Stuart, E.N. Ivanov, A.N. Luiten, A simple technique for accurate and complete characterisation of a Fabry-Perot cavity. Opt. Express **17**(24), 21935–21943 (2009)
II.7. G. Kortum, *Reflectance Spectroscopy* (Springer, Berlin, Heidelberg, 1969)
II.8. A.E. Siegman, *Lasers* (University Science, Mill Valley, 1986)
II.9. J.F. Ready, *Effects of High-Power Laser Radiation* (Academic, New York, 1971)
II.10. Y. Pao (ed.), *Optoacoustic Spectroscopy and Detection* (Academic, New York, 1977)
II.11. Yu.A. Ananiev, *Optical Resonators and Divergence of Laser Radiation* (Nauka, Moscow, 1979)
II.12. D. Kliger, *Ultrasensitive Laser Spectroscopy* (Academic, New York, 1983)
II.13. V.A. Shutilov, *Fundamental Physics of Ultrasound* (Gordon and Breach, New York, 1988)
II.14. J.A. Sell (ed.), *Photothermal Investigations of Solids and Fluids* (Academic, New York, 1989)
II.15. P. Hess (ed.), *Photoacoustic, Photothermal and Photochemical Processes in Gases* (Springer, New York, 1989)
II.16. F.V. Bunkin, A.A. Kolomensky, V.G. Mikhalevich, *Lasers in Acoustics* (Harwood, New York, 1991)
II.17. A. Mandelis (ed.), *Progress in Photothermal and Photoacoustic Science and Technology*, vol. 1 (Elsevier, New York, 1992)
II.18. V.E. Gusev, A.A. Karabutov, *Laser Optoacoustics* (Institute of Physics, New York, 1993)
II.19. M.W. Sigrist (ed.), *Air Monitoring by Spectroscopic Techniques*, Chemical Analysis Series, vol. 127 (Wiley, New York, 1994)
II.20. H.A. Macleod, *Thin-Film Optical Filters*, 3rd edn. (Institute of Physics Publishing, Tucson, 2001)
II.21. I.L. Fabelinskii, *Molecular Scattering of Light* (Plenum, New York, 1968; Nauka, Moscow, 1965)
II.22. H.C. van de Hulst, *Light Scattering by Small Particles* (Dover, New York, 1981)
II.23. R.M.A. Azzam, N.M. Bashara, *Ellipsometry and Polarized Light* (Elsevier, Amsterdam, 1996)
II.24. S. Chandrasekhar, *Radiative Transfer* (Dover, New York, 1960)
II.25. R. Siegel, J.R. Howell, *Thermal Radiation Heat Transfer* (Hemisphere, New York, 1981)
II.26. M. Francon, *Laser Speckle and Applications in Optics* (Academic Press, New York, 1979)
II.27. W. Demtroder, *Laser Spectroscopy: Basic Concepts and Instrumentation*, 2nd edn. (Springer, Berlin, 1996)
II.28. K. Petermann, *Laser Diode Modulation and Noise* (Kluwer, Dordrecht, 1988)
II.29. D.V. O'Connor, D. Phillips, *Time-Correlated Single Photon Counting* (Academic, New York, London, 1984)

II.30. P.R. Griffiths, J.A. De Haseth, J.D. Winefordner (eds.), *Fourier Transform Infrared Spectrometry*, 2nd edn. (Wiley, New York, 2007)
II.31. W. Koechner, *Solid-State Laser Engineering*, 3rd edn. (Springer, Heidelberg, 1992)
II.32. J. Ye, T.W. Lynn, Applications of optical cavities in modern atomic, molecular, and optical physics, in *Advances in Atomic Molecular and Optical Physics*, vol. 49, ed. by B. Bederson, H. Walther (Elsevier, 2003), pp. 1–83
II.33. A.W. Snyder, J.D. Love, *Optical waveguide theory* (Chapman & Hall, London, 1983, 1996)
II.34. R. März, *Integrated Optics: Design and Modeling* (Artech House, Norwood, 1995)
II.35. N. Kashima, *Passive Optical Components for Optical Fiber Transmission* (Artech House, Boston, 1995)
II.36. S.B. Alexander, *Optical Communication receiver design, Tutorials in Optical Engineering*, vol. TT22 (SPIE, 1997)
II.37. G.P. Agrawal, *Fiber-Optic Communication Systems*, 2nd edn. (Wiley, New York, 1997)
II.38. D. Derickson (ed.), *Fiber Optic Test and Measurement* (Prentice Hall, Englewood Cliffs, 1998)
II.39. U. Wiedmann, P. Gallion, G.-H. Duan, A generalized approach to optical low-coherence reflectometry including spectral filtering effects. J. Lightwave Technol. **16**(7), 1343–1347 (1998)
II.40. F. Mayinger, *Optical Measurement Techniques* (Springer, Berlin, 1994); O. Feldmann, F. Mayinger, *Optical Measurements: Techniques and Applications* (Springer, Berlin, 2001)
II.41. R.D. van Zee, J.P. Looney (eds.), *Cavity-Enhanced Spectroscopies,* Experimental Methods in the Physical Sciences, vol. 40 (Elsevier, New York, 2002)
II.42. A. Yariv, P. Yeh, *Optical Waves in Crystals: Propagation and Control of Laser Radiation* (Wiley, New York, 2002); *Photonics: Optical Electronics in Modern Communication*, 6th edn. (Oxford University Press, Oxford, 2006)
II.43. C.R. Wylie, *Advances in Engineering Mathematics* (McGraw-Hill, New York, 1960)
II.44. A. Papoulis, *Probability and Statistics* (Prentice-Hall, Englewood Cliffs, 1990)
II.45. G.B. Arfken, H.J. Weber, *Mathematical Methods for Physicists*, 4th edn. (Academic Press, San Diego, London, 1995)

Chapter 5

5.1. K.C. Kao, T.V. Davis, Spectrophotometric studies of ultra low loss optical glasses I: single beam method. J. Sci. Instrum. Ser. 2, **1**(11), 1063–1068 (1968)
5.2. M.W. Jones, K.C. Kao, Spectrophotometric studies of ultra low loss optical glasses II: double beam method. J. Sci. Instrum. Ser. 2, **2**(4), 331–335 (1969)
5.3. P.J.R. Laybourn, W.A. Gambling, D.T. Jones, Measurement of attenuation in low-loss optical glasses. Optoelectronics **3**(8), 137–144 (1971); J.P. Dakin, W.A. Gambling, Transmission measurements in optical glass with an improved twin-beam spectrophotometer. Opto-Electronics **5**(4), 335–344 (1973)
5.4. A.I. Kolyadin, A.A. Malygina, Use of least-square method for determining the extinction coefficient of high-transmission glass. J. Opt. Technol. **44**(11), 656–658 (1977)
5.5. S. Bosch, J. Roca, A method for the measurement of reflectances of spherical surfaces. Meas. Sci. Technol. **4**, 190–192 (1993)
5.6. G. Boivin, J.-M. Theriault, Reflectometer for precise measurement of absolute specular reflectance at normal incidence. Rev. Sci. Instrum. **52**(7), 1001–1002 (1981)
5.7. A. Bittar, J.D. Hamlin, High-accuracy true normal-incidence absolute reflectometer. Appl. Opt. **23**(22), 4054–4057 (1984)

5.8. K. Al-Marzouk, M. Jacobson, R. Parcs, M. Rodgers, New absolute reflectometer. Opt. Eng. **21**(6), 976–978 (1982)
5.9. V.R. Weidner, J.J. Hsia, NBS specular reflectometer-spectrophotometer. Appl. Opt. **19**(8), 1268–1273 (1980)
5.10. C. Castelini, G. Emiliani, E. Masetti, P. Poggi, P.P. Polato, Characterization and calibration of a variable angle absolute reflectometer. Appl. Opt. **29**(4), 538–543 (1990)
5.11. J.M. Bennett, E.J. Ashley, Calibration of instruments measuring reflectance and transmittance. Appl. Opt. **11**(8), 1749–1755 (1972)
5.12. A.Ya. Hairullina, L.Ch. Neverovich, A setup for measurements of back-scattering from laser mirrors (Institute of Physics AN BSSR, Minsk, 1974) Selected Reprint
5.13. P.J. Laybourn, J.P. Dakin, W.A. Gambling, A photometer to measure light scattering in optical glass. Optoelectronics **2**(1), 36–42 (1970)
5.14. J.M. Elson, J.P. Rahn, J.M. Bennett, Relationship of the total integrated scattering from multilayer coated optics to angle of incidence, polarization, correlation length, and roughness cross-correlation properties. Appl. Opt. **22**(20), 3207–3220 (1983)
5.15. A.C. Toporets, Light reflection by rough surface. J. Opt. Technol. **46**(1), 35–48 (1979)
5.16. W.R. Blevin, J. Geist, Infrared reflectometry with a cavity-shaped pyroelectric detector. Appl. Opt. **13**(10), 2212–2217 (1974)
5.17. P. Roche, E. Pelletier, Characterization of optical surfaces by measurement of scattering distribution. Appl. Opt. **23**(20), 3561–3566 (1984)
5.18. B.A. Mehmetli, K. Takahashi, S. Sato, Direct measurement of reflectance from aluminum alloys during CO_2 laser welding. Appl. Opt. **35**(18), 3237–3242 (1996)
5.19. B.T. McGuckin, D.A. Haner, R.T. Menzies, C. Esproles, A.M. Brothers, Directional reflectance characterization facility and measurement methodology. Appl. Opt. **35**(24), 4827–4834 (1996)
5.20. D.G. Goebel, B.P. Caldwell, H.K. Hammond III, Use of an auxiliary sphere with a spectroreflectometer to obtain absolute reflectance. J. Opt. Soc. Am. **56**(6), 783–788 (1966)
5.21. S.M. Jaffe, W.M. Yen, Phase-locked optical choppers. Rev. Sci. Instrum. **64**(2), 342–345 (1993)
5.22. W. Smith, Reflectometer for laser mirrors with accuracy better than 10^{-4}. Appl. Opt. **17**(16), 2476–2477 (1978)
5.23. R.E. Lindquist, A.W. Ewald, Optical constants from reflectance ratios by a geometric construction. J. Opt. Soc. Am. **53**(2), 247–249 (1963)
5.24. W.R. Hunter, Optical constants of metals in the extreme ultraviolet. I. A modified critical-angle technique for measuring the index of refraction of metals in the extreme ultraviolet. J. Opt. Soc. Am. **54**(1), 15–19 (1964)
5.25. R.F. Potter, Analytical determination of optical constants based on the polarized reflectance at a dielectric-conductor interface. J. Opt. Soc. Am. **54**(7), 904–906 (1964)
5.26. E. Schmidt, Simple method for the determination of optical constants of absorbing materials. Appl. Opt. **8**(9), 1905–1908 (1969)
5.27. T.E. Darcie, M.S. Whalen, Determination of optical constants using pseudo-Brewster angle and normal incidence reflectance measurements. Appl. Opt. **23**(8), 1130–1131 (1984)
5.28. K. Ogusu, K. Suzuki, H. Nishio, Simple and accurate measurement of the absorption coefficient of an absorbing plate by use of the Brewster angle. Opt. Lett. **31**(7), 909–911 (2006)
5.29. D. Roßkamp, F. Truffer, S. Bolay, M. Geiser, Forward scattering measurement device with a high angular resolution. Opt. Express **15**(5), 2683–2690 (2007)
5.30. F.D.J. Brunner, A. Schneider, P. Günter, A terahertz time-domain spectrometer for simultaneous transmission and reflection measurements at normal incidence. Opt. Express **17**(23), 20684–20693 (2009)

5.31. S.L. Berets, M. Milosevic, Extracting infrared absolute reflectance from relative reflectance measurements. Appl. Spectrosc. **66**(6), 680–684 (2012)
5.32. X. Liang, M. Li, J.Q. Lu, C. Huang, Y. Feng, Y. Sa, J. Ding, X.-H. Hu, Spectrophotometric determination of turbid optical parameters without using an integrating sphere. Appl. Opt. **55**(8), 2079–2085 (2016)

Chapter 6

6.1. D.M. Gates, C.C. Shaw, D. Beaumont, Infrared reflectance of evaporated metal films. J. Opt. Soc. Am. **48**(2), 88–89 (1958)
6.2. L.G. Schultz, F.R. Tangherlini, Optical constants of silver, gold, copper, and aluminum. II. The index of refraction n. J. Opt. Soc. Am. **44**(5), 362–368 (1954)
6.3. V.I. Kuprenuk, V.E. Sherstobitov, A simple method of reflectance measurements for metal mirrors at wavelength $\lambda = 10.6$ μm. J. Appl. Spectrosc. **25**(5), 926–928 (1974)
6.4. D. Kelsall, Absolute specular reflectance measurements of highly reflecting optical coatings at 10.6 μm. Appl. Opt. **9**(1), 85–90 (1970)
6.5. S. Chandra, R.S. Rohde, Ultrasensitive multiple-reflections interferometer. Appl. Opt. **21**(9), 1533–1535 (1982)
6.6. H. Hanada, Characteristics of a Fabry-Perot interferometer with two retroreflectors and two beam splitters. J. Opt. Soc. Am. A **9**(12), 2167–2172 (1992)
6.7. A.L. Vitushkin, L.F. Vitushkin, Design of a multipass optical cell based on the use of shifted corner cubes and right-angle prisms. Appl. Opt. **37**(9), 162–166 (1998)
6.8. J.U. White, Long optical path of large aperture. J. Opt. Soc. Am. **32**(5), 285–288 (1942)
6.9. T.H. Edwards, Multiple-traverse absorption cell design. J. Opt. Soc. Am. **51**(1), 98–102 (1961)
6.10. G.P. Semenova, V.G. Vorob'ev, Yu.D. Pushkin, Spectrophotometric attachment for absolute measurements of high specular reflectances. J. Opt. Technol. **43**(4), 78–79 (1976)
6.11. O. Arnon, P. Baumeister, Versatile high-precision multiple-pass reflectometer. Appl. Opt. **17**(18), 2913–2916 (1978)
6.12. R.P. Blickensderfer, G.E. Ewing, R. Leonard, A long path, low temperature cell. Appl. Opt. **7**(11), 2214–2217 (1968)
6.13. D. Horn, G.C. Pimentel, 2.5-km low-temperature multiple-reflection cell. Appl. Opt. **10**(8), 1892–1898 (1971)
6.14. P.L. Hanst, Spectroscopic methods for air pollution measurement, in *Advances in Environmental Science and Technology* ed. by J.N. Pitts, R.L. Metcalf (Wiley, New York, 1971), p. 91
6.15. E.O. Schulz-DuBois, Generation of square lattice of focal points by a modified white cell. Appl. Opt. **12**(7), 1391–1393 (1973)
6.16. D.M. Bakalyar, J.V. James, C.C. Wang, Absorption technique for OH measurements and calibration. Appl. Opt. **21**(16), 2901–2905 (1982)
6.17. P.L. Hanst, A.S. Lefohn, B.W. Gay Jr., Detection of atmospheric pollutants at parts-per-billion levels by infrared spectroscopy. Appl. Spectrosc. **27**(3), 188–198 (1973)
6.18. P.L. Hanst, Air pollution measurement by Fourier transform spectroscopy. Appl. Opt. **17**(9), 1360–1366 (1978)
6.19. H.J. Bernstein, J. Herzberg, Rotation-vibration spectra of diatomic and simple polyatomic molecules with long absorbing paths. J. Chem. Phys. **16**(1), 30–39 (1948)
6.20. W.R. Watkins, Path differencing: an improvement to multipass absorption cell measurements. Appl. Opt. **15**(1), 16–19 (1976)
6.21. J.U. White, Very long optical paths in air. J. Opt. Soc. Am. **66**(5), 411–416 (1976)

6.22. S.M. Chernin, E.G. Barskaya, Optical multipass matrix systems. Appl. Opt. **30**(1), 51–58 (1991)
6.23. H.D. Smith, J.K. Marshall, Method for obtaining long optical paths. J. Opt. Soc. Am. **30**(8), 338–342 (1940)
6.24. S.M. Chernin, Multipass V-shaped system with a large relative aperture: stages of development. Appl. Opt. **34**(34), 7857–7863 (1995)
6.25. K. Schäfer, K. Brockmann, J. Heland, P. Wiesen, C. Jahn, O. Legras, Multipass open-path Fourier-transform infrared measurements for nonintrusive monitoring of gas turbine exhaust composition. Appl. Opt. **44**(11), 2189–2201 (2005)
6.26. D.C. Tobin, L.L. Strow, W.J. Lafferty, W.B. Olson, Experimental investigation of the self- and N_2-broadened continuum within the ν_2 band of water vapor. Appl. Opt. **35**(24), 4724–4734 (1996)
6.27. P. Hannan, White cell design considerations. Opt. Eng. **28**(11), 1180–1184 (1989)
6.28. J.-F. Doussin, D. Ritz, P. Carlier, Multiple-pass cell for very-long-path infrared spectrometry. Appl. Opt. **38**(19), 4145–4150 (1999)
6.29. L. Grassi, R. Guzzi, Theoretical and practical consideration of the construction of a zero-geometric-loss multiple-pass cell based on the use of monolithic multiple-face retroreflectors. Appl. Opt. **40**(33), 6062–6071 (2001)
6.30. S.M. Chernin, Promising version of the three-objective multipass matrix system. Opt. Express **10**(2), 104–107 (2002)
6.31. D.R. Glowacki, A. Goddard, P.W. Seakins, Design and performance of a throughput-matched, zero-geometric-loss, modified three objective multipass matrix system for FTIR spectrometry. Appl. Opt. **46**(32), 7872–7883 (2007)
6.32. D. Herriott, H. Kogelnik, R. Kompfner, Off-axis parts in spherical mirror interferometers. Appl. Opt. **3**(4), 523–526 (1964)
6.33. D.R. Herriott, H.J. Schulte, Folded optical delay lines. Appl. Opt. **4**(8), 883–889 (1965)
6.34. J. Altman, R. Baumgart, C. Weitkamp, Two-mirror multipass absorption cell. Appl. Opt. **20**(6), 995–999 (1981)
6.35. P.L. Kebabian, Off-axis cavity absorption cell. U.S. Patent Number 5,291,265; 1 Mar 1994
6.36. J.B. McManus, P.L. Kebabian, M.S. Zahniser, Astigmatic mirror multipass absorption cells for long-path-length spectroscopy. Appl. Opt. **34**(18), 3336–3348 (1995)
6.37. L.-Y. Hao, S. Qiang, G.-R. Wu, L. Qi, D. Feng, Q.-S. Zhu, Cylindrical mirror multipass Lissajous system for laser photoacoustic spectroscopy. Rev. Sci. Instrum. **73**(5), 2079–2085 (2002); D. Das, A.C. Wilson, Very long optical path-length from a compact multi-pass cell. Appl. Phys. B **103**(3), 749–754 (2011)
6.38. J.A. Silver, Simple dense-pattern optical multipass cells. Appl. Opt. **44**(31), 6545–6556; Near re-entrant dense pattern optical multipass cell. U.S. Patent 7,307,716; 11 Dec 2007
6.39. C. Dyroff, A. Zahn, W. Freude, B. Jänker, P. Werle, Multipass cell design for Stark-modulation spectroscopy. Appl. Opt. **46**(19), 4000–4007 (2007)
6.40. G.S. Engel, E.J. Moyer, Precise multipass Herriott cell design: derivation of controlling design equations. Opt. Lett. **32**(6), 704–706 (2007)
6.41. G. Müller, E. Weimer, Multipass-Systeme für die Raman-Spectroscopie. Optic **56**(1), 1–19 (1980)
6.42. J.J. Barrett, N.I. Adams III, Laser-excited rotation-vibration Raman scattering in ultra-small gas samples. J. Opt. Soc. Am. **58**(3), 311–319 (1968)
6.43. W.R. Trutna, R.L. Byer, Multiple-pass Raman gain cell. Appl. Opt. **19**(2), 301–312 (1980)
6.44. H.L. Welsh, E.J. Stansbury, J. Romanko, T. Feldman, Raman spectroscopy of gases. J. Opt. Soc. Am. **45**(5), 338–343 (1955)
6.45. A. Weber, S.P.S. Porto, L.E. Cheesman, J.J. Barrett, High-resolution Raman spectroscopy of gases with cw-laser excitation. J. Opt. Soc. Am. **57**(1), 19–28 (1967)

6.46. J.J. Barrett, N.I. Adams, Laser-excited rotation-vibration Raman scattering in ultra-small gas samples. J. Opt. Soc. Am. **58**(3), 311–319 (1968)
6.47. R.A. Hill, D.L. Hartley, Focused, multiple-pass cell for Raman scattering. Appl. Opt. **13**(1), 186–192 (1974)
6.48. R.A. Hill, A.J. Mulac, C.E. Hackett, Retroreflecting multipass cell for Raman scattering. Appl. Opt. **16**(7), 2004–2006 (1977)
6.49. A.J. Mulac, W.L. Flower, R.A. Hill, D.P. Aeschliman, Pulsed spontaneous Raman scattering technique for luminous environments. Appl. Opt. **17**(17), 2695–2699 (1978)
6.50. M.A. Bukshtab, Configurable tunable resonant multipass cell for scattering and absorption measurements, 2007
6.51. G.A. Waldherr, H. Lin, Gain analysis of an optical multipass cell for spectroscopic measurements in luminous environments. Appl. Opt. **47**(7), 901–907 (2008)
6.52. R. Viola, High-luminosity multipass cell for infrared imaging spectroscopy. Appl. Opt. **45**(12), 2805–2809 (2006)
6.53. C.A. Arguello, G.F. Mendes, R.C.C. Leite, Simple technique to suppress spurious luminescence in Raman spectroscopy. Appl. Opt. **13**(8), 1731–1732 (1974)
6.54. D.A. Hatzenbuhler, Raman spectroscopy in the presence of fluorescence. U.S. Patent Number 3,807,862, 30 Apr 1974
6.55. E.C. Le Ru, L.C. Schroeter, P.G. Etchegoin, Direct measurement of resonance Raman spectra and cross sections by a polarization difference technique. Anal. Chem. **84**(5), 5074–5079 (2012)
6.56. M.A. Bukshtab, Fluorescence rejection techniques in Raman spectroscopy of carbohydrates (2013)
6.57. E.P. Yaney, Reduction of fluorescence background in Raman spectra by the pulsed Raman technique. JOSA **62**(11), 1297–1303 (1972)
6.58. A.Z. Genack, B.N. Perry, Phase resolved modulation Raman spectrometer. U.S. Patent Number 4,619,528, 28 Oct 1986
6.59. F.V. Bright, Multicomponent suppression of fluorescent interferents using phase-resolved Raman spectroscopy. Anal. Chem. **60**(15), 1622–1623 (1988)
6.60. D.V. Martyshkin, R.C. Ahuja, A. Kudriavtsev, S.B. Mirov, Effective suppression of fluorescence light in Raman measurements using ultrafast time gated charge coupled device camera. Rev. Sci. Instrum. **75**(3), 630–635 (2004)
6.61. P. Matousek, M. Towrie, A. Stanley, A.W. Parker, Efficient rejection of fluorescence from Raman spectra using picosecond Kerr gating. Appl. Spectrosc. **53**(12), 1485–1489 (1999)
6.62. F. Knorr, Z.J. Smith, S. Wachsmann-Hogiu, Development of a time-gated system for Raman spectroscopy of biological samples. Opt. Express **18**(19), 20049–20058 (2010)
6.63. V.S. Ban, B.L. Volodin, N.R. Stoker, Compact, low cost Raman monitor for single substances. US Patent 8,125,635, 28 Feb 2012
6.64. V.J. Hammond, W.C. Price, A new system for the elimination of scattered light effects in spectrophotometers. J. Opt. Soc. Am. **43**(10), 924 (1953)
6.65. J. Funfschilling, D.F. Williams, CW laser wavelength modulation in Raman and site selection fluorescence spectroscopy. Appl. Spectrosc. **30**(4), 443–446 (1976)
6.66. A.P. Shreve, N.J. Cherepy, R.A. Mathies, Effective rejection of fluorescence interference in Raman spectroscopy using a shifted excitation difference technique. Appl. Spectrosc. **46**(4), 707–711 (1992)
6.67. J.J. Baraga, M.S. Feld, R.P. Rava, Rapid near-infrared Raman spectroscopy of human tissue with a spectrograph and CCD detector. Appl. Spectrosc. **46**(2), 187–190 (1992)
6.68. P.A. Mosier-Boss, S.H. Lieberman, R. Newbery, Fluorescence rejection in Raman spectroscopy by shifted-spectra, edge detection, and FFT filtering techniques. Appl. Spectrosc. **49**(5), 630–7638 (1995)

6.69. G. Schulze, A. Jirasek, M.L. Yu, A. Lim, R.F.B. Turner, M.W. Blades, Investigation of selected baseline removal techniques as candidates for automated implementation. Appl. Spectrosc. **59**(5), 545–574 (2005)
6.70. J. Zhao, H. Lui, D.I. McLean, H. Zeng, Automated autofluorescence background subtraction algorithm for biomedical Raman spectroscopy. Appl. Spectrosc. **61**(11), 1225–1232 (2007)
6.71. Z.-M. Zhang, S. Chen, Y.-Z. Liang, Z.-X. Liu, Q.-M. Zhang, L.-X. Ding, F. Yec, H. Zhouc, An intelligent background-correction algorithm for highly fluorescent samples in Raman spectroscopy. J. Raman Spectrosc. **41**(6), 659–669 (2010)
6.72. J. Zhao, M.M. Carrabba, F.S. Allen, Automated fluorescence rejection using shifted excitation Raman difference spectroscopy. Appl. Spectrosc. **56**(7), 834–845 (2002)
6.73. P. Matousek, M. Towrie, A.W. Parker, Simple reconstruction algorithm for shifted excitation Raman difference spectroscopy. Appl. Spectrosc. **59**(6), 848–851 (2005)
6.74. A.C. De Luca, M. Mazilu, A. Riches, C.S. Herrington, K. Dholakia, Online fluorescence suppression in modulated Raman spectroscopy. Anal. Chem. **82**(2), 738–745 (2010)
6.75. J.A. Decker, Experimental realization of the multiplex advantage with a Hadamard-transform spectrometer. Appl. Opt. **10**(3), 510–514 (1971); W.H. Richardson, Bayesian-based iterative method of image restoration. J. Opt. Soc. Am. **62**(1), 55–59 (1972)
6.76. E. Voigtman, J.D. Winefordner, The multiplex disadvantage and excess low-frequency noise. Appl. Spectrosc. **41**(7), 1182–1184 (1987); S.E. Bialkowski, Overcoming the multiplex disadvantage by using maximum-likelihood inversion. Appl. Spectrosc. **52**(4), 591–598 (1998)
6.77. S.E.J. Bell, E.S.O. Bourguignon, A. Dennis, Analysis of luminescent samples using subtracted shifted Raman spectroscopy. Analyst **123**(8), 1729–1734 (1998)
6.78. S.T. McCain, R.M. Willett, D.J. Brady, Multi-excitation Raman spectroscopy technique for fluorescence rejection. Opt. Express **16**(15), 10975–10991 (2008)
6.79. M.A. da Silva Martins, D.G. Ribeiro, E.A. Pereira dos Santos, A.A. Martin, A. Fontes, H. da Silva Martinho, Shifted-excitation Raman difference spectroscopy for in vitro and in vivo biological samples analysis. Biomed. Opt. Express **1**(2), 617–626 (2010)
6.80. M. Mazilu, A.C. De Luca, A. Riches, C.S. Herrington, K. Dholakia, Optimal algorithm for fluorescence suppression of modulated Raman spectroscopy. Opt. Express **18**(11), 11382–11395 (2010)
6.81. B.B. Praveen, P.C. Ashok, M. Mazilu, A. Riches, S. Herrington, K. Dholakiaa, Fluorescence suppression using wavelength modulated Raman spectroscopy in fiber-probe-based tissue analysis. J. Biomed. Opt. **17**(7), Article 077006 (2012)
6.82. P.J. Cadusch, M.M. Hlaing, S.A. Wade, S.L. McArthur, P.R. Stoddart, Improved methods for fluorescence background subtraction from Raman spectra. J. Raman Spectrosc. **44**(11), 1587–1595 (2013)
6.83. S. Marshall, J.B. Cooper, Quantitative Raman spectroscopy when the signal-to-noise is below the limit of quantitation due to fluorescence interference: advantages of a moving window sequentially. Appl. Spectrosc. **70**(9), 1489–1501 (2016)
6.84. J. Blacksberg, E. Alerstam, Y. Maruama, C.J. Cochrane, G.R. Rossman, Miniaturized time-resolved Raman spectrometer for planetary science based on a fast single photon avalanche diode detector array. Appl. Opt. **55**(4), 739–748 (2016)
6.85. Y. Engelborghs, A.J.W.G. Visser, *Fluorescence Spectroscopy and Microscopy: Methods and Protocols* (Humana Press, Springer, New York, 2014)
6.86. B. Tuzson, M. Mangold, H. Looser, A. Manninen, L. Emmenegger, Compact multipass optical cell for laser spectroscopy. Opt. Lett. **38**(3), 257–259 (2013)
6.87. T. Mohamed, F. Zhu, S. Chen, J. Strohaber, A.A. Kolomenskii, A.A. Bengali, H.A. Schuessler, Multipass cell based on confocal mirrors for sensitive broadband laser spectroscopy in the near infrared. Appl. Opt. **52**(29), 7145–7151 (2013)

6.88. K. Krzempek, M. Jahjah, R. Lewicki, P. Stefanski, S. So, D. Thomazy, F.K. Tittel, CW DFB RT diode laser-based sensor for trace-gas detection of ethane using a novel compact multipass gas absorption cell. Appl. Phys. B **112**(4), 461–465 (2013)
6.89. D. Kaur, A.M. de Souza, J. Wanna, S.A. Hammad, L. Mercorelli, D.S. Perry, Multipass cell for molecular beam absorption spectroscopy. Appl. Opt. **29**(1), 119–124 (1990); K.C. Utsav, J.A. Silver, D.C. Hovde, P.L. Varghese, Improved multiple-pass Raman spectrometer. Appl. Opt. **50**(24), 4805–4816 (2011)
6.90. J. Thorstensen, K.H. Haugholt, A. Ferber, K.A.H. Bakke, J. Tschudi, Low-cost resonant cavity Raman gas probe for multi-gas detection. J. Eur. Opt. Soc. Rap. Public. **9**, Article 14054 (2014)
6.91. W. Muller, M. Kielhorn, M. Schmitt, J. Popp, R. Heintzmann, Light sheet Raman micro-spectroscopy. Optica **3**(4), 452–457 (2016)
6.92. V.N. Lednev, P.A. Sdvizhenskii, M.YA. Grishin, M.N. Filippov, A.N. Shchegolikhin, S.M. Pershin, Laser crater enhanced Raman spectroscopy. Opt. Lett. **42**(3), 607–610 (2017)

Chapter 7

7.1. A.B. Melnikov, Determination of transmittance of low-dense plasma by the intracavity method. J. Appl. Spectrosc. **6**(6), 821–823 (1967)
7.2. H.P. Brandli, Method for measuring of small optical losses using a He–Ne laser. Rev. Sci. Instrum. **39**(4), 583–587 (1968)
7.3. V.S. Burakov, V.V. Djukovsky, A.A. Stavrov, An increase of the dynamic range of the intra-cavity measurements of optical densities. Quantum Electron. **5**(1), 13–19 (1978)
7.4. V. Sanders, High-precision reflectivity measurement technique for low-loss laser mirrors. Appl. Opt. **16**(1), 19–20 (1977)
7.5. J.S. Shirk, T.D. Harris, J.W. Mitchell, Laser intracavity spectrophotometer. Anal. Chem. **52**(11), 1701–1705 (1980)
7.6. A.L. Bloom, *Gas Lasers* (Wiley, New York, 1968)
7.7. N. Konjevic, M. Kokovic, He–Ne laser for intra-cavity enhanced absorption measurement. Spectrosc. Lett. **7**(12), 615–620 (1974)
7.8. V.I. Makhorin, A.I. Popov, E.D. Protsenko, Influence of intra-resonator losses on power of a He–Ne laser at 3.39 μm region. J. Appl. Spectrosc. **27**(3), 418–422 (1977)
7.9. A.S. Burmistrov, A.I. Popov, Study of a sensitivity of the intra-cavity method of determination of low optical losses in a cw gas laser. J. Appl. Spectrosc. **37**(2), 205–209 (1982)
7.10. A.V. Lebedev, A.I. Popov, Computation of a sensitivity of method of low optical absorption study in a cw laser with internal cavity and narrow spectrum. J. Appl. Spectrosc. **44**(2), 219–225 (1986)
7.11. L.A. Pakhomyucheva, E.A. Sviridenkov, A.F. Sychkov, L.V. Titova, S.S. Kurilov, The linear structure of spectrums generated by solid-state lasers. Lett. JETF **12**(2), 60–63 (1970)
7.12. B.M. Baev, V.P. Dyubov, E.A. Sviridenkov, Increasing of sensitivity of the intra-cavity laser spectroscopy using Nd: glass laser. Quantum Electron. **12**(12), 2490–2491 (1985)
7.13. N.C. Peterson, M.J. Kurylo, W. Braun, A.M. Bass, R.A. Keller, Enhancement of absorption spectra by dye-laser quenching. J. Opt. Soc. Am. **61**(6), 746–750 (1971); R.A. Keller, E.F. Zalewski, N.C. Peterson, Enhancement of absorption spectra by die-laser quenching, II. J. Opt. Soc. Am. **62**(3), 319–326 (1972)
7.14. V.I. Baev, T.P. Belikova, E.A. Sviridenkov, A.F. Sychkov, Intra-cavity spectroscopy with cw and quasi-cw lasers. JTF **74**(1), 43–56 (1978)
7.15. A.A. Kachanov, T.V. Plakhotnik, Intracavity spectrometer with a ring traveling-wave dye laser: reduction of detection limit. Opt. Commun. **47**(4), 257–261 (1983)

7.16. A.V. Adamushko, M.V. Belokon, A.I. Rubinov, Intracavity spectrometer based on cw dye lasers. J. Appl. Spectrosc. **28**(3), 417–420 (1978)
7.17. D.A. Smith, D.I. Shernoff, Simple measurement of gain and loss in ultralow loss optical resonators. Appl. Opt. **24**(12), 1722–1723 (1985)
7.18. N. Dutta, R.T. Warner, G.J. Wolga, Sensitivity enhancement of a spin-flip Raman laser absorption spectrometer through use of an intracavity absorption cell. Opt. Lett. **1**(5), 155–157 (1977)
7.19. G.O. Brink, An alternate model of CW dye laser intracavity absorption. Opt. Commun. **32**(1), 123–128 (1980)
7.20. E.N. Antonov, A.A. Kachanov, V.R. Mironenko, T.V. Plakhotnik, Dependence of the sensitivity of intracavity laser spectroscopy on generation parameters. Opt. Commun. **46**(2), 126–130 (1983)
7.21. S.J. Harris, Intracavity laser spectroscopy: an old field with new prospects for combustion diagnostics. Appl. Opt. **23**(9), 1311–1318 (1984)
7.22. F. Stoeckel, G.H. Atkinson, Time evolution of a broadband quasi-cw dye laser: limitations of sensitivity in intracavity laser spectroscopy. Appl. Opt. **24**(21), 3591–3597 (1985)
7.23. A. O'Keefe, D.A.G. Deacon, Cavity ring-down optical spectrometer for absorption measurements using pulsed laser sources. Rev. Sci. Instrum. **59**(12), 2544–2551 (1988)
7.24. R. Engeln, G. Meijer, A Fourier transform cavity ring down spectrometer. Rev. Sci. Instrum. **67**(8), 2708–2714 (1996)
7.25. P. Zalicki, R.N. Zare, Cavity ring-down spectroscopy for quantitative absorption measurements. J. Chem. Phys. **102**(7), 2708–2717 (1995)
7.26. K.K. Lehman, D. Romanini, The superposition principle and cavity ring-down spectroscopy. J. Chem. Phys. **105**(23), 10263–10277 (1996)
7.27. J.T. Hodges, J.P. Looney, R.D. van Zee, Response of a ring-down cavity to an arbitrary excitation. J. Chem. Phys. **105**(23), 10278–10288 (1996)
7.28. J.T. Hodges, J.P. Looney, R.D. van Zee, Laser bandwidth effects in quantitative cavity ring-down spectroscopy. Appl. Opt. **35**(21), 4112–4116 (1996)
7.29. M. Billardon, M.E. Couprie, J.M. Ortega, M. Velghe, Fabry-Perot effects in the exponential decay and phase shift reflectivity measurement methods. Appl. Opt. **30**(3), 344–351 (1991)
7.30. R.D. van Zee, J.T. Hodges, J.P. Looney, Pulsed, single-mode cavity ringdown spectroscopy. Appl. Opt. **38**(18), 3951–3960 (1999)
7.31. J.L. Remo, Reflection losses for symmetrically perturbed curved reflectors in open resonators. Appl. Opt. **20**(17), 2997–3002 (1981)
7.32. H. Naus, I.H.M. van Stokkum, W. Hogervorst, W. Ubachs, Quantitative analysis of decay transients applied to a multimode pulsed cavity ringdown experiment. Appl. Opt. **40**(24), 4416–4426 (2001)
7.33. T. von Lerber, M.W. Sigrist, Cavity-ring-down principle for fiber-optic resonators: experimental realization of bending loss and evanescent-field sensing. Appl. Opt. **41**(18), 3567–3575 (2002)
7.34. K.K. Lehmann, Ring-down cavity spectroscopy cell using continuous wave excitation for trace species detection. U.S. Patent Number 5,528,040, 18 June 1996
7.35. B.A. Paldus, C.C. Harb, T.G. Spence, B. Wilke, J. Xie, J.S. Harris, R.N. Zare, Cavity-locked ringdown spectroscopy. J. Appl. Phys. **83**(8), 3991–3997 (1998)
7.36. J.W. Hahn, Y.S. Yoo, J.Y. Lee, J.W. Kim, H.-W. Lee, Cavity ringdown spectroscopy with a continuous-wave laser: calculation of coupling efficiency and a new spectrometer design. Appl. Opt. **38**(9), 1859–1866 (1999)
7.37. J.W. Kim, Y.S. Yoo, J.Y. Lee, J.B. Lee, J.W. Hahn, Uncertainty analysis of absolute concentration measurement with continuous-wave cavity ringdown spectroscopy. Appl. Opt. **40**(30), 5509–5516 (2001)

7.38. J.Y. Lee, H.-W. Lee, J.W. Kim, Y.S. Yoo, J.W. Hahn, Measurement of ultralow supermirror birefringence by use of the polarimetric differential cavity ringdown technique. Appl. Opt. **39**(12), 1941–1945 (2000)
7.39. G. Totschnig, D.S. Baer, J. Wang, F. Winter, H. Hofbauer, R.K. Hanson, Multiplexed continuous-wave diode-laser cavity ringdown measurements of multiple species. Appl. Opt. **39**(12), 2009–2016 (2000)
7.40. N.J. van Leeuwen, J.C. Diettrich, A.C. Wilson, Periodically locked continuous-wave cavity ringdown spectroscopy. Appl. Opt. **42**(18), 3670–3677 (2003)
7.41. A. Schocker, K. Kohse-Höinghaus, A. Brockhinke, Quantitative determination of combustion intermediates with cavity ring-down spectroscopy: systematic study in propene flames near the soot-formation limit. Appl. Opt. **44**(31), 6660–6672 (2005)
7.42. R.W.P. Drever, J.L. Hall, F.V. Kowalski, J. Hough, G.M. Ford, A.J. Munley, H. Ward, Laser phase and frequency stabilization using an optical resonator. Appl. Phys. B **31**(2), 97–105 (1983)
7.43. K. An, C. Yang, R.R. Dasari, M.S. Feld, Cavity ring-down technique and its application to the measurement of ultraslow velocities. Opt. Lett. **20**(9), 1068–1070 (1995)
7.44. M. Rakhmanov, Doppler-induced dynamics of fields in Fabry-Perot cavities with suspended mirrors. Appl. Opt. **40**(12), 1942–1949 (2001)
7.45. S.M. Ball, R.L. Jones, Broad-band cavity ring-down spectroscopy. Chem. Rev. **103**(12), 5239–5262 (2003)
7.46. S.E. Fiedler, A. Hese, A.A. Ruth, Incoherent broad-band cavity-enhanced absorption spectroscopy. Chem. Phys. Lett. **371**(3–4), 284–294 (2003)
7.47. J.M. Langridge, T. Laurila, R.S. Watt, R.L. Jones, C.F. Kaminski, J. Hult, Cavity enhanced absorption spectroscopy of multiple trace gas species using a supercontinuum radiation source. Opt. Express **16**(14), 10178–10188 (2007)
7.48. K.K. Lehmann, P.S. Johnston, P. Rabinowitz, Brewster angle prism retroreflectors for cavity enhanced spectroscopy. Appl. Opt. **48**(16), 2967–2978 (2009)
7.49. C. Petermann, P. Fischer, Actively coupled cavity ringdown spectroscopy with low-power broadband sources. Opt. Express **19**(11), 10164–10173 (2011)
7.50. J. Reid, M. El-Sherbiny, B.K. Garside, E.A. Ballik, Sensitivity limits of a tunable diode laser spectrometer, with application to the detection of NO_2 at the 100-ppt level. Appl. Opt. **19**(19), 3349–3354 (1980)
7.51. D.T. Cassidy, J. Reid, Harmonic detection with tunable diode lasers: two-tone modulation. Appl. Phys. B **29**(4), 279–285 (1982)
7.52. P. Werle, B. Jänker, High-frequency-modulation spectroscopy: phase noise and refractive index fluctuations in optical multipass cells. Opt. Eng. **35**(7), 2051–2057 (1996)
7.53. C.R. Webster, Brewster-plate spoiler: a novel method for reducing the amplitude of interference fringes that limit tunable-laser absorption sensitivities. J. Opt. Soc. Am. B **2**(9), 1464–1470 (1985)
7.54. J.A. Silver, A.C. Stanton, Optical interference fringe reduction in laser absorption experiments. Appl. Opt. **27**(10), 1914–1916 (1988)
7.55. A. Fried, J.R. Drummond, B. Henry, J. Fox, Reduction of interference fringes in small multipass absorption cells by pressure modulation. Appl. Opt. **29**(7), 900–902 (1990)
7.56. J.B. McManus, P.L. Kebabian, Narrow optical interference fringes for certain setup conditions in multipass absorption cells of the Herriott type. Appl. Opt. **29**(7), 898–900 (1990)
7.57. H.C. Sun, E.A. Whittaker, Novel etalon fringe rejection technique for laser absorption spectroscopy. Appl. Opt. **31**(24), 4998–5002 (1992)
7.58. D.E. Cooper, J.P. Watjen, Two-tone optical heterodyne spectroscopy with a tunable lead-salt diode laser. Opt. Lett. **11**(10), 606–608 (1986)
7.59. D.E. Cooper, C.B. Carlisle, High-sensitivity FM spectroscopy with a lead-salt diode laser. Opt. Lett. **13**(9), 719–721 (1988)

7.60. G. Durry, T. Danguy, I. Pouchet, Open multipass absorption cell for in situ monitoring of stratospheric trace gas with telecommunication laser diodes. Appl. Opt. **41**(3), 424–433 (2002)
7.61. S. Hocquet, D. Penninckx, E. Bordenave, C. Gouedard, Y. Jaouen, FM-to-AM conversion in high-power lasers. Appl. Opt. **47**(18), 3338–3349 (2008)
7.62. X. Dangpeng, W. Jianjun, L. Mingzhong, L. Honghuan, Z. Rui, D. Ying, D. Qinghua, H. Xiaodong, W. Mingzhe, D. Lei, T. Jun, Weak etalon effect in wave plates can introduce significant FM-to-AM modulations in complex laser systems. Opt. Express **18**(7), 6621–6627 (2010)
7.63. D. Romanini, A.A. Kachanov, J. Morville, M. Chenevier, Measurement of trace gases by diode laser cavity ringdown spectroscopy, in *Proceedings of SPIE*, vol. 3821, pp. 94–104, 1999; Z. Tan, X. Long, A developed optical-feedback cavity ring-down spectrometer and its application. Appl. Spectrosc. **66**(5), 492–495 (2012)
7.64. J. Courtois, J.T. Hodges, Coupled-cavity ring-down spectroscopy technique. Opt. Lett. **37**(16), 3354–3356 (2012); J. Courtois, K. Bielska, J.T. Hodges, Differential cavity ring-down spectroscopy. J. Opt. Soc. Am. B **30**(6), 1486–1495 (2013)
7.65. Z. Li, W. Ma, X. Fu, W. Tan, G. Zhao, L. Dong, L. Zhang, W. Yin, S. Jia, Continuous-wave cavity ringdown spectroscopy based on the control of cavity reflection. Opt. Express **21**(15), 17961–17971 (2013)
7.66. A. Cygan, D. Lisak, P. Morzynski, M. Bober, M. Zawada, E. Pazderski, R. Ciuryło, Cavity mode-width spectroscopy with widely tunable ultra narrow laser. Opt. Express **21**(24), 29744–29754 (2013)
7.67. J. Burkart, D. Romanini, S. Kassi, Optical feedback frequency stabilized cavity ring-down spectroscopy. Opt. Lett. **39**(16), 4695–4698 (2014)
7.68. B. Li, H. Cui, Y. Han, L. Gao, C. Guo, C. Gao, Y. Wang, Simultaneous determination of optical loss, residual reflectance and transmittance of highly anti-reflective coatings with cavity ring down technique. Opt. Express **22**(23), 29135–29142 (2014)
7.69. L.E. McHale, A. Hecobian, A.P. Yalin, Open-path cavity ring-down spectroscopy for trace gas measurements in ambient air. Opt. Express **24**(5), 5523–5535 (2016)
7.70. H. Cui, B. Li, Y. Han, J. Wang, C. Gao, Y. Wang, Extinction measurement with open-path cavity ring-down technique of variable cavity length. Opt. Express **24**(12), 13343–13350 (2016)
7.71. A. Karpf, G.N. Rao, Real-time trace gas sensor using a multimode diode laser and multiple-line integrated cavity enhanced absorption spectroscopy. Appl. Opt. **54**(19), 6085–6092 (2015)
7.72. G. Zhao, T. Hausmaninger, W. Ma, O. Axner, Whispering-gallery-mode laser-based noiseimmune cavity-enhanced optical heterodyne molecular spectrometry. Opt. Lett. **42**(16), 3109–3112 (2017)

Chapter 8

8.1. V.V. Appolonov, A.I. Barchukov, V.K. Konukhov, Measurements of scattering of laser mirrors reflecting main CO_2 laser beams. Quantum Electron. **4**(16), 103–105 (1973)
8.2. O. De-Lange, Long-distance directional transmission of light signals. Proc. IEEE **1**(10), 1350 (1963)
8.3. L.S. Kornienko, B.G. Skuibin, About a possibility of measurements of selective optical losses. Opt. Spectrosc. **40**(3), 571–573 (1976)
8.4. E.S. Voropai, A.M. Sarzhevskii, P.A. Torpachev, Procedure for measuring small optical losses. J. Appl. Spectrosc. **34**(1), 115–119 (1981)
8.5. J. Brochard, Ph. Cahuzac, Application des techniques d'absorption saturée á l'értitude de la relaxion des vitesses d'atomes me'tastables sous l'effet des choes e'lastiques. J. Phys. B: Atom. Mol. Phys. **9**(12), 2027–2034 (1976)

8.6. A.J. Rock, M.R. Biazzo, A technique for measuring small optical loss using an oscillating spherical interferometer. Bell Syst. Tech. J. **43**(4), 1563–1579 (1964)
8.7. N.K. Berger, E.N. Bondarchuk, V.V. Dembovetskiy, *Method of Laser-Mirror Reflectance Measurements* (Avtometria, Moscow, 1977), No. 1, pp. 109–111
8.8. Ph Cahuzac, G. Golman, Mesure des pouvoirs re'flecteurs e'leve's a l'aide d'une cavité optique a réflexion multiples. Nouv. Rev. Optique **7**(6), 363–367 (1976)
8.9. J.M. Herbelin, J.A. McKay, M.A. Kwok, R.H. Ueunten, D.S. Ureving, D.J. Spencer, D.J. Benard, Sensitive measurement of photon lifetime and true reflectances in an optical cavity by a phase-shift method. Appl. Opt. **19**(1), 144–147 (1980)
8.10. J.M. Herbelin, J.A. McKay, Development of laser mirrors of very high reflectivity using the cavity attenuated phase-shift method. Appl. Opt. **20**(19), 3341–3344 (1980)
8.11. M.A. Kwok, J.M. Herbelin, R.H. Ueunten, Cavity phase-shift method for high reflectance measurements at mid-infrared wavelength. Opt. Eng. **21**(6), 979–982 (1982)
8.12. D.Z. Anderson, J.C. Frisch, C.S. Masser, Mirror reflectometer based on optical cavity decay time. Appl. Opt. **23**(8), 1238–1245 (1984)
8.13. R. Engeln, G. von Helden, G. Berden, G. Meijer, Phase shift cavity ring down absorption spectroscopy. Chem. Phys. Lett. **262**(1–2), 105–109 (1996)
8.14. G. Rempe, R.J. Thompson, H.J. Kimble, R. Lalezari, Measurement of ultralow losses in an optical interferometer. Opt. Lett. **17**(5), 363–365 (1992)
8.15. M.A. Bukhshtab, Resonator technique for absolute reflection and transmission measurements. J. Appl. Spectrosc. **37**(5), 1330–1335 (1982)
8.16. Y. Le Grand, A. Le Floch, Measurement of residual reflectivities using the two eigenstates of a passive cavity. Appl. Opt. **27**(23), 4925–4930 (1988)
8.17. D. Jacob, F. Bretenaker, P. Pourcelot, Ph. Rio, M. Dumont, A. Dore, Pulsed measurement of high-reflectivity mirror phase retardance. Appl. Opt. **33**(15), 3175–3178 (1994)
8.18. E.R. Crosson, P. Haar, G.A. Marcus, H.A. Schwettman, B.A. Paldus, T.G. Spence, R.N. Zare, Pulse-stacked cavity ring-down spectroscopy. Rev. Sci. Instrum. **70**(1), 4–10 (1999)
8.19. W.H. Knox, N.M. Pearson, K.D. Li, Ch.A. Hirlimann, Interferometric measurements of femtosecond group delay in optical components. Opt. Lett. **13**(7), 574–576 (1988)
8.20. K. Naganuma, K. Mogi, H. Yamada, Group-delay measurement using the Fourier transform of an interferometric cross correlation generated by white light. Opt. Lett. **15**(7), 393–395 (1990)
8.21. A.P. Kovàcs, K. Osvay, Zs Bor, R. Szipöcs, Group-delay measurement on laser mirrors by spectrally resolved white light interferometry. Opt. Lett. **20**(7), 788–790 (1995)
8.22. W.H. Knox, In situ measurement of complete intracavity dispersion in an operating Ti: sapphire femtosecond laser. Opt. Lett. **17**(7), 514–516 (1992)
8.23. W.H. Knox, Dispersion measurements for femtosecond-pulse generation and applications. Appl. Phys. B **58**, 225–235 (1994)
8.24. K. Naganuma, Y. Sakai, Interferometric measurement of wavelength dispersion of femtosecond laser cavities. Opt. Lett. **19**(7), 487–489 (1994)
8.25. M.A. Bukhshtab, Low phase dispersion measurements of laser cavity components by spectro-photometric resonating technique, in *OSA Annual Meeting—ILS-X Conference*, Dallas, p. 145 (1994)
8.26. M.A. Bukhshtab, Spectrophotometric resonant measurement of wavelength phase dispersion on femtosecond laser cavities and single elements during their fabrication. Opt. Commun. **123**(4–6), 430–436 (1996)
8.27. Y. Le Grand, A. Le Froch, Sensitive dichroism measurement using eigenstate decay times. Appl. Opt. **29**(9), 1244–1246 (1990)
8.28. A. Miks, J. Novak, P. Novak, Colorimetric method for phase evaluation. J. Opt. Soc. Am. A **23**(4), 894–901 (2006)

8.29. T.G. Spence, C.C. Harb, B.A. Paldus, R.N. Zare, B. Willke, R.L. Byer, A laser-locked cavity ring-down spectrometer employing an analog detection scheme. Rev. Sci. Instrum. **71**(2), 347–353 (2000)
8.30. J.B. Paul, L. Lapson, J.G. Anderson, Ultrasensitive absorption spectroscopy with a high-finesse optical cavity and off-axis alignment. Appl. Opt. **40**(27), 4904–4910 (2001)
8.31. K.D. Skeldon, G.M. Gibson, C.A. Wyse, L.C. McMillan, S.D. Monk, C. Longbottom, M.J. Padgett, Development of high-resolution real-time sub-ppb ethane spectroscopy and some pilot studies in life science. Appl. Opt. **44**(22), 4712–4721 (2005)
8.32. S.D. Dyer, K.B. Rochford, A.H. Rose, Fast and accurate low-coherence interferometric measurements of fiber Bragg grating dispersion and reflectance. Opt. Express **5**(11), 262–266 (1999)
8.33. M.J. Thorpe, R.J. Jones, K.D. Moll, J. Ye, R. Lalezari, Precise measurements of optical cavity dispersion and mirror coating properties via femtosecond combs. Opt. Express **13**(3), 882–888 (2005)
8.34. N. Uehara, A. Ueda, K. Ueda, H. Sekiguchi, T. Mitake, K. Nakamura, N. Kitajima, I. Kataoka, Ultralow-loss mirror of parts-in-10^6 level at 1064 nm. Opt. Lett. **20**(6), 530–532 (1995)
8.35. K. An, B.A. Sones, C. Fang-Yen, R.R. Dasari, M.S. Feld, Optical bistability induced by mirror absorption: measurement of absorption coefficients at the sub-ppm level. Opt. Lett. **22**(18), 1433–1435 (1997)
8.36. C.J. Hood, H.J. Kimble, J. Ye, Characterization of high-finesse mirrors: loss, phase shifts, and mode structure in an optical cavity. Phys. Rev. A **64**, Article 033804 (2001)
8.37. G. Li, Y. Zhang, Y. Li, X. Wang, J. Zhang, J. Wang, T. Zhang, Precision measurement of ultralow losses of an asymmetric optical microcavity. Appl. Opt. **45**(29), 7628–7631 (2006)
8.38. M. Borselli, T.J. Johnson, O. Painter, Accurate measurement of scattering and absorption loss in microphotonic devices. Opt. Lett. **32**(20), 2954–2956 (2007)
8.39. G. Farca, S.I. Shopova, A.T. Rosenberger, Cavity-enhanced laser absorption spectroscopy using microresonator whispering-gallery modes. Opt. Express **15**(25), 17443–17448 (2007)
8.40. J. Poirson, F. Bretenaker, M. Vallet, A. Le Floch, Analytical and experimental study of ringing effects in a Fabry-Perot cavity. Application to the measurement of high finesses. JOSA B **14**(11), 2811–2817 (1997)
8.41. C.R. Bucher, K.K. Lehmann, D.F. Plusquellic, G.T. Fraser, Doppler-free nonlinear absorption in ethylene by use of continuous-wave cavity ringdown spectroscopy. Appl. Opt. **39**(18), 3154–3164 (2000)
8.42. I. Debecker, A.K. Mohamed, D. Romanini, High-speed cavity ringdown spectroscopy with increased spectral resolution by simultaneous laser and cavity tuning. Opt. Express **13**(8), 2906–2915 (2005)
8.43. Y. He, B.J. Orr, Continuous-wave cavity ringdown absorption spectroscopy with a swept-frequency laser: rapid spectral sensing of gas-phase molecules. Appl. Opt. **44**(31), 6752–6761 (2005)
8.44. J. Courtois, A.K. Mohamed, D. Romanini, High-speed off-axis cavity ring-down spectroscopy with a re-entrant configuration for spectral resolution enhancement. Opt. Express **18**(5), 4845–4858 (2010)
8.45. M.C. Kuoa, Y.R. Lina, W.A.A. Syeda, J.T. Shya, Precision continuous wave cavity ringdown spectroscopy of CO_2 at 1064 nm. Opt. Spectrosc. **108**(1), 29–36 (2010)
8.46. C. Froehly, A. Lacourt, J.C. Viénot, Time impulse response and time frequency response of optical pupils: experimental confirmations and applications. Nouv. Rev. Opt. **4**(4), 183–196 (1973)
8.47. A.M. Weiner, D.E. Leaird, D.H. Reitze, E.G. Paek, Femtosecond spectral holography. IEEE J. Quantum Electron. **28**(10), 2251–2261 (1992)

8.48. L. Lepetit, G. Chériaux, M. Joffre, Linear techniques of phase measurement by femtosecond spectral interferometry for applications in spectroscopy. J. Opt. Soc. Am. B **12**(12), 2467–2474 (1995)
8.49. D. Meshulach, D. Yelin, Y. Silberberg, White light dispersion measurements by one- and two-dimensional spectral interference. IEEE J. Quantum Electron. **33**(11), 1969–1974 (1997)
8.50. A. Börzsönyia, A.P. Kovácsa, M. Görbea, K. Osvaya, Advances and limitations of phase dispersion measurement by spectrally and spatially resolved interferometry. Opt. Commun. **281**(11), 3051–3061 (2008)
8.51. I. Pupeza, X. Gu, E. Fill, T. Eidam, J. Limpert, A. T¨unnermann, F. Krausz, T. Udem, Highly sensitive dispersion measurement of a high-power passive optical resonator using spatial-spectral interferometry. Opt. Express **18**(25), 26184–26195 (2010)
8.52. A. Schliesser, C. Gohle, T. Udem, T.W. Hänsch, Complete characterization of a broadband high-finesse cavity using an optical frequency comb. Opt. Express **14**(13), 5975–5983 (2006)
8.53. M. Milosevic, S.W. King, Spectroscopic method for measuring refractive index. Appl. Opt. **52**(19), 4477–4482 (2013)
8.54. M.I. Cheema, S. Mehrabani, A.A. Hayat, Y.-A. Peter, A.M. Armani, A.G. Kirk, Simultaneous measurement of quality factor and wavelength shift by phase shift microcavity ring down spectroscopy. Opt. Express **20**(8), 9090–9098 (2012)
8.55. K. Stamataki, V. Papadakis, M.A. Everest, S. Tzortzakis, B. Loppinet, T.P. Rakitzis, Monitoring adsorption and sedimentation using evanescent-wave cavity ringdown ellipsometry. Appl. Opt. **52**(5), 1086–1093 (2013)
8.56. T.H. Stievater, M.W. Pruessner, D. Park, W.S. Rabinovich, R.A. McGill, D.A. Kozak, R. Furstenberg, S.A. Holmstrom, J.B. Khurgin, Trace gas absorption spectroscopy using functionalized microring resonators. Opt. Lett. **39**(4), 969–972 (2014)
8.57. J.A. Barnes, G. Gagliardi, H.-P. Loock, Absolute absorption cross-section measurement of a submonolayer film on a silica microresonator. Optica **1**(2), 75–83 (2014)
8.58. T. Grosz, A.P. Kovacs, K. Varju, Chromatic dispersion measurement along both polarization directions of a birefringent hollow-core photonic crystal fiber using spectral interferometry. Appl. Opt. **56**(19), 5369–5376 (2017)

Chapter 9

9.1. H. Daglish, C. North, Watching light waves decline. New Sci. **48**(721), 14–15 (1970)
9.2. D.A. Pinnow, T.C. Rich, Development of a calorimetric method for making precision optical absorption measurements. Appl. Opt. **12**(5), 984–992 (1973)
9.3. L.H. Scolnic, A review of techniques for measuring small optical losses in infrared transmitting materials, in *Optical Properties of Highly Transparent Solids*, ed. by S.S. Mitra, B. Bendow (Plenum, New York, 1975), pp. 405–434
9.4. H.B. Rosenstock, M. Hass, D.A. Gregory, J.A. Harrington, Analysis of laser calorimetric data. Appl. Opt. **16**(11), 2837–2842 (1977)
9.5. H.B. Rosenstock, D.A. Gregory, J.A. Harrington, Infrared bulk and surface absorption by nearly transparent crystals. Appl. Opt. **15**(9), 2075–2079 (1976)
9.6. H.S. Carslaw, J.C. Jaeger, *Conduction of Heat in Solids* (Oxford University Press, London, 1969)
9.7. P.J. Severin, Calorimetric measurements of weakly absorbing materials: theory. Appl. Opt. **18**(10), 1546–1554 (1976); P.J. Severin, H. van Esveld, Calorimetric measurements of the absorption coefficient of fiber quality glass: experiment. Appl. Opt. **20**(10), 1833–1839 (1981)
9.8. P.A. Miles, Static profile calorimetry of laser materials. Appl. Opt. **16**(11), 2897–2901 (1977)

9.9. M. Hass, J.W. Davidson, H.B. Rosenstock, J. Babiskin, Measurement of very low absorption coefficient by laser calorimetry. Appl. Opt. **14**(5), 1128–1129 (1975)
9.10. J.E. Midwinter, *Optical Fibers for Transmission* (Wiley, New York, 1979)
9.11. D. Bunimovich, L. Nagli, A. Katzir, Absorption measurements of mixed silver halide crystals and fibers by laser calorimetry. Appl. Opt. **33**(1), 117–119 (1994)
9.12. J.A. Harrington, M. Braunstein, J.E. Rudisill, Measuring the infrared absorption in thin-film coatings. Appl. Opt. **16**(11), 2843–2846 (1977)
9.13. E.G. Bernal, Heat flow analysis of laser absorption calorimetry. Appl. Opt. **14**(2), 314–321 (1975)
9.14. H. Ahrens, H. Welling, H.E. Scheel, Measurement of optical absorption in dielectric reflectors. Appl. Phys. **1**, 69–71 (1973)
9.15. N.K. Sahoo, K.V.S.R. Apparao, Laser calorimeter for UV absorption measurement of dielectric thin films. Appl. Opt. **31**(28), 6111–6116 (1992)
9.16. P.A. Temple, Experimental and theoretical considerations in thin film laser calorimetry. Opt. Eng. **23**(3), 326–330 (1984)
9.17. R.A. Hoffman, Apparatus for the measurement of optical absorptivity in laser mirrors. Appl. Opt. **13**(6), 1405–1410 (1974)
9.18. D. Bunimovich, E. Belotserkovsky, L. Nagli, A. Katzir, Measurements of absorption coefficients using noncontact fiber-optic laser calorimetry. Appl. Opt. **34**(4), 743–745 (1995)
9.19. R.C.C. Leite, R.S. Moore, J.R. Whinnery, Low absorption measurements using an He–Ne laser. Appl. Phys. Lett. **5**(7), 141–14 (1964); J.P. Gordon, R.C.C. Leite, R.S. Moore, S.P.S. Porto, J.R. Whinnery, Long-transient effects in lasers with inserted liquid samples. J. Appl. Phys. **36**(1), 3–8 (1965)
9.20. Ch. Hu, J.R. Whinnery, New thermooptical measurement method and a comparison with other methods. Appl. Opt. **12**(1), 72–79 (1973)
9.21. J. Stone, Measurement of the absorption of light in low-loss liquids. J. Opt. Soc. Am. **62**(3), 327–333 (1972); Thermooptical technique for the measurement of absorption loss spectrum in liquids. Appl. Opt. **12**(8), 1828–1830 (1973)
9.22. D. Solimini, Accuracy and sensitivity of the thermal lens method for measuring absorption. Appl. Opt. **5**(12), 1931–1939 (1966)
9.23. S.J. Sheldon, L.V. Knight, J.M. Thorne, Laser-induced thermal lens effect: a new theoretical model. Appl. Opt. **21**(9), 1663–1669 (1982)
9.24. C.A. Carter, J.M. Harris, Comparison of models describing the thermal lens effect. Appl. Opt. **23**(3), 476–481 (1984)
9.25. S.E. Bialkowski, A. Chartier, Diffraction effects in single- and two-laser photothermal lens spectroscopy. Appl. Opt. **36**(27), 6711–6721 (1997)
9.26. J.F. Power, E.D. Salin, Mode-mismatched laser induced thermal lens effect detection via spatial fourier analysis of beam profiles. Anal. Chem. **60**(9), 838–842 (1988); J.F. Power, Pulsed mode thermal lens effect detection in the near field via thermally induced probe beam spatial phase modulation: a theory. Appl. Opt. **29**(1), 52–63 (1990)
9.27. A.C. Boccara, D. Fournier, W. Jackson, N.M. Amer, Sensitive photothermal deflection technique for measuring absorption in optically thin media. Opt. Lett. **5**(9), 377–379 (1980)
9.28. W.B. Jackson, N.M. Amer, A.C. Boccara, D. Fournier, Photothermal deflection spectroscopy and detection. Appl. Opt. **20**(8), 1333–1344 (1981)
9.29. M. Commandré, P. Roche, J.-P. Borgogno, G. Albrand, Absorption mapping for characterization of glass surfaces. Appl. Opt. **34**(13), 2372–2379 (1995)
9.30. M. Commandré, E. Pelletier, Measurements of absorption losses in TiO_2 films by a collinear photothermal deflection technique. Appl. Opt. **29**(28), 4276–4280 (1990)
9.31. M. Commandré, P. Roche, Characterization of optical coatings by photothermal deflection. Appl. Opt. **35**(25), 5021–5034 (1996)

9.32. A. Gatto, M. Commandré, Multiscale mapping technique for the simultaneous estimation of absorption and partial scattering in optical coatings. Appl. Opt. **41**(1), 225–234 (2002)
9.33. V. Loriette, C. Boccara, Absorption of low-loss optical materials measured at 1064 nm by a position-modulated collinear photothermal detection technique. Appl. Opt. **42**(4), 649–656 (2003)
9.34. R. Chow, J.R. Taylor, Z.L. Wu, Absorptance behavior of optical coatings for high-average-power laser applications. Appl. Opt. **39**(4), 650–658 (2000)
9.35. B. Li, S. Martin, E. Welsch, In situ measurement on ultraviolet dielectric components by a pulsed top-hat beam thermal lens. Appl. Opt. **39**(25), 4690–4697 (2000)
9.36. S.F. Pellicori, H.L. Hettich, Reversible spectral shift in coatings. Appl. Opt. **27**(15), 3061–3062 (1988)
9.37. H. Takashashi, Temperature stability of thin-film narrowbandpass filters produced by ion-assisted deposition. Appl. Opt. **34**(4), 667–675 (1995)
9.38. E. Welsch, D. Ristau, Photothermal measurements on optical thin films. Appl. Opt. **34**(31), 7239–7253 (1995)
9.39. L. Gallaisand, M. Commandré, Photothermal deflection in multilayer coatings: modeling and experiment. Appl. Opt. **44**(25), 5230–5238 (2005)
9.40. H. Hao, B. Li, Photothermal detuning for absorption measurement of optical coatings. Appl. Opt. **47**(2), 188–194 (2008)
9.41. B. Li, H. Blaschke, D. Ristau, Combined laser calorimetry and photothermal technique for absorption measurement of optical coatings. Appl. Opt. **45**(23), 5827–5831 (2006)
9.42. B. Li, S. Martin, E. Welsch, Pulsed top-hat beam thermal-lens measurement for ultraviolet dielectric coatings. Opt. Lett. **24**(20), 1398–1400 (1999)
9.43. S.E. Bialkowski, Accounting for absorption saturation effects in pulsed infrared laser-excited photothermal spectroscopy. Appl. Opt. **32**(18), 3177–3189 (1993)
9.44. A. Hordvic, Measurement techniques for small absorption coefficients: recent advances. Appl. Opt. **16**(11), 2827–2833 (1977)
9.45. M. Itoh, I. Ogura, Absorption measurements of laser optical materials by interferometric calorimetry. J. Appl. Phys. **53**(7), 5140–5145 (1982)
9.46. A.A. Gilionis, P.Yu. Krauialis, A.K. Maldutis, Yu.I. Reksnis, S.B. Sakalauskas, Evaluation of optical characteristics of solid materials by thermooptical method using pulsed laser radiation, in *Theses of the IVth Conference on Nonresonance Light Interactions with Mediums*, Leningrad, GOI, 1978, pp. 183–184
9.47. P.-K. Kuo, M. Munidasa, Single-beam interferometry of a thermal bump. Appl. Opt. **29**(36), 5326–5331 (1990)
9.48. A. Cournoyer, P. Baulaigue, E. Lazarides, H. Blancher, L. Bertrand, R. Occelli, Photothermal measurements with a Jamin interferometer. Appl. Opt. **36**(21), 5252–5261 (1997)
9.49. S. Hild, H. Lück, W. Winkler, K. Strain, H. Grote, J. Smith, M. Malec, M. Hewitson, B. Willke, J. Hough, K. Danzmann, Measurement of a low-absorption sample of OH-reduced fused silica. Appl. Opt. **45**(28), 7269–7272 (2006)
9.50. D. Ottaway, J. Betzwieser, S. Ballmer, S. Waldman, W. Kells, In situ measurement of absorption in high-power interferometers by using beam diameter measurements. Opt. Lett. **31**(4), 450–452 (2006)
9.51. L.B. Glebov, V.G. Dokuchaev, Measurements of low absorption extents by a polarization calorimetric method. J. Opt. Technol. **51**(2), 52–54 (1984)
9.52. D.A. Cremers, R.A. Keller, Thermooptic-based differential measurements of weak solute absorptions with an interferometer. Appl. Opt. **21**(9), 1654–1662 (1982)
9.53. A. Rosencwaig, A. Gersho, Theory of the photoacoustic effect with solids. J. Appl. Phys. **47**(1), 64–69 (1976)
9.54. A. Hordvic, H. Schlossberg, Photoacoustic technique for determining optical absorption coefficients in solids. Appl. Opt. **16**(1), 101–107 (1977)

9.55. A. Rosencwaig, *Photoacoustics and Photoacoustic Spectroscopy* (Wiley, New York, 1980)
9.56. V.P. Zharov, V.S. Letokhov, in *Laser Optoacoustic Spectroscopy*, ed. by A.M. Bonch-Bruevich (Moscow, Nauka, 1984; Springer, Berlin, 1986)
9.57. Y.C. Teng, B.S.H. Royce, Absolute optical absorption coefficient measurements using photoacoustic spectroscopy amplitude and phase information. J. Opt. Soc. Am. **70**(5), 557–560 (1980)
9.58. V.P. Novikov, M.A. Novikov, Pulsed photoacoustic method for measurement of bulk absorption in crystals. J. Appl. Spectrosc. **40**(3), 499–502 (1984)
9.59. A.A. Betin, O.V. Mitropolskii, V.P. Novikov, M.A. Novikov, Study of optical losses in IR optical materials by laser photoacoustic method. Quantum Electron. **12**(9), 1856–1862 (1985)
9.60. S.A. Vinokurov, Surface and bulk absorption at photoacoustic measurements. J. Opt. Technol. **50**(10), 14–16 (1983)
9.61. M. Itoh, H. Saito, Pulsed photoacoustic technique to measure the absorption coefficients of the highly transparent optical materials. Opt. Commun. **44**(4), 229–231 (1983)
9.62. M.Y. Raja, D.W. Reicher, S.R.J. Brueck, J.R. McNeil, D.E. Oates, High-sensitivity surface-photoacoustic spectroscopy. Opt. Lett. **15**(1), 66–68 (1990)
9.63. E.L. Kerr, J.G. Atwood, The laser illuminated absorptivity spectrophone: a method for measurement of weak absorptivity in gases at laser wavelengths. Appl. Opt. **7**(5), 915–921 (1968)
9.64. J.G. Parker, Optical absorption in glass: investigation using an acoustic technique. Appl. Opt. **12**(12), 2974–2977 (1973)
9.65. L.-G. Rosengren, Optimal optoacoustic detector design. Appl. Opt. **14**(8), 1960–1976 (1975)
9.66. J.F. McClelland, R.N. Kniseley, Photoacoustic spectroscopy with condensed samples. Appl. Opt. **15**(11), 2658–2663 (1976)
9.67. A.C. Tam, C.K.N. Patel, Optical absorptions of light and heavy water by laser optoacoustic spectroscopy. Appl. Opt. **18**(19), 3348–3358 (1979)
9.68. L.B. Kreuzer, Ultralow gas concentration infrared absorption spectroscopy. J. Appl. Phys. **42**(7), 2934–2943 (1971)
9.69. P.C. Claspy, C. Ha, Y.-H. Pao, Optoacoustic detection of NO_2 using a pulsed dye laser. Appl. Opt. **16**(11), 2972–2973 (1977)
9.70. C.F. Dewey Jr., R.D. Kamm, C.E. Hackett, Acoustic amplifier for detection of atmospheric pollutants. Appl. Phys. Lett. **23**(11), 633–635 (1973)
9.71. M.W. Sigrist, Laser generation of acoustic waves in liquids and gases. J. Appl. Phys. **60**(7), R83 (1986)
9.72. P.L. Meyer, M.W. Sigrist, Atmospheric pollution monitoring using CO_2-laser photoacoustic spectroscopy and other techniques. Rev. Sci. Instrum. **61**(7), 1779–1807 (1990)
9.73. R.P. Fiegel, P.B. Hays, W.M. Wright, Photoacoustic technique for the measurement of absorption line profiles. Appl. Opt. **28**(7), 1401–1408 (1989)
9.74. M.A. Gondal, Laser photoacoustic spectrometer for remote monitoring of atmospheric pollutants. Appl. Opt. **36**(15), 3195–3201 (1997)
9.75. M. Harris, G.N. Pearson, D.V. Willetts, K. Ridley, P.R. Tapster, B. Perrett, Pulsed indirect photoacoustic spectroscopy: application to remote detection of condensed phases. Appl. Opt. **39**(6), 1032–1040 (2000)
9.76. M. Fiedler, P. Hess, Frequency domain analysis of acoustic resonances excited with single laser pulses, in *Photoacoustic and Photothermal Phenomena*, ed. by J.C. Murphy, J.W. Maclachlan-Spicer, L.C. Aamodt, B.S.H. Royce. Springer Series in Optical Sciences, vol. 62 (Springer, Berlin, 1990), pp. 344–346

9.77. A. Miklós, C. Brand, A. Winkler, P. Hess, Effective noise reduction on pulsed laser excitation of modes in a high-Q photoacoustic resonator. J. Phys. IV **4**(7), 781–784 (1994)
9.78. C. Brand, A. Winkler, P. Hess, A. Miklós, Z. Bozoki, J. Sneider, Pulsed-laser excitation of acoustic modes in open high-Q photoacoustic resonators for trace gas monitoring: results for C_2H_4. Appl. Opt. **34**(18), 3257–3266 (1995)
9.79. P. Repond, M.W. Sigrist, Photoacoustic spectroscopy on trace gases with continuously tunable CO_2 laser. Appl. Opt. **35**(21), 4065–4085 (1996)
9.80. G. Busse, D. Herboeck, Differential Helmholtz resonator as an optoacoustic detector. Appl. Opt. **18**(23), 3959–3961 (1979)
9.81. J. Peizi, K. Klein, O. Nordhaus, Extended Helmholtz resonator in low-temperature photoacoustic spectroscopy. Appl. Opt. **21**(1), 94–99 (1982)
9.82. S. Schafer, A. Miklós, P. Hess, Quantitative signal analysis in pulsed resonant photoacoustics. Appl. Opt. **36**(15), 3202–3211 (1997)
9.83. A. Miklós, C.-H. Lim, W.-W. Hsiang, G.-C. Liang, A.H. Kung, A. Schmohl, P. Hess, Photoacoustic measurement of methane concentrations with a compact pulsed optical parametric oscillator. Appl. Opt. **41**(15), 2985–2993 (2002)
9.84. J. Henningsen, N. Melander, Sensitive measurement of adsorption dynamics with nonresonant gas phase photoacoustics. Appl. Opt. **36**(27), 7037–7045 (1997)
9.85. A. Schmohl, A. Miklós, P. Hess, Effects of adsorption–desorption processes on the response time and accuracy of photoacoustic detection of ammonia. Appl. Opt. **40**(15), 2571–2578 (2001)
9.86. A. Miklos, P. Hess, Z. Bozoki, Application of acoustic resonators in photoacoustic trace gas analysis and metrology. Rev. Sci. Instrum. **72**(4), 1937–1955 (2001)
9.87. M.E. Webber, M. Pushkarsky, C.N. Patel, Fiber-amplifier-enhanced photoacoustic spectroscopy with near-infrared tunable diode lasers. Appl. Opt. **42**(12), 2119–2126 (2003)
9.88. Z. Bozóki, A. Mohácsi, G. Szabó, Z. Bor, M. Erdélyi, W. Chen, F.K. Tittel, Near-infrared diode laser based spectroscopic detection of ammonia: a comparative study of photoacoustic and direct optical absorption methods. Appl. Spectrosc. **56**(6), 715–719 (2002)
9.89. H.O. McMahon, Thermal radiation from partially transparent reflecting bodies. J. Opt. Soc. Am. **40**(6), 376–380 (1950)
9.90. D. Weber, Low-temperature, directional, spectral emissivity of translucent solids. J. Opt. Soc. Am. **50**(8), 808–810 (1960)
9.91. D.L. Stierwalt, Infrared spectral emittance measurements of optical materials. Appl. Opt. **5**(12), 1911–1915 (1966)
9.92. R.P. Heinisch, R.N. Schmidt, Development and application of an instrument for the measurement of directional emittance of blackbody cavities. Appl. Opt. **9**(8), 1920–1925 (1970)
9.93. E.M. Sparrow, P.D. Kruger, R.P. Heinisch, Cavity methods for determining the emittance of solids. Appl. Opt. **12**(10), 2466–2471 (1973)
9.94. F.A. Benford, An absolute method for determining coefficients of diffuse reflection. Gen. Electr. Rev. **23**, 72–75 (1920)
9.95. F. Benford, The integrating factor of the photometric sphere. J. Opt. Soc. Am. **25**(10), 332–339 (1935)
9.96. P. Elterman, Integrating cavity spectroscopy. Appl. Opt. **9**(9), 2140–2142 (1970)
9.97. E.S. Fry, G.W. Kattawar, R.M. Pope, Integrating cavity absorption meter. Appl. Opt. **31**(12), 2055–2065 (1992)

9.98. R.M. Pope, E.S. Fry, Absorption spectrum 380–700 nm of pure water. II. Integrating cavity measurements. Appl. Opt. **36**(33), 8710–8722 (1997); see also: T.I. Quickenden, C.G. Freeman, R.A.J. Litjens, Some comments on the paper by E.S. Fry on the visible and near-ultraviolet absorption spectrum of liquid water. Appl. Opt. **39**(16), 2740–2742 (2000)
9.99. J.T.O. Kirk, Modeling the performance of an integrating-cavity absorption meter: theory and calculations for a spherical cavity. Appl. Opt. **34**(21), 4397–4408 (1995)
9.100. D.M. Hobbs, N.J. McCormick, Design of an integrating cavity absorption meter. Appl. Opt. **38**(3), 456–461 (1999)
9.101. J.T.O. Kirk, Point-source integrating-cavity absorption meter: theoretical principles and numerical modeling. Appl. Opt. **36**(24), 6123–6128 (1997)
9.102. R.A. Leathers, T.V. Downes, C.O. Davis, Analysis of a point-source integrating-cavity absorption meter. Appl. Opt. **39**(33), 6118–6127 (2000)
9.103. G.M. Hale, M.R. Querry, Optical constants of water in the 200-nm to 200-Mm wavelength region. Appl. Opt. **12**(3), 555–563 (1973)
9.104. R. Röttgers, W. Schönfeld, P.-R. Kipp, R. Doerffer, Practical test of a point-source integrating cavity absorption meter: the performance of different collector assemblies. Appl. Opt. **44**(26), 5549–5560 (2005)
9.105. D.J. Gray, G.W. Kattawar, E.S. Fry, Design and analysis of a flow-through integrating cavity absorption meter. Appl. Opt. **45**(35), 8990–8998 (2006)
9.106. J.A. Musser, E.S. Fry, D.J. Gray, Flow-through integrating cavity absorption meter: experimental results. Appl. Opt. **48**(19), 3596–3602 (2009)
9.107. S. Tranchart, I. Hadj Bachir, J.-L. Destombes, Sensitive trace gas detection with near-infrared laser diodes and an integrating sphere. Appl. Opt. **36**(35), 7070–7074 (1996)
9.108. J.L. Keef, J.F. Clare, K.J. Thome, Analytical solution for integrating sphere spectral efficiency inclusive of atmospheric attenuation. Appl. Opt. **47**(2), 253–262 (2008)
9.109. A.D. Clarke, Integrating sandwich: a new method of measurement of the light absorption coefficient for atmospheric particles. Appl. Opt. **21**(16), 3011–3020 (1982); R.M. Abdullin, A.V. Lebedev, Use of an integrating sphere as a multipass optical cell. J. Opt. Technol. **55**(3), 139–141 (1988)
9.110. E.S. Fry, J. Musser, G.W. Kattawar, P.-W. Zhai, Integrating cavities: temporal response. Appl. Opt. **45**(36), 9053–9065 (2006)
9.111. J. Hodgkinson, D. Masiyano, R.P. Tatam, Using integrating spheres as absorption cells: path-length distribution and application of Beer's law. Appl. Opt. **48**(30), 5748–5758 (2009)
9.112. N. Bosschaart, M.C.G. Aalders, D.J. Faber, J.J.A. Weda, M.J.C. van Gemert, T.G. van Leeuwen, Quantitative measurements of absorption spectra in scattering media by low-coherence spectroscopy. Opt. Lett. **34**(23), 3746–3748 (2009)
9.113. A.A. Kosterev, Yu.A. Bakhirkin, R.F. Curl, F.K. Tittel, Quartz-enhanced photoacoustic spectroscopy. Opt. Lett. **27**(21), 1902–1904 (2002)
9.114. A.A. Kosterev, F.K. Tittel, D.V. Serebryakov, A.L. Malinovsky, I.V. Morozov, Applications of quartz tuning forks in spectroscopic gas sensing. Rev. Sci. Instrum. **76**, Article 063102 (2005)
9.115. K. Liu, J. Li, L. Wang, T. Tan, W. Zhang, X. Gao, W. Chen, F.K. Tittel, Trace gas sensor based on quartz tuning fork enhanced laser photoacoustic spectroscopy. Appl. Phys. B **94**(3), 527–533 (2009)
9.116. V. Spagnolo, A.A. Kosterev, L. Dong, R. Lewicki, F.K. Tittel, NO trace gas sensor based on quartz-enhanced photoacoustic spectroscopy and external cavity quantum cascade laser. Appl. Phys. B **100**(1), 125–130 (2010)

9.117. J.H. Doty, A.A. Kosterev, F.K. Tittel, Recent advances in resonant optothermalacoustic detection, in *Quantum Sensing and Nanophotonic Devices VIII*, ed. by M. Razeghi, R. Sudharsanan, G.J. Brown, Proceedings of SPIE, 2011, vol. 7945, Article 79450Q
9.118. N. Petra, J. Zweck, A.A. Kosterev, S.E. Minkoff, D. Thomazy, Theoretical analysis of a quartz-enhanced photoacoustic spectroscopy sensor. Appl. Phys. B **94**(4), 673–680 (2009)
9.119. T. Laurila, H. Cattaneo, V. Koskinen, J. Kauppinen, R. Hernberg, Diode laser-based photoacoustic spectroscopy with interferometrically-enhanced cantilever detection. Opt. Express **13**(7), 2453–2458 (2005)
9.120. E.L. Holthoff, D.A. Heaps, P.M. Pellegrino, Development of a MEMS-scale photoacoustic chemical sensor using a quantum cascade laser. IEEE Sens. J. **10**(3), 572–577 (2010); R.G. Polcawich, P.M. Pellegrino, Microelectromechanical resonant photoacoustic Cell. U.S. Patent Number 7 304 732, 4 Dec 2003
9.121. B. Schäfer, J. Gloger, U. Leinhos, K. Mann, Photo-thermal measurement of absorptance losses, temperature induced wavefront deformation and compaction in DUV-optics. Opt. Express **17**(25), 23025–23036 (2009)
9.122. B. Schäfer, M. Schöneck, A. Bayer, K. Mann, Absolute measurement of surface and bulk absorption in DUV optics from temperature induced wavefront deformation. Opt. Express **18**(21), 21534–21539 (2010)
9.123. Y. Chen, S. Webster, B. Wickham, A. Bennett, M. Bass, Surface losses in the visible governed by Rayleigh scattering in synthetic diamonds. Opt. Mat. Express **5**(11), 2443–2447 (2015)
9.124. C. Bogan, P. Kwee, S. Hild, S.H. Huttner, B. Willke, Novel technique for thermal lens measurement in commonly used optical components. Opt. Express **23**(12), 15380–15389 (2015)
9.125. N. Shiokawa, E. Tokunaga, Quasi first-order Hermite Gaussian beam for enhanced sensitivity in Sagnac interferometer photothermal deflection spectroscopy. Opt. Express **24**(11), 11961–11974 (2016)
9.126. T. Berer, M. Brandstetter, A. Hochreiner, G. Langer, W. Märginger, P. Burgholzer, B. Lendl, Remote mid-infrared photoacoustic spectroscopy with a quantum cascade laser. Opt. Lett. **40**(15), 3476–3479 (2015)
9.127. R. Ellwood, O. Ogunlade, E. Zhang, P. Beard, B. Cox, Photoacoustic tomography using orthogonal Fabry–Pérot sensors. J. Biomed. Opt. **22**(4), Article 041009 (2017)
9.128. M. Leidinger, S. Fieberg, N. Waasem, F. Kuhnemann, K. Buse, I. Breunig, Comparative study on three highly sensitive absorption measurement techniques characterizing lithium niobate over its entire transparent spectral range. Opt. Express **23**(17), 21690–121705 (2015)
9.129. P.C. Dufour, N.L. Rowell, A.G. Steele, Fourier-transform radiation thermometry: measurements and uncertainties. Appl. Opt. **37**(25), 5923–5931 (1998)
9.130. L. González-Fernández, R.B. Pérez-Sáez, L. del Campo, M.J. Tello, Analysis of calibration methods for direct emissivity measurements. Appl. Opt. **49**(14), 2728–2735 (2010)
9.131. M. Honner, P. Honnerová, Survey of emissivity measurement by radiometric methods. Appl. Opt. **54**(4), 669–683 (2015)
9.132. M.T. Cone, J.A. Musser, E. Figueroa, J.D. Mason, E.S. Fry, Diffuse reflecting material for integrating cavity spectroscopy, including ring-down spectroscopy. Appl. Opt. **54**(2), 334–346 (2015)
9.133. S. Bergin, J. Hodgkinson, D. Francis, R.P. Tatam, Integrating cavity based gas cells: a multibeam compensation scheme for pathlength variation. Opt. Express **24**(12), 13647–13664 (2016)

Chapter 10

10.1. K.I. Tarasov, *Spectrophotometers* (Mashinostroenie, Leningrad, 1976)
10.2. V.G. Vorob'ev, Sources of photometric scale nonlinearity in optical-null spectrophotometers. J. Opt. Technol. **46**(9), 512–515 (1979)
10.3. Beckman Coulter Inc., DU® 800 UV/Vis Spectrophotometer Specifications (2010); H.H. Cary, A.O. Beckman, A quartz photoelectric spectrophotometer. J. Opt. Soc. Am. **31**(11), 682–689 (1941)
10.4. W. Swindell, Electronic circuits of visual radiation detectors, in *Applied Optics and Optical Engineering*, ed. by R.R. Shannon, J.C. Wyant (Academic Press, New York, 1980)
10.5. M.R. Querry, P.G. Cary, R.C. Waring, Split-pulse laser method for measuring attenuation coefficients of transparent liquids: application to deionized filtered water in the visible region. Appl. Opt. **17**(22), 3587–3592 (1978)
10.6. E.S. Voropay, V.I. Karas, P.A. Torpachev, Measurements of optical losses using two pairs of photodiode-transimpedance amplifiers. Meas. Tech. **26**(2), 33–35 (1984)
10.7. E.S. Voropay, V.I. Karas, P.A. Torpachev, Study of the possibility of measurements of the light flux with an amplitude resolution of 10^5. Metrologia, Moscow, 1985, No. 9, pp. 31–38
10.8. R.T.H. Collis, Lidar. Appl. Opt. **9**(8), 1782–1788 (1970)
10.9. S.A. Ahmed, Molecular air pollution monitoring by dye laser measurement of differential absorption of atmospheric elastic backscatter. Appl. Opt. **12**(4), 901–903 (1973)
10.10. J. Gelbwachs, NO_2 lidar comparison: fluorescence vs backscattered differential absorption. Appl. Opt. **12**(12), 2812–2813 (1973)
10.11. U. Platt, J. Stutz, *Differential Optical Absorption Spectroscopy – Principles and Applications* (Springer, Heidelberg, 2005)
10.12. T. Brauers, M. Hausmann, U. Brandenburger, H.-P. Dorn, Improvement of differential optical absorption spectroscopy with a multichannel scanning technique. Appl. Opt. **34**(21), 4472–4479 (1995)
10.13. M. Bartholdi, G.C. Salzman, R.D. Hiebert, M. Kerker, Differential light scattering photometer for rapid analysis of single particles in flow. Appl. Opt. **19**(10), 1573–1581 (1980)
10.14. G. Laufer, A. Ben-David, Optimized differential absorption radiometer for remote sensing of chemical effluents. Appl. Opt. **41**(12), 2263–2273 (2002)
10.15. V. Ebert, P. Vogel, Near shot noise detection of oxygen in the A-band with vertical-cavity surface-emitting lasers. Appl. Phys. B **72**(1), 127–135 (2001)
10.16. J.R. Schmidt, S.T. Sanders, Differential absorption sensor applied for liquid oxygen measurements. Appl. Opt. **44**(28), 6058–6066 (2005)
10.17. I. Pundt, K.U. Mettendorf, Multibeam long-path differential optical absorption spectroscopy instrument: a device for simultaneous measurements along multiple light paths. Appl. Opt. **44**(23), 4985–4994 (2005)
10.18. C. Kern, S. Trick, B. Rippel, U. Platt, Applicability of light-emitting diodes as light sources for active differential optical absorption spectroscopy measurements. Appl. Opt. **45**(9), 2077–2088 (2006)
10.19. J. Stutz, U. Platt, Numerical analysis and estimation of the statistical error of differential optical absorption spectroscopy measurements with least-squares methods. Appl. Opt. **35**(30), 6041–6053 (1996)
10.20. M. Wenig, B. Jähne, U. Platt, Operator representation as a new differential optical absorption spectroscopy formalism. Appl. Opt. **44**(16), 3246–3253 (2005)
10.21. C. Billet, R. Sablong, Differential optical spectroscopy for absorption characterization of scattering media. Opt. Lett. **32**(22), 3251–3253 (2007)

10.22. A.H. Carrieri, J. Copper, D.J. Owens, E.S. Roese, J.R. Bottiger, R.D. Everly, K.C. Hung, Infrared differential-absorption Mueller matrix spectroscopy and neural network-based data fusion for biological aerosol standoff detection. Appl. Opt. **49**(3), 382–393 (2010)
10.23. W. Heitmann, Attenuation measurement in low-loss optical glass by polarized radiation. Appl. Opt. **14**(12), 3047–3052 (1975)
10.24. W. Heitmann, Attenuation measurement in glass for optical communications: an immersion method. Appl. Opt. **15**(1), 256–260 (1976)
10.25. F. Ferri, A. Bassini, E. Paganini, Commercial spectrophotometer for particle sizing. Appl. Opt. **36**(4), 884–891 (1997)
10.26. G. Bonfiglioli, P. Brovetto, Principles of self-modulating derivative optical spectroscopy. Appl. Opt. **3**(12), 1417–1424 (1964)
10.27. G. Bonfiglioli, J. Trench, Signal recovering in wavelength modulated spectrometers. Opt. Commun. **10**(2), 207–210 (1974)
10.28. E.I. Moses, C.L. Tang, High-sensitivity laser wavelength-modulation spectroscopy. Opt. Lett. **1**(4), 115–117 (1977)
10.29. A.T. Forrester, Photoelectric mixing as a spectroscopic tool. J. Opt. Soc. Am. **51**(3), 253–259 (1961)
10.30. A.E. Siegman, The antenna properties of optical heterodyne receivers. Appl. Opt. **5**(10), 1588–1594 (1966)
10.31. D. Fink, Coherent detection signal-to-noise. Appl. Opt. **14**(3), 689–690 (1975)
10.32. L. Mandel, E. Wolf, Optimum conditions for heterodyne detection of light. J. Opt. Soc. Am. **65**(4), 413–420 (1975)
10.33. T. Takenaka, K. Tanaka, O. Fukumitsu, Signal-to-noise ratio in optical heterodyne detection for Gaussian fields. Appl. Opt. **17**(21), 3466–3470 (1978)
10.34. H.P. Yuen, V.W.S. Chan, Noise in homodyne and heterodyne detection. Opt. Lett. **8**(3), 177–179 (1983)
10.35. B.J. Rye, Differential absorption lidar system sensitivity with heterodyne reception. Appl. Opt. **17**(24), 3862–3864 (1978)
10.36. G.C. Bjorklund, Frequency-modulation spectroscopy: a new method for measuring weak absorptions and dispersions. Opt. Lett. **5**(1), 15–17 (1980)
10.37. W. Lenth, C. Ortiz, G.C. Bjorklund, Pulsed frequency-modulation spectroscopy as a means for fast absorption measurements. Opt. Lett. **6**(7), 351–353 (1981)
10.38. T.F. Gallagher, R. Kachru, F. Gounand, G.C. Bjorklund, W. Lenth, Frequency-modulation spectroscopy with a pulsed dye laser. Opt. Lett. **7**(1), 28–30 (1982)
10.39. M. Romagnoli, M.D. Levenson, G.C. Bjorklund, Frequency-modulation-polarization spectroscopy. Opt. Lett. **8**(12), 635–637 (1983)
10.40. N.H. Tran, R. Kachru, P. Pillet, H.V.L van den Heuvell, T.F. Gallagher, J.P. Watjen, Frequency-modulation spectroscopy with a pulsed dye laser: experimental investigations of sensitivity and useful features. Appl. Opt. **23**(9), 1353–1360 (1984)
10.41. C.S. Gudeman, M.H. Begemann, J. Pfaff, R.J. Saykally, Tone-burst modulated color-center-laser spectroscopy. Opt. Lett. **8**(6), 310–312 (1983)
10.42. H. Lotem, Extension of the spectral coverage range of frequency modulation spectroscopy by double frequency modulation. J. Appl. Phys. **54**(10), 6033–6035 (1983)
10.43. D.E. Cooper, T.F. Gallagher, Double frequency modulation spectroscopy: high modulation frequency with low-bandwidth detectors. Appl. Opt. **24**(9), 1327–1334 (1985)
10.44. G.R. Janik, C.B. Carlisle, T.F. Gallagher, Two-tone frequency-modulation spectroscopy. J. Opt. Soc. Am. B **3**(8), 1070–1074 (1986)
10.45. D.E. Cooper, J.P. Watjen, Two-tone optical heterodyne spectroscopy with a tunable lead-salt diode laser. Opt. Lett. **11**(10), 606–608 (1986)

10.46. D.E. Cooper, R.E. Warren, Two-tone optical heterodyne spectroscopy with diode lasers: theory of line shapes and experimental results. J. Opt. Soc. Am. B **4**(4), 470–480 (1987)
10.47. M. Gehrtz, W. Lenth, A.T. Young, H.S. Johnston, High-frequency-modulation spectroscopy with a lead-salt diode laser. Opt. Lett. **11**(3), 132–134 (1986)
10.48. N.-Y. Chou, G.W. Sachse, Single-tone and two-tone AM-FM spectral calculations for tunable diode laser absorption spectroscopy. Appl. Opt. **26**(17), 3584–3587 (1987)
10.49. L. Wang, H. Riris, C.B. Carlisle, T.F. Gallagher, Comparison of approaches to modulation spectroscopy with GaAIAs semiconductor lasers: application to water vapor. Appl. Opt. **27**(10), 2071–2077 (1988)
10.50. C.B. Carlisle, D.E. Cooper, H. Preier, Quantum noise-limited FM spectroscopy with a lead-salt diode laser. Appl. Opt. **28**(13), 2567–2576 (1989)
10.51. J.A. Silver, Frequency-modulation spectroscopy for trace species detection: theory and comparison among experimental methods. Appl. Opt. **31**(6), 707–717 (1992); D.S. Bomse, A.C. Stanton, J.A. Silver, Frequency modulation and wavelength modulation spectroscopies: comparison of experimental methods using a lead-salt diode laser. Appl. Opt. **31**(6), 718–731 (1992)
10.52. J.M. Supplee, E.A. Whittaker, W. Lenth, Theoretical description of frequency modulation and wavelength modulation spectroscopy. Appl. Opt. **33**(27), 6294–6302 (1994)
10.53. P. Kluczynski, O. Axner, Theoretical description based on Fourier analysis of wavelength-modulation spectrometry in terms of analytical and background signals. Appl. Opt. **38**(27), 5803–5815 (1999)
10.54. R.T. Ku, E.D. Hinkley, J.O. Sample, Long-path monitoring of atmospheric carbon monoxide with a tunable diode laser system. Appl. Opt. **14**(4), 854–861 (1975)
10.55. J. Shewchun, B.K. Garside, E.A. Ballik, C.C.Y. Kwan, M.M. Elsherbiny, G. Hogenkamp, A. Kazandjian, Pollution monitoring systems based on resonance absorption measurements of ozone with a "tunable" CO_2 laser: some criteria. Appl. Opt. **15**(2), 340–346 (1976)
10.56. J. Reid, J. Shewchun, B.K. Garside, E.A. Ballik, High sensitivity pollution detection employing tunable diode lasers. Appl. Opt. **17**(2), 300–307 (1978)
10.57. J. Reid, B.K. Garside, J. Shewchun, M. El-Sherbiny, E.A. Ballik, High sensitivity point monitoring of atmospheric gases employing tunable diode lasers. Appl. Opt. **17**(11), 1806–1810 (1978)
10.58. H. Flicker, J.P. Aldridge, H. Filip, N.G. Nereson, M.J. Reisfeld, W.H. Weber, WaveNumber calibration of tunable diode lasers using etalons. Appl. Opt. **17**(6), 851–852 (1978)
10.59. A.R. Chraplyvy, Diode laser spectra with simultaneous frequency calibration. Appl. Opt. **17**(17), 2674–2675 (1978)
10.60. D.E. Jennings, Absolute line strengths in v_4, $^{12}CH_4$: a dual-beam diode laser spectrometer with sweep integration. Appl. Opt. **19**(16), 2695–2700 (1980)
10.61. D.T. Cassidy, J. Reid, High-sensitivity detection of trace gases using sweep integration and tunable diode lasers. Appl. Opt. **21**(14), 2527–2530 (1982)
10.62. R.D. Schaeffer, J.C. Sproul, J. O'Connell, C. van Vloten, A.W. Mantz, Multipass absorption cell designed for high temperature UHV operation. Appl. Opt. **28**(9), 1710–1713 (1989)
10.63. M. Fehér, P.A. Martin, A. Rohrbacher, A.M. Soliva, J.P. Maier, Inexpensive near-infrared diode-laser-based detection system for ammonia. Appl. Opt. **32**(12), 2028–2030 (1993)
10.64. M.P. Arroyo, R.K. Hanson, Absorption measurements of water-vapor concentration, temperature, and line-shape parameters using a tunable InGaAsP diode laser. Appl. Opt. **32**(30), 6104–6116 (1993)

10.65. M.P. Arroyo, S. Langlois, R.K. Hanson, Diode-laser absorption technique for simultaneous measurements of multiple gasdynamic parameters in high-speed flows containing water vapor. Appl. Opt. **33**(15), 3296–3307 (1994)
10.66. S.C. Woodworth, D.T. Cassidy, M.J. Hamp, Sensitive absorption spectroscopy by use of an asymmetric multiple-quantum-well diode laser in an external cavity. Appl. Opt. **40**(36), 6719–6724 (2001)
10.67. W. Armerding, M. Spiekermann, J. Walter, F.J. Comes, Multipass optical absorption spectroscopy: a fast-scanning laser spectrometer for the in situ determination of atmospheric trace-gas components, in particular OH. Appl. Opt. **35**(21), 4206–4219 (1996)
10.68. D. Richter, D.G. Lancaster, F.K. Tittel, Development of an automated diode-laser-based multicomponent gas sensor. Appl. Opt. **39**(24), 4444–4450 (2000)
10.69. R. Claps, F.V. Englich, D.P. Leleux, D. Richter, F.K. Tittel, R.F. Curl, Ammonia detection by use of near-infrared diode-laser-based overtone spectroscopy. Appl. Opt. **40**(24), 4387–4394 (2001)
10.70. R.T. Ku, D.L. Spears, High-sensitivity infrared heterodyne radiometer using a tunable-diode-laser local oscillator. Opt. Lett. **1**(3), 84–86 (1977)
10.71. C.B. Carlisle, D.E. Cooper, Tunable-diode-laser frequency-modulation spectroscopy using balanced homodyne detection. Opt. Lett. **14**(23), 1306–1308 (1989)
10.72. G.D. Houser, E. Garmire, Balanced detection technique to measure small changes in transmission. Appl. Opt. **33**(6), 1059–1062 (1994)
10.73. P.C.D. Hobbs, Ultrasensitive laser measurements without tears. Appl. Opt. **36**(4), 903–920 (1997); Noise cancelling circuitry for optical systems with signal dividing and combining means. U.S. Patent 5,134,276; 28 July 1992
10.74. M.G. Allen, K.L. Carleton, S.J. Davis, W.J. Kessler, C.E. Otis, D.A. Palombo, D.M. Sonnenfroh, Ultrasensitive dual-beam absorption and gain spectroscopy: applications for near-infrared and visible diode laser sensors. Appl. Opt. **34**(18), 3240–3248 (1995)
10.75. D.M. Sonnenfroh, M.G. Allen, Ultrasensitive, visible tunable diode laser detection of NO_2. Appl. Opt. **35**(21), 4053–4058 (1996)
10.76. D.M. Sonnenfroh, W.T. Rawlins, M.G. Allen, C. Gmachl, F. Capasso, A.L. Hutchinson, D.L. Sivco, J.N. Baillargeon, A.Y. Cho, Application of balanced detection to absorption measurements of trace gases with room-temperature, quasi-cw quantum-cascade lasers. Appl. Opt. **40**(6), 812–820 (2001)
10.77. M.A. Bukhshtab, Absolute measurements of small specular reflection coefficients. Meas. Tech. **30**(3), 218–220 (1987)
10.78. M.A. Bukshtab, *Regarding Correlations Among Measurements of Low Optical Losses* (Central Institute "Information," Moscow, 1987)
10.79. M.A. Bukhshtab, *Measurements of Low Optical Loss in Reflected Radiation*. Svetotekhnika (6), 5–6 (1987)
10.80. M.A. Bukhshtab, V.N. Koromislichenko, A.Y. Kirillov, Two-channel system for determination of small optical losses of laser radiation with an amplitude resolution of more than 10,000. Instrum. Exp. Tech. **31**(2), 443–446 (1988)
10.81. A.Gh. Podoleanu, Unbalanced versus balanced operation in an optical coherence tomography system. Appl. Opt. **39**(1), 173–182 (2000)
10.82. O. Haderka, V. Michálek, V. Urbášek, M. Ježek, Fast time-domain balanced homodyne detection of light. Appl. Opt. **48**(15), 2884–2889 (2009)
10.83. S. Lambert-Girard, M. Allard, M. Piché, F. Babin, Differential optical absorption spectroscopy lidar for mid-infrared gaseous measurements. Appl. Opt. **54**(7), 1647–1656 (2015)
10.84. B. Zimmermann, A. Kohlerb, Optimizing Savitzky-Golay parameters for improving spectral resolution and quantification in infrared spectroscopy. Appl. Spectrosc. **67**(8), 892–902 (2013)

10.85. M.A. Czarnecki, Resolution enhancement in second-derivative spectra. Appl. Spectrosc. **69**(1), 67–74 (2015)
10.86. M. Vainio, M. Merimaa, L. Halonen, Frequency-comb-referenced molecular spectroscopy in the mid-infrared region. Opt. Lett. **36**(21), 4122–4124 (2011)
10.87. K.M. Manfred, J.M.R. Kirkbride, L. Ciaffoni, R. Peverall, G.A.D. Ritchie, Enhancing the sensitivity of mid-IR quantum cascade laser-based cavity-enhanced absorption spectroscopy using RF current perturbation. Opt. Lett. **39**(24), 6811–6814 (2014)
10.88. C.-Y. Chang, J.-T. Shy, Optimal power split ratio for autobalanced photodetection. Appl. Opt. **53**(3), 347–350 (2014)

Chapter 11

11.1. D. Marcuse, *Principles of Optical Fiber Measurements* (Academic Press, New York, 1981)
11.2. M.K. Barnoski, S.D. Personick, Measurements in fiber optics. Proc. IEEE **66**(4), 429–441 (1978)
11.3. D.B. Keck, P.C. Shultz, F. Zimar, Attenuation of multimode glass optical waveguides. Appl. Phys. Lett. **21**(5), 215–217 (1972)
11.4. A.R. Tynes, Integrating cube scattering detector. Appl. Opt. **9**(12), 2706–2710 (1970)
11.5. D. Marcuse, Loss analysis of single-mode fiber splices. Bell. Syst. Tech. J. **56**, 703–718 (1977)
11.6. M. Tachikura, Internal loss measurement technique for optical devices equipped with fiber connectors at both ends. Appl. Opt. **34**(34), 8056–8057 (1995)
11.7. A. Zaganiaris, Simultaneous measurement of absorption and scattering losses in bulk glasses and optical fibers by a microcalorimetric method. Appl. Phys. Lett. **25**(6), 345–347 (1974)
11.8. E.T. Stone, W.B. Gardner, C.R. Lovelace, Calorimetric measurement of absorption and scattering losses in optical fibers. Opt. Lett. **2**(2), 48–50 (1978)
11.9. A.R. Tynes, A.D. Pearson, D.L. Bisbee, Loss mechanisms and measurements in clad glass fibers and bulk glass. J. Opt. Soc. Am. **61**(2), 143–153 (1971)
11.10. S. Huard, D. Chardon, Measure de l'absorption d'une fibre optique par effet phot-acoustique. Opt. Commun. **39**(1–2), 59–63 (1981)
11.11. G. Ghosh, S. Kachi, Y. Sasaki, M. Kimura, New method to measure scattering and total losses of optical fibres. Electron. Lett. **21**(16), 670–671 (1985)
11.12. X. Zhou, S. Zhu, H. Shen, M. Liu, A new spatial integration method for luminous flux determination of light-emitting diodes. Meas. Sci. Technol. **21**, Article 105303 (2010)
11.13. R. Olshansky, S.M. Oaks, Differential mode attenuation measurements in graded-index fibers. Appl. Opt. **17**(11), 1830–1835 (1978)
11.14. L.E. Busse, G.H. McCabe, I.D. Aggarwal, Wavelength dependence of the scattering loss in fluoride optical fibers. Opt. Lett. **15**(8), 423–424 (1990)
11.15. N. Mekada, A. Al-Hamdan, T. Murakami, M. Miyoshi, New direct measurement technique of polarization dependent loss with high resolution and repeatability, in *Symposium on Optical Fiber Measurements, Technical Digest*, 1994, NIST Special Publication 864, pp. 189–192
11.16. R.C. Jones, A new calculus for the treatment of optical systems. VI. Experimental determination of the matrix. J. Opt. Soc. Am. **37**(2), 110–112 (1947)
11.17. B.L. Heffner, Deterministic, analytically complete measurement of polarization-dependent transmission through optical devices. IEEE Photon Technol. Lett. **4**(9), 451–454 (1992)

11.18. B.L. Heffner, Recent progress in polarization measurement techniques, in *Symposium on Optical Fiber Measurements, Technical Digest*, 1992, NIST Special Publication 839, pp. 131–136
11.19. N. Gisin, Statistics of polarization dependent losses. Opt. Commun. **114**(8), 399–405 (1995)
11.20. A. Elamari, N. Gisin, B. Perny, H. Zbinden, C. Zimmer, Polarization dependent loss of concatenated passive optical components, in *Symposium on Optical Fiber Measurements, Technical Digest*, 1996, NIST Special Publication 905, pp. 163–166
11.21. I. Molina-Fernández, J. de-Oliva-Rubio, Effects of phase noise in an optical six-port measurement technique. Opt. Express **13**(7), 2475–2486 (2005)
11.22. M. Bukhshtab, Interferometric noise in fiber transmission systems incorporating birefringent substances, in *Symposium on Optical Fiber Measurements, Technical Digest*, 1996, NIST Special Publication 905, pp. 211–214
11.23. D. Schicketanz, Method and apparatus for measuring the distance of a discontinuity of glass fiber from one end of the fiber. U.S. Patent 4,021,121; 3 May 1977; Deutche Auslegungsschrift No. 2451654 from 30 October 1974
11.24. M.K. Barnoski, S.M. Jensen, Fiber waveguides: a novel technique for investigating attenuation characteristics. Appl. Opt. **15**(9), 2112–2115 (1976)
11.25. S.D. Personick, Photon probe—an optical fiber time-domain reflectometer. Bell Syst. Tech. J. **56**(3), 355–366 (1977)
11.26. R.I. MacDonald, Frequency domain optical reflectometer. Appl. Opt. **20**(10), 1840–1844 (1981)
11.27. W. Eickhoff, R. Ulrich, Optical frequency reflectometry in single-mode fiber. Appl. Phys. Lett. **39**(9), 693–695 (1981)
11.28. D. Uttam, B. Culshaw, Precision time domain reflectometry in optical fiber systems using a frequency modulated continuous wave ranging technique. J. Lightwave Technol. **LT-3**(5), 971–977 (1985)
11.29. F.P. Kapron, R.D. Maurer, M.P. Teter, Theory of backscattering effects in waveguides. Appl. Opt. **11**(6), 1352–1356 (1972)
11.30. E. Brinkmeyer, Analysis of the backscattering method for single-mode optical fibers. J. Opt. Soc. Am. **70**(8), 1010–1012 (1980)
11.31. A.H. Hartog, M.P. Gold, On the theory of backscattering in single-mode optical fibers. J. Lightwave Technol. **LT-2**(2), 76–82 (1984)
11.32. F. Caviglia, P. Ricaldone, Noise error in OTDR splice loss measurement, in *Symposium on Optical Fiber Measurements: Technical Digest*, 1994, NIST Special Publication 864, pp. 49–52
11.33. M.P. Gold, A.H. Harotg, Improved-dynamic-range single-mode OTDR at 1.3 μm. Electron. Lett. **20**(7), 285–287 (1984)
11.34. H. Izumita, Y. Koyamada, S. Furukawa, I. Sankawa, Performance limits of coherent OTDR due to optical nonlinear effects, in *Symposium on Optical Fiber Measurements, Technical Digest*, 1994, NIST Special Publication 864, pp. 39–44
11.35. M. Ghioni, G. Ripamonti, S.V. Vanoli, S. Pitassi, Multiphoton pulse approach in photon-timing OTDR yields enhanced dynamic range and shorter measurement time, in *Symposium on Optical Fiber Measurements, Technical Digest*, 1990, NIST Special Publication 792, pp. 31–34
11.36. G. Pipamonti, S. Cova, Optical time-domain reflectometry with centimetre resolution at 10^{-15} W sensitivity. Electron. Lett. **22**(15), 818–819 (1986)
11.37. D. Dolfi, M. Nazarathy, S.A. Newton, 5-mm-resolution optical-frequency-domain reflectometry using a coded phase-reversal modulator. Opt. Lett. **13**(8), 678–680 (1988)
11.38. D. Dolfi, M. Nazarathy, Optical frequency domain reflectometry with high sensitivity and resolution using optical synchronous detection with coded modulators. Electron. Lett. **25**(2), 160–162 (1989)

11.39. V.C.Y. So, J.W. Jiang, J.A. Cargill, P.J. Vella, Automation of an optical time domain reflectometer to measure loss and return loss. J. Lightwave Technol. **8**(7), 1078–1082 (1990)
11.40. B.L. Danielson, C.D. Whittenberg, Guide-wave reflectometry with micrometer resolution. Appl. Opt. **26**(14), 2836–2842 (1987)
11.41. K. Takada, I. Yokohama, K. Chida, J. Noda, New measurement system for fault location in optical waveguide devices based on an interferometric technique. Appl. Opt. **26**(9), 1603–1606 (1987)
11.42. W.V. Sorin, D.K. Donald, Long and short range measurements using coherent FMCW reflectometry, in *Symposium on Optical Fiber Measurements, Technical Digest*, 1990, NIST Special Publication 792, pp. 27–30
11.43. K. Takada, A. Himeno, K. Yukimatsu, High sensitivity and submillimeter resolution optical-time domain reflectometry based on low-coherence interference. J. Lightwave Technol. **9**(11), 1534–1539 (1991)
11.44. K. Takada, K. Yukimatsu, M. Kobayashi, J. Noda, Rayleigh backscattering measurement of single-mode fibers by low coherence optical domain reflectometer with 14 μm spatial resolution. Appl. Phys. Lett. **59**(2), 143–145 (1991)
11.45. K. Takada, A. Himeno, K. Yukimatsu, Resolution-controllable optical time domain reflectometry based on low coherence interference. J. Lightwave Technol. **10**(12), 1998–2005 (1992)
11.46. E.A. Swanson, D. Huang, M.R. Hee, J.G. Fujimoto, C.P. Lin, C.A. Puliafito, High-speed optical coherence domain reflectometry. Opt. Lett. **17**(2), 151–153 (1992)
11.47. L.-T. Wang, K. Iiyama, F. Tsukada, N. Yoshida, K. Hayashi, Loss measurement in optical waveguide devices by coherent frequency-modulated continuous-wave reflectometry. Opt. Lett. **18**(13), 1095–1097 (1993)
11.48. S.K. Das, A.F. Judy, G.M. Alameel, R.M. Jopson, T.F. Adda, Reflectance measurement in lightwave systems: a comparison of various techniques, in *Symposium on Optical Fiber Measurements, Technical Digest*, 1988, NIST Special Publication 748, pp. 25–30
11.49. E.L. Buckland, M. Nishimura, Bidirectional OTDR measurements utilizing an improved folded-path technique, in *Symposium on Optical Fiber Measurements, Technical Digest*, 1988, NIST Special Publication 748, pp. 15–18
11.50. A.F. Judy, An OTDR based combined end-reflection and backscatter measurement, in *Symposium on Optical Fiber Measurements, Technical Digest*, 1992, NIST Special Publication 839, pp. 19–22
11.51. F.P. Kapron, B.P. Adams, E.A. Thomas, J.W. Peters, Fiber-optic reflection measurements using OCWR and OTDR techniques. J. Lightwave Technol. **7**(8), 1234–1241 (1989)
11.52. P. Blanchard, P.-H. Zongo, P. Facq, Accurate reflectance and optical fibre backscatter parameter measurements using an OTDR. Electron. Lett. **26**(25), 2060–2062 (1991)
11.53. L. Ducos, P. Facq, Windowing technique for accurate measurement of low reflectances by OTDR, in *Symposium on Optical Fiber Measurements, Technical Digest*, 1994, NIST Special Publication 864, pp. 45–48
11.54. D. Marcuse, Reflection losses from imperfectly broken fiber ends. Appl. Opt. **14**(12), 3016–3020 (1975)
11.55. M.A. Bukhshtab, V.N. Koromislichenko, A.A. Ovsiannikov, Method of determining optical losses at the ends and end joints of fiber light guides. U.S. Patent Number 5,037,197, 6 Aug 1991
11.56. M.A. Bukhshtab, V.N. Koromislichenko, Light reflection method for transmission-loss measurements in optical fiber lightguides. U.S. Patent 5,226,102, 6 July 1993
11.57. M.A. Bukhshtab, Method of determining the optical loss in a fiber-optic light guide in reflected radiation. U.S. Patent 5,331,391, 19 July 1994

11.58. M.M. Choy, J.M. Gimlett, R. Welter, L.G. Kasovsky, N.K. Cheung, Interferometric conversion of laser phase noise to intensity noise by single mode fiber optic components. Electron. Lett. **23**(21), 1151–1152 (1987)
11.59. L. Mandel, Phenomenological theory of laser beam fluctuations and beam mixing. Phys. Rev. **138**(3B), B753–B 762 (1965)
11.60. J.A. Armstrong, Theory of interferometric analysis of laser phase noise. J. Opt. Soc. Am. **56**(8), 1024–1031 (1966)
11.61. C.H. Henry, Theory of the linewidth of semiconductor lasers. IEEE J. Quantum Electron. **QE-18**(2), 259–264 (1982)
11.62. R.W. Tkach, A.R. Chraplyvy, Phase noise and linewidth in an InGaAsP DFB laser. J. Lightwave Technol. **4**(11), 1711–1716 (1986)
11.63. M. Tur, E.L. Goldstein, Dependence of error rate on signal-to-noise ratio in fiber-optic communication systems with phase-induced intensity noise. J. Lightwave Technol. **7**(12), 2055–2058 (1989)
11.64. A. Arie, M. Tur, E.L. Goldstein, Probability-density function of noise at the output of a two-beam interferometer. J. Opt. Soc. Am. A **8**(12), 1936–1942 (1991)
11.65. J.L. Gimlett, N.K. Cheung, Effects of phase-to-intensity noise conversion by multiple reflections on gigabit-per-second DFB laser transmission systems. J. Lightwave Technol. **7**(6), 888–895 (1989)
11.66. J.L. Gimlett, M.Z. Iqobal, N.K. Cheung, A. Righetti, F. Fontana, G. Grasso, Observation of equivalent Rayleigh scattering mirrors in lightwave systems with optical amplifiers. IEEE Photon. Technol. Lett. **2**(3), 211–213 (1990)
11.67. C. Desem, Optical Interference in subscriber multiplexed systems with multiple optical carriers. IEEE J. Sel. Areas Commun. **8**(7), 1290–1295 (1990)
11.68. M. Nazarathy, W. Sorin, D. Baney, S. Newton, Spectral analysis of optical mixing measurements. J. Lightwave Technol. **7**(7), 1083–1096 (1989)
11.69. M. Tur, E.L. Goldstein, Probability distribution of phase-induced intensity noise generated by distributed-feedback, lasers. Opt. Lett. **15**(1), 1–3 (1990)
11.70. P.J. Legg, D.K. Hunter, I. Andonovic, P.E. Barnsley, Inter-channel crosstalk phenomena in optical time division multiplexed switching networks. IEEE Photon. Technol. Lett. **6**(5), 661–663 (1994)
11.71. E.L. Goldstein, L. Eskildsen, A.F. Elrefaie, Performance implications of component crosstalk in transparent lightwave networks. IEEE Photon. Technol. Lett. **6**(5), 657–659 (1994)
11.72. E.L. Goldstein, L. Eskildsen, Scaling limitations in transparent optical networks due to low-level crosstalk. IEEE Photon. Technol. Lett. **7**(1), 93–94 (1995)
11.73. L. Eskildsen, P.B. Hunsen, Interferometric noise in lightwave systems with optical preamplifiers. IEEE Photon. Technol. Lett. **9**(11), 1538–1540 (1997)
11.74. H.J.S. Dorren, H. de Waardt, I.T. Monroy, Statistical analysis of crosstalk accumulation in WDM networks. J. Lightwave Technol. **17**(12), 2425–2430 (1999)
11.75. L. Gilner, Scalability of optical multiwavelength switching networks: crosstalk analysis. J. Lightwave Technol. **17**(1), 58–67 (1999)
11.76. Z. Meng, Y. Hu, S. Xiong, G. Stewart, G. Whitenett, B. Culshaw, Phase noise characteristics of a diode-pumped ND:YAG laser in an unbalanced fiber-optic interferometer. Appl. Opt. **44**(17), 3425–3428 (2005)
11.77. J.R. Folkenberg, M.D. Nielsen, N.A. Mortensen, C. Jakobsen, H.R. Simonsen, Polarization maintaining large mode area photonic crystal fiber. Opt. Express **12**(5), 956–960 (2004)
11.78. I. Fatadin, S.J. Savory, Impact of phase to amplitude noise conversion in coherent optical systems with digital dispersion compensation. Opt. Express **18**(15), 16273–16278 (2010)

11.79. I. Salinas, I. Garcés, R. Alonso, J. Pelayo, F. Villuendas, Experimental study on the origin of optical waveguide losses by means of Rayleigh backscattering measurement. Opt. Express **13**(2), 564–972 (2005)
11.80. P. Healy, P. Hensel, Optical time domain reflectometry by photon counting. Electron. Lett. **16**(16), 631–633 (1980)
11.81. R. Feced, M. Farhadiroushan, V.A. Handerek, Zero dead-zone OTDR with high-spatial resolution for short haul applications. IEEE Photon. Technol. Lett. **9**(5), 1140–1142 (1997)
11.82. M. Legré, R. Thew, H. Zbinden, N. Gisin, High resolution optical time domain reflectometer based on 1.55 μm up-conversion photon-counting module. Opt. Express **15**(13), 8237–8242 (2007)
11.83. P. Blanchard, J. Dubard, L. Ducos, R. Thauvin, Simulation method of reflectance measurement error using the OTDR. IEEE Photon. Technol. Lett. **10**(5), 705–706 (1998)
11.84. Y.-J. Rao, D.A. Jackson, Recent progress in fiber optic low-coherence interferometry. Meas. Sci. Technol. **7**(7), 910–999 (1996)
11.85. A.J. Rogers, Polarization-optical time domain reflectometry: a technique for the measurement of field distributions. Appl. Opt. **20**, 1060–1074 (1981)
11.86. J.G. Ellison, A.S. Siddiqui, A fully polarimetric optical time-domain reflectometer. IEEE Photon. Technol. Lett. **10**(2), 246–248 (1998)
11.87. B. Huttner, J. Reecht, N. Gizin, R. Passy, J.P. von der Weid, Local birefringence measurements in single-mode fibers with coherent optical frequency-domain reflectometry. IEEE Photon. Technol. Lett. **10**(10), 1458–1460 (1998)
11.88. M. Han, Y. Wang, A. Wang, Grating-assisted polarization optical time-domain reflectometry for distributed fiber-optic sensing. Opt. Lett. **32**(14), 2028–2030 (2007)
11.89. M.G. Shlyagin, A.V. Khomenko, D. Tentori, Birefringence dispersion measurement in optical fibers by wavelength scanning. Opt. Lett. **20**(8), 869–871 (1995)
11.90. V.V. Spirin, F.J. Mendieta, S.V. Miridonov, M.G. Shlyagin, A.A. Chtcherbakov, P.L. Swart, Localization of a loss-inducing perturbation with variable accuracy along a test fiber using transmission-reflection analysis. IEEE Photon. Technol. Lett. **16**(2), 569–571 (2004)
11.91. P. Hlubina, D. Ciprian, Spectral-domain measurement of phase modal birefringence in polarization-maintaining fiber. Opt. Express **15**(25), 17019–17024 (2007)
11.92. N.H. Zhu, J.H. Ke, H.G. Zhang, W. Chen, J.G. Liu, L.J. Zhao, W. Wang, Wavelength coded optical time-domain reflectometry. J. Lightwave Technol. **28**(6), 972–977 (2010)
11.93. V. Kalavally, I.D. Rukhlenko, M. Premaratne, T. Win, Multipath interference in pulse-pumped fiber Raman amplifiers: analytical approach. J. Lightwave Technol. **28**(18), 2701–2707 (2010)
11.94. B. Szafraniec, R. Mästle, B. Nebendahl, E. Thrush, D.M. Baney, Fast polarization-dependent loss measurement based on continuous polarization modulation. Appl. Opt. **48**(3), 573–578 (2009)
11.95. T. Geng, G. Li, Y. Zhang, J. Wang, T. Zhang, Phase noise of diode laser in self-mixing interference. Opt. Express **13**(16), 5904–5912 (2005)
11.96. P.K. Tien, Light waves in thin films and integrated optics. Appl. Opt. **10**(11), 2395–2413 (1971)
11.97. I. Awai, H. Onodera, Y.-K. Choi, M. Nakajima, J.-I. Ikenoue, Improved method of loss measurement for optical waveguides by use of a rectangular glass probe. Appl. Opt. **31**(12), 2078–2084 (1992)
11.98. J. Cardin, D. Leduc, Determination of refractive index, thickness, and the optical losses of thin films from prism–film coupling measurements. Appl. Opt. **47**(7), 894–900 (2008)
11.99. T.A. Strasser, M.C. Gupta, Optical loss measurement of low-loss thin-film waveguides by photographic analysis. Appl. Opt. **31**(12), 2041–2046 (1992)

11.100. S. Satoh, K. Susa, I. Matsuyama, Simple method of measuring scattering losses in optical fibers. Appl. Opt. **38**(34), 7080–7084 (1999)
11.101. D.F. Clark, M.S. Iqbal, Simple extension to the Fabry-Perot technique for accurate measurement of losses in semiconductor waveguides. Opt. Lett. **15**(22), 1291–1293 (1990)
11.102. R. Fazludeen, S. Barai, P.K. Pattnaik, T. Srinivas, A. Selvarajan, A novel technique to measure the propagation loss of integrated optical waveguides. IEEE Photon. Technol. Lett. **17**(2), 360–362 (2005)
11.103. Y.-P. Wang, J.-P. Chen, X.-W. Li, X.-H. Zhang, J.-X. Hong, A.-L. Ye, Simultaneous measurement of various optical parameters in a multilayer optical waveguide by a Michelson precision reflectometer. Opt. Lett. **30**(9), 979–981 (2005)
11.104. S. Taebi, M. Khorasaninejad, S.S. Saini, Modified Fabry-Perot interferometric method for waveguide loss measurement. Appl. Opt. **47**(35), 6625–6630 (2008)
11.105. H.L. Rogers, S. Ambran, C. Holmes, P.G.R. Smith, J.C. Gates, In situ loss measurement of direct UV-written waveguides using integrated Bragg gratings. Opt. Lett. **35**(17), 2849–2851 (2010)
11.106. T.-N. Nguyen, K. Lengle, M. Thual, P. Rochard, M. Gay, L. Bramerie, S. Malaguti, G. Bellanca, S.D. Le, T. Chartier, Nondestructive method to measure coupling and propagation losses in optical guided structures. J. Opt. Soc. Am. B **29**(12), 3393–3397 (2012)
11.107. S. Jeon, H. Kim, B.-S. Song, Y. Yamaguchi, T. Asano, S. Noda, Measurement of optical loss in nanophotonic waveguides using integrated cavities. Opt. Lett. **41**(23), 5486–5489 (2016)
11.108. V.G. Plotnichenko, V.O. Sokolov, E.B. Kryukova, G.E. Snopatin, I.V. Skripachev, M.F. Churbanov, Specifics of spectral loss measurement in infrared fibers. Appl. Opt. **56**(8), 2112–2118 (2017)
11.109. N. Riesen, T.T.-Y. Lam, J.H. Chow, Bandwidth-division in digitally enhanced optical frequency domain reflectometry. Opt. Express **21**(4), 4017–4026 (2013)
11.110. Q. Liu, X. Fan, Z. He, Time-gated digital optical frequency domain reflectometry with 1.6-m spatial resolution over entire 110-km range. Opt. Express **23**(20), 25988–25995 (2015)
11.111. A. Minardo, R. Bernini, R. Ruiz-Lombera, J. Mirapeix, J.M. Lopez-Higuera, L. Zeni, Proposal of Brillouin optical frequency domain reflectometry (BOFDR). Opt. Express **24**(26), 29994–30001 (2016)
11.112. F. Ito, T. Manabe, Recent developments of fiber diagnosis technologies in optical communication. J. Lightwave Technol. **35**(16), 3473–3482 (2017)
11.113. H. Li, J. Zhang, L. Wang, H. Ma, Z. Jin, Measurement of the reflection and loss of the hybrid air-core photonic-bandgap fiber ring resonator. Appl. Opt. **55**(32), 9329–9333 (2016)

Chapter 12

12.1. A.A. Michelson, The relative motion of the Earth and the luminiferous ether. Am. J. Sci. **22**, 120–129 (1881); A. Michelson, E. Morley, On the relative motion of the Earth and the luminiferous ether. Am. J. Sci. **34**, 333–345 (1887)
12.2. Lord Rayleigh, On the interference bands of approximately homogeneous light: in a letter to prof. A. Michelson, Philos. Mag. **34**, 407 (1892)
12.3. E.V. Loewenstein, The history and current status of Fourier transform spectroscopy. Appl. Opt. **5**(5), 845–852 (1966)
12.4. P. Jacquinot, The luminosity of spectrometers with prisms, gratings, or Fabry-Perot etalons. J. Opt. Soc. Am. **44**(10), 761–765 (1954)

12.5. P.B. Fellgett, Dynamic impedance and sensitivity of radiation thermocouples. Proc. Phys. Soc. B **62**(6), 351–359 (1949); On the ultimate sensitivity and practical performance of radiation detectors. J. Opt. Soc. Am. **39**(11), 970–976 (1949)
12.6. P. Connes, Spectromètre interférentiel à sélection par l'amplitude de modulation. J. Phys. Radium **19**(3), 215–222 (1958)
12.7. J. Connes, Spectroscopic studies using Fourier transformation. Nouv. Rev. Opt. **40**, 45–72, 116–140, 171–190, 231–265 (1961); J. Connes, P. Connes, Near-infrared planetary spectra by Fourier spectroscopy. I. Instruments and results. J. Opt. Soc. Am. **56**(7), 896–910 (1966)
12.8. E.R. Peck, A new principle in interferometer design. J. Opt. Soc. Am. **38**(1), 66 (1948); Theory of the corner-cube interferometer. J. Opt. Soc. Am. **38**(12), 1015–1024 (1948)
12.9. P.B. Fellgett, A contribution to the theory of the multiplex interferometric spectrometer. J. Phys. Radium **19**(3), 187–191 (1958)
12.10. J. Strong, G.A. Vanasse, Interferometric spectroscopy in the far infrared. J. Opt. Soc. Am. **49**(9), 844–850 (1959)
12.11. R.N. Ibbett, D. Aspinall, J.F. Grainger, Real-time multiplexing of dispersed spectra in any wavelength region. Appl. Opt. **7**(6), 1089–1093 (1968); J.A. Decker, Jr., Experimental realization of the multiplex advantage with a Hadamard-transform spectrometer. Appl. Opt. **10**(3), 510–514 (1971)
12.12. M.H. Tai, M. Harwit, Fourier and Hadamard transform spectrometers: a limited comparison. Appl. Opt. **15**(11), 2664–2666 (1976); R.R. Treffers, Signal-to-noise ratio in Fourier spectroscopy. Appl. Opt. **16**(12), 3103–3106 (1977); T. Hirschfeld, Conventions and values for the multiplex advantage in Fourier transform spectroscopy. Appl. Opt. **16**(12), 3070–3071 (1977)
12.13. Lord Rayleigh, On the interference-rings, described by Haidinger, observable by means of plates whose surfaces are absolutely parallel. Philos. Mag. **12**(71), 489–493 (1906)
12.14. D.B. Tanner, R.P. McCall, Source of a problem with Fourier transform spectroscopy. Appl. Opt. **23**(14), 2363–2368 (1984)
12.15. H.E. Revercomb, H. Buijs, H.B. Howell, D.D. LaPorte, W.L. Smith, L.A. Sromovsky, Radiometric calibration of IR Fourier transform spectrometers: solution to a problem with the high-resolution interferometer sounder. Appl. Opt. **27**(15), 3210–3218 (1988); L.A. Sromovsky, Radiometric errors in complex Fourier transform spectrometry. Appl. Opt. **42**(10), 1779–1787 (2003)
12.16. G.A. Vanasse, R.E. Murphy, F.H. Cook, Double-beaming technique in Fourier spectroscopy. Appl. Opt. **15**(2), 290–291 (1976)
12.17. L.B. Scott, Interferometer. US Patent 2,841,049, 1 July 1958
12.18. J. Pritchard, H. Sakai, W. Steel, G. Vanasse, Mobius band interferometer and its application to Fourier spectroscopy. J. de Physique Colloques **28**(C2), 91–96 (1967)
12.19. P. Burkert, Two beam interferometer for Fourier spectroscopy with rigid pendulum. US Patent 4,383,762, 17 May 1983
12.20. W.M. Doyle, High resolution spectrometer interferometer having an integrated alignment unit. US Patent 4,773,757, 27 Sept 1988
12.21. P.R. Solomon, System including unified beamsplitter and parallel reflecting element, and retroreflecting component. US Patent 5,675,412, 7 Oct 1997
12.22. G.W. Stroke, Photoelectric fringe signal information and range in interferometers with moving mirrors. J. Opt. Soc. Am. **47**(12), 1097–1103 (1957)
12.23. Q. Yang, B. Zhao, D. Wen, Principle and analysis of a moving double-sided mirror interferometer. Opt. Laser Technol. **44**(5), 1256–1260 (2012)
12.24. J. Kauppinen, T. Karkkainen, E. Kyro, Correcting errors in the optical path difference in Fourier spectroscopy: a new accurate method. Appl. Opt. **17**(10), 1587–1594 (1978)
12.25. P. Hlubina, J. Lunacek, D. Ciprian, R. Chlebus, Dispersion error of a beam splitter cube in white-light spectral interferometry. Opto-Electron. Rev. **16**(4), 439–443 (2008)

12.26. K.F. Lee, A. Bonvalet, P. Nuernberger, M. Joffre, Unobtrusive interferometer tracking by path length oscillation for multidimensional spectroscopy. Opt. Express **17**(15), 12379–12384 (2009)
12.27. J. Li, D. Lu, Z. Qi, A modified equation for the spectral resolution of Fourier transform spectrometers. J. Lightwave Technol. **33**(1), 19–24 (2015)
12.28. J. Strong, Interferometry for the far infrared. J. Opt. Soc. Am. **47**(5), 354–357 (1957)
12.29. J. Strong, G.A. Vanasse, Lamellar grating far-infrared interferometer. J. Opt. Soc. Am. **50**(2), 113–118 (1960)
12.30. P.L. Richards, High-resolution Fourier transform spectroscopy in the far-infrared. J. Opt. Soc. Am. **54**(12), 1474–1484 (1964)
12.31. J. Kauppinen, Double-beam high resolution Fourier spectrometer for the far infrared. Appl. Opt. **14**(8), 1987–1992 (1975)
12.32. J. Kauppinen, V.-M. Horneman, Large aperture cube corner interferometer with a resolution of 0.001 cm^{-1}. Appl. Opt. **30**(18), 2575–2578 (1991)
12.33. K. Strong, T.J. Johnson, G.W. Harris, Visible intracavity laser spectroscopy with a step-scan Fourier-transform interferometer. Appl. Opt. **36**(33), 8533–8540 (1997)
12.34. J. Cheng, H. Lin, S. Hu, S. He, Q. Zhu, A. Kachanov, Infrared intracavity laser absorption spectroscopy with a continuous-scan Fourier-transform interferometer. Appl. Opt. **39**(13), 2221–2229 (2000)
12.35. N. Picqué, G. Guelachvili, High-information time-resolved Fourier transform spectroscopy at work. Appl. Opt. **39**(22), 3984–3990 (2000)
12.36. N. Picqué, G. Guelachvili, A.A. Kachanov, High-sensitivity time-resolved intracavity laser Fourier transform spectroscopy with vertical-cavity surface-emitting multiple-quantum-well lasers. Opt. Lett. **28**(5), 313–315 (2003)
12.37. E. Hamers, D. Schram, R. Engeln, Fourier transform phase shift cavity ring down spectroscopy. Chem. Phys. Lett. **365**(3–4), 237–243 (2002)
12.38. A.A. Ruth, J. Orphal, S.E. Fiedler, Fourier-transform cavity-enhanced absorption spectroscopy using an incoherent broadband light source. Appl. Opt. **46**(17), 3611–3616 (2007)
12.39. G.W. Stroke, A.T. Funkhouser, Fourier-transform spectroscopy using holographic imaging without computing and with stationary interferometers. Phys. Lett. **16**(3), 272–274 (1965)
12.40. R.A. Kruger, L.W. Anderson, F.L. Roesler, All-reflection interferometer for use as a Fourier-transform spectrometer. J. Opt. Soc. Am. **62**(8), 938–945 (1972)
12.41. R.A. Kruger, L.W. Anderson, F.L. Roesler, New Fourier transform all-reflection interferometer. Appl. Opt. **12**(3), 533–540 (1973)
12.42. R.G. Sellar, G.D. Boreman, Comparison of relative signal-to-noise ratios of different classes of imaging spectrometer. Appl. Opt. **44**(9), 1614–1624 (2005)
12.43. T. Dohi, T. Suzuki, Attainment of high resolution holographic Fourier transform spectroscopy. Appl. Opt. **10**(5), 1137–1140 (1971)
12.44. G. Fortunato, A. Maréchal, Spectromètre interférentiel à modulation sélective. C. R. Acad. Sci. Ser. B **274**, 931–934 (1972)
12.45. T. Okamoto, S. Kawata, S. Minami, Fourier transform spectrometer with a self-scanning photodiode array. Appl. Opt. **23**(2), 269–273 (1984)
12.46. A. Maréchal, Theory and practice of image formation. J. Opt. Soc. Am. **56**(12), 1645–1648 (1966)
12.47. G.A. Vanasse, R.W. Esplin, R.J. Huppi, Selective modulation interferometric spectrometer (SIMS) technique applied to background suppression. Opt. Eng. **18**(4), 403–408 (1979)
12.48. R.A. Williams, W.S.C. Chang, Resolution and noise in Fourier-transform spectroscopy. J. Opt. Soc. Am. **56**(2), 167–170 (1966)

12.49. J.M. Harlander, F.L. Roesler, J.G. Cardon, C.R. Englert, R.R. Conway, SHIMMER: a spatial heterodyne spectrometer for remote sensing of Earth's middle atmosphere. Appl. Opt. **41**(7), 1343–1352 (2002)
12.50. I. Powell, P. Cheben, Modeling of the generic spatial heterodyne spectrometer and comparison with conventional spectrometer. Appl. Opt. **45**(36), 9079–9086 (2006)
12.51. J. Li, D. Lu, Z. Qi, A modified equation for the spectral resolution of Fourier transform spectrometers. J. Lightwave Technol. **33**(1), 19–24 (2015)
12.52. M.-L. Junttila, J. Kauppinen, E. Ikonen, Performance limits of stationary Fourier spectrometers. J. Opt. Soc. Am. A **8**(9), 1457–1462 (1991)
12.53. C.R. Englert, J.M. Harlander, Flatfielding in spatial heterodyne spectroscopy. Appl. Opt. **45**(19), 4583–4590 (2006)
12.54. B. Carli, V. Natale, Efficiency of spectrometers. Appl. Opt. **18**(23), 3954–3958 (1979)
12.55. D. Martin, E. Puplett, Polarised interferometric spectrometry for the millimetre and submillimetre spectrum. Infrared Phys. **10**, 105–109 (1970)
12.56. B. Carli, D.H. Martin, E.F. Puplett, J.E. Harries, Very-high-resolution far-infrared measurements of atmospheric emission from aircraft. J. Opt. Soc. Am. **67**(7), 917–921 (1977); B. Carli, F. Mencaraglia, A. Bonetti, Submillimeter high-resolution FT spectrometer for atmospheric studies. Appl. Opt. **23**(15), 2594–2603 (1984)
12.57. D.K. Lambert, P.L. Richards, Martin-Puplett interferometer: an analysis. Appl. Opt. **17**(10), 1595–1602 (1978)
12.58. B. Carli, F. Mencaraglia, Signal doubling in the Martin-Puplett interferometer. Int. J. Infrared Millim. Waves **2**(5), 1045–1051 (1981)
12.59. D.E. Jennings, Folded-beam design for a Martin-Puplett interferometer with substrate polarizers. Appl. Opt. **35**(16), 2910–2912 (1996)
12.60. P.A.R. Ade, P.A. Hamilton, D.A. Naylor, An absolute dual beam emission spectrometer – Fourier Transform Spectroscopy: New Methods and Applications, OSA Technical Digest, 1999, paper FWE3; L.D. Spencer, D.A. Naylor, P.A.R. Ade, J. Zhang, Beam-splitter effects in dual-input Fourier transform spectroscopy. J. Opt. Soc. Am. A **28**(9), 1805–1811 (2011)
12.61. M.A. Bukshtab, Lossless polarization double-pass dual cell FTIR (2015)
12.62. D.T. Chuss, E.J. Wollack, S.H. Moseley, G. Novak, Interferometric polarization control. Appl. Opt. **45**(21), 5107–5117 (2006)
12.63. S. Chandra, R.S. Rohde, Ultrasensitive multiple-reflections interferometer. Appl. Opt. **21**(9), 1533–1535 (1982); M. Pisani, Multiple reflection Michelson interferometer with picometer resolution. Opt. Express **16**(26), 21558–21563 (2008)
12.64. S. Amarie, T. Ganz, F. Keilmann, Mid-infrared near-field spectroscopy. Opt. Express **17**(24), 21794–21801 (2009)
12.65. G. D'Alessandro, P. de Bernardis, S. Masi, A. Schillaci, Common-mode rejection in Martin-Puplett spectrometers for astronomical observations at mm-wavelengths. Appl. Opt. **54**(31), 9269–9276 (2015)
12.66. R.T. Hall, D. Vrabec, J.M. Dowling, A high-resolution, far infrared double-beam lamellar grating interferometer. Appl. Opt. **5**(7), 1147–1158 (1966)
12.67. P. Luc, S. Gerstenkorn, Fourier transform spectroscopy in the visible and ultraviolet range. Appl. Opt. **17**(9), 1327–1331 (1978)
12.68. D. Debarre, A.C. Boccara, D. Fournier, High-luminosity visible and near-IR Fourier-transform photoacoustic spectrometer. Appl. Opt. **20**(24), 4281–4286 (1981)
12.69. C. Dorrer, N. Belabas, J.-P. Likforman, M. Joffre, Spectral resolution and sampling issues in Fourier-transform spectral interferometry. J. Opt. Soc. Am. B **17**(10), 1795–1802 (2000)
12.70. R.A. Palmer, C.J. Manning, J.A. Rzepiela, J.M. Widder, J.L. Chao, Time-resolved spectroscopy using step-scan Fourier transform interferometry. Appl. Spectrosc. **43**(2), 193–194 (1989)
12.71. C. Dorrer, Influence of the calibration of the detector on spectral interferometry. J. Opt. Soc. Am. B **16**(7), 1160–1168 (1999)

12.72. G. Guelachvili, High-accuracy Doppler-limited 10^6 samples Fourier transform spectroscopy. Appl. Opt. **17**(9), 1322–1326 (1978); Distortion free interferograms in Fourier transform spectroscopy with nonlinear detectors. Appl. Opt. **25**(24), 4644–4648 (1986)
12.73. M.J. Padgett, A.R. Harvey, A.J. Duncan, W. Sibbett, Single-pulse, Fourier-transform spectrometer having no moving parts. Appl. Opt. **33**(25), 6035–6040 (1994)
12.74. N.P. Ayerden, U. Aygun, S.T.S. Holmstrom, S. Olcer, B. Can, J.-L. Stehle, H. Urey, High-speed broadband FTIR system using MEMS. Appl. Opt. **53**(31), 7267–7272 (2014)
12.75. N. de Oliveira, D. Joyeux, D. Phalippou, J.C. Rodier, F. Polack, M. Vervloet, L. Nahon, A Fourier transform spectrometer without a beam splitter for the vacuum ultraviolet range: from the optical design to the first UV spectrum. Rev. Sci. Instrum. **80**, Article 043101 (2009)
12.76. J. Li, D.-F. Lu, Z.-M. Qi, Miniature Fourier transform spectrometer based on wavelength dependence of half-wave voltage of a $LiNbO_3$ waveguide interferometer. Opt. Lett. **39**(13), 3923–3926 (2014)
12.77. M. Mujat, E. Baleine, A. Dogariu, Interferometric imaging polarimeter. J. Opt. Soc. Am. A **21**(11), 2244–2249 (2004)
12.78. C. Oh, M.J. Escuti, Achromatic diffraction from polarization gratings with high efficiency. Opt. Lett. **33**(20), 2287–2289 (2008)
12.79. M.W. Kudenov, M.N. Miskiewicz, M.J. Escuti, E.L. Dereniak, Spatial heterodyne interferometry with polarization gratings. Opt. Lett. **37**(21), 4413–4415 (2012)
12.80. S. Amarie, T. Ganz, F. Keilmann, Mid-infrared near-field spectroscopy. Opt. Express **17**(24), 21794–21801 (2009)
12.81. L. Brillouin, Diffusion de la lumière et des rayons X par un corps transparent homogène: influence de l'agitation thermique. Ann. Phys. (Paris) **17**(1), 88–122 (1922)
12.82. L.I. Mandelstam, Light scattering by inhomogeneous media. Zh. Russ. Fiz-Khim. Ova. **58**, 381–385 (1926)
12.83. L. Landau, G. Placzek, Z. Phys. Sowjetunion **5**, 172 (1934); L.D. Landau, E.M. Lifshitz, *Statistical Physics* (Pergamon Press, New York, 1958)
12.84. H.Z. Cummins, R.W. Gammon, Rayleigh and Brillouin scattering in liquids: the Landau—Placzek ratio. J. Chem. Phys. **44**(7), 2785–2796 (1966)
12.85. M. Vaughan, *The Fabry-Perot Interferometer: History, Theory, Practice and Applications* (Taylor & Fransis, New York, 1989)
12.86. P. Jacquinot, C. Dufour, Condition optique d'emploi des cellules photo-électriques dans les spectrographes et les interférometrès. J. Recherche du Centre Natl. Recherche Sci. Lab. Bellevue, Paris **6**, 91–103 (1948)
12.87. S. Tolansky, D.J. Bradley, *Interferometry: N.P.L. Symposium* No. 11, pp. 375–386 (1960)
12.88. K.D. Mielenz, R.B. Stephens, K. Nefflen, A Fabry-Perot spectrometer for high-resolution spectroscopy and laser work. J. Res. Natl. Bur. Stand. **68C**(1), 1–6 (1964)
12.89. D.R. Herriott, Spherical-mirror oscillating interferometer. Appl. Opt. **2**(8), 865–866 (1963)
12.90. G. Hernandez, O.A. Mills, Feedback stabilized Fabry-Perot interferometer. Appl. Opt. **12**(1), 126–130 (1973)
12.91. R.A. McLaren, G.I.A. Stegeman, Technique for recording spectra in Fabry-Perot interferometry. Appl. Opt. **12**(7), 1396–1398 (1973)
12.92. J.R. Sandercock, Simple stabilization scheme for maintenance of alignment in a scanning Fabry-Perot interferometer. J. Phys. E **9**, 566–569 (1976)
12.93. R.A.D. Hewko, B.H. Torriea, Computer stabilization of Brillouin spectrograms. Appl. Spectrosc. **30**(2), 216–219 (1976)
12.94. A. Asenbaum, Computer-controlled Fabry-Perot interferometer for Brillouin spectroscopy. Appl. Opt. **18**(4), 540–544 (1979)

12.95. D.H. Rank, R.P. Ruth, K.L. Vander Sluis, The compound Fabry-Perot interferometer. J. Opt. Soc. Am. **41**(5), 351–353 (1951)
12.96. P. Hariharana, D. Sen, Double-passed Fabry-Perot interferometer. J. Opt. Soc. Am. **51**(4), 398–399 (1961)
12.97. J.R. Sandercock, Brillouin scattering study of SbSI using a double-passed, stabilized scanning interferometer. Opt. Commun. **2**(2), 73–76 (1970)
12.98. J.M. Vaughan, Brillouin scattering in nematic and isotropic phases of a liquid crystal. Phys. Lett. A **58**(5), 325–328 (1976)
12.99. C. Roychoudhuri, M. Hercher, Stable multipass Fabry-Perot interferometer: design and analysis. Appl. Opt. **16**(9), 2514–2520 (1977)
12.100. J.R. Sandercock, Fabry-Perot interferometer. US Patent 4,225,236, 30 Sept 1980; Trends in Brillouin scattering, in *Light Scattering in Solids III*, ed. by M. Cardona, G. Güntherodt (Springer, Berlin, 1982), pp. 173–206
12.101. I.M. Nagibina, A.N. Korolev, A study of some of the properties of a Fabry-Perot etalon with a small transparent window. Opt. Spectrosc. **15**, 225–226 (1963)
12.102. M. Shirasaki, Large angular dispersion by a virtually imaged phased array and its application to a wavelength demultiplexer. Opt. Lett. **21**(5), 366–368 (1996)
12.103. M. Bukshtab, M. Friedman, Multipass virtually imaged phased array etalon. US Patent Application 14/941214, 13 Nov 2015; Pub. No. 2016/0139390; Pub. Date: 19 May 2016
12.104. M. Bukshtab, Confocal virtual imaging phase array microscope spectrometer and method of calibration CMS-VIPA. US Patent Application 62/447,607, 18 Jan 2017
12.105. S. Xiao, A.M. Weiner, C. Lin, A dispersion law for virtually imaged phased-array spectral dispersers based on paraxial wave theory. IEEE J. Quantum Electron. **40**(4), 420–426 (2004)
12.106. D.J. Gauthier, Comment on "Generalized grating equation for virtually imaged phased-array spectral dispersers". Appl. Opt. **51**(34), 8184–8185 (2012)
12.107. M. Bukshtab, A. Paranjape, M. Friedman, D. Muller, Fast low-noise Brillouin spectroscopy measurements of elasticity for corneal cross-linking, in *Proceedings of SPIE*, vol. 9327, Article 932718 (2015)
12.108. W.G. Fastie, H.M. Crosswhite, P. Gloersen, Vacuum Ebert grating spectrometer. J. Opt. Soc. Am. **48**(2), 106–111 (1958)
12.109. J.C. Wyant, Double frequency grating lateral shear interferometer. Appl. Opt. **12**(9), 2057–2059 (1973)
12.110. V. Mazzacurati, P. Benassi, G. Ruocco, A new class of multiple dispersion grating spectrometers. J. Phys. E: Sci. Instrum. **21**, 798–804 (1988)
12.111. P. Benassi, R. Eramo, A. Giugni, M. Nardone, M. Sampoli, A spectrometer for high-resolution and high-contrast Brillouin spectroscopy in the ultraviolet. Rev. Sci. Instrum. **76**, Article 013904 (2005)
12.112. P.B. Hays, H.E. Snell, Multiplex Fabry-Perot interferometer. Appl. Opt. **30**(22), 3108–3113 (1991)
12.113. S. Xiao, A.M. Weiner, 2-D wavelength demultiplexer with potential for ≥ 1000 channels in the C-band. Opt. Express **12**(13), 2895–2902 (2004)
12.114. G. Scarcelli, P. Kim, S.H. Yun, Cross-axis cascading of spectral dispersion. Opt. Lett. **33**(24), 2979–2981 (2008)
12.115. G. Scarcelli, S.H. Yun, Multistage VIPA etalons for high-extinction parallel Brillouin spectroscopy. Opt. Express **19**(11), 10913–10922 (2011)
12.116. D. Heiman, D.S. Hamilton, R.W. Hellwarth, Brillouin scattering measurements on optical glasses. Phys. Rev. B **19**(12), 6583–6592 (1979)
12.117. P. Benassi, V. Mazzacurati, G. Monaco, G. Ruocco, G. Signorelli, Brillouin and Raman cross-sections in silicate glasses. Phys. Rev. B **52**(2), 976–981 (1995)

12.118. S. Gehrsitz, H. Sigg, H. Siegwart, M. Krieger, C. Heine, R. Morf, F.K. Reinhart, W. Martin, H. Rudigier, Tandem triple-pass Fabry-Perot interferometer for applications in the near infrared. Appl. Opt. **36**(22), 5355–5361 (1997)
12.119. D. Walton, J.J. Vanderwal, P. Zhao, The use of CCDs in Fabry-Perot spectrometers. Appl. Spectrosc. **46**(2), 373–375 (1992)
12.120. K.J. Koski, J. Muller, H.D. Hochheimer, J.L. Yargera, High pressure angle-dispersive Brillouin spectroscopy: a technique for determining acoustic velocities and attenuations in liquids and solids. Rev. Sci. Instrum. **73**(3), 1235–1241 (2002)
12.121. K.J. Koski, J.L. Yarger, Brillouin imaging. Appl. Phys. Lett. **87**, Article 061903 (2005)
12.122. Y. Ike, S. Tsukada, S. Kojima, High-resolution Brillouin spectroscopy with angular dispersion-type Fabry-Perot interferometer and its application to a quartz crystal. Rev. Sci. Instrum. **78**, Article 076104 (2007)
12.123. Z. Meng, A.J. Traverso, V.V. Yakovlev, Background clean-up in Brillouin microspectroscopy of scattering medium. Opt. Express **22**(5), 5410–5415 (2014)
12.124. I. Remer, A. Bilenca, Background-free Brillouin spectroscopy in scattering media at 780 nm via stimulated Brillouin scattering. Opt. Lett. **41**(5), 926–929 (2016)
12.125. J. Xu, X. Ren, W. Gong, R. Dai, D. Liu, Measurement of the bulk viscosity of liquid by Brillouin scattering. Appl. Opt. **42**(33), 6704–6709 (2003)
12.126. T.A. Litovitz, C.M. Davis, Structural and shear relaxation in liquids, in *Physical Acoustics*, ed. by W.P. Mason (Academic, New York, 1965), pp. 281–349; D.A. Pinnow, S.J. Candau, J.T. LaMacchia, T.A. Litovitz, Brillouin scattering: viscoelastic measurements in liquids. J. Acoust. Soc. Am. **43**(1), 131–142 (1968)
12.127. R. Harley, D. James, A. Miller, J.W. White, Phonons and the elastic moduli of collagen and muscle. Nature **267**(5), 285–287 (1977)
12.128. J. Randall, J.M. Vaughan, Brillouin scattering in systems of biological significance. Phil. Trans. R. Soc. Lond. **293**, 341–348 (1979)
12.129. A. Fiore, J. Zhang, P. Shao, S.H. Yun, G. Scarcelli, High-extinction virtually imaged phased array-based Brillouin spectroscopy of turbid biological media. Appl. Phys. Lett. **108**, Article 203701 (2016)
12.130. J.M. Vaughan, J.T. Randall, Brillouin scattering, density, and elastic properties of the lens and cornea of the eye. Nature **284**(3), 489–491 (1980)
12.131. J. Randall, J.M. Vaughan, The measurement and interpretation of Brillouin scattering in the lens of the eye. Proc. R. Soc. Lond. B **214**, 449–470 (1982)
12.132. G. Scarcelli, S.H. Yun, Confocal Brillouin microscopy for three-dimensional mechanical imaging. Nature Photon. **2**(1), 39–43 (2008)
12.133. S. Reiß, G. Burau, O. Stachs, R. Guthoff, H. Stolz, Spatially resolved Brillouin spectroscopy to determine the rheological properties of the eye lens. Biomed. Opt. Express **2**(8), 2144–2159 (2011)
12.134. R. Barer, S. Joseph, Refractometry of living cells, 1: basic principles. Q. J. Microsc. Sci. **95**(4), 399–423 (1954)
12.135. T.D. Wang, M.J. Mandella, C.H. Contag, G.S. Kino, Dual-axis confocal microscope for high-resolution in vivo imaging. Opt. Lett. **28**(6), 414–416 (2003)
12.136. G. Scarcelli, S.H. Yun, In vivo Brillouin optical microscopy of the human eye. Opt. Express **20**(8), 9197–9202 (2012)
12.137. F. Rasetti, Sopra lo spettro raman dell'ossido nitrico. Nuovo Cimento **7**(2), 261–269 (1930)
12.138. G.E. Devlin, J.L. Davis, L. Chase, S. Geschwind, Absorption of unshifted scattered light by a molecular I_2 filter in Brillouin and Raman scattering. Appl. Phys. Lett. **19**(5), 138–140 (1971)
12.139. P.J. Horoyski, M.L.W. Thewalt, Fourier transform Raman and Brillouin spectroscopy using atomic vapor filters. Appl. Spectrosc. **48**(7), 843–847 (1994)

12.140. Z. Meng, V.V. Yakovlev, Precise determination of Brillouin scattering spectrum using a virtually imaged phase array (VIPA) spectrometer and charge-coupled device (CCD) camera. Appl. Spectrosc. **70**(8), 1356–1363 (2016)
12.141. A. Battistoni, F. Bencivenga, D. Fioretto, C. Masciovecchio, Practical way to avoid spurious geometrical contributions in Brillouin light scattering experiments at variable scattering angles. Opt. Lett. **39**(20), 5858–5861 (2014)
12.142. G. Antonacci, G. Lepert, C. Paterson, P. Torok, Elastic suppression in Brillouin imaging by destructive interference. Appl. Phys. Lett. **107**, Article 061102 (2015)
12.143. D.G. Hall, Vector-beam solutions of Maxwell's wave equation. Opt. Lett. **21**(1), 9–11 (1996); D.P. Biss, K.S. Youngworth, T.G. Brown, Dark-field imaging with cylindrical-vector beams. Appl. Opt. **45**(3), 470–479 (2006); M. Duocastella, C.B. Arnold, Bessel and annular beams for materials processing. Laser Photon. Rev. **6**(5), 607–621 (2012)
12.144. G. Antonacci, Dark-field Brillouin microscopy. Opt. Lett. **42**(7), 1432–1435 (2017)
12.145. S.T. Bailey, M.D. Twa, J.C. Gump, M. Venkiteshwar, M.A. Bullimore, R. Sooryakumar, Light-scattering study of the normal human eye lens: elastic properties and age dependence. IEEE Trans. Biomed. Eng. **57**(12), 2910–2917 (2010)
12.146. H. Kogelnik, Bragg diffraction in hologram gratings with multiple internal reflections. J. Opt. Soc. Am. **57**(3), 431–433 (1967); G.A. Rakuljic, V. Leyva, Volume holographic narrow-band optical filter. Opt. Lett. **18**(6), 459–461 (1993)
12.147. O.M. Efimov, L.B. Glebov, L.N. Glebova, K.C. Richardson, V.I. Smirnov, High-efficiency Bragg gratings in photothermorefractive glass. Appl. Opt. **38**(4), 619–627 (1999)
12.148. C. Moser, B. Schupp, D. Psaltis, Localized holographic recording in doubly doped lithium niobate. Opt. Lett. **25**(3), 162–164 (2000)
12.149. S. Lebedkin, C. Blum, N. Stürzl, F. Hennrich, M.M. Kappes, A low-wavenumber-extended confocal Raman microscope with very high laser excitation line discrimination. Rev. Sci. Instrum. **82**, Article 013705 (2011)
12.150. T. Wilson, A.R. Carlini, Size of the detector in confocal imaging systems. Opt. Lett. **12**(4), 227–229 (1987); S. Kimura, T. Wilson, Confocal scanning optical microscope using single-mode fiber for signal detection. Appl. Opt. **30**(16), 2143–2150 (1991)
12.151. D.A. Steck, Rubidium 85 D Line Data, http://steck.us/alkalidata. Revision 0.1.1, 02 May 2008
12.152. L.P. Yaroslavsky, G. Shabat, B.G. Salomon, I.A. Ideses, B. Fishbain, Nonuniform sampling, image recovery from sparse data and the discrete sampling theorem. J. Opt. Soc. Am. A **26**(3), 566–575 (2009)
12.153. J. Ye, S.T. Cundiff (eds.), *Femtosecond Optical Frequency Comb: Principle, Operation, and Applications* (Springer, Norwell, 2005)
12.154. J.L. Hall, Nobel lecture: defining and measuring optical frequencies. Rev. Mod. Phys. **78**(4), 1279–1295 (2006)
12.155. T.W. Hänsch, Nobel lecture: passion for precision. Rev. Mod. Phys. **78**(4), 1297–1309 (2006)
12.156. A. Javan, E.A. Ballik, W.L. Bond, Frequency characteristics of a continuous-wave He–Ne optical maser. J. Opt. Soc. Am. **52**(1), 96–98 (1962)
12.157. K.M. Evenson, J.S. Wells, F.R. Petersen, B.L. Danielson, G.W. Day, R.L. Barger, J.L. Hall, Speed of light from direct frequency and wavelength measurements of the methane-stabilized laser. Phys. Rev. Lett. **29**(19), 1346–1349 (1972)
12.158. H.R. Telle, D. Meschede, T.W. Hänsch, Realization of a new concept for visible frequency division: phase locking of harmonic and sum frequencies. Opt. Lett. **15**(10), 532–534 (1990)
12.159. M. Kourogi, K. Nakagawa, M. Ohtsu, Wide-span optical frequency comb generator for accurate optical frequency difference measurement. IEEE J. Quantum Electron. **29**(10), 2693–2701 (1993)

12.160. Th. Udem, J. Reichert, R. Holzwarth, T.W. Hänsch, Accurate measurement of large optical frequency differences with a mode-locked laser. Opt. Lett. **24**(13), 881–883 (1999)
12.161. S.T. Cundiff, J. Ye, J.L. Hall, Optical frequency synthesis based on mode-locked lasers. Rev. Sci. Instrum. **72**(10), 3749–3771 (2001)
12.162. J. Ye, L.-S. Ma, T. Daly, J.L. Hall, Highly selective terahertz optical frequency comb generator. Opt. Lett. **22**(5), 301–303 (1997)
12.163. K. Imai, M. Kourogi, M. Ohtsu, 30-THz span optical frequency comb generation by self-phase modulation in an optical fiber. IEEE J. Quantum Electron. **34**(1), 54–60 (1998)
12.164. J.K. Ranka, R.S. Windeler, A.J. Stentz, Visible continuum generation in air–silica microstructure optical fibers with anomalous dispersion at 800 nm. Opt. Lett. **25**(1), 25–27 (2000)
12.165. S.A. Diddams, D.J. Jones, J. Ye, S.T. Cundiff, J.L. Hall, J.K. Ranka, R.S. Windeler, R. Holzwarth, Th. Udem, T.W. Hänsch, Direct link between microwave and optical frequencies with a 300 THz femtosecond laser comb. Phys. Rev. Lett. **84**(22), 5102–5105 (2000)
12.166. R. Holzwarth, Th. Udem, T.W. Hänsch, J.C. Knight, W.J. Wadsworth, P.S.J. Russell, Optical frequency synthesizer for precision spectroscopy. Phys. Rev. Lett. **85**(11), 2264–2267 (2000)
12.167. D.H. Auston, K.P. Cheung, Coherent time-domain far-infrared spectroscopy. J. Opt. Soc. Am. B **2**(4), 606–612 (1985)
12.168. S. Schiller, Spectrometry with frequency combs. Opt. Lett. **27**(9), 766–768 (2002)
12.169. M. Zimmermann, C. Gohle, R. Holzwarth, T. Udem, T.W. Hänsch, Optical clockwork with an offset-free difference-frequency comb: accuracy of sum- and difference-frequency generation. Opt. Lett. **29**(3), 310–312 (2004)
12.170. F. Keilmann, C. Gohle, R. Holzwarth, Time-domain mid-infrared frequency-comb spectrometer. Opt. Lett. **29**(33), 1542–1544 (2004)
12.171. I. Coddington, W.C. Swann, N.R. Newbury, Coherent multiheterodyne spectroscopy using stabilized optical frequency combs. Phys. Rev. Lett. **100**, Article 013902 (2008)
12.172. J. Mandon, G. Guelachvili, N. Picqué, Fourier transform spectroscopy with a laser frequency comb. Nature Photon. **3**(2), 99–102 (2009)
12.173. R.J. Jones, J. Ye, Femtosecond pulse amplification by coherent addition in a passive optical cavity. Opt. Lett. **27**(20), 1848–1850 (2002)
12.174. M.J. Thorpe, R.J. Jones, K.D. Moll, J. Ye, Precise measurements of optical cavity dispersion and mirror coating properties via femtosecond combs. Opt. Express **13**(3), 882–888 (2005)
12.175. R.J. Jones, I. Thomann, J. Ye, Precision stabilization of femtosecond lasers to high-finesse optical cavities. Phys. Rev. A **69**, Article 051803(R) (2004)
12.176. M.J. Thorpe, K.D. Moll, R.J. Jones, B. Safdi, J. Ye, Broadband cavity ringdown spectroscopy for sensitive and rapid molecular detection. Science **311**(3), 1595–1599 (2006)
12.177. M.J. Thorpe, D.D. Hudson, K.D. Moll, J. Lasri, J. Ye, Cavity-ringdown molecular spectroscopy based on an optical frequency comb at 1.45–1.65 μm. Opt. Lett. **32**(3), 307–309 (2007)
12.178. D. Strickland, G. Mourou, Compression of amplified chirped optical pulses. Opt. Commun. **56**(3), 219–221 (1985)
12.179. S.A. Diddams, L.W. Hollberg, V. Mbele, Molecular fingerprinting with spectrally-resolved modes of a femtosecond laser frequency comb. Nature **445**(2), 627–630 (2007)
12.180. M.J. Thorpe, D. Balslev-Clausen, M.S. Kirchner, J. Ye, Cavity-enhanced optical frequency comb spectroscopy: application to human breath analysis. Opt. Express **16**(4), 2387–2397 (2008)

12.181. K.C. Cossel, F. Adler, K.A. Bertness, M.J. Thorpe, J. Feng, M.W. Raynor, J. Ye, Analysis of trace impurities in semiconductor gas via cavity-enhanced direct frequency comb spectroscopy. Appl. Phys. B **100**, 917–924 (2010)
12.182. L. Nugent-Glandorf, T. Neely, F. Adler, A.J. Fleisher, K.C. Cossel, B. Bjork, T. Dinneen, J. Ye, S.A. Diddams, Mid-infrared virtually imaged phased array spectrometer for rapid and broadband trace gas detection. Opt. Lett. **37**(15), 3285–3287 (2012)
12.183. D.A. Long, A.J. Fleisher, K.O. Douglass, S.E. Maxwell, K. Bielska, J.T. Hodges, D.F. Plusquellic, Multiheterodyne spectroscopy with optical frequency combs generated from a continuous-wave laser. Opt. Lett. **39**(9), 2688–2690 (2014)
12.184. A. Khodabakhsh, C.A. Alrahman, A. Foltynowicz, Noise-immune cavity-enhanced optical frequency comb spectroscopy. Opt. Lett. **39**(17), 5034–5037 (2014)
12.185. P. Maslowski, K.F. Lee, A.C. Johansson, A. Khodabakhsh, G. Kowzan, L. Rutkowski, A.A. Mills, C. Mohr, J. Jiang, M.E. Fermann, A. Foltynowicz, Surpassing the path-limited resolution of Fourier-transform spectrometry with frequency combs. Phys. Rev. A. **93**, Article 021802(R) (2016)
12.186. A.C. Johansson, L. Rutkowski, A. Khodabakhsh, A. Foltynowicz, Signal line shapes of Fourier-transform cavity-enhanced frequency modulation spectroscopy with optical frequency combs. J. Opt. Soc. Am. B **34**(2), 358–365 (2017)
12.187. F. Zernike, P.R. Berman, Generation of far infrared as a difference frequency. Phys. Rev. Lett. **15**(12), 999 (1965); Erratum **16**(1), 117 (1966)
12.188. K.H. Yang, P.L. Richards, Y.R. Shen, Generation of far-infrared radiation by picosecond light pulses in $LiNb0_3$. Appl. Phys. Lett. **19**(9), 320–323 (1971)
12.189. D.H. Auston, K.P. Cheung, Coherent time-domain far-infrared spectroscopy. J. Opt. Soc. Am. B **2**(4), 606–612 (1985)
12.190. Ch. Fattinger, D. Grischkowsky, Point source terahertz optics. Appl. Phys. Lett. **53**(16), 1480–1482 (1988)
12.191. S. Keiding, D. Grischkowsky, Measurements of the phase shift and reshaping of terahertz pulses due to total internal reflection. Opt. Lett. **15**(1), 48–50 (1990)
12.192. D. Grischkowsky, S. Keiding, M. van Exter, Ch. Fattinger, Far-infrared time-domain spectroscopy with terahertz beams of dielectrics and semiconductors. J. Opt. Soc. Am. B **7**(10), 2006–2015 (1990)
12.193. M. Born, *Optik* (Springer, Berlin, 1933)
12.194. H.A. Kramers, The quantum theory of dispersion. Nature **114**, 310–311 (1924); R. de L. Kronig, On the theory of dispersion of x-rays. J. Opt. Soc. Am. **12**(5), 547–557 (1926)
12.195. V. Lucarini, J.J. Saarinen, K.-E. Peiponen, E.M. Vartiainen, *Kramers-Kronig Relations in Optical Materials Research* (Springer, Berlin, Heidelberg, 2005)
12.196. J.S. Toll, Casualty and the dispersion relation: logical foundations. Phys. Rev. **104**(6), 1760–1770 (1956)
12.197. G. Andermann, A. Caron, D.A. Dows, Kramers-Kronig dispersion analysis of infrared reflectance bands. J. Opt. Soc. Am. **55**(10), 1210–1216 (1965)
12.198. I. Simon, Spectroscopy in infrared by reflection and its use for highly absorbing substances. J. Opt. Soc. Am. **41**(5), 336–345 (1951)
12.199. F. Wooten, *Optical Properties of Solids* (Academic Press, New York, 1972)
12.200. S. Nashima, O. Morikawa, K. Takata, M. Hangyo, Measurement of optical properties of highly doped silicon by terahertz time domain reflection spectroscopy. Appl. Phys. Lett. **79**(24), 3923–3925 (2001)
12.201. P.U. Jepsen, B.M. Fischer, Dynamic range in terahertz time-domain transmission and reflection spectroscopy. Opt. Lett. **30**(1), 29–31 (2005)
12.202. L. Duvillaret, F. Garet, J.-L. Coutaz, A reliable method for extraction of material parameters in terahertz time-domain spectroscopy. IEEE J. Sel. Top. Quantum Electron. **2**(3), 739–746 (1996)

12.203. L. Duvillaret, F. Garet, J.-L. Coutaz, Highly precise determination of optical constants and sample thickness in terahertz time-domain spectroscopy. Appl. Opt. **38**(2), 409–615 (1999)
12.204. W. Withayachumnankul, B.M. Fischer, H. Lin, D. Abbott, Uncertainty in terahertz time-domain spectroscopy measurement. J. Opt. Soc. Am. B **25**(6), 1059–1072 (2008)
12.205. T.D. Dorney, R.G. Baraniuk, D.M. Mittleman, Material parameter estimation with terahertz time-domain spectroscopy. J. Opt. Soc. Am. A **18**(7), 1562–1571 (2008)
12.206. R.C. McPhedran, L.C. Botten, D.R. McKenzie, R.P. Netterfield, Unambiguous determination of optical constants of absorbing films by reflectance and transmittance measurements. Appl. Opt. **23**(6), 1197–1205 (1984)
12.207. K. Lamprecht, W. Papousek, G. Leising, Problem of ambiguity in the determination of optical constants of thin absorbing films from spectroscopic reflectance and transmittance measurements. Appl. Opt. **36**(25), 6364–6371 (1997)
12.208. X.C. Li, J.M. Zhao, L.H. Liu, J.Y. Tan, Optical properties of edible oils within spectral range from 300 to 2500 nm determined by double optical pathlength transmission method. Appl. Opt. **54**(13), 3886–3893 (2015)
12.209. X. Li, C. Wang, J. Zhao, L. Liu, A new method for determining the optical constants of highly transparent solids. Appl. Spectrosc. **71**(1), 70–77 (2017)
12.210. I. Pupeza, R. Wilk, M. Koch, Highly accurate optical material parameter determination with THz time-domain spectroscopy. Opt. Express **15**(7), 4335–4350 (2007)
12.211. S. Ohno, K. Miyamoto, H. Minamide, H. Ito, New method to determine the refractive index and the absorption coefficient of organic nonlinear crystals in the ultra-wideband THz region. Opt. Express **18**(16), 17306–17312 (2010)
12.212. B.S.-Y. Ung, J. Li, H. Lin, B.M. Fischer, W. Withayachumnankul, D. Abbott, Dual-mode terahertz time-domain spectroscopy system. IEEE Trans. Terahertz. Sci. Technol. **3**(2), 216–220 (2013)
12.213. C. D'Amico, A. Houard, M. Franco, B. Prade, A. Mysyrowicz, A. Couairon, V.T. Tikhonchuk, Conical forward THz emission from femtosecond-laser-beam filamentation in air. Phys. Rev. Lett. **98**, Article 235002 (2007)
12.214. T. Wang, E.A. Romanova, N. Abdel-Moneim, D. Furniss, A. Loth, Z. Tang, A. Seddon, T. Benson, A. Lavrinenko, P.U. Jepsen, Time-resolved terahertz spectroscopy of charge carrier dynamics in the chalcogenide glass. Photon. Res. **4**(3), A22–A28 (2016)
12.215. B.B. Hu, M.C. Nuss, Imaging with terahertz waves. Opt. Lett. **20**(16), 1716–1718 (1995)
12.216. Q. Wu, X.-C. Zhang, Free-space electro-optics sampling of mid-infrared pulses. Appl. Phys. Lett. **71**(10), 1285–1286 (1997)
12.217. Y. Cai, I. Brener, J. Lopata, J. Wynn, L. Pfeiffer, J.B. Stark, Q. Wu, X.C. Zhang, J.F. Federici, Coherent terahertz radiation detection: direct comparison between free-space electro-optic sampling and antenna detection. Appl. Phys. Lett. **73**(4), 444–446 (1998)
12.218. S.P. Kovalev, G.Kh. Kitaeva, Terahertz electro-optical detection: optical phase or energy measurements. J. Opt. Soc. Am. B **30**(10), 2650–2656 (2013)
12.219. S. Keiber, S. Sederberg, A. Schwarz, M. Trubetskov, V. Pervak, F. Krausz, N. Karpowicz, Electro-optic sampling of near-infrared waveforms. Nature Photon. **10**(3), 159–163 (2016)
12.220. B. Dahmani, L. Hollberg, R. Drullinger, Frequency stabilization of semiconductor lasers by resonant optical feedback. Opt. Lett. **12**(11), 876–878 (1987)
12.221. E.R. Brown, F.W. Smith, K.A. McIntosh, Coherent millimeter-wave generation by heterodyne conversion in low-temperature-grown GaAs photoconductors. J. Appl. Phys. **73**(3), 1480–1484 (1993)
12.222. A.S. Pine, R.D. Suenram, E.R. Brown, K.A. McIntosh, A terahertz photomixing spectrometer: application to SO_2 self broadening. J. Mol. Spectrosc. **175**, 37–47 (1996)

12.223. P. Chena, G.A. Blake, M.C. Gaidis, E.R. Brown, K.A. McIntosh, S.Y. Chou, M.I. Nathan, F. Williamson, Spectroscopic applications and frequency locking of THz photomixing with distributed-Bragg-reflector diode lasers in low-temperature-grown GaAs. Appl. Phys. Lett. **71**(12), 1601–1603 (1997)
12.224. S. Verghese, K.A. McIntosh, S. Calawa, W.F. Dinatale, E.K. Duerr, K.A. Molvar, Generation and detection of coherent terahertz waves using two photomixers. Appl. Phys. Lett. **73**(26), 3824–3826 (1998)
12.225. R. Mendis, C. Sydlo, J. Sigmund, M. Feiginov, P. Meissner, H.L. Hartnagel, Spectral characterization of broadband THz antennas by photoconductive mixing: toward optimal antenna design. IEEE Antennas Wirel. Propag. Lett. **4**, 85–88 (2005)
12.226. I. Park, C. Sydlo, I. Fischer, W. Elsäßer, and H.L. Hartnagel, Generation and spectroscopic application of tunable continuous-wave terahertz radiation using a dual-mode semiconductor laser. Meas. Sci. Technol. **19**, Article 065305 (2008)
12.227. T. Yasuia, Y. Kabetani, E. Saneyoshi, S. Yokoyama, T. Araki, Terahertz frequency comb by multifrequency heterodyning photoconductive detection for high-accuracy, high-resolution terahertz spectroscopy. Appl. Phys. Lett. **88**, Article 241104 (2006)
12.228. Y. Yang, D. Burghoff, D.J. Hayton, J.-R. Gao, J.L. Reno, Q. Hu, Terahertz multiheterodyne spectroscopy using laser frequency combs. Optica **3**(5), 499–502 (2016)
12.229. Z. Jiang, X.C. Zhang, Single-shot spatiotemporal terahertz field imaging. Opt. Lett. **23**(14), 1114–1116 (1998)
12.230. B.K. Russell, B.K. Ofori-Okai, Z. Chen, M.C. Hoffmann, Y.Y. Tsui, S.H. Glenzer, Self-referenced single-shot THz detection. Opt. Express **25**(14), 16140–16150 (2017)

Index

M. Bukshtab, *Photometry, Radiometry, and Measurements of Optical Losses*, Springer Series in Optical Sciences 209,
https://doi.org/10.1007/978-981-10-7745-6

D

O

T